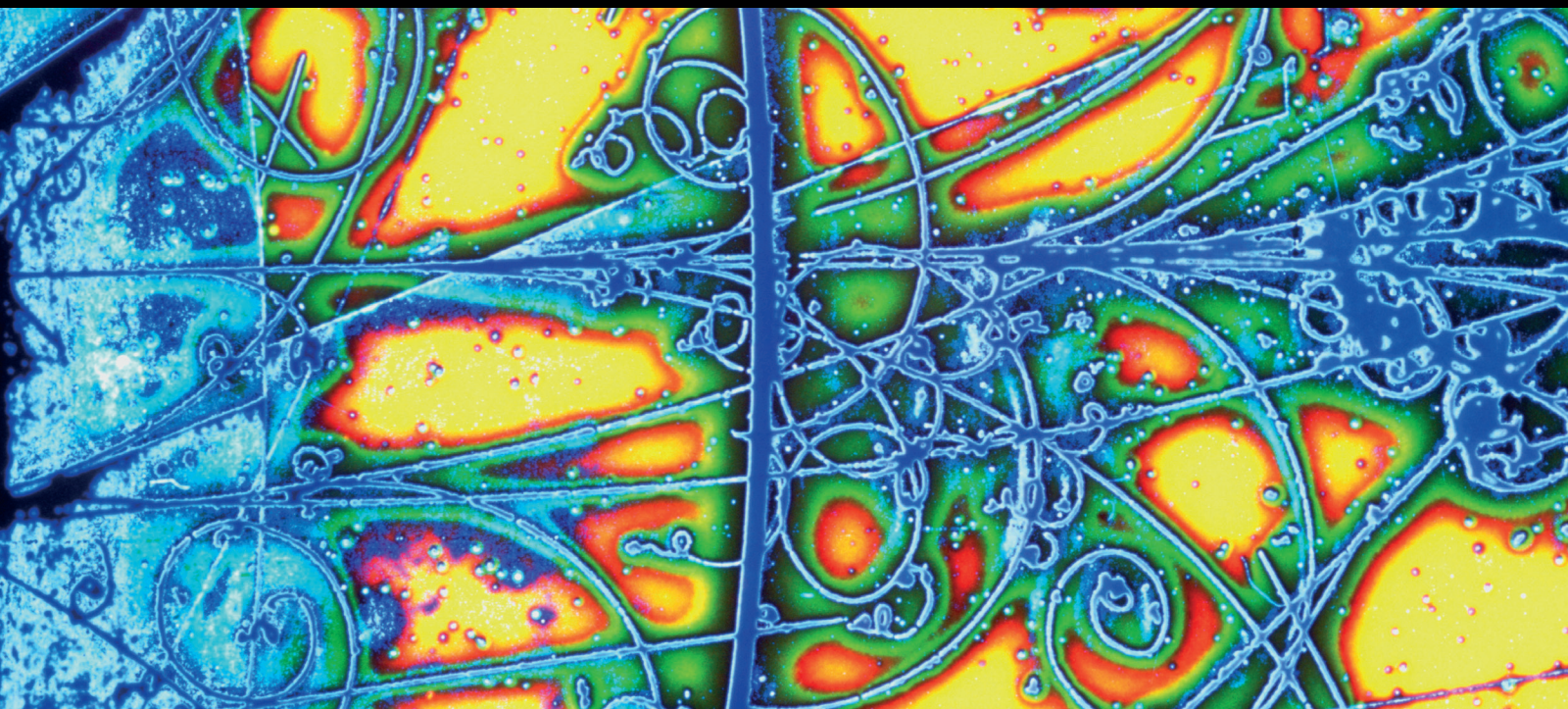


PHYSICS OF QUARK GLUON PLASMA: AN UPDATE AND THE STATUS REPORT

GUEST EDITORS: JAN E. ALAM, EDWARD SARKISYAN-GRINBAUM, AND SUBRATA BHATTACHARYYA





Physics of Quark Gluon Plasma: An Update and the Status Report

Advances in High Energy Physics

Physics of Quark Gluon Plasma: An Update and the Status Report

Guest Editors: Jan E. Alam, Edward Sarkisyan-Grinbaum,
and Subrata Bhattacharyya



Copyright © 2014 Hindawi Publishing Corporation. All rights reserved.

This is a special issue published in "Advances in High Energy Physics." All articles are open access articles distributed under the Creative Commons Attribution License, which permits unrestricted use, distribution, and reproduction in any medium, provided the original work is properly cited.

Editorial Board

Luis A. Anchordoqui, USA
Marco Battaglia, USA
Botio Betev, Switzerland
Rong-Gen Cai, China
Duncan L. Carlsmith, USA
Kingman Cheung, Taiwan
Ashot Chilingarian, Armenia
Sridhara Dasu, USA
Shi-Hai Dong, Mexico
Edmond C. Dukes, USA
Amir H. Fatollahi, Iran
Frank Filthaut, The Netherlands
Chao-Qiang Geng, Taiwan

Maria Giller, Poland
Xiaochun He, USA
Hong-Jian He, China
Ian Jack, UK
Filipe R. Joaquim, Portugal
Kyung K. Joo, Republic of Korea
Michal Kreps, UK
Ming Liu, USA
Piero Nicolini, Germany
Seog H. Oh, USA
Stephen Pate, USA
Anastasios Petkou, Greece
Alexey A. Petrov, USA

Reinhard Schlickeiser, Germany
Frederik G. Scholtz, South Africa
Sally Seidel, USA
George Siopsis, USA
Terry Sloan, UK
Luca Stanco, Italy
Elias C. Vagenas, Kuwait
Nikos Varelas, USA
Kadayam S. Viswanathan, Canada
Yau W. Wah, USA
Moran Wang, China
Gongnan Xie, China

Contents

Physics of Quark Gluon Plasma: An Update and the Status Report, Jan E. Alam,
Edward Sarkisyan-Grinbaum, and Subrata Bhattacharyya
Volume 2014, Article ID 825041, 1 page

Selected Experimental Results from Heavy-Ion Collisions at LHC, Ranbir Singh, Lokesh Kumar,
Pawan Kumar Netrakanti, and Bedangadas Mohanty
Volume 2013, Article ID 761474, 22 pages

Electromagnetic Radiations from Heavy Ion Collision, Payal Mohanty, Sabyasachi Ghosh,
and Sukanya Mitra
Volume 2013, Article ID 176578, 41 pages

Dilepton Spectroscopy of QCD Matter at Collider Energies, Ralf Rapp
Volume 2013, Article ID 148253, 17 pages

Viscous Hydrodynamic Model for Relativistic Heavy Ion Collisions, A. K. Chaudhuri
Volume 2013, Article ID 693180, 25 pages

Tubular Initial Conditions and Ridge Formation, M. S. Borysova, O. D. Borysov, Iu. A. Karpenko,
V. M. Shapoval, and Yu. M. Sinyukov
Volume 2013, Article ID 209182, 10 pages

Some Aspects of Anisotropic Quark-Gluon Plasma, Mahatsab Mandal and Pradip Roy
Volume 2013, Article ID 371908, 20 pages

Femtoscopic and Nonfemtoscopic Two-Particle Correlations in $A + A$ and $p + p$ Collisions at RHIC and LHC Energies, Yu. M. Sinyukov, S. V. Akkelin, Iu. A. Karpenko, and V. M. Shapoval
Volume 2013, Article ID 198928, 23 pages

QCD Thermodynamics on the Lattice, Sayantan Sharma
Volume 2013, Article ID 452978, 26 pages

Internal Cumulants for Femtoscopy with Fixed Charged Multiplicity, H. C. Eggers and B. Buschbeck
Volume 2013, Article ID 230515, 22 pages

A Random Walk with Heavy Flavours, Surasree Mazumder, Trambak Bhattacharyya, and Santosh K. Das
Volume 2013, Article ID 136587, 23 pages

Calibrating the In-Medium Behavior of Quarkonia, Helmut Satz
Volume 2013, Article ID 242918, 6 pages

On the Higher Moments of Particle Multiplicity, Chemical Freeze-Out, and QCD Critical Endpoint,

A. Tawfik

Volume 2013, Article ID 574871, 22 pages

Role of Magnetic Interaction in Dense Plasma, S. Sarkar, K. Pal, and A. K. Dutt-Mazumder

Volume 2013, Article ID 530895, 17 pages

Particle Production in Strong Electromagnetic Fields in Relativistic Heavy-Ion Collisions, Kirill Tuchin

Volume 2013, Article ID 490495, 34 pages

On Collective Properties of Dense QCD Matter, Igor Dremin, Martin Kirakosyan, and Andrei Leonidov

Volume 2013, Article ID 706521, 11 pages

Viscous Coefficients of a Hot Pion Gas, Sourav Sarkar

Volume 2013, Article ID 627137, 15 pages

Charge Radii and Quadrupole Moments of the Low-Lying Baryons in the Chiral Constituent Quark Model, Neetika Sharma and Harleen Dahiya

Volume 2013, Article ID 756847, 17 pages

Ridge and Transverse Correlation without Long-Range Longitudinal Correlation, Charles B. Chiu and Rudolph C. Hwa

Volume 2013, Article ID 728365, 11 pages

Editorial

Physics of Quark Gluon Plasma: An Update and the Status Report

Jan E. Alam,¹ Edward Sarkisyan-Grinbaum,^{2,3} and Subrata Bhattacharyya⁴

¹ *Theoretical Physics Division, Variable Energy Cyclotron Centre, Kolkata 700064, India*

² *PH Department, CERN, 1211 Geneva 23, Switzerland*

³ *Department of Physics, The University of Texas at Arlington, Arlington, TX 76019, USA*

⁴ *Physics & Applied Mathematics Unit, Indian Statistical Institute (ISI), Kolkata 700108, India*

Correspondence should be addressed to Jan E. Alam; jane@vecc.gov.in

Received 24 February 2014; Accepted 24 February 2014; Published 9 June 2014

Copyright © 2014 Jan E. Alam et al. This is an open access article distributed under the Creative Commons Attribution License, which permits unrestricted use, distribution, and reproduction in any medium, provided the original work is properly cited. The publication of this article was funded by SCOAP³.

The microsecond old universe was too hot for the nucleons to survive as bound states of quarks. When the temperature of the universe fell below $\sim 10^{13}$ K as a result of cooling due to expansion, the quarks got confined inside the nucleons to reside there ever after—making them inaccessible to any direct observation in isolation. Natural objects like the core of the compact astrophysical objects may also contain deconfined quark matter. Therefore, creation of a deconfined phase of thermal quarks and gluons will be very important for understanding the evolution of the early universe and the physics of compact astrophysical objects like neutron star. Calculations based on lattice QCD indicate that hadronic matter at high temperatures and densities undergoes a phase transition to a thermalized system of deconfined quarks and gluons, called quark gluon plasma (QGP). It is expected that such high densities and temperatures may be achieved by colliding two nuclei at RHIC, LHC, or FAIR energies. The present volume addresses some of the experimental and theoretical issues related to quark-hadron phase transition in the relativistic heavy ion collisions by the world experts in the field. On the experimental sides it contains results from CERN's Super Proton Synchrotron (SPS) and Large Hadron Collider (LHC) and Brookhaven National Laboratory's Relativistic Heavy Ion Collider (RHIC). Comparison of experimental results from RHIC and LHC is extremely useful to gain insights into the properties of the matter formed in these experiments. The present volume offers

a review on this subject. On the theoretical side the present volume contains papers on the space-time evolution of the system formed in heavy ion collisions including the effects of viscosities through hydrodynamic equations, issues of equilibration, electromagnetic and heavy quark probes of QGP, quarkonia suppression in QGP, ridge, and transverse correlations. Recent progress in the femtoscopy and particle production in strong electromagnetic fields in heavy ion collisions is also addressed adequately. In summary, the present volume brings out recent developments on almost all the relevant issues of heavy ion collisions like creation, evolution, and signals of QGP. We are sure that the volume will be useful for the current practitioners and young new entrants to this exciting field of research.

Acknowledgment

We sincerely thank all the authors who contributed to this volume.

*Jan E. Alam
Edward Sarkisyan-Grinbaum
Subrata Bhattacharyya*

Review Article

Selected Experimental Results from Heavy-Ion Collisions at LHC

Ranbir Singh,¹ Lokesh Kumar,^{2,3} Pawan Kumar Netrakanti,⁴ and Bedangadas Mohanty³

¹ Physics Department, University of Jammu, Jammu 180001, India

² Kent State University, Kent, OH 44242, USA

³ School of Physical Sciences, National Institute of Science Education and Research, Bhubaneswar 751005, India

⁴ Nuclear Physics Division, Bhabha Atomic Research Centre, Mumbai 400085, India

Correspondence should be addressed to Bedangadas Mohanty; bedanga@niser.ac.in

Received 10 April 2013; Revised 29 July 2013; Accepted 6 August 2013

Academic Editor: Edward Sarkisyan-Grinbaum

Copyright © 2013 Ranbir Singh et al. This is an open access article distributed under the Creative Commons Attribution License, which permits unrestricted use, distribution, and reproduction in any medium, provided the original work is properly cited.

We review a subset of experimental results from the heavy-ion collisions at the Large Hadron Collider (LHC) facility at CERN. Excellent consistency is observed across all the experiments at the LHC (at center of mass energy $\sqrt{s_{NN}} = 2.76$ TeV) for the measurements such as charged particle multiplicity density, azimuthal anisotropy coefficients, and nuclear modification factor of charged hadrons. Comparison to similar measurements from the Relativistic Heavy Ion Collider (RHIC) at lower energy ($\sqrt{s_{NN}} = 200$ GeV) suggests that the system formed at LHC has a higher energy density and larger system size and lives for a longer time. These measurements are compared to model calculations to obtain physical insights on the properties of matter created at the RHIC and LHC.

1. Introduction

The main goal of the high energy heavy-ion collisions is to study the phase structure of the quantum chromodynamic (QCD) phase diagram [1–3]. One of the most interesting aspects of these collisions is the possibility of forming a phase of deconfined quarks and gluons, a system that is believed to have existed in a few microseconds-old universe. First principle QCD calculations suggest that it is possible to have such a state of matter if the temperatures attained can be of the order of the QCD scale (~ 200 MeV) [4–6]. In laboratory, such temperatures could be attained by colliding heavy ions at relativistic energies. Furthermore, in very high energy collisions of heavy ions at the LHC and RHIC, the lifetime of the deconfined phase may be long enough to allow for the detailed study of the fundamental constituents (quarks and gluons) of the visible matter.

The results from heavy-ion collisions at RHIC have clearly demonstrated the formation of a deconfined system of quarks and gluons in Au + Au collisions at $\sqrt{s_{NN}} = 200$ GeV [7–11]. The produced system exhibits copious production of strange hadrons, shows substantial collectivity developed in the partonic phase, and exhibits suppression in high

transverse momentum (p_T) hadron production relative to $p + p$ collisions and small fluidity as reflected by a small value of viscosity to entropy density ratio (η/s). A factor of 14 increase in $\sqrt{s_{NN}}$ for Pb + Pb collisions at LHC is expected to unravel the temperature dependence of various observables and to extend the kinematic reach in rapidity and p_T of previous measurements at RHIC. On the other hand, the beam energy scan program at RHIC is expected to provide additional details of the QCD phase diagram not accessible at the LHC [12].

In this review paper, we discuss a subset of results that have come out from LHC Pb + Pb collisions at $\sqrt{s_{NN}} = 2.76$ TeV. We have divided the discussion into three sections. In the second section, we discuss the consistency of various measurements among the three LHC experiments that have heavy-ion programs: ALICE, ATLAS, and CMS. Section 2.1 discusses the results on the charged particle multiplicity, Section 2.2 discusses the results on azimuthal anisotropy, and Section 2.3 discusses the results on the nuclear modification factor.

In the third section, we make a comparative study between similar observables measured at lower energy collisions at RHIC and those from LHC. In doing this, we

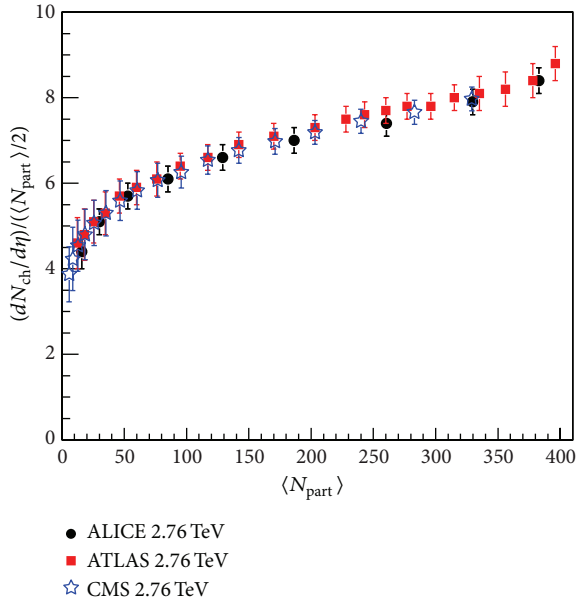


FIGURE 1: (Color online) Average charged particle multiplicity per unit pseudorapidity ($dN_{\text{ch}}/d\eta$) at midrapidity per participating nucleon ($\langle N_{\text{part}} \rangle$) pair plotted as a function of $\langle N_{\text{part}} \rangle$ for Pb + Pb collisions at $\sqrt{s_{\text{NN}}} = 2.76$ TeV. The measurements are shown from ALICE [14], CMS [15], and ATLAS [16] experiments.

highlight the additional information that heavy-ion collisions at LHC bring compared to RHIC. In Section 3.1, we discuss the bulk properties at freeze-out that include results on multiplicity, average transverse mass and Bjorken energy density, volume and decoupling time, kinetic freeze-out temperature and average flow velocity, and fluctuations. Section 3.2 is devoted on the results to azimuthal anisotropy, where we discuss the energy dependence of p_T integrated v_2 , dependence of various azimuthal anisotropy coefficients on p_T , and flow fluctuations. In Section 3.3, we discuss results for nuclear modification factor.

In the fourth section, we present a comparison of various model calculations to the corresponding measurements at LHC. We concentrate mainly on the results for charged particle multiplicity density and K/π ratio in Section 4.1, azimuthal anisotropy in Section 4.2, and nuclear modification factor in Section 4.3.

Finally, we summarize our observations in the last section of the paper.

2. Consistency of Results among LHC Experiments

2.1. Charged Particle Multiplicity. One of the first measurements to come out of the heavy-ion collision program at LHC is the charged particle multiplicity per unit pseudorapidity in Pb + Pb collisions at $\sqrt{s_{\text{NN}}} = 2.76$ TeV. Figure 1 shows the centrality (reflected by the number of participating nucleons, N_{part} , obtained from a Glauber model calculation [13]) dependence of $dN_{\text{ch}}/d\eta$ at midrapidity for Pb + Pb collisions at $\sqrt{s_{\text{NN}}} = 2.76$ TeV from ALICE [14], CMS [15],

and ATLAS [16] experiments. The error bars reflect statistical uncertainties. The ATLAS measurements of $dN_{\text{ch}}/d\eta|_{\eta=0}$ are obtained over $|\eta| < 0.5$ using a minimum bias trigger with a central solenoid magnet off data set. The charged particles are reconstructed using two different algorithms using the information from pixel detectors covering $|\eta| < 2.0$. The N_{part} values are obtained by comparing the summed transverse energy in the forward calorimeter over a pseudorapidity range $3.2 < |\eta| < 4.9$ to a Glauber model simulation. The CMS results for $dN_{\text{ch}}/d\eta|_{\eta=0}$ are from the barrel section of the pixel tracker covering $|\eta| < 2.5$. The minimum bias trigger data set was in the magnetic field off configuration so as to improve the acceptance of low p_T particles. The centrality determinations as in the case of ATLAS experiment are done using information from hadron forward calorimeter ($2.9 < |\eta| < 5.2$) and Glauber model simulations. The ALICE measurement uses a minimum bias data set from the silicon pixel detector ($|\eta| < 2.0$). The centrality selection is carried out using signals from VZERO detectors (2 arrays of 32 scintillator tiles) covering the regions $2.8 < \eta < 5.1$ and $-3.7 < \eta < -1.7$, along with the corresponding Glauber modeling of the data.

In spite of the difference in operating conditions and measurement techniques, the $dN_{\text{ch}}/d\eta$ versus N_{part} results for Pb + Pb collisions at $\sqrt{s_{\text{NN}}} = 2.76$ TeV show a remarkable consistency across the three experiments. The results show that the charged particle multiplicity per unit pseudorapidity per nucleon pair increases from peripheral to central collisions. This gradual increase in $dN_{\text{ch}}/d\eta$ per participating nucleon pair indicates that in central head-on collisions, where the number of participating nucleons is more, the charged particle production is different compared to that in peripheral collisions.

2.2. Azimuthal Anisotropy. Azimuthal anisotropy has been studied in great detail in heavy-ion collision experiments. It can provide information about initial stages of heavy-ion collisions. Figure 2 (top panels) shows the azimuthal anisotropy of produced charged particles ($v_n = \langle \cos(n(\phi - \Psi_n)) \rangle$) as a function of p_T for 30–40% Pb + Pb collisions at $\sqrt{s_{\text{NN}}} = 2.76$ TeV from the three different experiments: ATLAS, ALICE, and CMS. Here, ϕ is the azimuthal angle of the produced particles, and Ψ_n is the n th order reaction plane angle measured in the experiments. The left panel in the figure corresponds to v_2 , the middle panel corresponds to v_3 , and the right panel corresponds to v_4 , respectively. Bottom panels show the ratio of the experimental data to a polynomial fit to the ALICE data.

In the CMS experiment [17–20], the v_2 measurements use the information from the silicon tracker in the region $|\eta| < 2.5$ with a track momentum resolution of 1% at $p_T = 100$ GeV/c kept within a magnetic field of 3.8 Tesla. The event plane angle (Ψ_2) is obtained using the information on the energy deposited in the hadron forward calorimeter. A minimum η gap of 3 units is kept between the particles used for obtaining Ψ_2 and v_2 . This ensures suppression of nonflow correlations which could arise, for example, from dijets. The event plane resolution obtained using three subevents technique varies from 0.55 to 0.84, depending on the collision

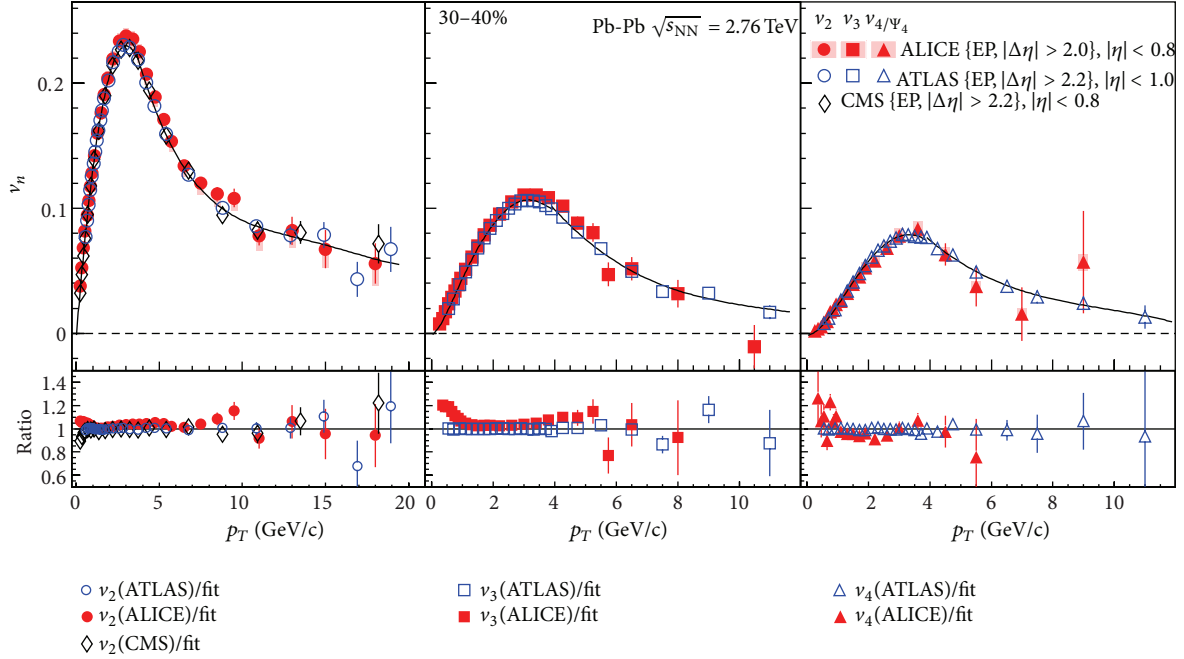


FIGURE 2: (Color online) v_n versus p_T at midrapidity for 30–40% Pb + Pb collisions at $\sqrt{s_{NN}} = 2.76$ TeV. The results are shown from different LHC experiments: CMS [17–20], ATLAS [21–24], and ALICE [25]. The bottom panels show the ratio of the experimental data to a polynomial fit to the ALICE data.

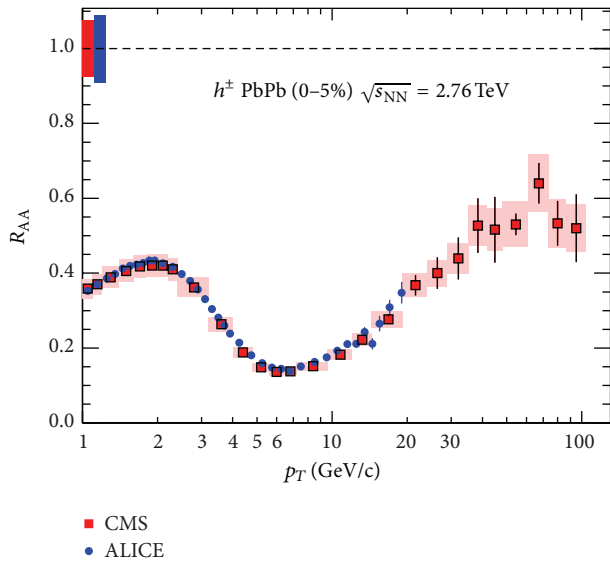


FIGURE 3: (Color online) Nuclear modification factor R_{AA} of charged hadrons measured by ALICE [26] and CMS [27] experiments at midrapidity for 0–5% most central Pb-Pb collisions at $\sqrt{s_{NN}} = 2.76$ TeV. The boxes around the data denote p_T -dependent systematic uncertainties. The systematic uncertainties on the normalization are shown as boxes at $R_{AA} = 1$.

centrality. The ATLAS experiment [21–24] measured v_n using the inner detectors in the $|\eta| < 2.5$, kept inside a 2 Tesla field of superconducting solenoid magnet. The event planes are obtained using forward calorimeter information,

with a resolution varying from 0.2 to 0.85, depending on collision centrality. The ALICE experiment [25] measured v_n using charged tracks reconstructed from the Time Projection Chamber ($|\eta| < 0.8$); the event plane was obtained using information from VZERO detectors kept at a large rapidity gap from the TPC. The momentum resolution of the tracks is better than 5%.

A very nice agreement for v_2 , v_3 , and v_4 versus p_T is found between all the experiments to a level of within 10% for most of the p_T ranges presented. The results show an increase of v_2 , v_3 , and v_4 values with p_T for the low p_T and a decrease for p_T above ~ 3 GeV/c. The hydrodynamical evolution of the system affects most of the low p_T particles and hence the increasing v_n at low p_T .

2.3. Nuclear Modification Factor. One of the established signatures of the QGP at top RHIC energy is the suppression of high transverse momentum (p_T) particles in heavy-ion collisions compared to corresponding data from the binary collisions scaled $p + p$ collisions. It has been interpreted in terms of energy loss of partons in QGP. This phenomenon is referred to as the jet quenching in a dense partonic matter. The corresponding measurement is called the nuclear modification factor (R_{AA}).

Figure 3 shows the nuclear modification factor for inclusive charged hadrons measured at midrapidity in LHC experiments for Pb + Pb collisions at $\sqrt{s_{NN}} = 2.76$ TeV. The nuclear modification factor is defined as $R_{AA} = (dN_{AA}/d\eta d^2 p_T)/(T_{AB} d\sigma_{NN}/d\eta d^2 p_T)$. Here, the overlap integral $T_{AB} = N_{\text{binary}}/\sigma_{\text{inelastic}}^{pp}$ with N_{binary} being the number of binary collisions commonly estimated from Glauber model

calculation and $d\sigma_{\text{NN}}/d\eta d^2p_T$ is the cross section of charged hadron production in $p + p$ collisions at $\sqrt{s} = 2.76$ TeV.

The ALICE experiment [26] uses the inner tracking system (ITS) and the time projection chamber (TPC) for vertex finding and tracking in a minimum bias data set. The CMS experiment [27] reconstructs charged particles based on hits in the silicon pixel and strip detectors. In order to extend the statistical reach of the p_T spectra in the highly prescaled minimum bias data recorded in 2011, it uses unprescaled single-jet triggers. Both experiments take the value of $\sigma_{\text{inelastic}}^{pp} = 64 \pm 5$ mb. The result shows that the charged particle production at high p_T in LHC is suppressed in heavy-ion collisions relative to nucleon-nucleon collisions. The suppression value reaches to a minimum at p_T 6-7 GeV/c and then gradually increases to attain an almost constant value at ~ 40 GeV/c. This can be understood in terms of energy loss mechanism differences in intermediate and higher p_T regions. The rise in the R_{AA} above p_T 6-7 GeV/c may imply the dominance of the constant fractional energy loss which is the consequence of flattening of the unquenched nucleon-nucleon spectrum. An excellent agreement for R_{AA} versus p_T for charged hadrons in 0-5% central Pb + Pb collisions at $\sqrt{s_{\text{NN}}} = 2.76$ TeV is observed between the two experiments.

Having discussed the consistency of these first measurements in Pb + Pb collisions among different experiments, the major detectors used, acceptances, and ways to determine centrality and event plane, we now discuss the comparison between measurements at RHIC and LHC heavy-ion collisions.

3. Comparison of LHC and RHIC Results

In the first subsection, we discuss the energy dependence of basic measurements made in heavy-ion collisions. These include $dN_{\text{ch}}/d\eta$, $\langle m_T \rangle$ ($m_T = \sqrt{p_T^2 + m^2}$; here, m represents mass of hadron), Bjorken energy density (ϵ_{Bj}), life time of the hadronic phase (τ_f), system volume at the freeze-out, kinetic and chemical freeze-out conditions, and finally, the fluctuations in net-charge distributions. In the next subsection, we discuss the energy dependence of p_T integrated v_2 , v_n versus p_T , and flow fluctuations at RHIC and LHC. In the final subsection, we compare the nuclear modification factor for hadrons produced in heavy-ion collisions at RHIC and LHC.

3.1. Bulk Properties at Freeze-Out

3.1.1. Multiplicity. Figure 4(a) shows the charged particle multiplicity density at midrapidity ($dN_{\text{ch}}/d\eta$) per participating nucleon pair produced in central heavy-ion collisions versus $\sqrt{s_{\text{NN}}}$. We observe that the charged particle production increases by a factor 2 as the energy increases from RHIC to LHC. The energy dependence seems to rule out a logarithmic dependence of particle production with $\sqrt{s_{\text{NN}}}$ and supports a power law type of dependence on $\sqrt{s_{\text{NN}}}$. The red solid curve seems to describe the full energy range. More detailed discussions on the energy dependence of these measurements can be found in [28].

Figure 4(b) shows the excess of $dN_{\text{ch}}/d\eta/\langle N_{\text{part}} \rangle$ in A + A collisions [15, 16, 29–37] over corresponding yields in $p + p(\bar{p})$ [38–47] and $p(d) + A$ collisions [29, 48, 49]. This observation also seen at RHIC persists at LHC but is proportionately larger at the higher energy collisions at the LHC. A power law fit to the $p + p$ collision charged particle multiplicity density leads to a dependence $\sim s^{0.11}$, while those for A + A collisions go as $\sim s^{0.15}$. There is no scaling observed in the charged particle multiplicity density per participating nucleon, when compared between elementary collisions like $p + p$ and heavy-ion collisions. This is a clear indication that A + A collisions at RHIC and LHC are not a simple superposition of several $p + p$ collisions, whereas the $p + A$ collisions scale with the $p + p$ collisions.

3.1.2. Average Transverse Mass and Bjorken Energy Density.

Figure 5(a) shows the $\langle m_T \rangle$ values for pions in central heavy-ion collisions as a function of $\sqrt{s_{\text{NN}}}$. The $\langle m_T \rangle$ value increases with $\sqrt{s_{\text{NN}}}$ at lower AGS energies [50, 51], stays independent of $\sqrt{s_{\text{NN}}}$ for the SPS energies [52, 53], and then tends to rise further with increasing $\sqrt{s_{\text{NN}}}$ at the higher beam energies of LHC. About 25% increase in $\langle m_T \rangle$ is observed from RHIC [41, 54] to LHC [55]. For a thermodynamic system, $\langle m_T \rangle$ can be an approximate representation of the temperature of the system, and $dN/dy \propto \ln(\sqrt{s_{\text{NN}}})$ may represent its entropy [56]. In such a scenario, the observations could reflect the characteristic signature of a phase transition, as proposed by Van Hove [57]. Then, the constant value of $\langle m_T \rangle$ versus $\sqrt{s_{\text{NN}}}$ has one possible interpretation in terms of formation of a mixed phase of a QGP and hadrons during the evolution of the heavy-ion system. The energy domains accessed at RHIC and LHC will then correspond to partonic phase, while those at AGS would reflect hadronic phase. However, there could be several other effects to which $\langle m_T \rangle$ is sensitive, which also need to be understood for proper interpretation of the data [56].

Figure 5(b) shows the product of the estimated Bjorken energy density ($\epsilon_{\text{Bj}} = (1/(A_{\perp}\tau))dE_T/dy$; A_{\perp} [58] is the transverse overlap area of the nuclei, and E_T is the transverse energy) and formation time (τ) as a function of $\sqrt{s_{\text{NN}}}$ [59–64]. The product of energy density and the formation time at LHC seem to be a factor of 3 larger compared to that attained at RHIC. If we assume the same value of τ_0 (=1 fm/c) for LHC and RHIC, the Bjorken energy density is about a factor of 3 larger at the LHC compared to that at RHIC in central collisions.

3.1.3. Volume and Decoupling Time. The top panel of Figure 6 shows the energy dependence of the product of the three radii (R_{out} , R_{side} , and R_{long}) obtained from pion HBT or Bose-Einstein correlation analysis. Here, the “out” corresponds to the axis pointing along the pair transverse momentum, the “side” to the axis perpendicular to it in the transverse plane, and the “long” corresponds to the axis along the beam (Bertsch-Pratt convention [65, 66]). The product of the radii is connected to the volume of the homogeneity region at the last interaction. The product of the three radii shows a linear dependence on the charged-particle pseudorapidity density.

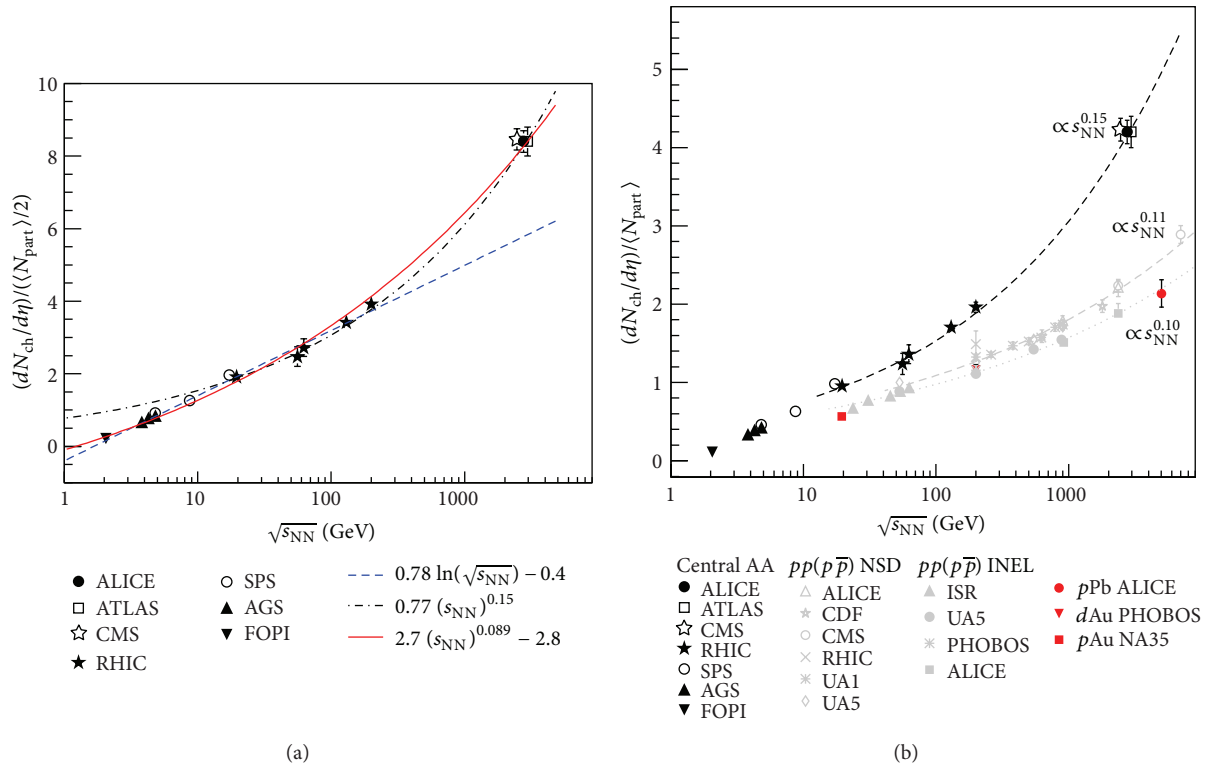


FIGURE 4: (Color online) (a) $dN_{ch}/d\eta$ per participating nucleon pair at midrapidity in central heavy-ion collisions as a function of $\sqrt{s_{NN}}$. (b) Comparison of $dN_{ch}/d\eta$ per participating nucleon at midrapidity in central heavy-ion collisions [15, 16, 29–37] to corresponding results from $p + p(\bar{p})$ [38–47] and $p(d) + A$ collisions [29, 48, 49].

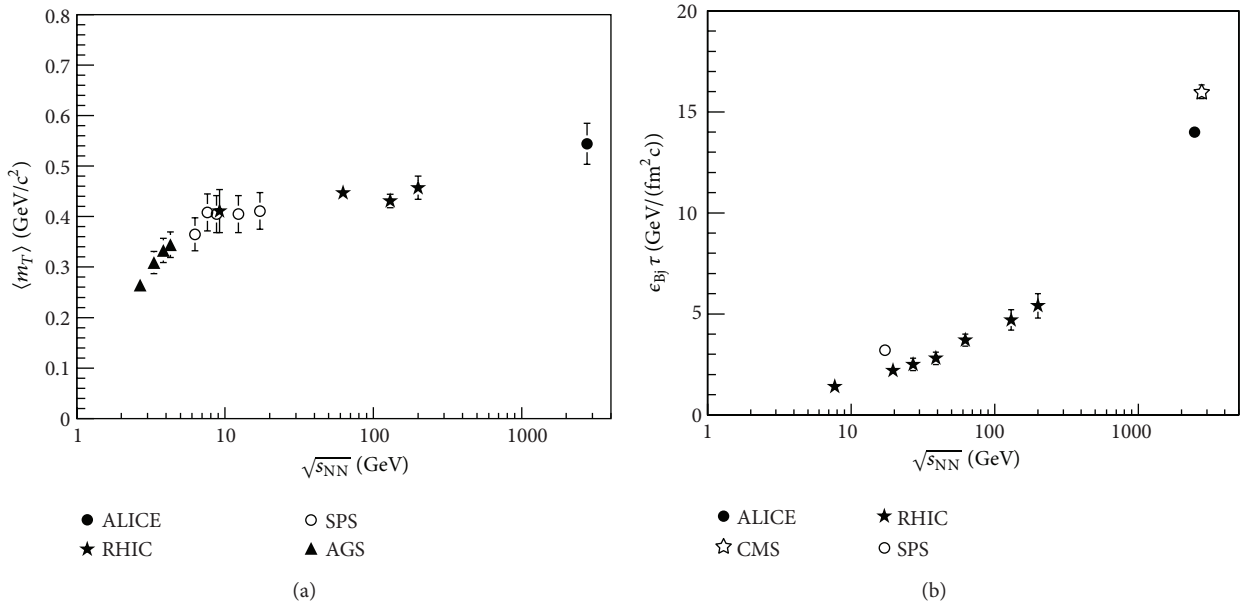


FIGURE 5: (a) $\langle m_T \rangle$ for charged pions in central heavy-ion collisions at midrapidity for AGS [50, 51], SPS [52, 53], RHIC [41, 54], and LHC [55] energies. The errors shown are the quadrature sum of statistical and systematic uncertainties. (b) The product of Bjorken energy density, ϵ_{Bj} [58], and the formation time (τ) in central heavy-ion collisions at midrapidity as a function of $\sqrt{s_{NN}}$ [59–64].

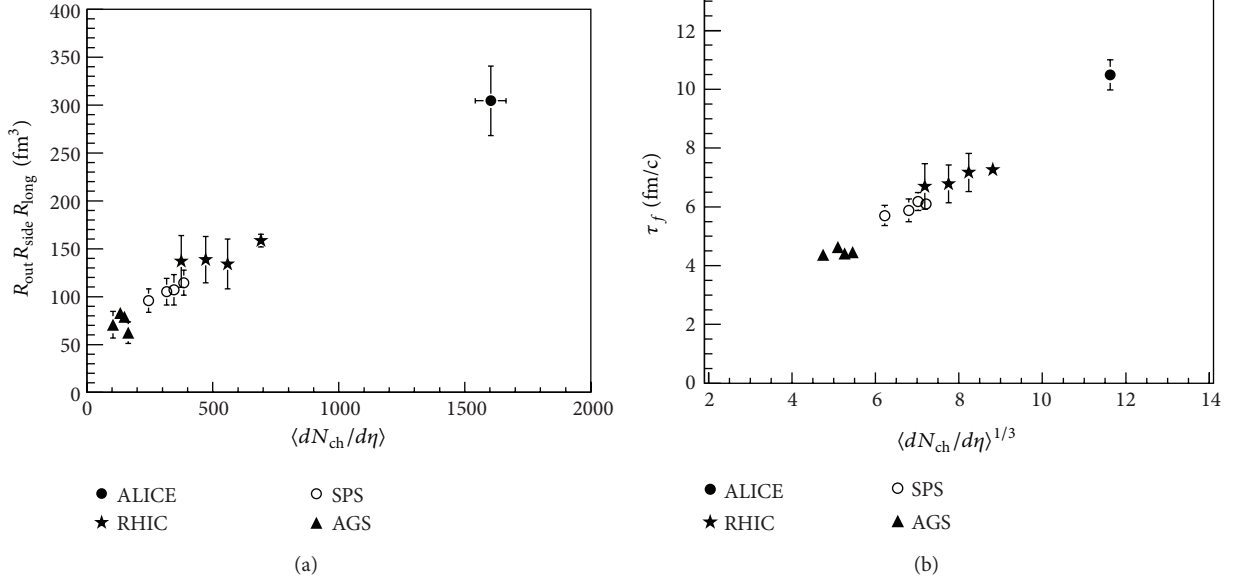


FIGURE 6: (a) Product of the three pion HBT radii at k_T (average transverse momenta of two pions) = 0.3 GeV/c for central heavy-ion collisions at AGS [68], SPS [69, 70], RHIC [71, 72], and LHC [73] energies. (b) The decoupling time extracted from $R_{\text{long}}(k_T)$ for central heavy-ion collisions at midrapidity at AGS, SPS, RHIC, and LHC energies as a function of $(dN_{\text{ch}}/d\eta)^{1/3}$.

The data indicates that the volume of homogeneity region is two times larger at the LHC than at RHIC.

Furthermore, within a hydrodynamic picture, the decoupling time for hadrons (τ_f) at midrapidity can be estimated from the magnitude of radii R_{long} as follows: $R_{\text{long}}^2 = \tau_f^2 TK_2(m_T/T)/m_T K_1(m_T/T)$, with $m_T = \sqrt{m_\pi^2 + k_T^2}$, where m_π is the mass of the pion, T is the kinetic freeze-out temperature, and K_1 and K_2 are the integer-order modified Bessel functions [67]. For the estimation of τ_f , the average value of the kinetic freeze-out temperature T is taken to be 120 MeV from AGS to LHC energies. However, the energy dependence of kinetic freeze-out temperature, as discussed in the next subsection, would provide a more accurate description of the τ_f values. The extracted τ_f values for central heavy-ion collisions at midrapidity at AGS [68], SPS [69, 70], RHIC [71, 72], and LHC [73] energies are shown as a function of cube root of $dN_{\text{ch}}/d\eta$ in the bottom panel of Figure 6. We observe that τ_f scales linearly with $(dN_{\text{ch}}/d\eta)^{1/3}$ and is about 10 fm/c at LHC energies. This value is about 40% larger than at RHIC. It may be noted that the above expression ignores transverse expansion of the system and finite chemical potential for pions. Also there are uncertainties associated with freeze-out temperature that could lead to variations in the extracted τ_f values.

3.1.4. Freeze-Out Temperature and Radial Flow Velocity. The hadron yields and spectra reflect the properties of the bulk matter at chemical and kinetic freeze-out, respectively. Generally, the point at which the inelastic collisions cease is called the chemical freeze-out, and the point where even the elastic collisions stop is called the kinetic freeze-out.

The transverse momentum distribution of different particles contains two components: one random and the other collective. The random component can be identified with the temperature of the system at kinetic freeze-out (T_{kin}). The collective component, which could arise from the matter density gradient from the center to the boundary of the fireball created in high energy nuclear collisions, is called collective flow in transverse direction ($\langle \beta \rangle$). Using the assumption that the system attains thermal equilibrium, the blast wave formulation can be used to extract T_{kin} and $\langle \beta \rangle$. These two quantities are shown in Figure 7 versus $\sqrt{s_{\text{NN}}}$ [41, 55, 74–77]. For beam energies at AGS and above, one observes a decrease in T_{kin} with $\sqrt{s_{\text{NN}}}$. This indicates that the higher the beam energy is, the longer interactions are among the constituents of the expanding system and the lower the temperature. From RHIC top energy to LHC, there seems to be, however, a saturation in the value of T_{kin} . In contrast to the temperature, the collective flow increases with the increase in beam energy, rapidly, reaching a value close to 0.6 times the speed of light at the LHC energy.

Figure 8 shows the chemical freeze-out temperature (T_{ch}) versus the baryon chemical potential (μ_B) in central heavy-ion collisions [41, 55, 78–85]. These quantities are obtained by fitting the particle yields to a statistical model assuming thermal equilibrium within the framework of a Grand Canonical ensemble. There are two values of temperature quoted for LHC energies. A T_{ch} value of about 164 MeV and fixed μ_B value of 1 MeV seem to reproduce the multistrange ratios (involving Ξ and Ω) quite well but were observed to miss the data for p/π and Λ/π . On the other hand, the statistical thermal model prediction with $T_{\text{ch}} = 152$ MeV and fixed $\mu_B = 1$ MeV fits the measured p/π and Λ/π ratios better but misses

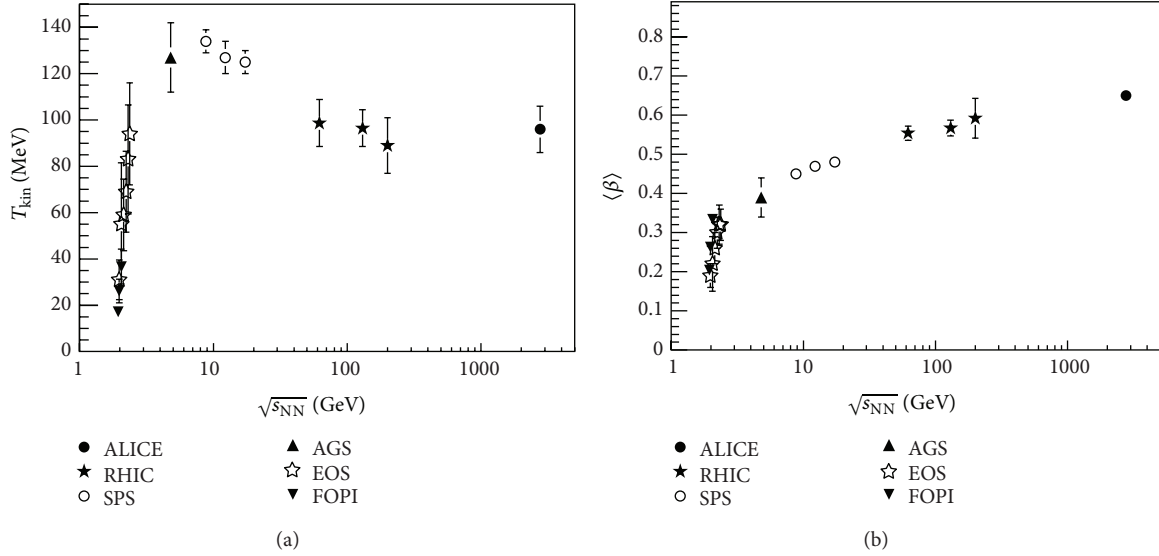


FIGURE 7: Kinetic freeze-out temperature (a) and radial flow velocity (b) in central heavy-ion collisions as a function of collision energy [41, 55, 74–77].

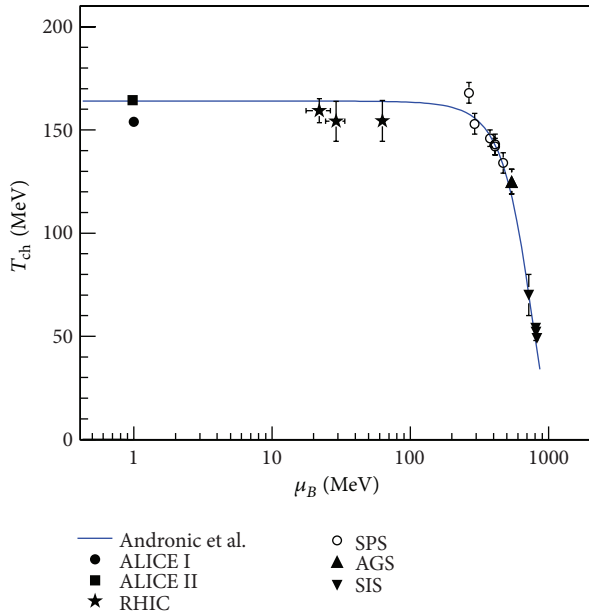


FIGURE 8: (Color online) Chemical freeze-out temperature versus baryon chemical potential in central heavy-ion collisions [41, 55, 78–85]. The curve corresponds to model calculations from [78, 79].

the ratios involving multistrange hadrons [86]. This issue is not yet resolved, being possibly related to hadronic final state interactions [87]. The curve corresponds to generalization of the energy dependence of $T_{\text{ch}} - \mu_B$ using statistical thermal model calculations [78, 79]. The model works within the framework of a Grand Canonical ensemble and takes as input the produced particle yields from experiments to extract the freeze-out parameters such as T_{ch} and μ_B .

3.1.5. Fluctuations. One of the proposed signatures to search for the phase transition from hadronic to partonic medium is to study the net-charge fluctuations in heavy-ion collisions. The partonic phase has constituents with fractional charges, while the hadronic phase has constituents with integral units of charge; hence, the measure of the fluctuations in the net-charge particle production is expected to be different in these two cases. Specifically, net-charge fluctuations are expected to be smaller if the system underwent a phase transition. However, it is important to address how these fluctuations may or may not survive the evolution of the system in the heavy-ion collisions. An experimental measure of net-charge fluctuations is defined as $\nu(+-, dyn) = (\langle N_+(N_+ - 1) \rangle / \langle N_+^2 \rangle) + (\langle N_-(N_- - 1) \rangle / \langle N_-^2 \rangle) - 2(\langle N_- N_+ \rangle / \langle N_- \rangle \langle N_+ \rangle)$, where $\langle N_- \rangle$ and $\langle N_+ \rangle$ are average negative and positive charged particle multiplicity, respectively [88].

Figure 9 shows the product of $\nu(+-, dyn)$ and $\langle N_{\text{ch}} \rangle$ (average number of charged particles) as a function of $\sqrt{s_{\text{NN}}}$ [89–91]. We find that this observable fluctuation rapidly decreases with $\sqrt{s_{\text{NN}}}$ and approaches expectation for a simple QGP-like scenario [92] as we move from RHIC to LHC energies. Given that several other observables already indicate that a hot and dense medium of color charges has been formed at RHIC and LHC, the net-charge fluctuation result may indicate that the observable $\nu(+-, dyn)$ is not sensitive enough to QGP physics or the process of hadronization washes out the QGP signal for this observable. It may be also noted that the model's results do not incorporate the acceptance effects and do not consider any dynamic evolution of the system like, for example, the dilution of the signals in the hadronization process.

3.2. Azimuthal Anisotropy

3.2.1. Energy Dependence of p_T Integrated v_2 . Figure 10 shows the p_T integrated v_2 close to midrapidity of charged particles

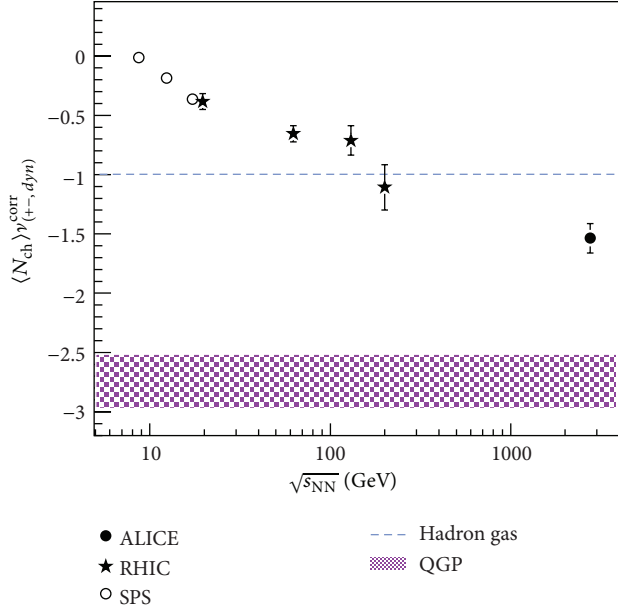


FIGURE 9: (Color online) Energy dependence of net-charge fluctuations about midrapidity in central heavy-ion collisions at SPS [89], RHIC [90], and LHC [91] energies. Also shown are the expectations from a hadron resonance gas model and for a simple QGP picture [92].

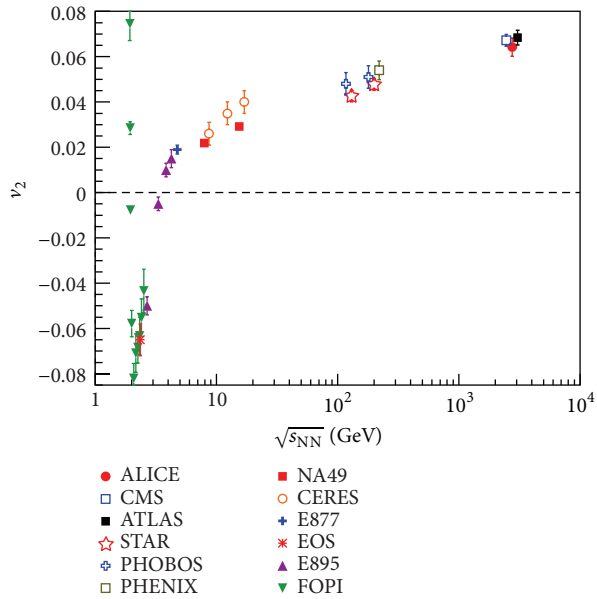


FIGURE 10: (Color online) Transverse momentum integrated v_2 close to midrapidity for charged ($Z = 1$) particles for collision centralities around 20–30% as a function of center of mass energy.

for collision centralities around 20–30% as a function of center of mass energy. We observe that there is an increase in magnitude of v_2 by about 30% from top RHIC energy ($\sqrt{s_{NN}} = 200$ GeV) to LHC energy ($\sqrt{s_{NN}} = 2.76$ TeV). This needs to be viewed within the context of a similar magnitude of increase in $\langle p_T \rangle$ of pions from RHIC to LHC energies. The increase of

v_2 beyond beam energy of 10 GeV is logarithmic in $\sqrt{s_{NN}}$. This is expected to be determined by the pressure gradient-driven expansion of the almond-shape fireball produced in the initial stages of a noncentral heavy-ion collision [93] while for v_2 measured at lower beam energies, the dependences observed are due to interplay of passing time of spectators and time scale of expansion of the system. A preference for an inplane emission versus out-of-plane (“squeeze-out”) pattern of particles as a function of beam energy is observed. The experimental data used are from FOPI [94, 95], EOS, E895 [96], E877 [97], CERES [98], NA49 [99], STAR [100], PHOBOS [101], PHENIX [102], ALICE [25], ATLAS [103], and CMS [17–20] experiments. Charged particles are used for LHC, RHIC, CERES, and E877 experiments, pion data is used from NA49 experiment, protons’ results are from EOS and E895 experiments, and FOPI results are for all particles with $Z = 1$.

3.2.2. Azimuthal Anisotropy Coefficients versus Transverse Momentum. Figure 11(a) shows the comparison of $v_2(p_T)$, $v_3(p_T)$, and $v_4(p_T)$ for 30–40% collision centrality at RHIC (PHENIX experiment [104]) and LHC (ALICE [105]) at midrapidity in Au + Au and Pb + Pb collisions, respectively. The bottom panel of this figure shows the ratio of LHC and RHIC results to a polynomial fit to the LHC data. The $v_n(p_T)$ measurement techniques are similar at RHIC and LHC energies. One observes that at lower p_T (< 2 GeV/c), the $v_2(p_T)$ and $v_3(p_T)$ are about 10–20% smaller at RHIC compared to the corresponding LHC results. However, at higher p_T , the results are quite similar. The $v_4(p_T)$ seems higher at RHIC compared to that at LHC.

One of the most striking observations to come out from RHIC is the number of constituent quark (n_q) scaling of $v_2(p_T)$ for identified hadrons. The basis of such a scaling is the splitting of $v_2(p_T)$ between baryons and mesons at intermediate p_T (2–6 GeV/c). This is shown in the bottom panels of Figure 11(b). Such a splitting between baryon and meson $v_2(p_T)$ is also observed at intermediate p_T at LHC energies (seen in the top panels of Figure 11(b)). However, the degree to which n_q scaling holds could be different at RHIC [106] and LHC [107] energies. The n_q scaling is much more closely followed at RHIC compared to LHC. It may be noted that there are several factors which could dilute such scaling, which include energy dependence of radial flow, an admixture of higher Fock states, and consideration of a realistic momentum distribution of quarks inside a hadron [108, 109]. The observation of the baryon-meson splitting is commonly interpreted as due to substantial amount of collectivity being generated in the deconfined phase. Another important feature is that at both RHIC and LHC energies, a clear hydrodynamic feature of mass dependence of $v_2(p_T)$ is observed at low p_T (< 2 GeV/c).

Figure 12 shows the charged hadron $v_2(p_T)$ for 30–40% collision centrality in Au + Au collisions at $\sqrt{s_{NN}} = 200$ GeV and Pb + Pb collisions at $\sqrt{s_{NN}} = 2.76$ TeV for $|\eta| < 1$ [17–20]. This figure demonstrates the kinematic reach for higher energy collisions at LHC relative to RHIC. LHC data allows us to study the $v_2(p_T)$ in the p_T range never measured

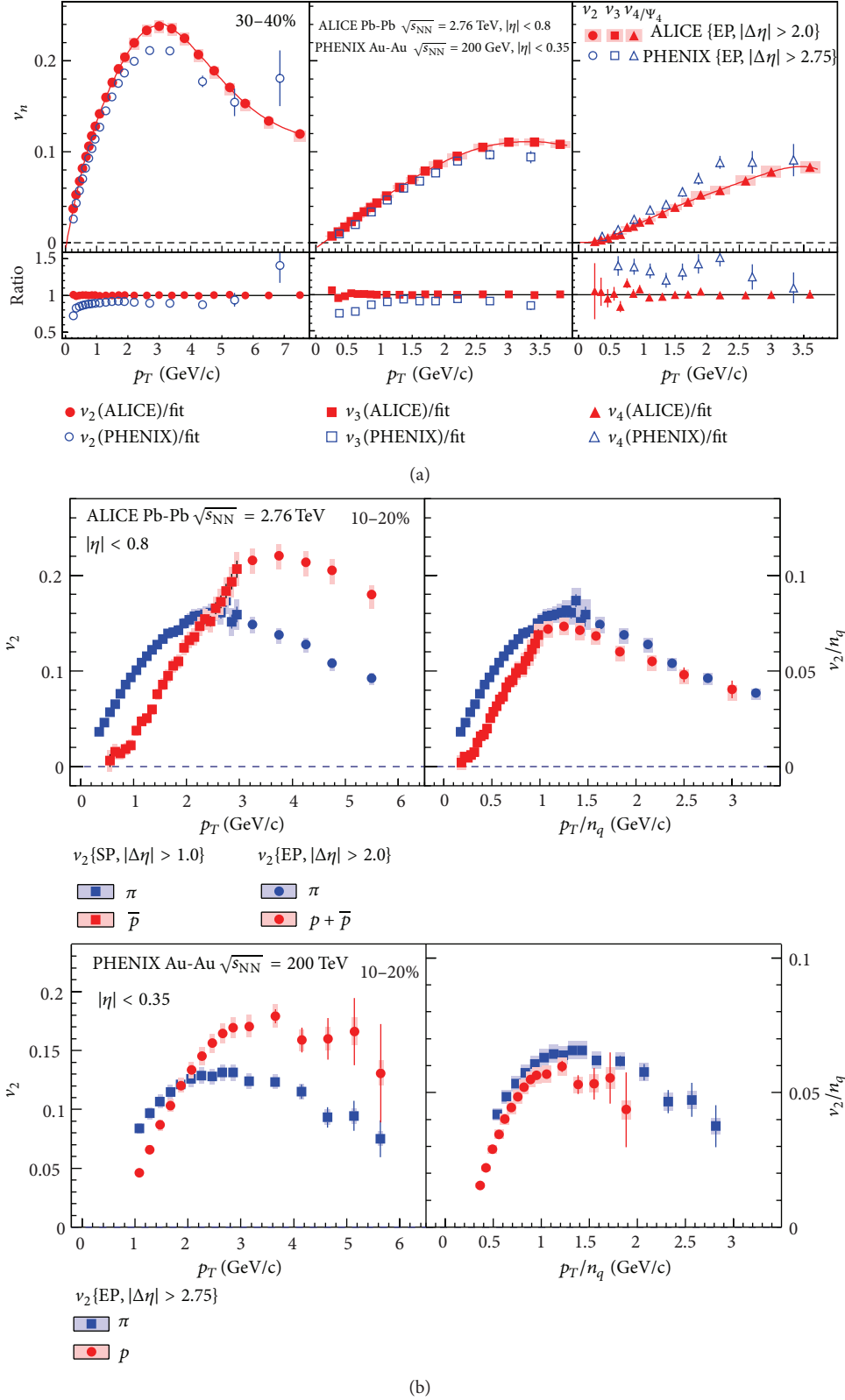


FIGURE 11: (Color online) (a) Comparison of $v_n(p_T)$ at midrapidity for 30–40% collision centrality at RHIC (Au + Au collisions at $\sqrt{s_{NN}} = 200$ GeV from PHENIX experiment [104]) and at LHC (Pb + Pb collisions at $\sqrt{s_{NN}} = 2.76$ TeV from ALICE experiment [105]). (b) show the ratio of v_n at LHC and RHIC. (b) v_2 versus p_T and v_2/n_q versus p_T/n_q for pions and protons at midrapidity for 10–20% collision centrality from Au + Au collisions at $\sqrt{s_{NN}} = 200$ GeV (PHENIX experiment [106]) and Pb + Pb collisions at $\sqrt{s_{NN}} = 2.76$ TeV (ALICE experiment [107]).

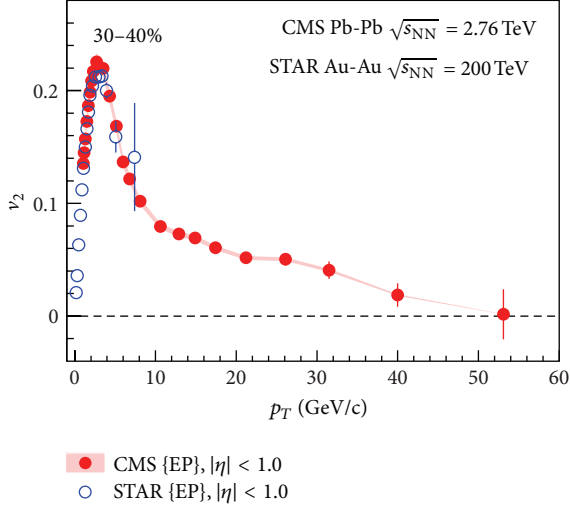


FIGURE 12: (Color online) Comparison of $v_2(p_T)$ at midrapidity for 30–40% collision centrality at RHIC (Au + Au collisions at $\sqrt{s_{NN}} = 200$ GeV from STAR experiment) and at LHC (Pb + Pb collisions at $\sqrt{s_{NN}} = 2.76$ TeV from CMS experiment [17–20]). The shaded band about CMS data point are systematic errors and vertical lines represent statistical errors.

before in heavy-ion collisions. The $v_2(p_T) \sim 0$ for $p_T > 40$ GeV/c might suggest that those particles must have been emitted very early in the interactions when the collective effects had not set in. These high transverse momentum data are useful to understand the effects of the initial geometry or path-length dependence of various properties associated with parton modification inside the hot QCD medium. In addition, it also provides significantly improved precision measurement of v_2 for $12 < p_T < 20$ GeV/c.

3.2.3. Flow Fluctuations. Fluctuations in azimuthal anisotropy coefficient v_2 have gained quite an attention in recent times. In particular, the measurement of event-by-event v_2 fluctuations can pose new constraints on the models of the initial state of the collision and their subsequent hydrodynamic evolution. In extracting event-by-event v_2 fluctuations, one needs to separate nonflow effects, and so far, there is no direct method to decouple v_2 fluctuations and nonflow effects in a model independent from the experimental measurements. However, several techniques exist where the nonflow effects can be minimized; for example, flow and non-flow contributions can be possibly separated to a great extent with a detailed study of two particle correlation function in $\Delta\phi$ and its dependence on η and $\Delta\eta$. Here, we discuss another technique to extract and compare the v_2 fluctuations at RHIC and LHC. We assume that the difference between $v_2\{2\}$ (two-particle cumulant) and $v_2\{4\}$ (four-particle cumulant) is dominated by v_2 fluctuations, and nonflow effect is negligible for $v_2\{4\}$. Then, the ratio $R_{v(2-4)} = \sqrt{(v_2\{2\}^2 - v_2\{4\}^2)/(v_2\{2\}^2 + v_2\{4\}^2)}$ can be considered as an estimate for v_2 fluctuations in the data. Figure 13 shows the

$R_{v(2-4)}$ as a function of collision centrality and $\langle dN_{ch}/d\eta \rangle$ for RHIC [110] and LHC [107] energies. The centrality dependence of $R_{v(2-4)}$ at RHIC or LHC as seen in Figure 13 could be an interplay of residual nonflow effects which increases for central collisions and multiplicity fluctuations which dominate smaller systems. It is striking to see that $R_{v(2-4)}$ when presented as a function of % cross section is similar at RHIC and LHC, suggesting it reflects features associated with initial state of the collisions, for example, the event-by-event fluctuations in the eccentricity of the system. But when presented as a function of $dN_{ch}/d\eta$, it tends to suggest a different behavior for most central collisions at RHIC.

Recently, a great interest has been generated on extracting initial condition and flow fluctuation information from the measurement of the probability distribution of v_n at LHC. The probability density of v_n can be expressed as a Gaussian function in transverse plane [111] as $p(v_n) = (1/2\pi\delta_{v_n}^2)e^{-(v_n - v_n^{RP})^2/(2\delta_{v_n}^2)}$ or as one dimensional Bessel-Gaussian function [112, 113] as $p(v_n) = (v_n/\delta_{v_n}^2)e^{-((v_n)^2 + (v_n^{RP})^2)/2\delta_{v_n}^2}I_0(v_n^{RP}v_n/\delta_{v_n}^2)$, where I_0 is the modified Bessel function of the first kind and δ_{v_n} is the fluctuation in v_n , with $\delta_{v_n} \approx \sigma_{v_n}$ for $\delta_{v_n} \ll v_n^{RP}$ (v_n measured with respect to reaction plane).

Figure 14 shows the v_2^{RP} and δ_{v_2} values extracted from the v_2 distributions as a function of $\langle N_{part} \rangle$ by fitting to the above probability functions [114]. They are compared with values of $\langle v_2 \rangle$ and σ_{v_2} obtained directly from the v_2 distributions. The v_2^{RP} value is always smaller than the value for $\langle v_2 \rangle$, and it decreases to zero in the 0–2% centrality interval. The value of δ_{v_2} is close to σ_{v_2} , except in the most central collisions. This leads to a value of δ_{v_2}/v_2^{RP} larger than $\sigma_{v_2}/\langle v_2 \rangle$ over the full centrality range as shown in Figure 14(c). The value of δ_{v_2}/v_2^{RP} decreases with $\langle N_{part} \rangle$ and reaches a minimum at $\langle N_{part} \rangle \approx 200$ but then increases for more central collisions. Thus, the event-by-event v_2 distribution brings additional insight for the understanding of v_2 fluctuations.

3.3. Nuclear Modification Factor. Figure 15 shows the R_{AA} of various particles produced in heavy-ion collisions at RHIC and LHC. In Figure 15(a), we observe that the shape of the R_{AA} versus p_T of charged hadrons at RHIC and LHC [26, 27] is very similar for the common p_T range of measurements. The values R_{AA} at RHIC are higher compared to those at LHC energies up to $p_T < 8$ GeV/c. The higher kinematic reach of LHC in p_T allows us to see the full p_T evolution of R_{AA} in high energy heavy-ion collisions. All these measurements suggest that the energy loss of partons in the medium formed in heavy-ion collisions at LHC energies is perhaps larger compared to that at RHIC. In Figure 15(b), we observe that the nuclear modification factors for $d + Au$ collisions at $\sqrt{s_{NN}} = 200$ GeV [115] and $p + Pb$ collisions at $\sqrt{s_{NN}} = 5.02$ TeV [116] are greater than unity for the $p_T > 2$ GeV/c. The values for RHIC are slightly larger compared to those for LHC. A value greater than unity for the nuclear modification factor in $p(d) + A$ collisions is generally interpreted as due to

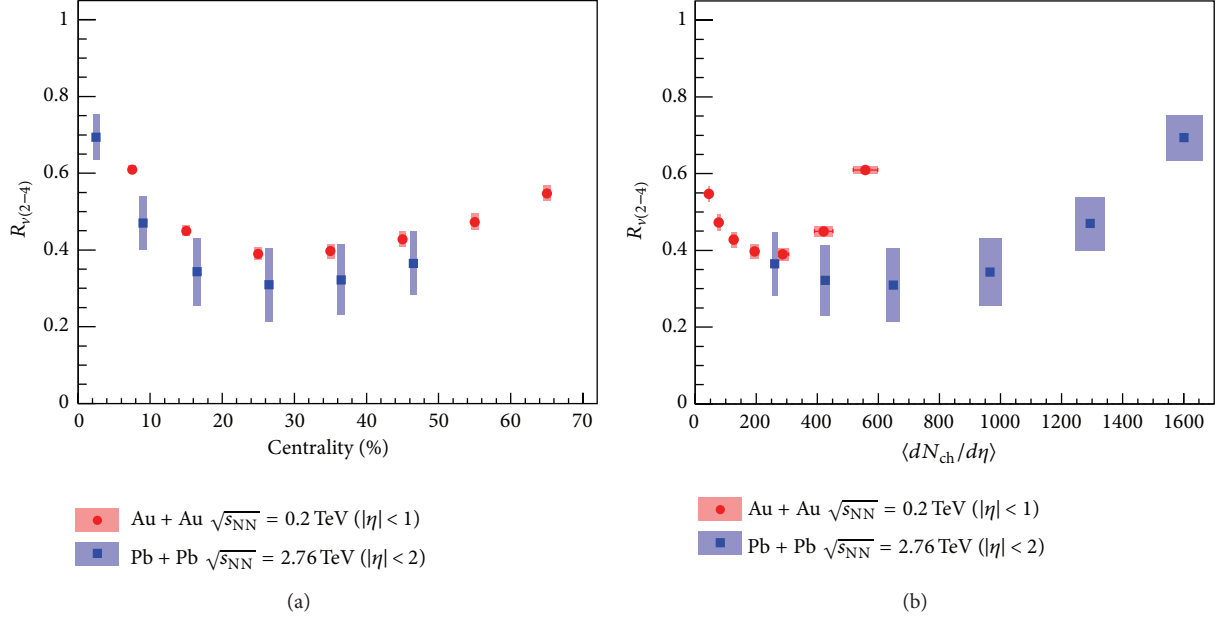


FIGURE 13: (Color online) The ratio $R_{v_2(2-4)} = \sqrt{(v_2\{2\}^2 - v_2\{4\}^2)/(v_2\{2\}^2 + v_2\{4\}^2)}$, an estimate of v_2 fluctuations plotted as a function of collision centrality (a) and $\langle dN_{ch}/d\eta \rangle$ (b) for RHIC (STAR experiment: Au + Au collisions at $\sqrt{s_{NN}} = 200 \text{ GeV}$ [110]) and LHC (ALICE: Pb + Pb collisions at $\sqrt{s_{NN}} = 2.76 \text{ TeV}$ [107]) at midrapidity. The bands reflect the systematic errors.

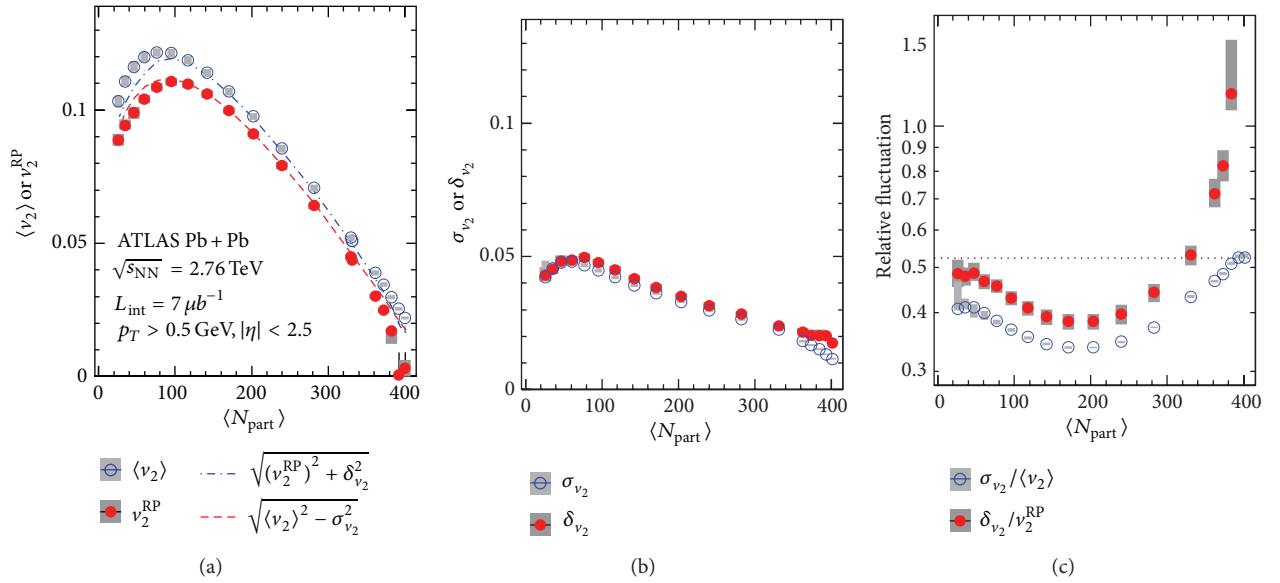


FIGURE 14: (Color online) The dependence of v_2^{RP} and $\langle v_2 \rangle$ (a), δ_{v_2} and σ_{v_2} (b), and δ_{v_2}/v_2^{RP} and $\sigma_{v_2}/\langle v_2 \rangle$ (c) on $\langle N_{part} \rangle$ [114]. The shaded boxes indicate the systematic uncertainties.

Cronin effect [117, 118]. However, several other physics effects could influence the magnitude of the nuclear modification factor in $p(d) + A$ collisions such as nuclear shadowing and gluon saturation effects. But the results that the nuclear modification factors in $p(d) + A$ collisions are not below

unity strengthen the argument (from experimental point of view) that a hot and dense medium of color charges is formed in $A + A$ collisions at RHIC and LHC. In Figure 15(c), we show the R_{AA} of particles that do not participate in strong interactions, and some of them are most likely formed in the

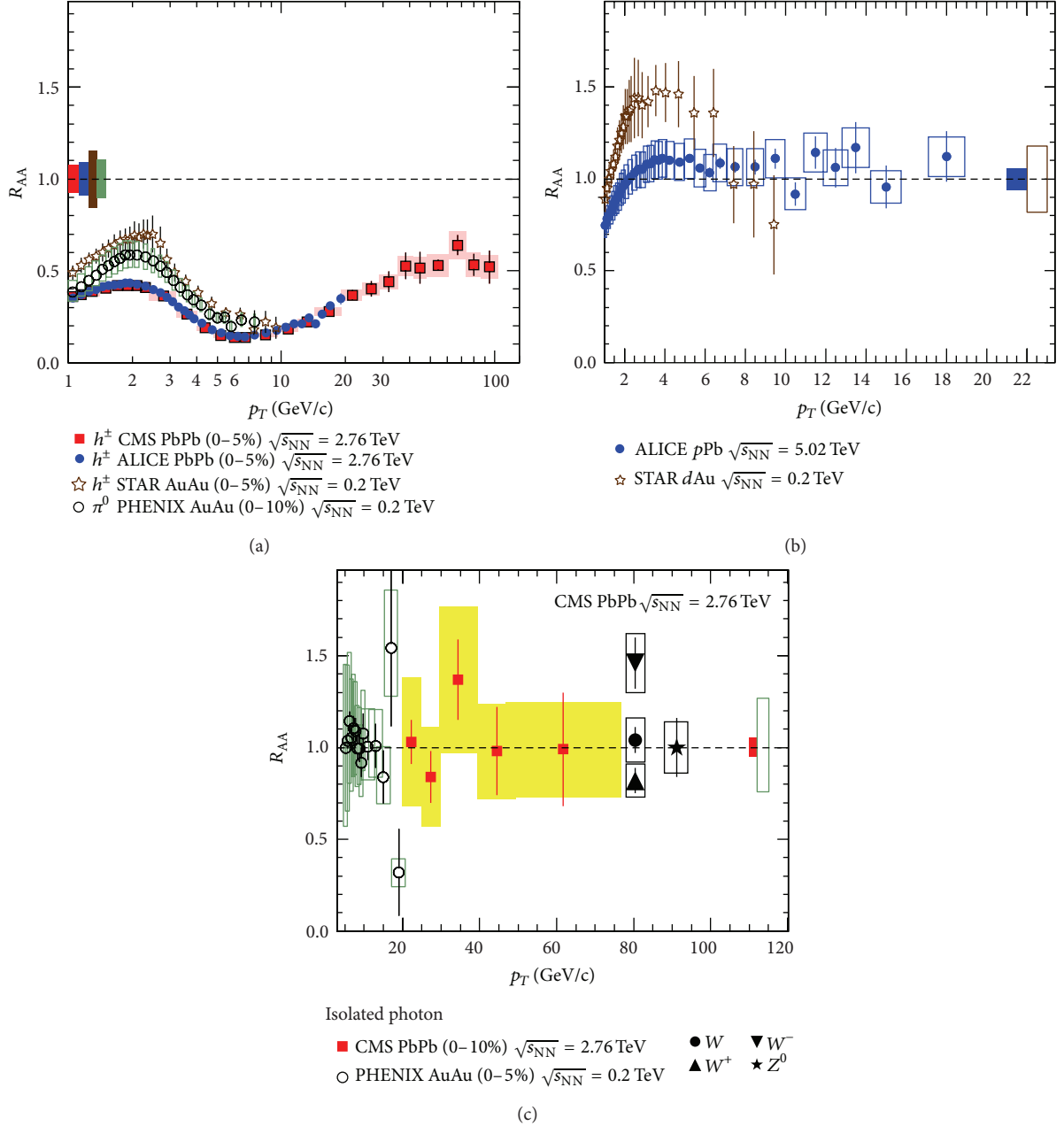


FIGURE 15: (Color online) (a) Nuclear modification factor R_{AA} of charged hadrons measured by ALICE [26] and CMS [27] experiments at midrapidity for 0–5% most central Pb+Pb collisions at $\sqrt{s_{NN}} = 2.76$ TeV. For comparison, shown are the R_{AA} of charged hadrons at midrapidity for 0–5% most central collisions measured by STAR [115] and R_{AA} of π^0 at midrapidity for 0–10% most central collisions measured by PHENIX [173] for Au + Au collisions at $\sqrt{s_{NN}} = 200$ GeV. (b) Comparison of nuclear modification factor for charged hadrons versus p_T at midrapidity for minimum bias collisions in $d + Au$ collisions at $\sqrt{s_{NN}} = 200$ GeV [115] and $p + Pb$ collisions at $\sqrt{s_{NN}} = 5.02$ TeV [116]. (c) The nuclear modification factor versus p_T for isolated photons in central nucleus-nucleus collisions at $\sqrt{s_{NN}} = 200$ GeV [119] and 2.76 TeV [120]. Also shown are the p_T integrated R_{AA} of W^\pm [121] and Z bosons [122] at corresponding m_T at LHC energies. Open and shaded boxes represent the systematic uncertainties in the experimental measurements and normalization uncertainties, respectively.

very early stages of the collisions. These particles (photon [119, 120], W^\pm [121], and Z [122] bosons) have an $R_{AA} \sim 1$, indicating that the $R_{AA} < 1$, observed for charged hadrons in A + A collisions, is due to the strong interactions in a dense medium consisting of color charges.

4. Comparison to Model Calculations

In this section, we compare some of the experimental observables discussed above with corresponding model calculations. This helps us to interpret the data at both RHIC and

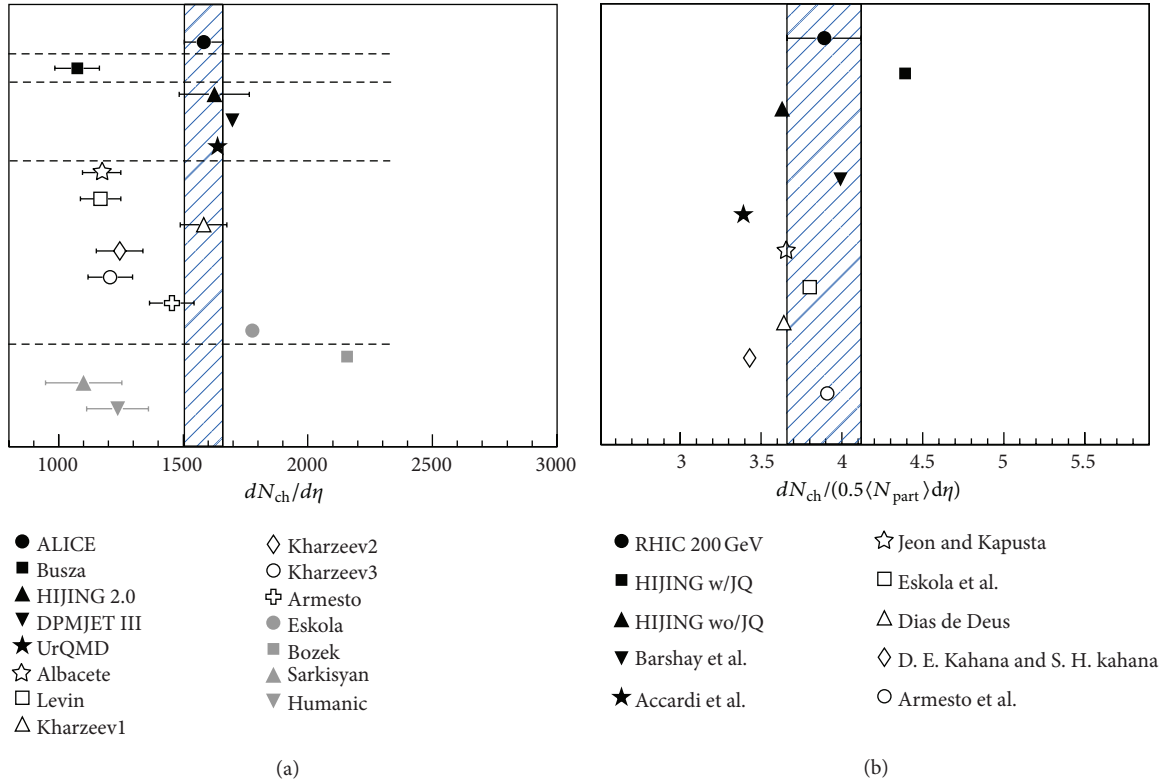


FIGURE 16: (Color online) Comparison of $dN_{ch}/d\eta$ measurement at midrapidity for central heavy-ion collisions at RHIC and LHC with model predictions.

LHC energies. We restrict our discussion on the comparison of the models with the experimental data for charged particle production, ratio of kaon to pion yields as a function of beam energy, p_T dependence of v_2 , and R_{AA} for charged particles and pions. For the charged particle production, we compare the experimental data with models inspired by the perturbative QCD-based calculations (HIJING, DPMJET) with macroscopic models (statistical and hydrodynamical), microscopic models (string, transport, cascade, etc.), and calculations which are derived by the different parametrizations of the nucleon-nucleon and nucleus-nucleus lower energy data. The ratio of kaon to pion yields for different beam energies is compared with the statistical and thermal models. The transverse momentum dependence of v_2 is compared with models incorporating the calculations based on hydrodynamic and transport approaches. Finally, the R_{AA} results are compared with the perturbative QCD-based calculations with different mechanism for the parton energy loss in the presence of colored medium.

4.1. Charged Particle Multiplicity Density and Particle Ratio. Figure 16 compares the measured charged particle pseudorapidity density at RHIC (0.2 TeV) and LHC (2.76 TeV) energies to various model calculations.

Empirical extrapolation from lower energy data (named “Busza” in the figure) [123] significantly under-predicts the measurement at LHC energies. A simple power-law growth of charged-particle multiplicities near midrapidity in central

Au + Au collisions seems to be followed up to RHIC energies (named as “Barshay and Kreyerhoff” in the figure) [124]. Perturbative QCD-inspired Monte Carlo event generators, the HIJING model without jet quenching [125], the Dual Parton Model [126] (named “DPMJET III” in the figure), and the Ultrarelativistic Quantum Molecular Dynamics model [127] (named “UrQMD” in the figure) are consistent with the measurement. The HIJING model results without jet quenching were also consistent with the RHIC measurements. The semimicroscopic models like LEXUS are successful in explaining the observed multiplicity at RHIC (named as “Jeon and Kapusta” in the figure) [128]. Models based on initial-state gluon density saturation have a range of predictions depending on the specifics of the implementation [129–133]. The best agreement with LHC data happens for model as described in (named as “Kharzeev et al.” and “Armesto et al.” in the figure) [131, 133]. Conclusions for RHIC energy from these models are similar. The prediction of a hybrid model based on hydrodynamics and saturation of final-state phase space of scattered partons (named as “Eskola et al.” in the figure) [134] is slightly on a higher side compared to the measurement at LHC. But such a model seems to do a reasonable job for RHIC energies [135]. Another hydrodynamic model in which multiplicity is scaled from $p + p$ collisions overpredicts the measurement (named as “Bozek et al.” in the figure) [136]. Models incorporating constituent quark scaling and Landau hydrodynamics (named as “Sarkisyan and Sakharov” in the figure) [137, 138] and based on modified PYTHIA

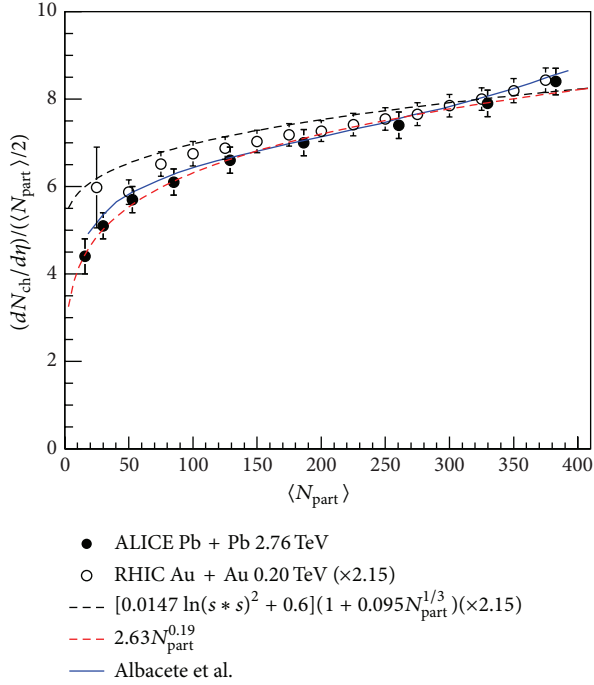


FIGURE 17: (Color online) Centrality dependence of $(dN_{\text{ch}}/d\eta)/(\langle N_{\text{part}} \rangle/2)$ for Pb + Pb collisions at $\sqrt{s_{\text{NN}}} = 2.76$ TeV [14] and Au + Au collisions at $\sqrt{s_{\text{NN}}} = 200$ GeV. The RHIC results are scaled up by a factor of 2.15. Also shown are comparisons to theoretical model calculations [144] and some parametrization based on detail shape of $dN_{\text{ch}}/d\eta$ distributions at RHIC [47] and $\langle N_{\text{part}} \rangle$.

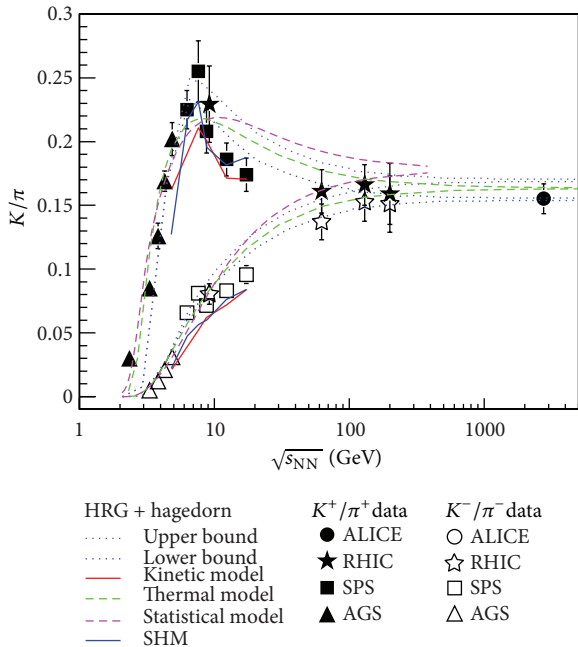


FIGURE 18: (Color online) Energy dependence of K^\pm/π^\pm ratio for central collisions at midrapidity. Errors are statistical and systematic added in quadrature. Results are also compared with various theoretical model predictions [79, 147–150].

and hadronic re-scattering (named as “Humanic” in the figure) [139] underpredict the measurement at LHC energy. At RHIC energies, models considering minijet production in ultrarelativistic heavy-ion collisions by taking semihard parton rescatterings explicitly into account underpredict the multiplicities (named as “Accardi” in the figure) [140]. It is also seen at RHIC energies that models based on string fusion [141] and dual string model [142] seem to work well, whereas those based on heavy-ion cascade LUCIFER model [143] underpredict the data.

Figure 17 shows the $(dN_{\text{ch}}/d\eta)/(\langle N_{\text{part}} \rangle/2)$ versus $\langle N_{\text{part}} \rangle$ for Pb + Pb collisions at $\sqrt{s_{\text{NN}}} = 2.76$ TeV [14]. Also shown are the corresponding RHIC results scaled up by a factor 2.15. Remarkable similarity is observed in the shape of the distributions at RHIC and LHC energies. Particle production based on saturation model explains the trends nicely (named as “Albacete and Dumitru” in the figure) [144] (published after the most central $dN_{\text{ch}}/d\eta$ value [25] was known). simple fit to the data using a power law form for the $\langle N_{\text{part}} \rangle$ also explains the measurements. In addition, a functional form inspired by the detailed shape of pseudorapidity distribution of charged particle multiplicity distributions at RHIC [47] explains the centrality trends nicely.

Strangeness production in heavy-ion collisions is a classic signature for formation of QGP [145]. The particle yield ratio K/π could reflect the strangeness enhancement in heavy-ion collisions with respect to the elementary collisions. Figure 18 shows the energy dependence of K^\pm/π^\pm ratio for central collisions at midrapidity. It will be interesting to see which model explains such an impressive collection of systematic data on K/π ratio. Figure 18 also shows the energy dependence of K/π ratio from various theoretical model calculations. The energy dependence of K^+/π^+ ratio has been interpreted using the Statistical Model of Early Stage (SMES) [146]. The model predicts first-order phase transition and the existence of mixed phase around beam energy of 7-8 GeV. The SHM or statistical hadronization model [147] assumes that the strong interactions saturate the particle production matrix elements. This means that the yield of particles is controlled predominantly by the magnitude of the accessible phase space. The system is in chemical nonequilibrium for $\sqrt{s_{\text{NN}}} < 7.6$ GeV, while for higher energies, the oversaturation of chemical occupancies is observed. The statistical model [148] assumes that the ratio of entropy to T^3 as a function of collision energy increases for mesons and decreases for baryons. Thus, a rapid change is expected at the crossing of the two curves, as the hadronic gas undergoes a transition from a baryon-dominated to a meson-dominated gas. The transition point is characterized by $T = 140$ MeV, $\mu_B = 410$ MeV, and $\sqrt{s_{\text{NN}}} = 8.2$ GeV. In the thermal model [79], the energy dependence of K^\pm/π^\pm is studied by including σ -meson, which is neglected in most of the models, and many higher mass resonances ($m > 2$ GeV/ c^2) into the resonance spectrum employed in the statistical model calculations. The hadronic nonequilibrium kinetic model [149] assumes that the surplus of strange particles is produced in secondary reactions of hadrons generated in nuclear collisions. Then, the two important aspects are the available energy density and the

lifetime of the fireball. It is suggested that these two aspects combine in such a way so as to show a sharp peak for the strangeness-to-entropy or K/π ratio as a function of beam energy. In the hadron resonance gas and hagedorn (HRG + Hagedorn) model [150], all hadrons as given in PDG with masses up to $2 \text{ GeV}/c^2$ are included. The unknown hadron resonances in this model are included through Hagedorn's formula for the density of states. The model assumes that the strangeness in the baryon sector decays to strange baryons and does not contribute to the kaon production. The energy dependence of K^\pm/π^\pm ratio seems to be best explained using HRG + Hagedorn model.

This systematic measurement of K/π ratio reveals two interesting pieces of information. (a) The K^+/π^+ ratio shows a peak around $\sqrt{s_{\text{NN}}} = 8 \text{ GeV}$, while the K^-/π^- ratio increases monotonically; the peak indicates the role of the maximum baryon density at freeze-out around this collision energy. (b) For $\sqrt{s_{\text{NN}}} > 100 \text{ GeV}$, pair production becomes the dominant mechanism for K^\pm production, so both the ratios K^+/π^+ and K^-/π^- approach the value of 0.16. Taking into account the different masses between pions and kaons, this asymptotic value corresponds to a temperature of the order of 160 MeV.

4.2. Azimuthal Anisotropy. The azimuthal anisotropy parameter v_2 , measured at RHIC and LHC, provides a unique opportunity to study the transport properties of the fundamental constituents of any visible matter, a system of quarks and gluons. Furthermore, it provides an opportunity to understand whether the underlying dynamics of the evolution of the system formed in the collisions are governed by macroscopic hydrodynamics [151–153] or by microscopic transport approach [154]. Figure 19 shows the v_2 versus p_T for 30–40% collision centrality Au + Au and Pb + Pb collisions at midrapidity for $\sqrt{s_{\text{NN}}} = 200 \text{ GeV}$ and 2.76 TeV , respectively. The measurements are compared to a set of model calculations based on hydrodynamic approach (including THERMINATOR [155, 156]) and another set of calculations based on transport approach. It is observed that hydrodynamic-based models explain the v_2 measurements both at RHIC and LHC energies. Transport-based models including partonic interactions (like AMPT [154]) also explain the v_2 measurements. However, those transport models which do not incorporate partonic interactions like UrQMD [157, 158] fail to explain the data. The model comparison also reveals that the data favors a high degree of fluidity reflected by a small value of shear viscosity to entropy density ratio (η/s) < 0.2 . A more detailed comparison of the model calculations with various order azimuthal anisotropy parameters v_n would in the near future give us a more quantitative picture of the temperature (or energy) dependence of transport coefficients of the system formed in the heavy-ion collisions.

4.3. Nuclear Modification Factor. The nuclear modification factor (R_{AA}) is an observable used to study the structure of strongly interacting dense matter formed in heavy-ion collisions. Here, we discuss the observation of $R_{\text{AA}} < 1$ at high p_T seen at RHIC and LHC by comparing two models within perturbative QCD- (pQCD-) based formalisms. In

this picture, the high p_T hadrons are expected to originate from the fragmentation of hard partons (hard scattering scales larger than QCD scales of 200 MeV). The hard partons lose energy through interactions with the hot and dense mediums, which get reflected in the observed values of R_{AA} . The processes by which they could lose energy includes radiative energy loss and elastic energy loss. For a more elaborate discussion on these models, we refer the reader to the review article [159].

In Figure 20, we show a comparison between experimentally measured R_{AA} versus p_T at LHC and RHIC energies and corresponding pQCD-based model calculations. All theoretical formalisms require a microscopic model of the medium to set the input parameters for the energy loss calculation. These parameters, for example, are denoted as $\langle \hat{q} \rangle$, the transport coefficient of the medium or the gluon number density dN^g/dy per unit rapidity. The parameter P_{esc} , on the other hand, reflects the strength of elastic energy loss put in the model calculations. Without going into deeper theoretical discussions of each model, we refer the readers to the following related publications: PQM [160], GLV [161], ASW [162], YaJEM [163], WHDG [164], and ZOWW [165]. However, for completeness and to elucidate the approach taken in the model calculations, we briefly mention two formalisms as examples: the GLV approach named after their authors Gyulassy, Levai, and Vitev and ASW approach named after the corresponding authors Armesto, Salgado and Wiedemann, where the medium is defined as separated heavy static scattering centers with color screened potentials, where as in some other formalism, a more precise definition of the medium is considered as being composed of quark gluon quasiparticles with dispersion relations and interactions given by the hard thermal loop effective theory.

We observe that most models predict the p_T dependence of R_{AA} well for collisions both at RHIC and LHC energies. The models specially capture the generally rising behavior of R_{AA} that is observed in the data at high p_T for the LHC energies. The magnitude of the predicted slope of R_{AA} versus p_T varies between models, depending on the assumptions for the jet-quenching mechanism. The models shown do not need larger values of medium density in the calculation to explain the R_{AA} for $3 < p_T < 20 \text{ GeV}/c$ at RHIC and LHC for the common kinematic range. They however, require a high medium density at LHC energy to explain the values of R_{AA} for $p_T > 20 \text{ GeV}/c$.

5. Summary

In summary, the results on multiplicity density in pseudo-rapidity, HBT, azimuthal anisotropy, and nuclear modification factor from LHC experiments indicate that the fireball produced in these nuclear collisions is hotter, lives longer, and expands to a larger size at freeze-out compared to lower energies. These results also confirm the formation of a deconfined state of quarks and gluons at RHIC energies. The measurements at LHC provide a unique kinematic access to study in detail the properties (such as transport coefficients) of this system of quarks and gluons.

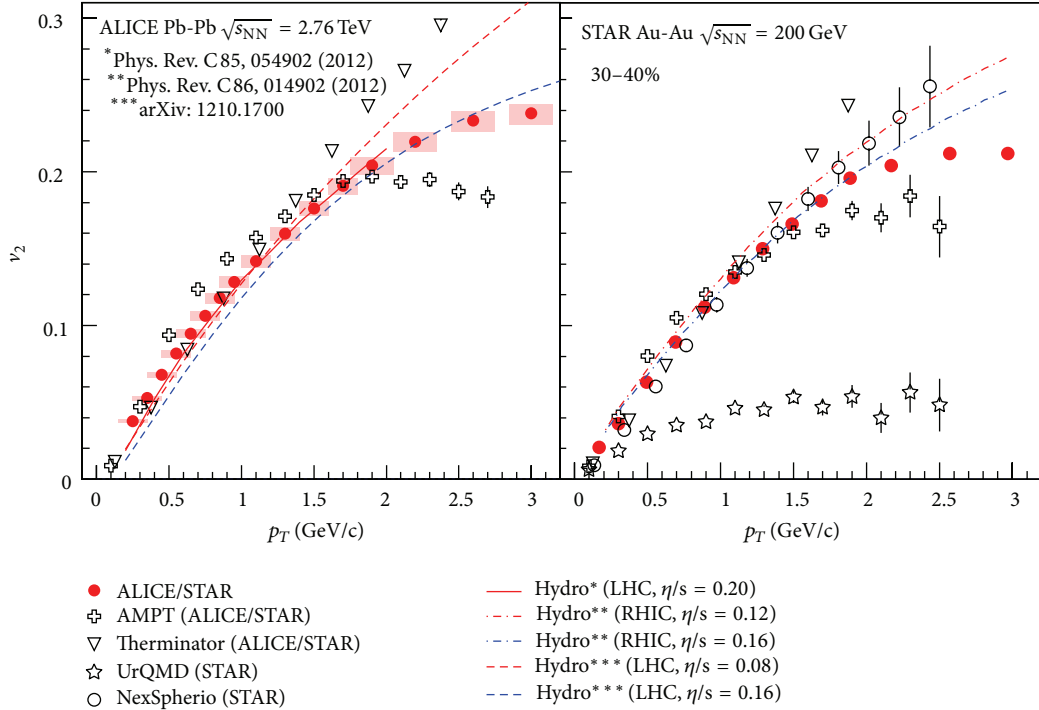


FIGURE 19: (Color online) The azimuthal anisotropy parameter v_2 , measured in noncentral heavy-ion collisions at midrapidity for RHIC and LHC energies. For comparison, shown are the various theoretical calculations based on hydrodynamic and transport approaches (see text for details).

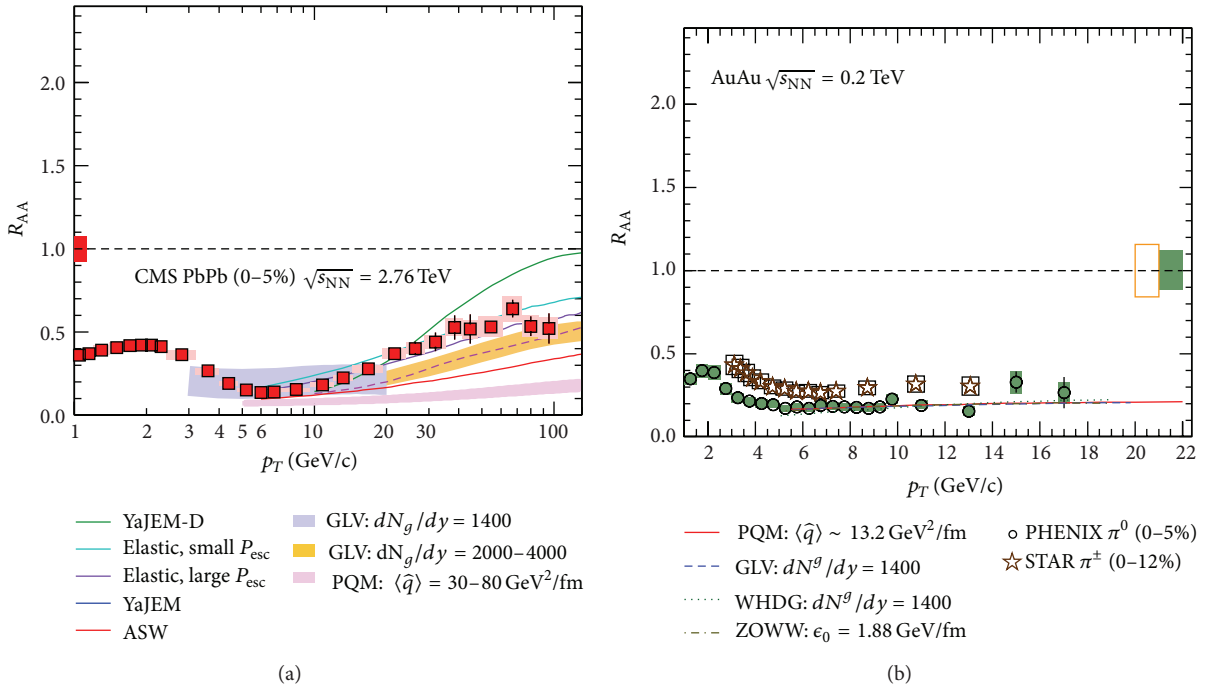


FIGURE 20: (Color online) Measurements of the nuclear modification factor R_{AA} in central heavy-ion collisions at two different center-of-mass energies, as a function of p_T , for pions ($\pi^{\pm,0}$) [174, 175] and charged hadrons [26, 27], compared to several theoretical predictions (see text). The error bars on the points are the statistical uncertainties, and the boxes around the data points are the systematic uncertainties. Additional absolute normalization uncertainties of order 5% to 10% are not plotted. The bands for several of the theoretical calculations represent their uncertainties.

In this review, we showed that the first set of measurements made by the three LHC experiments within the heavy-ion programs, ALICE, ATLAS, and CMS, show a high degree of consistency. These measurements include centrality dependence of charged particle multiplicity, azimuthal anisotropy, and nuclear modification factor versus transverse momentum. Next, we discussed the comparison of various measurements made at RHIC and LHC energies. LHC measurements of $dN_{ch}/d\eta$ clearly demonstrated the power law dependence of charged particle multiplicity on the beam energy. They also reconfirmed the observation at RHIC that particle production mechanism is not a simple superposition of several $p + p$ collisions. The values of $\langle m_T \rangle$, ϵ_{BJ} , freeze-out volume, decoupling time for hadrons, and $\langle v_2 \rangle$ and $\langle \beta \rangle$ are larger at LHC energies compared to those at RHIC energies, even though the freeze-out temperatures are comparable. The value of the net-charge fluctuation measure is observed to rapidly approach towards a simple model-based calculation for QGP state. However, the sensitivity of this observable for a heavy-ion system as well as the lack of proper modeling of the heavy-ion system theoretically for such an observable needs careful consideration. The v_2 fluctuations as a function of centrality fraction have a similar value at both RHIC and LHC. This reflects their sensitivity to initial state effects. Just like at RHIC, the R_{dAu} and direct photon R_{AA} measurements experimentally demonstrated that the observed $R_{AA} < 1$ for charged hadrons is a final state effect; also at LHC, the R_{pPb} , direct photon, and W^\pm and Z^0 R_{AA} measurements showed that the observed $R_{AA} < 1$ is indeed due to formation of a dense medium of colored charges in central heavy-ion collisions. All these conclusions were further validated by the comparison of several observables to corresponding model calculations. Further, it was found that the fluid at LHC shows a comparable degree of fluidity as that at RHIC. This is reflected by a small value of shear viscosity to entropy density ratio.

Measurements-related heavy quark production [166–168], dilepton production, jet-hadron correlations [169, 170], and higher-order azimuthal anisotropy [171, 172] which are now coming out of both RHIC and LHC experiments will provide a much more detailed characterization of the properties of the QCD matter formed in heavy-ion collisions.

Acknowledgments

The authors would like to thank F. Antinori, S. Gupta, D. Keane, A. K. Mohanty, Y. P. Viyogi, and N. Xu for reading the paper and for their helpful discussions and comments. Bedangadas Mohanty is supported by the DAE-SRC project fellowship for this work. Lokesh Kumar is partly supported by the DOE Grant DE-FG02-89ER40531 for carrying out this work.

References

- [1] B. Mohanty, “Exploring the quantum chromodynamics landscape with high-energy nuclear collisions,” *New Journal of Physics*, vol. 13, Article ID 065031, 2011.
- [2] B. Mohanty, “QCD phase diagram: phase transition, critical point and fluctuations,” *Nuclear Physics A*, vol. 830, no. 1–4, pp. 899C–907C, 2009.
- [3] K. Fukushima and T. Hatsuda, “The phase diagram of dense QCD,” *Reports on Progress in Physics*, vol. 74, no. 1, Article ID 014001, 2011.
- [4] S. Gupta, X. Luo, B. Mohanty, H. G. Ritter, and N. Xu, “Scale for the phase diagram of quantum chromodynamics,” *Science*, vol. 332, no. 6037, pp. 1525–1528, 2011.
- [5] A. Bazavov, T. Bhattacharya, M. Cheng et al., “Chiral and deconfinement aspects of the QCD transition,” *Physical Review D*, vol. 85, no. 5, Article ID 054503, 37 pages, 2012.
- [6] S. Borsányi, Z. Fodor, C. Hoelbling et al., “Is there still any T_c mystery in lattice QCD? Results with physical masses in the continuum limit III,” *Journal of High Energy Physics*, vol. 2010, article 73, 2010.
- [7] I. Arsene, I. G. Bearden, D. Beavis et al., “Quark-gluon plasma and color glass condensate at RHIC? The perspective from the BRAHMS experiment,” *Nuclear Physics A*, vol. 757, no. 1–2, pp. 1–27, 2005.
- [8] B. B. Back, M. D. Baker, M. Ballintijn et al., “The PHOBOS perspective on discoveries at RHIC,” *Nuclear Physics A*, vol. 757, no. 1–2, pp. 28–101, 2005.
- [9] J. Adams, M. M. Aggarwal, Z. Ahammed et al., “Experimental and theoretical challenges in the search for the quark-gluon plasma: the STAR collaboration’s critical assessment of the evidence from RHIC collisions,” *Nuclear Physics A*, vol. 757, no. 1–2, pp. 102–183, 2005.
- [10] K. Adcox, S. S. Adler, S. Afanasiev et al., “Formation of dense partonic matter in relativistic nucleus-nucleus collisions at RHIC: experimental evaluation by the PHENIX collaboration,” *Nuclear Physics A*, vol. 757, no. 1–2, pp. 184–283, 2005.
- [11] M. Gyulassy and L. McLerran, “New forms of QCD matter discovered at RHIC,” *Nuclear Physics A*, vol. 750, no. 1, pp. 30–63, 2005.
- [12] B. Mohanty and STAR Collaboration, “STAR experiment results from the beam energy scan program at the RHIC,” *Journal of Physics G*, vol. 38, no. 12, Article ID 124023, 2011.
- [13] M. L. Miller, K. Reygers, S. J. Sanders, and P. Steinberg, “Glauber modeling in high-energy nuclear collisions,” *Annual Review of Nuclear and Particle Science*, vol. 57, pp. 205–243, 2007.
- [14] K. Aamodt, A. A. Quintana, D. Adamová et al., “Centrality dependence of the charged-particle multiplicity density at midrapidity in Pb-Pb collisions at $\sqrt{s_{NN}} = 2.76$ TeV,” *Physical Review Letters*, vol. 106, no. 3, Article ID 032301, 10 pages, 2011.
- [15] S. Chatrchyan, V. Khachatryan, A. M. Sirunyan et al., “Dependence on pseudorapidity and on centrality of charged hadron production in PbPb collisions at $\sqrt{s_{NN}} = 2.76$ TeV,” *Journal of High Energy Physics*, vol. 2011, article 141, 2011.
- [16] G. Aad, B. Abbott, J. Abdallah et al., “Measurement of the centrality dependence of the charged particle pseudorapidity distribution in lead-lead collisions at $\sqrt{s_{NN}} = 2.76$ TeV with the ATLAS detector,” *Physics Letters B*, vol. 710, no. 3, pp. 363–382, 2012.
- [17] S. Chatrchyan, V. Khachatryan, A. M. Sirunyan et al., “Azimuthal anisotropy of charged particles at high transverse momenta in Pb-Pb collisions at $\sqrt{s_{NN}} = 2.76$ TeV,” *Physical Review Letters*, vol. 109, no. 2, Article ID 022301, 15 pages, 2012.
- [18] S. Chatrchyan, V. Khachatryan, A. M. Sirunyan et al., “Measurement of the azimuthal anisotropy of neutral pions in Pb-Pb collisions at $\sqrt{s_{NN}} = 2.76$ TeV,” *Physical Review Letters*, vol. 110, no. 4, Article ID 042301, 15 pages, 2013.

- [19] S. Chatrchyan, V. Khachatryan, A. M. Sirunyan et al., “Measurement of the elliptic anisotropy of charged particles produced in PbPb collisions at $\sqrt{s_{NN}} = 2.76$ TeV,” *Physical Review C*, vol. 87, no. 1, Article ID 014902, 34 pages, 2013.
- [20] S. Chatrchyan, V. Khachatryan, A. M. Sirunyan et al., “Centrality dependence of dihadron correlations and azimuthal anisotropy harmonics in PbPb collisions at $\sqrt{s_{NN}} = 2.76$ TeV,” *European Physical Journal C*, vol. 72, Article ID 10052, 2012.
- [21] G. Aad, B. Abbott, J. Abdallah et al., “Measurement of the pseudorapidity and transverse momentum dependence of the elliptic flow of charged particles in lead-lead collisions at $\sqrt{s_{NN}} = 2.76$ TeV with the ATLAS detector,” *Physics Letters B*, vol. 707, no. 3-4, pp. 330–348, 2012.
- [22] G. Aad, B. Abbott, J. Abdallah et al., “Measurement of the distributions of event-by-event flow harmonics in lead-lead collisions at $\sqrt{s_{NN}} = 2.76$ TeV with the ATLAS detector at the LHC,” <http://arxiv.org/abs/1305.2942>.
- [23] G. Aad, B. Abbott, J. Abdallah et al., “Measurement of the azimuthal anisotropy for charged particle production in $\sqrt{s_{NN}} = 2.76$ TeV lead-lead collisions with the ATLAS detector,” *Physical Review C*, vol. 86, no. 1, Article ID 014907, 41 pages, 2012.
- [24] J. Jia and ATLAS Collaboration, “Measurement of event plane correlations in Pb-Pb collisions at $\sqrt{s_{NN}} = 2.76$ TeV with the ATLAS detector,” *Nuclear Physics A*, vol. 910-911, pp. 276–280, 2013.
- [25] K. Aamodt, B. Abelev, A. A. Quintana et al., “Elliptic flow of charged particles in Pb-Pb collisions at $\sqrt{s_{NN}} = 2.76$ TeV,” *Physical Review Letters*, vol. 105, no. 25, Article ID 252302, 11 pages, 2010.
- [26] K. Aamodt, B. Abelev, A. A. Quintana et al., “Suppression of charged particle production at large transverse momentum in central Pb-Pb collisions at $\sqrt{s_{NN}} = 2.76$ TeV,” *Physics Letters B*, vol. 696, no. 1-2, pp. 30–39, 2011.
- [27] S. Chatrchyan, V. Khachatryan, A. M. Sirunyan et al., “Study of high- p_T charged particle suppression in PbPb compared to pp collisions at $\sqrt{s_{NN}} = 2.76$ TeV,” *European Physical Journal C*, vol. 72, article 1945, 2012.
- [28] A. N. Mishra and R. Sahoo, “Towards a universality in particle production in heavy-ion collisions,” <http://arxiv.org/abs/1304.2113>.
- [29] B. B. Back, M. D. Baker, M. Ballintijn et al., “Pseudorapidity distribution of charged particles in $d+Au$ collisions at $\sqrt{s_{NN}} = 200$ GeV,” *Physical Review Letters*, vol. 93, no. 8, Article ID 082301, 5 pages, 2004.
- [30] M. C. Abreu, B. Alessandro, C. Alexa et al., “Pseudorapidity distributions of charged particles as a function of centrality in Pb-Pb collisions at 158 and 40 GeV per nucleon incident energy,” *Physics Letters B*, vol. 530, no. 1-4, pp. 33–42, 2002.
- [31] C. Adler, Z. Ahammed, C. Allgower et al., “Multiplicity distribution and spectra of negatively charged hadrons in $Au+Au$ collisions at $\sqrt{s_{NN}} = 130$ GeV,” *Physical Review Letters*, vol. 87, no. 11, Article ID 112303, 5 pages, 2001.
- [32] I. G. Bearden, D. Beavis, C. Besliu et al., “Charged particle densities from $Au+Au$ collisions at $\sqrt{s_{NN}} = 130$ GeV,” *Physics Letters B*, vol. 523, no. 3-4, pp. 227–233, 2001.
- [33] I. G. Bearden, D. Beavis, C. Besliu et al., “Pseudorapidity distributions of charged particles from $Au+Au$ collisions at the maximum RHIC energy, $\sqrt{s_{NN}} = 200$ GeV,” *Physical Review Letters*, vol. 88, no. 20, Article ID 202301, 4 pages, 2002.
- [34] K. Adcox, S. S. Adler, N. N. Ajitanand et al., “Centrality dependence of charged particle multiplicity in $Au-Au$ collisions at $\sqrt{s_{NN}} = 130$ GeV,” *Physical Review Letters*, vol. 86, no. 16, pp. 3500–3505, 2001.
- [35] B. B. Back, M. D. Baker, D. S. Barton et al., “Charged-particle multiplicity near midrapidity in central $Au+Au$ collisions at $\sqrt{s_{NN}} = 130$ GeV,” *Physical Review Letters*, vol. 85, no. 15, pp. 3100–3104, 2000.
- [36] B. B. Back, M. D. Baker, D. S. Barton et al., “Significance of the fragmentation region in ultrarelativistic heavy-ion collisions,” *Physical Review Letters*, vol. 91, no. 5, Article ID 052303, 4 pages, 2003.
- [37] W. Thome, K. Eggert, K. Giboni et al., “Charged particle multiplicity distributions in pp collisions at ISR energies,” *Nuclear Physics B*, vol. 129, no. 3, pp. 365–389, 1977.
- [38] C. Albajar, M. G. Albrow, O. C. Allkofer et al., “A study of the general characteristics of proton-antiproton collisions at $\sqrt{s} = 0.2$ to 0.9 TeV,” *Nuclear Physics B*, vol. 335, no. 2, pp. 261–287, 1990.
- [39] K. Alpgard, R. E. Ansorge, B. Åsman et al., “Particle multiplicities in $\bar{p}p$ interactions at $\sqrt{s} = 540$ GeV,” *Physics Letters B*, vol. 121, no. 2-3, pp. 209–215, 1983.
- [40] G. Alner, R. E. Ansorge, B. Åsman et al., “Scaling of pseudorapidity distributions at c.m. energies up to 0.9 TeV,” *Zeitschrift für Physik C*, vol. 33, no. 1, pp. 1–6, 1986.
- [41] T. Alber and NA35 Collaboration, “Charged particle production in proton-, deuteron-, oxygen- and sulphur-nucleus collisions at 200 GeV per nucleon,” *The European Physical Journal C*, vol. 2, no. 4, pp. 643–659, 1998.
- [42] F. Abe, D. Amidei, G. Apollinari et al., “Pseudorapidity distributions of charged particles produced in $\bar{p}p$ interactions at $\sqrt{s} = 630$ and 1800 GeV,” *Physical Review D*, vol. 41, no. 7, pp. 2330–2333, 1990.
- [43] K. Aamodt, B. Abelev, A. Quintana et al., “Charged-particle multiplicity measurement in proton-proton collisions at $\sqrt{s} = 7$ TeV with ALICE at LHC,” *The European Physical Journal C*, vol. 68, no. 3-4, pp. 345–354, 2010.
- [44] V. Khachatryan, M. Sirunyan, A. Tumasyan et al., “Transverse momentum and pseudorapidity distributions of charged hadrons in pp collisions at $\sqrt{s} = 0.9$ and 2.36 TeV,” *Journal of High Energy Physics*, vol. 1002, article 41, 2010.
- [45] W. Thome, K. Eggert, K. Giboni et al., “Charged particle multiplicity distributions in pp collisions at ISR energies,” *Nuclear Physics B*, vol. 129, no. 3, pp. 365–389, 1977.
- [46] K. Aamodt, N. Abel, U. Abeysekara et al., “Charged-particle multiplicity measurement in proton-proton collisions at $\sqrt{s} = 0.9$ and 2.36 TeV with ALICE at LHC,” *European Physical Journal C*, vol. 68, no. 1-2, pp. 89–108, 2010.
- [47] B. Alver, B. B. Back, M. D. Baker et al., “Charged-particle multiplicity and pseudorapidity distributions measured with the PHOBOS detector in $Au+Au$, $Cu+Cu$, $d+Au$, and $p+p$ collisions at ultrarelativistic energies,” *Physical Review C*, vol. 83, no. 2, Article ID 024913, 24 pages, 2011.
- [48] B. Abelev, J. Adam, D. Adamová et al., “Pseudorapidity density of charged particles in $p+Pb$ collisions at $\sqrt{s_{NN}} = 5.02$ TeV,” *Physical Review Letters*, vol. 110, no. 3, Article ID 032301, 10 pages, 2013.
- [49] T. Alber and NA35 Collaboration, “Charged particle production in proton-, deuteron-, oxygen- and sulphur-nucleus collisions at 200 GeV per nucleon,” *The European Physical Journal C*, vol. 2, no. 4, pp. 643–659, 1998.
- [50] L. Ahle, Y. Akibad, K. Ashktorab et al., “Excitation function of K^+ and π^+ production in $Au+Au$ reactions at $2-10$ AGeV,” *Physics Letters B*, vol. 476, no. 1-2, pp. 1–8, 2000.

- [51] J. Barrette, R. Bellwied, S. Bennett et al., “Proton and pion production in Au+Au collisions at 10.8A GeV/c,” *Physical Review C*, vol. 62, no. 2, Article ID 024901, 8 pages, 2000.
- [52] J. T. Mitchell and PHENIX Collaboration, “The RHIC beam energy scan program: results from the PHENIX experiment,” *Nuclear Physics A*, vol. 904-905, pp. 903c-906c, 2013.
- [53] C. Alt, T. Anticic, B. Baatar et al., “Pion and kaon production in central Pb+Pb collisions at 20A and 30A GeV: evidence for the onset of deconfinement,” *Physical Review C*, vol. 77, no. 2, Article ID 024903, 10 pages, 2008.
- [54] B. I. Abelev, M. M. Aggarwal, Z. Ahammed et al., “Identified particle production, azimuthal anisotropy, and interferometry measurements in Au+Au collisions at $\sqrt{s_{NN}} = 9.2$ GeV,” *Physical Review C*, vol. 81, no. 2, Article ID 024911, 19 pages, 2010.
- [55] B. Abelev, J. Adam, D. Adamová et al., “Pion, kaon, and proton production in central Pb-Pb collisions at $\sqrt{s_{NN}} = 2.76$ TeV,” *Physical Review Letters*, vol. 109, no. 25, Article ID 252301, 11 pages, 2012.
- [56] B. Mohanty, J. E. Alam, S. Sarkar, T. K. Nayak, and B. K. Nandi, “Indication of a coexisting phase of quarks and hadrons in nucleus-nucleus collisions,” *Physical Review C*, vol. 68, no. 2, Article ID 021901, 4 pages, 2003.
- [57] L. Van Hove, “Multiplicity dependence of pt spectrum as a possible signal for a phase transition in hadronic collisions,” *Physics Letters B*, vol. 118, no. 1-3, pp. 138-140, 1982.
- [58] J. D. Bjorken, “Highly relativistic nucleus-nucleus collisions: the central rapidity region,” *Physical Review D*, vol. 27, no. 1, pp. 140-151, 1983.
- [59] C. Loizides, “Charged-particle multiplicity and transverse energy in Pb-Pb collisions at $\sqrt{s_{NN}} = 2.76$ TeV with ALICE,” *Journal of Physics G*, vol. 38, no. 12, Article ID 124040, 2011.
- [60] S. Chatrchyan, V. Khachatryan, A. M. Sirunyan et al., “Measurement of the pseudorapidity and centrality dependence of the transverse energy density in Pb-Pb collisions at $\sqrt{s_{NN}} = 2.76$ TeV,” *Physical Review Letters*, vol. 109, no. 15, Article ID 152303, 16 pages, 2012.
- [61] J. T. Mitchell and PHENIX Collaboration, “The RHIC beam energy scan program: results from the PHENIX experiment,” <http://arxiv.org/abs/1211.6139>.
- [62] S. S. Adler, S. Afanasiev, C. Aidala et al., “Systematic studies of the centrality and $\sqrt{s_{NN}}$ dependence of the $dET/d\eta$ and $dNch/d\eta$ in heavy ion collisions at midrapidity,” *Physical Review C*, vol. 71, no. 3, Article ID 034908, 25 pages, 2005, Erratum in *Physical Review C*, vol. 71, Article ID 049901, 2005.
- [63] K. Adcox, S. S. Adler, N. N. Ajitanand et al., “Measurement of the midrapidity transverse energy distribution from $\sqrt{s_{NN}} = 130$ GeV Au+Au collisions at RHIC,” *Physical Review Letters*, vol. 87, no. 5, Article ID 052301, 6 pages, 2001.
- [64] M. M. Aggarwal, A. Agnihotri, Z. Ahammed et al., “Scaling of particle and transverse energy production in $^{208}\text{Pb}+^{208}\text{Pb}$ collisions at 158-A GeV,” *The European Physical Journal C*, vol. 18, no. 4, pp. 651-663, 2001.
- [65] G. F. Bertsch, “Pion interferometry as a probe of the plasma,” *Nuclear Physics A*, vol. 498, pp. 173-179, 1989.
- [66] S. Pratt, “Pion interferometry of quark-gluon plasma,” *Physical Review D*, vol. 33, no. 5, pp. 1314-1327, 1986.
- [67] D. Teaney, “Effect of shear viscosity on spectra, elliptic flow, and Hanbury Brown-Twiss radii,” *Physical Review C*, vol. 68, no. 3, Article ID 034913, 11 pages, 2003.
- [68] M. A. Lisa, N. N. Ajitanand, J. M. Alexander et al., “Bombarding energy dependence of π -interferometry at the Brookhaven AGS,” *Physical Review Letters*, vol. 84, no. 13, pp. 2798-2802, 2000.
- [69] C. Alt, T. Anticic, B. Baatar et al., “Bose-Einstein correlations of π - π -pairs in central Pb+Pb collisions at 20A,30A,40A,80A, and 158A GeV,” *Physical Review C*, vol. 77, no. 6, Article ID 064908, 20 pages, 2008.
- [70] D. Adamova, G. Agakichiev, H. Appelshäuser et al., “Beam energy and centrality dependence of two-pion Bose-Einstein correlations at SPS energies,” *Nuclear Physics A*, vol. 714, no. 1-2, pp. 124-144, 2003.
- [71] B. I. Abelev, M. M. Aggarwal, Z. Ahammed et al., “Pion interferometry in Au+Au and Cu+Cu collisions at $\sqrt{s_{NN}} = 62.4$ and 200 GeV,” *Physical Review C*, vol. 80, no. 2, Article ID 024905, 12 pages, 2009.
- [72] B. B. Back, M. D. Baker, M. Ballintijn et al., “Transverse momentum and rapidity dependence of Hanbury-Brown-Twiss correlations in Au+Au collisions at $\sqrt{s_{NN}} = 62.4$ and 200 GeV,” *Physical Review C*, vol. 73, no. 3, Article ID 031901, 5 pages, 2006.
- [73] K. Aamodt, A. A. Quintana, D. Adamová et al., “Two-pion Bose-Einstein correlations in central Pb-Pb collisions at $\sqrt{s_{NN}} = 2.76$ TeV,” *Physics Letters B*, vol. 696, no. 4, pp. 328-337, 2011.
- [74] W. Reisdorfa, D. Besta, A. Gobbi et al., “Central collisions of Au on Au at 150, 250 and 400 A·MeV,” *Nuclear Physics A*, vol. 612, pp. 493-556, 1997.
- [75] M. A. Lisa, S. Albergo, F. Bieser et al., “Radial flow in Au+Au collisions at $E = (0.25-1.15)$ AGeV,” *Physical Review Letters*, vol. 75, pp. 2662-2665, 1995.
- [76] C. Muntz and E802 Collaboration, “Recent results from E866 at BNL,” <http://arxiv.org/abs/nucl-ex/9806002>.
- [77] H. Appelshäuser, J. Bächler, S. J. Bailey et al., “Hadronic expansion dynamics in central Pb+Pb collisions at 158 GeV per nucleon,” *European Physical Journal C*, vol. 2, pp. 661-670, 1998.
- [78] A. Andronic, P. Braun-Munzinger, and J. Stachel, “Hadron production in central nucleus-nucleus collisions at chemical freeze-out,” *Nuclear Physics A*, vol. 772, no. 3-4, pp. 167-199, 2006.
- [79] A. Andronic, P. Braun-Munzinger, and J. Stachel, “Thermal hadron production in relativistic nuclear collisions: the hadron mass spectrum, the horn, and the QCD phase transition,” *Physics Letters B*, vol. 673, no. 2, pp. 142-145, 2009, Erratum in *Physics Letters B*, vol. 678, p. 516, 2009.
- [80] J. Cleymans, H. Oeschler, and K. Redlich, “Particle ratios at SPS, AGS and SIS,” *Journal of Physics G*, vol. 25, no. 2, p. 281, 1999.
- [81] J. Cleymans, D. Elliott, A. Keranen, and E. Suhonen, “Thermal model analysis of particle ratios in Ni+Ni experiments using exact strangeness conservation,” *Physical Review C*, vol. 57, no. 6, pp. 3319-3323, 1998.
- [82] P. Braun-Munzinger, J. Stachel, J. P. Wessels, and N. Xu, “Thermal equilibration and expansion in nucleus-nucleus collisions at the AGS,” *Physics Letters B*, vol. 344, no. 1-4, pp. 43-48, 1995.
- [83] P. Braun-Munzinger, I. Heppe, and J. Stachel, “Chemical equilibration in Pb+Pb collisions at the SPS,” *Physics Letters B*, vol. 465, no. 1-4, pp. 15-20, 1999.
- [84] F. Becattini and G. Pettini, “Strange quark production in a statistical effective model,” *Physical Review C*, vol. 67, no. 1, Article ID 015205, 12 pages, 2003.
- [85] F. Becattini, J. Cleymans, A. Keranen, E. Suhonen, and K. Redlich, “Features of particle multiplicities and strangeness production in central heavy ion collisions between 1.7A and 158A GeV/c,” *Physical Review C*, vol. 64, no. 2, Article ID 024901, 9 pages, 2001.

- [86] L. Milano and ALICE Collaboration, “Identified charged hadron production in Pb-Pb collisions at the LHC with the ALICE Experiment,” *Nuclear Physics A*, vol. 904-905, pp. 531c–534c, 2013.
- [87] J. Steinheimer, J. Aichelin, and M. Bleicher, “Nonthermal p/π ratio at LHC as a consequence of hadronic final state interactions,” *Physical Review Letters*, vol. 110, no. 4, Article ID 042501, 4 pages, 2013.
- [88] C. Pruneau, S. Gavin, and S. Voloshin, “Methods for the study of particle production fluctuations,” *Physical Review C*, vol. 66, no. 4, Article ID 044904, 12 pages, 2002.
- [89] H. Sako, H. Appelshäuser, and CERES/NA45 Collaboration, “vent-by-event fluctuations at 40, 80 and 158A GeV/c in Pb+Au collisions,” *Journal of Physics G*, vol. 30, no. 8, Article ID S1371, 2004.
- [90] B. I. Abelev, M. M. Aggarwal, Z. Ahammed et al., “Beam-energy and system-size dependence of dynamical net charge fluctuations,” *Physical Review C*, vol. 79, no. 2, Article ID 024906, 14 pages, 2009.
- [91] B. Abelev, J. Adam, D. Adamová et al., “Net-charge fluctuations in Pb-Pb collisions at $\sqrt{s_{NN}} = 2.76$ TeV,” *Physical Review Letters*, vol. 110, no. 15, Article ID 152301, 11 pages, 2013.
- [92] S. Jeon and V. Koch, “Charged particle ratio fluctuation as a signal for quark-gluon plasma,” *Physical Review Letters*, vol. 85, no. 10, pp. 2076–2079, 2000.
- [93] J. Y. Ollitrault, “Anisotropy as a signature of transverse collective flow,” *Physical Review D*, vol. 46, no. 1, pp. 229–245, 1992.
- [94] A. Andronic, V. Barret, Z. Basrak et al., “Excitation function of elliptic flow in Au+Au collisions and the nuclear matter equation of state,” *Physics Letters B*, vol. 612, no. 3-4, pp. 173–180, 2005.
- [95] N. Bastidm, A. Andronic, V. Barret et al., “First analysis of anisotropic flow with Lee-Yang zeros,” *Physical Review C*, vol. 72, no. 1, Article ID 011901, 5 pages, 2005.
- [96] ATLAS Collaboration, “Search for supersymmetry in events with at least one photon, one lepton, and large missing transverse momentum in proton—proton collision at a center-of-mass energy of 7 TeV with the ATLAS detector,” ATLAS-CONF-2012-117.
- [97] C. Pinkenburg, N. N. Ajitanand, J. M. Alexander et al., “Elliptic flow: transition from out-of-plane to in-plane emission in Au+Au collisions,” *Physical Review Letters*, vol. 83, no. 7, pp. 1295–1298, 1999.
- [98] D. Adamova and CERES collaboration, “New results from CERES,” *Nuclear Physics A*, vol. 698, no. 1–4, pp. 253–260, 2002.
- [99] C. Alt, T. Anticic, B. Baatar et al., “Directed and elliptic flow of charged pions and protons in Pb+Pb collisions at 40A and 158A GeV,” *Physical Review C*, vol. 68, no. 3, Article ID 034903, 32 pages, 2003.
- [100] J. Adams, M. M. Aggarwal, Z. Ahammed et al., “Azimuthal anisotropy in Au+Au collisions at $\sqrt{s_{NN}} = 200$ GeV,” *Physical Review C*, vol. 72, no. 1, Article ID 014904, 23 pages, 2005.
- [101] B. B. Back, M. D. Baker, M. Ballintijn et al., “Energy dependence of elliptic flow over a large pseudorapidity range in Au+Au collisions at the BNL relativistic heavy ion collider,” *Physical Review Letters*, vol. 94, no. 12, Article ID 122303, 4 pages, 2005.
- [102] S. Afanasiev, C. Aidala, N. N. Ajitanand et al., “Systematic studies of elliptic flow measurements in Au+Au collisions at $\sqrt{s_{NN}} = 200$ GeV,” *Physical Review C*, vol. 80, no. 2, Article ID 024909, 25 pages, 2009.
- [103] ATLAS Collaboration, ATLAS-CONF-2012-117.
- [104] A. Adare, S. Afanasiev, C. Aidala et al., “Measurements of higher order flow harmonics in Au+Au collisions at $\sqrt{s_{NN}} = 200$ GeV,” *Physical Review Letters*, vol. 107, no. 25, Article ID 252301, 7 pages, 2011.
- [105] K. Aamodt, B. Abelev, A. A. Quintana et al., “Higher harmonic anisotropic flow measurements of charged particles in Pb-Pb collisions at $\sqrt{s_{NN}} = 2.76$ TeV,” *Physical Review Letters*, vol. 107, no. 3, Article ID 032301, 10 pages, 2011.
- [106] A. Adare, S. Afanasiev, C. Aidala et al., “Deviation from quark number scaling of the anisotropy parameter v_2 of pions, kaons, and protons in Au+Au collisions at $\sqrt{s_{NN}} = 200$ GeV,” *Physical Review C*, vol. 85, no. 6, Article ID 064914, 14 pages, 2012.
- [107] B. Abelev, J. Adam, D. Adamová et al., “Anisotropic flow of charged hadrons, pions and (anti-)protons measured at high transverse momentum in Pb-Pb collisions at $\sqrt{s_{NN}} = 2.76$ TeV,” *Physics Letters B*, vol. 719, no. 1–3, pp. 18–28, 2013.
- [108] B. Müller, R. J. Fries, and S. A. Bass, “Thermal recombination: beyond the valence quark approximation,” *Physics Letters B*, vol. 618, no. 1–4, pp. 77–83, 2005.
- [109] V. Greco and C. M. Ko, “Effect of space-momentum correlations on the constituent quark number scaling of hadron elliptic flows,” <http://arxiv.org/abs/nucl-th/0505061>.
- [110] G. Agakishiev, M. M. Aggarwal, Z. Ahammed et al., “Energy and system-size dependence of two- and four-particle v_2 measurements in heavy-ion collisions at $\sqrt{s_{NN}} = 62.4$ and 200 GeV and their implications on flow fluctuations and nonflow,” *Physical Review C*, vol. 86, no. 1, Article ID 014904, 15 pages, 2012.
- [111] S. A. Voloshin, A. M. Poskanzer, A. Tang, and G. Wang, “Elliptic flow in the Gaussian model of eccentricity fluctuations,” *Physics Letters B*, vol. 659, no. 3, pp. 537–541, 2008.
- [112] S. Voloshin and Y. Zhang, “Flow study in relativistic nuclear collisions by Fourier expansion of Azimuthal particle distributions,” *Zeitschrift für Physik C*, vol. 70, no. 4, pp. 665–671, 1996.
- [113] S. A. Voloshin, A. M. Poskanzer, and R. Snellings, “Collective phenomena in non-central nuclear collisions,” <http://arxiv.org/abs/0809.2949>.
- [114] G. Aad and ATLAS Collaboration, “Measurement of the distributions of event-by-event flow harmonics in lead-lead collisions at $\sqrt{s_{NN}} = 2.76$ TeV with the ATLAS detector at the LHC,” <http://arxiv.org/abs/1305.2942>.
- [115] J. Adams, C. Adler, M. M. Aggarwal et al., “Evidence from d+Au measurements for final-state suppression of high- p_T hadrons in Au+Au collisions at RHIC,” *Physical Review Letters*, vol. 91, no. 7, Article ID 072304, 6 pages, 2003.
- [116] B. Abelev, J. Adam, D. Adamová et al., “Transverse momentum distribution and nuclear modification factor of charged particles in p+Pb collisions at $\sqrt{s_{NN}} = 5.02$ TeV,” *Physical Review Letters*, vol. 110, no. 8, Article ID 082302, 11 pages, 2013.
- [117] D. Antreasyan, J. W. Cronin, H. J. Frisch et al., “Production of kaons, protons, and antiprotons with large transverse momentum in p-p and p-d collisions at 200, 300, and 400 GeV,” *Physical Review Letters*, vol. 38, no. 3, pp. 115–117, 1977.
- [118] D. Antreasyan, J. W. Cronin, H. J. Frisch et al., “Production of π^+ and π^- at large transverse momentum in p-p and p-d collisions at 200, 300, and 400 GeV,” *Physical Review Letters*, vol. 38, no. 3, pp. 112–114, 1977.
- [119] S. S. Adler, S. Afanasiev, C. Aidala et al., “Centrality dependence of direct photon production in $\sqrt{s_{NN}} = 200$ GeV Au+Au collisions,” *Physical Review Letters*, vol. 94, no. 23, Article ID 232301, 6 pages, 2005.

- [120] S. Chatrchyan, V. Khachatryan, A.M. Sirunyan et al., “Measurement of isolated photon production in pp and PbPb collisions at $\sqrt{s_{NN}} = 2.76$ TeV,” *Physics Letters B*, vol. 710, no. 2, pp. 256–277, 2012.
- [121] S. Chatrchyan, V. Khachatryan, A.M. Sirunyan et al., “Study of W boson production in PbPb and pp collisions at $\sqrt{s_{NN}} = 2.76$ TeV,” *Physics Letters B*, vol. 715, no. 1–3, pp. 66–87, 2012.
- [122] S. Chatrchyan, V. Khachatryan, A. M. Sirunyan et al., “Study of Z boson production in PbPb collisions at $\sqrt{s_{NN}} = 2.76$ TeV,” *Physical Review Letters*, vol. 106, no. 21, Article ID 212301, 14 pages, 2011.
- [123] W. Busza, “Trends in multiparticle production and some “predictions” for pp and PbPb collisions at LHC,” *Journal of Physics G*, vol. 35, no. 4, Article ID 044040, 2008.
- [124] S. Barshay and G. Kreyerhoff, “Related power-law growth of particle multiplicities near midrapidity in central Au+Au collisions and in \bar{p} -p collisions,” *Nuclear Physics A*, vol. 697, no. 1-2, pp. 563–568, 2002, Erratum in *Nuclear Physics A*, vol. 703, p. 891, 2002.
- [125] W. T. Deng, X. N. Wang, and R. Xu, “Hadron production in p+p, p+Pb, and Pb+Pb collisions with the hijing 2.0 model at energies available at the CERN large hadron collider,” *Physical Review C*, vol. 83, no. 1, Article ID 014915, 9 pages, 2011.
- [126] F. W. Bopp, R. Engel, J. Ranft, and S. Roesler, “Inclusive distributions at the LHC as predicted from the DPMJET-III model with chain fusion,” <http://arxiv.org/abs/0706.3875>.
- [127] M. Mitrovski, T. Schuster, G. Graf, H. Petersen, and M. Bleicher, “Charged-particle (pseudo-)rapidity distributions in p+ \bar{p} /p+p and Pb+Pb/Au+Au collisions from UrQMD calculations at energies available at the CERN super proton synchrotron to the large hadron collider,” *Physical Review C*, vol. 79, no. 4, Article ID 044901, 6 pages, 2009.
- [128] S. Jeon and J. I. Kapusta, “Interpretation of the first data on central Au+Au collisions at $\sqrt{s} = 56A$ and 130A GeV,” *Physical Review C*, vol. 63, no. 1, Article ID 011901, 3 pages, 2001.
- [129] J. L. Albacete, “CGC and initial state effects in heavy ion collisions,” *Journal of Physics: Conference Series*, vol. 270, no. 1, Article ID 012052, 2011.
- [130] E. Levin and A. H. Rezaeian, “Hadron multiplicity in pp and AA collisions at LHC from the color glass condensate,” *Physical Review D*, vol. 82, no. 5, Article ID 054003, 6 pages, 2010.
- [131] D. Kharzeev, E. Levin, and M. Nardi, “Color glass condensate at the LHC: hadron multiplicities in pp, pA and AA collisions,” *Nuclear Physics A*, vol. 747, no. 2–4, pp. 609–629, 2005.
- [132] D. Kharzeev, E. Levin, and M. Nardi, “Hadron multiplicities at the LHC,” <http://arxiv.org/abs/0707.0811>.
- [133] N. Armesto, C. A. Salgado, and U. A. Wiedemann, “Relating high-energy Lepton-Hadron, proton-nucleus, and nucleus-nucleus collisions through geometric scaling,” *Physical Review Letters*, vol. 94, no. 2, Article ID 022002, 4 pages, 2005.
- [134] K. J. Eskola, P. V. Ruuskanen, S. S. Räsänen, and K. Tuominen, “Multiplicities and transverse energies in central AA collisions at RHIC and LHC from pQCD, saturation and hydrodynamics,” *Nuclear Physics A*, vol. 696, no. 3–4, pp. 715–728, 2001.
- [135] K. J. Eskola, K. Kajantie, and K. Tuominen, “Heavy-ion collision multiplicities and gluon distribution functions,” *Nuclear Physics A*, vol. 700, no. 1-2, pp. 509–522, 2002.
- [136] P. Bozek, M. Chojnacki, W. Florkowski, and B. Tomášik, “Hydrodynamic predictions for Pb+Pb collisions at $\sqrt{s_{NN}} = 2.76$ TeV,” *Physics Letters B*, vol. 694, no. 3, pp. 238–241, 2010.
- [137] E. K. G. Sarkisyan and A. S. Sakharov, “Relating multihadron production in hadronic and nuclear collisions,” *European Physical Journal C*, vol. 70, no. 3, pp. 533–541, 2010.
- [138] E. K. G. Sarkisyan and A. S. Sakharov, “Multihadron production features in different reactions,” *AIP Conference Proceedings*, vol. 828, pp. 35–41, 2006.
- [139] T. J. Humanic, “Predictions of hadronic observables in Pb+Pb collisions at $\sqrt{s_{NN}} = 2.76$ TeV from a hadronic rescattering model,” <http://arxiv.org/abs/1011.0378>.
- [140] A. Accardi, “Semi-hard scatterings at RHIC and LHC: initial conditions and charged multiplicities,” <http://arxiv.org/abs/hep-ph/0104060>.
- [141] N. Armesto, C. Pajares, and D. Sousa, “Analysis of the first RHIC results in the string fusion model,” *Physics Letters B*, vol. 527, no. 1-2, pp. 92–98, 2002.
- [142] J. D. de Deus and R. Ugoccioni, “Particle densities in heavy ion collisions at high energy and the dual string model,” *Physics Letters B*, vol. 491, no. 3-4, pp. 253–256, 2000.
- [143] D. E. Kahana and S. H. Kahana, “Inclusive particle spectra at (56 and 130)A GeV,” *Physical Review C*, vol. 63, no. 3, Article ID 031901, 4 pages, 2001.
- [144] J. L. Albacete and A. Dumitru, “A model for gluon production in heavy-ion collisions at the LHC with rcBK unintegrated gluon densities,” <http://arxiv.org/abs/1011.5161>.
- [145] P. Koch, B. Muller, and J. Rafelski, “Strangeness in relativistic heavy ion collisions,” *Physics Reports*, vol. 142, no. 4, pp. 167–262, 1986.
- [146] M. Gaździcki and M. I. Gorenstein, “On the early stage of nucleus-nucleus collisions,” *Acta Physica Polonica B*, vol. 30, p. 2705, 1999.
- [147] I. Kuznetsova and J. Rafelski, “Non-equilibrium heavy-flavored hadron yields from chemical equilibrium strangeness-rich QGP,” *Journal of Physics G*, vol. 35, no. 4, Article ID 044011, 2008.
- [148] J. Cleymans, H. Oeschler, K. Redlich, and S. Wheaton, “The thermal model and the transition from baryonic to mesonic freeze-out,” *European Physical Journal A*, vol. 29, no. 1, pp. 119–121, 2006.
- [149] B. Tomasik and E.E. Kolomeitsev, “Strangeness production time and the K+/ π + horn,” *European Physical Journal C*, vol. 49, no. 1, pp. 115–120, 2007.
- [150] S. Chatterjee, R. M. Godbole, and S. Gupta, “Stabilizing hadron resonance gas models,” *Physical Review C*, vol. 81, no. 4, Article ID 044907, 7 pages, 2010.
- [151] C. Shen and U. Heinz, “Collision energy dependence of viscous hydrodynamic flow in relativistic heavy-ion collisions,” *Physical Review C*, vol. 85, no. 5, Article ID 054902, 12 pages, 2012, Erratum in *Physical Review C*, vol. 86, Article ID 049903, 2012.
- [152] V. Roy, A. K. Chaudhuri, and B. Mohanty, “Comparison of results from a (2+1)-D relativistic viscous hydrodynamic model to elliptic and hexadecapole flow of charged hadrons measured in Au-Au collisions at $\sqrt{s_{NN}} = 200$ GeV,” *Physical Review C*, vol. 86, no. 1, Article ID 014902, 9 pages, 2012.
- [153] V. Roy, B. Mohanty, and A. K. Chaudhuri, “Elliptic and hexadecapole flow of charged hadrons in viscous hydrodynamics with Glauber and color glass condensate initial conditions for Pb-Pb collision at $\sqrt{s_{NN}} = 2.76$ TeV,” *Journal of Physics G*, vol. 40, no. 6, Article ID 065103, 2013.
- [154] J. Xu and C. M. Ko, “Pb-Pb collisions at $\sqrt{s_{NN}} = 2.76$ TeV in a multiphase transport model,” *Physical Review C*, vol. 83, no. 3, Article ID 034904, 5 pages, 2011.

- [155] M. Chojnacki, A. Kisiel, W. Florkowski, and W. Broniowski, "THERMINATOR 2: THERMal heavy IoN generATOR 2," *Computer Physics Communications*, vol. 183, no. 3, pp. 746–773, 2012.
- [156] A. Kisiel, T. Tałuć, W. Broniowski, and W. Florkowski, "THERMINATOR: THERMal heavy-IoN generATOR," *Computer Physics Communications*, vol. 174, no. 8, pp. 669–687, 2006.
- [157] S. A. Bass, M. Belkacem, M. Bleicher et al., "Microscopic models for ultrarelativistic heavy ion collisions," *Progress in Particle and Nuclear Physics*, vol. 41, pp. 255–369, 1998.
- [158] M. Bleicher, E. Zabrodin, C. Spieles et al., "Relativistic hadron-hadron collisions in the ultra-relativistic quantum molecular dynamics model," *Journal of Physics G*, vol. 25, no. 9, pp. 1859–1896, 1999.
- [159] A. Majumder and M. van Leeuwen, "The theory and phenomenology of perturbative QCD based jet quenching," *Progress in Particle and Nuclear Physics*, vol. 66, no. 1, pp. 41–92, 2011.
- [160] A. Dainese, C. Loizides, and G. Paic, "Leading-particle suppression in high energy nucleus-nucleus collisions," *European Physical Journal C*, vol. 38, no. 4, pp. 461–474, 2005.
- [161] I. Vitev and M. Gyulassy, "High-pT tomography of d+Au and Au+Au at SPS, RHIC, and LHC," *Physical Review Letters*, vol. 89, no. 25, Article ID 252301, 4 pages, 2002.
- [162] N. Armesto, A. Dainese, C. A. Salgado, and U. A. Wiedemann, "Testing the color charge and mass dependence of parton energy loss with heavy-to-light ratios at BNL RHIC and CERN LHC," *Physical Review D*, vol. 71, no. 5, Article ID 054027, 10 pages, 2005.
- [163] T. Renk, H. Holopainen, R. Paatelainen, and K. J. Eskola, "Systematics of the charged-hadron PT spectrum and the nuclear suppression factor in heavy-ion collisions from $\sqrt{s_{NN}} = 200$ GeV to $\sqrt{s_{NN}} = 2.76$ TeV," *Physical Review C*, vol. 84, no. 1, Article ID 014906, 11 pages, 2011.
- [164] S. Wicks, W. Horowitz, M. Djordjevic, and M. Gyulassy, "Elastic, inelastic, and path length fluctuations in jet tomography," *Nuclear Physics A*, vol. 784, no. 1–4, pp. 426–442, 2007.
- [165] H. Zhang, J. F. Owens, E. Wang, and X. N. Wang, "Dihadron tomography of high-energy nuclear collisions in next-to-leading order perturbative QCD," *Physical Review Letters*, vol. 98, no. 21, Article ID 212301, 4 pages, 2007.
- [166] S. Chatrchyan, V. Khachatryan, A. M. Sirunyan et al., "Suppression of non-prompt J/ψ , prompt J/ψ , and Y (1S) in PbPb collisions at $\sqrt{s_{NN}} = 2.76$ TeV," *Journal of High Energy Physics*, vol. 1205, no. 5, article 63, 2012.
- [167] E. Abbas and ALICE Collaboration, " J/ψ elliptic flow in Pb-Pb collisions at $\sqrt{s_{NN}} = 2.76$ TeV," <http://arxiv.org/abs/1303.5880>.
- [168] L. Adamczyk, J. K. Adkins, G. Agakishiev et al., "Measurement of J/ψ azimuthal anisotropy in Au+Au collisions at $\sqrt{s_{NN}} = 200$ GeV," <http://arxiv.org/abs/1212.3304>.
- [169] L. Adamczyk, J. K. Adkins, G. Agakishiev et al., "Jet-Hadron correlations in $\sqrt{s_{NN}} = 200$ GeV Au+Au and p+p collisions," <http://arxiv.org/abs/1302.6184>.
- [170] S. Chatrchyan, V. Khachatryan, A.M. Sirunyan et al., "Observation of long-range, near-side angular correlations in pPb collisions at the LHC," *Physics Letters B*, vol. 718, no. 3, pp. 795–814, 2013.
- [171] L. Adamczyk, J. K. Adkins, G. Agakishiev et al., "Third harmonic flow of charged particles in Au+Au collisions at $\sqrt{s_{NN}} = 200$ GeV," *Physical Review C*, vol. 88, no. 1, Article ID 014904, 11 pages, 2013.
- [172] G. Aad, T. Abajyan, B. Abbott et al., "Measurement with the ATLAS detector of multi-particle azimuthal correlations in p+Pb collisions at $\sqrt{s_{NN}} = 5.02$ TeV," *Physics Letters B*, vol. 725, no. 1–3, pp. 60–78, 2013.
- [173] S. S. Adler, S. Afanasiev, C. Aidala et al., "Detailed study of high-pT neutral pion suppression and azimuthal anisotropy in Au+Au collisions at $\sqrt{s_{NN}} = 200$ GeV," *Physical Review C*, vol. 76, no. 3, Article ID 034904, 26 pages, 2007.
- [174] A. Adare, S. Afanasiev, C. Aidala et al., "Quantitative constraints on the transport properties of hot partonic matter from semi-inclusive single high transverse momentum pion suppression in Au+Au collisions at $\sqrt{s_{NN}} = 200$ GeV," *Physical Review C*, vol. 77, no. 6, Article ID 064907, 12 pages, 2008.
- [175] B. I. Abelev, M.M. Aggarwal, Z. Ahammed et al., "Energy dependence of π^\pm , p and \bar{p} transverse momentum spectra for Au+Au collisions at $\sqrt{s_{NN}} = 2.76$ and 200 GeV," *Physics Letters B*, vol. 655, no. 3–4, pp. 104–113, 2007.

Review Article

Electromagnetic Radiations from Heavy Ion Collision

Payal Mohanty,^{1,2} Sabyasachi Ghosh,^{2,3} and Sukanya Mitra²

¹ HENPP Division, Saha Institute of Nuclear Physics, 1/AF Bidhan Nagar, Kolkata 700064, India

² Theoretical Physics Division, Variable Energy Cyclotron Centre, 1/AF Bidhan Nagar, Kolkata 700064, India

³ Ctr. for Astroparticle Physics and Space Bose Institute, 5/EN Bidhan Nagar, Kolkata 700091, India

Correspondence should be addressed to Payal Mohanty; payal.mohanty@saha.ac.in

Received 15 April 2013; Accepted 5 July 2013

Academic Editor: Jan E. Alam

Copyright © 2013 Payal Mohanty et al. This is an open access article distributed under the Creative Commons Attribution License, which permits unrestricted use, distribution, and reproduction in any medium, provided the original work is properly cited.

In this review, we have discussed the different sources of photons and dileptons produced in heavy ion collision (HIC). The transverse momentum (p_T) spectra of photons for different collision energies are analyzed with a view of extracting the thermal properties of the system formed in HIC. We showed the effect of viscosity on p_T spectra of produced thermal photons. The dilepton productions from hot hadrons are considered including the spectral change of light vector mesons in the thermal bath. We have analyzed the p_T and invariant mass (M) spectra of dileptons for different collision energies too. As the individual spectra are constrained by certain unambiguous hydrodynamical inputs, so we evaluated the ratio of photon to dilepton spectra, R_{em} , to overcome those quantities. We argue that the variation of the radial velocity extracted from R_{em} with M is indicative of a phase transition from the initially produced partons to hadrons. In the calculations of interferometry involving dilepton pairs, it is argued that the nonmonotonic variation of HBT radii with invariant mass of the lepton pairs signals the formation of quark gluon plasma in HIC. Elliptic flow (v_2) of dilepton is also studied at $\sqrt{s_{NN}} = 2.76$ TeV for 30–40% centrality using the $(2 + 1)d$ hydrodynamical model.

1. Introduction

The main objective of relativistic heavy ion collisions is to study the transient phase, that is, *quark gluon plasma* (QGP) which is believed to permeate the early universe a few microseconds after the *Big Bang*. Collision between nuclei at ultrarelativistic energies produces charged particles either in hadronic or in partonic state depending on the collision energy. Interaction among these charged particles produces electromagnetic (EM) radiation [1–9]. However, hadrons being strongly interacting objects give snapshot of evolution only from the freezeout surface. So they have hardly any information about the interior of the plasma. Whereas EM radiations, for example, the thermal photons and dileptons, are expected to provide an accurate information about the initial condition and the history of evolution of the plasma. This is possible since photons and dileptons interact only through the EM interaction. The EM interaction strength is small compared to that of strong interaction ($\alpha \ll \alpha_s$) and thus dominates the dynamics of nuclear collision processes. Therefore, its mean free path ($\lambda = 1/n\sigma$) is larger than

the size of the system. Because of their negligible final-state interactions with the hadronic environment, once produced it brings the electromagnetic particles about to escape unscathed carrying the clean information of all stages of the collision. The EM radiations produce all stages of collision process which contribute to the measured photon spectra; in principle, a careful analysis may be useful to uncover the whole space-time history of nuclear collision. Hence EM radiations—real and the virtual photons (dilepton)—are considered as efficient probes to study dynamical evolution of the matter formed in relativistic heavy ion collision. However, as they are emitted continuously, they sense in fact the entire space-time history of the reaction. This expectation has led to an intense and concerted efforts toward the identification of various sources of such radiations. While initially these signals were treated as *thermometer* of the dense medium created, but later on recent calculations suggest it might serve as *chronometer* [10] and *flow-meter* [11–16] of HIC.

The review is organized as follows. In Section 2, we start with possible sources of photons and dileptons that were produced in HIC. We have discussed the formalism of static

emission rate of photons and dileptons in Section 3. To get total yield, we need concept of hydrodynamics. So, we briefly outlined relativistic hydrodynamics in Section 4 which takes care of the evolution. In Section 5 we have presented the thermal emission rate of photons from QGP (Section 5.1) and hadronic matter (Section 5.2) which is used to produce the results, and total invariant yield of direct photon for different collision energy is shown in Section 5.4. The effect of viscosity on the transverse momentum (p_T) spectra of photon is discussed in Section 5.5. Similarly, the details of the emission rate of dileptons from QGP and hot hadrons are given in Sections 6.1 and 6.2, respectively. Using these rates, the results of p_T and invariant mass (M) spectra of dileptons are presented in Section 6.4. In Section 7 the radial flow is extracted by simultaneous use of p_T spectra of photons and dileptons and ratio of the spectra, and R_{em} is conferred. The correlation function for dilepton has been calculated and HBT radii are extracted as function of M in Section 8. We have also evaluated the dilepton v_2 in Section 9 taking into account the medium effect on the spectral function of the vector mesons. Finally, we have summarized the work in Section 10.

2. Various Sources of EM Radiations

As argued previously that EM radiations emerge out copiously from all stages of collision, so, in order to proceed, it is useful to identify various sources of photons and dileptons produced in the HIC. So the “inclusive” photon spectrum coming from such collision in usual sense can be defined as the unbiased photon spectrum observed in pp, pA, or AA collision. This spectrum is built up from a cocktail of various components.

Depending on their origin, there are two different types of sources which are “direct photons” and “photons from decay of hadrons.” The term “direct photons” is meant for those photons and dileptons which produce directly from collision between the particles. One can subdivide this broad category of “direct photons” into “prompt photons,” “preequilibrium photons” and “thermal photons,” depending on their origin. On the other hand, the decay photons do not come directly from the collision, rather from the decay of hadrons.

2.1. Transverse Momentum (p_T) Dependence of EM Radiations. The EM spectra provided by the experimentalist are mingled with various sources of photons and dileptons and it is difficult to distinguish different sources experimentally. However, real interest lies in the thermal photons and dileptons since it is expected to render information about the initial condition and the history of evolution of the plasma while it cools and hadronizes. Thus, theoretical models are used with great advantage to identify these sources of photons and their relative importance and characteristics in the spectrum.

Depending on the process through which photons/dileptons produce, they are categorized as follows.

- (1) *Prompt:* the EM radiations produced by hard scattering of the partons inside the nucleons of incoming

nuclei in the initial stage of collision, before the thermalization sets in, are known as prompt photons and dileptons (Drell Yan). This contribution may be evaluated by using pQCD.

- (2) *Preequilibrium:* the *preequilibrium photons and dileptons* are produced in the preequilibrium stage, that is, before the thermalization sets in the system. In such scenario the contribution from preequilibrium stage will be very small and hence neglected.
- (3) *Thermal:* EM radiations which are emitted from the thermalized systems of quarks and gluons or hadronic gas.
- (4) *Decay:* after the freezeout of the fireball, photons and dileptons are also produced from the decays of long-lived (compared to strong interaction time scale) hadrons and known as “*photons from decay.*”

Out of different sources, the thermal photons and dileptons are privileged as they carry information about the formation of QGP. As indicated in Figure 1, the hard photons dominate the high p_T part of the invariant momentum spectra, and decay photon populates the low p_T part and rest over thermal contribution shines in the intermediate domain of the p_T spectra $\sim 1-3$ GeV. And the calculations based on theory infer that the photons and lepton pairs from hadronic matter dominate the spectrum at lower p_T ($\sim 1-2$ GeV) whereas photons and dileptons from QGP dominate in the intermediate p_T range, that is, $p_T \sim 2-3$ GeV (depending on the models) [17]. This small window may help in learning the properties of QGP. Thus one has to subtract out the nonthermal sources to understand the properties of the QGP. However, it is not possible experimentally to distinguish between different sources. Thus, theoretical models and calculations can be used to great advantage to identify different sources of direct photons and their relative importance and characteristics in the spectrum. The hard photons and dileptons are well understood in the framework of pQCD, and decay contributions can be filtered out experimentally using different subtraction methods, like invariant mass analysis, mixed event analysis, internal conversion method, and so forth.

The invariant momentum distribution of photons and dileptons produce from a thermal source depends on the temperature (T) of the source through the thermal phase space distributions of the participants of the reaction that produces the photons and dileptons [18]. As a result the p_T spectra of thermal photons and dileptons reflect the temperature of the source through the phase space factor ($e^{-E/T}$). Hence ideally the photons with intermediate p_T values ($\sim 2-3$ GeV, depending on the value of initial temperature) reflect the properties of QGP (realized when $T > T_c$, T_c is the transition temperature). Therefore, one should look into the p_T spectra for these values of p_T for the detection of QGP. However, for an expanding system the situation is far more complex. The thermal phase space factor changes by flow; for example, the transverse kick received by low p_T photons due to flow originating from the low temperature hadronic phase (realized when $T < T_c$) populates the high p_T part of the

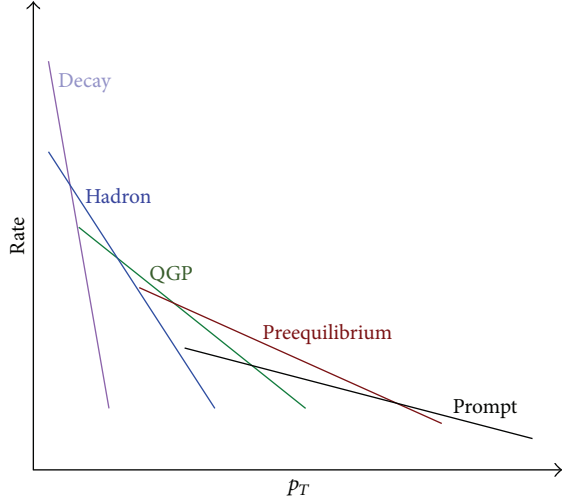


FIGURE 1: Schematic diagram of different sources of photon production in heavy ion collision as function of transverse momentum (p_T).

spectra [19]. As a consequence the intermediate or the high p_T part of the spectra contains contributions from both QGP and hadrons. Thus, it is not an easy task to disentangle the photons coming from pure partonic phase. Thus photons appear to be a more restrictive probe since they are characterized only by their momentum whereas the dileptons have two kinematic variable, p_T and invariant mass (M) to play with. A soft photon (low p_T) in one frame of reference can be hard (high p_T) in another frame, whereas the p_T integrated invariant mass distribution of dileptons is independent of any frame. In addition to it the p_T spectra are affected by the flow; however, the p_T integrated M spectra remain unaltered by the flow in the system. Also in the M spectra of dileptons, again in M spectra, the dileptons from QGP dominates over its hadronic counterpart above the ϕ peak. All these suggests that a judicious choice of p_T and M windows will be very useful to characterize the QGP and hadronic phase separately.

2.2. Invariant Mass (M) Dependence of EM Radiations. Being massive, dileptons make situation different from photons. They have two kinematic variables— p_T and M . As argued before, the p_T spectra are affected by the flow; however, the p_T -integrated M spectra remain unaltered by the flow in the system. It should be mentioned here that for M below ρ peak and above ϕ peak dileptons from QGP dominates over its hadronic counterpart (assuming the contributions from hadronic cocktails are subtracted out) if the medium effect of spectral function of the low mass vector mesons are not taken into account. However, the spectral function of low mass vector mesons (mainly ρ) may shift toward lower invariant mass region due to nonzero temperature and density effects. As a consequence the contributions from the decays of ρ mesons to lepton pairs could populate the low M window and may dominate over the contributions from the QGP phase [5, 8, 20]. All these suggest that the invariant mass distribution of dilepton can be used as a clock for HIC, and a

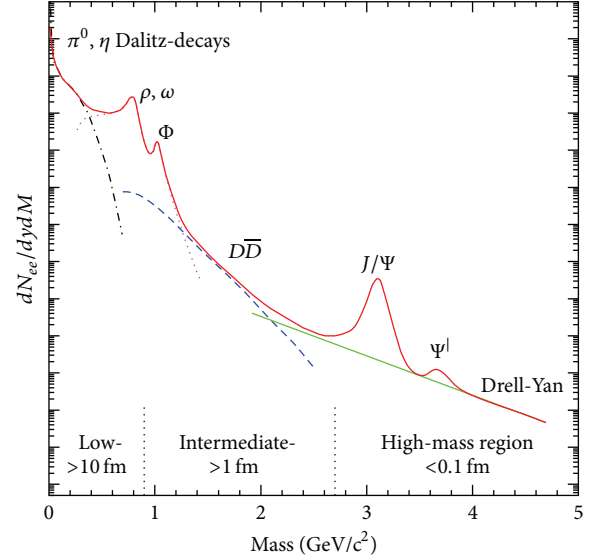


FIGURE 2: Expected different sources of dilepton production in HIC as function of invariant mass [5].

judicious choice of p_T and M windows will be very useful to characterize the flow in QGP and hadronic phase.

The measured dilepton spectra can be divided into several phases. Depending on the invariant mass of the emitted dileptons, it can be classified into three distinct regimes (discussed below [5]), and a schematic diagram of dilepton mass distribution is shown in Figure 2.

(i) High mass region (HMR):

$$(M \geq M_{J/\Psi} (= 3.1 \text{ GeV}), p_T \sim 3-5 \text{ GeV}). \quad (1)$$

The HMR region corresponds to early preequilibrium phase ($\tau < \tau_i$), where the lepton pairs are produced with large invariant mass ($M > 3 \text{ GeV}$) and the dominant contributions are from the hard scattering between the partons, like Drell Yan annihilation [21, 22]. The final abundance of the heavy quarkonia ($J/\Psi, \Upsilon$) and their contribution to the spectrum is suppressed due to the Debye screening and as a result the bound states are dissolved.

(ii) Intermediate mass region (IMR):

$$(M_\phi \leq M \leq M_{J/\Psi}, p_T \sim 1-3 \text{ GeV}). \quad (2)$$

Thermalization is achieved in the system after a time scale ($> \tau_i$). In this domain, the dileptons from the QGP are produced via quark-antiquark annihilation. In this regime, due to higher temperature the continuum radiation from QGP dominates the dilepton mass spectrum and thus this region is important for the detection of QGP. The decays of “open charm” mesons, that is, pairwise produced $D\bar{D}$ mesons [23] followed by semileptonic decays, contribute largely in this domain of M . Although an enhanced charm production is interesting in itself—probably related to the very early collision states—it may easily mask the thermal plasma

signal. To somewhat lesser extent, this also holds true for the lower-mass tail of Drell-Yan production [21, 22]. If the heavy quark does not get thermalized, then their contribution may be estimated from pp collision data with the inclusion of nuclear effects like shadowing, and so forth, and they do not contribute to the flow also [24].

(iii) Low mass region (LMR):

$$(M \leq M_\phi (= 1.02 \text{ GeV}), p_T < 1 \text{ GeV}). \quad (3)$$

With subsequent expansion and cooling, the QGP converts into a hot hadron gas at the transition temperature, T_c . At later stages, the dileptons are preferentially radiated from hot hadron gas from the decay of (light) vector meson, such as the ρ , ω , and ϕ . The low M domain of the lepton pairs is dominated by the decays of ρ . Medium modification of ρ will change the yield in this domain of M . The change of ρ spectral function is connected with the chiral symmetry in the bath; therefore, the measurement of low M lepton pairs has great importance to study the chiral symmetry restoration [25, 26] at high temperature and density. Thus the invariant mass of the lepton pair directly reflects the mass distribution of the light vector mesons. This explains the distinguished role that vector mesons in conjunction with their in-medium modifications play for dilepton measurements in HIC.

So far, we have discussed the different sources of photons and dileptons. As QGP is expected to form in the HIC experiments, the basic intention of the present study is to study the properties of QGP. Therefore, we have emphasized more on the study of thermal photons and dileptons in this review, as they may provide information to understand the formation and unique properties of the novel matter.

The emission of thermal photons and dileptons coming from HIC consists of two important segments:

$$\frac{dN}{d^4p} = \int \frac{dR}{d^4x}, \quad (4)$$

- (1) firstly, static emission rate (dR/d^4p) which takes care of the basic interactions in respective phases (QGP or hadronic phase),
- (2) Secondly, the space-time integration over four volume (d^4x) which takes care of the evolution of the thermal matter created in HIC. As the EM radiations produced from each space-time point of the evolving matter, we need the concept of relativistic hydrodynamics (described in Section 4) for understanding the evolution.

3. Formulation of Thermal Emission Rate of EM Radiations

The importance of the electromagnetic probes for the study of thermodynamic state of the evolving matter was first proposed by Feinberg in 1976 [27]. Feinberg showed that the emission rates can be related to the electromagnetic current-current correlation function in a thermalized system.

3.1. Dilepton Emission Rate from Thermal Medium. Let us consider an initial state $|I\rangle$ which goes to a final state $|F\rangle$ producing a lepton pair l^+l^- with momenta p_1 and p_2 , respectively. The dilepton multiplicity thermally averaged over initial states is given by [4, 28]

$$N = \sum_I \sum_F \left| \langle F, l^+l^- \left| e^{i \int \mathcal{L}_{\text{int}} d^4x} \right| I \rangle \right|^2 \times \frac{e^{-\beta E_l}}{Z} \frac{d^3 p_1}{(2\pi)^3 2E_1} \frac{d^3 p_2}{(2\pi)^3 2E_2}, \quad (5)$$

where $\mathcal{L}_{\text{int}} = e\bar{\psi}_l(x)\gamma_\mu\psi_l(x)A^\mu(x) + eJ_\mu(x)A^\mu(x)$ in which $\psi_l(x)$ is the lepton field operator and $J_\mu(x)$ is the electromagnetic current and $Z = \text{Tr}[e^{-\beta H}]$. Following [1, 4, 8] this expression can be put in the form

$$\frac{dN}{d^4q d^4x} = -\frac{\alpha^2}{6\pi^3 q^2} L(M^2) f_{BE}(q_0) g^{\mu\nu} W_{\mu\nu}(q_0, \vec{q}), \quad (6)$$

where the factor $L(M^2) = (1 + 2m_l^2/M^2)(1 - 4m_l^2/M^2)^{1/2}$ is of the order of unity for electrons, $M(= \sqrt{q^2})$ being the invariant mass of the pair, and the electromagnetic (e.m.) current correlator $W_{\mu\nu}$ is defined by

$$W_{\mu\nu}(q_0, \vec{q}) = \int d^4x e^{iq \cdot x} \langle [J_\mu^{\text{em}}(x), J_\nu^{\text{em}}(0)] \rangle. \quad (7)$$

Here $J_\mu^{\text{em}}(x)$ is the electromagnetic current and $\langle \rangle$ indicates ensemble average. The rate given by (6) is to leading order in electromagnetic interactions but exact to all orders in the strong coupling encoded in the current correlator $W_{\mu\nu}$. The q^2 in the denominator indicates the exchange of a single virtual photon and the Bose distribution implies the thermal weight of the source. We can also express the dilepton rate in terms of a photon spectral function $A_\gamma^{\mu\nu}$. Using the relation [4],

$$4\pi\alpha W_{\mu\nu} = 2\pi (q^2 g_{\mu\alpha} - q_\mu q_\alpha) A_\gamma^{\alpha\beta}(-q) (q^2 g_{\beta\nu} - q_\beta q_\nu) \quad (8)$$

in (6), we have

$$\frac{dN}{d^4q d^4x} = -\frac{\alpha}{(\dots)} \frac{L^{\mu\nu}}{q^4} f_{BE}(q_0) \text{Im} \Pi_{\mu\nu}^{\text{em}}(q_0), \quad (9)$$

where $A_{\mu\nu}(q_0, \vec{q}) = \text{Im} \Pi_{\mu\nu}^{\text{em}}(q_0)$.

3.2. Photon Emission Rate from Thermal Medium. The photon emission rate is calculated in the similar way to that of dilepton rate. The photon emission rate differs from the dilepton rate in the following way: the factor $e^2 L_{\mu\nu}/q^4$ appearing in the dilepton rate (in (9)) which is nothing but the product of electromagnetic vertex $\gamma^* \rightarrow l^+l^-$, the leptonic current involving Dirac spinors, and the square of the photon propagator should be replaced by the factor $\sum e^\mu e^{\nu*} (= -g^{\mu\nu})$. And the phase space factor $d^3 p_1/(2\pi)^3 E_1 d^3 p_2/(2\pi)^3 E_2$ should be replaced by $d^3 p/(2\pi)^3 E$. Then the photon emission rate becomes

$$q_0 \frac{dR}{d^3 q} = \frac{\alpha}{2\pi^3} g^{\mu\nu} f_{BE}(q_0) \text{Im} \Pi_{\mu\nu}^{\text{em}}. \quad (10)$$

The above emission rate is correct up to order e^2 in electromagnetic interaction but exact, in principle, to all order in strong interaction. However, for all practical purposes, one is able to evaluate up to a finite order of loop expansion. Now it is clear from the above results that to evaluate photon and dilepton emission rate from a thermal system we need to evaluate the imaginary part of the photon self-energy. The Cutkosky rules at finite temperature or the thermal cutting rules [29–32] give a systematic procedure to calculate the imaginary part of a Feynman diagram. The Cutkosky rule expresses the imaginary part of the n -loop amplitude in terms of physical amplitude of lower order ($n - 1$ loop or lower). This is shown schematically in Figure 3. When the imaginary part of the self-energy is calculated up to and including L order loops where L satisfies $x + y < L + 1$, then one obtains the photon emission rate for the reaction x particles $\rightarrow y$ particles $+\gamma$, and the above formalism becomes equivalent to the relativistic kinetic theory formalism [2, 3].

3.3. Emission Rate Using Relativistic Kinetic Theory Formalism. According to relativistic kinetic theory formulation, the production of i -type particles from the reaction of type $1(p_1) + 2(p_2) \rightarrow 3(p_3) + 4(p)$ is given as follows:

$$\begin{aligned} \mathcal{R}_i = \mathcal{N} \int & \frac{d^3 p_1}{(2\pi)^3 2E_1} \frac{d^3 p_2}{(2\pi)^3 2E_2} \frac{d^3 p_3}{(2\pi)^3 2E_3} \frac{d^3 p}{(2\pi)^3 2E} \\ & \times (2\pi)^4 \delta^{(4)}(p_1 + p_2 - p_3 - p) \overline{|\mathcal{M}|^2} \\ & \times f_1 f_2 (1 \pm f_3) (1 \pm f_4), \end{aligned} \quad (11)$$

where \mathcal{N} is the overall degeneracy for the reaction under consideration, $\overline{|\mathcal{M}|^2}$ is the square of the invariant amplitude for the process under consideration, p_i , E_i , and $f_i(E_i)$ are the three momentum, energy, and thermal distribution functions (Fermi-Dirac or Bose-Einstein) of the incoming and outgoing particles “ i .”

The transverse momentum (p_T) distribution of photons from a reaction of the type: $1 + 2 \rightarrow 3 + \gamma$ taking place in a thermal bath at a temperature, T is given by [2, 3]:

$$\begin{aligned} E \frac{dR}{d^3 p} = \frac{\mathcal{N}}{2(2\pi)^8} \int & \frac{d^3 p_1}{2E_1} \frac{d^3 p_2}{2E_2} \frac{d^3 p_3}{2E_3} f_1 f_2 (1 \pm f_3) \\ & \times \delta^{(4)}(p_1 + p_2 - p_3 - p) \overline{|\mathcal{M}|^2}. \end{aligned} \quad (12)$$

Using the Mandelstam variables (s, t, u) we can write the differential photon production rate as [33]

$$\begin{aligned} E \frac{dR}{d^3 p} = \frac{\mathcal{N}}{16(2\pi)^7 E} \int_{(m_1+m_2)^2}^{\infty} ds \int_{t_{\min}}^{t_{\max}} dt & |\mathcal{M}(s, t, u)|^2 \\ & \times \int dE_1 \int dE_2 \frac{f(E_1) f(E_2) [1 + f(E_3)]}{\sqrt{aE_2^2 + 2bE_2 + c}}, \end{aligned} \quad (13)$$

FIGURE 3: Optical Theorem in Quantum Field Theory.

where

$$\begin{aligned} a &= -(s + t - m_2^2 - m_3^2)^2, \\ b &= E_1 (s + t - m_2^2 - m_3^2) (m_2^2 - t) \\ &+ E [(s + t - m_2^2 - m_3^2)(s - m_1^2 - m_2^2) - 2m_1^2 (m_2^2 - t)], \\ c &= -E_1^2 (m_2^2 - t)^2 - E^2 [(s - m_1^2 - m_2^2)^2 - 4m_1^2 m_2^2] \\ &+ m_2^2 (s + t - m_2^2 - m_3^2)^2 + m_1^2 (m_2^2 - t)^2 - 2E_1 E \\ &\times [2m_2^2 (s + t - m_2^2 - m_3^2) - (m_2^2 - t)(s - m_1^2 - m_2^2)] \\ &- (s + t - m_2^2 - m_3^2)(m_2^2 - t)(s - m_1^2 - m_2^2), \\ E_{1 \min} &= \frac{(s + t - m_2^2 - m_3^2)}{4E} + \frac{Em_1^2}{s + t - m_2^2 - m_3^2}, \\ E_{2 \min} &= \frac{Em_2^2}{m_2^2 - t} + \frac{m_2^2 - t}{4E}, \\ E_{2 \max} &= -\frac{b}{a} + \frac{\sqrt{b^2 - ac}}{a}. \end{aligned} \quad (14)$$

In a similar way the dilepton emission rate for a reaction $a\bar{a} \rightarrow l^+ l^-$ can be obtained as

$$\begin{aligned} \frac{dR}{d^4 p} = \mathcal{N} \int & \frac{d^3 p_a}{2E_a (2\pi)^3} \frac{d^3 p_{\bar{a}}}{2E_{\bar{a}} (2\pi)^3} \frac{d^3 p_1}{2E_1 (2\pi)^3} \frac{d^3 p_2}{2E_2 (2\pi)^3} \\ & \times (2\pi)^4 \delta^{(4)}(p_a + p_{\bar{a}} - p_1 - p_2) \delta^{(4)} \\ & \times (p - p_a - p_{\bar{a}}) \overline{|\mathcal{M}|^2}_{a\bar{a} \rightarrow l^+ l^-} f(p_a) f(p_{\bar{a}}), \end{aligned} \quad (15)$$

where $f(p_a)$ is the appropriate occupation probability for bosons or fermions.

4. Relativistic Hydrodynamics

To evaluate the photon and dilepton production from HIC we need to convolute the static rate over space-time integration. Thus, we need to know hydrodynamics which takes care of the evolution of the matter. In this section, we briefly discuss the relativistic hydrodynamics for an ideal as well as viscous medium formed in HIC. Ideally, one cannot describe heavy ion experimental data from the first principle, that is, quantum chromodynamics (QCD) due to its complexity which mainly arises from nonlinearity of interactions of gluons, strong coupling, dynamical many body system, and color confinement. One promising strategy to connect the first

principle with phenomena is to introduce hydrodynamics as a phenomenological theory. *Relativistic hydrodynamics* [18, 34–43] plays an important role for an expanding system where pressure, temperature, and so forth vary with space and time. It is assumed that, due to intense rescatterings among the produced secondaries, the system reaches a state of local thermal equilibrium and then the evolution of the system is described by relativistic fluid dynamics. To describe the space-time evolution of such expanding system during the collision, the prescription of relativistic hydrodynamics is essential which assumes the system to be in local thermodynamic equilibrium, which means that pressure and temperature are not constant but rather are the function of space and time. This prescription is valid in the regime where the mean-free path in this “thermalised” system λ is much smaller than the characteristic dimensions of the system (L); that is, $L \geq \lambda$.

4.1. Basic Equations of Ideal Hydrodynamics. The space-time evolution of the pressure, energy density, particle densities, and the local fluid velocities is controlled by energy momentum conservation equations from hydrodynamics. The basic equations of relativistic hydrodynamics which result from applying constraints of energy-momentum conservations relevant for heavy ion collision at relativistic energies are expressed in

$$\partial_\mu T^{\mu\nu} = 0, \quad (16)$$

where $T^{\mu\nu}$ is the energy-momentum tensor of fluid element, and in its local rest frame it is given by

$$T_0^{\mu\nu} = \text{diag}[\epsilon(x), -P(x), -P(x), -P(x)]. \quad (17)$$

Local rest frame is the frame in which the velocity of the fluid element is zero. In such a frame the $T^{\mu\nu}$ becomes diagonal since the energy flux of the fluid T^{i0} and the momentum density T^{0j} turns to be zero. In absence of any dissipative processes the T^{00} component becomes the energy density ϵ and $T^{ij} = P\delta^{ij}$ since $T^{ij}dS_j$ is the i th component of force acting on the surface element which according to Pascal’s law is isotropic and perpendicular to the surface. P is the pressure of the fluid element in the local rest frame. Isotropy implies that the energy flux T_{i0} and the momentum density T_{0j} vanish in the rest frame of fluid. In addition, it implies that the pressure tensor is proportional to the identity matrix, that is, $T_{ij} = P\delta_{ij}$, where P is the thermodynamic pressure.

By doing a proper Lorentz transformation, the energy-momentum tensor $T^{\mu\nu}$ in a moving frame, where the fluid moves with an arbitrary four-velocity, $u^\mu = \gamma(1, \vec{v})$ where $\gamma = (1 - v^2)^{-1/2}$, is given in

$$T^{\mu\nu} = [\epsilon(x) + P(x)] u^\mu u^\nu - P(x) g^{\mu\nu}, \quad (18)$$

where $g^{\mu\nu} \equiv \text{diag}(1, -1, -1, -1)$ is the Minkowski metric tensor and u^μ is the fluid 4-velocity referred to as “collectivity” of the system which can be defined as $u^\mu = \gamma(1, \vec{v})$ with $\gamma = 1/\sqrt{1 - v^2}$ and $u^\mu u_\mu = 1$, where \vec{v} is the velocity of fluid element. In the above equation, the ϵ and P are the energy

density and pressure, respectively, in the fluid rest frame, and both are functions of space time coordinate x^μ .

Apart from the energy-momentum conservation, a fluid may contain several conserved charges, such as total electric charge, and net baryon number. The conserved charges obey the following continuity equation given in (19):

$$\partial_\mu N_B^\mu = 0. \quad (19)$$

$N_B^\mu = n_B u^\mu$ is the conserved net baryonic current and n_B is baryon number density. For the present work the net baryon number is assumed to be negligible small, so (16) is the only relevant equation to deal with. In addition to it, the total entropy of an inviscid fluid is conserved throughout ($S = \text{constant}$). If we define the entropy current: $s^\mu = su^\mu$, then the conservation of entropy results in $\partial_\mu s^\mu = 0$ [44].

4.2. Basic Equations of Viscous Hydrodynamics. In the above discussion we considered an idealized situation of a perfect fluid with no internal friction or energy dissipation. But in practice most of the times we have to deal with a system of imperfect fluid in which the density, pressure, and fluid velocity changes over a distance of the order of mean-free path. Such presence of a space-time gradient of those thermodynamic quantities results in modifying the energy momentum tensor $T^{\mu\nu}$ and the conserved current N^μ to the first-order gradient of these quantities:

$$\begin{aligned} T^{\mu\nu} &= (\epsilon + P) u^\mu u^\nu - P g^{\mu\nu} + \Delta T^{\mu\nu}, \\ N^\mu &= n u^\mu + \Delta N^\mu. \end{aligned} \quad (20)$$

One thing should be mentioned here that for a relativistic fluid it is necessary to specify whether u^μ is the velocity of energy transport or velocity of particle transport. In the approach of Landau and Lifshitz, u^μ is taken to be the velocity of energy transport and so T^{i0} vanishes in a comoving frame. In the approach of Eckart, u^μ is taken to be the velocity of particle transport and so $N^i = n u^i = 0$ in a comoving frame. The second approach is adopted here to obtain the following assumptions. The modification in the energy momentum tensor $\Delta T^{\mu\nu}$ and conserved current ΔN^μ is such that in a comoving frame:

$$\begin{aligned} u_\mu u_\nu \Delta T^{\mu\nu} &= 0, \\ \Delta N^\mu &= 0. \end{aligned} \quad (21)$$

With these assumptions we need to construct $\Delta T^{\mu\nu}$ to quantify the dissipative processes within the system. This has to be done in such a way that the rate of entropy production per unit volume is positive, which is again required from second law of thermodynamics. To accomplish this task some guidelines are to be followed.

- (1) The thermodynamic quantities ϵ , P , and u^μ vary slightly over the mean-free path of the particles within the fluid; that is, the system is only very slightly away from equilibrium. So the dissipative term in energy momentum tensor $\Delta T^{\mu\nu}$ must be a linear combination of space-time derivatives of ϵ , P , u^μ , and so forth.

- (2) Only the space time derivative of T and u^μ can occur in $\Delta T^{\mu\nu}$ because if derivative of ϵ , P , or n appeared in $\Delta T^{\mu\nu}$, then $\partial_\mu S^\mu$ would contain pressure or density gradient, with velocity or temperature gradient and these products are not always positive for all fluid configurations.

The entropy production rate comes out to be

$$\frac{\partial S^\mu}{\partial x^\mu} = \left[\frac{1}{T} \dot{u}_i - \frac{1}{T^2} \frac{\partial T}{\partial x^i} \right] \Delta T^{i0} + \frac{1}{T} (\partial_j u_i) \Delta T^{ij}. \quad (22)$$

From the condition that $\partial_\mu S^\mu \geq 0$ for all fluid configuration we obtain

$$\begin{aligned} \Delta T^{ij} &= \eta \left(\frac{\partial u^i}{\partial x^j} + \frac{\partial u^j}{\partial x^i} - \frac{2}{3} \vec{\nabla} \cdot \vec{u} \delta^{ij} \right) + \zeta \vec{\nabla} \cdot \vec{u} \delta^{ij}, \\ \Delta T^{i0} &= -\chi \frac{\partial T}{\partial x^i} + \zeta \frac{\partial u^i}{\partial t}, \\ \Delta T^{00} &= 0, \end{aligned} \quad (23)$$

where η is the coefficient of shear viscosity, ζ is coefficient of bulk viscosity, and χ is thermal conductivity.

Generalizing this expression $\Delta^{\mu\nu}$ comes out to be [45]

$$\Delta T^{\mu\nu} = \eta \left(\nabla^\mu u^\nu + \nabla^\nu u^\mu - \frac{2}{3} \Delta^{\mu\nu} \nabla_\rho u^\rho \right) + \zeta \Delta^{\mu\nu} \nabla_\rho u^\rho. \quad (24)$$

Here we have ignored the terms related to thermal conductivity since we are not showing any effect of that on any observables. We have defined $\nabla^\mu = \Delta^{\mu\nu} \partial_\nu$, where $\Delta^{\mu\nu} = g^{\mu\nu} - u^\mu u^\nu$ is the projection operator.

For the present study, the evaluation of matter from QGP (initial) to the hadronic system (final) via an intermediate quark-hadron transition is studied by applying relativistic hydrodynamics.

4.3. Space-Time Evolution. Hydrodynamics is a general framework to describe the space-time evolution of locally thermalized matter for a given equation of state (EoS). The basic ingredients required to solve the ideal hydrodynamic equations are EoS and initial conditions. As the system expands from its initial state, the mean-free path between particles within the system increases. At certain stage, the mean-free path becomes comparable to the system size, and then the hydrodynamic description breaks down and the phase space distribution of the particle gets fixed by the temperature of the system at this stage. This stage of evolution is called freezeout state and the corresponding temperature of the system is called thermal freezeout temperature (T_f). The hydrodynamic evolution stops at the freezeout point.

4.3.1. Initial Condition. The initial conditions are crucial to the description of space-time evolution. Initial conditions in hydrodynamics may be constrained in the following ways to reproduce the measured final multiplicity. We assume that the system reaches equilibration at a time τ_i (called initial thermalization time) after the collision. The T_i can be

related to the measured hadronic multiplicity (dN/dy) by the following relation [46]:

$$T_i^3 \tau_i \approx \frac{2\pi^4}{45\zeta(3)} \frac{1}{4a_{\text{eff}}} \frac{1}{\pi R_A^2} \frac{dN}{dy}, \quad (25)$$

where $R_A \sim 1.1N_{\text{part}}^{1/3}$ is the radius of the system, $\zeta(3)$ is the Riemann zeta function, and $a_{\text{eff}} = \pi^2 g_{\text{eff}}/90$, $g_{\text{eff}} (= 2 \times 8 + (7/8) \times 2 \times 2 \times N_c \times N_F)$ is the degeneracy of quarks and gluons in QGP, $N_c =$ number of colors, $N_F =$ number of flavors. The factor “7/8” originates from the difference between the Bose-Einstein and the Fermi-Dirac statistics. T_i depends on the centrality through the multiplicity, dN/dy . The value of dN/dy for various beam energies and centralities can be obtained directly from experiment or calculated using the following relation [47]:

$$\frac{dN}{dy} = (1-x)n_{\text{pp}} \frac{\langle N_{\text{part}} \rangle}{2} + xn_{\text{pp}} \langle N_{\text{coll}} \rangle, \quad (26)$$

where n_{pp} is the multiplicity per unit rapidity measured in pp collisions: $n_{\text{pp}} = 2.5 - 0.25 \ln(s) + 0.023 \ln^2(s)$, the fraction x of n_{pp} is due to “hard” processes, with the remaining fraction $(1-x)$ being “soft” processes. The multiplicity in nuclear collision has then two components: “soft,” which is proportional to number of participants, N_{part} and “hard,” which is proportional to number of binary collision, N_{coll} .

After the initial thermalization time, τ_i , the system can be treated hydrodynamically. The initial conditions to solve the hydrodynamic equations are given through the energy density and velocity profile:

$$\begin{aligned} \epsilon(\tau_i, r) &= \frac{\epsilon_0}{1 + \exp((r - R_A)/\delta)}, \\ v(\tau_i, r) &= 0, \end{aligned} \quad (27)$$

where ϵ_0 is the initial energy density which is related to initial (T_i), R_A is the nuclear radius, and δ is the diffusion parameter taken as 0.5 fm.

4.3.2. Equation of State (EoS). The set of hydrodynamic equations are not closed by itself; the number of unknown variable exceeds the number of equations by one. Thus a functional relation between any two variables is required so that the system become deterministic. The most natural course is to look for such relation between the pressure P and the energy density ϵ . Under the assumption of local thermal equilibrium, this functional relation between P , ϵ , and n_B is the EoS:

$$P = P(\epsilon, n_B) \quad (28)$$

which expresses the pressure as function of energy density, ϵ , and baryon density, n_B . This can be obtained by exploiting numerical lattice QCD simulation [48].

Different EoSs (corresponding to QGP vis-a-vis that of hadronic matter) will govern the hydrodynamic flow quite differently. It is thus imperative to understand in what

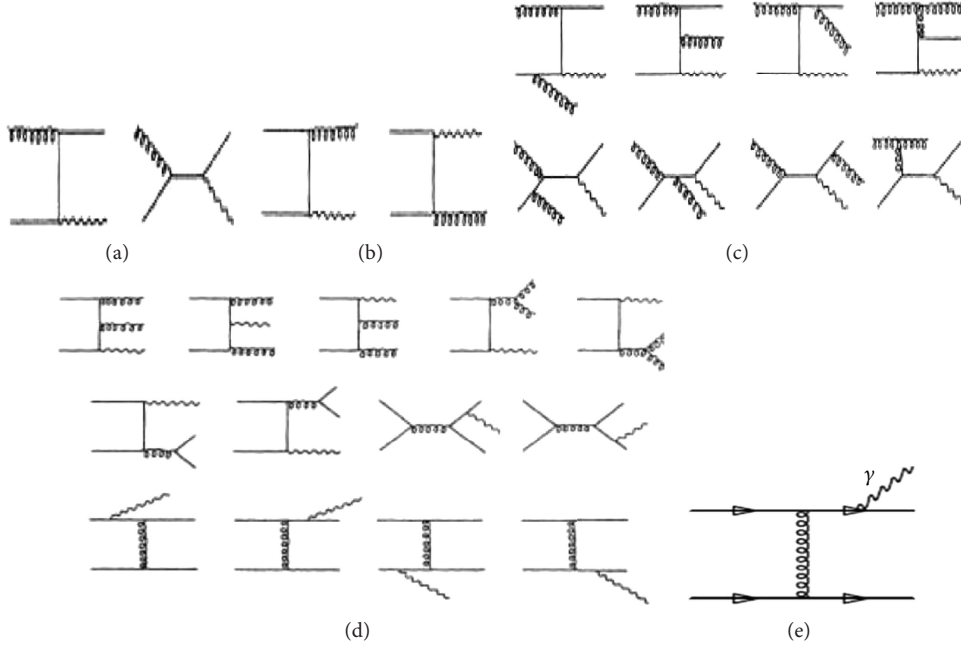


FIGURE 4: Partonic processes for production of photons.

respects the two EoSs differ and how they affect the evolution in space and time. The role of the EoS in governing the hydrodynamic flow lies in the fact that the velocity of sound, $c_s^2 = (\partial P/\partial \epsilon)$ sets an intrinsic scale in hydrodynamic evolution. One can thus write simple parametric form of the EoS: $P = c_s^2 \epsilon$, for baryon-free system which is relevant for the present study.

4.3.3. Freeze-Out Criteria. The expansion persists as long as the fluid particles interact. At sufficiently longer λ when it is comparable to system size the particles decouple to behave as free particles which is called “freeze-out” stage. This freeze-out scenario is characterized by a system temperature T_f which is of the order of pion mass and defines a space-time surface $T(x, t) = T_f$ which serves as the boundary of the hydrodynamical flow [49].

5. Emission of Thermal Photons from Heavy Ion Collision

The *thermal* photons emerge just after the system thermalizes ($\tau > \tau_i$) from both QGP due to partonic interactions and hot hadrons due to interactions among the hadrons. Now with the formalism discussed in Section 3, the production of thermal photons from QGP and hot hadronic gas is given in Sections 5.1 and 5.2, respectively. And using the hydrodynamic equations, we have convoluted these static rates by space-time integration (discussed in Section 4) and obtained the total invariant yield of photon for different collision energies. The space-time integration is constrained to the hydrodynamical inputs which has been discussed elaborately in this section.

5.1. Photons Emission from Quark Gluon Plasma. The contribution from QGP to the spectrum of thermal photons due to annihilation ($q\bar{q} \rightarrow g\gamma$) and Compton ($q(\bar{q})g \rightarrow q(\bar{q})\gamma$) processes has been calculated in [17, 50] using hard thermal loop (HTL) approximation [51, 52]. The rate of hard photon emission is then obtained as [17]

$$E \frac{dR_\gamma^{\text{QGP}}}{d^3q} = \sum_f e_f \frac{\alpha \alpha_s}{2\pi^2} T^2 e^{-E/T} \ln \left(\frac{2.912E}{g_s^2 T} \right), \quad (29)$$

where α_s is the strong coupling constant. Later, it was shown that photons from the processes [53]: $gq \rightarrow gq\gamma$, $qq \rightarrow qq\gamma$, $q\bar{q}\bar{q} \rightarrow q\gamma$, and $gq\bar{q} \rightarrow g\gamma$ contribute in the same order $O(\alpha\alpha_s)$ as Compton and annihilation processes (shown in Figure 4). The complete calculation of emission rate from QGP to order α_s has been performed by resumming ladder diagrams in the effective theory [54, 55]. In the present work this rate has been used. The temperature dependence of the strong coupling, α_s , has been taken from [56].

5.2. Photons Emission from Hot Hadronic Gas. For the photon spectra from hadronic phase we consider an exhaustive set of hadronic reactions and the radiative decay of higher resonance states [33, 57, 58].

To evaluate the photon emission rate from a hadronic gas we model the system as consisting of π , ρ , ω , and η . The relevant vertices for the reactions $\pi\pi \rightarrow \rho\gamma$ and $\pi\rho \rightarrow \pi\gamma$ and the decay $\rho \rightarrow \pi\pi\gamma$ are obtained from the following Lagrangian [57] (see Figure 5):

$$\mathcal{L} = -g_{\rho\pi\pi} \vec{\rho}^\mu \cdot (\vec{\pi} \times \partial_\mu \vec{\pi}) - e J^\mu A_\mu + \frac{e}{2} F^{\mu\nu} (\vec{\rho}_\mu \times \vec{\rho}_\nu)_3, \quad (30)$$

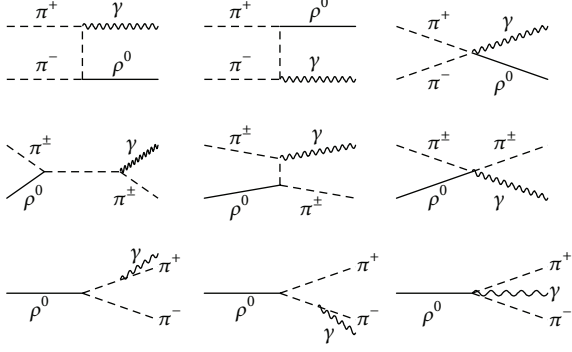


FIGURE 5: Photon-producing reactions and decays in hadronic gas.

where $F_{\mu\nu} = \partial_\mu A_\nu - \partial_\nu A_\mu$ is the Maxwell field tensor and J^μ is the hadronic part of the electromagnetic current given by

$$J^\mu = (\vec{\rho}_\nu \times \vec{B}^{\nu\mu})_3 + (\vec{\pi} \times (\partial^\mu \vec{\pi} + g_{\rho\pi\pi} \vec{\pi} \times \vec{\rho}^\mu))_3 \quad (31)$$

with $\vec{B}_{\mu\nu} = \partial_\mu \vec{\rho}_\nu - \partial_\nu \vec{\rho}_\mu - g_{\rho\pi\pi} (\vec{\rho}_\mu \times \vec{\rho}_\nu)$.

For the sake of completeness we have also considered the photon production due to the reactions $\pi\eta \rightarrow \pi\gamma$, $\pi\pi \rightarrow \eta\gamma$, and the decay $\omega \rightarrow \pi\gamma$ using the following interaction:

$$\begin{aligned} \mathcal{L} = & \frac{g_{\rho\rho\eta}}{m_\eta} \epsilon_{\mu\nu\alpha\beta} \partial^\mu \rho^\nu \partial^\alpha \rho^\beta \eta \\ & + \frac{g_{\omega\rho\pi}}{m_\pi} \epsilon_{\mu\nu\alpha\beta} \partial^\mu \omega^\nu \partial^\alpha \rho^\beta \pi + \frac{em_p^2}{g_{\rho\pi\pi}} A_\mu \rho^\mu. \end{aligned} \quad (32)$$

The last term in the above Lagrangian is written down on the basis of vector meson dominance (VMD) [60, 61]. To evaluate the photon spectra, we have taken the relevant amplitudes for the abovementioned interactions from [33, 57]. The effects of hadronic form factors [62] have also been incorporated in the present calculation. The reactions involving strange mesons: $\pi K^* \rightarrow K\gamma$, $\pi K \rightarrow K^*\gamma$, $\rho K \rightarrow K\gamma$, and $KK^* \rightarrow \pi\gamma$ [62, 63] have also been incorporated in the present work. Contributions from other decays, such as $K^*(892) \rightarrow K\gamma$, $\phi \rightarrow \eta\gamma$, $b_1(1235) \rightarrow \pi\gamma$, $a_2(1320) \rightarrow \pi\gamma$, and $K_1(1270) \rightarrow \pi\gamma$, have been found to be small [63] for $p_T > 1$ GeV.

With all photon-producing hadronic reaction, the static thermal emission rate of photons for hadronic phase has been evaluated [17, 33, 54, 55, 57, 62]. The reaction involving ρ mesons has dominant contribution. The rate at low photon energy is dominated by reaction with ρ in final state, because these reactions are endothermic with most of the available energy going into rho mass. At high photon energy reactions with the ρ in initial state are dominant because these reactions are exothermic; most of the rho mass is available for the production of high energy photons. Similar remarks can be made concerning reactions involving η mesons, but as the value of $g_{\rho\rho\eta}$ is smaller, thus so are the rates. All the isospin combinations for the above processes have properly been implemented.

5.3. Total Invariant Momentum Spectra of Thermal Photons.

In this section we evaluate photon spectrum from a dynamically evolving system. The evolution of the system is governed by relativistic hydrodynamic. The photon production from an expanding system can be calculated by convoluting the static thermal emission rate with the expansion dynamics, which can be expressed as follows:

$$\frac{dN_\gamma}{d^2 p_T dy} = \sum_i \int_i \left[\frac{dR_\gamma}{d^2 p_T dy} (E^*, T) \right]_i d^4 x, \quad (33)$$

where the $d^4 x$ is the four volume. The energy, E^* , appearing in (33) should be replaced by $u^\mu p_\mu$ for a system expanding with space-time-dependent four-velocity u^μ . Under the assumption of cylindrical symmetry and longitudinal boost invariance, u^μ can be written as

$$\begin{aligned} u &= \gamma_T (\tau, r) \left(\frac{t}{\tau}, v_r(\tau, r), \frac{z}{\tau} \right) \\ &= \gamma_T (M_T \cosh \eta, u_x, u_y, M_T \sinh \eta) \\ &= \gamma_T (M_T \cosh \eta, v_r \cos \phi, v_r \sin \phi, M_T \sinh \eta), \end{aligned} \quad (34)$$

where $v_r(\tau, r)$ is the radial velocity, $\gamma_r(\tau, r) = (1 - v_r(\tau, r))^{-1/2}$ and, therefore, for the present calculations,

$$u^\mu p_\mu = \gamma_r (M_T \cosh(y - \eta) - v_r p_T \cos \phi). \quad (35)$$

For massless photon the factor $u^\mu p_\mu$ can be obtained by replacing M_T in (35) by p_T . For the system produced in QGP phase reverts to hot hadronic gas at a temperature $T \sim T_c$. Thermal equilibrium may be maintained in the hadronic phase until the mean-free path remains comparable to the system size. The term " $(dR/d^2 p_T dy)_i = [(\dots) f_{BE}]$ " is the static rate of photon production where i stands for quark matter (QM), mixed phase (M) (in a 1st-order phase transition scenario), and hadronic matter (HM), respectively. The p_T dependence of the photon and dilepton spectra originating from an expanding system is predominantly determined by the thermal factor f_{BE} . The total momentum distribution can be obtained by summing the contribution from QM and HM, where the distribution for both the phases can be obtained by choosing the phase space appropriately.

The $d^4 x$ integration has been performed by using relativistic hydrodynamics with longitudinal boost invariance [41] and cylindrical symmetry [64] along with the inputs (given in Table 1) as the initial conditions for SPS and RHIC energies.

To estimate dN/dy for RHIC, we have taken $dn_{pp}/dy = 2.43$ and $x = 0.1$ at $\sqrt{s_{NN}} = 200$ GeV. It should be mentioned here that the values of dN/dy (through N_{part} and N_{coll} in (26)) and hence the T_i (through dN/dy in (25)) depend on the centrality of the collisions. For SPS, dN/dy is taken from experimental data [65]. We use the EoS obtained from the lattice QCD calculations by the MILC collaboration [66]. We consider kinetic freeze-out temperature, $T_f = 140$ MeV for all the hadrons. The ratios of various hadrons measured experimentally at different $\sqrt{s_{NN}}$ indicate that the system formed in heavy ion collisions chemically decouple at T_{ch}

TABLE 1: The values of various parameters—thermalization time (τ_i), initial temperature (T_i), and hadronic multiplicity dN/dy (the value of dN/dy for various beam energies and centralities is calculated from (26))—used in the present calculations.

$\sqrt{s_{NN}}$	Centrality	dN/dy	τ_i (fm)	T_i (MeV)
17.3 GeV	0–06%	700	1.0	200
	0–20%	496	0.6	227
200 GeV	20–40%	226	0.6	203
	min. bias	184	0.6	200
2.76 TeV	0–40%	1212	0.1	553

which is higher than T_f which can be determined by the transverse spectra of hadrons [67, 68]. Therefore, the system remains out of chemical equilibrium from T_{ch} to T_f . The deviation of the system from the chemical equilibrium is taken into account by introducing chemical potential for each hadronic species. The chemical nonequilibrium affects the yields through the phase space factors of the hadrons which in turn affects the productions of the EM probes. The value of the chemical potential has been taken into account following [69].

5.4. Results and Discussion on p_T Distributions of Photons.

For comparison with direct photon spectra as extracted from HIC two further ingredients are required. With all the ingredients we have reproduced the p_T spectra of direct photon for both SPS and RHIC energies. The prompt photons are normally estimated by using perturbative QCD. However, to minimize the theoretical model dependence here, we use the available experimental data from p-p collisions to estimate the hard photon and normalized it to A-A data with $T_{AA}(b)$ for different centrality; that is, the photon production from A-A collision and p-p collision are related to the following relation:

$$\frac{dN^{AA}}{d^2 p_T dy} = \frac{N_{coll}(b)}{\sigma_{in}^{pp}} \frac{d\sigma^{NN}}{d^2 p_T dy} = T_{AA}(b) \frac{d\sigma^{NN}}{d^2 p_T dy}, \quad (36)$$

where $N_{coll}(b)$ is taken for the corresponding experiments and the typical σ_{in}^{pp} (σ_{in}^{pp} 41 mb for RHIC and 30 mb for SPS).

5.4.1. Photon Spectrum for WA98 Collaboration. The WA98 photon spectra from Pb+Pb collisions are measured at $\sqrt{s_{NN}} = 17.3$ GeV. However, no data at this collision energy is available for pp interactions. Therefore, prompt photons for p+p collision at $\sqrt{s_{NN}} = 19.4$ GeV have been used [70] to estimate the hard contributions for nuclear collisions at $\sqrt{s_{NN}} = 17.3$ GeV. Appropriate scaling [65] has been used to obtain the results at $\sqrt{s_{NN}} = 17.3$ GeV. For the Pb+Pb collisions the result has been appropriately scaled by the number of collisions at this energy (this is shown in Figure 6 as prompt photons). The high p_T part of the WA98 data is reproduced by the prompt contributions reasonably well. At low p_T the hard contributions underestimate the data indicating the presence of a thermal source. The thermal photons with initial temperature = 200 MeV along with the

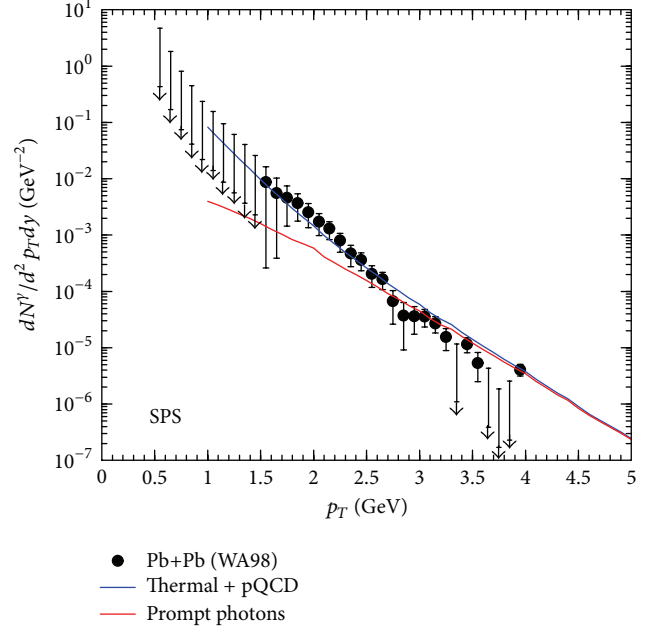


FIGURE 6: Transverse momentum spectra of photon at SPS energy for Pb+Pb collision at midrapidity [12].

prompt contributions explain the WA98 data well (Figure 6), with the inclusion of nonzero chemical potentials for all hadronic species considered [25, 26, 69, 71, 72]. In some of the previous works [73–78] the effect of chemical freezeout is ignored. As a result either a higher value of T_i or a substantial reduction of hadronic masses in the medium was required [73]. In the present work, the data has been reproduced without any such effects.

5.4.2. Photon Spectrum for PHENIX Collaboration. In Figure 7, transverse momentum spectra of photons at RHIC energy for Au-Au collision for three different centralities (0–20%, 20–40%, and min. bias.) at midrapidity shown, where the red tangles are the direct photon data measured by PHENIX collaboration [79] from Au-Au collision at $\sqrt{s_{NN}} = 200$ GeV, blue-dashed line is the contribution of the prompt photons and the black solid line is thermal + prompt photons. For the prompt photon contribution at $\sqrt{s_{NN}} = 200$ GeV, we have used the available experimental data from pp collision and normalized it to Au-Au data with $T_{AA}(b)$ for different centrality [80] (using (36)). At low p_T the prompt photons underestimate the data indicating the presence of a possible thermal source. The thermal photons along with the prompt contributions explain the data [79] from Au-Au collisions at $\sqrt{s_{NN}} = 200$ GeV reasonably well. The reproduction of data is satisfactory (Figure 7) for all the centralities with the initial temperature shown in Table 1 [81].

5.4.3. Photon Spectrum for ALICE Collaboration. The direct photon spectra from Pb+Pb collisions are measured at $\sqrt{s_{NN}} = 2.76$ TeV for 0–40% centrality by ALICE collaboration. However, no data at this collision energy is available

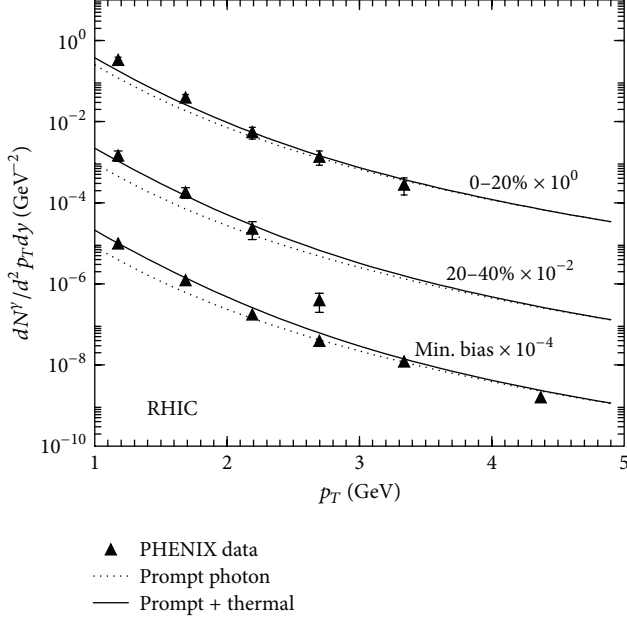


FIGURE 7: Transverse momentum spectra of photons at RHIC energy for Au-Au collision for different centralities at midrapidity [12].

for pp interactions. Therefore, prompt photons from p+p collision at $\sqrt{s_{NN}} = 7$ TeV have been used to estimate the hard contributions for nuclear collisions at $\sqrt{s_{NN}} = 2.76$ TeV by using the scaling (with $\sqrt{s_{NN}}$) procedure used in [65]. For the Pb+Pb collisions the result has been scaled up by the number of collisions at this energy (this is shown in Figure 8 as prompt photons). The high p_T part of the data is reproduced by the prompt contributions reasonably well. At low p_T the hard contributions underestimate the data indicating the presence of a possible thermal source.

The thermal photons with initial temperature ~ 553 MeV along with the prompt contributions explain the data well (Figure 8), with the inclusion of nonzero chemical potentials for all hadronic species considered [69] (see also [71, 72]).

It is well known that transverse momentum spectra of photons act as a thermometer of the interior of the plasma. The inverse slope of the thermal distribution is a measure of the average (over evolution) effective (containing flow) temperature of the system. We have extracted the average effective temperature ($\sim \langle p_T \rangle$) from the thermal distributions of photons at different collision energies—that is, for SPS, RHIC, and LHC energies. Figure 9 shows the variation of $\langle p_T \rangle$ with multiplicity for different collision energies. To minimize the centrality dependence of the results the $dN_{ch}/d\eta$ is normalized by N_{part} . The results clearly indicate a significant rise in the average p_T ($\langle p_T \rangle$) while going from SPS to RHIC to LHC. The values of $\langle p_T \rangle$ for different collision energies are given in Table 1. Since photons are emitted from each space time point of the system, therefore, the measured slope of the p_T spectra represents the average effective temperature of the system.

The quantity, $\rho_{eff}^{av} (= 1/N_{part} dN_{ch}/d\eta)$, is proportional to the entropy density. Therefore, $\rho_{eff}^{av}/\langle p_T \rangle^3 \propto g_{eff}^{av}$, the average

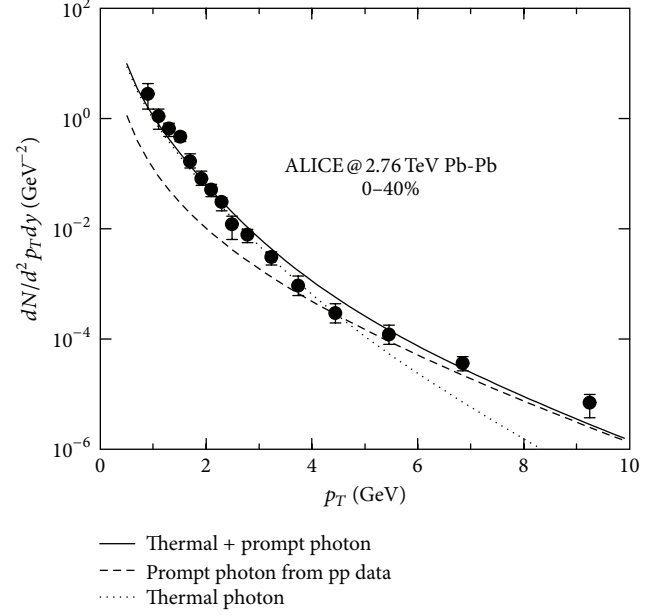


FIGURE 8: Transverse momentum spectra of photons at LHC energy for Pb-Pb collision for different 0–40% centrality at midrapidity [59].

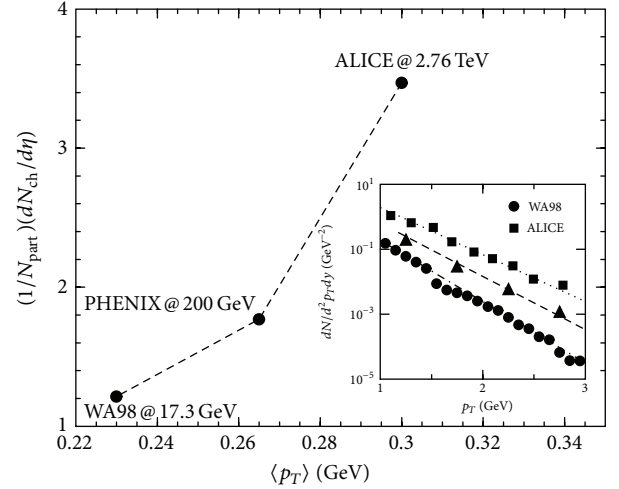


FIGURE 9: The variation of $\langle p_T \rangle$ with the increase in multiplicity for different collision energies.

effective statistical degeneracy, a quantity which changes drastically if the colour degrees of freedoms deconfined; that is, if a phase transition takes place in the system. We find that the entropy density ($s \sim g_{eff} T^3$) at LHC increases by almost 96% compared to RHIC, and there is an enhancement of 46% at RHIC compared to SPS. However, part of this increase is due to the increase in the temperature and part is due to increase in degeneracy. To estimate the increase in the degeneracy we normalize the quantity ρ_{eff}^{av} by $\langle p_T \rangle^3$. Therefore, we estimate $\rho_{eff}^{av}/\langle p_T \rangle^3$ from the analysis of the experimental data and found that there is a 15% increase in this quantity from SPS to RHIC and 35% increase from RHIC to LHC.

5.5. *Total Invariant Momentum Spectra of Thermal Photons in Viscous Medium.* Effects of viscosity on the transverse momentum distribution of photons were earlier considered in [82, 83] and recently the interest in this field is renewed [84–86]. The measured photon spectra ($dN/d^2 p_T dy$) are the yield obtained after performing the space time integration over the entire evolution history—from the initial state to the freezeout point using (33). Beyond a certain threshold in collision energy the system is expected to be formed in QGP phase which will inevitably make a transition to the hadronic matter later. The measured spectra contain contributions from both QGP and hadronic phases. Therefore, it becomes imperative to estimate the photon emission with viscous effects from QGP as well as hadrons and identify a kinematic window where photons from QGP dominate. While in some of the earlier works [84–86] contributions from hadrons were ignored, in others [82, 83] the effects of dissipation on the phase space factors were omitted. In the present work we study the effects of viscosity on the thermal photon spectra originating from QGP and hadronic matter and argue that photons can be used as a very useful tool to estimate η/s and hence characterize the matter.

Equation (12) can be simplified to the following form (see the appendix) [87]:

$$\begin{aligned} \frac{dR}{d^2 p_T dy} &= \frac{\mathcal{N}}{16(2\pi)^8} \int p_{1T} dp_{1T} dp_{2T} d\phi_1 dy_1 dy_2 \\ &\times f_1(p_1) f_2(p_2) (1 \pm f_3(p_3)) \times \overline{|\mathcal{M}|^2} \\ &\times |p_{1T} \sin(\phi_1 - \phi_2) + p_T \sin \phi_2|_{\phi_2=\phi_0}^{-1}. \end{aligned} \quad (37)$$

The effects of viscosity on the photon spectra resulting from HIC enter through two main factors: (i) the modification of the phase space factor due to the deviation of the system from equilibrium and (ii) the space time evolution of the matter governed by dissipative hydrodynamics. One more important issue deserves to be mentioned here. Normally, the initial temperature (T_i) and the thermalization time (τ_i) are constrained by the measured hadron multiplicity (dN/dy). This approach is valid for a system where there is no viscous loss and the time reversal symmetry is valid. However, for a viscous system the entropy at the freezeout point (which is proportional to the multiplicity) contains the initially produced entropy as well as the entropy produced during the space time evolution due to nonzero shear and bulk viscosity. Therefore, the amount of entropy generated during the evolution has to be subtracted from the total entropy at the freezeout point, and the remaining part which is produced initially should be used to estimate the initial temperature. Therefore, for a given dN/dy (which is associated with the freezeout point) and τ_i the magnitude of T_i will be lower in case of viscous dynamics compared to ideal flow.

5.5.1. *Viscous Correction to the Distribution Function.* We assume that the system is slightly away from equilibrium which relaxes back to equilibrium through dissipative processes. Here we briefly recall the main considerations leading

to the commonly used form for the first viscous correction, δf , to the phase space factor, f , defined as follows [88]:

$$\begin{aligned} f_i(p) &= f_{i0} (1 + \delta f_i) \\ &= f_{i0} \left(1 + \frac{p^\alpha p^\beta}{2T^3} [C \langle \nabla_\alpha u_\beta \rangle + A \Delta_{\alpha\beta} \nabla \cdot u] \right), \end{aligned} \quad (38)$$

where f_{i0} is the equilibrium distribution function of “ith” particle, $\langle \nabla_\alpha u_\beta \rangle \equiv \nabla_\alpha u_\beta + \nabla_\beta u_\alpha - (2/3) \Delta_{\alpha\beta} \nabla_\gamma u^\gamma$, $\Delta_{\alpha\beta} = g_{\alpha\beta} - u_\alpha u_\beta$, $\nabla_\alpha = (g_{\alpha\beta} - u_\alpha u_\beta) \partial^\beta$, u_μ being the four-velocity of the fluid. The coefficients C and A can be determined in the following way. Substituting f in the expression for stress-energy tensor $T^{\mu\nu}$ we get

$$\begin{aligned} T^{\mu\nu} &= \int \frac{d^3 p}{(2\pi)^3 E} p^\mu p^\nu f_0 (1 + \delta f) \\ &= T_0^{\mu\nu} + \Delta T^{\mu\nu}, \end{aligned} \quad (39)$$

where $T_0^{\mu\nu} = (\epsilon + P)u^\mu u^\nu - g^{\mu\nu} P$ is the energy momentum tensor for ideal fluid. From general considerations [44] the dissipative part can be written as

$$\Delta T^{\mu\nu} = \eta \langle \nabla^\mu u^\nu \rangle + \zeta \Delta^{\mu\nu} \nabla \cdot u. \quad (40)$$

Equating the part containing δf from (38) with (40), C and A can be expressed in terms of the coefficients of shear (η) and bulk (ζ) viscosity, respectively, in terms of which the phase space distribution for the system can be written as

$$f = f_0 \left(1 + \frac{\eta/s}{2T^3} p^\alpha p^\beta \langle \nabla_\alpha u_\beta \rangle - \frac{\zeta/s}{5T^3} p^\alpha p^\beta \Delta_{\alpha\beta} \nabla \cdot u \right). \quad (41)$$

For a boost invariant expansion in (1 + 1) dimension this can be simplified to get

$$f = f_0 [1 + \delta f_\eta - \delta f_\zeta], \quad (42)$$

where

$$\begin{aligned} \delta f_\eta &= \frac{\eta/s}{3T^3 \tau} (p_T^2 - 2p_z'^2), \\ \delta f_\zeta &= \frac{\zeta/s}{5T^3 \tau} (p_T^2 + p_z'^2), \end{aligned} \quad (43)$$

where $p_z' = m_T \sinh(y - \eta)$ is the z -component of the momentum in the fluid comoving frame. The phase space distribution with viscous correction (42) thus enters the production rate of photon through (37).

5.5.2. *Viscous Correction to the Expansion Dynamics.* As mentioned before the p_T distribution of thermal photons is obtained by integrating the emission rate over the evolution history of the expanding fluid. Relativistic viscous hydrodynamics can be used as a tool for the space-time dynamics of the fluid.

For a (1 + 1) dimensional boost invariant expansion [41] the evolution equation, $\partial_\mu T^{\mu\nu} = 0$, can be written as [89]

$$\frac{d\epsilon}{d\tau} + \frac{\epsilon + P}{\tau} = \frac{(4/3)\eta + \zeta}{\tau^2}, \quad (44)$$

where P is the pressure and ϵ is the energy density. We assume that the baryonic chemical potential is small in the central rapidity region for RHIC/LHC collision energies. Therefore, the equation corresponding to the net baryon number conservation need not be considered in these situations.

We assume that the system achieves thermal equilibrium at a time τ_i after the collision at an initial temperature T_i . With this initial condition and equation of state (EoS) $P = \epsilon/3$ the solution of (44) can be written as [82]

$$T = T_i \left(\frac{\tau_i}{\tau} \right)^{1/3} + \frac{A_Q}{8a_Q\tau_i} \left[\left(\frac{\tau_i}{\tau} \right)^{1/3} - \frac{\tau_i}{\tau} \right], \quad (45)$$

where $A_Q = ((4/3)\eta_{Q0} + \zeta_{Q0})$, $\eta_{Q0} = \eta_Q/T^3 = 4a_Q(\eta/s)_Q$, and $\zeta_{Q0} = \zeta_Q/T^3 = 4a_Q(\zeta/s)_Q$.

Equation (45) dictates the cooling of the QGP phase from its initial state to the transition temperature, T_c , at a time, τ_q , when the QGP phase ends.

In a first-order phase transition scenario, the pure QGP phase is followed by a coexistence phase of QGP and hadrons. The energy density, shear, and bulk viscosities in the mixed phase can be written in terms of the corresponding quantities of the quark and hadronic phases at temperature T_c as follows [82]:

$$\begin{aligned} \epsilon_M(\tau) &= f_Q\epsilon_Q(T_c) + (1 - f_Q(\tau))\epsilon_H(T_c), \\ \eta_M(\tau) &= f_Q\eta_Q(T_c) + (1 - f_Q(\tau))\eta_H(T_c), \\ \zeta_M(\tau) &= f_Q\zeta_Q(T_c) + (1 - f_Q(\tau))\zeta_H(T_c), \end{aligned} \quad (46)$$

where $f_Q(\tau)$ ($f_H(\tau)$) indicates the fraction of the quark (hadronic) matter in the mixed phase at a proper time τ . We have $\epsilon_Q(T_c) = 3a_Q T_c^4 + B$, $\epsilon_H(T_c) = 3a_H T_c^4$, $a_Q = g_Q\pi^2/90$, $a_H = g_H\pi^2/90$, B is the bag constant, g_Q (g_H) denote statistical degeneracy for the QGP (hadronic) phase. In the mixed phase the temperature remains constant but the energy density varies with time as the conversion of QGP to hadrons continues. This time variation is executed through $f_Q(\tau)$. Substituting (46) in (44) and solving for $f_Q(\tau)$ we get [82]

$$f_Q = \frac{e^{-b/\tau}}{\tau} \int_{\tau_Q}^{\tau'} \left[\frac{ce^{b/\tau'}}{\tau'} - ae^{b/\tau'} \right] d\tau' + \frac{\tau_Q}{\tau} e^{(b/\tau_Q - b/\tau)}, \quad (47)$$

where $a = 4\epsilon_H/(3\Delta\epsilon)$, $b = [4(\eta_Q - \eta_H)/3 + 2(\zeta_Q - \zeta_H)]/\Delta\epsilon$, $c = ((4/3)\eta_H + 2\zeta_H)/\Delta\epsilon$, and $\Delta\epsilon = \epsilon_Q - \epsilon_H$. Equation (47) indicates how the fraction of QGP in the coexistence phase evolves with time.

The variation of T with τ in the hadronic phase can be obtained by solving (44) with the boundary condition $T = T_c$ and $\tau = \tau_H$, where τ_H is the (proper) time at which the mixed

TABLE 2: The values of various η/s and parameters—initial temperature (T_i), starting time of mixed phase (τ_q), and ending time of mixed phase (τ_h)—used in the present calculations.

η/s	T_i (MeV)	τ_q (fm)	τ_h (fm)
0	328	3.95	8.8
1/4 π	315	3.93	8.78
2/4 π	302	3.92	8.76

phase ends; that is, when the conversion of QGP to hadronic matter is completed,

$$T = T_c \left(\frac{\tau_H}{\tau} \right)^{1/3} + \frac{A_H}{8a_H\tau_H} \left[\left(\frac{\tau_H}{\tau} \right)^{1/3} - \frac{\tau_H}{\tau} \right]. \quad (48)$$

Similar to QGP, $P = \epsilon/3$ has been used for hadronic phase. For a vanishing bulk viscosity ($\zeta = 0$) the cooling of the QGP is dictated by

$$T = T_i \left(\frac{\tau_i}{\tau} \right)^{1/3} + \frac{2}{3\tau_i} \left(\frac{\eta}{s} \right)_Q \left[\left(\frac{\tau_i}{\tau} \right)^{1/3} - \frac{\tau_i}{\tau} \right]. \quad (49)$$

Similarly the time variation of temperature in the hadronic phase is given by

$$T = T_c \left(\frac{\tau_H}{\tau} \right)^{1/3} + \frac{2}{3\tau_H} \left(\frac{\eta}{s} \right)_H \left[\left(\frac{\tau_H}{\tau} \right)^{1/3} - \frac{\tau_H}{\tau} \right]. \quad (50)$$

In a realistic scenario the value of η/s may be different for QGP [90–94] and hadronic phases [95–98]. However, in the present work we take the same value of η/s both for QGP and hadronic matter as shown in Table 2.

5.5.3. Results and Discussion on Viscous Effect on p_T Distributions of Photons. In case of an ideal fluid, the conservation of entropy implies that the rapidity density dN/dy is a constant of motion for the isentropic expansion [41]. In such circumstances, the experimentally observed (final) multiplicity, dN/dy , may be related to a combination of the initial temperature T_i and the initial time τ_i as $T_i^3\tau_i$. Assuming an appropriate value of τ_i (taken to be ~ 0.6 fm/c in the present case), one can estimate T_i .

For dissipative systems, such an estimate is obviously inapplicable. Generation of entropy during the evolution invalidates the role of dN/dy as a constant of motion. Moreover, the irreversibility arising out of dissipative effects implies that estimation of the initial temperature from the final rapidity density is no longer a trivial task. We can, nevertheless, relate the experimental dN/dy to the freezeout temperature, T_f , and the freezeout time, τ_f , by the relation:

$$\frac{dN}{dy} = \frac{\pi R_A^2 4a_H T_f^3 \tau_f}{\kappa}, \quad (51)$$

where R_A is the radius of the colliding nuclei (we consider AA collision for simplicity) and κ is a constant ~ 3.6 for massless bosons.

To estimate the initial temperature for the dissipative fluid we follow the following algorithm. We treat T_i as a parameter;

for each T_i , we let the system evolve forward in time under the condition of dissipative fluid dynamics (44) till a given freezeout temperature T_f is reached. Thus τ_f is determined. We then compute dN/dy at this instant of time from (51) and compare it with the experimental dN/dy . The value of T_i for which the calculated dN/dy matches the experimental number is taken to be the value of the initial temperature. Once T_i is determined, the evolution of the system from the initial to the freezeout stage is determined by (45), (47), and (48).

In Figure 10 we display the variation of temperature with proper time. It is clear from the results shown in the inset (Figure 10) that initial temperature for system which evolves with nonzero viscous effects is lower compared to the ideal case for a fixed dN/dy . Because of a nonviscous isentropic evolution scenario the multiplicity (measured at the freezeout point) is fixed by the initial entropy. However, for a viscous evolution scenario the generation of entropy due to dissipative effects contributes to the multiplicity. Therefore, for a given multiplicity (which is proportional to the entropy) at the freezeout point one requires lower initial entropy; hence, initial temperature will be lower. It is also seen (Figure 10) that the cooling of the system is slower for viscous dynamics because of the extra heat generated during the evolution.

In this section we present the shift in the p_T distribution of the photons due to viscous effects. The integrand in (33) is a Lorentz scalar; consequently the Lorentz transformation of the integrand from the laboratory to the comoving frame of the fluid can be effected by just transforming the argument; that is, the energy of the photon ($E = p_T \cosh(y)$) in the laboratory frame should be replaced by $u_\mu p^\mu$ in the comoving frame of the fluid, where p^μ is the four momenta of the photon.

The results presented here are obtained with vanishing bulk viscosity. The effects of viscosity enter into the photon spectra through the phase space factor as well as through the space time evolution. We would like to examine these two effects separately. For convenience we define two scenarios:

- (i) the effects of viscosity on the phase space factor are included ($\delta f_\eta \neq 0$) in (42), but the viscous effects on the evolution are neglected ($\eta = 0$) in (44),
- (ii) the effects of $\eta \neq 0$ are taken into account in the phase space factors as well as in the evolution dynamics.

The space time-integrated photon yield originating from the QGP in scenario (i) is displayed in Figure 11. Note that the value of the initial temperatures for the results displayed in Figure 11 is the same (for all η/s) because the viscous effects on the evolution are ignored in scenario (i). The viscous effects on the p_T distribution of the photons are distinctly visible. The higher values of η/s make the spectra flatter through the p_T dependence of the correction, δf_η .

Next we assess the effects of viscosity on photon spectra for scenario (ii). In Figure 12 we depict the photon spectra for various values of η/s . In this scenario the value of T_i is lower for higher η/s for reasons described above. As a result the enhancement in the photon production due to change

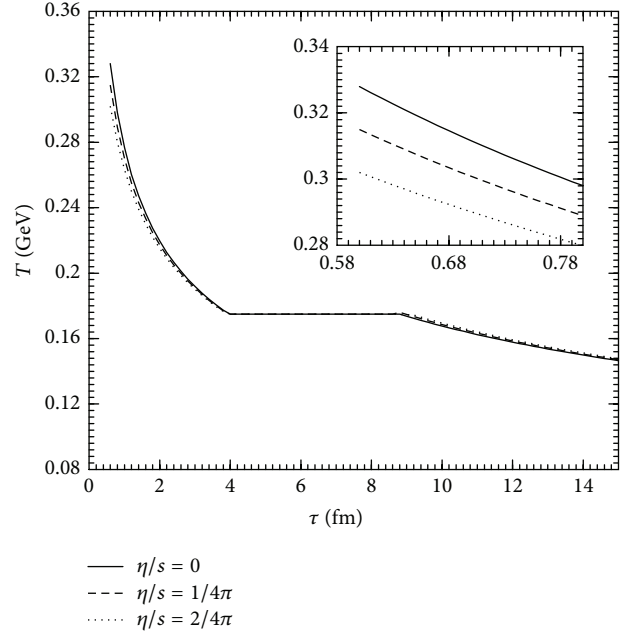


FIGURE 10: Variation of temperature with proper time for different phases for various values of the shear viscosities. Inset shows the effect of viscosity on the cooling of the QGP phase (in an amplified scale) for different values of η/s .

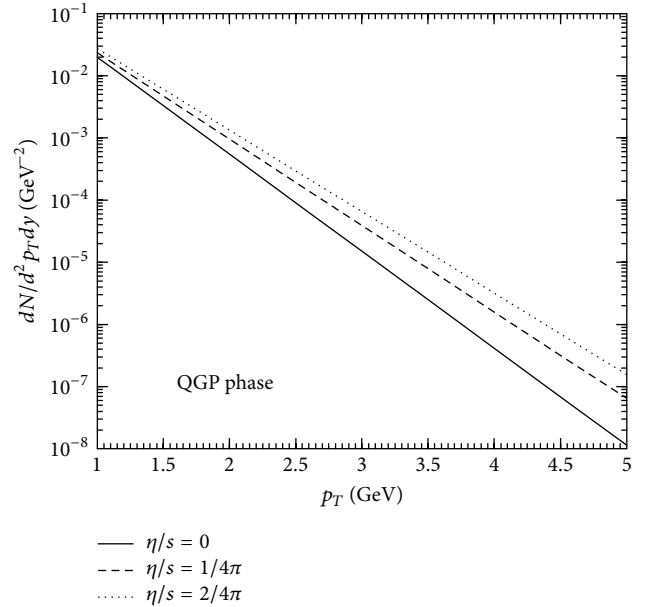


FIGURE 11: Transverse momentum distribution of thermal photons from QGP for various values of η/s in the scenario (i).

in phase space factor, δf_η , is partially compensated by the reduction in T_i for nonzero η , which is clearly seen in the results displayed in Figures 11 and 12.

In Figures 13 and 14 we exhibit results for the hadronic phase for scenarios (i) and (ii), respectively. The effects of dissipation on the p_T distribution of photons from hadronic phase are qualitatively similar to the QGP phase; that is,

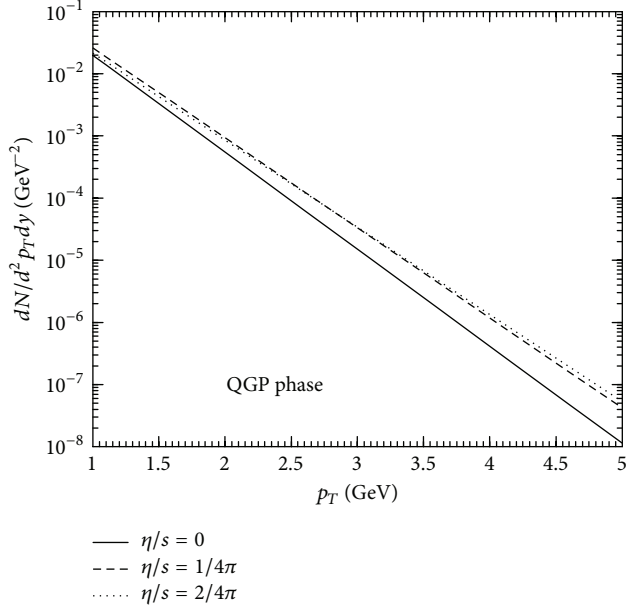


FIGURE 12: Transverse momentum distribution of thermal photons from QGP for various values of η/s in the scenario (ii).

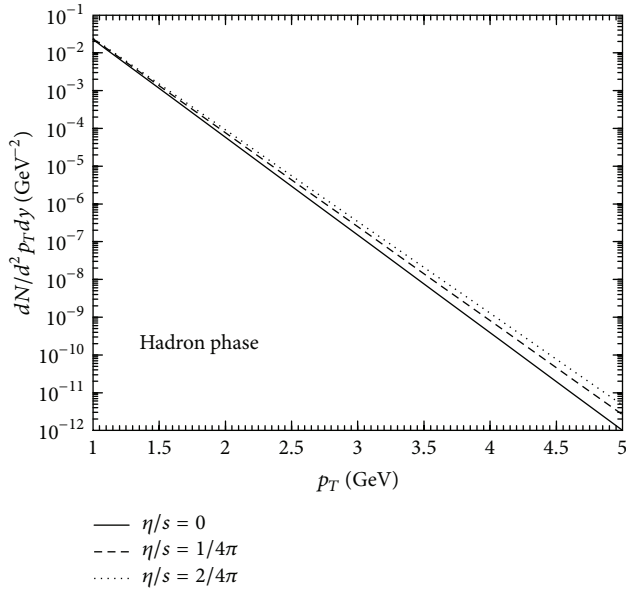


FIGURE 13: Transverse momentum distribution of photons from thermal hadrons for various values of η/s in the scenario (i).

the effect is more prominent in scenario (i) than in (ii). It is also clearly seen that the effects of viscosity though the effect is stronger in the QGP phase than in the hadronic phase. It is expected that the observed shift in the photon spectra due to viscous effects may be detected in future high precision experiments.

Finally in Figures 15 and 16 we plot the p_T spectra of photons for the entire life time of the thermal system; that is, the photon yield is obtained by summing up contributions from QGP, mixed and hadronic phases for different values of

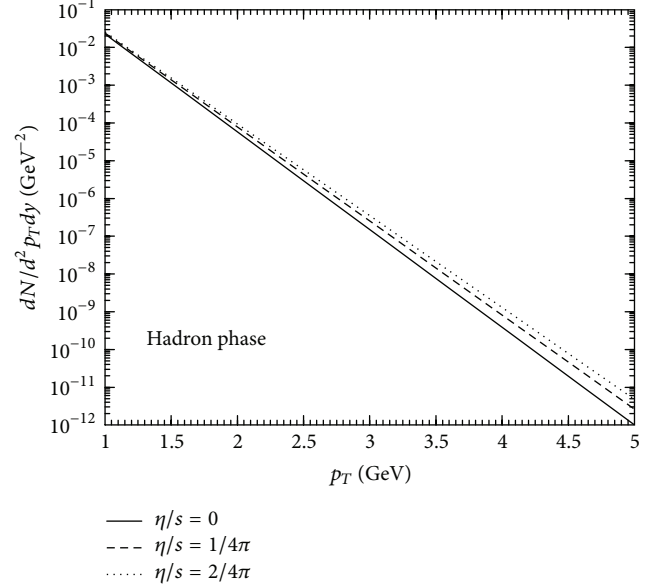


FIGURE 14: Transverse momentum distribution of photons from thermal hadrons for various values of η/s in the scenario (ii).

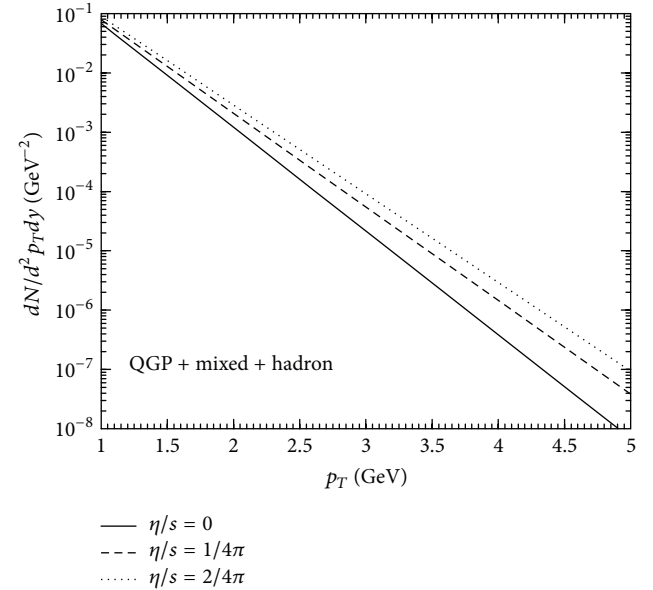


FIGURE 15: Transverse momentum distribution of thermal photons from the entire evolution history of the system for various values of η/s in the scenario (i).

η/s for scenario (i) and (ii), respectively. The effect of viscosity for the scenario (i) is stronger than (ii).

6. Emission of Thermal Dileptons from Heavy Ion Collision

Unlike real photon, dilepton is massive. Thus dilepton has two kinematic variables, invariant mass (M) and transverse momentum (p_T). Again, the p_T spectra are affected due to

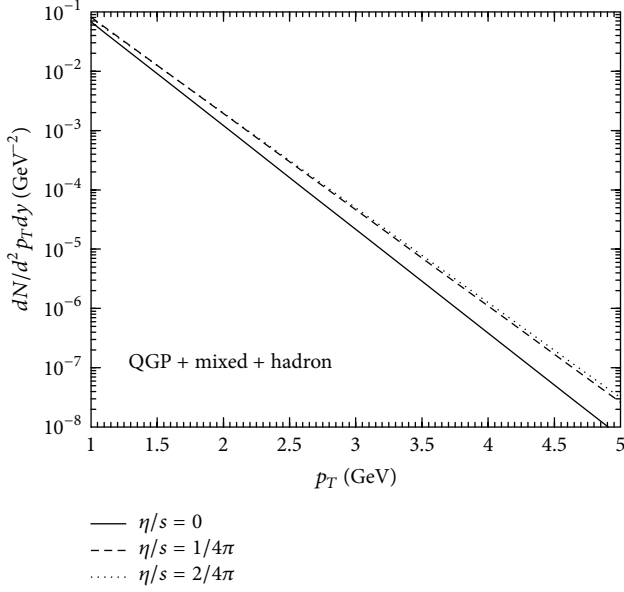


FIGURE 16: Transverse momentum distribution of thermal photons from the entire evolution history of the system for various values of η/s in the scenario (ii).

flow, whereas the p_T -integrated M spectra remain unaltered by flow. By tuning these two parameters, different stages of expanding fireball can be understood. Dileptons having large M and high p_T are emitted early from the hot zone of the system. On the other hand, those having lower M and p_T produced at later stage of the fireball when the temperature is low. Because of an additional variable, the invariant pair mass M , dileptons have the advantage over real photons [99].

The production of thermal dileptons from QGP (Section 6.1) and hot hadronic gas (Section 6.2) is described below.

6.1. Dileptons Emission from QGP. In the QGP, where quarks and gluons are the relevant degrees of freedom, the $W_{\mu\nu}$ can be directly evaluated by writing the electromagnetic current in terms of quarks of flavor f , that is, $J_\mu^{\text{em}} = \sum_f e_f \bar{\psi}_f \gamma_\mu \psi_f$. Confining to the leading order contribution we obtain

$$g^{\mu\nu} W_{\mu\nu} = -\frac{3q^2}{2\pi} \sum_f e_f^2 \left(1 - \frac{4m_q^2}{q^2} \right). \quad (52)$$

The rate in this case corresponds to dilepton production due to process $q\bar{q} \rightarrow \gamma^* \rightarrow l^+l^-$. The static thermal emission rate of dilepton from QM is given by $(q\bar{q} \rightarrow \gamma^* \rightarrow l^+l^-)$ [100, 101] (also [102, 103]),

$$\frac{dR_{l^+l^-}}{d^4p} = -\frac{\alpha^2}{4\pi^4} L(M^2) f_{BE} \sum_f e_f^2 \left[1 + \frac{2T}{\bar{p}} \ln \left(\frac{n_+}{n_-} \right) \right], \quad (53)$$

where e_f is the charge of the quark and $n_\pm = 1/(e^{(p_0 \pm |\bar{p}|/2T)} + 1)$.

6.2. Dileptons Emission from Hot Hadronic Gas. To obtain the rate of dilepton production from hadronic interactions it is

convenient to break up the quark current J_μ^h into parts with definite isospin:

$$\begin{aligned} J_\mu^h &= \frac{1}{2} (\bar{u}\gamma_\mu u - \bar{d}\gamma_\mu d) + \frac{1}{6} (\bar{u}\gamma_\mu u + \bar{d}\gamma_\mu d) + \dots \\ &= J_\mu^V + J_\mu^S + \dots = J_\mu^\rho + \frac{J_\mu^\omega}{3} + \dots, \end{aligned} \quad (54)$$

where V and S denote iso-vector and iso-scalar currents and the dots denote currents comprising of quarks with strangeness and heavier flavors. These currents couple to individual hadrons as well as multiparticle states with the same quantum numbers and are usually labeled by the lightest meson in the corresponding channel [104]. We thus identify the isovector and isoscalar currents with the ρ and ω mesons, respectively. Defining the correlator of these currents $W_{\mu\nu}^{\rho,\omega,\phi}$ analogously as in (7), we can write

$$W_{\mu\nu} = W_{\mu\nu}^\rho + \frac{W_{\mu\nu}^\omega}{9} + \dots \quad (55)$$

The correlator of vector-isovector currents $W_{\mu\nu}^\rho$ has in fact been measured [105, 106] in vacuum along with the axial-vector correlator by studying τ decays into even and odd number of pions. The former is found to be dominated at lower energies by the prominent peak of the ρ meson followed by a continuum at high energies. The axial correlator, on the other hand, is characterized by the broad hump of the a_1 . The distinctly different shape in the two spectral densities is an experimental signature of the fact that chiral symmetry of QCD is dynamically broken by the ground state [107]. It is expected that this symmetry may be restored at high temperature and/or density and will be signaled by a complete overlap of the vector and axial-vector correlators [17].

In the medium, both the pole and the continuum structure of the correlation function gets modified [8, 108]. We will first evaluate the modification of the pole part due to the self-energy of vector mesons in the following. Using vector meson dominance the isovector and scalar currents are written in terms of dynamical field operators for the mesons allowing us to express the correlation function in terms of the exact (full) propagators or the interacting spectral functions of the vector mesons in the medium. To reach that goal we have to specify the coupling of the currents to the corresponding vector fields. For this purpose we write, in the narrow width approximation [104],

$$\langle 0 | J_\mu^{\text{em}}(0) | R \rangle = F_R m_R \epsilon_\mu, \quad (56)$$

where R denotes the resonance in a particular channel and ϵ_μ is the corresponding polarization vector. The coupling constants F_R are obtained from the partial decay widths into e^+e^- through the relation

$$F_R^2 = \frac{3m_R \Gamma_{R \rightarrow e^+e^-}}{4\pi\alpha^2} \quad (57)$$

yielding $F_R = 0.156 \text{ GeV}$, 0.046 GeV , and 0.079 GeV for ρ , ω , and ϕ , respectively. Equation (56) suggests the operator relations:

$$\begin{aligned} J_\mu^\rho(x) &= F_\rho m_\rho V_\mu^\rho(x), \\ J_\mu^\omega(x) &= 3F_\omega m_\omega V_\mu^\omega(x), \text{ and so forth,} \end{aligned} \quad (58)$$

where $V_\mu^{\rho(\omega)}(x)$ denotes the field operator for the $\rho(\omega)$ meson. So using the above relations connecting currents to fields (so-called field-current identity), the current commutator becomes

$$\begin{aligned} W_{\mu\nu} &= \sum_{R=\rho,\omega,\dots} F_R^2 m_R^2 \int d^4x e^{iq \cdot x} \langle [V_\mu^R(x), V_\nu^R] \rangle \\ &= \sum_{R=\rho,\omega,\dots} F_R^2 m_R^2 A_{\mu\nu}^R(q_0, \vec{q}) \\ &= 2\epsilon(q_0) \sum_{R=\rho,\omega,\dots} F_R^2 m_R^2 \text{Im} \bar{D}_{\mu\nu}^R(q_0, \vec{q}), \end{aligned} \quad (59)$$

where $A_{\mu\nu}^R$ are the spectral functions of corresponding vector meson resonances (R) and $\bar{D}_{\mu\nu}^R$ is the diagonal element of the thermal propagator matrix. The form of the diagonal element of the exact thermal propagator matrix for the spin 1 particle is given by

$$\bar{D}_{\mu\nu}^R(q) = \bar{G}_{\mu\nu}^R - \frac{q_\mu q_\nu}{q^2 m_R^2}, \quad (60)$$

where

$$\bar{G}_{\mu\nu}^R = -\frac{P_{\mu\nu}}{q^2 - m_R^2 - \bar{\Pi}_t^R(q)} - \frac{Q_{\mu\nu}/q^2}{q^2 - m_R^2 - q^2 \bar{\Pi}_l^R(q)}. \quad (61)$$

The imaginary part is then put in (59) and then in (6) to arrive at the dilepton emission rate:

$$\begin{aligned} \frac{dN}{d^4q d^4x} &= \frac{\alpha^2}{\pi^3 q^2} L(q^2) f_{BE}(q_0) \\ &\times \left[F_\rho^2 m_\rho^2 A_\rho(q_0, \vec{q}) + F_\omega^2 m_\omega^2 A_\omega(q_0, \vec{q}) + \dots \right], \end{aligned} \quad (62)$$

where, for example, $A_\rho (= -g^{\mu\nu} \text{Im} \bar{D}_{\mu\nu}^\rho / 3)$ is given by

$$\begin{aligned} A_\rho &= -\frac{1}{3} \left[\frac{2 \sum \text{Im} \bar{\Pi}_t^R}{\left(q^2 - m_\rho^2 - \sum \text{Re} \bar{\Pi}_t^R \right)^2 + \left(\sum \text{Im} \bar{\Pi}_t^R \right)^2} \right. \\ &\quad \left. + \frac{q^2 \sum \text{Im} \bar{\Pi}_l^R}{\left(q^2 - m_\rho^2 - q^2 \sum \text{Re} \bar{\Pi}_l^R \right)^2 + q^4 \left(\sum \text{Im} \bar{\Pi}_l^R \right)^2} \right], \end{aligned} \quad (63)$$

the sum running overall meson loops πH and baryon loops NB . Here $\bar{\Pi}_{t,l}^R$ is the diagonal element of vector meson ($R = \rho$ and ω) self-energy at finite temperature and density which

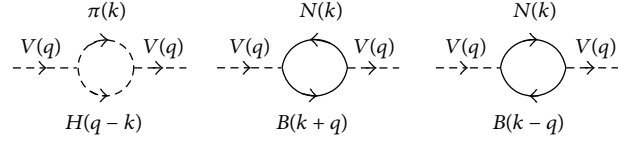


FIGURE 17: One-loop Feynman diagrams for ρ or ω self-energy involving mesons (first figure) and baryons (second and third figures). V stands for the ρ or ω in the external line. In the internal lines of meson loops, $H = \pi, \omega, a_1,$ and h_1 for $V = \rho$ whereas $H = \rho$ for $V = \omega$. For the baryonic loops, N and B indicate, respectively, nucleon and baryonic internal lines.

is also a matrix in the real-time formalism. We have taken $H = \pi, \omega, a_1, h_1$ [109] and $B = N(940), N^*(1520), N^*(1650), N^*(1700), N^*(1720), \Delta(1230),$ and $\Delta^*(1620)$ [110] for ρ meson whereas for ω meson, $H = \rho$ (with $\pi\pi$ folding), and $B = N(940), N^*(1440), N^*(1520), N^*(1535), N^*(1650),$ and $N^*(1720)$ [111] are taken. These self-energy graphs are diagrammatically represented in Figure 17.

The general expression of $\bar{\Pi}_{t,l}^R$ for meson loop πH (representing the first diagram of Figure 17) is given by [109, 111]

$$\begin{aligned} \bar{\Pi}_{t,l}^R(q) &= \int \frac{d^3k}{(2\pi)^3} \frac{1}{4\omega_\pi \omega_H} \\ &\times \left[\frac{(1+n^\pi) L_{t,l}^1 + n^H L_{t,l}^3}{q_0 - \omega_\pi - \omega_H + i\eta\epsilon(q_0)} \right. \\ &\quad + \frac{-n^\pi L_{t,l}^1 + n^H L_{t,l}^4}{q_0 - \omega_\pi + \omega_H + i\eta\epsilon(q_0)} \\ &\quad + \frac{n^\pi L_{t,l}^2 - n^H L_{t,l}^3}{q_0 + \omega_\pi - \omega_H + i\eta\epsilon(q_0)} \\ &\quad \left. + \frac{-n^\pi L_{t,l}^2 - (1+n^H) L_{t,l}^4}{q_0 + \omega_\pi + \omega_H + i\eta\epsilon(q_0)} \right], \end{aligned} \quad (64)$$

where n 's are Bose-Einstein distribution functions for the internal meson lines and ω 's are their on-shell energies. In the above expression $L_{t,l}^{i=1,\dots,4}$ denote the values of $L_{t,l}(k_0)$ for $k_0 = \omega_\pi, -\omega_\pi, q_0 - \omega_H,$ and $q_0 + \omega_H,$ respectively. The corresponding expression for the baryon loop NB (second diagram of Figure 17) is given by [110, 111]

$$\begin{aligned} \bar{\Pi}_{t,l}^R(q) &= \int \frac{d^3k}{(2\pi)^3} \frac{1}{4\omega_N \omega_B} \\ &\times \left[\frac{(1-n_+^N) L_{t,l}^1 - n_-^B L_{t,l}^3}{q_0 - \omega_N - \omega_B + i\eta\epsilon(q_0)} \right. \\ &\quad + \frac{n_+^N L_{t,l}^1 - n_+^B L_{t,l}^4}{q_0 - \omega_N + \omega_B + i\eta\epsilon(q_0)} \\ &\quad + \frac{-n_-^N L_{t,l}^2 + n_-^B L_{t,l}^3}{q_0 + \omega_N - \omega_B + i\eta\epsilon(q_0)} \\ &\quad \left. + \frac{n_-^N L_{t,l}^2 + (-1+n_+^B) L_{t,l}^4}{q_0 + \omega_N + \omega_B + i\eta\epsilon(q_0)} \right], \end{aligned} \quad (65)$$

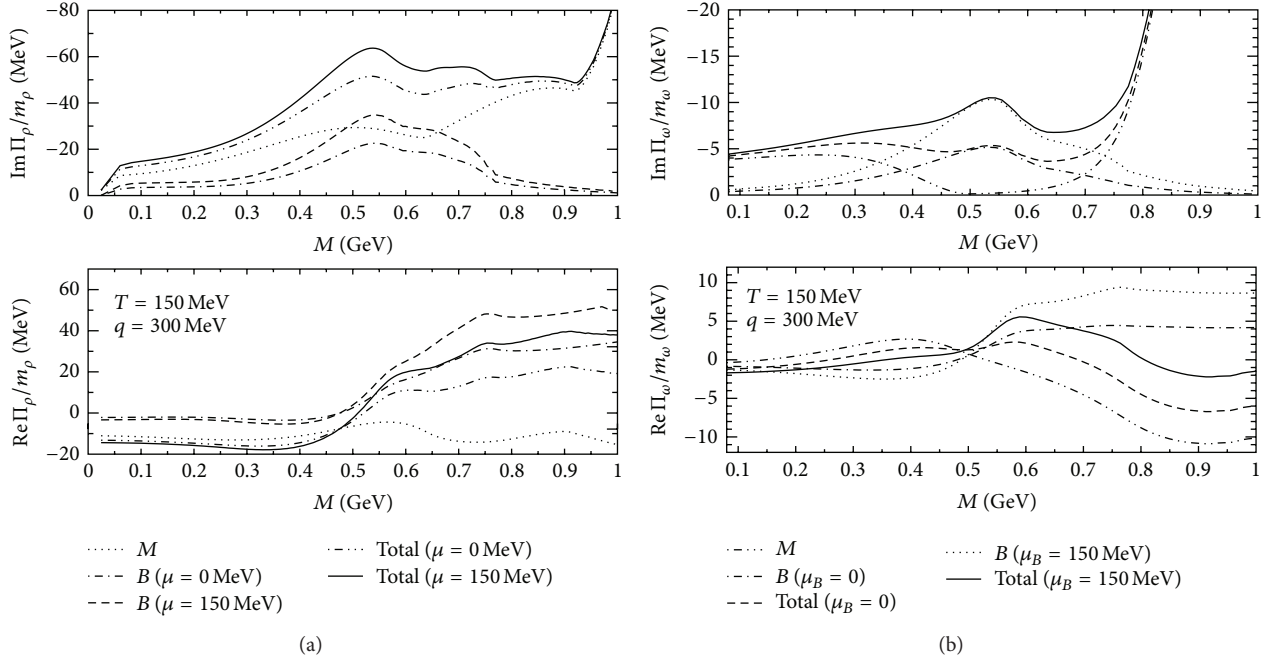


FIGURE 18: The imaginary (upper) and real (lower) part of self-energy function of ρ (a) and ω (b) at different chemical potential (μ or μ_B). The contribution coming from meson, baryon loops, and their sum is shown.

where $n_{+(-)}$'s are Fermi-Dirac distribution functions for the internal baryon (antibaryon) lines. Here, $L_{t,l}^{i=1,\dots,4}$ denote the values of $L_{t,l}(k_0)$ for $k_0 = \omega_N, -\omega_N, q_0 - \omega_B, q_0 + \omega_B$, respectively. The expression for the third diagram of Figure 17 can be obtained by changing the sign of the external momentum q in (65).

The numerical results for the ρ and ω meson self-energy are, respectively, shown in Figures 18(a) and 18(b). The individual contribution from the meson and baryon loops is also shown for two values of the baryon chemical potential. For both ρ and ω mesons, the small positive contribution from the baryon loops to the real part is partly compensated by the negative contributions from the meson loops which can be clearly seen in the lower panels of Figure 18.

We now use these self-energy functions in the expression for the exact propagator (60) to obtain an explicit results of in-medium spectral functions for ρ and ω meson. In view of the fact that the ρ and ω peaks are close to each other, it is worthwhile to compare their relative spectral strengths below their nominal masses. This is shown in Figure 19 for two values of the chemical potential. The characteristic 2π and 3π thresholds for the ρ and ω in the vacuum case are also visible. At fixed temperature and density, the ω contribution is lower than ρ but of comparable magnitude below their nominal masses. However, the fact that the ω is suppressed by a factor ~ 10 ($\approx F_{\rho}^2/F_{\omega}^2$) compared to the ρ in the dilepton emission rate makes a quantitative study of the ω difficulty. In the above expressions the meson (H) and baryon resonances (B) have been treated in the narrow width approximation. These have then been folded with the width of the resonances as shown in [110].

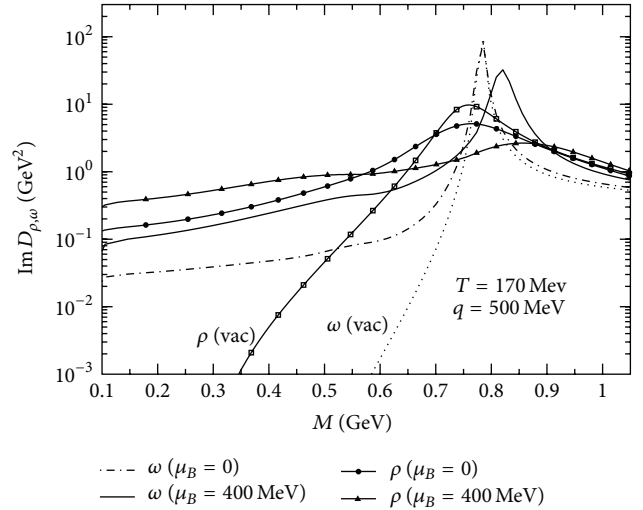


FIGURE 19: The ω spectral function seen in comparison with the ρ .

Thus, the dilepton emission rate in the present scenario actually boils down to the evaluation of the self-energy graphs of ρ and ω as a function of q_0 , \vec{q} , temperature (T), and net baryon density (ρ_B). Using those functions in (63) we can get a numerical estimation of dilepton static rates. With all the ingredients discussed previously, we have calculated the static emission rate of dilepton from QGP and hadronic matter. The emission rate from both the phases is plotted in Figure 20 for a given temperature of 175 MeV and baryonic chemical potential of 30 MeV. We observe significant enhancement in the dilepton yield in the mass region below the ρ pole

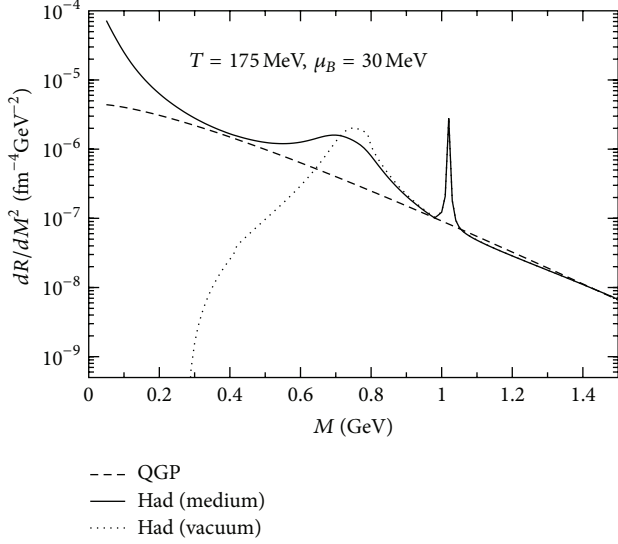


FIGURE 20: The dilepton emission rate from different sources at $T = 175$ MeV and $\mu_B = 30$ MeV.

compared to vacuum. This rate has been used in the analysis of the dimuon spectra obtained from In-In collisions at 17.3 GeV at CERN SPS [112, 113] (discussed in Section 6.4.1). The calculations show a reasonable agreement with the invariant mass spectra for different p_T ranges as well as the M_T spectra for different M bins.

As indicated earlier, coupling of the hadronic current to multiparticle states gives rise to a continuum structure in the current correlation function $W^{\mu\nu}$. Following [104], we take a parameterized form for this contribution and augment the dilepton emission rate with

$$\frac{dN}{d^4q d^4x} = \frac{\alpha^2}{\pi^3} L(q^2) f_{BE}(q_0) \sum_{V=\rho,\omega} A_V^{\text{cont}}, \quad (66)$$

where

$$A_\rho^{\text{cont}} = \frac{1}{8\pi} \left(1 + \frac{\alpha_s}{\pi}\right) \frac{1}{1 + \exp(\omega_0 - q_0)/\delta} \quad (67)$$

with $\omega_0 = 1.3, 1.1$ GeV for ρ, ω , and $\delta = 0.2$ for both ρ and ω . The continuum contribution for the ω contains an additional factor of $1/9$.

6.3. Invariant Mass and Momentum Spectra of Dileptons. The total invariant transverse momentum distribution of thermal dileptons (l^+l^-) is obtained as follows:

$$\frac{d^2 N_{l^+l^-}}{d^2 p_T dy} = \sum_{i=Q,M,H} \int_i \left(\frac{dR_{l^+l^-}}{d^2 p_T dy dM^2} \right)_i M dM d^4 x. \quad (68)$$

In a similar manner, the invariant transverse mass distribution of thermal dileptons (l^+l^-) can be obtained by integrating static emission rate over certain p_T window and by convoluting that by four volume and expressed as follows:

$$\frac{d^2 N_{l^+l^-}}{2M dM dy} = \sum_{i=Q,M,H} \int_i \left(\frac{dR_{l^+l^-}}{d^2 p_T dy dM^2} \right)_i p_T d p_T d^4 x. \quad (69)$$

The limits for integration over p_T and M can be fixed judiciously to detect contributions either from quark matter or hadronic matter. Experimental measurements [79, 114, 115] are available for different M window.

6.4. Results and Discussion on p_T and M Distributions of Dileptons. Thus far we have discussed the dilepton emission rate for a given temperature. In HIC the dilepton yield is obtained by convoluting the static emission rate over space and time.

6.4.1. Dileptons at SPS Energy. With all these ingredients the M_T and M spectra of dileptons measured by NA60 collaboration at SPS energy are reproduced as follows.

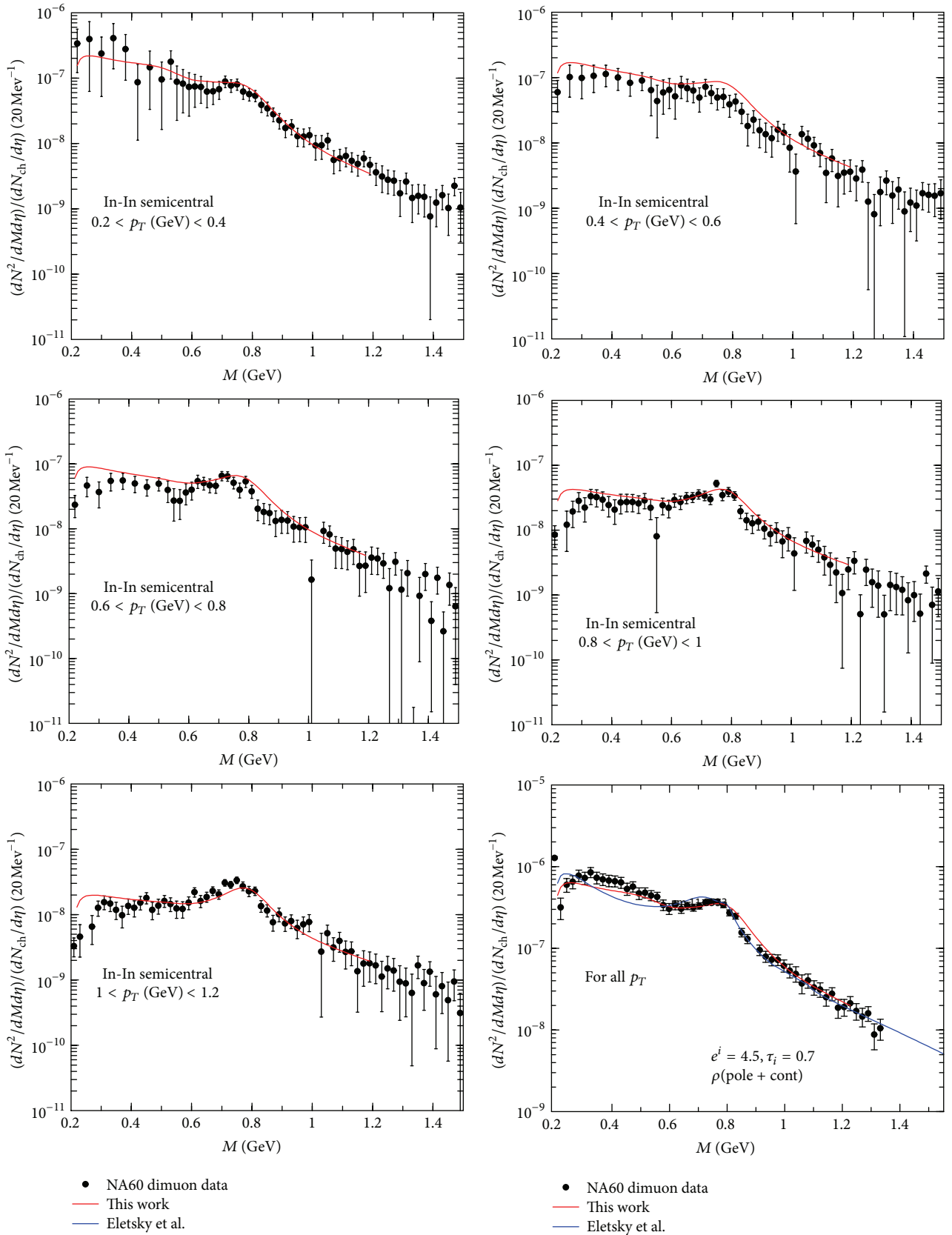
Finally, we have obtained the dimuon yield (dN/dM) in In-In collisions at SPS at a center of mass energy of 17.3 GeV. The initial energy density is taken as 4.5 GeV/fm³ corresponding to a thermalisation time $\tau_i = 0.7$ fm, the QGP to hadronic matter transition temperature $T_c = 175$ MeV, and the freezeout temperature $T_f = 120$ MeV (fixed from the slope of the hadronic spectra measured by the NA60 Collaboration) has been taken to compare the data measured by NA60 collaboration. In Figure 21 we have shown the invariant mass spectra for different transverse momentum (p_T) windows calculated for 17.3 GeV energies.

The theoretical curves agree quite well with the experimental data [114, 115] for all the p_T ranges. The strong enhancement in the low M domain is clearly due to the large broadening of the ρ in the thermal medium which comes entirely from the Landau cut in the self-energy diagrams. In the last panel, the blue-dashed line curve is the result of a previous calculation [113] where the self-energy due to baryons has been evaluated following the approach of [116]. In the present work [112] we have included an exhaustive set of baryon loops using the real-time thermal field theoretical approach where we have employed the full relativistic baryon propagators in which baryons and anti-baryons appear on an equal footing. This [112] is seen to be in better agreement with the experimental data [114, 115] than [113] in the range $0.35 \leq M \leq 0.65$ GeV.

Apart from the M spectra, we have also evaluated the transverse mass spectra of dimuon pairs at SPS energy measured by NA60 collaboration [114, 115].

The results are compared with the data obtained by NA60 collaborations [114, 115, 117, 118] at SPS energy (Figure 22). Theoretical results contain contributions from the thermal decays of light vector mesons (ρ, ω , and ϕ) and also from the decays of vector mesons at the freezeout [10, 49] of the system has also been considered. The nonmonotonic variation of the effective slope parameter extracted from the M_T spectra of the lepton pair with $\langle M \rangle$ evaluated within the ambit of the present model [113] reproduces the NA60 [114, 115] results reasonably well.

6.4.2. Dileptons at RHIC Energy. For Au+Au collisions at $\sqrt{s_{NN}} = 200$ GeV, we have evaluated the dilepton spectra for different invariant mass bins with the initial condition (min bias) shown in Table 1 and lattice QCD equation of


 FIGURE 21: Dilepton invariant mass spectra for different p_T bins compared with the NA60 data.

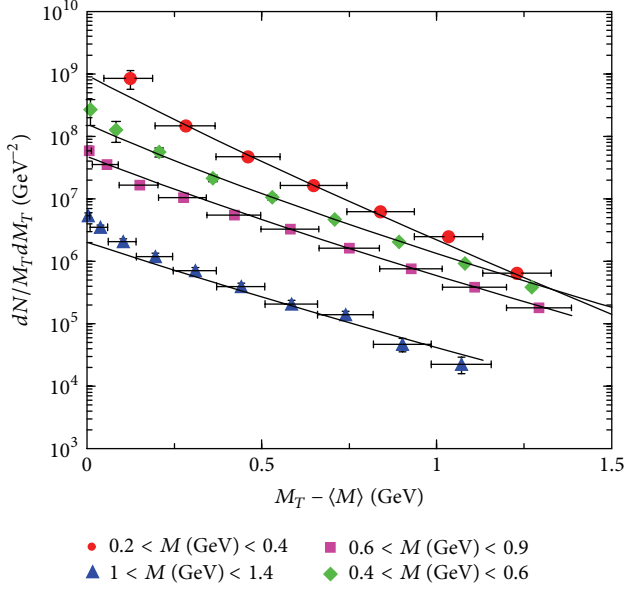


FIGURE 22: Transverse mass spectra of dimuons in In+In collisions at SPS energy. Solid lines denote the theoretical results [12].

state. The results are displayed in Figure 23. The slopes of the experimental data on p_T distribution of lepton pairs for different invariant mass windows measured by the PHENIX collaboration [119, 120] could be reproduced well with the same initial condition that reproduces photon spectra [79]. In fact, the reproduction of data for the mass bins $0.5 < M(\text{GeV}) < 0.75$ and $0.81 < M(\text{GeV}) < 0.99$ does not need any normalization factors (Figure 23). For lower mass windows slopes are reproduced well but fail to reproduce the absolute normalization. Therefore, it should be clarified here that the theoretical results shown in Figure 22 for lower mass windows (to be precise for $0.1 < M(\text{GeV}) < 0.2$, $0.2 < M(\text{GeV}) < 0.3$ and $0.3 < M(\text{GeV}) < 0.5$) contain arbitrary normalization constant.

Assuming 10% hard (i.e., $x = 0.10$) and 90% soft collisions for initial entropy production the value of dN_{pp}^{ch}/dy turns out to be about 2.43 at $\sqrt{s} = 200$ GeV. For RHIC energy, we take $T_i = 320$ MeV with initial time $\tau_i = 0.2$ fm/c which acts as inputs to the hydrodynamic evolution.

For studying thermal dileptons at the RHIC energy (as well as the LHC energy) we have included the vacuum spectral function of ϕ meson because its mass appears at a boundary between quark and hadronic sources of dileptons.

We begin by plotting the space-time integrated invariant mass spectra of dileptons. In Figure 24 we plot the yield of lepton pairs from the hadronic matter (HM), evaluated with and without the modified ρ spectral function for RHIC energy. The enhancement in the region $0.1 \leq M \leq 0.7$ GeV is purely a medium effect and is a contribution from the Landau cut of the meson and baryon loops. In contrast, the vacuum spectral function naturally starts from the $2m_\pi$ threshold coming from the unity in the unitary cut contribution. The (small) kink at 0.42 GeV in this curve is due to the $3m_\pi$

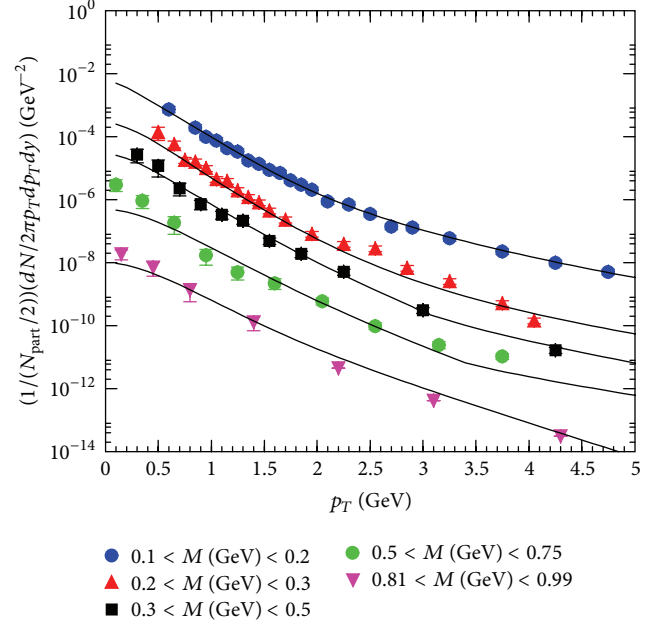


FIGURE 23: Transverse momentum spectra of dileptons for different invariant mass windows for minimum bias Au-Au collisions at RHIC energy [12].

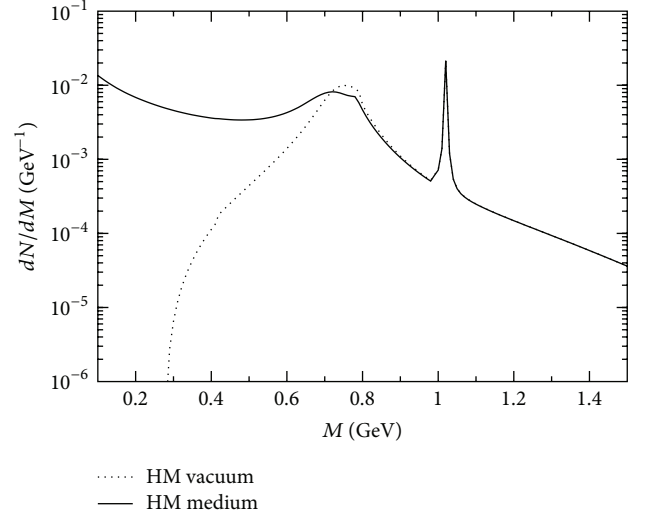


FIGURE 24: Invariant mass distribution of dileptons from hadronic matter (HM) for modified and unmodified ρ meson for RHIC energy.

threshold for ω production. The enhancement in the yield due to medium effects is ~ 20 for M around 400 MeV.

In Figure 25, we have shown the dependence of the yield from the two phases on the EoS. Dilepton radiation from hadronic phase outshines the emission from quark matter for M up to ϕ mass. Since the internal loops of ρ self-energy contain $a_{1\pi}$ and ω_π interactions, we ignore the four pion annihilation process [121] to avoid double counting. The contributions from quark matter phase dominate over its hadronic counter part for both the EoS for M beyond ϕ

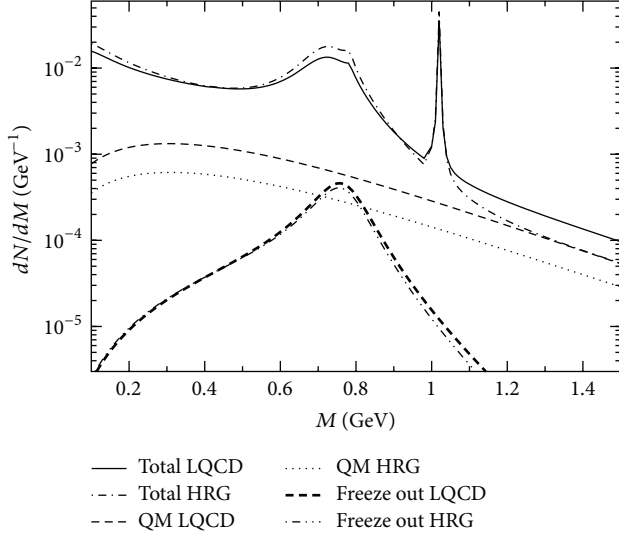


FIGURE 25: FreeZE-out, QGP, and total contribution for EoS (a) HRG (dash-double dotted, dotted, and dash-dotted lines) and EoS (b) LQCD (bold dashed, dashed, and solid lines) at RHIC energy.

peak. This fact may be used to extract various properties, that is, *average flow, temperature, and so forth* of quark matter and hadronic matter by selecting M windows judiciously. The dilepton yield from hadronic matter is observed to be larger when the HRG EoS is employed in comparison with LQCD. This can be understood in terms of the velocity of sound $c_s^2 (= dP/de$ evaluated at constant entropy) which controls the rate of expansion. For EoS of the type (a) $c_s^2 \sim 1/3$ in the QGP phase which is larger than the value of the corresponding quantity for EoS of the type (b). Therefore, the rate of expansion in the scenario (b) is comparatively slower, allowing the QGP to emit lepton pairs for a longer time resulting in greater yield for LQCD EoS. In contrast, for the EoS (a), the lower value of c_s^2 for the hadronic phase results in a slower cooling and hence a larger yield. Also shown for comparison is the yield from the decays of ρ mesons at the freezeout for the two types of EoS used. The yield from this source is much smaller and we will not consider it any further.

6.5. Dileptons at LHC Energy. At LHC the measured values of dN_{pp}^{ch}/dy for $\sqrt{s_{NN}} = 900$ GeV, 2.36 TeV, and 7 TeV are 3.02, 3.77, and 6.01, respectively [122]. The value dN_{pp}^{ch}/dy at $\sqrt{s_{NN}} = 5.25$ TeV is obtained by interpolating the above experimental data mentioned above. Assuming $x = 0.2$ in (26) we obtain $dN/dy = 2607$ in Pb+Pb collision for 0–10% centrality. For $\tau_i = 0.1$ fm/c we get $T_i = 756$ MeV.

The invariant mass spectra of lepton pairs are displayed for LHC initial conditions in Figure 26. Although the results are qualitatively similar to RHIC, quantitatively the yield at LHC is larger by an order of magnitude, primarily because of the large initial temperature. This enhancement is also seen in the transverse mass distributions of the lepton pairs at LHC.

All the results presented above for photon and dilepton production are reproduced using hydrodynamical model

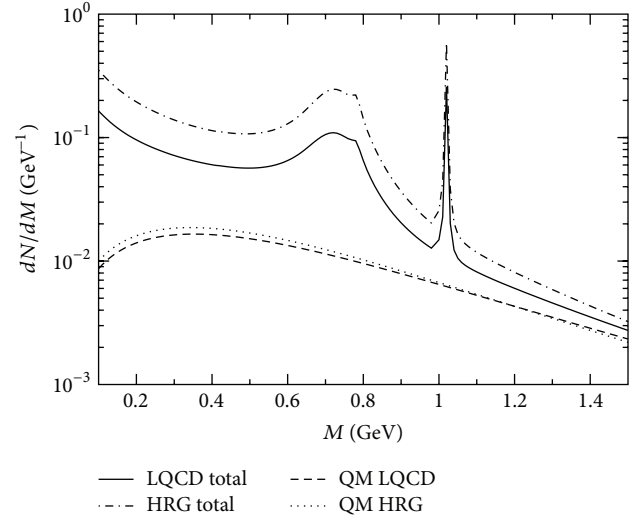


FIGURE 26: QGP and total contribution for EoS (a) HRG (dotted and dash-dotted lines) and EoS (b) LQCD (dashed and solid lines) at LHC energy.

with cylindrical symmetry [64] and boost invariance along the longitudinal direction [41]. The two approximations, such as cylindrical symmetry and boost invariance, remain intact at very high p_T and in central collision. So our results will not differ much even if (3 + 1) hydrodynamics is used at very high p_T and in central collision. In [123], the transverse momentum spectra of photons and v_2 of photons are calculated at RHIC energy using (3 + 1) hydrodynamical model. Recently, in [124, 125], a realistic (3 + 1) hydrodynamical model is established which can be used further to calculate the dilepton production, higher harmonics of flow of dileptons, interferometry with dileptons, and many more.

7. Radial Flow of Thermal Photons and Dileptons

The average magnitude of radial flow can be extracted from the transverse mass spectra $m_T (= \sqrt{p_T^2 + m_h^2})$ spectra of the hadrons only at freezeout surface. However, hadrons being strongly interacting objects can bring the information of the state of the system when it is too dilute to support collectivity; that is, the parameters of collectivity extracted from the hadronic spectra are limited to the evolution stage where the collectivity ceases to exist. These collective parameters have hardly any information about the interior of the matter. On the other hand, electromagnetic (EM) probes; that is, photons and dileptons are produced and emitted [1–8] from each space time point. Therefore, estimating radial flow from the EM probes will shed light on the time evolution of the collectivity in the system.

The calculations of EM probes from thermal sources depend on the parameters such as T_i , τ_i , T_{ch} , T_f , are EoS, which are not known uniquely. These abovementioned uncertainties have been used in the evaluation of individual single spectra of photon as well as dilepton. In order to

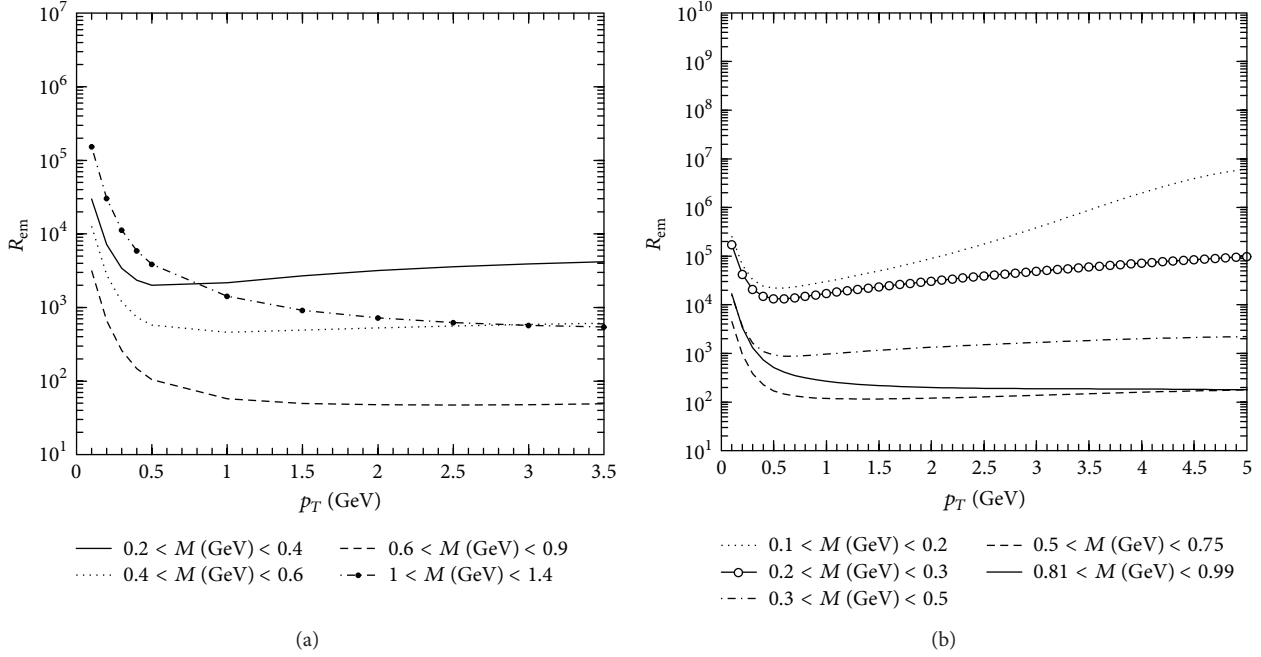


FIGURE 27: Variation thermal photon to dilepton ratio, R_{em} , with p_T for different invariant mass windows at SPS energy (a) and RHIC energy (b) (see text).

overcome the uncertainties and minimize the dependence of thermal sources on these parameters, the importance of the ratio of the transverse momentum spectra of photon to dilepton (R_{em}) has been emphasized in the present study (see [12, 16, 126, 127]), where the uncertainties are canceled out partially. It may be mentioned here that in the limit of $M \rightarrow 0$ the lepton pairs (virtual photons) emerge as real photons. Therefore, the evaluation of the ratio of the p_T spectra of photons to dileptons for various invariant mass bins along with a judicious choice of the p_T and M windows will be very useful to extract the properties of QGP as well as those of hadronic phase. This will be demonstrated in the present work by analyzing WA98 and PHENIX photons (results are shown in Section 5.4) and NA60 and PHENIX dilepton (results are shown in Section 6.4) spectra.

The p_T spectra of photon and dilepton can be parametrized as follows:

$$\left(\frac{dN}{d^2p_T dy}\right)_\gamma = A_1 \left(\frac{1}{p_T}\right)^{B_1} \exp[-c_1 p_T]; \quad c_1 = \frac{1}{T_{eff_1}},$$

$$\left(\frac{dN}{d^2p_T dy}\right)_{l^+l^-} = A_2 \left(\frac{1}{M_T}\right)^{B_2} \exp[-c_2 M_T]; \quad c_2 = \frac{1}{T_{eff_2}},$$
(70)

where $T_{eff_1} = T_{av} \sqrt{(1 + v_r)/(1 - v_r)}$ is the blue-shifted effective temperature for massless photons and $T_{eff_2} = T_{av} + Mv_r^2$ is the effective temperature for massive dileptons. T_{av} is the average temperature and v_r is the average radial flow of the system. The $T_{eff_{1,2}}$ can be obtained by parameterizing the p_T spectra of photons and dileptons (see Sections 5.4 and 6.4), respectively, with the expressed form of (70). The ratio, R_{em} ,

for different M windows (Figure 27) can be parametrized as follows:

$$R_{em} = A \left(\frac{M_T}{p_T}\right)^B \exp[-c(M_T - p_T)]; \quad c = \frac{1}{T_{eff}} \quad (71)$$

with different values of T_{eff} for different invariant mass windows. The argument of the exponential in (71) can be written as [126]

$$\frac{M_T - p_T}{T_{eff}} = \frac{M_T}{T_{eff_2}} - \frac{p_T}{T_{eff_1}}$$

$$= \frac{M_T}{T_{av} + Mv_r^2} - \frac{p_T}{T_{av} \sqrt{(1 + v_r)/(1 - v_r)}}. \quad (72)$$

As mentioned before some of the uncertainties prevailing in the individual spectra may be removed by taking the ratio, R_{em} , of the p_T distribution of thermal photon to dileptons. In the absence of experimental data for both photon and dilepton from the same colliding system for SPS energies, we have calculated the ratio R_{em} for Pb+Pb system, where the initial condition and the EoS are constrained by the measured WA98 photon spectra. The results are displayed in Figure 27.

Also we evaluate the ratio of the thermal photon to dilepton spectra constrained by the experimental data from Au+Au collisions measured by PHENIX collaboration. The results for the thermal ratio, R_{em} , displayed in Figure 27(b) are constrained by the experimental data on the single-photon and -dilepton spectra. The behavior of R_{em} with p_T for different invariant mass windows which is extracted from the available data is similar to the theoretical results obtained

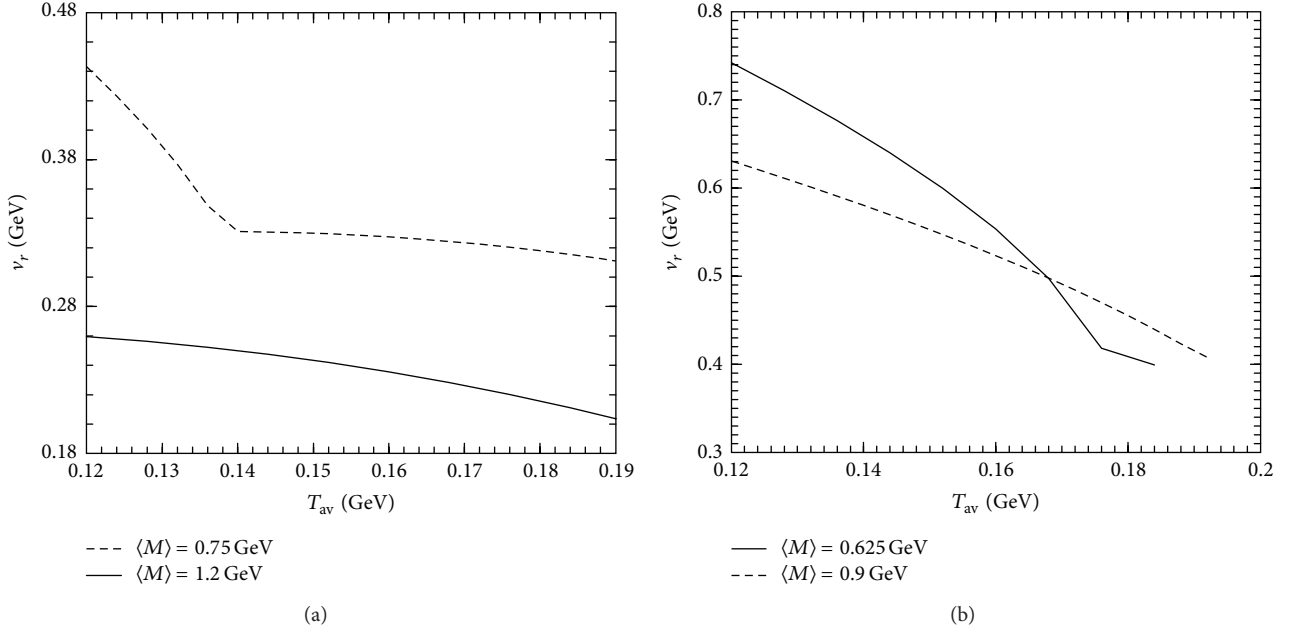


FIGURE 28: The variation of radial flow velocity with average temperature of the system for $\langle M \rangle = 0.75$ GeV and 1.2 GeV at SPS energy (a) and for $\langle M \rangle = 0.625$ GeV and 0.9 GeV at RHIC energy (b).

in [16, 126]. It is observed that the ratio decreases sharply and reaches a plateau beyond $p_T > 1.5$ GeV.

This behavior of R_{em} as a function of p_T can be understood as follows: (i) for $p_T \gg M$, $M_T \sim p_T$ and consequently $R_{em} \sim A$ giving rise to a plateau at large p_T . The height of the plateau is sensitive to the initial temperature of the system [16, 126] and (ii) for $p_T < M$, $R_{em} \sim \exp(-p_T/T_{eff})/p_T^B$ indicating a decrease of the ratio with p_T (at low p_T) as observed in Figure 27.

7.1. Variation of Radial Flow with Average Temperature. For a given p_T and M , (72) can be written as $v_r = f(T_{av})$. The T_{eff} 's are obtained from the ratio of individual spectra of photon and dilepton (by parametrising the R_{em} in Figure 27 using (71)). Thus we obtained the variation of radial flow with average temperature ($v_r(T_{av})$) for SPS (a) and RHIC (b) that has been depicted in Figure 28. It is clear from Figure 28 that the magnitude of the flow is larger in case of RHIC than SPS because of the higher initial pressure. Because of the larger initial pressure and QGP life time the radial velocity for QGP at RHIC is larger compared to SPS.

The T_{eff} obtained from the parametrization of ratio at SPS energy is 263 MeV and 243 MeV for $M = 0.75$ and 1.2 GeV, respectively. The average flow velocity v_r versus T_{av} has been displayed for $M = 0.75$ GeV and 1.2 GeV in Figure 28(a). The hadronic matter (QGP) dominates the $M \sim 0.75(1.2)$ GeV region. Therefore, these two mass windows are selected to extract the flow parameters for the respective phases. The v_r increases with decreasing T_{av} (increase in time) and reaches its maximum when the temperature of the system is minimum; that is, when the system attains T_f , the freezeout temperature. Therefore, the variation of v_r with T_{av} may be

treated as to show how the flow develops in the system. The v_r is larger in the hadronic phase because the velocity of sound in this phase is smaller, which makes the expansion slower, as a consequence system lives longer—allowing the flow to fully develop. On the other hand, v_r is smaller in the QGP phase because it has smaller life time where the flow is only partially developed. In Figure 28(b) the variation of average transverse velocity with average temperature for RHIC initial conditions is depicted.

7.2. Variation of Radial Flow with Invariant Mass. Obtaining T_{eff_1} and T_{eff_2} from the individual spectra and eliminating T_{av} one gets the variation of v_r with M . Figure 29(a) shows the variation of v_r with M for SPS conditions. The radial flow velocity increases with invariant mass M up to $M = M_\rho$ and then drops. How can we understand this behavior? From the invariant mass spectra, it is well known that the low M (below ρ mass) and high M (above ϕ peak) pairs originate from a partonic source [16]. The collectivity (or flow) does not develop fully in the QGP because of the small life time of this phase, which means that the radial velocity in QGP will be smaller for both low and high M . Whereas the lepton pairs with mass around ρ -peak mainly originate from a hadronic source (at a late stage of the evolution of system) are largely affected by the flow resulting in higher values of flow velocity. In summary, the value of v_r for M below and above the ρ -peak is small but around the ρ peak is large—with the resulting behavior displayed in Figure 29. Similar nonmonotonic behavior is observed in case of elliptic flow of photon as a function of p_T [128]. The variation of v_r with M in RHIC (Figure 29(b)) is similar to SPS though the values

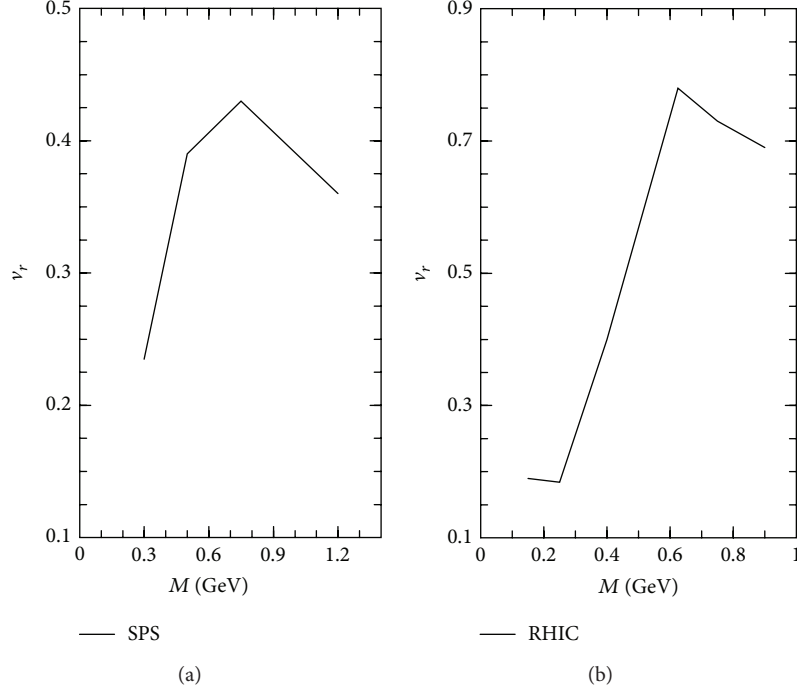


FIGURE 29: The variation of radial flow with invariant mass pairs for SPS (a) and RHIC (b) energies.

of v_r at RHIC are larger than those of SPS as expected due to higher initial pressure.

It is shown that simultaneous measurements of photon and dilepton spectra in HIC will enable us to quantify the evolution of the average radial flow velocity for the system, and the nature of the variation of radial flow with invariant mass indicates the formation of partonic phase at SPS and RHIC energy. The stronger radial flow at RHIC compared to SPS is due to higher initial energy densities and a longer lifetime of the reaction zone.

8. Dilepton Interferometry

The two-particle intensity interferometry, commonly known as Hanbury Brown Twiss (HBT) interferometry [129], is considered as one of the efficient methods to extract the information of space-time structure of the fireball formed in HIC. The utility of the intensity interferometry with dileptons [14, 15] for extracting fireball properties is as follows. As EM radiation produces from each stages of HIC, it retains information of the fireball at each space-time point. In contrast to correlation studies with hadrons which give information of the system when the system has frozen out, two-particle intensity interferometry using lepton pairs [14, 15], or photon [130, 131], can provide the information on the history of evolution of hot matter efficiently because EM probes do not rescatter after its production. As argued previously, photons appear to be more restrictive compared to dilepton, and we have attempted to do the correlation calculations with dileptons. So that with judicious choice of p_T and M windows we can get the spatial as well as temporal information of QGP and the hadronic phases separately by making use of correlations between two dilepton pairs.

8.1. Formalism and Equation of Bose-Einstein Correlation Function (BECF). As interferometry of the dilepton pairs actually reflects correlations between two virtual photons, the analysis then concentrates on computing the Bose-Einstein correlation function (BECF) for two identical particles defined as

$$C_2(\vec{p}_1, \vec{p}_2) = \frac{P_2(\vec{p}_1, \vec{p}_2)}{P_1(\vec{p}_1)P_1(\vec{p}_2)}, \quad (73)$$

where \vec{p}_i is the three momenta of the particle i , and $P_1(\vec{p}_i)$ and $P_2(\vec{p}_1, \vec{p}_2)$ represent the one- and two-particle inclusive lepton pair spectra, respectively, and is expressed as follows:

$$\begin{aligned} P_1(\vec{p}) &= \int d^4x \omega(x, K), \\ P_2(\vec{p}_1, \vec{p}_2) &= P_1(\vec{p}_1)P_1(\vec{p}_2) \\ &+ \frac{\lambda}{3} \int d^4x_1 d^4x_2 \omega(x_1, K) \\ &\quad \times \omega(x_2, K) \cos(\Delta x^\mu q_\mu), \end{aligned} \quad (74)$$

where $K = (p_1 + p_2)/2$, $q_\mu = p_{1\mu} - p_{2\mu} = q_\mu$, $\Delta x_\mu = x_{1\mu} - x_{2\mu}$, $x_{i\mu}$ and $p_{i\mu}$ are four coordinates for position and momentum variables, respectively, and $\omega(x, K)$ is the source function related to the thermal emission rate of lepton pairs per unit four volume, expressed as as follows:

$$\omega(x, K) = \int_{M_1^2}^{M_2^2} dM^2 \frac{dR}{dM^2 d^2K_T dy}. \quad (75)$$

TABLE 3: Values of the various parameters used in the relativistic hydrodynamical calculations.

Input	RHIC	LHC
dN/dy	1100	2376
T_i	290 MeV	640 MeV
τ_i	0.6 fm	0.1 fm
T_c	175 MeV	175 MeV
T_{ch}	170 MeV	170 MeV
T_{fo}	120 MeV	120 MeV
EoS	2 + 1 Lattice QCD	2 + 1 Lattice QCD

With further simplification, the C_2 can be redefined as

$$C_2(\vec{p}_1, \vec{p}_2) = 1 + \left(\frac{\lambda}{3} \frac{[\int d^4x \omega(x, K) \cos(\Delta\alpha)]^2}{P_1(\vec{p}_1) P_1(\vec{p}_2)} + \frac{[\int d^4x \omega(x, K) \sin(\Delta\alpha)]^2}{P_1(\vec{p}_1) P_1(\vec{p}_2)} \right), \quad (76)$$

where $\Delta\alpha = \alpha_1 - \alpha_2$, $\alpha_i = \tau M_{iT} \cosh(y_i - \eta) - r p_{iT} \cos(\theta - \psi_i)$, $M_{iT} = \sqrt{p_{iT}^2 + M^2}$ is the transverse mass, y_i is the rapidity, and ψ_i 's are the angles made by p_{iT} with the x -axis.

The inclusion of the spin of the virtual photon will reduce the value of $C_2 - 1$ by 1/3. The correlation functions can be evaluated for different average mass windows, $\langle M \rangle (\equiv M_{1+T}) = (M_1 + M_2)/2$. The leading order process through which lepton pairs are produced in QGP is $q\bar{q} \rightarrow l^+l^-$ [100, 101]. For the low M dilepton production from the hadronic phase the decays of the light vector mesons ρ , ω , and ϕ have been considered including the continuum [1, 5, 7, 8, 104]. Since the continuum part of the vector meson spectral functions is included in the current work, the processes like four pions annihilations [121] are excluded to avoid double counting.

For the space time the evolution of the system relativistic hydrodynamical model with cylindrical symmetry [64] and boost invariance along the longitudinal direction [41] has been used. The values of the parameters required for space-time evolution are displayed in Table 3. With all these ingredients we evaluate the correlation function C_2 for 0–5% Au+Au collisions centrality for RHIC at $\sqrt{s_{NN}} = 200$ GeV [132] and Pb+Pb collisions at for LHC at $\sqrt{s_{NN}} = 2.76$ TeV [133] for different invariant mass windows as a function of q_{side} and q_{out} which are related to transverse momenta of individual pair [134, 135]. By choosing appropriate phase space for the QGP and hadron gas and performing the space time integration using the initial condition tabulated in Table 3, the C_2 for different phase has been evaluated. We have evaluated the C_2 for $\langle M \rangle = 0.3, 0.5, 0.7, 1.2, 1.6$, and 2.5 GeV. In Figure 30 the results for only three values of $\langle M \rangle$ corresponding to low and high mass which are expected to be dominated by radiations from QGP ($\langle M \rangle \sim 1.6$ GeV) and hadronic phase ($\langle M \rangle \sim 0.77$ GeV), respectively, are displayed.

In Figure 30, we plot the C_2 as a function of q_{side} and q_{out} for RHIC initial conditions as tabulated in Table 3. A clear difference of dilepton pair mass dependence of the BEC studied as a function of q_{side} is observed for the contributions from different M domains. The differences are however small when BEC is studied as a function of q_{out} .

8.2. *Source Dimension.* The source dimensions can be obtained by parameterizing the calculated correlation function of the dilepton pairs with the empirical (Gaussian) form:

$$C_2(q, K) = 1 + \lambda \exp(-R_i^2(K) q_i^2), \quad (77)$$

where i stands for side, out, and long. Thus R_{side} , R_{out} , and R_{long} appearing in (77) are commonly referred to as HBT radii, which is measure of Gaussian widths of source size and can be expressed as follows:

$$\begin{aligned} R_{\text{side}}^2(K) &= \langle \tilde{y}^2 \rangle, \\ R_{\text{out}}^2(K) &= \langle (\tilde{x} - v_r \tilde{t})^2 \rangle, \\ R_{\text{long}}^2(K) &= \langle (\tilde{z} - v_z \tilde{t})^2 \rangle. \end{aligned} \quad (78)$$

The q_{out} , q_{side} , and q_{long} can be expressed in terms of individual particle momenta as [136]

$$\begin{aligned} q_{\text{side}} &= \left| \vec{q}_T - q_{\text{out}} \frac{\vec{K}_T}{K_T} \right| = \frac{2p_{1T} p_{2T} \sqrt{1 - \cos^2(\psi_1 - \psi_2)}}{f(k_{1T}, k_{2T})}, \\ q_{\text{out}} &= \frac{\vec{q}_T \cdot \vec{K}_T}{|K_T|} = \frac{(p_{1T}^2 - p_{2T}^2)}{f(k_{1T}, k_{2T})}, \\ q_{\text{long}} &= p_{1z} - p_{2z} = p_{1T} \sinh y_1 - p_{2T} \sinh y_2, \end{aligned} \quad (79)$$

where $f(k_{1T}, k_{2T}) = \sqrt{p_{1T}^2 + p_{2T}^2 + 2p_{1T} p_{2T} \cos(\psi_1 - \psi_2)}$ and λ (in this review, $\lambda = 1/3$) represents the degree of chaotic of the source. The deviation of λ from 1/3 will indicate the presence of nonthermal sources. A representative fit to the correlation functions is shown in Figure 30 (solid lines). While the radius (R_{side}) corresponding to q_{side} is closely related to the transverse size of the system and considerably affected by the collectivity, the radius (R_{out}) corresponding to q_{out} measures both the transverse size and duration of particle emission [136–139]. The extracted R_{side} and R_{out} for different $\langle M \rangle$ are shown in Figures 31(a) and 31(b), respectively.

8.2.1. Variation of R_{side} and R_{out} with $\langle M \rangle$

R_{side} . The variation of R_{side} for QGP, hadronic and QGP + hadronic phase, is obtained from the respective C_2 in that phase with an appropriate selection of phase space in space-time integration. Figure 31(a) shows nonmonotonic dependence of R_{side} on M , starting from a value close to QGP value (indicated by the dashed line); it drops with increase in M finally again approaching the QGP value for $\langle M \rangle > m_\phi$. It can be shown that $R_{\text{side}} \sim 1/(1 + E_{\text{collective}}/E_{\text{thermal}})$ [134, 135].

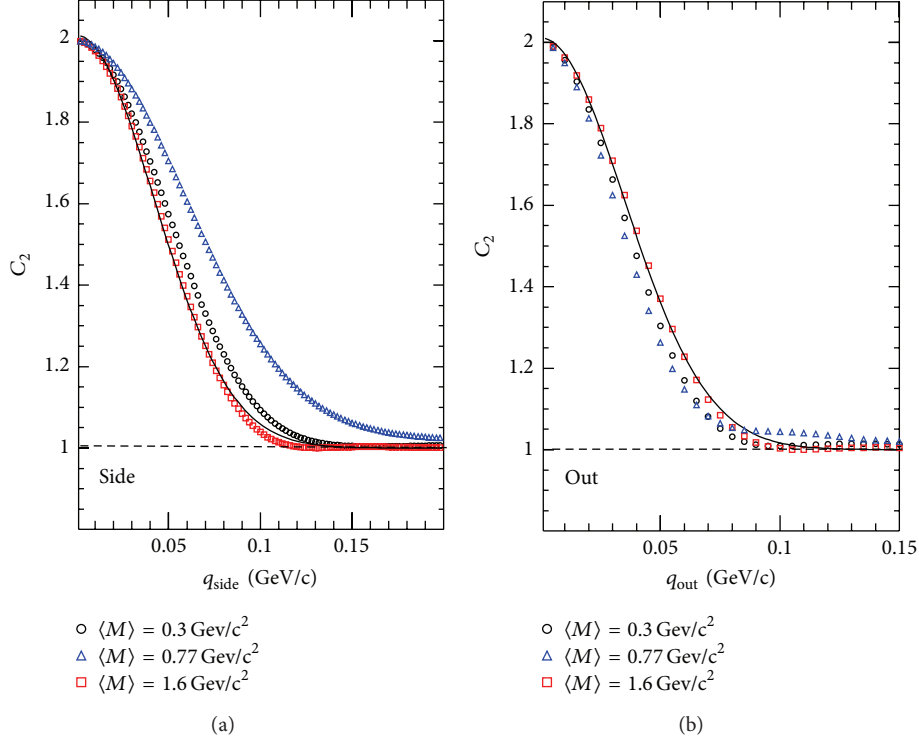


FIGURE 30: Correlation function for dilepton pairs as a function of q_{side} ((a), for $p_{1T} = p_{2T} = 2 \text{ GeV}$ and $\psi_2 = 0$) and q_{out} ((b), for $\psi_1 = \psi_2 = 0$ and $p_{1T} = 2 \text{ GeV}$) for three values of $\langle M \rangle$ [14, 15]. The solid lines show the parameterization of C_2 using (77).

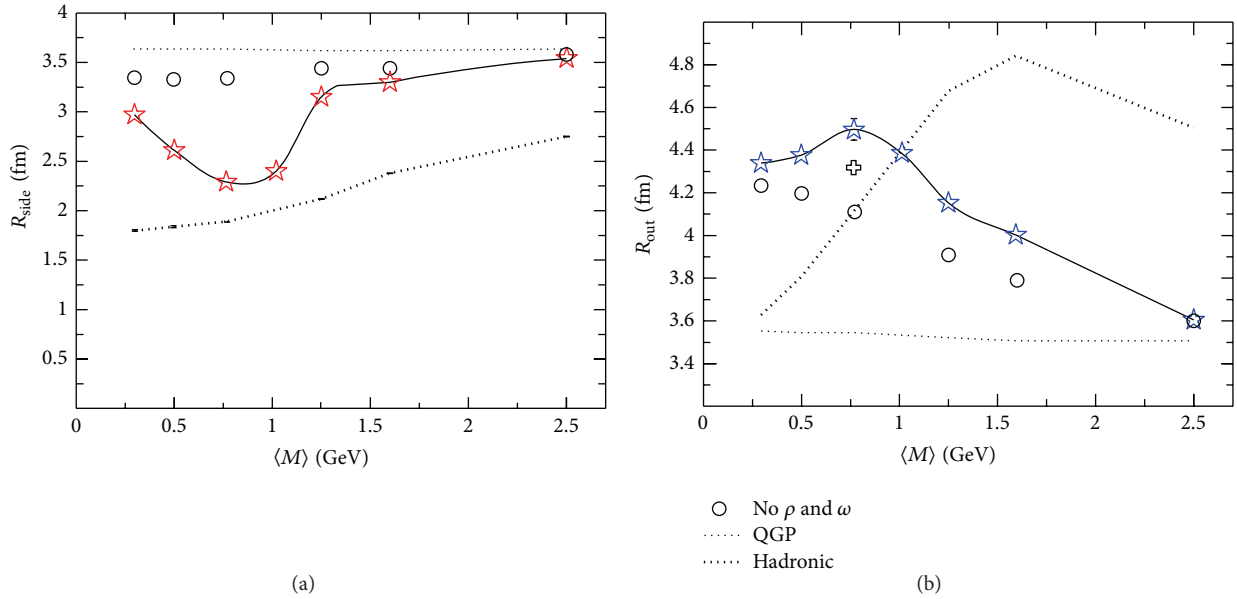


FIGURE 31: (a) R_{side} is evaluated with $p_{1T} = p_{2T} = 2 \text{ GeV}$ and $\psi_2 = 0$ as a function of $\langle M \rangle$ for RHIC energy and (b) R_{out} is evaluated with $\psi_1 = \psi_2 = 0$ and $p_{1T} = 2$ as a function of $\langle M \rangle$ for RHIC [14, 15].

In the absence of radial flow, R_{side} is independent of q_{side} . With the radial expansion of the system a rarefaction wave moves toward the center of the cylindrical geometry; as a consequence the radial size of the emission zone decreases with time. Therefore, the size of the emission zone is larger at

early times and smaller at late time. The high $\langle M \rangle$ regions are dominated by the early partonic phase where the collective flow has not been developed fully; that is, the ratio of collective-to-thermal energy is small, and hence the source has larger R_{side} . In contrast, the lepton pairs with $M \sim m_\rho$

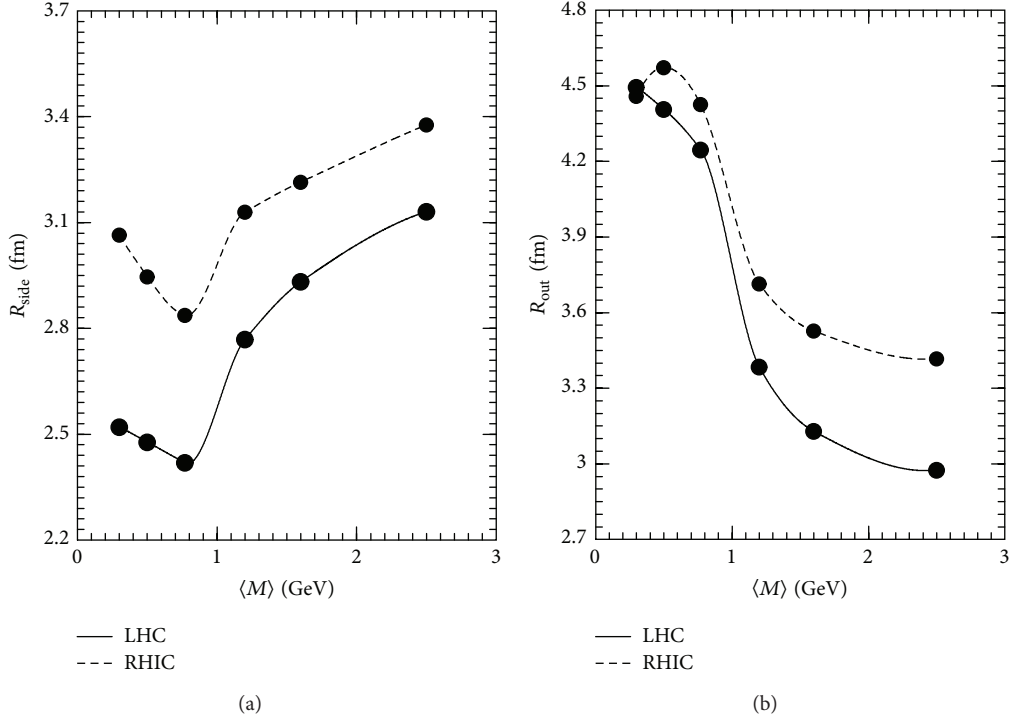


FIGURE 32: R_{side} (a) is evaluated with $p_{1T} = p_{2T} = 1$ GeV and $\psi_2 = 0$ and R_{out} (b) is evaluated with $p_{1T} = 1$ GeV and $\psi_1 = \psi_2 = 0$ as a function of $\langle M \rangle$ for RHIC (dashed line) and LHC (solid line) energies [14, 15].

are emitted from the late hadronic phase where the size of the emission zone is smaller due to larger collective flow giving rise to a smaller R_{side} . The ratio of collective to thermal energy for such cases is quite large, which is reflected as a dip in the variation of R_{side} with $\langle M \rangle$ around the ρ -mass region (Figure 31(a)). Thus the variation of R_{side} with M can be used as an efficient tool to measure the collectivity in various phases of matter. The dip in R_{side} at $\langle M \rangle \sim m_\rho$ is due to the contribution dominantly from the hadronic phase. We observe that, by keeping the ρ and ω contributions and setting radial velocity, $v_r = 0$, the dip in R_{side} vanishes, confirming the fact that the dip is caused by the radial flow of the hadronic matter. Therefore, the value of R_{side} at $\langle M \rangle \sim m_\rho$ may be used to estimate the average v_r in the hadronic phase.

R_{out} . The R_{out} probes both the transverse dimension and the duration of emission, and unlike R_{side} it does not remain constant even in the absence of radial flow. As a result its variation with M is complicated. The values R_{out} for different phases are obtained in a similar fashion as followed for obtaining the R_{side} values for the different phases. The large M regions are populated by lepton pairs from early partonic phase where the effect of flow is small and the duration of emission is also small—resulting in smaller values of R_{out} . For lepton pair from $M \sim m_\rho$ the flow is large which could have resulted in a dip as in R_{side} in this M region. However, R_{out} probes the duration of emission too which is large for hadronic phase because the expansion is slower in this phase for the EoS used in the present work. The velocity of sound which controls the rate of expansion and hence the

duration of the phase has larger value in hadronic phase than in the partonic phase. Thus resulting in the larger R_{out} in the hadronic phase than that in partonic phase, the larger duration compensates the reduction of R_{out} due to flow in the hadronic phase resulting is a bump in R_{out} in this region of M (Figure 31(b)). Again the duration of particle emission from both the phases obviously is larger than that from the individual phases.

Both R_{side} and R_{out} approach QGP values for $\langle M \rangle \sim 2.5$ GeV implying dominant contributions from partonic phase.

8.3. Comparison of HBT Radii with Different Collision Energies. Now we study the sensitivity of the HBT radii on the different collision energy. The R_{side} and R_{out} extracted from the C_2 's evaluated for 0–5% centrality in Au+Au collisions for RHIC at $\sqrt{s_{NN}} = 200$ GeV [132] and Pb+Pb collisions for LHC at $\sqrt{s_{NN}} = 2.76$ TeV [133] for different invariant mass windows as a function of q_{side} and q_{out} are shown in Figure 32. The change of R_{side} with $\langle M \rangle$ for RHIC and LHC is qualitatively similar but quantitatively different. The smaller values of R_{side} for LHC are due to the larger radial expansion which can be understood from the fact that the quantity $E_{\text{collective}}/E_{\text{thermal}}$ is larger at LHC than RHIC. So, the dip in the R_{side} variation at LHC is below than that at RHIC confirming a larger flow at LHC than RHIC. As the R_{out} probes both the transverse size and the duration of emission, from the previous discussion in Section 8.2.1, the larger duration compensates the reduction of R_{out} due to that flow resulting is a bump in R_{out} for $M \sim m_\rho$.

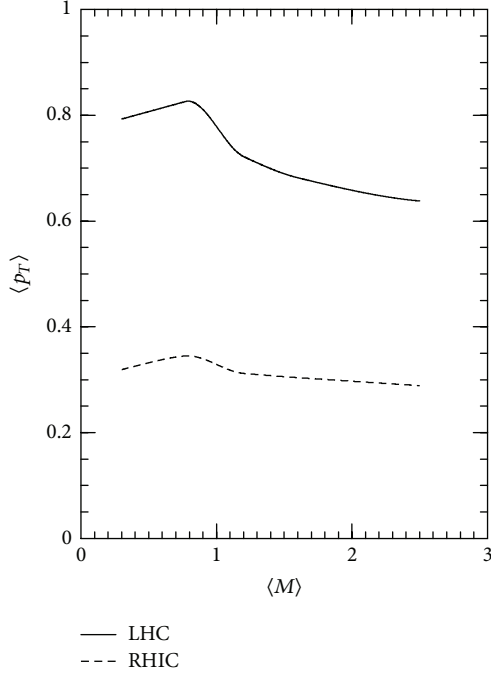


FIGURE 33: Variation of $\langle p_T \rangle$ as function of M (see (80)).

Though the duration of particle emission is more at LHC compared to RHIC (shown in Figure 36), the larger flow (corresponds to smaller size) at LHC [126] than that of RHIC compensates other factor (like duration of emission) which has an enhancing effect on R_{out} . So the value R_{out} at LHC is smaller than that of RHIC.

8.4. Radial Flow from HBT Radii. According to the discussion given in the Section 8.2, R_{side} is independent of q_{side} in the absence of radial flow. R_{side} is related to radial flow as follows:

$$R_{\text{side}}(M) = \frac{\mathcal{K}}{\langle p_T(M) \rangle}; \quad \langle p_T(M) \rangle = T_{\text{av}} + Mv_r^2. \quad (80)$$

The values of $R_{\text{side}}(M)$ are obtained for different $\langle M \rangle$ windows (shown in Figure 31). The higher mass, that is, $\langle M \rangle = 2.5$ GeV, corresponds to the initial stage of collision where the flow is not developed fully. So assume for $\langle M \rangle = 2.5$, $v_r = 0$, and $T = T_i$ the value of $\mathcal{K} = T_i \times R_{\text{side}}|_{\langle M \rangle = 2.5}$. Once we know the value of \mathcal{K} , we can calculate the $\langle p_T(M) \rangle (= \mathcal{K}/R_{\text{side}}(M))$. The variation of $\langle p_T \rangle$ with $\langle M \rangle$ has been displayed in Figure 33.

The high $\langle M \rangle$ regions are dominated by the early partonic phase where the collective flow has not been developed fully and hence show smaller $\langle p_T \rangle$. In contrast, due to larger collective flow for the lepton pairs with $M \sim m_\rho$, emitted from the late hadronic phase, $\langle p_T \rangle$ is larger. The larger value of $\langle p_T \rangle$ around the ρ -mass region is due to the contribution of large flow in the hadronic phase. Thus the variation of R_{side} with M (Figure 31) can be used as an efficient tool to measure the collectivity in various phases of matter.

8.5. Sensitivity of HBT Radii on p_{iT} . In this section, the sensitivity of the HBT radii for different values of the individual transverse momentum of the pairs is described. In Figure 34, the variation of R_{side} and R_{out} with $\langle M \rangle$ is shown for $p_{iT} = 1$ and 2 GeV. The lepton pairs coming from higher p_T and high mass region enable us to quantify the size of hotter zone. As mentioned before, the p_T contains the effect of flow as well as thermal motion. Hence the larger R_{side} at $M \sim M_\rho$ for $p_T = 2$ GeV is associated with longer flow and hence smaller source size. The observed bump in R_{out} (Figure 34(b)) is resulted from the fact that it contains both the size of the system as well as the duration of dilepton emission as discussed earlier.

8.6. Duration of Particle Emission from HBT Radii. The HBT radii, R_{out} and R_{side} , provide the information of average source size. However, in the ratio, $R_{\text{out}}/R_{\text{side}}$, some of the uncertainties associated with the space time evolution get canceled out. The quantity, $R_{\text{out}}/R_{\text{side}}$ gives the duration of particle emission [134, 135, 140, 141] for various domains of M . The difference between $R_{\text{side}}^2(K)$ and $R_{\text{out}}^2(K)$ at nonzero in K is then only due to the explicit K dependence in (78), that is, the term $v_r \langle t^2 \rangle$. This implies that the explicit K dependence dominates if the emission duration is sufficiently large or if the position-momentum correlations in the source are sufficiently weak:

$$R_{\text{diff}}^2 = R_{\text{out}}^2(K) - R_{\text{side}}^2(K) = v_r \langle t^2 \rangle. \quad (81)$$

In this case, the difference between these two HBT radius parameters gives direct access to the average emission duration $\langle t^2 \rangle$ of the source and allows to partially disentangle the spatial and temporal information contained in (78).

Figure 35 shows the $R_{\text{out}}/R_{\text{side}}$ and the difference $\sqrt{R_{\text{out}}^2 - R_{\text{side}}^2}$ as a function of $\langle M \rangle$ for Au+Au collisions at $\sqrt{s_{NN}} = 200$ GeV. Both show a nonmonotonic dependence on $\langle M \rangle$. The smaller values of both the quantities, particularly at high mass region, reflect the contributions from the early partonic phase of the system. The peak around ρ -meson mass reflects dominance of the contribution from hadronic phase as discussed before. Figure 36 shows a comparative study of the above two quantities (the ratio and the difference of R_{out} and R_{side}) for RHIC and LHC energies. They reflect a larger life time of thermal system for LHC than RHIC.

9. Elliptic Flow of Thermal Dileptons

It has been argued that the anisotropic momentum distribution of the hadrons can bring the information on the interaction of the dense phase of the system [142] despite the fact that the hadrons are emitted from the freezeout surfaces when the system is too dilute to support collectivity. Therefore, a suitable dynamical model is required to extrapolate the final hadronic spectra backward in time to get the information about the early dense phase. Such an extrapolation is not required for lepton pairs because they are emitted from the entire space-time volume of the system. Therefore, the v_2 of lepton pairs provides information of the hot and dense

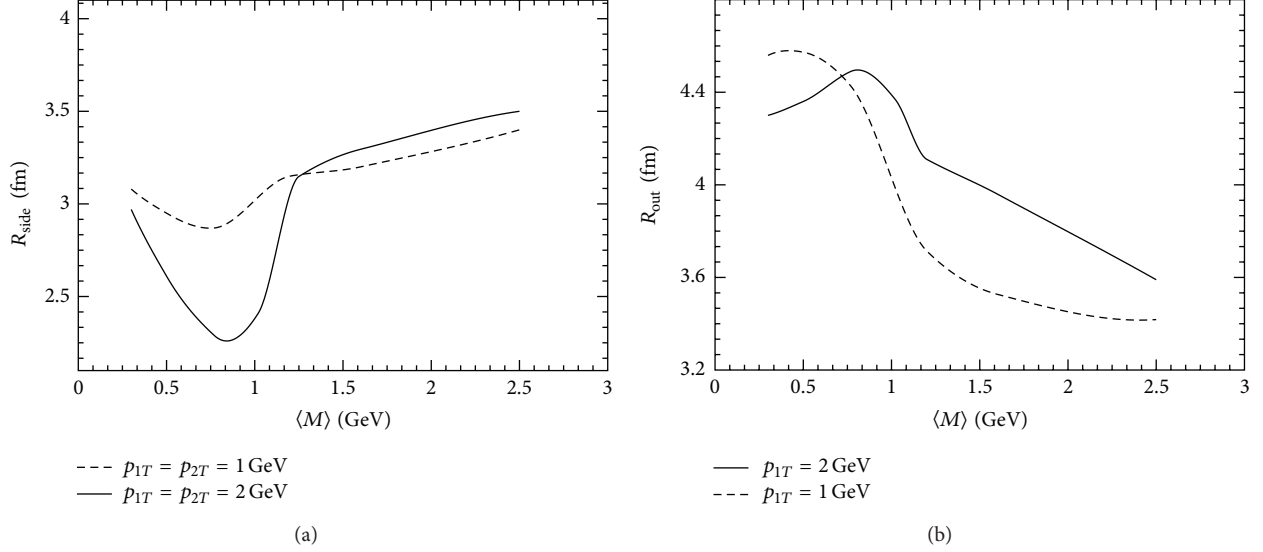


FIGURE 34: (a) Shows R_{side} as a function of $\langle M \rangle$ which is evaluated with $p_{1T} = p_{2T} = 1$ and 2 GeV and $\psi_2 = 0$ and similarly (b) shows R_{out} as a function of for $\psi_1 = \psi_2 = 0$ and $p_{1T} = 1$ and 2 GeV $\langle M \rangle$. The $p_{1T} = 1$ and 2 GeV results are shown as dashed line and solid line, respectively.

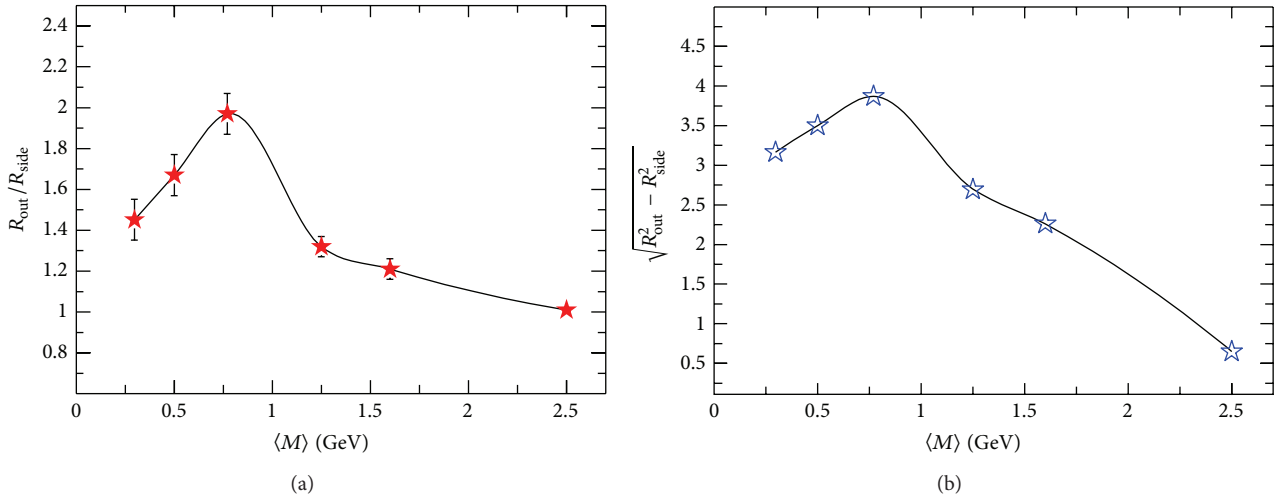


FIGURE 35: The ratio $R_{\text{out}}/R_{\text{side}}$ and the difference $\sqrt{R_{\text{out}}^2 - R_{\text{side}}^2}$ as a function of $\langle M \rangle$ [14, 15].

phase directly. The v_2 of dileptons can also be used to test the validity and efficiency of the extrapolation required for hadronic v_2 . The v_2 of real photons and dileptons [128, 143–146] has been evaluated for RHIC energies and shown that it can be used as effective probes to extract the properties of the partonic plasma. The sensitivity of the v_2 of lepton pairs on EoS has been elaborated in [145] for RHIC collision conditions. The lepton pairs are produced from each space time point of the system and hence the study of v_2 of lepton pairs will shed light on the time evolution of collectivity in the system [12, 147]. The radial flow alters the shape of the p_T spectra of dileptons; it kicks the low p_T pairs to the higher p_T domain, making the spectra flatter. Therefore, the presence of large radial flow may diminish the magnitude of v_2 at low p_T [37, 38], and this effect will be larger when the radial flow

is large, that is, in the hadronic phase which corresponds to lepton pairs with $M \sim m_\rho$.

9.1. Formalism of Elliptic Flow of Dilepton. The elliptic flow of dilepton, v_2 , can be defined as

$$\begin{aligned}
 v_2(p_T, M) &= \langle \cos 2\phi \rangle \\
 &= \frac{\sum_{i=Q,H} \int \cos(2\phi) \left(\frac{dN^{*}}{d^2 p_T dM^2 dy} \Big|_{y=0} \right)_i d\phi}{\sum_{i=Q,H} \int \left(\frac{dN^{*}}{d^2 p_T dM^2 dy} \Big|_{y=0} \right)_i d\phi},
 \end{aligned} \tag{82}$$

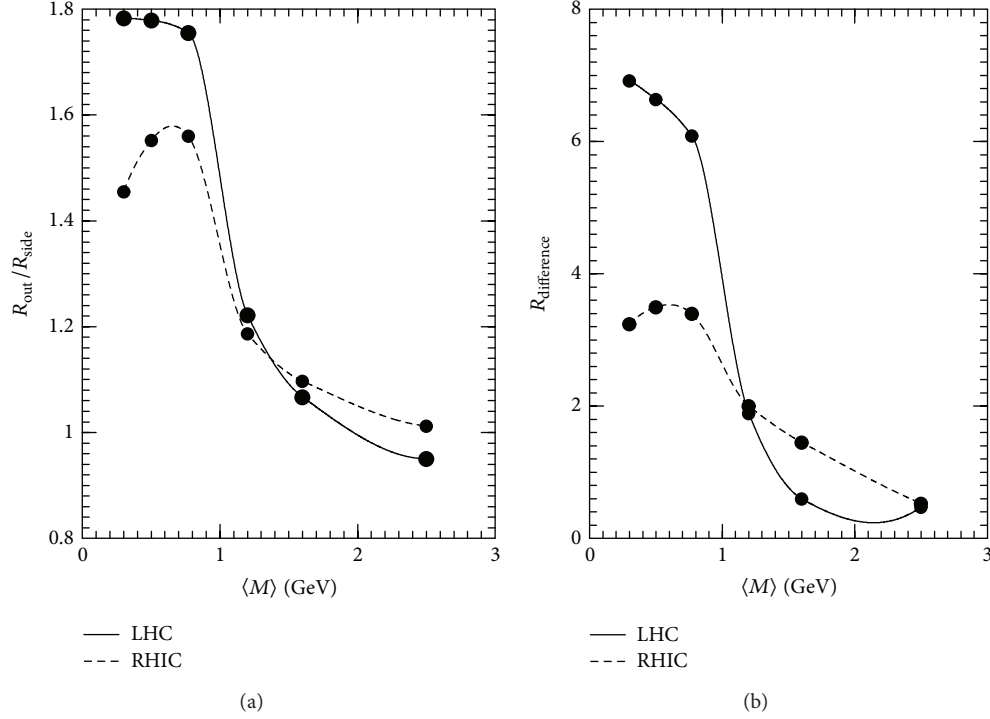


FIGURE 36: The ratio $R_{\text{out}}/R_{\text{side}}$ (a) and the difference $\sqrt{R_{\text{out}}^2 - R_{\text{side}}^2}$ (b) as a function of $\langle M \rangle$ for RHIC (dashed line) and LHC (solid line) energies are shown.

where the \sum stands for summation over quark matter (QM) and hadronic matter (HM) phases. The quantity $dN/d^2 p_T dM^2 dy|_{y=0}$ appearing in (82) can be obtained from the dilepton production per unit four volume, $dN/d^4 p d^4 x$ in a thermalized medium by integrating over the space-time evolution of the system. The $dN/d^4 p d^4 x$ for lepton pairs for QGP and hadrons are discussed in Sections 6.1 and 6.2, respectively (see [13, 109] for details).

To evaluate v_2 from (82) one needs to integrate the fixed temperature production rate given by (9) over the space time evolution of the system—from the initial QGP phase to the final hadronic freezeout state through a phase transition in the intermediate stage. The space-time evolution is done over the 4-volume, which is defined as $d^4 x (= \tau d\tau dx dy d\eta)$ are expressed in terms of $x^\mu = (\tau, x, y, \eta)$. We assume that the matter is formed in QGP phase with zero net baryon density in Pb+Pb collision at $\sqrt{s_{NN}} = 2.76$ TeV. The energy of the lepton pair (p_0) should be replaced by its value in the comoving frame of the expanding system which is given by $[p \cdot u = \gamma_T (M_T \cosh(y - \eta) - v_x p_T \cos \phi - v_y p_T \sin \phi)]$, $p_\mu = (M_T \cosh y, p_T \cos \phi, p_T \sin \phi, M_T \sinh y)$, and $u^\mu = \gamma_T (\cosh \eta, v_x, v_y, \sinh \eta)$. The EoS required to close the hydrodynamic equations is constructed by complementing Wuppertal-Budapest lattice simulation [48] with a hadron resonance gas comprising all the hadronic resonances up to mass of 2.5 GeV [148, 149]. The necessary initial conditions to solve the hydrodynamic equations are $T_i = 456$ MeV, the value of the temperature corresponding to the maximum of the initial energy profile for 30–40%

centrality at $\sqrt{s_{NN}} = 2.76$ TeV, with $\tau_i = 0.6$ fm/c, the thermalization time. The transition temperature, T_c , for quark hadron conversion is taken as 175 MeV. The system is assumed to get out of chemical equilibrium at $T = T_{\text{ch}} = 170$ MeV [69]. The kinetic freezeout temperature $T_F = 130$ MeV is fixed from the p_T spectra of the produced hadrons at the same collision energy of Pb+Pb system. The EoS and the values of the parameters mentioned above are constrained by the p_T spectra (for 0–5% centrality) and elliptic flow (for 10–50% centrality) of charged hadrons [148] measured by ALICE collaboration [150, 151].

9.2. Results and Discussion. In Figure 37 we depict the constant temperature contours corresponding to $T_c = 175$ MeV and $T_f = 130$ MeV in the τ - x plane (at zero abscissa) indicating the boundaries for the QM and HM phases, respectively.

The life time of the QM phase ~ 6 fm/c and the duration of the HM are ~ 6 –12 fm/c. Throughout this work by early and late will approximately mean the duration of the QM and HM, respectively.

With all the ingredients mentioned above we evaluate the p_T integrated M distribution of lepton pairs originating from QM and HM (with and without medium effects on the spectral functions of ρ and ω). The results are displayed in Figure 38 for the initial conditions and centrality mentioned above. We observe that for $M > M_\phi$ the QM contributions dominate. For $M_\rho \leq M \leq M_\phi$ the HM shines brighter than QM. For $M < M_\rho$, the HM (solid line) over shines

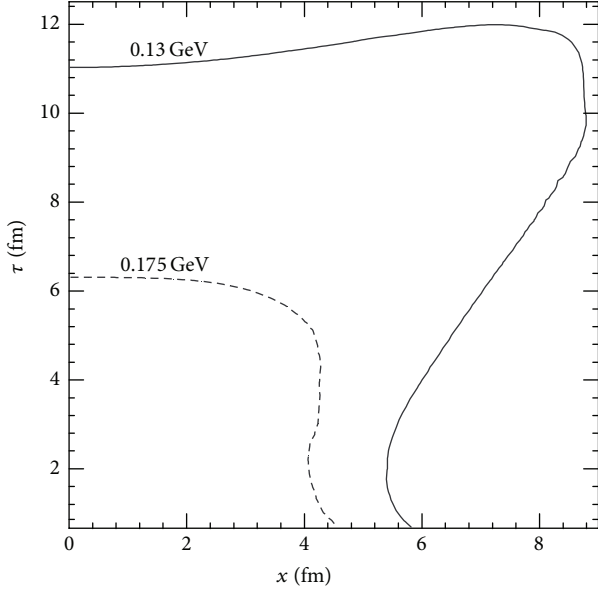


FIGURE 37: Constant temperature contours denoting space-time boundaries of the QGP and hadronic phase.

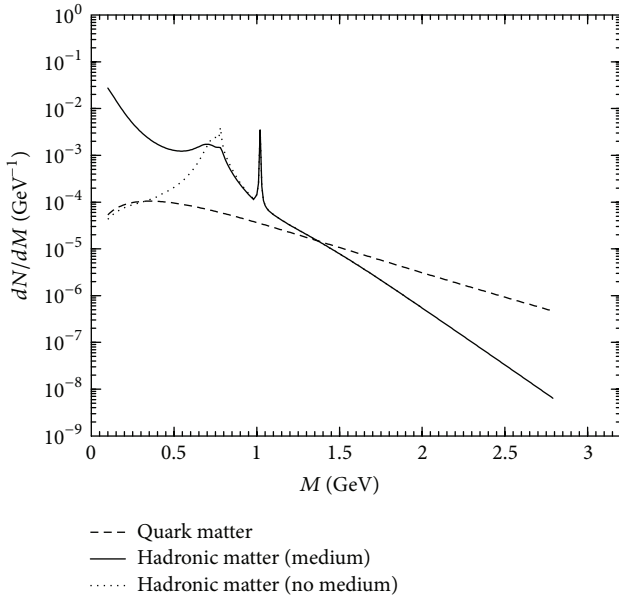


FIGURE 38: Invariant mass distribution of lepton pairs from quark matter and hadronic matter [13].

the QM due to the enhanced contributions primarily from the medium-induced broadening of ρ spectral function. However, the contributions from QM and HM become comparable in this region of M if the medium effects on ρ spectral function are ignored (dotted line). Therefore, the results depicted in Figure 38 indicate that a suitable choice of M window will enable us to unravel the contributions from a particular phase (QM or HM).

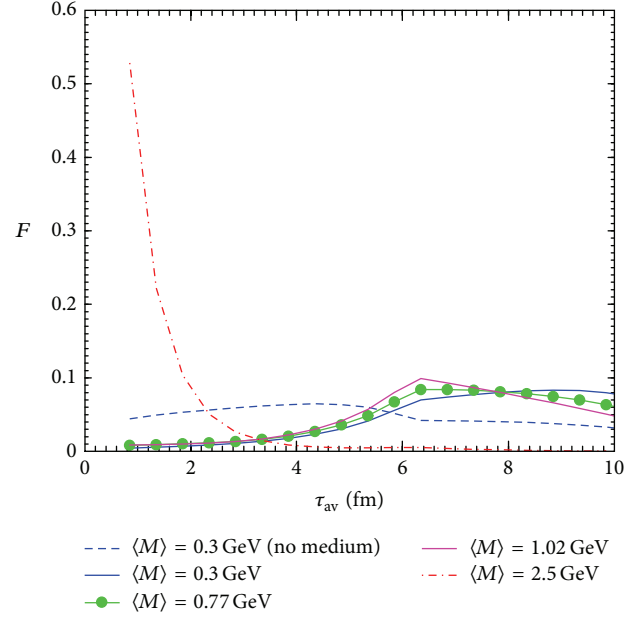


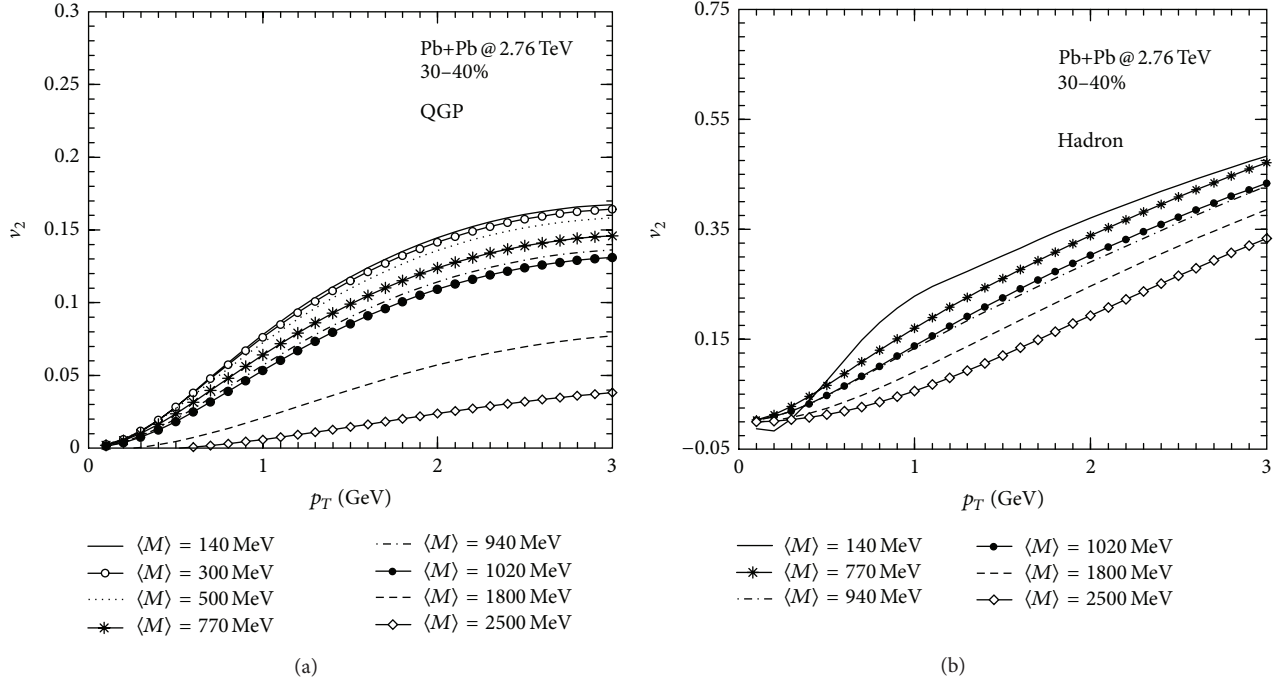
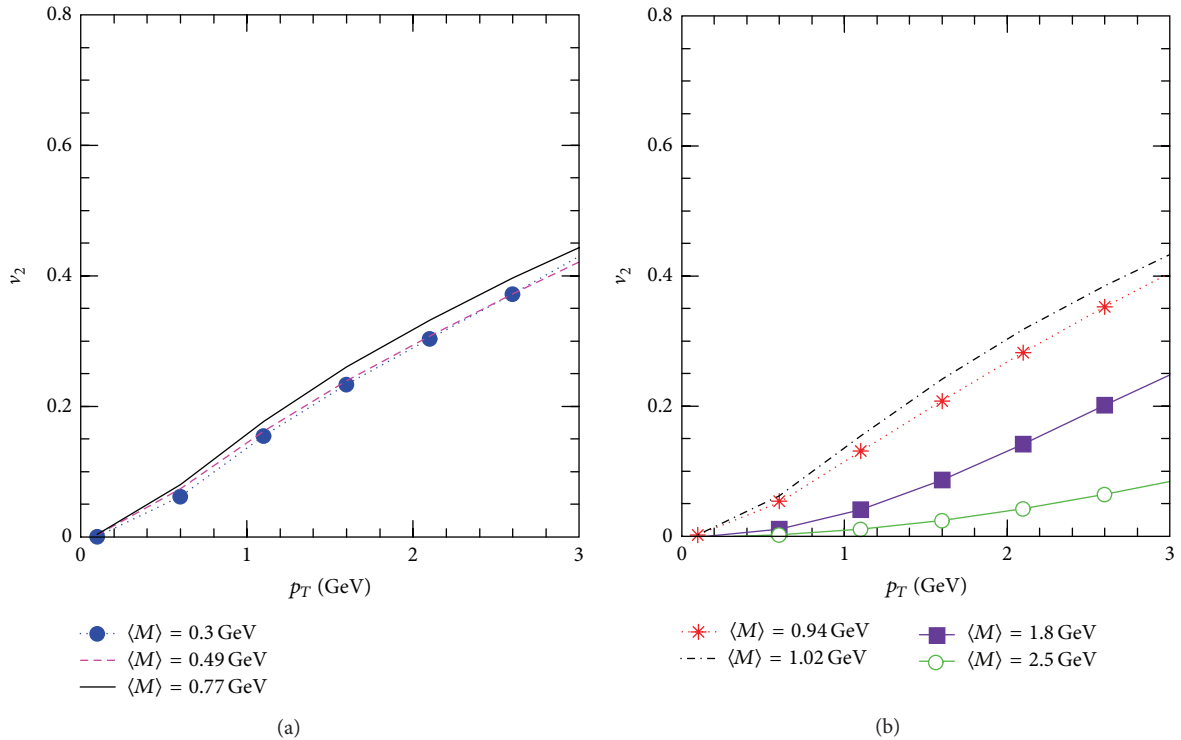
FIGURE 39: Fractional contribution of lepton pairs for various invariant mass windows as a function of average proper time (see text for details) [13].

To further quantify these issues we evaluate the following quantity:

$$F = \frac{\int' (dN/d^4x d^2p_T dM^2 dy) dx dy d\eta d\tau d^2p_T dM^2}{\int (dN/d^4x d^2p_T dM^2 dy) dx dy d\eta d\tau d^2p_T dM^2}, \quad (83)$$

where the M integration in both the numerator and denominator is performed for selective M windows from M_1 to M_2 with mean M defined as $\langle M \rangle = (M_1 + M_2)/2$. The prime in \int' in the numerator indicates that the τ integration in the numerator is done from $\tau_1 = \tau_i$ to $\tau_2 = \tau_i + \Delta\tau$ with progressive increment of $\Delta\tau$, while in the denominator the integration is done over the entire lifetime of the system. In Figure 39, F is plotted against $\tau_{av} (= (\tau_1 + \tau_2)/2)$. The results substantiate the fact that pairs with high $\langle M \rangle \sim 2.5$ GeV originate from QM ($\tau_{av} \leq 6$ fm/c, QGP phase) and pairs with $\langle M \rangle \sim 0.77$ GeV mostly emanate from the HM phase ($\tau_{av} \geq 6$ fm/c). The change in the properties of ρ due to its interaction with thermal hadrons in the bath is also visible through F evaluated for $\langle M \rangle \sim 0.3$ GeV with and without medium effects. This clearly indicates that the $\langle M \rangle$ distribution of lepton pairs can be exploited to extract collectivity of different phases of the evolving matter.

Figure 40(a) shows the differential elliptic flow, $v_2(p_T)$, of dileptons arising from various $\langle M \rangle$ domains in quark matter. Similarly Figure 40(b) shows the differential elliptic flow, $v_2(p_T)$, of dileptons arising from various $\langle M \rangle$ domains from hadronic matter. The individual v_2 for QM and HM is obtained by doing an integration over specific invariant masses (M) window as well as space time integration over the regime where $T_c < T(\tau, x, y) < T_i$ and $T_f < T(\tau, x, y) < T_c$, respectively. The v_2 is small at low p_T and gradually increases


 FIGURE 40: Elliptic flow of quark matter (a) and hadronic matter (b) as a function of p_T for various mass windows.

 FIGURE 41: Total elliptic flow as function of p_T for various mass windows.

and attains large value around $p_T \sim 2-3$ GeV/c. Also there is clear mass ordering that has been observed for $v_2(p_T)$ for QM; that is, v_2 decreases with increase in M . This is because dileptons come from high M region, $M > M_\phi$, come mostly from hot partonic phase where the fluid velocity is not strong to support the collectivity but the spatial eccentricity

of the source is large. On the other hand dileptons that come from low M region, M below ϕ peak dominantly come from late hadronic matter where the collectivity is strong and the spatial asymmetry dissolve into momentum asymmetry.

Figure 41 shows the differential elliptic flow, $v_2(p_T)$ of dileptons arising from various $\langle M \rangle$ domains. We observe

that, for $\langle M \rangle = 2.5 \text{ GeV}$, v_2 is small for the entire p_T range because these pairs arise from the early epoch (see Figure 39) when the flow is not developed entirely. However, the v_2 is large for $\langle M \rangle = 0.77 \text{ GeV}$ as these pairs originate predominantly from the late hadronic phase when the flow is fully developed.

It is also interesting to note that the medium-induced enhancement of ρ spectral function provides a visible modification in v_2 for dileptons below ρ peak. Figure 42 shows the comparison between $v_2(p_T)$ of dilepton at $\langle M \rangle = 300 \text{ MeV}$ with and without medium effects.

In Figure 43 we depict the variation of R_Q with p_T for $\langle M \rangle = 0.3 \text{ GeV}$ (line with solid circle) 0.77 GeV (solid line) and 2.5 GeV (line with open circle). The quantity R_Q and R_H is defined as

$$R_Q = \frac{v_2^{\text{QM}}}{v_2^{\text{QM}} + v_2^{\text{HM}}}, \quad (84)$$

$$R_H = \frac{v_2^{\text{HM}}}{v_2^{\text{QM}} + v_2^{\text{HM}}},$$

where v_2^{QM} and v_2^{HM} are the elliptic flow of QM and HM phases, respectively. The results clearly illustrate that v_2 of lepton pairs in the large $\langle M \rangle (= 2.5 \text{ GeV})$ domain (open circle in Figure 43) originates from QM for the entire p_T range considered here. The value of R_Q is large in this domain because of the large (negligibly small) contributions from QM (HM) phase. f_{QM} is large here. It is also clear that the contribution from QM phase to the elliptic flow for $\langle M \rangle (= 0.77 \text{ GeV})$ is very small (solid line in Figure 43). The value of R_H for $\langle M \rangle = 0.77 \text{ GeV}$ is large (not shown in the figure). The v_2 at the (late) hadronic phase (either at ρ or ϕ peak) is larger than the (early) QGP phase (say at $\langle M \rangle = 2.5 \text{ GeV}$) for the entire p_T range considered here. Therefore, the p_T -integrated values of v_2 should also retain this character of v_2 at the corresponding values of $\langle M \rangle$. It is also important to note that the differential elliptic flow, $v_2(p_T)$, obtained here at LHC is larger than the values obtained at RHIC [143–145] for all the invariant mass windows. The value of R_H for $\langle M \rangle = 0.77 \text{ GeV}$ is large (not shown in the figure).

The v_2 at the HM phase (either at ρ or ϕ peak) is larger than its value in the QGP phase (say at $\langle M \rangle = 2.5 \text{ GeV}$) for the entire p_T -range considered here. Therefore, the p_T integrated values of v_2 should also retain this character at the corresponding values of $\langle M \rangle$, which is clearly observed in Figure 44 which displays the variation of $v_2(\langle M \rangle)$ with $\langle M \rangle$. The $v_2(\propto \epsilon_p)$ of QM is small because of the small pressure gradient in the QGP phase. The v_2 resulting from hadronic phase has a peak around ρ pole indicating the full development of the flow in the HM phase. For $\langle M \rangle > m_\phi$ the v_2 obtained from the combined phases approaches the value corresponding to the v_2 for QGP. Therefore, measurement of v_2 for large $\langle M \rangle$ will bring information of the QGP phase at the earliest time of the evolution. It is important to note that the p_T -integrated $v_2(\langle M \rangle)$ of lepton pairs with $\langle M \rangle \sim m_\pi, m_K$ is close to the hadronic v_2^π and v_2^K (symbol * in Figure 44) if the thermal effects on ρ properties are included. Exclusion of

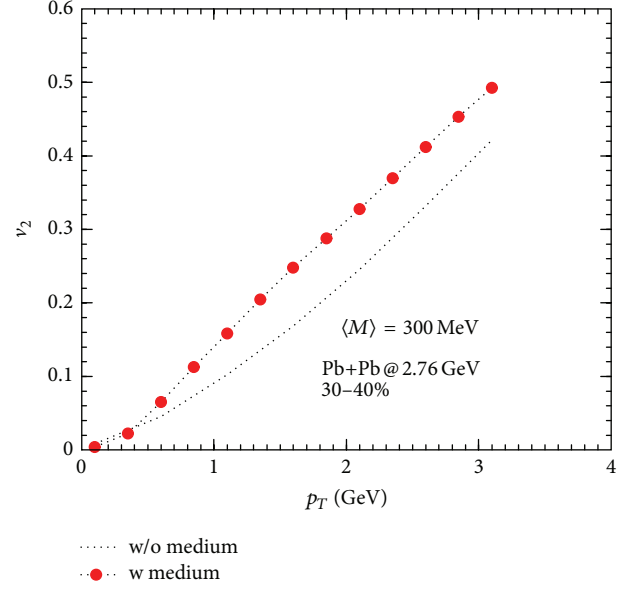


FIGURE 42: The figure displays the effect of the broadening of ρ spectral function on the elliptic flow for $\langle M \rangle = 300 \text{ MeV}$.

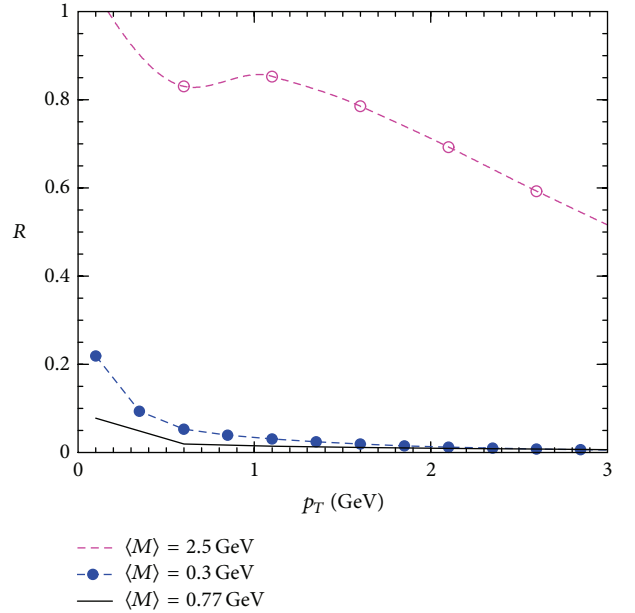


FIGURE 43: It shows the variation of R_Q (see text) with p_T for $\langle M \rangle = 0.3 \text{ GeV}$, 0.77 GeV and 2.5 GeV .

medium effects gives lower v_2 for lepton pairs compared to hadrons. The fact that the v_2 of the (penetrating) lepton pairs is similar in magnitude to the v_2 of hadrons for ($\langle M \rangle \sim m_\pi, m_K, m_{\text{proton}}$, etc.) ascertains that the anisotropic momentum distribution of hadrons carries the information of the HM phase with duration $\sim 6\text{--}12 \text{ fm/c}$ [13]. We also observe that the variation of $v_2(\langle M \rangle)$ with $\langle M \rangle$ has a structure similar to dN/dM versus M . As indicated by (82) we can write

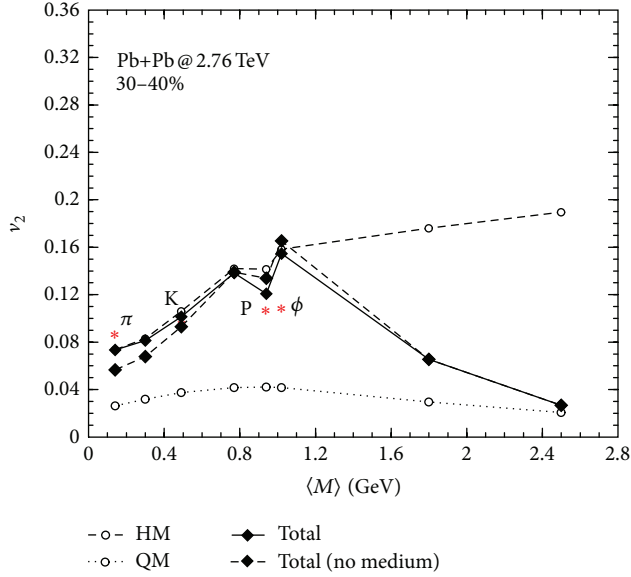


FIGURE 44: (Color online) Variation of dilepton elliptic flow as function of $\langle M \rangle$ for QM, HM (with and without medium effects), and for the entire evolution. The symbol * indicates the value of v_2 for hadrons, for example, π , kaon, proton, and ϕ .

$v_2(\langle M \rangle) \sim \sum_{i=QM, HM} v_2^i \times f_i$, where f_i is the fraction of QM or HM from various space-time regions. The structure of dN/dM is reflected in $v_2(\langle M \rangle)$ through f_i . We find that the magnitude of $v_2(\langle M \rangle)$ at LHC is larger than its value at RHIC [143–145].

10. Summary

In this review, we have attempted to summarize the photon and dilepton spectra measured at different beam energies by different experimental collaborations which have been analyzed to understand the evaluation of collectivity in the system. The initial conditions of the evolving matter required to calculate the photon and dilepton spectra have been constrained to reproduce the measured multiplicity in these collisions. The EoS, the other crucial input to the calculations, has been taken from lattice QCD calculations. The deviation of the hadronic phase from chemical equilibrium is taken into account by introducing nonzero chemical potential for each hadronic species. For dilepton emission from hot hadrons, the spectral function of ρ , ω at finite temperature and ϕ in vacuum is considered. We have also observed the dissipative effects on the photon spectra by taking into account the viscous contribution to phase space factors of all the participating partons/hadrons in the photon production rate as well as to the expansion dynamics with finite shear viscosity.

It is shown that simultaneous measurements of photon and dilepton spectra in heavy ion collisions will enable us to quantify the evolution of the average radial flow velocity for the system, and the nature of the variation of radial flow with invariant mass will indicate the formation of partonic phase. All this study suggests with judicious choice of p_T and

M window will infer information of partonic and hadronic phase separately.

In this work, we present a new proposal for carrying out an experimental measurement of dilepton interferometry both for RHIC and LHC. We establish through a hydrodynamical model-based space-time evolution the promise of such a dilepton interferometry analysis that will be useful to understand the properties of the partonic phase. We have evaluated the correlation function, C_2 , for two dilepton pairs for various invariant mass domains and extracted the HBT radii, that is R_{side} and R_{out} as a function of M . These HBT radii show a nonmonotonic dependence on the invariant mass, reflecting the evolution of collective flow in the system which can be considered as a signal of the QGP formation in heavy ion collisions. The M dependence of the $R_{\text{out}}/R_{\text{side}}$ and $\sqrt{R_{\text{out}}^2 - R_{\text{side}}^2}$ which can be experimentally measured could be used to characterize the source properties at various instances of the evolution.

We have evaluated the v_2 of dileptons originating from the Pb+Pb collisions at $\sqrt{s_{NN}} = 2.76$ TeV for 30–40% centrality. Our study shows that $v_2(M)$ provides useful information on the collective motion of the evolving QCD matter formed in high energy heavy-ion collisions. The present work indicates that experimental observation of the reduction of $v_2(M)$ with increasing M beyond ϕ mass would reflect the presence of small momentum space anisotropy through small collective motion in the partonic phase. We observe that $v_2(\langle M \rangle)$ of the penetrating probe (lepton pairs) for $\langle M \rangle = m_\pi$ and m_K is similar to the hadronic v_2^π and v_2^K when the medium-induced change in the ρ spectral function is included in evaluating the dilepton spectra. Since the medium effects are large during the dense phase of the system, therefore, this validates the statement that the hadronic v_2 carries the information of the early dense phase of the collisions. Our study also establishes the fact that the invariant mass dependence of dilepton v_2 can in principle act as a clock for the space time evolution of the system formed in HIC.

Some comments on effect of magnetic field on photon and dilepton production are in order here. The magnetic contribution is significant when photons propagate perpendicular to magnetic field or in reaction plane in noncentral collision [152]. Recently, Tuchin has implemented the magnetic field effect on the photon as well as dilepton production which is summarized here. Recently in [153, 154], it has been argued that photons, in particular thermal and direct photons from earliest times of QGP, will be affected by the magnetic field. In dilepton sector, the magnetic contribution is important at lower electron energies (below ~ 0.5 GeV at midrapidity at RHIC). In fact, it becomes dominant source of dileptons at lower electron energies. For LHC energies, the effect of magnetic field on dilepton should be taken seriously because 40% of energy density of the QGP resides in the strong magnetic field ($\sim 10^{18}$ Gauss [152]), which can be generated in heavy ion collision at LHC. Whereas in RHIC energy this fraction is within 3% so can be safely ignored. Some more realistic calculation and hydrodynamic model with magnetic field are required to conclude anything in future.

Appendix

Phase Space

In this appendix we derive (37) from (12). The photon production rate from the process, $1 + 2 \rightarrow 3 + \gamma$ is given by

$$E \frac{dR}{d^3 p} = \frac{1}{2} \frac{\mathcal{N}}{(2\pi)^8} \times \int \frac{d^3 p_1}{2E_1} \int \frac{d^3 p_2}{2E_2} \int \frac{d^3 p_3}{2E_3} f_1(E_1) f_2(E_2) \times [1 \pm f_3(E_3)] \overline{|M|^2} \delta \times (p_1 + p_2 - p_3 - p). \quad (\text{A.1})$$

Performing the $d^3 p_3$ integration using the delta function and using $d^3 p/E = p_T dp_T dy d\phi$ we get

$$E \frac{dR}{d^3 p} = \frac{1}{16} \frac{\mathcal{N}}{(2\pi)^8} \int p_{1T} dp_{1T} dy_1 d\phi_1 p_{2T} dp_{2T} dy_2 d\phi_2 \times \frac{1}{E_3} f_1(E_1) f_2(E_2) [1 \pm f_3(E_3)] \times \overline{|M|^2} \delta(E_1 + E_2 - E_3 - E), \quad (\text{A.2})$$

where ϕ_1 and ϕ_2 are the angles made by the transverse momenta of first and second particles with the transverse momentum of the emitted photon. The momentum conservation along the z -direction: $p_{3z} = p_{1z} + p_{2z} - p_z$ can be written in terms of rapidity as

$$m_{3T} \sinh y_3 = m_{1T} \sinh y_1 + m_{2T} \sinh y_2 - p_T \sinh y. \quad (\text{A.3})$$

Now the energy, E_3 , can be written as

$$E_3 = m_{3T} \cosh y_3 = \sqrt{m_{3T}^2 + m_{3T}^2 \sinh^2 y_3}. \quad (\text{A.4})$$

Substituting (A.3) in (A.4) we get

$$E_3 = \left[(m_{1T} \sinh y_1 + m_{2T} \sinh y_2 - p_T \sinh y)^2 + m_{3T}^2 \right]^{1/2}. \quad (\text{A.5})$$

Considering the energy conservation ($E_3 = E_1 + E_2 - E$) and writing the energies in terms of rapidity ($E_i = m_{iT} \cosh y_i$) we get

$$E_3 = m_{1T} \cosh y_1 + m_{2T} \cosh y_2 - p_T \cosh y. \quad (\text{A.6})$$

Equating (A.5) and (A.6) we have

$$m_{3T} = \left[m_{1T}^2 + m_{2T}^2 + p_T^2 + 2m_{1T}m_{2T} \cosh(y_1 - y_2) - 2m_{1T}p_T \cosh(y_1 - y) - 2m_{2T}p_T \cosh(y_2 - y) \right]^{1/2}. \quad (\text{A.7})$$

However, we also have

$$m_{3T} = (p_{3T}^2 + m_3^2)^{1/2} = \left[(p_{1T} + p_{2T} - p_T)^2 + m_3^2 \right]^{1/2} = \left[p_{1T}^2 + p_{2T}^2 + p_T^2 + 2p_{1T}p_{2T} \cos(\phi_{12}) - 2p_T p_{1T} \cos(\phi_1) - 2p_T p_{2T} \cos(\phi_2) + m_3^2 \right]^{1/2}, \quad (\text{A.8})$$

where

$$\cos(\phi_{12}) = \cos(\phi_1) \cos(\phi_2) + \sin(\phi_1) \sin(\phi_2). \quad (\text{A.9})$$

Equating (A.7) with (A.8) leads to the expression:

$$\left[(p_{1T} \cos \phi_1 - p_T) \cos \phi_2 + p_{1T} \sin \phi_1 \sin \phi_2 \right] = \frac{1}{2p_{2T}} \left[(m_1^2 + m_2^2 - m_3^2) + 2m_{1T}m_{2T} \cosh(y_1 - y_2) - 2m_{1T}p_T \cosh(y_1 - y) - 2m_{2T}p_T \cosh(y_2 - y) + 2p_T p_{1T} \cos \phi_1 \right]. \quad (\text{A.10})$$

Solving (A.10) for ϕ_2 one gets

$$\phi_2^0 = \tan^{-1} \left(\frac{p_{1T} \sin \phi_1}{p_{1T} \cos \phi_1 - p_T} \right) - \cos^{-1} \frac{H}{2Rp_{2T}}, \quad (\text{A.11})$$

where

$$R = \sqrt{p_{1T}^2 + p_T^2 - 2p_{1T}p_T \cos \phi_1}, \quad (\text{A.12})$$

$$H = (m_1^2 + m_2^2 - m_3^2) + 2m_{1T}m_{2T} \cosh(y_1 - y_2) - 2m_{1T}p_T \cosh(y_1 - y) - 2m_{2T}p_T \cosh(y_2 - y) + 2p_T p_{1T} \cos \phi_1. \quad (\text{A.13})$$

Now we express the argument of the delta function in (A.2) as function of ϕ_2 as

$$f(\phi_2) = E_1 + E_2 - E_3 - E = m_{1T} \cosh y_1 + m_{2T} \cosh y_2 - p_T \cosh y - \left[m_{3T}^2 + (m_{1T} \sinh y_1 + m_{2T} \sinh y_2 - p_T \sinh y)^2 \right]^{1/2}, \quad (\text{A.14})$$

and performing the ϕ_2 integration in (A.2) we get

$$\begin{aligned}
 E \frac{dR}{d^3p} &= \frac{1}{16} \frac{\mathcal{N}}{(2\pi)^8} \int_0^\infty p_{1T} dp_{1T} \int_0^\infty dp_{2T} \\
 &\times \int_{-\infty}^\infty dy_1 \int_{-\infty}^\infty dy_2 \int_0^{2\pi} d\phi_1 \\
 &\times f_1(E_1) f_2(E_2) [1 \pm f_3(E_3)] \\
 &\times \frac{|M|^2}{|p_{1T} \sin(\phi_1 - \phi_2) + p_T \sin \phi_2|_{\phi_0^0}}
 \end{aligned} \tag{A.15}$$

with the constraint $|H/2Rp_{2T}| \leq 1$ originating from $|\cos(\phi)| \leq 1$.

Acknowledgments

The authors thank Sourav Sarkar and Jan E. Alam for their major collaborative contribution in these works presented here and also for comments and suggestions to complete the paper. Payal Mohanty and Sabyasachi Ghosh thank Victor Roy, Santosh K. Das, Jajati K. Nayak, Bedangadas Mohanty, and Asis K. Chaudhuri for their assistance in the work presented in the review.

References

- [1] L. D. McLerran and T. Toimela, "Photon and dilepton emission from the quark-gluon plasma: some general considerations," *Physical Review D*, vol. 31, pp. 545–563, 1985.
- [2] C. Gale and J. Kapusta, "Dilepton radiation from high temperature nuclear matter," *Physical Review C*, vol. 35, no. 6, pp. 2107–2116, 1987.
- [3] C. Gale and J. I. Kapusta, "Vector dominance model at finite temperature," *Nuclear Physics B*, vol. 357, no. 1, pp. 65–89, 1991.
- [4] H. A. Weldon, "Reformulation of finite-temperature dilepton production," *Physical Review D*, vol. 42, pp. 2384–2387, 1990.
- [5] R. Rapp and J. Wambach, "Chiral symmetry restoration and dileptons in relativistic heavy-ion collisions," *Advances in Nuclear Physics*, vol. 25, pp. 1–205, 2000.
- [6] "Elementary particles, nuclei and atoms," *Relativistic Heavy Ion Physics*, vol. 23, pp. 134–175, 2010.
- [7] J.-E. Alam, S. Raha, and B. Sinha, "Electromagnetic probes of quark gluon plasma," *Physics Reports*, vol. 273, no. 5–6, pp. 243–362, 1996.
- [8] J.-E. Alam, S. Sarkar, P. Roy, T. Hatsuda, and B. Sinha, "Thermal photons and Lepton pairs from Quark Gluon plasma and hot hadronic matter," *Annals of Physics*, vol. 286, no. 2, pp. 159–248, 2000.
- [9] R. Chatterjee, L. Bhattacharya, and D. K. Shrivastava, "Electromagnetic probes," *Lecture Notes in Physics*, vol. 785, pp. 219–264, 2010.
- [10] H. van Hees and R. Rapp, "Dilepton radiation at the CERN super-proton synchrotron," *Nuclear Physics A*, vol. 806, no. 1–4, pp. 339–387, 2008.
- [11] R. Rapp, "Theory of soft electromagnetic emission in heavy-ion collisions," *Acta Physica Polonica B*, vol. 42, no. 12, p. 2823, 2011.
- [12] P. Mohanty, J. K. Nayak, J.-E. Alam, and S. K. Das, "Radial flow from electromagnetic probes and signal of quark gluon plasma," *Physical Review C*, vol. 82, no. 3, Article ID 034901, 2010.
- [13] P. Mohanty, V. Roy, S. Ghosh, S. K. Das, B. Mohanty et al., "Elliptic flow of thermal dileptons as a probe of QCD matter," *Physical Review C*, vol. 85, Article ID 031903, 2012.
- [14] P. Mohanty, J.-E. Alam, and B. Mohanty, "Evolution of collectivity as a signal of quark gluon plasma formation in heavy ion collisions," *Physical Review C*, vol. 84, no. 2, Article ID 024903, 2011.
- [15] P. Mohanty, J.-E. Alam, and B. Mohanty, "Characterizing quark gluon plasma by dilepton interferometry," *Nuclear Physics A*, vol. 862, pp. 301–303, 2011.
- [16] J. K. Nayak, J.-E. Alam, S. Sarkar, and B. Sinha, "Thermal photon to dilepton ratio in high energy nuclear collisions," *Physical Review C*, vol. 78, no. 3, Article ID 034903, 2008.
- [17] J. I. Kapusta and E. V. Shuryak, "Weinberg-type sum rules at zero and finite temperature," *Physical Review D*, vol. 49, pp. 4694–4704, 1994.
- [18] C. Y. Wong, *Introduction of High Energy Heavy Ion Collisions*, World Scientific, Singapore, 1994.
- [19] J.-E. Alam, D. K. Srivastava, B. Sinha, and D. N. Basu, "Transverse flow effects on high-energy photons emitted by expanding quark-gluon plasma," *Physical Review D*, vol. 48, pp. 1117–1131, 1993.
- [20] J. Ruppert, C. Gale, T. Renk, P. Lichard, and J. I. Kapusta, "Low mass dimuons produced in relativistic nuclear collisions," *Physical Review Letters*, vol. 100, Article ID 162301, 2008.
- [21] S. D. Drell and T.-M. Yan, "Massive lepton-pair production in hadron-hadron collisions at high energies," *Physical Review Letters*, vol. 25, no. 5, pp. 316–320, 1970.
- [22] S. D. Drell and T. M. Yan, "Massive Lepton-pair production in Hadron-Hadron collisions at high energies," *Physical Review Letters*, vol. 25, p. 902, 1970.
- [23] S. Gavin, P. L. McGaughey, P. V. Ruuskanen, and R. Vogt, "Lepton production from charm decay in nuclear collisions at $\sqrt{s} = 200$ GeV and 5.5 TeV per nucleon," *Physical Review C*, vol. 54, no. 5, pp. 2606–2623, 1996.
- [24] N. Armesto, N. Borghini, S. Jeon, U. A. Wiedemann et al., "Heavy-ion collisions at the LHC-Last call for predictions," *Journal of Physics G*, vol. 35, Article ID 054001, 2008.
- [25] R. Rapp, "Duality and chiral restoration from low-mass dileptons at the CERN-SpS," *Nuclear Physics A*, vol. 661, no. 1–4, Article ID 990734, pp. 33–44, 1999.
- [26] R. Rapp and J. Wambach, "Low-mass dileptons at the CERN-SpS: evidence for chiral restoration?" *The European Physical Journal A*, vol. 6, pp. 415–420, 1999.
- [27] E. L. Feinberg, "Direct production of photons and dileptons in thermodynamical models of multiple hadron production," *Nuovo Cimento A*, vol. 34, pp. 391–412, 1976.
- [28] S. Sarkar, "Photons from ultra-relativistic heavy ion collisions," <http://arxiv.org/abs/nucl-th/0007011>.
- [29] A. Das, *Finite Temperature Field Theory*, World Scientific, Singapore, 1997.
- [30] R. Kobes and G. Semenoff, "Discontinuities of green functions in field theory at finite temperature and density," *Nuclear Physics B*, vol. 260, no. 3–4, pp. 714–746, 1985.
- [31] R. Kobes and G. Semenoff, "Discontinuities of green functions in field theory at finite temperature and density (II)," *Nuclear Physics B*, vol. 272, no. 2, pp. 329–364, 1986.
- [32] F. Gelis, "Cutting rules in the real-time formalisms at finite temperature," *Nuclear Physics B*, vol. 508, no. 1-2, pp. 483–505, 1997.

- [33] S. Sarkar, J.-E. Alam, P. Roy, A. K. Dutt-Mazumder, B. Dutta-Roy, and B. Sinha, "Photons from hadronic matter at finite temperature," *Nuclear Physics A*, vol. 634, no. 1–2, pp. 206–230, 1998.
- [34] T. Hirano and Y. Nara, "Hydrodynamic afterburner for the color glass condensate and the parton energy loss," *Nuclear Physics A*, vol. 743, no. 4, pp. 305–328, 2004.
- [35] D. Teaney, J. Lauret, and E. V. Shuryak, "Flow at the SPS and RHIC as a Quark-Gluon plasma signature," *Physical Review Letters*, vol. 86, pp. 4783–4786, 2001.
- [36] P. F. Kolb, P. Huovinen, U. W. Heinz, and H. Heiselberg, "Elliptic flow at SPS and RHIC: from kinetic transport to hydrodynamics," *Physics Letters B*, vol. 500, no. 3–4, pp. 232–240, 2001.
- [37] P. Huovinen, P. F. Kolb, U. Heinz, P. V. Ruuskanen, and S. A. Voloshin, "Radial and elliptic flow at RHIC: further predictions," *Physics Letters, Section B*, vol. 503, no. 1–2, pp. 58–64, 2001.
- [38] T. Hirano and M. Gyulassy, "Perfect fluidity of the quark-gluon plasma core as seen through its dissipative hadronic corona," *Nuclear Physics A*, vol. 769, no. 1–4, pp. 71–94, 2006.
- [39] C. Nokana and S. A. Bass, "Space-time evolution of bulk QCD matter," *Physical Review C*, vol. 75, Article ID 014902, 2007.
- [40] L. D. Landau, "On the multiple production of particles in high energy collisions," *Izvestiya Akademii Nauk Azerbaidzhanskoi SSR. Seriya Fiziko-Tekhnicheskikh*, vol. 17, p. 51, 1953.
- [41] J. D. Bjorken, "Highly relativistic nucleus-nucleus collisions: the central rapidity region," *Physical Review D*, vol. 27, no. 1, pp. 140–151, 1983.
- [42] T. Hirano, N. van der Kolk, and A. Bilandzic, "Hydrodynamics and flow," *Lecture Notes in Physics*, vol. 785, pp. 139–178, 2010.
- [43] J.-Y. Ollitrault, "Relativistic hydrodynamics for heavy-ion collisions," *European Journal of Physics*, vol. 29, no. 2, pp. 275–302, 2008.
- [44] S. Weinberg, "Entropy generation and the survival of protogalaxies in an expanding universe," *The Astronomical Journal*, vol. 168, pp. 175–194, 1971.
- [45] P. Danielewicz and M. Gyulassy, "Dissipative phenomena in quark-gluon plasmas," *Physical Review D*, vol. 31, pp. 53–62, 1985.
- [46] R. C. Hwa and K. Kajantie, "Diagnosing quark matter by measuring the total entropy and the photon or dilepton emission rates," *Physical Review D*, vol. 32, pp. 1109–1118, 1985.
- [47] D. Kharzeev and M. Nardi, "Hadron production in nuclear collisions at RHIC and high-density QCD," *Physics Letters B*, vol. 507, no. 1–4, pp. 121–128, 2001.
- [48] S. Borsanyi, G. Endrodi, Z. Fodor, A. Jakovac et al., "The QCD equation of state with dynamical quarks," *Journal of High Energy Physics*, vol. 1011, p. 077, 2010.
- [49] F. Cooper and G. Frye, "Single-particle distribution in the hydrodynamic and statistical thermodynamic models of multiparticle production," *Physical Review D*, vol. 10, no. 1, pp. 186–189, 1974.
- [50] R. Bair, H. Nakagawa, A. Niegawa, and K. Redlich, "Production rate of hard thermal photons and screening of quark mass singularity," *Zeitschrift für Physik C Particles and Fields*, vol. 53, no. 3, pp. 433–438, 1992.
- [51] E. Braaten and R. D. Pisarski, "Soft amplitudes in hot gauge theories: a general analysis," *Nuclear Physics B*, vol. 337, no. 3, pp. 569–634, 1990.
- [52] E. Braaten and R. D. Pisarski, "Deducing hard thermal loops from Ward identities," *Nuclear Physics B*, vol. 339, no. 2, pp. 310–324, 1990.
- [53] P. Aurenche, F. Gelis, R. Kobes, and H. Zaraket, "Bremsstrahlung and photon production in thermal QCD," *Physical Review D*, vol. 58, Article ID 085003, 1998.
- [54] P. Arnold, G. D. Moore, and L. G. Yaffe, "Photon emission from ultrarelativistic plasmas," *Journal of High Energy Physics*, vol. 0111, Article ID 057, 2001.
- [55] P. Arnold, G. D. Moore, and L. G. Yaffe, "Photon emission from Quark-Gluon plasma: complete leading order results," *Journal of High Energy Physics*, vol. 0112, Article ID 009, 2001.
- [56] O. Kaczmarek and F. Zantow, "Static quark-antiquark interactions in zero and finite temperature QCD: I. Heavy quark free energies, running coupling, and quarkonium binding," *Physical Review D*, vol. 71, Article ID 114510, 2005.
- [57] P. Roy, S. Sarkar, J.-E. Alam, and B. Sinha, "Electromagnetic radiation from hot and dense hadronic matter," *Nuclear Physics A*, vol. 653, no. 3, pp. 277–300, 1999.
- [58] J.-E. Alam, P. Roy, and S. Sarkar, "Comment on "Hadronic production of thermal photons,"" *Physical Review C*, vol. 71, Article ID 059802, 2005.
- [59] S. Mitra, P. Mohanty, S. Ghosh, S. Sarkar, and J.-E. Alam, "Characterizing quark gluon plasma by thermal photons and lepton pairs," <http://arxiv.org/abs/1303.0675>.
- [60] J. J. Sakurai, *Currents and Mesons*, The University of Chicago Press, Chicago, Ill, USA, 1969.
- [61] R. K. Bhaduri, *Models of Nucleon—From Quarks to Soliton*, Addison-Wesley, 1988.
- [62] S. Turbide, R. Rapp, and C. Gale, "Hadronic production of thermal photons," *Physical Review C*, vol. 69, no. 1, Article ID 014903, 2004.
- [63] K. L. Haglin, "Photon production from hot hadronic matter," *Journal of Physics G*, vol. 30, p. L27, 2004.
- [64] H. Von Gersdorff, L. D. McLerran, M. Kataja, and P. V. Ruuskanen, "Studies of the hydrodynamic evolution of matter produced in fluctuations in $p\bar{p}$ collisions and in ultrarelativistic nuclear collisions," *Physical Review D*, vol. 34, pp. 794–810, 1986.
- [65] M. M. Aggarwal, A. Agnihotri, Z. Ahammed, WA98 Collaboration et al., "Observation of direct photons in central 158A GeV $^{208}\text{Pb}+^{208}\text{Pb}$ collisions," *Physical Review Letters*, vol. 85, pp. 3595–3599, 2000.
- [66] C. Bernard, T. Burch, C. DeTar et al., "QCD equation of state with 2+1 flavors of improved staggered quarks," *Physical Review D*, vol. 75, Article ID 094505, 2007.
- [67] I. Arsene, I. G. Bearden, D. Beavis, BRAHMS Collaboration et al., "Quark-gluon plasma and color glass condensate at RHIC? The perspective from the BRAHMS experiment," *Nuclear Physics A*, vol. 757, no. 1–2, pp. 1–27, 2005.
- [68] B. B. Back, M. D. Baker, M. Ballintijn, PHOBOS Collaboration et al., "The PHOBOS perspective on discoveries at RHIC," *Nuclear Physics A*, vol. 757, no. 1–2, pp. 28–101, 2005.
- [69] T. Hirano and K. Tsuda, "Collective flow and two-pion correlations from a relativistic hydrodynamic model with early chemical freeze-out," *Physical Review C*, vol. 66, Article ID 054905, 2002.
- [70] D. L. Adams, N. Achurin, N. I. Belikov, E704 Collaboration et al., "Measurement of single spin asymmetry for direct photon production in pp collisions at 200 GeV/c," *Physics Letters B*, vol. 345, no. 4, pp. 569–575, 1995.

- [71] T. Renk, “A comprehensive description of multiple observables in heavy-ion collisions at SPS,” *Journal of Physics G*, vol. 30, Article ID 064905, p. 1495, 2004.
- [72] T. Renk, “Photonic measurements of the longitudinal expansion dynamics in relativistic heavy-ion collisions,” *Physical Review C*, vol. 71, Article ID 064905, 2005.
- [73] J.-E. Alam, S. Sarkar, T. Hatsuda, T. K. Nayak, and B. Sinha, “Photons from Pb-Pb collisions at ultrarelativistic energies,” *Physical Review C*, vol. 63, Article ID 021901, 2001.
- [74] D. K. Srivastava and B. Sinha, “Radiation of single photons from Pb+Pb collisions at relativistic energies and the quark-hadron phase transition,” *Physical Review C*, vol. 64, Article ID 034902, 2001.
- [75] P. Huovinen, P. V. Ruuskanen, and S. S. Räsänen, “Photon emission in heavy ion collisions at the CERN SPS,” *Physics Letters, Section B*, vol. 535, no. 1–4, pp. 109–116, 2002.
- [76] K. Gallmeister, B. Kämpfer, and O. P. Pavlenko, “Unique large thermal source of real and virtual photons in the reactions Pb(158A GeV) + Pb, Au,” *Physical Review C*, vol. 62, Article ID 057901, 2000.
- [77] F. D. Steffen and M. H. Thoma, “Hard thermal photon production in relativistic heavy ion collisions,” *Physics Letters B*, vol. 510, no. 1–4, pp. 98–106, 2001.
- [78] R. Chatterjee, D. K. Srivastava, and S. Jeon, “Single photons from relativistic collisions of lead nuclei at energies available at the CERN Super Proton Synchrotron (SPS): a reanalysis,” *Physical Review C*, vol. 79, Article ID 034906, 2009.
- [79] A. Adare, S. Afanasiev, C. Aidala, PHENIX collaboration et al., “Enhanced production of direct photons in Au+Au collisions at $\sqrt{s_{NN}} = 200$ GeV and implications for the initial temperature,” *Physical Review Letters*, vol. 104, Article ID 132301, 2010.
- [80] S. S. Adler, S. Afanasiev, C. Aidala, PHENIX collaboration et al., “Suppressed π^0 Production at Large Transverse Momentum in Central Au+Au Collisions at $\sqrt{s_{NN}} = 200$ GeV,” *Physical Review Letters*, vol. 91, Article ID 072301, 2003.
- [81] F. M. Liu, T. Hirano, K. Werner, and Y. Zhu, “Centrality-dependent direct photon pt spectra in Au+Au collisions at the BNL Relativistic Heavy Ion Collider (RHIC) energy $\sqrt{s_{NN}} = 200$ GeV,” *Physical Review C*, vol. 79, Article ID 014905, 2009.
- [82] S. Sarkar, P. Roy, J.-E. Alam, S. Raha, and B. Sinha, “Dissipative effects in photon diagnostics of quark—gluon plasma,” *Journal of Physics G*, vol. 23, p. 469, 1997.
- [83] A. K. Chaudhuri, “Effect of viscosity on one dimensional hydrodynamic flow and direct photons from 200 AGeV S+Au collisions at CERN SPS,” *Physica Scripta*, vol. 61, p. 311, 2000.
- [84] A. K. Chaudhuri and B. Sinha, “Direct photon production from viscous quark-gluon plasma,” *Physical Review C*, vol. 83, Article ID 034905, 2010.
- [85] J. R. Bhatt, H. Mishra, and V. Sreekanth, “Thermal photons in QGP and non-ideal effects,” *Journal of High Energy Physics*, vol. 1011, p. 106, 2010.
- [86] K. Dusling, “Photons as a viscometer of heavy ion collisions,” *Nuclear Physics A*, vol. 839, no. 1–4, pp. 70–77, 2010.
- [87] S. Mitra, P. Mohanty, S. Sarkar, and J.-E. Alam, “Thermal radiation from an evolving viscous Quark Gluon plasma,” *International Journal of Modern Physics E*, vol. 22, Article ID 1350004, 2013.
- [88] D. Teaney, “Effect of shear viscosity on spectra, elliptic flow, and Hanbury Brown-Twiss radii,” *Physical Review C*, vol. 68, Article ID 034913, 2003.
- [89] P. Danielewicz and M. Gyulassy, “Dissipative phenomena in quark-gluon plasmas,” *Physical Review D*, vol. 31, no. 1, pp. 53–62, 1985.
- [90] H. B. Meyer, “Calculation of the shear viscosity in SU(3) gluodynamics,” *Physical Review D*, vol. 76, Article ID 101701, 2007.
- [91] P. Arnold, G. D. Moore, and L. G. Yaffe, “Transport coefficients in high temperature gauge theories: (II) Beyond leading log,” *Journal of High Energy Physics*, vol. 0305, Article ID 051, 2003.
- [92] J.-W. Chen, H. Dong, K. Ohnishi, and Q. Wang, “Shear viscosity of a gluon plasma in perturbative QCD,” *Physics Letters, Section B*, vol. 685, no. 4–5, pp. 277–282, 2010.
- [93] S. K. Das and J. Alam, “Transport coefficients of gluonic fluid,” *Physical Review D*, vol. 83, Article ID 114011, 2011.
- [94] Z. Xu and C. Greiner, “Shear viscosity in a Gluon gas,” *Physical Review Letters*, vol. 100, Article ID 172301, 2008.
- [95] K. Itakura, O. Morimatsu, and H. Otomo, “Shear viscosity of a hadronic gas mixture,” *Physical Review D*, vol. 77, no. 1, Article ID 014014, 2008.
- [96] A. Dobado and I. J. Llanes-Estrada, “Viscosity of meson matter,” *Physical Review D*, vol. 69, Article ID 116004, 2004.
- [97] P. Chakraborty and J. I. Kapusta, “Quasiparticle theory of shear and bulk viscosities of hadronic matter,” *Physical Review C*, vol. 83, no. 1, Article ID 014906, 2011.
- [98] A. S. Khvorostukhin, V. D. Toneev, and D. N. Voskresensky, “Viscosity coefficients for hadron and quark-gluon phases,” *Nuclear Physics A*, vol. 845, no. 1–4, pp. 106–146, 2010.
- [99] I. Tseruya, “Summary of low-mass dilepton and direct photon results,” *Nuclear Physics A*, vol. 590, no. 1–2, pp. 127–138, 1995.
- [100] J. Cleymans, J. Fingberg, and K. Redlich, “Transverse-momentum distribution of dileptons in different scenarios for the QCD phase transition,” *Physical Review D*, vol. 35, pp. 2153–2165, 1987.
- [101] K. Dusling and I. Zahed, “Transverse momentum spectra of dileptons measured by the NA60 Collaboration in In+In collisions at 158 GeV/nucleon,” *Physical Review C*, vol. 80, no. 1, Article ID 014902, 2009.
- [102] T. Altherr and P. V. Ruuskanen, “Low-mass dileptons at high momenta in ultra-relativistic heavy-ion collisions,” *Nuclear Physics B*, vol. 380, no. 3, pp. 377–390, 1992.
- [103] M. H. Thoma and C. T. Traxler, “Production of energetic dileptons with small invariant masses from the quark-gluon plasma,” *Physical Review D*, vol. 56, no. 1, pp. 198–202, 1997.
- [104] E. V. Shuryak, “Correlation functions in the QCD vacuum,” *Reviews of Modern Physics*, vol. 65, pp. 1–46, 1993.
- [105] R. Barate, D. Buskulic, D. Decamp, ALEPH Collaboration et al., “Measurement of the axial-vector τ spectral functions and determination of $\alpha_3(M_\tau^2)$ from hadronic τ decays,” *The European Physical Journal C*, vol. 4, no. 3, pp. 409–431, 1998.
- [106] K. Ackerstaff, G. Alexander, J. Allison et al., “Measurement of the strong coupling constant and the vector α_3 and axial-vector spectral functions in hadronic tau decays,” *The European Physical Journal C*, vol. 7, pp. 571–593, 1999.
- [107] S. Sarkar, “Hadrons at finite temperature,” *Nuclear Physics A*, vol. 862–863, pp. 13–19, 2011.
- [108] S. Mallik and S. Sarkar, “Vector and axial-vector mesons at finite temperature,” *The European Physical Journal C*, vol. 25, pp. 445–452, 2002.
- [109] S. Ghosh, S. Mallik, and S. Sarkar, “Analytic structure of ρ meson propagator at finite temperature,” *The European Physical Journal C*, vol. 70, pp. 251–262, 2010.

- [110] S. Ghosh and S. Sarkar, “ ρ self-energy at finite temperature and density in the real-time formalism,” *Nuclear Physics A*, vol. 870-871, no. 1, pp. 94–111, 2011.
- [111] S. Ghosh and S. Sarkar, “Analysis of self-energy at finite temperature and density in the real-time formalism,” *The European Physical Journal A*, vol. 49, article 97, 2013.
- [112] S. Sarkar and S. Ghosh, “In-medium vector mesons and low mass lepton pairs from heavy ion collisions,” *Journal of Physics*, vol. 374, Article ID 012010, 2012.
- [113] J. K. Nayak, J.-E. Alam, T. Hirano, S. Sarkar, and B. Sinha, “Muon pairs from In + In collision at energies available at the CERN Super Proton Synchrotron,” *Physical Review C*, vol. 85, Article ID 064906, 2012.
- [114] R. Arnaldi, R. Averbeck, K. Banicz et al., “First measurement of the ρ spectral function in high-energy nuclear collisions,” *Physical Review Letters*, vol. 96, Article ID 162302, 2006.
- [115] R. Arnaldi, R. Averbeck, K. Banicz et al., “Evidence for radial flow of thermal dileptons in high-energy nuclear collisions,” *Physical Review Letters*, vol. 100, Article ID 022302, 2008.
- [116] V. L. Eletsky, M. Belkacem, P. J. Ellis, and J. I. Kapusta, “Properties of ρ and ω mesons at finite temperature and density as inferred from experiment,” *Physical Review C*, vol. 64, Article ID 035202, 2001.
- [117] H. Van Hees and R. Rapp, “Comprehensive interpretation of thermal dileptons measured at the CERN super proton synchrotron,” *Physical Review Letters*, vol. 97, no. 10, Article ID 102301, 2006.
- [118] R. Rapp, G. Chanfray, and J. Wambach, “Rho Meson propagation and dilepton enhancement in hot hadronic matter,” *Nuclear Physics A*, vol. 617, pp. 472–495, 1997.
- [119] A. Toia and PHENIX Collaboration, “ e^+e^- pairs: a clock and a thermometer of heavy ion collisions,” *Journal of Physics G*, vol. 35, Article ID 104037, 2008.
- [120] A. Adare, S. Afanasiev, C. Aidala, PHENIX Collaboration et al., “Detailed measurement of the e^+e^- pair continuum in p+p and Au+Au collisions at $\sqrt{s_{NN}} = 200$ GeV and implications for direct photon production,” *Physical Review C*, vol. 81, Article ID 034911, 2010.
- [121] P. Lichard and J. Jura, “Electron-positron annihilation into four charged pions and the $a_1\rho\pi$ Lagrangian,” *Physical Review D*, vol. 76, Article ID 094030, 2007.
- [122] K. Aamodt, N. Abel, U. Abeysekara, ALICE collaboration et al., “Charged-particle multiplicity measurement in proton-proton collisions at $\sqrt{s} = 0.9$ and 2.36 TeV with ALICE at LHC,” *The European Physical Journal C*, vol. 68, pp. 89–108, 2010.
- [123] F.-M. Liu, T. Hirano, K. Werner, and Y. Zhu, “Centrality-dependent direct photon p_t spectra in Au+Au collisions at the BNL Relativistic Heavy Ion Collider (RHIC) energy $\sqrt{s_{NN}} = 200$ GeV,” *Physical Review C*, vol. 79, Article ID 014905, 2009.
- [124] B. Schenke, S. Jeon, and C. Gale, “(3+1)D hydrodynamic simulation of relativistic heavy-ion collisions,” *Physical Review C*, vol. 82, Article ID 014903, 2010.
- [125] B. Schenke, S. Jeon, and C. Gale, “Higher flow harmonics from (3+1)D event-by-event viscous hydrodynamics,” *Physical Review C*, vol. 85, Article ID 024901, 2012.
- [126] J. K. Nayak and J. Alam, “Measuring radial flow of partonic and hadronic phases in relativistic heavy-ion collisions,” *Physical Review C*, vol. 80, Article ID 064906, 2009.
- [127] B. Sinha, “Universal signals of a quark-gluon plasma,” *Physics Letters B*, vol. 128, no. 1-2, pp. 91–94, 1983.
- [128] R. Chatterjee, E. S. Frodermann, U. Heinz, and D. K. Srivastava, “Elliptic flow of thermal photons in relativistic nuclear collisions,” *Physical Review Letters*, vol. 96, no. 20, Article ID 202302, 2006.
- [129] R. Hanbury Brown and R. Q. Twiss, “A test of a new type of stellar interferometer on sirius,” *Nature*, vol. 178, pp. 1046–1048, 1956.
- [130] D. Peressounko, “Hanbury Brown-Twiss interferometry of direct photons in heavy ion collisions,” *Physical Review C*, vol. 67, Article ID 014905, 2003.
- [131] Y. M. Sinyukov, “Hanbury Brown/Twiss correlations for expanding hadron and quark-gluon matter,” *Nuclear Physics A*, vol. 498, pp. 151–159, 1989.
- [132] A. Adare, S. Afanasiev, C. Aidala et al., “Energy loss and flow of heavy Quarks in Au+Au collisions at $\sqrt{s_{NN}} = 200$ GeV,” *Physical Review Letters*, vol. 98, Article ID 172301, 2007.
- [133] B. Abelev, B. Abelev, A. A. Quintana, The ALICE Collaboration et al., “Charged-particle multiplicity density at Midrapidity in central Pb-Pb collisions at $\sqrt{s_{NN}} = 2.76$ TeV,” *Physical Review Letters*, vol. 105, Article ID 252301, 2010.
- [134] S. Pratt, “Pion interferometry for exploding sources,” *Physical Review Letters*, vol. 53, no. 13, pp. 1219–1221, 1984.
- [135] S. Pratt, “Pion interferometry of quark-gluon plasma,” *Physical Review D*, vol. 33, pp. 1314–1327, 1986.
- [136] U. A. Wiedemann and U. Heinz, “Particle interferometry for relativistic heavy-ion collisions,” *Physics Reports*, vol. 319, no. 4–5, pp. 145–230, 1999.
- [137] U. Heinz and B. V. Jacak, “Two-particle correlations in relativistic heavy-ion collisions,” *Annual Review of Nuclear and Particle Science*, vol. 49, no. 1, pp. 529–579, 1999.
- [138] T. Csörgő and B. Lörstad, “Bose-Einstein correlations for three-dimensionally expanding, cylindrically symmetric, finite systems,” *Physical Review C*, vol. 54, pp. 1390–1403, 1996.
- [139] D. H. Rischke and M. Gyulassy, “The time-delay signature of quark-gluon plasma formation in relativistic nuclear collisions,” *Nuclear Physics A*, vol. 608, no. 4, pp. 479–512, 1996.
- [140] S. Chapman, P. Scotto, and U. Heinz, “New cross term in the two-particle Hanbury-Brown-Twiss correlation function in ultrarelativistic heavy-ion collisions,” *Physical Review Letters*, vol. 74, no. 22, pp. 4400–4403, 1995.
- [141] M. Herrmann and G. F. Bertsch, “Source dimensions in ultrarelativistic heavy-ion collisions,” *Physical Review C*, vol. 51, pp. 328–338, 1995.
- [142] P. Huovinen and P. V. Ruuskanen, “Hydrodynamic models for heavy ion collisions,” *Annual Review of Nuclear and Particle Science*, vol. 56, pp. 163–206, 2006.
- [143] R. Chatterjee, D. K. Srivastava, U. W. Heinz, and C. Gale, “Elliptic flow of thermal dileptons in relativistic nuclear collisions,” *Physical Review C*, vol. 75, Article ID 054909, 2007.
- [144] R. Chatterjee, D. K. Srivastava, U. W. Heinz, and C. Gale, “Elliptic flow of thermal dileptons in relativistic nuclear collisions,” *Physical Review C*, vol. 75, Article ID 054909, 2007.
- [145] J. Deng, Q. Wang, N. Xu, and P. Zhuang, “Dilepton flow and deconfinement phase transition in heavy ion collisions,” *Physics Letters B*, vol. 701, pp. 581–586, 2011.
- [146] H. Van Hees, C. Gale, and R. Rapp, “Thermal photons and collective flow at energies available at the BNL relativistic heavy-ion collider,” *Physical Review C*, vol. 84, no. 5, Article ID 054906, 2011.
- [147] T. Renk and J. Ruppert, “Dimuon transverse momentum spectra as a tool to characterize the emission region in heavy-ion

- collisions,” *Physical Review C*, vol. 77, no. 2, Article ID 024907, 2008.
- [148] V. Roy and A. K. Choudhuri, “Charged particle’s elliptic flow in (2+1)D viscous hydrodynamics at LHC ($\sqrt{s} = 2.76$ TeV) energy in Pb + Pb collision,” *Physics Letters B*, vol. 703, no. 3, pp. 313–317, 2011.
- [149] B. Mohanty and J. Alam, “Velocity of sound in relativistic heavy-ion collisions,” *Physical Review C*, Article ID 064903, 2003.
- [150] K. Aamodt, A. Abrahantes Quintana, D. Adamova, ALICE Collaboration et al., “Centrality dependence of the charged-particle multiplicity density at midrapidity in Pb-Pb collisions at $\sqrt{s_{NN}} = 2.76$ TeV,” *Physical Review Letters*, vol. 106, Article ID 032301, 2011.
- [151] K. Aamodt, A. Abrahantes Quintana, D. Adamova, ALICE Collaboration et al., “Suppression of charged particle production at large transverse momentum in central Pb-Pb collisions at $\sqrt{s_{NN}} = 2.76$ TeV,” *Physics Letters B*, vol. 696, p. 30, 2011.
- [152] K. Itakura, “Strong-field physics as a new probe of early-time dynamics in heavy-ion collisions,” *Journal of Physics*, vol. 422, Article ID 012029, 2013.
- [153] K. Tuchin, “Photon decay in a strong magnetic field in heavy-ion collisions,” *Physical Review C*, vol. 83, Article ID 017901, 2011.
- [154] K. Tuchin, “Electromagnetic radiation by quark-gluon plasma in a magnetic field,” *Physical Review C*, vol. 87, Article ID 024912, 2013.

Research Article

Dilepton Spectroscopy of QCD Matter at Collider Energies

Ralf Rapp

Cyclotron Institute and Department of Physics & Astronomy, Texas A&M University, College Station, TX 77843-3366, USA

Correspondence should be addressed to Ralf Rapp; rapp@comp.tamu.edu

Received 3 April 2013; Accepted 4 July 2013

Academic Editor: Edward Sarkisyan-Grinbaum

Copyright © 2013 Ralf Rapp. This is an open access article distributed under the Creative Commons Attribution License, which permits unrestricted use, distribution, and reproduction in any medium, provided the original work is properly cited.

Low-mass dilepton spectra as measured in high-energy heavy-ion collisions are a unique tool to obtain spectroscopic information about the strongly interacting medium produced in these reactions. Specifically, in-medium modifications of the vector spectral function, which is well known in the vacuum, can be deduced from the thermal radiation off the expanding QCD fireball. This, in particular, allows to investigate the fate of the ρ resonance in the dense medium and possibly infer from it signatures of the (partial) restoration of chiral symmetry, which is spontaneously broken in the QCD vacuum. After briefly reviewing calculations of thermal dilepton emission rates from hot QCD matter, utilizing effective hadronic theory, lattice QCD, or resummed perturbative QCD, we focus on applications to dilepton spectra at heavy-ion collider experiments at RHIC and LHC. This includes invariant-mass spectra at full RHIC energy with transverse-momentum dependencies and azimuthal asymmetries, as well as a systematic investigation of the excitation function down to fixed-target energies, thus making contact to previous precision measurements at the SPS. Furthermore, predictions for the energy frontier at the LHC are presented in both dielectron and dimuon channels.

1. Introduction

The exploration of matter at extremes of temperature (T) and baryon density (ρ_B) is at the forefront of research in contemporary nuclear physics, with intimate connections to high-energy, condensed-matter, and even atomic physics [1]. Theoretical efforts over the last few decades are suggesting an extraordinary richness of the phase diagram of strongly interacting matter, which should ultimately emerge from the underlying theory of quantum chromodynamics (QCD) as part of the standard model. However, several basic questions, both qualitative and quantitative, such as the possible existence of first order transitions and their location as function of baryon-chemical potential (μ_B) and temperature, remain open to date [2]. A close interplay of experiment and theory is needed to create a robust knowledge about the QCD phase structure. On one hand, naturally occurring matter at temperatures close to or beyond the expected pseudo-critical one, $T_{pc} \approx 160$ MeV [3, 4], may last have existed ~ 14 billion years ago, during the first tens of microseconds of the Universe. On the other hand, at small temperatures, matter with baryon densities close to or beyond the critical one for the transition into quark matter may prevail in the interior of compact stars today, but its verification and exploration from observational

data are challenging [5]. It is quite fascinating that tiny man-made samples of hot QCD matter can nowadays be created and studied in the laboratory using ultrarelativistic heavy-ion collisions (URHICs). Significant progress has been made in understanding the properties of this medium through analyses of experiments conducted at the CERN's Super-Proton Synchrotron (SPS), BNL's Relativistic Heavy-Ion Collider (RHIC), and CERN's Large Hadron Collider (LHC) (see, e.g., the recent Quark Matter conference proceedings [6, 7]). For example, systematic investigations of the produced hadron spectra have revealed a hydrodynamic behavior of the bulk matter in the region of low transverse momenta ($q_t \lesssim 2$ -3 GeV) and a strong absorption of hadrons with high transverse momentum ($q_t \gtrsim 6$ GeV). Even hadrons containing a heavy quark (charm or bottom) exhibit substantial energy loss and collectivity due to their coupling to the expanding fireball. While the total charm and bottom yields are essentially conserved, the production of heavy quark-antiquark bound states (charmonia and bottomonia) is largely suppressed. The relation of the above hadronic observables to spectral properties of the medium is, however, rather indirect. Low-mass dileptons, on the other hand, are radiated from the interior of the medium throughout the fireball's lifetime, as

their mean-free path is much larger than the size of the fireball. Thus, their invariant-mass spectra directly measure the in-medium vector spectral function, albeit in a superposition of the varying temperature in the fireball's expansion.

The dilepton program at the SPS has produced remarkable results. The CERES/NA45 dielectron data in Pb-Au collisions, and particularly the NA60 dimuon spectra in In-In collisions, have shown that the ρ -meson undergoes a strong broadening, even complete melting, of its resonance structure, with quantitative sensitivity to its spectral shape, see [8–10] for recent reviews. The QCD medium at SPS energies is characterized by a significant net-baryon content with chemical potentials of $\mu_B \approx 250$ MeV at chemical freezeout, $T_{\text{ch}} \approx 160$ MeV [11], and further increasing as the system cools down [12]. Baryons have been identified as a dominant contributor to the medium modifications of the ρ 's spectral function [10]. The question arises how these develop when moving toward the net baryon-free regime in the QCD phase diagram, $\mu_B \ll T$. Theoretical expectations based on the hadronic many-body approach [13] suggest comparable medium effects in this regime, since the relevant quantity is the *sum* of baryon and antibaryon densities, and this turns out to be similar at SPS and RHIC/LHC [12], at least close to T_{pc} . Since $T_{\text{ch}} \approx T_{\text{pc}}$ at collider energies, the total baryon density at RHIC and LHC in the subsequent hadronic evolution of the fireball will remain similar. We also note that the $\mu_B \approx 0$ MeV regime is amenable to numerical lattice QCD calculations, both for the equation of state of the medium evolution, and in particular for the microscopic dilepton production rate, at least in the QGP phase for now [14, 15]. Furthermore, since the phase transition at $\mu_B \approx 0$ MeV presumably is a continuous crossover [16], a realistic dilepton rate should vary smoothly when changing the temperature through T_{pc} . Thus, after the successful fixed-target dilepton program at the CERN-SPS, the efforts and attention are now shifting to collider energies around experiments at RHIC and LHC.

In the present paper we will focus on the theory and phenomenology of dilepton production at collider energies (for a recent overview including an assessment of SPS data, see, e.g., [17]). The presented material is partly of review nature, but also contains thus far unpublished results, for example, updates in the use of nonperturbative QGP dilepton rates and equation of state, and detailed predictions for invariant-mass and transverse-momentum spectra for ongoing and upcoming experiments at RHIC and LHC, including an excitation function of the beam energy scan program at RHIC.

This paper is organized as follows. In Section 2, we briefly review the calculation of the thermal dilepton emission rates from hadronic matter and the quark-gluon plasma (QGP). We elaborate on how recent lattice-QCD results at vanishing three-momentum ($q = 0$) may be extended to finite q to enable their application to URHICs. In Section 3, we discuss in some detail the calculations of dilepton spectra suitable for comparison with experiment; this involves a brief discussion of the medium evolution in URHICs (including an update of the equation of state) in Section 3.1 and of nonthermal sources (primordial production and final-state decays) in Section 3.2. It will be followed by analyses of mass and momentum spectra, as well as elliptic flow at full

RHIC energy in Section 3.3, and of an excitation function as obtained from the RHIC beam energy scan in Section 3.4; predictions for dielectron and dimuon spectra at current (2.76 ATeV) and future (5.5 ATeV) LHC energies are presented in Section 3.5. We end with a summary and outlook in Section 4.

2. Thermal Dilepton Rates in QCD Matter

The basic quantity for connecting calculations of the electromagnetic (EM) spectral function in QCD matter to measurements of dileptons in heavy-ion collisions is their thermal emission rate; per unit phase space, it can be written as

$$\frac{dN_{ll}}{d^4x d^4q} = -\frac{\alpha_{\text{EM}}^2 L(M)}{\pi^3 M^2} f^B(q_0; T) \text{Im} \Pi_{\text{EM}}(M, q; \mu_B, T), \quad (1)$$

where $L(M)$ is a lepton phase-space factor (=1 for vanishing lepton mass), f^B denotes the thermal Bose distribution, and $q_0 = \sqrt{M^2 + q^2}$ is the energy of the lepton pair (or virtual photon) in terms of its invariant mass and 3-momentum. As mentioned above, this observable is unique in its direct access to an in-medium spectral function of the formed system, namely, in the vector (or EM) channel, $\text{Im} \Pi_{\text{EM}} \equiv (1/3)g_{\mu\nu} \text{Im} \Pi_{\text{EM}}^{\mu\nu}$. It is defined via the correlation function of the EM current, j_{EM}^μ , as transported by the electric-charge carriers in the system. In quark basis, the EM current is given by the charge-weighted sum over flavor:

$$j_{\text{EM}}^\mu = \sum_{q=u,d,s} e_q \bar{q} \gamma^\mu q, \quad (2)$$

while in hadronic basis, it is in good approximation given by the vector-meson fields:

$$j_{\text{EM}}^\mu = \sum_{V=\rho,\omega,\phi} \frac{m_V^2}{g_V} V^\mu, \quad (3)$$

known as vector-dominance model (VDM). Since the significance of thermal dilepton radiation is limited to masses below the J/ψ mass, $M \lesssim 3$ GeV, we will focus on the light- and strange-quark sector in this article.

In the vacuum, the EM spectral function is well known from the e^+e^- annihilation cross section into hadrons, usually quoted relative to the annihilation into dimuons as the ratio $R = -(12\pi/s) \text{Im} \Pi_{\text{EM}}$ (cf. Figure 1). It illustrates that the non-perturbative hadronic description in terms of VDM works well in the low-mass region (LMR), $M \lesssim 1$ GeV, while the perturbative partonic description appears to apply for $M \gtrsim 1.5$ GeV. Thus, in URHICs, dilepton spectra in the LMR are ideally suited to study the properties of vector mesons in the medium. A central question is if and how these medium modifications can signal (the approach to) deconfinement and the restoration of the dynamical breaking of chiral symmetry (DBCS). After all, confinement and DBCS govern the properties of hadrons in vacuum. At masses $M \gtrsim 1.5$ GeV, the perturbative nature of the EM spectral function suggests that in-medium modifications are suppressed, coming in as

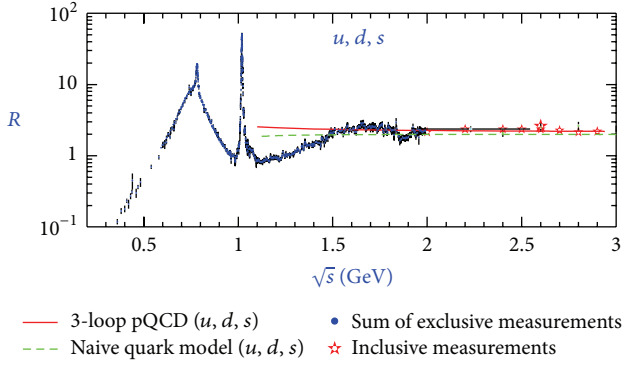


FIGURE 1: Compilation of experimental data for the ratio, R , of cross sections for $e^+e^- \rightarrow \text{hadrons}$ over $e^+e^- \rightarrow \mu^+\mu^-$, as a function of invariant mass $\sqrt{s} = M$. Figure taken from [33].

corrections in powers of T/M and α_s . In this case, invariant-mass spectra of thermal radiation become an excellent measure for the prevalent temperatures of the produced system, free from blue shifts due to the medium expansion which strongly affect p_t spectra.

2.1. Hadronic Matter. Over the last two decades, broad efforts have been undertaken to evaluate the medium modifications of the ρ -meson. The latter dominates in the EM spectral function over the ω by about a factor of 10 (the ϕ appears to be rather protected from hadronic medium effects, presumably due to the OZI rule, at least for its coupling to baryons). Recent overviews of these efforts can be found, for example, in [10, 18, 19]. Most approaches utilize effective hadronic (chiral) Lagrangians and apply them in diagrammatic many-body theory to compute thermal (or density) loop corrections. The generic outcome is that of a substantial broadening of the ρ 's spectral shape, with little mass shift (in a heat bath, chiral symmetry protects the ρ from mass shifts at order $\mathcal{O}(T^2)$ [20]). The magnitude of the ρ 's in-medium width (and/or its precise spectral shape) varies in different calculations, but the discrepancies can be mostly traced back to the differing contributions accounted for in the Lagrangian (e.g., the set of baryon and/or meson resonance excitations, or medium effects in the ρ 's pion cloud). Similar findings arise when utilizing empirically extracted on-shell ρ -meson scattering amplitudes off hadrons in linear-density approximation [21]. Since these calculations are restricted to resonances above the nominal ρN (or $\rho\pi$) threshold, quantitative differences to many-body (field-theoretic) approaches may arise; in particular, the latter account for subthreshold excitations, for example, $\rho + N \rightarrow N^*(1520)$, which induce additional broadening and associated enhancement of the low-mass part in the ρ spectral function (also causing marked deviations from a Breit-Wigner shape). Appreciable mass shifts are typically found in mean-field approximations (due to large in-medium scalar fields) or in calculations where the bare parameters of the underlying Lagrangian are allowed to be temperature dependent [22].

An example for dilepton rates following from a ρ spectral function calculated in hot and dense hadronic matter at SPS energies is shown in Figure 2(a). The EM spectral function

follows from the ρ -meson using VDM, (3), although corrections to VDM are necessary for quantitative descriptions of the EM couplings in the baryon sector [23, 24]. When extrapolated to temperatures around T_{pc} , the resonance peak has essentially vanished leading to a structureless emission rate with a large enhancement in the mass region below the free ρ mass. The decomposition of the rate into in-medium self-energy contributions illustrates the important role of the pion cloud modifications and of multiple low-energy excitations below the free ρ mass, for example, resonance-hole BN^{-1} , that is, $\rho + N \rightarrow B$ for off-shell ρ -mesons. The hadronic medium effects are slightly reduced at collider energies (Figure 2(b)), where a faint resonance structure appears to survive at around T_{pc} (it is significantly more suppressed at $T = 180$ MeV). A recent calculation in a similar framework, combining thermal field theory with effective hadron Lagrangians [25] and including both finite-temperature and -density contributions to the ρ self-energy through baryon and meson resonances, shows fair agreement with the results shown in Figure 2(a).

2.2. Quark-Gluon Plasma. In a perturbative QGP (pQGP), the leading-order (LO) mechanism of dilepton production is EM quark-antiquark annihilation as following from a free quark current in (2). The corresponding EM spectral function is essentially given by the “naive quark model” curve in Figure 1, extended all the way down to vanishing mass,

$$\begin{aligned} \text{Im } \Pi_{\text{EM}}^{\text{pQGP}} &= -\frac{C_{\text{EM}} N_c}{12\pi} M^2 \left(1 + \frac{2T}{q} \ln \left[\frac{1+x_+}{1+x_-} \right] \right) \\ &\equiv \frac{C_{\text{EM}} N_c}{12\pi} M^2 \hat{f}_2(q_0, q; T), \end{aligned} \quad (4)$$

where $C_{\text{EM}} \equiv \sum_{q=u,d,s} e_q^2$ (an additional phase-space factor occurs for finite current quark masses) and $x_{\pm} = \exp[-(q_0 \pm q)/2T]$. Finite-temperature corrections are induced by a quantum-statistical Pauli-blocking factor (written for $\mu_q = 0$) which produces a nontrivial 3-momentum dependence [26]; for $q = 0$, it simplifies to $\hat{f}_2(q_0, q = 0; T) = [1 - 2f^F(q_0/2)]$, where f^F is the thermal Fermi distribution. The pertinent 3-momentum integrated dilepton rate is structureless (cf. long-dashed curve in Figure 2(b)). Its finite value at $M = 0$ implies that no real photons can be produced from this mechanism.

A consistent implementation of α_s corrections in a thermal QGP at vanishing quark chemical potential has been achieved by resumming the hard-thermal-loop (HTL) action [27]. Quarks and gluons acquire thermal masses $m_{q,g}^{\text{th}} \sim gT$, but bremsstrahlung-type contributions lead to a marked enhancement of the rate over the LO pQCD results (cf. the dash-dotted line in Figure 2(b)).

Recent progress in calculating dilepton rates nonperturbatively using thermal lattice QCD (lQCD) has been reported in [14, 15, 28]. The basic quantity computed in these simulations is the Euclidean-time correlation function which is related to the spectral function, $\rho_V \equiv -2 \text{Im } \Pi_V^i$, via

$$\Pi_V(\tau, q; T) = \int_0^\infty \frac{dq_0}{2\pi} \rho_V(q_0, q; T) \frac{\cosh[q_0(\tau - 1/2T)]}{\sinh[q_0/2T]}. \quad (5)$$

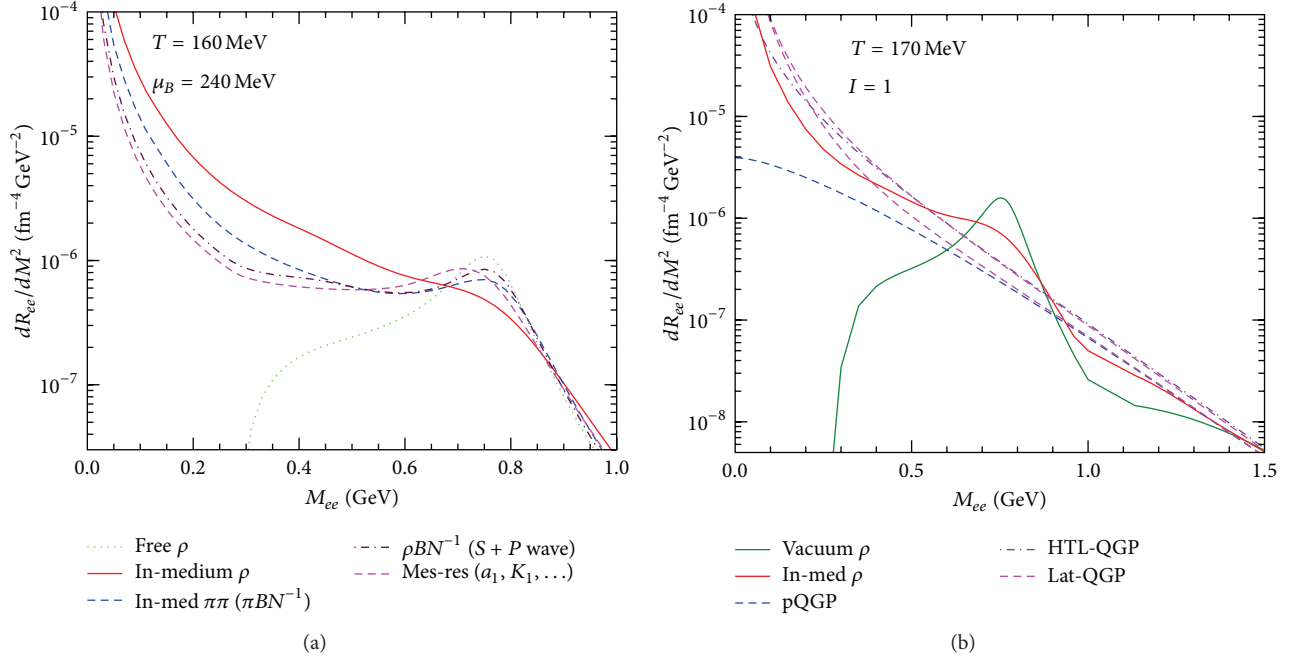


FIGURE 2: Dilepton rates from hot QCD matter in the isovector (ρ) channel. (a) Effective hadronic Lagrangian plus many-body approach for the in-medium ρ spectral function (solid line) at a temperature and chemical potential characteristic for chemical freezeout at full SPS energy; the effects of in-medium pion-cloud (long-dashed line), baryon resonances (dash-dotted line), and meson resonances (short-dashed line) are shown separately along with the rate based on the vacuum spectral function (dotted line). (b) Comparison of free and in-medium hadronic and partonic calculations at temperature $T = 170 \text{ MeV}$ and small baryon chemical potential characteristic for RHIC and LHC conditions; the free and in-medium hadronic rates are based on [35, 36]; the “lat-QGP” rates (2 short-dashed lines) are based on fits to the $q = 0$ IQCD rate with extensions to finite 3-momentum utilizing perturbative photon rates (see Section 2.2 for details).

Results for Π_V obtained in quenched QCD for $T = 1.45 T_c$ at vanishing q (in which case $M = q_0$) are shown by the data points in Figure 3(a), normalized to the free (noninteracting) pQGP limit. At small τ , corresponding to large energies in the spectral function, this ratio tends to one as expected for the perturbative limit. For larger τ , a significant enhancement develops which is associated with a corresponding enhancement in the low-energy (or low-mass) regime of the spectral function (and thus dilepton rate). This enhancement may be quantified by making an ansatz for the spectral function in terms of a low-energy Breit-Wigner part plus a perturbative continuum [14],

$$\rho_V^{\text{ii}}(q_0) = S_{\text{BW}} \frac{q_0 \Gamma / 2}{q_0^2 + \Gamma^2 / 4} + \frac{C_{\text{EM}} N_c}{2\pi} (1 + \kappa) q_0^2 \tanh\left(\frac{q_0}{4T}\right) \quad (6)$$

(note that $\tanh(q_0/4T) = 1 - 2f^F(q_0/2)$). The strength (S_{BW}) and width (Γ) of the Breit-Wigner, as well as a perturbative α_s correction (κ), are then fit to the Euclidean correlator. The large- τ enhancement in the correlator generates an appreciable low-energy enhancement in the spectral function (cf. Figure 3(b)). The zero-energy limit of the spectral function defines a transport coefficient, the electric conductivity, $\sigma_{\text{EM}} = (1/6) \lim_{q_0 \rightarrow 0} (\rho_V^{\text{ii}}/q_0)$. Similar to the viscosity or heavy-quark diffusion coefficient, a small value for σ_{EM} , implied by a large value for Γ , indicates a strong coupling of the medium; for example, in pQCD, $\sigma_{\text{EM}} \propto T/\alpha_s^2$ [29].

The results for the dilepton rate (or spectral function) at a smaller temperature of $1.1 T_c$ are found to be similar to the ones at $1.45 T_c$ [28], suggesting a weak temperature dependence in this regime. Note, however, that the phase transition in quenched QCD is of first order; that is, a stronger variation is expected when going across T_c . Recent results for two-flavor QCD [15] also indicate rather structureless spectral functions similar to the quenched results. Ultimately, at sufficiently small temperatures, the lattice computations should recover a ρ -meson resonance peak; it will be interesting to see at which temperatures this occurs.

For practical applications, a finite 3-momentum dependence of the IQCD dilepton rate is needed, which is currently not available from the simulations. We here propose a “minimal” construction which is based on a matching to the 3-momentum dependence obtained from the LO pQCD photon rate [30]. The latter reads

$$\begin{aligned} q_0 \frac{dR_V}{d^3q} &= -\frac{\alpha_{\text{EM}}}{\pi^2} \text{Im} \Pi_T(M=0, q) f^B(q_0, T) \\ &= \frac{C_{\text{EM}} \alpha_s}{2\pi^2} T^2 f^B(q_0, T) \ln\left(1 + \frac{2.912 q_0}{4\pi \alpha_s T}\right). \end{aligned} \quad (7)$$

The idea is now to adopt the transverse part of the EM spectral function as given by (7) for the 3-momentum dependence of

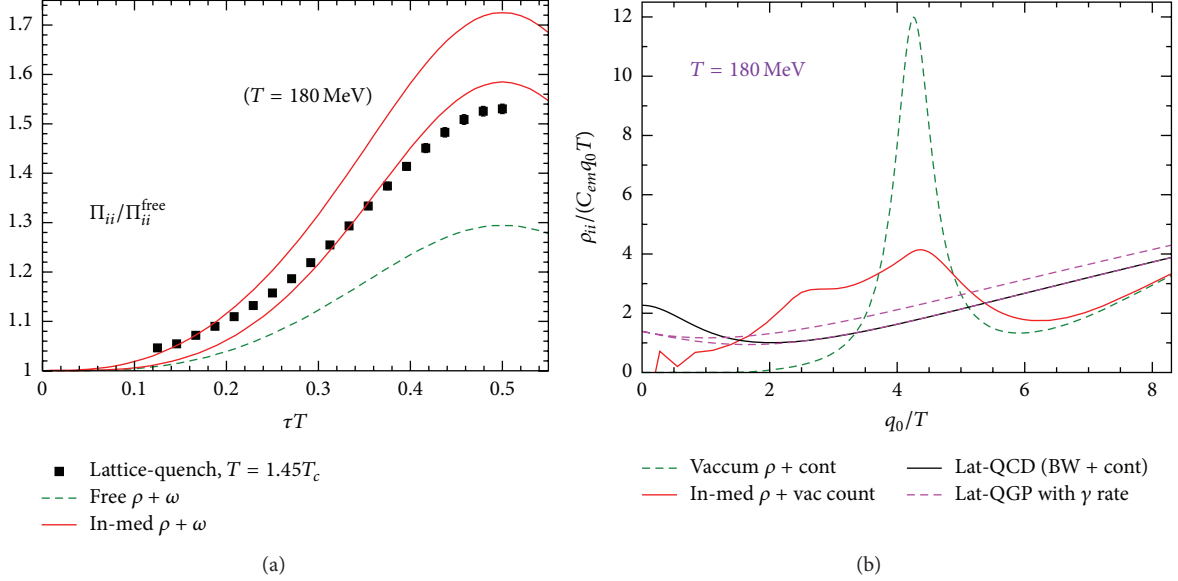


FIGURE 3: (a) Euclidean correlators of the EM current as computed in quenched thermal IQCD (data points) [14], compared to results from integrating hadronic spectral functions using (5) without (dashed green line) and with in-medium effects (red lines, with free and in-medium continuum threshold) [37]. (b) Vector-isovector spectral functions at $q = 0$ corresponding to the Euclidean correlators in (a) in vacuum (green dashed line), in hadronic matter calculated from many-body theory at $T = 180 \text{ MeV}$ [13] (red solid line), and in a gluon plasma at $1.4T_c$ extracted from thermal lattice-QCD (black solid line) [14]; the 3-momentum extended IQCD rates according to (8) are shown for $K = 2$ (short-dashed lines, with (lower) and without (upper) form factor correction).

the spectral function in (6) by replacing the Breit-Wigner part with it; that is,

$$\begin{aligned}
 -\text{Im } \Pi_T &= \frac{C_{\text{EM}} N_c}{12\pi} M^2 \\
 &\times \left(\hat{f}_2(q_0, q; T) \right. \\
 &\quad \left. + 2\pi\alpha_s \frac{T^2}{M^2} K F(M^2) \ln \left(1 + \frac{2.912 q_0}{4\pi\alpha_s T} \right) \right) \\
 &\equiv \frac{C_{\text{EM}} N_c}{12\pi} M^2 \left(\hat{f}_2(q_0, q; T) + Q_{\text{LAT}}^T(M, q) \right). \tag{8}
 \end{aligned}$$

Here, we have introduced a K factor into Q_{LAT}^T , which serves two purposes: (i) with $K = 2$, it rather accurately accounts for the enhancement of the complete LO photon rate calculation [31] over the rate in (7); (ii) it better reproduces the low-energy regime of the IQCD spectral function; for example, for $K = 2$, the electric conductivity following from (8) is $\sigma_{\text{EM}}/T \approx 0.23 C_{\text{EM}}$, not far from the IQCD estimate with the fit ansatz (6), $\sigma_{\text{EM}}/T \approx (0.37 \pm 0.01) C_{\text{EM}}$ (also compatible with [32]; the systematic uncertainty in the lattice result, due to variations in the ansatz, is significantly larger). The resulting spectral function (upper dashed line in Figure 3(b)) somewhat overestimates the IQCD result at high energies, where the latter coincides with the annihilation term. This can be improved by an additional form factor, $F(M^2) = \Lambda^2/(\Lambda^2 + M^2)$, resulting in the lower dashed line in Figure 3(b) (using $\Lambda = 2T$).

Finally, care has to be taken to include a finite longitudinal part which develops in the timelike regime. Here, we employ a dependence that follows, for example, from standard constructions of gauge-invariant S-wave ρ -baryon interactions, yielding $\Pi_L = (M^2/q_0^2)\Pi_T$ [34]. Thus, we finally have

$$Q_{\text{LAT}}^{\text{tot}} = \frac{1}{3} (2Q_{\text{LAT}}^T + Q_{\text{LAT}}^L) = \frac{1}{3} Q_{\text{LAT}}^T \left(2 + \frac{M^2}{q_0^2} \right). \tag{9}$$

The IQCD results for the isovector spectral function are compared to hadronic calculations in Figure 3(b). Close to the phase transition temperature, the ‘‘melting’’ of the in-medium ρ spectral function suggests a smooth transition from its prominent resonance peak in vacuum to the rather structureless shape extracted from IQCD, signaling a transition from hadronic to partonic degrees of freedom. It would clearly be of interest to extract the conductivity from the hadronic calculations, which currently is not well resolved from the $q = 0, q_0 \rightarrow 0$ limit of the spectral function. The mutual approach of the nonperturbative hadronic and IQCD spectral functions is also exhibited in the 3-momentum integrated dilepton rate shown in Figure 2(b), especially when compared to the different shapes of the LO pQCD and vacuum hadronic rates. Arguably, the in-medium hadronic rate still shows an indication of a broad resonance. A smooth matching of the rates from above and below T_{pc} might therefore require some additional medium effects in the hot and dense hadronic medium and/or the emergence of resonance correlations in the $q\bar{q}$ correlator in the QGP. Unless otherwise noted, the thermal emission rates used in the calculations of dilepton spectra discussed below will be based

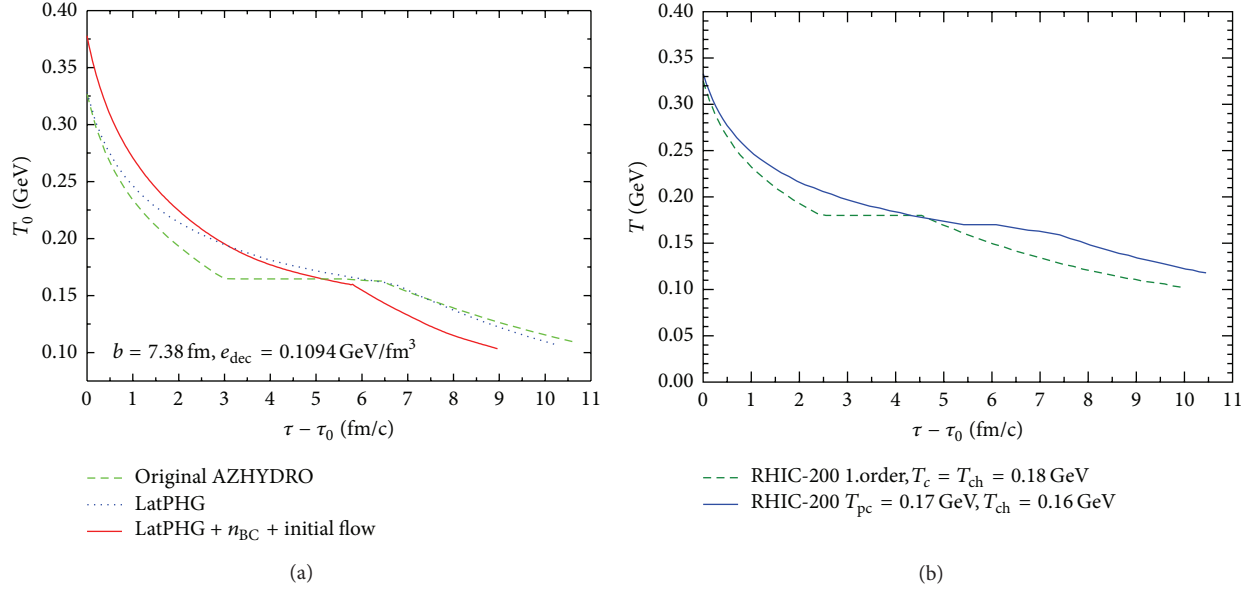


FIGURE 4: Time evolution of fireball temperature in semicentral Au-Au ($\sqrt{s} = 0.2$ GeV) collisions at RHIC within (the central cell of) ideal hydrodynamics (a) [42] and an expanding fireball model (b). The dashed green and dotted blue lines in (a) are to be compared to the dashed green and solid blue lines in (b), respectively.

on the in-medium hadronic rates of [35] and the lQCD-inspired QGP rates [14], extended to finite 3-momentum as constructed above (with $K = 2$ and form factor).

3. Dilepton Spectra at RHIC and LHC

The calculation of dilepton mass and transverse-momentum (q_t) spectra, suitable for comparison to data in heavy-ion collisions, requires an integration of the thermal rates of hadronic matter and QGP over a realistic space-time evolution of the AA reaction:

$$\frac{dN_{ll}}{dM} = \int d^4x \frac{Md^3q}{q_0} \frac{dN_{ll}}{d^4x d^4q}. \quad (10)$$

In addition to the thermal yield, nonthermal sources have to be considered, for example, primordial Drell-Yan annihilation and electromagnetic final-state decays of long-lived hadrons. We will briefly discuss space-time evolutions in Section 3.1 and nonthermal sources in Section 3.2, before proceeding to a more detailed discussion of thermal spectra and comparisons to data, as available, in Sections 3.3, 3.4, and 3.5 for full RHIC energy, the beam-energy scan, and LHC, respectively.

3.1. Medium Expansion. The natural framework to carry out the space-time integral over the dilepton rate in URHICs is relativistic hydrodynamics. The application of this approach to AA collisions at RHIC and LHC works well to describe bulk hadron observables (e.g., p_t spectra and elliptic flow) up to momenta of $p_t \approx 2$ -3 GeV, which typically comprises more than 90% of the total yields. Some uncertainties remain, for example, as to the precise initial conditions at thermalization, viscous corrections, or the treatment of the late stages where

the medium becomes dilute and the hadrons decouple (see, e.g., [38] for a recent review). Another key ingredient is the equation of state (EoS) of the medium, $\varepsilon(P)$, which drives its collective expansion. Figure 4(a) illustrates the effects of updating a previously employed bag-model EoS (a quasiparticle QGP connected to a hadron resonance gas via a first-order phase transition) [39] by a recent parametrization of a nonperturbative QGP EoS from lQCD data [40, 41] (continuously matched to a hadron-resonance gas at $T_{pc} = 170$ MeV) [42]; within a 2+1-D ideal hydro calculation, the most notable change is a significant increase of the temperature (at fixed entropy density) in the regime just above the transition temperature (up to ca. 30 MeV at the formerly onset of the first-order transition). Together with the fact that the hadronic portion of the formerly mixed phase is now entirely associated with the QGP, this will lead to an increase (decrease) of the QGP (hadronic) contribution to EM radiation relative to the first-order scenario. In addition, the harder lattice EoS induces a stronger expansion leading to a slightly faster cooling and thus reduction in the lifetime by about 5%. This effect becomes more pronounced when modifying the initial conditions of the hydrodynamic evolution, for example, by introducing a more compact spatial profile (creating larger gradients) and/or initial transverse flow (associated with interactions prior to the thermalization time, τ_0) [42] (cf. the solid line in Figure 4(a)). The resulting more violent expansion plays an important role in understanding the HBT radii of the system [43]. The relevance for EM radiation pertains to reducing the fireball lifetime by up to $\sim 20\%$.

More simplistic parametrizations of the space-time evolution of AA collisions have been attempted with longitudinally and transversely expanding fireballs. With an appropriate choice of the transverse acceleration (in all applications below

it is taken as $a_t = 0.12/\text{fm}$ at the surface), an approximate reproduction of the basic features (timescales and radial flow) of hydrodynamic evolutions can be achieved, see Figure 4(b). Most of the results shown in the remainder of this article are based on such simplified fireball parametrizations, utilizing the EoS of [42] where a parametrization of IQCD results is matched with a hadron resonance gas at $T_{\text{pc}} = 170$ MeV and subsequent chemical freezeout at $T_{\text{ch}} = 160$ MeV (see also [44]). We note that the use of this EoS, together with the IQCD-based QGP emission rates, constitutes an update of our earlier calculations [45] where a quasiparticle bag-model EoS was employed in connection with HTL rates in the QGP. We have checked that the previous level of agreement with the acceptance-corrected NA60 spectra is maintained, which is essentially due to the duality of the QGP and hadronic rates around T_{pc} (a more detailed account in the context of the SPS dilepton data will be given elsewhere [46]). For our discussion of collider energies below, the initialization (or thermalization times) are chosen at 0.33 fm/c at full RHIC energy (increasing smoothly to 1 fm/c at $\sqrt{s} = 20$ GeV) and 0.2 fm/c in the LHC regime. This results in initial temperatures of 225 MeV and 330 MeV in minimum-bias (MB) Au-Au collisions at 20 and 200 GeV, respectively, increasing to ~ 380 MeV in central Au-Au (200 GeV) and $\sim 560(620)$ MeV in central Pb-Pb at $2.76(5.5)$ ATeV. These values differ slightly from previous calculations with a quasiparticle EoS; they are also sensitive to the initial spatial profile (cf. Figure 4(a)). However, for our main objective of calculating low-mass dilepton spectra, the initial temperature has little impact.

3.2. Nonthermal Sources. In addition to thermal radiation from the locally equilibrated medium, dilepton emission in URHICs can arise from interactions prior to thermalization (e.g., Drell-Yan annihilation) and from EM decays of long-lived hadrons after the fireball has decoupled (e.g., Dalitz decays $\pi^0, \eta \rightarrow \gamma l^+ l^-$ or $\omega, \phi \rightarrow l^+ l^-$). Furthermore, paralleling the structure in hadronic spectra, a nonthermal component from hard production will feed into dilepton spectra, for example, via bremsstrahlung from hard partons traversing the medium [47] or decays of both short- and long-lived hadrons which have not thermalized with the bulk (e.g., “hard” ρ -mesons or long-lived EM final-state decays). Hadronic final-state decays (including the double semileptonic decay of two heavy-flavor hadrons originating from a $c\bar{c}$ or $b\bar{b}$ pair produced together in the same hard process) are commonly referred to as the “cocktail,” which is routinely evaluated by the experimental collaborations using the vacuum properties of each hadron with p_t spectra based on measured spectra or appropriately extrapolated using thermal blast-wave models. In URHICs, the notion of the cocktail becomes problematic for short-lived resonances whose lifetime is comparable to the duration of the freezeout process of the fireball (e.g., for ρ, Δ , etc.). In their case, a better approximation is presumably to run the fireball an additional ~ 1 fm/c to treat their final-decay contribution as thermal radiation including medium effects. However, care has to be taken in evaluating their dilepton p_t -spectra, as the latter are slightly different for thermal radiation and final-state decays

(cf. [45] for a discussion and implementation of this point). For light hadrons at low p_t , the cocktail scales with the total number of charged particles, N_{ch} , at given collision energy and centrality, while for hard processes, a collision-number scaling $\propto N_{\text{coll}}$ is in order (and compatible with experiment where measured, modulo the effects of “jet quenching”). The notion of “excess dileptons” is defined as any additional radiation observed over the cocktail, sometimes quantified as an “enhancement factor” in a certain invariant-mass range. The excess radiation is then most naturally associated with thermal radiation, given the usual limitation where hard processes take over, that is, $M, q_t \lesssim 2\text{-}3$ GeV.

3.3. RHIC-200. We start our discussion of low-mass dilepton spectra at full RHIC energy where most of the current experimental information at collider energies is available, from both PHENIX [48] and STAR [49] measurements.

3.3.1. Invariant-Mass Spectra. Figure 5 shows the comparison of thermal fireball calculations with low-mass spectra from STAR [49]. As compared to earlier calculations with a bag-model EoS [13], the use of IQCD-EoS and emission rates for the QGP enhances the pertinent yield significantly. It is now comparable to the in-medium hadronic contribution for masses below $M \approx 0.3$ GeV and takes over in the intermediate-mass region ($M \geq 1.1$ GeV). The hadronic part of the thermal yield remains prevalent in a wide range around the free ρ mass, with a broad resonance structure and appreciable contributions from 4π annihilation for $M \geq 0.9$ GeV. Upon adding the thermal yield to the final-state decay cocktail by the STAR collaboration (without ρ decay), the MB data are well described. For the central data, a slight overestimate around $M \approx 0.2$ GeV and around the ω peak is found. A similar description [51] of the STAR data arises in a viscous hydrodynamic description of the medium using the ρ spectral function from on-shell scattering amplitudes [21] (see also [52]) and in the parton-hadron string dynamics transport approach using a schematic temperature- and density-dependent broadening in a Breit-Wigner approximation of the ρ spectral function [53]. More studies are needed to discern the sensitivity of the data to the in-medium spectral shape, as the latter significantly varies in the different approaches. For the PHENIX data (not shown), the enhancement as recently reported in [54] for noncentral collisions (carried out with the hadron-blind detector (HBD) upgrade) agrees with earlier measurements [48], is consistent with the STAR data, and thus should also agree with theory. For the most central Au-Au data, however, a large enhancement was reported in [48], which is well above theoretical calculations with broad spectral functions [13, 53, 55, 56], even in the MB sample. More “exotic” explanations of this effect, which did not figure at the SPS, for example, a Bose-condensed like glasma in the pre-equilibrium stages [57], have been put forward to explain the “PHENIX puzzle.” However, it is essential to first resolve the discrepancy on the experimental side, which is anticipated with the HBD measurement for central collisions.

To quantify the centrality dependence of the thermal radiation (or excess) yield, one commonly introduces an

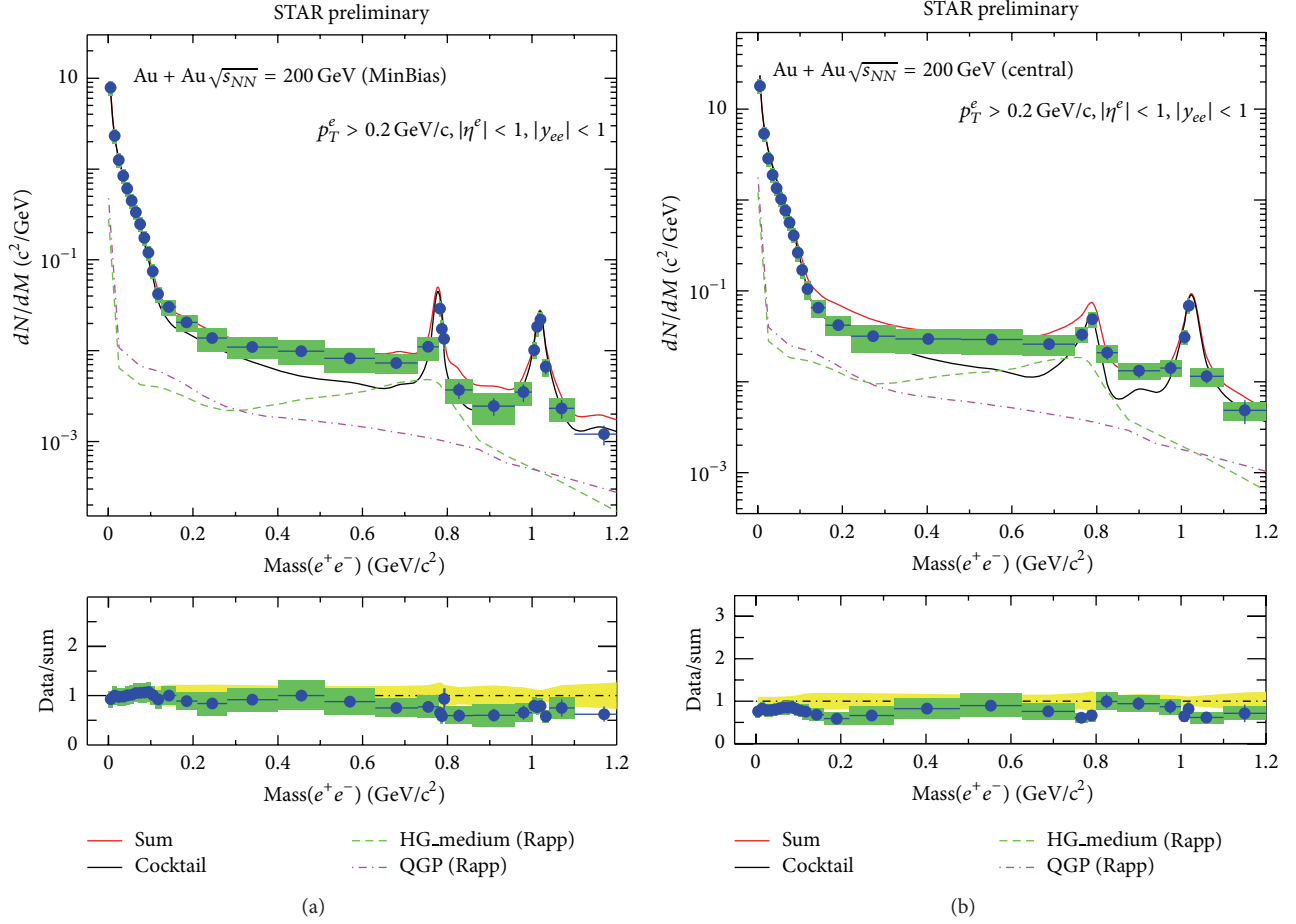


FIGURE 5: Dilepton invariant-mass spectra in Au-Au(200 AGeV) for minimum-bias (a) and central (b) collisions. Theoretical calculations for thermal radiation from a nonperturbative QGP and in-medium hadronic spectral functions are compared to STAR data [49, 50].

exponent α_c as $Y_M(N_{ch})/N_{ch} = CN_{ch}^{\alpha_c}$, which describes how the excess (or thermal) yield in a given mass range scales relative to the charged-particle multiplicity. For full RHIC energy, the theoretical calculation gives $\alpha_c \approx 0.45$ (with a ca. 10% error), similar to what had been found for integrated thermal photon yields [58].

3.3.2. Transverse-Momentum Dependencies. When corrected for acceptance, invariant-mass spectra are unaffected by any blue-shift of the expanding medium, which renders them a pristine probe for in-medium spectral modifications. However, the different collective flow associated with different sources may be helpful in discriminating them by investigating their q_t spectra, see, for example, [26, 59–64]. As is well known from the observed final-state hadron spectra, particles of larger mass experience a larger blue-shift than lighter particles due to collective motion with the expanding medium. Schematically, this can be represented by an effective slope parameter which for sufficiently large masses takes an approximate form of $T_{\text{eff}} = T + M\bar{\beta}^2$, where T and $\bar{\beta}$ denote the local temperature and average expansion velocity of the emitting source cell. Dileptons are well suited to systematically scan the mass dependence of T_{eff}

by studying q_t spectra for different mass bins (provided the data have sufficient statistics). At the SPS, this has been done by the NA60 collaboration [65], who found a gradual increase in the slope from the dimuon threshold to the ρ mass characteristic for a source of hadronic origin (a.k.a in-medium ρ mesons), a maximum around the ρ mass (late ρ decays), followed by a decrease and leveling off in the intermediate-mass region (IMR, $M \geq 1$ GeV) indicative for early emission at temperatures $T \approx 170$ –200 MeV (where at the SPS the collective flow is still small).

Figure 6 shows the q_t spectra for thermal radiation from hadronic matter and QGP in MB Au-Au(200 AGeV) in two typical mass regions where either of the two sources dominates. In the low-mass region (LMR), both sources have a surprisingly similar slope ($T_{\text{slope}} \approx 280$ –285 MeV), reiterating that the emission is from mostly around T_{pc} where the slope of both sources is comparable (also recall from Figure 5 that in the mass window $M = 0.3$ –0.7 GeV the QGP emission is largest at the lower mass end, while the hadronic one is more weighted toward the higher end). For definiteness, assuming $T = 170$ MeV and $M = 0.5$ GeV, one finds that $\bar{\beta} \approx 0.45$ –0.5, which is right in the expected range [42]. On the other hand, in the IMR, where the QGP dominates, the hadronic

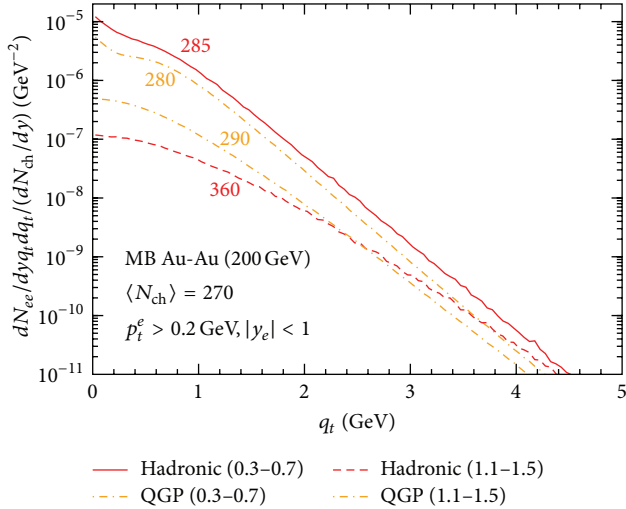


FIGURE 6: Dilepton transverse-momentum spectra from thermal radiation of QGP and hadronic matter in MB Au-Au(200 AGeV) collisions. The numbers next to each curve indicate the effective slope parameter, T_{eff} (MeV), as extracted from a two parameter fit using $dN/(q_t dq_{t'}) = C \exp[-M_t/T_{\text{eff}}]$ [45] with the transverse mass $M_t = \sqrt{M^2 + q_t^2}$ and an average mass of 0.5 GeV and 1.25 GeV for the low- and intermediate-mass windows, respectively.

slope has significantly increased to ca. 360 MeV due to the larger mass in the collective-flow term. On the other hand, the slope of the QGP emission has only slightly increased over the LMR, indicating that the increase in mass in the flow term is essentially offset by an earlier emission temperature, as expected for higher mass (for hadronic emission, the temperature is obviously limited by T_{pc}). Consequently, at RHIC, the effective slope of the total thermal radiation in the IMR exceeds the one in the LMR, contrary to what has been observed at SPS. Together with blue-shift free temperature measurements from slopes in invariant-mass spectra, this provides a powerful tool for disentangling collective and thermal properties through EM radiation from the medium.

Alternatively, one can investigate the mass spectra in different momentum bins, possibly revealing a q_t -dependence of the spectral shape, as was done for both e^+e^- data in Pb-Au [66] and $\mu^+\mu^-$ in In-In [65] at SPS. Calculations for thermal radiation in Au-Au at full RHIC energy are shown in Figure 7 for four bins from $q_t = 0-2$ GeV. One indeed recognizes that the ρ resonance structure becomes more pronounced as transverse momentum is increased. In the lowest bin, the minimum structure around $M \approx 0.2$ GeV is caused by the experimental acceptance, specifically the single-electron $p_t^e > 0.2$ GeV, which for vanishing q_t suppresses all dilepton yields below $M \approx 2p_t^{e,\text{min}} = 0.4$ GeV.

3.3.3. Elliptic Flow. Another promising observable to diagnose the collectivity, and thus the origin of the EM emission source, is its elliptic flow [64, 69, 70]. The latter is particularly useful to discriminate early from late(r) thermal emission sources; contrary to the slope parameter, which is subject to an interplay of decreasing temperature and increasing flow,

the medium's ellipticity is genuinely small (large) in the early (later) phases. Figure 8(a) shows hydrodynamic calculations of the inclusive thermal dilepton ν_2 as a function of invariant mass (using the same emission rates and EoS as in the previous figures) [67]. One nicely recognizes a broad maximum structure around the ρ mass, indicative for predominantly later emission in the vicinity of its vacuum mass, a characteristic mass dependence (together with an increasing QGP fraction) below, and a transition to a dominant QGP fraction with reduced ν_2 above. All these features are essentially paralleling the mass dependence of the *slope* parameter at SPS, while the latter exhibits a marked increase at RHIC in the IMR due to the increased radial flow in the QGP and early hadronic phase. Rather similar results are obtained in hydrodynamic calculations with in-medium spectral functions from on-shell scattering amplitudes [51]. When using a less pronounced in-medium broadening, the peak structure in $\nu_2(M)$ tends to become narrower [64, 69, 70]. First measurements of the dilepton- ν_2 have been presented by STAR [68], see Figure 8(b). The shape of the data is not unlike the theoretical calculations, while it is also consistent with the simulated cocktail contribution. Note that the total ν_2 is essentially a weighted sum of cocktail and excess radiation. Thus, if the total ν_2 were to agree with the cocktail, it would imply that the ν_2 of the excess radiation is as large as that of the cocktail. Clearly, future ν_2 measurements with improved accuracy will be a rich source of information.

Significant ν_2 measurements of EM excess radiation have recently been reported in the $M = 0$ limit, that is, for direct photons, by both PHENIX [71, 72] and ALICE [73, 74]. A rather large ν_2 signal has been observed in both experiments [72, 74], suggestive for rather late emission [75] (see also [76–79]). In addition, the effective slope parameters of the excess radiation have been extracted, $T_{\text{eff}} = 219 \pm 27$ MeV [71] at RHIC-200 and 304 ± 51 MeV at LHC-2760 [73], which are rather soft once blue-shift effects are accounted for. In fact, these slopes are not inconsistent with the trends in the LMR dileptons when going from RHIC (Figure 6) to LHC (Figure 12). This would corroborate their main origin from around T_{pc} .

3.4. RHIC Beam Energy Scan. A central question for studying QCD phase structure is how the spectral properties of excitations behave as a function of chemical potential and temperature. With the EM (or vector) spectral function being the only one directly accessible via dileptons, systematic measurements as a function of beam energy are mandatory. At fixed target energies, this is being addressed by the current and future HADES efforts ($E_{\text{beam}} = 1-10$ AGeV) [80, 81], by CBM for E_{beam} (Au) up to ~ 35 AGeV [2], and has been measured at SPS energies at $E_{\text{beam}} = 158$ AGeV, as well as in a CERES run at 40 AGeV [82].

At collider energies, a first systematic study of the excitation function of dilepton spectra has been conducted by STAR [68] as part of the beam-energy scan program at RHIC. The low-mass excess radiation develops smoothly when going down from $\sqrt{s_{NN}} = 200$ GeV via 62 GeV to 20 GeV (cf. Figure 9). Closer inspection reveals that the enhancement factor of excess radiation over cocktail in the region below

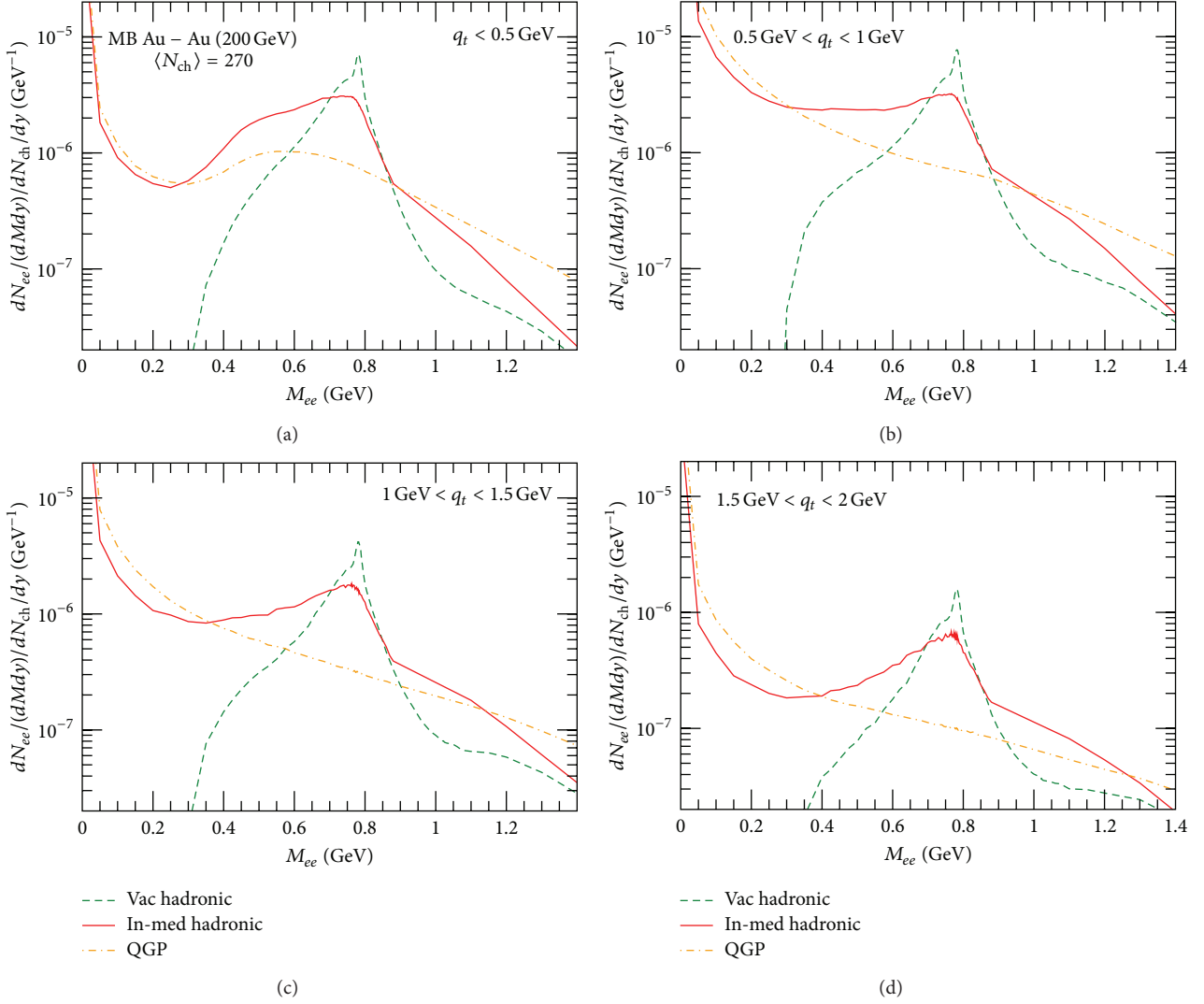


FIGURE 7: Dilepton invariant mass spectra in different bins of transverse momentum from thermal radiation of QGP (dash-dotted line) and hadronic matter (solid line: in medium, dashed line: vacuum spectral function) in MB Au-Au(200 AGeV) collisions; experimental acceptance as in Figures 5 and 6.

the ρ mass increases as the energy is reduced [68]. An indication of a similar trend was observed when comparing the CERES measurements in Pb-Au at $\sqrt{s_{NN}} = 17.3$ GeV and 8.8 GeV. Theoretically, this can be understood by the importance of baryons in the generation of medium effects [24], specifically, the low-mass enhancement in the ρ spectral function. These medium effects become stronger as the beam energy is reduced since the hadronic medium close to T_{pc} becomes increasingly baryon rich. At the same time, the cocktail contributions, which are mostly made up by meson decays, decrease. The hadronic in-medium effects are expected to play a key role in the dilepton excess even at collider energies. The comparison with the STAR excitation function supports the interpretation of the excess radiation as originating from a melting ρ resonance in the vicinity of T_{pc} .

A major objective of the beam-energy program is the search for a critical point. One of the main effects associated

with a second-order endpoint is the critical slowing down of relaxation rates due to the increase in the correlation length in the system. For the medium expansion in URHICs, this may imply an “anomalous” increase in the lifetime of the interacting fireball. If this is so, dileptons may be an ideal tool to detect this phenomenon, since their total yield (as quantified by their enhancement factor) is directly proportional to the duration of emission. The NA60 data have shown that such a lifetime measurement can be carried out with an uncertainty of about ± 1 fm/c [45]. In the calculations shown in Figure 9, no critical slowing down has been assumed; as a result, the average lifetime in MB Au-Au collisions increases smoothly from ca. 8 to 10 fm/c. Thus, if a critical point were to exist and lead to a, say, 30% increase in the lifetime in a reasonably localized range of beam energies, dilepton yields ought to be able to detect this signature. This signal would further benefit from the fact that the prevalent radiation arises from around

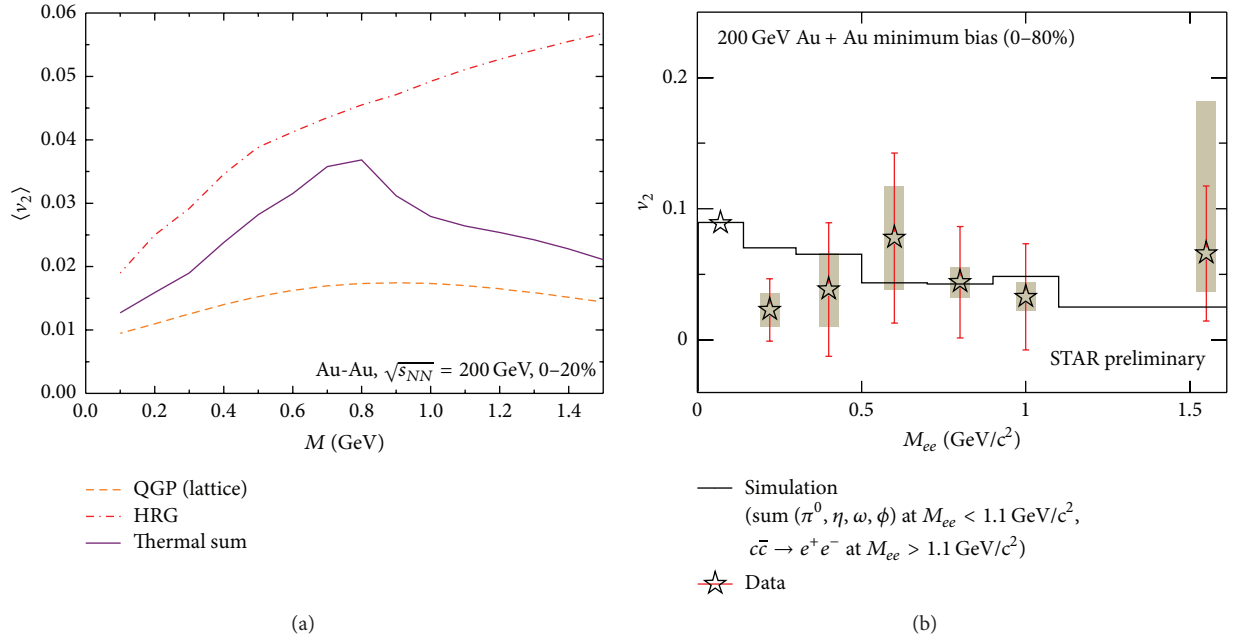


FIGURE 8: (a) Inclusive elliptic flow of thermal dileptons in 0–20% central Au-Au(200 AGeV) collisions, calculated within an ideal hydrodynamic model with lattice EoS using lQCD-based QGP and medium-modified hadronic rates [67]. (b) Dielectron- v_2 measured by STAR in MB Au-Au [68], including the cocktail contribution; the latter has been simulated by STAR and is shown separately by the solid histogram.

T_{pc} where the largest effect from the slowing down is expected.

3.5. LHC. The previous section raises the question whether the smooth excitation function of dilepton invariant-mass spectra in the RHIC regime will continue to LHC energies, which increase by another factor of ~ 20 . On the other hand, the dilepton q_t spectra, especially their inverse-slope parameters, indicate an appreciable variation from SPS to RHIC, increasing from ca. 220 to 280 MeV in the LMR, and, more pronounced, from ca. 210 to about 320 MeV in the IMR. This is a direct consequence of the stronger (longer) development of collective flow in the QGP phase of the fireball evolution. This trend will continue at the LHC, as we will see below. In the following Section 3.5.1, we will first discuss the dielectron channel at LHC and highlight the excellent experimental capabilities that are anticipated with a planned major upgrade program of the ALICE detector [83]. In addition, ALICE can measure in the dimuon channel, albeit with somewhat more restrictive cuts whose impact will be illustrated in Section 3.5.2.

3.5.1. Dielectrons. The invariant-mass spectra of thermal radiation at LHC energies show a very similar shape and hadronic/QGP composition as at RHIC energy, see Figure 10. This is not surprising given the virtually identical in-medium hadronic and QGP rates along the thermodynamic trajectories at RHIC and LHC (where $\mu_B \ll T$ at chemical freezeout). It implies that the thermal radiation into the LMR is still dominated by temperatures around T_{pc} , with little (if any) sensitivity to the earliest phases. The total yield, on

the other hand, increases substantially due to the larger fireball volumes created by the larger multiplicities. More quantitatively, the (N_{ch} -normalized) enhancement around, for example, $M = 0.4$ GeV, approximately scales as $N_{ch}^{\alpha_E}$ with $\alpha_E \approx 0.8$ relative to central Au-Au at full RHIC energy. This is a significantly stronger increase than the centrality dependent enhancement at fixed collision energy, $\alpha_c \approx 0.45$ as quoted in Section 3.3.1.

Detailed simulation studies of a proposed major upgrade of the ALICE detector have been conducted in the context of a pertinent letter of intent [83]. The final results after subtraction of uncorrelated (combinatorial) background are summarized in Figure 11, based on an excess signal given by the thermal contributions in Figure 10. (The thermal yields provided for the simulations were later found to contain a coding error in the author's implementation of the experimental acceptance; the error turns out to be rather inconsequential for the shape and relative composition of the signal, as a close comparison of Figures 10(b) and 11(b) reveals; the absolute differential yields differ by up to 20–30%.) Figure 10(a) shows that the thermal signal is dominant for the most part of the LMR (from ca. 0.2–1. GeV), while in the IMR it is outshined by correlated heavy-flavor decays. However, the latter can be effectively dealt with using displaced vertex cuts, while the excellent mass resolution, combined with measured and/or inferred knowledge of the Dalitz spectra of π^0 (from charged pions), η (from charged kaons), and ω (from direct dilepton decays), facilitates a reliable subtraction of the cocktail. The resulting excess spectra shown in Figure 10(b) are of a quality comparable to the NA60 data. This will allow for quantitative studies of the in-medium EM spectral

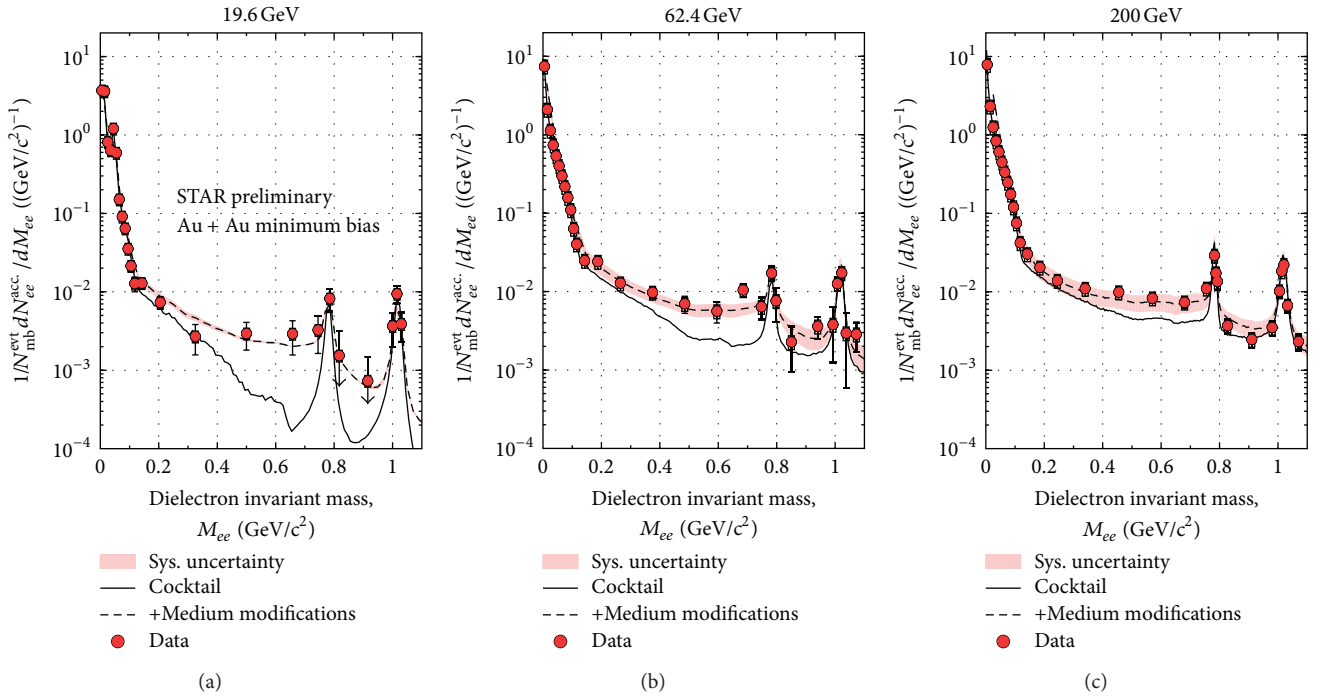


FIGURE 9: Low-mass dilepton spectra as measured by STAR in the RHIC beam-energy scan [68]; MB spectra are compared to theoretical predictions for the in-medium hadronic + QGP radiation, added to the cocktail contribution.

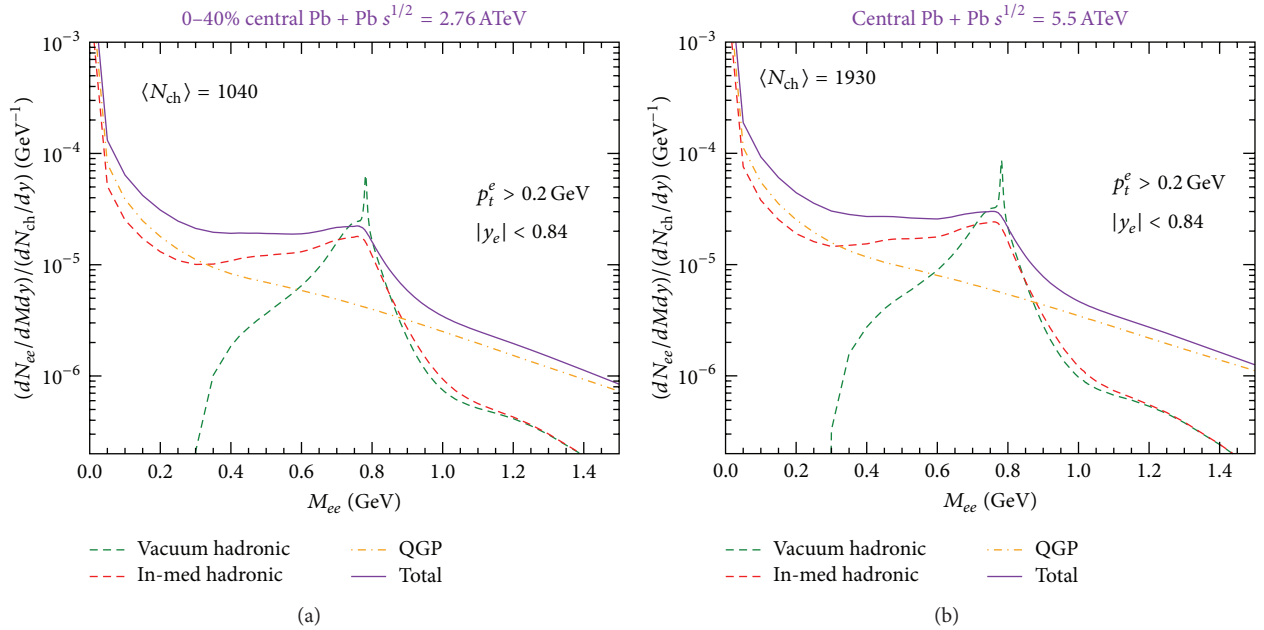


FIGURE 10: Dielectron invariant-mass spectra from thermal radiation in 0-40% central Pb-Pb(2.76 ATeV) (a) and 0-10% central Pb-Pb(5.5 ATeV) (b), including single-electron cuts to simulate the ALICE acceptance. Hadronic (with in-medium or vacuum EM spectral function) and QGP contributions are shown separately along with the sum of in-medium hadronic plus QGP. Here and in the following LHC plots, both vacuum and in-medium hadronic emission rates in the LMR have been supplemented with the vacuum spectral function in the LMR; that is, no in-medium effects due to chiral mixing have been included (for all RHIC calculations shown in the previous sections, full chiral mixing was included).

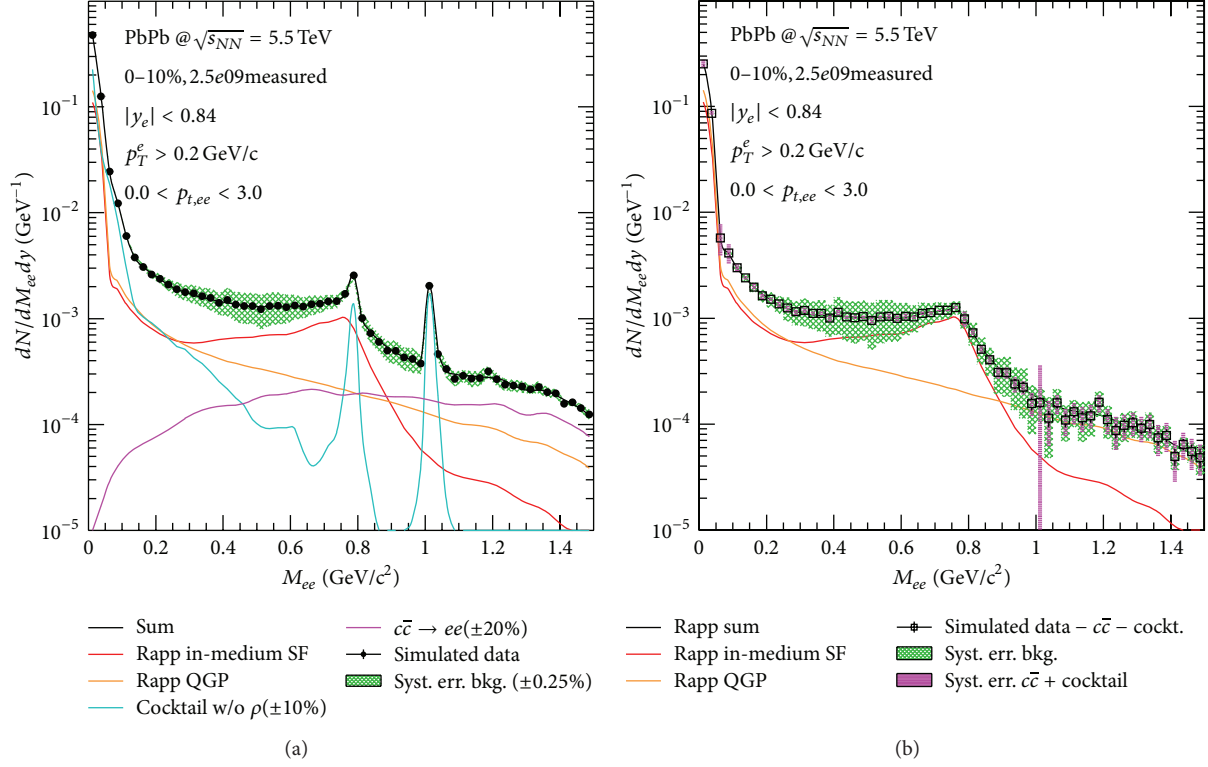


FIGURE 11: Simulations of dielectron invariant-mass spectra in Pb-Pb(5.5 ATeV) collisions assuming the thermal spectra shown in (a) of Figure 10 as the excess signal [83, 84]. In addition to the acceptance cuts on single-electron rapidity and momentum, pair efficiency and displaced vertex cuts are included here. (a) Invariant-mass spectra after subtraction of combinatorial background; in addition to the thermal signal, the simulated data contain the hadronic cocktail and correlated open-charm decays. (b) Simulated excess spectra after subtraction of the cocktail and the open-charm contribution using displaced vertex cuts.

function in the LMR which are critical for being able to evaluate signatures of chiral restoration (as discussed elsewhere, see, e.g., [17, 85]). In addition, the yield and spectral slope of the dominantly QGP emission in the IMR will open a pristine window on QGP lifetime and temperature (recall that the M spectra, which are little affected by the acceptance cuts in the IMR, are unaffected by blue shifts).

Let us turn to the dilepton q_t spectra at full LHC energy, displayed again for two mass bins representing the LMR and IMR in Figure 12. Compared to RHIC, the LHC fireball is characterized by a marked increase in QGP lifetime and associated build-up of transverse flow by the time the system has cooled down to T_{pc} . Consequently, the q_t spectra exhibit an appreciable increase in their inverse-slope parameters, by about 60% in the LMR (for both hadronic and QGP parts) and for the QGP part in the IMR, and up to 80% for the hadronic IMR radiation (recall that in a scenario with chiral mixing, the hadronic radiation for $M = 1.1\text{--}1.5$ GeV is expected to increase by about a factor of 2, so that its larger slope compared to the QGP will become more significant for the total).

3.5.2. Dimuons. Low-mass dilepton measurements are also possible with ALICE in the dimuon channel at forward rapidities, $2.5 < y_\mu < 4$, albeit with somewhat more restrictive momentum cuts [86]. The charged-particle multiplicity

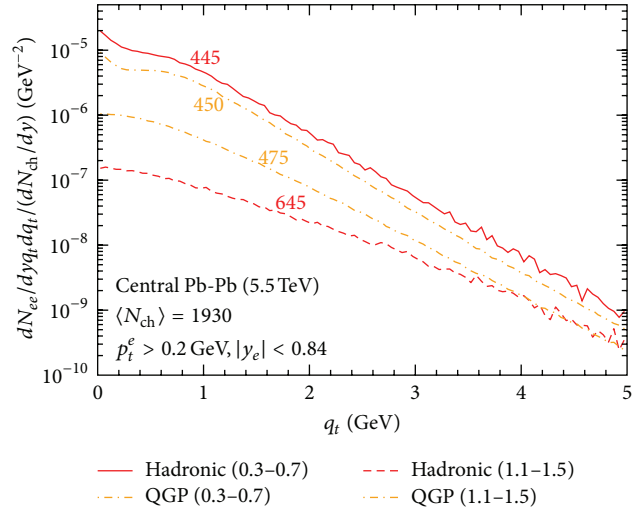


FIGURE 12: Same as Figure 6, but for central Pb-Pb(5.5 ATeV).

in this rapidity range is reduced by about 30% compared to midrapidity [87] but, at 2.76 ATeV, is still ca. 30% above central rapidities in central Au-Au at RHIC.

Figure 13 illustrates the expected thermal mass spectra in central Pb-Pb(2.76 ATeV). For “conservative” cuts on

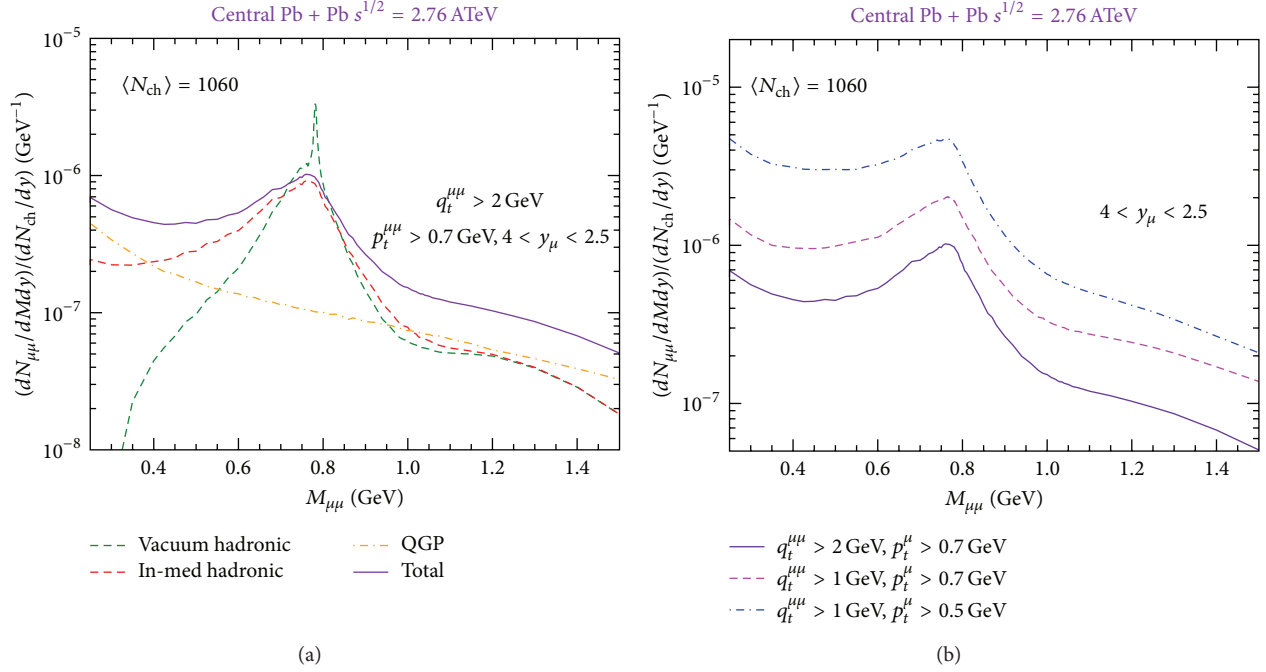


FIGURE 13: Calculations of thermal dimuon invariant-mass spectra in central Pb-Pb(2.76 ATeV) collisions at forward rapidity, $y = 2.5-4$. (a) in-medium hadronic, vacuum hadronic, QGP and the sum of in-medium hadronic plus QGP, are shown with “strong” cuts on single and dimuon transverse momenta. Part (b) illustrates how the total yield increases when the two cuts are relaxed.

the di-/muons ($q_t^{\mu\mu} > 2 \text{ GeV}$, $p_t^{\mu\mu} > 0.7 \text{ GeV}$), their yield is substantially suppressed (see Figure 13(a)), by about one order of magnitude, compared to a typical single- e cut of $p_t^e > 0.2 \text{ GeV}$. In addition, the spectral broadening of the in-medium ρ meson is less pronounced, a trend that was also observed in the q_t -sliced NA60 dimuon spectra. Here, it is mostly due to the suppression of medium effects at larger ρ -meson momentum relative to the heat bath, caused by hadronic form factors (analogous to RHIC, recall Figure 7). It is, in fact, mostly the pair cut which is responsible for the suppression, since $q_t^{\mu\mu, \text{cut}}$ is significantly larger than $2p_t^{\mu\mu, \text{cut}}$. If the former can be lowered to, say, 1 GeV, the thermal yield of accepted pairs increases by about a factor 3 in the IMR and 2 in the LMR (see dashed line in Figure 13(b)). The LMR acceptance is now mainly limited by the single- μ cut, as the latter suppresses low-mass pairs whose pair momentum is not at least $2p_t^{\mu\mu, \text{cut}}$ (the same effect is responsible for the rather sharp decrease in acceptance for low-momentum electron pairs below $M \approx 0.4 \text{ GeV}$ in Figure 7(a), leading to a dip toward lower mass in the thermal spectra, even though the thermal rate increases approximately exponentially). This could be much improved by lowering the single- μ cut to, for example, 0.5 GeV, which would increase the low-mass yield by about a factor of 3. At the same time, the spectral broadening of the ρ becomes more pronounced in the accepted yields; that is, the data would be more sensitive to medium effects.

4. Summary and Outlook

In this article, we have given an overview of medium modifications of the electromagnetic spectral function under

conditions expected at collider energies (high temperature and small baryon chemical potential) and how these medium effects manifest themselves in experimental dilepton spectra at RHIC and LHC. For the emission rates from the hadronic phase, we have focused on predictions from effective hadronic Lagrangians evaluated with standard many-body (or thermal field-theory) techniques; no in-medium changes of the parameters in the Lagrangian (masses and couplings) have been assumed. Since this approach turned out to describe dilepton data at the SPS well, providing testable predictions for upcoming measurements at RHIC and LHC is in order. As collision energy increases, the QGP occupies an increasing space-time volume of the fireball evolution. To improve the description of the pertinent dilepton radiation, information from lattice-QCD has been implemented on (i) the equation of state around and above T_{pc} and (ii) nonperturbative dilepton emission rates in the QGP. The latter have been “minimally” extended to finite 3-momentum to facilitate their use in calculations of observables. Since these rates are rather similar to previously employed perturbative (HTL) rates, an approximate degeneracy of the in-medium hadronic and the IQCD rates close to T_{pc} still holds. This is welcome in view of the smooth crossover transition as deduced from bulk properties and order parameters at $\mu_q = 0$.

The main features of the calculated thermal spectra at RHIC and LHC are as follows. The crossover in the IQCD EoS produces a noticeable increase of the QGP fraction of the yields (compared to a bag-model EoS), while the hadronic portion decreases (its former mixed-phase contribution has been swallowed by the QGP). However, due to the near-degeneracy of the QGP and hadronic emission rates near

T_{pc} , both the total yield and its spectral shape change little; the hadronic part remains prevalent in an extended region around the ρ mass at all collision energies. The very fact that an appreciable reshuffling of hadronic and QGP contributions from the transition region occurs indicates that the latter is a dominant source of low-mass dileptons at both RHIC and LHC. This creates a favorable setup for in-depth studies of the chiral restoration transition in a regime of the phase diagram where quantitative support from IQCD computations for order parameters and the EM correlator is available. Current ideas of how to render these connections rigorous have been reported elsewhere. Phenomenologically, it turns out that current RHIC data for LMR dilepton spectra are consistent with the melting ρ scenario (with the caveat of the central Au-Au PHENIX data), including a recent first measurement of an excitation function all the way down to SPS energies. However, the accuracy of the current data does not yet suffice to discriminate in-medium spectral functions which differ considerably in detail. These “details” will have to be ironed out to enable definite tests of chiral restoration through the EM spectral function.

While the low-mass shape of the spectra is expected to be remarkably stable with collision energy, large variations are predicted in the excitation function of other dilepton observables. First, the total yields increase substantially with collision energy. In the LMR, the dependence on charged-particle rapidity density, N_{ch}^α , is estimated to scale as $\alpha_E \approx 1.8$ from RHIC to LHC, significantly stronger than as function of centrality at fixed \sqrt{s} . This is, of course, a direct consequence of the longer time it takes for the fireball to cool down to thermal freezeout. For the RHIC beam-energy scan program, this opens an exciting possibility to search for a non-monotonous behavior in the fireball’s lifetime due to a critical slowing down of the system’s expansion. If the LMR radiation indeed emanates largely from the transition region, a slowed expansion around T_c would take maximal advantage of this, thus rendering an “anomalous dilepton enhancement” a promising signature of a critical point.

Second, the transverse-momentum spectra of thermal dileptons are expected to become much harder with collision energy, reflecting the increase in the collective expansion generated by the QGP prior to the transition region. This “QGP barometer” provides a higher sensitivity than final-state hadron spectra which include the full collectivity of the hadronic evolution. The inverse-slope parameters for q_t spectra in the LMR are expected to increase from ~ 220 MeV at SPS to ~ 280 MeV at RHIC-200 and up to ~ 450 MeV at LHC-5500. Even larger values are reached in the IMR, although the situation is a bit more involved here, since (a) the QGP emission is increasingly emitted from earlier phases and (b) the hadronic emission, while picking up the full effect of additional collectivity at T_{pc} , becomes subleading relative to the QGP. The trend in the LMR seems to line up with the recent slope measurements in photon excess spectra at RHIC and LHC. A similar connection exists for the elliptic flow; pertinent data will be of great interest. Invariant-mass spectra in the IMR remain the most promising observable to measure early QGP temperatures, once the correlated heavy-flavor

decays can be either subtracted or reliably evaluated theoretically.

The versatility of dileptons at collider energies comprises a broad range of topics, ranging from chiral restoration to direct-temperature measurements, QGP collectivity, and fireball lifetime. Experimental efforts are well underway to exploit these, while sustained theoretical efforts will be required to provide thorough interpretations.

Acknowledgments

The author gratefully acknowledges the contributions of his collaborators, in particular Charles Gale, Min He, and Hendrik van Hees. He also thanks the STAR and ALICE collaborations for making available their plots shown in this article. This work has been supported by the U.S. National Science Foundation under Grant nos. PHY-0969394 and PHY-1306359 and by the A.-v.-Humboldt Foundation (Germany).

References

- [1] E. Shuryak, “Physics of strongly coupled quark-gluon plasma,” *Progress in Particle and Nuclear Physics*, vol. 62, no. 1, pp. 48–101, 2009.
- [2] B. Friman, C. Höhne, J. Knoll et al., Eds., *The CBM Physics Book: Compressed Baryonic Matter in Laboratory Experiments*, vol. 814 of *Lecture Notes in Physics*, 2011.
- [3] S. Borsanyi, Z. Fodor, C. Hoelbling et al., “QCD equation of state at nonzero chemical potential: continuum results with physical quark masses at order μ^2 ,” *Journal of High Energy Physics*, vol. 1009, article 073, 2010.
- [4] A. Bazavov, T. Bhattacharya, M. Cheng et al., “Chiral and deconfinement aspects of the QCD transition,” *Physical Review D*, vol. 85, no. 5, Article ID 054503, 2012.
- [5] F. Weber, “Strange quark matter and compact stars,” *Progress in Particle and Nuclear Physics*, vol. 54, no. 1, pp. 193–288, 2005.
- [6] Y. Schutz and U. A. Wiedemann, Eds., “Proceedings of XXII International Conference on Ultrarelativistic Nucleus-Nucleus Collisions, Annecy (France, May 23–28, 2011),” *Journal of Physics G*, vol. 38, 2012.
- [7] T. Ulrich, B. Wyslouch, and J. W. Harris, Eds., “Proceedings of XXIII International Conference on Ultrarelativistic Nucleus-Nucleus Collisions, Washington (DC, Aug. 12–18, 2012),” *Nuclear Physics A*, vol. 904-905, 2013.
- [8] I. Tserruya, “Electromagnetic probes,” in *Relativistic Heavy-Ion Physics*, R. Stock and L. Börnstein, Eds., New Series I/23A, Springer, 2010.
- [9] H. J. Specht, “Thermal dileptons from hot and dense strongly interacting matter,” in *Proceedings of International Workshop on Chiral Symmetry in Hadrons and Nuclei*, vol. 1322 of *AIP Conference Proceedings*, pp. 1–10, Valencia, Spain, June 2010.
- [10] R. Rapp, J. Wambach, and H. van Hees, “The chiral restoration transition of QCD and low mass dileptons,” in *Relativistic Heavy-Ion Physics*, R. Stock and L. Börnstein, Eds., New Series I/23A, Springer, 2010.
- [11] P. Braun-Munzinger and J. Stachel, “Hadron production in ultra-relativistic nuclear collisions and the QCD phase diagram: an update,” in *From Nuclei to Stars: Festschrift in Honor of Gerald E Brown’s 85th Birthday*, S. Lee, Ed., World Scientific, Singapore, 2011.

- [12] R. Rapp, “Hadrochemistry and evolution of (anti)baryon densities in ultrarelativistic heavy-ion collisions,” *Physical Review C*, vol. 66, no. 1, Article ID 017901, 4 pages, 2002.
- [13] R. Rapp, “Signatures of thermal dilepton radiation at ultrarelativistic energies,” *Physical Review C*, vol. 63, no. 5, Article ID 054907, 13 pages, 2001.
- [14] H.-T. Ding, A. Francis, O. Kaczmarek, F. Karsch, E. Laermann, and W. Soeldner, “Thermal dilepton rate and electrical conductivity: an analysis of vector current correlation functions in quenched lattice QCD,” *Physical Review D*, vol. 83, no. 3, Article ID 034504, 2011.
- [15] B. B. Brandt, A. Francis, H. B. Meyer, and H. Wittig, “Thermal correlators in the ρ channel of two-flavor QCD,” *Journal of High Energy Physics*, vol. 1303, article 100, 2013.
- [16] Y. Aoki, G. Endrodi, Z. Fodor, S. D. Katz, and K. K. Szabó, “The order of the quantum chromodynamics transition predicted by the standard model of particle physics,” *Nature*, vol. 443, no. 7112, pp. 675–678, 2006.
- [17] R. Rapp, “Update on chiral symmetry restoration in the context of dilepton data,” *Journal of Physics: Conference Series*, vol. 420, Article ID 012017, 2013.
- [18] S. Leupold, V. Metag, and U. Mosel, “Hadrons in strongly interacting matter,” *International Journal of Modern Physics E*, vol. 19, no. 2, pp. 147–224, 2010.
- [19] E. Oset, A. Ramos, E. J. Garzon et al., “Interaction of vector mesons with baryons and nuclei,” *International Journal of Modern Physics E*, vol. 21, no. 11, Article ID 1230011, 2012.
- [20] M. Dey, V. L. Eletsky, and B. L. Ioffe, “Mixing of vector and axial mesons at finite temperature: an indication towards chiral symmetry restoration,” *Physics Letters B*, vol. 252, no. 4, pp. 620–624, 1990.
- [21] V. L. Eletsky, M. Belkacem, P. J. Ellis, and J. I. Kapusta, “Properties of ρ and ω mesons at finite temperature and density as inferred from experiment,” *Physical Review C*, vol. 64, no. 3, Article ID 035202, 2001.
- [22] M. Harada and K. Yamawaki, “Hidden local symmetry at loop: a new perspective of composite gauge boson and chiral phase transition,” *Physics Reports*, vol. 381, no. 1–3, pp. 1–233, 2003.
- [23] B. Friman and H. J. Pirner, “P-wave polarization of the ρ -meson and the dilepton spectrum in dense matter,” *Nuclear Physics A*, vol. 617, no. 4, pp. 496–509, 1997.
- [24] R. Rapp, G. Chanfray, and J. Wambach, “Rho meson propagation and dilepton enhancement in hot hadronic matter,” *Nuclear Physics A*, vol. 617, no. 4, pp. 472–495, 1997.
- [25] S. Ghosh and S. Sarkar, “ ρ self-energy at finite temperature and density in the real-time formalism,” *Nuclear Physics A*, vol. 870–871, pp. 94–111, 2011, Erratum in *Nuclear Physics A*, vol. 888, p. 44, 2012.
- [26] J. Cleymans, J. Fingberg, and K. Redlich, “Transverse-momentum distribution of dileptons in different scenarios for the QCD phase transition,” *Physical Review D*, vol. 35, no. 7, pp. 2153–2165, 1987.
- [27] E. Braaten, R. D. Pisarski, and T. C. Yuan, “Production of soft dileptons in the quark-gluon plasma,” *Physical Review Letters*, vol. 64, no. 19, pp. 2242–2245, 1990.
- [28] O. Kaczmarek, E. Laermann, M. Mueller et al., “Thermal dilepton rates from quenched lattice QCD,” *PoS Confinement X*, vol. 2012, pp. 185–192, 2012.
- [29] G. D. Moore and J.-M. Robert, “Dileptons, spectral weights, and conductivity in the quark-gluon plasma,” <http://arxiv.org/abs/hep-ph/0607172>.
- [30] J. Kapusta, P. Lichard, and D. Seibert, “High-energy photons from quark-gluon plasma versus hot hadronic gas,” *Physical Review D*, vol. 44, no. 9, pp. 2774–2788, 1991, Erratum in *Physical Review D*, vol. 47, no. 9, p. 4171, 1993.
- [31] P. B. Arnold, G. D. Moore, and L. G. Yaffe, “Photon emission from quark-gluon plasma: complete leading order results,” *Journal of High Energy Physics*, vol. 2001, no. 12, article 009, 2001.
- [32] G. Aarts, C. Allton, J. Foley, S. Hands, and S. Kim, “Spectral functions at small energies and the electrical conductivity in hot quenched lattice QCD,” *Physical Review Letters*, vol. 99, no. 2, Article ID 022002, 4 pages, 2007.
- [33] K. Nakamura, “Review of particle physics,” *Journal of Physics G*, vol. 37, no. 7A, Article ID 075021, 2010.
- [34] R. Rapp and J. Wambach, “Chiral symmetry restoration and dileptons in relativistic heavy-ion collisions,” in *Advances in Nuclear Physics*, J. W. Negele and E. Vogt, Eds., vol. 25, pp. 1–205, 2002.
- [35] R. Rapp and J. Wambach, “Low-mass dileptons at the CERN-SpS: evidence for chiral restoration?” *The European Physical Journal A*, vol. 6, no. 4, pp. 415–420, 1999.
- [36] M. Urban, M. Buballa, R. Rapp, and J. Wambach, “Momentum dependence of the pion cloud for ρ -mesons in nuclear matter,” *Nuclear Physics A*, vol. 641, no. 4, pp. 433–460, 1998.
- [37] R. Rapp, “Hadrons in hot and dense matter,” *European Physical Journal A*, vol. 18, no. 2-3, pp. 459–462, 2003.
- [38] U. W. Heinz and R. Snellings, “Collective flow and viscosity in relativistic heavy-ion collisions,” *Annual Review of Nuclear and Particle Science*, vol. 63, 2013.
- [39] P. F. Kolb and U. W. Heinz, “Hydrodynamic description of ultrarelativistic heavy-ion collisions,” in *Quark Gluon Plasma** 634–714, R. C. Hwa and X.-N. Wang, Eds., World Scientific, Singapore, 2004.
- [40] S. Borsanyi, G. Endrodi, Z. Fodor et al., “The QCD equation of state with dynamical quarks,” *Journal of High Energy Physics*, vol. 2010, no. 5, article 077, 2010.
- [41] M. Cheng, S. Ejiri, P. Hegde et al., “Equation of state for physical quark masses,” *Physical Review D*, vol. 81, no. 5, Article ID 054504, 2010.
- [42] M. He, R. J. Fries, and R. Rapp, “Ideal hydrodynamics for bulk and multistrange hadrons in $\sqrt{s_{NN}} = 200$ A GeV Au-Au collisions,” *Physical Review C*, vol. 85, no. 4, Article ID 044911, 9 pages, 2012.
- [43] S. Pratt, “Resolving the hanbury brown-twiss puzzle in relativistic heavy ion collisions,” *Physical Review Letters*, vol. 102, no. 23, Article ID 232301, 4 pages, 2009.
- [44] T. Renk, R. Schneider, and W. Weise, “Phases of QCD, thermal quasiparticles, and dilepton radiation from a fireball,” *Physical Review C*, vol. 66, no. 1, Article ID 014902, 19 pages, 2002.
- [45] H. van Hees and R. Rapp, “Dilepton radiation at the CERN super-proton synchrotron,” *Nuclear Physics A*, vol. 806, no. 1–4, pp. 339–387, 2008.
- [46] H. van Hees et al., In preparation.
- [47] S. Turbide, C. Gale, D. K. Srivastava, and R. J. Fries, “High momentum dilepton production from jets in a quark gluon plasma,” *Physical Review C*, vol. 74, no. 1, Article ID 014903, 2006.
- [48] A. Adare, S. Afanasiev, C. Aidala et al., “Detailed measurement of the e^+e^- pair continuum in $p + p$ and Au + Au collisions at $\sqrt{s_{NN}} = 200$ GeV and implications for direct photon production,” *Physical Review C*, vol. 81, no. 3, Article ID 034911, 56 pages, 2010.

- [49] J. Zhao, “Dielectron continuum production from $\sqrt{s_{NN}} = 200$ GeV $p + p$ and Au + Au collisions at STAR,” *Journal of Physics G*, vol. 38, no. 12, Article ID 124134, 2011.
- [50] J. Zhao, Private Communication, 2012.
- [51] G. Vujanovic, C. Young, B. Schenke, S. Jeon, R. Rapp, and C. Gale, “Dilepton production in high energy heavy ion collisions with 3 + 1D relativistic viscous hydrodynamics,” *Nuclear Physics A*, vol. 904-905, pp. 557c–560c, 2013.
- [52] H.-J. Xu, H.-F. Chen, X. Dong, Q. Wang, and Y.-F. Zhang, “Di-electron production from vector mesons with medium modifications in heavy ion collisions,” *Physical Review C*, vol. 85, no. 2, Article ID 024906, 8 pages, 2012.
- [53] O. Linnyk, W. Cassing, J. Manninen, E. L. Bratkovskaya, and C. M. Ko, “Analysis of dilepton production in Au + Au collisions at $\sqrt{s_{NN}} = 200$ GeV within the parton-hadron-string dynamics transport approach,” *Physical Review C*, vol. 85, no. 2, Article ID 024910, 2012.
- [54] I. Tserruya, “Photons and low-mass dileptons: results from PHENIX,” *Nuclear Physics A*, vol. 904-905, pp. 225c–232c, 2013.
- [55] K. Dusling and I. Zahed, “Low mass dilepton radiation at RHIC,” *Nuclear Physics A*, vol. 825, no. 3-4, pp. 212–221, 2009.
- [56] S. Ghosh, S. Sarkar, and J.-E. Alam, “Observing many-body effects on lepton pair production from low mass enhancement and flow at RHIC and LHC energies,” *The European Physical Journal C*, vol. 71, article 1760, 2011.
- [57] M. Chiu, T. K. Hemmick, V. Khachatryan, A. Leonidov, J. Liao, and L. McLerran, “Production of photons and dileptons in the glasma,” *Nuclear Physics A*, vol. 900, pp. 16–37, 2013.
- [58] S. Turbide, R. Rapp, and C. Gale, “Hadronic production of thermal photons,” *Physical Review C*, vol. 69, no. 1, Article ID 014903, 13 pages, 2004.
- [59] P. J. Siemens and S. A. Chin, “Testing of QCD plasma formation by dilepton spectra in relativistic nuclear collisions,” *Physical Review Letters*, vol. 55, no. 12, pp. 1266–1268, 1985.
- [60] K. Kajantie, J. Kapusta, L. McLerran, and A. Mekjian, “Dilepton emission and the QCD phase transition in ultrarelativistic nuclear collisions,” *Physical Review D*, vol. 34, no. 9, pp. 2746–2754, 1986.
- [61] B. Kämpfer and O. P. Pavlenko, “Probing meson spectral functions with double differential dilepton spectra in heavy-ion collisions,” *The European Physical Journal A*, vol. 10, no. 1, pp. 101–107, 2001.
- [62] T. Renk and J. Ruppert, “Dimuon transverse momentum spectra as a tool to characterize the emission region in heavy-ion collisions,” *Physical Review C*, vol. 77, no. 2, Article ID 024907, 7 pages, 2008.
- [63] J. K. Nayak, J.-E. Alam, T. Hirano, S. Sarkar, and B. Sinha, “Muon pairs from In + In collision at energies available at the CERN super proton synchrotron,” *Physical Review C*, vol. 85, no. 6, Article ID 064906, 6 pages, 2012.
- [64] J. Deng, Q. Wang, N. Xu, and P. Zhuang, “Dilepton flow and deconfinement phase transition in heavy ion collisions,” *Physics Letters B*, vol. 701, no. 5, pp. 581–586, 2011.
- [65] R. Arnaldi, K. Banicz, K. Borer et al., “NA60 results on thermal dimuons,” *The European Physical Journal C*, vol. 61, no. 4, pp. 711–720, 2009.
- [66] G. Agakichiev, H. Appelshäuser, J. Bielcikova et al., “ e^+e^- pair production in Pb-Au collisions at 158 GeV per nucleon,” *The European Physical Journal C*, vol. 41, no. 4, pp. 475–513, 2005.
- [67] M. He, R. J. Fries, and R. Rapp, In preparation.
- [68] F. Geurts, “The STAR dilepton physics program,” *Nuclear Physics A*, vol. 904-905, pp. 217c–224c, 2013.
- [69] R. Chatterjee, D. K. Srivastava, U. Heinz, and C. Gale, “Elliptic flow of thermal dileptons in relativistic nuclear collisions,” *Physical Review C*, vol. 75, no. 5, Article ID 054909, 2007.
- [70] P. Mohanty, V. Roy, S. Ghosh et al., “Elliptic flow of thermal dileptons as a probe of QCD matter,” *Physical Review C*, vol. 85, no. 3, Article ID 031903, 2012.
- [71] A. Adare, S. Afanasiev, C. Aidala et al., “Enhanced production of direct photons in Au + Au collisions at $\sqrt{s_{NN}} = 200$ GeV and implications for the initial temperature,” *Physical Review Letters*, vol. 104, no. 13, Article ID 132301, 6 pages, 2010.
- [72] A. Adare, S. Afanasiev, C. Aidala et al., “Observation of direct-photon collective flow in Au + Au collisions at $\sqrt{s_{NN}} = 200$ GeV,” *Physical Review Letters*, vol. 109, no. 12, Article ID 122302, 7 pages, 2012.
- [73] M. Wilde, A. Deloff, I. Ilkiv et al., “Measurement of direct photons in $p + p$ and Pb-Pb collisions with ALICE,” *Nuclear Physics A*, vol. 904-905, pp. 573c–576c, 2013.
- [74] D. Lohner, “Measurement of direct-photon elliptic flow in Pb-Pb collisions at $\sqrt{s_{NN}} = 2.76$ TeV,” <http://arxiv.org/abs/1212.3995>.
- [75] H. van Hees, C. Gale, and R. Rapp, “Thermal photons and collective flow at energies available at the BNL relativistic heavy-ion collider,” *Physical Review C*, vol. 84, no. 5, Article ID 054906, 2011.
- [76] F. M. Liu, T. Hirano, K. Werner, and Y. Zhu, “Elliptic flow of thermal photons in Au + Au collisions at $\sqrt{s_{NN}} = 200$ GeV,” *Physical Review C*, vol. 80, no. 3, Article ID 034905, 5 pages, 2009.
- [77] H. Holopainen, S. Rasanen, and K. J. Eskola, “Elliptic flow of thermal photons in heavy-ion collisions at energies available at the BNL relativistic heavy ion collider and at the CERN large hadron collider,” *Physical Review C*, vol. 84, no. 6, Article ID 064903, 11 pages, 2011.
- [78] M. Dion, J.-F. Paquet, B. Schenke, C. Young, S. Jeon, and C. Gale, “Viscous photons in relativistic heavy ion collisions,” *Physical Review C*, vol. 84, no. 6, Article ID 064901, 13 pages, 2011.
- [79] G. Başar, D. E. Kharzeev, and V. Skokov, “Conformal anomaly as a source of soft photons in heavy ion collisions,” *Physical Review Letters*, vol. 109, no. 20, Article ID 202303, 5 pages, 2012.
- [80] G. Agakichiev, A. Balanda, D. Berver et al., “Origin of the low-mass electron pair excess in light nucleus-nucleus collisions,” *Physics Letters B*, vol. 690, no. 2, pp. 118–122, 2010.
- [81] R. Holzmann, “The experimental quest for in-medium effects,” in *Proceedings of the 6th International Conference on Quarks and Nuclear Physics (QNP '12)*, vol. 5, Paris, France, April 2012.
- [82] D. Adamová, G. Agakichiev, H. Appelshäuser et al., “Enhanced production of low-mass electron-positron pairs in 40-AGeV Pb-Au collisions at the CERN SPS,” *Physical Review Letters*, vol. 91, no. 4, Article ID 042301, 5 pages, 2003.
- [83] L. Musa and K. Safarik, “Letter of intent for the upgrade of the ALICE experiment,” CERN-LHCC-2012-012, CERN, Geneva, Switzerland, 2012, <http://cds.cern.ch/record/1475243>.
- [84] P. Reichelt and H. Appelshäuser, Private Communication, 2013.
- [85] P. M. Hohler and R. Rapp, “Evaluating chiral symmetry restoration through the use of sum rules,” *EPJ Web of Conferences*, vol. 36, article 00012, 2012.
- [86] R. Tieulent, Private Communication, 2012.
- [87] K. Gulbrandsen et al., “Charged-particle pseudorapidity density and anisotropic flow over a wide pseudorapidity range using ALICE at the LHC,” in *Proceedings of the Hot Quarks Workshop*, Copamarina, Puerto Rico, October 2012.

Review Article

Viscous Hydrodynamic Model for Relativistic Heavy Ion Collisions

A. K. Chaudhuri

Theoretical Physics Division, Variable Energy Cyclotron Centre, 1/AF, Bidhan Nagar, Kolkata 700 064, India

Correspondence should be addressed to A. K. Chaudhuri; akc@vecc.gov.in

Received 11 April 2013; Accepted 20 June 2013

Academic Editor: Jan E. Alam

Copyright © 2013 A. K. Chaudhuri. This is an open access article distributed under the Creative Commons Attribution License, which permits unrestricted use, distribution, and reproduction in any medium, provided the original work is properly cited.

Viscous hydrodynamical modeling of relativistic heavy ion collisions has been highly successful in explaining bulk of the experimental data in RHIC and LHC energy collisions. We briefly review viscous hydrodynamics modeling of high energy nuclear collisions. Basic ingredients of the modeling, the hydrodynamic equations, relaxation equations for dissipative forces, are discussed. Hydrodynamical modeling being a boundary value problem, we discuss the initial conditions, freeze-out process. We also show representative simulation results in comparison with experimental data. We also discuss the recent developments in event-by-event hydrodynamics.

1. Introduction

Lattice QCD simulations of strongly interacting nuclear matter suggests that, under appropriate conditions (e.g., high temperature, high density), the normally confining nuclear matter can exist in a deconfined state, commonly called Quark-Gluon Plasma (QGP). Lattice simulations also predict that the confinement-deconfinement transition is not a phase transition rather a crossover transition [1–6], with the crossover temperature (or pseudocritical temperature) $T_c \approx 150$ – 170 MeV. It also appears that the deconfined matter is not entirely interaction free even at very high temperature. Thermodynamic quantities, for example, energy density, pressure, and entropy density, are significantly below the interaction free values. It is thus appropriate to call the deconfined matter strongly interacting Quark-Gluon Plasma (sQGP). Recent experiments in $\sqrt{s_{NN}} = 200$ GeV Au+Au collisions at Relativistic Heavy Ion Collider (RHIC) [7–10] and $\sqrt{s_{NN}} = 2.76$ TeV Pb+Pb collisions at Large Hadron Collider (LHC) [11–15] produced convincing evidences that in RHIC and LHC collisions a deconfined medium or Quark-Gluon Plasma is produced.

A nucleus-nucleus collision at relativistic energy passes through different stages. Schematic picture of different stages

of the collision are shown in Figure 1. One can broadly classify the following stages.

- (i) Preequilibrium stage: at relativistic energy, initial collisions are expected to be in the partonic level. Initial partonic collisions produce a fireball in a highly excited state. In all possibility, the fireball is not in equilibrium. Constituents of the fireball collide frequently to establish a “local” equilibrium’ state. The time taken to establish the local equilibrium is called the “thermalisation” or “equilibration” time.
- (ii) Expansion stage: in the equilibrium or the thermalised state, the constituents of the fireball, the partons or more specifically, the quarks and gluons are in the deconfined state. The system has thermal pressure which acts against the surrounding vacuum. The fireball then undergoes collective (hydrodynamic) expansion. As it expands, density (energy density) decreases, and the system cools. If the system supports phase transition, then below a critical temperature, the deconfined quarks and gluons will hadronise. In the hadronisation stage, over a small temperature interval, entropy density will decrease very fast. Since total entropy cannot decrease, it implies that the fire

ball will expand rapidly, while temperature remains approximately constant.

- (iii) Freeze-out: even after the hadronisation, the matter can also be in thermal equilibrium. Constituent hadrons will collide to maintain local equilibrium. The system will expand and cool. A stage will come when inelastic collisions, in which hadron changes identity, become too small to keep up with expansion. The stage is called chemical freeze-out. Hadron abundances will remain fixed after the chemical freeze-out. However, due to elastic collisions, local equilibrium can still be maintained, and the system will further expands and cool, with fixed hadron abundances. Eventually a stage will come when average distance between the constituents will be larger than strong interaction range. Collisions between the constituents will be so infrequent that “local” thermal equilibrium cannot be maintained. The hydrodynamic description will break down. The hadrons decouple or freeze-out. It is called kinetic freeze-out. Hadrons from the kinetic freeze out surface will be detected in the detector.

From the expansion stage to freeze-out, the collision process can be modeled by relativistic hydrodynamic equations. If the macroscopic properties of the fluid, for example, local energy density, pressure, fluid velocity, and so forth, are known at the initial time τ_i , hydrodynamic equations can be solved to obtain the space-time evolution of the fireball till the freeze-out. At the freeze-out suitable algorithm (e.g., Cooper-Frye [16]) can be used to convert the fluid information at the freeze-out into particle’s invariant yield and compare with experimental data. Hydrodynamic models are unique that it is imperative to use an equation of state (EoS), a thermodynamic relation between the energy density, pressure, and number density of the fluid. By explicitly incorporating phase transition in the equation of state, one can study, dynamically, the effect of phase transition on the fluid evolution and associated particle production. Ideal hydrodynamic models have been largely successful in explaining a variety of experimental data, for example, transverse momentum spectra, elliptic flow of identified particles in $\sqrt{s_{NN}} = 200$ GeV Au+Au collisions [17]. Indeed, success of *ideal* fluid dynamics in explaining several experimental data, together with the string theory motivated lower limit of shear viscosity over entropy ratio $\eta/s \geq 1/4\pi$ [18–20], leads to a paradigm that in Au+Au collisions, a nearly “perfect” fluid, is created.

However, the paradigm of “perfect fluid” produced in Au+Au collisions at RHIC needs to be clarified. It so happens that the ideal fluid dynamic models do have their limitations [21]. For example, experimentally, elliptic flow tends to saturate at large transverse momentum. The ideal fluid dynamics on the other hand predicts a continually increasing elliptic flow. The transverse momentum spectra of identified particles also start to deviate from ideal fluid dynamics prediction beyond $p_T \approx 1.5$ GeV. Experimentally determined HBT radii are not reproduced in the ideal fluid dynamic models, the famous “HBT puzzle” [22]. Ideal fluid dynamics also works best in central collisions and gets poorer in more peripheral

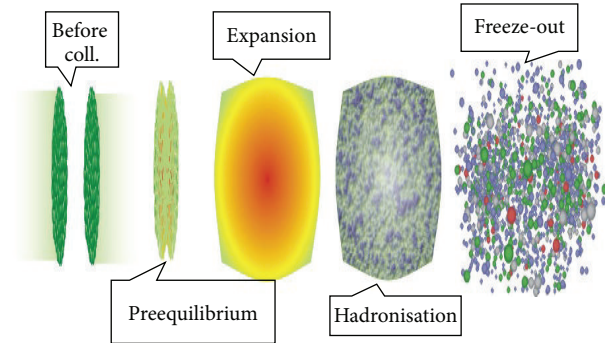


FIGURE 1: Different stages of nuclear collisions at ultrarelativistic energy.

collisions. The shortcomings of ideal fluid dynamics possibly indicate greater importance of dissipative effects in the p_T ranges greater than 1.5 GeV or in more peripheral collisions. Indeed, ideal fluid is a concept, which is never realized in nature. As suggested in string theory motivated models, QGP viscosity could be small, $\eta/s \geq 1/4\pi$, nevertheless it is nonzero. Indeed, much earlier, Danielewicz and Gyulassy [23], from the uncertainty principle, estimated the lower bound of viscosity to entropy ratio, $\eta/s \geq 1/12$, a value very close to the AdS/CFT estimate. It is thus important to study the effect of viscosity, even if small, on space-time evolution of QGP fluid and quantify its effect. Furthermore, QGP fluid has to be characterized by its transport coefficients, for example, heat conductivity, bulk and shear viscosity. Theoretically, it is possible to obtain those transport coefficients in a kinetic theory model. However, in the present status of theory, the goal cannot be achieved immediately, even more so for a strongly interacting QGP (sQGP). Alternatively, one can compare viscous hydrodynamic simulations to experimental data and obtain a “phenomenological” limit to the transport coefficients of sQGP. There is another incentive to study dissipative hydrodynamics. Ideal hydrodynamics depends on the assumption of local equilibrium. In dissipative hydrodynamics, the strict assumption of local thermal equilibrium is relaxed to the assumption of “near” local thermal equilibrium, extending the range of validity of hydrodynamic description. Indeed, one can explore early times of fluid evolution better in dissipative hydrodynamics. It may be mentioned here that success of hydrodynamical modeling of relativistic heavy ion collisions does not necessarily imply the realisation of local thermodynamic equilibrium, although the inverse is true. Whether or not local equilibrium is achieved in high energy nuclear collisions is still in debate.

Theory of dissipative relativistic fluid has been formulated quite early. The original dissipative relativistic fluid equations were given by Eckart [24] and Landau and Lifshitz [25]. They are called first order theories. Formally, relativistic dissipative hydrodynamic equations are obtained from an expansion of entropy 4-current, in terms of the dissipative fluxes. In first order theories, entropy 4-current contains terms linear in dissipative quantities. First order theory of dissipative hydrodynamics suffers from the problem of causality violation and

instabilities [26, 27]. Causality violation is unwarranted in any theory, even more in a relativistic theory. The problem of causality violation is removed in the Israel-Stewart's second order theory of dissipative fluid [28, 29]. In second order theory, expansion of entropy 4-current contains terms second order in dissipative fluxes. However, these leads to complications that dissipative fluxes are no longer function of the state variables only. They become dynamic. The space of thermodynamic variables has to be extended to include the dissipative fluxes (e.g., heat conductivity, bulk, and shear viscosity). In the following section Israel-Stewart's phenomenological theory of dissipative hydrodynamics is briefly discussed. More detailed exposition can be found in [29, 30].

2. Dissipative Fluid Dynamics

A simple fluid, in an arbitrary state, is fully specified by primary variables: particle current (N^μ), energy-momentum tensor ($T^{\mu\nu}$), entropy current (S^μ), and a number of additional (unknown) variables. Primary variables satisfy the conservation laws:

$$\begin{aligned}\partial_\mu N^\mu &= 0, \\ \partial_\mu T^{\mu\nu} &= 0,\end{aligned}\tag{1}$$

and the second law of thermodynamics,

$$\partial_\mu S^\mu \geq 0.\tag{2}$$

In relativistic fluid dynamics, one defines a time-like hydrodynamic 4-velocity, u^μ (normalized as $u^2 = 1$). One also defines a projector, $\Delta^{\mu\nu} = g^{\mu\nu} - u^\mu u^\nu$, orthogonal to the 4-velocity ($\Delta^{\mu\nu} u_\nu = 0$). In equilibrium, an unique 4-velocity (u^μ) exists such that the particle density (n), energy density (ϵ), and the entropy density (s) can be obtained from

$$\begin{aligned}N_{\text{eq}}^\mu &= nu^\mu, \\ T_{\text{eq}}^{\mu\nu} &= \epsilon u^\mu u^\nu - p \Delta^{\mu\nu}, \\ S_{\text{eq}}^\mu &= su^\mu.\end{aligned}\tag{3}$$

An equilibrium state is assumed to be fully specified by 5 parameters (n, ϵ, u^μ) or equivalently by the thermal potential $\alpha = \mu/T$ (μ being the chemical potential) and inverse 4-temperature, $\beta^\mu = u^\mu/T$. Given an equation of state, $s = s(\epsilon, n)$, pressure p can be obtained from the generalized thermodynamic relation:

$$S_{\text{eq}}^\mu = p\beta^\mu - \alpha N_{\text{eq}}^\mu + \beta_\lambda T_{\text{eq}}^{\lambda\mu}.\tag{4}$$

Using the Gibbs-Duhem relation, $d(p\beta^\mu) = N_{\text{eq}}^\mu d\alpha - T_{\text{eq}}^{\lambda\mu} d\beta_\lambda$, following relations can be established on the equilibrium hypersurface $\Sigma_{\text{eq}}(\alpha, \beta^\mu)$,

$$dS_{\text{eq}}^\mu = -\alpha dN_{\text{eq}}^\mu + \beta_\lambda dT_{\text{eq}}^{\lambda\mu}.\tag{5}$$

In a nonequilibrium system, no 4-velocity can be found such that (3) remains valid. Tensor decomposition leads to additional terms:

$$N^\mu = N_{\text{eq}}^\mu + \delta N^\mu = nu^\mu + V^\mu,$$

$$\begin{aligned}T^{\mu\nu} &= T_{\text{eq}}^{\mu\nu} + \delta T^{\mu\nu} \\ &= [\epsilon u^\mu u^\nu - p \Delta^{\mu\nu}] + \Pi \Delta^{\mu\nu} + \pi^{\mu\nu} \\ &\quad + (W^\mu u^\nu + W^\nu u^\mu), \\ S^\mu &= S_{\text{eq}}^\mu + \delta S^\mu = su^\mu + \Phi^\mu.\end{aligned}\tag{6}$$

The new terms describe a net flow of charge $V^\mu = \Delta^{\mu\nu} N_\nu$, energy flow $W^\mu = (\epsilon + p)/nV^\mu + q^\mu$ (where q^μ is the heat flow vector), and entropy flow Φ^μ . $\Pi = -(1/3)\Delta_{\mu\nu} T^{\mu\nu} - p$ is the bulk viscous pressure, and $\pi^{\mu\nu} = [(1/2)(\Delta^{\mu\sigma} \Delta^{\nu\tau} + \Delta^{\nu\sigma} \Delta^{\mu\tau} - (1/3)\Delta^{\mu\nu} \Delta^{\sigma\tau}] T_{\sigma\tau}$ is the shear stress tensor. Hydrodynamic 4-velocity can be chosen to eliminate either V^μ (the Eckart frame, u^μ is parallel to particle flow) or the energy flow W^μ (the Landau frame, u^μ is eigenvector of energy-momentum tensor). In relativistic heavy ion collisions, central rapidity region is nearly baryon free, and Landau's frame is more appropriate than the Eckart's frame. Dissipative flows are transverse to u^μ , and additionally, shear stress tensor is traceless. Thus a nonequilibrium state requires $1 + 3 + 5 = 9$ additional quantities, the dissipative flows Π, q^μ (or V^μ), and $\pi^{\mu\nu}$. In kinetic theory, N^μ and $T^{\mu\nu}$ are the first and second moments of the distribution function. Unless the function is known a-priori, two moments do not furnish enough information to enumerate the microscopic states required to determine S^μ , and in an arbitrary nonequilibrium state, no relation exists between $N^\nu, T^{\mu\nu}$, and S^μ . *Only in a state, close to an equilibrium one, such a relation can be established.* Assuming that the equilibrium relation (5) remains valid in a "near equilibrium state," also the entropy current can be generalized as

$$S^\mu = S_{\text{eq}}^\mu + dS^\mu = p\beta^\mu - \alpha N^\mu + \beta_\lambda T^{\lambda\mu} + Q^\mu,\tag{7}$$

where Q^μ is an undetermined quantity in second order in deviations, $\delta N^\mu = N^\mu - N_{\text{eq}}^\mu$ and $\delta T^{\mu\nu} = T^{\mu\nu} - T_{\text{eq}}^{\mu\nu}$. Detail form of Q^μ is constrained by the second law $\partial_\mu S^\mu \geq 0$. With the help of conservation laws and Gibbs-Duhem relation, entropy production rate can be written as

$$\partial_\mu S^\mu = -\delta N^\mu \partial_\mu \alpha + \delta T^{\mu\nu} \partial_\mu \beta_\nu + \partial_\mu Q^\mu.\tag{8}$$

Choice of Q^μ leads to first order or second order theories of dissipative hydrodynamics. In first order theories the simplest choice is made, $Q^\mu = 0$, and entropy current contains terms up to first order in deviations, δN^μ and $\delta T^{\mu\nu}$. Entropy production rate can be written as

$$T \partial_\mu S^\mu = \Pi X - q^\mu X_\mu + \pi^{\mu\nu} X_{\mu\nu},\tag{9}$$

where $X = -\nabla \cdot u$, $X^\mu = \nabla^\mu / T - u^\nu \partial_\nu u^\mu$, and $X^{\mu\nu} = \nabla^{(\mu} u^{\nu)}$.

The second law, $\partial_\mu S^\mu \geq 0$, can be satisfied by postulating a linear relation between the dissipative flows and thermodynamic forces:

$$\Pi = -\zeta \theta,$$

$$q^\mu = -\lambda \frac{nT^2}{\epsilon + p} \nabla^\mu \left(\frac{\mu}{T} \right),\tag{10}$$

$$\pi^{\mu\nu} = 2\eta \nabla^{(\mu} u^{\nu)},$$

where ζ, λ , and η are the positive transport coefficients, bulk viscosity, heat conductivity, and shear viscosity, respectively.

In first order theories, causality is violated [26, 27]. Causality violation is corrected in second order theories [29]. In second order theories, entropy current contain terms up to second order in the deviations, $Q^\mu \neq 0$. The most general Q^μ containing terms up to second order in deviations can be written as

$$Q^\mu = -\left(\beta_0 \Pi^2 - \beta_1 q^\nu q_\nu + \beta_2 \pi_{\nu\lambda} \pi^{\nu\lambda}\right) \frac{u^\mu}{2T} - \frac{\alpha_0 \Pi q^\mu}{T} + \frac{\alpha_1 \pi^{\mu\nu} q_\nu}{T}, \quad (11)$$

where β_0 , β_1 , and β_2 are thermodynamic coefficients for the bulk stress (Π), heat flow (q^μ), and shear viscous stress ($\pi^{\mu\nu}$), respectively. α_0 and α_1 are thermodynamic coefficients for the coupling between the heat flow and bulk and shear stress, respectively. As before, one can cast the entropy production rate ($T\partial_\mu S^\mu$) in the form of (9). Neglecting the terms involving dissipative flows with gradients of equilibrium thermodynamic quantities (both are assumed to be small) and demanding that a linear relation exists between the dissipative flows and thermodynamic forces, the following *relaxation* equations for the dissipative flows can be obtained:

$$\tau_\Pi \dot{\Pi} + \Pi = -\zeta\theta - \left[\frac{1}{2} \zeta T \partial_\mu \left(\frac{\tau_0}{\zeta T} u^\mu \right) \Pi \right] + I_{\Pi q} \nabla_\mu q^\mu, \quad (12)$$

$$\tau_\pi \Delta_\mu^\alpha \Delta_\nu^\beta \dot{\pi}_{\alpha\beta} + \pi_{\mu\nu} = 2\eta \sigma_{\mu\nu} - \left[\eta T \partial_\lambda \left(\frac{\tau_2}{2\eta T} u^\lambda \right) \pi_{\mu\nu} \right] + I_{\pi q} \nabla_{(\mu} q_{\nu)}, \quad (13)$$

$$\tau_q \Delta_\mu^\nu \dot{q}_\nu + q_\mu = \lambda (\nabla_\mu T - T \dot{u}_\mu) + \left[\frac{1}{2} \lambda T^2 \partial_\nu \left(\frac{\tau_1}{\lambda T^2} u^\nu \right) q_\mu \right] - I_{q\Pi} \nabla_\mu - I_{q\pi} \nabla_\mu \pi_\mu^\nu. \quad (14)$$

The relaxation times are

$$\tau_\Pi = \zeta \beta_0, \quad \tau_\pi = 2\eta \beta_2, \quad \tau_q = \lambda T \beta_1. \quad (15)$$

I_{ab} s are coupling coefficients between different dissipative flows, specifically,

$$I_{\Pi q} = \zeta \alpha_0, \quad I_{q\Pi} = \lambda T \alpha_0, \quad I_{\pi q} = 2\eta \alpha_1, \quad I_{q\pi} = \lambda T \alpha_1. \quad (16)$$

Unlike in the first order theories, in second order theories, dynamical equations control the dissipative flows. Even if thermodynamic forces vanish, dissipative flows do not vanish instantly. It is important to mention that the parameters, α and β_λ , are not connected to the actual state ($N^\mu, T^{\mu\nu}$). The pressure p in (7) is also not the ‘‘actual’’ thermodynamics pressure, that is, not the work done in an isentropic expansion. Chemical potential α and 4-inverse temperature β_λ have meaning only for the equilibrium state. Their meaning need not to be extended to nonequilibrium states also. However, it is possible to fit a fictitious ‘‘local equilibrium’’ state, point by

point, such that pressure p in (7) can be identified with the thermodynamic pressure, at least up to first order. The conditions of fit fix the underlying nonequilibrium phase-space distribution.

It may be mentioned here that relaxation equations for the dissipative fluxes can also be derived in kinetic theory [29, 31–34]. In kinetic theory, relaxation equations as well as explicit expressions for transport coefficients, relaxation times, and so forth can be obtained. There is no unique method to obtain the relaxation equations from kinetic theory. For example, Israel-Stewart obtained the relaxation equations from the second moment of kinetic equation. Betz et al. [31] on the other hand obtained them from the kinetic equation itself. Both the methods gave identical relaxation equations. However, while the relaxation equations remain unchanged, the relaxation time and coupling coefficients do depend on whether the zeroth moment or the second moment of the kinetic equation is used to derive the relaxation equation.

Among the three dissipative coefficients, shear viscosity appears to be most important in heavy ion collisions. In a collision, initial momentum is predominantly longitudinal. Some shear force must act on it to isotropise the momentum distribution (as required by the assumption of thermal equilibrium). Most of the dissipative hydrodynamic studies for heavy ion collisions thus concern with the effect of shear viscosity on fluid evolution and subsequent particle emission. Bulk viscosity, in general is order of magnitude less than shear viscosity. However, there are indications that, in QGP, near the transition point, bulk viscosity can be large [35, 36]. Recently, effect of bulk viscosity on particle production is being investigated [37–42]. There is some uncertainty about the correct form of the nonequilibrium correction to the equilibrium distribution function in presence of bulk viscosity. Grad’s 14-moment method for nonequilibrium correction appears to give very large correction even for small bulk viscosity [42]. In [41], a different conclusion was reached. Using Grad’s 14-moment method in orthogonal basis form [32] along with bulk viscosity relaxation time of [34] does not lead to such problems. Conductivity of QGP fluid is the least studied dissipative coefficient. The central rapidity region in ultra-relativistic heavy ion collisions is essentially baryon free, and effect of conductivity is minimum. However, in future FAIR energy collisions, effect of conductivity may be important.

3. Equation of State

Hydrodynamic equations are closed with an equation of state (EOS) $p = p(\epsilon, n_B)$. As it was mentioned earlier, hydrodynamic models are unique that the effect of phase transition can be studied, dynamically, by including the phase transition in the equation of state. Earlier, hydrodynamical simulations of relativistic heavy ion collisions used EOS with first-order confinement-deconfinement phase transition. The simple Bag model equation of state was used extensively to model EOS of the QGP phase. The confined phase is generally modeled as interaction free hadron resonance gas. At sufficiently low temperature, thermodynamics of a strongly interacting matter is dominated by pions. As the temperature increases, larger and larger fraction of available energy goes into

excitation of more and more heavier resonances. For temperature $T \geq 150$ MeV, heavy states dominate the energy density. However, densities of heavy particles are still small, $\rho_i \sim e^{-M_i/T}$. Their mutual interaction, being proportional to $\rho_i \rho_j \sim e^{-(M_i+M_j)/T}$, is suppressed. One can use Virial expansion to obtain an effective interaction. Virial expansion together with experimental phase shifts was used by Venugopalan and Prakash to study thermodynamics of low temperature hadronic matter [43]. It was shown that interplay of attractive interactions (characterised by positive phase shifts) and repulsive interactions (characterised by negative phase shifts) is such that, effectively, theory is interaction free. One can then consider that interaction-free resonances constitute the hadronic matter at low temperature.

In recent years, there is much progress in lattice simulation of QCD. In particular, thermodynamic properties of baryon free QCD have been studied accurately and extensively. Currently, there is consensus that the confinement-deconfinement transition is a crossover, and the crossover or the pseudocritical temperature for the transition is $T_c \approx 170$ MeV [3–6]. Accurate lattice simulations also show that at low temperature, interaction-free hadron resonance gas correctly reproduces lattice simulation results. Recent hydrodynamical simulations generally use EOS where the lattice simulation results for the deconfined phase are smoothly joined at $T = T_c$ MeV, with hadronic resonance gas EOS [44, 45]. In Figure 2, Wuppertal-Budapest simulations for entropy density and pressure are shown. The lines in Figure 2 are for a lattice-based EOS [45], where the lattice simulations for entropy density are smoothly joined at $T = T_c \approx 170$ MeV, with the entropy density of the hadronic resonance gas result. The energy density and pressure are then obtained from the thermodynamical relation:

$$P(T) = \int_0^T dT' s(T'), \quad (17)$$

$$\varepsilon(T) = sT - P. \quad (18)$$

4. Initial Condition

One understands that hydrodynamics is an initial value problem. To solve the conservation one has to initialise the (baryon) number density $n_B(x, y, \eta)$, energy density $\varepsilon(x, y, \eta)$, and velocity $\mathbf{u}(x, y, \eta) = \gamma \mathbf{v}(x, y, \eta)$ distributions at the initial time τ_i , beyond which hydrodynamics is applicable. In viscous hydrodynamics, the viscous stresses have also to be initialised. In relativistic heavy ion collisions, rather than (t, x, y, z) , more appropriate coordinates are $(\tau = \sqrt{t^2 - z^2}, x, y, \eta_s = (1/2) \ln(t+z)/(t-z))$. In (τ, x, y, η_s) coordinate system, for the initial energy density, a common practice is to assume a factorised form:

$$e(x, y, \eta_s) = \varepsilon(x, y) H(\eta_s), \quad (19)$$

where $\varepsilon(x, y)$ is the initial energy density in the transverse plane and $H(\eta_s)$ is in the direction of (spatial) rapidity η_s . One can use a Gaussian distribution for $H(\eta_s)$. Transverse energy density $\varepsilon(x, y)$ can be conveniently parameterised in

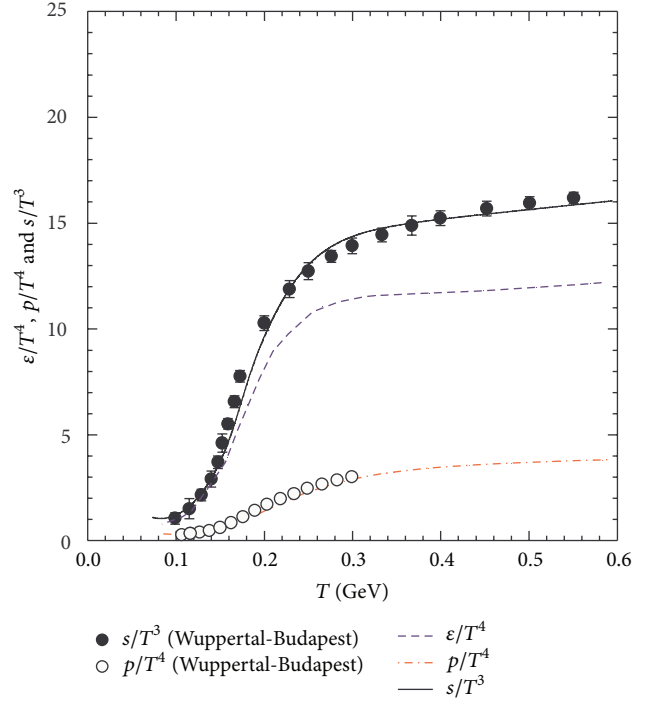


FIGURE 2: Lattice simulations [6] for energy density and entropy density are shown. The lines are parameterised EOS. For details of the parametric EOS, see [45].

a Glauber model [17] or in color glass condensate (CGC) model [46–48]. I briefly discuss the Glauber and CGC initial conditions. In Glauber model, in A+B collisions at impact parameter \mathbf{b} , at the initial time τ_i , the initial entropy density $(s(x, y))$ or energy density $(\varepsilon(x, y))$ is parameterised as

$$s(x, y) = s_0 \left[(1-f) N_{\text{part}}(x, y) + f N_{\text{coll}}(x, y) \right] \quad (20)$$

or

$$\varepsilon(x, y) = \varepsilon_0 \left[(1-f) N_{\text{part}}(x, y) + f N_{\text{coll}}(x, y) \right], \quad (21)$$

where $N_{\text{part}}(x, y)$ and $N_{\text{coll}}(x, y)$ are the transverse profile of participant nucleons and binary collision number and can easily be computed in Glauber model:

$$\begin{aligned} N_{\text{coll}}(x, y) &= \sigma_{NN} T_A \left(x + \frac{\mathbf{b}}{2}, y \right) T_B \left(x - \frac{\mathbf{b}}{2}, y \right), \\ N_{\text{part}}(x, y) &= T_A \left(x + \frac{\mathbf{b}}{2}, y \right) \left(1 - \left[1 - \sigma_{NN} T_B \left(x - \frac{\mathbf{b}}{2}, y \right) \right]^B \right) \\ &\quad + T_B \left(x - \frac{\mathbf{b}}{2}, y \right) \left(1 - \left[1 - \sigma_{NN} T_A \left(x + \frac{\mathbf{b}}{2}, y \right) \right]^A \right), \end{aligned} \quad (22)$$

where the thickness function is $T_A(x, y) = \int dz \rho_A(x, y, z)$, with ρ being the density distribution. f in (20), (21) is the hard scattering fraction (to be fitted to experimental data).

CGC model initial condition relies on the physical argument that gluon production saturates at high energies [49–51], and prior to QGP, a new form of matter, “Color Glass Condensate (CGC)” is formed. The new form of matter then evolves into QGP. Evolution of CGC is governed by complicated nonlinear JIMWLK equation [50–53]. For hydrodynamical application, one generally uses the Kharzeev-Levin-Nardi (KLN) approach (which captures the essential features of the gluon saturation) [54, 55] and computes the transverse profile of the gluons in A+A collisions. Transverse profile of gluons in A+B collision can be computed as

$$\frac{dN_g}{d^2r_T dY} = \frac{4\pi^2 N_c}{N_c^2 - 1} \int \frac{d^2 p_T}{p_T^2} \int d^2 k_T \alpha_s(k_T) \times \phi_A(x_1, p_T^2, r_T) \phi_B(x_2, (p_T - k_T)^2, r_T), \quad (23)$$

where p_T and Y are the transverse momentum and rapidity of the produced gluon. $x_{1,2} = (p_T/\sqrt{s})e^{\pm Y}$ is the momentum fraction of colliding gluons ladders at c.m. energy \sqrt{s} . $\alpha_s(k_T)$ is the strong coupling constant at the momentum scale k_T . $\phi_{A(B)}$ are unintegrated gluon distribution functions in nuclei A and B . In KLN approach [56], the unintegrated gluon distribution function (ϕ_A) is taken as [55, 56]:

$$\phi_A(x, k_T^2, r_T) \sim \frac{1}{\alpha_s(Q_s^2)} \frac{Q_s^2}{\max(Q_s^2, k_T^2)}, \quad (24)$$

where Q_s is saturation momentum at the given momentum fraction x and at the transverse position r_T . In the KLN approach, the saturation scale in AB collision is parameterised as [55, 56]:

$$Q_{s,A(B)}(x, r_T) = 2 \text{ GeV}^2 \left(\frac{N_{\text{part}}^{A(B)}(r_T)}{1.53} \right) \left(\frac{0.01}{x} \right)^\lambda. \quad (25)$$

The form $Q_s(x) \sim x^{-\lambda}$ with $\lambda \approx 0.2-0.3$ is motivated from DIS experiments. $N_{\text{part}}^{A(B)}$ in the above equation is the transverse density of participant nucleons, which can be calculated in a Glauber model.

In the CGC model, the transverse energy density should follow the gluon density distribution (23). However, (23) is valid in the time scale $\tau_s \sim 1/Q_s$, when the medium may not be in thermal equilibrium. One assumes that the medium undergoes one-dimensional Bjorken (longitudinal, isentropic) expansion during the period τ_s to τ_i . The density at the time τ_i , when hydrodynamic becomes applicable, is easily obtained as $n(\tau_i) = (\tau_s/\tau_i)n(\tau_s)$. The transverse energy density profile at the initial time τ_i is

$$e(x, y, b) = e_0 \left[\frac{dN_g}{dx dy dY} \right]^{4/3}. \quad (26)$$

It may be mentioned here that, in general, in a given impact parameter, hydrodynamical simulation with CGC initial condition generates more elliptic flow than the Glauber model initial condition. The reason is also understood. Elliptic flow is proportional to initial eccentricity of the medium.

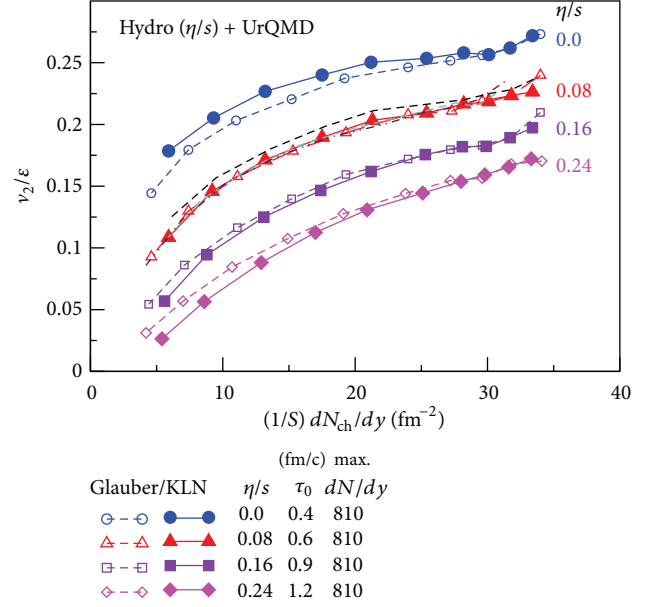


FIGURE 3: Hybrid model simulation for the eccentricity-scaled elliptic flow v_2/ϵ as a function of multiplicity density $(1/S)(dN_{\text{ch}}/dy)$, for different values of $(\eta/s)_{\text{QGP}}$. Eccentricity-scaled elliptic flow does not depend on the details of the model for initial density distribution but only on the QGP viscosity. See [57] for details.

In CGC model initial condition, initial eccentricity is comparatively larger than that in the Glauber model. Recently, in an important publication, Song et al. [57] resolved the uncertainty in the initial conditions in viscous hydrodynamics. They used a hybrid model, where viscous fluid dynamics for the QGP was coupled with a microscopic transport model (UrQMD) for hadronic freeze-out. Hybrid models, without additional parameters, govern the complex hadron kinetic freeze-out and allow quantitative exploration of the transport properties of the earlier QGP phase using measured final hadron spectra. It was shown that at least in a fixed energy collision, the relation between the eccentricity scaled elliptic flow (v_2/ϵ) and the multiplicity density $(1/S)(dN_{\text{ch}}/dy)$ is approximately universal function, only depending on the value of QGP viscosity over entropy ratio, $(\eta/s)_{\text{QGP}}$, but not on any details of the model from which ϵ and $S = \pi \sqrt{\langle x^2 \rangle \langle y^2 \rangle}$ is computed. Results of their simulations are shown in Figure 3 (for details see [57]).

The number density distribution at the initial time can be similarly parameterised. In general, one assumes zero initial fluid velocity at the initial time, though it is possible that fluid has nonzero velocity, especially near the surface of the fluid. The reasoning is simple. Fluid constituents have random velocity. In the interior of the fluid, the random velocities will balance to produce net zero velocity, but near the surface random velocities will not be balanced. In viscous hydrodynamics, one also needs to initialise the viscous stresses. One common practice is to assume that at the initial time τ_i , viscous stresses are zero, $\Pi(x, y, \eta) = \pi^{\mu\nu}(x, y, \eta) = 0$ [58]. In hydrodynamic models with the assumption of boost-invariance, boost-invariant values can also be used [59].

It may be mentioned here that the initial time τ_i is also a parameter of the model. It is essentially the thermalisation time. One important finding of hydrodynamical analysis of $\sqrt{s_{NN}} = 200$ GeV Au+Au and $\sqrt{s_{NN}} = 2.76$ TeV Pb+Pb collisions is that hydrodynamical simulations require small thermalisation time $\tau_i \approx 0.5$ –1.0 fm. Origin of small thermalisation time is not properly understood. In QGP, nonabelian version of Weibel instabilities can grow very fast, isotropizing the medium [60]. The maximum growth rate is $\gamma \sim g\sqrt{n/p_{\text{hard}}}$, with n being the density and p_{hard} the characteristic momentum scale dominating the excitations in nonequilibrium QGP [60]. In high energy collisions, a large number of gluons will be freed in the first moments after the collisions, n is large, and instabilities can grow fast. However, it must be mentioned here that Chromo-Weibel instabilities have never been shown to be able to isotropize the system in the time scale 0.5–1 fm/c. In a recent publication it was shown that in nucleus-nucleus collisions at LHC energy, Chromo-Weibel instabilities can isotropise the system in the time as large as ~ 5 fm [61]. It is even more ~ 10 fm in RHIC energy scale.

Another important input to viscous hydrodynamics simulation is the relaxation time for bulk stress (τ_{Π}) and shear (τ_{π}) stress. In principle, relaxation times τ_{Π} and τ_{π} could be calculated from the underlying kinetic theory, which for strongly coupled QCD plasma, is a complex problem. Relaxation times τ_{Π} and τ_{π} were calculated in [28, 29], for simple relativistic Boltzmann, Bose, and Fermi gases with mass m using Grad 14 moment approximation in relativistic kinetic theory. For a Boltzmann gas, in the nonrelativistic limit ($\beta = m/T \rightarrow \infty$), $\tau_{\Pi} = \zeta\beta_0 \approx (6/5)(m^2/T^2)(\zeta/P)$ and $\tau_{\pi} = 2\eta\beta_2 \approx \eta/P$. In the relativistic limit ($\beta \rightarrow 0$), $\tau_{\Pi} = \zeta\beta_0 = \zeta(216/P)(kT/m)^4$ and $\tau_{\pi} = 2\eta\beta_2 = 3\eta/2P$. Note that in the relativistic limit, the mass term appears in the denominator with a quartic power. Two phases in heavy ion collision, that is, QGP and hadronic phases, consist of quasiparticles of different masses; the dependence of this mass with temperature as well as the ambiguity around the crossover makes it difficult to use τ_{Π} as given here. In most of the simulation, τ_{Π} is either taken as a constant or kept same as τ_{π} . Recently, Jaiswal et al. [34] solved the long-standing ambiguity in the relaxation time for bulk viscosity. They derived causal dissipative hydrodynamic equations by invoking second law of thermodynamics from entropy four-current expressed in terms of distribution function. The bulk relaxation time thus obtained shows critical slowing down near transition temperature and does not lead to cavitation.

5. Shear and Bulk Viscosity Coefficients

In viscous hydrodynamic simulations, one also needs to specify the dissipative coefficients. The shear or bulk viscosity for a strongly interacting system can be calculated by using Kubo formula [65, 66] as given in the following:

$$\eta = \lim_{\omega \rightarrow 0} \frac{1}{2\omega\hbar} \int dt dx e^{i\omega t} \langle [T_{\mu\nu}(t, x), T_{\mu\nu}(0, \mathbf{0})] \rangle, \quad (27)$$

$$\zeta = \lim_{\omega \rightarrow 0} \frac{1}{6\omega\hbar} \int dt dx e^{i\omega t} \langle [T_{\mu\mu}(t, x), T_{\mu\mu}(0, \mathbf{0})] \rangle.$$

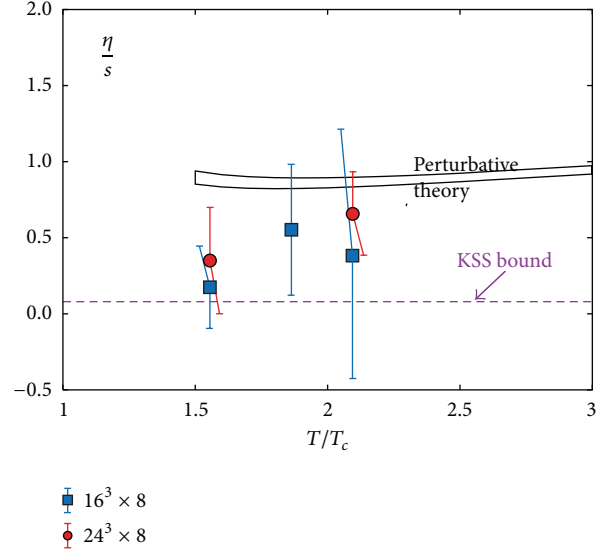


FIGURE 4: Viscosity over entropy ratio (η/s) as a function of temperature from perturbative calculation [62, 63], lattice QCD calculation [64]. AdS/CFT bound $\eta/s = 1/4\pi$ is also shown.

However, first principle calculations of viscosity coefficients are very difficult for sQGP. See [67] for a detailed discussion of viscous properties of QCD matter. In Figure 4, I have shown some results from first principle attempts to obtain (shear) viscosity over entropy ratio of sQGP. Applicability of perturbative QCD in sQGP is questionable. Still, in [62, 63], η/s was obtained in pQCD approach. pQCD leads to very large (shear) viscosity over entropy ratio $\eta/s \sim 1$, too large to explain experimental elliptic flow. Lattice QCD calculations [64, 68] require analytic continuation from imaginary to real time and results can be obtained only with large uncertainty. As shown in Figure 4, QGP viscosity over entropy ratio appears to increase with temperature, though very large error bars preclude any definite conclusion. In AdS/CFT approach, one relates the correlator to Graviton absorption cross-section. AdS/CFT correspondence is based on Maldacena's gauge/gravity duality conjecture. It is conjectured that string theory with gravity defined on a product space $\text{AdS}_5 \times S^5$ is equivalent to quantum field theory without gravity defined on the conformal boundary of AdS_5 ; here AdS_5 is the 5-dimensional anti-deSitter space, and S^5 is a five-dimensional sphere. For more details, see [69]. In this approach, energy-momentum tensor $T_{\mu\nu}$ couples to gravity at the boundary, and one can calculate the absorption cross-section of a graviton. Absorption cross-section of a graviton of frequency ω , polarised in xy direction, is the imaginary part of the retarded Green function:

$$\sigma_{\text{abs}}(\omega) = -\frac{2\kappa^2}{\omega} \text{Im}G^R(\omega) \quad (28)$$

$$= \frac{\kappa^2}{\omega} \int dt dx e^{i\omega t} \langle [T_{\mu\nu}(t, x), T_{\mu\nu}(0, \mathbf{0})] \rangle,$$

where $\kappa = \sqrt{8\pi G}$ appears due to normalisation of the graviton action. One can show that absorption cross-section

of graviton is equal to that of a minimally coupled scalar, in the low energy limit which can be identified with the area (A) of the horizon [70]. Considering that black hole entropy is $s = A/4G$, one can easily obtain the AdS/CFT limit for shear viscosity over entropy ratio [18–20]:

$$\frac{\eta}{s} \geq \frac{1}{4\pi}. \quad (29)$$

Bulk viscosity is proportional to interaction measure $\varepsilon - 3P$, and in a purely conformal system it is identical to zero. In QCD conformal symmetry is broken by the running coupling constant, α_s , and can be nonzero. Leading log perturbative limit for bulk viscosity is very small, to within 10% for $0.06 \leq \alpha_s \leq 0.3$ $\zeta/s = 0.020\alpha_s^2$ [71], and is consistent with the old relation, $\zeta = 15\eta(1/3 - c_s^2)^2$ [72], with c_s^2 being the speed of sound in the medium. AdS/CFT calculations that incorporate deviations from conformality at strong coupling find $\zeta \approx 2\eta(1/3 - c_s^2)$ [73, 74]. However, there are indications that in QGP, near the transition point, bulk viscosity can be large [35, 36].

Bulk and shear viscosity of the hadronic matter has been also been calculated, either in effective hadronic interaction model or in the transport model [75–78]. QGP viscosity over entropy ratio of the hadronic gas decreases with increasing temperature, bulk viscosity over entropy ratio and on the other hand shows opposite behavior increase with temperature. Present paradigm is that while shear viscosity over entropy ratio has a minimum at $T \approx T_c$ [79, 80], bulk viscosity over entropy ratio has a maxima at $T \approx T_c$.

Considering the limited theoretical knowledge of the viscosity over entropy ratio, an alternative approach is to extract the ratio by comparing viscous fluid dynamical simulations with experimental data. This is the approach taken in most of the hydrodynamical simulations.

6. Freeze-Out

In addition to the initialisation of the fluid, hydrodynamic models also require a freeze-out condition. As it was mentioned earlier, there are two types of freeze-out, in hydrodynamical evolution, the chemical freeze-out and the kinetic freeze-out. Hadron abundances remain fixed after the chemical freeze-out. Statistical models, based on Grand Canonical ensemble, surprisingly give correct values for hadron ratios [81, 82]. Chemical freeze-out temperature and baryonic chemical potentials have been parameterised as a function of collision energy. The parameterised forms can be used to obtain the chemical freeze-out temperature for application in hydrodynamical modeling. The kinetic freeze-out temperature, generally, is treated as a parameter, and its value is obtained from fitting experimental data. Freeze-out temperature $T_F = 110\text{--}150$ MeV has been used in hydrodynamic simulations.

At kinetic freeze-out, Cooper-Frye prescription [16] is used to obtain the particle (invariant) distribution:

$$E \frac{dN}{d^3p} = \frac{dN}{dyd^2p_T} = \int_{\Sigma} d\Sigma_{\mu} p^{\mu} f(x, p), \quad (30)$$

where $d\Sigma_{\mu}$ is the freeze-out hypersurface and $f(x, p)$ is the one-body distribution function. Now in ideal dynamics, the fluid is in local equilibrium, and the one-body distribution function is well approximated by the equilibrium distribution function:

$$f(x, p) = f^{\text{eq}}(x, p) = \frac{g}{2\pi^3} \frac{1}{\exp[\beta(u_{\mu}p^{\mu} - \mu)] \pm 1} \quad (31)$$

with inverse temperature $\beta = 1/T$ and chemical potential μ . g is the degeneracy factor. In viscous dynamics on the other hand, the fluid is not in equilibrium, and $f(x, p)$ cannot be approximated by the equilibrium distribution function $f^{\text{eq}}(x, p)$. In a highly nonequilibrium system, distribution function $f(x, p)$ is unknown. If the system is slightly off-equilibrium, then it is possible to calculate correction to equilibrium distribution function due to (small) nonequilibrium effects. Slightly off-equilibrium distribution function can be approximated as

$$f^{\text{neq}}(x, p) = f^{\text{eq}}(x, p) [1 + r f^{\text{eq}}(x, p)] [1 + \phi(x, p)], \quad (32)$$

where $r = 1, -1$, and 0 for Fermi, Bose, and Boltzmann gas, respectively. $\phi(x, p) \ll 1$ is the deviation from equilibrium distribution function f^{eq} . With shear viscosity as the only dissipative forces, $\phi(x, p)$ can be locally approximated by a quadratic function of 4-momentum:

$$\phi(x, p) = \frac{1}{2(\varepsilon + p)T^2} \pi_{\mu\nu} p^{\mu} p^{\nu}, \quad (33)$$

completely specifying the nonequilibrium distribution functions. As expected, correction factor increases with increasing viscosity. We also note that nonequilibrium correction depends quadratically on particle momentum. The effect of dissipation is more on large momentum particles. For bulk viscosity, the situation is more complicated. The nonequilibrium correction can be written as

$$\phi(x, p) = [D_0 p_{\mu} u^{\mu} + B_0 p_{\mu} p_{\nu} \Delta^{\mu\nu} + \bar{B}_0 p_{\mu} p_{\nu} u^{\mu} u^{\nu}] \Pi, \quad (34)$$

where D_0 , B_0 , and \bar{B}_0 are space-time-dependent parameters, explicit expression for which can be found in [38]. It appears that even for small bulk viscosity, the correction factor can be very large, invalidating viscous hydrodynamics at momenta $p_T > 1$ GeV or so [42].

In the late stage of evolution, applicability of hydrodynamics may be poor. In more realistic models, hydrodynamic models are coupled with hadron-based transport models [83–87]. In the hybrid models, below a switching temperature $T_{\text{sw}} < T_c$, motion of hadrons is governed by transport equations, for example, UrQMD model. At the switching temperature T_{sw} hadron abundances can be computed using the Cooper-Frye formalism. The initial state of the transport models is produced through the Monte-Carlo sampling. Agreement with data appears to improve in hybrid models.

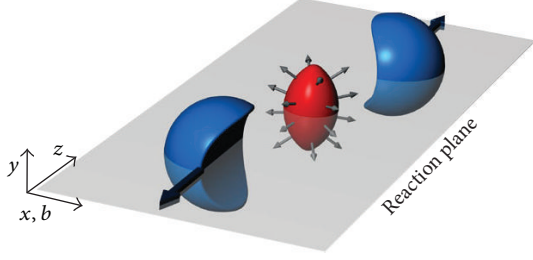


FIGURE 5: Schematic picture of a nonzero impact parameter collision.

7. Collective Flow

In relativistic heavy ion collisions, one of the important observables is the azimuthal distribution of produced particles. In Figure 5, geometry of a collision at nonzero impact parameter is shown. The overlap region of the two nuclei is the participant region, where most of the collisions occur. The target and projectile remnants on the periphery act as spectator. It is obvious from Figure 5 that, in nonzero impact parameter collisions, the participant or the reaction zone in coordinate space does not possess azimuthal symmetry. Multiple collisions among the constituent particles translate this spatial anisotropy into momentum anisotropy of the produced particles. The observed momentum anisotropy is called collective flow and has a natural explanation in a hydrodynamic model [17]. In the following we briefly discuss collective flow phenomena. More detailed expositions can be found in [88–90].

Momentum anisotropy is best studied by decomposing the invariant distribution in a Fourier series. For example, the momentum integrated invariant distribution of a particle can be expanded as

$$\frac{dN}{d\phi} = \frac{N}{2\pi} \left[1 + 2 \sum_n v_n \cos [n(\phi - \psi)] + 2 \sum_n w_n \sin [n(\phi - \psi)] \right], \quad n = 1, 2, 3 \dots, \quad (35)$$

where ϕ is the azimuthal angle of the detected particle and ψ is the plane of the symmetry of initial collision zone. For smooth initial matter distribution (obtained from geometric overlap of the colliding nuclei, e.g., Glauber model), plane of symmetry of the collision zone coincides with the reaction plane Ψ_{RP} (the plane containing the impact parameter and the beam axis). The sine terms of the Fourier expansion does not contribute due to symmetry with respect to the reaction plane.

Flow coefficients v_n are easily obtained,

$$v_n = \langle \cos(n\phi - n\psi) \rangle = \frac{\int d\phi (dN/d\phi) \cos(n\phi - n\psi)}{\int d\phi (dN/d\phi)}. \quad (36)$$

v_1 is called (integrated) directed flow, v_2 is called (integrated) elliptic flow, v_3 is called (integrated) triangular flow, v_4 is called (integrated) hexadecapole flow, and so forth.

Similar to (35), one can Fourier expand the invariant distribution

$$E \frac{d^3N}{d^3p} = \frac{1}{2\pi} \frac{d^2N}{p_T dp_T dy} \left[1 + 2 \sum_n v_n(p_T) \cos [n(\phi - \psi)] \right]. \quad (37)$$

The coefficients $v_n(p_T)$ are called differential flow coefficient. Second flow coefficient or elliptic flow has been studied extensively in RHIC and LHC energy collisions. Finite-nonzero value of v_2 is thought to be direct signature of production of thermalised medium. Elliptic flow is best understood in a hydrodynamic model [17]. Elliptic flow measures the momentum anisotropy. In nonzero impact parameter collisions, the reaction zone is spatially asymmetric (see Figure 5). Spatial asymmetry of the initial reaction zone can be quantified in terms of eccentricity, defined as

$$\varepsilon = \frac{\langle y^2 - x^2 \rangle}{\langle y^2 + x^2 \rangle}, \quad (38)$$

where $\langle \dots \rangle$ indicates energy/entropy density weighted averaging. In nonzero impact parameter collision, initial eccentricity is positive. If a thermalised medium is produced in the reaction zone, due to thermodynamic pressure, the medium will expand against the outside vacuum. One can immediately see that pressure gradient will be more along the minor axis than along the major axis. Due to differential pressure gradient, as the system evolves with time, eccentricity will reduce. Momentum distribution of particles is isotropic initially. If momentum anisotropy is measured as

$$\varepsilon_p = \frac{\int dx dy [T^{xx} - T^{yy}]}{\int dx dy [T^{xx} + T^{yy}]}, \quad (39)$$

initially ε_p will be zero. However, as the fluid evolves, rescattering of particles will introduce asymmetry, and ε_p will grow. Beyond certain time, when reaction zone attains azimuthal symmetry, it is expected to saturate. In a sense, elliptic flow is self-quenching phenomena, and driving force of the flow (the reaction zone asymmetry) continuously reduces to quench the flow. In Figure 6, hydrodynamic model simulations for temporal evolution of spatial eccentricity and momentum anisotropy, in ideal and viscous fluid, are shown [96]. As expected, in simulations also, while the eccentricity decreases with time, the momentum anisotropy increases and tends to saturate at large time. Effect of viscosity is not large on the evolution of spatial eccentricity. In viscous fluid, eccentricity decrease marginally faster. The effect is, however, more pronounced on momentum anisotropy. Viscosity hinders the growth of the momentum anisotropy. Saturation value of momentum anisotropy in viscous fluid is lower than that in ideal fluid.

The second harmonic coefficient or the elliptic flow (v_2) has been studied extensively in $\sqrt{s_{NN}} = 200$ GeV Au+Au collisions at RHIC [9, 10]. Recently, ALICE collaboration measured elliptic flow in $\sqrt{s_{NN}} = 2.76$ TeV Pb+Pb collisions at LHC [14, 15]. Large elliptic flow has provided compelling evidence that at RHIC and LHC, nearly perfect fluid is produced.

TABLE I: Various viscous hydrodynamics models are listed.

Reference	Dim.	IC	EOS	Scheme	Freeze-out	Obs.
P. Romatschke and U. Romatschke [58]	2 + 1	G	IQCD	CD	Single T_F	v_2
Dusling and Teaney [91]	2 + 1	G	Ideal gas	—	Viscous correction	v_2
Luzum and Romatschke [47]	2 + 1	G, CGC	IQCD	CD	Resonance decay	v_2
Schenke et al. [92]	3 + 1	MC-G	IQCD	KT	Viscous correction	v_2, v_3
Song et al. [57]	2 + 1	MC-G, MC-CGC	IQCD	SHASTA	Cascade (UrQMD)	v_2
Chaudhuri [59], Roy and Chaudhuri [42]	2 + 1	G, CGC, MC-G	IQCD	SHASTA	Viscous correction	v_2, v_3
Bozek [93]	3 + 1	G	IQCD	—	THERMINATOR2	v_1, v_2, HBT
Denicol et al. [94]	3 + 1	G	IQCD	SPH	Viscous correction	v_2

G: Glauber model, CGC: color glass condensate, MC-G: Monte-Carlo Glauber, MC-CGC: Monte Carlo color glass condensate, and CD: central difference. The table is from [95]. I have added the last reference, which uses smooth particle hydrodynamics (SPH) for solving hydrodynamic equations.

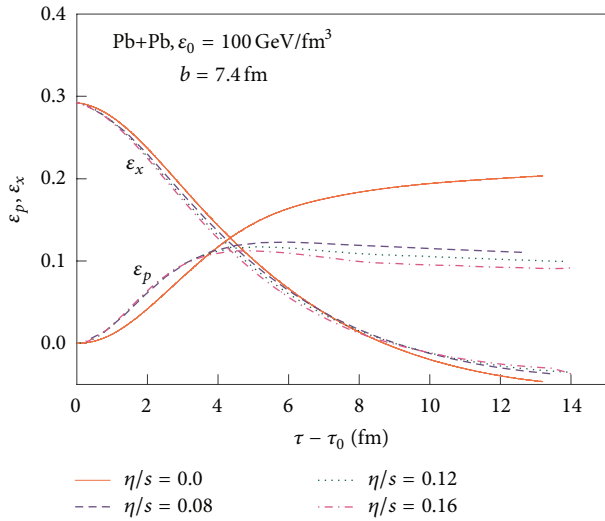


FIGURE 6: Ideal and viscous hydrodynamic simulations for evolution of spatial eccentricity (ϵ_x) and momentum anisotropy (ϵ_p) in $b = 7.4$ fm Pb+Pb collisions.

Deviation from the ideal fluid behavior is controlled by shear viscosity to entropy ratio (η/s). Effect of shear viscosity is to dampen the flow coefficients. Elliptic flow has sensitive dependence on η/s . In smooth hydrodynamics, sensitivity of elliptic flow has been utilised to obtain phenomenological estimates of η/s [47, 85, 97–102]. It appears that QGP viscosity over entropy ratio is close to $\eta/s \approx 1/4\pi$.

8. Hydrodynamic Simulation of Heavy Ion Collisions and Comparison with Experiment

Even though Israel-Stewart formulated second order theory for dissipative fluid some 30 years back, significant progress towards its numerical implementation has only been made very recently. In Table I, I have listed the various viscous hydrodynamic models, developed across the world. Several algorithms can be used to solve the energy momentum conservation equations and the relaxation equations. One widely used algorithm is the Smooth and Sharp Transport Algorithm (SHASTA) followed by Flux Corrected Transport (FCT) [103]. SHASTA-FCT algorithm is known to be an accurate

and effective algorithm to solve nonlinear generalized continuity equation of the type which occurs in fluid dynamics [103, 104]. It is essentially a three-step process. In the first step, called transport, the velocities of the fluid and the source term are first calculated at half time steps $t_{n+1/2}$. In the second step, using the new velocity and the new source term in the n th step, one calculates the quantities at the $n+1$ th step. The third step is called the antidiffusive step, designed to remove the numerical diffusion inherent to the transport scheme. This is done by calculating an antidiffusive flux, which is subtracted from the time-advanced quantities at the $n+1$ th step to get the final result at the $n+1$ th step. The calculation of the antidiffusion is carried out by a method called “flux correction.” For details of the method, see [103, 104].

In the following, some representative viscous hydrodynamic simulation results are discussed in brief. In Figure 7 viscous hydrodynamic simulation results [47] for the centrality dependence of pions, kaons, and protons multiplicity, in $\sqrt{s_{NN}} = 200$ GeV Au+Au collisions, are compared with experimental data. In the simulations, it was assumed that viscosity over entropy ratio remains a constant throughout the evolution. Three values, $\eta/s = 0$ (ideal fluid), 0.08 (AdS/CFT limit), and 0.16, were used in the simulation. In [47], both Glauber model initial condition and CGC initial conditions were used to simulate Au+Au collisions. Figure 7 was obtained with Glauber model initial condition. Simulation results indicate that particle’s multiplicity is not sensitive to viscosity when fluid is appropriately initialised (see [47] for details), viscosity over entropy ratio $\eta/s \approx 0, 0.08$ and 0.16 describes the data equally well. In Figure 8, viscous hydrodynamic simulations for charged particle’s integrated elliptic flow are compared with the experimental data. Simulation results for integrated elliptic flow, however, show sensitive dependence on viscosity over entropy ratio, decreasing with increasing viscosity. Similar results are also obtained with CGC initial condition, and particle multiplicity is not sensitive to η/s , but elliptic flow is. We will not discuss in detail but from the analysis of $\sqrt{s_{NN}} = 200$ GeV Au+Au collision data, the viscosity over entropy ratio was estimated as $\eta/s = 0.1 \pm 0.1$ (theory) ± 0.08 (experiment) [47].

In Figure 9, viscous hydrodynamic simulation results [48] for transverse momentum spectra in $\sqrt{s_{NN}} = 200$ GeV Au+Au collisions are compared with the PHENIX experiment. Glauber model initial condition was used for these

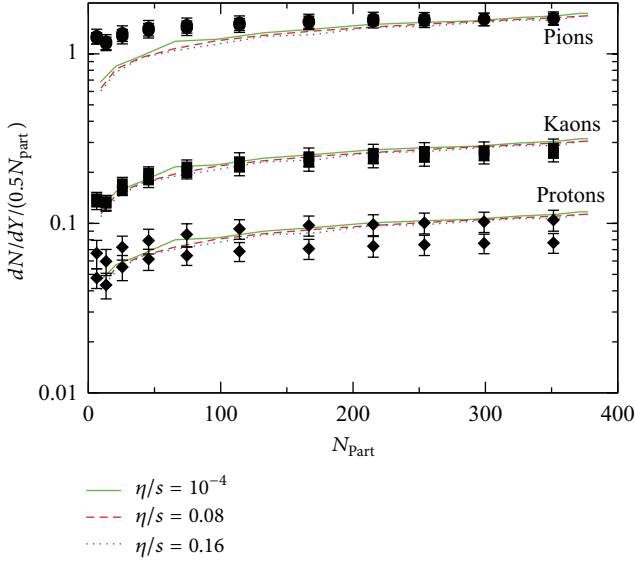


FIGURE 7: Centrality dependence of particle's multiplicity in a 2 + 1D hydrodynamical simulation is compared with experimental data. The figure is from [47].

simulations. Here also, viscosity over entropy ratio assumed to be temperature-independent. Effect of viscosity is manifest, and p_T spectra is hardened. More viscous is the fluid, and more is the hardening. From the figures, one conclude that charged particles p_T spectra in 0–50% collision are best described with viscosity to entropy ratio $\eta/s \approx 0.08$ –0.12. In Figure 10, hydrodynamic simulations for elliptic flow are compared with PHENIX data. Elliptic flow is reduced in viscous fluid. In more viscous fluid elliptic flow is reduced even more. One observes that the experimental data on elliptic flow prefers higher values of η/s in more peripheral collisions than in central collisions. For example, elliptic flow in 0–10% collisions is consistent with ideal fluid simulation. Elliptic flow in 20–30% collisions however prefer, $\eta/s \approx 0.12$, and still higher value, $\eta/s \approx 0.16$, in 40–50% collision. In [48], PHENIX data were also analysed with CGC initial condition. Conclusions were similar. While charged particles spectra prefer fluid viscosity $\eta/s = 0.08$ –0.12, elliptic flow data demand more viscous fluid in more peripheral collision. That the elliptic flow data demand-dependent QGP viscosity was obtained in an earlier analysis [99] also.

Centrality dependence of η/s is essentially manifest of temperature dependence of viscosity over entropy ratio. As mentioned earlier, simulation results depicted in Figures 7–10 were obtained with temperature-independent η/s . However, viscosity over entropy ratio does have temperature dependence [79, 80]. Viscosity over entropy ratio of hadronic matter increases with lowering of temperature [76]. Lattice QCD simulations do indicate that η/s for QGP increases with temperature [68]. Present paradigm is that the viscosity over entropy ratio for strongly interacting matter has a minimum, possibly with a cusp, around the critical temperature $T = T_c$. Demand of higher η/s in peripheral collisions in simulations with constant η/s is not at variance with the prevailing paradigm. Rather it indicates the increasingly important role

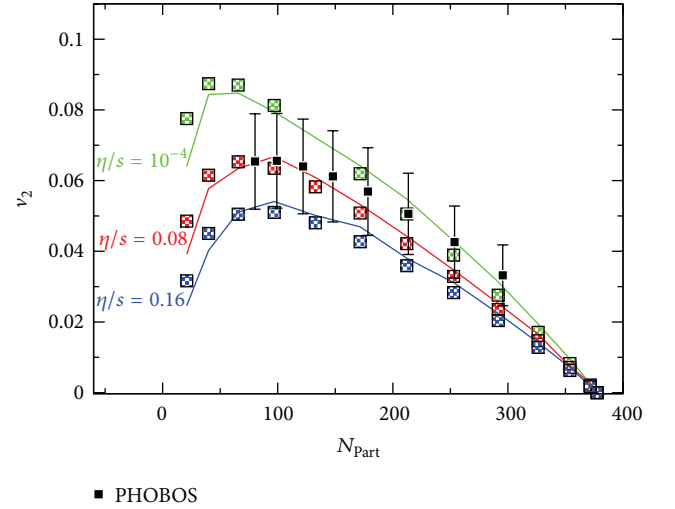


FIGURE 8: Centrality dependence of charged particles (integrated) elliptic flow compared with experimental data. The figure is from [47].

of hadronic matter in the development of elliptic flow in peripheral collisions. η/s of hadronic matter increase with lowering of temperature.

In recent years, temperature dependence of QGP viscosity over entropy ratio was investigated by several authors [85, 105–108]. In [105], four different temperatures dependence for η/s were considered: (i) LH-LQ: $\eta/s = 0.08$ for all temperatures, (ii) LH-HQ: $\eta/s = 0.08$ in the hadron gas and above $T = 180$ MeV η/s increases according to lattice QCD data [68], (iii) HH-LQ: below $T = 180$ MeV, η/s is that of a hadron gas [76], and $\eta/s = 0.08$, and (iv) HH-HQ: a realistic parametrization for both the hadron gas and the QGP viscosity [68, 76]. Simulation results for transverse momentum spectra and elliptic flow for pions are shown in Figure 11. One finds that the elliptic flow in $\sqrt{s_{NN}} = 200$ GeV Au+Au collisions at RHIC is dominated by the viscosity in the hadronic phase. It is largely insensitive to QGP viscosity. QGP viscosity dominates only at LHC energy $\sqrt{s_{NN}} = 2.76$ TeV.

In [108], attempt was made to obtain the temperature dependence of η/s empirically. A linear temperature dependence of η/s for the QGP phase was assumed:

$$\left(\frac{\eta}{s}\right)_{\text{QGP}} = \frac{1}{4\pi} + \alpha \frac{T - T_c}{T_c}, \quad (40)$$

and it was smoothly joined with hadronic viscosity [68] at $T = T_c$. Experimental data in $\sqrt{s} = 200$ GeV Au+Au and $\sqrt{s_{NN}} = 2.76$ TeV Pb+Pb collisions were confronted with three slope parameters: (i) $\alpha = 0$ (ii) $\alpha = 0.2$ and (iii) $\alpha = 0.4$. Slope parameter $\alpha = 0$ –0.2 appears to be consistent with experimental data in $\sqrt{s_{NN}} = 2.76$ TeV Pb+Pb collisions. LHC data clearly disfavor very strong temperature dependence. At RHIC energy, however, strong temperature dependence $\alpha = 0.4$ was indicated. It was concluded that a unique, linear temperature-dependent QGP viscosity over entropy ratio fails to explain, simultaneously, the experimental elliptic flow data at RHIC and LHC energies. In [85, 107] a similar conclusion that

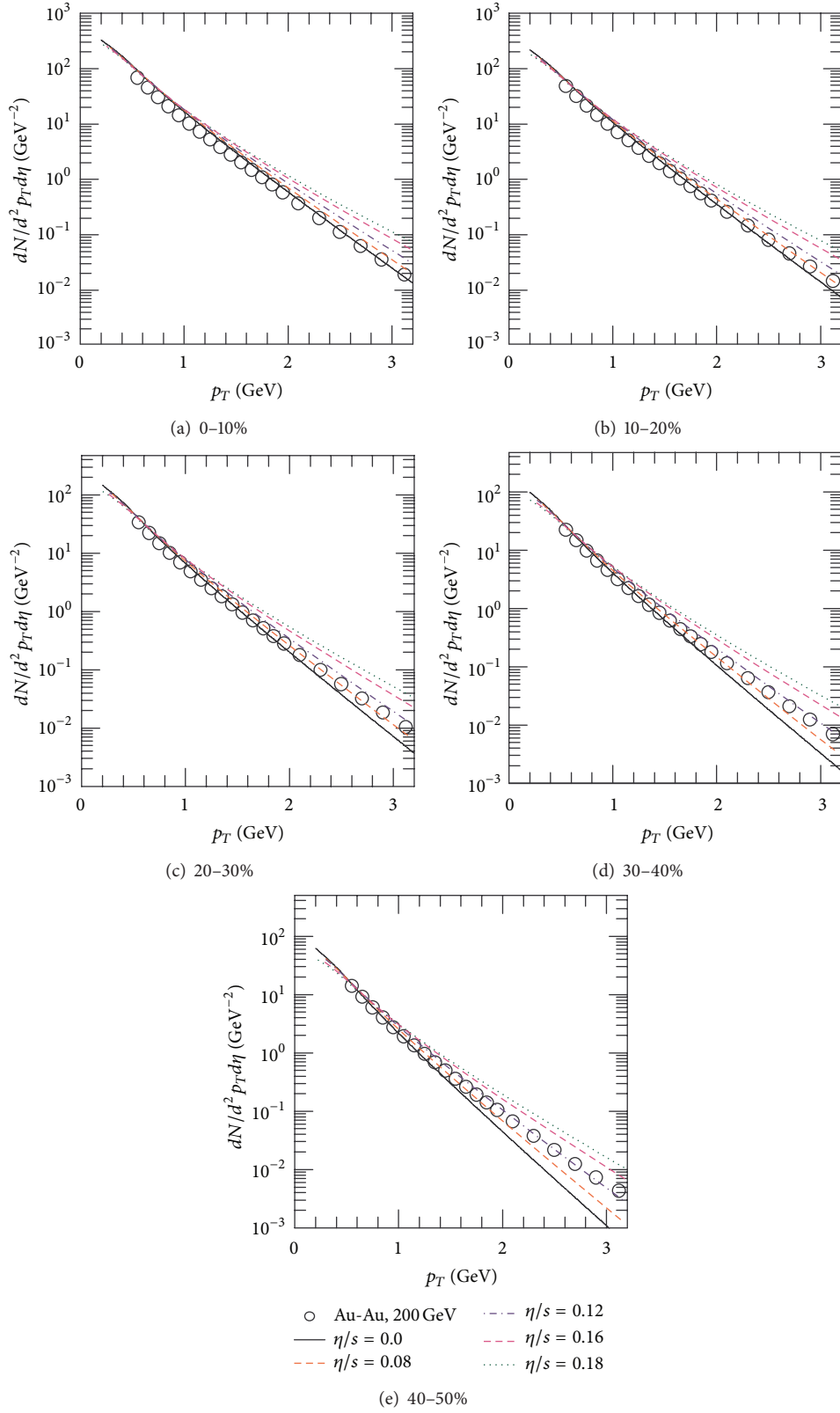


FIGURE 9: PHENIX measurements of charged particles p_T spectra in $\sqrt{s_{NN}} = 200$ GeV Au+Au collisions are compared with viscous hydrodynamic simulations. The figures are from [48].

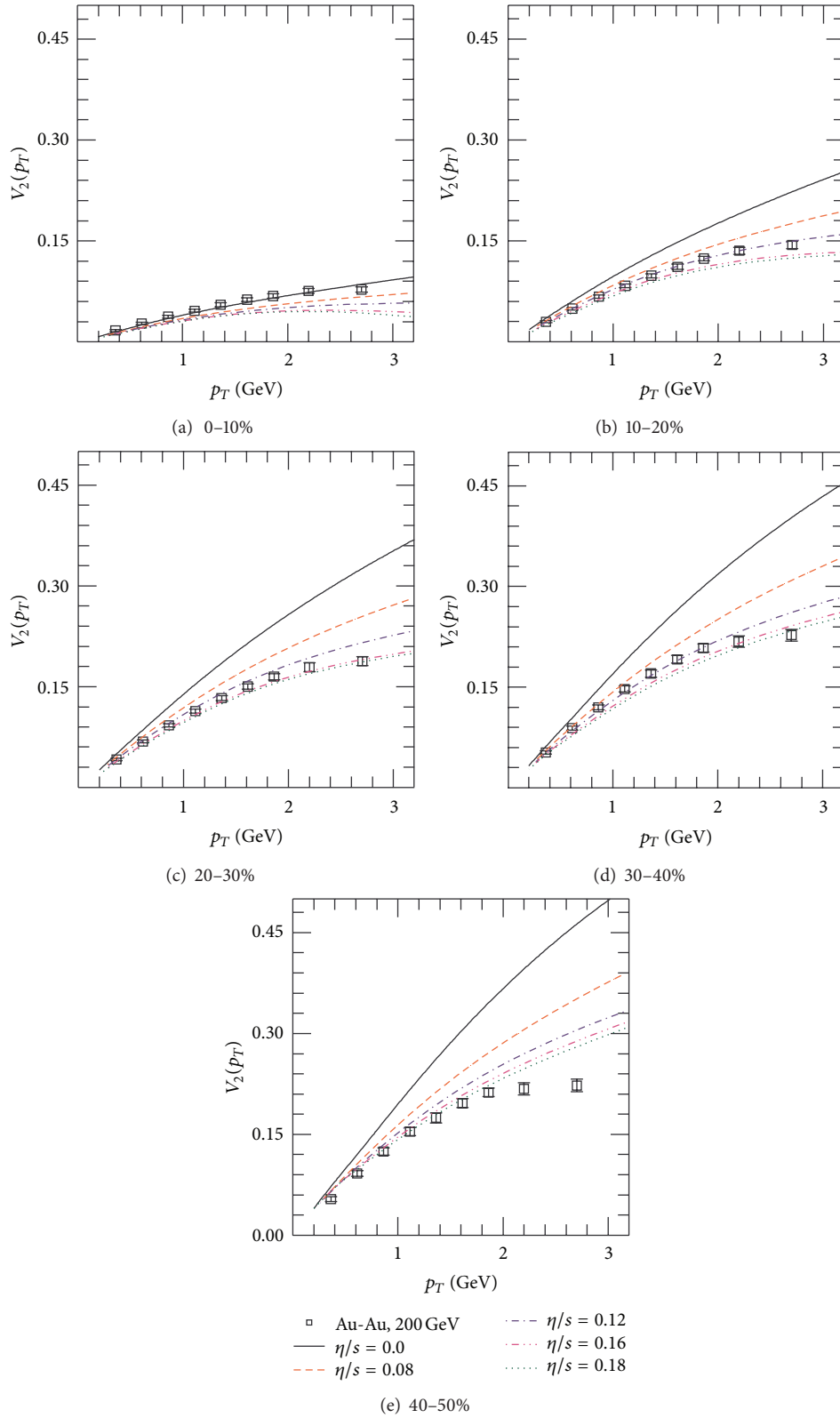


FIGURE 10: Same as in Figure 9 but for elliptic flow. The figures are from [48].

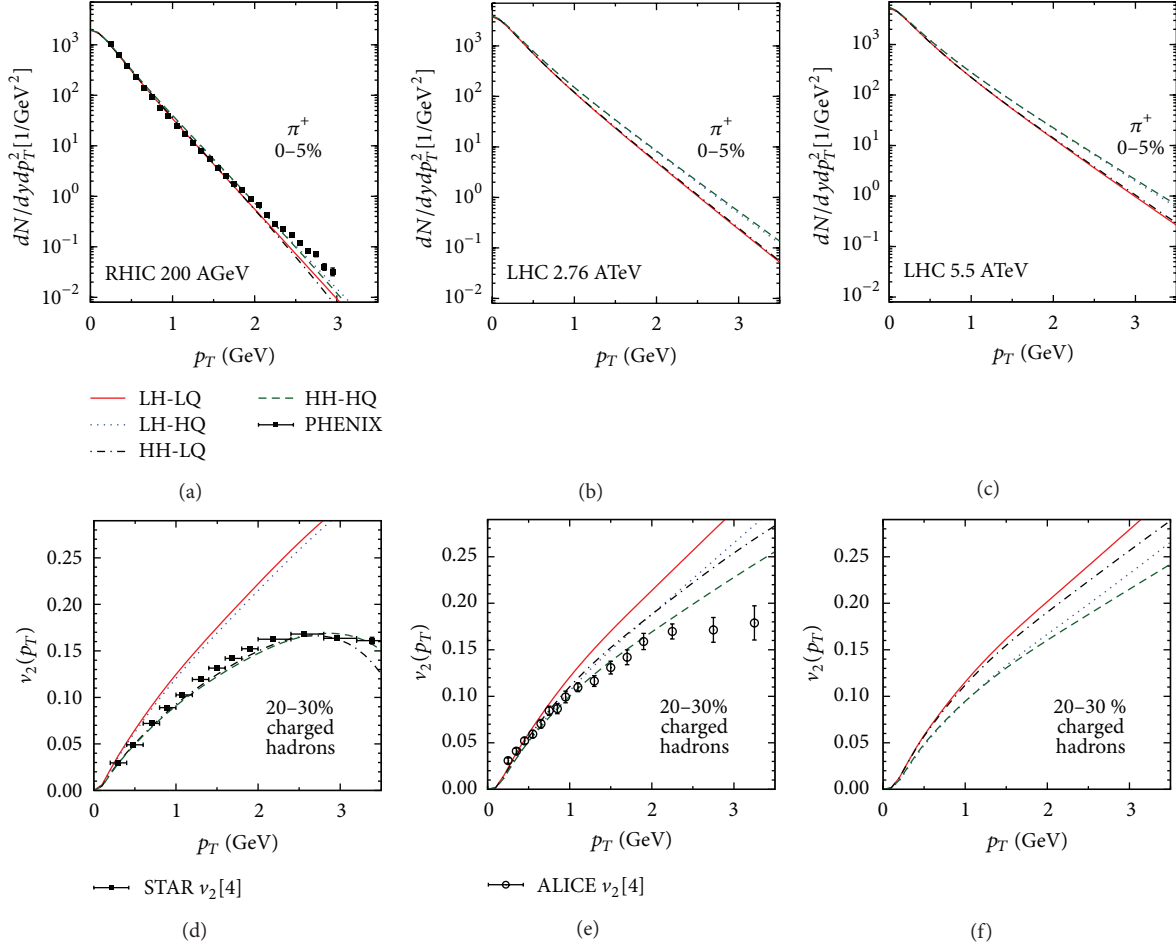


FIGURE 11: Transverse momentum spectra of positive pions in the 0–5% most central collisions and elliptic flow coefficients in the 20–30% centrality class at RHIC and LHC. Different curves correspond to the different parametrizations of the temperature dependence of η/s described in the text. For details, see [105].

was reached the temperature dependence of QGP viscosity over entropy ratio cannot be constrained by fitting p_T spectra and elliptic flow data alone.

9. Event-by-Event Viscous Hydrodynamics

In the preceding section, hydrodynamical simulations discussed used smooth initial condition, either Glauber model or CGC model for initial condition. In recent years, there is much interest in event-by-event hydrodynamics. Unlike in smooth hydrodynamics, in event-by-event hydrodynamics, initial conditions fluctuate event-by-event. Event-by-event hydrodynamics takes into account the possibility that participant positions can fluctuate from event to event. It was also realised in recent years that the participating nucleons, rather than the reaction plane, determine the symmetry plane of the initial collision zone [109]. In Figure 12, a schematic representation of participating nucleons in the transverse plane in a Monte-Carlo event is shown. Geometric overlap region does not coincide with the participating nucleons. It is obvious that the symmetry plane of the participating nucleons is

tilted with respect to the reaction plane. In such a situation, azimuthal angle should be measured with respect to the participant plane rather than the reaction plane. Participant plane can fluctuate, event-by-event, and give rise to the novel phenomena like triangular flow, the third flow harmonic in the Fourier expansion of azimuthal distribution, which will be absent in smooth initial condition. Triangular flow is instrumental in explaining the peculiar structures (known as Ridge) seen in the two particle correlation in $\Delta\phi - \Delta\eta$ plane [110–112]. In Figure 13 two particle correlations in $\Delta\phi - \Delta\eta$ plane, in d+Au and Au+Au collisions are shown. One notices the marked differences in the correlation. Unlike in d+Au collisions, in Au+Au collisions, two particles are correlated over a many units of pseudorapidity $\Delta\eta$. Correlation in the azimuth, however, is narrow. The peculiar structure in two particle correlations known as “ridge” observed both in STAR and PHENIX experiments. The ridge like structure that is also observed in $p\bar{p}$ collisions [113, 114]. The ridge structure has most compelling explanation provided the third flow harmonic, and the triangular flow v_3 develops in the collisions [115–117]. Specifically, if initial condition is parameterized with quadrupole and triangular moments, response of

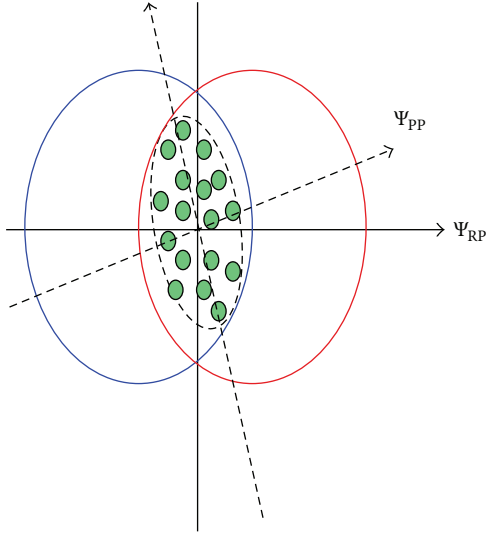


FIGURE 12: A schematic representation for distribution of participant nucleons on the transverse plane in Au+Au collisions in a Monte-Carlo event. The participant plane angle (ψ_{pp}) is tilted with respect to the reaction plane (ψ_{RP}).

the medium to these anisotropies is reflected in the two body correlation as ridge [115, 116].

For example, the azimuthal correlation function can be Fourier decomposed as

$$\frac{dN^{\text{pairs}}}{d\Delta\phi} = \frac{N^{\text{pairs}}}{2\pi} \left(1 + \sum_n 2V_{n\Delta} \cos(n\Delta\phi) \right), \quad (41)$$

where the first component $V_{1\Delta}$ is understood to be due to momentum conservation and directed flow, the second component $V_{2\Delta}$ is dominated by the contribution from elliptic flow, and the third component $V_{3\Delta}$ is dominated by the triangular flow. In Figure 14, PHOBOS and STAR measurements of long range azimuthal correlation in 200 GeV Au+Au collisions are shown. In the top panel of Figure 14, the first three Fourier components of the azimuthal correlations are shown. The bottom panels show the residual after these components are taken out. Evidently, experimental data on two particle correlation are very well described by the three Fourier components. The analysis indicates that the two particle correlation in $\Delta\eta - \Delta\phi$ plane is consistent with hydrodynamic models, if triangular flow develops during the evolution, which is possible only when initial condition fluctuates. Recently, ALICE collaboration has measured triangular flow in $\sqrt{s_{NN}} = 2.76$ TeV Pb+Pb collisions [15]. In most central collisions, the elliptic flow (v_2) and triangular flow (v_3) are of similar magnitude. In peripheral collisions, however, elliptic flow dominates. More recently, PHENIX collaboration [118–120] measured triangular flow in $\sqrt{s_{NN}} = 200$ GeV Au+Au collisions.

In recent years, several authors have simulated Au+Au/Pb+Pb collisions at RHIC/LHC, in event-by-event hydrodynamics [92, 121–132]. Some of the simulation results for event-by-event viscous hydrodynamics are briefly discussed here.

In event-by-event hydrodynamics, one generally uses Monte-Carlo Glauber model or Monte-Carlo CGC (the Kharzeev-Levin-Nardi version) to obtain the initial conditions, event-by-event. Recently, Monte-Carlo CGC model is improved by combining the impact parameter-dependent saturation model [133, 134] of high energy nucleon or nuclear wave function with the classical Yang-Mills description of Glasma fields [135]. The model is called IP-Glasma model [122] for initial condition. In addition to fluctuations of nucleon positions, IP-Glasma description includes quantum fluctuations of color charges on the length scale determined by the inverse nuclear saturation scale Q_s , missed in MC-KLN models [136]. In Figure 15, initial energy density distribution in three types of model, MC-Glauber, MC-KLN, and IP-Glasma is shown. Color charge fluctuations in the length scale Q_s^{-1} introduces addition fluctuations, and in IP-Glasma model, initial density has finer structures than in MC-KLN model or in MC-Glauber model.

Fluid dynamical models require continuous density distribution; however, in event-by-event hydrodynamics, initial conditions are generated using Monte-Carlo algorithm, and in general the distribution is not continuous. For example, in MC-Glauber model, in an event, participants nucleons positions can be obtained. If a particular MC event has N_{part} participants, participants positions in the transverse plane can be labeled as $(x_1, y_1), (x_2, y_2) \dots (x_{N_{\text{part}}}, y_{N_{\text{part}}})$. The energy density in the transverse plane can be approximated as

$$\varepsilon(x, y) \propto \sum_{i=1}^{N_{\text{part}}} \delta(x - x_i, y - y_i). \quad (42)$$

However, the discrete distribution as in (42) cannot be evolved. To use in a hydrodynamic model, the discrete density distribution has to be converted into a smooth energy-density distribution. This can be done by smearing the discrete participant positions by some smoothing function, $\delta(x - x_i, y - y_i) \rightarrow g(x - x_i, y - y_i, \zeta_1, \zeta_2, \dots)$, with ζ_i being parameters of the smoothing function g . Effect of smoothing of was studied in [137]. In Monte-Carlo Glauber model initial participant positions were smoothed with a Gaussian function of various width and Woods-Saxon function of various diffuseness. It was shown that effect of smoothing of participant positions, on elliptic and triangular flow, is minimum.

One important aspect of event-by-event hydrodynamics is the characterisation of the asymmetry of the initial collision zone as well as the azimuthal angle of the participant plane. Each flow harmonics can have their own participant plane. One can generalise the definition of eccentricity to give a simple ansatz to characterise the asymmetry of the initial collision zone [129],

$$\varepsilon_n e^{in\psi_n^{PP}} = - \frac{\int \int \varepsilon(x, y) r^n e^{i2\phi} dx dy}{\int \int \varepsilon(x, y) r^n dx dy}, \quad (43)$$

$$n = 1, 2, 3, 4, 5,$$

where $x = r \cos \phi$ and $y = r \sin \phi$. Equation (43) also determines the participant plane angle ψ_n^{PP} . Asymmetry measures, ε_2 and ε_3 , are called eccentricity and triangularity. ε_4 and ε_5

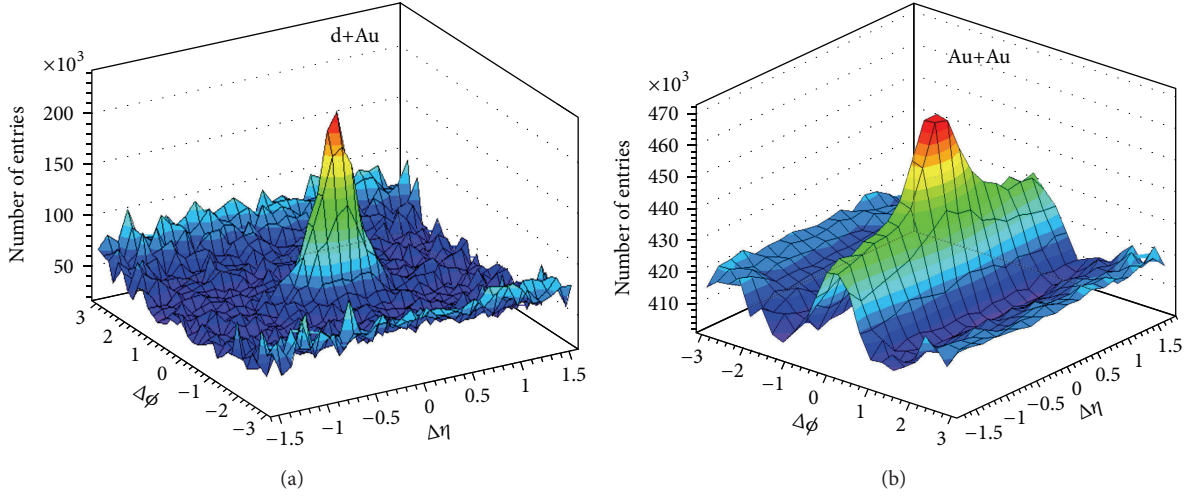


FIGURE 13: Two particle correlations in $\Delta\phi - \Delta\eta$ in d+Au and Au+Au collisions are shown. The results are from STAR experiment.

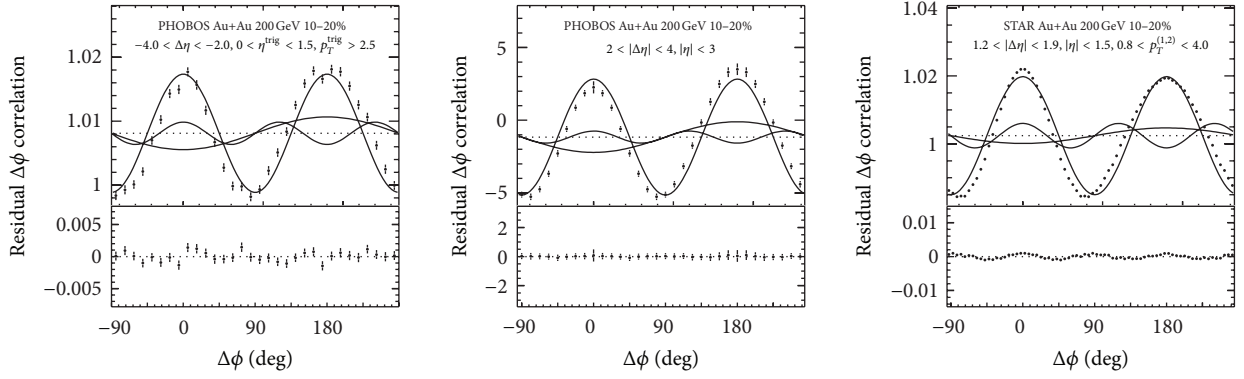


FIGURE 14: Azimuthal correlation functions for midcentral (10–20%) Au+Au collisions at $\sqrt{s_{NN}} = 200$ GeV obtained from projections of two-dimensional $\Delta\phi - \Delta\eta$ correlation measurements by PHOBOS [19, 25] and STAR [41]. The residual correlation functions after the first three Fourier components that are subtracted are shown in the bottom panel. The figure is from [115].

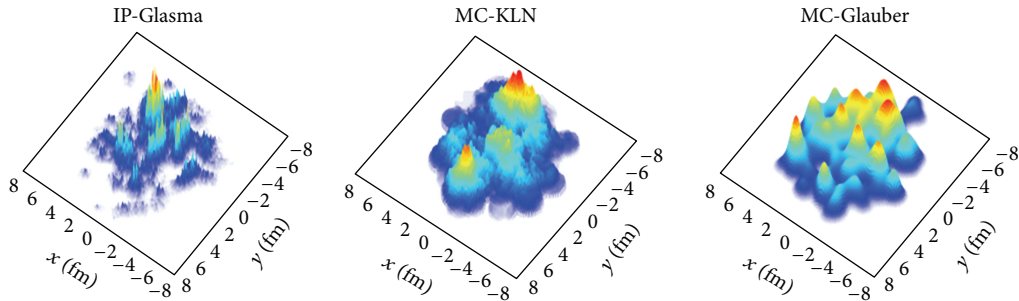


FIGURE 15: Initial energy density (arbitrary units) in the transverse plane in three different heavy ion collision events: from top to bottom, IP-Glasma, MC-KLN, and MC-Glauber models. The figure is from [122].

essentially measure the squareness and five sidedness of the initial distribution. They may be called rectangularity and pentangularity, respectively. Fourth flow coefficient v_4 is generally referred as hexadecapole flow, and rectangular flow may be more appropriate. Similarly v_5 may be referred to as the pentangular flow.

Viscous effects on elliptic and triangular flow, in event-by-event hydrodynamics, were studied in [92]. The results are shown in Figures 16 and 17. In [92], a 3 + 1 dimensional hydrodynamical model was used. As it was in smooth hydrodynamics, effect of viscosity is to reduce the elliptic flow. More viscous is the fluid, and less is the elliptic flow. Except in

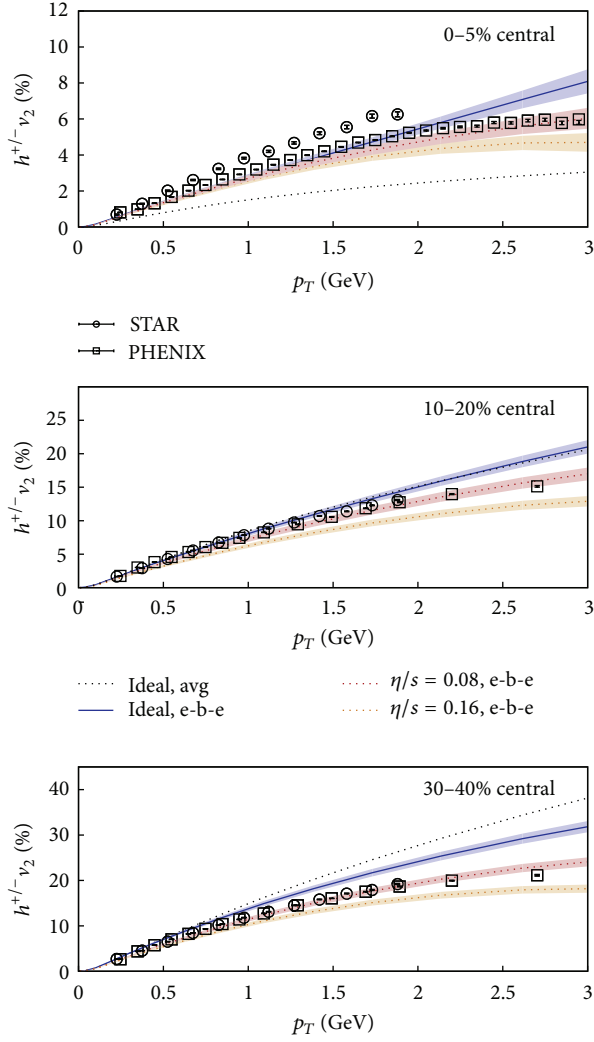


FIGURE 16: Charged hadron elliptic flow (v_2) for different centralities as a function of transverse momentum for averaged initial conditions (avg) and event-by-event simulations (e-b-e) using different viscosity to entropy density ratios compared to STAR [33] and PHENIX [34] data. The figures are from [92].

very central collision, where event-by-event hydrodynamics produces less flow than that in smooth hydrodynamics (the curve labeled as “avg”), the increase of v_2 in central 0–5% collision is understood. In event-by-event hydrodynamics, v_2 is determined in each event. Single events have a larger anisotropy with respect to the event plane than the average with respect to the reaction plane, and v_2 is increased. In more peripheral collisions, the effect reduces, and event-by-event v_2 becomes smaller than that for smooth initial condition. Triangular flow is completely fluctuation driven and depend less strongly on collision centrality than the elliptic flow. Triangular flow also reduces with viscosity. One also understands that triangular flow is more sensitive to viscosity than the elliptic flow. For example, in 30–40% collision, at $p_T \approx 1.5$ GeV, elliptic flow reduces by $\sim 15\%$ and 30% when η/s is increased from 0 to 0.08 and 0.12, respectively. The reduction in triangular flow is much larger, respectively, $\sim 30\%$ and 45% .

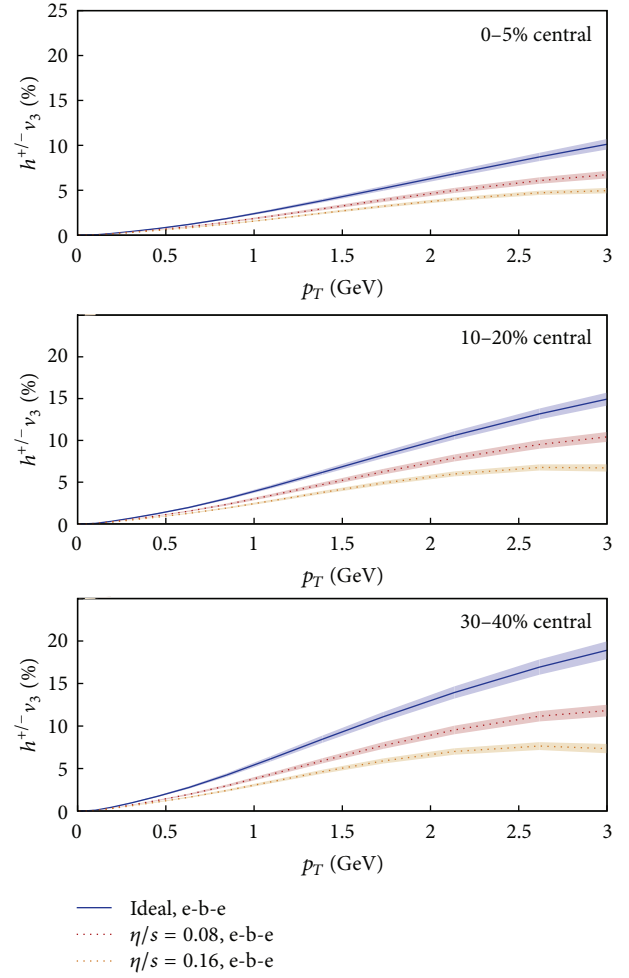


FIGURE 17: Same as in Figure 16 but for triangular flow. The figures are from [92].

One expects that experimental data on triangular flow can constrain viscosity over entropy ratio much better than the elliptic flow data.

In Figure 18, event-by-event hydrodynamic simulations, with IP-Glasma initial condition, are compared with ALICE measurements for p_T spectra of pion, kaon, and proton [92]. Viscosity over entropy ratio was fixed at $\eta/s = 0.2$. One find that simulations with IP-Glasma initial condition explains the p_T spectra of charged particles rather nicely. IP-Glasma initial condition also explain the measured flow coefficients rather nicely. In Figure 19, simulations results are compared with ATLAS measurements. Charged particles flow coefficients v_2 , v_3 , v_4 , and v_5 appear to agree with the experimental measurements. However, whether or not similar fit can be obtained with other values of viscosity over entropy ratio was not explored in [92].

In Figures 16 and 17, only event averaged flows are shown. In event-by-event hydrodynamics, participant plane fluctuates. It is natural then the flow coefficient also fluctuates. Unless the fluctuations are within some reasonable limit, sensitivity of the flow to viscosity over entropy ratio will reduce greatly. In [138] fluctuations in elliptic and triangular flow in

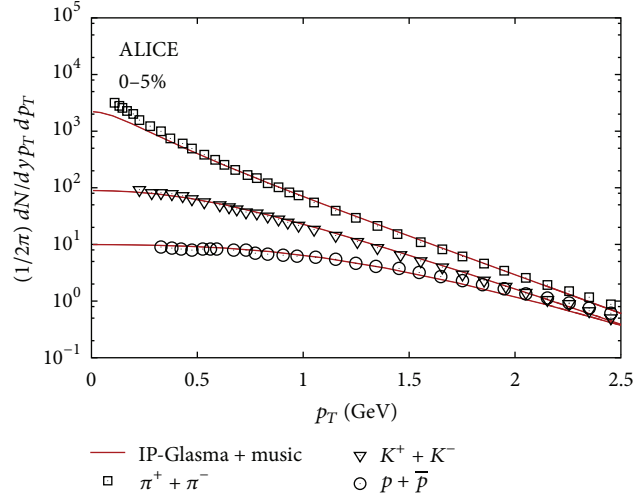


FIGURE 18: ALICE measurements for the transverse momentum spectra of pion, kaon, and protons in 0–5% Pb+Pb collisions at LHC energy are compared with IP-Glasma model predictions with viscosity over entropy ratio $\eta/s = 0.08$. The figures are from [123].

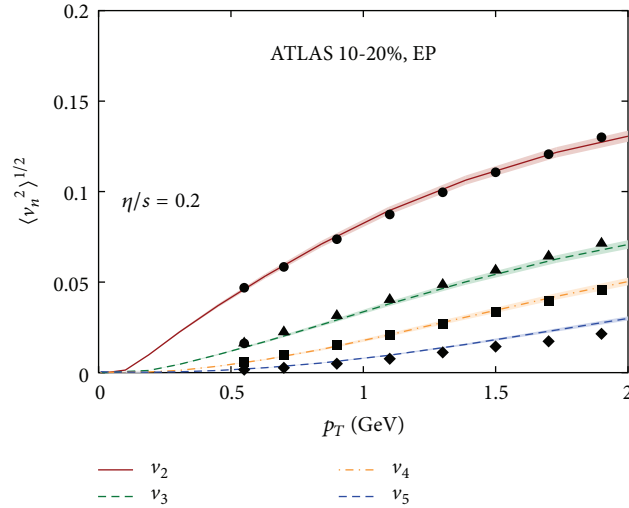


FIGURE 19: ATLAS measurements for the flow coefficients v_n , $n = 2, 3, 4, 5$ are compared with IP-Glasma model predictions. The figures are from [123].

event-by-event hydrodynamic were studied. 30–40% Pb+Pb collisions at $\sqrt{s_{NN}} = 2.76$ TeV was simulated in event-by-event hydrodynamics. Four values of viscosity over entropy ratio were considered, $\eta/s = 0, 0.08, 0.12,$ and 0.16 . Simulation results are shown in Figures 20 and 21. In Figures 20 and 21, the symbols represent the event averaged values and the bars the variances. As it was shown earlier, event-averaged flow coefficients smoothly decrease with increasing viscosity. However, both elliptic and triangular flow fluctuates strongly. For example, in the p_T range 1–3 GeV, fluctuations in $v_2(p_T)$ are $\sim 15\text{--}20\%$. Fluctuations in $v_3(p_T)$ are even more $\sim 70\text{--}80\%$. The fluctuations in anisotropic flow greatly reduce their efficacy as a diagnostic tool. For example, within the fluctuations, differential elliptic flow does not distinguish between ideal fluid and fluid with viscosity to entropy ratio 0.08. Triangular flow is even more insensitive. Fluid viscosity over entropy ratio η/s varying between 0 and 0.16 is not

distinguished. It was also shown in [138] that the fluctuations are not statistical and cannot be eliminated by increasing the number of events. Reduced sensitivity of elliptic and triangular flow towards viscosity belies the possibility of constraining shear viscosity from a simultaneous fit to elliptic and triangular flow.

In a hydrodynamic model, collective flow is a response of the spatial asymmetry of the initial state. For example, elliptic flow is the response of ellipticity of the initial medium. If ellipticity in the initial medium is characterized by spatial eccentricity, $\epsilon_2 = \langle y^2 - x^2 \rangle / \langle y^2 + x^2 \rangle$, more eccentric is the initial medium, and more flow will be generated, $v_2 \propto \epsilon_2$. Similar correlation is expected between the triangular flow and initial triangularity. Recently in [131], the correlation between asymmetry measures ϵ_n and flow coefficients v_n was studied in event-by-event hydrodynamics. As it was in smooth hydrodynamics, in event-by-event hydrodynamics

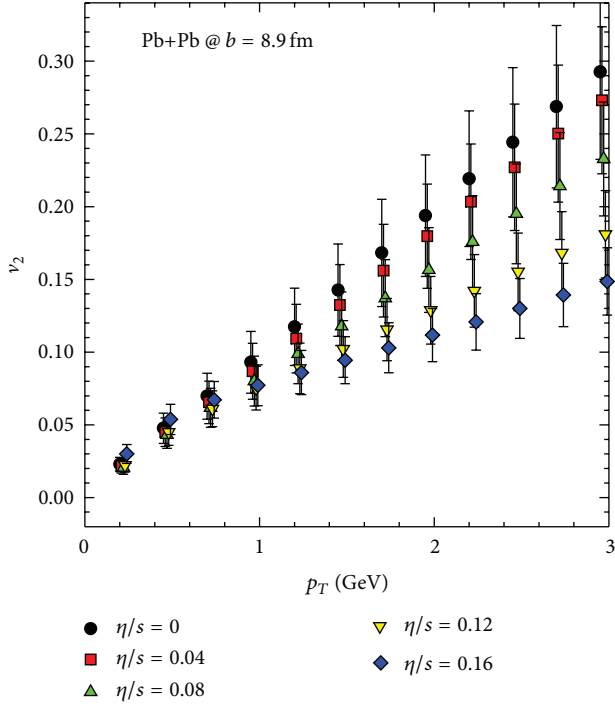


FIGURE 20: Differential elliptic flow (v_2) for viscosity to entropy ratio $\eta/s = 0, 0.04, 0.08, 0.12,$ and 0.16 . The colored symbols represent the event average, bars, and the variance. The figures are from [138].

also, elliptic flow is strongly correlated with initial eccentricity. Triangular flow was also found to be correlated with initial triangularity. Higher flow harmonics, however, are only weakly correlated with initial eccentricity measured. It was shown that to correctly predict v_4 and v_5 , one must take into account nonlinear terms proportional ϵ_2^2 and $\epsilon_2\epsilon_3$, respectively. Correlation between initial (spatial) asymmetry measures and flow coefficients was also studied in [140]. Similar results were obtained. Higher flow coefficients are only weakly correlated with initial asymmetry measures, and the correlations are weakened in more peripheral collisions. However, in [131, 140] only ideal fluid was considered, dependence on viscosity was not investigated. Since viscosity introduces additional length scales, qualitatively, one can argue that correlation between momentum anisotropy of the produced particles and asymmetry of initial density distribution will reduce in presence of viscosity. Effect of viscosity on the correlation between elliptic flow and initial eccentricity and between triangular flow and initial triangularity was studied in [139]. In Figure 22, event-by-event hydrodynamic simulations for elliptic flow in 30–40% Pb+Pb collisions are plotted against the initial eccentricity. For perfect correlation $v_2 \propto \epsilon_2$, all the points should lie on a straight line. In ideal hydrodynamics, elliptic flow is strongly correlated with initial eccentricity. Scattering of the points around a common straight line is very small. Scattering increases in viscous evolution indicating that the correlation is weakened. Even then scattering of the points is not large even for large viscosity $\eta/s = 0.16$, and one understands that the correlation between initial eccentricity and elliptic flow remains strong in ideal

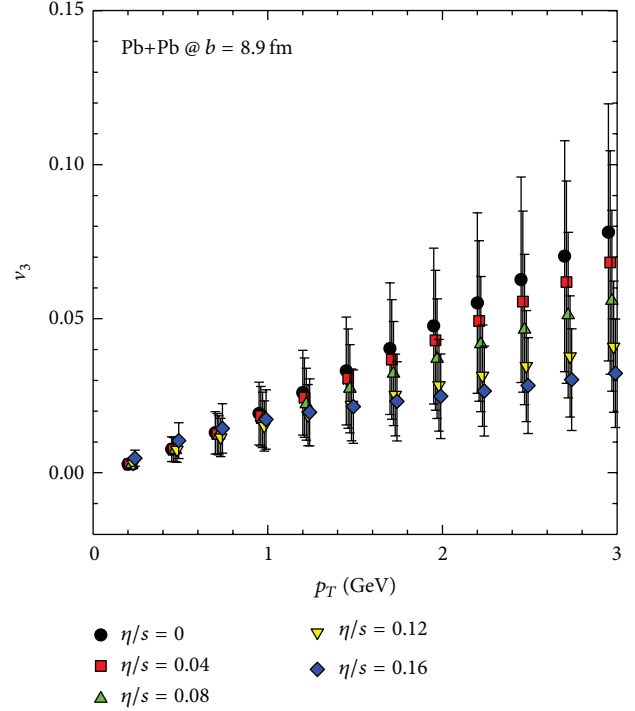


FIGURE 21: Same as in Figure 20 but for triangular flow. The figures are from [138].

and viscous hydrodynamics. Simulation result for triangular flow is shown in Figure 23. Comparatively large scattering of the points indicates that the correlation between triangular flow and initial triangularity is comparatively weak. Viscosity further weakens the correlation. In [139], a viscous effect on higher flow correlations was not studied. It will be interesting to see the effect of viscosity on higher flow coefficients and in other collision centralities.

Comparatively weak correlation in higher flow harmonics with the eccentricity measures can be understood, qualitatively. In Figure 24, primary shapes of the collision zone, responsible elliptic, triangular, rectangular, and pentangular flow are shown. Thick arrows attached to the shapes indicate the primary direction of particle emission. One notices that elliptic shape for elliptic flow can contribute both to elliptic and to rectangular flow (indicated by the thin arrows) and vice versa. However, since $v_4 \ll v_2$, elliptic flow will be less affected by the contamination than the rectangular flow. Then while elliptic flow and initial eccentricity will be correlated strongly, correlation between rectangular flow and initial rectangularity will be comparatively weak. Similarly, triangular shape can contribute both to triangular flow and pentangular flow. Here again, since $v_5 \ll v_3$, triangular flow will be less affected than the pentangular flow.

10. Summary

In the preceding sections, I have briefly discussed some aspects of viscous hydrodynamics. Viscous hydrodynamics has been greatly successful in explaining many experimental

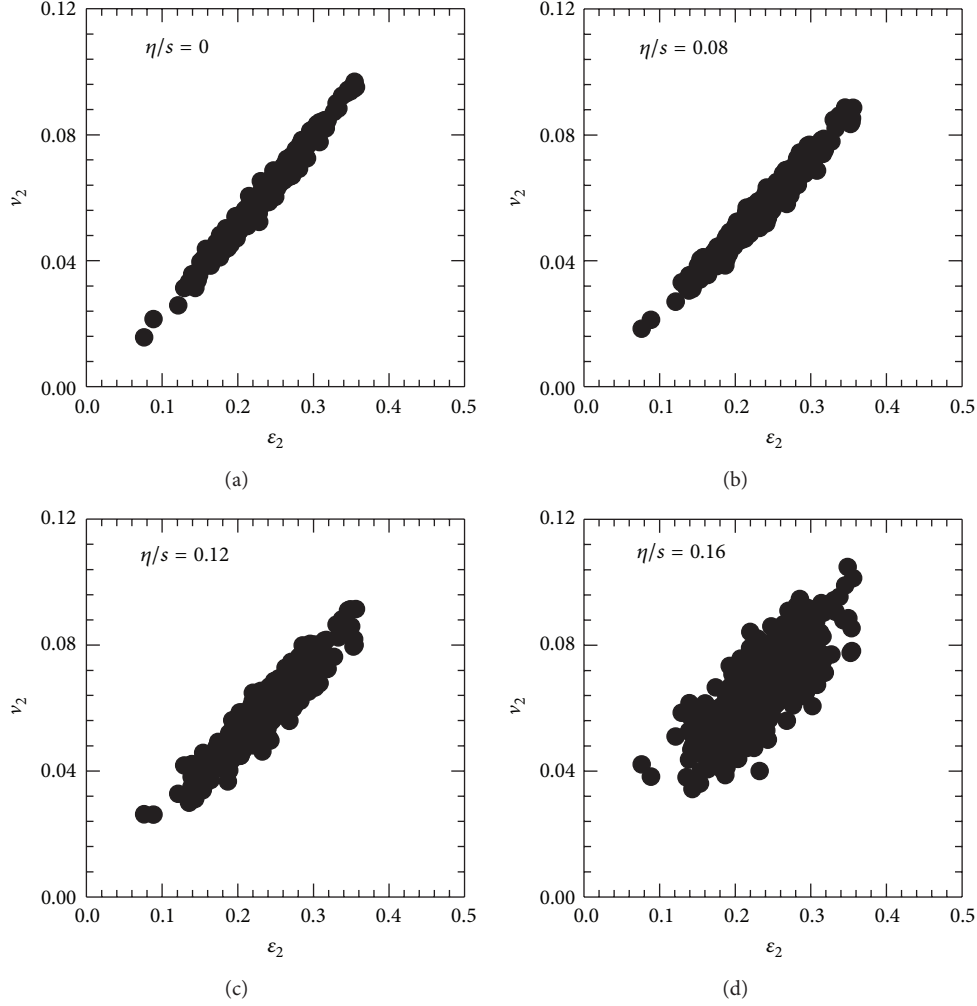


FIGURE 22: Correlation between elliptic flow (v_2) and initial eccentricity (ϵ_2) is shown for four values of fluid viscosity to entropy ratio $\eta/s = 0, 0.08, 0.12, \text{ and } 0.16$. The figure is from [139].

data in high energy collisions, in particular, data related to the bulk production. However, there are several issues that need to be investigated. For example, hydrodynamics modeling of nuclear collisions require a number of parameters to be fixed initially, for example, initial time, initial energy density/velocity/shear (bulk) stress tensor profile, freeze-out, and so forth. Intercorrelation between these parameters is not fully investigated. How the intercorrelations affect sensitive observables like elliptic or triangular flow is not known. Several attempts have been made to extract QGP viscosity over entropy ratio from hydrodynamical analysis of experimental data. However, how the extracted viscosity over entropy ratio depends on the intercorrelation between different initial conditions was not investigated. In [98], an attempt was made to obtain systematic uncertainty in extracted η/s due to uncertain initial conditions, but the investigation was not complete. The small thermalisation time used in most of the simulations is also an issue. The mechanism of fast thermalisation is not understood. It was mentioned previously that chromo-Weibel instability was found to be inadequate to thermalise the medium in the time scale ~ 1 fm. If indeed,

thermalisation takes longer time, for example, ~ 5 fm in LHC energy and ~ 10 fm in RHIC energy [61], then many of our understanding, in particular regarding elliptic flow, need to be readjusted. Freeze-out is also an issue, in particular in event-by-event hydrodynamics. Unlike in smooth initial condition, in event-by-event hydrodynamic, the initial condition is granular. Some interior parts of the fluid can freeze-out early, but the hadrons emitted from that part may not come out but absorbed in the medium. The medium can be reheated. The issue needs to be investigated. Freeze out issue may be less important in hybrid models, where the late stage of evolution is governed by transport equations. But hybrid model requires an arbitrary parameter, the switching temperature, below which hydrodynamic description give way to transport description. The issue of temperature dependence of viscosity over entropy ratio is also not fixed. Is the temperature dependence linear or more complex? Whether or not the experimental data on bulk production can fix empirically the temperature dependence of QGP viscosity over entropy ratio is uncertain. In the present review, bulk viscosity was not discussed in details. Bulk viscosity may also become

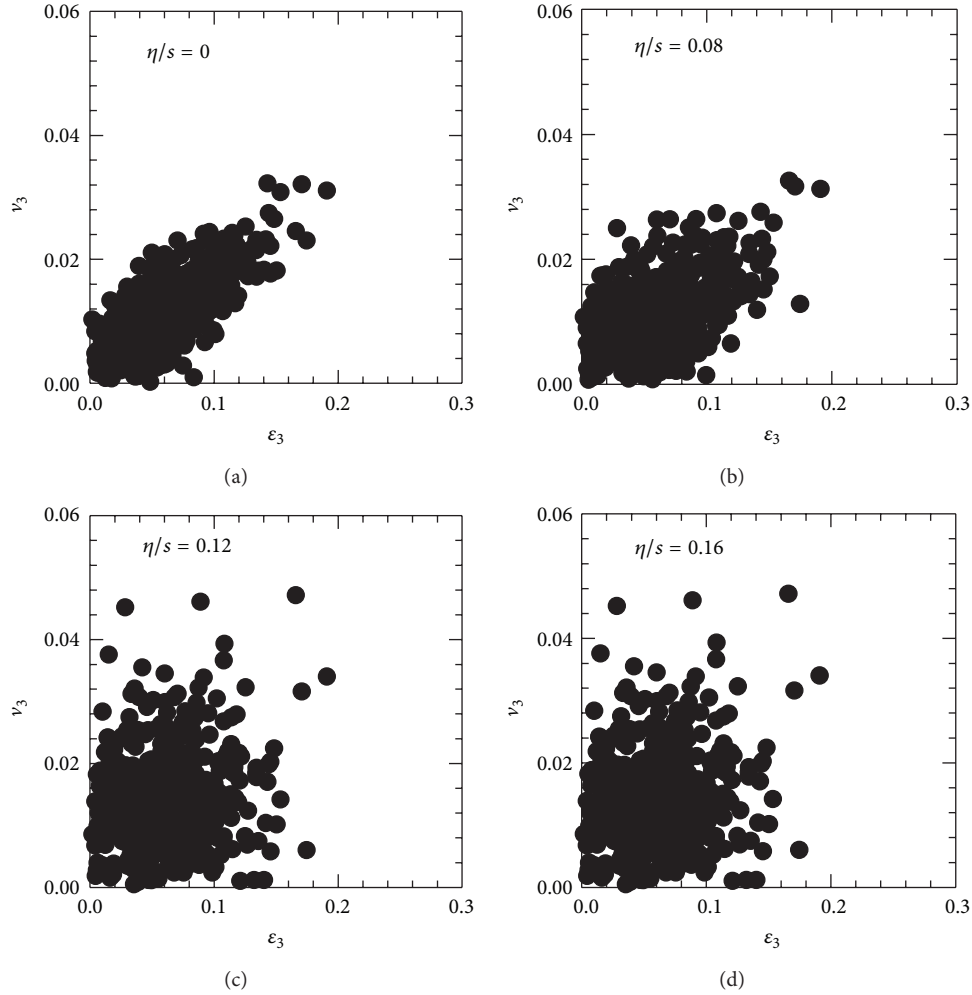


FIGURE 23: Correlation between triangular flow (v_3) and initial triangularity (ϵ_3) is shown for four values of fluid viscosity to entropy ratio $\eta/s = 0, 0.08, 0.12,$ and 0.16 . The figure is from [139].

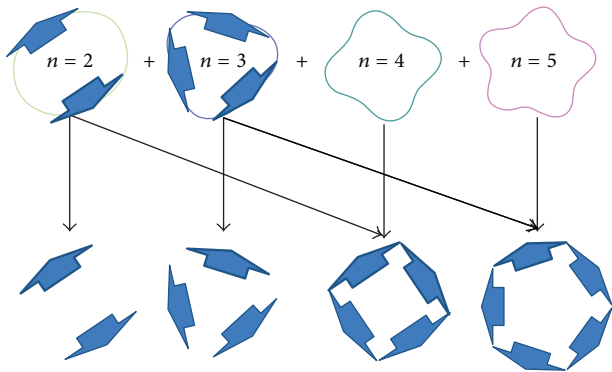


FIGURE 24: Primary shapes for v_n , $n = 2-5$ are shown. The thick arrows indicate the dominant directions of particle emission. The thin arrows indicate the shapes which contribute to each other.

an important issue in understanding experimental data in terms of hydrodynamic models. As it was noted earlier, correct form for the nonequilibrium correction due to bulk

viscosity is still an issue and needed to be investigated in detail.

References

- [1] F. Karsch, “Equation of state and more from lattice regularized QCD,” *Journal of Physics G*, vol. 35, no. 10, Article ID 104096, 2008.
- [2] M. Cheng, S. Ejiri, P. Hegde et al., “Equation of State for physical quark masses,” *Physical Review D*, vol. 81, no. 5, Article ID 054504, 8 pages, 2010.
- [3] Y. Aoki, G. Endrodi, Z. Fodor, S. D. Katz, and K. K. Szabó, “The order of the quantum chromodynamics transition predicted by the standard model of particle physics,” *Nature*, vol. 443, no. 7112, pp. 675–678, 2006.
- [4] Z. Fodor, “QCD thermodynamics on the lattice: approaching the continuum limit with physical quark masses,” *Journal of Physics: Conference Series*, vol. 230, Article ID 012013, 2010.
- [5] Y. Aoki, S. Borsanyi, S. Durr et al., “QCD transition temperature: approaching the continuum on the lattice,” *Nuclear Physics A*, vol. 830, no. 1–4, 2009.

- [6] S. Borsányi, G. Endrődi, Z. Fodor et al., “The QCD equation of state with dynamical quarks,” *Journal of High Energy Physics*, vol. 1011, 077, 2010.
- [7] I. Arsene, I. G. Bearden, D. Beavis et al. et al., “Quark-gluon plasma and the color glass condensate at RHIC? The perspective from the BRAHMS experiment,” *Nuclear Physics A*, vol. 757, p. 1, 2005.
- [8] B. B. Back, M. D. Baker, M. Ballintijn et al., “The PHOBOS perspective on discoveries at RHIC,” *Nuclear Physics A*, vol. 757, p. 28, 2005.
- [9] K. Adcox, S. S. Adler, S. Afanasiev et al., “Formation of dense partonic matter in relativistic nucleus nucleus collisions at RHIC: experimental evaluation by the PHENIX collaboration,” *Nuclear Physics A*, vol. 757, pp. 184–283, 2005.
- [10] J. Adams, M. M. Aggarwal, Z. Ahammed et al., “Experimental and theoretical challenges in the search for the quark gluon plasma: the STAR Collaboration’s critical assessment of the evidence from RHIC collisions,” *Nuclear Physics A*, vol. 757, p. 102, 2005.
- [11] K. Aamodt, B. Abelev, A. A. Quintana et al., “Charged-particle multiplicity density at mid-rapidity in central Pb-Pb collisions at $\sqrt{s_{NN}} = 2.76$ TeV,” *Physical Review Letters*, vol. 105, no. 25, Article ID 252301, 11 pages, 2010.
- [12] K. Aamodt, A. A. Quintana, D. Adamová et al., “Centrality dependence of the charged-particle multiplicity density at mid-rapidity in Pb-Pb collisions at $\sqrt{s_{NN}} = 2.76$ TeV,” *Physical Review Letters*, vol. 106, no. 3, Article ID 032301, 10 pages, 2011.
- [13] K. Aamodt, A. A. Quintana, D. Adamová et al., “Suppression of charged particle production at large transverse momentum in central Pb-Pb collisions at $\sqrt{s_{NN}} = 2.76$ TeV,” *Physics Letters B*, vol. 696, no. 1-2, pp. 30–39, 2011.
- [14] K. Aamodt, B. Abelev, A. A. Quintana et al., “Elliptic flow of charged particles in Pb-Pb collisions at $\sqrt{s_{NN}} = 2.76$ TeV,” *Physical Review Letters*, vol. 105, no. 25, Article ID 252302, 11 pages, 2010.
- [15] K. Aamodt, B. Abelev, A. A. Quintana et al., “Higher harmonic anisotropic flow measurements of charged particles in Pb-Pb collisions at $\sqrt{s_{NN}} = 2.76$ TeV,” *Physical Review Letters*, vol. 107, no. 3, Article ID 032301, 10 pages, 2011.
- [16] F. Cooper and G. Frye, “Single-particle distribution in the hydrodynamic and statistical thermodynamic models of multiparticle production,” *Physical Review D*, vol. 10, no. 1, pp. 186–189, 1974.
- [17] P. F. Kolb and U. Heinz, “Hydrodynamic description of ultra-relativistic heavy-ion collisions,” in *Quark-Gluon Plasma 3*, R. C. Hwa and X. N. Wang, Eds., pp. 634–714, World Scientific, Singapore, 2004.
- [18] G. Policastro, D. T. Son, and A. O. Starinets, “Shear viscosity of strongly coupled $N = 4$ supersymmetric Yang-Mills plasma,” *Physical Review Letters*, vol. 87, no. 8, Article ID 081601, pp. 816011–816014, 2001.
- [19] G. Policastro, D. T. Son, and A. O. Starinets, “From AdS/CFT correspondence to hydrodynamics,” *Journal of High Energy Physics*, vol. 2002, article 0209, 043, 2002.
- [20] P. Kovtun, D. T. Son, and A. O. Starinets, “Holography and hydrodynamics: diffusion on stretched horizons,” *Journal of High Energy Physics*, vol. 2003, article 0310, 064, 2003.
- [21] U. Heinz, “Hydrodynamics at RHIC: how well does it work, where and how does it break down?” *Journal of Physics G*, vol. 31, no. 6, pp. S717–S724, 2005.
- [22] U. W. Heinz and P. F. Kolb, “Two RHIC puzzles: early thermalization and the HBT problem,” <http://arxiv.org/abs/hep-ph/0204061>.
- [23] P. Danielewicz and M. Gyulassy, “Dissipative phenomena in quark-gluon plasmas,” *Physical Review D*, vol. 31, no. 1, pp. 53–62, 1985.
- [24] C. Eckart, “The thermodynamics of irreversible processes. II,” *Physical Review*, vol. 58, no. 10, pp. 919–924, 1940.
- [25] L. D. Landau and E. M. Lifshitz, *Fluid Mechanics*, section 127, Pergamon, Oxford, UK, 1963.
- [26] W. A. Hiscock and L. Lindblom, “Generic instabilities in first-order dissipative relativistic fluid theories,” *Physical Review D*, vol. 31, no. 4, pp. 725–733, 1985.
- [27] W. A. Hiscock and L. Lindblom, “Stability and causality in dissipative relativistic fluids,” *Annals of Physics*, vol. 151, no. 2, pp. 466–496, 1983.
- [28] W. Israel, “Nonstationary irreversible thermodynamics: a causal relativistic theory,” *Annals of Physics*, vol. 100, no. 1-2, pp. 310–331, 1976.
- [29] W. Israel and J. M. Stewart, “Transient relativistic thermodynamics and kinetic theory,” *Annals of Physics*, vol. 118, no. 2, pp. 341–372, 1979.
- [30] A. Muronga, “Causal theories of dissipative relativistic fluid dynamics for nuclear collisions,” *Physical Review C*, vol. 69, no. 3, pp. 034903–1, 2004.
- [31] B. Betz, G. S. Denicol, T. Koide, E. Molnar, H. Niemi, and D. H. Rischke, “Second order dissipative fluid dynamics from kinetic theory,” in *Proceedings of the International Workshop on Hot and Cold Baryonic Matter (HCBM ’10)*, vol. 13, p. 8, 2011.
- [32] G. S. Denicol, H. Niemi, E. Molnar, and D. H. Rischke, “Derivation of transient relativistic fluid dynamics from the Boltzmann equation,” *Physical Review D*, vol. 85, no. 11, Article ID 114047, 22 pages, 2012.
- [33] A. Jaiswal, R. S. Bhalerao, and S. Pal, “New relativistic dissipative fluid dynamics from kinetic theory,” *Physics Letters B*, vol. 720, no. 4-5, pp. 347–351, 2013.
- [34] A. Jaiswal, R. S. Bhalerao, and S. Pal, “Complete relativistic second-order dissipative hydrodynamics from the entropy principle,” *Physical Review C*, vol. 87, Article ID 021901, 2013.
- [35] F. Karsch, D. Kharzeev, and K. Tuchin, “Universal properties of bulk viscosity near the QCD phase transition,” *Physics Letters B*, vol. 663, no. 3, pp. 217–221, 2008.
- [36] D. Kharzeev and K. Tuchin, “Bulk viscosity of QCD matter near the critical temperature,” *Journal of High Energy Physics*, vol. 2008, article 093, 2008.
- [37] R. J. Fries, B. Muller, and A. Schafer, “Stress tensor and bulk viscosity in relativistic nuclear collisions,” *Physical Review C*, vol. 78, no. 3, Article ID 034913, 7 pages, 2008.
- [38] A. Monnai and T. Hirano, “Effects of bulk viscosity at freezeout,” *Physical Review C*, vol. 80, no. 5, Article ID 054906, 10 pages, 2009.
- [39] K. Dusling and T. Schfer, “Bulk viscosity, particle spectra and flow in heavy-ion collisions,” *Physical Review C*, vol. 85, no. 4, Article ID 044909, 19 pages, 2012.
- [40] H. Song and U. Heinz, “Viscous hydrodynamics with bulk viscosity—uncertainties from relaxation time and initial conditions,” *Nuclear Physics A*, vol. 830, no. 1–4, 2009.
- [41] H. Song and U. Heinz, “Interplay of shear and bulk viscosity in generating flow in heavy-ion collisions,” *Physical Review D*, vol. 81, no. 2, Article ID 024905, 12 pages, 2010.

- [42] V. Roy and A. K. Chaudhuri, “2 + 1 dimensional hydrodynamics including bulk viscosity: a systematic study,” *Physical Review C*, vol. 85, no. 2, Article ID 024909, 13 pages, 2012, Erratum in *Physical Review C*, vol. 85, Article ID 049902, 2012.
- [43] R. Venugopalan and M. Prakash, “Thermal properties of interacting hadrons,” *Nuclear Physics, Section A*, vol. 546, no. 4, pp. 718–760, 1992.
- [44] P. Huovinen and P. Petreczky, “QCD equation of state and hadron resonance gas,” *Nuclear Physics A*, vol. 837, no. 1-2, pp. 26–53, 2010.
- [45] V. Roy and A. K. Chaudhuri, “Charged particle’s elliptic flow in (2+1)D viscous hydrodynamics at LHC ($\sqrt{s} = 2.76$ TeV) energy in Pb+Pb collision,” *Physics Letters, Section B*, vol. 703, no. 3, pp. 313–317, 2011.
- [46] T. Hirano and Y. Nara, “Hydrodynamic afterburner for the color glass condensate and the parton energy loss,” *Nuclear Physics A*, vol. 743, no. 4, pp. 305–328, 2004.
- [47] M. Luzum and P. Romatschke, “Conformal relativistic viscous hydrodynamics: applications to RHIC results at $\sqrt{s_{NN}} = 2.76$ GeV,” *Physical Review C*, vol. 79, no. 3, Article ID 034915, 778.
- [48] V. Roy, A. K. Chaudhuri, and B. Mohanty, “Comparison of results from a 2+1D relativistic viscous hydrodynamic model to elliptic and hexadecapole flow of charged hadrons measured in Au-Au collisions at $\sqrt{s_{NN}} = 200$ GeV,” *Physical Review C*, vol. 86, no. 1, Article ID 014902, 9 pages, 2012.
- [49] L. McLerran, “A brief introduction to the color glass condensate and the glasma,” <http://arxiv.org/abs/0812.4989>.
- [50] E. Iancu, A. Leonidov, and L. McLerran, “The renormalization group equation for the color glass condensate,” *Physics Letters, Section B*, vol. 510, no. 1-4, pp. 133–144, 2001.
- [51] E. Iancu, A. Leonidov, and L. McLerran, “Nonlinear gluon evolution in the color glass condensate: I,” *Nuclear Physics A*, vol. 692, no. 3-4, pp. 583–645, 2001.
- [52] J. Jalilian-Marian, A. Kovner, A. Leonidov, and H. Weigert, “The BFKL equation from the Wilson renormalization group,” *Nuclear Physics B*, vol. 504, no. 1-2, pp. 415–431, 1997.
- [53] J. Jalilian-Marian, A. Kovner, A. Leonidov, and H. Weigert, “Wilson renormalization group for low x physics: towards the high density regime,” *Physical Review D*, vol. 59, no. 1, Article ID 014014, 6 pages, 1999.
- [54] D. Kharzeev, E. Levin, and M. Nardi, “Color glass condensate at the LHC: Hadron multiplicities in pp, pA and AA collisions,” *Nuclear Physics A*, vol. 747, no. 2-4, pp. 609–629, 2005.
- [55] A. Adil, H.-J. Drescher, A. Dumitru, A. Hayashigaki, and Y. Nara, “Eccentricity in heavy-ion collisions from color glass condensate initial conditions,” *Physical Review C*, vol. 74, no. 4, Article ID 044905, 2006.
- [56] D. Kharzeev, E. Levin, and M. Nardi, “QCD saturation and deuteron-nucleus collisions,” *Nuclear Physics A*, vol. 730, no. 4, pp. 448–459, 2004, Erratum in *Nuclear Physics A*, vol. 743, pp. 329–331, 2004.
- [57] H. Song, S. A. Bass, U. Heinz, T. Hirano, and C. Shen, “200 A GeV Au+Au collisions serve a nearly perfect quark-gluon liquid,” *Physical Review Letters*, vol. 106, Article ID 192301, 4 pages, 2011, Erratum in *Physical Review Letters*, vol. 109, Article ID 139904, 2012.
- [58] P. Romatschke and U. Romatschke, “Viscosity information from relativistic nuclear collisions: how perfect is the fluid observed at RHIC?” *Physical Review Letters*, vol. 99, no. 17, Article ID 172301, 2007.
- [59] A. K. Chaudhuri, “Viscous fluid dynamics in Au+Au collisions at RHIC,” <http://arxiv.org/abs/0801.3180>.
- [60] P. Arnold, J. Lenaghan, G. D. Moore, and L. G. Yaffe, “Apparent thermalization due to plasma instabilities in the quark-gluon plasma,” *Physical Review Letters*, vol. 94, no. 7, Article ID 072302, 2005.
- [61] M. Attems, A. Rebhan, and M. Strickland, “Longitudinal thermalization via the chromo-Weibel instability,” <http://arxiv.org/abs/1301.7749>.
- [62] P. B. Arnold, G. D. Moore, and L. G. Yaffe, “Transport coefficients in high temperature gauge theories (I): leading-log results,” *Journal of High Energy Physics*, vol. 2000, article 11, 001, 2000.
- [63] P. B. Arnold, G. D. Moore, and L. G. Yaffe, “Transport coefficients in high temperature gauge theories, 2. Beyond leading log,” *Journal of High Energy Physics*, vol. 2003, article 05, 051, 2003.
- [64] A. Nakamura and S. Sakai, “Transport coefficients of a gluon plasma,” *Physical Review Letters*, vol. 94, no. 7, Article ID 072305, 4 pages, 2005.
- [65] R. Kubo, “Statistical-mechanical theory of irreversible processes. I. General theory and simple applications to magnetic and conduction problems,” vol. 12, pp. 570–586, 1957.
- [66] R. Kubo, “The fluctuation-dissipation theorem,” *Reports on Progress in Physics*, vol. 29, article 255, 1966.
- [67] J. I. Kapusta, “Viscous properties of strongly interacting matter at high temperature,” <http://arxiv.org/abs/0809.3746>.
- [68] A. Nakamura and S. Sakai, “Viscosities of Hot Gluon—a Lattice QCD Study,” *Nuclear Physics A*, vol. 774, no. 1-4, pp. 775–778, 2006.
- [69] O. Aharony, S. S. Gubser, J. Maldacena, H. Ooguri, and Y. Oz, “Large N field theories, string theory and gravity,” *Physics Report*, vol. 323, no. 3-4, pp. 183–386, 2000.
- [70] S. R. Das, G. Gibbons, and S. D. Mathur, “Universality of low energy absorption cross sections for black holes,” *Physical Review Letters*, vol. 78, no. 3, pp. 417–419, 1997.
- [71] P. Arnold, C. Dogan, and G. D. Moore, “Bulk viscosity of high-temperature QCD,” *Physical Review D*, vol. 74, no. 8, Article ID 085021, 13 pages, 2006.
- [72] S. Weinberg, “Entropy generation and the survival of protogalaxies in an expanding universe,” *Astrophysical Journal*, vol. 168, p. 175, 1971.
- [73] P. Benincasa, A. Buchel, and A. O. Starinets, “Sound waves in strongly coupled non-conformal gauge theory plasma,” *Nuclear Physics B*, vol. 733, no. 1-2, pp. 160–187, 2006.
- [74] A. Buchel, “Bulk viscosity of gauge theory plasma at strong coupling,” *Physics Letters B*, vol. 663, no. 3, pp. 286–289, 2008.
- [75] M. Prakash, M. Prakash, R. Venugopalan, and G. Welke, “Nonequilibrium properties of hadronic mixtures,” *Physics Report*, vol. 227, no. 6, pp. 321–366, 1993.
- [76] J. Noronha-Hostler, J. Noronha, and C. Greiner, “Transport coefficients of hadronic matter near T_c ,” *Physical Review Letters*, vol. 103, no. 17, Article ID 172302, 2009.
- [77] N. Demir and S. A. Bass, “Shear-viscosity to entropy-density ratio of a relativistic hadron gas,” *Physical Review Letters*, vol. 102, no. 17, Article ID 172302, 4 pages, 2009.
- [78] A. El, A. Muronga, Z. Xu, and C. Greiner, “Shear viscosity and out of equilibrium dynamics,” *Physical Review C*, vol. 79, no. 4, Article ID 044914, 10 pages, 2009.

- [79] L. P. Csernai, J. I. Kapusta, and L. D. McLerran, “Strongly interacting low-viscosity matter created in relativistic nuclear collisions,” *Physical Review Letters*, vol. 97, no. 15, Article ID 152303, 2006.
- [80] R. A. Lacey, N. N. Ajitanand, J. M. Alexander et al., “Has the QCD critical point been signaled by observations at the BNL relativistic heavy ion collider?” *Physical Review Letters*, vol. 98, no. 9, Article ID 092301, 2007.
- [81] J. Cleymans, H. Oeschler, K. Redlich, and S. Wheaton, “Status of chemical freeze-out,” *Journal of Physics G*, vol. 32, no. 12, article no. S21, 2006.
- [82] F. Becattini, J. Manninen, and M. Gaździcki, “Energy and system size dependence of chemical freeze-out in relativistic nuclear collisions,” *Physical Review C*, vol. 73, no. 4, Article ID 044905, 2006.
- [83] S. A. Bass and A. Dumitru, “Dynamics of hot bulk QCD matter: from the quark-gluon plasma to hadronic freeze-out,” *Physical Review C*, vol. 61, no. 6, Article ID 064909, 24 pages, 2000.
- [84] T. Hirano, U. Heinz, D. Kharzeev, R. Lacey, and Y. Nara, “Hadronic dissipative effects on elliptic flow in ultrarelativistic heavy-ion collisions,” *Physics Letters, Section B*, vol. 636, no. 6, pp. 299–304, 2006.
- [85] H. Song, S. A. Bass, and U. Heinz, “Elliptic flow in $\sqrt{s} = 200$ GeV Au+Au collisions and $\sqrt{s} = 2.76$ TeV Pb+Pb collisions: insights from viscous hydrodynamics + hadron cascade hybrid model,” *Physical Review C*, vol. 83, no. 5, Article ID 054912, 6 pages, 2011, Erratum in *Physical Review C*, vol. 87, Article ID 019902, 2013.
- [86] H. Song, S. A. Bass, U. Heinz, T. Hirano, and C. Shen, “Hadron spectra and elliptic flow for 200 A GeV Au+Au collisions from viscous hydrodynamics coupled to a Boltzmann cascade,” *Physical Review C*, vol. 83, no. 5, Article ID 054910, 2011, Erratum in *Physical Review C*, vol. 86, Article ID 059903, 2012.
- [87] H. Song, S. A. Bass, and U. Heinz, “Viscous QCD matter in a hybrid hydrodynamic+Boltzmann approach,” *Physical Review C*, vol. 83, no. 2, Article ID 024912, 16 pages, 2011.
- [88] A. M. Poskanzer and S. A. Voloshin, “Methods for analyzing anisotropic flow in relativistic nuclear collisions,” *Physical Review C*, vol. 58, no. 3, pp. 1671–1678, 1998.
- [89] S. A. Voloshin, A. M. Poskanzer, and R. Snellings, “Collective phenomena in non-central nuclear collisions,” in *Relativistic Heavy Ion Physics*, vol. 23 of *Landolt-Börnstein-Group I Elementary Particles, Nuclei and Atoms*, pp. 293–333, Springer, Berlin, Germany, 2010.
- [90] J.-Y. Ollitrault, “Anisotropy as a signature of transverse collective flow,” *Physical Review D*, vol. 46, no. 1, pp. 229–245, 1992.
- [91] K. Dusling and D. Teaney, “Simulating elliptic flow with viscous hydrodynamics,” *Physical Review C*, vol. 77, no. 3, Article ID 034905, 2008.
- [92] B. Schenke, S. Jeon, and C. Gale, “Elliptic and triangular flow in event-by-event D=3+1 viscous hydrodynamics,” *Physical Review Letters*, vol. 106, no. 4, Article ID 042301, 2011.
- [93] P. Bozek, “Flow and interferometry in 3 + 1 dimensional viscous hydrodynamics,” *Physical Review C*, vol. 85, Article ID 034901, 9 pages, 2012.
- [94] G. S. Denicol, T. Kodama, and T. Koide, “The effect of shear and bulk viscosities on elliptic flow,” *Journal of Physics G*, vol. 37, no. 9, Article ID 094040, 2010.
- [95] C. Nonaka and M. Asakawa, “Modeling a realistic dynamical model for high energy heavy ion collisions,” *Progress of Theoretical and Experimental Physics*, vol. 2012, Article ID 01A208, 2012.
- [96] V. Roy, *Dissipative fluid dynamics for ultra-relativistic nuclear collisions [Ph.D. thesis]*, Homi Bhabha National Institute, 2012.
- [97] H. Song and U. Heinz, “Extracting the QGP viscosity from RHIC data—a status report from viscous hydrodynamics,” *Journal of Physics G*, vol. 36, no. 6, Article ID 064033, 2009.
- [98] A. K. Chaudhuri, “Nearly perfect fluid in Au + Au collisions at RHIC,” *Physics Letters, Section B*, vol. 681, no. 5, pp. 418–422, 2009.
- [99] A. K. Chaudhuri, “Centrality dependence of elliptic flow and QGP viscosity,” *Journal of Physics G*, vol. 37, no. 7, Article ID 075011, 2010.
- [100] V. Roy and A. K. Chaudhuri, “Charged particle’s elliptic flow in 2+1D viscous hydrodynamics at LHC, ($\sqrt{s} = 2.76$ TeV) energy in Pb+Pb collision,” *Physics Letters B*, vol. 703, no. 313, p. 317, 2011.
- [101] B. Schenke, S. Jeon, and C. Gale, “Anisotropic flow in $\sqrt{s} = 2.76$ TeV Pb+Pb collisions at the LHC,” *Physics Letters, Section B*, vol. 702, no. 1, pp. 59–63, 2011.
- [102] P. Bozek, “Components of the elliptic flow in Pb-Pb collisions at $\sqrt{s} = 2.76$ TeV,” *Physics Letters, Section B*, vol. 699, no. 4, pp. 283–286, 2011.
- [103] J. P. Boris and D. L. Book, “Flux-corrected transport. I. SHASTA, a fluid transport algorithm that works,” *Journal of Computational Physics*, vol. 11, no. 1, pp. 38–69, 1973.
- [104] D. H. Rischke, S. Bernard, and J. A. Maruhn, “Relativistic hydrodynamics for heavy-ion collisions. I. General aspects and expansion into vacuum,” *Nuclear Physics A*, vol. 595, no. 3, pp. 346–382, 1995.
- [105] H. Niemi, G. S. Denicol, P. Huovinen, E. Molnár, and D. H. Rischke, “Influence of shear viscosity of quark-gluon plasma on elliptic flow in ultrarelativistic heavy-ion collisions,” *Physical Review Letters*, vol. 106, no. 21, Article ID 212302, 2011.
- [106] G. S. Denicol, T. Kodama, and T. Koide, “The effect of shear and bulk viscosities on elliptic flow,” *Journal of Physics G*, vol. 37, no. 9, Article ID 094040, 2010.
- [107] C. Shen and U. Heinz, “Hydrodynamic flow in heavy-ion collisions with large hadronic viscosity,” *Physical Review C*, vol. 83, no. 4, Article ID 044909, 10 pages, 2011.
- [108] A. K. Chaudhuri, “Temperature dependence of QGP viscosity over entropy ratio from hydrodynamical analysis of ALICE data in $\sqrt{s_{NN}} = 2.76$ TeV Pb+Pb collisions,” *Journal of Physics G*, vol. 39, no. 12, Article ID 125102, 2012.
- [109] S. Manly, “System size, energy and pseudorapidity dependence of directed and elliptic flow at RHIC,” *Nuclear Physics A*, vol. 774, no. 1–4, pp. 523–526, 2006.
- [110] J. Adams, C. Adler, M. M. Aggarwal et al., “Distributions of charged hadrons associated with high transverse momentum particles in *pp* and Au + Au collisions at $\sqrt{s_{NN}} = 200$ GeV,” *Physical Review Letters*, vol. 95, no. 15, Article ID 152301, 6 pages, 2005.
- [111] J. Putschke, “Intra-jet correlations of high-pt hadrons from STAR,” *Journal of Physics G*, vol. 34, no. 8, article no. S72, pp. S679–S683, 2007.
- [112] B. I. Abelev, M. M. Aggarwal, Z. Ahammed et al., “Indications of conical emission of charged hadrons at RHIC,” *Physical Review Letters*, vol. 102, no. 5, Article ID 052302, 7 pages, 2009.
- [113] V. Khachatryan, M. Sirunyan, A. Tumasyan et al., “Observation of long-range, near-side angular correlations in proton-proton collisions at the LHC,” *Journal of High Energy Physics*, article 91, 2010.

- [114] D. Velicanu, “Ridge correlation structure in high-multiplicity pp collisions with CMS,” *Journal of Physics G*, vol. 38, no. 12, Article ID 124051, 2011.
- [115] B. Alver and G. Roland, “Collision-geometry fluctuations and triangular flow in heavy-ion collisions,” *Physical Review C*, vol. 81, Article ID 054905, 2010.
- [116] B. H. Alver, C. Gombeaud, M. Luzum, and J.-Y. Ollitrault, “Triangular flow in hydrodynamics and transport theory,” *Physical Review C*, vol. 82, no. 3, Article ID 034913, 2010.
- [117] P. Sorensen, “Implications of space-momentum correlations and geometric fluctuations in heavy-ion collisions,” *Journal of Physics G*, vol. 37, no. 9, Article ID 094011, 2010.
- [118] A. Adare, S. Afanasiev, C. Aidala et al., “Elliptic and hexadecapole flow of charged hadrons in Au+Au collisions at $\sqrt{s_{NN}} = 200$ GeV,” *Physical Review Letters*, vol. 105, no. 6, Article ID 062301, 6 pages, 2010.
- [119] A. Adare, S. Afanasiev, C. Aidala et al., “Measurements of higher order flow harmonics in Au + Au Collisions at $\sqrt{s_{NN}} = 200$ GeV,” *Physical Review Letters*, vol. 107, no. 25, Article ID 252301, 7 pages, 2011.
- [120] R. Lacey, “PHENIX measurements of higher order flow harmonics in Au+Au collisions at $\sqrt{s_{NN}} = 200$ GeV,” *Journal of Physics G*, vol. 38, no. 12, Article ID 124048, 2011.
- [121] B. Schenke, S. Jeon, and C. Gale, “Higher flow harmonics from (3 + 1)D event-by-event viscous hydrodynamics,” *Physical Review C*, vol. 85, no. 2, Article ID 024901, 2012.
- [122] B. Schenke, P. Tribedy, and R. Venugopalan, “Fluctuating Glasma initial conditions and flow in heavy ion collisions,” *Physical Review Letters*, vol. 108, no. 25, Article ID 252301, 5 pages, 2012.
- [123] C. Gale, S. Jeon, B. Schenke, P. Tribedy, and R. Venugopalan, “Event-by-event anisotropic flow in heavy-ion collisions from combined Yang-Mills and viscous fluid dynamics,” *Physical Review Letters*, vol. 110, no. 1, Article ID 012302, 5 pages, 2013.
- [124] H. Petersen, G.-Y. Qin, S. A. Bass, and B. Muller, “Triangular flow in event-by-event ideal hydrodynamics in Au+Au collisions at $\sqrt{s_{NN}} = 200$ A GeV,” *Physical Review C*, vol. 82, no. 4, Article ID 041901, 5 pages, 2010.
- [125] H. Holopainen, H. Niemi, and K. J. Eskola, “Event-by-event hydrodynamics and elliptic flow from fluctuating initial states,” *Physical Review C*, vol. 83, no. 3, Article ID 034901, 2011.
- [126] H. Niemi, G. S. Denicol, H. Holopainen, and P. Huovinen, “Event-by-event distributions of azimuthal asymmetries in ultrarelativistic heavy-ion collisions,” *Physical Review C*, no. 5, Article ID 054901, 8 pages, 2013.
- [127] K. Werner, I. Karpenko, T. Pierog, M. Bleicher, and K. Mikhailov, “Event-by-event simulation of the three-dimensional hydrodynamic evolution from flux tube initial conditions in ultrarelativistic heavy ion collisions,” *Physical Review C*, vol. 82, no. 4, Article ID 044904, 2010.
- [128] C. E. Aguiar, Y. Hama, T. Kodama, and T. Osada, “Event-by-event fluctuations in hydrodynamical description of heavy-ion collisions,” *Nuclear Physics A*, vol. 698, no. 1–4, 2002.
- [129] Z. Qiu and U. Heinz, “Event-by-event shape and flow fluctuations of relativistic heavy-ion collision fireballs,” *Physical Review C*, vol. 84, no. 2, Article ID 024911, 2011.
- [130] P. Boek and W. Broniowski, “Transverse-momentum fluctuations in relativistic heavy-ion collisions from event-by-event viscous hydrodynamics,” *Physical Review C*, vol. 85, no. 4, Article ID 044910, 2012.
- [131] F. G. Gardim, F. Grassi, M. Luzum, and J.-Y. Ollitrault, “Mapping the hydrodynamic response to the initial geometry in heavy-ion collisions,” *Physical Review C*, vol. 85, no. 2, Article ID 024908, 2012.
- [132] F. G. Gardim, F. Grassi, M. Luzum, and J.-Y. Ollitrault, “Characterizing the hydrodynamic response to the initial conditions,” *Nuclear Physics A*, vol. 904–905, pp. 503–506, 2013.
- [133] J. Bartels, K. J. Golec-Biernat, and H. Kowalski, “A modification of the saturation model: DGLAP evolution,” *Physical Review D*, vol. 66, no. 1, Article ID 014001, 9 pages, 2002.
- [134] H. Kowalski and D. Teaney, “Impact parameter dipole saturation model,” *Physical Review D*, vol. 68, no. 11, Article ID 114005, 2003.
- [135] A. Kovner, L. McLerran, and H. Weigert, “Gluon production from non-Abelian Weizsäcker-Williams fields in nucleus-nucleus collisions,” *Physical Review D*, vol. 52, no. 11, pp. 6231–6237, 1995.
- [136] A. Dumitru and Y. Nara, “KNO scaling of fluctuations in pp and pA, and eccentricities in heavy-ion collisions,” *Physical Review C*, vol. 85, no. 3, Article ID 034907, 2012.
- [137] M. Rihan Haque, V. Roy, and A. K. Chaudhuri, “Fluctuating initial condition and smoothening effect on elliptic and triangular flow,” *Physical Review C*, vol. 86, no. 3, Article ID 037901, 2012.
- [138] A. K. Chaudhuri, “Fluctuating initial conditions and fluctuations in elliptic and triangular flow,” *Physics Letters B*, vol. 710, no. 2, pp. 339–342, 2012.
- [139] A. K. Chaudhuri, “Influence of shear viscosity on the correlation between the triangular flow and initial spatial triangularity,” *Physics Letters B*, vol. 713, pp. 91–94, 2012.
- [140] A. K. Chaudhuri, M. R. Haque, V. Roy, and B. Mohanty, “Event-by-event hydrodynamical simulations for $\sqrt{s_{NN}} = 200$ GeV Au+Au collisions and the correlation between flow coefficients and initial asymmetry measures,” *Physical Review C*, vol. 87, Article ID 034907, 2013.

Research Article

Tubular Initial Conditions and Ridge Formation

M. S. Borysova,¹ O. D. Borysov,² Iu. A. Karpenko,^{3,4} V. M. Shapoval,³ and Yu. M. Sinyukov³

¹ Kyiv Institute for Nuclear Research, Kiev 03083, Ukraine

² FNAL, Batavia, IL 60510, USA

³ Bogolyubov Institute for Theoretical Physics, Kiev 03680, Ukraine

⁴ FIAS, Ruth Moufang Street 1, 60438 Frankfurt am Main, Germany

Correspondence should be addressed to Yu. M. Sinyukov; sinyukov@bitp.kiev.ua

Received 13 April 2013; Revised 12 June 2013; Accepted 10 July 2013

Academic Editor: Edward Sarkisyan-Grinbaum

Copyright © 2013 M. S. Borysova et al. This is an open access article distributed under the Creative Commons Attribution License, which permits unrestricted use, distribution, and reproduction in any medium, provided the original work is properly cited.

The 2D azimuth and rapidity structure of the two-particle correlations in relativistic A+A collisions is altered significantly by the presence of sharp inhomogeneities in superdense matter formed in such processes. The causality constraints enforce one to associate the long-range longitudinal correlations observed in a narrow angular interval, the so-called (soft) ridge, with peculiarities of the initial conditions of collision process. This study's objective is to analyze whether multiform initial tubular structures, undergoing the subsequent hydrodynamic evolution and gradual decoupling, can form the soft ridges. Motivated by the flux-tube scenarios, the initial energy density distribution contains the different numbers of high density tube-like boost-invariant inclusions that form a bumpy structure in the transverse plane. The influence of various structures of such initial conditions in the most central A+A events on the collective evolution of matter, resulting spectra, angular particle correlations and v_n -coefficients is studied in the framework of the hydrokinetic model (HKM).

1. Introduction

The correlation and fluctuation study is a valuable tool for probing the dynamics of heavy-ion collisions, the initial conditions, and for exploring the thermodynamic properties of strongly interacting matter at extremely high temperatures and/or densities. The data from the experiments at RHIC revealed interesting features in the two-particle correlation landscape [1–6]. Specifically, an excess of correlated particles in a wide pseudorapidity interval and a narrow azimuthal angle range $\Delta\phi$ was firstly measured in the relativistic heavy-ion collisions by the STAR collaboration [1]. The pair correlation on the near side of the trigger particle (with $p_T = 2.5$ –15 GeV) was found to be extended across the entire detector pseudorapidity acceptance region $\Delta\eta \sim 3$ –4 units. Such a correlation structure was called “the ridge.” The ridges are observed both in the correlations of particles with a jet triggering (the “hard” ridge) and in the correlations without a high p_T trigger particle (the “soft” ridge). The analyses of measurements by the PHENIX [5] and PHOBOS [6] RHIC collaborations confirmed the STAR results. In ALICE LHC

experiment it was found that the soft ridge is consistent with expectations from collective response to anisotropic initial conditions [7]. Moreover, the recent measurements by CMS collaboration [8, 9] detected unexpected similar effect in proton-proton collisions at LHC. The clear and significant ridge structure emerges at $\Delta\phi \approx 0$, extending to $|\Delta\eta|$ of at least 4 units. This novel feature of the data has never been seen in two-particle correlation functions in pp or $p\bar{p}$ collisions before.

The discovery of the ridge structures has aggravated quantitative theoretical analyses of nucleus-nucleus and proton-proton collisions but brought the new physical ideas. Early models of the ridge formation were based on the opposite physical mechanisms. Some authors treated the ridge as an initial-state effect [10]; the others explored final-state effects, soft interactions, and jet propagation in anisotropic plasma as the origin of the ridge [11]. In the former case the authors argued that due to causality constraints the long-range correlations within 4 units of pseudorapidity could be explained only if they originated from the very initial collision stage. They could be a consequence of the correlations

in the classical color fields responsible for multiparticle production in relativistic heavy-ion collisions. Then, due to fluctuations of color charges in colliding nuclei, the longitudinally boost-invariant and transversally bumpy structure of the matter can be formed. As for the hard ridges, these correlations are associated with jet propagation that gives relatively narrow correlations in pseudorapidity. The interesting attempt to combine soft and hard ridge structures is done in [12]. It is based on interaction of jets with pieces of expanding bulk matter boosted by the transverse flow.

The role of fluctuations in the formation of the soft observables was first considered in [13, 14], and their ability to produce ridges in [15]. Alver and Roland [16] observed that the correlations arising from geometrical fluctuations in the initial conditions result in odd flow harmonics such as a triangular flow v_3 . Then one can suppose that v_3 , together with flow harmonics of all higher orders, could explain the excess in the long-ranged two-particle correlations. It has been recently shown in measurements [8, 9, 17–19] and demonstrated in various modelings [20–22] that there are fairly strong fluctuations in the initial matter profile from event to event. Such fluctuations contain various higher order harmonics in azimuthal angle $\sim \cos(n\phi)$. After the collective expansion of the bulk matter, these fluctuations lead to observed harmonic flows up to about $n = 6$. There is a hope that such high harmonics can explain the soft dihadron azimuthal correlations—the soft ridge. It means, in fact, that the soft ridges originate from the fluctuating initial conditions altogether with the specific set of Fourier n -harmonics. It also seems that the fluctuations of the initial conditions, associated with ridges, are of specific type. This issue is studied in the present paper.

If the soft ridge is caused by the peculiarities of the initial space structure of the bulk matter, then this effect should be analyzed within hydrodynamics models of A+A collisions, which are now the standard approach to the description of such processes. During more than 50 years the hydrodynamic models were based on the smooth initial energy density profiles (see, e.g., [23, 24] for the ridge problem). However, it has been shown that fluctuations in the positions of nucleons within the colliding nuclei from event to event may lead to significant deviations from the smooth regular profiles in one event [25]. The similar effect can be caused by the fluctuations of the local color charge in color glass condensate effective field theory [26]. This irregular structure of the initial conditions for hydrodynamic evolution was explored in [15, 27, 28] for analysis of the ridge phenomenon. It becomes clear that the most important factor for ridge formation is not just the variation of the geometry form of initial system from event to event, but strongly inhomogeneous bumpy structure of the initial energy density profile in the transverse plane. Such initial structure is subjected to further nontrivial evolution during the system expansion. The different mechanisms can be responsible for the formation of the bumps in the initial energy density profile, for example, it can be longitudinal strings as in Nexus [15], color flux tubes, arising between large locally fluctuating color charges in colliding nuclei. These fluctuations have the form of very narrow and dense, approximately boost-invariant longitudinal tubes, shifted

differently from the center in transverse plane, on the top of smoothly distributed energy density. The number of the tubes also can be different. The analysis of the ridge formation in the case of one peripheral tube has been done in [15] with the Cooper-Frye prescription for freeze-out. The analogous analysis for multitube systems was provided in [29, 30].

In this work we continue to analyze possibilities of ridge formation at sharp disturbances of the initial energy density. The evolution and spectra formation for the system with bumpy initial energy density profile is analyzed within the hydrokinetic model (HKM) [31–34] which incorporates description of all the stages of the system evolution, including the afterburn one, responsible for continuous particle liberation from expanding decoupling system. Previously it was found that the effect of the initial bump-like fluctuations is not washed out during the system expansion and leads to the specific final energy density distributions [30, 35, 36]. In this paper we examine the influence of tube-like fluctuations of different type on the observed particle spectra, azimuthal correlations, and magnitudes of the Fourier harmonics. To highlight the role of the bumpy structure, we limit our present study to the most central collisions only, say $c = 0$ –2%. In contrast to the noncentral collisions, with strong initial eccentricity already in average (in the framework of the variable geometry analysis) and large 2nd flow harmonic produced, in the perfectly central collisions ($b = 0$) the background geometry is isotropic, and the anisotropy and v_n -coefficients, caused by the fluctuating bumpy structure only, will be best manifested.

2. Model Description

The hydrokinetic approach, which we use as the basic model of the matter evolution, is described in detail in [32, 33]. It contains the perfect hydrodynamic component, related to expanding quark-gluon matter, and the kinetic one, describing the system decay and the spectra formation due to gradual particle liberation from expanding hadron-resonance matter. We consider the transversally bumpy, tube-like IC aiming to study how the initial fluctuations in the energy density distribution affect the spectra, azimuthal correlations, and flows. For the sake of simplicity, these results are presented only for one kind of particles—negative pions π^- .

The HKM in its original version [32, 33] is (2+1)D model based on the boost-invariant Bjorken-type IC, where the longitudinal flow has quasi-inertial form and is related to the initial proper time $\tau_i = \sqrt{t^2 - z^2}$, when (partial) thermalization is established and further evolution can be described by hydrodynamics. The transverse dynamics of the prethermal stage starts at very early time $\tau_0 = 0.1$ –0.2 fm/c just after the c.m.s. energy in the overlapping region of colliding nuclei exceeds their binding energy. The thermalization can hardly happen before 1 fm/c (1–1.5 fm/c is the lowest known estimate of the thermalization time). However, if one starts hydrodynamics at that time, neither radial nor elliptic flow can develop well enough to explain experimental transverse spectra and their anisotropy (v_2 -coefficients). The solution of this problem was proposed in the papers [34, 37], where it

was demonstrated how efficiently the transverse collective flow and its anisotropy can develop at prethermal stage (even without pressure) in spatially finite systems typical for A+A collisions. Now the description of this prethermal stage based on [38] is in progress. Meanwhile, in [39] a rough approach was proposed, which allows one to calculate the developing of the transverse flow and its anisotropy at the prethermal stage by means of hydroevolution that starts at very early time (0.1 fm/c) just to account for the energy-momentum conservation law. It brings a good agreement with all bulk observables. It does not mean that thermalisation actually happens at the proper time 0.1–0.2 fm/c (the same concerns the hydrodynamic models where the starting time is 0.4–0.6 fm/c), but only that hydrodynamic approach introduces no big errors being applied out of its applicability region, at the prethermal stage, to describe collective flow and its anisotropy at the thermalization time ~ 1 fm/c. With this in mind, the hydrodynamic evolution in our approach begins from the starting time of the collision process, $\tau_i = \tau_0$. Here we use the starting proper time $\tau_0 = 0.2$ fm/c. At this very early moment there is no collective transverse flow, and our analysis is related just to this case.

We assume the initial energy density distribution in the corresponding flux tubes (produced by the fluctuating local nucleons distribution or color charge fluctuations in colliding nuclei) to be fairly homogeneous in a long rapidity interval because of the boost invariance and rather thin transversally with the transverse (Gaussian) radii $a_i = 1$ fm. The initial energy-density distribution $\epsilon(x, y)$ at τ_0 is supposed to be decomposed in general case as

$$\epsilon(x, y) = \epsilon_{\text{bkg}}(r) + \sum_{i=0}^{N_t} \epsilon_i e^{-(((x-x_i)^2 + (y-y_i)^2)/a^2)}, \quad (1)$$

where $r^2 = x^2 + y^2$, $\mathbf{r}_i = (x_i, y_i)$ are the positions of the tubes' centers, N_t is the number of tubes, and ϵ_i are the values of maximal energy density in the tube-like fluctuations. In our analysis we use the two different types of the background ϵ_{bkg} , on which tubes are placed: it takes either the Gaussian form

$$\epsilon_{\text{bkg}}^G(r) = \epsilon_b e^{-r^2/R^2} \quad (2)$$

or the Woods-Saxon form with the surface thickness parameter δ

$$\epsilon_{\text{bkg}}^{\text{WS}}(r) = \frac{\epsilon_b}{e^{(\sqrt{r^2 - R_a})/\delta} + 1}, \quad (3)$$

where ϵ_b is the maximum value of the background energy-density distribution.

The results are demonstrated for various kinds of the bumpy IC structure with different number N_t of tubes—two odd ones ($N_t = 1$ and 3) and two even ones ($N_t = 4$ and 10) having variable radial distances from the center. Also the two previously mentioned types of the background are utilized. Specifically, the analysis is carried out for the following tube-like initial configurations.

- (i) The configuration with a smooth Gaussian profile without fluctuations, as it was considered in [34],

where the parameters obtained from the fit to the color glass condensate model result are as follows: $R = 5.4$ fm and maximum energy density at $r = 0$ is $\epsilon_b = 90$ GeV/fm³.

- (ii) The configuration with one tube in the center, where the tube energy density profile is the Gaussian one with $a = 1.0$ fm and $\epsilon_i = 270$ GeV/fm³. The background corresponds to the case (i).
- (iii) The configuration with one tube shifted from the center, where $\epsilon_i = 270$ GeV/fm³, $r_1 = 3$ fm or $r_1 = 5.6$ fm, and $a = 1$ fm. The background corresponds to item (i). The initial configuration with $r_1 = 3$ fm is presented in Figure 1(a).
- (iv) The configuration with three tubes: $\epsilon_i = 250$ GeV/fm³; $\mathbf{r}_i = (0, 5.6), (-1, 3.6), (-1, -3.6)$ fm or $\mathbf{r}_i = (0, 0), (-1, 3.6), (-1, -3.6)$ fm; $a_i = 1$ fm. The background is Gaussian with $\epsilon_b = 85$ GeV/fm³, $R = 5.4$ fm.
- (v) The configuration with four symmetrically located tubes: $\epsilon_i = 250$ GeV/fm³, $r_i = 5.6$ fm, and $a_i = 1$ fm. The background is the Gaussian one with $\epsilon_b = 85$ GeV/fm³. The corresponding initial energy density profile is presented in Figure 1(b).
- (vi) The configuration with ten tubes, $\epsilon_b = 25$ GeV/fm³, $R = 5.4$ fm, $r_1 = 0$ fm, $r_{2,3,4} = 2.8$ fm, $r_{i>4} = 4.7$ fm, $a = 1$ fm, and $\epsilon_i = 4\epsilon_b$ (see Figure 1(c)).
- (vii) Besides these configurations, we also consider the case of IC with background profile $\epsilon_{\text{bkg}}(r)$ in the form (3) ($\epsilon_b = 90$ GeV/fm³, $R = 6.37$ fm, and $\delta = 0.54$ fm) and one tube shifted from the center and placed at $r_i = 0.5R$ or $1.1R$. The maximum energy densities are $\epsilon_i = 270$ GeV/fm³, $a = 1$ fm. This type of IC with $r_i = 0.5R$ is presented in Figure 2.

The configurations described above serve as the initial conditions for hydrodynamic evolution of the superdense system. The quark-gluon plasma and hadron gas are supposed to be in complete local equilibrium above the chemical freeze-out temperature T_{ch} with EoS described below. With the given IC, the evolution of thermally and chemically equilibrated matter is described with the help of the ideal hydrodynamics approximation. The latter is based on (2+1)D numerical hydrodynamic code, described in [33]. For this stage of evolution we use the lattice QCD-inspired equation of state of quark-gluon phase [40] together with corrections for small but nonzero baryon chemical potentials [33], matched with chemically equilibrated hadron-resonance gas via crossover-type transition. The hadron-resonance gas consists of all ($N = 329$) well-established hadron states made of u,d,s-quarks, including σ -meson, $f_0(600)$. The chemical freeze-out hypersurface at $T = 165$ MeV, which corresponds to the end of chemically and thermally equilibrated evolution and start of the hydrokinetic stage of A+A collision process, is presented in Figure 3 for the initial configuration (iii).

At the temperatures below T_{ch} the system loses chemical and thermal equilibrium and gradually decays. In the

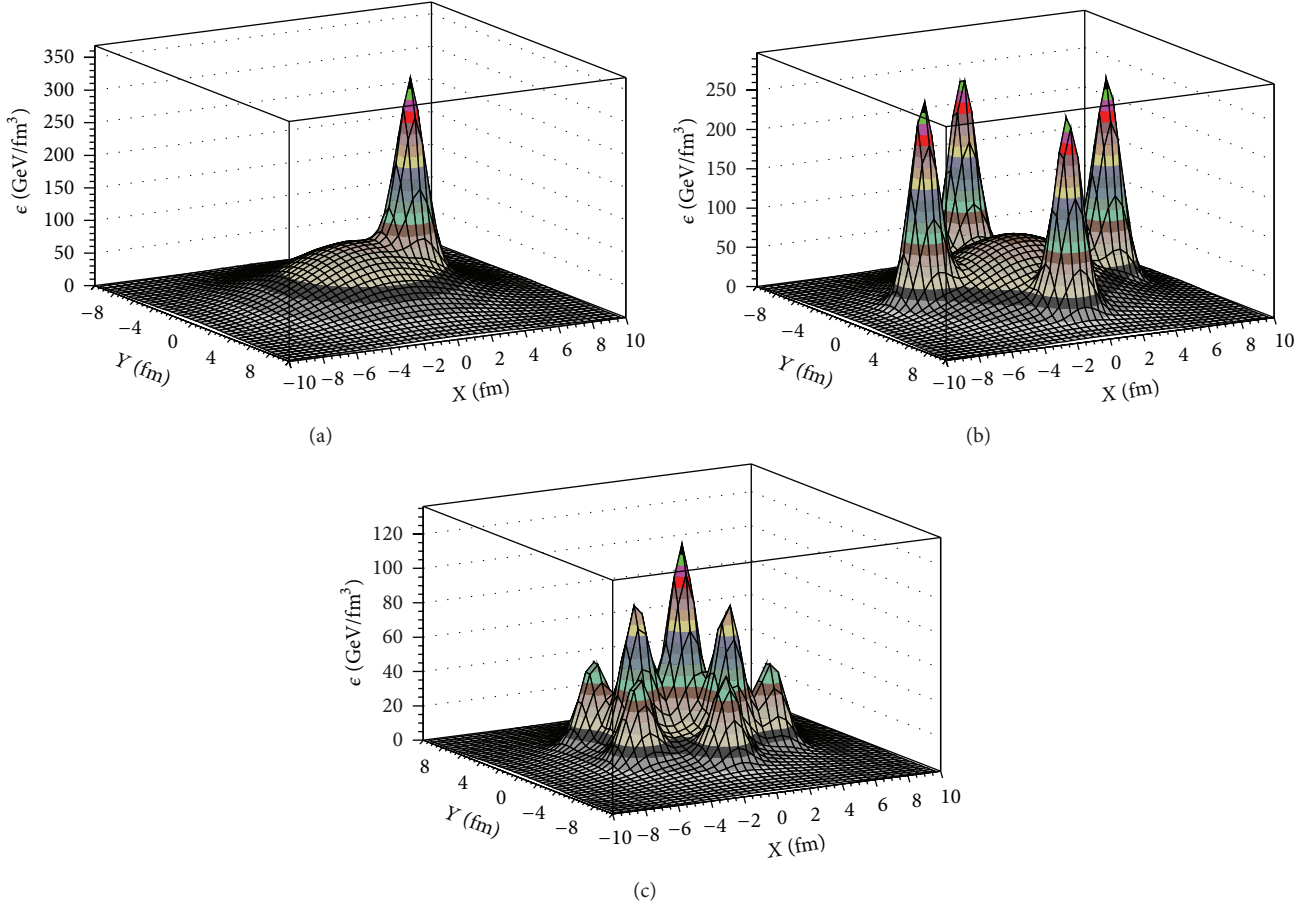


FIGURE 1: 3D plots of the initial energy density profiles with tube-like IC on the Gaussian background in the form (2) for $\tau_0 = 0.2$ fm/c. (a) 1 tube (iii) displaced at $r_1 = 3$ fm. (b) 4 tubes (v). (c) 10 tubes (vi).

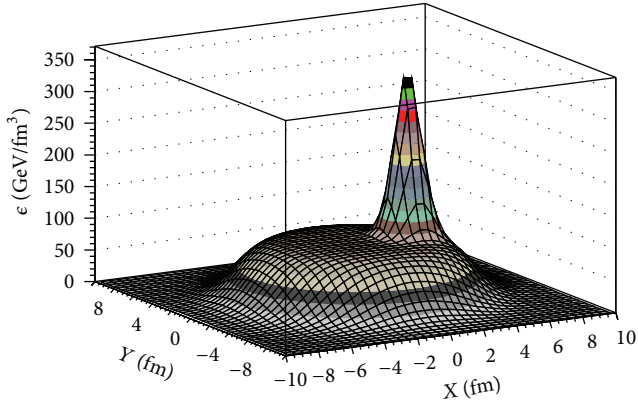


FIGURE 2: 3D plot of the initial energy density profile with one tube-like fluctuation (vii) placed at $r_i = 0.5R$ on the Woods-Saxon background (3).

hydrokinetic approach, HKM, the dynamical decoupling, is described by the particle escape probabilities from the inhomogeneous hydrodynamically expanding system (with resonance decays taken into account) in a way consistent with the kinetic equations in the relaxation-time approximation

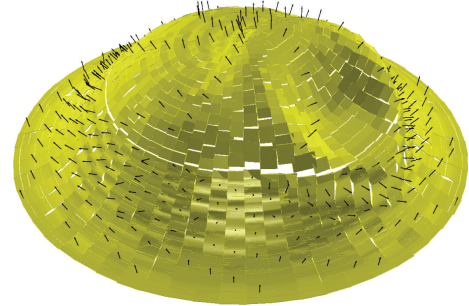


FIGURE 3: The chemical freeze-out hypersurface $\tau(x, y)$ at $T = 165$ MeV for 1 tube (iii) placed at $r_1 = 3$ fm from the center with the vector field of velocities.

for emission functions [32, 33]. The HKM gives the possibility to calculate the momentum spectra formation during continuous process of the particle liberation. Within HKM one can consider the single event (=fixed IC) basing on numerical calculations of the analytical formulas for spectra using the temperatures and particle concentrations from numerical hydrodynamic solution. An extensive description of the approach can be found in [32, 33]. In the employed

version of HKM there is no Monte Carlo cascade algorithm for the hadron stage that typically brings the new ensemble of events with energy-momentum conservation fulfilled only in average for the fixed initial conditions and fixed hydrodynamic evolution (in this aspect the results of some studies do not correspond, strictly speaking, to the true event-by-event analysis). We just calculate the analytical structure describing gradual decay of expanding fluid into the particles in the single event (related to the fixed IC) in the sense that solutions of the Boltzmann equation describe continuously the *mean* distribution functions at given IC in correspondence with the energy-momentum conservation law.

In this paper the HKM is applied to the systems with the bumpy ICs which are described above.

3. Results and Discussion

In this section we present the results obtained within HKM model with the tube-like IC. It is obvious that the angular dependence of transverse pion spectra in the cases (i) and (ii), described in the previous section, is flat, and the effective temperature of the p_T -spectrum (its inverse slope) is higher for configuration (ii). A nontrivial angular dependence appears for the other ICs, where at least one tube is shifted from the center and so brings an azimuthal asymmetry into the system. In Figure 3, which fully corresponds to the actual calculations, one can see that the fluctuation in the initial distribution leads to the appearance of concavity on freeze-out hypersurface in the azimuthal direction corresponding to the initial high-energy fluctuation. It means, in particular, that the freeze-out temperature is reached earlier in this domain.

3.1. Integrated Pion Spectra. The analysis of the spectra at various p_T shows their angular dependence to be different. In this subsection we demonstrate the results for integrated over p_T spectra, aiming to see a possibility for the ridge formation in such a tubular picture. In Figure 4 we present $|p_T|$ -integrated pion spectra $dN/d\phi$ for different initial configurations. The black line corresponds to the integrated spectra at $p_T > 0.9$ GeV, and the red one corresponds to the momentum values $p_T > 2.5$ GeV (It is demonstrated in different hydrodynamic models, see, e.g., [39], that the hydrodynamics works in p_T -region until 3 GeV for the central events; here we consider very central collisions with $b \approx 0$. Note that we analyze the contribution of only hydrocomponent to the soft ridge formation.) One can see that behavior of the curves in the case of the Woods-Saxon background distribution with the single very peripheral tube (Figure 4, 2nd row, right) is similar to the results obtained in [41] for similar configuration; in particular, both local minima coincide at $\phi = 0$, but in contrast to [41], for $p_T > 2.5$ GeV the minimum is not absolute but local. This probably points out that Woods-Saxon background is not similar to the one used in [41], for the Nexus-inspired IC. For the Gaussian-like background or not so peripheral single-tube disposition (Figure 4, top left), the angular behavior of the spectrum is different from the above result. Nevertheless, the azimuthal

positions of the maximal values of the spectra are correlated for high momentum “trigger” component and “associated” soft one. In the 3rd row of Figure 4 for three initial tubes there are no positive correlations in a front of the initial tube at $\phi = 0$. Nevertheless, there are such correlations at the left figure at the points $-\pi$ and π and at the right figure at -1 and 1 rad. The angular positions of the maximal values are synchronized for 4 and, partially, for 10 tubes (Figure 4, bottom).

The results demonstrate that if one particle with relatively large p_T is triggered, then, most probably, its azimuthal direction will correspond to the one of the peaks in the distributions $dN/d\phi$. Then, as it follows from the $dN/d\phi$ distributions for $p_T > 0.9$ GeV and $p_T > 2.5$ GeV, the probability to find the second “associated” particle with the same or smaller transverse momentum will be maximal in a narrow range $\Delta\phi$ near this peak. Such effects are typically expressed through the ratio $C(\Delta\phi)$ of the dihadron distribution in $\Delta\phi$ for the *same* events to the one extracted from the *mixed* events:

$$C(\Delta\phi) - 1 = \left(\frac{dN^{\text{mixed}}}{d\Delta\phi} \right)^{-1} \left(\frac{dN^{\text{same}}}{d\Delta\phi} - \frac{dN^{\text{mixed}}}{d\Delta\phi} \right), \quad (4)$$

where in our model for each identical (in the sense of variable geometry analysis) initial tube-like configuration we have

$$\begin{aligned} \frac{dN^{\text{same}}}{d\Delta\phi} &= \int_{-\pi}^{\pi} f\left(\phi + \frac{\Delta\phi}{2}\right) \cdot g\left(\phi - \frac{\Delta\phi}{2}\right) d\phi, \\ \frac{dN^{\text{mixed}}}{d\Delta\phi} &= \frac{1}{2\pi} \int_{-\pi}^{\pi} \int_{-\pi}^{\pi} d\phi_1 d\phi_2 f\left(\phi_1 + \frac{\Delta\phi}{2}\right) \cdot g\left(\phi_2 - \frac{\Delta\phi}{2}\right) \\ &= \frac{1}{2\pi} N_{\text{as}} N_{\text{tr}}. \end{aligned} \quad (5)$$

Here $f(\phi) = \int_{0.9}^{3.0} s(p, \phi) dp$ and $g(\phi) = \int_{2.5}^{3.0} s(p, \phi) dp$ are $dN/d\phi$ distributions for $p_T > 0.9$ GeV and $p_T > 2.5$ GeV, respectively, $s(p, \phi)$ are the pion spectra, and $N_{\text{tr}} = \int_{-\pi}^{\pi} g(\phi) d\phi$ and $N_{\text{as}} = \int_{-\pi}^{\pi} f(\phi) d\phi$ are the normalization constants for the “trigger” and “associated” components, respectively.

The correlation functions $C(\Delta\phi)$ are presented in Figure 5 for the different initial configurations. One can see that for many of the considered initial configurations (but not for all of them!) there are narrow azimuthal near-side correlations which are typical for the ridge. The inclusive correlations between the triggered particle and the particle corresponding to the other peaks will be relatively weak, since these peaks will change their angular location from event to event with respect to the “triggered,” or near-side, peak, and this will wash out the two-particle correlations outside the near-side peak. It is not unlikely, however, that the doubly-peaked away-side structure, which is seen in Figure 5 (2nd row right and 3rd right), can be supported by the multi-peak configurations similar to those presented in Figure 5 (bottom), and so the doubly peaked away-side structure may survive, if the weights of such triangular initial configurations

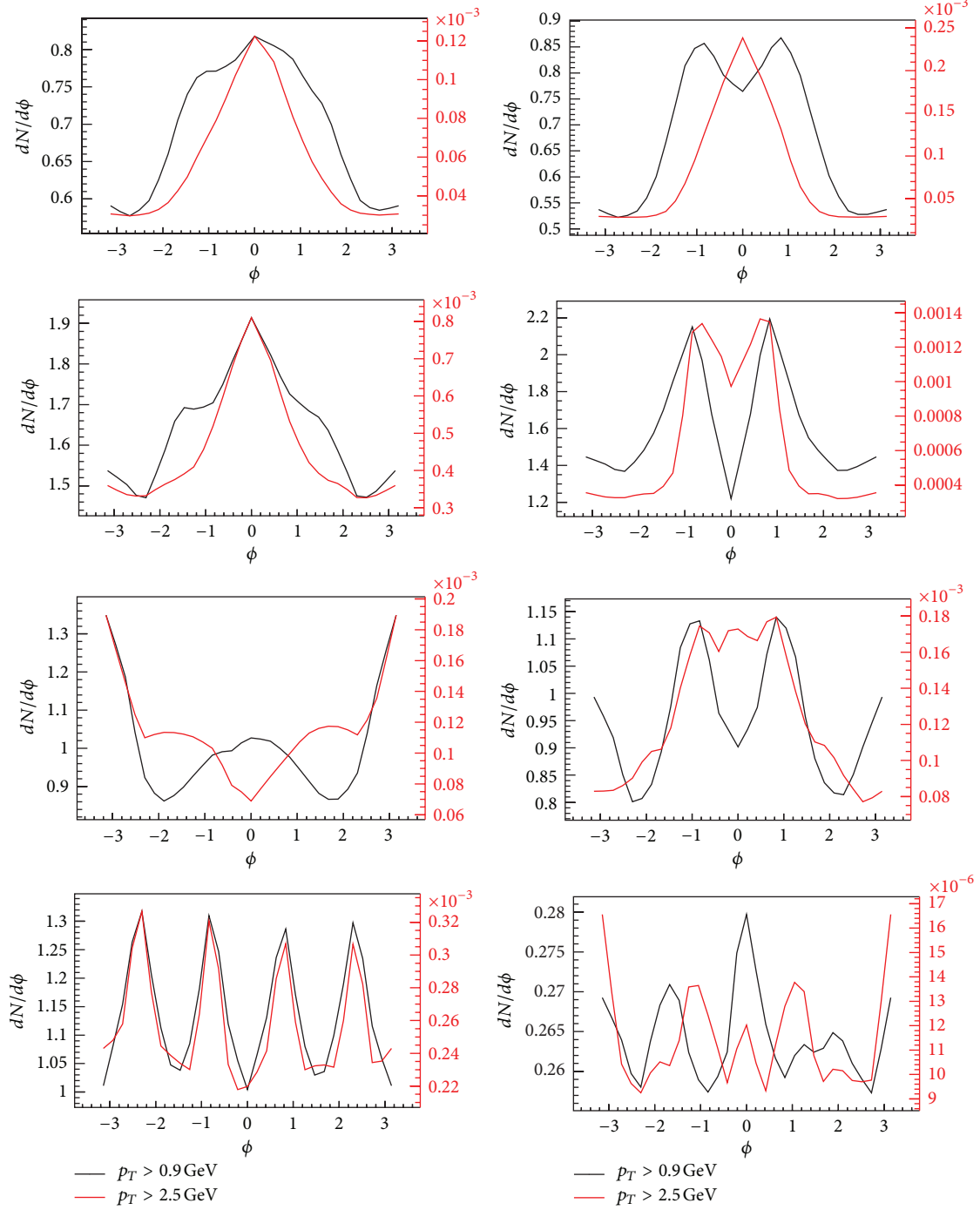


FIGURE 4: The integrated spectra with the tube-like ICs. The top row demonstrates the case of 1 displaced tube with the Gaussian background (iii): left: at $r_1 = 0.55R$, right: at $r_1 = 1.04R$. The 2nd row corresponds to the case of 1 displaced tube with the Woods-Saxon background (vii): left: at $r_i = 0.5R$, right: at $r_i = 1.1R$. The 3rd row is related to the IC with 3 tubes and the Gaussian background (iv): left: $\mathbf{r}_i = (0, 0), (-1, 3.6), (-1, -3.6)$ fm, right: $\mathbf{r}_i = (0, 5.6), (-1, 3.6), (-1, -3.6)$ fm. The 4th row is related to the Gaussian background: left: 4 tubes (v), right: 10 tubes (vi).

are fairly big. One can also see that if the tube is not in the IC peripheral region, just the near-side ridge structure appears, and the away-side structure is washed out. Thus, not only the number of the tubes is important, but also

their positions. The comparison of the ridge and doubly-peaked away-side structure with the data of ALICE LHC [7] supports such a hypothesis. This is the possible mechanism of formation of the so-called soft ridge structure. Note that

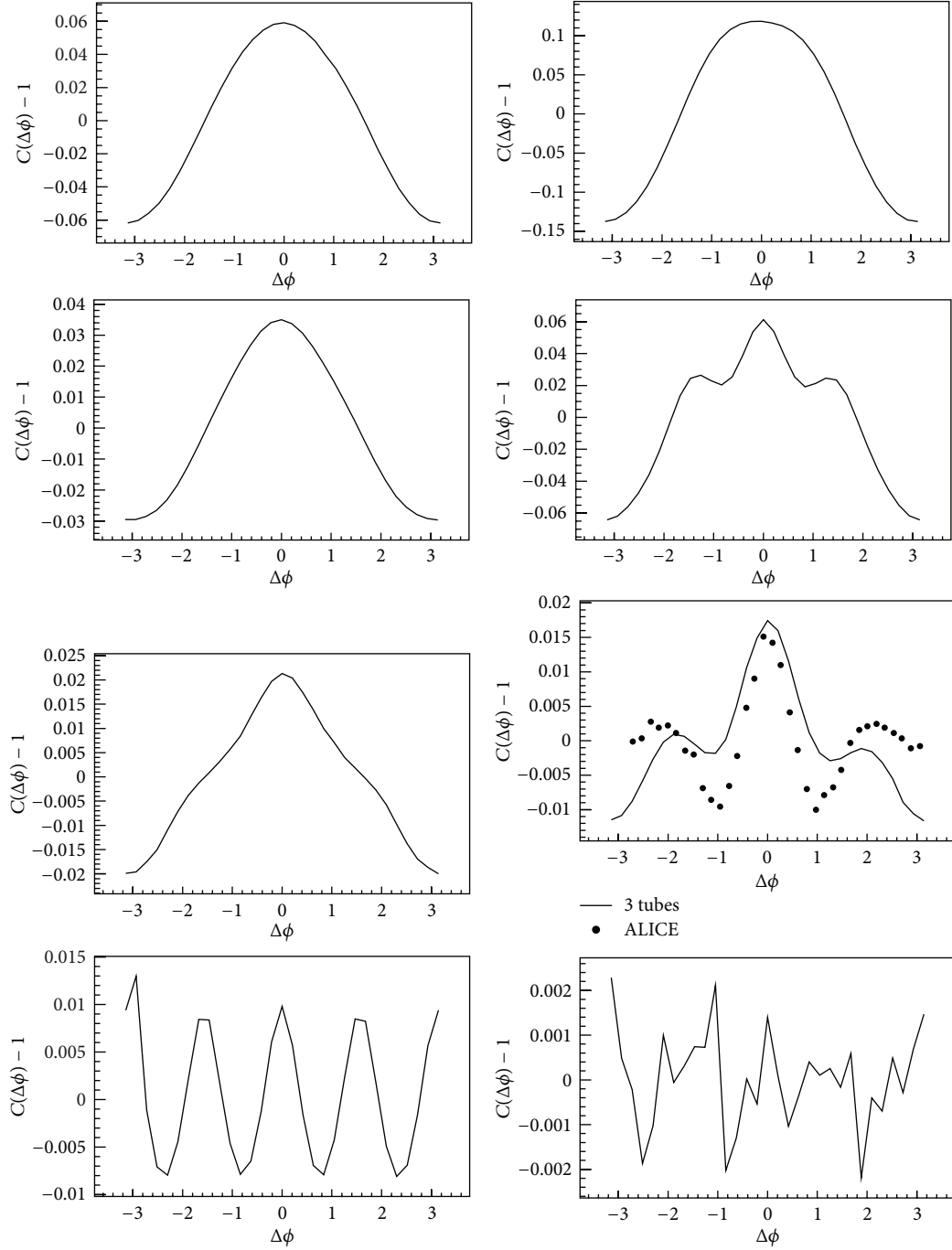


FIGURE 5: The correlation function $C(\Delta\phi)$ for various ICs. The top row demonstrates the case of 1 displaced tube with the Gaussian background (iii): left: at $r_i = 0.55R$, right: at $r_i = 1.04R$. The 2nd row corresponds to the case of 1 displaced tube with the Woods-Saxon background (vii): left: at $r_i = 0.5R$, right: at $r_i = 1.1R$. The 3rd row describes 3 tubes with the Gaussian background (iv): left: $\mathbf{r}_i = (0, 0), (-1, 3.6), (-1, -3.6)$ fm, right: $\mathbf{r}_i = (0, 5.6), (-1, 3.6), (-1, -3.6)$ fm. The 4th row is related to the Gaussian background: left: 4 tubes (v), right: 10 tubes (vi). The ALICE LHC data are taken from [7].

the dihadron correlations are sensitive not only to the tube configurations, but also to the tube energy, as it is analyzed for one-tube case in [15, 41]. The comparison between the results for the Gaussian background (Figure 5, 1st row, right) and the Woods-Saxon one (Figure 5, 2nd row, right) demonstrates a sensitivity of ridge formation to the background initial

profile: in the case of one tube the ridges prefer Woods-Saxon type of the profile.

As for the formation of the hard ridges with triggered particle momenta $p_T > 5-6$ GeV, it is very likely that they are the result of superposition of the bulk spectrum structure, caused by the tubular bumpy IC, and the jet spectrum one,

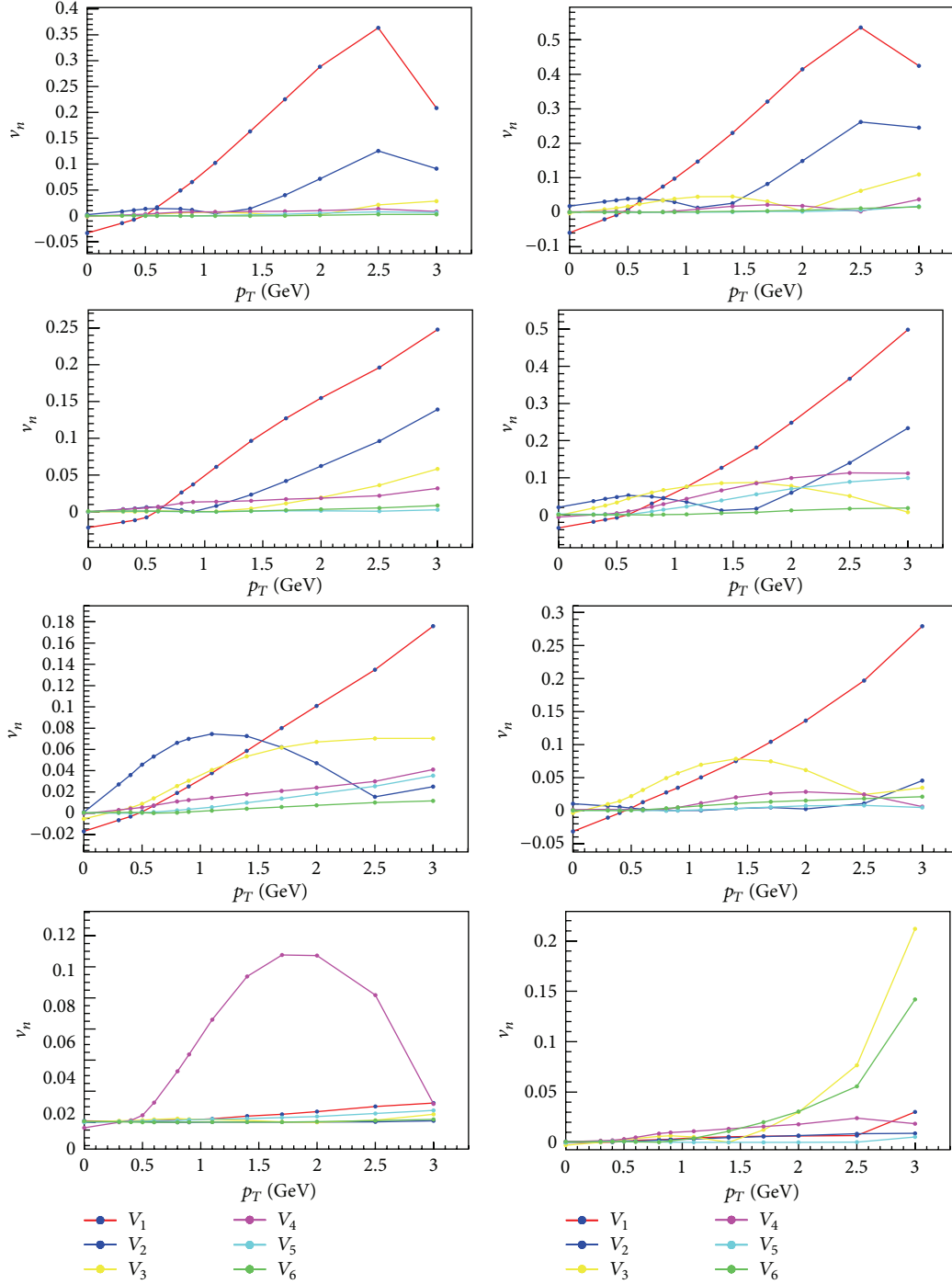


FIGURE 6: The v_n -coefficients for different tube-like ICs. The top row demonstrates the case of 1 displaced tube with the Gaussian background (iii): left: at $r_1 = 0.55R$, right: at $r_1 = 1.04R$. The 2nd row represents 1 displaced tube on the top of the Woods-Saxon distribution (vii): left: at $r_i = 0.5R$, right: at $r_i = 1.1R$. The 3rd row corresponds to 3 tubes on the top of the Gaussian distribution (iv): left: $\mathbf{r}_i = (0, 5.6), (-1, 3.6), (-1, -3.6)$ fm, right: $\mathbf{r}_i = (0, 0), (-1, 3.6), (-1, -3.6)$ fm. The 4th row is related to: left: 4 tubes with the Gaussian background (v), right: 10 tubes with the Gaussian background (vi).

conditioned by the jet formation mechanism accounting for the interaction with the bulk matter. Even a 10% coincidence between the azimuth jet direction and the angular position of one of the peaks in soft spectra, similar to those in Figure 4, can be enough to form the observed hard ridge [12].

3.2. *The Flow Harmonics and p_T Dependence of Their Magnitudes.* The anisotropy of the initial tubular conditions that leads to nontrivial ridge structure, results also in a non-trivial transverse momentum spectrum angular structure, even in the most central collisions. This structure can be investigated

quantitatively using a discrete Fourier decomposition. Then the azimuthal momentum distribution of the emitted particles is commonly expressed as

$$\frac{dN}{p_T dp_T d\phi dy} = \frac{1}{2\pi} \frac{dN}{p_T dp_T dy} \times \left(1 + \sum_{n=1}^{\infty} 2v_n(p_T) \cos(n(\phi - \Psi_n(p_T))) \right), \quad (6)$$

where v_n is the magnitude of the n th order harmonic term, relative to the angle of the initial-state spatial plane of symmetry Ψ_n . In Figure 6 we show our results for the p_T dependence of v_n for different initial configurations. Here, since our purpose is to show clearly the effects of bumpy IC, we plot the results obtained for v_n up to $n = 6$. One can note that v_1 coefficients take negative and positive values, and so the integral $\int_0^{3.5 \text{ GeV}} dp_T p_T^2 v_1(dN/p_T dp_T)$ is close to zero. In fact, this integral is less than 10% of the differences between its values in the regions where $v_1 > 0$ (large p_T) and $v_1 < 0$ (small p_T). This smallness of the integral (for different configurations it is 0.004–0.029 GeV) reflects the transverse momentum (it is zero initially) conservation. Since we consider v_n coefficients for the pion subsystem only, one cannot expect exact zero value for considered integral.

Note that for configurations (ii)–(vii) for odd number of the initial tubes the odd harmonics are dominating, and the analogous tendency takes place for the even harmonics at even number of the tubes. However, to make general conclusion, more configurations have to be considered.

The experimentally valuable results have to be based on some model of the tube-like initial conditions and the correspondingly built event generator for IC and also include an event by event evolution procedure. It will define the weight of the single events, such as those presented in Figure 6, and finally give the resulting event-averaged v_n -coefficients and the quantitative structure of the ridge. We plan to realize such a quantitative experimental analysis in subsequent studies.

4. Conclusions

The tube-like fluctuating structures in the initial energy density distribution are considered with the aim to study the influence of their presence on the pion spectra, flow harmonics, and ridge formation. These very dense color-field flux tubes are formed at the very initial stage of the nucleus-nucleus collision and lead to the long-range longitudinal correlations in pseudorapidity. It is found that the presence of the corresponding bumpy structures in transverse direction in IC strongly affects the hydrodynamic evolution and leads to emergence of conspicuous structures in azimuthal distributions of the pion transverse momentum spectra. The hydrokinetic evolution for different initial configurations with different numbers of tubes is calculated. As the result, one can see that most configurations can bring the ridge structure accompanied by the specific set of $v_n(p_T)$ -coefficients. Not only the triangular structures of

the initial conditions are responsible for the soft ridge formation, but also the odd number of the initial tubes can support this job. It means that the hydrodynamic mechanism of the near-side “soft ridges” formation is sufficiently plausible. Also one can note that the doubly peaked away-side structure appears when there is one outer/peripheral tube in the initial conditions. To constrain event by event fluctuating IC in A+A collisions with subsequent hydrodynamic expansion within the viscous HKM and provide the detailed quantitative analysis of the ridge structure, a further systematic analysis is planned.

Acknowledgments

Yu. M. Sinyukov thanks Y. Hama for the fruitful discussions and FAPESP (Contract 2013/10395-2) for financial support. The research was carried out within the scope of the European Ultra Relativistic Energies Agreement (EUREA) of the European Research Group GDRE: Heavy ions at ultrarelativistic energies and is supported by the State Fund for Fundamental Researches of Ukraine, Agreement F33/24-2013, and the National Academy of Sciences of Ukraine, Agreement F4-2013. Iu. A. Karpenko acknowledges the financial support by the ExtreMe Matter Institute EMMI and Hessian LOEWE initiative.

References

- [1] M. G. Horner and STAR Collaboration, “Low- and intermediate- p_T di-hadron distributions in Au + Au collisions at $\sqrt{s_{NN}} = 200$ GeV from STAR,” *Journal of Physics G*, vol. 34, no. 8, article S995, 2007.
- [2] B. Alver, B. B. Back, M. D. Baker et al., “System size dependence of cluster properties from two-particle angular correlations in Cu + Cu and Au + Au collisions at $\sqrt{s_{NN}} = 200$ GeV,” *Physical Review C*, vol. 81, no. 2, Article ID 024904, 9 pages, 2010.
- [3] B. Alver, M. M. Aggarwal, Z. Ahammed et al., “Three-particle coincidence of the long range pseudorapidity correlation in high energy nucleus-nucleus collisions,” *Physical Review Letters*, vol. 105, no. 2, Article ID 022301, 7 pages, 2010.
- [4] B. I. Abelev, B. B. Back, M. D. Baker et al., “High transverse momentum triggered correlations over a large pseudorapidity acceptance in Au + Au collisions at $\sqrt{s_{NN}} = 200$ GeV,” *Physical Review Letters*, vol. 104, no. 6, Article ID 062301, 4 pages, 2010.
- [5] A. Adare, S. Afanasiev, C. Aidala et al., “Dihadron azimuthal correlations in Au + Au collisions at $\sqrt{s_{NN}} = 200$ GeV,” *Physical Review C*, vol. 78, no. 1, Article ID 014901, 42 pages, 2008.
- [6] B. Wosiek and PHOBOS Collaboration, “Latest results from the PHOBOS experiment,” *Journal of Physics G*, vol. 35, no. 10, Article ID 104005, 2008.
- [7] K. Aamodt, B. Abelev, A. A. Quintana et al., “Harmonic decomposition of two particle angular correlations in Pb-Pb collisions at $\sqrt{s_{NN}} = 2.76$ TeV,” *Physics Letters B*, vol. 708, no. 3–5, pp. 249–264, 2012.
- [8] V. Khachatryan, A. M. Sirunyan, A. Tumasyan et al., “Observation of long-range, near-side angular correlations in proton-proton collisions at the LHC,” *Journal of High Energy Physics*, vol. 2010, article 91, 2010.
- [9] W. Li and CMS collaboration, “Correlations and fluctuations measured by the CMS experiment in pp and PbPb,” *Journal*

- of *Physics G*, vol. 38, Article ID 124027, 2011, <http://arxiv.org/abs/1107.2452>.
- [10] A. Dumitru, "Glasma flux tubes and the near side ridge phenomenon at RHIC," *Nuclear Physics A*, vol. 810, no. 1–4, pp. 91–108, 2008.
 - [11] B. Schenke, A. Dumitru, Y. Nara, and M. Strickland, "QGP collective effects and jet transport," *Journal of Physics G*, vol. 35, no. 10, Article ID 104109, 2008.
 - [12] K. Werner, Iu. Karpenko, M. Bleicher, T. Pierog, and S. Porteboeuf-Houssais, "Jets, bulk matter, and their interaction in heavy ion collisions at several TeV," *Physical Review C*, vol. 85, no. 6, Article ID 064907, 14 pages, 2012.
 - [13] O. Socolowski Jr., F. Grassi, Y. Hama, and T. Kodama, "Fluctuations of the initial conditions and the continuous emission in the hydrodynamical description of two-pion interferometry," *Physical Review Letters*, vol. 93, no. 18, Article ID 182301, 4 pages, 2004.
 - [14] C. E. Aguiar, Y. Hama, T. Kodama, and T. Osada, "Event-by-event fluctuations in hydrodynamical description of heavy-ion collisions," *Nuclear Physics A*, vol. 698, no. 1–4, pp. 639–642, 2002.
 - [15] Y. Hama, R. P. G. Andrade, F. Grassi, and W. L. Qian, "Trying to understand the ridge effect in hydrodynamic model," *Nonlinear Phenomena in Complex Systems*, vol. 12, no. 4, pp. 466–470, 2009.
 - [16] B. Alver and G. Roland, "Collision-geometry fluctuations and triangular flow in heavy-ion collisions," *Physical Review C*, vol. 81, no. 5, Article ID 054905, 7 pages, 2010.
 - [17] R. Lacey and PHENIX Collaboration, "PHENIX measurements of higher order flow harmonics in Au + Au collisions at $\sqrt{s_{NN}} = 200$ GeV," *Journal of Physics G*, vol. 38, no. 12, Article ID 124048, 2011.
 - [18] J. F. Grosse-Oetringhaus and ALICE Collaboration, "Hadron correlations in Pb-Pb collisions at $\sqrt{s_{NN}} = 2.76$ TeV with ALICE," *Journal of Physics G*, vol. 38, no. 12, Article ID 124028, 2011.
 - [19] J. Jia and ATLAS Collaboration, "Measurement of elliptic and higher order flow from ATLAS experiment at the LHC," *Journal of Physics G*, vol. 38, no. 12, Article ID 124012, 2011.
 - [20] B. H. Alver, C. Gombeaud, M. Luzum, and J. Y. Ollitrault, "Triangular flow in hydrodynamics and transport theory," *Physical Review C*, vol. 82, no. 3, Article ID 034913, 9 pages, 2010.
 - [21] M. Luzum, "Flow fluctuations and long-range correlations: elliptic flow and beyond," *Journal of Physics G*, vol. 38, no. 12, Article ID 124026, 2011.
 - [22] G. Y. Qin, H. Petersen, S. A. Bass, and B. Muller, "Translation of collision geometry fluctuations into momentum anisotropies in relativistic heavy-ion collisions," *Physical Review C*, vol. 82, no. 6, Article ID 064903, 14 pages, 2010.
 - [23] G. Moschelli and S. Gavin, "Soft contribution to the hard ridge in relativistic nuclear collisions," *Nuclear Physics A*, vol. 836, no. 1–2, pp. 43–58, 2010.
 - [24] T. Hirano and K. Tsuda, "Collective flow and two-pion correlations from a relativistic hydrodynamic model with early chemical freeze-out," *Physical Review C*, vol. 66, no. 5, Article ID 054905, 14 pages, 2002.
 - [25] S. Manly and PHOBOS Collaboration, "System size, energy and pseudorapidity dependence of directed and elliptic flow at RHIC," *Nuclear Physics A*, vol. 774, pp. 523–526, 2006.
 - [26] S. Gavin, L. McLerran, and G. Moschelli, "Long range correlations and the soft ridge in relativistic nuclear collisions," *Physical Review C*, vol. 79, no. 5, Article ID 051902, 4 pages, 2009.
 - [27] K. Werner, Iu. Karpenko, T. Pierog, M. Bleicher, and K. Mikhailov, "Event-by-event simulation of the three-dimensional hydrodynamic evolution from flux tube initial conditions in ultrarelativistic heavy ion collisions," *Physical Review C*, vol. 82, no. 4, Article ID 044904, 26 pages, 2010.
 - [28] H. Petersen, J. Steinheimer, G. Baur, M. Bleicher, and H. Stöcker, "Fully integrated transport approach to heavy ion reactions with an intermediate hydrodynamic stage," *Physical Review C*, vol. 78, no. 4, Article ID 044901, 18 pages, 2008.
 - [29] Y. Hama, R. P. G. Andrade, F. Grassi, J. Noronha, and W. L. Qian, "Further results on peripheral-tube model for ridge correlation," *Acta Physica Polonica B*, vol. 6, no. 2, pp. 513–518, 2013.
 - [30] M. S. Borysova, Iu. A. Karpenko, and Yu. M. Sinyukov, "Fluctuations in initial energy density distributions in A + A collisions," *Nuclear Physics and Atomic Energy*, vol. 11, no. 3, pp. 269–274, 2010.
 - [31] Yu. M. Sinyukov, S. V. Akkelin, and Y. Hama, "Freeze-out problem in hydrokinetic approach to A + A collisions," *Physical Review Letters*, vol. 89, no. 5, Article ID 052301, 4 pages, 2002.
 - [32] S. V. Akkelin, Y. Hama, Iu. A. Karpenko, and Yu. M. Sinyukov, "Hydro-kinetic approach to relativistic heavy ion collisions," *Physical Review C*, vol. 78, no. 3, Article ID 034906, 15 pages, 2008.
 - [33] Iu. Karpenko and Yu. M. Sinyukov, "Kaon and pion femtoscopy at the highest energies available at the BNL Relativistic Heavy Ion Collider (RHIC) in a hydrokinetic model," *Physical Review C*, vol. 81, no. 5, Article ID 054903, 14 pages, 2010.
 - [34] Yu. M. Sinyukov, Iu. A. Karpenko, and A. V. Nazarenko, "Spacetime scales and initial conditions in relativistic A + A collisions," *Journal of Physics G*, vol. 35, no. 10, Article ID 104071, 2008.
 - [35] M. S. Borysova, Yu. M. Sinyukov, and Iu. A. Karpenko, "Evolution of energy density fluctuations in A + A collisions," *Physics of Particles and Nuclei Letters*, vol. 8, no. 9, pp. 915–917, 2011.
 - [36] M. S. Borysova, "Bumping structure of initial energy density distributions and peculiarities of pion spectra in A + A collisions," *Nuclear Physics and Atomic Energy*, vol. 13, no. 1, p. 39, 2012.
 - [37] Yu. M. Sinyukov, "Matter evolution and soft physics in A + A collisions," *Acta Physica Polonica B*, vol. 37, no. 12, article 3343, 2006.
 - [38] S. V. Akkelin and Yu. M. Sinyukov, "Matching of nonthermal initial conditions and hydrodynamic stage in ultrarelativistic heavy-ion collisions," *Physical Review C*, vol. 81, no. 6, Article ID 064901, 6 pages, 2010.
 - [39] Iu. A. Karpenko, Yu. M. Sinyukov, and K. Werner, "Uniform description of bulk observables in the hydrokinetic model of A + A collisions at the BNL Relativistic Heavy Ion Collider and the CERN Large Hadron Collider," *Physical Review C*, vol. 87, no. 2, Article ID 024914, 13 pages, 2013.
 - [40] M. Laine and Y. Schroder, "Quark mass thresholds in QCD thermodynamics," *Physical Review D*, vol. 73, no. 8, Article ID 085009, 13 pages, 2006.
 - [41] R. P. G. Andrade, F. Gardim, F. Grassi, Y. Hama, and W. L. Qian, "Influence of tubular initial conditions on two-particle correlations," *Journal of Physics G*, vol. 38, no. 12, Article ID 124123, 2011.

Review Article

Some Aspects of Anisotropic Quark-Gluon Plasma

Mahatsab Mandal and Pradip Roy

Saha Institute of Nuclear Physics, 1/AF Bidhannagar, Kolkata 700064, India

Correspondence should be addressed to Mahatsab Mandal; mahatsab.mandal@saha.ac.in

Received 5 April 2013; Revised 5 July 2013; Accepted 19 July 2013

Academic Editor: Edward Sarkisyan-Grinbaum

Copyright © 2013 M. Mandal and P. Roy. This is an open access article distributed under the Creative Commons Attribution License, which permits unrestricted use, distribution, and reproduction in any medium, provided the original work is properly cited.

We review the various aspects of anisotropic quark-gluon plasma (AQGP) that have recently been discussed by a number of authors. In particular, we focus on the electromagnetic probes of AQGP, inter quark potential, quarkonium states in AQGP, and the nuclear modifications factor of various bottomonium states using this potential. In this context, we will also discuss the radiative energy loss of partons and nuclear modification factor of light hadrons in the context of AQGP. The features of the wake potential and charge density due to the passage of jet in AQGP will also be demonstrated.

1. Introduction

Ever since the possibility of creating the quark-gluon plasma (QGP) in relativistic heavy ion collision was envisaged, numerous indirect signals were proposed to probe the properties of such an exotic state of matter. For example, electromagnetic probes (photon and dilepton) [1], J/ψ suppression [2], jet quenching vis-a-vis energy loss [3–10], and many more. In spite of these, many properties of the QGP are poorly understood. The most pertinent question is whether the matter produced in relativistic heavy ion collisions is in thermal equilibrium or not. Studies on elliptical flow (up to about $p_T \sim 1.5$ GeV) using ideal hydrodynamics indicate that the matter produced in such collisions becomes isotropic with $\tau_{\text{iso}} \sim 0.6$ fm/c [11–13]. On the other hand, using second-order transport coefficients with conformal field theory, it has been found that the isotropization/thermalization time has sizable uncertainties [14] leading to uncertainties in the initial conditions, such as the initial temperature.

In the absence of a theoretical proof favoring the rapid thermalization and the uncertainties in the hydrodynamical fits of experimental data, it is very hard to assume hydrodynamical behavior of the system from the very beginning. The rapid expansion of the matter along the beam direction causes faster cooling in the longitudinal direction than in the transverse direction [18]. As a result, the system becomes anisotropic with $\langle p_L^2 \rangle \ll \langle p_T^2 \rangle$ in the local rest frame. At some later time when the effect of parton interaction rate

overcomes the plasma expansion rate, the system returns to the isotropic state again and remains isotropic for the rest of the period. If the QGP, just after formation, becomes anisotropic, soft unstable modes are generated characterized by the exponential growth of the transverse chromomagnetic/chromoelectric fields at short times. Thus, it is very important to study the collective modes in an AQGP and use these results to calculate relevant observables. The instability, thus developed, is analogous to QED Weibel instability. The most important collective modes are those which correspond to transverse chromomagnetic field fluctuations, and these have been studied in great detail in [19–26]. This is known as chromo-Weibel instability, and it differs from its QED analogue because of nonlinear gauge self-interactions. Because of this fact, anisotropy driven plasma instabilities in QCD may slow down the process of isotropization whereas, in QED, it can speed up the process [27].

To characterize the presence of initial state of momentum space anisotropy, it has been suggested to look for some observables which are sensitive to the early time after the collision. The effects of preequilibrium momentum anisotropy on various observables have been studied quite extensively over the past few years. The collective oscillations in an AQGP have been studied in [28, 29]. Heavy quark energy loss and momentum broadening in anisotropic QGP have been investigated in [30, 31]. However, the radiative energy loss of partons in AQGP has recently been calculated in [32]. Another aspect of jet propagation in hot and dense medium

is the wake that it creates along its path. First, Ruppert and Muller [33] have investigated that when a jet propagates through the medium, a wake of current and charge density is induced which can be studied within the framework of linear-response theory. The result shows the wake in both the induced charge and current density due to the screening effect of the moving parton. In the quantum liquid scenario, the wake exhibits an oscillatory behavior when the charge parton moves very fast. Later, Chakraborty et al. [34] also found the oscillatory behavior of the induced charge wake in the backward direction at a large parton speed using HTL perturbation theory. In a collisional quark-gluon plasma, it is observed that the wake properties change significantly compared to the collisionless case [35]. Recently, Jiang and Li [36, 37] have investigated the color response wake in the viscous QGP with the HTL resummation technique. It is shown that the increase of the shear viscosity enhances the oscillation of the induced charge density as well as the wake potential. The effect of momentum space anisotropy on the wake potential and charge density has recently been considered in [38].

Effects of anisotropy on photon and dilepton yields have been investigated rigorously in [16, 39–43]. Recently, the authors in [44] calculated the nuclear modification factor for light hadrons assuming an anisotropic QGP and showed how the isotropization time can be extracted by comparing with the experimental data.

The organization of the review is as follows. In Section 2 we will briefly discuss various models of space-time evolution in AQGP along with the electromagnetic probes which can be used to extract the isotropization time of the plasma. Section 3 will be devoted to discuss the works on heavy quark potential and related phenomena (such as gluon J/ψ dissociation cross-section in an AQGP) that have been investigated so far. We will also discuss the radiative energy loss of partons in AQGP and nuclear modification factor of light hadrons due to the energy loss of the jet in Section 4. In Section 5, the effect of momentum anisotropy on wake potential and charge density due to the passage of a jet will be presented. Finally we summarize in Section 6.

2. Electromagnetic Probes

Photons and dileptons have long been considered to be the good probes to characterize the initial stages of heavy ion collisions as these interact “weakly” with the constituents of the medium and can come out without much distortion in their energy and momentum. Thus, they carry the information about the space-time point where they are produced. Since anisotropy is an early stage phenomena, photons and dileptons are the efficient probes to characterize this stage. The yield of dileptons (henceforth called medium dileptons/photons) in an AQGP has been calculated using a phenomenological model of space-time evolution in $(1+1)$ dimension [42, 43]. This model (henceforth referred to as model I) introduces two parameters: p_{hard} and ξ which are functions of time. The former is called the hard momentum scale and is related to the average momentum of the particles in the medium. In isotropic case this can be identified with the temperature of the system. The latter is called the anisotropy

parameter and $-1 < \xi < \infty$. Furthermore, the model interpolates between early-time $1+1$ free streaming behavior ($\tau \ll \tau_{\text{iso}}$) and late-time ideal hydrodynamical behavior ($\tau \gg \tau_{\text{iso}}$). We first discuss various space-time evolution models of AQGP. In model I the time dependence of ξ is given by [42, 43]

$$\xi(\tau, \delta) = \left(\frac{\tau}{\tau_i}\right)^\delta - 1, \quad (1)$$

where the exponent $\delta = 2(2/3)$ corresponds to free streaming (collisionally broadened) preequilibrium state momentum space anisotropy and $\delta = 0$ corresponds to thermalization. τ_i is the formation time of the QGP. For smooth transition from free streaming to hydrodynamical behavior a transition width γ^{-1} is introduced. The time dependences of various relevant parameters are obtained in terms of a smeared step function [42, 43] as follows:

$$\lambda(\tau) = \frac{1}{2} \left(\tanh \left[\frac{\gamma(\tau - \tau_{\text{iso}})}{\tau_i} \right] + 1 \right). \quad (2)$$

For $\tau \ll \tau_{\text{iso}}$ ($\gg \tau_{\text{iso}}$), we have $\lambda = 0(1)$ which corresponds to free streaming (hydrodynamics). Thus, the time dependences of ξ and p_{hard} are as follows [42, 43]:

$$\xi(\tau, \delta) = \left(\frac{\tau}{\tau_i}\right)^{\delta(1-\lambda(\tau))} - 1, \quad (3)$$

$$p_{\text{hard}}(\tau) = T_i \overline{\mathcal{U}}^{1/3}(\tau),$$

where

$$\mathcal{U}(\tau) \equiv \left[\mathcal{R} \left(\left(\frac{\tau_{\text{iso}}}{\tau} \right)^\delta - 1 \right) \right]^{3\lambda(\tau)/4} \left(\frac{\tau_{\text{iso}}}{\tau} \right)^{1-\delta(1-\lambda(\tau))/2}, \quad (4)$$

$$\overline{\mathcal{U}} \equiv \frac{\mathcal{U}(\tau)}{\mathcal{U}(\tau_i)},$$

$$\mathcal{R}(x) = \frac{1}{2} \left[\frac{1}{(x+1)} + \frac{\tan^{-1} \sqrt{x}}{\sqrt{x}} \right],$$

and T_i is the initial temperature of the plasma. In our calculation, we assume a fast-order phase transition beginning at the time τ_f and ending at $\tau_H = r_d \tau_f$, where $r_d = g_Q/g_H$ is the ratio of the degrees of freedom in the two (QGP phase and hadronic phase) phases and τ_f is obtained by the condition $p_{\text{hard}}(\tau_f) = T_c$, which we take as 192 MeV. We also include the contribution from the mixed phase.

The other model (referred to as model II hereafter) of space-time evolution of highly AQGP is the boost invariant dissipative dynamics in $(0+1)$ dimension [45]. This model can reproduce both the hydrodynamics and the free streaming limits. The time evolution of the phase space distribution $f(t, z, \mathbf{p})$ can be described by Boltzmann equation. Thus, as a starting point, we write the Boltzmann equation in $(0+1)$ dimension in the lab frame as follows:

$$p^t \partial_t f(t, z, \mathbf{p}) + p^z \partial_z f(t, z, \mathbf{p}) = -\mathcal{C}[f(t, z, \mathbf{p})], \quad (5)$$

where homogeneity in the transverse direction is assumed and $\mathcal{C}[f(t, z, \mathbf{p})]$ is the collision kernel. We assume that the phase-space distribution for the anisotropic plasma is given by the following ansatz [28, 29]:

$$f(\mathbf{p}, \xi(\tau), p_{\text{hard}}(\tau)) = f_{\text{iso}} \left(\frac{[\mathbf{p}^2 + \xi(\tau)(\mathbf{p} \cdot \hat{\mathbf{n}})]^2}{p_{\text{hard}}^2(\tau)} \right), \quad (6)$$

where $\hat{\mathbf{n}}$ is the direction of anisotropy. Note that, in subsequent sections, this distribution function will be used to calculate various observables. Now it is convenient to write (5) in the comoving frame. Introducing space-time rapidity (Θ), particle rapidity (y), and proper time (τ) one can write (5) in terms of the comoving coordinates as [45]

$$\begin{aligned} & \left(p_T \cosh(y - \Theta) \frac{\partial}{\partial \tau} + \frac{p_T \sinh(y - \Theta)}{\tau} \frac{\partial}{\partial \tau} \right) \\ & \times f(\mathbf{p}, \xi, p_{\text{hard}}) \\ & = -\Gamma p_T \cosh(y - \Theta) \left[f(\mathbf{p}, \xi, p_{\text{hard}}) - f_{\text{eq}}(\mathbf{p}, T(\tau)) \right], \end{aligned} \quad (7)$$

where $\Gamma = 2T(\tau)/(5\bar{\eta})$ and $\bar{\eta} = \eta/s$, η is the shear viscosity coefficient.

The zeroth-order and first-order moments of the Boltzmann equation give the time dependence for ξ and p_{hard} as described in [45]. Without going into further details we simply quote the coupled differential equations that have to be solved to get the time dependence of ξ and p_{hard} [45] as follows:

$$\begin{aligned} \frac{1}{1 + \xi} \partial_\tau \xi &= \frac{2}{\tau} - 4\Gamma \mathcal{R}(\xi) \frac{\mathcal{R}^{3/4} \sqrt{1 + \xi} - 1}{2\mathcal{R}(\xi) + 3(1 + \xi) \mathcal{R}'(\xi)}, \\ \frac{1}{1 + \xi} \frac{1}{p_{\text{hard}}} \partial_\tau p_{\text{hard}} &= \frac{2}{\tau} - 4\Gamma \mathcal{R}'(\xi) \frac{\mathcal{R}^{3/4} \sqrt{1 + \xi} - 1}{2\mathcal{R}(\xi) + 3(1 + \xi) \mathcal{R}'(\xi)}. \end{aligned} \quad (8)$$

The previous two coupled differential equations have to be solved numerically. The results are shown in Figure 1. It is seen that the anisotropy parameter falls much rapidly compared to the case when model II is used. There is a narrow window in τ where ξ dominates in case of model I. The cooling is slower in case of model II as can be seen from the right panel of Figure 1. These observations have important consequence on various observables.

The assumption of boost invariant in the longitudinal direction can be relaxed and such a space-time model (the so called AHYDRO) has been proposed in [46]. As before, the time evolutions of various quantities can be obtained by taking moments of the Boltzmann equation. However, in this case, instead of two one obtains three coupled differential equations. The third variable is the longitudinal flow velocity (see [46] for details). The observations of this work are as follows. It removes the problem of negative longitudinal pressure sometimes obtained in 2nd-order viscous hydrodynamics and this model leads to much slower relaxation towards isotropy. In this review, for the sake of simplicity, the observables of AQGP will be calculated using space-time model

I. The same can also be calculated using other space-time models of AQGP, and the results may differ from case to case.

2.1. Photons. We first consider the medium photon production from AQGP. The detail derivation of the differential rate is standard and can be found in [16, 39–41]. Here we will quote only the final formula for total photon yield after convoluting with the space-time evolution. The total medium photon yield, arising from the pure QGP phase and the mixed phase is given by

$$\begin{aligned} \frac{dN^\gamma}{dy d^2 p_T} &= \pi R_\perp^2 \left[\int_{\tau_i}^{\tau_f} \tau d\tau \int d\eta \frac{dN^\gamma}{d^4 x dy d^2 p_T} \right. \\ & \left. + \int_{\tau_f}^{\tau_H} f_{\text{QGP}}(\tau) \tau d\tau \int d\eta \frac{dN^\gamma}{d^4 x dy d^2 p_T} \right], \end{aligned} \quad (9)$$

where $f_{\text{QGP}}(\tau) = (r_d - 1)^{-1} (r_d \tau_f \tau^{-1} - 1)$ is the fraction of the QGP phase in the mixed phase [47] and $R_\perp = 1.2A^{1/3}$ fm is the radius of the colliding nucleus in the transverse plane. The energy of the photon in the fluid rest frame is given by $E_\gamma = p_T \cosh(y - \Theta)$, where Θ and y are the space-time and photon rapidities, respectively. The anisotropy parameter and the hard momentum scale enter through the differential rate via $dN^\gamma/d^4 x dy d^2 p_T$ (see [16, 39–41] for details).

We plot the total photon yield coming from thermal QGP, thermal hadrons and the initial hard contribution in Figure 2 and compare it with the RHIC data for various values of τ_{iso} . In the hadronic sector, we include photons from baryon-meson (BM) and meson-meson (MM) reactions. Two scenarios have been considered: (i) pure hydrodynamics from the beginning and (ii) inclusion of momentum state anisotropy. We observe that (i) photons from BM reactions are important, (ii) pure hydro is unable to reproduce the data, that is, some amount of momentum anisotropy is needed, and (iii) exclusion of BM reactions underpredict the data. We note that the value of τ_{iso} needed to describe the data also lies in the range $1.5 \text{ fm}/c \geq \tau_{\text{iso}} \geq 0.5 \text{ fm}/c$ for both values of the transition temperatures.

2.2. Dileptons. The dilepton production from AQGP has been estimated in [17, 42, 43] using the same space-time model. It is argued in [17] that the transverse momentum distribution of lepton pair in AQGP could provide a good insight about the estimation of τ_{iso} . We will briefly discuss the high mass dilepton yield along with the p_T distribution in AQGP. Here we consider only the QGP phase as in the high mass region the yield from the hadronic reactions and decay should be suppressed. The dilepton production from quark-antiquark annihilation can be calculated from kinetic theory and is given by

$$\begin{aligned} E \frac{dR}{d^3 P} &= \int \frac{d^3 \mathbf{p}_1}{(2\pi)^3} \frac{d^3 \mathbf{p}_2}{(2\pi)^3} f_q(\mathbf{p}_1) f_{\bar{q}}(\mathbf{p}_2) v_{q\bar{q}} \sigma_{q\bar{q}}^{J\Gamma} \delta^{(4)}(P - p_1 - p_2), \end{aligned} \quad (10)$$

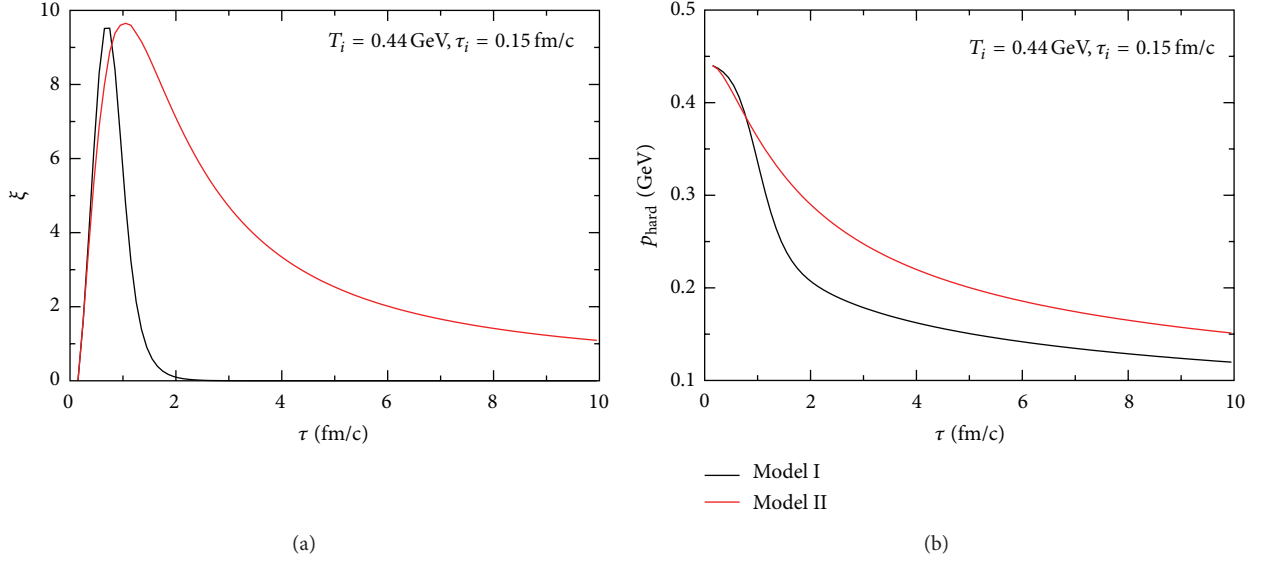


FIGURE 1: (Color online) Time evolutions of (a) the anisotropy parameter ξ and (b) the hard momentum scale p_{hard} in the two space-time models described in the text. The graphs are taken from [15].

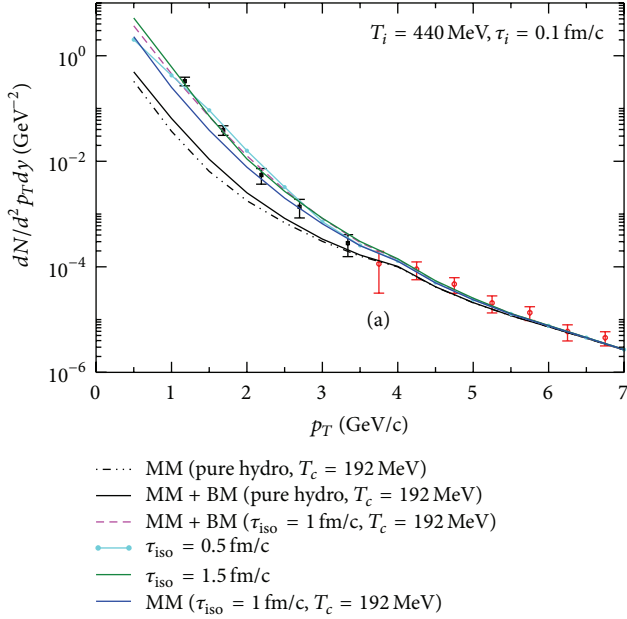


FIGURE 2: (Color online) Photon transverse momentum distributions at RHIC energies. The initial conditions are taken as $T_i = 440$ MeV, $\tau_i = 0.1$ fm/c, and $T_c = 192$ MeV [16].

where $f_{q(\bar{q})}$ is the phase space distribution function of the medium quarks (anti-quarks), $v_{q\bar{q}}$ is the relative velocity between quark and anti-quark, and $\sigma_{q\bar{q}}^{I^+I^-}$ is the total cross-section. Consider

$$\sigma_{q\bar{q}}^{I^+I^-} = \frac{4\pi}{3} \frac{\alpha^2}{M^2} \left(1 + \frac{2m_l^2}{M^2}\right) \left(1 - \frac{4m_l^2}{M^2}\right)^{1/2}. \quad (11)$$

Using the anisotropic distribution functions for the quark (antiquark) defined earlier the differential dilepton production rate can be written as [43]

$$\begin{aligned} \frac{dR}{d^4P} &= \frac{5\alpha^2}{18\pi^5} \times \int_{-1}^1 d(\cos\theta_{p_1}) \\ &\times \int_{a_+}^a \frac{dp_1}{\sqrt{\chi}} p_1 f_q \left(\sqrt{\mathbf{p}_1^2 (1 + \xi \cos^2\theta_{p_1})}, p_{\text{hard}} \right) \\ &\times f_{\bar{q}} \left(\sqrt{(\mathbf{E} - \mathbf{p}_1)^2 + \xi (\mathbf{p}_1 \cos\theta_{p_1} - \mathbf{P} \cos\theta_P)^2}, p_{\text{hard}} \right). \end{aligned} \quad (12)$$

The invariant mass and p_T distributions of lepton pair can be obtained after space-time integration using the evolution model described earlier. The final rates are as follows [17]:

$$\begin{aligned} \frac{dN}{dM^2 dy} &= \pi R_{\perp}^2 \int d^2 P_T \int_{\tau_i}^{\tau_f} \int_{-\infty}^{\infty} \frac{dR}{d^4 P} \tau d\tau d\eta, \\ \frac{dN}{d^2 P_T dy} &= \pi R_{\perp}^2 \int dM^2 \int_{\tau_i}^{\tau_f} \int_{-\infty}^{\infty} \frac{dR_{\text{ann}}}{d^4 P} \tau d\tau d\eta. \end{aligned} \quad (13)$$

The numerical results are shown in Figure 3 for the initial conditions $\tau_i = 0.88$ fm/c and $T_i = 845$ MeV corresponding to the LHC energies. For $\tau_{\text{iso}} \sim 2$ fm/c, it is observed that the dilepton yield from AQGP is comparable to Drell-Yan process. The p_T distribution shows (Figure 3(b)) that the medium contribution dominates over all the other contributions upto $p_T \sim 9$ GeV. The extraction of the isotropization time can only be determined if these results are confronted with the data after the contributions from

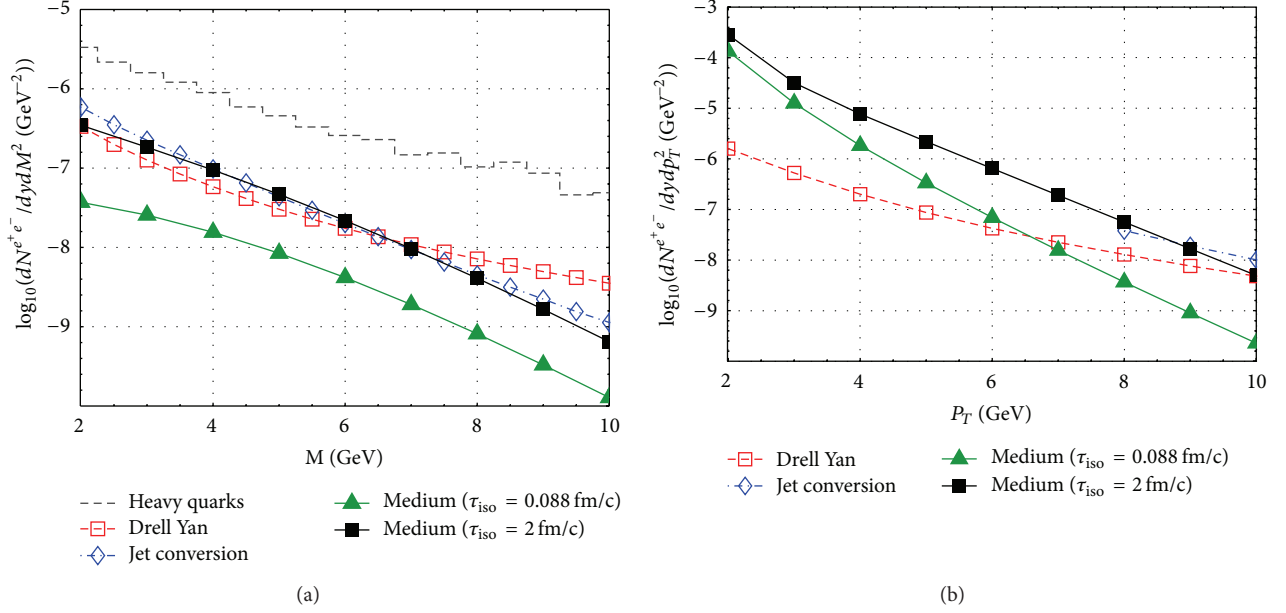


FIGURE 3: (Color online) Invariant mass (a) and momentum (b) distribution of midrapidity dileptons in central Pb + Pb collisions at LHC. The figures are taken from [17].

the semileptonic decay from heavy quarks and Drell-Yan processes are subtracted from the total yield.

3. Heavy Quark Potential and Quarkonium States in AQGP

In this section, we will discuss the heavy quark potential in AQGP that has been calculated in [48]. It is to be noted that this formalism will enable us to calculate the radiative energy loss of both heavy and light quarks, and this will be discussed in Section 4. To calculate the interquark potential one starts with the retarded gluon self-energy expressed as [49]

$$\Pi^{\mu\nu}(K) = g^2 \int \frac{d^3 p}{(2\pi)^3} P^\mu \frac{\partial f(\mathbf{p})}{\partial P_\beta} \left(g^{\beta\nu} - \frac{P^\nu K^\beta}{K \cdot P + i\epsilon} \right). \quad (14)$$

This tensor is symmetric, $\Pi^{\mu\nu}(K) = \Pi^{\nu\mu}(K)$, and transverse, $K_\mu \Pi^{\mu\nu}(K) = 0$. The spatial components of the self-energy tensor can be written as

$$\Pi^{ij}(K) = -g^2 \int \frac{d^3 p}{(2\pi)^3} v^i \partial^j f(\mathbf{p}) \left(\delta^{jl} + \frac{v^j k^l}{K \cdot V + i\epsilon} \right), \quad (15)$$

where $f(\mathbf{p})$ is the arbitrary distribution function. To include the local anisotropy in the plasma, one has to calculate the gluon polarization tensor incorporating anisotropic distribution function of the constituents of the medium. We assume that the phase-space distribution for the anisotropic plasma is given by (6). Using the ansatz for the phase space distribution given in (6), one can simplify (15) to

$$\Pi^{ij}(K) = m_D^2 \int \frac{d\Omega}{(4\pi)} v^i \frac{v^j + \xi(\mathbf{v} \cdot \hat{\mathbf{n}}) n^j}{(1 + \xi(\mathbf{v} \cdot \hat{\mathbf{n}})^2)^2} \left(\delta^{jl} + \frac{v^j k^l}{K \cdot V + i\epsilon} \right), \quad (16)$$

where m_D is the Debye mass for isotropic medium represented by

$$m_D^2 = -\frac{g^2}{2\pi^2} \int_0^\infty dp p^2 \frac{df_{\text{iso}}(p^2)}{dp}. \quad (17)$$

Due to the anisotropy direction, the self-energy, apart from momentum \mathbf{k} , also depends on the anisotropy vector \mathbf{n} , with $n^2 = 1$. Using the proper tensor basis [28], one can decompose the self-energy into four structure functions as

$$\Pi^{ij}(k) = \alpha A^{ij} + \beta B^{ij} + \gamma C^{ij} + \delta D^{ij}, \quad (18)$$

where

$$A^{ij} = \delta^{ij} - \frac{k^i k^j}{k^2}, \quad B^{ij} = k^i k^j, \quad (19)$$

$$C^{ij} = \frac{\tilde{n}^i \tilde{n}^j}{\tilde{n}^2}, \quad D^{ij} = k^i \tilde{n}^j + \tilde{n}^i k^j,$$

with $\tilde{n}^i = A^{ij} n^j$ which obeys $\tilde{n} \cdot k = 0$. α , β , γ , and δ are determined by the following contractions:

$$k^i \Pi^{ij} k^j = \mathbf{k}^2 \beta, \quad \tilde{n}^i \Pi^{ij} k^j = \tilde{n}^2 \mathbf{k}^2 \delta, \quad (20)$$

$$\tilde{n}^i \Pi^{ij} \tilde{n}^j = \tilde{n}^2 (\alpha + \gamma), \quad \text{Tr} \Pi^{ij} = 2\alpha + \beta + \gamma.$$

Before going to the calculation of the quark-quark potential let us study the collective modes in AQGP which have been thoroughly investigated in [28, 29], and we briefly discuss this here. The dispersion law for the collective modes of anisotropic plasma in temporal axial gauge can be determined by finding the poles of propagator Δ^{ij} as follows:

$$\Delta^{ij}(K) = \frac{1}{[(\mathbf{k}^2 - \omega^2) \delta^{ij} - k^i k^j + \Pi^{ij}(k)]}. \quad (21)$$

Substituting (19) in the previous equation and performing the inverse formula [28], one finds

$$\Delta(K) = \Delta_A [\mathbf{A} - \mathbf{C}] + \Delta_G \left[(\mathbf{k}^2 - \omega^2 + \alpha + \gamma) \mathbf{B} + (\beta - \omega^2) \mathbf{C} - \delta \mathbf{D} \right]. \quad (22)$$

The dispersion relation for the gluonic modes in anisotropic plasma is given by the zeros of

$$\Delta_A^{-1}(k) = k^2 - \omega^2 + \alpha = 0, \quad (23)$$

$$\Delta_G^{-1}(k) = (k^2 - \omega^2 + \alpha + \gamma)(\beta - \omega^2) - k^2 \tilde{n}^2 \delta^2 = 0.$$

Let us first consider the stable modes for real $\omega > k$ in which case there are at most two stable modes stemming from $\Delta_G^{-1} = 0$. The other stable mode comes from zero of Δ_A^{-1} . Thus, for finite ξ , there are three stable modes. Note that these modes depend on the angle of propagation with respect to the anisotropy axis. The dispersion relation for the unstable modes can be obtained by letting $\omega \rightarrow i\Gamma$ in $\Delta_G^{-1} = 0$ and Δ_A^{-1} leading to two unstable modes and these modes again depend the direction of propagation with respect to the anisotropy axis.

The collective modes in a collisional AQGP have been investigated in [50] using Bhatnagar-Gross-Krook collisional kernel. It has been observed that inclusion of the collisions slows down the growth rate of unstable modes and the instabilities disappear at certain critical values of the collision frequency.

In order to calculate the quark-quark potential, we resort to the covariant gauge. Using the previous expression for gluon self-energy in anisotropic medium the propagator, in covariant gauge, can be calculated after some cumbersome algebra [48] as follows:

$$\Delta^{\mu\nu} = \frac{1}{(K^2 - \alpha)} [A^{\mu\nu} - C^{\mu\nu}] + \Delta_G \left[(K^2 - \alpha - \gamma) \frac{\omega^4}{K^4} B^{\mu\nu} + (\omega^2 - \beta) C^{\mu\nu} + \delta \frac{\omega^2}{K^2} D^{\mu\nu} \right] - \frac{\lambda}{K^4} K^\mu K^\nu, \quad (24)$$

where

$$\Delta_G^{-1} = (K^2 - \alpha - \gamma)(\omega^2 - \beta) - \delta^2 [K^2 - (n \cdot K)^2]. \quad (25)$$

The structure functions (α , β , γ , and δ) depend on ω , \mathbf{k} , ξ , and on the angle (θ_n) between the anisotropy vector and the momentum \mathbf{k} . In the limit $\xi \rightarrow 0$, the structure functions γ and δ are identically zero, and α and β are directly related to the isotropic transverse and longitudinal self-energies, respectively [28]. In anisotropic plasma, the two-body interaction, as expected, becomes direction dependent. Now the momentum space potential can be obtained from the static gluon propagator in the following way [32, 48]:

$$V(k_\perp, k_z, \xi) = g^2 \Delta^{00}(\omega = 0, k_\perp, k_z, \xi) = g^2 \frac{\mathbf{k}^2 + m_\alpha^2 + m_\gamma^2}{(\mathbf{k}^2 + m_\alpha^2 + m_\gamma^2)(\mathbf{k}^2 + m_\beta^2) - m_\delta^2}, \quad (26)$$

where

$$m_\alpha^2 = -\frac{m_D^2}{2k_\perp^2 \sqrt{\xi}} \times \left[k_z^2 \tan^{-1}(\sqrt{\xi}) - \frac{k_z \mathbf{k}^2}{\sqrt{\mathbf{k}^2 + \xi k_\perp^2}} \times \tan^{-1} \left(\frac{\sqrt{\xi} k_z}{\sqrt{\mathbf{k}^2 + \xi k_\perp^2}} \right) \right],$$

$$m_\beta^2 = m_D^2 \left(\left(\sqrt{\xi} + (1 + \xi) \tan^{-1}(\sqrt{\xi}) (\mathbf{k}^2 + \xi k_\perp^2) + \xi k_z \left(\xi k_z + (\mathbf{k}^2 (1 + \xi) / \sqrt{\mathbf{k}^2 + \xi k_\perp^2}) \right) \times \tan^{-1} \left(\sqrt{\xi} k_z / \sqrt{\mathbf{k}^2 + \xi k_\perp^2} \right) \right) \right) \times \left(2\sqrt{\xi} (1 + \xi) (\mathbf{k}^2 + \xi k_\perp^2) \right)^{-1}, \quad (27)$$

$$m_\gamma^2 = -\frac{m_D^2}{2} \left(\frac{\mathbf{k}^2}{\mathbf{k}^2 + \xi k_\perp^2} - \frac{1 + 2k_z^2/k_\perp^2}{\sqrt{\xi}} \tan^{-1}(\sqrt{\xi}) + \frac{k_z \mathbf{k}^2 (2\mathbf{k}^2 + 3\xi k_\perp^2)}{\sqrt{\xi} (\mathbf{k}^2 + \xi k_\perp^2)^{3/2} k_\perp^2} \times \tan^{-1} \left(\frac{\sqrt{\xi} k_z}{\sqrt{\mathbf{k}^2 + \xi k_\perp^2}} \right) \right),$$

$$m_\delta^2 = -\frac{\pi m_D^2 \xi k_z k_\perp |\mathbf{k}|}{4(\mathbf{k}^2 + \xi k_\perp^2)^{3/2}},$$

where $\alpha_s = g^2/4\pi$ is the strong coupling constant, and we assume constant coupling. The coordinate space potential can be obtained by taking Fourier transform of (26):

$$V(\mathbf{r}, \xi) = -g^2 C_F \int \frac{d^3 k}{(2\pi)^3} e^{-i\mathbf{k} \cdot \mathbf{r}} V(k_\perp, k_z, \xi), \quad (28)$$

which, under small ξ limit, reduces to [48]

$$V(\mathbf{r}, \xi) \approx V_{\text{iso}}(r) - g^2 C_F \xi m_D^2 \int \frac{d^3 k}{(2\pi)^3} e^{-i\mathbf{k} \cdot \mathbf{r}} \frac{2/3 - (\mathbf{k} \cdot \mathbf{n})^2 / \mathbf{k}^2}{(\mathbf{k}^2 + m_D^2)^2}, \quad (29)$$

where $V_{\text{iso}}(r) = -g^2 C_F e^{-m_D r} / (4\pi r)$. As indicated earlier, the potential depends on the angle between \mathbf{r} and \mathbf{n} . When $\mathbf{r} \parallel \mathbf{n}$ the potential (V_{\parallel}) is given by [48]

$$V_{\parallel}(\mathbf{r}, \xi) = V_{\text{iso}}(r) \left[1 + \xi \left(2 \frac{e^{\hat{r}} - 1}{\hat{r}^2} - \frac{2}{\hat{r}} - 1 - \frac{\hat{r}}{6} \right) \right], \quad (30)$$

whereas [48]

$$V_{\perp}(\mathbf{r}, \xi) = V_{\text{iso}}(r) \left[1 + \xi \left(\frac{1 - e^{\hat{r}}}{\hat{r}^2} + \frac{1}{\hat{r}} + \frac{1}{2} + \frac{\hat{r}}{3} \right) \right], \quad (31)$$

where $\hat{r} = r m_D$.

For arbitrary ξ , (28) has to be evaluated numerically. It has been observed that because of the lower density of the plasma particles in AQGP, the potential is deeper and closer to the vacuum potential than for $\xi = 0$ [48]. This means that the general screening is reduced in an AQGP.

Next, we consider quarkonium states in an AQGP where the potential, to linear order in ξ , is given by (29) which can also be written as [51]

$$V(\mathbf{r}, \xi) = V_{\text{iso}}(r) [1 - \xi (f_0(\hat{r}) + f_1(\hat{r}) \cos 2\theta)], \quad (32)$$

where $\cos \theta = \hat{r} \cdot \hat{n}$ and the functions are given by [51]

$$\begin{aligned} f_0(\hat{r}) &= \frac{6(1 - e^{\hat{r}}) + \hat{r}[6 - \hat{r}(\hat{r} - 3)]}{12\hat{r}^2} = -\frac{\hat{r}}{6} - \frac{\hat{r}^2}{48} + \dots, \\ f_1(\hat{r}) &= \frac{6(1 - e^{\hat{r}}) + \hat{r}[6 + \hat{r}(\hat{r} + 3)]}{12\hat{r}^2} = -\frac{\hat{r}^2}{16} + \dots \end{aligned} \quad (33)$$

With the previous expressions, the real part of the heavy quark potential in AQGP, after finite quark mass correction, becomes [51]

$$\begin{aligned} V(\mathbf{r}) &= -\frac{\alpha}{r} (1 + \mu r) \exp(-\mu r) + \frac{2\sigma}{\mu} [1 - \exp(-\mu r)] \\ &\quad - \sigma r \exp(-\mu r) - \frac{0.8}{m_{\text{Q}}^2 r}, \end{aligned} \quad (34)$$

where $\mu/m_D = 1 + \xi(3 + \cos 2\theta)/16$ and the previous expression is the minimal extension of the KMS potential [52] in AQGP. The ground states and the excited states of the quarkonium states in AQGP have been found by solving the three-dimensional Schrodinger equation using the finite difference time domain method [53]. Without going into further details, we will quote the main findings of the work of [51]. The binding energies of charmonium and bottomonium states are obtained as a function of the hard momentum scale. For a fixed hard momentum scale, it is seen that the binding energy increases with anisotropy. Note that the potential (34) is obtained by replacing m_D by μ in KMS equation [52]. For a given hard momentum scale $\mu < m_D$, the quarkonium states are more strongly bound than the isotropic case. This implies that the dissociation temperature for a particular quarkonium state is more in AQGP. It is found that the dissociation temperature for J/ψ in AQGP is $1.4T_c$, whereas for isotropic case it is $1.2T_c$ [51].

Quarkonium binding energies have also been calculated using a realistic potential including the complex part in [54] by solving the 3D Schrodinger equation where the potential has the form

$$V(\mathbf{r}, \xi) = V_R(\mathbf{r}, \xi) + iV_I(\mathbf{r}, \xi), \quad (35)$$

where the real part is given by (34) and the imaginary part is given in [55]. The main results of this calculations are as follows. For J/ψ , the dissociation temperature obtained in this case is $2.3T_c$ in isotropic case. It has been found that with anisotropy the dissociation temperature increases as the binding of quarkonium states becomes stronger in AQGP.

Thermal bottomonium suppression (R_{AA}) at RHIC and LHC energies has been calculated in [56, 57] in an AQGP. Two types of potentials have been considered there coming from the free energy (case A) and the internal energy (case B), respectively. By solving the 3D Schrodinger equation with these potentials, it has been found that the dissociation temperature for $\Upsilon(1s)$ becomes 373 MeV and 735 MeV for the cases A and B, respectively, whereas in case of $\xi = 0$, these become 298 MeV and 593 MeV. Thus, the dissociation temperature increases in case of AQGP irrespective of the choice of the potential. In case of other bottomonium states, the dissociation temperatures increase compared to the isotropic case. The nuclear modification factor has been calculated by coupling AHYDRO [46] with the solutions of Schrodinger equation. Introduction of AHYDRO into the picture makes p_{hard} and ξ functions of proper time (τ), transverse coordinate (\mathbf{x}_\perp), and the space-time rapidity (Θ). As a consequence, both the real and imaginary part of the binding energies become functions of τ , \mathbf{x}_\perp , and Θ . Now the nuclear modification factor (R_{AA}) is related to the decay rate (Γ) of the state in question, where $\Gamma = -2\mathcal{I}[E]$. Thus, R_{AA} is given by [56, 57]

$$R_{AA}(p_T, \mathbf{x}_\perp, \Theta) = e^{-\zeta(p_T, \mathbf{x}_\perp, \Theta)}, \quad (36)$$

where $\zeta(p_T, \mathbf{x}_\perp, \Theta)$ is given by

$$\zeta(p_T, \mathbf{x}_\perp, \Theta) = \theta(\tau_f - \tau_{\text{form}}) \int_{\max(\tau_{\text{form}}, \tau_i)}^{\tau_f} d\tau \Gamma(p_T, \mathbf{x}_\perp, \Theta). \quad (37)$$

Here, τ_{form} is the formation time of the particular state in the laboratory frame and τ_f is the time when the hard momentum scale reaches T_c . To study the nuclear suppression of a particular state, one needs to take into account the decay of the excited states to this particular state (so-called feed down). For RHIC energies, using the value of $dN_{\text{ch}}/dy = 620$ and various values of η/S (note that η/S is related to the anisotropy parameter, ξ) the corresponding initial temperatures are estimated with $\tau_i = 0.3 \text{ fm}/c$. p_T integrated R_{AA} values of individual bottomonium states (direct production) have been calculated using both the potentials A and B [56, 57] as functions of number of participants and rapidity. It is seen that for both potentials, more suppression is observed in case of anisotropic medium than in the isotropic case. However, the suppression is more in case of potential model A. There is also indication of sequential suppression [56, 57]. Similar exercise has also been done in case of LHC energies ($\sqrt{s} = 2.76 \text{ TeV}$) using a constant value of η/S . It is again observed that the suppression in case of potential A is more. These findings can be used to constrain η/S by comparing with the RHIC and LHC data.

Next, we discuss the effect of the initial state momentum anisotropy on the survival probability of J/ψ due to gluon dissociation. This is important as we have to take into account all possibilities of quarkonium getting destroyed in the QGP to estimate the survival probability and hence R_{AA} . In contrast to Debye screening, this is another possible mechanism of J/ψ suppression in QGP. In QGP, the gluons have much harder momentum, sufficient to dissociate the charmonium.

Such a study was performed in an isotropic plasma [58]. In this context, we will study the thermally weighted gluon dissociation cross of J/ψ in an anisotropic media.

Bhanot and Peskin first calculated the quarkonium-hadron interaction cross-section using operator product expansion [59]. The perturbative prediction for the gluon J/ψ dissociation cross-section is given by [60]

$$\sigma(q^0) = \frac{2\pi}{3} \left(\frac{32}{3}\right)^2 \left(\frac{16\pi}{3g_2}\right) \frac{1}{m_Q^2} \frac{(q^0/\epsilon_0 - 1)^{3/2}}{(q^0/\epsilon_0)^5}, \quad (38)$$

where q^0 is the energy of the gluon in the stationary J/ψ frame; ϵ_0 is the binding energy of the J/ψ where $q_0 > \epsilon_0$, and m_Q is charm quark mass. It is to be noted that we have used the constant binding energy of the J/ψ in AQGP at finite temperature. We assume that the J/ψ moves with four momentum P given by

$$P = (M_T \cosh y, 0, P_T, M_T \sinh y), \quad (39)$$

where $M_T = \sqrt{M_{J/\psi}^2 + P_T^2}$ is the J/ψ transverse mass and y is the rapidity of the J/ψ . A gluon with a four momentum $K = (k^0, \mathbf{k})$ in the rest frame of the parton gas has energy $q^0 = K \cdot u$ in the rest frame of the J/ψ . The thermal gluon J/ψ dissociation cross-section in anisotropic media is defined as [15, 58]

$$\langle \sigma(K \cdot u) v_{\text{rel}} \rangle_k = \frac{\int d^3k \sigma(K \cdot u) v_{\text{rel}} f(k^0, \xi, p_{\text{hard}})}{\int d^3k f(k^0, \xi, p_{\text{hard}})}, \quad (40)$$

where $v_{\text{rel}} = 1 - (\mathbf{k} \cdot \mathbf{P})/(k^0 M_T \cosh y)$ is the relative velocity between J/ψ and the gluon. Now changing the variable ($K \leftrightarrow Q$), one can obtain by using Lorentz transformation [15], the following relations:

$$k^0 = \frac{(q^0 E + q(\sin \theta_p \sin \theta_q \sin \phi_q + \cos \theta_p \cos \theta_q))}{M_{J/\psi}},$$

$$\mathbf{k} = \mathbf{q} + \frac{qE}{|\mathbf{P}| M_{J/\psi}} \times \left[(q M_T \cosh y - M_{J/\psi}) \times (\sin \theta_p \sin \theta_q \sin \phi_q + \cos \theta_p \cos \theta_q) + |\mathbf{P}| \right] \mathbf{v}_{J/\psi}, \quad (41)$$

where $\mathbf{v}_{J/\psi} = \mathbf{P}/E$, $P = (E, 0, |\mathbf{P}| \sin \theta_p, |\mathbf{P}| \cos \theta_p)$, and $\mathbf{q} = (q \sin \theta_q \cos \phi_q, q \sin \theta_q \sin \phi_q, q \cos \theta_q)$. In the rest frame of J/ψ , numerator of (40) can be written as

$$\int d^3q \frac{M_{J/\psi}}{E} \sigma(q^0) f(k^0, \xi, p_{\text{hard}}), \quad (42)$$

while, the denominator of (40) can be written as [30]

$$\int d^3k f(k^0, \xi, p_{\text{hard}}) = \int d^3k f_{\text{iso}} \left(\sqrt{\mathbf{k}^2 + \xi(\mathbf{k} \cdot \hat{\mathbf{n}})^2}, p_{\text{hard}} \right) = \frac{1}{\sqrt{1 + \xi}} 8\pi \zeta(3) p_{\text{hard}}^3, \quad (43)$$

where $\zeta(3)$ is the Riemann zeta function. The maximum value of the gluon J/ψ dissociation cross-section [60] is about 3 mb in the range $0.7 \leq q^0 \leq 1.7$ GeV. Therefore high-momentum gluons do not see the large object and simply passes through it, and the low-momentum gluons cannot resolve the compact object and cannot raise the constituents to the continuum.

To calculate the survival probability of J/ψ in an anisotropic plasma, we consider only the longitudinal expansion of the matter. The survival probability of the J/ψ in the deconfined quark-gluon plasma is

$$S(P_T) = \frac{\int d^2r (R_A^2 - r^2) \exp \left[- \int_{\tau_i}^{\tau_{\text{max}}} d\tau n_g(\tau) \langle \sigma(K \cdot u) v_{\text{rel}} \rangle_k \right]}{\int d^2r (R_A^2 - r^2)}, \quad (44)$$

where $\tau_{\text{max}} = \min(\tau_\psi, \tau_f)$ and τ_i are the QGP formation time. $n_g(\tau) = 16\zeta(3) p_{\text{hard}}^3(\tau)/[\pi^2 \sqrt{1 + \xi(\tau)}]$ is the gluon density at a given time τ . Now the J/ψ will travel a distance in the transverse direction with velocity $\mathbf{v}_{J/\psi}$ given by

$$d = -r \cos \phi + \sqrt{R_A^2 - r^2 (1 - \cos^2 \phi)}, \quad (45)$$

where $\cos \phi = \hat{\mathbf{v}}_{J/\psi} \cdot \hat{\mathbf{r}}$. The time interval $\tau_\psi = M_T d/P_T$ is the time before J/ψ escapes from a gluon gas of transverse extension R_\perp . The time evaluation of ξ and p_{hard} is determined by (3) and (4).

We now first discuss the numerical result of the thermal averaged gluon dissociation cross-section in the anisotropic system. The results are displayed in Figure 4 for $P_T = 0$ and $P_T = 8$ GeV for a set of values of the anisotropy parameter. It is seen that the velocity averaged cross-section decreases with ξ for p_{hard} up to ~ 500 MeV and then increases as compared to the isotropic case ($\xi = 0$) (see Figure 4(a)). For higher P_T , a similar feature has been observed in Figure 4(b), where the cross-section starts to increase beyond $p_{\text{hard}} \sim 200$ MeV. For fixed p_{hard} , the dissociation cross-section as a function of P_T shows that the cross-section first decreases and then marginally increases [15].

Equation (44) has been used to calculate the survival probability. Figure 5 describes the survival probability of J/ψ for various values of the isotropization time τ_{iso} at RHIC energy. Left (Right) panel corresponds to $\theta_p = \pi/2$ ($\theta_p = \pi/3$). It is observed that the survival probability remains the same as in the isotropic case upto $P_T = 4$ GeV in the central region. Beyond that marginal increase is observed with the increase of τ_{iso} . In the forward rapidity, the results are almost the same as the isotropic case throughout the whole P_T region. For this set of initial conditions, the argument of the exponential in (44) becomes similar to that of the isotropic case. Also the dissociation cross-section first decreases with P_T and then increases. Because of these reasons, we observe minor change in the survival probability [15]. Therefore, the survival probability is more or less independent of the direction of propagation of the J/ψ with respect to the anisotropy axis, whereas in the case of radiative energy loss of

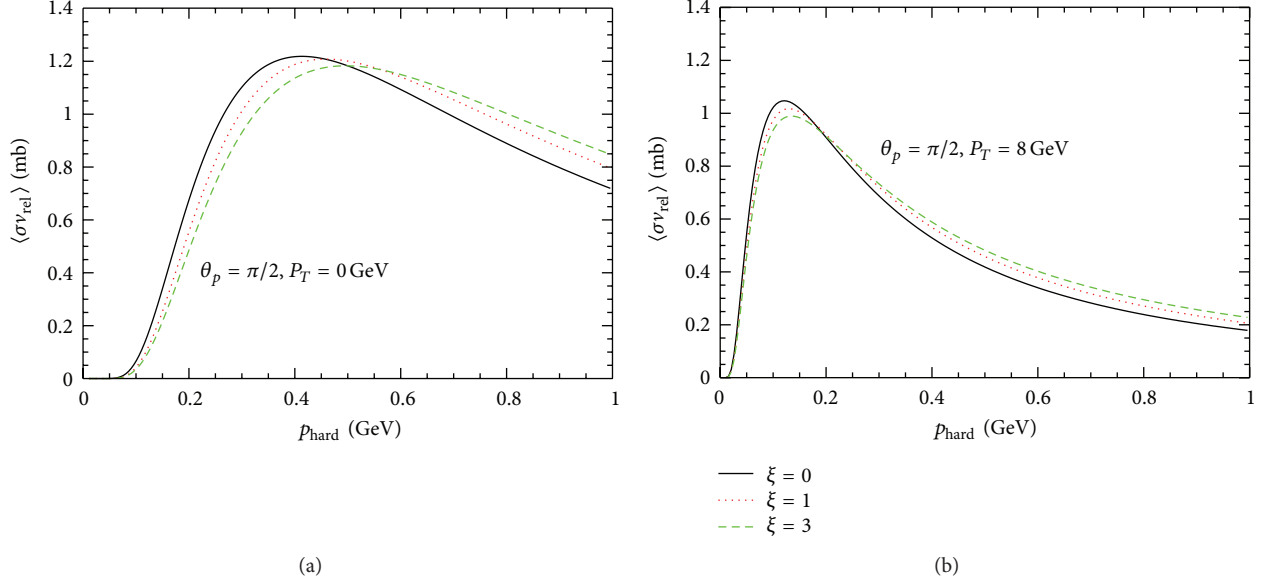


FIGURE 4: (Color online) The thermal-averaged gluon J/ψ dissociation cross-section as function of the hard momentum scale at central rapidity ($\theta_p = \pi/2$) for $\xi = \{0, 1, 3, 5\}$. (a) corresponds to $P_T = 0$ and (b) is for $P_T = 8$ GeV.

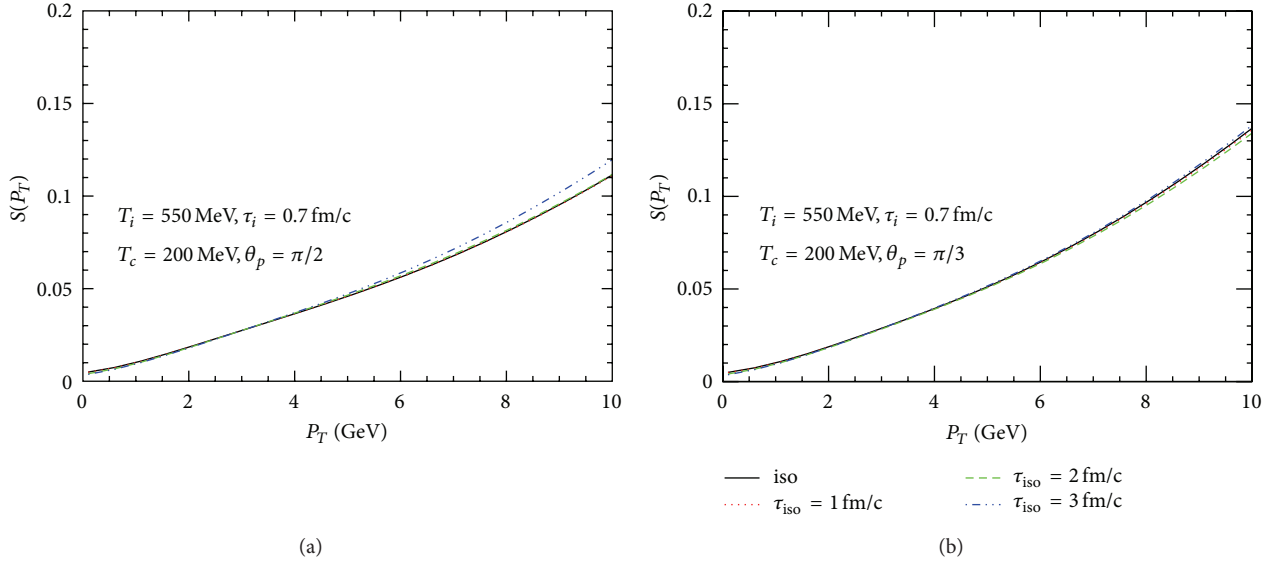


FIGURE 5: (Color online) The survival probability of J/ψ in an anisotropic plasma at central and forward rapidity region. The initial conditions are taken as $T_i = 550$ MeV, $T_c = 200$ MeV, and $\tau_i = 0.7$ fm/c.

fast partons in anisotropic media the result has been shown to depend strongly on the direction of propagation [32]. The results for the LHC energies for the two sets of initial conditions at two values of the transition temperatures are shown in Figure 6. For set I, we observe marginal increase as in the case for set I at RHIC energies. However, for set II substantial modification is observed for the reason stated earlier.

4. Radiative Energy Loss and R_{AA} of Light Hadrons

In this section, we calculate the radiative energy loss in an infinitely extended anisotropic plasma. We assume that an

on-shell quark produced in the remote past is propagating through an infinite QCD medium that consists of randomly distributed static scattering centers which provide a color-screened Yukawa potential originally developed for the isotropic QCD medium given by [61]

$$\begin{aligned}
 V_n &= V(q_n) e^{i\mathbf{q}_n \cdot \mathbf{x}_n} \\
 &= 2\pi\delta(q^0) v(q_n) e^{-i\mathbf{q}_n \cdot \mathbf{x}_n} T_{a_n}(R) \otimes T_{a_n}(n),
 \end{aligned} \tag{46}$$

with $v(\mathbf{q}_n) = 4\pi\alpha_s/(q_n^2 + m_D^2)$. x_n is the location of the n th scattering center, T denotes the color matrices of the parton and the scattering center. It is to be noted that the

In the previous expression, λ denotes the average mean-free path of the quark scattering and is given by

$$\frac{1}{\lambda} = \frac{1}{\lambda_g} + \frac{1}{\lambda_q}, \quad (50)$$

which depends on the strength of the anisotropy. In the last expression λ_q and λ_g correspond to the contributions coming from q - q and q - g scattering, respectively. Consider

$$\frac{1}{\lambda_i} = \frac{C_R C_2(i) \rho(i)}{N_c^2 - 1} \int \frac{d^2 q_\perp}{(2\pi)^2} |V(q_\perp, 0, \xi)|^2, \quad (51)$$

where $C_2(i)$ is the Casimir for the d_i -dimensional representation and $C_2(i) = (N_c^2 - 1)/(2N_c)$ for quark and $C_2(i) = N_c$ for gluon scatterers. ρ_i is the density of the scatterers. Using $\rho_i = \rho_i^{\text{iso}} \sqrt{1 + \xi}$, we obtain

$$\frac{1}{\lambda} = \frac{18\alpha_s p_{\text{hard}} \zeta(3)}{\pi^2 \sqrt{1 + \xi}} \frac{1}{R(\xi)} \frac{1 + N_F/6}{1 + N_F/4}, \quad (52)$$

where N_F is the numbers of flavors.

The fractional energy loss in anisotropy medium for the light quark is shown in Figure 7. We consider a plasma at a temperature $T = 250$ MeV with the effective number of degrees of freedom $N_F = 2.5$, $\alpha_s = 0.3$ and the length of the medium is $L = 5$ fm. The energy loss in the anisotropic media depends on the angle of propagation of the fast parton with respect to the anisotropy axis ($\hat{\mathbf{n}}$). We see that the fractional energy loss increases in the direction parallel to the anisotropy axis. With the increase of anisotropy parameter ξ the fractional energy loss subsequently increases for $\theta_n = \pi/6$. However, away from the anisotropy axis ($\theta_n = \pi/2$), the fractional energy loss decreases because the quark-quark potential is stronger in the anisotropy direction [32]. In the perpendicular direction to the anisotropy axis, the fractional energy loss is quite small. The fractional energy loss for the heavy quarks (i.e., for charm and bottom) is shown in Figure 8. The fractional energy loss is enhanced in the direction parallel to anisotropy axis as well as for $\theta_n = \pi/6$. However, for $\theta_n = \pi/2$, the fractional energy loss decreases for both heavy and light quarks.

Next, we consider the nuclear modification factor of light hadrons incorporating the light quark energy loss in AQGP discussed in the previous paragraphs. When a parton is propagating in the direction of anisotropy it is found that the fractional energy loss increases. In this section, we will apply this formalism to calculate the nuclear modification factor of the light hadrons. Starting with two-body scattering at the parton level, the differential cross-section for the hadron production is [63]

$$\begin{aligned} E \frac{d\sigma}{d^3 p} (AB \rightarrow \text{jet} + X) \\ = K \sum_{abcd} \int dx_a dx_b G_{a/h_A}(x_a, Q^2) G_{b/h_B} \\ \times (x_b, Q^2) \frac{\hat{s}}{\pi} \frac{d\sigma}{dt} (ab \rightarrow cd) \delta(\hat{s} + \hat{t} + \hat{u}). \end{aligned} \quad (53)$$

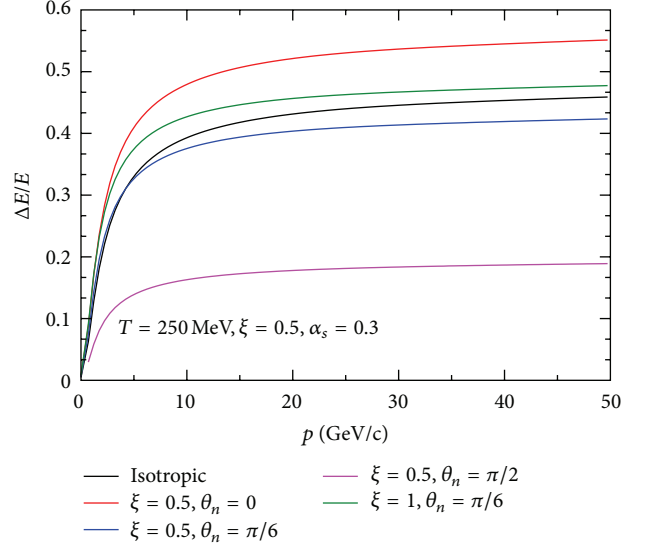


FIGURE 7: Color online: fractional energy loss for the light quark for $\xi = (0.5, 1)$.

The argument of the δ function can be expressed in terms of x_a and x_b , and doing the x_b integration we arrive at the final expression as follows:

$$\begin{aligned} E \frac{d\sigma}{d^3 p} (AB \rightarrow \text{jet} + X) \\ = K \sum_{abcd} \int_{x_{\min}}^1 dx_a G_{a/h_A}(x_a, Q^2) G_{b/h_B} \\ \times (x_b, Q^2) \frac{2}{\pi} \frac{x_a x_b}{2x_a - x_T e^{-y}} \frac{d\sigma}{dt} (ab \rightarrow cd), \end{aligned} \quad (54)$$

where $x_b = (x_a x_T e^{-y}) / (2x_a - x_T e^{-y})$, $x_T = 2p_T / \sqrt{s}$, and $x_{\min} = x_T e^y / (2 - x_T e^{-y})$, and the factor K is introduced to take into account the higher-order effects. It should be noted that to obtain single-particle inclusive invariant cross-section, the fragmentation function $D_{h/c}(z, Q^2)$ must be included. To obtain the hadronic p_T spectra in A-A collisions, we multiply the result by the nuclear overlap function for a given centrality. The inclusion of jet quenching as a final state effect in nucleus-nucleus collisions can be implemented in two ways: (i) modifying the partonic p_T spectra [64] and (ii) modifying the fragmentation function [65] but keeping the partonic p_T spectra unchanged. In this calculation we intend to modify the fragmentation function. The effective fragmentation function can be written as

$$D_{h/c}(z, Q^2) = \frac{z^*}{z} D_{h/c}(z^*, Q^2), \quad (55)$$

where $z^* = z / (1 - \Delta E/E)$ is the modified momentum fraction. Now we take into account the jet production geometry. We assume that all the jets are not produced at the same point; therefore, the path length transversed by the partons before

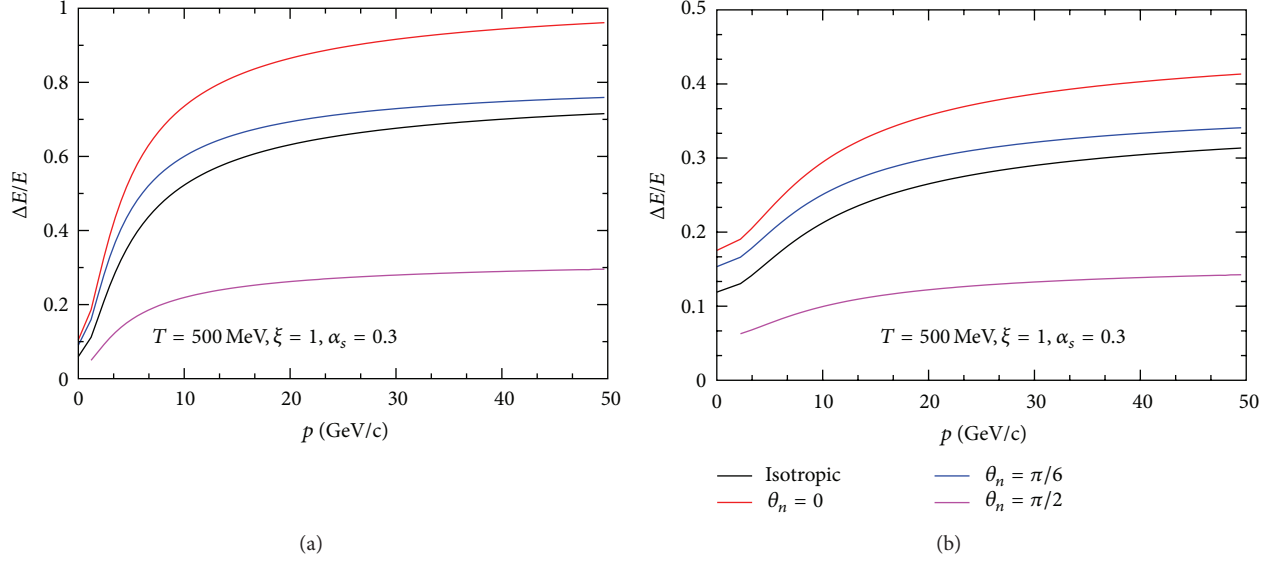


FIGURE 8: (Color online) Same as 7 for charm quark (a) and bottom quark (b) with $\xi = 1$ and $T = 500$ MeV.

the fragmentation is not the same. We consider a jet initially produced at (r, ϕ) and leaves the plasma after a proper time (t_L) or equivalently after traversing a distance L (for light quarks $t_L = L$) where

$$L(r, \phi) = \sqrt{R_\perp^2 - r^2 \sin^2 \phi} - R_\perp \cos \phi, \quad (56)$$

where R_\perp is the transverse dimension of the system. Since the number of jets produced at \mathbf{r} is proportional to the number of binary collisions, the probability is proportional to the product of the thickness functions as follows:

$$\mathcal{P}(\vec{r}) \propto T_A(\vec{r}) T_B(\vec{r}). \quad (57)$$

In case of hard sphere $\mathcal{P}(r)$ is given by [66]

$$\mathcal{P}(r) = \frac{2}{\pi R_\perp^2} \left(1 - \frac{r^2}{R_\perp^2}\right) \theta(R_\perp - r), \quad (58)$$

where $\int d^2r \mathcal{P}(r) = 1$. To obtain the hadron p_T spectra, we have to convolute the resulting expression over all transverse positions and the expression is

$$\begin{aligned} & \frac{dN^{\pi^0(\eta)}}{d^2p_T dy} \\ &= \sum_f \int d^2r \mathcal{P}(r) \int_{t_i}^{t_L} \frac{dt}{t_L - t_i} \\ & \quad \times \int \frac{dz}{z^2} D_{\pi^0(\eta)/f}(z, Q^2) \Big|_{z=p_T/p_T^f} E \frac{dN}{d^3p^f}. \end{aligned} \quad (59)$$

The quantity $E(dN/d^3p^f)$ is the initial momentum distribution of jets and can be computed using LO-pQCD. Here, we use average distance traversed by the partons, $\langle L \rangle$ is given by

$$\langle L \rangle = \frac{\int_0^{R_T} r dr \int_0^{2\pi} L(\phi, r) T_{AA}(r, b=0) d\phi}{\int_0^{R_T} r dr \int_0^{2\pi} T_{AA}(r, b=0) d\phi}, \quad (60)$$

where $\langle L \rangle \sim 5.8(6.2)$ fm for RHIC (LHC). Finally, the nuclear modification factor (R_{AA}) becomes [44]

$$R_{AA}(p_T) = \frac{dN_{AA}^{\pi^0(\eta)}/d^2p_T dy}{\left[dN_{AA}^{\pi^0(\eta)}/d^2p_T dy \right]_0}, \quad (61)$$

where $[dN_{AA}^{\pi^0(\eta)}/d^2p_T dy]_0$ corresponds to the hadron p_T distribution without the energy loss.

For an expanding plasma, the anisotropy parameter p_{hard} and ξ are time dependent. The time evaluation is again given by (3) and (4). In the present work, it is assumed that an isotropic QGP is formed at an initial time τ_i and initial temperature T_i . Rapid longitudinal expansion of the plasma leads to an anisotropic QGP which lasts till τ_{iso} . For 0–10% centrality (relevant for our case), we obtain $T_i = 440(350)$ MeV for $\tau_i = 0.147(0.24)$ fm/c. at RHIC energy [44].

Figure 9 describes the nuclear modification factor for two different initial conditions with various values of isotropization time, τ_{iso} along with the PHENIX data [67]. It is quite clear from Figure 9(a) that the value of R_{AA} for anisotropic medium is lower than that for the isotropic media as the energy loss in the anisotropy medium is higher [32]. It is also observed that as τ_{iso} increases the value of R_{AA} decreases compared to its isotropic value [44]. This is because the hard scale decreases slowly as compared to the isotropic case, that is, the cooling is slow. For reasonable choices of τ_{iso} , the experimental data is well described. It is seen that increasing the value of τ_{iso} beyond 1.5 fm/c grossly underpredict the data. We find that the extracted value of isotropization time lies in the range $0.5 \leq \tau_{\text{iso}} \leq 1.5$ fm/c [44]. This is in agreement with the earlier finding of τ_{iso} using PHENIX photon data [16]. In order to see the sensitivity on the initial conditions we now consider another set of initial conditions, $T_i = 350$ MeV and $\tau_i = 0.24$ fm/c. The result is shown in Figure 9(b). It is observed that to reproduce the data a larger value of τ_{iso} is

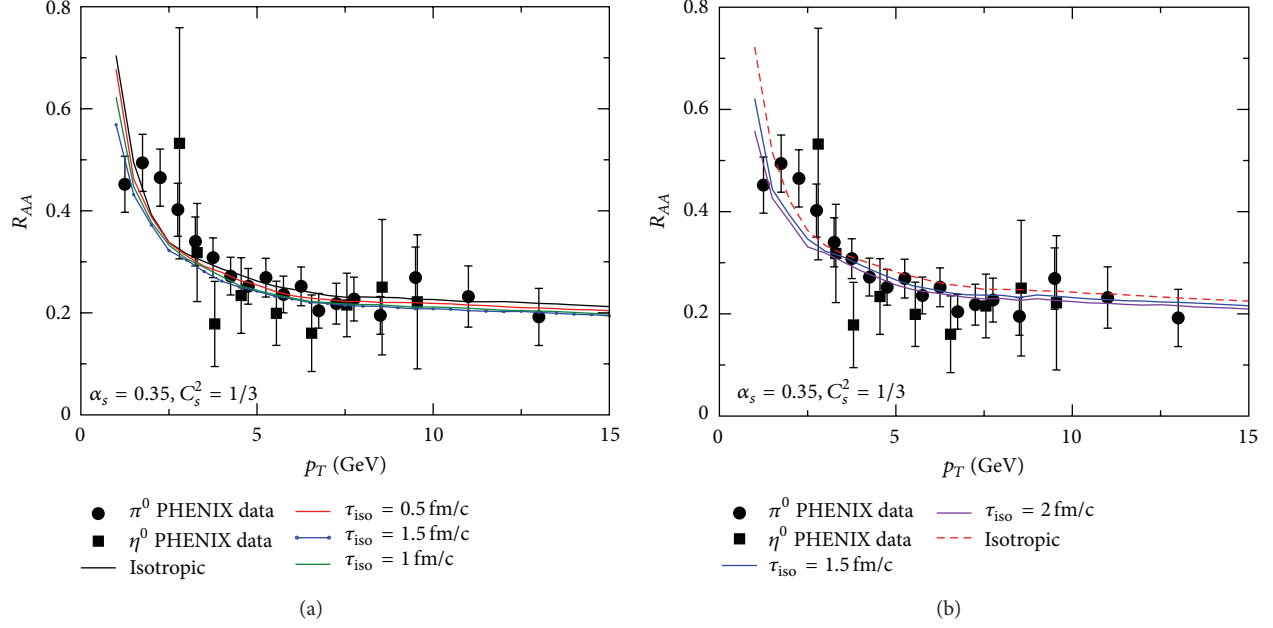


FIGURE 9: (Color Online) Nuclear modification factor at RHIC energies. The initial conditions are taken as (a) $T_i = 440$ MeV and $\tau_i = 0.147$ fm/c and (b) $T_i = 350$ MeV and $\tau_i = 0.24$ fm/c.

needed as compared to the case of higher initial temperature. We extract an upper limit of $\tau_{\text{iso}} = 2$ fm/c [44] in this case.

5. Plasma Wakes

It is mentioned earlier that when a jet propagates through hot and dense medium it loses energy mainly by the radiative process. As mentioned earlier, it also creates wake in the charge density as well as in the potential. Now, we calculate the wake in charge density and the wake potential due to the passage of a fast parton in a small ξ limit. Dielectric function contains essentially all the information of the chromoelectromagnetic properties of the plasma. The dielectric function $\epsilon(\mathbf{k}, \omega)$ can be calculated from the dielectric tensor using the following relation:

$$\epsilon(\mathbf{k}, \omega) = \frac{k_i e^{ij}(\mathbf{k}, \omega) k_j}{k^2}, \quad (62)$$

where the dielectric tensor e^{ij} can be written in terms of the gluon polarization tensor as follows (given by (18)):

$$e^{ij} = \delta^{ij} - \frac{\Pi^{ij}}{\omega^2}. \quad (63)$$

Therefore, the dielectric function is directly related to the structure functions mentioned in Section 3 through (18), (63), and (62). To get the analytic expressions for the structure functions, one must resort to small ξ limit. To linear order in ξ , we have [28]

$$\alpha = \Pi_T(z) + \xi \left[\frac{z^2}{12} (3 + 5 \cos 2\theta_n) m_D^2 - \frac{1}{6} (1 + \cos 2\theta_n) m_D^2 \right],$$

$$+ \frac{1}{4} \Pi_T(z) \left((1 + 3 \cos 2\theta_n) - z^2 (3 + 5 \cos 2\theta_n) \right) \Big],$$

$$\beta = z^2 \left[\Pi_L(z) + \xi \left[\frac{1}{6} (1 + 3 \cos 2\theta_n) m_D^2 + \Pi_L(z) \left(\cos 2\theta_n - \frac{z^2}{2} (1 + 3 \cos 2\theta_n) \right) \right] \right],$$

$$\gamma = \frac{\xi}{3} (3\Pi_T(z) - m_D^2) (z^2 - 1) \sin^2 \theta_n,$$

$$\delta = \frac{\xi}{3k} \left[4z^2 m_D^2 + 3\Pi_T(z) (1 - 4z^2) \right] \cos \theta_n, \quad (64)$$

with

$$\Pi_T(K) = \frac{m_D^2}{2} z^2 \times \left[1 - \frac{1}{2} \left(z - \frac{1}{z} \right) \left(\ln \left| \frac{z+1}{z-1} \right| - i\pi \Theta(1-z^2) \right) \right],$$

$$\Pi_L(K) = m_D^2 \left[\frac{z}{2} \left(\ln \left| \frac{z+1}{z-1} \right| - i\pi \Theta(1-z^2) \right) - 1 \right], \quad (65)$$

where $z = \omega/k$.

In the presence of the test charge particle, the induced charge density and the wake potential depend on the velocity of the external charged parton and also on the distribution

of the background particle [68]. When a static test charge is introduced in a plasma, it acquires a shielding cloud. As a result, the induced charge distribution is spherically symmetric. When a charge particle is in motion relative to the plasma, the induced charge distribution no longer remains symmetric. As a result spherical symmetry of the screening cloud reduces to ellipsoidal shape.

The passage of external test charge through the plasma also disturbs the plasma and creates induced color charge density [69]. Therefore, the total color charge density is given as

$$\rho_{\text{tot}}^a(\mathbf{k}, \omega) = \rho_{\text{ext}}^a(\mathbf{k}, \omega) + \rho_{\text{ind}}^a(\mathbf{k}, \omega), \quad (66)$$

where a represents the color index. However, the total color charge density is linearly related to ρ_{ext}^a through the dielectric response function ($\rho_{\text{tot}}^a(\mathbf{k}, \omega) = \rho_{\text{ext}}^a(\mathbf{k}, \omega)/\epsilon(\mathbf{k}, \omega)$). Therefore, the induced color charge density is explicitly written as

$$\rho_{\text{ind}}^a(\mathbf{k}, \omega) = \left(\frac{1}{\epsilon(\mathbf{k}, \omega)} - 1 \right) \rho_{\text{ext}}^a(\mathbf{k}, \omega). \quad (67)$$

Now, we consider a charge particle Q^a moving with a constant velocity \mathbf{v} and interacting with the anisotropic plasma. The external charge density associated with the test charge particle can be written as [33, 34, 38]

$$\rho_{\text{ext}}^a = 2\pi Q^a \delta(\omega - \mathbf{k} \cdot \mathbf{v}). \quad (68)$$

The delta function indicates that the value of ω is real and the velocity of the charge particle is restricted between $0 < v < 1$, which is known as the Cerenkov condition for the moving parton in the medium. Therefore, the collective modes are determined in the space-like region of the ω - k plane [34, 38]. According to Cerenkov condition, there will be two important scenarios which occur due to the interaction of the particle and the plasmon wave: first, the modes which are moving with a speed less than the average speed of the plasmon modes can be excited, but the particle moving slightly slower than the wave will be accelerated. While the charge particle moving faster than the wave will decrease its average velocity [69]. The slowly moving particle absorbs energy from the wave, the faster moving particle transfers its extra energy to the wave. The absorption and emission of energy result in a wake in the induced charge density as well as in the potential. Second, when the charge particle moving with a speed greater than the average phase velocity v_p , the modes are excited and they may not be damped. Such excited modes can generate Cerenkov-like radiation and a Mach stem [70] which leads to oscillation both in the induced charge density and in the wake potential.

Substituting (68) into (67) and transforming into \mathbf{r} - t space, the induced charge density becomes

$$\begin{aligned} \rho_{\text{ind}}^a(\mathbf{r}, t) &= 2\pi Q^a \int \frac{d^3k}{(2\pi)^3} \\ &\times \int \frac{d\omega}{2\pi} \exp^{i(\mathbf{k} \cdot \mathbf{r} - \omega t)} \left(\frac{1}{\epsilon(\mathbf{k}, \omega)} - 1 \right) \\ &\times \delta(\omega - \mathbf{k} \cdot \mathbf{v}). \end{aligned} \quad (69)$$

First, we consider the case where the fast parton is moving in the beam direction, that is, $\mathbf{v} \parallel \hat{\mathbf{n}}$. In spherical coordinate system $\mathbf{k} = (k \sin \theta_n \cos \phi, k \sin \theta_n \sin \phi, k \cos \theta_n)$ and the cylindrical coordinate for $\mathbf{r} = (\rho, 0, z)$; therefore, the induced charge density can be written as

$$\begin{aligned} \rho_{\text{ind}}^a(\mathbf{r}, t) &= \frac{Q^a m_D^3}{2\pi^2} \int_0^\infty dk k^2 \\ &\times \int_0^1 d\chi J_0 \left(k\rho \sqrt{1 - \chi^2 m_D} \right) \\ &\times \left[\cos \Gamma \left(\frac{\text{Re } \epsilon(\mathbf{k}, \omega)}{\Delta} - 1 \right) \right. \\ &\quad \left. + \sin \Gamma \frac{\text{Im } \epsilon(\mathbf{k}, \omega)}{\Delta} \right] \Big|_{\omega=\mathbf{k} \cdot \mathbf{v}}, \end{aligned} \quad (70)$$

where χ is represented as $\cos \theta_n$, J_0 is the zeroth-order Bessel function, $\Gamma = k\chi(z - vt)m_D$, and $\Delta = (\text{Re } \epsilon(\mathbf{k}, \omega))^2 + (\text{Im } \epsilon(\mathbf{k}, \omega))^2$. To get the previous equation, we use the simple transformation $\omega \rightarrow \omega m_D$ and $k \rightarrow km_D$. It is seen that the charge density ρ_{ind}^a is proportional to m_D^3 .

Numerical evaluation of the previous equation leads to the contour plots of the induced charge density shown in Figure 10 with two different speeds of the fast parton. The contour plot of the equicharge lines shows a sign flip along the direction of the moving parton in Figure 10. The left (right) panel shows the contour plot of the induced color charge density in both isotropic and anisotropic plasma with parton velocity $v = 0.55(0.99)$. It is clearly seen that, because of anisotropy, the positive charge lines appear alternately in the backward space which indicates a small oscillatory behavior of the color charge wake (see Figure 10(c)). When the charge particle moves faster than the average plasmon speed, the induced charge density forms a cone-like structure which is significantly different from when the parton velocity is $v = 0.55$. It is also seen that the induced charge density is oscillatory in nature. The supersonic nature of the parton leads to the formation of Mach cone and the plasmon modes could emit a Cerenkov-like radiation, which spatially limits the disturbances in the induced charge density [71]. In the backward space ($(z - vt) < 0$), induced color charge density is very much sensitive to the anisotropic plasma than that in the forward space ($(z - vt) > 0$). Due to the effect of the anisotropy, the color charge wake is modified significantly and the oscillatory behavior is more pronounced than the isotropic case. It is also seen that the oscillatory nature increases with the increase of the anisotropic parameter ξ .

Next, we consider the case when the parton moves perpendicular to the anisotropy direction in which case the induced charge density can be written as

$$\begin{aligned} \rho_{\text{ind}}^a(\mathbf{r}, t) &= \frac{Q^a m_D^3}{2\pi^2} \int_0^\infty dk k^2 \\ &\times \int_0^1 d\chi \int_0^{2\pi} \frac{d\phi}{2\pi} \left[\cos \Omega \left(\frac{\text{Re } \epsilon(\mathbf{k}, \omega)}{\Delta} - 1 \right) \right. \\ &\quad \left. + \sin \Omega \frac{\text{Im } \epsilon(\mathbf{k}, \omega)}{\Delta} \right] \Big|_{\omega=\mathbf{k} \cdot \mathbf{v}}, \end{aligned} \quad (71)$$

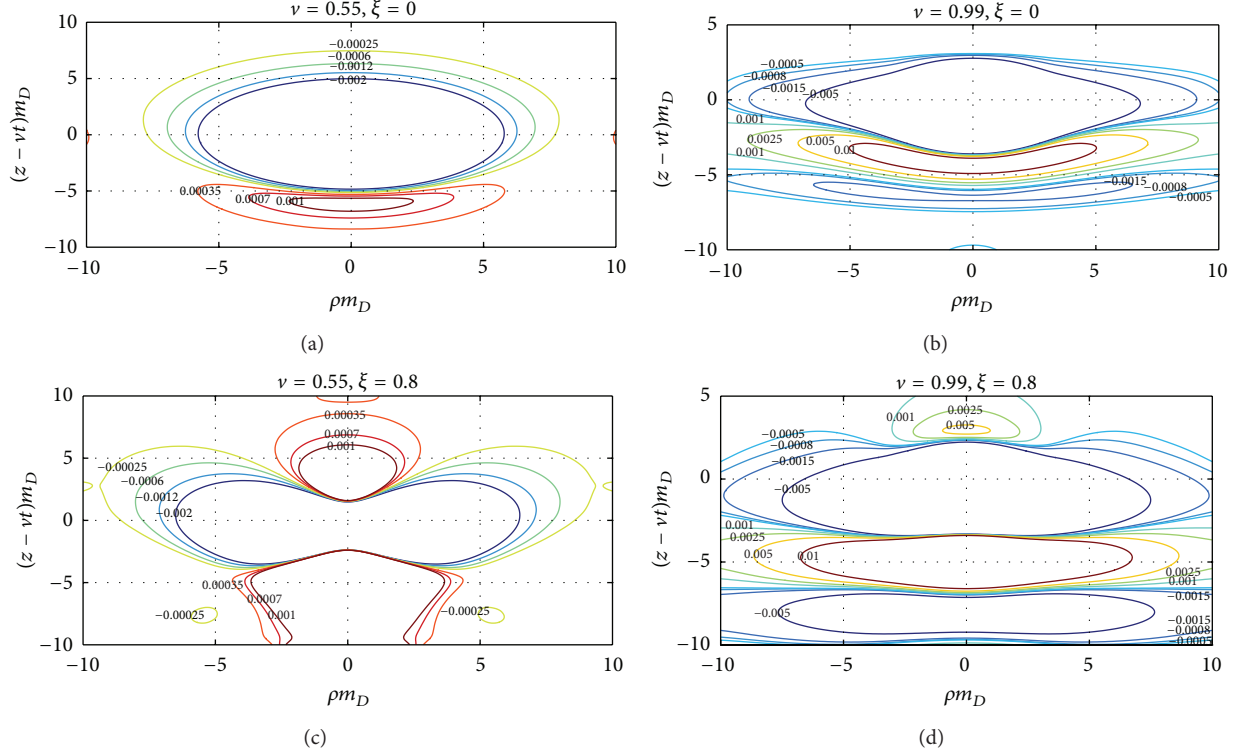


FIGURE 10: (Color online) Left Panel: the plot shows equicharge line with parton velocity $\nu = 0.55$ for different $\xi(0, 0.8)$. Right Panel: same as left panel with parton velocity $\nu = 0.99$.

with $\Omega = k(z\chi + (\rho - vt)\sqrt{1 - \chi^2} \cos \phi)m_D$. Numerical results of the equicharge lines are shown in Figure 11. The left (right) panel shows the contour plots of the induced charge density for the parton velocity $\nu = 0.55(0.99)$. When $\nu = 0.99$, the number of induced charge lines that appear alternately in the backward space is reduced for the anisotropic plasma in comparison to the isotropic plasma. Therefore, the anisotropy reduces the oscillatory behavior of the induced color charge density when the parton moves perpendicular to the anisotropy direction.

According to the Poisson equation, the wake potential induced by the fast parton reads as [33]

$$\Phi^a(\mathbf{k}, \omega) = \frac{\rho_{\text{ext}}^a(\mathbf{k}, \omega)}{k^2 \epsilon(\mathbf{k}, \omega)}. \quad (72)$$

Substituting (68) into (72) and transforming to the configuration space, the wake potential is given by [38]

$$\begin{aligned} \Phi^a(\mathbf{r}, t) &= 2\pi Q^a \int \frac{d^3 k}{(2\pi)^3} \int \frac{d\omega}{2\pi} \exp^{i(\mathbf{k}\cdot\mathbf{r} - \omega t)} \frac{1}{k^2 \epsilon(\omega, \mathbf{k})} \delta(\omega - \mathbf{k} \cdot \mathbf{v}). \end{aligned} \quad (73)$$

Using similar coordinate system as before, the screening potential turns into

$$\Phi^a(\mathbf{r}, t) = \frac{Q^a m_D}{2\pi^2} \int_0^\infty dk$$

$$\begin{aligned} &\times \int_0^1 d\chi J_0(k\rho\sqrt{1 - \chi^2}m_D) \\ &\times \left[\cos \Gamma \frac{\text{Re } \epsilon(\omega, \mathbf{k})}{\Delta} \right. \\ &\quad \left. + \sin \Gamma \frac{\text{Im } \epsilon(\omega, \mathbf{k})}{\Delta} \right] \Big|_{\omega=\mathbf{k}\cdot\mathbf{v}}. \end{aligned} \quad (74)$$

We solve the wake potential for the two special cases: (i) along the parallel direction of the fast parton, that is, $\mathbf{r} \parallel \mathbf{v}$ and also $\rho = 0$ and (ii) perpendicular to direction of the parton, that is, $\mathbf{r} \perp \mathbf{v}$. The potential for the parallel case is obtained as

$$\begin{aligned} \Phi_{\parallel}^a(\mathbf{r}, t) &= \frac{Q^a m_D}{2\pi^2} \int_0^\infty dk \\ &\times \int_0^1 d\chi \left[\cos \Gamma \frac{\text{Re } \epsilon(\omega, \mathbf{k})}{\Delta} \right. \\ &\quad \left. + \sin \Gamma \frac{\text{Im } \epsilon(\omega, \mathbf{k})}{\Delta} \right] \Big|_{\omega=\mathbf{k}\cdot\mathbf{v}}, \end{aligned} \quad (75)$$

whereas that for the perpendicular case, we have

$$\begin{aligned} \Phi_{\perp}^a(\mathbf{r}, t) &= \frac{Q^a m_D}{2\pi^2} \int_0^\infty dk \\ &\times \int_0^1 d\chi J_0(k\rho\sqrt{1 - \chi^2}m_D) \end{aligned}$$

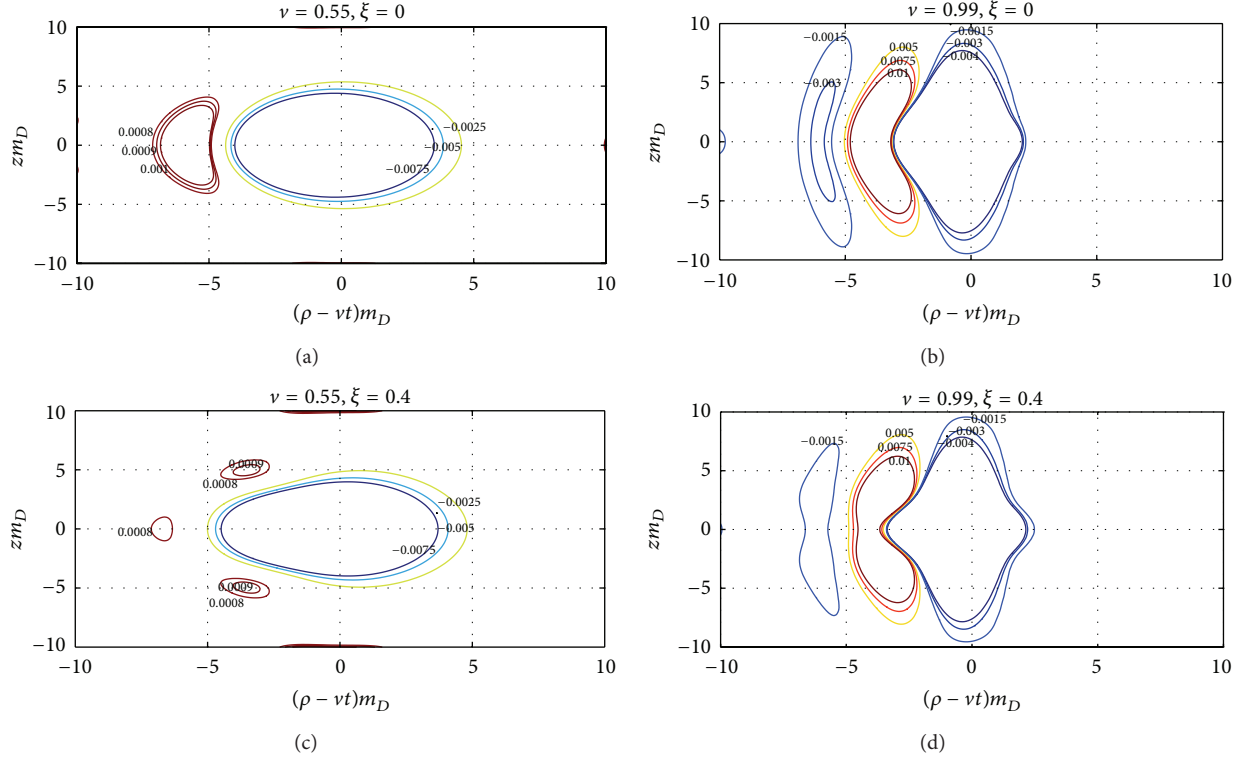


FIGURE 11: (Color online) The left (right) panel shows the equicharge lines for $\nu = 0.55(0.99)$. In this case the parton moves perpendicular to the direction of anisotropy [38].

$$\times \left[\cos \Gamma' \frac{\text{Re} \epsilon(\omega, \mathbf{k})}{\Delta} - \sin \Gamma' \frac{\text{Im} \epsilon(\omega, \mathbf{k})}{\Delta} \right] \Big|_{\omega=\mathbf{k}\cdot\mathbf{v}}, \quad (76)$$

with $\Gamma' = k\chi\nu t m_D$.

Figure 12 describes the scaled wake potential in two specified directions. In these figures, the scaled parameter Φ_0^a is given by $(2\pi^2/m_D)\Phi^a$. The left panel shows the wake potential along the direction of the moving color charge. In the backward direction, the wake potential for isotropic plasma decreases with the increase of $z - vt$ and exhibits a negative minimum when $\nu = 0.55$. With the increase of the anisotropic parameter ξ , the depth of the negative minimum decreases for $\nu = 0.55$. At large $\xi(0.8)$, there is no negative minimum and the wake potential behaves like a modified Coulomb potential. For $\nu = 0.99$, the wake potential is Lennard-Jones potential type which has a short range repulsive part as well as a long range attractive part [34, 38] in both isotropic and anisotropic plasma. It is also seen that the wake potential is oscillatory in nature in the backward direction. It is clearly visible that the depth of the negative minimum is increased compared to the case when $\nu = 0.55$. Because of the anisotropy effect, the oscillation of the wake potential is more pronounced, and it extends to a large distance [38]. In the forward direction, the screening

potential is a modified Coulomb potential in both types of plasma. Figure 12(b) describes the wake potential along the perpendicular direction of the moving parton. It can be seen that the wake potential is symmetric in backward and forward direction, no matter what the speed is [38]. In presence of the moving charge particle, the wake potential is Lennard-Jones type. When $\nu = 0.55$, the value of negative minimum is increased with increase of ξ but in case of $\nu = 0.99$, it decreases with ξ . However, with the increase of ξ , the depth of negative minimum is moving away from the origin for both the jet velocities considered here.

Next, we consider the case when the parton moves perpendicular to the beam direction. The wake potential in (74) is also evaluated for the two spacial cases: (i) along the direction of the moving parton, that is, $\mathbf{r} \parallel \mathbf{v}$ and (ii) perpendicular direction of the parton, that is, $\mathbf{r} \perp \mathbf{v}$. The wake potential for the parallel case can be written as [38]

$$\begin{aligned} \Phi_{\parallel}^a(\mathbf{r}, t) = & \frac{Q^a m_D}{2\pi^2} \int_0^{\infty} dk \int_0^1 d\chi \\ & \times \int_0^{2\pi} \frac{d\phi}{2\pi} \\ & \times \left[\cos \Omega' \frac{\text{Re} \epsilon(\omega, \mathbf{k})}{\Delta} \right. \\ & \left. + \sin \Omega' \frac{\text{Im} \epsilon(\omega, \mathbf{k})}{\Delta} \right] \Big|_{\omega=\mathbf{k}\cdot\mathbf{v}}, \end{aligned} \quad (77)$$

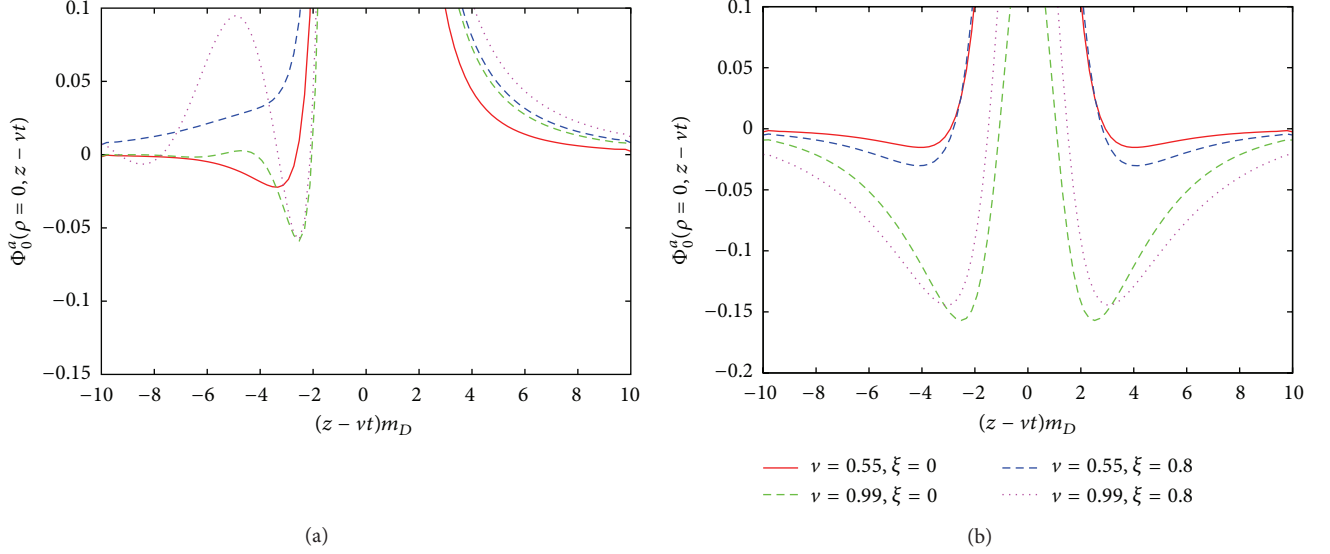


FIGURE 12: (Color online) (a): scaled wake potential along the motion of the fast parton, that is, z -axis for different ξ with two different parton velocity $v = 0.55$ and $v = 0.99$. (b) same as (a) but perpendicular to direction of motion of the parton.

where $\Omega' = k(\rho - vt)\sqrt{1 - \chi^2} \cos \phi m_D$. For the perpendicular case it is given by

$$\begin{aligned} \Phi_{\perp}^a(\mathbf{r}, t) = & \frac{Q^a m_D}{2\pi^2} \int_0^{\infty} dk \int_0^1 d\chi \\ & \times \int_0^{2\pi} \frac{d\phi}{2\pi} \\ & \times \left[\cos \Omega'' \frac{\text{Re } \epsilon(\omega, \mathbf{k})}{\Delta} \right. \\ & \left. + \sin \Omega'' \frac{\text{Im } \epsilon(\omega, \mathbf{k})}{\Delta} \right] \Big|_{\omega=\mathbf{k}\cdot\mathbf{v}}, \end{aligned} \quad (78)$$

with $\Omega'' = k(z\chi - vt)\sqrt{1 - \chi^2} \cos \phi m_D$. The left panel in Figure 13 shows screening potential along the parallel direction of the moving color charge. The behavior of the wake potential is more like a modified Coulomb (Lennard-Jones) potential at parton velocity $v = 0.55(0.99)$. For $v = 0.99$, the wake potential shows an oscillatory behavior in an isotropic plasma [34] but in anisotropic case, oscillatory structure of the wake potential is smeared out for $\xi = 0.5$ and $\mathbf{v} \perp \hat{\mathbf{n}}$ [38]. But the depth of the negative minimum increases in the case of anisotropic plasma for both the parton velocities considered here. The behavior of the wake potential in the perpendicular direction of the moving parton is shown in the right panel of Figure 13. At $v = 0.55$, the anisotropy modifies the structure of the wake potential significantly, that is, it becomes modified Coulomb potential instead of Lennard-Jones potential. For $v = 0.99$, the wake potential is a Lennard-Jones potential type but the depth of the minimum decreases in anisotropic plasma [38].

6. Summary and Discussions

We have reviewed the effect of initial state momentum anisotropy that can arise in an AQP on various observables. It is shown that electromagnetic probes could be a good signal that can be used to characterize this anisotropic state as this can only be realized in the early stages of heavy ion collisions. It has been demonstrated that the isotropization time of the QGP can be extracted by comparing the photon yield with the experimental data. We further estimate the radiative energy loss of a fast moving parton (both heavy and light flavours) in an AQP and show that it is substantially different from that in the isotropic QGP. Moreover, it depends on the direction of propagation of the parton with the anisotropic axis. Related to this is the nuclear modification factor of light hadrons that is produced due to the fragmentation of light partons which lose energy in the medium. Thus, we have also discussed the nuclear modification factor in the context of AQP and compared it with the RHIC data to extract the isotropization time. The extracted value is compatible with that obtained from photon data.

It might be mentioned here that the presence of unstable modes in AQP may affect radiative energy loss. However, in [72, 73] the authors have shown that the polarization loss (collisional loss) remains unaffected by the unstable modes, but in a recent paper [74] it is shown that the polarisation loss indeed has strong time and directional dependence and also the nature of the loss is oscillatory. Such effect may be present in radiative energy loss. In this review, we did not consider it.

The heavy quark potential and the quarkonium states in AQP have also been reviewed with both real and complex valued potential. In all these calculations, it has been found that the dissociation temperature of various quarkonium states increases in comparison with the isotropic case. We have also focused on the nuclear modification factors of various bottomonium states which have been calculated by

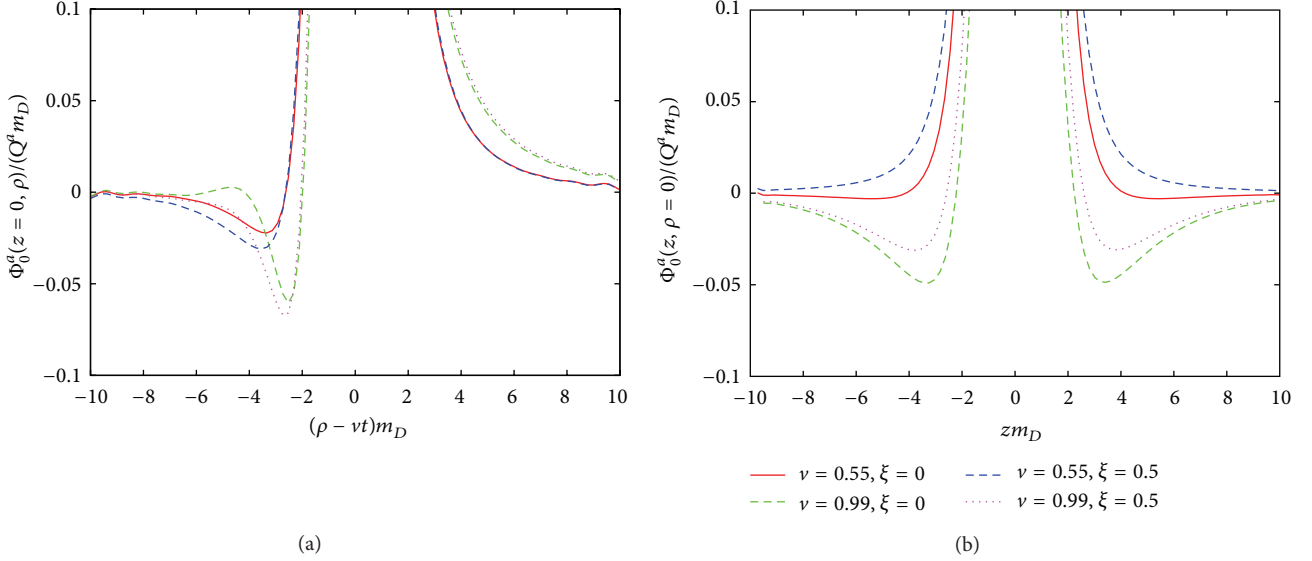


FIGURE 13: (Color online) The left (right) panel shows scaled wake potential for $\xi = \{0, 0.5\}$ with parton velocity $v = 0.55(0.99)$. In this case the parton moves perpendicular to the direction of anisotropy [38].

combining hydrodynamics and solutions of 3D Schrodinger equation using two types of complex valued potentials.

Apart from the energy loss of a jet in a medium, the jet also creates wake in the plasma. We have demonstrated that due to the jet propagation in an AQGP, the wake potential and the charge density are significantly modified in comparison with the isotropic case.

We end by mentioning that the ADS/CFT calculation of the electromagnetic correlator has been performed in strongly coupled $\mathcal{N} = 4$ super Yang-Mills theory using anisotropic momentum distribution [75]. Photon production rate is then estimated and it is concluded that in the weak coupling limit, the rate is consistent with that in [41] with an oblate phase space distribution in momentum space. There are other models that deal with the gravity dual theory for anisotropic plasma with additional bulk fields [76, 77]. Thus, a comparative study of various observables in gravity dual theory should be done in the future.

References

- [1] J.-E. Alam, S. Sarkar, P. Roy, T. Hatsuda, and B. Sinha, “Thermal photons and lepton pairs from quark gluon plasma and hot hadronic matter,” *Annals of Physics*, vol. 286, no. 2, pp. 159–248, 2000.
- [2] H. Satz and T. Matsui, “ J/ψ suppression by quark-gluon plasma formation,” *Physics Letters B*, vol. 178, no. 4, pp. 416–422, 1986.
- [3] J. D. Bjorken, “Partons lose energy due to interactions with the medium,” *FERMILAB-Pub-82/59-THY*, Erratum, 1982.
- [4] M. Gyulassy, P. Levai, and I. Vitev, “Jet quenching in thin quark-gluon plasmas I: formalism,” *Nuclear Physics B*, vol. 571, pp. 197–233, 2000.
- [5] B. G. Zakharov, “On the energy loss of high energy quarks in a finite-size quark-gluon plasma,” *JETP Letters*, vol. 73, no. 2, pp. 49–52, 2001.
- [6] M. Djordjevic and U. Heinz, “Radiative energy loss in a finite dynamical QCD medium,” *Physical Review Letters*, vol. 101, no. 2, Article ID 022302, 4 pages, 2008.
- [7] G.-Y. Qin, J. Ruppert, C. Gale, S. Jeon, G. D. Moore, and M. G. Mustafa, “Radiative and collisional jet energy loss in the quark-gluon plasma at the BNL relativistic heavy ion collider,” *Physical Review Letters*, vol. 100, no. 7, Article ID 072301, 2008.
- [8] R. Baier, Y. L. Dokshitzer, A. H. Mueller, and D. Schiff, “Quenching of hadron spectra in media,” *Journal of High Energy Physics*, vol. 2001, article 033, 2001.
- [9] A. K. Dutt-Mazumder, J. Alam, P. Roy, and B. Sinha, “Stopping power of hot QCD plasma,” *Physical Review D*, vol. 71, no. 9, Article ID 094016, 9 pages, 2005.
- [10] P. Roy, J.-E. Alam, and A. K. Dutt-Mazumder, “Quenching of light hadrons at RHIC in a collisional energy loss scenario,” *Journal of Physics G*, vol. 35, no. 10, Article ID 104047, 2008.
- [11] P. Huovinen, P. Kolb, U. Heinz, and P. V. Ruuskanen, “Radial and elliptic flow at RHIC: further predictions,” *Physics Letters B*, vol. 503, no. 1-2, pp. 58–64, 2001.
- [12] T. Hirano and K. Tsuda, “Collective flow and two-pion correlations from a relativistic hydrodynamic model with early chemical freeze-out,” *Physical Review C*, vol. 66, no. 5, Article ID 054905, 14 pages, 2002.
- [13] M. J. Tannenbaum, “Recent results in relativistic heavy ion collisions: from ‘a new state of matter’ to ‘the perfect fluid,’” *Reports on Progress in Physics*, vol. 69, no. 7, 2005.
- [14] M. Luzum and P. Romatschke, “Conformal relativistic viscous hydrodynamics: applications to RHIC results at $\sqrt{s_{NN}} = 200$ GeV,” *Physical Review C*, vol. 78, no. 3, Article ID 034915, 17 pages, 2008.
- [15] M. Mandal and P. Roy, “Gluon dissociation of J/ψ in anisotropic quark-gluon plasma,” *Physical Review C*, vol. 86, no. 2, Article ID 024915, 7 pages, 2012.
- [16] L. Bhattacharya and P. Roy, “Measuring the isotropization time of quark-gluon plasma from direct photons at energies available at the BNL Relativistic Heavy Ion Collider (RHIC),” *Physical Review C*, vol. 79, no. 5, Article ID 054910, 7 pages, 2009.

- [17] M. Martinez and M. Strickland, “Dilepton production as a measure of QGP thermalization time,” *Journal of Physics G*, vol. 35, no. 10, Article ID 104162, 2008.
- [18] R. Baier, A. H. Muller, D. Schiff, and D. T. Son, “‘Bottom-up’ thermalization in heavy ion collisions,” *Physics Letters B*, vol. 502, no. 1–4, pp. 51–58, 2001.
- [19] E. Weibel, “Spontaneously growing transverse waves in a plasma due to an anisotropic velocity distribution,” *Physical Review Letters*, vol. 2, no. 3, p. 83, 1959.
- [20] S. Mrowczynski, “Plasma instability at the initial stage of ultrarelativistic heavy-ion collisions,” *Physics Letters B*, vol. 314, no. 1, pp. 118–121, 1993.
- [21] S. Mrowczynski, “Color collective effects at the early stage of ultrarelativistic heavy-ion collisions,” *Physical Review C*, vol. 49, no. 4, pp. 2191–2197, 1994.
- [22] S. Mrowczynski, “Color filamentation in ultrarelativistic heavy-ion collisions,” *Physics Letters B*, vol. 393, no. 1–2, pp. 26–30, 1997.
- [23] S. Mrowczynski, “Instabilities driven equilibration of the quark–gluon plasma,” *Acta Physica Polonica B*, vol. 37, pp. 427–454, 2006.
- [24] P. Arnold, J. Lenghan, G. D. Moore, and L. G. Yaffe, “apparent thermalization due to plasma instabilities in the quark-gluon plasma,” *Physical Review Letters*, vol. 94, no. 7, Article ID 072302, 4 pages, 2005.
- [25] A. Rebhan, P. Romatschke, and M. Strickland, “Hard-loop dynamics of non-abelian plasma instabilities,” *Physical Review Letters*, vol. 94, no. 10, Article ID 102303, 4 pages, 2005.
- [26] P. Romatschke and R. Venugopalan, “Collective non-abelian instabilities in a melting color glass condensate,” *Physical Review Letters*, vol. 96, no. 6, Article ID 062302, 4 pages, 2006.
- [27] M. Strickland, “The chromo-weibel instability,” *Brazilian Journal of Physics*, vol. 37, no. 2, p. 702, 2007.
- [28] P. Romatschke and M. Strickland, “Collective modes of an anisotropic quark-gluon plasma,” *Physical Review D*, vol. 68, no. 3, Article ID 036004, 8 pages, 2003.
- [29] P. Romatschke and M. Strickland, “Collective modes of an anisotropic quark-gluon plasma: II,” *Physical Review D*, vol. 70, no. 11, Article ID 116006, 9 pages, 2004.
- [30] P. Romatschke and M. Strickland, “Collisional energy loss of a heavy quark in an anisotropic quark-gluon plasma,” *Physical Review D*, vol. 71, no. 12, Article ID 125008, 2005.
- [31] P. Romatschke, “Momentum broadening in an anisotropic plasma,” *Physical Review C*, vol. 75, no. 1, Article ID 014901, 8 pages, 2007.
- [32] P. Roy and A. K. Dutt-Mazumder, “Radiative energy loss in an anisotropic quark-gluon plasma,” *Physical Review C*, vol. 83, no. 4, Article ID 044904, 6 pages, 2011.
- [33] J. Ruppert and B. Muller, “Waking the colored plasma,” *Physics Letters B*, vol. 618, no. 1–4, pp. 123–130, 2005.
- [34] P. Chakraborty, M. G. Mustafa, and M. H. Thoma, “Wakes in the quark-gluon plasma,” *Physical Review D*, vol. 74, no. 9, Article ID 094002, 16 pages, 2006.
- [35] P. Chakraborty, M. G. Mustafa, R. Ray, and M. H. Thoma, “Wakes in a collisional quark-gluon plasma,” *Journal of Physics G*, vol. 34, no. 10, p. 2141, 2007.
- [36] B.-F. Jiang and J.-R. Li, “The wake potential in the viscous quark-gluon plasma,” *Nuclear Physics A*, vol. 856, no. 1, pp. 121–133, 2011.
- [37] B.-f. Jiang and J.-r. Li, “The polarized charge distribution induced by a fast parton in the viscous quark-gluon plasma,” *Journal of Physics G*, vol. 39, no. 2, Article ID 025007, 2012.
- [38] M. Mandal and P. Roy, “Wake in anisotropic quark-gluon plasma,” *Physical Review D*, vol. 86, no. 11, Article ID 114002, 9 pages, 2012.
- [39] L. Bhattacharya and P. Roy, “Photons from anisotropic quark-gluon plasma,” *Physical Review C*, vol. 78, no. 6, Article ID 064904, 2008.
- [40] L. Bhattacharya and P. Roy, “Rapidity distribution of photons from an anisotropic quark-gluon plasma,” *Physical Review C*, vol. 81, no. 5, Article ID 054904, 2010.
- [41] B. Schenke and M. Strickland, “Photon production from an anisotropic quark-gluon plasma,” *Physical Review D*, vol. 76, no. 2, Article ID 025023, 5 pages, 2007.
- [42] M. Martinez and M. Strickland, “Measuring quark-gluon-plasma thermalization time with dileptons,” *Physical Review Letters*, vol. 100, no. 10, Article ID 102301, 4 pages, 2008.
- [43] M. Martinez and M. Strickland, “Pre-equilibrium dilepton production from an anisotropic quark-gluon plasma,” *Physical Review C*, vol. 78, no. 3, Article ID 034917, 19 pages, 2008.
- [44] M. Mandal, L. Bhattacharya, and P. Roy, “Nuclear modification factor in an anisotropic quark-gluon plasma,” *Physical Review C*, vol. 84, no. 4, Article ID 044910, 10 pages, 2011.
- [45] M. Martinez and M. Strickland, “Dissipative dynamics of highly anisotropic systems,” *Nuclear Physics A*, vol. 848, no. 1–2, pp. 183–197, 2010.
- [46] M. Martinez and M. Strickland, “Non-boost-invariant anisotropic dynamics,” *Nuclear Physics A*, vol. 856, no. 1, pp. 68–87, 2011.
- [47] K. Kajantie, J. Kapusta, L. McLerran, and A. Mekjian, “Dilepton emission and the QCD phase transition in ultrarelativistic nuclear collisions,” *Physical Review D*, vol. 34, no. 9, pp. 2746–2754, 1986.
- [48] A. Dumitru, Y. Guo, and M. Strickland, “The heavy-quark potential in an anisotropic plasma,” *Physics Letters B*, vol. 662, no. 1, pp. 37–42, 2008.
- [49] J. P. Blaizot and E. Iancu, “The quark-gluon plasma: collective dynamics and hard thermal loops,” *Physics Reports*, vol. 359, no. 5–6, pp. 155–528, 2002.
- [50] B. Schenke, M. Strickland, C. Greiner, and M. Thoma, “Model of the effect of collisions on QCD plasma instabilities,” *Physical Review D*, vol. 73, no. 12, Article ID 125004, 12 pages, 2006.
- [51] A. Dumitru, Y. Gao, A. Mocsy, and M. Strickland, “Quarkonium states in an anisotropic QCD plasma,” *Physical Review D*, vol. 79, no. 5, Article ID 054019, 10 pages, 2009.
- [52] F. Karsch, M. T. Mehr, and H. Satz, “Color screening and deconfinement for bound states of heavy quarks,” *Zeitschrift für Physik C*, vol. 37, no. 4, pp. 617–622, 1988.
- [53] I. D. Sudiarta and D. J. W. Geldart, “Solving the Schrödinger equation using the finite difference time domain method,” *Journal of Physics A*, vol. 40, no. 8, pp. 1885–1896, 2007.
- [54] M. Margotta, K. McCarty, C. McGahan, M. Strickland, and D. Yager-Elorriaga, “Quarkonium states in a complex-valued potential,” *Physical Review D*, vol. 83, Article ID 105019, 2011.
- [55] A. Dumitru, Y. Gao, and M. Strickland, “Imaginary part of the static gluon propagator in an anisotropic (viscous) QCD plasma,” *Physical Review D*, vol. 79, no. 11, Article ID 114003, 7 pages, 2009.
- [56] M. Strickland, “Thermal $\Upsilon(1_s)$ and χ_{b1} Suppression at $\sqrt{\langle s_{NN} \rangle} = 2.76$ TeV Pb-Pb Collisions at the LHC,” *Physical Review Letters*, vol. 107, no. 13, Article ID 132301, 4 pages, 2011.
- [57] M. Strickland and D. Bazow, “Thermal bottomonium suppression at RHIC and LHC,” *Nuclear Physics A*, vol. 879, pp. 25–58, 2012.

- [58] X.-M. Xu, D. Kharzeev, H. Satz, and X.-N. Wang, “ J/ψ suppression in an equilibrating parton plasma,” *Physical Review C*, vol. 53, no. 6, pp. 3051–3056, 1996.
- [59] G. Bhanot and M. E. Peskin, “Short-distance analysis for heavy-quark systems. (II). Applications,” *Nuclear Physics B*, vol. 156, no. 3, pp. 391–416, 1979.
- [60] D. Kharzeev and H. Satz, “Colour deconfinement and quarkonium dissociation,” in *Quark-Gluon Plasma II*, R. C. Hwa, Ed., World Scientific, Singapore, 1995.
- [61] M. Gyulassy and X. N. Wang, “Multiple collisions and induced gluon bremsstrahlung in QCD,” *Nuclear Physics B*, vol. 420, no. 3, pp. 583–614, 1994.
- [62] M. Djordjevic, “Theoretical formalism of radiative jet energy loss in a finite size dynamical QCD medium,” *Physical Review C*, vol. 80, no. 6, Article ID 064909, 27 pages, 2009.
- [63] J. F. Owens, “Large-momentum-transfer production of direct photons, jets, and particles,” *Reviews of Modern Physics*, vol. 59, no. 2, pp. 465–503, 1987.
- [64] P. Roy, A. K. Dutt-Mazumder, and J.-E. Alam, “Energy loss and dynamical evolution of quark p_T spectra,” *Physical Review C*, vol. 73, no. 4, Article ID 044911, 4 pages, 2006.
- [65] X. N. Wang, “Effects of jet quenching on high p_T hadron spectra in high-energy nuclear collisions,” *Physical Review C*, vol. 58, no. 4, pp. 2321–2330, 1998.
- [66] S. Turbide, C. Gale, S. Jeon, and G. D. Moore, “Energy loss of leading hadrons and direct photon production in evolving quark-gluon plasma,” *Physical Review C*, vol. 72, no. 1, Article ID 014906, 15 pages, 2005.
- [67] S. S. Adler, S. Afanasiev, C. Aidala et al., “Common suppression pattern of η and π^0 mesons at high transverse momentum in Au+Au collisions at $\sqrt{\langle s_{NN} \rangle} = 200$ GeV,” *Physical Review Letters*, vol. 96, no. 20, Article ID 202301, 6 pages, 2006.
- [68] N. A. Krall and A. W. Trivelpiece, *Principles of Plasma Physics*, McGraw-Hill, New York, NY, USA, 1973.
- [69] S. Ichimaru, *Basic Principles of Plasma Physics*, W. A. Benjamin, Menlo Park, Calif, USA, 1973.
- [70] L. D. Landau and E. M. Lifshitz, *Fluid Mechanics*, Butterworth-Heinemann, Woburn, Mass, USA, 2nd edition, 1987.
- [71] W. J. Miloch, “Wake effects and Mach cones behind objects,” *Plasma Physics and Controlled Fusion*, vol. 52, no. 12, Article ID 124004, 2010.
- [72] P. Romatschke and M. strickland, “Energy loss of a heavy fermion in an anisotropic QED plasma,” *Physical Review D*, vol. 69, no. 6, Article ID 065005, 13 pages, 2005.
- [73] P. Romatschke and M. strickland, “Collisional energy loss of a heavy quark in an anisotropic quark-gluon plasma,” *Physical Review D*, vol. 71, no. 12, Article ID 125008, 12 pages, 2005.
- [74] M. E. Carrington, K. Deja, and S. Mrówczyński, “Energy loss in unstable quark-gluon plasma with extremely prolate momentum distribution,” *Acta Physica Polonica B*, vol. 6, supplement, p. 545, 2013.
- [75] A. Rebhan and D. Steineder, “Electromagnetic signatures of a strongly coupled anisotropic plasma,” *Journal of High Energy Physics*, vol. 2011, article 153, 2011.
- [76] D. Mateos and D. Trancanelli, “Anisotropic $N = 4$ Super-Yang-Mills Plasma and Its Instabilities,” *Physical Review Letters*, vol. 107, no. 10, 4 pages, 2011.
- [77] D. Mateos and D. Trancanelli, “Thermodynamics and instabilities of a strongly coupled anisotropic plasma,” *Journal of High Energy Physics*, vol. 2011, article 54, 2011.

Review Article

Femtoscopic and Nonfemtoscopic Two-Particle Correlations in $A + A$ and $p + p$ Collisions at RHIC and LHC Energies

Yu. M. Sinyukov,¹ S. V. Akkelin,¹ Iu. A. Karpenko,^{1,2} and V. M. Shapoval¹

¹ Bogolyubov Institute for Theoretical Physics, Kiev 03680, Ukraine

² FIAS, 60438 Frankfurt am Main, Germany

Correspondence should be addressed to Yu. M. Sinyukov; sinyukov@bitp.kiev.ua

Received 15 April 2013; Accepted 16 June 2013

Academic Editor: Edward Sarkisyan-Grinbaum

Copyright © 2013 Yu. M. Sinyukov et al. This is an open access article distributed under the Creative Commons Attribution License, which permits unrestricted use, distribution, and reproduction in any medium, provided the original work is properly cited.

The theoretical review of the last femtoscopy results for the systems created in ultrarelativistic $A + A$, $p + p$, and $p + Pb$ collisions is presented. The basic model, allowing to describe the interferometry data at SPS, RHIC, and LHC, is the hydrokinetic model. The model allows one to avoid the principal problem of the particlization of the medium at nonspace-like sites of transition hypersurfaces and switch to hadronic cascade at a space-like hypersurface with nonequilibrated particle input. The results for pion and kaon interferometry scales in $Pb + Pb$ and $Au + Au$ collisions at LHC and RHIC are presented for different centralities. The new theoretical results as for the femtoscopy of small sources with sizes of 1-2 fm or less are discussed. The uncertainty principle destroys the standard approach of completely chaotic sources: the emitters in such sources cannot radiate independently and incoherently. As a result, the observed femtoscopy scales are reduced, and the Bose-Einstein correlation function is suppressed. The results are applied for the femtoscopy analysis of $p + p$ collisions at $\sqrt{s} = 7$ TeV LHC energy and $p + Pb$ ones at $\sqrt{s} = 5.02$ TeV. The behavior of the corresponding interferometry volumes on multiplicity is compared with what is happening for central $A + A$ collisions. In addition the nonfemtoscopic two-pion correlations in proton-proton collisions at the LHC energies are considered, and a simple model that takes into account correlations induced by the conservation laws and minijets is analyzed.

1. Introduction

The two-particle correlation femtoscopy of identical particles allows one to analyze the space-time structure of a particle emission from the systems created in heavy ion, hadron and lepton collisions (for recent reviews see, e.g., [1–3]). The femtoscopy method, which is based on the Bose-Einstein or Fermi-Dirac interference of identical particles, has been proposed first in [4–7] for measurements of the geometrical sizes and shapes of the interaction region in hadronic collisions. Then it has been developed in [8–14] as a tool for a study of rapidly expanding fireballs formed in ultrarelativistic heavy ion collisions. Despite the extremely small sizes of such systems (the order of the value is around 10^{-14} m), they have a pronounced inhomogeneous structure. The generalized treatment of the interferometry measurements asserts that the measured scales—the interferometry radii—are associated just with the homogeneity lengths in the system [15–18]. Only in the very particular case of a

finite homogeneous system such lengths correspond to the total geometrical sizes, but normally they are smaller than the latter. The interferometry scanning of femtosystems at various total momenta of pion pairs allows one to analyze the homogeneity lengths related to different space-time regions of the expanding fireball [11, 12, 17, 18]. An understanding of interferometry in terms of the homogeneity lengths, as opposed to the simple-mind geometrical picture, provides explanation to some, at first sight paradoxical, results at RHIC.

The long-term study of the peculiarities of the interferometry scales behavior in heavy ion collisions, in particular, the so-called RHIC HBT puzzle [19–21], relatively small observed radii and close to unity ratio of the two transverse femtoscales, helps much in clearing up the underlying properties of the matter created in these processes. The physical conditions explaining the RHIC HBT puzzle are [22–28] a relatively hard EoS because of a crossover transition (instead of the 1st order one) between quark-gluon and hadron

phases, the presence of prethermal anisotropic transverse flow developed to thermalization time, and an “additional portion” of the transverse flow caused by the shear viscosity effect and fluctuations of the initial conditions. An account for these factors gives the possibility to describe well the hadron spectra together with the femtoscopy data within a realistic freeze-out hydrokinetic model (HKM) with a gradual decay of the fluid into observed particles [28–30].

Soon after the first Large Hadron Collider (LHC) heavy ion results were received, it became evident that the hydrodynamic picture of the collision processes, confirmed at RHIC, is clearly seen also at much higher energy. This conclusion is based on the two classes of observables. The first one is related to the azimuthal anisotropy of particle spectra expressed basically through their second harmonics or v_2 coefficients. The obtained LHC results for the transverse momentum dependence of $v_2(p_T)$ at a given centrality bin (here and below for the quantities depending on one particle momentum p_T means the transverse momentum of one particle, whereas for the pair quantities p_T means the average pair transverse momentum, $p_T = (p_{1T} + p_{2T})/2$) were found to be similar to the ones at RHIC, except for the higher momentum range at LHC [31]. This is the evidence of the same hydrodynamic mechanism of the anisotropy formation as at RHIC. The second type of observables deals with the direct measurements of the space-time structure of nucleus-nucleus collisions by means of the correlation femtoscopy. The hydrodynamic predictions [32] for p_T behavior of the interferometry radii at the LHC energies were confirmed by the ALICE experiment [33]. The most impressive hydrodynamic prediction [28, 34], that the ratio of the two transverse interferometry radii, *out* to *side*, will drop in the whole p_T -interval with increasing collision energy and will reach a value close to unity at the LHC, has been discovered experimentally [33].

However, quantitative application of the hydrodynamic approach is a nontrivial problem, because it depends on both the initial conditions for the continuous matter evolution and final state treatments for the particles production. The hydrokinetic model (HKM) [23, 29, 35] allows one to apply hydrodynamics also at the late nonequilibrated stage of gradual system decay, where it can be matched, in its hybrid version (hHKM) [30, 36], with the ultrarelativistic quantum molecular dynamics (UrQMD) cascade [37, 38]. A utilization of the UrQMD ensures an adequate description of the very rarefied stage of matter evolution and transition to particle free-streaming regime. It is especially important at the LHC energies because of relatively prolonged duration of the interacting nonequilibrated stage. It was shown that the hydrokinetic approach without such correction of later-time evolution results in overestimated effective temperature of proton spectra at RHIC energy and insufficient rise of interferometry radii and volume from top RHIC to LHC energies [36]. It is important to note that utilization of hydrokinetic model in between pure hydrodynamics and UrQMD gives the possibility to switch correctly to the UrQMD cascade at any space-like hypersurface, in particular, at isochronic one. It allows one to avoid problems that usually appear in hybrid models matching hydrodynamics with hadronic cascade at hadronisation hypersurface. The latter typically contains

nonspace-like sectors that cannot be correctly accounted for in initial conditions for hadronic cascade model.

In the recent paper [39] the correlation femtoscopy analysis is going beyond the model of independent particle emitters, which is fairly good for the systems formed in heavy ion collisions but not for small systems (with sizes about 1 fm) created in $p + p$, $p + Pb$, and $e^+ + e^-$ collisions. It is found that the uncertainty principle leads to (partial) indistinguishability of closely located emitters that fundamentally impedes their full independence and incoherence. The partial coherence of emitted particles is because of the quantum nature of particle emission and happens even if there is no specific mechanism to produce a coherent component of the source radiation. The found effect leads to reduction of the interferometry radii and suppression of the Bose-Einstein correlation functions. We review briefly the observed results and their application [40] to $p + p$ collisions at $\sqrt{s} = 7$ TeV LHC energy.

As for the elementary particle collisions, like $p + p$, there is no unambiguous interpretation of the HBT radii p_T -dependence. It became clear [41–43] that for relatively small systems the additional two-particle correlations affect the correlation functions in the kinematic region where quantum statistical (QS) and final state interaction (FSI) correlations are usually observed. These correlations can be induced by total energy and momentum conservation laws (see, e.g., [44, 45]) and minijets [39, 46, 47]. As opposed to the QS and FSI correlations, which are familiar from the correlation femtoscopy method and so are sometimes called femtoscopy correlations, these correlations are not directly related to the spatiotemporal scales of the emitter and are therefore called nonfemtoscopic correlations. Since the latter noticeably affects correlation functions for small systems, the interferometry radii extracted from the complete correlation function in $p + p$ collisions depend strongly on the assumption about the so-called correlation baseline—the strength and momentum dependence of the nonfemtoscopic correlations [41–43]. It has an influence on the interpretation of the momentum dependence of the interferometry radii in $p + p$ collisions, where the possibility of hydrodynamic behavior of matter is questionable.

2. Escape Function Dynamics of Expanding Medium Particlization

Let us start with discussion of hydrokinetic approach to $A + A$ collisions and explain how it helps switch from hydrodynamical expansion to molecular dynamics of hadronic particles. It was proposed in [35] to describe the hadronic momentum spectra in $A + A$ collisions basing on the escape function of particles which are gradually liberated from hydrodynamically expanding systems. The escape function, first introduced in hydrodynamic framework in [48, 49] without a resort to the Boltzmann kinetics, was utilized in [35] within the Boltzmann equations in a specific approximation based on hydrodynamic approach. It was shown that such a picture corresponds to a relativistic kinetic equation with the relaxation time approximation for the collision term, where the relaxation time tends to infinity, $\tau_{\text{rel}} \rightarrow \infty$, when

$t \rightarrow \infty$, indicating a gradual transition to the free-streaming regime. It is worth noting that the hydrodynamics at fairly large times play no role in formation of locally anisotropic particle spectra.

The Boltzmann equation for the distribution function $f(x, p)$ in the case of no external forces has the form

$$\frac{p^i}{p^0} \frac{\partial f(x, p)}{\partial x^i} = F^{\text{gain}}(x, p) - F^{\text{loss}}(x, p). \quad (1)$$

The terms F^{gain} and F^{loss} are associated with number of particles which, correspondingly, came to point (x, p) and left this point because of collisions. Term $F^{\text{loss}}(x, p) = R(x, p)f(x, p)$ can easily be expressed in terms of the rate of collisions of the particle with momentum p , $R(x, p) = \langle \sigma v_{\text{rel}} \rangle n(x)$. The term F^{gain} has, in general, more complicated integral structure and depends on differential cross-section.

The escape fraction, $f_{\text{esc}}^\sigma(x, p)$, describes the (probabilistic) distribution of the particles that reaches the hypersurface σ without interactions. At asymptotic hypersurface σ where times $t \rightarrow \infty$, the distribution function corresponds to free quanta: $f_{\text{esc}}^\sigma(x, p) \rightarrow f(x, p)$. In general cases, which we will need, when the space-like hypersurface σ is situated at the final times, we define the escape function as

$$f_{\text{esc}}^\sigma(x, p) = \mathcal{P}_\sigma(x, p) f(x, p), \quad (2)$$

where $\mathcal{P}_\sigma(x, p)$ is the escape probability for particle to reach freely the hypersurface σ at some point $(t_\sigma, \mathbf{x}_\sigma)$ starting from the point (t, \mathbf{x}) . If the point x belongs to this hypersurface σ , then $\mathcal{P}_\sigma(x, p) = 1$, and so

$$f_{\text{esc}}^\sigma(x, p)|_\sigma = f(x, p)|_\sigma. \quad (3)$$

The escape probability is the relativistic invariant and can be expressed explicitly through the rate of collisions along the world line of free particle with momentum p :

$$\mathcal{P}_\sigma(x, p) = \exp\left(-\int_t^{t_\sigma} d\bar{t} R(\bar{x}, p)\right), \quad (4)$$

where $\bar{x} \equiv (\bar{t}, \mathbf{x}_\sigma + (\mathbf{p}/p_0)(\bar{t} - t_\sigma))$. It satisfies the differential equation

$$\frac{1}{\mathcal{P}_\sigma(x, p)} \frac{p^\mu}{p^0} \frac{\partial}{\partial x^\mu} \mathcal{P}_\sigma(x, p) = R(x, p) = \frac{F^{\text{loss}}(x, p)}{f(x, p)}. \quad (5)$$

It follows from (1) and (5) that

$$\frac{p^\mu}{\mathcal{P}_\sigma} \frac{\partial}{\partial x^\mu} f_{\text{esc}}^\sigma(x, p) = \mathcal{P}_\sigma(x, p) F^{\text{gain}}(x, p). \quad (6)$$

The formal solution of (6) can be presented in the following form:

$$f_{\text{esc}}^\sigma(x, p) = f_{\text{esc}}^\sigma(x_0, p) + \int_{t_{\sigma_0}(\mathbf{x}_0)}^t dt' \mathcal{P}_\sigma(x', p) F^{\text{gain}}(x', p), \quad (7)$$

where $x = (t, \mathbf{x})$, $\sigma : t = \text{const}$, $f_{\text{esc}}^\sigma(x_0, p)$ with $x_0 \equiv (t_{\sigma_0}(\mathbf{x}_0), \mathbf{x}_0 = \mathbf{x} + (\mathbf{p}/p_0)(t_{\sigma_0}(\mathbf{x}_0) - t))$ corresponds to the portion of the system, which propagates without collisions until some time t starting from initial hypersurface σ_0 , $x' \equiv (t', \mathbf{x} + (\mathbf{p}/p_0)(t' - t))$.

The expression (7) for escape function $f_{\text{esc}}^\sigma(x, p)$ can be explained in simple heuristic way as follows. Let us split the distribution function at each space-time point into two parts: $f(x, p) = f_{\text{int}}^\sigma(x, p) + f_{\text{esc}}^\sigma(x, p)$, $x = (t, \mathbf{x})$. The first part, $f_{\text{int}}^\sigma(x, p)$, describes the fraction of the system which will continue to interact before reaching the hypersurface σ . The second fraction, $f_{\text{esc}}^\sigma(x, p)$, describes the particles that reach the hypersurface σ without interactions. Denote again by $x' \equiv (t', \mathbf{x} + (\mathbf{p}/p_0)(t' - t))$ the space-time point where the particle at x with momentum p would be, if it moved freely. Consider, at each vicinity of the phase-space point (x, p) , the number of particles that have escaped from the interacting system during the time interval $(t', t' + dt')$. First, this *additional* portion of escaped particles can be produced only from the interacting part of the system. Second, these particles are only among particles that came to the phase-space vicinity of the point (x', p) *just after* the interaction during the time dt' . Indeed, if some particles from the interacting part of the system $f_{\text{int}}^\sigma(x', p)$ do not interact during the given time interval $(t', t' + dt')$, then they will interact without fail at some future time; thus, they cannot contribute to the additional portion of particles escaping during dt' . Therefore, the additional contribution $\Delta f_{\text{esc}}^\sigma(x, p; t')$, from the time interval $(t', t' + dt')$ to the distribution function $f_{\text{esc}}^\sigma(x, p)$, is $\Delta f_{\text{esc}}^\sigma(x, p; t') = \mathcal{P}_\sigma(x', p) F^{\text{gain}}(x', p) dt'$ for $t' < t$ and is zero for $t' > t$. Here $\mathcal{P}_\sigma(x', p)$ is probability for any *given* particle at point x' with momentum p to reach without interaction the hypersurface σ . The summation of such contributions is presented by (7), and the differential of this equation leads to (6).

Utilization of the escape function for the momentum spectra formation is based on (3) which can be used to describe inclusive spectra of particles,

$$p^0 \frac{dN}{d\mathbf{p}} = \langle a_p^+ a_p \rangle, \quad p_1^0 p_2^0 \frac{dN}{d\mathbf{p}_1 d\mathbf{p}_2} = \langle a_{p_1}^+ a_{p_2}^+ a_{p_1} a_{p_2} \rangle, \dots, \quad (8)$$

that are constructed in the standard way by means of the averages of product of creation and annihilation operators. Namely, on the hypersurface σ_{out}

$$\langle a_{p_1}^+ a_{p_2} \rangle = \int_{\sigma_{\text{out}}} d\sigma_\mu(x) p^\mu \exp(iqx) f_{\text{esc}}(x, p), \quad (9)$$

where $p = (p_1 + p_2)/2$, $q = p_1 - p_2$. Then, using the Gauss theorem, (6) and (1) analytically continued to

off-mass-shell four-momenta p , and taking into account that $\partial_\mu(p^\mu \exp(iqx)) = 0$ for particles on mass shell, one can get

$$\begin{aligned} \langle a_{p_1}^+ a_{p_2} \rangle &= p_0 \int_{\sigma_0} d^3 \sigma_\mu(x_0) p^\mu f_{\text{esc}}^\sigma(x_0, p) e^{-iqx_0} \\ &+ p_0 \int_{\sigma_0} d^4 x \mathcal{P}_\sigma(x, p) F^{\text{gain}}(x, p) e^{-iqx}, \end{aligned} \quad (10)$$

$$\begin{aligned} \langle a_{p_1}^+ a_{p_2} \rangle &= p^0 \int_{\sigma_0} d^3 \sigma_\mu(x_0) p^\mu f(x_0, p) e^{-iqx_0} \\ &+ p^0 \int_{\sigma_0} d^4 x \\ &\times [F^{\text{gain}}(x, p) - F^{\text{loss}}(x, p)] e^{-iqx}, \end{aligned} \quad (11)$$

respectively, where $\mathcal{P}_{\sigma_{\text{out}}}(x, p)$ is the probability for particle to reach the hypersurface σ from the space-time point x , $f_{\text{esc}}^\sigma(x_0, p) = f(x_0, p) \mathcal{P}_\sigma(x_0, p)$ is a portion of the particles at the initial hypersurface σ_0 that reach hypersurface σ moving freely without interactions, $f(x_0, p)$ is the distribution function at σ_0 , and $p^0 \mathcal{P} F^{\text{gain}}$ is the Lorentz-invariant emission density.

The hydrokinetic approach is based on (10) where one utilizes the escaping function dynamics (6) for finding solution of the Boltzmann equation at hypersurface σ and calculation there the particle momentum spectra. The escaped functions and escape probabilities are calculated within the local equilibrium approximation for the term F^{gain} and the collision term R . The latter is defined from the particle cross-sections which are similar to those in the UrQMD. The equation of state is supposed to be the same as in the Boltzmann hadron gas with changing in time chemical composition. The evolution of the parameters, such as the temperature, chemical potentials, particle concentrations, and collective velocities in the hadron-resonance gas, are defined by the equations of relativistic hydrodynamics. All the details are presented in [23, 29, 35]. The resulting distribution function at σ , found from the integral form (7) of the equation for escaped functions, is, of course, far from the local equilibrium one.

In the models like UrQMD, distribution function dynamics (1) is utilized for calculation of the momentum spectra in accordance with (11). Both approaches coincide in the case of free-streaming, when $F^{\text{gain}}(x, p) = F^{\text{loss}}(x, p) \equiv 0$ and therefore $\mathcal{P}_\sigma(x_0, p) \equiv 1$, then the second terms in (10), (11) are equal to zero and the first terms are coincided (note that it is not the case when $F^{\text{gain}}(x, p) = F^{\text{loss}}(x, p) \neq 0$). Then distribution function dynamics (1) is still as at a free-streaming, while the escaping function dynamics (6) becomes nontrivial). It is worth noting that if the initial hypersurface σ_0 has nonspace-like sites, $\Delta\sigma_\mu(x_1)$, then for some momenta p_1 we have $p_1^\mu \Delta\sigma_\mu(x_1) < 0$, and so these parts give the negative contribution to the particle number density according to (10) and (11). It happens because the particles are going inside the hypersurface σ_0 near the point x_1 . This negative contribution will

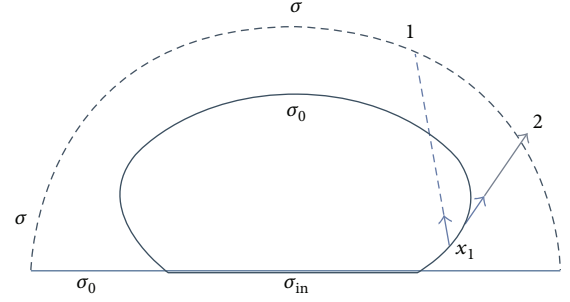


FIGURE 1: The cartoon of the particlization at the hypersurface σ_0 (solid line) and spectra formation at σ (dashed line). The very initial system forms at the hypersurface σ_{in} (double line) and then evolves. The Gauss theorem in (10) and (11) is applied to enclosed hypersurface $\sigma_0 \oplus \sigma$. In the case of large opacity $f_{\text{esc}}^\sigma(x_1, p_1) \approx 0$ for particle 1, also is small for particle 2, and so $p_\mu \Delta\sigma_\mu^\sigma(x_1) f_{\text{esc}}^\sigma(x_1, p) \approx 0$, while for the distribution function $f(x_1, p)$ the similar value $p_\mu \Delta\sigma_\mu^\sigma(x_1) f(x_1, p)$ is not zero, and for $p = p_1$ it is negative if $\Delta\sigma_0$ is a nonspace-like site of the hypersurface σ_0 .

be compensated when the particle crosses the hypersurface again in another point x_2 of the hypersurface to go out. See the possible trajectory of the particle 1 in Figure 1. Of course, the Gauss theorem applied to the enclosed hypersurface $\sigma_0 \oplus \sigma$ guarantees the correct positive result for particle momentum spectra, no matter how complicated structure σ_0 has and how many times the negative contributions happen. As for the external hypersurface σ , it can be chosen as a space-like one.

Typically at a modeling of $A + A$ collisions the initial conditions for the Boltzmann equations are selected at the hypersurface σ_0 close to the hadronisation hypersurface. Such a hypersurface is not everywhere a space-like one, but at sites with $p^\mu \Delta\sigma_\mu < 0$ particles cannot go deeply inside because of high opacity (see Figure 1). It is taken into account in the escape function formalism, where the escape probability for the particles with momentum directed into the fluid is about zero at these sites, $\mathcal{P}_\sigma(x_0, p) \approx 0$, and so the escape function is about zero, $f_{\text{esc}}^\sigma(x_0, p) \approx 0$, resulting in suppression of the negative contributions to particle momentum density in (10) from the σ_0 hypersurface. Note that within the escape function formalism a transition from continuous medium to particles is described as a gradual process, because escape function and escape probability can be defined for both sides of the hypersurface σ_0 (in other words, hadronisation process is treated as gradual in the escape function dynamics, and the very initial system state is defined, in fact, on a space-like hypersurface). The latter fact, accounting for (2), implies the continuity of the distribution function through σ_0 in accordance with Boltzmann kinetics (1). It means that if it is the local equilibrium on the one side of the hypersurface, it will be the same on the other side, no matter whether they are space-like or nonspace-like sectors. Then in (11), dealing with the full distribution function, the negative contributions at the nonspace-like sites really exist and have to be preserved to maintain true dynamics. Summarizing, the hydrokinetic model is based on continuous behavior of the physical values. It implies a continuous

behavior of the locally isotropic distribution function at any parts of the hypersurface σ_0 , including “bad” nonspace-like sites. It is implemented through a continuous hydrodynamic description of the matter crossing the σ_0 that is utilized for calculation of the escape probability and emission function. Therefore no discontinuity in the energy and momentum flows through σ_0 arises. The hydrokinetic approach accounts also for the smooth time behavior of the escape function that forms the distribution function at some space-like hypersurface σ that can be used then to provide the input of the nonlocally equilibrium distribution function (the output of HKM) to the UrQMD [30].

In cascade models, which solve the Boltzmann equation in the form (11), one does not deal with the small fraction of the particles that are already free at σ_0 but brings into play the distribution function $f(x, p)$ itself for further numerical simulations of the collisions in the Boltzmann gas. Then one can see from (11) that near the nonspace-like site at x_1 a negative number of the particles with corresponding momenta p_1 has to be “injected” (see Figure 1). Typically, to cure this dilemma people just cut them in the full distribution function $f(x_1, p)$, that leads to discontinuity of the energy and momentum flows through the corresponding sites of σ_0 [50]. Such a cut, introduced through the Heaviside function $\Theta(d\sigma_\mu p^\mu)$ in the Cooper-Frye prescription [51], destroys the basic equation (11) where the negative contributions have to be preserved! Also locally, it obviously violates the continuity of the particle current $n^\mu = nu^\mu : \partial_\mu n^\mu(x)|_{\Delta\sigma_0(x_1)} \neq 0$. The error of such prescription is that it considers a decaying hadronic system rather as a star, practically unlimited reservoir of emitted photons/particles, while the hadronic medium formed in the heavy ion collisions is a small compact holder of emitted particles and it is rearranged when the system loses them (back reaction).

The situation can be improved if one introduces some model of the surface layer with the locally isotropic thermal distribution that includes also the particles with momenta p_1 moving towards the nonspace-like sites where $p_1^\mu \Delta\sigma_0(x_1) < 0$. These particles have to collide with the particles that move from the inside of $\Delta\sigma_0(x_1)$ to outside. The attempt to substitute such real collisions inside the surface layer by the elastic reflection from the moving (with the “velocity” of the nonspace-like site) wall was performed in [52]. It results in the specific combination of the Heaviside Θ -functions in the Cooper-Frye formula and provides the local conservation law for particles $\partial_\mu n^\mu(x)|_{\Delta\sigma_0(x_1)} = 0$. Such a prescription is utilized in the FAST MC Freeze-out Generator [53] and is planned to be used in UrQMD [54]. However, the method [52] ensures continuity of particle and energy flows but not the momentum flow and so preserves discontinuity of momentum-energy tensor at nonspace-like segments of σ_0 [52].

Because of the difficulties in building the model of the surface layer, one can use hydrokinetics, that does not deal directly with the distribution function at σ_0 but only with the distributions of particles continuously escaping from the hydrodynamically expanding matter and calculate a nonequilibrated distribution function with (2) and (4) on

a space-like hypersurface σ where one can switch to UrQMD cascade without troubles described.

Theoretical calculations, presented in the next section, are performed in hybrid hydrokinetic model (hHKM) [30]. At the initial state the Monte-Carlo Glauber model of the initial conditions is used (see [30]). After the thermalization stage of the system’s evolution, the matter is supposed to be chemically and thermally equilibrated, and its expansion is described within perfect $(2 + 1)D$ boost-invariant relativistic hydrodynamics with the lattice QCD-inspired equation of state in the quark-gluon phase [55] matched with chemically equilibrated hadron-resonance gas via crossover-type transition. The hadron-resonance gas consists of 329 well-established hadron states (according to Particle Data Group compilation [56]) made of u , d , and s quarks, including σ -meson ($f_0(600)$). With such an equilibrated evolution the system reaches the chemical freeze-out isotherm with the temperature $T_{\text{ch}} = 165$ MeV. At the second stage with $T < T_{\text{ch}}$, the hydrodynamically expanding hadron system gradually loses its (local) thermal and chemical equilibrium, and particles continuously escape from the system. This stage is described within the hydrokinetic approach [35] to the problem of dynamical decoupling. In hHKM model [30] the hydrokinetic stage is matching with hadron cascade UrQMD one [37, 38] at the isochronic hypersurface $\sigma : t = \text{const}$ (with $T_\sigma(r = 0) = T_{\text{ch}}$) that guarantees the correctness of the matching (see [29, 30] for details). In the latter case of transition from the hydrokinetics to cascade, the following distribution functions are used:

$$\begin{aligned}
 f_i(\tau, \vec{x}, \vec{p}) &= f_i^{\text{L,eq.}}(\tau_0, \vec{x}^{(\tau_0)}(\tau), \vec{p}) \\
 &\times \exp\left(-\int_{\tau_0}^{\tau} \tilde{R}_i(s, \vec{x}^{(s)}(\tau), \vec{p}) ds\right) \\
 &+ \int_{\tau_0}^{\tau} d\lambda [f_i^{\text{L,eq.}}(\lambda, \vec{x}^{(\lambda)}(\tau), \vec{p}) \\
 &\quad \times \tilde{R}_i(\lambda, \vec{x}^{(\lambda)}(\tau), \vec{p}) \\
 &\quad + \tilde{G}_i^{\text{decay}}(\lambda, \vec{x}^{(\lambda)}(\tau), \vec{p})] \\
 &\times \exp\left(-\int_{\lambda}^{\tau} [\tilde{R}_i(s, \vec{x}^{(s)}(\tau), \vec{p}) \right. \\
 &\quad \left. + \tilde{D}_i(s, \vec{x}^{(s)}(\tau), \vec{p})] ds\right).
 \end{aligned} \tag{12}$$

The different terms in (12) correspond to the following: $\tilde{R}_i(\lambda, \vec{x}, \vec{p})$ is the collision rate of the i th sort of hadrons with the rest of particles, $\tilde{G}_i^{\text{decay}}(\lambda, \vec{x}, \vec{p})$ is an income of particles into the phase-space point owing to resonance decays, and $\tilde{D}_i(\lambda, \vec{x}, \vec{p})$ is the decay rate of a given resonance species. To calculate the collision rates, we assume meson-meson, meson-baryon, and baryon-baryon cross-sections in a way similar to the UrQMD code [37, 38].

3. Femtoscopic Correlations in Relativistic $A + A$ Collisions

In the processes of multiparticle production the two-particle correlation function is defined through the ratio of the one- and two-particle (semi)inclusive spectra as follows:

$$C(p_1, p_2) = \frac{p_1^0 p_2^0 (dN/d\mathbf{p}_1 d\mathbf{p}_2)}{p_1^0 (dN/d\mathbf{p}_1) p_2^0 (dN/d\mathbf{p}_2)}. \quad (13)$$

Experimentally, the two-particle correlation function is defined as the ratio of the distribution of particle pairs from the same collision event to the distribution of pairs with particles taken from different events. In heavy ion collisions almost all the correlations between identical pions with low relative momentum are due to quantum statistics and final state interactions. As for the latter, in this review we suppose that they are already extracted from the total correlation function (the method is well known and has been proposed in [57]).

The quantum-statistical enhancement of the pairs of identical pions produced with close momenta was observed first in $\bar{p} + p$ collisions in 1959 [58]. It took more than a decade to develop the method of pion interferometry microscope based on the discovered phenomenon. This was done at the beginning of 70s by Kopylov and Podgoretsky [4–6]. Their theoretical analysis assumed the radiating source to consist of independent incoherent emitters. In fact, such a representation is used for a long time for the analysis of the space-time structure of particle sources. For such chaotic sources the four-point average in (8) can be decomposed in the following sum of pair products:

$$\langle a_{p_1}^+ a_{p_2}^+ a_{p_1} a_{p_2} \rangle = \langle a_{p_1}^+ a_{p_1} \rangle \langle a_{p_2}^+ a_{p_2} \rangle + \langle a_{p_1}^+ a_{p_2} \rangle \langle a_{p_2}^+ a_{p_1} \rangle. \quad (14)$$

Then using (8) and (10) one can express the correlation function (13) for chaotic sources

$$C(p, q) = 1 + \frac{\int d^4 x_1 d^4 x_2 S(x_1, p) S(x_2, p) e^{iq(x_1 - x_2)}}{\left(\int d^4 x_1 S(x_1, p_1)\right) \left(\int d^4 x_2 S(x_2, p_2)\right)}, \quad (15)$$

where $p = (p_1 + p_2)/2$, $q = p_1 - p_2$, $S(x, p)$ is the emission function; if $f_{\text{esc}|\sigma_0}^\sigma \approx 0$, then $S(x, p) = p^0 F^{\text{gain}}(x, p) \mathcal{P}_\sigma(x, p)$ as it follows from (10) (in general case it includes in addition the contribution from σ_0).

When calculating these femtoscopic correlation functions in a quasiclassical particle production model (or event generator) that produces particles without any quantum correlations, the output of event generator is the list of particle positions (at the point of their last interaction) and their momenta, and $C(p, q)$ is equal to unity there. So one has to construct in addition a numerical procedure to calculate quantum-statistical correlations in accordance with (15). It is done usually in a way that is similar to the final state interaction method: one takes outcome of a given classical event generator and then constructs a numerical approximation of (15) based on smoothness conditions [59]. This can be done using the binning technique, also used in several event

generators [53, 60] including hHKM. One takes outcome of a given distribution of the particle pairs in the bins according to their relative momentum \vec{q} and the average momentum of the particle pair \vec{p} . If one calculates the correlations arising only due to the Bose-Einstein enhancement, for example, for pion pairs, the corresponding numerical equivalent of (15) at each transverse p_T bin looks like

$$C(\vec{q}) = \frac{\sum_i \sum_{j \neq i} \delta_\Delta(\vec{q} - \vec{p}_i + \vec{p}_j) (1 + \cos((p_j - p_i)(x_j - x_i)))}{\sum_i \sum_j \delta_\Delta(\vec{q} - \vec{p}_i + \vec{p}_j)}, \quad (16)$$

where $\delta_\Delta(x) = 1$ if $|x| < \Delta p/2$ and 0 otherwise, with Δp being the bin size in histograms. We decompose the relative momentum \vec{q} into $(q_{\text{out}}, q_{\text{side}}, q_{\text{long}})$ projections and perform analysis in the longitudinal center of mass system (LCMS), where the mean longitudinal momentum of the pair vanishes. Evaluation according to (16) can be done with the help of 3D histograms, implemented in ROOT library classes [61], and in hHKM two separate histograms are used to calculate the numerator and the denominator of (16), which are divided one by another to get the correlation function.

Some remarks to such a receipt are in order here. First, note that this procedure does not change single-particle momentum spectra, while one can expect that they will be changed if the quantum statistics were taken into account in the event generators. Even if hydrodynamic evolution accounts for the quantum statistics through corresponding EoS and gives Bose-Einstein and Fermi-Dirac heat distributions as the input for event generator like UrQMD, the subsequent quasiclassical UrQMD hadronic cascade destroys the true quantum-statistical picture. Unfortunately, an account for the quantum statistics is still not realized for realistic event generators because, in particular, any direct account of quantum statistics is very time consuming (for current developments and recent attempts to overcome this problem see [62, 63] and references therein). Therefore, the theoretical analysis of the quantum effects at multiparticle production, that goes beyond the simple prescription (16), is still very important. Some significant results have been already obtained. One of them concerns quantum corrections to spectra and correlations in the case when homogeneity length λ in the system is less than the particle wavelength, $\lambda < 1/p^0$ [15, 16, 64, 65]—this drastically changes the form of the spectra and BE correlations. The other is the multibosonic effects when particle number is close to the Bose-Einstein condensation [65–67]—this leads to decrease of the interferometry radii. Also, the effects of coherence for femtoscopic correlations of charged particles were considered in detail in [68] based on the formalism of generalized coherent states—it gives the tool for the correlation search of a coherence component by measuring the correlations between like and oppositely charged pions. One more quantum effect, which also cannot be taken into account by prescription (16), is connected with the uncertainty principle and is analyzed very recently in [39, 40]. We will discuss this effect in Sections 4 and 5.

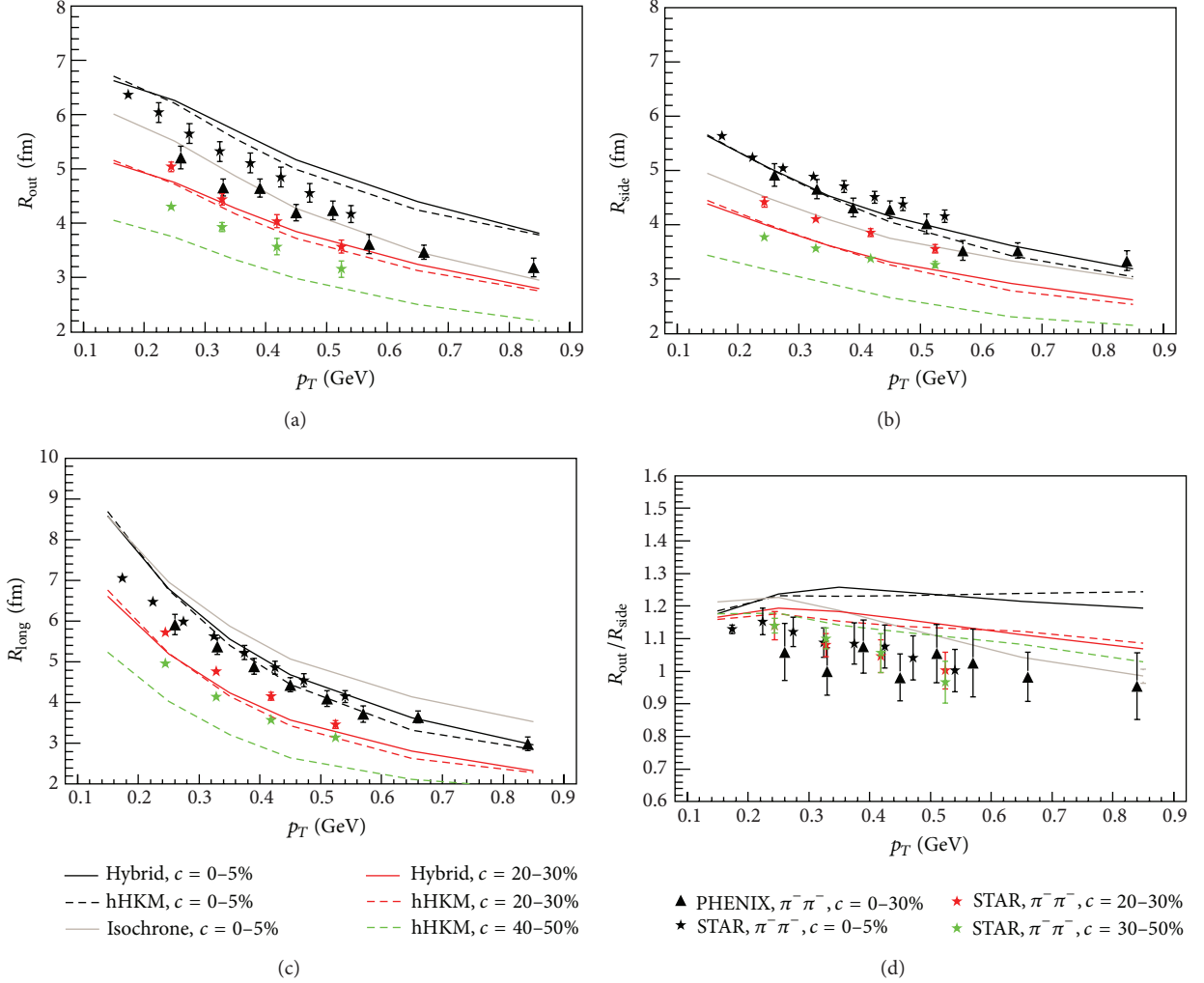


FIGURE 2: HBT radii of π^- pairs at 200 A GeV RHIC energy, calculated in different models and compared to experimental data from the STAR [69] and PHENIX [70] collaborations. Dashed lines correspond to the hydrokinetic procedure of matching (hHKM), while solid lines stand for the “hybrid” model case. The results for the “hybrid-isochronic” model are presented for central $c = 0-5\%$ events with a gray solid line. The ICs used for hydrodynamic evolution: $\tau_0 = 0.1$ fm/c with zero initial transverse flow and the MC-Glauber profiles for initial entropy density.

The resulting correlation function obtained with (16) is fitted with the Bertsch-Pratt parameterization

$$C(q) = 1 + \lambda \cdot \exp \left(-R_{out}^2 q_{out}^2 - R_{side}^2 q_{side}^2 - R_{long}^2 q_{long}^2 - R_{os}^2 q_{out} q_{side} - R_{sl}^2 q_{side} q_{long} - R_{ol}^2 q_{out} q_{long} \right). \quad (17)$$

Next, we show some results for the correlation radii from hHKM model. Following the experimental cuts (which are somewhat different for STAR, PHENIX, and ALICE Collaborations), we consider pions in central pseudorapidity region $|\eta| < 0.5$. Owing to longitudinal boost invariance and approximate azimuthal symmetry for the most central collisions which we consider for the present HBT studies, the cross-terms R_{os}^2 , R_{sl}^2 , and R_{ol}^2 are neglected.

The comparison of interferometry radii, calculated in hHKM with the experimental data from $\sqrt{s} = 200$ GeV $Au + Au$ collisions at RHIC, is shown in Figure 2. The parameters of the model are chosen to reproduce the basic set of observables: charged hadron density at midrapidity as a function of collision centrality [30]. Note that PHENIX presented its results for the 0–30% centrality bin, which corresponds to a smaller average multiplicity than the 0–5% STAR bin; thus PHENIX radii lie slightly below the ones calculated by STAR; in our model we observe the same tendency with the initial conditions set for 0–30% centrality.

From Figure 2 one can conclude that both the hHKM and the “hybrid” cases describe the data quite satisfactory, except for HBT radii for 30–50% centrality, which are clearly underestimated (and here we note that the hHKM results for 40–50% centrality, which describe well the hadron spectra and flow [30], seem to correspond to smaller effective system

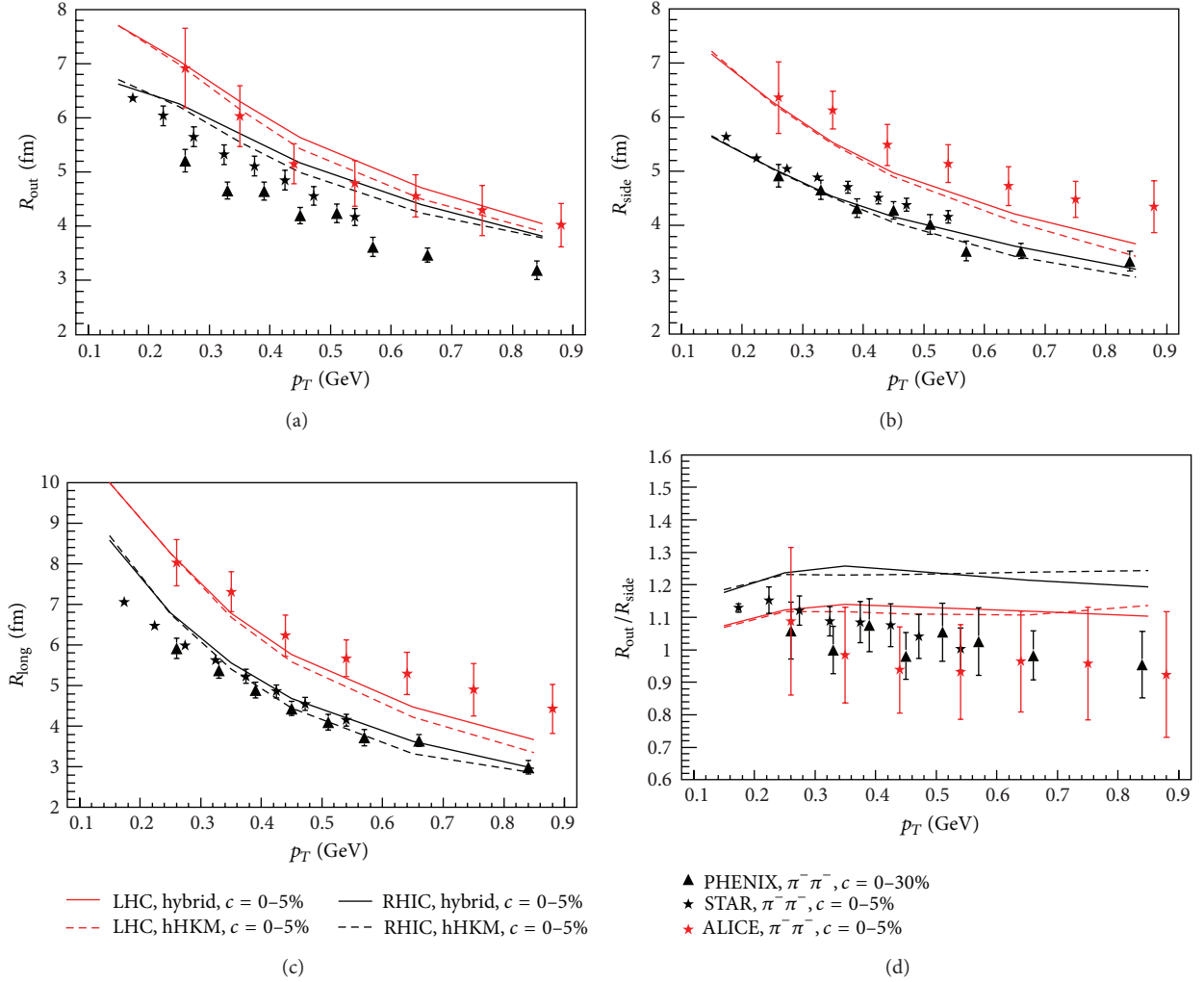


FIGURE 3: HBT radii of $\pi^- \pi^-$ pairs for the most central events, calculated in the hHKM model and compared to experimental data from ALICE [33]. Dashed lines correspond to hydrokinetic procedure of matching, while solid lines stand for the “hybrid” model case. Corresponding HBT radii for top RHIC energy are shown for comparison purposes.

size). The shear viscosity should also reduce the R_{out}/R_{side} ratio because it enhances the transverse flow, and the corresponding influence on HBT radii is shown in [71] (however the model presented in [71] does not include cascade stage; thus only resonance decays are considered after the hydrodynamic freezeout at isothermal hypersurface). As for the “hybrid-isochrone” model, it fails to describe the shape of pion, kaon, and proton transverse spectra, v_2 , and long-, side- and out-interferometry radii. The main difference between the first two (hHKM, hybrid) and “hybrid-isochrone” scenarios is that the first two matching procedures do not use the local equilibrium particle distribution functions as input for UrQMD cascade at the space-time regions where the system should be far from equilibrium. The peripheral regions at isochronic hypersurface are spatially and temporally distant from the freeze-out isotherm and have rather small temperatures, and in this transition area the finite and rapidly expanding system cannot be described hydrodynamically: the free-streaming regime of particle propagation already starts there.

Next, recent results from ALICE Collaboration show considerable rise of both R_{side} and R_{long} (and the corresponding rise of interferometric volume) with increase of collision energy from 200 A GeV RHIC to 2.76 TeV LHC. As one can see from Figure 3, this behavior is well reproduced in hHKM (see also [36]), and it is found to be caused by the protracted cascade stage at LHC energy. We keep unchanged the model parameters when passing from RHIC to LHC energies, except for a general normalization of initial entropy (or energy) density for increased dN/dy , contribution from binary collisions, and the baryonic chemical potentials at freeze-out; we also find a decent reproduction of basic set of observables with hHKM at LHC. One can conclude that this supports the same physical picture of bulk matter evolution at both top RHIC and LHC energies.

In Figure 4 (taken from recent STAR publication [72]) we show HBT radii of kaon pairs measured recently by STAR collaboration, compared to the older results by PHENIX and to the ones calculated in hHKM. The figure demonstrates

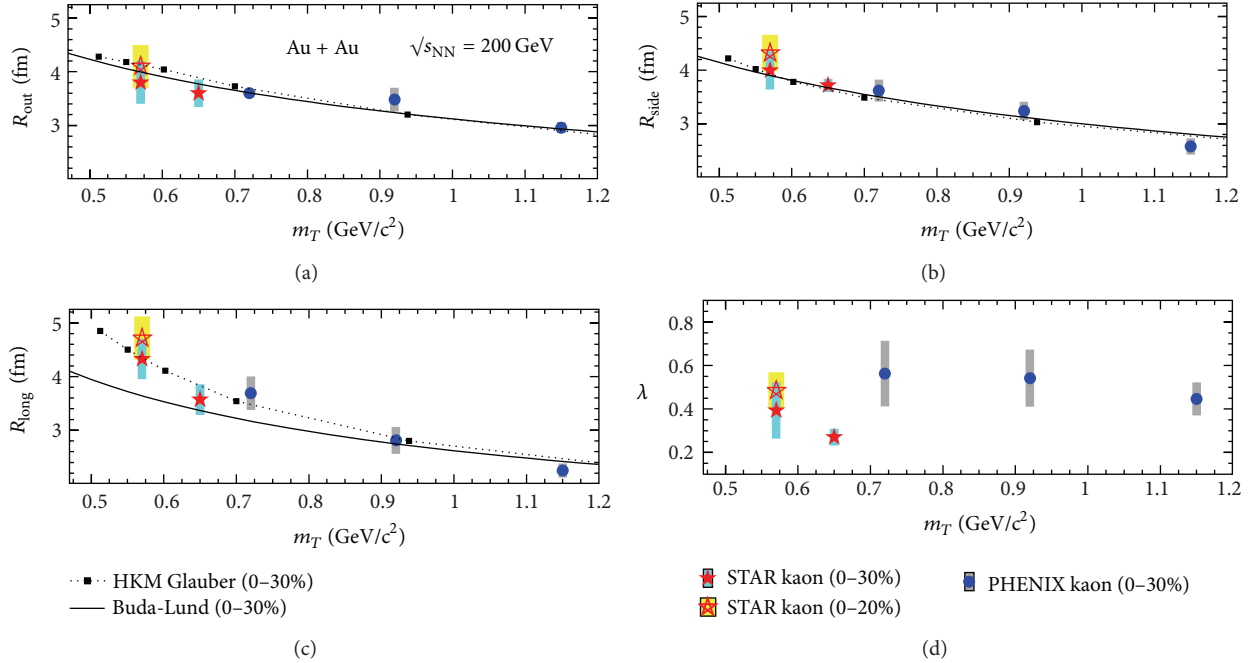


FIGURE 4: Transverse mass dependence of Gaussian radii (a) R_{out} , (b) R_{side} , and (c) R_{long} for midrapidity kaon pairs from the 30% most central Au + Au collisions at $\sqrt{s_{NN}} = 200$ GeV. The results from STAR [72] and PHENIX [73] are compared to the calculations in hHKM model (dotted lines).

a good reproduction of kaon femtoscopy in hHKM and Buda-Lund models. This is connected with the fact that in hHKM we see no exact scaling between kaon and pion radii. Generally, due to different cross-sections with the hadron mixture, pions and kaons decouple (i.e., suffer their last interactions) from the system at different times and have different contributions from strong resonance decays. It was demonstrated in the pure HKM [29] that, despite the smaller cross-section, the emission duration of kaons with the same m_T as for pions is slightly larger than for pions, at least for intermediate m_T , because the same m_T corresponds to smaller p_T for kaons (and the duration of emission process is highly p_T dependent), which results in somewhat larger values of HBT radii for kaons. Generally, HBT measurements for different particle species seem to be a valuable tool to study the details of the particle liberation process and discriminate between models of particle production.

4. Correlation Femtoscopy for Small Systems

In the work [39] it is shown that for small systems formed in particle collisions (e.g., pp , e^+e^-), where the observed interferometry radii are about 1-2 fm or smaller, the uncertainty principle does not allow one to distinguish completely between individual emission points. Also the phases of closely emitted wave packets are mutually coherent. All that is taken into account in the formalism of partially coherent phases in the amplitudes of closely spaced individual emitters. The measure of distinguishability and partial coherence is then the overlap integral of the two emitted wave packets. In thermal systems the role of corresponding coherent length

is played by the thermal de Broglie wavelength that defines also the size of a single emitter. The Monte-Carlo method (16) cannot account for such effects since it deals with classical particles and point-like emitters (points of the particle's last collision). The classical probabilities are summarized according to the event generator method (16), while in the quantum approach a superposition of partially coherent amplitudes, associated with different possible emission points, serves as the input for further calculations [39]. Such approach leads to the reduction of the interferometry radii as compared to (16). In addition, the ascription of the factor $1 + \cos((x_1 - x_2)(p_1 - p_2))$ to the weight of the pion pair in (16) is not correct for very closely located points x_1 and x_2 , because there is no Bose-Einstein enhancement if the two identical bosons are emitted from the same point [39, 74]. The effect is small for large systems with large number of independent emitters, but for small systems it can be significant, and one has to exclude the excessive contributions (“double counting” [39]) in the two-particle emission amplitude. Such corrections lead to a suppression of the Bose-Einstein correlations that is manifested as a reduction of the observed correlation function intercept as compared to one in the standard method (16).

The results of [39] are presented in the nonrelativistic approximation related to the rest frame of the source moving with four-velocity u^μ . In hydrodynamic/hydrokinetic approach the role of such a source at given pair's half-momentum bin near some value p is played by the fluid element or piece of the matter with the sizes equal to the homogeneity lengths $\lambda(p)$ [15, 16]. These lengths are extracted from the HKM simulations, namely, from the interferometry radii defined by the Gaussian fits to the correlation functions

obtained in HKM. All the pairs in procedure (1) are considered in the longitudinally comoving system (LCMS) in the boost-invariant approximation automatically selects the longitudinal rest frame of the source and longitudinal homogeneity length in this frame (it is Lorentz dilated as compared to one in the global system [13]). The femtoscopy analysis is typically related to some p_T bin, and so one needs also to determine the transverse source size in the transverse rest frame, marked by the asterisk. The corresponding Lorentz transformations do not change the *side*-homogeneity length; as for the *out*-direction, we proceed in the way proposed first in [13]. The corresponding transformations then are [13, 40]

$$\begin{aligned} R_{\text{out}}^*(p) &= R_{\text{out}}(p) \frac{\cosh y_T}{\cosh(y_T - \eta_T)}, \\ R_{\text{side}}^* &= R_{\text{side}} = \lambda_{\text{side}}, \\ R_{\text{long}}^* &= R_{\text{long}} = \lambda_{\text{long}}, \\ \lambda_{\text{out}}^* &= \lambda_{\text{out}} \frac{\cosh y_T}{\cosh(y_T - \eta_T)}, \\ \frac{p_{\text{out}}^* T^*}{p_0^*} &= T \frac{\sinh y_T}{\cosh(y_T - \eta_T)}. \end{aligned} \quad (18)$$

Here $R_{\text{out}}^{*2}(p) = \lambda_{\text{out}}^{*2} + (p_{\text{out}}^*/p_0^*)T^{*2}$, T is the emission duration, η_T is a rapidity of the source in transverse direction, and $y_T = (y_{1T} + y_{2T})/2$ is half sum of transverse rapidities of the particles forming the pair. Note that $y_T^* = y_T - \eta_T$, and if rapidity of the pair is equal to the rapidity of the source, $y_T^* = 0$, then in this particular case the radius in the rest frame is Lorentz-dilated by the factor γ . Generally, the reference system where the pair's momentum is zero does not coincide with the rest frame of the source that emits the pair. Therefore the direct application of these formulas is not an easy task for rather complicated emission structure in hypothetical hydrodynamic/hydrokinetic model of $p + p$ collisions. Of course, the details of the transformation will be different for the string event generator; therefore one can estimate the theoretical uncertainties using the radii transformation just in the two limiting cases $R_{\text{out}}^* = R_{\text{out}}$ and $R_{\text{out}}^* = \gamma R_{\text{out}}$ ($\gamma = \cosh y_T$).

In [40] the quantum corrections are calculated at each p_T -bin in the rest frame of the corresponding source using (18), and then a transition is made again to the global reference system. In what follows the *asterisk* mark is omitted and all values are related to the source rest frame. To account that due to the uncertainty principle the emitters (strictly speaking emitted wave packets) have the finite sizes $\langle (\Delta x)^2 \rangle \sim k^2$ (k is the momentum variance of the particle radiation) when defining the lengths of coherence, one should at first consider the amplitude of the radiation processes and only then make statistical averaging over phases of the wave packets using the overlap integral as the coherence measure [39].

Following to [39] we present the quantum state $\psi_{x_i}(p, t)$ corresponding to a boson with mass m emitted at the time t_i

from the point \mathbf{x}_i as a wave packet with momentum variance k which then propagates freely:

$$\psi_{x_i}(p, t) = e^{ipx_i - iEt} e^{i\varphi(x_i)} \tilde{f}(\mathbf{p}), \quad (19)$$

where $\varphi(x_i)$ is some phase and \tilde{f} defines the primary momentum spectrum $f(\mathbf{p})$ that we take in the Gaussian form,

$$f(\mathbf{p}) = \tilde{f}^2(\mathbf{p}) = \frac{1}{(2\pi k^2)^{3/2}} e^{-(\mathbf{p}^2/2k^2)}, \quad (20)$$

with the variance $k^2 = mT$. The effective temperature of particle emission in the local rest frames in HKM, T , is close to the chemical freeze-out temperature T_{ch} .

The amplitude of the single-particle radiation from some 4-volume is supposed to be a superposition of the wave functions $\psi_x(p)$ with the Gaussian coefficients $\hat{\rho}(x) = \sqrt{\rho(x)}$, where $\rho(x)$ is the probability distribution in the case of random phases:

$$\rho(x, t) \propto e^{-\sum_i x_i^2/2\lambda_i^{*2}(p) - t^2/2T^{*2}(p)}. \quad (21)$$

Then in the rest frame of the source

$$A(p, t) = c \int d^4x \psi_x(p, t) \hat{\rho}(x), \quad (22)$$

where c is the normalization constant.

The single- and two-particle spectra, averaged over the ensemble of emission events with partially correlated phases $\varphi(x)$ are

$$\begin{aligned} \overline{W(p)} &= c^2 \int d^4x d^4x' e^{ip(x-x')} \hat{\rho}(x) \hat{\rho}(x') \\ &\quad \times f(\mathbf{p}) \left\langle e^{i(\varphi(x) - \varphi(x'))} \right\rangle, \\ \overline{W(p_1, p_2)} &= c^4 \int d^4x_1 d^4x_2 d^4x'_1 d^4x'_2 e^{i(p_1x_1 + p_2x_2 - p_1x'_1 - p_2x'_2)} \\ &\quad \cdot f(\mathbf{p}_1) f(\mathbf{p}_2) \hat{\rho}(x_1) \hat{\rho}(x_2) \hat{\rho}(x'_1) \hat{\rho}(x'_2) \\ &\quad \times \left\langle e^{i(\varphi(x_1) + \varphi(x_2) - \varphi(x'_1) - \varphi(x'_2))} \right\rangle. \end{aligned} \quad (23)$$

The phase averages are associated with corresponding overlap integrals [39]

$$\left\langle e^{i(\varphi(x) - \varphi(x'))} \right\rangle = G_{xx'} = I_{xx'} = \left| \int d^3\mathbf{r} \psi_x(t, \mathbf{r}) \psi_{x'}^*(t, \mathbf{r}) \right|, \quad (24)$$

$$\begin{aligned} \left\langle e^{i(\varphi(x_1) + \varphi(x_2) - \varphi(x'_1) - \varphi(x'_2))} \right\rangle &= G_{x_1x'_1} G_{x_2x'_2} + G_{x_1x'_2} G_{x_2x'_1} \\ &\quad - G_{x_1x'_2} G_{x_2x'_1} G_{x_1x_2}, \end{aligned} \quad (25)$$

where $\psi_{x_i}(t, \mathbf{r}) = (1/(2\pi)^{3/2}) \int f(\mathbf{p}) e^{-i\mathbf{p}(\mathbf{r}-\mathbf{x}_i)} e^{-i(\mathbf{p}^2/2m)(t_i-t)} d^3p$ are the wave functions of single bosonic states in coordinate representation.

Then the correlation function $C(\mathbf{p}, \mathbf{q})$ can be expressed through the homogeneity lengths in the local rest frame $R_L \equiv \lambda_{\text{long}}^*(p)$, $R_S \equiv \lambda_{\text{side}}^*(p)$, and $R_O \equiv \lambda_{\text{out}}^*(p)$ which in its turn are expressed through the HBT radii obtained from the Gaussian fit (17) of the HKM correlation functions and transformation law (18) as described above:

$$C(\mathbf{p}, \mathbf{q}) = \frac{\overline{W(p_1, p_2)}}{W(p_1)W(p_2)} = 1 + e^{-q_O^2 R_O^2 (4k_0^2 R_O^2 / (1+4k_0^2 R_O^2)) - q_S^2 R_S^2 (4k_0^2 R_S^2 / (1+4k_0^2 R_S^2))} \times e^{-q_L^2 R_L^2 (4k_0^2 R_L^2 / (1+4k_0^2 R_L^2))} \times e^{-((\mathbf{q}\mathbf{p})^2 T^2 / m^2) (4k^2 T^2 / (1+4k^2 T^2))} - C_d(\mathbf{p}, \mathbf{q}), \quad (26)$$

where $k_0^2 = k^2 / (1 + \alpha k^4 T^2 / m^2)$, parameter $\alpha(k^2 R^2)$ is defined from the model numerically (it is the order of unity for $R \sim 1$ fm and tends to zero for the large sources—see [39] for details), and the subtracted term

$$C_d(\mathbf{p}, \mathbf{q}) = e^{-2q_O^2 k_0^2 R_O^4 (1+8k_0^2 R_O^2) / (1+4k_0^2 R_O^2) (1+8k_0^2 R_O^2 + 8k_0^4 R_O^4)} \times e^{-2q_S^2 k_0^2 R_S^4 (1+8k_0^2 R_S^2) / (1+4k_0^2 R_S^2) (1+8k_0^2 R_S^2 + 8k_0^4 R_S^4)} \times e^{-2q_L^2 k_0^2 R_L^4 (1+8k_0^2 R_L^2) / (1+4k_0^2 R_L^2) (1+8k_0^2 R_L^2 + 8k_0^4 R_L^4)} \times e^{-2k^2 T^4 (\mathbf{p}\mathbf{q})^2 (1+8k^2 T^2) / m^2 (1+4p^2 T^2) (1+8k^2 T^2 + 8k^4 T^4)} \times F(k_0^2 R_i^2, k^2 T^2), \quad (27)$$

$$F(k_0^2 R_i^2, k^2 T^2) = \left(\frac{k_0}{k}\right)^{3/2} \times \left(\frac{(1+4k^2 T^2)}{(1+8k^2 T^2 + 8k^4 T^4)} \frac{(1+4k_0^2 R_O^2)}{(1+8k_0^2 R_O^2 + 8k_0^4 R_O^4)} \frac{(1+4k_0^2 R_S^2)}{(1+8k_0^2 R_S^2 + 8k_0^4 R_S^4)} \frac{(1+4k_0^2 R_L^2)}{(1+8k_0^2 R_L^2 + 8k_0^4 R_L^4)}\right)^{1/2}$$

responds for the elimination of the double counting.

Now we can see that the apparent interferometry radii extracted from the Gaussian fits to the correlation function (26) are reduced as compared to those obtained in the standard approach.

Particularly, if we neglect the double counting effects, truncate the subtracted term $C_d(\mathbf{p}, \mathbf{q})$ in (26), and fit the correlation function with the Gaussian form (17), we obtain

the femtoscopic radii R_{out} , R_{side} , and R_{long} related to the standard ones $R_{\text{out,st}}$, $R_{\text{side,st}}$, and $R_{\text{long,st}}$ as follows:

$$\frac{R_{\text{out}}^2}{R_{\text{out,st}}^2} = \left(R_O^2 \frac{4k_0^2 R_O^2}{1+4k_0^2 R_O^2} + T^2 v_{\text{out}}^2 \frac{4k^2 T^2}{1+4k^2 T^2} \right) \times (R_O^2 + T^2 v_{\text{out}}^2)^{-1}, \quad (28)$$

$$\frac{R_{\text{side}}^2}{R_{\text{side,st}}^2} = \frac{4k_0^2 R_S^2}{1+4k_0^2 R_S^2},$$

$$\frac{R_{\text{long}}^2}{R_{\text{long,st}}^2} = \frac{4k_0^2 R_L^2}{1+4k_0^2 R_L^2},$$

where $v_{\text{out}} = p_{\text{out}}^* / p_0^* \ll 1$ according to the nonrelativistic approximation. At large source sizes, for example, when the homogeneity lengths correspond to $A + A$ -collisions, $k_0^2 R^2 \gg 1$, $k^2 T^2 \gg 1$, all these ratios tend to unity.

The mean emission duration is supposed to be proportional to the average system's size, $T = a(R_O + R_S + R_L)/3$, that leads to the quadratic equation expressing R_O (and T) through $R_{i,\text{st}}$. The latter are connected with ones taken in the global reference system according to transformation laws (18). The value a is a free model parameter. Then we put these extracted values into the expression (26) for the correlation function and perform its fitting with the Gaussian (17). This gives us finally the interferometry radii R_{out} , R_{side} , and R_{long} in view of the uncertainty principle. The radii are presented then in the global system using the transformations inverse to (18).

The correlation function is the ratio of the two- and one-particle spectra. It is found [39] that quantum corrections to this ratio are not so sensitive to different forms of the wave packets as the spectra itself. In particular, the effective temperature of the *corrected* transverse spectra depends on whether the parameter of mean particle momentum is included or not into the wave packet formalism. If yes, the corrected effective temperature for small sources $R \sim 1$ fm is equal or even higher than that the individual emitters have, $T = k^2/m$, while for the wave packets in the form (19) it is lower [39]. Besides this, in the nonrelativistic approximation one can describe only very soft part of the spectra. That is why we focus in the paper on the corrections to the Bose-Einstein correlation functions where in the rest frame of the source the total and relative momenta of the boson pairs are fairly small.

5. Femtoscopy of $p + p$ Collisions in View of the Uncertainty Principle

This section of the review is based on the results of [40].

The attempt of the systematic theoretical analysis of the pion femtoscopy of $p + p$ collisions at the top RHIC and $\sqrt{s} = 0.9$ TeV LHC energies was made in [75] within Quark-Gluon String Model (QGSM). It was found that for a satisfactory description of the interferometry radii one needs to reduce significantly the formation time by increasing the string tension value relative to the one fixed by the QGSM

description of the spectra and multiplicity. Otherwise, the radii obtained within QGSM are too large as compared to the measured femtoscopy scales. Hypothetically one can hope to reduce the predicted radii suggesting the other approach—the hydrodynamic mechanism of the bulk matter production in $p + p$ collisions, at least, for high multiplicity events. Although the applicability of hydrodynamics to $p + p$ collisions is still questionable, there are certain arguments in its favor. For instance, in [76, 77] multiparticle production in nuclear collisions is related to that in hadronic ones within the model based on dissipating energy of participants and their types, which includes Landau relativistic hydrodynamics and constituent quark picture. Then to reproduce high multiplicity, the initially very small $p + p$ system has to be initially superdense. This leads to very large collective velocity gradients, and so the homogeneity lengths should be fairly small. However, as we will demonstrate, even at the maximally possible velocity gradients at the given multiplicity, one gets again an overestimate of the interferometry radii in $p + p$ collisions. Therefore, one can conclude that the problem of theoretical description of the interferometry radii in $p + p$ collisions may be a general one for different types of event generators associated with various particle production mechanisms. Here we try to correct the femtoscopic results of event generators using for this aim the quantum effects accounting for partial indistinguishability and mutual coherence described in the previous section.

We will employ the hydrokinetic model (HKM) [23, 29, 35] in its hybrid form [30] where the UrQMD hadronic cascade is considered as the semiclassical event generator at postfreeze-out (“afterburn”) stage of the hydrodynamic/hydrokinetic evolution. The analysis provided in [30] shows a fairly small difference of the one- and two-particle spectra obtained in hHKM and in the case of the direct matching of hydrodynamics and UrQMD cascade at the chemical freeze-out hypersurface. Thus, in this paper we utilize just the latter simplified “hybrid” variant for the afterburn stage.

Let us try to apply the above hydrokinetic picture to the LHC $p + p$ collisions at $\sqrt{s} = 7$ TeV aiming to get the minimal interferometry radii/volume at the given multiplicity bin. As it is known [23] the maximal average velocity gradient and so the minimal homogeneity lengths can be reached at the Gaussian-like initial energy density profile. For the same aim we use the minimal transverse scale in ultrahigh energy $p + p$ collision, close to the size of gluon spots [78, 79] in proton moving with a speed $v \approx c$. In detail, the initial boost-invariant tube for $p + p$ collisions has the energy density Gaussian distribution in transverse plane with the width (rms) $R = 0.3$ fm [78, 79], and, following [30], we attribute it to the initial proper time $\tau_0 = 0.1$ fm/c. At this time there is no initial transverse collective flow. The maximal initial energy density is defined by all charged particle multiplicity bin.

In Figures 5 and 6, taken from [40], for the two multiplicity classes $\langle dN_{\text{ch}}/d\eta \rangle = 9.2$ and $\langle dN_{\text{ch}}/d\eta \rangle = 17.9$ we present the three curves for interferometry radii as a function of p_T : the experimental one, the one taken just from the HKM simulations, and the other one obtained after application of the quantum corrections. The basic parameters

used correspond to the limiting case, when the homogeneity lengths in the source rest frame coincide with the ones taken from the model, $\gamma = 1$. For this case $a \approx 1$, $k = 0.18$ GeV/c, and $p_T^* = 0.13$ GeV/c. The α parameter values linearly increase with p_T from 1.15 to 1.35 for the $\langle dN_{\text{ch}}/d\eta \rangle = 9.2$ case and from 1.02 to 1.1 for $\langle dN_{\text{ch}}/d\eta \rangle = 17.9$. As one can see, the quantum corrected p_T -dependency of the radii gets closer to the experimental values, but for large p_T the corrections are insufficient to fully describe the observable femtoscopy scales behavior. This fact may indicate that sources of particles with large p_T cannot be described in hydrodynamical approximation. Note that just for such large p_T the nontrivial baseline corrections, already provided in presented experimental data, are very essential.

Considering the multiplicity dependence of femtoscopy scales in $p + p$ and $p + Pb$ collisions we cannot bypass the scaling hypothesis issue [44, 45], that suggests a universal linear dependence of the HBT volume on the particle multiplicity. It means that the observed interferometry volume depends roughly only on the multiplicity of particles produced in collision but not on the geometrical characteristics of the collision process. At the same time, as it was found in the theoretical analysis in [88, 89], the interferometry volume should depend not only on the multiplicity but also on the initial size of colliding systems. In more detail, the intensity of the transverse flow depends on the initial geometrical size R_0^g of the system: roughly, if the pressure is $p = c_0^2 \epsilon$, then the transverse acceleration $a = \nabla_{x_T} p / \epsilon \propto p(\mathbf{x}_T = 0) / (R_0^g \epsilon) = c_0^2 / R_0^g$. The interferometry radii R_T , that are associated with the homogeneity lengths, depend on the velocity gradient and geometrical size and for nonrelativistic transverse expansion can be approximately expressed through R_0^g , the averaged transverse velocity $\langle |v_T| \rangle$, and inverse of the temperature β at some final moment τ [17, 18, 90, 91]:

$$R_T = \frac{R^g(\tau)}{\sqrt{1 + (2/\pi) \langle |v_T| \rangle^2 \beta m_T}} \quad (29)$$

$$\approx R_0^g \left(1 + \frac{\tau^2 c_0^2}{2(R_0^g)^2} - \beta m_T \frac{\tau^2 c_0^2}{\pi^2 (R_0^g)^2} \right).$$

The result (29) for the HBT radii depends obviously on R_0^g and, despite its roughness, demonstrates the possible mechanism of compensation of the growing geometrical radii of an expanding fireball in the femtoscopy measurements. For some dynamical models of expanding fireballs the interferometry radii, measured at the final time of system’s decoupling, are coincided with the initial geometrical ones, no matter how large the multiplicity is [35, 92]. The reason for such a behavior is clear from (11): if there is no dissipation in the expanding system, $F^{\text{gain}}(t, \mathbf{x}) = F^{\text{loss}}(t, \mathbf{x})$, then the spectra and correlation functions are coincided with the initial ones. The detail study of hydrodynamically expanding systems is provided in [88, 89]. It is found that at the boost-invariant isentropic and chemically frozen evolution

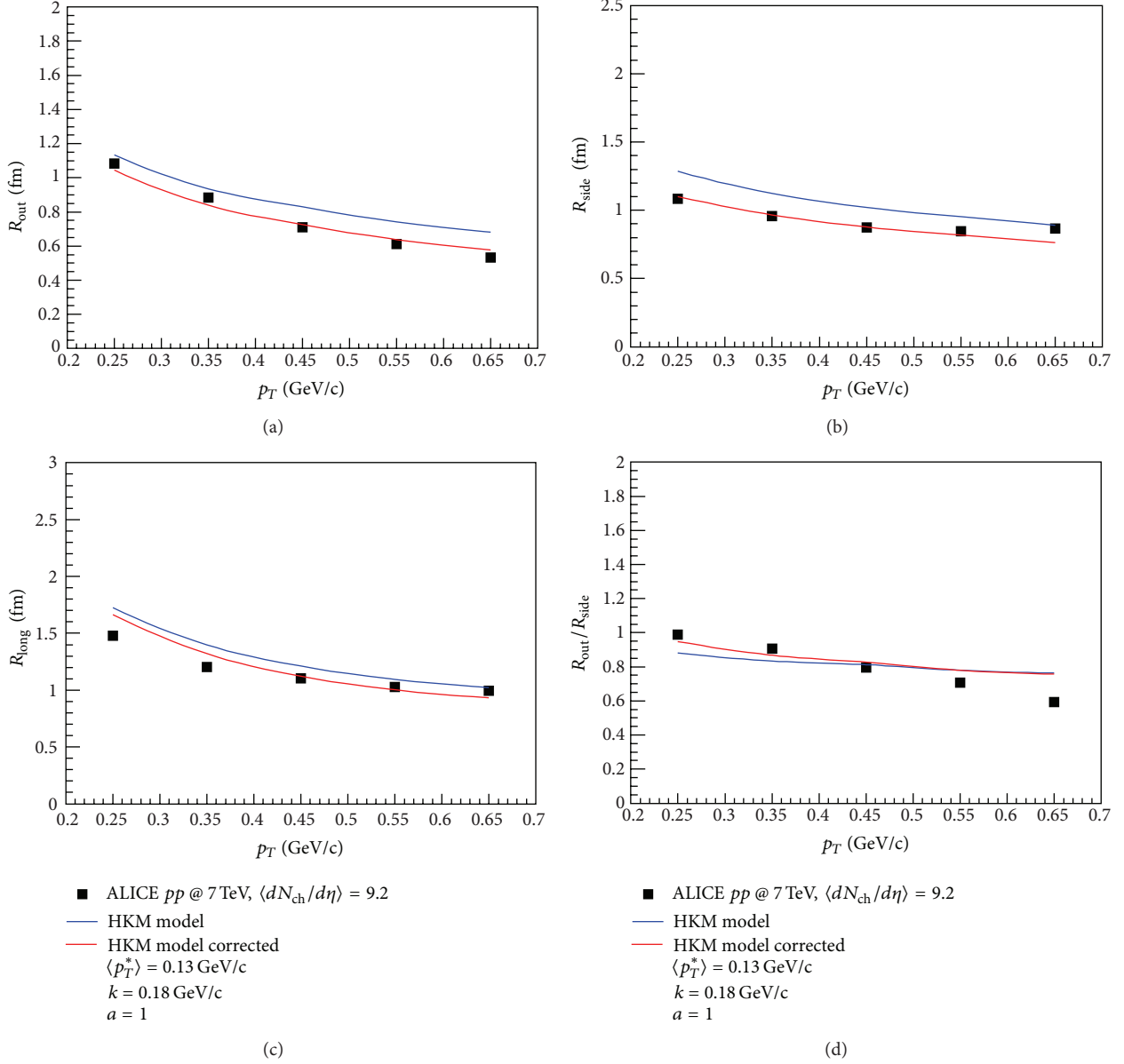


FIGURE 5: Interferometry radii dependency on p_T , $\langle dN_{ch}/d\eta \rangle = 9.2$. The data are taken from [42].

the interferometry volume, if it were possible to measure at some evolution time τ , is approximately constant:

$$V_{int}(\tau) \simeq C(\sqrt{s}) \frac{dN/dy(\tau)}{\langle f \rangle_{\tau} T_{eff}^3(\tau)}, \quad (30)$$

where $\langle f \rangle$ is the averaged phase-space density [93, 94] which is found to be approximately conserved during the hydrodynamic evolution under the above conditions as well as dN/dy [88, 89]. As for the effective temperature of the hadron spectra, $T_{eff}(\tau) = T(\tau) + m(\langle v_T(\tau) \rangle^2/2)$, one can see that, when the system's temperature T drops, the mean v_T^2 increases; therefore T_{eff} does not change much during the evolution (it slightly decreases with time for pions and increases for protons). Hence V_{int} , if it has been measured

at some evolution time τ , will also approximately conserve. Of course, the real evolution is neither isentropic nor chemically frozen and includes also QGP stage, but significant dependence of the femtoscopy scales on the initial system size preserves anyway.

Figure 7 shows the dependency $V_{int}(\langle dN_{ch}/d\eta \rangle)$ for considered case of $p + p$ collisions at the LHC, $\sqrt{s} = 7$ TeV, and for the most central (only!) collisions of nuclei having similar sizes, $Pb + Pb$ and $Au + Au$, at the SPS, RHIC, and LHC. We have also put on the plot our prediction for the interferometry volume of pPb -system, that has initially larger size than pp -system. As one can see, the different groups of points corresponding to $p + p$, $p + Pb$, and $A + A$ events cannot be fitted by the same straight line. This apparently confirms the result obtained in [88, 89] that the interferometry volume

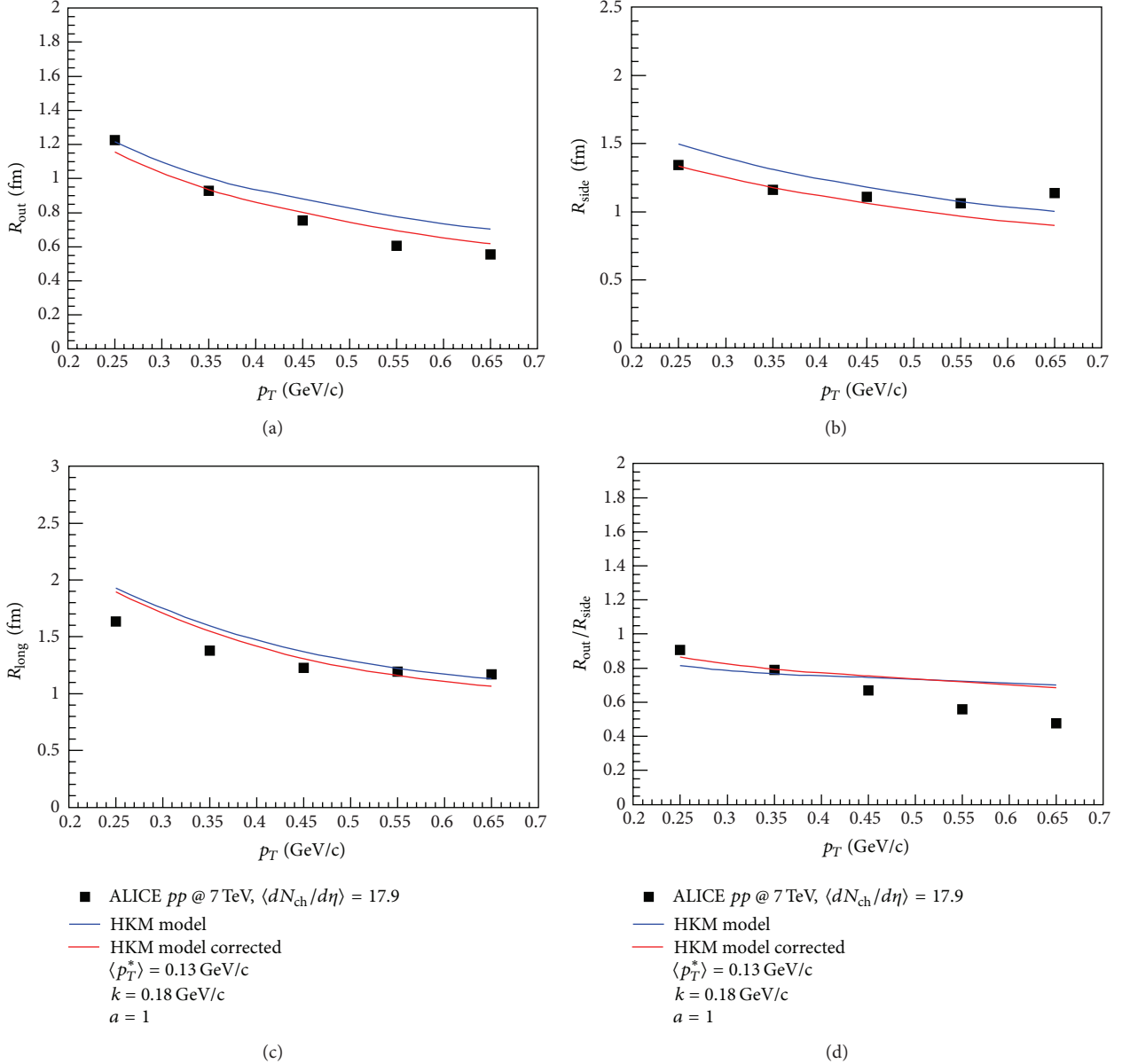


FIGURE 6: Interferometry radii dependency on p_T , $\langle dN_{ch}/d\eta \rangle = 17.9$. The data are taken from [42].

is a function of both variables: the multiplicity and the initial size of colliding system. The latter depends on the atomic number A of colliding objects and the collision centrality c .

One can conclude that quantum corrections to the pion interferometry radii in $p + p$ collisions at the LHC can significantly improve the (semiclassical) event generator results that typically give an overestimate of the experimental interferometry radii and volumes. The corrections account for the basic (partial) indistinguishability and mutual coherence of the closely located emitters because of the uncertainty principle [39]. The additional suppression of the Bose-Einstein correlation function also appears. The effects become important for small sources, 1-2 fm or smaller. Such systems cannot be completely random and so require the modification of the standard theoretical approach for

the correlation femtoscopy. The predicted femtosopic scales for $p + Pb$ collisions need some small corrections only for its minimal values corresponding to the *initial* transverse size of pPb system 0.9 fm.

6. Nonfemtoscopic Two-Pion Correlations in Small Systems

The interest to the nonfemtoscopic correlations is motivated in particular by the fact that for relatively small systems they appreciably affect the complete two-particle correlation function, forming the so-called correlation baseline. It has an influence on the interpretation of the interferometry radii momentum dependence in $p + p$ collisions with high multiplicities, where the different mechanisms of spectra

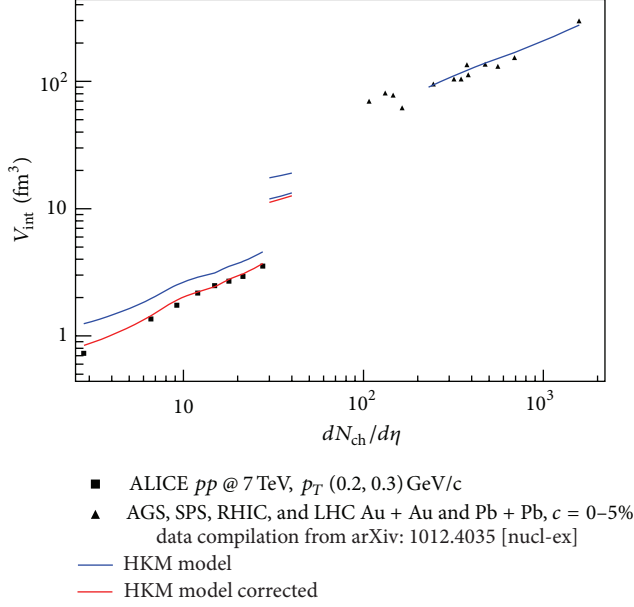


FIGURE 7: The interferometry volume dependency on charged particles multiplicity. The curve fragments in the middle correspond to the HKM prediction for $p + Pb$ collision at the LHC energy $\sqrt{s} = 5.02$ GeV. The upper one is related to the initial transverse system size $R = 1.5$ fm and for the two lower ones $R = 0.9$ fm. The curves at the left and at the right represent the HKM results for $p + p$ and $A + A$ central collisions respectively, compared to the experimental data at AGS, SPS, RHIC, and LHC, taken from papers [42, 80–87]. The pp volumes are calculated as a product $R_{\text{out}}R_{\text{side}}R_{\text{long}}$ of respective experimental radii. The blue lines correspond to pure HKM results, whereas the quantum corrections to them are presented by the red lines. Figure is taken from [40].

formation are under discussion. Therefore, for successful and unambiguous application of the correlation femtoscopy method to the case of elementary particle collisions, one needs to know the mechanisms of nonfemtoscopic correlations to separate the femtoscopic and nonfemtoscopic ones.

The two-particle correlation function is defined as

$$C(p_1, p_2) = \frac{P(p_1, p_2)}{P(p_1)P(p_2)}, \quad (31)$$

where $P(p_1, p_2)$ is the probability of observing two particles with momenta \mathbf{p}_1 and \mathbf{p}_2 , while $P(p_1)$ and $P(p_2)$ designate the single-particle probabilities. In heavy ion collisions

$$C(p_1, p_2) \approx C_F(\mathbf{p}, \mathbf{q}), \quad (32)$$

where $\mathbf{p} = (\mathbf{p}_1 + \mathbf{p}_2)/2$, $\mathbf{q} = \mathbf{p}_2 - \mathbf{p}_1$, and C_F denotes the femtoscopic correlation function that takes into account quantum statistics and final state interactions. In elementary particle collisions additional (nonfemtoscopic) correlations, like those arising from jet/string fragmentation and from energy and momentum conservation (see, e.g., [41–43]), can also give a significant contribution. The important problem

in this regard is whether we can factorize out the part corresponding to the nonfemtoscopic correlations, C_{NF} , from the total correlation function:

$$C(p_1, p_2) = C_F(\mathbf{p}, \mathbf{q}) C_{NF}(\mathbf{p}, \mathbf{q}). \quad (33)$$

It [39], such a factorization, was demonstrated numerically within the simple models of three- and two-particle emission accounting for minijets fragmentation and event-by-event initial state fluctuation induced nonfemtoscopic correlations, and below we will assume this factorization property.

Recently, the ALICE Collaboration utilized some event generators, which do not include effects of quantum statistics, for an estimate of the correlation baseline (i.e., nonfemtoscopic correlation function of identical pions) under the Bose-Einstein peak at LHC energies [41, 42]. It was motivated by a reasonable agreement of the corresponding event generator simulations with the experimental data for correlation functions of oppositely charged pions in $p + p$ collisions at the same energy [41, 42]. The calculated correlation baseline has been utilized by the ALICE Collaboration to extract femtoscopic correlations from measured identical pion two-particle correlation functions [41]. Because the utilized event generators account for energy-momentum conservation and emission of minijets, it was conjectured in [41, 42] that some specific peculiarities of the unlike-sign pion correlations as well as like-sign nonfemtoscopic pion correlations can be caused by the jet-like and energy-momentum conservation induced correlations. In [46], we support this conjecture. There, to describe the nonfemtoscopic pion correlations in a simple analytical model, we assume that N pions are produced with momenta $\mathbf{p}_1, \dots, \mathbf{p}_N$ in $(N + X)$ multiparticle production events and consider pions as distinguishable, yet equivalent particles with symmetrical probability density functions. A distinguishability of equivalent particles means that there is no quantum interference between possibilities that correspond to all $N!$ permutations of the particle momenta p_i . Then single-particle probability, $P_N(p_1)$, and the two-particle probability, $P_N(p_1, p_2)$, can be written as

$$P_N(p_1) = \frac{1}{N} \sum_{i=1}^N \int d\Omega_{p^*} E_i^* \delta^{(3)}(\mathbf{p}_1 - \mathbf{p}_i^*) \hat{P}_N(p_1^*, \dots, p_N^*), \quad (34)$$

$$\begin{aligned} P_N(p_1, p_2) &= \frac{1}{N(N-1)} \sum_{i \neq j=1}^N \int d\Omega_{p^*} E_i^* \delta^{(3)}(\mathbf{p}_1 - \mathbf{p}_i^*) E_j^* \\ &\quad \times \delta^{(3)}(\mathbf{p}_2 - \mathbf{p}_j^*) \hat{P}_N(p_1^*, \dots, p_N^*), \end{aligned} \quad (35)$$

where $d\Omega_p = (d^3 p_1)/E_1 \cdots (d^3 p_N)/E_N$. The nonsymmetrized N -pion probability density in such events reads as

$$\begin{aligned} \widehat{P}_N(p_1, \dots, p_N) \\ = \frac{1}{K} \sum_X \int d\Omega_k \delta^{(4)} \left(p_a + p_b - \sum_{i=1}^N p_i - \sum_{j=1}^X k_j \right) \\ \times |M_{N+X}(p_1, \dots, k_X)|^2, \end{aligned} \quad (36)$$

where $M_{N+X}(p_1, \dots, k_X)$ is nonsymmetrized $(N+X)$ -particle production amplitude, p_a and p_b are 4-momenta of colliding particles (protons), and K is the normalization factor,

$$\begin{aligned} K = \sum_X \int d\Omega_k d\Omega_p \delta^{(4)} \left(p_a + p_b - \sum_{i=1}^N p_i - \sum_{j=1}^X k_j \right) \\ \times |M_{N+X}(p_1, \dots, k_X)|^2. \end{aligned} \quad (37)$$

Expression (36) for $\widehat{P}_N(p_1, \dots, p_N)$ is rather complicated because, in particular, it depends on X particles that are produced in addition to N pions. The latter means also that one can hardly expect that total energy or momentum of the pion subsystems are constants in the system's center of mass; instead, one can expect that they fluctuate in event-by-event basis. Here we assume that the total transverse momentum of N pions is equal to zero in the system's center of mass (keeping, however, in mind that this constraint is, in fact, too strong and can be weakened if necessary) and neglect the constraints conditioned by the conservation of energy and longitudinal momentum supposing that the system under consideration is barely N -pion subsystem in a small midrapidity region of the total system. Then, motivated by (36), we assume that a nonsymmetrized N -pion probability density can be written as

$$\widehat{P}_N(p_1, \dots, p_N) = \frac{1}{K} \delta(p_1, \dots, p_N) F_N(p_1, \dots, p_N), \quad (38)$$

where $F_N(p_1, \dots, p_N)$ is a nonsymmetrized function of pionic momenta, $\delta(p_1, \dots, p_N)$ denotes average constraints on the N -pion states that appear due to energy and momentum conservations in multiparticle production events, and we assume that

$$\delta(p_1, \dots, p_N) = \delta^{(2)}(\mathbf{p}_{T1} + \mathbf{p}_{T2} + \cdots + \mathbf{p}_{TN}), \quad (39)$$

where $\mathbf{p}_{T1}, \mathbf{p}_{T2}, \dots, \mathbf{p}_{TN}$ are transverse components of the momenta of the N particles. Then the normalization factor is

$$K = \int d\Omega_p \delta(p_1, \dots, p_N) F_N(p_1, \dots, p_N). \quad (40)$$

Now, to describe the nonfemtoscopic pion correlations in a simple analytical model, we assume that there are no other correlations in the production of N -pion states except for the correlations induced by transverse momentum conservation and cluster (minijet) structures in momentum space. For the

sake of simplicity we assume here that the only two-particle clusters appear. Then one can write for fairly large $N \gg 1$

$$\begin{aligned} F_N(p_1, \dots, p_N) \\ = f(p_1) \cdots f(p_N) Q(p_1, p_2) \cdots Q(p_{N-1}, p_N), \end{aligned} \quad (41)$$

where $Q(p_i, p_j)$ denotes the jet-like correlations between momenta \mathbf{p}_i and \mathbf{p}_j ; existence of such correlations means that F_N cannot be expressed as a product of one-particle distributions. Then, utilizing the integral representation of the δ -function by means of the Fourier transformation, $\delta^{(2)}(\mathbf{p}_T) = (2\pi)^{-2} \int d^2 r_T \exp(i\mathbf{r}_T \mathbf{p}_T)$, and accounting for (34), (38), (39), and (41), the single-particle probability reads as

$$P_N(p_1) = \frac{1}{(2\pi)^2 K} \int d^2 r_T G_N(\mathbf{p}_1, \mathbf{r}_T), \quad (42)$$

where

$$\begin{aligned} G_N(\mathbf{p}_1, \mathbf{r}_T) = \int d\Omega_{p^*} E_i^* \delta^{(3)}(\mathbf{p}_1 - \mathbf{p}_1^*) \\ \times e^{i\mathbf{r}_T(\mathbf{p}_{T1}^* + \cdots + \mathbf{p}_{TN}^*)} \\ \times F_N(p_1^*, \dots, p_N^*). \end{aligned} \quad (43)$$

A possibility of different cluster configurations of particles means, in particular, that registered particles with momenta \mathbf{p}_1 and \mathbf{p}_2 can belong either to different minijets or to the same minijet. Then, taking into account (35), (38), (39), and (41), we get

$$\begin{aligned} P_N(p_1, p_2) = \frac{N}{N(N-1)} P_N^{\text{1jet}}(p_1, p_2) \\ + \frac{N(N-1) - N}{N(N-1)} P_N^{\text{2jet}}(p_1, p_2), \end{aligned} \quad (44)$$

where

$$P_N^{\text{1jet}}(p_1, p_2) = \frac{1}{(2\pi)^2 K} \int d^2 r_T G_N^{\text{1jet}}(\mathbf{p}_1, \mathbf{p}_2, \mathbf{r}_T), \quad (45)$$

$$P_N^{\text{2jet}}(p_1, p_2) = \frac{1}{(2\pi)^2 K} \int d^2 r_T G_N^{\text{2jet}}(\mathbf{p}_1, \mathbf{p}_2, \mathbf{r}_T), \quad (46)$$

$$\begin{aligned} G_N^{\text{1jet}}(\mathbf{p}_1, \mathbf{p}_2, \mathbf{r}_T) = \int d\Omega_{p^*} E_i^* \delta^{(3)}(\mathbf{p}_1 - \mathbf{p}_1^*) E_j^* \\ \times \delta^{(3)}(\mathbf{p}_2 - \mathbf{p}_2^*) e^{i\mathbf{r}_T(\mathbf{p}_{T1}^* + \cdots + \mathbf{p}_{TN}^*)} F_N, \end{aligned} \quad (47)$$

$$\begin{aligned} G_N^{\text{2jet}}(\mathbf{p}_1, \mathbf{p}_2, \mathbf{r}_T) = \int d\Omega_{p^*} E_i^* \delta^{(3)}(\mathbf{p}_1 - \mathbf{p}_1^*) E_j^* \\ \times \delta^{(3)}(\mathbf{p}_2 - \mathbf{p}_3^*) e^{i\mathbf{r}_T(\mathbf{p}_{T1}^* + \cdots + \mathbf{p}_{TN}^*)} F_N. \end{aligned} \quad (48)$$

Here $F_N \equiv F_N(p_1^*, \dots, p_N^*)$. The first term in the right hand side of (44) is associated with events where the two registered particles belong to the same minijet, and the second term

corresponds to events where the particles are from different minijets. Evidently, the former is relatively rare; however, notice that the first term can be significant for small systems with not very large N .

It was demonstrated in [46] that this model can reproduce, with reasonable parameters, the correlation functions of unlike-sign pions measured by the ALICE Collaboration [41] and nonfemtoscopic correlations of like-sign pions that are generated in the PHOJET simulations and utilized as the correlation baseline by the ALICE Collaboration [41]. To calculate nonfemtoscopic correlations, analytical parameterizations of the functions in interest were used, namely,

$$f(p_i) = E_i \exp\left(-\frac{\mathbf{p}_{i,T}^2}{T_T^2}\right) \exp\left(-\frac{\mathbf{p}_{i,L}^2}{T_L^2}\right), \quad (49)$$

$$Q(p_i, p_j) = \exp\left(-\frac{(\mathbf{p}_i - \mathbf{p}_j)^2}{\alpha^2}\right), \quad (50)$$

where T_T, T_L , and α are some parameters, and we assume that $T_L \gg T_T$. In accordance with ALICE baseline obtained from the PHOJET event generator simulations, we assume that only $q_{\text{inv}} = \sqrt{(\mathbf{p}_2 - \mathbf{p}_1)^2 - (E_2 - E_1)^2}$ is measured for each \mathbf{p}_T bin. Assuming that longitudinal components of the registered particles are equal to zero, $p_{1L} = p_{2L} = 0$, we approximate q_{inv}^2 as

$$q_{\text{inv}}^2 \approx \mathbf{q}_T^2 \left(\frac{m^2 + \mathbf{p}_T^2 \sin^2 \phi}{m^2 + \mathbf{p}_T^2} \right), \quad (51)$$

where ϕ denotes unregistered angle between \mathbf{p}_T and \mathbf{q}_T , $\mathbf{p}_T \cdot \mathbf{q}_T = |\mathbf{p}_T| |\mathbf{q}_T| \cos \phi$. Then

$$C_{NF}(|\mathbf{p}_T|, q_{\text{inv}}) = \frac{\int_0^{2\pi} d\phi P_N(p_1, p_2)}{\int_0^{2\pi} d\phi P_N(p_1) P_N(p_2)}, \quad (52)$$

and, taking into account (44), we get

$$\begin{aligned} C_{NF}(|\mathbf{p}_T|, q_{\text{inv}}) &= \frac{N-2}{N-1} \\ &\times \left(C_N^{2\text{jet}}(|\mathbf{p}_T|, q_{\text{inv}}) \right. \\ &\left. + \frac{1}{N-2} C_N^{1\text{jet}}(|\mathbf{p}_T|, q_{\text{inv}}) \right), \end{aligned} \quad (53)$$

where

$$C_N^{2\text{jet}}(|\mathbf{p}_T|, q_{\text{inv}}) = \frac{\int_0^{2\pi} d\phi P_N^{2\text{jet}}(p_1, p_2)}{\int_0^{2\pi} d\phi P_N(p_1) P_N(p_2)}, \quad (54)$$

$$C_N^{1\text{jet}}(|\mathbf{p}_T|, q_{\text{inv}}) = \frac{\int_0^{2\pi} d\phi P_N^{1\text{jet}}(p_1, p_2)}{\int_0^{2\pi} d\phi P_N(p_1) P_N(p_2)}. \quad (55)$$

It is well known (see, e.g., [44, 45]) that the influence of exact conservation laws on single-particle and two-particle momentum probability densities at the N -particle production process depends on the value of N and disappears

at $N \rightarrow \infty$. Since one considers a subsystem of N pions but not the total system, to weaken the influence of the total transverse momentum conservation on pions we will consider $C_M^{1\text{jet}}$ and $C_M^{2\text{jet}}$ with $M > N$ instead of $C_N^{1\text{jet}}$ and $C_N^{2\text{jet}}$ in (53). This is the simplest way to account for a weakened conservation law in our model. At the same time, the factor $1/(N-2)$ in (53) remains the same since it is associated with the combinatorics of the distribution of particles between clusters in momentum space (“minijets”), which happens whether or not one weakens the total momentum conservation law. Also, for more exact fitting of the data points in each average transverse momentum bin, we utilize the auxiliary factors Λ ; when we compared results of our calculations with ALICE two-pion correlation and simulation data, these proportionality factors differ slightly from unit in our calculations (nearly 0.9). Then (53) gets the form

$$\begin{aligned} C_{NF}(|\mathbf{p}_T|, q_{\text{inv}}) &= \Lambda(|\mathbf{p}_T|) \\ &\times \left(C_M^{2\text{jet}}(|\mathbf{p}_T|, q_{\text{inv}}) \right. \\ &\left. + \frac{1}{N-2} C_M^{1\text{jet}}(|\mathbf{p}_T|, q_{\text{inv}}) \right). \end{aligned} \quad (56)$$

The results of our calculations of the nonfemtoscopic correlation functions C_{NF} are shown in Figures 8 and 9 in comparison with correlation functions reported by the ALICE Collaboration [41] for different transverse momenta of pion pairs (actually, we performed calculations for the mean value in each bin). The data for unlike-sign pion correlations measured by the ALICE Collaboration as well as for the PHOJET simulations of like-sign two-pion nonfemtoscopic correlation functions at midrapidity for the total charged multiplicity $N_{\text{ch}} \geq 12$ bin in $p + p$ collisions at $\sqrt{s} = 900$ GeV are taken from [41, 95]. Note that correlations of nonidentical pions measured by the ALICE Collaboration, as well as the PHOJET simulations of identical two-pion correlation functions, demonstrate Coulomb FSI correlations at the lowest q_{inv} bin and peaks coming from resonance decays. These Coulomb FSI and contributions from resonance production are not taken into account and so are not reproduced in our model. The presented results are obtained for $M = 50$, $T_T = \alpha = 0.65$ GeV (to minimize the number of fit parameters, we fixed $T_T = \alpha$ for all calculations. Note that with these parameter values the mean transverse momentum $\langle p_T \rangle$ is about 0.58 GeV), and the fitted values of N are different for like-sign and unlike-sign pion pairs, namely, $N^{\pm\pm} = 20$ for the former and $N^{+-} = 11$ for the latter. The relatively high value of M can be interpreted as a residual effect on the pion subsystem of total energy-momentum conservation in a multiparticle production process. The relation $N^{+-} < N^{\pm\pm}$ between fitted N values means that the magnitude of the correlations induced by a minijet for unlike-sign pion pairs is higher than that for like-sign ones. This happens because in the former there is no local charge conservation constraint for the production of oppositely charged pion pairs, and, therefore, one can expect less identically charged pion pairs from the fragmenting minijets than oppositely charged ones. One can

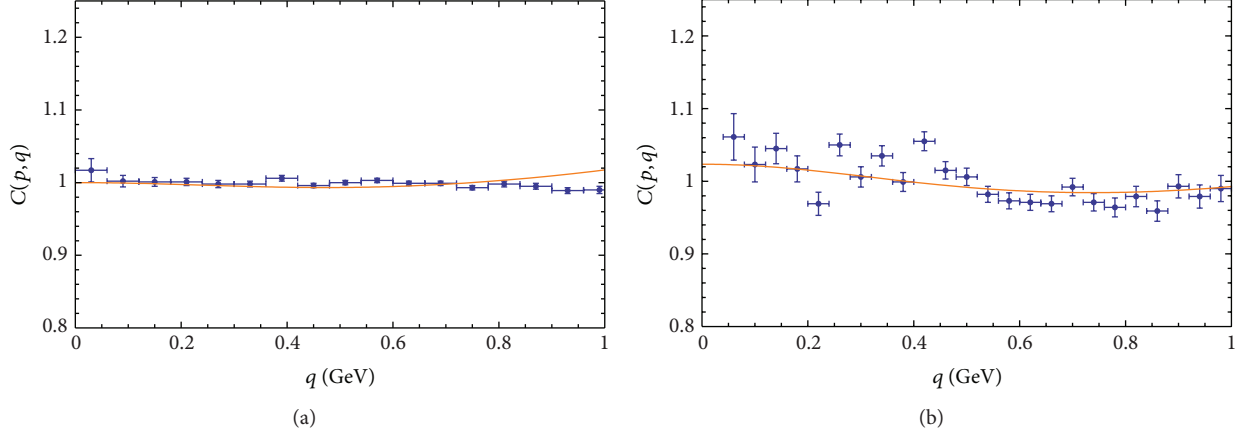


FIGURE 8: The nonfemtoscopic correlation functions of like-sign (a) and unlike-sign (b) pions in the $0.1 < p_T < 0.25$ GeV bin from a simulation using PHOJET [41, 95] (solid dots) and those calculated from the analytical model: minijets + momentum conservation (solid line). See the text for details.

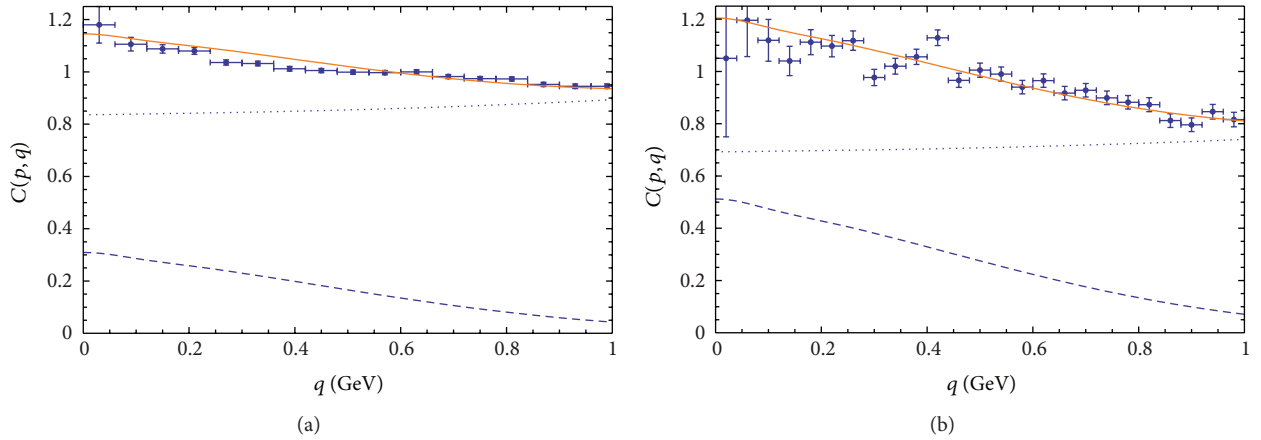


FIGURE 9: The nonfemtoscopic correlation functions of like-sign pions (a) from a simulation using PHOJET and unlike-sign pions (b) measured by the ALICE Collaboration in the $0.7 < p_T < 1.0$ GeV bin from [41, 95] (solid dots) and those calculated from the analytical model (solid line). The contributions to the nonfemtoscopic correlation function from the first term of (56) (dotted line) and from the second one (dashed line) are also presented.

see from the figures that the behavior of the nonfemtoscopic correlation functions of pions, C_{NF} , is reproduced well despite the simplicity of our model. This is a result of the competition of the two trends: an increase of the correlation function with q_{inv} because of momentum conservation and its decrease due to fragmentation of one minijet into the registered pion pair. Figure 9 also demonstrates the relative contribution of the first and second terms in (56) to the nonfemtoscopic correlation functions.

Another type of correlations not induced by the QS effects is the correlations connected with existence of subensembles of events with different emission functions that leads to the corresponding fluctuations in single-particle and two-particle momentum spectra. In hydrodynamical models of nucleus-nucleus and proton-proton collisions these fluctuations can be caused by asymmetrically fluctuating initial densities used for the hydrostage of the model. Let us consider the effect of such correlations on the resulting correlation

function on the example of a simple analytical model [46]. Disregarding the QS correlations (for model of two-particle emission that accounts for the QS see [39]) we suppose that the N -particle probability density is defined as

$$P_N(p_1, p_2, \dots, p_N) = \sum_i w(u_i) P_N(p_1, p_2, \dots, p_N; u_i), \quad (57)$$

where $P_N(p_1, p_2, \dots, p_N; u_i)$ is the N -particle probability density for some u_i type of the initial conditions, and $w(u_i)$ denotes the distribution over initial conditions, $\sum_i w(u_i) = 1$. To analyze the possible effect of fluctuating initial conditions, here we neglect conservation law constraints and the production of minijets. Because we assume uncorrelated particle emissions for each specific initial condition, one can write

$$P_N(p_1, p_2, \dots, p_N; u_i) = f(p_1; u_i) f(p_2; u_i) \cdots f(p_{N-1}; u_i) f(p_N; u_i), \quad (58)$$

where we normalize $f(p; u_i)$ as $\int (d^3 p/E) f(p; u_i) = 1$, and then $K = 1$; see (38) and (40). The two-particle nonfemtoscopic correlation function C_{NF} then reads as

$$C_{NF}(p_1, p_2) = \frac{\sum_i w(u_i) f(p_1; u_i) f(p_2; u_i)}{\sum_i w(u_i) f(p_1; u_i) \sum_j w(u_j) f(p_2; u_j)}. \quad (59)$$

Evidently, the different type of fluctuation, that is, the form of the distribution $w(u_i)$, leads to a different behavior of the nonfemtoscopic correlations. To illustrate that fluctuations can lead to the nonfemtoscopic correlation functions that are similar to the ones induced by minijets, let us consider the toy model where

$$w(\mathbf{u}_T) = \frac{\alpha^2}{\pi} \exp(-\mathbf{u}_T^2 \alpha^2), \quad (60)$$

$$f(p; \mathbf{u}_T) = \frac{\beta^2 \gamma}{\pi^{3/2}} E \exp(-(\mathbf{p}_T - \mathbf{u}_T)^2 \beta^2) \exp(-p_L^2 \gamma^2), \quad (61)$$

and normalization is chosen in such a way that $\int d^2 u_T w(\mathbf{u}_T) = 1$ and $\int (d^3 p/E) f(p; \mathbf{u}_T) = 1$. The main feature of such a model is that event-by-event single-particle transverse momentum spectra have a maximum for event-by-event fluctuating \mathbf{p}_T values. Such momentum spectrum fluctuations could take place, for example, in hydrodynamics with a highly inhomogeneous initial energy density profile without cylindrical or elliptic symmetry. One can easily see that in this case C_{NF} decreases with q_T^2 ,

$$C_{NF}(p, q) \sim \exp\left(-\frac{\beta^4}{2(\alpha^2 + \beta^2)} q_T^2\right), \quad (62)$$

and this means (after taking into account (51) and (52)) that C_{NF} decreases with q_{inv}^2 too, which is similar to the behavior of C_{NF} if the nonfemtoscopic correlations are induced by minijets. At the same time, unlike the latter, the hydrodynamical fluctuations lead to similar correlations for like-sign and unlike-sign pion pairs. Then, our analysis suggests that, up to different resonance yields, the value of the slope of the correlation baseline at relatively low q_{inv} can be somewhere between pure hydrodynamic (i.e., the same as for nonidentical pion pairs) and pure minijet (i.e., lower than for nonidentical pion pairs) scenarios.

7. Summary

It is often said that the femtoscopic measurements allow one to restore the space-time structure of the particle/nucleus collision processes. It is really possible but only through the theoretical constructions allowing to interpret these processes and describe the wide range of the corresponding experimental data. If such an advanced model is based on some kind of the space-time picture, then the crucial point for the model is a recreation of the femtoscopic data. If it is successful, then, first, this model claims to be true, and,

second, the same is related to recover by the model the space-time structure of a collision process.

In this review we analyzed hydrokinetic model (HKM) for $A + A$ collisions as the reliable theoretical construction for description of the momentum spectra of pions, kaons, protons/antiprotons, all charged particles, and elliptic flows, in wide range of different centralities [29, 30] at RHIC and LHC. We demonstrate here that it describes well the available femtoscopic data for $Au + Au$ and $Pb + Pb$ collisions.

A particular interest is the theoretical basis of HKM which is grounded on the escape functions (not on the distribution ones) when the particle liberation process from the expanding medium is described within the Boltzmann equation. This allows one to avoid the principal problem of the particlization of a medium at nonspace-like sites of transition hypersurfaces, where medium evolution converts into hadronic cascade, like the UrQMD one. So, using the hydrokinetics, as the ‘‘buffer’’ zone, one can switch to hadronic cascade at some space-like hypersurface with a nonequilibrium particle input from HKM. In review we describe just this hybrid variant of the HKM + UrQMD (hHKM).

The HKM, UrQMD, and other existing models/event generators are quasiclassical constructions, and quantum elements, like Bose-Einstein correlations, are inputted typically at the very late stage as the external weights of the boson pair states. In its turn such a procedure is based on the model of independent chaotic sources [4–6]. It is found recently [39] that such a model is inadequate for fairly small sources where the uncertainty principle leads to (partial) indistinguishability of closely located emitters that fundamentally impedes their full independence and incoherence. We review the recent results as for the correlation femtoscopy method that is going beyond the standard approach of independent/random particle emission. The partial coherence of emitted particles is because of the quantum nature of particle emission and happens even if there is no specific mechanism to produce a coherent component of the source radiation. The measure of distinguishability/indistinguishability and mutual coherence of the two emitted wave packets is associated with their overlap integral. In thermal systems the role of corresponding coherent length is played by the thermal de Broglie wavelength.

The application of the new femtoscopy method is demonstrated using the results of [40], where it was found that quantum corrections to the pion interferometry radii in $p + p$ collisions at the LHC can significantly improve the (semiclassical) event generator results that typically give an overestimate of the experimental interferometry radii and volumes. The effects become important for small sources, 1–2 fm or smaller. Such systems cannot be completely random and so require the modification of the standard theoretical approach for the correlation femtoscopy.

More sophisticated result of this study is a good applicability of the hydrodynamics/hydrokinetics with the quantum corrections for description of the femtoscopy scales not only in $A + A$ collisions but also, at least for large multiplicities, in $p + p$ events. These scales are well reproduced for not

large p_T . Whether it means the validity of the hydrodynamic mechanism for the bulk matter production in the LHC $p + p$ collisions is still an open question. It is also related to the problem of early thermalization in the processes of heavy ion collisions; the nature of such phenomenon is still a fundamental theoretical issue.

For small systems the specific nonfemtoscopic correlations can appear in the same kinematic region as the femtoscopic ones. They could be a result of the cluster (minijet) structures in final momentum space of produced particles and the global energy-momentum conservation constraints. The latter typically result in an increase with q_{inv} for fairly high q_{inv} of the nonfemtoscopic two-pion correlation functions of small systems, whereas the former mostly determines a decrease of the ones at relatively low q_{inv} . We discuss the simple analytical model [46] that takes into account correlations induced by the total transverse momentum conservation as well as minijets and show that the model gives reasonable description of the two-pion nonfemtoscopic correlations of identical and nonidentical pions in proton-proton collision events at $\sqrt{s} = 900$ GeV reported by the ALICE Collaboration [41]. The important issue is that femtoscopic and nonfemtoscopic correlations are factorized [39].

There can be different types of multiparticle production mechanisms in $p + p$ collisions, and some of them could result in qualitatively similar nonfemtoscopic correlation functions. We discuss heuristic arguments [46] that the two-pion nonfemtoscopic correlation functions calculated in hydrodynamics with event-by-event fluctuating initial conditions can be qualitatively similar at relatively low q_{inv} to the ones calculated in the PHOJET-like generators, where the nonfemtoscopic correlations for low q_{inv} are mainly caused by minijets. It is worth noting an important difference between the nonfemtoscopic correlations induced by minijets and hydrodynamical fluctuations: while the former leads to a higher magnitude of the nonfemtoscopic correlations for unlike-sign pion pairs as compared to like-sign pions, the latter results in a similar (up to the resonance contributions) strength of the nonfemtoscopic correlations for identical and nonidentical pions. Then, if the applicability of hydrodynamics to $p + p$ collisions will be justified, such an analysis allows one to estimate the correlation baseline and, so, to extract the femtoscopic scales in these collisions by means of tuning the hydrokinetic model to reproduce the experimental unlike-sign pion correlations.

Acknowledgments

The research was carried out within the scope of the EUREA: European Ultra Relativistic Energies Agreement (European Research Group: "Heavy ions at ultrarelativistic energies") and is supported by the National Academy of Sciences of Ukraine (Agreement F4-2013) and by the State fund for Fundamental Researches of Ukraine (Agreement F33/24-2013). The work was supported by the Program of Fundamental Research of the Department of Physics and Astronomy of NAS Ukraine.

References

- [1] M. A. Lisa, S. Pratt, R. Soltz, and U. Wiedemann, "Femtосcopy in relativistic heavy ion collisions: two decades of progress," *Annual Review of Nuclear and Particle Science*, vol. 55, pp. 357–402, 2005.
- [2] M. Lisa and S. Pratt, "Femtoscopically probing the freeze-out configuration in heavy ion collisions," in *The Final Expansion State of Relativistic Nuclear Collisions*, R. Stock, Ed., vol. 23 of *Relativistic Heavy Ion Physics*, pp. 653–685, 2010.
- [3] Z. Chajęcki, "Femtосcopy in hadron and lepton collisions: world systematics," *Acta Physica Polonica B*, vol. 40, no. 4, pp. 1119–1136, 2009.
- [4] G. I. Kopylov and M. I. Podgoretsky, "Correlations of identical particles emitted by highly excited nuclei," *Soviet Journal of Nuclear Physics*, vol. 15, p. 219, 1972.
- [5] G. I. Kopylov and M. I. Podgoretsky, "Multiple production and interference of particles emitted by moving sources," *Soviet Journal of Nuclear Physics*, vol. 18, p. 336, 1974.
- [6] G. I. Kopylov and M. I. Podgoretsky, "Mutual coherence functions of elementary particles and multiple production," *Soviet Journal of Nuclear Physics*, vol. 19, p. 215, 1974.
- [7] G. Cocconi, "Second-order interference as a tool for the determination of hadron fireball dimensions," *Physics Letters B*, vol. 49, no. 5, pp. 459–461, 1974.
- [8] S. Pratt, "Pion interferometry for exploding sources," *Physical Review Letters*, vol. 53, no. 13, pp. 1219–1221, 1984.
- [9] S. Pratt, "Pion interferometry of quark-gluon plasma," *Physical Review D*, vol. 33, no. 5, pp. 1314–1327, 1986.
- [10] A. N. Makhlin and Yu. M. Sinyukov, "The pion interferometry theory for the hydrodynamic stage of multiple processes," *Soviet Journal of Nuclear Physics*, vol. 46, p. 345, 1987.
- [11] V. A. Averchenkov, A. N. Makhlin, and Yu. M. Sinyukov, "Study of collective motion in hadronic matter by a pion interferometry method," *Soviet Journal of Nuclear Physics*, vol. 46, p. 905, 1987.
- [12] A. N. Makhlin and Yu. M. Sinyukov, "The hydrodynamics of hadron matter under a pion interferometric microscope," *Zeitschrift für Physik C*, vol. 39, no. 1, pp. 69–73, 1988.
- [13] Yu. M. Sinyukov, "Hanbury Brown/Twiss correlations for expanding hadron and quark-gluon matter," *Nuclear Physics A*, vol. 498, no. C, pp. 151–159, 1989.
- [14] Y. Hama and S. S. Padula, "Bose-Einstein correlation of particles produced by expanding sources," *Physical Review D*, vol. 37, no. 11, pp. 3237–3245, 1988.
- [15] Yu. M. Sinyukov, "Spectra and correlations in locally equilibrium hadron and quark-gluon systems," *Nuclear Physics A*, vol. 566, no. C, pp. 589–592, 1994.
- [16] Yu. M. Sinyukov, "Boson spectra and correlations in small thermalized systems," in *Hot Hadronic Matter: Theory and Experiment*, J. Letessier, H. H. Gutbrod, and J. Rafelski, Eds., pp. 309–322, Plenum, New York, NY, USA, 1995.
- [17] S. V. Akkelin and Yu. M. Sinyukov, "The HBT-interferometry of expanding sources," *Physics Letters B*, vol. 356, no. 4, pp. 525–530, 1995.
- [18] S. V. Akkelin and Yu. M. Sinyukov, "The HBT-interferometry of expanding inhomogeneous sources," *Zeitschrift für Physik C*, vol. 72, no. 3, pp. 501–507, 1996.
- [19] U. Heinz, "The quark-gluon plasma at RHIC," *Nuclear Physics A*, vol. 721, pp. C30–C39, 2003.
- [20] S. Pratt, "Correlations and fluctuations, a summary of Quark Matter 2002," *Nuclear Physics A*, vol. 715, pp. 389c–398c, 2003.

- [21] S. Soff, S. A. Bass, D. H. Hardtke, and S. Y. Panitkin, “Particle correlations at RHIC—scrutiny of a puzzle,” *Nuclear Physics A*, vol. 715, pp. 801c–804c, 2003.
- [22] Yu. M. Sinyukov, “Matter evolution and soft physics in $A + A$ collisions,” *Acta Physica Polonica B*, vol. 37, no. 12, pp. 3343–3369, 2006.
- [23] S. V. Akkelin, Y. Hama, Iu. A. Karpenko, and Yu. M. Sinyukov, “Hydro-kinetic approach to relativistic heavy ion collisions,” *Physical Review C*, vol. 78, no. 3, Article ID 034906, 2008.
- [24] Yu. M. Sinyukov, A. V. Nazarenko, and Iu. A. Karpenko, “Is early thermalization really needed in $A + A$ collisions?” *Acta Physica Polonica B*, vol. 40, no. 4, pp. 1109–1117, 2009.
- [25] M. Gyulassy, Iu. Karpenko, A. V. Nazarenko, and Yu. M. Sinyukov, “HBT and initial conditions for hydrodynamic expansion in $A + A$ collisions,” *Brazilian Journal of Physics*, vol. 37, no. 3A, pp. 1031–1038, 2007.
- [26] W. Broniowski, W. Florkowski, M. Chojnacki, and A. Kisiel, “Free-streaming approximation in early dynamics of relativistic heavy-ion collisions,” *Physical Review C*, vol. 80, no. 3, Article ID 034902, 2009.
- [27] S. Pratt, “The long slow death of the HBT puzzle,” *Nuclear Physics A*, vol. 830, no. 1–4, pp. 51c–57c, 2009.
- [28] Iu. A. Karpenko and Yu. M. Sinyukov, “Energy dependence of pion interferometry scales in ultra-relativistic heavy ion collisions,” *Physics Letters B*, vol. 688, no. 1, pp. 50–54, 2010.
- [29] Iu. A. Karpenko and Yu. M. Sinyukov, “Kaon and pion femtoscopy at the highest energies available at the BNL Relativistic Heavy Ion Collider (RHIC) in a hydrokinetic model,” *Physical Review C*, vol. 81, no. 5, Article ID 054903, 2010.
- [30] Iu. A. Karpenko, Yu. M. Sinyukov, and K. Werner, “description of bulk observables in the hydrokinetic model of $A + A$ collisions at the BNL Relativistic Heavy Ion Collider and the CERN Large Hadron Collider,” *Physical Review C*, vol. 87, Article ID 024914, 2013.
- [31] K. Aamodt, B. Abelev, A. A. Quintana et al., “Elliptic flow of charged particles in Pb-Pb collisions at $\sqrt{s_{NN}} = 2.76$ TeV,” *Physical Review Letters*, vol. 105, Article ID 252302, 11 pages, 2010.
- [32] N. Armesto, N. Borghini, S. Jeon et al., Eds., “Heavy-ion collisions at the LHC—last call for predictions,” *Journal of Physics G*, vol. 35, no. 5, Article ID 054001, 2008.
- [33] K. Aamodt, A. A. Quintana, D. Adamová et al., “Two-pion Bose-Einstein correlations in central Pb-Pb collisions at $\sqrt{s_{NN}} = 2.76$ TeV,” *Physics Letters B*, vol. 696, no. 4, pp. 328–337, 2011.
- [34] M. Chojnacki, W. Florkowski, W. Broniowski, and A. Kisiel, “Soft heavy-ion physics from hydrodynamics with statistical hadronization: Predictions for collisions at $\sqrt{s_{NN}} = 5.5$ TeV,” *Physical Review C*, vol. 78, no. 1, Article ID 014905, 13 pages, 2008.
- [35] Yu. M. Sinyukov, S. V. Akkelin, and Y. Hama, “Freeze-out problem in hydrokinetic approach to $A + A$ collisions,” *Physical Review Letters*, vol. 89, no. 5, pp. 052301/1–052301/4, 2002.
- [36] Iu. A. Karpenko and Yu. M. Sinyukov, “Femtoscopic scales in central $A + A$ collisions at RHIC and LHC energies in a hydrokinetic model,” *Journal of Physics G*, vol. 38, no. 12, Article ID 124059, 2011.
- [37] S. A. Bass, M. Belkacem, M. Bleicher et al., “Microscopic models for ultrarelativistic heavy ion collisions,” *Progress in Particle and Nuclear Physics*, vol. 41, pp. 255–369, 1998.
- [38] M. Bleicher, E. Zabrodin, C. Spieles et al., “Relativistic hadron-hadron collisions in the ultra-relativistic quantum molecular dynamics model,” *Journal of Physics G*, vol. 25, no. 9, Article ID 1859, 1999.
- [39] Yu. M. Sinyukov and V. M. Shapoval, “Correlation femtoscopy of small systems,” *Physical Review D*, vol. 87, no. 9, Article ID 094024, 15 pages, 2013.
- [40] V. M. Shapoval, P. Braun-Munzinger, Iu. A. Karpenko, and Yu. M. Sinyukov, “Femtoscopic scales in $p + p$ and $p + Pb$ collisions in view of the uncertainty principle,” *Physics Letters B*, vol. 725, no. 1–3, pp. 139–147, 2013.
- [41] K. Aamodt, N. Abel, U. Abeysekara et al., “Two-pion Bose-Einstein correlations in pp collisions at $\sqrt{s} = 900$ GeV,” *Physical Review D*, vol. 82, no. 5, Article ID 052001, 14 pages, 2010.
- [42] K. Aamodt, A. A. Quintana, D. Adamová et al., “Femtoscopic study of pp collisions at $\sqrt{s} = 0.9$ and 7 TeV at the LHC with two-pion Bose-Einstein correlations,” *Physical Review D*, vol. 84, no. 11, Article ID 112004, 22 pages, 2011.
- [43] M. M. Aggarwal, Z. Ahammed, A. V. Alakhverdyants et al., “Pion femtoscopy in $p + p$ collisions at $\sqrt{s} = 200$ GeV,” *Physical Review C*, vol. 83, Article ID 064905, 17 pages, 2011.
- [44] Z. Chajęcki and M. Lisa, “Global conservation laws and femtoscopy of small systems,” *Physical Review C*, vol. 78, no. 6, Article ID 064903, 2008.
- [45] Z. Chajęcki and M. Lisa, “Conservation laws and multiplicity evolution of spectra at energies available at the BNL Relativistic Heavy Ion Collider,” *Physical Review C*, vol. 79, no. 3, p. 034908, 2009.
- [46] S. V. Akkelin and Yu. M. Sinyukov, “Deciphering nonfemtoscopic two-pion correlations in $p + p$ collisions with simple analytical models,” *Physical Review D*, vol. 85, no. 7, Article ID 074023, 2012.
- [47] M. Janik, “ $\Delta\eta\Delta\phi$ angular correlations in pp collisions at the LHC registered by the ALICE experiment,” <http://arxiv.org/abs/1203.2844>.
- [48] F. Grassi, Y. Hama, and T. Kodama, “Continuous particle emission: a probe of thermalized matter evolution?” *Physics Letters B*, vol. 355, no. 1–2, pp. 9–14, 1995.
- [49] F. Grassi, Y. Hama, and T. Kodama, “Particle emission in the hydrodynamical description of relativistic nuclear collisions,” *Zeitschrift für Physik C*, vol. 73, pp. 153–160, 1996.
- [50] K. A. Bugaev, “Shock-like freeze-out in relativistic hydrodynamics,” *Nuclear Physics A*, vol. 606, no. 3–4, pp. 559–567, 1996.
- [51] F. Cooper and G. Frye, “Single-particle distribution in the hydrodynamic and statistical thermodynamic models of multiparticle production,” *Physical Review D*, vol. 10, no. 1, pp. 186–189, 1974.
- [52] Yu. M. Sinyukov, “Direct conversion of mixed phase into free hadronic gas and transverse pion momenta in ultra-relativistic nuclear collisions,” *Zeitschrift für Physik C*, vol. 43, pp. 401–409, 1989.
- [53] N. S. Amelin, R. Lednicky, T. A. Pocheptsov et al., “Fast hadron freeze-out generator,” *Physical Review C*, vol. 74, no. 6, Article ID 064901, 2006.
- [54] P. Huovinen and H. Petersen, “Particle production in hybrid models,” *The European Physical Journal A*, vol. 48, article 171, 2012.
- [55] M. Laine and Y. Schroder, “Quark mass thresholds in QCD thermodynamics,” *Physical Review D*, vol. 73, Article ID 085009, 13 pages, 2006.
- [56] K. Nakamura, J. Beringer, J.-F. Arguin et al., “Review of particle physics,” *Journal of Physics G*, vol. 37, Article ID 075021, 2010.

- [57] Yu. M. Sinyukov, R. Lednicky, S. V. Akkelin, J. Pluta, and B. Erazmus, "Coulomb corrections for interferometry analysis of expanding hadron systems," *Physics Letters B*, vol. 432, no. 3-4, pp. 248–257, 1998.
- [58] G. Goldhaber, S. Goldhaber, W. Lee, and A. Pais, "Influence of Bose-Einstein statistics on the antiproton-proton annihilation process," *Physical Review*, vol. 120, no. 1, pp. 300–312, 1960.
- [59] S. Pratt, "Validity of the smoothness assumption for calculating two-boson correlations in high-energy collisions," *Physical Review C*, vol. 56, no. 2, pp. 1095–1098, 1997.
- [60] A. Kisiel, W. Florkowski, W. Broniowski, and J. Pluta, "Femtoscopy in hydrodynamics-inspired models with resonances," *Physical Review C*, vol. 73, no. 6, Article ID 064902, 2006.
- [61] "ROOT Data Analysis Framework," <http://root.cern.ch/drupal/>.
- [62] O. Utyuzh, G. Wilk, and Z. Włodarczyk, "Modeling Bose-Einstein correlations via elementary emitting cells," *Physical Review D*, vol. 75, no. 7, Article ID 074030, 2007.
- [63] G. A. Kozlov, O. V. Utyuzh, G. Wilk, and Z. Włodarczyk, "Some forgotten features of the Bose-Einstein correlations," *Physics of Atomic Nuclei*, vol. 71, no. 9, pp. 1502–1504, 2008.
- [64] Yu. M. Sinyukov, "Boson spectra and correlations for thermal locally equilibrium systems," *Acta Physica Hungarica Series A*, vol. 10, pp. 113–136, 1999.
- [65] Yu. M. Sinyukov and B. Lorstad, "On intensity interferometry at high multiplicities," *Zeitschrift für Physik C*, vol. 61, pp. 587–592, 1994.
- [66] Yu. M. Sinyukov, S. V. Akkelin, and R. Lednicky, "Thermodynamics of multi-boson phenomena," in *Proceedings of the 8th International Workshop on Multiparticle Production in Matrahaza*, T. Csorgo, S. Hegyi, G. Hwa et al., Eds., p. 66, World Scientific.
- [67] R. Lednicky, V. Lyuboshitz, K. Mikhailov, Yu. M. Sinyukov, A. Stavinsky, and B. Erazmus, "Multiboson effects in multiparticle production," *Physical Review C*, vol. 61, no. 3, pp. 349011–349019, 2000.
- [68] S. V. Akkelin, R. Lednicky, and Yu. M. Sinyukov, "Correlation search for coherent pion emission in heavy ion collisions," *Physical Review C*, vol. 65, no. 6, pp. 649041–649046, 2002.
- [69] STAR Collaboration, "Pion interferometry in $Au + Au$ collisions at $\sqrt{s_{NN}} = 200$ GeV," *Physical Review C*, vol. 71, no. 4, Article ID 044906, 21 pages, 2005.
- [70] S. S. Adler, S. Afanasiev, C. Aidala et al., "Bose-Einstein correlations of charged pion pairs in $Au + Au$ collisions at $\sqrt{s_{NN}} = 200$ GeV," *Physical Review Letters*, vol. 93, no. 15, Article ID 152302, 6 pages, 2004.
- [71] P. Bozek, "Flow and interferometry in $(3 + 1)$ -dimensional viscous hydrodynamics," *Physical Review C*, vol. 85, no. 3, Article ID 034901, 9 pages, 2012.
- [72] L. Adamczyk, J. K. Adkins, G. Agakishiev et al., "Freeze-out dynamics via charged kaon femtoscopy in $\sqrt{s_{NN}} = 200$ GeV central $Au + Au$ collisions," <http://arxiv.org/abs/1302.3168>.
- [73] S. Afanasiev, C. Aidala, N. N. Ajitanand et al., "Charged kaon interferometric probes of space-time evolution in $Au + Au$ collisions at $\sqrt{s_{NN}} = 200$ GeV," *Physical Review Letters*, vol. 103, no. 14, Article ID 142301, 6 pages, 2009.
- [74] R. Lednicky, V. L. Lyuboshitz, and M. I. Podgoretsky, "Interference correlations of identical particles in models with closely spaced sources," *Yad. Fiz.*, vol. 38, p. 251, 1983, *Soviet Journal of Nuclear Physics*, vol. 38, pp. 147, 1983.
- [75] M. S. Nilsson, L. V. Bravina, E. E. Zabrodin, L. V. Malinina, and J. Bleibel, "Study of $\pi\pi$ correlations at LHC and RHIC energies in pp collisions within the quark-gluon string model," *Physical Review D*, vol. 84, no. 5, Article ID 054006, 2011.
- [76] E. K. G. Sarkisyan and A. S. Sakharov, "Relating multihadron production in hadronic and nuclear collisions," *The European Physical Journal C*, vol. 70, no. 3, pp. 533–541, 2010.
- [77] E. K. G. Sarkisyan and A. S. Sakharov, "Multihadron production features in different reactions," *AIP Conference Proceedings*, vol. 828, pp. 35–41, 2006.
- [78] B. Kopeliovich, A. Schäfer, and A. Tarasov, "Nonperturbative effects in gluon radiation and photoproduction of quark pairs," *Physical Review D*, vol. 62, no. 5, Article ID 054022, pp. 1–31, 2000.
- [79] E. V. Shuryak and I. Zahed, "Understanding nonperturbative deep-inelastic scattering: instanton-induced inelastic dipole-dipole cross section," *Physical Review D*, vol. 69, no. 1, Article ID 014011, 2004.
- [80] K. Aamodt, A. A. Quintanab, D. Adamová et al., "Two-pion Bose-Einstein correlations in central Pb-Pb collisions at $\sqrt{s_{NN}} = 2.76$ TeV," *Physics Letters B*, vol. 696, no. 4, pp. 328–337, 2011.
- [81] D. Antończyk, "Two pion correlations at SPS energies," *Acta Physica Polonica B*, vol. 40, no. 4, pp. 1137–1144, 2009.
- [82] S. V. Afanasiev, T. Anticic, D. Barna et al., "Energy dependence of pion and kaon production in central $Pb + Pb$ collisions," *Physical Review C*, vol. 66, no. 5, Article ID 054902, 9 pages, 2002.
- [83] C. Alt, T. Anticic, B. Baatar et al., "Bose-Einstein correlations of $\pi-\pi$ pairs in central $Pb + Pb$ collisions at 20A,30A,40A,80A, and 158A GeV," *Physical Review C*, vol. 77, no. 6, Article ID 064908, 20 pages, 2008.
- [84] J. Adams, C. Adler, M. M. Aggarwal et al., "Identified particle distributions in pp and $Au + Au$ collisions at $\sqrt{s_{NN}} = 200$ GeV," *Physical Review Letters*, vol. 92, no. 11, Article ID 112301, 6 pages, 2004.
- [85] J. Adams, M. M. Aggarwal, Z. Ahammed et al., "Pion interferometry in $Au + Au$ collisions at $\sqrt{s_{NN}} = 200$ GeV," *Physical Review C*, vol. 71, no. 4, Article ID 044906, 21 pages, 2004.
- [86] S. S. Adler, S. Afanasiev, C. Aidala et al., "Identified charged particle spectra and yields in $Au + Au$ collisions at $\sqrt{s_{NN}} = 200$ GeV," *Physical Review C*, vol. 69, no. 3, Article ID 034909, 32 pages, 2004.
- [87] S. S. Adler, S. Afanasiev, C. Aidala et al., "Bose-Einstein correlations of charged pion pairs in $Au + Au$ collisions at $\sqrt{s_{NN}} = 200$ GeV," *Physical Review Letters*, vol. 93, no. 15, Article ID 152302, 6 pages, 2004.
- [88] S. V. Akkelin and Yu. M. Sinyukov, "Phase-space densities and effects of resonance decays in a hydrodynamic approach to heavy ion collisions," *Physical Review C*, vol. 70, no. 6, Article ID 064901, 17 pages, 2004.
- [89] S. V. Akkelin and Yu. M. Sinyukov, "Hanbury-Brown-Twiss search for new states of matter in $A + A$ collisions," *Physical Review C*, vol. 73, no. 3, Article ID 034908, 2006.
- [90] T. Csorgo and B. Lorstad, "Bose-Einstein correlations for three-dimensionally expanding, cylindrically symmetric, finite systems," *Physical Review C*, vol. 54, no. 3, pp. 1390–1403, 1996.
- [91] S. V. Akkelin, P. Braun-Munzinger, and Yu. M. Sinyukov, "Reconstruction of hadronization stage in $Pb + Pb$ collisions at 158 A GeV/c," *Nuclear Physics A*, vol. 710, no. 3-4, pp. 439–465, 2002.
- [92] P. Cszizmadia, T. Csorgo, and B. Lukacs, "New analytic solutions of the non-relativistic hydrodynamical equations," *Physics Letters B*, vol. 443, no. 1–4, pp. 21–25, 1998.

- [93] G. F. Bertsch, “Meson phase space density in heavy ion collisions from interferometry,” *Physical Review Letters*, vol. 72, no. 15, pp. 2349–2350, 1994.
- [94] G. F. Bertsch, “Meson phase space density in heavy ion collisions from interferometry,” *Physical Review Letters*, vol. 77, pp. 789–789, 1996.
- [95] “The Durham HepData Project,” <http://hepdata.cedar.ac.uk/>.

Review Article

QCD Thermodynamics on the Lattice

Sayantana Sharma

Fakultät für Physik, Universität Bielefeld, 33615 Bielefeld, Germany

Correspondence should be addressed to Sayantan Sharma; sayantana@physik.uni-bielefeld.de

Received 11 April 2013; Accepted 3 June 2013

Academic Editor: Jan E. Alam

Copyright © 2013 Sayantan Sharma. This is an open access article distributed under the Creative Commons Attribution License, which permits unrestricted use, distribution, and reproduction in any medium, provided the original work is properly cited.

A remarkable progress has been made in the understanding of the hot and dense QCD matter using lattice gauge theory. The issues which are very well understood as well as those which require both conceptual and algorithmic advances are highlighted. The recent lattice results on QCD thermodynamics which are important in the context of the heavy ion experiments are reviewed. Instances of greater synergy between the lattice theory and the experiments in the recent years are discussed where lattice results could be directly used as benchmarks for experiments, and results from the experiments would be a crucial input for lattice computations.

1. Introduction

A large part of the visible matter in our universe is made out of protons and neutrons, collectively called hadrons. Hadrons are made out of more fundamental particles called quarks and gluons. The quantum theory for these particles is quantum chromodynamics (QCD). QCD is a strongly interacting theory, and the strength of interaction becomes vanishingly small only at asymptotically high energies. Due to this reason, the quarks and gluons are not visible directly in our world and remain confined within the hadrons. Lattice gauge theory has emerged as the most successful nonperturbative tool to study QCD, with very precise lattice results available for hadron masses and decay constants which are in excellent agreement with the experimental values [1].

It is expected that at high enough temperatures that existed in the early universe, the hadrons would melt into a quark gluon plasma (QGP) phase. Signatures of such a phase have been seen during the last decade in the heavy ion collision experiments at the relativistic heavy ion collider (RHIC), in Brookhaven National Laboratory. This is particularly exciting for the lattice theory community which has been predicting such a phase transition since a long time [2]. The formation of the QGP phase occurs at temperatures near Λ_{QCD} , where QCD is strongly interacting, which means lattice is the most reliable tool to understand the properties of the hot QCD medium. Over the past three decades, the lattice community has contributed significantly

to the understanding of the physics of heavy ion experiments and strongly interacting matter under extreme conditions, in general. Lattice computations are entering into the precision regime, where lattice data can be directly used for interpreting the experimental results and set benchmarks for the heavy ion experiments at RHIC and at the ALICE facility in CERN. It is now generally believed that the hot and dense matter created due to the collision of two heavy nuclei at RHIC and ALICE equilibrates within 1 fm/c of the initial impact. The equilibrated QGP medium then expands and cools down in the process, ultimately forming hadrons at the chemical freezeout. The evolution of the fireball from its equilibration till the chemical freezeout is described by relativistic hydrodynamics [3]. The QCD Equation of State (EoS) is an input for the hydrodynamic equations, and lattice can provide a nonperturbative estimate of this quantity from first principles. The lattice data for the speed of sound in the QCD medium is also an important input for the hydrodynamic study, once bulk viscosity is considered.

In this paper, I have selected the most recent results from lattice QCD thermodynamics that are relevant for the heavy ion phenomenology. I have tried to review the necessary background but not attempted to provide a comprehensive account of the development of the subject throughout these years. I have divided this paper into two major sections. The first section deals with QCD at finite temperature and zero baryon density, where lattice methods are very robust. I have given a basic introduction to the lattice techniques,

and how the continuum limit is taken, which is essential to relate the lattice data with the real world experiments. I have discussed the current understanding we have of the nature of QCD phase transition as a function of quark masses, inferred from lattice studies. Subsequently, the different aspects of the hot QCD medium for physical quark masses are discussed; the EoS, the nature and the temperature of transition, and the behaviour of various thermodynamic observables in the different phases. In the study of thermodynamics, the contribution of the lighter u , d , and s quarks is usually considered. The effect of heavier charm quarks on QCD thermodynamics is discussed in this section, in view of their relevance for the heavy ion experiments at LHC, where hydrodynamic evolution is expected to set in already at temperatures about 500 MeV and also for the physics of early universe. The relevance of chiral symmetry for the QCD phase diagram and the effects of chiral anomaly are discussed in detail. The chiral anomaly is believed to have an important role in shaping the phase diagram, and several lattice studies in the recent years are trying to understand its effect. It is a difficult problem, and I have tried to compile the recent results and review the general understanding within the community, about how to improve upon them.

The second section is about lattice QCD at finite density, where there is an inherent short coming of the lattice algorithms due to the so-called sign problem. A brief overview of the different methods used, and those being developed by the lattice practitioners to circumvent this problem, is given. It is an active field of research, with a lot of understanding of the origin and the severity of this problem gained in recent years, which is motivating the search for its possible cure. In the regime where the density of baryons is not too large, which is being probed by the experiments at RHIC, lattice techniques have been used successfully to produce some interesting results. One such important proposal in the recent time is the first principles determination of the chemical freezeout curve using experimental data on the electric charge fluctuations. This and the lattice results on the fluctuations of different quantum numbers in the hot medium and the EoS at finite baryon density are discussed in detail. An important feature of the QCD phase diagram is the possible presence of a critical end-point for the chiral first order transition. Since critical end-point search is one of the main objectives at RHIC, I have reviewed the current lattice results on this topic. The presence of the critical end-point is still not conclusively proven from lattice studies. It is a very challenging problem and I mention the further work in progress to address this problem effectively. Fermions with exact chiral symmetry on the lattice are important in this context. I have discussed the recent successful development to construct fermion operators that have exact chiral symmetry even at finite density which would be relevant for future studies on the critical end-point. The signatures of the critical end-point could be detected in the experiments if the critical region is not separated from the freezeout curve. It is thus crucial to estimate the curvature of the critical line from first principles, and I devote an entire subsection to discuss the lattice results on this topic.

I apologize for my inability to include all the pioneering works that have firmly established this subject and also to review the extensive set of interesting contemporary works. For a comprehensive review of the current activity in lattice thermodynamics, at finite temperature and density, I refer to the excellent review talks of the lattice conference, 2012 [4, 5].

2. QCD at Finite Temperature on the Lattice

The starting point of any thermodynamic study is the partition function. The QCD partition function for N_f flavours of quarks in the canonical ensemble is given as

$$\mathcal{Z}_{\text{QCD}}(T, V) = \int \mathcal{D}U_\mu(x) \prod_{f=1}^{N_f} \det D_f e^{-S_G}, \quad (1)$$

where D_f is the fermion operator for each flavour of quark f . U_μ is the gauge link defined as $U_\mu(x) = \exp(-ig \int^x A_\mu(x') dx')$ in terms of gauge fields A_μ , which are adjoint representation of the SU(3) color group, and g is the strength of the gauge coupling. S_G is the gluon action in Euclidean space of finite temporal extent of size denoted by the inverse of the temperature of the system, T . Lattice QCD involves discretizing the spacetime into a lattice with a spacing denoted by a . The volume of the lattice is given as $V = N^3 a^3$, where N are the number of lattice sites along the spatial directions and the temperature being $T = 1/(N_\tau a)$, where N_τ are the number of sites along the temporal direction. The lattice is usually denoted as $N^3 \times N_\tau$. The gluon action and the fermion determinant are discretized on the lattice. The simplest gluon action, known as Wilson plaquette action is of the form

$$S_G = \frac{6}{g^2} \sum_{x, \mu, \nu, \mu < \nu} \left(1 - \frac{1}{3} \text{Tr Re } U_{\mu, \nu}(x) \right), \quad (2)$$

$$U_{\mu, \nu}(x) = U_\mu(x) U_\nu(x + \mu) U_\mu^\dagger(x + \nu) U_\nu^\dagger(x),$$

where $U_{\mu, \nu}(x)$ is called a plaquette. The naive discretization of the continuum Dirac equation on the lattice results in the fermion operator of the form

$$\begin{aligned} D_f(x, y) &= \sum_{x, y} \left[\sum_{\mu=1}^4 \frac{1}{2} \gamma_\mu \left(U_\mu(x) \delta_{y, x+\mu} - U_\mu^\dagger(y) \delta_{y, x-\mu} \right) + am_f \delta_{x, y} \right], \end{aligned} \quad (3)$$

where in each of the expressions the site index $x = 1 - N^3 \times N_\tau$. The discretization of the gluon and fermion operators are not unique, and there are several choices which give the correct continuum limit. Usually discretized operators with small finite a corrections are preferred. Reducing a -dependent corrections by adding suitable ‘‘irrelevant’’ terms in the Renormalization Group (RG) sense, is known as the improvement of the operator. Another issue related to the discretization of the fermion operator is called the ‘‘fermion doubling problem.’’ It arises because the naive

discretization of the continuum fermion operator introduces extra unphysical fermion species called the doublers. The existence of the doublers can be traced back to a No-Go theorem [6] on the lattice which states that fermion actions, which are ultralocal, have exact chiral symmetry, and have the correct continuum limit, cannot be free from the doublers. Doublers are problematic since in the continuum limit we would get a theory with 16 fermion species and QCD with 16 flavours which is very close to the upper bound of the number of flavours beyond which the asymptotic freedom is lost. It is thus important to ensure that the discrete fermion operator should be free of the doublers. In order to do so the chiral symmetry is explicitly broken on the lattice, like for the case of Wilson fermions [7], or only a remnant of it is preserved for the staggered fermions [8]. The staggered fermion discretization retains the doubling problem in a milder form. In the continuum limit, the staggered fermion determinant would give contribution of four degenerate fermion species or tastes. However, on a finite lattice, there is a considerable mixing among the tastes so a simple fourth root of the determinant would not yield the contribution of a single fermion flavour. This is called the rooting problem. The severity of rooting problem can be minimized by choosing either the stout-smearred staggered quarks [9] or the highly Improved staggered suarks (HISQ) [10]. Other improved versions of staggered fermions used for QCD thermodynamics are the p4 and asqtad fermions [11–14]. Only the overlap [15, 16] and the domain wall fermions [17] have exact chiral symmetry on the lattice at the expense of breaking the ultralocality condition of the Nielsen-Ninomiya No-go theorem. As a result, overlap and domain wall fermions are much more expensive to simulate compared to the staggered and the Wilson fermions. For QCD thermodynamics, the staggered and to some extent the Wilson fermions are favourites, with very high precision data available with improved versions of staggered quarks [18, 19]. With the advent of faster computing resources and smarter algorithms, even large scale simulations with chiral fermions are becoming a reality [20–23].

With the choice of a suitable gauge and the fermion operators on the lattice, different physical observables are measured on statistically independent configurations generated using suitable Monte-Carlo algorithms. To make connection with the continuum physics, one needs to take the $a \rightarrow 0$ limit of the observables measured on the lattice. The gauge coupling is related to the lattice spacing through the beta-function, and the continuum limit, in turn, implies $g \rightarrow 0$. In the space of coupling constants and the fermion masses, the continuum limit is a second order fixed point, and the approach to the fixed point should be done along the correct RG trajectory or the lines of constant physics. The line of constant physics is defined by setting the mass of hadrons on the lattice to the continuum values, at each value of the coupling constant. The number of such relations required depends on the number of fermion flavours. To relate the lattice hadron masses to their experimental values, one has to define a scale to express the lattice spacing a , in terms of some physical units. There are two often used methods in QCD to set the scale, using the quantities r_1 and the kaon decay constant f_K . The r_1

scale is defined from the quark-antiquark potential $V_{\bar{q}q}(r)$ as

$$\left(r^2 \frac{\partial V_{\bar{q}q}(r)}{\partial r} \right)_{r=r_1} = 1.0. \quad (4)$$

On the lattice, one measures $V_{\bar{q}q}(r)$ and r_1 is extracted from it using a suitable fit ansatz for the potential. To quantify the value of r_1 in physical units, one uses either the pion decay constant or the splitting of energy levels of bottom mesons to set the lattice spacing [24]. Advantage of this scale is that it is not sensitive to fermion discretization effects and to the choice of quark masses that defines the line of constant physics. However, the accurate determination of the potential requires very good statistics. One can also set the scale by choosing the f_K measured on the lattice to its physical value. The f_K is known with very high accuracy from the experiments. Once the line of constant physics is set, one has to take care of the finite size and lattice spacing effects such that the continuum extrapolation is correctly performed. To minimize such corrections, the correlation length which is given by the inverse of the mass of the lowest excitation of the system should be much larger than the lattice spacing but sufficiently smaller than the spatial size. Also for thermodynamics, it is crucial to minimize finite volume corrections which is ensured for the choice $\zeta \geq 3$, where $\zeta = N/N_\tau$.

To characterize different phases, one needs to define a suitable order parameter which depends on the symmetries of the theory. In the limit of infinitely heavy quark masses, QCD is just a pure gauge theory with an exact order parameter; the expectation value of the Polyakov loop is given as

$$L(\mathbf{x}) = \frac{1}{3} \text{Tr} P \prod_{x_4=1}^{N_\tau} U_4(\mathbf{x}, x_4), \quad P \implies \text{path ordering.} \quad (5)$$

The phase transition from a phase of confined colour degrees of freedom to the deconfined regime of free gluons is of first order and is established very firmly from lattice studies [25]. The corresponding transition temperature is T_c (pure gauge) = 276(2) MeV [26] using string tension, $\sqrt{\sigma}$, value to be 425 MeV, to set the scale. If the quarks are massless, the QCD partition function with N_f quark flavours has an exact $SU(N_f) \otimes SU(N_f)$ chiral symmetry. At some temperature, there is a phase transition from a chiral symmetry broken phase to the symmetry restored phase, characterized by the order parameter called the chiral condensate,

$$\langle \bar{\psi}_f \psi_f \rangle = \lim_{m_f \rightarrow 0} \lim_{V \rightarrow \infty} \frac{T}{V} \frac{\partial \ln \mathcal{Z}_{\text{QCD}}}{\partial m_f}, \quad f = 1, \dots, N_f. \quad (6)$$

The phase transition in the chiral limit for $N_f = 3$ is expected to be of first order, and there are several lattice results supporting this [27–31]. For $N_f = 2$, the lattice results are contradictory with some claiming a first order transition [32, 33] whereas recent results showing that the second order transition is also a possibility [34]. The current status of

$N_f = 2$ QCD phase transition in the chiral limit would be discussed again in a later subsection. For any finite value of quark masses, however there is no unique order parameter, and no sharp phase transition is expected but only a gradual crossover.

Based on effective field theories with same symmetries as QCD, using universality arguments and renormalization group inspired techniques, a schematic diagram of different phases of QCD as a function of quark mass is summarized in the famous ‘‘Columbia plot’’ [35]. The first order regions in the quenched and the chiral limits are separated from the crossover region by second order lines belonging to the $Z(2)$ universality class. These boundaries are schematic, though, and it is important to estimate the precise location of the physical point in this diagram. Lattice studies over the years have helped to redraw the boundaries more quantitatively. A latest version of the ‘‘Columbia plot’’ is shown in Figure 1. With the high precision lattice data with physical light and strange quark masses, it is now known that the QCD transition in our world is a crossover [36–38]. The boundary of the first order region in the upper right hand corner of Figure 1 is fairly well known [39]. The extent of the first order region in the bottom left hand corner is now believed to be small and much far away from the physical point [40, 41]. However the extent of the $Z(2)$ line in the left hand corner is still not well established; it can either continue along the $m_{u,d} = 0$ axis to the $m_s \rightarrow \infty$ corner or end at a tricritical point. A better understanding of this issue is currently underway. The key to the resolution of this issue is to understand the effects of chiral anomaly through rigorous lattice computations. Since the light u, d -quark masses are much smaller than Λ_{QCD} ; the QCD action has an approximate $SU(2) \times SU(2) \times U_B(1)$ symmetry with an additional classical $U_A(1)$ symmetry broken explicitly by quantum effects. This is known as the $U_A(1)$ anomaly [42–44]. At zero temperature, the magnitude of this anomaly is related to the instanton-density. If the magnitude of this anomaly is temperature independent, the phase transition along the $m_{u,d} = 0$ axes has to be of second order, belonging to the $O(4)$ universality class [45]. This would mean that the $Z(2)$ line has to end at a tricritical point characterized by the strange quark mass, m_s^{tric} . The difference between the physical and tricritical mass for the strange quark is not yet known with a good precision.

In the following subsections, the lattice results for the QCD EoS for physical quark masses are discussed, which is an input for the hydrodynamics of the QGP medium. The current results on the pseudocritical temperature, the entropy density, and the speed of sound are also shown. All the results are for $2 + 1$ flavour QCD, that is, two light degenerate u and d quarks and a heavier strange quark mass. The effect of the heavy charm quarks on the thermodynamic quantities is also highlighted. At the end of this section, I touch upon the $N_f = 2$ QCD near the chiral limit and the effects of the $U_A(1)$ anomaly for QCD thermodynamics.

2.1. Equation of State. The Equation of State (EoS) is the relation between the pressure and energy density of a system in thermal equilibrium. For estimating the QCD EoS, the most frequently used method by the lattice practitioners is

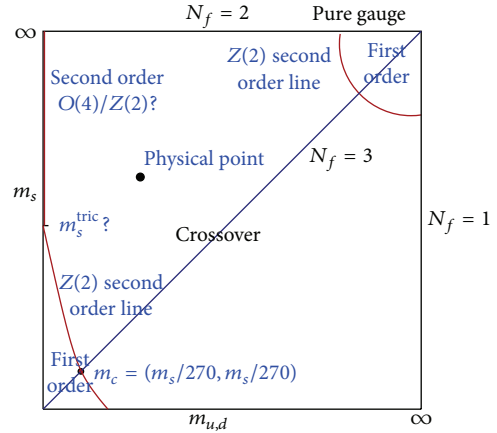


FIGURE 1: The present status of the Columbia plot.

the integral method [46]. In this method, one first computes the trace anomaly $I(T)$, which is the trace of the energy-momentum tensor. This is equal to the quantity $\epsilon - 3p$ where ϵ is the energy density of the system and p is the pressure. Moreover, it is related to the pressure of the system through the following relation:

$$I(T) = T^5 \frac{\partial p}{\partial T T^4}. \quad (7)$$

So if $I(T)$ is known, the pressure can be computed by integrating $I(T)$ over a range of temperature, with the lower value of temperature chosen such that the corresponding value of pressure is vanishingly small. The trace anomaly is related to the chiral condensate and the gluon action as

$$\begin{aligned} \frac{I(T)}{T^4} = & -N_\tau^4 \left(a \frac{d\beta}{da} (\langle S_G \rangle - \langle S_G \rangle_0) \right. \\ & \left. + \sum_f a \frac{d(m_f a)}{da} (\langle \bar{\psi}_f \psi_f \rangle - \langle \bar{\psi}_f \psi_f \rangle_0) \right), \\ & \beta = \frac{6}{g^2}, \end{aligned} \quad (8)$$

where the subscript zero denotes the vacuum expectation values of the corresponding quantities. The subtraction is necessary to remove the zero temperature ultraviolet divergences, and the vacuum expectation values are usually computed on a lattice with number of sites $(N_\tau)_0$ in the temporal direction, equal to the corresponding spatial number of sites, N . The subtraction is an unavoidable expense of this method. A new idea of deriving thermodynamic observables from cumulants of momentum distribution has emerged, where the vacuum subtraction is not required [47], and it would be interesting to check the application of this method in QCD. Also one needs to know the functional dependence of the inverse of QCD coupling constant β and the quark masses with the lattice spacing a along the line of constant physics.

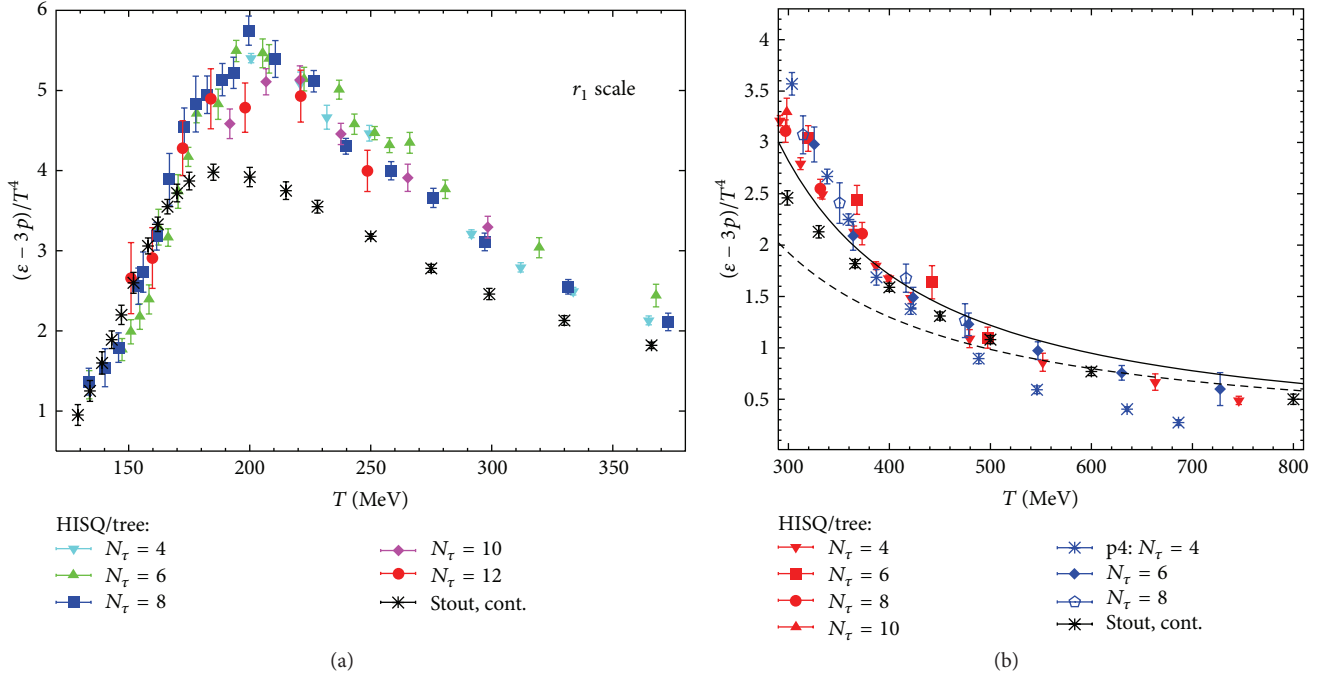


FIGURE 2: The results for the trace anomaly using the HISQ action for low (a) and high (b) temperatures for lattice sizes with temporal extent N_τ and spatial size $4N_\tau$, from [48]. Also in (b), the HISQ results are compared to the results using p4 fermions, which has an improved behaviour at high temperatures and to the continuum perturbation theory results at 1-loop (solid line) and 2-loop (dashed line) for the trace anomaly. The stout data are the continuum estimates from the $N_\tau = 6, 8, 10$ data in [19].

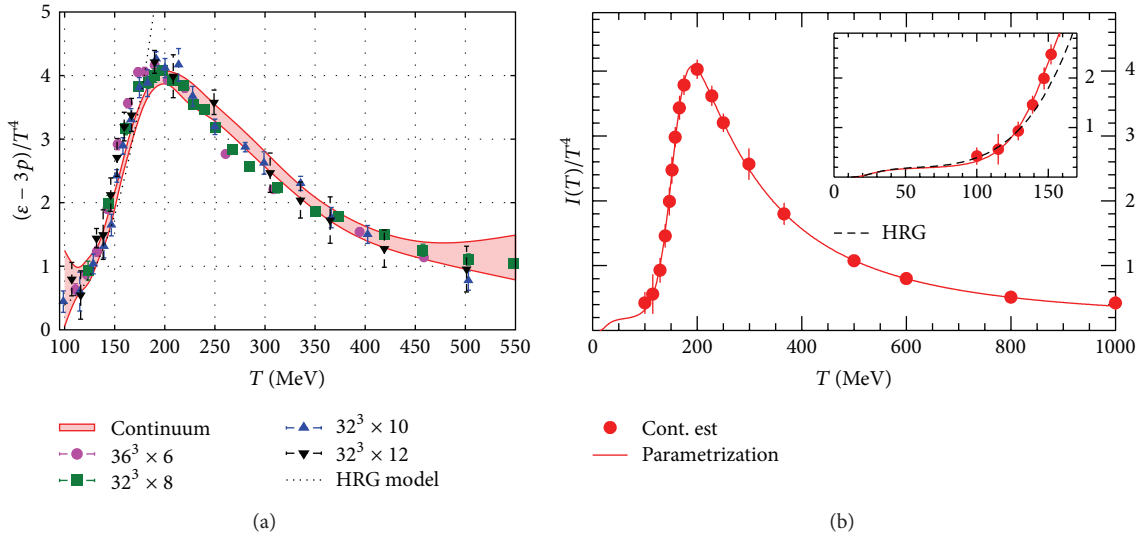


FIGURE 3: The latest data with the stout smeared fermions (a), from [50]. In (b), the fit to the trace anomaly data from the continuum extrapolation of the $N_\tau = 6, 8$ results, from [19]. The results are in perfect agreement with the Hadron resonance gas model calculations for $T < 140$ MeV.

On the lattice, $I(T)$ is known only for a finite number of temperature values. The pressure computed by the numerical integration of the $I(T)$ data has errors both due to statistical fluctuations and systematic uncertainties involved in the numerical interpolation of the data.

The results for the trace anomaly are available for different lattice discretizations of the fermions. For staggered quarks,

there are two sets of results, one from the HotQCD collaboration using HISQ discretization [48, 49] and the other from the Budapest-Wuppertal collaboration using stout smeared staggered quarks [19, 50]. These results are compiled in Figures 2 and 3. For the HISQ results, the bare lattice parameters are fixed by setting the lowest strange pseudoscalar meson mass to its physical value at about 686 MeV and $m_\pi = 160$ MeV,

which defines the line of constant physics. The kaon decay constant $f_K = 156.1$ MeV or alternatively the $r_1 = 0.3106$ fm from the static quark potential is used to set the scale. The corresponding parameters for the stout smeared quarks are $m_\pi = 135$ MeV, $m_K = 498$ MeV, and the kaon decay constant. From Figure 2, it is evident that there is a good agreement between the two sets of results for $T < 180$ MeV and also for high enough temperatures $T > 350$ MeV. The stout continuum results in the figure were obtained extrapolation with the $N_\tau = 6, 8, 10$ data from [19]. In the intermediate temperature range, there is some discrepancy, specially the peaks of the interaction measure do not coincide for these two different discretization schemes, which may be due to finite lattice spacing effects. However, the HISQ $N_\tau = 12$ data is inching closer to the stout results in this regime. The recent continuum stout results, obtained from continuum extrapolation of the new $N_\tau = 12$ data in addition to the older data, are consistent with the HISQ results, with the peak position shifting to 200 MeV (Figure 3(a)). There is also a good agreement of the HISQ and stout data with the trace anomaly obtained from the Hadron Resonance Gas (HRG) model for $T < 140$ MeV and with the resummed perturbation theory results at high temperatures. Using the $N_\tau = 6, 8$ data which is available upto temperatures of 1000 MeV, a continuum extrapolation of the stout data was performed, the result of which is shown in Figure 3(b). For this entire range of temperature, there is a useful parameterization characterizing the trace anomaly [19] with the following parametric form:

$$\frac{I(T)}{T^4} = e^{-h_1/t - h_2/t^2} \cdot \left(h_0 + \frac{f_0 [\tanh(f_1 t + f_2) + 1]}{1 + g_1 t + g_2 t^2} \right), \quad (9)$$

$$t = \frac{T}{200 \text{ MeV}},$$

where the best fit parameters are

$$\begin{aligned} h_0 &= 0.1396, & h_1 &= -0.18, & h_2 &= 0.035, \\ f_0 &= 2.76, & f_1 &= 6.79, & f_2 &= -5.29, \\ g_1 &= -0.47, & g_2 &= 1.04. \end{aligned} \quad (10)$$

This parametric form could be a useful input for the hydrodynamical simulations, which usually uses the lattice EoS before hadronization and that from the HRG after the freezeout of hadrons.

There are lattice results for the EoS using alternative fermion discretizations, the Wilson fermions. The WHOT-QCD collaboration has results for 2 + 1 flavours of improved Wilson fermions [51] with the physical value of strange quark mass but a large pion mass equal to $0.63m_\rho$. The tmfT collaboration has results for 2 flavours of maximally twisted Wilson fermions [52] with $m_\pi > 400$ MeV. Both these results are compiled in Figure 4. These are in rough qualitative agreement with the staggered fermion data, specially the peak for the WHOT-QCD data occurring at 200 MeV is consistent with the HISQ and stout results. A more quantitative agreement at this stage is difficult, since the pion masses for the Wilson fermions are much larger than the physical value.

2.2. The Pseudocritical Temperature. We recall that the QCD transition, from a phase of color singlet states to a phase of colored quantum states, is an analytic crossover, for physical quark masses. This is fairly well established by now from lattice studies using two different approaches. One approach is to monitor the behaviour of the thermodynamic observables in the transition region for physical values of quark masses while the other is to map out the chiral critical line as a function of light quark mass [53]. The absence of a sharp phase transition implies that there is no unique transition temperature but only different pseudocritical temperatures corresponding to different observables. There is no order parameter but the observables like the renormalized Polyakov loop; L_R has a point of inflexion across the crossover region. Another observable relevant in the crossover regime is the renormalized chiral condensate, which has been defined [54] in the following manner to take into account the multiplicative renormalization as well as additive ones due to a finite bare quark mass,

$$\Delta_{l,s}(T) = \frac{\langle \bar{\psi}\psi \rangle_{l,T} - (m_l/m_s) \langle \bar{\psi}\psi \rangle_{s,T}}{\langle \bar{\psi}\psi \rangle_{l,0} - (m_l/m_s) \langle \bar{\psi}\psi \rangle_{s,0}}, \quad l = u, d. \quad (11)$$

The normalized chiral susceptibility χ_R for the light quarks defined as

$$\chi_R = \frac{1}{VT^3} m_l^2 \frac{\partial^2}{\partial m_l^2} (\ln \mathcal{Z}(T) - \ln \mathcal{Z}(0)) \quad (12)$$

is a good observable as well. Both L_R and $\Delta_{l,s}(T)$ have a point of inflexion at the pseudocritical temperature, and χ_R has a smooth peak. From the continuum extrapolated data of the stout-smeared staggered fermions, the pseudocritical temperatures corresponding to these observables for physical quark masses are

$$T_c = \begin{cases} 170(4)(3) & \text{for } L_R \\ 157(3)(3) & \Delta_{l,s} \\ 147(2)(3) & \chi_R. \end{cases} \quad (13)$$

The data for L_R and $\Delta_{l,s}$ with the HISQ discretization is shown in Figure 5. These are for lattices of size $N_\tau \times (4N_\tau)^3$. The HISQ data are in good agreement with the continuum extrapolated stout-smeared staggered results from [55]. The fact that the rise of L_R is more gradual than the corresponding rise of $\Delta_{l,s}$ signals that the crossover is more likely influenced by the chiral symmetry restoration. Previous scaling studies of the renormalized chiral condensate with the p4-staggered quarks showed that the physical light quarks already approximate the $O(4)$ critical behaviour of the chiral quarks [34]. Using the $O(4)$ scaling of the renormalized chiral condensate, the T_c obtained for HISQ quarks through chiral and continuum extrapolation is 154 ± 9 MeV. This value is in excellent agreement with the stout result, implying that the continuum extrapolation done with the staggered fermions is quite robust.

2.3. Comparing Results for Different Fermion Discretizations. The results for the EoS and the pseudocritical temperature

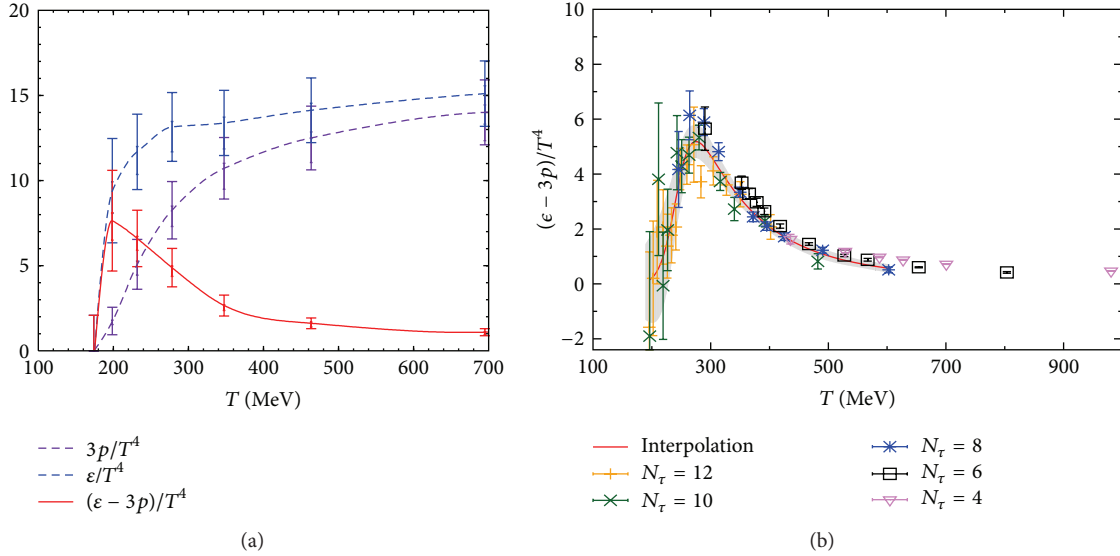


FIGURE 4: The results for the pressure, energy density, and the trace anomaly with clover-improved Wilson fermions on a $32^3 \times 8$ lattice, from [51] (a) and the trace anomaly data with the twisted mass Wilson fermions, from [52] (b).

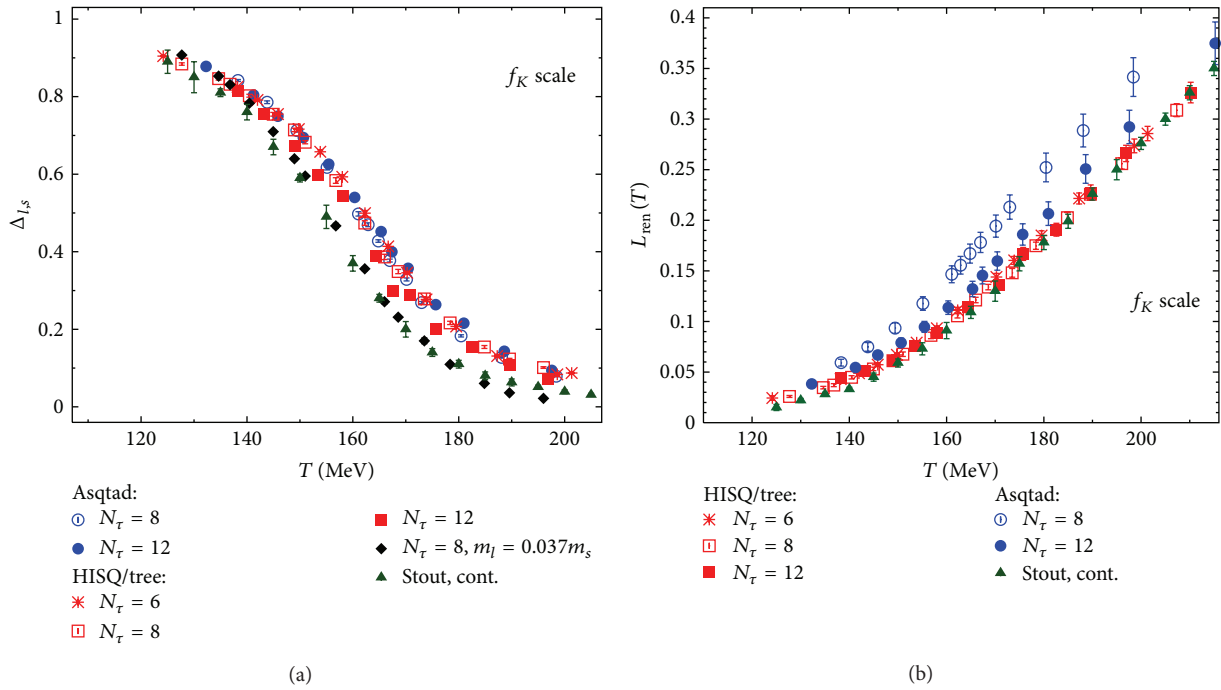


FIGURE 5: The results for the subtracted chiral condensate (a) and the renormalized Polyakov loop (b) from the HotQCD collaboration, from [49]. These data are compared with the continuum results using stout smeared fermions, from [55].

discussed so far have been obtained using different improved versions of the staggered quarks. For these fermion species, the so called “rooting” problem may alter the continuum limit due to breaking of the $U_A(1)$ anomaly [56] though some other work refutes this claim [57]. It is important to check the effects of the rooting procedure on the continuum extrapolation of finite temperature observables. The Budapest-Wuppertal

collaboration has recently compared the continuum extrapolated results for different observables using the Wilson and staggered fermions [58] as the former discretization does not suffer from the rooting problem. The scale for the Wilson fermions was determined using $m_\Omega = 1672$ MeV and the line of constant physics was set using $m_\pi/m_\Omega \sim 0.3$ and $m_K/m_\Omega \sim 0.36$. For the staggered quarks, the line of constant

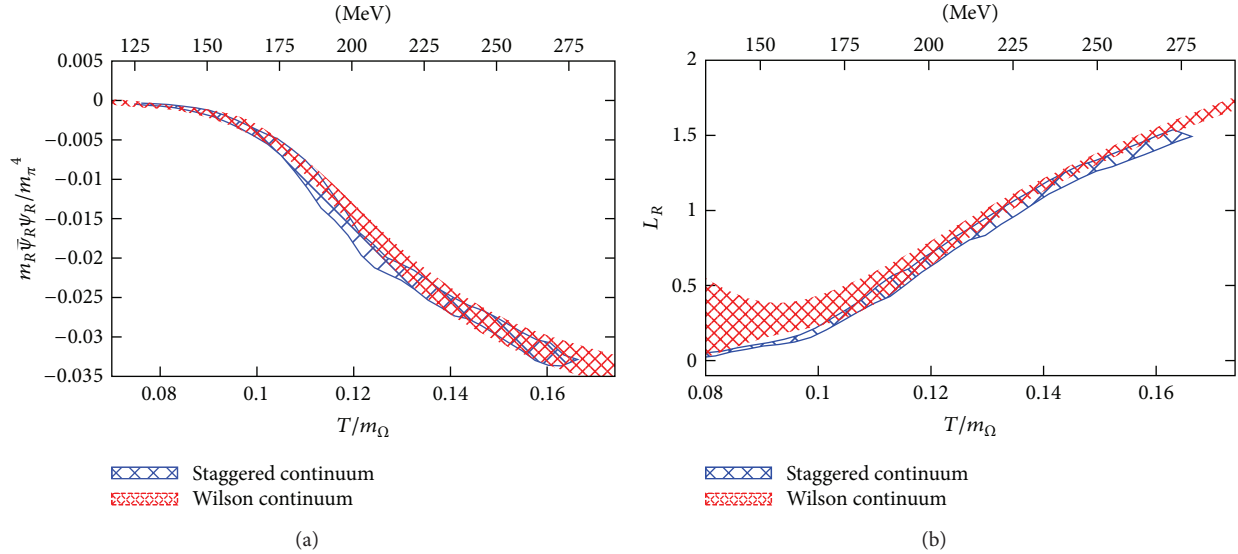


FIGURE 6: The continuum extrapolated renormalized chiral condensate (a) and the Polakov loop (b) are compared for Wilson and stout-smear staggered fermions, from [58].

physics was set such that the ratios m_π/m_Ω and m_K/m_Ω are within 3% of the corresponding values for the Wilson fermions. This means that the pions are quite heavy with $m_\pi \sim 540$ MeV for both these discretizations. The continuum extrapolated results for L_R and the renormalized chiral condensate are shown in Figure 6. The continuum results for both these quantities are in good agreement for the whole range of temperature, implying that these two different fermion discretizations indeed have the correct continuum limit. In all these computations an improved Wilson operator was used, in which the dominant $\mathcal{O}(a)$ correction terms due to explicit breaking of chiral symmetry by these fermions were cancelled. It ensured that in both the studies the approach to the continuum limit was chosen to be the same. However at this large value of quark masses, the rooting problem may be mild enough to show any adverse effects and it would be desirable to perform a similar comparison at physical value of the quark masses.

Since the effects of chiral symmetry persist in the crossover region, it is important to compare the existing results for T_c with those using fermions with exact chiral symmetry on the lattice. For the Wilson and the staggered action, even for massless quarks, the full $SU(2) \otimes SU(2)$ chiral symmetry is realized only in the continuum limit. For chiral fermions on the lattice, like the overlap or the domain wall fermions, the chiral and the continuum limits are disentangled, allowing us to understand the remnant effects of chiral symmetry in the crossover region even on a finite lattice. However, lattice QCD with overlap fermions is computationally prohibitive [59], and currently better algorithms are being developed to simulate them with comparatively lesser effort [60]. The domain wall fermions have exact chiral symmetry only when the extent of the fifth dimension, N_5 , of the five dimensional lattice on which these fermions are defined, is infinite. For smooth gauge fields, the chiral symmetry violation on

a finite lattice is suppressed as an exponential of N_5 but the suppression could be much slower, as $1/N_5$ for rough gauge configurations in the crossover region. Better algorithms have been employed to ensure exponential suppression even for rough gauge fields [61]. The most recent results for the overlap fermions from the Budapest-Wuppertal collaboration [21] and the domain wall fermions from the HotQCD collaboration [61] are shown in Figure 7. The renormalized chiral condensate for the overlap fermions is qualitatively consistent with the continuum staggered fermion results, even for small volumes and large pion masses of about 350 MeV around the crossover region. The lattice cut-off effects seem to be quite small for $N_\tau = 8$. The renormalized chiral condensate and the $\Delta_{l,s}$ for the domain wall fermions are shown in Figure 7. The lattice size is $16^3 \times 8$ with the number of lattice sites along the fifth dimension taken to be 32 for $T > 160$ MeV and 48 otherwise, and the pion mass is about 200 MeV. The lattice volume is comparatively small; therefore, these results do not show a sharp rise in the crossover region. With larger volumes, the rise in these thermodynamic quantities is expected to be much steeper. The value of T_c estimated from the peak of the chiral susceptibility, that is, the derivative of the chiral condensate is between 160–170 MeV which is consistent with the continuum results from the HISQ fermions.

2.4. The Thermodynamical Observables. Thermodynamical observables characterize the different phases across a phase transition. From the behaviour of these observables, one can infer about the degrees of freedom of the different phases and the nature of the interactions among the constituents. It was already known from an important lattice study that the pressure in high temperature phase of QCD showed a strong dependence on the number of quark flavours [62], signaling deconfinement of the quark and gluon degrees of freedom.

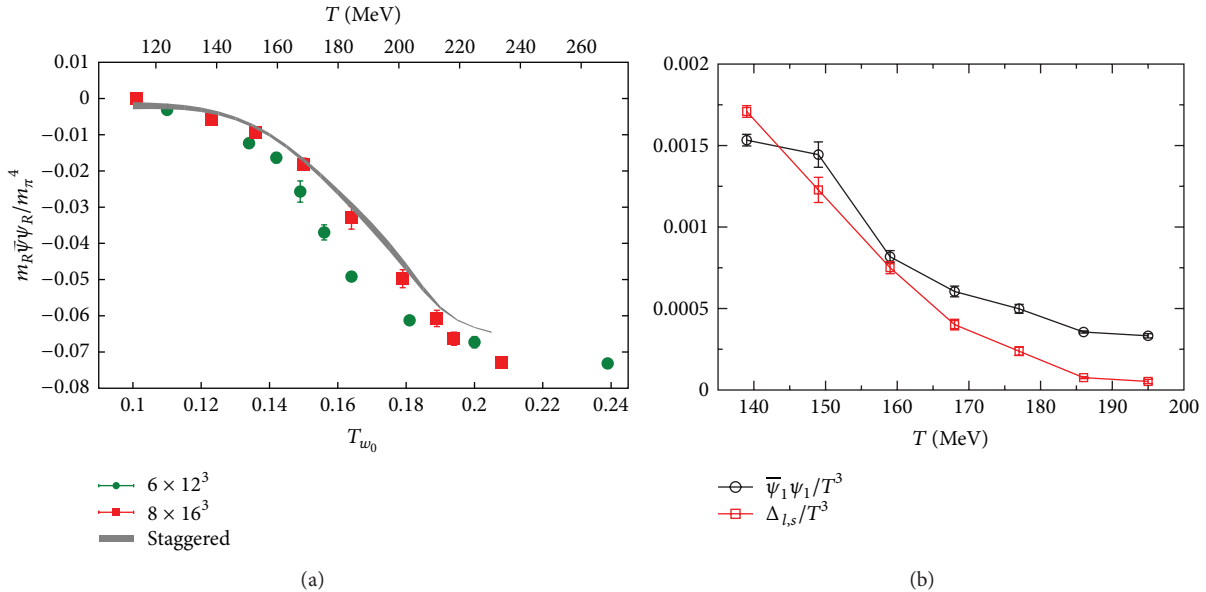


FIGURE 7: The renormalized chiral condensate for the overlap quarks is compared to the continuum extrapolated results using the stout smeared staggered quarks in (a), from [21]. In (b), the behaviour of different chiral condensates defined using the domain wall fermions is shown in the critical region, from [61].

Recent results for the pressure, entropy density, and the speed of sound for QCD, using the stout-smeared staggered quarks, are compiled in Figure 8. Though in our world there is no real phase transition, the entropy density increases rapidly with temperature, again signaling the liberation of a large number of colour degrees of freedom. The entropy density for QCD is almost 20% off from the value of a free gas of quarks and gluons, even at temperatures about 1000 MeV. The deviation of the pressure of QGP computed at similar temperatures, from its free theory value, is even more close to about 25% of its value. Another observable that characterizes the different phases is the speed of sound c_s . If QGP at high temperatures was qualitatively close to a strongly interacting conformal theory, then the speed of sound would be exactly $1/\sqrt{3}$. However, the deviation from conformality is quite significant even at temperatures about $T = 500$ MeV which hints that the AdS-CFT inspired study of the QGP medium should be done with more care. The values of entropy density computed with different discretizations of staggered fermions like the asqtad or the p4 fermions [63] show about 10% deviation from the free theory value at very high temperatures. The departure from AdS-CFT values is even more severe using these fermions. The stout results are about 10% lower than the corresponding asqtad and p4 results. This deviation is attributed to the fact that the latter discretizations have smaller cut-off effects at higher temperatures and would be more closer to the continuum results. The stout continuum values shown in the figure were obtained by averaging the $N_\tau = 8, 10$ data. A proper continuum extrapolation of the results for both the fermion discretizations is necessary for resolving the difference and for use of these values for the real world calculations. However, the lattice results with at least 10% off from the free theory values even at very

high temperatures implies that the QGP phase is strongly interacting, more like a liquid rather than a gas of quarks and gluons, confirming the similar prediction from the RHIC experiments. For $T < T_c$, the results for all these observables are in agreement with Hadron resonance gas model predictions.

2.5. Effects of Charm Quarks on the EoS. The effects of charm quarks to the pressure in the QGP phase were estimated sometime ago, using next-to leading order perturbation theory [64]. It was observed that the contribution of charm quarks becomes significant for temperatures $T > 2T_c$. Preliminary data from the LHC already indicates that the charm quarks would thermalize quickly as the lighter quarks. It would then affect the EoS and thus the hydrodynamical evolution of the fireball formed at LHC energies. Lattice studies are important to quantify the contribution of charm to the EoS in the QGP phase. The first lattice studies were done by the RBC [65] as well as the MILC collaboration [66] with quenched charm quarks, that is, by neglecting quantum fluctuations due to the charm quarks. The quenched charm results for the EoS differ from the $2 + 1$ flavour results, already at $1.2T_c$. Recent results from the Budapest-Wuppertal collaboration with dynamical charm quarks [50], however, show that the effects of charm quarks show up only around 300 MeV, more in agreement with the perturbative estimates (Figure 9). Both the approaches highlight the fact that the effects of charm quark should be considered for the EoS used as an input for the hydrodynamical evolution of the fireball at LHC energies, which may set in at $T \sim 500$ MeV. It would be also important for the EoS of the standard model, important for the cosmological evolution in the early universe [67, 68].

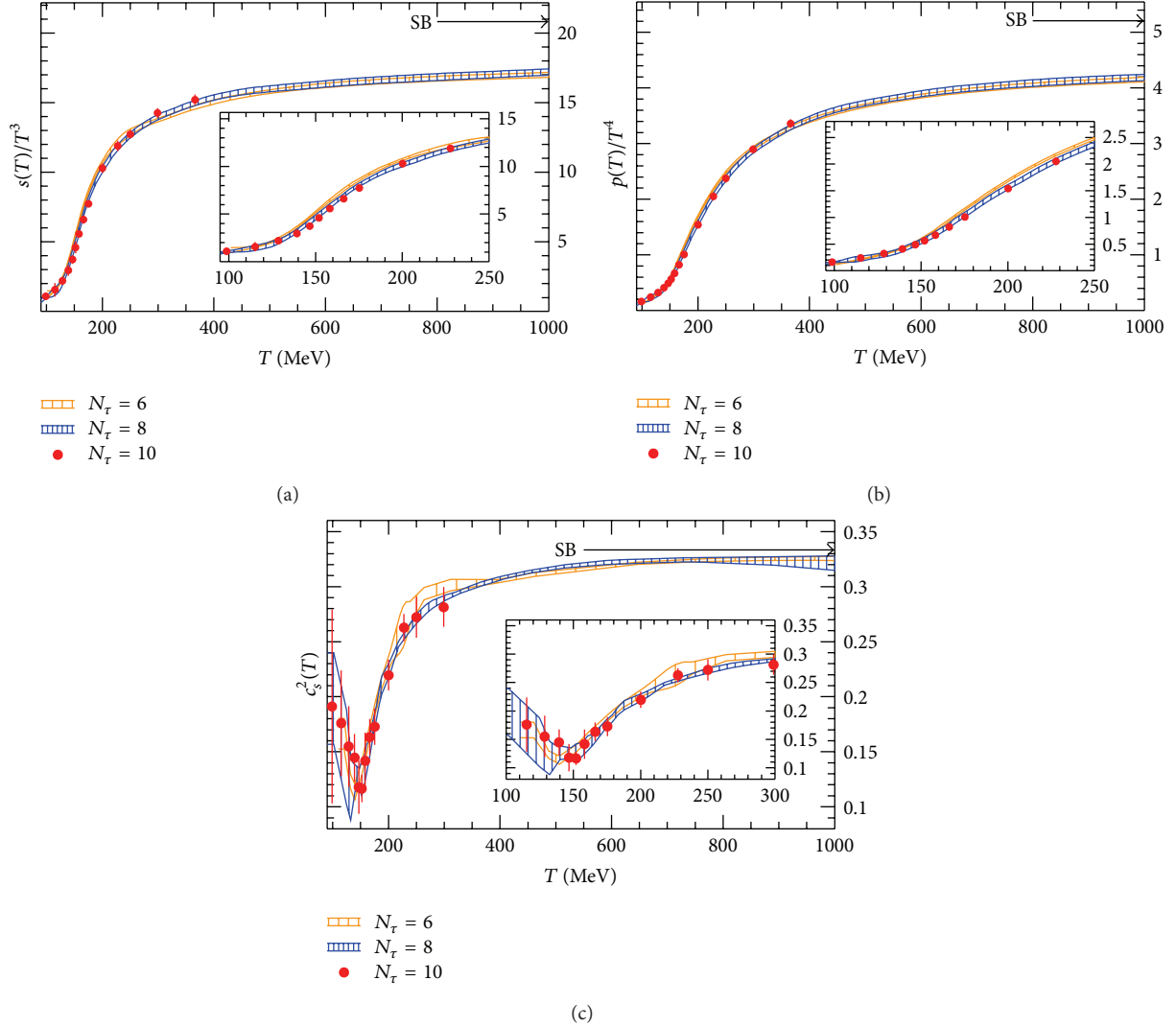


FIGURE 8: The entropy density, pressure, and the speed of sound for the stout-smear fermions as a function of temperature, from [19].

2.6. The 2 Flavour QCD Transition and the Fate of the $U_A(1)$ Anomaly. The chiral phase transition for $N_f = 2$ QCD is still not well understood from lattice studies, as was emphasized at the beginning of this section. Though the lattice results for 2+1 flavours with different fermion discretizations are in good agreement, the corresponding ones for the two light flavour case are still inconclusive. Two major approaches have been undertaken in the recent years to understand the order of this transition. One of them is to check the scaling properties of the order parameter. If the phase transition is indeed a second order one, then the order parameter would show $O(4)$ scaling in the transition region. The second approach is to understand the effects of the $U_A(1)$ anomaly near the phase transition. If the quantum fluctuations responsible for this $U_A(1)$ anomaly decrease significantly with temperature, it would result in the degeneracy of the masses of mesons of certain quantum numbers and a characteristic behaviour of the density of low lying eigenmodes of the fermion operator. I discuss the major lattice results using both these approaches,

in the following paragraphs. Most of these approaches are hinting that the two flavour chiral phase transition may be a second order one.

2.6.1. Scaling Analysis in the Critical Region. The order parameter that characterizes the chiral phase transition is the chiral condensate. A suitable dimensionless definition of the chiral condensate used in the lattice study by the BNL-Bielefeld collaboration [34] is

$$M_b = m_s \frac{\langle \bar{\psi}\psi \rangle}{T^4}. \quad (14)$$

The additive ultraviolet divergences are not explicitly subtracted from the condensate, and hence it is the bare value denoted by subscript b . This additive divergence would be included in the regular part, and in the transition region would be much smaller in magnitude than the singular part

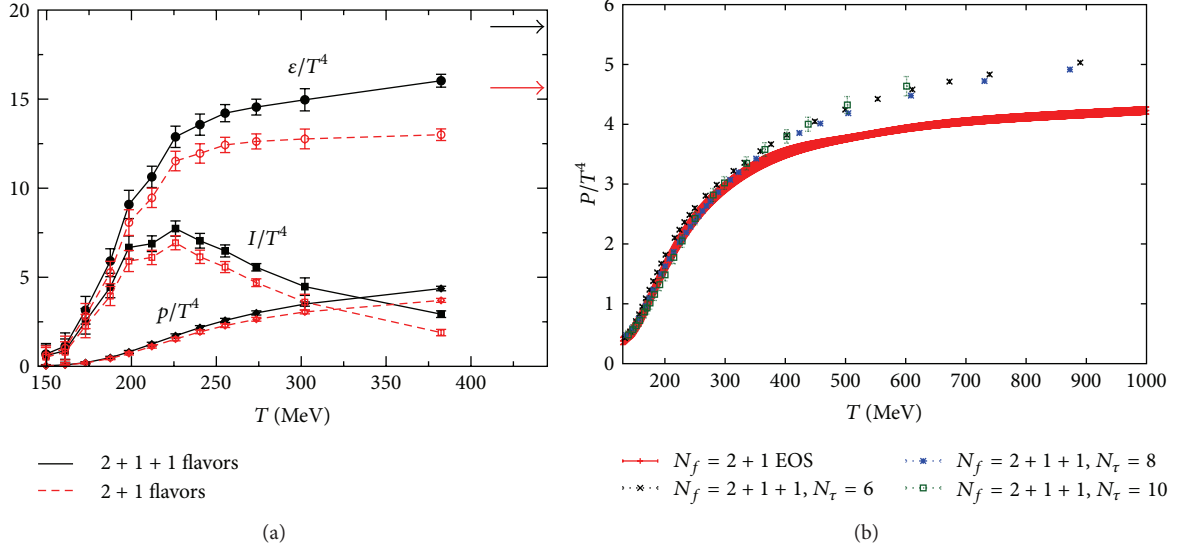


FIGURE 9: In (a), the effects of quenched charm quark to the pressure, energy density, and trace anomaly are shown as a function of temperature, from [66]. The lattice size is $24^3 \times 6$. In (b); the effects of dynamical charm quarks to the pressure are shown as a function of temperature, from [50].

of M_b . In the vicinity of the transition region, the order parameter can be written as

$$M_b(T, H) = h^{1/\delta} f_G\left(\frac{t}{h^{1/\beta\delta}}\right) + f_{\text{reg}}(T, H), \quad (15)$$

where f_G is the universal scaling function, known from analysis of the $O(N)$ spin models [69–71] with β and δ being the corresponding critical exponents. The quantities h and t are dimensionless parameters that determine the deviations from the critical point and are defined as

$$t = \frac{1}{t_0} \frac{T - T_{c,0}}{T_{c,0}}, \quad h = \frac{H}{h_0}, \quad H = \frac{m_l}{m_s}, \quad (16)$$

with $T_{c,0}$ being the transition temperature in the chiral regime, that is, for $h \rightarrow 0$, and h_0 and t_0 are nonuniversal constants. One of the choices of the regular part of the order parameter used in the lattice study is

$$f_{\text{reg}} = H \left(a_0 + a_1 \frac{T - T_{c,0}}{T_{c,0}} + a_2 \left(\frac{T - T_{c,0}}{T_{c,0}} \right)^2 \right), \quad (17)$$

where one assumes that the regular part is an analytic function of the relevant parameters around the transition point. The BNL-Bielefeld collaboration used an improved variety of the staggered quarks, called the p4 quarks, to compute the order parameter defined in (14) and χ_m , its derivative with respect to m_l for different values of the light quark masses, m_l . The strange quark mass was fixed at its physical value. These quantities were fitted to the functional form given in (15) and its derivative, respectively. The scaling analysis was done for a fixed lattice of size $N^3 \times 4$, so the order parameter and its derivatives are expected to have an $O(2)$ scaling in the chiral regime since the fermion discretization

only retains a remnant of the continuum $O(4)$ symmetry group. From the plots for the order parameter in Figure 10(a), it is evident that for $m_l/m_s = 1/80$ the phase transition is indeed a second order one with $O(2)$ critical exponents, though $O(4)$ scaling cannot be ruled out completely with the current precision available. In the scaling regime, the variable $M_b/h^{1/\delta}$ should be a universal function of $t/h^{1/\beta\delta}$. In Figure 10(b), the scaled chiral condensate is seen to be almost universal for $m_l/m_s < 1/20$, which provides a hint that even for the physical quark masses there is a remnant effect of the chiral symmetry. The crossover transition for 2 + 1 flavour QCD should be sensitive to the effects of chiral symmetry and therefore also to the effects of the $U_A(1)$ anomaly.

2.6.2. The Effects of $U_A(1)$ Anomaly. The QCD partition function breaks $U_A(1)$ symmetry explicitly. However, its effect varies with temperature since we know that at asymptotically high temperatures, we approach the ideal Fermi gas limit where this symmetry is restored. It is important to understand the temperature dependence of $U_A(1)$ breaking near the chiral phase transition. If $U_A(1)$ breaking is significantly reduced from that at zero temperature, one would then claim that the symmetry is effectively restored. This would result in the degeneracy of the mass of the isospin triplet pseudoscalar (pion) and scalar (delta) mesons. The order parameter for such an effective restoration is the quantity defined as

$$\chi_\pi - \chi_\delta = \int d^4x \left[\langle \bar{\psi}(x) \tau_2 \gamma_5 \psi(x) \bar{\psi}(0) \tau_2 \gamma_5 \psi(0) \rangle - \langle \bar{\psi}(x) \tau_2 \psi(x) \bar{\psi}(0) \tau_2 \psi(0) \rangle \right], \quad (18)$$

and the order parameter for the restoration of the chiral symmetry is the chiral condensate. These quantities are also

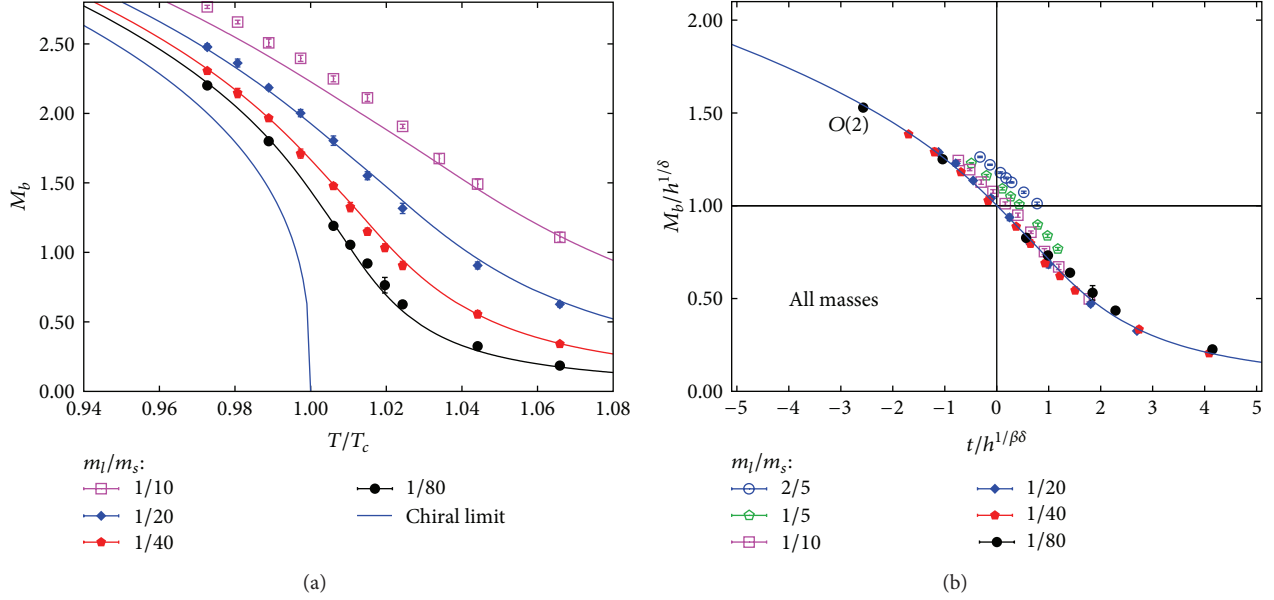


FIGURE 10: The interpolated data for M_b for different light quark masses are compared with the corresponding plot for an $O(4)$ spin model in the continuum, denoted by the solid blue line (a). In (b), the scaling plots for the chiral condensate for QCD are shown to match with the universal function with $O(2)$ symmetry for $m_l/m_s < 1/20$. Both the plots are for p4 staggered quarks, from [34].

related to the fundamental theory through the density of eigenvalues, $\rho(\lambda)$ of the Dirac operator as

$$\begin{aligned} \langle \bar{\psi}\psi \rangle &= \int d\lambda \rho(\lambda, m) \frac{2m}{m^2 + \lambda^2}, \\ \chi_\pi - \chi_\delta &= \int d\lambda \rho(\lambda, m) \frac{4m^2}{(m^2 + \lambda^2)^2}. \end{aligned} \quad (19)$$

Different scenarios that could lead to different functional behaviour of $\rho(\lambda)$ were discussed in detail in [61]. I summarize the arguments below.

- (i) From dilute instanton gas approximation, $\rho(\lambda, m) = c_0 m^2 \delta(\lambda) \Rightarrow \langle \bar{\psi}\psi \rangle \sim m$ and $\chi_\pi - \chi_\delta \sim 2$.
- (ii) Analyticity of $\rho(\lambda, m)$ as a function of λ and m when chiral symmetry is restored. To the leading order $\rho(\lambda, m) = c_m m + c_\lambda \lambda + \mathcal{O}(m^2, \lambda^2)$.
If $\rho(\lambda, m) \sim \lambda \Rightarrow \langle \bar{\psi}\psi \rangle \sim -2m \ln m$, $\chi_\pi - \chi_\delta \sim 2$.
If $\rho(\lambda, m) \sim m \Rightarrow \langle \bar{\psi}\psi \rangle \sim \pi m$, $\chi_\pi - \chi_\delta \sim \pi$.

In fact, to understand the effect of anomaly, it is desirable to use fermions with exact chiral symmetry on the lattice. The overlap and the domain wall fermions are such candidates, for which the chiral anomaly can be defined. Indeed, the overlap fermions satisfy an exact index theorem on the lattice [72]. A recent study of the eigenvalue spectrum with the domain wall fermions from the HotQCD collaboration [73] seems to favour $\rho(\lambda, m) = c_0 m^2 \delta(\lambda) + c_1 \lambda$, for the density of eigenvalues. This would imply that in the chiral limit, the $U_A(1)$ anomaly would still survive when the chiral symmetry is restored. This is also consistent with the behaviour of $\chi_\pi - \chi_\delta$ as a function of temperature, shown in Figure 11(a).

At crossover temperature around 160 MeV, the $\chi_\pi - \chi_\delta$ is far from zero, implying that the effects of the anomaly may be large in the crossover region.

A recent theoretical study [74] with the overlap fermions shows that in the chiral symmetry restored phase where $\langle \bar{\psi}\psi \rangle = 0$, the eigenvalue density in the chiral limit should behave as

$$\lim_{m \rightarrow 0} \langle \rho(\lambda, m) \rangle = \lim_{m \rightarrow 0} \langle \rho(m) \rangle \frac{\lambda^3}{3!} + \mathcal{O}(\lambda^4) \quad (20)$$

which would imply that $\chi_\pi - \chi_\delta \rightarrow 0$ as $m \rightarrow 0$. Moreover, it is argued that if an operator is invariant under some symmetry transformation then its expectation value becoming zero would not necessarily imply that the symmetry is restored, whereas the converse is true [74]. This would mean that the observable $\chi_\pi - \chi_\delta$ may not be a good candidate to study the $U_A(1)$ restoration. Rather, the equality of the correlators of the pion and delta meson could be a more robust observable to indicate the restoration of the $U_A(1)$ symmetry. Recent results from the JLQCD collaboration with 2 flavours of overlap fermions seem to indicate that the $U_A(1)$ may be restored near the chiral symmetry restoration temperature, making it a first order transition [75, 76]. Two of their main results are compiled in Figure 12. The correlators of the scalar mesons become degenerate at about 196 MeV, and at the same temperature a gap opens up in the small eigenvalue region of the eigenvalue spectrum. $T = 196$ MeV is slightly above the transition temperature which is nearly about 177 MeV. For $T = 177$ MeV, there is no degeneracy between the scalar and the pseudoscalar correlators, and the density of zero modes is finite implying that the chiral symmetry is broken, which means that the $U_A(1)$ changes rapidly near the phase transition. However, the lattice size is $16^3 \times 8$, which is small

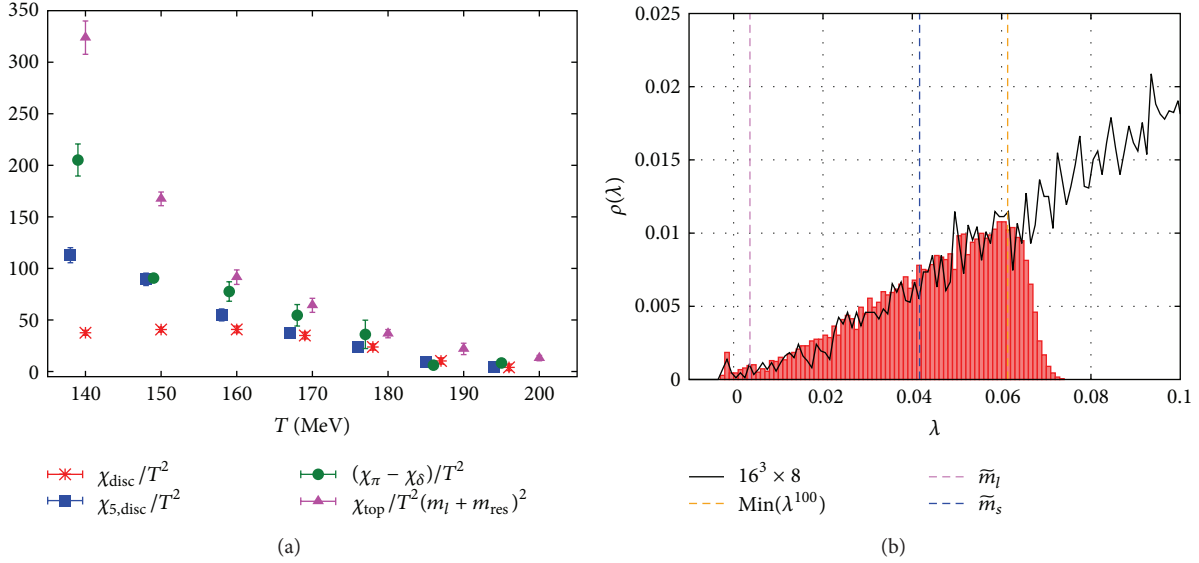


FIGURE 11: The susceptibilities for different meson quantum states constructed with the domain wall fermions are shown as a function of temperature in (a), from [61]. The eigenvalue distribution with domain wall fermions, shown in (b), from [73], has a peak in the near zero mode distribution at 177 MeV. The lattice size is $16^3 \times 8 \times N_5$ where $N_5 = 32$ for $T \geq 160$ MeV and $N_5 = 48$ otherwise.

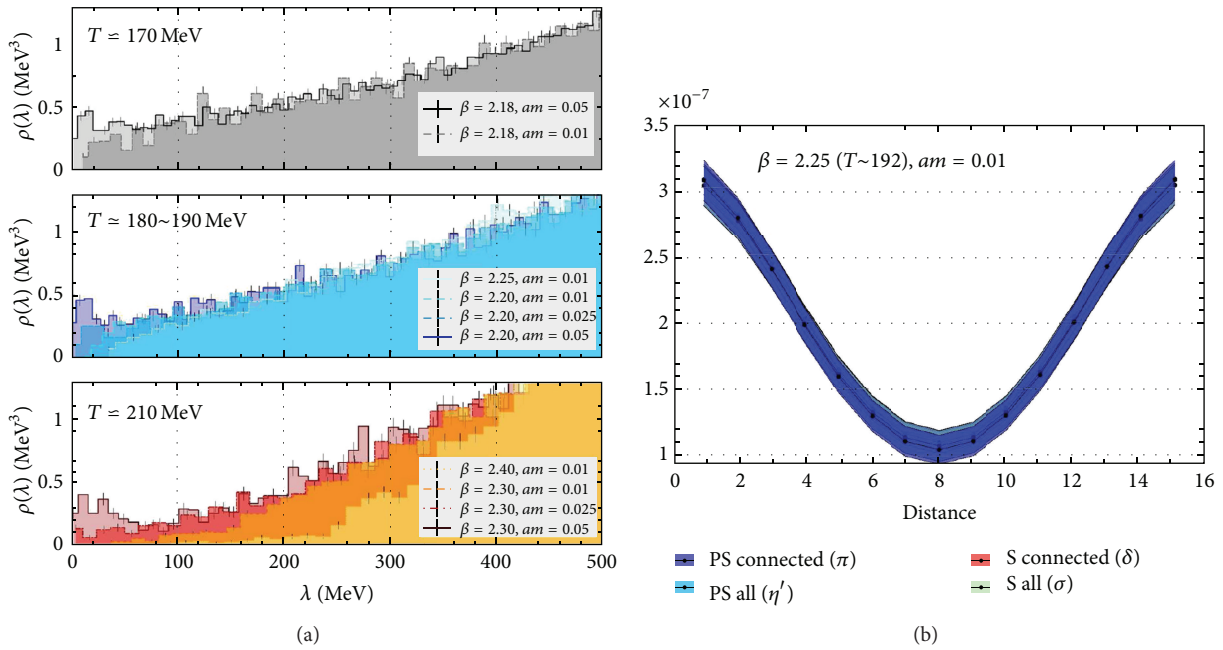


FIGURE 12: In (a), the quark mass dependence of eigenvalue distribution for the overlap quarks is compared at different temperatures, from [75, 76]. In (b), the degeneracy of the scalar and pseudoscalar mesons for overlap quarks are shown at a temperature of 192 MeV which is slightly higher than the corresponding pseudocritical temperature, from [75, 76].

enough to introduce significant finite volume and cut-off effects in the present results.

With the chiral fermions, the fate of $U_A(1)$ in the crossover region is still undetermined, and more work needs to be done for conclusive understanding of this issue. With Wilson and staggered quarks, the anomaly is recovered only in the continuum limit. For fine enough lattice spacings, one can

however check the behaviour of the low lying eigenmodes and the meson masses for different quantum numbers, to understand the effects of the remnant $U_A(1)$ anomaly using these fermions. From the eigenvalue distribution of HISQ operator shown in Figure 13(a) [77], it is evident that the effect of $U_A(1)$ still persists at $T = 330$ MeV. The long tail in the low lying eigenmodes is not a finite volume artifact

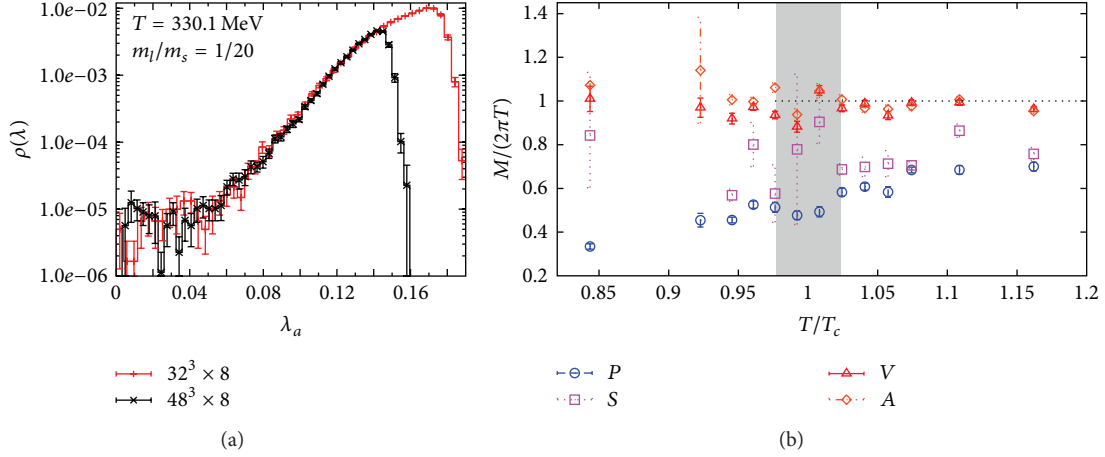


FIGURE 13: The density of eigenvalues at $T = 330.1$ MeV for HISQ discretization showing a long tail even with large volumes, from [77] (a). In (b), the screening masses for scalar, pseudo-scalar, vector, and axial vector mesons using Wilson fermions are shown as a function of temperature, from [78].

since it persists even for very large volumes. However, the data is quite noisy, and more statistics are required for making a final conclusion. The screening masses for the mesons of different quantum numbers were obtained from lattice studies with improved Wilson fermions (Figure 13(b), [78]). In the transition region, the scalar and pseudoscalar mesons are not degenerate and an agreement seen only for temperatures above $1.2T_c$. However, the input quark masses are quite large compared to the physical values, and more data is needed to take a final call. At present, the effects of quantum anomalies are not yet understood from lattice studies.

3. Lattice QCD at Finite Density

QCD with a finite number of baryons is relevant for the physics of neutron stars and supernovae. It is the theoretical setup for the heavy ion physics phenomena occurring at low center of mass energy, \sqrt{s} , of the colliding nuclei. Some of these low \sqrt{s} collisions are being investigated at the RHIC and to be probed further with the start of the heavy ion experiments at FAIR, GSI, and NICA, Dubna. In fact, an interesting feature of the QCD phase diagram is the critical end-point related to chiral symmetry restoration. The existence of the critical point has important consequences on the QCD phase diagram, and it is the aim of the extensive beam energy scan (BES) program at the RHIC to search for it.

To explain these experimental results from first principles, we need to extend the lattice QCD formulation to include the information of finite baryon density. One of the methods is to work in a grand canonical ensemble. In such an ensemble, the partition function is given by

$$\mathcal{Z}_{\text{QCD}}(T, \mu) = \text{Tr} \left(e^{\mathcal{H}_{\text{QCD}} - \mu N} \right) = \int \mathcal{D}U_\mu \prod_{f=1}^{N_f} \det D_f(\mu) e^{-S_G}, \quad (21)$$

where the chemical potential μ is the Lagrange multiplier corresponding to the conserved number density N that commutes with the QCD Hamiltonian H_{QCD} . N can be the baryon number or the net electric charge. The μ enters into the lattice fermion action as $\exp(\pm \mu a)$ factors multiplying the forward and backward temporal links, respectively [79, 80], referred to as the Hasenfratz-Karsch method. The naive fermion operator at finite μ on the lattice would be of the form

$$D_f(\mu)_{x,y} = \left[\sum_{i=1}^3 \frac{1}{2} \gamma_i (U_i(x) \delta_{y,x+i} - U_i^\dagger(y) \delta_{y,x-i}) + \frac{1}{2} \gamma_4 (e^{\mu a} U_4(x) \delta_{y,x+4} - e^{-\mu a} U_4^\dagger(y) \delta_{y,x-4}) + am_f \delta_{x,y} \right]. \quad (22)$$

This is not a unique way of introducing μ , and it could be also done in several different ways [81]. The lattice fermion determinant at finite μ , like in the continuum, is no longer positive definite since

$$\det D_f^\dagger(\mu) = \det D_f(-\mu) \implies \det D_f(\mu) = |\det D_f(\mu)| e^{i\theta}, \quad (23)$$

and the interpretation of $\int \mathcal{D}U \det D_f(\mu) e^{-S_G}$ as a probability weight in the standard Monte Carlo simulations is no longer well defined. This is known as the “sign problem.” One may consider only the real part of the fermion determinant for Monte Carlo algorithms and generate configurations, by the so-called phase quenching. Once the partition function is known in the phase quenched limit, one can then use the reweighting techniques to generate the partition function of the full theory at different values of μ . The expectation value

of the phase of the determinant, needed for reweighting, at some finite μ , is given as

$$\langle e^{i\theta} \rangle = \frac{\int \mathcal{D}U \prod_{f=1}^{N_f} |\det D_f(\mu)| e^{i\theta} e^{-S_G}}{\int \mathcal{D}U \prod_{f=1}^{N_f} |\det D_f(\mu)| e^{-S_G}} = e^{-V\Delta F/T}, \quad (24)$$

where ΔF is the difference between the free energy densities of the full and the phase quenched QCD. For two degenerate quark flavours, the phase quenched theory is equivalent to a theory with a finite isospin chemical potential [82], and ΔF is the difference of free energies of QCD with finite baryon (quark) chemical potential and that at an isospin chemical potential. These two theories are qualitatively quite different, and the sign problem results in a very small overlap between these two theories. For isospin QCD, the charged pions are the lightest excitations, and these can undergo a Bose-Einstein condensation for $\mu > m_\pi/2$. The difference between the respective free energies in this regime is quite large, leading to a severe sign problem. This is an algorithmic problem that can arise for any theory which has chiral symmetry breaking. A better understanding of the sign problem has been achieved in the recent years with a knowledge of the regions in the phase diagram with severe sign problem and those where it is controllable [83–85]. There are several methods followed to circumvent this problem on the lattice, some of which are listed below:

- (i) reweighting of the $\mu = 0$ partition function [86–89],
- (ii) Taylor series expansion [90–92],
- (iii) canonical ensemble method [93–96],
- (iv) imaginary chemical potential approach [97–100],
- (v) complex Langevin algorithm [101–105],
- (vi) worm algorithms [106, 107].

The Taylor series method has been widely used in the lattice QCD studies in the recent years, which has led to interesting results relevant for the experiments. One such proposal is the determination of the line of chemical freezeout for the hadrons in the phase diagram at small baryon density, from first principles lattice study. It was first proposed that cumulants of baryon number fluctuations could be used for determining the freezeout parameters [108] on the lattice. Last year, another interesting suggestion was made [109], where the experimental data on cumulants of electric charge fluctuations could be used as an input to compute the freezeout curve using lattice data. This and some other results are discussed in the subsequent subsections. Most of the results are obtained with improved versions of staggered fermions. It has been known that the rooting problem may be more severe at finite density [110]. It is thus important to explore other fermion formulations as well for lattice studies. Wilson fermions have been used but it is important to use chiral fermions, especially for the study of the critical point. I outline in the next subsection, the theoretical efforts in the recent years that have led to the development of fermion operators at finite density with exact chiral symmetry on the lattice which can be used for future lattice studies on the critical point.

3.1. Chiral Fermions at Finite Density. The contribution of the $U_A(1)$ anomaly is believed to affect the order of the chiral phase transition at zero density and hence is crucial for the presence or absence of the critical point. If the anomaly is not represented correctly at finite density, it may affect the location of the critical point in the phase diagram, if it exists. Overlap fermions have exact chiral symmetry on the lattice, in the sense that the overlap action is invariant under suitable chiral transformations known as the Luscher transformations [111]. It can be further shown that the fermion measure in the path integral is not invariant under Luscher transformations, and its change gives the chiral anomaly. The index theorem, relating the anomaly to the difference between the fermion zero modes, can be proved for them [72]. Thus, the overlap fermions have the properties analogous to the fermions in the continuum QCD. In the continuum, it is known that the anomaly is not affected in presence of a finite baryon chemical potential. It would be desirable to preserve this continuum property with the overlap fermions as well, such that the physical properties important for the existence of the critical point are faithfully presented on a finite lattice. Defining an overlap fermion action at finite chemical potential is non-trivial as the conserved currents have to be defined with care [112]. The first attempt to define an overlap fermion operator at finite density [113] was done in the last decade, and an index theorem at finite μ was also derived for them. However, these overlap fermions did not have exact chiral symmetry on a finite lattice [114]. Moreover, the index theorem for them was μ -dependent, unlike in the continuum. Recently, overlap fermion at finite density has been defined from the first principles [115], which has exact chiral symmetry on the lattice [116] and preserves the μ -independent anomaly as well. A suitable domain wall fermion action has been also defined at finite density [116], which was shown to reproduce the overlap action in the appropriate limit. It would be important to check the application of these overlap and domain wall fermion operators at finite μ for future large scale QCD simulations.

3.2. Correlations and Fluctuations on the Lattice. The studies of fluctuations of the conserved charges are important to understand the nature of the degrees of freedom in a thermalized medium and the interactions among them [117, 118]. The diagonal susceptibility of order n , defined as

$$\chi_n^X = \frac{T}{V} \frac{\partial^n \ln \mathcal{Z}}{\partial \mu_X^n}, \quad X \equiv B, S, Q, \quad (25)$$

measures the fluctuations of the conserved quantum number X . In a heavy-ion experiment, the relevant conserved numbers are the baryon number B and electric charge Q . The strangeness S is zero at the initial time of collision of heavy nuclei, but strange quark excitations are produced at a later time in the QGP, and is also believed to be a good quantum number. These fluctuations can be computed exactly on the lattice at $\mu = 0$ from the quark number susceptibilities [119]. Continuum extrapolated results for the second order susceptibilities of baryon number, strangeness,

and electric charge exist for both HISQ [120] and stout smeared staggered quarks [121]. The fluctuations of baryon number are very well explained by the hadron resonance gas model for $T < 160$ MeV. However, the fluctuations of the strangeness are usually larger than the HRG values by about 20% in the freezeout region characterized by $160 \leq T \leq 170$ MeV. The electric charge fluctuations, on the other hand, are smaller than the corresponding HRG values by 10% in the same region. The ratio of χ_2^Q/χ_2^B ($\mu = 0$) $\simeq 0.29$ – 0.35 in the freezeout region. A first principle determination of this ratio is crucial, as it would allow us to relate the net baryon number fluctuations with the net proton number fluctuations, which is an observable in the heavy ion experiments [120]. At high temperatures, these fluctuations slowly approach the corresponding free theory value, with the continuum extrapolated data for the baryon number susceptibility showing about 20% deviation from the free theory value even at $2T_c$ [120]. The data are in good agreement with resummed perturbation theory estimates at these temperatures [122, 123] indicating that the QGP is still fairly strongly interacting even at temperatures around $2T_c$.

To relate to the results of the heavy ion experiments at a lower collision energy, \sqrt{s} , one has to compute the fluctuations on the lattice at a finite value of μ . The most widely used lattice method to compute the susceptibilities at a finite value of quark chemical potential μ is through the Taylor expansion of the corresponding quantity at $\mu = 0$, for example,

$$\frac{\chi_2^B(\mu)}{T^2} = \frac{\chi_2^B(0)}{T^2} + \frac{\mu^2}{2!T^2}\chi_4^B(0) + \frac{\mu^4}{4!T^4}\chi_6^B(0)T^2 + \dots \quad (26)$$

The light and strange quark susceptibilities have been computed at finite but small densities from Taylor expansion, using asqtad staggered quarks [66] and the ratios of baryon number susceptibilities using the unimproved staggered fermions [108] in the region of interest for the RHIC experiments. All these ratios agree well with the estimates from the HRG model [108], the results for which are compiled in Figure 16(b). The ratios of susceptibilities serve as a good observable for comparing the lattice and the experimental data since these are free from the unknown quantities, like the volume of the fireball during freezeout [124].

The higher order susceptibilities χ_n , for $n > 4$, are important even in the $\mu = 0$ regime. In the chiral limit, it is expected that the fourth order baryon number susceptibility would have a cusp, and the sixth order would diverge with $O(4)$ scaling at the critical temperature. Even for physical quark masses, χ_6^B for QCD would show oscillations near the pseudocritical temperature, and χ_8^B would have negative values in the same region [125], quite contrary to the HRG predictions. Thus, the signatures of critical behaviour could be understood by the careful study of these quantities already at $\mu \sim 0$, which is probed by the experiments at LHC [125].

Other important quantities of relevance are the off-diagonal susceptibilities. These defined as

$$\chi_{ijk}^{BSQ} = \frac{T}{V} \frac{\partial^{i+j+k} \ln \mathcal{Z}}{\partial \mu_B^i \partial \mu_S^j \partial \mu_Q^k} \quad (27)$$

are a measure of the correlations between different quantum numbers and hence good observables to estimate the effects of interactions in the different phases of the QCD medium. It has been suggested that the quantity $C_{BS} = -3\chi_{11}^{BS}/\chi_2^S$ is a good observable to characterize the deconfinement in thermal QCD [126]. If the strangeness is carried by quark like excitations, the value of C_{BS} would be identity and would be much smaller than unity in the phase where only the baryons and mesons carry the strangeness quantum number. Recent results from the HotQCD collaboration using HISQ action [120] show that C_{BS} approaches unity very quickly at around 200 MeV implying that almost no strange hadrons survive in the QGP phase above T_c . This is compiled in Figure 14(a). The HotQCD data is consistent with the corresponding continuum extrapolated data with the stout smeared fermions [121]. Also C_{BS} is not sensitive to the sea strange quark masses for $T > T_c$ since the first partially quenched results [127] for this quantity are consistent with the full QCD results. The other important observable is the baryon-electric charge correlation. In the confined phase, electric charge in the baryon sector is mainly carried by protons and antiprotons; therefore, the correlation would rise exponentially with temperature if this phase could be described as a noninteracting gas consisting of these particles. At high temperatures, however, quark-like excitations would be important and their masses being much smaller than the temperature, this correlation would fall to zero. From the behaviour of the continuum extrapolated HISQ data for χ_{11}^{BQ} , compiled in Figure 14(b), it is evident that near the pseudocritical temperature there is a change in the fundamental properties of the degrees of freedom of the medium, with quark-like excitations dominating at $1.5T_c$.

3.3. The Freezeout Curve from Lattice. To relate the results from heavy ion experiments with the lattice data, it is crucial to map the center of mass energy of the colliding nuclei in the heavy ion collisions, \sqrt{s} , to the corresponding point in the $T - \mu_B$ plane of the QCD phase diagram. This is called the freezeout curve. Phenomenologically, the freezeout curve is obtained from a particular parameterization of the HRG model obtained through fitting the experimental data on hadron abundances [128]. At chemical freezeout, the chemical composition of the baryons gets frozen, meaning that the inelastic collisions between these species become less probable under further cooling of the system. However, the systematic uncertainties in determining the hadron yields are not taken into account in the phenomenological determination of the freezeout curve. Recent work by the BNL-Bielefeld collaboration shows how lattice techniques can provide first principle determination of the freezeout curve through suitable experimental observables. As emphasized in

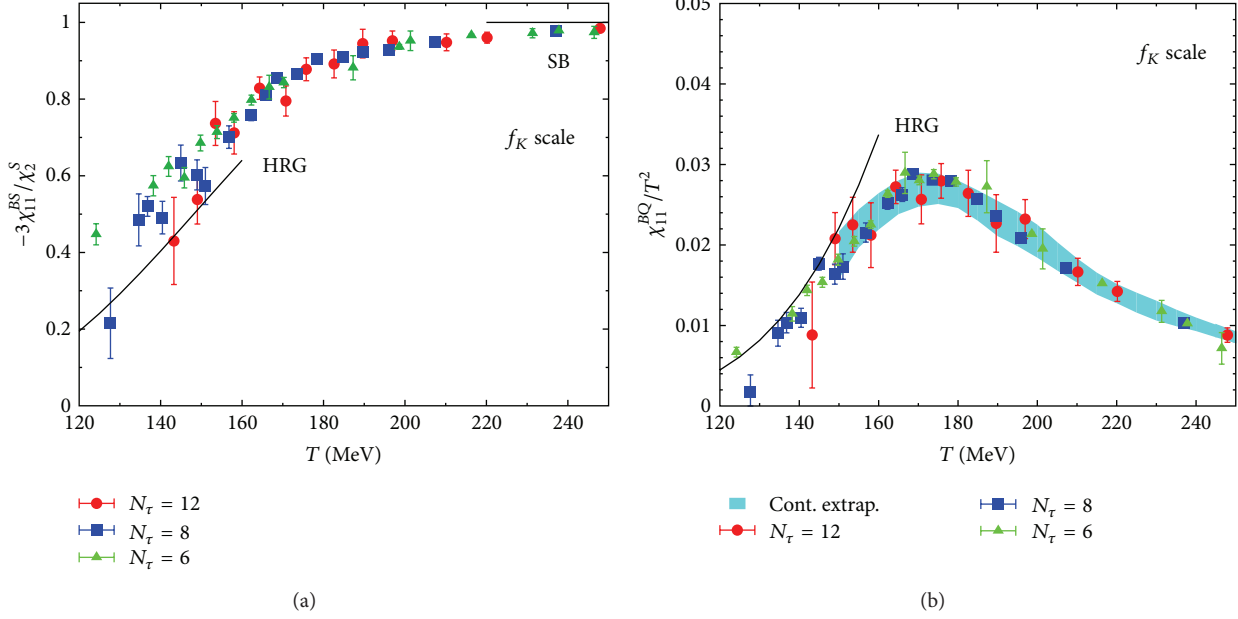


FIGURE 14: The HISQ data for C_{BS} (a) and χ_{11}^{BQ}/T^2 (b) as a function of temperature, from [120].

the last subsection, the ratios of susceptibilities are believed to be good observables for comparing the lattice and the experimental data. Two such observables proposed in [109] are

$$R_{12}^X \equiv \frac{M_X}{\sigma_X^2} = \frac{\mu_B}{T} \left(R_{12}^{X,1} + \frac{\mu_B^2}{T^2} R_{12}^{X,3} + \mathcal{O}(\mu_B^4) \right), \quad (28)$$

$$R_{31}^X \equiv \frac{S_X \sigma_X^3}{M_X} = R_{31}^{X,1} + \frac{\mu_B^2}{T^2} R_{31}^{X,3} + \mathcal{O}(\mu_B^4),$$

where M_X, σ_X, S_X denotes the mean, variance, and the skewness in dimensionless units for the conserved quantum number X . These observables are chosen because these are odd and even functions of μ_B , allowing us to independently determine T and μ_B from these two quantities. The quantum number X can either be chosen to be the net electric charge Q or the net baryon number B . In the experiments, one can only measure the proton number fluctuations, and it is not clear whether the proton number fluctuations could be a proxy for the net baryon fluctuation [129]. It was thus suggested that the ratios of net charge fluctuations would be a better observable to compare with the experiments. Once the R_{31}^Q is known from experiments, one can determine the freezeout temperature T_f from it by comparing with the continuum extrapolated lattice data. Analogously, one can obtain the μ_B at freezeout from comparison of the R_{12}^Q data. In Figure 15(a), the results for R_{31}^Q are shown as a function of temperature. It is evident that the first order correction to the value of the ratio is within 10% of the leading order value for $\mu_B/T < 1.3$ and in the freezeout region, that is, $T > 140$ MeV. From the leading order results of R_{31}^Q , one can estimate the freezeout temperature. For \sqrt{s} in the range of 39–200 GeV currently probed in the beam energy scan (BES)

experiment at RHIC, the freezeout temperature from the HRG parameterization of the hadron multiplicities is about 165 MeV. At this temperature, the ratio R_{31}^Q calculated from the HRG model is quite larger than the lattice estimate which would mean that the freezeout temperature estimated from lattice data would differ from the model results by at least 5%. Similarly, if R_{12}^Q is known from the experiments, μ_B can be accurately estimated and is expected to be different from the current HRG estimates. This is not very surprising because the freezeout of the fluctuations happens due to diffusive processes and is due to a different mechanism from the freezeout of hadrons due to decreasing probability of inelastic collisions. Another question that was addressed in this work was how relevant are the other parameters like μ_S and μ_Q for the phase diagram and the freezeout curve. It was seen that μ_S and μ_Q are significantly smaller than μ_B , and the ratios of these quantities have a very small μ_B dependence in the entire temperature range of 140–170 MeV relevant for the freezeout studies. It signifies that the relevant axes for the phase diagram are indeed T and μ_B , and these two parameters are sufficient for characterizing the freezeout curve.

3.4. Physics Near the Critical Point. It is known from models with the same symmetries as QCD that the chiral phase transition at $T = 0$ and finite μ is a first order one. At zero density and high enough temperatures, QCD undergoes a crossover from the hadron to the QGP phase. By continuity, it is expected that the first order line should end at a critical end-point in the phase diagram [130–132]. The determination of its existence from first principles lattice computation has been quite challenging, and the currently available lattice results are summarized in Figure 16(a). These are all obtained using staggered fermions. The first lattice study on the critical point was done using reweighting technique. Configurations

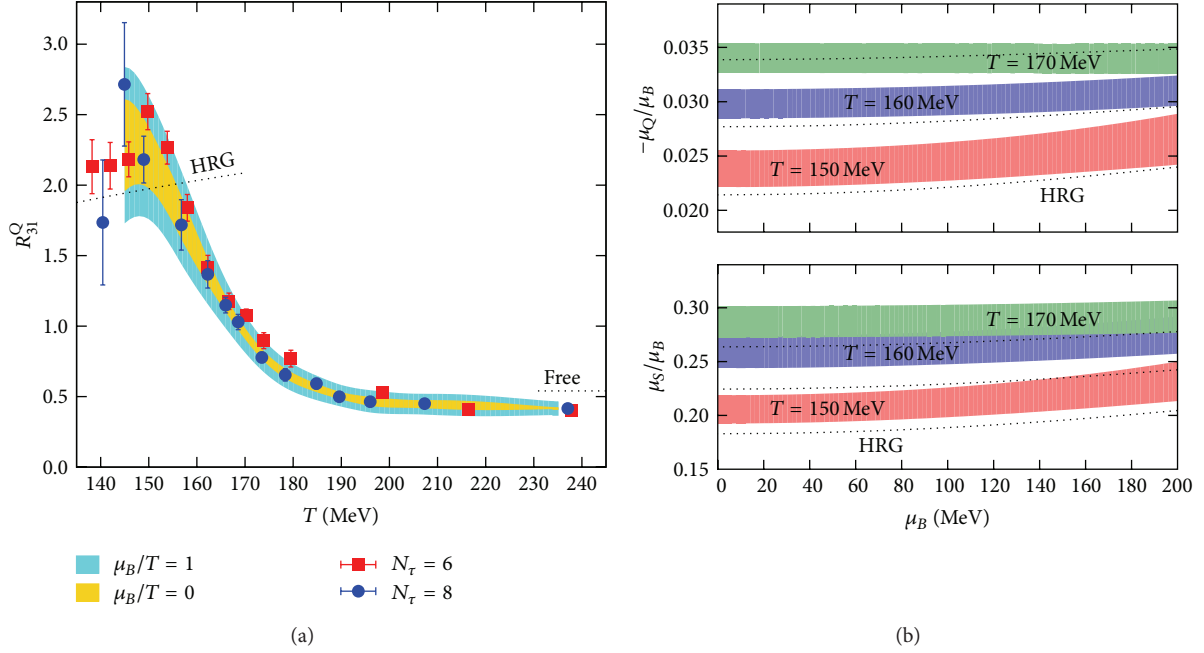


FIGURE 15: In (a), the leading term for R_{31}^Q shown in the yellow band is compared to its NLO term denoted by the blue band in the continuum limit. In (b), the ratios of μ_Q and μ_S with respect to μ_B are compared with the HRG model predictions at different temperatures. Both figures are from [109].

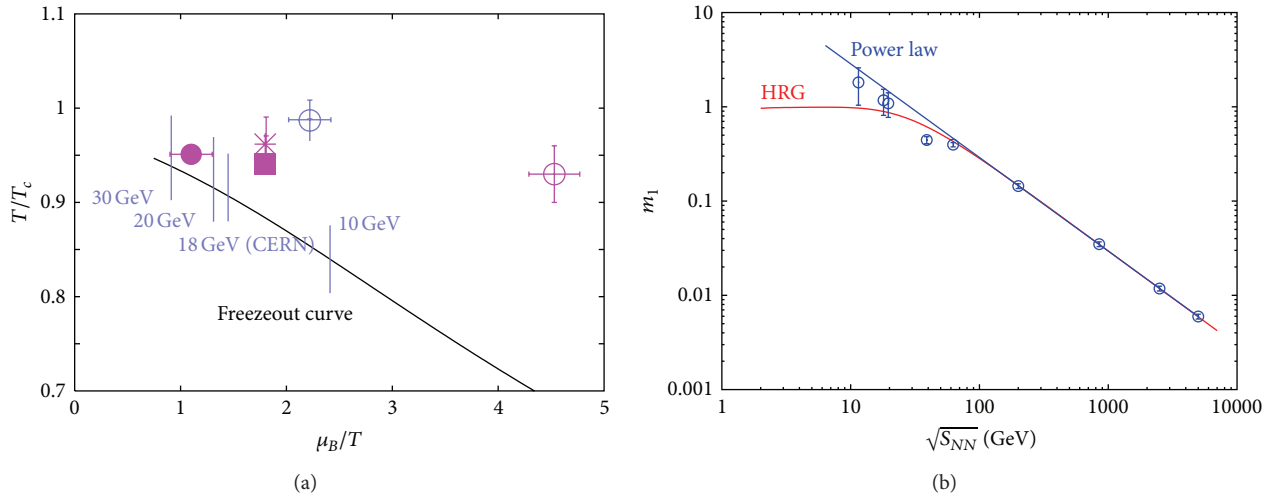


FIGURE 16: The estimates of the critical point from lattice studies are shown in (a), from [137]. The magenta solid circle, box, and star denote the $N_\tau = 4, 6, 8$ data, respectively, for 2 flavours of staggered quarks [135–137], and the open circles denote $N_\tau = 4$ data for 2 + 1 flavours obtained with reweighting techniques [87, 133]. In (b), the ratio of the third and the second order baryon number susceptibility is plotted as a function of \sqrt{s} relevant for the RHIC and LHC experiments and compared with the HRG model data, from [108].

generated at the critical value of the gauge coupling for $\mu_B = 0$ were used to determine the partition function at different values of T and μ_B using two-parameter reweighting [87]. By observing the finite volume behaviour of the Lee-Yang zeroes of the partition function, it was predicted that for 2 + 1 flavour QCD, there is a critical end-point at $T_E = 160(4)$ MeV and $\mu_B = 725(35)$ MeV. In this study, the light quark was four times heavier than its physical value. Reducing the light quark mass shifted the critical end-point to $\mu_B = 360(40)$ MeV

with $T_E = 162(2)$ remaining the same [133]. However, this result is for a rather small lattice of size $16^3 \times 4$ and is expected to change in the continuum limit and with larger volumes. Reweighting becomes more expensive with increasing volume of the lattice, so going to a larger lattice seems difficult with this method.

The other results for the critical point were obtained using the Taylor series method. In this method, the baryon number susceptibility at finite density is expanded in powers

of μ_B/T as a Taylor series as shown in (26), for each value of temperature. The baryon number susceptibility is expected to diverge at the critical end-point [134], so the radius of convergence of the series would give the location of the critical end-point [92]. However, on a finite lattice, there are no divergences but the different estimates of the radius of convergence given as

$$r_n \ (n = \text{odd}) = \sqrt{\frac{\chi_{n+1}^B}{T^2 \chi_{n+3}^B}}, \quad r_n \ (n = \text{even}) = \left[\frac{\chi_2^B}{T^n \chi_{n+2}^B} \right]^{1/n} \quad (29)$$

should all be positive and equal within errors at the critical end-point. Currently, the state of the art on the lattice is estimates of baryon number susceptibilities upto χ_8^B . This gives five different independent estimates of the radius of convergence upto r_6 , which were shown to be consistent within errors for $N_\tau = 4, 6, 8$ at $T_E = 0.94(1)T_c$ [135–137]. The radius of convergence after finite volume correction is $\mu_B/T_E = 1.7(1)$ [137], which means $\mu_B = 246(15)$ MeV at the critical end-point if we choose $T_c = 154$ MeV. The input pion mass for this computation is about 1.5 times the physical value and could affect the final coordinates of the end-point. Moreover the different estimates for the radius of convergence r_n in (29), agrees with each other for asymptotically large values of n and one might need to check the consistency of the results with the radii of convergence estimates beyond r_6 . Hints of the critical end-point were also obtained [138] using a different fermion discretization and a different methodology as well. Working with the canonical ensemble of improved Wilson fermions, the presence of a critical point was reported at $T_E = 0.925(5)T_c$ and $\mu_B/T_c = 2.60(8)$. This is a very preliminary study though, with a small lattice volume and a very heavy pion mass of about 700 MeV.

Though there is growing evidence in support for the existence of the critical end-point, the systematics for all these lattice studies are still not under control. It would be desirable to follow a different strategy to determine its existence. The alternate method suggested [139] was to determine the curvature of the surface of second order chiral phase transitions as a function of the baryon chemical potential μ_B . If the chiral critical surface bends towards larger values of $m_{u,d}$ with increasing baryon chemical potential and for a fixed value of the strange quark mass, it would pass through the physical point, ensuring the existence of a critical end-point. However if the curvature is of opposite sign, the chiral critical end-point would not exist. For lattice size of $8^3 \times 4$, the critical value of the light quarks was estimated upto $\mathcal{O}(\mu_B^4)$ [140],

$$\frac{m_c(\mu_B)}{m_c(0)} = 1 - 39(8) \left(\frac{\mu_B}{3\pi T} \right)^2 - \dots, \quad (30)$$

with the strange quark mass fixed at its physical value. The leading value of the curvature has the same sign even for a finer lattice of extent $N_\tau = 6$ [141]. These studies show that the region of first order transition shrinks for small values of μ_B , which would mean that the critical point may not exist in this regime of μ_B . However for larger values of μ_B , the higher order

terms could be important and may bend the chiral critical line towards the physical values of quark masses. The finite cut-off effects are still sizeable and it is currently premature to make any definite predictions in the continuum limit with this method.

It is equally important to understand the possible experimental signatures of the critical point. The search of the critical end-point is one of the important aims for the extensive BES program at RHIC. In a heavy ion experiment, one measures the number of charged hadrons at the chemical freezeout and its cumulants. During the expansion of the fireball, the hot and dense QCD medium would pass through the critical region and cool down eventually forming hadrons. If the freezeout and the critical regions are far separated, the system would have no memory of the critical fluctuations and the baryon number susceptibility measured from the experiments could be consistent with the predictions from thermal HRG models which has no critical behaviour. If the freezeout region is within the critical region, the critical fluctuations would be larger than the thermal fluctuations. It is thus important to estimate the chiral critical line for QCD from first principles. The curvature of the chiral critical line has been estimated by the BNL-Bielefeld collaboration [142], by extending the scaling analysis of the dimensionless chiral condensate M_b outlined in Section 2.6.1 for finite values of baryon chemical potential, using Taylor series expansion. The corresponding scaling variables at finite μ_B are

$$t = \frac{1}{t_0} \left(\frac{T - T_{c,0}}{T_{c,0}} + \kappa_B \frac{\mu_B}{3T} \right), \quad h = \frac{m_l}{h_0 m_s}. \quad (31)$$

The quantity M_b can be expanded as a Taylor series in $\mu_B/3T$ as

$$M_b(\mu) = M_b(0) + \frac{\chi_{m,B}}{2T} \left(\frac{\mu_B}{3T} \right)^2 + \mathcal{O} \left(\frac{\mu_B}{3T} \right)^4, \quad (32)$$

where $\chi_{m,B}$ is the mixed susceptibility defined as $\chi_{m,B} = (T^2/m_s) \partial^2 M_b / \partial (\mu_B/3T)^2$ computed at $\mu_B = 0$. In the critical region, it would show a scaling behaviour of the form

$$\frac{\chi_{m,B}}{T} = \frac{2\kappa_B T}{t_0 m_s} h^{-(1-\beta)/\beta\delta} f'_G \left(\frac{t}{h^{1/\beta\delta}} \right). \quad (33)$$

The universality of the scaled $\chi_{m,B}$ data is clearly visible in Figure 17(b), both for p4 staggered quarks on $N_\tau = 4$ lattice with mass ratios of light and strange quarks varying from 1/20 to 1/80 and with HISQ discretization on a $32^3 \times 8$ lattice with the mass ratio fixed at 1/20. The fit of the complete lattice data set to the scaling relation for $\chi_{m,B}$, gave the value of $\kappa_B = 0.00656(66)$. At non-vanishing μ_B , the phase transition point is located at $t = 0$, which implies that the critical temperature at finite density can be parameterized as

$$\begin{aligned} \frac{T_c(\mu_B)}{T_c(0)} &= 1 - \kappa_B \left(\frac{\mu_B}{3T} \right)^2 + \mathcal{O} \left(\frac{\mu_B}{3T} \right)^4 \\ \Rightarrow T_c(\mu_B) &\simeq 154 \left(1 - 0.0066 \left(\frac{\mu_B}{3T} \right)^2 \right) \text{ MeV.} \end{aligned} \quad (34)$$

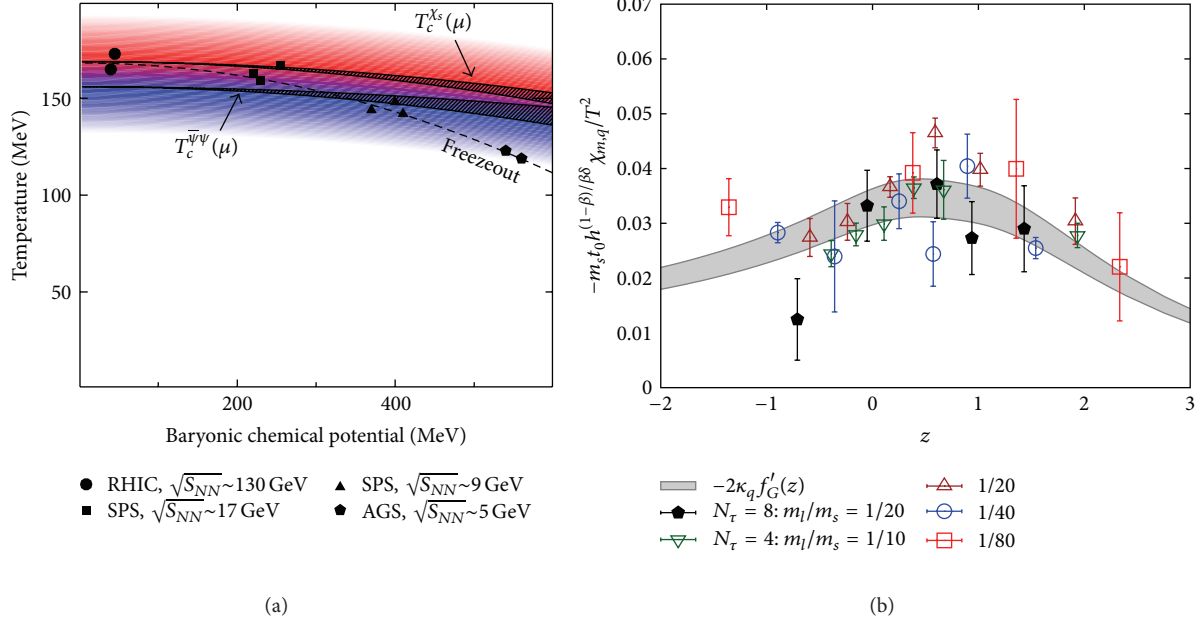


FIGURE 17: In (a), the width of the pseudocritical region for chiral condensate is shown as a blue curve and that for strange quark susceptibility is shown as a red curve, from [143]. In (b), the scaling of the mixed susceptibility is shown for different light quark masses and at the physical value of strange quark mass, from [142].

This estimate of the curvature is about three times larger than the corresponding prediction from the hadron resonance gas model. It would be interesting to compare the curvature of the freezeout line computed on the lattice with that of the critical line, once the experimental data for the electric charge cumulants are available.

Another complimentary study about the fate of the critical region at finite density was done by the Budapest-Wuppertal group [143]. It was suggested that if the critical region shrinks with increasing μ_B , it would imply that one slowly converges to the critical end-point. The width of the critical region was measured from two different observables, the renormalized chiral condensate and the strange quark number susceptibility. Stout smeared staggered quarks were employed and the continuum limit was taken with the $N_\tau = 6, 8, 10$ data. The results are summarized in Figure 17(a). From the plots, it seems that the width of the crossover region does not change from its $\mu_B = 0$ value significantly for $\mu_B < 500$ MeV, which implies either that the critical end-point does not exist at all or is present at a higher value of μ_B . The corresponding curvature measured for the light quark chiral condensate is 0.0066(20) which is consistent with the result from the BNL-Bielefeld collaboration. The results indicate that the chiral pseudocritical line and the phenomenological freezeout curve would separate apart at larger values of μ_B and would be further away at the critical end-point.

It was noted that the higher order fluctuations are more strongly dependent on the correlation length of the system [144] and would survive even if the chiral and freezeout lines are far apart. It has been proposed [125], that the signature of the critical point can be detected by monitoring the behaviour of the sixth and higher order fluctuations of the electric charge along the freezeout curve.

3.5. The EoS at Finite Density. The EoS at finite density would be the important input for understanding the hydrodynamical evolution of the fireball formed at low values of the collisional energy, at the RHIC and the future experiments at FAIR and NICA. It is believed that there is no generation of entropy once the fireball thermalizes [145]. In that case, as pointed out in [146], it is important to determine the EoS along lines of constant entropy per net baryon number, S/n_B to relate the lattice results with the experiments. The isentrope, determined by a fixed value of S/n_B that characterizes the evolution of the fireball, is $S/n_B \approx 300$ for RHIC experiments, at $\sqrt{s} = 200$ GeV. For the future experiments at FAIR, the isentropes would be labelled by $S/n_B = 30$ nearly as same as the early SPS experiments at CERN where $S/n_B \sim 45$. For two flavour QCD with p4 staggered quarks and with pion mass heavier than its physical value, it was already observed that the ratio of pressure and energy density showed little variation as a function of S/n_B . The pressure and the energy density at finite μ are usually computed on the lattice as a Taylor series about its value at zero baryon density as

$$\frac{P(\mu_l, \mu_s)}{T^4} = \frac{P(0)}{T^4} + \sum_{i,j} \frac{\chi_{ij}(T)}{T^{4-i-j}} \left(\frac{\mu_l}{T}\right)^i \left(\frac{\mu_s}{T}\right)^j. \quad (35)$$

The formula is valid for two degenerate light quark flavours and a heavier strange quark. The coefficients χ_{ij} are the quark number susceptibilities at $\mu = 0$ and are non-zero for $i + j = \text{even}$. The corresponding expression for the trace anomaly is given as

$$\frac{I(\mu_l, \mu_s)}{T^4} = -\frac{N_\tau^3}{N^3} \frac{d \ln \mathcal{Z}}{d \ln a} = \frac{I(0)}{T^4} + \sum_{i,j} b_{ij}(T) \left(\frac{\mu_l}{T}\right)^i \left(\frac{\mu_s}{T}\right)^j. \quad (36)$$

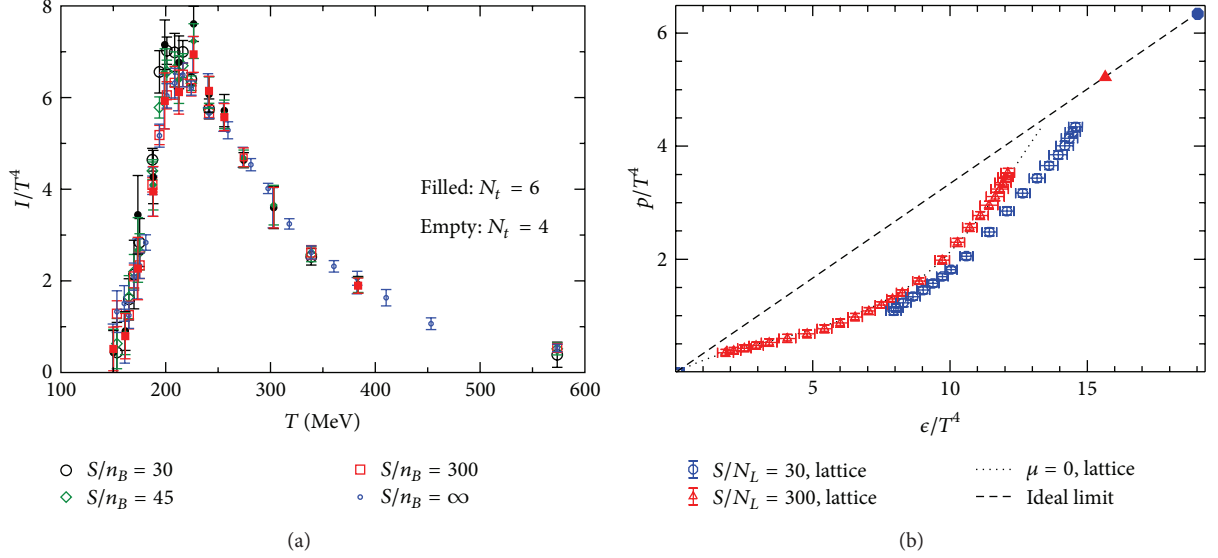


FIGURE 18: The EoS for different isentropes using asqtad quarks is shown in (a), from [66]. In (b), the data for the energy density and pressure is compared for different isentropes using stout-smearred staggered quarks, from [147].

The χ_{ij} s can be also obtained from the coefficients b_{ij} by integrating the latter along the line of constant physics. For 2+1 flavours of improved asqtad staggered quarks with physical strange quark mass and $m_l = m_s/10$, the interaction measure was computed upto $\mathcal{O}(\mu^6)$ for two different lattice spacings (Figure 18(a)). The interaction measure did not change significantly from the earlier results with heavier quarks and showed very little sensitivity to the cut-off effects along the isentropes [66]. However, it was observed that the light and the strange quark number susceptibilities change significantly from the zero temperature values along the isentropes. No peaks were found in the quark number susceptibilities at isentropes $S/n_b = 300$, which led to the conclusion that the critical point may not be observed at the RHIC [66]. The EoS and the thermodynamic quantities were computed for physical values of quark masses by the Budapest-Wuppertal collaboration [147]. In this study, they set the values of the light quark chemical potentials such that $\mu_l = \mu_B/3$ and the strange quark susceptibility is $\mu_s = -2\mu_l\chi_{11}^{us}/\chi_2^s$ to mimic the experimental conditions where the net strangeness is zero. The pressure and the energy density was computed upto $\mathcal{O}(\mu^2)$. The ingredients that went into the computations were (a) the near continuum values of the interaction measure data from the $N_\tau = 10$ lattice and (b) the spline interpolated values of χ_2^s, χ_{11}^{us} for the range $125 < T < 400$ MeV obtained using the continuum extrapolated data for χ_2^s, χ_{11}^{us} . It was observed, as evident from Figure 18(b), that the finite density effects along the RHIC isentropes are negligible consistent with the earlier work. However for isentropes given by $S/n_B = 30$, the finite density effects become more important. The effect of truncation at $\mathcal{O}(\mu^2)$ was also estimated on a reasonably large $N_\tau = 8$ lattice. It was observed that

$$\frac{p \text{ up to } \mathcal{O}((\mu_B/T)^4)}{p \text{ up to } \mathcal{O}((\mu_B/T)^2)} \leq \begin{cases} 1.1, & \text{for } \frac{\mu_B}{T} \leq 2, \\ 1.35, & \text{for } \frac{\mu_B}{T} \leq 3, \end{cases} \quad (37)$$

implying that the fourth and higher order terms need to be determined for even modest values of μ_B in the Taylor series method. An independent study about the truncation effects of the Taylor series was performed in [148]. The derivatives of pressure were computed for two flavour QCD with staggered quarks at imaginary chemical potential. These derivatives are related to the successive terms of the Taylor coefficients of pressure evaluated at $\mu = 0$. By fitting the imaginary μ data with a polynomial ansatz, these Taylor coefficients were obtained and compared with the exact values. It was observed that for $T_c \leq T \leq 1.04T_c$, atleast the 8th order Taylor coefficient is necessary for a good fit. This highlights the necessity to evaluate higher order susceptibilities, beyond the currently measured eighth order in the studies of EoS or the critical end-point. New ideas to extend the Taylor series to higher order susceptibilities are evolving [148, 149] and these should be explored in full QCD simulations.

4. Summary

As emphasized in the introduction, I have tried to compile together some of the important instances to show that the lattice results have already entered into the precision regime with different fermion discretizations giving consistent continuum results for the pseudocritical temperature and fluctuations of different quantum numbers. The continuum result for the EoS would be available in very near future, with consistency already observed for different discretizations. The lattice community has opened the door for a very active collaboration between the theorists and experimentalists. With the EoS as an input, one can study the phenomenology of the hot and dense matter created at the heavy ion colliders. On the hand, there is a proposal of nonperturbative determination of the freezeout curve using lattice techniques, once the experimental data on cumulants of the charged hadrons are available.

A good understanding of the QCD phase diagram at zero baryon density has been achieved from the lattice studies. While the early universe transition from the QGP to the hadron phase is now known to be an analytic crossover and not a real phase transition, it is observed that the chiral dynamics will have observable effects in the crossover region. One of the remnant effects of the chiral symmetry would be the presence of a critical end-point. The search for the still elusive critical endpoint is one of the focus areas of lattice studies, and the important developments made so far in this area are reviewed.

While QCD at small baryon density is reasonably well understood with lattice techniques, the physics of baryon rich systems cannot be formulated satisfactorily on the lattice due to the infamous sign-problem. A lot of conceptual work, in understanding the severity and consequences of the sign problem as well algorithmic developments in circumventing this problem is ongoing which is one of the challenging problems in the field of lattice thermodynamics.

Acknowledgments

Sayantan Sharma would like to thank all the members of the Theoretical Physics Group at Bielefeld University, and in particular, Frithjof Karsch, Edwin Laermann, Olaf Kaczmarek, and Christian Schmidt for a lot of discussions that have enriched the author's knowledge about QCD thermodynamics and lattice QCD. The author expresses gratitude to Edwin Laermann for a careful reading of the paper and his helpful suggestions and Toru Kojo and Amaresh Jaiswal for their constructive criticism that has led to a considerable improvement of this paper. The author also acknowledges Rajiv Gavai and Rajamani Narayanan for very enjoyable collaboration, in which the author learnt many aspects of the subject.

References

- [1] C. Hoelbling, "Light hadron spectroscopy and pseudoscalar decay constants," in *International Symposium on Lattice Field Theory (LATTICE '10)*, PoS, Villasimius, Italy, June 2010, <http://arxiv.org/abs/1102.0410>.
- [2] F. Karsch, "Lattice QCD at finite temperature: a status report," *Zeitschrift Fur Physik C*, vol. 38, no. 1, pp. 147–155, 1988, <http://arxiv.org/abs/1302.3028>.
- [3] P. F. Kolb and U. W. Heinz, *Quark Gluon Plasma 3*, Edited by R. C. Hwa and X.-N. Wang, World Scientific, Singapore, 2003.
- [4] M.-P. Lombardo, "High Temperature QCD," in *International Symposium on Lattice Field Theory (LATTICE '12)*, PoS, Cairns, Australia, June 2012.
- [5] G. Aarts, "Complex Langevin dynamics and other approaches at finite chemical potential," in *International Symposium on Lattice Field Theory (LATTICE '12)*, PoS, Cairns, Australia, June 2012.
- [6] S. B. Nielsen and M. Ninomiya, "Absence of neutrinos on a lattice: (I). Proof by homotopy theory," *Nuclear Physics B*, vol. 185, no. 1, pp. 20–40, 1981.
- [7] K. G. Wilson, "Confinement of quarks," *Physical Review D*, vol. 10, no. 8, pp. 2445–2459, 1974.
- [8] J. Kogut and L. Susskind, "Hamiltonian formulation of Wilson's lattice gauge theories," *Physical Review D*, vol. 11, no. 2, pp. 395–408, 1975.
- [9] C. Morningstar and M. J. Peardon, "Analytic smearing of SU(3) link variables in lattice QCD," *Physical Review D*, vol. 69, no. 5, Article ID 054501, 9 pages, 2004.
- [10] E. Follana, Q. Mason, and C. Davies, "Highly improved staggered quarks on the lattice, with applications to charm physics," *Physical Review D*, vol. 75, Article ID 054502, 23 pages, 2007, <http://arxiv.org/abs/hep-lat/0610092>.
- [11] J. Engels, R. Joswig, F. Karsch, E. Laermann, M. Lütgemeier, and B. Petersson, "Thermodynamics of four-flavour QCD with improved staggered fermions," *Physics Letters B*, vol. 396, pp. 210–216, 1997, <http://arxiv.org/abs/0911.2215>.
- [12] K. Orginos and D. Toussaint, "Testing improved actions for dynamical Kogut-Susskind quarks," *Physical Review D*, vol. 59, no. 1, Article ID 014501, 7 pages, 1998, <http://arxiv.org/abs/hep-lat/9805009>.
- [13] J. F. Lagae and D. K. Sinclair, "Improved staggered quark actions with reduced flavor symmetry violations for lattice QCD," *Physical Review D*, vol. 59, no. 1, Article ID 014511, 6 pages, 1998, <http://arxiv.org/abs/hep-lat/9806014>.
- [14] G. P. Lepage, "Flavor-symmetry restoration and Symanzik improvement for staggered quarks," *Physical Review D*, vol. 59, no. 7, Article ID 074502, 4 pages, 1999, <http://arxiv.org/abs/hep-lat/9809157>.
- [15] R. Narayanan and H. Neuberger, "Chiral fermions on the lattice," *Physical Review Letters*, vol. 71, no. 20, pp. 3251–3254, 1993.
- [16] H. Neuberger, "Exactly massless quarks on the lattice," *Physics Letters B*, vol. 417, no. 1-2, pp. 141–144, 1998.
- [17] D. B. Kaplan, "A method for simulating chiral fermions on the lattice," *Physics Letters B*, vol. 288, no. 3-4, pp. 342–347, 1992.
- [18] M. Cheng, S. Ejiri, P. Hegde et al., "Equation of state for physical quark masses," *Physical Review D*, vol. 81, no. 5, Article ID 054504, 8 pages, 2010, <http://arxiv.org/abs/0911.2215>.
- [19] S. Borsanyi, G. Endrodi, Z. Fodor et al., "The QCD equation of state with dynamical quarks," *Journal of High Energy Physics*, vol. 2010, article 77, 2010, <http://arxiv.org/abs/1007.2580>.
- [20] G. Cossu et al., "Finite temperature QCD at fixed Q with overlap fermions," in *International Symposium on Lattice Field Theory (LATTICE '10)*, PoS, Villasimius, Italy, June 2010, <http://arxiv.org/abs/1011.0257>.
- [21] S. Borsanyi, Y. Delgado, S. Durr et al., "QCD thermodynamics with dynamical overlap fermions," *Physics Letters B*, vol. 713, no. 3, pp. 342–346, 2012, <http://arxiv.org/abs/1204.4089>.
- [22] M. Cheng, N. H. Christ, P. Hegde et al., "The finite temperature QCD using 2+1 flavors of domain wall fermions at $N_t = 8$," *Physical Review D*, vol. 81, no. 5, Article ID 054510, 14 pages, 2010.
- [23] T.-W. Chiu, "Simulation of lattice QCD with domain-wall fermions," In press, <http://arxiv.org/abs/1302.6918>.
- [24] A. Bazavov, C. Bernard, C. DeTar et al., "Nonperturbative QCD simulations with 2+1 flavors of improved staggered quarks," *Reviews of Modern Physics*, vol. 82, no. 2, pp. 1349–1417, 2010.
- [25] G. Boyd, J. Engels, F. Karsch et al., "Thermodynamics of SU(3) lattice gauge theory," *Nuclear Physics B*, vol. 469, no. 3, pp. 419–444, 1996, <http://arxiv.org/abs/hep-lat/9602007>.
- [26] F. Karsch, "Lattice QCD at finite temperature and density," *Nuclear Physics B-Proceedings Supplements*, vol. 83, Article ID 990900, p. 14, 2000, <http://arxiv.org/abs/hep-lat/9909006>.

- [27] F. Karsch, E. Laermann, and C. Schmidt, “The chiral critical point in 3-flavour QCD,” *Physics Letters B*, vol. 520, p. 41, 2001.
- [28] P. de Forcrand and O. Philipsen, “The QCD phase diagram for three degenerate flavors and small baryon density,” *Nuclear Physics B*, vol. 673, pp. 170–186, 2003.
- [29] D. Smith and C. Schmidt, “On the universal critical behavior in 3-flavor QCD,” in *International Symposium on Lattice Field Theory (LATTICE '11)*, vol. 216 of *PoS*, 2011.
- [30] X.-Y. Jin and R. D. Mawhinney, “Lattice QCD with 12 degenerate quark flavors,” in *International Symposium on Lattice Field Theory (LATTICE '11)*, *PoS*, 2011.
- [31] M. Cheng et al., “Study of the finite temperature transition in 3-flavor QCD,” *Physical Review D*, vol. 75, no. 3, Article ID 034506, 11 pages, 2007.
- [32] M. D’Elia, A. Di Giacomo, and C. Pica, “Two flavor QCD and confinement,” *Physical Review D*, vol. 27, no. 11, Article ID 114510, 27 pages, 2005, <http://arxiv.org/abs/hep-lat/0503030>.
- [33] C. Bonati, G. Cossu, M. D’Elia, A. Di Giacomo, and C. Pica, “A test of first order scaling in $N_f=2$ QCD: a progress report,” in *International Symposium on Lattice Field Theory (LATTICE '08)*, vol. 204 of *PoS*, July 2008, <http://arxiv.org/abs/0901.3231>.
- [34] S. Ejiri, F. Karsch, E. Laermann et al., “Magnetic equation of state in (2+1)-flavor QCD,” *Physical Review D*, vol. 80, no. 9, Article ID 094505, 16 pages, 2009, <http://arxiv.org/abs/0909.5122>.
- [35] S. Gavin, A. Gocksch, and R. D. Pisarski, “QCD and the chiral critical point,” *Physical Review D*, vol. 49, no. 7, pp. R3079–R3082, 1994.
- [36] C. Bernard, T. Burch, C. DeTar et al., “QCD thermodynamics with three flavors of improved staggered quarks,” *Physical Review D*, vol. 71, no. 3, Article ID 034504, 11 pages, 2005.
- [37] M. Cheng, N. Christ, S. Datta et al., “Transition temperature in QCD,” *Physical Review D*, vol. 74, no. 5, Article ID 054507, 15 pages, 2006.
- [38] Y. Aoki, G. Endrodi, Z. Fodor, S. D. Katz, and K. K. Szabó, “The order of the quantum chromodynamics transition predicted by the standard model of particle physics,” *Nature*, vol. 443, no. 7112, pp. 675–678, 2006.
- [39] H. Saito, S. Ejiri, S. Aoki et al., “Phase structure of finite temperature QCD in the heavy quark region,” *Physical Review D*, vol. 84, no. 5, Article ID 054502, 9 pages, 2011.
- [40] H.-T. Ding, A. Bazavov, P. Hegde, F. Karsch, S. Mukherjee, and P. Petreczky, “Exploring phase diagram of $N_f = 3$ QCD at $\mu = 0$ with HISQ fermions,” in *International Symposium on Lattice Field Theory (LATTICE '11)*, vol. 191 of *PoS*, 2011, <http://arxiv.org/abs/1111.0185>.
- [41] G. Endrodi, Z. Fodor, S. D. Katz, and K. K. Szabo, “The nature of the finite temperature QCD transition as a function of the quark masses,” in *International Symposium on Lattice Field Theory (LATTICE '07)*, vol. 182, 2007.
- [42] S. L. Adler, “Axial-vector vertex in spinor electrodynamics,” *Physical Review*, vol. 177, no. 5, pp. 2426–2438, 1969.
- [43] J. Bell and R. Jackiw, “A PCAC puzzle: $\pi^0 \rightarrow \gamma\gamma$ in the σ -model,” *Nuovo Cimento A*, vol. 60, no. 1, pp. 47–61, 1969.
- [44] K. Fujikawa, “Path integral for gauge theories with fermions,” *Physical Review D*, vol. 21, no. 10, p. 2848, 1980.
- [45] R. D. Pisarski and F. Wilczek, “Remarks on the chiral phase transition in chromodynamics,” *Physical Review D*, vol. 29, no. 2, pp. 338–341, 1984.
- [46] J. Engels, J. Fingberg, F. Karsch, D. Miller, and M. Weber, “Non-perturbative thermodynamics of $SU(N)$ gauge theories,” *Physics Letters B*, vol. 252, no. 4, pp. 625–630, 1990.
- [47] L. Giusti and H. B. Meyer, “Thermal momentum distribution from path integrals with shifted boundary conditions,” *Physical Review Letters*, vol. 106, no. 13, Article ID 131601, 4 pages, 2011, <http://arxiv.org/abs/1011.2727>.
- [48] P. Petreczky, “On trace anomaly in 2+1 flavor QCD,” in *International Symposium on Lattice Field Theory (LATTICE '12)*, vol. 069 of *PoS*, 2012, <http://arxiv.org/abs/1211.1678>.
- [49] A. Bazavov, T. Bhattacharya, M. Cheng et al., “The chiral and deconfinement aspects of the QCD transition,” *Physical Review D*, vol. 85, no. 5, Article ID 054503, 37 pages, 2012, <http://arxiv.org/abs/1111.1710>.
- [50] S. Borsanyi, G. Endrodi, Z. Fodor et al., “The QCD equation of state and the effects of the charm,” in *International Symposium on Lattice Field Theory (LATTICE '11)*, vol. 201 of *PoS*, July 2011, <http://arxiv.org/abs/1204.0995>.
- [51] T. Umeda, S. Aoki, S. Ejiri et al., “Equation of state in 2+1 flavor QCD with improved Wilson quarks by the fixed scale approach,” *Physical Review D*, vol. 85, no. 9, Article ID 094508, 11 pages, 2012, <http://arxiv.org/abs/1202.4719>.
- [52] F. Burger, M. Kirchner, M. Muller-Preussker et al., “Pseudo-critical temperature and thermal equation of state from $N_f = 2$ twisted mass lattice QCD,” in *Proceedings of the 30th International Symposium on Lattice Field Theory (LATTICE '12)*, vol. 68 of *PoS*, Cairns, Australia, June 2012, <http://arxiv.org/abs/1212.0982>.
- [53] P. de Forcrand and O. Philipsen, “The chiral critical line of $N_f = 2 + 1$ QCD at zero and non-zero baryon density,” *Journal of High Energy Physics*, vol. 2007, article 77, 2007, <http://arxiv.org/abs/hep-lat/0607017>.
- [54] M. Cheng, N. Christ, S. Datta et al., “QCD equation of state with almost physical quark masses,” *Physical Review D*, vol. 77, no. 1, Article ID 014511, 20 pages, 2008.
- [55] S. Borsanyi, Z. Fodor, C. Hoelbling et al., “Is there still any Tc mystery in lattice QCD? Results with physical masses in the continuum limit III,” *Journal of High Energy Physics*, vol. 2010, article 73, 2010.
- [56] M. Creutz, *PoS CONFINEMENT8*, article 016, 2008.
- [57] C. Bernard, M. Golterman, Y. Shamir, and S. R. Sharpe, “t Hooft vertices, partial quenching, and rooted staggered QCD,” *Physical Review D*, vol. 77, no. 11, Article ID 114504, 11 pages, 2008.
- [58] S. Borsanyi, S. Durr, Z. Fodor et al., “QCD thermodynamics with continuum extrapolated Wilson fermions I,” *Journal of High Energy Physics*, vol. 2012, article 126, 2012, <http://arxiv.org/abs/1205.0440>.
- [59] Z. Fodor, S. D. Katz, and K. K. Szabo, “Dynamical overlap fermions, results with hybrid Monte-Carlo algorithm,” *Journal of High Energy Physics*, vol. 2004, article 3, 2004.
- [60] S. Aoki, H. Fukaya, S. Hashimoto, and T. Onogi, “Finite volume QCD at fixed topological charge,” *Physical Review D*, vol. 76, no. 5, Article ID 054508, 11 pages, 2007.
- [61] A. Bazavov, T. Bhattacharya, M. I. Buchoff et al., “The chiral transition and $U(1)_A$ symmetry restoration from lattice QCD using Domain Wall Fermions,” *Physical Review D*, vol. 86, no. 9, Article ID 094503, 30 pages, 2012, <http://arxiv.org/abs/1205.3535>.
- [62] F. Karsch, E. Laermann, and A. Peikert, “The Pressure in 2, 2+1 and 3 Flavour QCD,” *Physics Letters B*, vol. 478, no. 4, pp. 447–455, 2000, <http://arxiv.org/abs/hep-lat/0002003>.

- [63] P. Petreczky, “Review of recent highlights in lattice calculations at finite temperature and finite density,” in *Proceedings of the Xth Quark Confinement and the Hadron Spectrum conference (ConfinementX '12)*, vol. 28 of *PoS*, 2012, <http://arxiv.org/abs/1301.6188>.
- [64] M. Laine and Y. Schroeder, “Quark mass thresholds in QCD thermodynamics,” *Physical Review D*, vol. 73, no. 8, Article ID 085009, 13 pages, 2006, <http://arxiv.org/abs/hep-ph/0603048>.
- [65] M. Cheng, “Charm quarks and the QCD equation of state,” in *International Symposium on Lattice Field Theory (LATTICE '07)*, vol. 173 of *PoS*, 2007.
- [66] C. DeTar, L. Levkova, S. Gottlieb et al., “QCD thermodynamics with nonzero chemical potential at $N_f = 6$ and effects from heavy quarks,” *Physical Review D*, vol. 81, no. 11, Article ID 114504, 17 pages, 2010, <http://arxiv.org/abs/1003.5682>.
- [67] M. Hindmarsh and O. Philipsen, “WIMP dark matter and the QCD equation of state,” *Physical Review D*, vol. 71, no. 8, Article ID 087302, 4 pages, 2005, <http://arxiv.org/abs/hep-ph/0501232>.
- [68] M. McGuigan and W. Soldner, “QCD cosmology from the lattice equation of state,” In press, <http://arxiv.org/abs/0810.0265>.
- [69] J. Engels, S. Holtmann, T. Mendes, and T. Schulze, “Equation of state and Goldstone-mode effects of the three-dimensional $O(2)$ model,” *Physics Letters B*, vol. 492, no. 1-2, pp. 219–227, 2000.
- [70] D. Toussaint, “Scaling functions for $O(4)$ in three dimensions,” *Physical Review D*, vol. 55, no. 1, pp. 362–366, 1997.
- [71] J. Engels and T. Mendes, “Goldstone-mode effects and scaling function for the three-dimensional $O(4)$ model,” *Nuclear Physics B*, vol. 572, no. 1-2, pp. 289–304, 2000.
- [72] P. Hasenfratz, V. Laliena, and F. Niedermayer, “The index theorem in QCD with a finite cut-off,” *Physics Letters B*, vol. 427, no. 1-2, pp. 125–131, 1998.
- [73] Z. Lin, *PoS Lattice*, article 084, 2012.
- [74] S. Aoki, H. Fukaya, and Y. Taniguchi, “Chiral symmetry restoration, the eigenvalue density of the Dirac operator, and the axial $U(1)$ anomaly at finite temperature,” *Physical Review D*, vol. 86, no. 11, Article ID 114512, 18 pages, 2012.
- [75] G. Cossu, S. Aoki, S. Hashimoto et al., “Topological susceptibility and axial symmetry at finite temperature,” in *International Symposium on Lattice Field Theory (LATTICE '11)*, vol. 188 of *PoS*, July 2011, <http://arxiv.org/abs/1204.4519>.
- [76] G. Cossu, S. Aoki, H. Fukaya et al., “Finite temperature study of the axial $U(1)$ symmetry on the lattice with overlap fermion formulation,” <http://arxiv.org/abs/1304.6145>.
- [77] H. Ohno, U. M. Heller, F. Karsch, and S. Mukherjee, “ $U_A(1)$ breaking at finite temperature from the Dirac spectrum with the dynamical HISQ action,” in *The 30th International Symposium on Lattice Field Theory (LATTICE '12)*, vol. 95 of *PoS*, Cairns, Australia, June 2012, <http://arxiv.org/abs/1211.2591>.
- [78] B. B. Brandt, A. Francis, H. B. Meyer, H. Wittig, and O. Philipsen, “QCD thermodynamics with two flavours of Wilson fermions on large lattices,” in *Proceedings of the 30th International Symposium on Lattice Field Theory (LATTICE '12)*, vol. 073 of *PoS*, Cairns, Australia, June 2012, <http://arxiv.org/abs/1210.6972>.
- [79] P. Hasenfratz and F. Karsch, “Chemical potential on the lattice,” *Physics Letters B*, vol. 125, no. 4, pp. 308–310, 1983.
- [80] J. Kogut, H. Matsuoka, M. Stone et al., “Chiral symmetry restoration in baryon rich environments,” *Nuclear Physics B*, vol. 225, no. 1, pp. 93–122, 1983.
- [81] R. V. Gavai, “Chemical potential on the lattice,” *Physical Review D*, vol. 32, no. 2, pp. 519–521, 1985.
- [82] D. T. Son and M. A. Stephanov, “QCD at finite isospin density,” *Physical Review Letters*, vol. 86, no. 4, pp. 592–595, 2001, <http://arxiv.org/abs/hep-ph/0005225>.
- [83] K. Splittorff, “Lattice simulations of QCD with $\mu_B=0$ versus phase quenched QCD,” <http://arxiv.org/abs/hep-lat/0505001>.
- [84] J. Han and M. A. Stephanov, “A random matrix study of the QCD sign problem,” *Physical Review D*, vol. 78, no. 5, Article ID 054507, 7 pages, 2008, <http://arxiv.org/abs/0805.1939>.
- [85] M. P. Lombardo, K. Splittorff, and J. J. M. Verbaarschot, “Distributions of the phase angle of the fermion determinant in QCD,” *Physical Review D*, vol. 80, no. 5, Article ID 054509, 19 pages, 2009.
- [86] I. M. Barbour, S. E. Morrison, E. G. Klepfish, J. B. Kogut, and M.-P. Lombardo, “Results on finite density QCD,” *Nuclear Physics B*, vol. 60, pp. 220–234, 1998, <http://arxiv.org/abs/hep-lat/9705042>.
- [87] Z. Fodor and S. D. Katz, “A new method to study lattice QCD at finite temperature and chemical potential,” *Physics Letters B*, vol. 534, no. 1–4, pp. 87–92, 2002, <http://xxx.lanl.gov/abs/hep-lat/0104001>.
- [88] Z. Fodor, S. D. Katz, and K. K. Szabo, “The QCD equation of state at nonzero densities: lattice result,” *Physics Letters B*, vol. 568, no. 1-2, pp. 73–77, 2003.
- [89] F. Csikor, G. I. Egri, Z. Fodor, S. D. Katz, K. K. Szabo, and A. I. Toth, “Equation of state at finite temperature and chemical potential, lattice QCD results,” *Journal of High Energy Physics*, vol. 2004, article 46, 2004.
- [90] C. R. Allton, S. Ejiri, S. J. Hands et al., “Equation of state for two flavor QCD at nonzero chemical potential,” *Physical Review D*, vol. 68, no. 1, Article ID 014507, 2003.
- [91] C. Allton, M. Doring, S. Ejiri et al., “Thermodynamics of two flavor QCD to sixth order in quark chemical potential,” *Physical Review D*, vol. 71, no. 5, Article ID 054508, 20 pages, 2005, <http://arxiv.org/abs/hep-lat/0501030>.
- [92] R. V. Gavai and S. Gupta, “Pressure and non-linear susceptibilities in QCD at finite chemical potentials,” *Physical Review D*, vol. 68, no. 3, Article ID 034506, 6 pages, 2003, <http://arxiv.org/abs/hep-lat/0303013>.
- [93] J. Engels, O. Kaczmarek, F. Karsch, and E. Laermann, “The quenched limit of lattice QCD at non-zero baryon number,” *Nuclear Physics B*, vol. 558, no. 1-2, pp. 307–326, 1999, <http://arxiv.org/abs/hep-lat/9903030>.
- [94] K.-F. Liu, “Finite density algorithm in lattice QCD—a canonical ensemble approach,” *International Journal of Modern Physics B*, vol. 16, no. 14, Article ID 020202, p. 2017, 2002, <http://arxiv.org/abs/hep-lat/0202026>.
- [95] A. Alexandru, M. Faber, I. Horvath, and K.-F. Liu, “Lattice QCD at finite density via a new canonical approach,” *Physical Review D*, vol. 72, no. 11, Article ID 114513, 13 pages, 2005.
- [96] P. de Forcrand and S. Kratochvila, “Finite density QCD with a canonical approach,” *Nuclear Physics B*, vol. 153, no. 1, pp. 62–67, 2006, <http://arxiv.org/abs/hep-lat/0602024>.
- [97] M. G. Alford, A. Kapustin, and F. Wilczek, “Imaginary chemical potential and finite fermion density on the lattice,” *Physical Review D*, vol. 59, no. 5, Article ID 054502, 4 pages, 1999, <http://arxiv.org/abs/hep-lat/9807039>.
- [98] M.-P. Lombardo, “Finite density (might well be easier) at finite temperature,” *Nuclear Physics B*, vol. 83, p. 375, 2000, <http://arxiv.org/abs/hep-lat/9908006>.
- [99] M. D’Elia and M.-P. Lombardo, “QCD thermodynamics from an imaginary μ_B : results on the four flavor lattice model,”

- Physical Review D*, vol. 70, no. 7, Article ID 074509, 11 pages, 2004.
- [100] P. de Forcrand and O. Philipsen, “The QCD phase diagram for small densities from imaginary chemical potential,” *Nuclear Physics B*, vol. 642, no. 1-2, pp. 290–306, 2002, <http://arxiv.org/abs/hep-lat/0205016>.
- [101] G. Parisi, “On complex probabilities,” *Physics Letters B*, vol. 131, no. 4–6, pp. 393–395, 1983.
- [102] F. Karsch and H. W. Wyld, “Complex langevin simulation of the SU(3) spin model with nonzero chemical potential,” *Physical Review Letters*, vol. 55, no. 21, pp. 2242–2245, 1985.
- [103] J. Ambjorn and S.-K. Yang, “Numerical problems in applying the langevin equation to complex effective actions,” *Physics Letters B*, vol. 165, no. 1–3, pp. 140–146, 1985.
- [104] G. Aarts, F. A. James, E. Seiler, and I. O. Stamatescu, “Adaptive stepsize and instabilities in complex Langevin dynamics,” *Physics Letters B*, vol. 687, no. 2-3, pp. 154–159, 2010, <http://arxiv.org/abs/0912.0617>.
- [105] G. Aarts, E. Seiler, and I. O. Stamatescu, “Complex Langevin method: when can it be trusted?” *Physical Review D*, vol. 81, no. 5, Article ID 054508, 13 pages, 2010.
- [106] S. Chandrasekharan, “Fermion bag approach to lattice field theories,” *Physical Review D*, vol. 82, no. 2, Article ID 025007, 15 pages, 2010.
- [107] C. Gattringer, “Flux representation of an effective Polyakov loop model for QCD thermodynamics,” *Nuclear Physics B*, vol. 850, no. 2, pp. 242–252, 2011.
- [108] R. V. Gavai and S. Gupta, “Lattice QCD predictions for shapes of event distributions along the freezeout curve in heavy-ion collisions,” *Physics Letters B*, vol. 696, no. 5, pp. 459–463, 2011.
- [109] A. Bazavov, H.-T. Ding, P. Hegde et al., “Freeze-out conditions in heavy Ion collisions from QCD thermodynamics,” *Physical Review Letters*, vol. 109, no. 19, Article ID 192302, 5 pages, 2012, <http://arxiv.org/abs/1208.1220>.
- [110] M. Golterman, Y. Shamir, and B. Svetitsky, “Breakdown of staggered fermions at nonzero chemical potential,” *Physical Review D*, vol. 74, no. 7, Article ID 071501, 5 pages, 2006, <http://arxiv.org/abs/hep-lat/0602026>.
- [111] M. Luscher, “Exact chiral symmetry on the lattice and the Ginsparg-Wilson relation,” *Physics Letters B*, vol. 428, no. 3-4, pp. 342–345, 1998.
- [112] J. Mandula, “Note on the lattice fermion chiral symmetry group,” In press, <http://arxiv.org/abs/0712.0651>.
- [113] J. C. R. Bloch and T. Wettig, “Overlap dirac operator at nonzero chemical potential and random matrix theory,” *Physical Review Letters*, vol. 97, no. 1, Article ID 012003, 4 pages, 2006.
- [114] D. Banerjee, R. V. Gavai, and S. Sharma, “Thermodynamics of the ideal overlap quarks on the lattice,” *Physical Review D*, vol. 78, no. 1, Article ID 014506, 13 pages, 2008, and PoS (LATTICE 2008), 177.
- [115] R. Narayanan and S. Sharma, “Introduction of the chemical potential in the overlap formalism,” *Journal of High Energy Physics*, vol. 2011, article 151, 2011.
- [116] R. V. Gavai and S. Sharma, “Exact chiral invariance at finite density on the lattice,” *Physics Letters B*, vol. 716, no. 3–5, pp. 446–449, 2012.
- [117] S. Jeon and V. Koch, “Charged particle ratio fluctuation as a signal for quark-gluon plasma,” *Physical Review Letters*, vol. 85, no. 10, pp. 2076–2079, 2000.
- [118] M. Asakawa, U. W. Heinz, and B. Muller, “Fluctuation probes of quark deconfinement,” *Physical Review Letters*, vol. 85, no. 10, pp. 2072–2075, 2000, <http://arxiv.org/abs/hep-ph/0003169>.
- [119] S. A. Gottlieb, W. Liu, D. Toussaint, R. L. Renken, and R. L. Sugar, “Quark-number susceptibility of high-temperature QCD,” *Physical Review Letters*, vol. 59, no. 20, pp. 2247–2250, 1987.
- [120] A. Bazavov, T. Bhattacharya, C. E. DeTar et al., “Fluctuations and Correlations of net baryon number, electric charge, and strangeness: a comparison of lattice QCD results with the hadron resonance gas model,” *Physical Review D*, vol. 86, no. 3, Article ID 034509, 15 pages, 2012, <http://arxiv.org/abs/1203.0784>.
- [121] S. Borsanyi, Z. Fodor, S. D. Katz et al., “Fluctuations of conserved charges at finite temperature from lattice QCD,” *Journal of High Energy Physics*, vol. 2012, article 138, 2012, <http://arxiv.org/abs/1112.4416>.
- [122] J. O. Andersen, S. Mogliacci, N. Su, and A. Vuorinen, “Quark number susceptibilities from resummed perturbation theory,” *Physical Review D*, vol. 87, no. 7, Article ID 074003, 6 pages, 2013, <http://arxiv.org/abs/1210.0912>.
- [123] N. Haque, M. G. Mustafa, and M. Strickland, “Quark number susceptibilities from two-loop hard thermal loop perturbation theory,” In press <http://arxiv.org/abs/1302.3228>.
- [124] S. Gupta, “Finding the critical end point of QCD: lattice and experiment,” in *Proceedings of Critical Point and Onset of Deconfinement (CPOD '09)*, vol. 25 of PoS, 2009, <http://arxiv.org/abs/0909.4630>.
- [125] F. Karsch and K. Redlich, “Probing freeze-out conditions in heavy ion collisions with moments of charge fluctuations,” *Physics Letters B*, vol. 695, no. 1–4, pp. 136–142, 2011.
- [126] V. Koch, A. Majumder, and J. Randrup, “Baryon-strangeness correlations: a diagnostic of strongly interacting matter,” *Physical Review Letters*, vol. 95, no. 18, Article ID 182301, 4 pages, 2005.
- [127] R. V. Gavai and S. Gupta, “Fluctuations, strangeness, and quasiquarks in heavy-ion collisions from lattice QCD,” *Physical Review D*, vol. 73, no. 1, Article ID 014004, 11 pages, 2006.
- [128] J. Cleymans, H. Oeschler, K. Redlich, and S. Wheaton, “Comparison of chemical freeze-out criteria in heavy-ion collisions,” *Physical Review C*, vol. 73, no. 3, Article ID 034905, 10 pages, 2006.
- [129] M. Kitazawa and M. Asakawa, “Revealing baryon number fluctuations from proton number fluctuations in relativistic heavy ion collisions,” *Physical Review C*, vol. 85, no. 2, Article ID 021901, 5 pages, 2012, <http://arxiv.org/abs/1107.2755>.
- [130] M. Asakawa and K. Yazaki, “Chiral restoration at finite density and temperature,” *Nuclear Physics A*, vol. 504, no. 4, pp. 668–684, 1989.
- [131] J. Berges and K. Rajagopal, “Color superconductivity and chiral symmetry restoration at non-zero baryon density and temperature,” *Nuclear Physics B*, vol. 538, no. 1-2, pp. 215–232, 1999.
- [132] A. M. Halasz, A. D. Jackson, R. E. Shrock, M. A. Stephanov, and J. J. M. Verbaarschot, “Phase diagram of QCD,” *Physical Review D*, vol. 58, no. 9, Article ID 096007, 11 pages, 1998.
- [133] Z. Fodor and S. D. Katz, “Critical point of QCD at finite T and μ , lattice results for physical quark masses,” *Journal of High Energy Physics*, vol. 2004, article 50, 2004.
- [134] M. Stephanov, K. Rajagopal, and E. Shuryak, “Signatures of the tricritical point in QCD,” *Physical Review Letters*, vol. 81, no. 22, pp. 4816–4819, 1998.
- [135] R. V. Gavai and S. Gupta, “The critical end point of QCD,” *Physical Review D*, vol. 71, no. 11, Article ID 114014, 21 pages, 2005, <http://arxiv.org/abs/hep-lat/0412035>.

- [136] R. V. Gavai and S. Gupta, “QCD at finite chemical potential with six time slices,” *Physical Review D*, vol. 78, no. 11, Article ID 114503, 15 pages, 2008, <http://arxiv.org/abs/0806.2233>.
- [137] S. Datta, R. V. Gavai, and S. Gupta, “The QCD Critical Point: marching towards continuum,” *Nuclear Physics A*, vol. 904-905, pp. 883c–886c, 2013, <http://arxiv.org/abs/1210.6784>.
- [138] A. Li, A. Alexandru, and K.-F. Liu, “Critical point of $N_f = 3$ QCD from lattice simulations in the canonical ensemble,” *Physical Review D*, vol. 84, no. 7, Article ID 071503, 5 pages, 2011, <http://arxiv.org/abs/1103.3045>.
- [139] Ph. de Forcrand and O. Philipsen, “The Chiral critical point of $N_f = 3$ QCD at finite density to the order $(\mu/T)^4$,” *Journal of High Energy Physics*, vol. 2008, article 12, 2008.
- [140] J. T. Mościcki, M. Woś, M. Lamanna, P. de Forcrand, and O. Philipsen, “Lattice QCD thermodynamics on the Grid,” *Computer Physics Communications*, vol. 181, no. 10, pp. 1715–1726, 2010, <http://arxiv.org/abs/0911.5682>.
- [141] O. Philipsen, “Status of the QCD phase diagram from lattice calculations,” *Acta Physica Polonica*, vol. 5, p. 825, 2012, <http://arxiv.org/abs/1111.5370>.
- [142] O. Kaczmarek, F. Karsch, E. Laermann et al., “The phase boundary for the chiral transition in (2+1)-flavor QCD at small values of the chemical potential,” *Physical Review D*, vol. 83, no. 1, Article ID 014504, 9 pages, 2011, <http://arxiv.org/abs/1011.3130>.
- [143] G. Endrodi, Z. Fodor, S. Katz, and K. Szabo, “The QCD phase diagram at nonzero quark density,” *Journal of High Energy Physics*, vol. 2011, article 1, 2011, <http://arxiv.org/abs/1102.1356>.
- [144] M. A. Stephanov, “Non-gaussian fluctuations near the QCD critical point,” *Physical Review Letters*, vol. 102, no. 3, Article ID 032301, 4 pages, 2009.
- [145] M. Stephanov, K. Rajagopal, and E. Shuryak, “Event-by-event fluctuations in heavy ion collisions and the QCD critical point,” *Physical Review D*, vol. 60, no. 11, Article ID 114028, 32 pages, 1999.
- [146] S. Ejiri, F. Karsch, E. Laermann, and C. Schmidt, “The isentropic equation of state of 2-flavor QCD,” *Physical Review D*, vol. 73, no. 5, Article ID 054506, 6 pages, 2006, <http://arxiv.org/abs/hep-lat/0512040>.
- [147] Sz. Borsanyi, G. Endrodi, Z. Fodor et al., “QCD equation of state at nonzero chemical potential: continuum results with physical quark masses at order μ^2 ,” *Journal of High Energy Physics*, vol. 1208, article 53, 2012, <http://arxiv.org/abs/1204.6710>.
- [148] T. Takaishi, P. de Forcrand, and A. Nakamura, “Equation of State at Finite Density from Imaginary Chemical Potential,” in *International Symposium on Lattice Field Theory (LATTICE '09)*, vol. 198 of *PoS*, 2009, <http://arxiv.org/abs/1002.0890>.
- [149] R. V. Gavai and S. Sharma, “Faster method of computation of lattice quark number susceptibilities,” *Physical Review D*, vol. 85, no. 5, Article ID 054508, 8 pages, 2012.

Research Article

Internal Cumulants for Femtoscopy with Fixed Charged Multiplicity

H. C. Eggers¹ and B. Buschbeck²

¹ Department of Physics, University of Stellenbosch, Stellenbosch 7602, South Africa

² Institut für Hochenergiephysik, Nikolsdorfergasse 18, 1050 Vienna, Austria

Correspondence should be addressed to H. C. Eggers; eggers@physics.sun.ac.za

Received 14 March 2013; Accepted 20 May 2013

Academic Editor: Edward Sarkisyan-Grinbaum

Copyright © 2013 H. C. Eggers and B. Buschbeck. This is an open access article distributed under the Creative Commons Attribution License, which permits unrestricted use, distribution, and reproduction in any medium, provided the original work is properly cited.

A detailed understanding of all effects and influences on higher-order correlations is essential. At low charged multiplicity, the effect of a non-Poissonian multiplicity distribution can significantly distort correlations. Evidently, the reference samples with respect to which correlations are measured should yield a null result in the absence of correlations. We show how the careful specification of desired properties necessarily leads to an average-of-multinomials reference sample. The resulting internal cumulants and their averaging over several multiplicities fulfill all requirements of correctly taking into account non-Poissonian multiplicity distributions as well as yielding a null result for uncorrelated fixed- N samples. Various correction factors are shown to be approximations at best. Careful rederivation of statistical variances and covariances within the frequentist approach yields errors for cumulants that differ from those used so far. We finally briefly discuss the implementation of the analysis through a multiple event buffer algorithm.

1. Introduction and Motivation

The understanding of hadronic collisions is now considered an essential baseline for ultrarelativistic heavy-ion collisions. Given the correspondingly low final-state multiplicities, there are significant deviations, even for inclusive samples, from assumptions commonly made both in the general theory and in the definition of experimentally measured quantities such as a non-Gaussian shape of the correlation function and non-Poissonian multiplicity distributions. Constraints such as energy-momentum conservation [1, 2] would also play a role in at least some regions of phase space. Multiplicity-class and fixed-multiplicity analysis differ increasingly from Poissonian and inclusive distributions, and with the good statistics now available, measurements have become accurate enough to require proper understanding and treatment of these assumptions and deviations, which play an ever larger role with increasing order of correlation.

1.1. Correlations as a Function of Charged Multiplicity. There are a number of reasons to study correlations at fixed charged multiplicity N or, if necessary, charged-multiplicity classes.

Firstly, the physics of multiparticle correlations will evidently change with N , and indeed the multiplicity dependence of various quantities such as the intercept parameter and radii associated with Gaussian parametrisations is under constant scrutiny [3–12]. Measurement of many observables as a function of multiplicity class, regarded a proxy for centrality dependence, has been routine for years. Corresponding theoretical considerations, for example, in the quantum optical approach go back a long time [13]. Secondly, correlations for fixed- N are the building blocks which are combined into multiplicity-class and inclusive correlations [14].

However, such fixed- N correlations have been beset by an inconsistency in that they are nonzero even when the underlying sample is uncorrelated and do not integrate to zero either. This has been recognised from the start [15], and various attempts have been made to fix the problem.

Combining events from several fixed- N subsamples into multiplicity classes does not solve these problems. To quote an early reference [16], “*Averaging over multiplicities inextricably mixes the properties of the correlation mechanism with those of the multiplicity distribution. Instead, the study of*

correlations at fixed multiplicities allows one to separate both effects and to investigate the behaviour of correlation functions as a function of multiplicity.” Under the somewhat inappropriate name of “Long-Range Short-Range correlations” [15, 17], an attempt was made to separate these multiplicity-mixing correlations from the fixed- N correlations, but the inconsistencies inherent in the underlying fixed- N correlations were not addressed. Building on [18], we propose doing so now.

1.2. Cumulants in Multiparticle Physics. Multiparticle cumulants have entered the mainstream of analysis, as shown by the following incomplete list of topics. In principle, the considerations presented in this paper would apply to any, and all such cumulants to the degree that their reference distribution deviates from a Poisson process or that the type of particle kept fixed differs from the particle being analysed.

Integrated cumulants of multiplicity distributions have a long history in multiparticle physics [19]. Second-order differential cumulants, normally termed “correlation functions,” have likewise been ubiquitous for decades [7] both in charged-particles correlations [15] and in femtoscopy since they provide information on spacetime characteristics of the emitting sources, most recently at the LHC [10, 11, 20]. Differential three-particle cumulants generically measure asymmetries in source geometry and exchange amplitude phases [21]. They also provide consistency checks [22] and a tool to disentangle the coherence parameter from other effects [23, 24]. Three-particle cumulants are also sensitive to differences between longitudinal and transverse correlation lengths in the Lund model [25]. Inclusive three-particle cumulants have been measured, albeit with different methodologies, in, for example, hadronic [26–29], leptonic [30–33], and nuclear collisions [34–37]. They play a central role in direct QCD-based calculations [38–40], in some recent theory, and in experiment of azimuthal and jet-like correlations [41–45]. Net-charge and other charge combinations are considered probes of the QCD phase diagram [46–48]. Cumulants of order 4 or higher are, of course, increasingly difficult to measure, and so early investigations were largely confined to their scale dependence [49–52]. The large event samples now available have, however, made feasible measurements of fourth- and higher-order cumulants in other variables as proposed in [13, 53–56] as, for example, recently measured by ALICE [57]. Reviews of femtoscopy theory range from [58–60] to more recent ones such as [8].

1.3. Outline of This Paper. It has long been obvious that the root cause of the problems and inconsistencies set out in Section 1.1 was the reference sample [61]. Insofar as cumulants are concerned, the solution was outlined in [18] as a subtraction of the reference sample cumulant from the measured one; important pieces of the puzzle were, however, still missing at that stage. In this paper, we clarify and extend the basic concept of internal cumulants and consider in detail the case of second- and third-order differential cumulants in the invariant $Q = \sqrt{-(p_1 - p_2)^2}$ for fixed charged multiplicity N . The method may be implemented for other variables without much fuss.

A second cornerstone of the present paper is the recognition that the n particles which enter a correlation analysis are usually only a subset of the N charged pions. While in the case of charged-particle correlations, all N particles are used in the analysis, Bose-Einstein correlations, for example, would use only the $n \equiv n_+$ positive pions (and, in a separate analysis, only the $n_- = N - n_+$ negatives). In addition, there may be reasons to restrict the analysis itself to subregions of the total acceptance Ω in which N was measured, as exemplified in this paper by restriction to a “good azimuthal region” subinterval around the beam axis, $\mathcal{A} \subset [0, 2\pi]$, in which detection efficiency is high. \mathcal{A} can, however, be reinterpreted generically as any restriction in momentum space compared to Ω and/or as a selection such as charge or particle species. Even when setting $\mathcal{A} = \Omega$, that is, doing the femtoscopy analysis in the full acceptance, n still does not equal N but fluctuates around $N/2$. The trivial observation that $n \neq N$ fundamentally changes the analysis: *identical-particle correlations at fixed N and charged-particle correlations at fixed N require different definitions.*

As we will show, ad hoc prescriptions such as simply inserting prefactors or implementing event mixing using only events of the same N do alleviate the effect of the overall non-Poissonian multiplicity distribution in part but fail to remove them completely. The same issues will, of course, arise in any other correlation type of, for example, nonidentical particles or net charge correlations. The formalism set out here can be easily extended to such cases. A refined version of the abovementioned Long-Range-Short-Range method, which we term “Averaged-Internal” cumulants, will be presented in Section 5. Along the way, we document in Section 2 extended versions of the particle counters [62, 63] which we need as the basis for correlation studies and in Section 4 demonstrate from first principles that statistical errors for cumulants used so far have captured only some of the terms and with partly incorrect prefactors. Section 6 outlines the implementation of event mixing for fixed- N analysis. While experimental results will be published elsewhere, preliminary results in Figures 2 and 3 show that, in third and even in second order, corrections due to proper treatment of fixed- N reference samples can be large.

2. Raw Data, Counters, and Densities

2.1. Raw Data. The starting point for experimental correlation analysis is the inclusive sample \mathcal{S} , made up of \mathcal{E} events $a = 1, \dots, \mathcal{E}$. Each event consists of a varying number of final-state elementary particles and photons; for our purposes, we consider only the $N(a)$ charged pions of event a in Ω , the maximal acceptance region used. Each pion $i = 1, \dots, N(a)$ is characterised by a data vector $(\mathbf{P}_i^a, \mathbf{s}_i^a, \mathbf{e}_i^a)$ containing its measured information, including the three components of its momentum, $\mathbf{P}_i^a = (p_{ix}^a, p_{iy}^a, p_{iz}^a)$ or $(y_i^a, \phi_i^a, p_{ti}^a)$, while its discrete attributes such as mass and charge are captured in a data vector \mathbf{s}_i^a of discrete values; for the moment, we will consider only the charge, $\mathbf{s}_i^a \rightarrow c_i^a$. From the sample’s raw data, we can immediately find derived quantities such as the total charged multiplicity $N(a)$ and the total transverse energy, and such derived quantities are hence considered

part of the raw data. The list of particle attributes should be augmented by an error vector \mathbf{e}_i^a containing the measurement errors for each track, but we will not consider detector resolution errors here. In summary, the inclusive data sample is fully described in terms of $\mathcal{S} = \{\mathbf{P}^a, \mathbf{s}^a\}_{a=1}^{\mathcal{E}}$ consisting of lists of vectors in continuous and discrete spaces

$$\mathbf{P}^a = \{\mathbf{P}_1^a, \mathbf{P}_2^a, \dots, \mathbf{P}_{N(a)}^a\}, \quad \mathbf{s}^a = \{\mathbf{s}_1^a, \mathbf{s}_2^a, \dots, \mathbf{s}_{N(a)}^a\}. \quad (1)$$

2.2. Data after Conditioning and Cuts. For a particular analysis, the inclusive sample is invariably subdivided and modified through “conditioning,” the statistics terminology for semiinclusive or triggered analysis. From the total sample of events, a subsample is selected according to some restriction or precondition. In our case, this conditioning proceeds in the following steps.

(i) *Conditioning into Fixed- N Subsamples.* For the fixed-multiplicity analyses that form the subject of this paper, \mathcal{S} is subdivided into a set of fixed- N subsamples \mathcal{S}_N , each of which contains only events a whose measured multiplicity $N(a)$ is equal to the constant N characterising $\mathcal{S}_N = \{\mathbf{P}^a, \mathbf{s}^a \mid \delta(N, N(a))\}$, $N = 0, 1, 2, \dots$. We use the vertical bar \mid here and everywhere in the usual sense of “conditioning” whereby the events in sample \mathcal{S}_N must satisfy the condition that their charged multiplicity must equal the specified constant N , denoted in this case by the Kronecker delta $\delta(N, N(a))$. Quantities to the right of the vertical bar are generally considered known and fixed, while quantities to the left of the bar are variable or unknown. The number of events in \mathcal{S}_N equals the δ -restricted sum over the inclusive sample,

$$\mathcal{E}_N = \sum_{a=1}^{\mathcal{E}} \delta(N, N(a)), \quad \sum_{N=0}^{\infty} \mathcal{E}_N = \mathcal{E}. \quad (2)$$

The usual multiplicity distribution is the list of relative frequencies,¹

$$\mathcal{R}_N = \frac{\mathcal{E}_N}{\mathcal{E}}, \quad \sum_{N=0}^{\infty} \mathcal{R}_N = 1. \quad (3)$$

While desirable, it is not easy to measure the total multiplicity of final-state charged pions, a quantity which approximately tracks the variation in the physics. Choosing charged pions measured within the maximal detector acceptance $N = N(\Omega)$ as marker is in any case only an approximation because it excludes charged particles outside the primary cuts and also ignores final-state particles other than charged pions. Nevertheless, we expect N to be a reasonable measure of the multiplicity dependence of the physics. Alternatively, the multiplicity density in pseudorapidity at central rapidities $dN/d\eta$ can be used as a model-dependent proxy for N .

(ii) *Azimuthal Cut.* While $N(a)$ is the charged multiplicity measured in Ω , there is no *a priori* reason why the correlation analysis itself may not be conducted within a restricted part $\mathcal{A} \subset \Omega$ of momentum space within which the actual analysis is done. In the case of the UA1 detector from which the data used in the examples below was drawn, \mathcal{A} refers to azimuthal

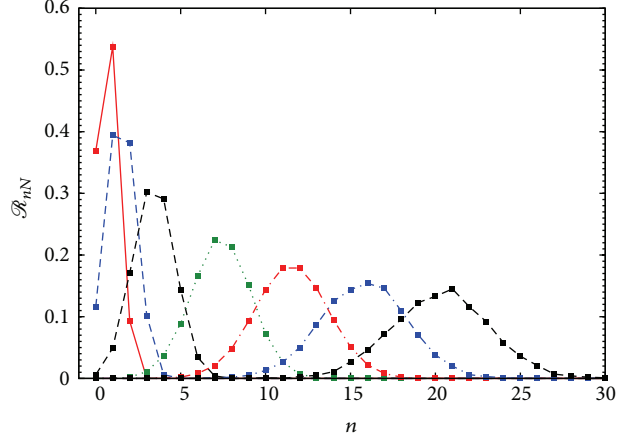


FIGURE 1: Conditional normalised multiplicity distribution (relative frequency) of the number of positive pions n in restricted azimuthal region $\mathcal{A} = \{20^\circ \leq |\phi| \leq 160^\circ\}$ for, respectively, fixed charged multiplicity $N = 3, 5, 10, 20, 30, 40,$ and 50 , for the UA1 dataset used in [65]. In accordance with (6), $\langle n \rangle_N = 0.39N$.

regions within which measurement efficiency was high, and pions found in the low-efficiency azimuthal regions were excluded. Correspondingly, the multiplicity $n(a)$ which enters the correlation analysis itself differs from $N(a)$ and will, for a given fixed- N , fluctuate with relative frequency

$$\mathcal{R}_{nN} = \frac{\mathcal{E}_{nN}}{\mathcal{E}_N} \quad \text{for each fixed } N = 1, 2, \dots, \quad (4)$$

where \mathcal{E}_{nN} is the number of events for which $N(a) = N$ and $n(a) = n$. The outcome space for $n(a)$ will depend on its definition; in the present case where only positive (or only negative) pions within \mathcal{A} are used in the analysis, it will be $[0, 1, \dots, N]$ so that the relative frequency is normalised by

$$\sum_{n=0}^N \mathcal{R}_{nN} = 1 \quad \forall N = 1, 2, \dots \quad (5)$$

With approximate charge conservation $n_+ \approx n_-$, we expect the fixed- N average for positive (or negative) pions in \mathcal{A} to hover around

$$\langle n \rangle_N \approx \frac{N}{2} \frac{\text{volume of } \mathcal{A}}{\text{volume of } \Omega}. \quad (6)$$

An example of the resulting relative frequencies (conditional normalised multiplicity distributions) is shown in Figure 1. Since $n \leq N$, these conditional multiplicity distributions are almost always sub-Poissonian, that is, narrower than a Poisson distribution with the same $\langle n \rangle_N$ would be.

(iii) *Generalisation.* While in this paper the analysis will be carried out for the $n(a)$ positive pions of event a falling into \mathcal{A} , the same formalism obviously applies to negative pions and may equally refer to any other particles such as kaons, baryons, and photons, in any combination which depends on N . There is no *a priori* connection between the definitions of N and n .

(iv) *Identical-Particle versus Multispecies Analysis.* While we do not develop the formalism for correlations between two or

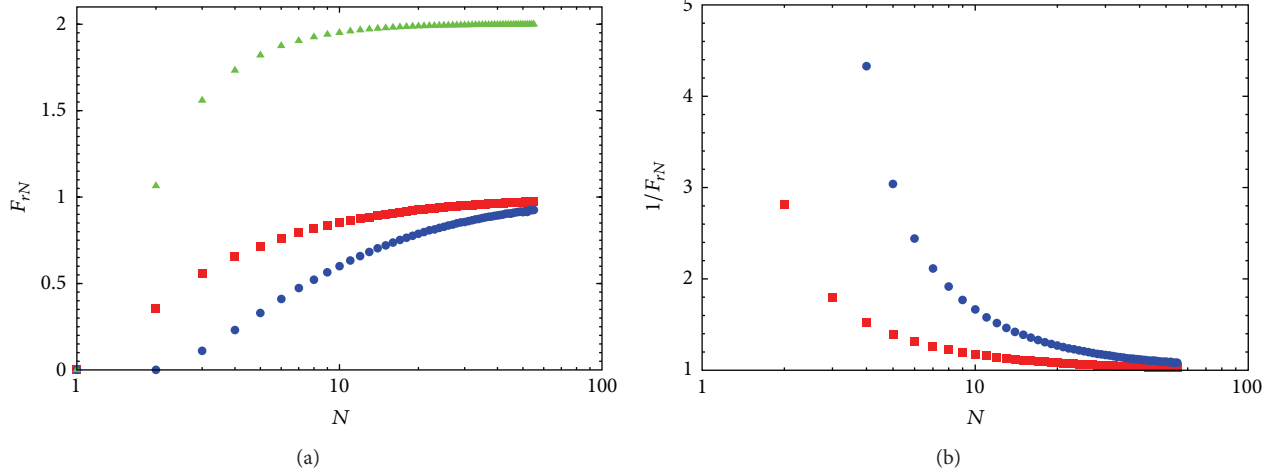


FIGURE 2: (a) Correction factors $F_{2N} = \langle n(n-1) \rangle_N / \langle n \rangle_N^2$ (red squares) and $F_{3N} = \langle n(n-1)(n-2) \rangle_N / \langle n \rangle_N^3$ (blue circles) as defined in (57) as well as G_{3N} (green triangles) of (70), for the UA1 dataset used in [65]. (b) Inverse factors as used in the normalisation of internal cumulants (74)-(75) and (83)-(84).

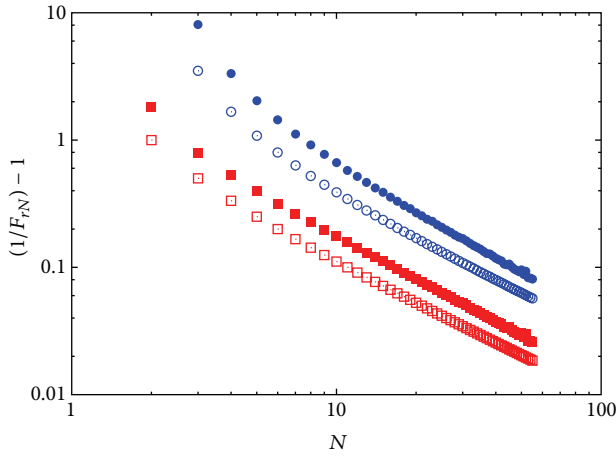


FIGURE 3: Comparison, for the same UA1 data and cuts, of $(1/F_{2N}) - 1$ (red filled squares), $(1/F_{3N}) - 1$ (blue filled circles), and both averages over n for fixed N , with prefactors $[N^2/N(N-1)] - 1$ (red open squares) and $[N^3/N(N-1)(N-2)] - 1$ (blue open circles). The Poissonian limit is represented by zero on the y -axis; that is, 100 times the y -scale represents the percentage deviation from the Poissonian limit.

three particles of different species or charge, the methodology developed here can be easily modified to deal with such cases. For example, positive-negative pion combinations and “charge balance correlations” [64] can be handled by inserting delta functions $\delta(c, c_i^a)$, where c is the desired charge and c_i^a the measured charge of track i in event a , into the definitions of the counters in Section 2.3.

2.3. Counters and Densities for Fixed N . This section is based on an old formalism [53, 62, 63] which must, however, be updated to accommodate the issues being considered here. The basic building block of correlation analysis is the *counter*;

it is a particular projection of the raw data particularly suited to the construction of histograms. Eventwise counters $\hat{\rho}$ for a given event a are averaged to give sample counters ρ .

We take the simple case where event a contains $N(a)$ tracks with three-momenta $\mathbf{P}^a = \{\mathbf{P}_1^a, \dots, \mathbf{P}_{N(a)}^a\}$, no discrete attributes \mathbf{s} and no further cuts or selection. For each point \mathbf{p}_1 in momentum space, only that particle i (if any) whose momentum \mathbf{P}_i^a happens to coincide with \mathbf{p} is to be counted,

$$\hat{\rho}(\mathbf{p}_1 | \mathbf{P}^a) = \sum_{i=1}^{N(a)} \delta(\mathbf{p}_1 - \mathbf{P}_i^a). \quad (7)$$

Such counters always appear under an integral over some region of the \mathbf{P} space, so that the delta functions fulfill the purpose of counting those particles falling within that region. Alternatively, one can consider the delta functions here and below to represent small nonoverlapping intervals around the specified momenta. The integral over the full momentum space Ω yields

$$\int_{\Omega} d\mathbf{p}_1 \hat{\rho}(\mathbf{p}_1 | \mathbf{P}^a) = N(a), \quad (8)$$

while an integral over some subspace or bin $\Omega_b \subset \Omega$ will yield the number of particles of event a in bin Ω_b . The second-order eventwise counter for event a is²

$$\hat{\rho}(\mathbf{p}_1, \mathbf{p}_2 | \mathbf{P}^a) = \sum_{i \neq j=1}^{N(a)} \delta(\mathbf{p}_1 - \mathbf{P}_i^a) \delta(\mathbf{p}_2 - \mathbf{P}_j^a), \quad (9)$$

with the inequality $i \neq j$ ensuring that a single particle is not counted as a “pair.” The counter integrates to

$$\int_{\Omega} d\mathbf{p}_1 d\mathbf{p}_2 \hat{\rho}(\mathbf{p}_1, \mathbf{p}_2 | \mathbf{P}^a) = N(a)(N(a) - 1) = N(a)^2, \quad (10)$$

using the falling factorial notation

$$N^{\underline{r}} = N(N-1)\cdots(N-r+1) \quad r = 1, 2, \dots, \quad (11)$$

as contrasted to the rising factorial (Pochhammer symbol) $N^{\overline{r}} = N(N+1)\cdots(N+r-1)$. The single-particle counter is a projection of $\widehat{\rho}(\mathbf{p}_1, \mathbf{p}_2 | \mathbf{P}^a)$ because

$$\int_{\Omega} d\mathbf{p}_2 \widehat{\rho}(\mathbf{p}_1, \mathbf{p}_2 | \mathbf{P}^a) = [N(a) - 1] \widehat{\rho}(\mathbf{p}_1 | \mathbf{P}^a). \quad (12)$$

The most general eventwise counter which enters the exclusive cross-section for events with charged multiplicity $N(a)$

$$\begin{aligned} & \widehat{\rho}(\mathbf{p}_1, \mathbf{p}_2, \dots, \mathbf{p}_{N(a)} | \mathbf{P}^a) \\ &= \sum_{i_1 \neq i_2 \neq \dots \neq i_{N(a)}=1}^{N(a)} \prod_{d=1}^{N(a)} \delta(\mathbf{p}_d - \mathbf{P}_{i_d}^a) \end{aligned} \quad (13)$$

fully describes the event, including any and all correlations between its particles. It integrates to the factorial of the event multiplicity

$$\int_{\Omega} d\mathbf{p}_1 d\mathbf{p}_2 \cdots d\mathbf{p}_{N(a)} \widehat{\rho}(\mathbf{p}_1, \mathbf{p}_2, \dots, \mathbf{p}_{N(a)} | \mathbf{P}^a) = N(a)! \quad (14)$$

and contains all counters of lower order by projection. An r th-order counter $\widehat{\rho}(\mathbf{p}_1, \mathbf{p}_2, \dots, \mathbf{p}_r | \mathbf{P}^a)$ is zero whenever there are more observation points than particles being observed, $r > N(a)$.³

To distinguish eventwise counters for nonfixed- N from eventwise counters for fixed N , we define the separate eventwise counter for fixed N by specifying an additional Kronecker delta,

$$\begin{aligned} & \widehat{\rho}(\mathbf{p}_1, \dots, \mathbf{p}_r | \mathbf{P}^a, N) \\ &= \delta(N, N(a)) \sum_{i_1 \neq \dots \neq i_r}^N \prod_d \delta(\mathbf{p}_d - \mathbf{P}_{i_d}^a) \end{aligned} \quad (15)$$

$r = 1, 2, \dots, N.$

While the counters and densities defined above and below are clearly frame dependent, it is easy to define corresponding Lorentz-invariant versions by supplementing each delta function in 3 momenta with the corresponding energy; thus (7) would become, for example,

$$\widehat{\rho}(\mathbf{p}_1 | \mathbf{P}^a) = \sum_{i=1}^{N(a)} E(\mathbf{p}_1) \delta(\mathbf{p}_1 - \mathbf{P}_i^a), \quad (16)$$

with $E(\mathbf{p}_1) = E_1 = \sqrt{\mathbf{p}_1^2 + m^2}$ the on-shell energy, and in general

$$\begin{aligned} & \widehat{\rho}(\mathbf{p}_1, \mathbf{p}_2, \dots, \mathbf{p}_r | \mathbf{P}^a) \\ &= \sum_{i_1 \neq i_2 \neq \dots \neq i_r=1}^{N(a)} \prod_{d=1}^{N(a)} E_d \delta(\mathbf{p}_d - \mathbf{P}_{i_d}^a) \end{aligned}$$

$r = 1, \dots, N(a),$

$$\begin{aligned} & \widehat{\rho}(\mathbf{p}_1, \dots, \mathbf{p}_r | \mathbf{P}^a, N) \\ &= \delta(N, N(a)) \sum_{i_1 \neq \dots \neq i_r}^N \prod_d E_d \delta(\mathbf{p}_d - \mathbf{P}_{i_d}^a) \end{aligned}$$

$r = 1, \dots, N,$

(17)

which are manifestly invariant. Because such counters and densities are, however, always integrated over some Ω_b by $\prod_d (d\mathbf{p}_d / E_d)$, the additional factors E_d always cancel and play no role on this level of analysis and will be ignored for the time being. The bin boundaries of Ω_b do, however, remain frame dependent.

Charge-, spin-, or species-specific counters are defined in the same way, that is, by supplying appropriate Kronecker deltas to the counters; for example, the particle counter for pions with charge c_1 at \mathbf{p}_1 for fixed N is

$$\widehat{\rho}(\mathbf{p}_1 | c_1, \mathbf{P}^a, N) = \delta(N, N(a)) \sum_{i=1}^{N(a)} \delta(c_1, c_i^a) \delta(\mathbf{p}_1 - \mathbf{P}_i^a), \quad (18)$$

while the two-particle counter for charge combination (c_1, c_2) at momenta $(\mathbf{p}_1, \mathbf{p}_2)$ for any N is, for example,

$$\begin{aligned} & \widehat{\rho}(\mathbf{p}_1, \mathbf{p}_2 | c_1, c_2, \mathbf{P}^a) \\ &= \sum_{i,j=1}^{N(a)} \delta(c_1, c_i^a) \delta(\mathbf{p}_1 - \mathbf{P}_i^a) \delta(c_2, c_j^a) \delta(\mathbf{p}_2 - \mathbf{P}_j^a). \end{aligned} \quad (19)$$

In contrast to (18), charge counters rather than particle counters would be

$$\widehat{\rho}_c(\mathbf{p}_1 | c_1, \mathbf{P}^a) = \sum_{i=1}^{N(a)} c_1 \delta(c_1, c_i^a) \delta(\mathbf{p}_1 - \mathbf{P}_i^a), \quad (20)$$

so that $\widehat{\rho}_c(\mathbf{p}_1 | +1, \mathbf{P}^a) + \widehat{\rho}_c(\mathbf{p}_1 | -1, \mathbf{P}^a)$ represents the net charge of event a at \mathbf{p}_1 . The two-particle counter for charges (c_1, c_2) at momenta $(\mathbf{p}_1, \mathbf{p}_2)$ is

$$\begin{aligned} & \widehat{\rho}^{c_1 c_2} \equiv \widehat{\rho}_c(\mathbf{p}_1, \mathbf{p}_2 | c_1, c_2, \mathbf{P}^a) \\ &= \sum_{i,j=1}^{N(a)} c_1 \delta(c_1, c_i^a) \delta(\mathbf{p}_1 - \mathbf{P}_i^a) c_2 \delta(c_2, c_j^a) \delta(\mathbf{p}_2 - \mathbf{P}_j^a), \end{aligned} \quad (21)$$

and “charge flow” correlations can be constructed from this (for rapidities (y, y') in the case of [66]) such as

$$\Phi(y, y') = - \left\langle \sum_{i \neq j} c_i^a c_j^a \delta(y - Y_i^a) \delta(y' - Y_j^a) \right\rangle, \quad (22)$$

which can be expressed as $\Phi = \langle \widehat{\rho}^{+-} + \widehat{\rho}^{+--} - \widehat{\rho}^{++-} - \widehat{\rho}^{---} \rangle$ and the related “charge balance functions” described in for example [46].

Returning to the fixed- N case, eventwise counters will usually be combined with similar events to form event averages. The simplest average is the fixed- N density for the subsample of fixed \mathcal{S}_N ,

$$\rho(\mathbf{p}_1 | \mathcal{S}_N) = \frac{1}{\mathcal{E}_N} \sum_a \hat{\rho}(\mathbf{p}_1 | \mathbf{P}^a, N), \quad (23)$$

with the Kronecker delta in (15) ensuring that only events in \mathcal{S}_N are considered, so we need not further specify the individual terms or limits of the a -sum. Using (2), it is immediately clear that

$$\int_{\Omega} d\mathbf{p}_1 \rho(\mathbf{p}_1 | \mathcal{S}_N) = N \quad (24)$$

compared to the integral over the corresponding eventwise counter

$$\int_{\Omega} d\mathbf{p} \hat{\rho}(\mathbf{p} | \mathbf{P}^a, N) = N \delta(N, N(a)) \quad (25)$$

and to the integral (8); similarly

$$\begin{aligned} \int_{\Omega} d\mathbf{p}_1 \cdots d\mathbf{p}_r \rho(\mathbf{p}_1, \dots, \mathbf{p}_r | \mathcal{S}_N) \\ = N(N-1) \cdots (N-r+1) = N^{\underline{r}}. \end{aligned} \quad (26)$$

The inclusive averaged density $\rho(\mathbf{p}_1 | \mathcal{S})$ is the weighted average over all N of the fixed- N averages,

$$\rho(\mathbf{p}_1 | \mathcal{S}) = \sum_{N=1}^{\infty} \mathcal{R}_N \rho(\mathbf{p}_1 | \mathcal{S}_N). \quad (27)$$

Using (3), (15), and (23), this can be written as

$$\rho(\mathbf{p}_1 | \mathcal{S}) = \frac{1}{\mathcal{E}} \sum_a \sum_i \delta(\mathbf{p}_1 - \mathbf{P}_i^a), \quad (28)$$

and for general $r = 1, 2, \dots$

$$\begin{aligned} \rho(\mathbf{p}_1, \dots, \mathbf{p}_r | \mathcal{S}) &= \sum_{N=r}^{\infty} \mathcal{R}_N \rho(\mathbf{p}_1, \dots, \mathbf{p}_r | \mathcal{S}_N) \\ &= \frac{1}{\mathcal{E}} \sum_a \sum_{i_1 \neq \dots \neq i_r} \prod_{d=1}^r \delta(\mathbf{p}_d - \mathbf{P}_{i_d}^a), \end{aligned} \quad (29)$$

keeping in mind that $\hat{\rho}(\mathbf{p}_1, \dots, \mathbf{p}_r | \mathcal{S}_N)$ will be zero whenever $N(a) < r$. The integral of any r th-order inclusive averaged density is the r th-order factorial moment of the multiplicity distribution,

$$\int_{\Omega} d\mathbf{p}_1 \cdots d\mathbf{p}_r \rho(\mathbf{p}_1, \dots, \mathbf{p}_r | \mathcal{S}) = \sum_{N=r}^{\infty} \mathcal{R}_N N^{\underline{r}} = \langle N^{\underline{r}} \rangle, \quad (30)$$

with simple angle brackets denoting inclusive averaging.

The averaged counters are of course directly related to the traditional definitions in terms of cross-sections. If \mathcal{L} is the integrated luminosity of incoming particles, the topological

cross-section is $\sigma_N = \mathcal{E}_N/\mathcal{L}$, the inelastic cross-section is $\sigma_I = \mathcal{E}/\mathcal{L}$, and the inclusive cross-section is $\sigma_{\text{incl}} = \sum_N N \sigma_N = \langle N \rangle \sigma_I$ while the relative frequency (multiplicity distribution) can be written as usual as $\mathcal{R}_N = \sigma_N/\sigma_I$. The relation between the differential cross sections and our counters is

$$\begin{aligned} \rho_{\text{incl}}(\mathbf{p}_1, \dots, \mathbf{p}_N) &= \rho(\mathbf{p}_1, \dots, \mathbf{p}_N | \mathcal{S}) = \frac{1}{\sigma_I} \frac{d^{3N} \sigma_{\text{incl}}}{d\mathbf{p}_1 \cdots d\mathbf{p}_N}, \\ \rho(\mathbf{p}_1, \dots, \mathbf{p}_N | \mathcal{S}_N) &= \frac{1}{\sigma_N} \frac{d^{3N} \sigma_{\text{excl}}}{d\mathbf{p}_1 \cdots d\mathbf{p}_N}, \end{aligned} \quad (31)$$

and so as usual inclusive and exclusive densities are related by [14]

$$\begin{aligned} \rho(\mathbf{p}_1, \dots, \mathbf{p}_N | \mathcal{S}) \\ = \sum_{N=r}^{\infty} \frac{\mathcal{R}_N}{(N-r)!} \int \rho(\mathbf{p}_1, \dots, \mathbf{p}_N | \mathcal{S}_N) d\mathbf{p}_{r+1} \cdots d\mathbf{p}_N, \end{aligned} \quad (32)$$

while the semi-inclusive cross sections and counters follow by the usual projections.

2.4. Counters and Densities for Fixed (N, n) . Our choice of a basic counter is motivated by the experimental situation set out in Section I: we wish to work in event subsamples of fixed total charged multiplicity $N(a)$ in the entire momentum space Ω but do the differential correlation analysis using only those pions n which fall into the restricted space \mathcal{A} and of a particular charge $+1$ or -1 . This requires the use of “sub-subsamples” for which both N and n are kept fixed,

$$\mathcal{S}_{nN} = \{\mathbf{P}^a, \text{ with } a \text{ constrained by } \delta(n, n_+(a)) \delta(N, N(a))\}, \quad (33)$$

with $n_+(a)$ being the number of positive pions of event a in \mathcal{A} , and eventwise sub-subsample counters

$$\begin{aligned} \hat{\rho}(\mathbf{p}_1, \dots, \mathbf{p}_r | n, N, \mathbf{P}^a) \\ = \delta(n, n_+(a)) \delta(N, N(a)) \end{aligned} \quad (34)$$

$$\times \sum_{i_1 \neq \dots \neq i_r=1}^n \delta(\mathbf{p}_1 - \mathbf{P}_{i_1}^a) \cdots \delta(\mathbf{p}_r - \mathbf{P}_{i_r}^a).$$

As in (2), the number of events in a sub-subsample $\mathcal{E}_{nN} = \sum_a \delta(n, n_+(a)) \delta(N, N(a))$ enters the relevant event averages

$$\rho(\mathbf{p}_1, \dots, \mathbf{p}_r | \mathcal{S}_{nN}) = \frac{1}{\mathcal{E}_{nN}} \sum_a \hat{\rho}(\mathbf{p}_1, \dots, \mathbf{p}_r | n, N, \mathbf{P}^a), \quad (35)$$

where once again the double Kronecker deltas in (34) ensure selection of events in \mathcal{S}_{nN} only. Integrals of the counters over

the good-azimuth region \mathcal{A} yield, for the eventwise and \mathcal{S}_{nN} -averaged counters,

$$\begin{aligned} & \int_{\mathcal{A}} d\mathbf{p}_1 \cdots d\mathbf{p}_r \hat{\rho}(\mathbf{p}_1, \dots, \mathbf{p}_r | n, N, \mathbf{P}^a) \\ &= n^r \delta(n, n_+(a)) \delta(N, N(a)), \quad (36) \\ & \int_{\mathcal{A}} d\mathbf{p}_1 \cdots d\mathbf{p}_r \rho(\mathbf{p}_1, \dots, \mathbf{p}_r | \mathcal{S}_{nN}) = n^r. \end{aligned}$$

Bearing in mind that observation points $\mathbf{p}_1, \mathbf{p}_2, \dots$ refer to positive pions in \mathcal{A} only, the event-averaged counters for fixed N but any n are given by the average weighted in terms of the relative frequency $\mathcal{R}_{nN} = \mathcal{E}_{nN} / \mathcal{E}_N$,

$$\begin{aligned} \rho(\mathbf{p}_1, \dots, \mathbf{p}_r | \mathcal{S}_N) &= \sum_{n=r}^N \mathcal{R}_{nN} \rho(\mathbf{p}_1, \dots, \mathbf{p}_r | \mathcal{S}_{nN}) \\ &= \langle \rho(\mathbf{p}_1, \dots, \mathbf{p}_r | \mathcal{S}_{nN}) \rangle_N, \quad (37) \end{aligned}$$

for $r = 1, 2, 3, \dots$, which integrate to

$$\int_{\mathcal{A}} d\mathbf{p}_1 \cdots d\mathbf{p}_r \rho(\mathbf{p}_1, \dots, \mathbf{p}_r | \mathcal{S}_N) = \langle n^r \rangle_N. \quad (38)$$

3. Construction of Correlation Quantities

3.1. Criteria. Correlation measurements of any sort are only meaningful if a reference baseline signifying ‘‘independence’’ or ‘‘lack of correlation’’ is defined quantitatively; indeed, many different kinds of correlations may be defined and measured on the same data, depending on which particular physical and mathematical scenario is considered to be known or trivial and taken to be the baseline [61]. In our case, we require the reference distribution to have the following properties.

- (1) *The number of charged pions in all phase space N is an important parameter as a measure of possibly different physics, but only the n positive pions in \mathcal{A} are to be considered in the differential analysis.*
- (2) *For a given (N, n) , the momenta of the reference density $\rho^{\text{ref}}(\mathbf{p}_1, \dots, \mathbf{p}_r | \mathcal{S}_{nN})$ should be mutually independent for any order $1 \leq r \leq n$. This and the previous requirement imply that the reference should be a n multinomial distributed over continuous momentum space; see Section 3.2.1.*
- (3) *Given fixed N , the reference density $\rho^{\text{ref}}(\mathbf{p}_1, \dots, \mathbf{p}_r | \mathcal{S}_N)$ must reproduce the n -multiplicity structure of the sub-samples \mathcal{S}_{nN} as embodied in \mathcal{R}_{nN} . As set out further in Section 3.2.2, this translates into an average of multinomials,*

$$\begin{aligned} \rho^{\text{ref}}(\mathbf{p}_1, \dots, \mathbf{p}_r | \mathcal{S}_N) &= \sum_{n=r}^N \mathcal{R}_{nN} \rho^{\text{mult}}(\mathbf{p}_1, \dots, \mathbf{p}_r | \boldsymbol{\alpha}, \mathcal{S}_{nN}) \\ &= \langle \rho^{\text{mult}}(\mathbf{p}_1, \dots, \mathbf{p}_r | \boldsymbol{\alpha}, \mathcal{S}_{nN}) \rangle_N. \quad (39) \end{aligned}$$

(4) *The reference density should reproduce the measured one-particle density in momentum space. This can in principle be satisfied by three different expressions for the multinomial’s parameters $\boldsymbol{\alpha}$: see Section 3.2.3.*

(5) *Measures of correlation must reduce to zero even on a differential basis whenever the data is, in fact, uncorrelated. While this may seem self-evident, this requirement is often ignored or not satisfied in the literature. We address the resulting proper baseline through the use of internal cumulants in Section 3.3.*

(6) *The measure of correlation should be insensitive to the one-particle distribution. This is addressed as usual by normalisation; see Section 3.3.*

3.2. The Reference Distribution

3.2.1. Multinomials in Discrete and Continuous Spaces. Before (39) can be developed further, it is necessary to take a detour into discrete outcome spaces before tackling the continuous outcome space defined by \mathbf{p} and \mathbf{P}^a . The reason is that multinomial distributions for continuous arguments \mathbf{p} can be written only as a limit of the discrete precursor.

Let there be bins Ω_b , $b = 1, \dots, B$ with the corresponding set of Bernoulli probabilities $\boldsymbol{\alpha} = \{\alpha(b)\}_{b=1}^B$ of a single particle falling into bin Ω_b , normalised by $\sum_b \alpha(b) = 1$. Independent tossing of n particles into these bins results in the multinomial for the bin counts $\mathbf{n} = \{n_b\}_{b=1}^B$,

$$p(\mathbf{n} | \boldsymbol{\alpha}, n) = n! \prod_{b=1}^B \frac{\alpha(b)^{n_b}}{n_b!}, \quad (40)$$

with normalisation

$$\sum_{U(\mathbf{n})} p(\mathbf{n} | \boldsymbol{\alpha}, n) = 1, \quad (41)$$

where the sum must be taken over the ‘‘universal set’’

$$U(\mathbf{n}) = \left\{ \mathbf{n} \mid n_b \geq 0; \sum_b n_b = n \right\}. \quad (42)$$

The multivariate factorial moment generating function (FMGF) for this multinomial for the set of source parameters $\boldsymbol{\lambda} = \{\lambda(b)\}_{b=1}^B$ can be solved in closed form,

$$\begin{aligned} Q^{\text{mult}}(\boldsymbol{\lambda} | \boldsymbol{\alpha}, n) &= \sum_U p(\mathbf{n} | \boldsymbol{\alpha}, n) \prod_b (1 - \lambda(b))^{n_b} \\ &= \left[1 - \sum_b \lambda(b) \alpha(b) \right]^n. \quad (43) \end{aligned}$$

The FMGF $Q(\boldsymbol{\lambda})$ can generally be used to find multivariate factorial moments $\rho(b_1, b_2, \dots, b_r)$ and factorial cumulants

$\kappa(b_{i_1}, b_{i_2}, \dots, b_{i_r})$ for any selection of bins $(b_{i_1}, b_{i_2}, \dots, b_{i_r}) \in (1, \dots, B)$, including repeated indices, by differentiation

$$\rho(b_{i_1}, b_{i_2}, \dots, b_{i_r}) = \frac{(-1)^r \partial^r Q(\boldsymbol{\lambda})}{\partial \lambda(b_{i_1}) \partial \lambda(b_{i_2}) \cdots \partial \lambda(b_{i_r})} \Big|_{\boldsymbol{\lambda}=0}, \quad (44)$$

$$\kappa(b_{i_1}, b_{i_2}, \dots, b_{i_r}) = \frac{(-1)^r \partial^r \ln Q(\boldsymbol{\lambda})}{\partial \lambda(b_{i_1}) \partial \lambda(b_{i_2}) \cdots \partial \lambda(b_{i_r})} \Big|_{\boldsymbol{\lambda}=0}.$$

For the multinomial case (43), the factorial moments and cumulants are therefore

$$\rho^{\text{mult}}(b_{i_1}, b_{i_2}, \dots, b_{i_r} | \boldsymbol{\alpha}, n) = n^r \prod_{d=1}^r \alpha(i_d) \quad \forall r \leq n,$$

$$\kappa^{\text{mult}}(b_{i_1}, b_{i_2}, \dots, b_{i_r} | \boldsymbol{\alpha}, n) = (-1)^{r-1} (r-1)! \cdot n \prod_{d=1}^r \alpha(i_d). \quad (45)$$

The multinomial for variable \mathbf{p} in continuous outcome space \mathbb{R} is derived by keeping n constant while taking the limit $B \rightarrow \infty$ with bin sizes tending to zero and changing to a Bernoulli probability density $\alpha(b) \rightarrow d\mathbf{p}\alpha(\mathbf{p})$ normalised by $\int_{\mathcal{S}} d\mathbf{p}\alpha(\mathbf{p}) = 1$. The result is the *point process* where the probability for the count $n(\mathbf{p})$ in the infinitesimal “bin” around any \mathbf{p} to be larger than 1 becomes negligible; that is, we have at most one particle at a given \mathbf{p} . While the multinomial probability itself can be written only as a limit, the FMGF can be written analytically as the functional [67]

$$Q^{\text{mult}}[\boldsymbol{\lambda}(\mathbf{p}) | \boldsymbol{\alpha}(\mathbf{p}), n] = \left[1 - \int_{\mathcal{S}} d\mathbf{p} \boldsymbol{\lambda}(\mathbf{p}) \boldsymbol{\alpha}(\mathbf{p}) \right]^n. \quad (46)$$

Factorial moments and factorial cumulants are found generically from functional derivatives [14]

$$\rho(\mathbf{p}_{i_1}, \mathbf{p}_{i_2}, \dots, \mathbf{p}_{i_r}) = \frac{(-1)^r \delta^r Q[\boldsymbol{\lambda}(\mathbf{p})]}{\delta \lambda(\mathbf{p}_{i_1}) \delta \lambda(\mathbf{p}_{i_2}) \cdots \delta \lambda(\mathbf{p}_{i_r})} \Big|_{\boldsymbol{\lambda}(\mathbf{p})=0},$$

$$\kappa(\mathbf{p}_{i_1}, \mathbf{p}_{i_2}, \dots, \mathbf{p}_{i_r}) = \frac{(-1)^r \delta^r \ln Q[\boldsymbol{\lambda}(\mathbf{p})]}{\delta \lambda(\mathbf{p}_{i_1}) \delta \lambda(\mathbf{p}_{i_2}) \cdots \delta \lambda(\mathbf{p}_{i_r})} \Big|_{\boldsymbol{\lambda}(\mathbf{p})=0}, \quad (47)$$

which for the multinomial $Q[\boldsymbol{\lambda}(\mathbf{p})] = Q^{\text{mult}}[\boldsymbol{\lambda}(\mathbf{p}) | \boldsymbol{\alpha}(\mathbf{p}), n]$ of (46) yield

$$\rho^{\text{mult}}(\mathbf{p}_{i_1}, \mathbf{p}_{i_2}, \dots, \mathbf{p}_{i_r} | \boldsymbol{\alpha}(\mathbf{p}), n) = n^r \prod_{k=1}^r \alpha(\mathbf{p}_{i_k}), \quad (48)$$

$$1 \leq r \leq n,$$

$$\kappa^{\text{mult}}(\mathbf{p}_{i_1}, \mathbf{p}_{i_2}, \dots, \mathbf{p}_{i_r} | \boldsymbol{\alpha}(\mathbf{p}), n)$$

$$= (-1)^{r-1} (r-1)! \cdot n \prod_{k=1}^r \alpha(\mathbf{p}_{i_k}). \quad (49)$$

3.2.2. Multinomial Reference for Fixed N . Applying the above general case to our reference distribution (39), we must rewrite (46) to make provision for the fact that $\boldsymbol{\alpha}$ may in general depend not only on N but also on n ,

$$Q^{\text{mult}}[\boldsymbol{\lambda}(\mathbf{p}) | \boldsymbol{\alpha}(\mathbf{p} | \mathcal{S}_{nN})] = \left[1 - \int d\mathbf{p} \boldsymbol{\lambda}(\mathbf{p}) \boldsymbol{\alpha}(\mathbf{p} | \mathcal{S}_{nN}) \right]^n. \quad (50)$$

Inserting (50) into (39), we find the FMGF for the reference distribution of subsample \mathcal{S}_N to be

$$Q^{\text{ref}}[\boldsymbol{\lambda}(\mathbf{p}) | \boldsymbol{\alpha}(\mathbf{p}), \mathcal{S}_N]$$

$$= \sum_n \mathcal{R}_{nN} Q^{\text{mult}}[\boldsymbol{\lambda}(\mathbf{p}) | \boldsymbol{\alpha}(\mathbf{p} | \mathcal{S}_{nN})]$$

$$= \left\langle \left[1 - \int d\mathbf{p} \boldsymbol{\lambda}(\mathbf{p}) \boldsymbol{\alpha}(\mathbf{p} | \mathcal{S}_{nN}) \right]^n \right\rangle_N.$$

Using (48), the reference factorial moments are therefore

$$\rho^{\text{ref}}(\mathbf{p}_1, \mathbf{p}_2, \dots, \mathbf{p}_r | \mathcal{S}_N) = \left\langle n^r \prod_{k=1}^r \alpha(\mathbf{p}_k | \mathcal{S}_{nN}) \right\rangle_N, \quad (52)$$

$$\forall r \leq n,$$

with corresponding expressions for the reference factorial cumulants.

3.2.3. Reproducing the One-Particle Distribution. The set of functions $\boldsymbol{\alpha}(\mathbf{p} | \mathcal{S}_{nN})$ are as yet undetermined, apart from the general constraints $\boldsymbol{\alpha}(\mathbf{p} | \mathcal{S}_{nN}) \geq 0$ and $\int_{\mathcal{S}} d\mathbf{p} \boldsymbol{\alpha}(\mathbf{p} | \mathcal{S}_{nN}) = 1$. In multinomials of all kinds, the Bernoulli probabilities $\boldsymbol{\alpha}$ are fixed parameters and therefore are the conveyers of whatever remains constant in the outcomes while the detailed outcomes fluctuate as statistical outcomes do. The “field” $\boldsymbol{\alpha}(\mathbf{p} | \mathcal{S}_{nN})$ can and must therefore be seen as the quantity encompassing the “physics” of the one-particle distributions, which, in the absence of additional external information, is embodied by our experimental data sample: the experimental densities $\rho(\mathbf{p}_1, \dots, \mathbf{p}_N | \mathcal{S}_N)$ “are” the physics, including all correlations, and their first-order projections $\rho(\mathbf{p}_1 | \mathcal{S}_N)$ “are” the one-particle physics. The question immediately arises whether $\boldsymbol{\alpha}(\mathbf{p} | \mathcal{S}_{nN})$ should be fixed by $\rho(\mathbf{p} | \mathcal{S}_{nN})$ or the n -average $\rho(\mathbf{p} | \mathcal{S}_N) = \langle \rho(\mathbf{p} | \mathcal{S}_{nN}) \rangle_N$. Three possible choices come to mind.

- (1) It is tempting to define it in terms of the density for each sub-subsample \mathcal{S}_{nN} ,

$$\boldsymbol{\alpha}(\mathbf{p} | \mathcal{S}_{nN}) = \frac{\rho(\mathbf{p} | \mathcal{S}_{nN})}{n} \quad \forall (N, n), \quad (53)$$

which is correctly normalised since $\int d\mathbf{p} \rho(\mathbf{p} | \mathcal{S}_{nN}) = n$. As this choice would attribute physical significance to n , it would be appropriate whenever n is associated with additionally measured experimental information. If, however, n fluctuates randomly from event to event based in part on unmeasured or unmeasurable properties such as an event’s azimuthal orientation, use of (53) makes no sense.

If n is deemed physically relevant, correlations in terms of $\rho(\mathbf{p}_1, \dots, \mathbf{p}_r | \mathcal{S}_{nN})$ of (35) may be feasible, conditional on the availability of a sufficient number of events \mathcal{E}_{nN} . Where sample sizes do not permit this, one could nevertheless attempt to measure what have historically been termed “short-range correlations” but in this case not in the traditional sense of fixed- N correlations versus inclusive ones but rather of fixed- n -fixed- N correlations versus fluctuating- n -fixed- N correlations. See Section 3.6.

(2) A second choice

$$\alpha(\mathbf{p} | \mathcal{S}_{nN}) = \left\langle \frac{\rho(\mathbf{p} | \mathcal{S}_{nN})}{n} \right\rangle_N \quad (54)$$

would be properly normalised but fails to satisfy the crucial relations (71)–(73) below and is hence discarded.

(3) While remaining open-minded towards Choice 1, we therefore choose the third possibility, the ratio of the average density divided by the average, all for fixed N ,

$$\alpha(\mathbf{p} | \mathcal{S}_{nN}) = \frac{\langle \rho(\mathbf{p} | \mathcal{S}_{nN}) \rangle_N}{\langle n \rangle_N} = \frac{\rho(\mathbf{p} | \mathcal{S}_N)}{\langle n \rangle_N}, \quad (55)$$

which would be appropriate for samples where \mathcal{E}_{nN} is too small or physical significance can be attributed only to N but not to n . According to (38), it is also correctly normalised and ensures that the Bernoulli parameters are the same for all events in \mathcal{S}_N , independent of n . Substituting this into (52), the differential reference factorial moments orders become

$$\begin{aligned} \rho^{\text{ref}}(\mathbf{p}_1, \mathbf{p}_2, \dots, \mathbf{p}_r | \mathcal{S}_N) &= \frac{\langle n^r \rangle_N}{\langle n \rangle_N^r} \prod_{d=1}^r \rho(\mathbf{p}_d | \mathcal{S}_N) \\ &= F_{rN} \prod_{d=1}^r \rho(\mathbf{p}_d | \mathcal{S}_N), \end{aligned} \quad (56)$$

where we identify the prefactor as the normalised factorial moments of the n -multiplicity distribution for given N ,

$$F_{rN} = \frac{\langle n^r \rangle_N}{\langle n \rangle_N^r}, \quad (57)$$

while the generating functional (51) becomes (see also [13])

$$\begin{aligned} Q^{\text{ref}}[\lambda(\mathbf{p}) | \alpha(\mathbf{p}), \mathcal{S}_N] \\ = \left\langle \left[1 - \int d\mathbf{p} \lambda(\mathbf{p}) \frac{\rho(\mathbf{p} | \mathcal{S}_N)}{\langle n \rangle_N} \right]^n \right\rangle_N. \end{aligned} \quad (58)$$

Taking functional derivatives of the logarithm of (58), the first-, second-, and third-order cumulants of the reference density are

$$\begin{aligned} \kappa^{\text{ref}}(\mathbf{p}_1 | \mathcal{S}_N) &= \rho^{\text{ref}}(\mathbf{p}_1 | \mathcal{S}_N) = \rho(\mathbf{p}_1 | \mathcal{S}_N), \\ \kappa^{\text{ref}}(\mathbf{p}_1, \mathbf{p}_2 | \mathcal{S}_N) &= \rho^{\text{ref}}(\mathbf{p}_1, \mathbf{p}_2 | \mathcal{S}_N) \\ &\quad - \rho(\mathbf{p}_1 | \mathcal{S}_N) \rho(\mathbf{p}_2 | \mathcal{S}_N) \end{aligned} \quad (59)$$

$$\begin{aligned} &= \left(\frac{\langle n^2 \rangle_N}{\langle n \rangle_N^2} - 1 \right) \rho(\mathbf{p}_1 | \mathcal{S}_N) \\ &\quad \times \rho(\mathbf{p}_2 | \mathcal{S}_N), \end{aligned} \quad (60)$$

$$\begin{aligned} \kappa^{\text{ref}}(\mathbf{p}_1, \mathbf{p}_2, \mathbf{p}_3 | \mathcal{S}_N) \\ &= \rho^{\text{ref}}(\mathbf{p}_1, \mathbf{p}_2, \mathbf{p}_3 | \mathcal{S}_N) \\ &\quad - [3] \rho^{\text{ref}}(\mathbf{p}_1, \mathbf{p}_2 | \mathcal{S}_N) \rho(\mathbf{p}_3 | \mathcal{S}_N) \\ &\quad + 2\rho(\mathbf{p}_1 | \mathcal{S}_N) \rho(\mathbf{p}_2 | \mathcal{S}_N) \rho(\mathbf{p}_3 | \mathcal{S}_N) \\ &= \left(\frac{\langle n^3 \rangle_N}{\langle n \rangle_N^3} - 3 \frac{\langle n^2 \rangle_N}{\langle n \rangle_N^2} + 2 \right) \\ &\quad \times \rho(\mathbf{p}_1 | \mathcal{S}_N) \rho(\mathbf{p}_2 | \mathcal{S}_N) \rho(\mathbf{p}_3 | \mathcal{S}_N), \end{aligned} \quad (61)$$

where the square bracket [3] indicates the number of distinct permutations which must be taken into account. The terms in the rounded brackets are readily recognised as the normalised factorial cumulants of the n distribution for a given fixed N

$$K_{rN} = \frac{1}{\langle n \rangle_N^r} \frac{(-\partial)^r}{\partial \Lambda^r} \ln \left(\sum_{n=0}^N \mathcal{R}_{nN} (1 - \Lambda)^n \right)_{\Lambda=0}, \quad (63)$$

and so generalisation to arbitrary orders is immediate,

$$\kappa^{\text{ref}}(\mathbf{p}_1, \dots, \mathbf{p}_r | \mathcal{S}_N) = K_{rN} \prod_{k=1}^r \rho(\mathbf{p}_k | \mathcal{S}_N). \quad (64)$$

This can be proven generally by defining the functional $\Lambda[\lambda(\mathbf{p})] = \int d\mathbf{p} \lambda(\mathbf{p}) \rho(\mathbf{p} | \mathcal{S}_N) / \langle n \rangle_N$ which has only a first nonzero functional derivative $\delta \Lambda / \delta \lambda(\mathbf{p}_1) = \rho(\mathbf{p}_1 | \mathcal{S}_N) / \langle n \rangle_N$ and the multiplicity generating function $\mathcal{Z}(\Lambda | \mathcal{S}_N) = \sum_n \mathcal{R}_{nN} (1 - \Lambda)^n$, in terms of which $Q^{\text{ref}}[\lambda] = \mathcal{Z}[\Lambda[\lambda]]$.

3.3. Internal Cumulants for Fixed \mathcal{S}_N . Equation (64) shows that the differential cumulants of the reference distribution are directly proportional to the integrated cumulants K_{rN} of n , which are zero only if \mathcal{R}_{nN} is Poissonian. For fixed N , neither the integrated cumulants K_{rN} nor the differential ones are zero. While this has long been recognised in the literature

[15], the inevitable consequence was not drawn; namely, that “Poissonian” cumulants for fixed N

$$\begin{aligned} \kappa(\mathbf{p}_1, \mathbf{p}_2 | \mathcal{S}_N) &= \rho(\mathbf{p}_1, \mathbf{p}_2 | \mathcal{S}_N) \\ &\quad - \rho(\mathbf{p}_1 | \mathcal{S}_N) \rho(\mathbf{p}_2 | \mathcal{S}_N), \end{aligned} \quad (65)$$

$$\begin{aligned} \kappa(\mathbf{p}_1, \mathbf{p}_2, \mathbf{p}_3 | \mathcal{S}_N) &= \rho(\mathbf{p}_1, \mathbf{p}_2, \mathbf{p}_3 | \mathcal{S}_N) \\ &\quad - [3] \rho(\mathbf{p}_1, \mathbf{p}_2 | \mathcal{S}_N) \rho(\mathbf{p}_3 | \mathcal{S}_N) \\ &\quad + 2\rho(\mathbf{p}_1 | \mathcal{S}_N) \rho(\mathbf{p}_2 | \mathcal{S}_N) \rho(\mathbf{p}_3 | \mathcal{S}_N), \end{aligned} \quad (66)$$

and so forth cannot possibly represent true correlations because they are nonzero even when the momenta are fully independent. It is known that the theory of cumulants needs improvement on a fundamental level which reaches well beyond the scope of this paper [68, 69], but those difficulties are irrelevant here. A first step which does address the above concerns was taken in [18], where it was shown very generally on the basis of generating functionals that correlations for samples of fixed N are best measured using the *internal cumulants* κ^I , which are defined as the differences between the measured and the reference cumulants of the same order

$$\begin{aligned} \kappa^I(\mathbf{p}_1, \dots, \mathbf{p}_r | \mathcal{S}_N) &= \kappa(\mathbf{p}_1, \dots, \mathbf{p}_r | \mathcal{S}_N) \\ &\quad - \kappa^{\text{ref}}(\mathbf{p}_1, \dots, \mathbf{p}_r | \mathcal{S}_N). \end{aligned} \quad (67)$$

For our averaged-multinomial reference case, the internal cumulants of second and third-orders are given by the differences between (65) and (60) and between (66) and (62), resulting in

$$\begin{aligned} \kappa^I(\mathbf{p}_1, \mathbf{p}_2 | \mathcal{S}_N) &= \rho(\mathbf{p}_1, \mathbf{p}_2 | \mathcal{S}_N) - F_{2N} \rho(\mathbf{p}_1 | \mathcal{S}_N) \rho(\mathbf{p}_2 | \mathcal{S}_N), \end{aligned} \quad (68)$$

$$\begin{aligned} \kappa^I(\mathbf{p}_1, \mathbf{p}_2, \mathbf{p}_3 | \mathcal{S}_N) &= \rho(\mathbf{p}_1, \mathbf{p}_2, \mathbf{p}_3 | \mathcal{S}_N) \\ &\quad - [3] \rho(\mathbf{p}_1, \mathbf{p}_2 | \mathcal{S}_N) \rho(\mathbf{p}_3 | \mathcal{S}_N) \\ &\quad + G_{3N} \rho(\mathbf{p}_1 | \mathcal{S}_N) \rho(\mathbf{p}_2 | \mathcal{S}_N) \rho(\mathbf{p}_3 | \mathcal{S}_N), \end{aligned} \quad (69)$$

with

$$G_{3N} = 3F_{2N} - F_{3N} = 3 \frac{\langle n(n-1) \rangle_N}{\langle n \rangle_N^2} - \frac{\langle n(n-1)(n-2) \rangle_N}{\langle n \rangle_N^3}, \quad (70)$$

and so on for higher orders. These internal cumulants are identically zero if and when the measured densities for fixed \mathcal{S}_{nN} are multinomials since then from (56)

$$\begin{aligned} \rho(\mathbf{p}_1, \mathbf{p}_2 | \mathcal{S}_N) &\longrightarrow \rho^{\text{ref}}(\mathbf{p}_1, \mathbf{p}_2 | \mathcal{S}_N) \\ &= F_{2N} \rho(\mathbf{p}_1 | \mathcal{S}_N) \rho(\mathbf{p}_2 | \mathcal{S}_N), \end{aligned} \quad (71)$$

so that $\kappa^I(\mathbf{p}_1, \mathbf{p}_2 | \mathcal{S}_N) \rightarrow 0$ whenever the data is multinomial, while

$$\begin{aligned} \rho(\mathbf{p}_1, \mathbf{p}_2, \mathbf{p}_3 | \mathcal{S}_N) &\longrightarrow F_{3N} \rho(\mathbf{p}_1 | \mathcal{S}_N) \rho(\mathbf{p}_2 | \mathcal{S}_N) \rho(\mathbf{p}_3 | \mathcal{S}_N) \end{aligned} \quad (72)$$

ensures that $\kappa^I(\mathbf{p}_1, \mathbf{p}_2, \mathbf{p}_3 | \mathcal{S}_N) \rightarrow 0$ in the same case. On another level, the internal cumulants always integrate to zero over the full good-azimuth space \mathcal{A} , irrespective of the presence of correlations,

$$\begin{aligned} \int_{\mathcal{A}} d\mathbf{p}_1 d\mathbf{p}_2 \kappa^I(\mathbf{p}_1, \mathbf{p}_2 | \mathcal{S}_N) &= \int_{\mathcal{A}} d\mathbf{p}_1 d\mathbf{p}_2 d\mathbf{p}_3 \kappa^I(\mathbf{p}_1, \mathbf{p}_2, \mathbf{p}_3 | \mathcal{S}_N) = 0, \end{aligned} \quad (73)$$

and so on for all orders. Both properties will remain valid after transformation from three-momentum to invariant four-momentum differences in Section 3.4. In the case of Poissonian statistics, $F_{rN} = 1$ for all r , so that the above internal cumulants revert to their usual definitions.

As stated in Section 3.1, the measured correlations may in addition be made insensitive to the one-particle distribution through normalisation. As set out in [18], such normalisation is achieved for fixed N by dividing the internal cumulants by the corresponding reference distribution density, which for the case at hand is given by (56). This leads to the second-order normalised internal cumulant

$$K^I(\mathbf{p}_1, \mathbf{p}_2 | \mathcal{S}_N) = \frac{1}{F_{2N}} \frac{\rho(\mathbf{p}_1, \mathbf{p}_2 | \mathcal{S}_N)}{\rho(\mathbf{p}_1 | \mathcal{S}_N) \rho(\mathbf{p}_2 | \mathcal{S}_N)} - 1, \quad (74)$$

while in third-order we get

$$\begin{aligned} K^I(\mathbf{p}_1, \mathbf{p}_2, \mathbf{p}_3 | \mathcal{S}_N) &= \frac{1}{F_{3N}} \\ &\quad \times \left(\frac{\rho(\mathbf{p}_1, \mathbf{p}_2, \mathbf{p}_3 | \mathcal{S}_N) - [3] \rho(\mathbf{p}_1, \mathbf{p}_2 | \mathcal{S}_N) \rho(\mathbf{p}_3 | \mathcal{S}_N)}{\rho(\mathbf{p}_1 | \mathcal{S}_N) \rho(\mathbf{p}_2 | \mathcal{S}_N) \rho(\mathbf{p}_3 | \mathcal{S}_N)} \right) \\ &\quad + 3 \frac{F_{2N}}{F_{3N}} - 1. \end{aligned} \quad (75)$$

3.4. Correlation Integrals for Momentum Differences. In femtoscopy, correlations are mostly expressed in terms of pair variables $\mathbf{K} = (1/2)(\mathbf{p}_1 + \mathbf{p}_2)$ and difference $\mathbf{q} = \mathbf{p}_1 - \mathbf{p}_2$ or the invariant four-momenta [70] $Q = \sqrt{-(p_1 - p_2)^2} = \sqrt{(\mathbf{p}_1 - \mathbf{p}_2)^2 - (E_1 - E_2)^2}$ where the energies are on-shell, $E_r = \sqrt{\mathbf{p}_r^2 + m^2}$. As shown in [53], the formulation of event-wise counters as sums and products of Dirac delta functions makes it easy to change variables. Writing $\rho_{rN}(\mathbf{p}_1, \dots, \mathbf{p}_r)$ as shorthand for $\rho(\mathbf{p}_1, \dots, \mathbf{p}_r | \mathcal{S}_N)$ and so forth, the second-order unnormalised internal cumulant in terms of

Q is, for example, found from the identity $\int dQ \kappa_{2N}^I(Q) = \int dQ \int_{\mathcal{S}} d\mathbf{p}_1 d\mathbf{p}_2 \kappa_{2N}^I(\mathbf{p}_1, \mathbf{p}_2) \delta(Q - \sqrt{(\mathbf{p}_1 - \mathbf{p}_2)^2 - (E_1 - E_2)^2})$ to be

$$\begin{aligned} \kappa_{2N}^I(Q) &= \left\langle \left\langle \sum_{i \neq j} \delta(Q - Q_{ij}^{aa}) \right\rangle \right\rangle_{Na} \\ &\quad - F_{2N} \left\langle \left\langle \left\langle \sum_{i,j} \delta(Q - Q_{ij}^{ab}) \right\rangle \right\rangle \right\rangle_{Nb} \quad (76) \\ &= \rho_{2N}(Q) - F_{2N} \rho_{1N} \otimes \rho_{1N}(Q), \end{aligned}$$

where the counters in the second line are defined by the terms in the first, while $Q_{ij}^{aa} = [-(P_i^a - P_j^a)^2]^{1/2}$ and $Q_{ij}^{ab} = [-(P_i^a - P_j^b)^2]^{1/2}$ are four-momentum differences between sibling pairs aa and event mixing pairs ab , respectively. It is easy to show that $\int_0^\infty dQ \rho_{2N}(Q) = \langle n^2 \rangle_N$ and $\int_0^\infty dQ \rho_{1N} \otimes \rho_{1N}(Q) = \langle n \rangle_N^2$ and hence, as before, $\int_0^\infty dQ \kappa_{2N}^I(Q) = 0$, which will be true for any correlation whatsoever. The double event averages in the product term

$$\rho_{1N} \otimes \rho_{1N}(Q) = \left\langle \left\langle \left\langle \sum_{i,j} \delta(Q - Q_{ij}^{ab}) \right\rangle \right\rangle \right\rangle_{Nb} \quad (77)$$

are the theoretical foundations of event mixing [53]; the inner b -average is usually shortened to a smaller ‘‘moving average tail’’ subsample of \mathcal{S}_N .

In third-order, the ‘‘GHP average’’ invariant is defined as the average of three two-momentum differences over all pairs (with or without the $\sqrt{3}$),

$$Q_a = \frac{\sqrt{-(p_1 - p_2)^2 - (p_2 - p_3)^2 - (p_3 - p_1)^2}}{\sqrt{3}}, \quad (78)$$

and it is related to the invariant mass of three pions $M_3 = (p_1 + p_2 + p_3)^2$ by $Q_a^2 = (1/3)M_3^2 - m^2$. Other ‘‘topologies’’ such as the ‘‘GHP max’’ $Q_m = \sqrt{\max[-(p_1 - p_2)^2, -(p_2 - p_3)^2, -(p_3 - p_1)^2]}$ can also be employed. For large multiplicities, the ‘‘Star’’ topology may be preferred [71], but we will not pursue it here. For the GHP average, the third internal cumulant is given by

$$\begin{aligned} \kappa_{3N}^I(Q_a) &= \left\langle \left\langle \sum_{i \neq j \neq k} \delta(Q_a - Q_{ijk}^{aaa}) \right\rangle \right\rangle_{Na} \\ &\quad - 3 \left\langle \left\langle \left\langle \sum_{i \neq j} \sum_k \delta(Q_a - Q_{ijk}^{aab}) \right\rangle \right\rangle \right\rangle_{Nb} \quad (79) \\ &\quad + G_{3N} \left\langle \left\langle \left\langle \left\langle \sum_{i,j,k} \delta(Q_a - Q_{ijk}^{abc}) \right\rangle \right\rangle \right\rangle \right\rangle_{Nc} \quad (79) \end{aligned}$$

with $Q_{ijk}^{abc} = \sqrt{(1/3)[-(P_i^a - P_j^b)^2 - (P_j^b - P_k^c)^2 - (P_k^c - P_i^a)^2]}$ and similarly for Q_{ijk}^{aaa} and Q_{ijk}^{aab} . Second- and third-order cumulants are normalised by, respectively,

$$\begin{aligned} F_{2N} \rho_{1N} \otimes \rho_{1N}(Q) &= F_{2N} \left\langle \left\langle \left\langle \sum_{i,j} \delta(Q - Q_{ij}^{ab}) \right\rangle \right\rangle \right\rangle_{Nb} \quad (80) \\ F_{3N} \rho_{1N} \otimes \rho_{1N} \otimes \rho_{1N}(Q_a) &= F_{3N} \left\langle \left\langle \left\langle \left\langle \sum_{i,j,k} \delta(Q_a - Q_{ijk}^{abc}) \right\rangle \right\rangle \right\rangle \right\rangle_{Nc} \quad (80) \end{aligned}$$

After transforming from momenta to Q , the formulae of Section 3.3 become

$$\kappa_{2N}^I(Q) = \rho_{2N}(Q) - F_{2N} \rho_{1N} \otimes \rho_{1N}(Q), \quad (81)$$

$$\begin{aligned} \kappa_{3N}^I(Q_a) &= \rho_{3N}(Q_a) - [3] \rho_{2N} \otimes \rho_{1N}(Q_a) \\ &\quad + G_{3N} \rho_{1N} \otimes \rho_{1N} \otimes \rho_{1N}(Q_a), \end{aligned} \quad (82)$$

while the normalised cumulants of Section 3.3 become

$$K_2^I(Q | \mathcal{S}_N) = \frac{\rho_{2N}(Q)}{F_{2N} \rho_{1N} \otimes \rho_{1N}(Q)} - 1, \quad (83)$$

$$\begin{aligned} K_3^I(Q_a | \mathcal{S}_N) &= \frac{\rho_{3N}(Q_a) - [3] \rho_{2N} \otimes \rho_{1N}(Q_a)}{F_{3N} \rho_{1N} \otimes \rho_{1N} \otimes \rho_{1N}(Q_a)} \\ &\quad + 3 \frac{F_{2N}}{F_{3N}} - 1. \end{aligned} \quad (84)$$

3.5. Effect of Fixed- N Correction Factors. To get a feeling for the size of the corrections involved, we measured the correction factors F_{rN} and G_{3N} with the same UAI dataset and the same cuts as in Figure 1. As shown in Figure 2, the consequence of the clearly sub-Poissonian multiplicity distributions shown in Figure 1 is that these factors are significantly *less* than 1, in contrast to the usual factorial moments of the charged multiplicity distribution which are super-Poissonian with factors *exceeding* 1. For very low multiplicities $N < 10$, normalised internal cumulants are hence larger than their Poissonian counterparts but converge to them with increasing N . Nevertheless, up to $N \approx 30$ corrections of more than 5% for K_2^I and more than 20% for K_3^I compared to their uncorrected counterparts can be expected. By contrast, the additive correction G_{3N} does not deviate much from the Poissonian limit of 2 except for very small N . By contrast, unnormalised internal cumulants (81) and (82) are far less sensitive to the multinomial correction.

It is of interest to zoom in on the approach to the Poissonian limit of 1 and to compare these corrections to the equivalent charged-multiplicity-based ones, which for the case of fixed N , would be just $N(N-1)/N^2$ and $N(N-1)(N-2)/N^3$. In Figure 3, the Poissonian limit corresponds to zero on the y -axis. It is clear that the fixed- N factors go some way to correct for the fixed- N conditioning; the gap between

them is approximately determined by $\langle n^x \rangle_N / N^x$, that is, by the exact definition and outcome space for n .

3.6. Eliminating Fluctuations in n . We return briefly to the first choice in Section 3.2.3, that is, $\alpha(\mathbf{p} \mid \mathcal{S}_{nN}) = \rho(\mathbf{p} \mid \mathcal{S}_{nN})/n$ which would permit different physics for each (N, n) combination. If we were willing and able to do analyses for each \mathcal{S}_{nN} , we would use the fixed- (N, n) equivalent of (68) and (69) derived from $\kappa^{\text{ref}}(\mathbf{p}_1, \dots, \mathbf{p}_r \mid \mathcal{S}_{nN}) = (-1)^{r-1} (r-1)! n \prod_{k=1}^r \rho(\mathbf{p}_k \mid \mathcal{S}_{nN})$,

$$\begin{aligned} \kappa^I(\mathbf{p}_1, \mathbf{p}_2 \mid \mathcal{S}_{nN}) &= \rho(\mathbf{p}_1, \mathbf{p}_2 \mid \mathcal{S}_{nN}) \\ &\quad - \left(1 - \frac{1}{n}\right) \rho(\mathbf{p}_1 \mid \mathcal{S}_{nN}) \rho(\mathbf{p}_2 \mid \mathcal{S}_{nN}), \\ \kappa^I(\mathbf{p}_1, \mathbf{p}_2, \mathbf{p}_3 \mid \mathcal{S}_{nN}) &= \rho(\mathbf{p}_1, \mathbf{p}_2, \mathbf{p}_3 \mid \mathcal{S}_{nN}) \\ &\quad - [3] \rho(\mathbf{p}_1, \mathbf{p}_2 \mid \mathcal{S}_{nN}) \rho(\mathbf{p}_3 \mid \mathcal{S}_{nN}) \\ &\quad + 2 \left(1 - \frac{1}{n^2}\right) \rho(\mathbf{p}_1 \mid \mathcal{S}_{nN}) \\ &\quad \times \rho(\mathbf{p}_2 \mid \mathcal{S}_{nN}) \rho(\mathbf{p}_3 \mid \mathcal{S}_{nN}), \end{aligned} \quad (85)$$

and normalise by $\rho^{\text{ref}}(\mathbf{p}_1, \dots, \mathbf{p}_r \mid \mathcal{S}_{nN}) = (n^x/n^r) \prod_{k=1}^r \rho(\mathbf{p}_k \mid \mathcal{S}_{nN})$. Where that is not possible, we can still average over the above to form ‘‘Averaged Internal’’ (AI) correlations (see Section 5), but in this case averaging over n for fixed N ,

$$\begin{aligned} \kappa^{\text{SRC}}(\mathbf{p}_1, \mathbf{p}_2 \mid \mathcal{S}_N) &= \langle \kappa^I(\mathbf{p}_1, \mathbf{p}_2 \mid \mathcal{S}_{nN}) \rangle_N, \\ \kappa^{\text{SRC}}(\mathbf{p}_1, \mathbf{p}_2, \mathbf{p}_3 \mid \mathcal{S}_N) &= \langle \kappa^I(\mathbf{p}_1, \mathbf{p}_2, \mathbf{p}_3 \mid \mathcal{S}_{nN}) \rangle_N, \end{aligned} \quad (86)$$

and normalise if necessary by the moment $\rho^{\text{SRC}}(\mathbf{p}_1, \dots, \mathbf{p}_r \mid \mathcal{S}_N) = \langle (n^x/n^r) \prod_{k=1}^r \rho(\mathbf{p}_k \mid \mathcal{S}_{nN}) \rangle_N$. Given that this involves products of moments in the sub-subsample \mathcal{S}_{nN} , event mixing would have to be restricted to the same sub-samples also, for example

$$\begin{aligned} &\left\langle \left(1 - \frac{1}{n}\right) \rho(\mathbf{p}_1 \mid \mathcal{S}_{nN}) \rho(\mathbf{p}_2 \mid \mathcal{S}_{nN}) \right\rangle_N \\ &= \sum_{n=2}^N \frac{\mathcal{E}_{nN}}{\mathcal{E}_N} \left(1 - \frac{1}{n}\right) \frac{1}{(\mathcal{E}_{nN})^2} \\ &\quad \times \sum_{a,b \in \mathcal{S}_{nN}} \hat{\rho}(\mathbf{p}_1 \mid n, N, \mathbf{P}^a) \hat{\rho}(\mathbf{p}_2 \mid n, N, \mathbf{P}^b). \end{aligned} \quad (87)$$

The transformation to pair variables works in the same way as in previous sections.

4. Statistical Errors

While the various versions of internal cumulants constructed above may all be relevant at some point, we concentrate on

finding expressions for experimental standard errors for the unnormalised and normalised internal cumulants of (81)–(84). This turns out to be more subtle than merely applying a generic root-mean-square prescription. We will show in this section that standard errors implemented thus far may have been underestimated even in the standard two-particle case.

The calculations performed in this section belong to the ‘‘frequentist’’ view of probability; a proper Bayesian analysis, which can be expected to rest on more solid foundations, is beyond the scope of this paper. The two viewpoints can reasonably be expected to yield similar results in the limit of large bin contents and sample sizes.

In this section, we often simplify notation by writing $\rho_r(Q \mid \mathcal{S}_N) \rightarrow \rho_{rN}$ and $\rho_1 \otimes \rho_1(Q \mid \mathcal{S}_N) \rightarrow \rho_{1N}^2$ and so forth, since the formulae apply to samples and variables of any kind.

4.1. Propagation of Statistical Errors. Because cumulants can be measured only through the moments that enter their definitions, the first task is to identify which moment variances and covariances are needed. By means of standard error propagation [68], we find the sample variances for second-order internal cumulants of (81) and (83) to be

$$\begin{aligned} \text{var}(\kappa_2^I(Q \mid \mathcal{S}_N)) &= \text{var}(\rho_{2N} - F_{2N} \rho_{1N}^2) \\ &= \text{var}(\rho_{2N}) + F_{2N}^2 \text{var}(\rho_{1N}^2) - 2 F_{2N} \text{cov}(\rho_{2N}, \rho_{1N}^2), \end{aligned} \quad (88)$$

$$\begin{aligned} \text{var}(K_2^I(Q \mid \mathcal{S}_N)) &= \text{var}\left(\frac{1}{F_{2N}} \frac{\rho_{2N}}{\rho_{1N}^2} - 1\right) \\ &= \left[\frac{1}{F_{2N}} \frac{\rho_{2N}}{\rho_{1N}^2}\right]^2 \\ &\quad \times \left[\frac{\text{var}(\rho_{2N})}{\rho_{2N}^2} + \frac{\text{var}(\rho_{1N}^2)}{\rho_{1N}^4} - 2 \frac{\text{cov}(\rho_{2N}, \rho_{1N}^2)}{\rho_{2N} \cdot \rho_{1N}^2}\right], \end{aligned} \quad (89)$$

under the assumption that $\text{var}(F_{2N})$ is much smaller than the other variances, so that F_{2N} can be treated as a constant; this is the case if there are many bins for Q . Similarly, from (69), the variance of the unnormalised internal cumulant is, assuming G_3 of (70) to be constant,

$$\begin{aligned} \text{var}(\kappa_3^I(Q_a \mid \mathcal{S}_N)) &= \text{var}[\rho_{3N} - 3\rho_{2N}\rho_{1N} + G_3\rho_{1N}^3] \\ &= \text{var}(\rho_{3N}) + 9\text{var}(\rho_{2N}\rho_{1N}) + G_3^2\text{var}(\rho_{1N}^3) \\ &\quad - 6\text{cov}(\rho_{3N}, \rho_{2N}\rho_{1N}) + 2G_3\text{cov}(\rho_{3N}, \rho_{1N}^3) \\ &\quad - 6G_3\text{cov}(\rho_{2N}\rho_{1N}, \rho_{1N}^3), \end{aligned} \quad (92)$$

while the normalised version has variance (again assuming $\text{var}(G_3) \ll \text{var}\rho_r$)

$$\begin{aligned}
& \text{var}\left(K_3^I(Q_a | \mathcal{S}_N)\right) \\
&= \text{var}\left[\frac{\rho_{3N} - 3\rho_{2N}\rho_{1N} + G_3\rho_{1N}^3}{F_{3N}\rho_{1N}^3}\right] \\
&= \frac{1}{F_{3N}^2} \text{var}\left[\frac{\rho_{3N} - 3\rho_{2N}\rho_{1N}}{\rho_{1N}^3} + G_3\right] \\
&= \left[\frac{\rho_{3N} - 3\rho_{2N}\rho_{1N}}{F_{3N}\rho_{1N}^3}\right]^2 \\
&\quad \times \left[\frac{\text{var}(\rho_{3N} - 3\rho_{2N}\rho_{1N})}{(\rho_{3N} - 3\rho_{2N}\rho_{1N})^2} + \frac{\text{var}(\rho_{1N}^3)}{\rho_{1N}^6}\right. \\
&\quad \left. - \frac{2\text{cov}(\rho_{3N} - 3\rho_{2N}\rho_{1N}, \rho_{1N}^3)}{(\rho_{3N} - 3\rho_{2N}\rho_{1N})\rho_{1N}^3}\right] \\
&= \left[\frac{\rho_{3N} - 3\rho_{2N}\rho_{1N}}{F_{3N}\rho_{1N}^3}\right]^2 \\
&\quad \times \left[\frac{\text{var}(\rho_{3N}) + 9\text{var}(\rho_{2N}\rho_{1N}) - 6\text{cov}(\rho_{3N}, \rho_{2N}\rho_{1N})}{(\rho_{3N} - 3\rho_{2N}\rho_{1N})^2}\right. \\
&\quad \left. + \frac{\text{var}(\rho_{1N}^3)}{\rho_{1N}^6}\right. \\
&\quad \left. + \frac{6\text{cov}(\rho_{2N}\rho_{1N}, \rho_{1N}^3) - 2\text{cov}(\rho_{3N}, \rho_{1N}^3)}{(\rho_{3N} - 3\rho_{2N}\rho_{1N})\rho_{1N}^3}\right]. \tag{94}
\end{aligned}$$

The unnormalised cumulants (81) and (82) and their variances (88) and (92) require knowledge of the multiplicity factorial moments F_{2N} , F_{3N} , so that the individual terms must be accumulated until the entire sample has been analysed. By contrast, the normalised cumulants (83) and (84) and their variances (90) and (94) contain the multiplicity moments only as prefactors.

4.2. Expectation Values of Counters. While we will not make direct use of the results in this section, it is nevertheless useful briefly to consider what we might mean by an “expectation value of experimental counters and densities.” For any scalar function $f(\mathbf{p})$ of the momenta, the theoretical expectation value $E[f]$ is defined as the integral over the entire outcome space Ω of f weighted by a “parent distribution” $P(\mathbf{p})$, an abstract entity supposedly containing everything there is to know on this level,

$$E[f(\mathbf{p})] = \int_{\Omega} d\mathbf{p} P(\mathbf{p}) f(\mathbf{p}). \tag{95}$$

Purely theoretical concepts such as $P(\mathbf{p})$ and $E[f]$ should be given little or no room in a strongly experimentally-oriented study. In calculating standard errors on counters

below, we will, however, make use of the exact factorisation that expectation values provide whenever two variables x, y are statistically independent, $E[xy] = \int dx dy P(x, y) xy = E[x]E[y]$.

Expectation values for pairwise variables such as the four-momentum difference Q we are considering here must be based on the underlying physics. We can deduce some properties of the parent distribution based on the usual definition of the femtosopic correlation function:

$$C_2(Q) \equiv K_2(Q) + 1 = \frac{\rho_2^{\text{sibling}}(Q)}{\rho_2^{\text{reference}}(Q)} = \frac{\langle \hat{\rho}(Q^{aa}) \rangle}{\langle \langle \hat{\rho}(Q^{ab}) \rangle \rangle}, \tag{96}$$

which is a function of two entirely different quantities: the four-momentum differences Q^{aa} of “sibling” tracks taken from the same event a and one constructed from the mixed-event sample using tracks from different events, written as Q^{ab} , Q^{bc} , and so forth. For second-order correlations, the parent distribution is therefore necessarily a two-variable probability⁴ $P(Q^{aa}, Q^{bc})$ which, depending on whether the cases $b = a$ and $c = a$ occur, may or may not factorise into “sibling” and “mixed” marginal probabilities

$$P(Q^{aa}, Q^{bc}) = P_s(Q^{aa}) P_m(Q^{bc}) \quad \text{iff } a \neq b \neq c, \tag{97}$$

but (unless $a = b = c$), the marginals will always be

$$\begin{aligned}
P_s(Q^{aa}) &= \int dQ^{bc} P(Q^{aa}, Q^{bc}), \\
P_m(Q^{bc}) &= \int dQ^{aa} P(Q^{aa}, Q^{bc}).
\end{aligned} \tag{98}$$

The shapes of $P_s(Q)$ and $P_m(Q)$ must necessarily be different since it is precisely this difference that leads to a nontrivial signal in (96). In terms of this joint probability, we can write expectation values of eventwise counters (separately for inclusive, fixed- N , or fixed- n cases) as

$$\begin{aligned}
E[\hat{\rho}(Q^{aa})] &= \int_{\Omega} dQ^{aa} dQ^{bc} P(Q^{aa}, Q^{bc}) \hat{\rho}_{aa} \\
&= \sum_{i \neq j} \int_{\Omega} dQ^{aa} P_s(Q^{aa}) \delta(Q^{aa} - Q_{ij}^{aa}) \\
&= \sum_{i \neq j} P_s(Q_{ij}^{aa}), \\
E[\hat{\rho}(Q^{bc})] &= \int_{\Omega} dQ^{aa} dQ^{bc} P(Q^{aa}, Q^{bc}) \hat{\rho}_{bc} \\
&= \sum_{i, j} \int_{\Omega} dQ^{bc} P_m(Q^{bc}) \delta(Q^{bc} - Q_{ij}^{bc}) \\
&= \sum_{i, j} P_m(Q_{ij}^{bc}).
\end{aligned} \tag{99}$$

Later, we will meet expectation values for cases such as $a = c$,

$$\begin{aligned} E[\hat{\rho}(Q^{aa})\hat{\rho}(Q^{ab})] &= \sum_{i \neq j,k,\ell} \sum_{\Omega} dQ^{aa} dQ^{ab} P(Q^{aa}, Q^{ab}) \\ &\quad \times \delta(Q^{aa} - Q_{ij}^{aa}) \delta(Q^{ab} - Q_{k\ell}^{ab}) \\ &= \sum_{i \neq j,k,\ell} P(Q_{ij}^{aa}, Q_{k\ell}^{ab}), \end{aligned} \quad (100)$$

which definitely do not factorise. The above expressions can be simplified because we know that the parent distribution is not a function of the individual track indices i, j, k , and ℓ

$$P(Q_{ij}^{aa}, Q_{k\ell}^{bc}) = P(Q^{aa}, Q^{bc}) \quad \forall i, j, k, \ell \quad (101)$$

and similarly $P_s(Q_{ij}^{aa}) = P_s(Q^{aa})$ and $P_m(Q_{k\ell}^{bc}) = P_m(Q^{bc})$. For the event-averaged counters, this results in

$$\begin{aligned} E[\rho_{aa}(Q)] &= \langle n_a^2 \rangle_N P_s(Q^{aa}), \\ E[\rho_{bc}(Q)] &= \langle n_b \rangle_N \langle n_c \rangle_N P_m(Q^{bc}), \end{aligned} \quad (102)$$

or in terms of the notation of Section 3.4,

$$\begin{aligned} E[\rho_{2N}(Q)] &= \langle n^2 \rangle_N P_s(Q^{aa}), \\ E[\rho_{1N} \otimes \rho_{1N}(Q)] &= \langle n \rangle_N^2 P_m(Q^{bc}). \end{aligned} \quad (103)$$

As mentioned, we do not need the factorisation (97) of $P(Q^{aa}, Q^{bc})$ as long as we keep careful track of the equal-event-indices cases. Whenever $a \neq b$ or $a \neq c$, independence of the events ensures that expectation values of products of any functions $f(Q^{aa})$ and $g(Q^{ab})$ of the pair variables do factorise,

$$E[f(Q^{aa})g(Q^{ab})] = E[f(Q^{aa})]E[g(Q^{ab})] \quad a \neq b. \quad (104)$$

For third-order correlations, the parent distribution is a function of three different variables Q^{aaa} , Q^{bbc} , and Q^{def} containing, respectively, three, two, or one track from the same event, and corresponding considerations regarding equal and unequal event indices apply there, too.

4.3. Statistical Error Calculation from First Principles. It was shown in Section 4.2 that expectation values would have well-defined meanings in terms of underlying parent distributions and their marginals if their parent distributions were known, which, however, they are not. We are therefore forced to revert from expectation values $E[\cdot]$ to sample averages $\langle \cdot \rangle$ after completing a calculation. The real use of such expectation values in frequentist statistics has been in the form of a gedankenexperiment which we now reproduce from Kendall [68]. Let x be any generic eventwise counter or any other eventwise statistic. Since the formulae in this section remain true for inclusive and fixed- N samples, we omit any notation

related to N in this derivation. In this simplified notation, the well-known standard error of the sample mean $\langle x \rangle$ is given by (simplifying $\mathcal{E} - 1 \rightarrow \mathcal{E}$)

$$\sigma(\langle x \rangle) = \sqrt{\text{var}(\langle x \rangle)} = \sqrt{\frac{1}{\mathcal{E}} [\langle x^2 \rangle - \langle x \rangle^2]}, \quad (105)$$

which follows from the combinatorics of equal and unequal event indices by the above artificial use of expectation values, reverting from expectation values $E[\cdot]$ to sample means $\langle \cdot \rangle$ in the last step:

$$\begin{aligned} \text{var}(\langle x \rangle) &= E[\langle x \rangle^2] - E[\langle x \rangle]^2 \\ &= \frac{1}{\mathcal{E}^2} \sum_{a,b} [E[x_a x_b] - E[x_a]E[x_b]] \\ &= \frac{1}{\mathcal{E}^2} \sum_{a=b} [E[x_a x_b] - E[x_a]E[x_b]] \\ &\quad + \frac{1}{\mathcal{E}^2} \sum_{a \neq b} [E[x_a]E[x_b] - E[x_a]E[x_b]] \\ &= \frac{1}{\mathcal{E}^2} \sum_a [E[x^2] - E[x]^2] + 0 = \frac{1}{\mathcal{E}} [\langle x^2 \rangle - \langle x \rangle^2], \end{aligned} \quad (106)$$

where we have used the fact that $E[x_a x_b] = E[x_a]E[x_b]$ for all $a \neq b$ and assumed that all x are identically distributed, $E[x_a] = E[x]$ for all a . Equality or inequality of event indices is thus crucial. We will follow the same approach below, keeping careful track of equal and unequal event indices, factorising expectation values for unequal event indices, and reverting to sample means in the last step.

4.4. Variances and Covariances for Multiple Event Averages

4.4.1. Statistical Errors for Second-Order Cumulants. According to (88)–(94), we must handle variances and covariances of products of several event averages. To derive these, we will use the following shortened notation: letting $\delta_{ij}^{ab} \equiv \delta(Q - Q_{ij}^{ab})$ and so forth, then $\hat{\rho}_{aa} = \sum_{i \neq j} \delta(Q - Q_{ij}^{aa}) = \sum_{i \neq j} \delta_{ij}^{aa}$ is the eventwise pair counter for event a , while $\hat{\rho}_{bc} = \sum_{i,j} \delta(Q - Q_{ij}^{bc}) = \sum_{i,j} \delta_{ij}^{bc}$ is the mixed-event counter of events b and c (with $b \neq c \neq a$ assumed), so that $\rho_2(Q) = \langle \hat{\rho}_{aa} \rangle_a$ while $\rho_1 \otimes \rho_1(Q) = \langle \hat{\rho}_{ab} \rangle_{ab}$ is a double event average. We reserve the event index a for the “sibling” event whose correlations are currently being analysed and use indices $b, c, \dots, t, u, v, w, \dots$ for events entering the event-mixing parts.⁵ All quantities are assumed to be measured within a particular subsample \mathcal{S}_N , but we omit the N -subscript and the argument. The event-index subscripts such as $\langle \cdot \rangle_{bc}$ above are included or omitted depending on whether they convey relevant information on the specific averaging.

In this notation, the method that led to (107) reads

$$\begin{aligned} \text{var}(\rho_2) &= \text{var}(\langle \hat{\rho}_{aa} \rangle_a) \\ &= \frac{1}{\mathcal{E}^2} \sum_{a,b} [E(\hat{\rho}_{aa}\hat{\rho}_{bb}) - E(\hat{\rho}_{aa})E(\hat{\rho}_{bb})] \\ &= \frac{1}{\mathcal{E}} [\langle (\hat{\rho}_{aa})^2 \rangle - \langle \hat{\rho}_{aa} \rangle^2]. \end{aligned} \quad (108)$$

The same method of disentangling the combinatorics of equal and unequal event indices is applied consistently to all variances and covariances below. The ρ_1^2 term in second-order cumulants has variance

$$\begin{aligned} \text{var}(\rho_1 \otimes \rho_1) &= \text{var}(\langle \hat{\rho}_{bc} \rangle_{bc}) \\ &= \frac{1}{(\mathcal{E}^2)^2} \sum_{b \neq c} \sum_{d \neq e} [E(\hat{\rho}_{bc}\hat{\rho}_{de}) - E(\hat{\rho}_{bc})E(\hat{\rho}_{de})]. \end{aligned} \quad (109)$$

The case $b \neq c \neq d \neq e$ yields zero, but the cases $b = d \neq c \neq e$ and three other equivalent combinations yield

$$\begin{aligned} \text{var}(\rho_1 \otimes \rho_1) &= \frac{4\mathcal{E}^3}{(\mathcal{E}^2)^2} [E[\hat{\rho}_{bc}\hat{\rho}_{be}] - E[\hat{\rho}_{bc}]E[\hat{\rho}_{be}]] \\ &\rightarrow \frac{4\mathcal{E}^3}{(\mathcal{E}^2)^2} [\langle \hat{\rho}_{bc}\hat{\rho}_{be} \rangle_{bce} - \langle \hat{\rho}_{bc} \rangle \langle \hat{\rho}_{be} \rangle] \\ &\rightarrow \frac{4}{\mathcal{E}} [\langle \hat{\rho}_{bc}\hat{\rho}_{be} \rangle - (\rho_1 \otimes \rho_1)^2], \end{aligned} \quad (110)$$

where in the second step we reverted $E[\cdot] \rightarrow \langle \cdot \rangle$ and in the third⁶ assumed $\mathcal{E} \gg 1$. Note that the requirement $b \neq c \neq e$ implies that $\langle \hat{\rho}_{bc}\hat{\rho}_{be} \rangle_{bce} = \langle \langle \sum_{i \neq j} \delta_{ij}^{bc} \rangle_c \langle \sum_{k \neq l} \delta_{kl}^{be} \rangle_e \rangle_b$ cannot be simplified to the square of a single counter $\langle \langle \sum_{i \neq j} \delta_{ij}^{bc} \rangle_c^2 \rangle_b$: the event mixing involves three different events, not two. Secondly, the combinations of two equalities $b = d \neq c = e$ and $b = e \neq c = d$ in (109) yield another term of order \mathcal{E}^{-2} ,

$$\frac{2}{\mathcal{E}^2} [\langle \hat{\rho}_{bd}\hat{\rho}_{bd} \rangle_{bd} - (\rho_1 \otimes \rho_1)^2], \quad (111)$$

which we can safely neglect when $\langle n^2 \rangle / \mathcal{E} \ll 1$ except when there are few bins or large multiplicities even in small bins. It is worth emphasising that the extra factor 4 which appears in (110) arises from the same method that has been used for decades to justify use of (105). We find, by the same method, that the covariance between ρ_2 and $\rho_1 \otimes \rho_1$ is given by

$$\begin{aligned} \text{cov}(\rho_2, \rho_1 \otimes \rho_1) &= \text{cov}(\langle \hat{\rho}_{aa} \rangle, \langle \hat{\rho}_{bc} \rangle) \\ &= \frac{1}{\mathcal{E}\mathcal{E}^2} \sum_d \sum_{b \neq c} [E(\hat{\rho}_{da}\hat{\rho}_{bc}) - E(\hat{\rho}_{da})E(\hat{\rho}_{bc})] \\ &= \frac{2}{\mathcal{E}} [\langle \hat{\rho}_{da}\hat{\rho}_{db} \rangle - \langle \hat{\rho}_{da} \rangle \langle \hat{\rho}_{db} \rangle] \\ &= \frac{2}{\mathcal{E}} [\langle \hat{\rho}_{da}\hat{\rho}_{dc} \rangle - (\rho_2)(\rho_1 \otimes \rho_1)], \end{aligned} \quad (112)$$

so that we must, in addition, accumulate, for every event d , the product of the counters

$$\hat{\rho}_{da}\hat{\rho}_{dc} = \sum_{i \neq j} \delta_{ij}^{dd} \sum_k \left\langle \sum_{\ell} \delta_{k\ell}^{dc} \right\rangle_c. \quad (113)$$

Note that there is no restriction on track indices $k \neq i$ or $k \neq j$ in the d -event, meaning that events with $n(a) = 2$ contribute to this counter which would otherwise not be the case. Combining these, we find, to leading order in \mathcal{E}^{-1} and renaming mixed-event indices,

$$\begin{aligned} \text{var}(\kappa_2^I) &= \frac{1}{\mathcal{E}} \left\{ \langle (\hat{\rho}_{aa} - 2F_{2N}\hat{\rho}_{ac})(\hat{\rho}_{aa} - 2F_{2N}\hat{\rho}_{ad}) \rangle_a \right. \\ &\quad \left. - (\rho_2 - 2F_{2N}\rho_1 \otimes \rho_1)^2 \right\}, \end{aligned} \quad (114)$$

with all event indices strictly unequal and c - and d event averages understood where appropriate.⁷ Contrasting this with the traditional way to calculate the same variance,

$$\begin{aligned} \text{var}(\kappa_2^I) &= \frac{1}{\mathcal{E}} \left\{ \langle (\hat{\rho}_{aa} - F_{2N}\hat{\rho}_{ac})(\hat{\rho}_{aa} - F_{2N}\hat{\rho}_{ad}) \rangle \right. \\ &\quad \left. - (\rho_2 - F_{2N}\rho_1 \otimes \rho_1)^2 \right\}, \end{aligned} \quad (115)$$

it is clear that in previous analyses the two possible ways to set a equal to b or c were overlooked, while normal (non-internal) cumulants also omit the F_{2N} .

4.4.2. Statistical Errors for Third-Order Cumulants. In third-order, we will need $\delta_{ijk}^{abc} \equiv \delta(Q_a - Q_{ijk}^{abc})$ and similar quantities and the notation for counters $\hat{\rho}_{aaa}$, $\hat{\rho}_{aab}$, and $\hat{\rho}_{abc}$ corresponding to the event averages $\rho_3(Q_a) = \langle \hat{\rho}_{aaa} \rangle$, $\rho_2 \otimes \rho_1(Q_a) = \langle \hat{\rho}_{aab} \rangle$, and $\rho_1 \otimes \rho_1 \otimes \rho_1(Q_a) = \langle \hat{\rho}_{abc} \rangle$, respectively. Clearly, $a \neq b \neq c$ must hold in the third-order case. We obtain for the necessary third-order quantities (shuffling and/or renaming indices if necessary)

$$\text{var}(\rho_3) = \frac{1}{\mathcal{E}} [\langle (\hat{\rho}_{aaa})^2 \rangle_a - \rho_3^2]$$

$$\begin{aligned} \text{cov}(\rho_3, \rho_2 \otimes \rho_1) &= \frac{1}{\mathcal{E}\mathcal{E}^2} \sum_r \sum_{s \neq t} [E(\hat{\rho}_{rrr}\hat{\rho}_{sst}) - E(\hat{\rho}_{rrr})E(\hat{\rho}_{sst})] \\ &= \frac{1}{\mathcal{E}} [\langle \hat{\rho}_{rrr}\hat{\rho}_{rrs} \rangle + \langle \hat{\rho}_{rrr}\hat{\rho}_{rss} \rangle - 2\rho_3(\rho_2 \otimes \rho_1)], \end{aligned} \quad (116)$$

with $\hat{\rho}_{rrr}\hat{\rho}_{rrs} = \sum_{i \neq j \neq k} \delta_{ijk}^{rrr} \sum_{\ell \neq m} \langle \sum_n \delta_{\ell mn}^{rs} \rangle_s$ and $\hat{\rho}_{rrr}\hat{\rho}_{rss} = \sum_{i \neq j \neq k} \delta_{ijk}^{rrr} \sum_{\ell} \langle \sum_{m \neq n} \delta_{\ell mn}^{rs} \rangle_s$. The remaining variances and covariances needed for third-order correlations with GHP topology are, after renaming of indices,

$$\begin{aligned} \text{var}(\rho_2 \otimes \rho_1) &= \frac{\mathcal{E}^3}{(\mathcal{E}^2)^2} \sum_{g \neq e} \sum_{c \neq d} [E(\hat{\rho}_{gge}\hat{\rho}_{ccd}) - E(\hat{\rho}_{gge})E(\hat{\rho}_{ccd})] \end{aligned}$$

$$= \frac{\mathcal{E}^3}{(\mathcal{E}^2)^2} \left[\langle \hat{\rho}_{ggd} [\hat{\rho}_{ggc} + \hat{\rho}_{gcc} + \hat{\rho}_{ddc} + \hat{\rho}_{dcc}] \rangle - 4(\rho_2 \otimes \rho_1)^2 \right], \quad (117)$$

while we neglect

$$\frac{1}{\mathcal{E}^2} [\hat{\rho}_{ggc}\hat{\rho}_{ggc} + \hat{\rho}_{ggc}\hat{\rho}_{gcc} - 2(\rho_2 \otimes \rho_1)^2]. \quad (118)$$

The next term is simpler,

$$\begin{aligned} \text{cov}(\rho_3, \rho_1^3) &= \frac{1}{\mathcal{E}^2 \mathcal{E}^3} \sum_t \sum_{u \neq v \neq w} [E(\hat{\rho}_{ttt}\hat{\rho}_{uvw}) - E(\hat{\rho}_{ttt})E(\hat{\rho}_{uvw})] \\ &= \frac{3}{\mathcal{E}} [\langle \hat{\rho}_{ttt}\hat{\rho}_{tuv} \rangle - \rho_3 \rho_1^3], \end{aligned} \quad (119)$$

but the following is not,

$$\begin{aligned} \text{cov}(\rho_2 \otimes \rho_1, \rho_1^3) &= \frac{1}{\mathcal{E}^2 \mathcal{E}^3} \sum_{u \neq v \neq x \neq y \neq z} [E(\hat{\rho}_{uuv}\hat{\rho}_{xyz}) - E(\hat{\rho}_{uuv})E(\hat{\rho}_{xyz})] \\ &= \frac{3\mathcal{E}^4}{\mathcal{E}^2 \mathcal{E}^3} [\langle \hat{\rho}_{uwx}\hat{\rho}_{wyz} \rangle + \langle \hat{\rho}_{wx}\hat{\rho}_{wyz} \rangle - 2(\rho_2 \rho_1)(\rho_1^3)] \\ &\quad + \frac{6}{\mathcal{E}^2} [\langle \hat{\rho}_{wvx}\hat{\rho}_{wxy} \rangle - (\rho_2 \rho_1)(\rho_1^3)], \end{aligned} \quad (120)$$

and the large number of combinations makes the variance of ρ_1^3 particularly complicated,

$$\begin{aligned} \text{var}(\rho_1 \otimes \rho_1 \otimes \rho_1) &= \frac{1}{(\mathcal{E}^3)^2} \sum_{d \neq e \neq h \neq b \neq p \neq q} [E(\hat{\rho}_{deh}\hat{\rho}_{bpq}) - E(\hat{\rho}_{deh})E(\hat{\rho}_{bpq})] \\ &= \frac{9\mathcal{E}^5}{(\mathcal{E}^3)^2} [\langle \hat{\rho}_{beh}\hat{\rho}_{bpq} \rangle - (\rho_1^3)(\rho_1^3)] \\ &\quad + \frac{18\mathcal{E}^4}{(\mathcal{E}^3)^2} [\langle \hat{\rho}_{beh}\hat{\rho}_{beq} \rangle - (\rho_1^3)(\rho_1^3)] \\ &\quad + \frac{6}{\mathcal{E}^3} [\langle \hat{\rho}_{beh}\hat{\rho}_{beh} \rangle - (\rho_1^3)(\rho_1^3)]. \end{aligned} \quad (121)$$

For large \mathcal{E} , the leading order terms will usually dominate, so that we can neglect the subleading terms.⁸ To leading

order, we therefore obtain after substitution in (91) and again omitting brackets for non- a event averages

$$\begin{aligned} \text{var}(\kappa_3^I) &= \frac{1}{\mathcal{E}} \left\{ \langle \hat{\rho}_{aaa}^2 + 9\hat{\rho}_{aab}(\hat{\rho}_{aac} + \hat{\rho}_{acc} + \hat{\rho}_{bbc} + \hat{\rho}_{bcc}) \right. \\ &\quad + 9G_3^2 \hat{\rho}_{aaa}(\hat{\rho}_{abc}\hat{\rho}_{ade}) - 6\hat{\rho}_{aaa}(\hat{\rho}_{aab} + \hat{\rho}_{abb}) \\ &\quad + 6G_3 \hat{\rho}_{aaa}\hat{\rho}_{abc} - 18G_3 \hat{\rho}_{aab}(\hat{\rho}_{acd} + \hat{\rho}_{bcd}) \rangle_a \\ &\quad - [\rho_3^2 + 36(\rho_2 \otimes \rho_1)^2 + 9G_3^2(\rho_1^3)^2 \\ &\quad - 12\rho_3(\rho_2 \otimes \rho_1) + 6G_3\rho_3(\rho_1)^3 \\ &\quad \left. - 36G_3^2(\rho_2 \otimes \rho_1)(\rho_1^3) \right\}, \\ &= \frac{1}{\mathcal{E}} \left\{ \langle (\hat{\rho}_{aaa} - 3\hat{\rho}_{aab} - 3\hat{\rho}_{abb} + 3G_3\hat{\rho}_{abc}) \right. \\ &\quad \times (\hat{\rho}_{aaa} - 3\hat{\rho}_{aad} - 3\hat{\rho}_{add} + 3G_3\hat{\rho}_{ade}) \rangle_a \\ &\quad \left. - [\rho_3 - 6\rho_2 \otimes \rho_1 + 3G_3(\rho_1)^3]^2 \right\}. \end{aligned} \quad (122)$$

While the factorised form is again instructive, it cannot be calculated in this form within the a -loop in the analysis since the G_{3N} constants are known only on completion of the entire sample analysis. Rather, the full palette of product counters $\hat{\rho}\hat{\rho}$ has to be accumulated and averaged and combined only in the final phase of the analysis.

5. Averaged Internal Cumulants

As N is only an approximation for the true total event multiplicity anyway, and for cases of small sample statistics, it may be necessary or desirable to group subsamples of fixed N into multiplicity classes $N \in [A, B]$. It is important, however, not to simply lump all events within this multiplicity class into a single ‘‘half-inclusive’’ subsample, because, as has long been known [15], that results in terms entering the cumulants which arise solely to ‘‘multiplicity mixing’’ (MM) of events of different N . Given the arbitrary choice of $[A, B]$, such MM correlations are spurious and avoided in favour of ‘‘Averaged-Internal’’ (AI) correlations⁹ defined as follows. Using the renormalised multiplicity distribution

$$\mathcal{R}'_N = \frac{\mathcal{R}_N}{\sum_{N=A}^B \mathcal{R}_N} = \frac{\mathcal{E}_N}{\sum_{N=A}^B \mathcal{E}_N}, \quad (123)$$

the AI unnormalised cumulants, reference distributions, and normalised AI cumulants are

$$\kappa_2^{\text{AI}}(Q | \mathcal{S}_{AB}) = \sum_{N=A}^B \mathcal{R}'_N \kappa_2^I(Q | \mathcal{S}_N), \quad (124)$$

$$\rho_1 \otimes \rho_1(Q | \mathcal{S}_{AB}) = \sum_{N=A}^B \mathcal{R}'_N F_{2N} \rho_1 \otimes \rho_1(Q | \mathcal{S}_N), \quad (125)$$

$$\begin{aligned} K_2^{\text{AI}}(Q | \mathcal{S}_{AB}) &= \frac{\kappa_2^{\text{AI}}(Q | \mathcal{S}_{AB})}{\rho_1 \otimes \rho_1(Q | \mathcal{S}_{AB})} \\ &= \frac{\sum_{N=A}^B \mathcal{R}'_N \rho_2(Q | \mathcal{S}_N)}{\sum_{N=A}^B \mathcal{R}'_N F_{2N} \rho_1 \otimes \rho_1(Q | \mathcal{S}_N)} - 1. \end{aligned} \quad (126)$$

Note that the correction factors F_{2N} , which are normalised factorial moments of n for fixed N , are part of the summed normalisations.¹⁰ In third-order, we have correspondingly

$$\kappa_3^{\text{AI}}(Q_a | \mathcal{S}_{AB}) = \sum_{N=A}^B \mathcal{R}'_N \kappa_3^I(Q_a | \mathcal{S}_N), \quad (127)$$

$$\begin{aligned} \rho_1 \otimes \rho_1 \otimes \rho_1(Q_a | \mathcal{S}_{AB}) \\ = \sum_{N=A}^B \mathcal{R}'_N F_{3N} \rho_1 \otimes \rho_1 \otimes \rho_1(Q_a | \mathcal{S}_N), \end{aligned} \quad (128)$$

$$K_3^{\text{AI}}(Q_a | \mathcal{S}_{AB}) = \frac{\kappa_3^{\text{AI}}(Q_a | \mathcal{S}_{AB})}{\rho_1 \otimes \rho_1 \otimes \rho_1(Q_a | \mathcal{S}_{AB})}. \quad (129)$$

Note also that (128) holds for the normalisation only and not for the last term in κ_3^I , which is $(3F_{2N} - F_{3N})\rho_1 \otimes \rho_1 \otimes \rho_1$ — but that is already taken care of in the formula (69) for κ_3^I itself. Expressions for an inclusive (all- N) multiplicity summation of internal cumulants are obtained from the above by setting $A = 0$ and $B = \infty$. The AI (Averaged Internal) correlations (124) and (127) represent refined versions of what has traditionally been termed “Short-Range Correlations,” differing from the original formulae [15, 17] by the F_{2N} and G_{3N} factors, respectively. This was originally pointed out in [18] but only for multinomials in N .

Regarding variances and standard errors for AI correlations, we first note that, since subsamples \mathcal{S}_N are strictly mutually independent, a variance over the $[A, B]$ range is simply the weighted sum of the corresponding fixed- N variances. From (124) and (129), we have for all orders r

$$\kappa_r^{\text{AI}}(Q | \mathcal{S}_{AB}) = \sum_{N=A}^B \mathcal{R}'_N \kappa_r^I(Q | \mathcal{S}_N) \quad r = 2, 3, \dots, \quad (130)$$

and given the independence of any functions f and g of different multiplicity subsamples, $E[f(\mathcal{S}_N) \cdot g(\mathcal{S}_{N'})] = E[f(\mathcal{S}_N)] \cdot E[g(\mathcal{S}_{N'})]$ for all $N \neq N'$, we conclude that

$$\text{var}[\kappa_r^{\text{AI}}(Q | \mathcal{S}_{AB})] = \sum_N (\mathcal{R}'_N)^2 \text{var}[\kappa_r^I(Q | \mathcal{S}_N)], \quad (131)$$

$$\text{var}[\rho_1^r(Q | \mathcal{S}_{AB})] = \sum_N (\mathcal{R}'_N)^2 (F_{rN})^2 \text{var}[\rho_1^r(Q | \mathcal{S}_N)], \quad (132)$$

$$\begin{aligned} \text{cov}[\kappa_r^{\text{AI}}(Q | \mathcal{S}_{AB}), \rho_1^r(Q | \mathcal{S}_{AB})] \\ = \sum_N (\mathcal{R}'_N)^2 F_{rN} \text{cov}[\kappa_r^I(Q | \mathcal{S}_N), \rho_1^r(Q | \mathcal{S}_N)], \end{aligned} \quad (133)$$

which are known functions in terms of Sections 4.4.1 and 4.4.2, while for the normalised cumulants in $[A, B]$, covariances between numerator and denominator are (omitting the Q)

$$\begin{aligned} \text{cov}[\kappa_2^I(\mathcal{S}_N), \rho_1^2(\mathcal{S}_N)] &= \text{cov}[\rho_2(\mathcal{S}_N), \rho_1 \otimes \rho_1(\mathcal{S}_N)] \\ &\quad - F_{2N} \text{var}(\rho_1 \otimes \rho_1(\mathcal{S}_N)), \\ \text{cov}[\kappa_3^I(\mathcal{S}_N), \rho_1^3(\mathcal{S}_N)] &= \text{cov}[\rho_3(\mathcal{S}_N), \rho_1^3(\mathcal{S}_N)] \\ &\quad - 3 \text{cov}[\rho_2 \otimes \rho_1(\mathcal{S}_N), \rho_1^3(\mathcal{S}_N)] \\ &\quad + G_3 \text{var}[\rho_1^3(\mathcal{S}_N)], \end{aligned} \quad (134)$$

so that the normalised range cumulants have variances

$$\begin{aligned} \text{var}[K_r^{\text{AI}}(Q | \mathcal{S}_{AB})] &= (K_r^{\text{AI}})^2 \\ &\quad \cdot \left[\frac{\text{var}[\kappa_r(\mathcal{S}_{AB})]}{(\kappa_r(\mathcal{S}_{AB}))^2} + \frac{\text{var}[\rho_1^r(\mathcal{S}_{AB})]}{(\rho_1^r(\mathcal{S}_{AB}))^2} \right. \\ &\quad \left. - 2 \frac{\text{cov}[\kappa_r(\mathcal{S}_{AB}), \rho_1^r(\mathcal{S}_{AB})]}{\kappa_r(\mathcal{S}_{AB}) \cdot \rho_1^r(\mathcal{S}_{AB})} \right], \end{aligned} \quad (135)$$

and standard errors are given by¹¹

$$\sigma(K_r^{\text{AI}}(\mathcal{S}_{AB})) = \sqrt{\text{var}(K_r^{\text{AI}}(Q | \mathcal{S}_{AB}))}. \quad (136)$$

6. Event Mixing Algorithms

“Event mixing” [72] is widely used to simulate uncorrelated or semicorrelated quantities such as ρ_1^3 and $\rho_2 \otimes \rho_1$. The idea has always been to use the experimental sample at hand to simulate the baseline of independence referred to in Section 3.1 in such a way that criteria 2 (independence of momenta), 4 (reproducing the one-particle momentum space distribution), and 6 (normalisation) are all addressed simultaneously. Ideally, all effects bar the desired correlation are elegantly removed in this way.

For the internal cumulants and their variances and covariances derived above, event mixing requires keeping track of counters of all orders in each of the subsamples \mathcal{S}_N . A count of event indices in Section 4 shows that in a brute-force calculation we would need, for each subsample, a minimum of five independent event averages or $O(\mathcal{E}^5)$ event combinations; furthermore, caution would advise not to use the same event in calculating related counters, so that selection and use of more than five events in mixing are advisable. The resulting excessive number of full event averages, mixing every (sub) sample event with every other one, is therefore not feasible.

If the order of events in the sample is random, the multiple event averages can be simplified by the use of the following multiple event buffer algorithm.

- (1) A single overall event loop equivalent to the event index a runs over the entire inclusive sample \mathcal{S} . A given event a will have a multiplicity $N = N(a)$, so for that particular a correlation analysis for subsample \mathcal{S}_N is advanced by one event while the others remain dormant.¹² In this way, a , which always refers to the sibling event, runs over all \mathcal{E}_N events of every subsample \mathcal{S}_N . There is no need to either explicitly sort the inclusive sample into subsamples or to run multiple jobs for fixed N .
- (2) The first \mathcal{E}_B events¹³ of a given multiplicity N are used solely to fill up the buffer without doing any analysis. Once a given buffer has been filled, event mixing analysis proceeds for that subsample as follows.
 - (a) A newly read a -event is assigned to the $N = N(a)$ buffer, the earliest event in that buffer is discarded, and sums for averages entering F_{2N} and F_{3N} as well as the sibling counters $\hat{\rho}_{aa}$, $\hat{\rho}_{aa}$, $(\hat{\rho}_{aa})^2$, and $(\hat{\rho}_{aaa})^2$ are updated.
 - (b) Event combinations for mixed-event counters are built up by picking any one of the $\mathcal{E}_B - 1$ other events in that buffer and calling it b , thereafter picking any one of the remaining $\mathcal{E}_B - 2$ events in the buffer, calling it c and so on. While for third-order, only five events (including the sibling event) are needed to construct all the counters required; in practice it is better to use different mixing events for different counters to root out even traces of unwanted correlations between different mixing counters. The random selection of events rather than tracks for mixing is necessary to ensure that more than one track per event can be used as required for counters of Sections 3 and 4 such as $\hat{\rho}_{bbc}$.
 - (c) For a given event set b, c, d, \dots , the mixing counters are incremented using all possible combinations of the n_a tracks in event a together with all the n_b, n_c, \dots tracks in the selected events b, c, \dots mixing events. For example, $\hat{\rho}_{bbc}$ would use all possible $n_b(n_b - 1)$ pairs of b -tracks¹⁴ together with all possible n_c single c -tracks. The mixing of all tracks of a given event rather than just selected ones ensures that the fluctuations in n for given fixed N are automatically contained in the counters.
 - (d) For constant a , the process of selecting events b, c, \dots is repeated $C_{\text{mix}} = 10\text{--}100$ times to reduce the statistical errors, avoiding events that have been used in previous selections. Efficiency can be maximised by tuning of both the number of events \mathcal{E}_B stored in each buffer and by the number of resamples C_{mix} .

- (3) Once the entire sample has been processed via the a -event loop, the b - c - d -event averages are normalised by $C_{\text{mix}}(\mathcal{E}_N - \mathcal{E}_B)$, while the primary a -average is normalised by $(\mathcal{E}_N - \mathcal{E}_B)$.
- (4) Unnormalised and normalised correlation quantities, their standard errors, and correction factors are constructed by appropriate combinations of averaged counters.
- (5) Results from fixed- N subsamples can then be combined into AI correlations over partial ranges of N or the entire inclusive sample at the end of the event loop using the methods outlined in Section 5.

7. Discussion and Conclusions

(1) Correlations are only defined properly if the null case or reference distribution is defined on the same level of sophistication as the correlation itself. Translated into statistics, the six criteria set out in Section 3.1 for a reference sample for correlations at fixed charged multiplicity N lead straight to the definition of the reference sample as the average of multinomials given in (51), weighted by the conditional multiplicity distribution \mathcal{R}_{nN} . Assigning Bernoulli probabilities $\alpha(\mathbf{p} \mid \mathcal{S}_{nN}) = \langle \rho(\mathbf{p} \mid \mathcal{S}_{nN}) \rangle_N / \langle n \rangle_N$ yields the reference density (56) and generating functional (58).

(2) From the theorem that internal cumulants are given by the difference between measured and reference cumulants, we obtain normalised and unnormalised internal cumulants which satisfy every stated criterion for proper correlations for fixed- N samples.

(3) We have highlighted the distinction between n , the particles entering the correlation analysis itself, and N , the particles determining the event selection criterion for a particular semi-inclusive subsample. Various correction factors are shown to be fair to good approximations of these exact results in some cases but far off the mark in others. Surprisingly, normalised cumulants are far more sensitive to these corrections, through the normalisation prefactor, than their unnormalised counterparts. To belabour the point, for any variables (x_1, x_2) , different definitions for correction factor $1/F$ for fixed- N correlations of positive pions,

$$K_2(x_1, x_2 \mid \mathcal{S}_N) = \frac{1}{F} \frac{\rho(x_1, x_2 \mid \mathcal{S}_N)}{\rho(x_1 \mid \mathcal{S}_N) \rho(x_2 \mid \mathcal{S}_N)} - 1, \quad (137)$$

can be very important at low multiplicities, with $F = 1$ (Poisson) being the worst approximation, $F = N(N - 1)/N^2$ being a fair one, and $\langle n(n - 1) \rangle_N / \langle n \rangle_N^2$ being the best.

For inclusive correlations, correction factors such as $\langle n \rangle^2 / \langle n(n - 1) \rangle_{\text{incl}}$ were proposed early on in [73, 74] in an approach based on probabilities rather than densities. Reference [75] specifically calls the inclusion of these correction factors meaningless because the theory then requires that the emission function be identically zero. We note that the argument in all those references relates to inclusive samples, while for the samples of fixed N considered in this paper the prefactor, which is *an average of n at fixed N* , is a necessity. Either way, the arbitrariness of the use or nonuse

of the prefactor has been eliminated here based solely on considerations related to the reference distribution.

(4) The problem posed in this paper, namely, the relation between charged multiplicity on the one hand and correlations based on the conditional n -distribution \mathcal{R}_{nN} has attracted little attention in the literature. Indeed, almost all theoretical work on multipion correlations, as for example summarised in [76], starts from the projection of final-state events, with all their different particle species, onto the single-species subspace of either n_+ (positive pions) or n_- (negative pions) correlations, to the exclusion of the other charge. It would be interesting to see a combined theory for both n_+ and n_- , which would encompass all the work done so far plus correlations between unlike-sign pions and, of course, the issue raised by us here.

(5) As shown in Figures 2 and 3, correction factors for third-order are larger than the second-order ones. For higher r th-order correlations, the effect of using a fixed- N subsample is suppressed by approximately $1/\langle n^{r-1} \rangle_N$ for unnormalised cumulants but actually worsens for normalised cumulants due to the normalisation prefactors $\langle n \rangle_N^r / \langle n^r \rangle_N$ for small n . The importance of accurate correction of normalised quantities therefore rises with order of correlation.

(6) The difference between Poissonian and internal cumulants is largest at small multiplicities n . The mixed-multinomial prescription will therefore be required for *any* correlation analysis involving small n , independently of the magnitude of N . Apart from the usual suspects of leptonic, hadronic, and low-energy collisions, the low- n case occurs both for very restricted phase space (such as in spectrometer experiments) and for correlations of rare particles such as kaons and baryons, even for large N .

(7) Since n fluctuates according to the conditional multiplicity distribution \mathcal{R}_{nN} , the degree to which fixed- N correlations differ from inclusive ones is strongly coupled to the character of \mathcal{R}_{nN} . In general, \mathcal{R}_{nN} is sub-Poissonian and so F_{rN} falls below the Poisson limit of 1. The correction from fixed- N Poissonian to internal normalised cumulants is hence upward, not downward as in the case of multiplicity-mixing corrections.

(8) While not the main subject of the present paper, some light is cast on the relationship between three levels of correlation, namely, correlations inherent in the overall multiplicity distribution, multiplicity-mixing correlations, and the true internal correlations for fixed N . Each of these can and should be treated separately. The averaged-internal correlations of Section 5 are a compromise solution which may be useful both for physics reasons and for small datasets.

(9) The fixed- N corrections discussed here are separate and complementary to other important effects at low multiplicity. References [76, 77] highlight, for example, possible effects of “residual correlations” resulting from projecting from multipion to two-pion correlations.

Energy-momentum conservation would also play a role. Borghini [78, 79] has, for example, calculated the effect of momentum conservation for normalised two- and three-particle cumulants in momenta and \mathbf{p}_t . However, the saddlepoint method used applies to the large- N limit, and

the results cannot be directly applied to the low- N (and hence low- n) samples under discussion here. Indeed, momentum conservation will be near-irrelevant for cases of large N and small n as discussed above, but the small- n corrections of this paper will remain important. For the specific case of like-sign pion femtoscopy, the fact that only $n \sim \mathcal{A}N/2\Omega$ out of the N charged pions are used and that momentum conservation constraints include all other final-state particles both imply that momentum conservation constraints may be less important than the internal-cumulant correction introduced here.

For the specific choice of correlation variables Q and Q_a for two- and three-particle cumulants, the contribution of momentum conservation to cumulants at small Q will be small since the counts will be dominated by pairs at small $(\Delta\phi, \Delta y)$ and intermediate (p_{t1}, p_{t2}) . As pointed out by [1], momentum conservation exerts the greatest influence at large pair or triplet momenta and hence mostly at large Q , where it may lead to moments and cumulants which do not converge to a constant as presupposed in most fits. The ad hoc method of multiplying fit parametrisations by a prefactor $1 + cQ$ with c a free parameter does not adequately address the problem.

Regarding the multiplicity dependence of the influence of energy-momentum conservation, [2] calculates the effect of energy-momentum conservation on single-particle differential observables and finds significant systematic effects. No doubt this must also be the case for multiparticle observables, although as we have pointed out above, the effect of conservation laws will be diluted by the fact that fewer than half of the final-state particles of any given event are actually used in the present analysis. Detailed investigations are beyond the scope of this paper.

(10) We have also recalculated statistical errors for products of event averages starting from the original prescription which forms the basis of frequentist statistical error calculations. Compared to conventional statistical error calculations, new prefactors appear in our calculations — see for example (110) and the results in Section 4.4.2—which have surprisingly been missed so far.

(11) We note that the present formalism is still in the frequentist statistics mindset, which may be inaccurate for low multiplicities and should be supplanted by a proper Bayesian analysis. The final word has certainly not been spoken about correlation analysis of small- n datasets.

Acknowledgment

This work was supported in part by the National Research Foundation of South Africa.

Endnotes

1. These event ratios are not probabilities in the strict sense; in the frequentist definition of probability, the two are equal only in the limit $\mathcal{E} \rightarrow \infty$. We therefore avoid the use of the symbol P_N for such and similar data ratios.
2. Pairs are *ordered*, for example, a particular pair is counted twice. Unordered pair counting is possible but unnecessarily complicates sum limits.

3. A counter of order $N(a)$ can be made to behave like one of order $N(a) + 1$ by defining an additional dummy data point $\mathbf{P}_{N(a)+1}$ which lies *outside* the normal domain Ω , but we will not pursue this here.
4. We could argue that there are three different variables Q^{aa} , Q^{ab} , and Q^{bc} , where the last two differ in the sense that Q^{ab} contains a track from the “current” event while Q^{bc} does not. As shown below, this distinction is unnecessary as long as we keep careful track of possible occurrences of equal event indices.
5. While it is irrelevant whether event a is included or excluded in theoretical calculations of event mixing, it should never be used in actual implementations of mixing.
6. Due to the factorisation of the expectation values earlier on, the fact that index b appears in two separate sample averages does *not* prevent us from replacing $\langle \hat{\rho}_{bc} \rangle$ and $\langle \hat{\rho}_{be} \rangle$ by $(\rho_1 \otimes \rho_1)^2$.
7. While this factorised form is instructive, it cannot be used directly since F_{2N} can be determined only on completion of the entire sample analysis. Each of the counter products in (114) must hence be implemented separately.
8. If and when large bins are used and the sixth power of the measured positive-pion multiplicity becomes comparable to \mathcal{E} , subleading terms will have to be included. This requirement is less trivial than it may sound, since for subsamples of fixed multiplicity N , the number of events \mathcal{E}_N is much smaller than \mathcal{E} , while of course n may be substantial when N is large. For UA1, $\mathcal{E}_N = O(10^4)$ while $\mathcal{E} = O(10^6)$.
9. Historically, this issue was discussed under the name “Short-Range Correlations” and “Long-Range Correlations” [15]. Since current usage of the term “Short-Range Correlations” refers to correlations over small scales in momentum space, we rather define them more accurately as “Averaged Internal” (AI) correlations and “Multiplicity-Mixing” (MM) correlations, noting also that the correction factors in (124)–(129) do not appear in the earlier literature.
10. An expression with a correction factor outside the sums such as

$$K_2 = \frac{\langle n \rangle^2}{\langle n(n-1) \rangle} \cdot \frac{\sum_N \mathcal{R}'_N \kappa_2^I(Q | \mathcal{S}_N)}{\sum_N \mathcal{R}'_N \rho_1 \otimes \rho_1(Q | \mathcal{S}_N)} \quad (138)$$

is inconsistent with AI correlation averaging if the single-particle spectra or some other physical effect change significantly within the range $[A, B]$. We also note that the above differs from the formula used in [65] for second-order correlations in \mathbf{q} . In the present notation, the cumulant used in [65] reads

$$K_2(\mathbf{q}) = \frac{\sum_N \mathcal{R}'_N \rho_2(\mathbf{q} | \mathcal{S}_N)}{\sum_N \mathcal{R}'_N ((N-1)/N) \rho_1 \otimes \rho_1(\mathbf{q} | \mathcal{S}_N)} - 1, \quad (139)$$

that is a correction for an N -multinomial rather than the weighted sum of n -multinomials used in (124)–(126).

11. One might expect $\sigma(K_r^{AI}(\mathcal{S}_{AB}))$ to include a prefactor of the sort seen in (105) that is something like $\sqrt{[\text{var}(K_r^{AI}(Q | \mathcal{S}_{AB}))/[B-A]]}$, but this would be incorrect. The reason is that the formulae (131)–(133) for range AB can be considered as an average, so that we can apply the methods of Section 4.3 to obtain the same results. For example, considering $\kappa_2^{AI}(Q | \mathcal{S}_{AB}) \equiv \bar{\kappa}_2$ of (124) as an average and writing $\kappa_2^I(Q | \mathcal{S}_N) \equiv \kappa_{2N}$, the variance on this average is

$$\begin{aligned} \text{var}[\bar{\kappa}_2] &= E[(\bar{\kappa}_2)^2] - E[\bar{\kappa}_2]^2 \\ &= E\left[\left(\sum_N \mathcal{R}'_N \kappa_{2N}\right) \cdot \left(\sum_{N'} \mathcal{R}'_{N'} \kappa_{2N'}\right)\right] \\ &\quad - E\left[\left(\sum_N \mathcal{R}'_N \kappa_{2N}\right)\right] E\left[\left(\sum_{N'} \mathcal{R}'_{N'} \kappa_{2N'}\right)\right] \quad (140) \\ &= \sum_{N=N'} (\mathcal{R}'_N)^2 \left(E[\kappa_{2N}^2] - E[\kappa_2^I(Q | \mathcal{S}_N)]^2\right) \\ &= \sum_N (\mathcal{R}'_N)^2 \text{var}(\kappa_{2N}), \end{aligned}$$

which is identical with (131). Therefore, division by $B-A$ is incorrect.

12. Inevitably, there are very few events in the high-multiplicity tail of the entire sample. These must be treated separately, for example, by putting all events with N greater than some threshold into a single buffer.
13. The number of events in a buffer \mathcal{E}_B is usually kept the same for each buffer.
14. As in the definition of the counters, each pair is counted twice: these are *ordered pairs*.

References

- [1] Z. Chajecski and M. Lisa, “Global conservation laws and femtoscopy of small systems,” *Physical Review C*, vol. 78, no. 6, Article ID 064903, 17 pages, 2008.
- [2] Z. Chajecski and M. Lisa, “Conservation laws and the multiplicity evolution of spectra at the relativistic heavy ion collider,” *Physical Review C*, vol. 79, no. 3, Article ID 034908, 15 pages, 2009.
- [3] A. Breakstone, R. Campanini, H. B. Crawley et al., “Multiplicity dependence of the average transverse momentum and of the particle source size in $\bar{p}p$ interactions at $\sqrt{s} = 62, 44$ and 31 GeV,” *Zeitschrift für Physik C*, vol. 33, no. 3, pp. 333–338, 1987.
- [4] B. Buschbeck, H. C. Eggers, and P. Lipa, “Multiplicity dependence of correlation functions in $\bar{p}p$ reactions at $\sqrt{s} = 630$ GeV,” *Physics Letters B*, vol. 481, pp. 187–193, 2000.
- [5] B. Buschbeck and H. C. Eggers, “Multiplicity dependence of Bose-Einstein correlations in antiproton-proton reactions: a discussion of possible origins,” in *Proceedings of the 9th International Workshop on Multiparticle Production*, A. Giovannini and R. Ugoccioni, Eds., Torino, Italy, June 2000.

- [6] B. Buschbeck and H. C. Eggers, "Multiplicity dependence of Bose-Einstein correlations in $\bar{p}p$ reactions: a discussion of possible origins," *Nuclear Physics B*, vol. 92, no. 1-3, pp. 235-246, 2001.
- [7] W. Kittel and E. A. de Wolf, *Soft Multihadron Dynamics*, World Scientific, Singapore, 2005.
- [8] M. Lisa, S. Pratt, R. Soltz, and U. A. Wiedemann, "Femtoscopy in relativistic heavy ion collisions: two decades of progress," *Annual Review of Nuclear and Particle Science*, vol. 55, pp. 357-402.
- [9] Z. Chajecski, "Femtoscopy in hadron and lepton collisions: RHIC results and world systematics," *Acta Physica Polonica B*, vol. 40, pp. 1119-1136, 2009.
- [10] V. Khachatryan, A. M. Sirunyan, A. Tumasyan et al., "First measurement of Bose-Einstein correlations in proton-proton collisions at $\sqrt{s} = 0.9$ and 2.36 TeV at the LHC," *Physical Review Letters*, vol. 105, Article ID 032001, 2010.
- [11] V. Khachatryan, A. M. Sirunyan, A. Tumasyan et al., "Measurement of Bose-Einstein correlations in pp collisions at $\sqrt{s} = 0.9$ and 7 TeV," *Journal of High Energy Physics*, vol. 5, article 029, 2011.
- [12] G. Alexander, "The dependence of Bose-Einstein correlations, on energy, multiplicity and hadronic jets," *Journal of Physics G*, vol. 39, Article ID 085007, 2012.
- [13] N. Suzuki and M. Biyajima, "Multiplicity dependence of identical particle correlations in the quantum optical approach," *Physical Review C*, vol. 60, no. 3, Article ID 034903, 1999.
- [14] Z. Koba, "Many-particle inclusive cross-sections and correlations in hadronic production processes at very high energy," *Acta Physica Polonica B*, vol. 4, pp. 95-143, 1973.
- [15] L. Foà, "Inclusive study of high-energy multiparticle production and two-body correlations," *Physics Reports*, vol. 22, no. 1, pp. 1-56, 1975.
- [16] K. Eggert, H. Frenzel, W. Thomé et al., "Angular correlations between the charged particles produced in pp collisions at ISR energies," *Nuclear Physics B*, vol. 86, no. 2, pp. 201-215, 1975.
- [17] P. Carruthers, "Structure of correlation functions," *Physical Review A*, vol. 43, no. 6, pp. 2632-2639, 1991.
- [18] H.C. Eggers, P. Lipa, and B. Buschbeck, "Generalized moments and cumulants for samples of fixed multiplicity," *Physical Review D*, vol. 53, pp. R4711-R4714, 1996.
- [19] A. H. Mueller, "Multiplicity distributions in regge-pole-dominated inclusive reactions," *Physical Review D*, vol. 4, pp. 150-155, 1971.
- [20] K. Aamodt, N. Abel, U. Abeyssekara et al., "Two-pion Bose-Einstein correlations in pp collisions at $\sqrt{s} = 900$ GeV," *Physical Review D*, vol. 82, Article ID 052001, 2010.
- [21] U. Heinz and Q. H. Zhang, "What can we learn from three-pion interferometry?" *Physical Review C*, vol. 56, no. 1, pp. 426-431, 1997.
- [22] H. C. Eggers, P. Lipa, and B. Buschbeck, "A sensitive test for models of Bose-Einstein correlations," *Physical Review Letters* 79, no. 2, pp. 197-200, 1997.
- [23] I. V. Andreev, M. Plümer, and R. M. Weiner, "Quantum-statistical space-time approach to Bose-Einstein correlations and multiplicity distributions," *International Journal of Modern Physics A*, vol. 8, no. 26, pp. 4577-4625, 1993.
- [24] T. Csörgö, W. Kittel, W. J. Metzger, and T. Novak, "Parametrization of Bose-Einstein correlations and reconstruction of the space-time evolution of pion production in e^+e^- annihilation," *Physics Letters B*, vol. 663, no. 3, pp. 214-216, 2008.
- [25] B. Andersson and M. Ringner, "Transverse and longitudinal Bose-Einstein correlations," *Physics Letters B*, vol. 421, no. 1-4, pp. 283-288, 1998.
- [26] V. P. Kenney, N. N. Biswas, J. M. Bishop et al., "Observation of three-particle correlations in inclusive $\pi\bar{p}$ reactions at 200 GeV/c," *Nuclear Physics B*, vol. 144, pp. 312-316, 1978.
- [27] N. Neumeister, T. Gajdosik, B. Buschbeck et al., "Higher order Bose-Einstein correlations in $\bar{p}p$ collisions at $\sqrt{s} = 630$ and 900 GeV," *Physics Letters B*, vol. 275, no. 1-2, pp. 186-194, 1992.
- [28] N. M. Agababyan, I. V. Azhinenko, M. R. Ataian et al., "Genuine higher order correlations in π^+p and K^+p collisions at 250-GeV/c," *Physics Letters B*, vol. 332, pp. 458-464, 1994.
- [29] N. M. Agababyan, I. V. Ajinenko, M. R. Atayan et al., "Higher order Bose-Einstein correlations in π^+p and K^+p collisions at 250 GeV/c," *Zeitschrift für Physik C*, vol. 68, no. 2, pp. 229-237, 1995.
- [30] P. Abreu, W. Adam, T. Adye et al., "Observation of short range three-particle correlations in e^+e^- annihilations at LEP energies," *Physics Letters B*, vol. 355, no. 1-2, pp. 415-424, 1995.
- [31] K. Ackerstaff, G. Alexander, Allison et al., "Bose-Einstein correlations of three charged pions in Hadronic Z^0 decays," *European Physical Journal C*, vol. 5, no. 2, pp. 239-248, 1998.
- [32] P. Achardu, O. Adriani, M. Aguilar-Benitez et al., "Measurement of genuine three-particle Bose-Einstein correlations in Hadronic Z^0 decay," *Physics Letters B*, vol. 540, no. 3-4, pp. 185-198, 2002.
- [33] G. Abbiendi, C. Ainsley, P. F. Åkesson et al., "Genuine correlations of like-sign particles in Hadronic Z^0 decays," *Physics Letters B*, vol. 523, no. 1-2, pp. 35-52, 2001.
- [34] M. M. Aggarwal, A. Agnihotri, Z. Ahammed et al., "Three-pion interferometry results from central Pb+Pb collisions at 158 A GeV/c," *Physical Review Letters*, vol. 85, no. 14, pp. 2895-2899, 2000.
- [35] J. Adams, C. Adler, Z. Ahammed et al., "Three-pion Hanbury-Brown-Twiss correlations in relativistic heavy-ion collisions from the STAR experiment," *Physical Review Letters*, vol. 91, no. 26, Article ID 262301, 2003.
- [36] A. Sakaguchi, I. G. Bearden, H. B. Bøggild et al., "One-, two- and three-particle hadron spectra: recent results from CERN/SPS experiment NA44," *Nuclear Physics A*, vol. 638, no. 1-2, pp. 103c-114c, 1998.
- [37] I. G. Bearden, H. Bøggild, J. G. Boissevain et al., "One and two dimensional analysis of 3pi correlations measured in Pb+Pb interactions," *Physics Letters B*, vol. 517, pp. 25-31, 2001.
- [38] V. A. Khoze and W. Ochs, "Perturbative QCD approach to multiparticle production," *International Journal of Modern Physics A*, vol. 12, no. 17, Article ID 2949, 1997.
- [39] P. Abreu, W. Adam, T. Adye et al., "Multiplicity fluctuations in one- and two-dimensional angular intervals compared with analytic QCD calculations," *Physics Letters B*, vol. 457, no. 4, pp. 368-382, 1999.
- [40] R. Pérez-Ramos, V. Mathieu, and M. A. Sanchis-Lozano, "Three-particle correlations in QCD parton showers," *Physical Review D*, vol. 84, Article ID 034015, 2011.
- [41] C. A. Pruneau, "Methods for Jet studies with three-particle correlations," *Physical Review C*, vol. 74, no. 6, Article ID 064910, 2006.
- [42] J. G. Ulery and F. Wang, "Analysis method for jet-like three-particle azimuthal correlations," *Nuclear Instruments and Methods in Physics Research A*, vol. 595, no. 2, pp. 502-511, 2008.

- [43] C. A. Pruneau, “Three-particle cumulant study of conical emission,” *Physical Review C*, vol. 79, no. 4, Article ID 044907, 2009.
- [44] G. Aad, B. Abbott, J. Abdallah et al., “Forward-backward correlations and charged-particle azimuthal distributions in pp interactions using the ATLAS detector,” *Journal of High Energy Physics*, vol. 2012, article 19, 2012.
- [45] L. Yi, “Isolation of flow and nonflow by two- and multi-particle cumulant measurements of v_n in $\sqrt{s_{NN}} = 200$ GeV Au + Au collisions by STAR,” *Nuclear Physics A*, vol. 904-905, pp. 401c–404c, 2013.
- [46] S. Pratt, “General charge balance functions, a tool for studying the chemical evolution of the quark-gluon plasma,” *Physical Review C*, vol. 85, no. 1, Article ID 014904, 2012.
- [47] A. Bzdak and V. Koch, “Acceptance corrections to net baryon and net charge cumulants,” *Physical Review C*, vol. 86, no. 4, Article ID 044904, 7 pages, 2012.
- [48] B. Abelev, J. Adam, D. Adamová et al., “Charge separation relative to the reaction plane in Pb-Pb collisions at $\sqrt{s_{NN}} = 2.76$ TeV,” *Physical Review Letters*, vol. 110, no. 1, Article ID 012301, 2013.
- [49] P. Carruthers, H. C. Eggers, and I. Sarcevic, “Analysis of multiplicity moments for hadronic multiparticle data,” *Physics Letters B*, vol. 254, no. 1-2, pp. 258–266, 1991.
- [50] E. A. De Wolf, I. M. Dremin, and W. Kittel, “Scaling laws for density correlations and fluctuations in multiparticle dynamics,” *Physics Reports*, vol. 270, no. 1-2, pp. 1–141, 1996.
- [51] E. K. G. Sarkisyan, “Description of local multiplicity fluctuations and genuine multiparticle correlations,” *Physics Letters B*, vol. 477, no. 1–3, pp. 1–12, 2000.
- [52] G. Alexander and E. K. G. Sarkisyan, “The effect of many sources on the genuine multiparticle correlations,” *Physics Letters B*, vol. 487, no. 3-4, pp. 215–223, 2000.
- [53] H. C. Eggers, P. Lipa, P. Carruthers, and B. Buschbeck, “Higher order pion interferometry. Moments and cumulants,” *Physics Letters B*, vol. 301, no. 2-3, pp. 298–306, 1993.
- [54] J. G. Cramer and K. Kadija, “Cumulants, coherence, and contamination in multiparticle Bose-Einstein interferometry,” *Physical Review C*, vol. 53, no. 2, pp. 908–917, 1996.
- [55] T. Csörgö, B. Lörstad, J. Schmidt-Sørensen, and A. Ster, “Partial coherence in the core/halo picture of Bose-Einstein n-particle correlations,” *European Physical Journal C*, vol. 9, no. 2, pp. 275–281, 1999.
- [56] N. Borghini, P. M. Dinh, and J. Y. Ollitrault, “Flow analysis from multiparticle azimuthal correlations,” *Physical Review C*, vol. 64, no. 5, Article ID 054901, 2001.
- [57] K. Aamodt, B. Abelev, A. Abrahantes Quintana et al., “Elliptic flow of charged particles in Pb-Pb collisions $\sqrt{s_{NN}} = 2.76$ TeV,” *Physical Review Letters*, vol. 105, no. 25, Article ID 252302, 2010.
- [58] M. I. Podgoretsky, “Interference correlations of identical pions: theory,” *Soviet Journal of Particles and Nuclei*, vol. 20, p. 266, 1989.
- [59] N. Amelin and R. Lednicky, “Multi-boson correlations and classical transport models,” *Acta Physica Hungarica New Series Heavy Ion Physics*, vol. 4, no. 1–4, pp. 241–247, 1996.
- [60] U. Heinz and B. Jacak, “Two-particle correlations in relativistic heavy-ion collisions,” *Annual Review of Nuclear and Particle Science*, vol. 49, pp. 529–579.
- [61] H. C. Eggers, “Experimental correlation analysis: foundations and practice,” in *Proceedings of the 30th International Symposium on Multiparticle Dynamics*, T. Csörgö, S. Hegyi, and W. Kittel, Eds., pp. 291–302, World Scientific, Tihany, Hungary, 2001.
- [62] L. Yu. Klimontovich, *The Statistical Theory of Non-Equilibrium Processes in a Plasma*, MIT Press, 1967.
- [63] R. Brout and P. Carruthers, *Lectures on the Many-Electron Problem*, John Wiley Interscience, New York, NY, USA, 1963.
- [64] S. Schlichting and S. Pratt, “Charge conservation in RHIC and contributions to local parity violation observables,” *Physical Review C*, vol. 83, Article ID 014913, 2011.
- [65] H. C. Eggers, F. J. October, and B. Buschbeck, “Transverse-longitudinal HBT correlations in $p\bar{p}$ collisions at $\sqrt{s} = 630$ GeV,” *Physics Letters B*, vol. 635, no. 5-6, pp. 280–285, 2006.
- [66] R. Brandelik, W. Braunschweig, K. Gather et al., “Evidence for charged primary partons in $e^+e^- \rightarrow 2$ jets,” *Physics Letters B*, vol. 100, no. 4, pp. 357–363, 1981.
- [67] Z. Koba, H. B. Nielsen, and P. Olesen, “Generating functionals for multiple particle production: semi-inclusive cross sections, momentum distributions and correlations,” *Nuclear Physics B*, vol. 43, pp. 125–146, 1972.
- [68] A. Stuart and J. K. Ord, *Kendall’s Advanced Theory of Statistics*, vol. 1, Charles Griffin, London, UK, 1986.
- [69] M. B. de Kock, *Gaussian and non-Gaussian-based Gram-Charlier and Edgeworth expansions for correlations of identical particles in HBT interferometry [M.S. thesis]*, University of Stellenbosch, 2009.
- [70] I. V. Andreev, M. Biyajima, I. M. Dremin, and N. Suzuki, “Intermittency and Bose-Einstein correlations,” *International Journal of Modern Physics A*, vol. 10, no. 28, Article ID 3951, 1995.
- [71] H. C. Eggers, P. Lipa, P. Carruthers, and B. Buschbeck, “Integral correlation measures for multiparticle physics,” *Physical Review D*, vol. 48, no. 5, pp. 2040–2053, 1993.
- [72] G. I. Kopylov, “Like particle correlations as a tool to study the multiple production mechanism,” *Physics Letters B*, vol. 50, no. 4, pp. 472–474, 1974.
- [73] M. Gyulassy, S. K. Kauffmann, and L. W. Wilson, “Pion interferometry of nuclear collisions. I. Theory,” *Physical Review C*, vol. 20, no. 6, pp. 2267–2292, 1979.
- [74] W. Zajc, “Bose-Einstein correlations: from statistics to dynamics,” in *Hadronic Multiparticle Production*, P. Carruthers, Ed., vol. 2 of *Advanced Series on Directions in High Energy Physics*, World Scientific, 1988.
- [75] D. Miskowiec and S. Voloshin, “On the normalization of the HBT correlation function,” *Heavy Ion Physics*, vol. 9, pp. 283–287, 1999.
- [76] U. Heinz, P. Scotto, and Q. H. Zhang, “Multi-boson effects in Bose-Einstein interferometry and the multiplicity distribution,” *Annals of Physics*, vol. 288, no. 2, pp. 325–360, 2001.
- [77] W. Zajc, “Monte Carlo calculational methods for the generation of events with Bose-Einstein correlations,” *Physical Review D*, vol. 35, pp. 3396–3408, 1987.
- [78] N. Borghini, “Multiparticle correlations from momentum conservation,” *European Physical Journal C*, vol. 30, no. 3, pp. 381–385, 2003.
- [79] N. Borghini, “Momentum conservation and correlation analyses in heavy-ion collisions at ultrarelativistic energies,” *Physical Review C*, vol. 75, no. 2, Article ID 021904, 2007.

Research Article

A Random Walk with Heavy Flavours

Surasree Mazumder,¹ Trambak Bhattacharyya,¹ and Santosh K. Das²

¹ Variable Energy Cyclotron Center, 1/AF, Bidhan Nagar, Kolkata 700064, India

² Department of Physics and Astronomy, University of Catania, Via S. Sofia 64, 95125 Catania, Italy

Correspondence should be addressed to Surasree Mazumder; surasree.mazumder@gmail.com

Received 14 March 2013; Accepted 5 June 2013

Academic Editor: Jan E. Alam

Copyright © 2013 Surasree Mazumder et al. This is an open access article distributed under the Creative Commons Attribution License, which permits unrestricted use, distribution, and reproduction in any medium, provided the original work is properly cited.

We focus on evaluating transport coefficients like drag and diffusion of heavy quarks (HQ) passing through quark-gluon plasma using perturbative QCD (pQCD). Experimental-observable-like nuclear suppression factor (R_{AA}) of HQ is evaluated for both zero and nonzero baryonic chemical potential (μ_B) scenarios using Fokker-Planck equation. Theoretical estimates of R_{AA} are contrasted with experiments.

1. Introduction

When nuclear matter is subjected to an ambience of very high density, the individual quarks and gluons would no longer be confined within the hadrons but melt into a deconfined state of quarks and gluons. Just after the discovery of asymptotic freedom [1–3], Collins and Perry [4] also suggested that at very high density the degrees of freedom of the strongly interacting matters are not hadrons but quarks and gluons. The same is true when QCD vacuum is excited to high temperatures, too [5]. With increasing temperature, new and new hadrons are produced thereby increasing the corresponding number density, and at a certain temperature, there is an overlap of hadrons. Such a phase of matter is called quark-gluon plasma (QGP) and its study needs QCD, the theory of strong interaction which is extremely successful in vacuum, to be applied in a thermal medium. So, the deconfined state of quarks and gluons gives an opportunity to peruse “condensed matter physics” of elementary particles in the new domain of nonabelian gauge theory.

Lattice-QCD-based calculations predict that the typical value of the temperature for the quark-hadron transition, T_c , is ~ 170 MeV [6, 7] (latest lattice QCD results show that $T_c \sim 160$ MeV [8–10]). According to the cosmological big bang model, the universe has undergone several phase transitions (GUT, electroweak, quark to hadron, etc.) at different stages of its evolution. The quark-hadron transition occurred when

the universe was few microseconds (μs) old and this is the only transition which can be accessed in the laboratory currently. The study of quark-hadron transition demands special importance in understanding the evolution of the μs old early universe. The issue is very crucial for astrophysics too, as the core of the compact astrophysical objects like neutron stars may contain quark matter at high baryon density and low temperature. So there is a multitude of reasons behind creating QGP in laboratories.

Temperature and energy density required to produce QGP in the laboratory can be achieved by colliding heavy ions at relativistic energies, under controlled laboratory environment. The nuclear collisions at Relativistic Heavy Ion Collider (RHIC) and the Large Hadron Collider (LHC) energies (200 GeV/A and 2.76 TeV/A, resp.) are aimed at creating QGP. Once the QGP medium is created, we must try to understand the transport properties of the medium, that is, whether it is liquid or gas. The study of the transport coefficients of strongly correlated system is a field of high contemporary interest both theoretically and experimentally. In one hand, the calculation of the lower bound on the shear viscosity (η) to entropy density (s) ratio (η/s) within the framework of AdS/CFT model [11] has ignited enormous interests among the theorists. On the other hand, the experimental study of the η/s for cold atomic systems and QGP and their similarities has generated huge interest across various branches of physics (see [12] for a review).

In general, the interaction of probes with a medium brings out useful information about the nature of the medium. As the magnitude of the transport coefficients is sensitive to the coupling strength, so these quantities qualify as useful quantities to characterize a medium.

In context of probing QGP, the heavy quarks (HQs), mainly, charm and bottom quarks, play a vital role. The reasons are as follows.

- (i) HQ mass is significantly larger than the typically attained temperatures and other nonperturbative scales $M \gg T_c, \Lambda_{\text{QCD}}$ (intrinsic energy scale for the strong interaction); that is, the production of HQs is essentially constrained to the early, primordial stage of a heavy-ion collision and they do not dictate the bulk properties of the matter. Therefore, the heavy flavours are the witness to the entire space-time evolution of the system.
- (ii) Their thermalization time scale is larger by a factor of m/T , where m is the mass of heavy quarks and T is the temperature, than that of the light quarks and gluons and hence heavy quarks can retain the interaction history very effectively.

From experimental point of view, however, the issue of HQ thermalization in QGP can be addressed by measuring the elliptic flow (v_2) of leptons from the decays of HQs. Moreover, the observed transverse momentum suppression (R_{AA}) of leptons originating from the decays of D and B mesons produced in nuclear collisions as compared to those produced in proton + proton (pp) collisions at the same colliding energy [13–15] offers us an opportunity to estimate the drag and diffusion coefficients of QGP. (It is now possible to detect directly D mesons at LHC detectors like ALICE, see [16]). Hence, no wonder that in the recent past a large number of attempts have been made to study both heavy flavour suppression [13, 14] and elliptic flow [17] within the framework of perturbative QCD (pQCD) [18–34].

2. Motion of Heavy Quarks (HQs) in QGP

In the introduction, we have already discussed that HQs act as effective probes to look into the properties of QGP. As HQs are much heavier than the particles constituting the QGP thermal bath, one expects that they will execute Brownian motion in QGP medium [35, 36]. The system under study, then, would have two components: (i) the QGP formed at an initial temperature T_i and initial thermalization time τ_i consisting of light quarks and gluons and (ii) heavy quark, the Brownian particle formed due to hard collisions at very early stage of heavy ion collision. The momentum distribution of HQ is governed by a nonlinear integrodifferential equation which is the Boltzman transport equation (BTE) as

$$\left[\frac{\partial}{\partial t} + \frac{\mathbf{p}}{E} \cdot \frac{\partial}{\partial \mathbf{x}} + \mathbf{F} \cdot \frac{\partial}{\partial \mathbf{p}} \right] f(x, \mathbf{p}, t) = \left[\frac{\partial f}{\partial t} \right]_{\text{collisions}}. \quad (1)$$

\mathbf{F} is the force exerted on the HQ by the surrounding colour field. \mathbf{p} and E denote the three momentums and the energy of

the HQ, respectively. The right hand side of (1), which is called the collision integral, $C[f]$, is attributed to the QCD interactions of HQ with light quarks (q), antiquarks (\bar{q}), and gluons (g). One should, in principle, solve this differential equation under the influence of potential involving interaction of HQs with light quarks/anti-quarks and the background colour field in the force term. But, here, we will set $\mathbf{F} = 0$ and will treat QGP to be uniform. Therefore, the second and the third term of the left hand side of (1) vanish under these approximations. Again defining

$$f(\mathbf{p}, t) = \frac{1}{V} \int d^3 \mathbf{x} f(\mathbf{x}, \mathbf{p}, t) \quad (2)$$

which is the normalized probability distribution in the momentum space, we have

$$\frac{\partial f(\mathbf{p}, t)}{\partial t} = \left[\frac{\partial f}{\partial t} \right]_{\text{collisions}}. \quad (3)$$

Equation (3) signifies that all variation of the distribution function of HQ with time is due to the collisions only.

3. Formalism

Our main aim is to determine the collision integral of the transport (3). Once, we determine certain form of $C[f]$, we can proceed towards solving the differential equation. There are lots of approximations through which the integrodifferential equation can be solved. Of course, under certain conditions, (3) can be reduced to the simple form

$$\frac{\partial f(\mathbf{p}, t)}{\partial t} = -\frac{f - f_0}{\tau} \quad (4)$$

which is a useful first approximation. Here, f_0 is the equilibrium distribution function and τ is the relaxation time that determines the rate at which the fluctuations in the system drive it to a state of equilibrium again. In this form, the equation is very easy to solve. But, our case is not so simple. We will deal with a more sophisticated approximation that leads to the Fokker-Planck equation [37].

To start with, we apply the Landau approximation which allows only soft scattering in the collision integral. If we define $w(\mathbf{p}, \mathbf{k})$ to be the rate of collisions which change the momentum of the HQ from \mathbf{p} to $\mathbf{p} - \mathbf{k}$, we have

$$\begin{aligned} \left[\frac{\partial f}{\partial t} \right]_{\text{collisions}} \\ = \int d^3 \mathbf{k} [w(\mathbf{p} + \mathbf{k}, \mathbf{k}) f(\mathbf{p} + \mathbf{k}) - w(\mathbf{p}, \mathbf{k}) f(\mathbf{p})]. \end{aligned} \quad (5)$$

The second part of the integral corresponds to all those transitions that remove HQ from momentum \mathbf{p} to $\mathbf{p} - \mathbf{k}$ and therefore represents a net loss to the distribution function. Likewise, the first part of the integral represents a net gain to the distribution function of HQ. With these, (3) becomes

$$\frac{\partial f(\mathbf{p}, t)}{\partial t} = \int d^3 \mathbf{k} [w(\mathbf{p} + \mathbf{k}, \mathbf{k}) f(\mathbf{p} + \mathbf{k}) - w(\mathbf{p}, \mathbf{k}) f(\mathbf{p})]. \quad (6)$$

Equation (6) is a linear equation in f . We can simplify it by assuming the previously discussed Landau approximation. Mathematically, this approximation amounts to assuming $w(\mathbf{p}, \mathbf{k})$ to fall off rapidly to zero with $|\mathbf{k}|$; that is, transition probability function, $w(\mathbf{p}, \mathbf{k})$, is sharply peaked around $|\mathbf{k}| = 0$. Therefore, if we expand the integrand in the right hand side of (6) in powers of \mathbf{k} , we have

$$\begin{aligned} w(\mathbf{p} + \mathbf{k}, \mathbf{k}) f(\mathbf{p} + \mathbf{k}) &\approx w(\mathbf{p}, \mathbf{k}) f(\mathbf{p}) + \mathbf{k} \cdot \frac{\partial}{\partial \mathbf{p}} (wf) \\ &+ \frac{1}{2} k_i k_j \frac{\partial^2}{\partial p_i \partial p_j} (wf). \end{aligned} \quad (7)$$

Retaining terms up to the second order only, we obtain Fokker-Planck equation [37]

$$\frac{\partial f}{\partial t} = \frac{\partial}{\partial p_i} \left[A_i(\mathbf{p}) f + \frac{\partial}{\partial p_j} [B_{ij}(\mathbf{p}) f] \right], \quad (8)$$

where the kernels are defined as follows:

$$\begin{aligned} A_i &= \int d^3 \mathbf{k} w(\mathbf{p}, \mathbf{k}) k_i, \\ B_{ij} &= \frac{1}{2} \int d^3 \mathbf{k} w(\mathbf{p}, \mathbf{k}) k_i k_j. \end{aligned} \quad (9)$$

In the present formalism, we considered the elastic scattering of the HQ with the gluon, light quark, and the corresponding anti-quarks. All these processes contribute to determine $w(\mathbf{p}, \mathbf{k})$ [37] and, in turn, the above defined kernels. Now, to explore the physical significance of the A and B coefficients, let us consider $A_i = p_i \gamma(p)$ and $B_{ij} = D(p) \delta_{ij}$, which assume very low \mathbf{p} ; that is, the medium of QGP is isotropic to the HQ. If, in this limit, we neglect all the derivatives of A and B coefficients with momentum of HQ, (8) reduces to

$$\frac{\partial f}{\partial t} = \gamma \frac{\partial}{\partial \mathbf{p}} \cdot (\mathbf{p} f) + D \left[\frac{\partial}{\partial \mathbf{p}} \right]^2 f. \quad (10)$$

The method of solution of this equation is elaborately discussed in [37]. Now, if we want to extend this formalism to the regime where the momentum of the HQ is no longer small, that is, the particular kinematic domain where HQ becomes relativistic, obviously, we would like to know how the transport coefficients drag (γ) and diffusion (D) behave at high \mathbf{p} region. In order to do so, we extrapolate the concept of isotropy to the higher momentum of HQ in such a way that only the first derivatives of the drag and diffusion coefficients are considered and the momentum dependence of A and B coefficients is encoded inside γ and D . Therefore, the Fokker-Planck equation, under this approximation, in Cartesian coordinate system becomes [28]

$$\begin{aligned} \frac{\partial f}{\partial t} &= C_1(p_x, p_y, t) \frac{\partial^2 f}{\partial p_x^2} + C_2(p_x, p_y, t) \frac{\partial^2 f}{\partial p_y^2} \\ &+ C_3(p_x, p_y, t) \frac{\partial f}{\partial p_x} + C_4(p_x, p_y, t) \frac{\partial f}{\partial p_y} \\ &+ C_5(p_x, p_y, t) f + C_6(p_x, p_y, t), \end{aligned} \quad (11)$$

where,

$$\begin{aligned} C_1 &= D, \\ C_2 &= D, \\ C_3 &= \gamma p_x + 2 \frac{\partial D}{\partial p_T} \frac{p_x}{p_T}, \\ C_4 &= \gamma p_y + 2 \frac{\partial D}{\partial p_T} \frac{p_y}{p_T}, \\ C_5 &= 2\gamma + \frac{\partial \gamma}{\partial p_T} \frac{p_x^2}{p_T} + \frac{\partial \gamma}{\partial p_T} \frac{p_y^2}{p_T}, \\ C_6 &= 0, \end{aligned} \quad (12)$$

where the momentum $\mathbf{p} = (\mathbf{p}_T, p_z) = (p_x, p_y, p_z)$. We numerically solve (11) [38] with the boundary conditions $f(p_x, p_y, t) \rightarrow 0$ for $p_x, p_y \rightarrow \infty$, and the initial (at time $t = \tau_i$) momentum distribution of charm and bottom quarks is taken from MNR code [39]. It is evident from (11) that with the momentum-dependent transport coefficients the FP equation becomes complicated.

It is possible to write down the solution of the FP equation in closed analytical form [40] in the special case of momentum-independent drag and diffusion coefficients. To find out the solution f for momentum independent drag and diffusion coefficients, we can consider the one-dimensional version of (10) as

$$\frac{\partial f}{\partial t} = \gamma \frac{\partial}{\partial p} (pf) + D \frac{\partial^2 f}{\partial p^2}, \quad (13)$$

which is also called the Rayleigh's equation. For the initial condition $f(p, t = 0) = \delta(p - p_0)$, the solution of f is

$$\begin{aligned} f(p, t) &= \left(\frac{\gamma}{2\pi D} (1 - e^{-2\gamma t}) \right)^{-1/2} \\ &\times \exp \left(-\frac{\gamma}{2D} \frac{(p - p_0 e^{-\gamma t})^2}{1 - e^{-2\gamma t}} \right). \end{aligned} \quad (14)$$

However, (14) is solution for a very simplified scenario and we will study the momentum dependence of drag and diffusion coefficients and their effects on R_{AA} in the sections to come.

4. Drag Coefficients

4.1. Elastic Processes. We need to evaluate the drag coefficient as a function of temperature and momentum of HQ. The expression to evaluate collisional drag can be written as [37]

$$\begin{aligned} \gamma_{\text{coll}} &= \frac{1}{2E_p} \int \frac{d^3 \mathbf{q}}{(2\pi)^3 2E_q} \int \frac{d^3 \mathbf{q}'}{(2\pi)^3 2E_{q'}} \\ &\times \int \frac{d^3 \mathbf{p}'}{(2\pi)^3 2E_{p'}} \frac{1}{\gamma_Q} \sum |M|^2 \\ &\times (2\pi)^4 \delta^4(p + q - p' - q') f'(\mathbf{q}) \left[1 - \frac{\mathbf{p} \cdot \mathbf{p}'}{p^2} \right], \end{aligned} \quad (15)$$

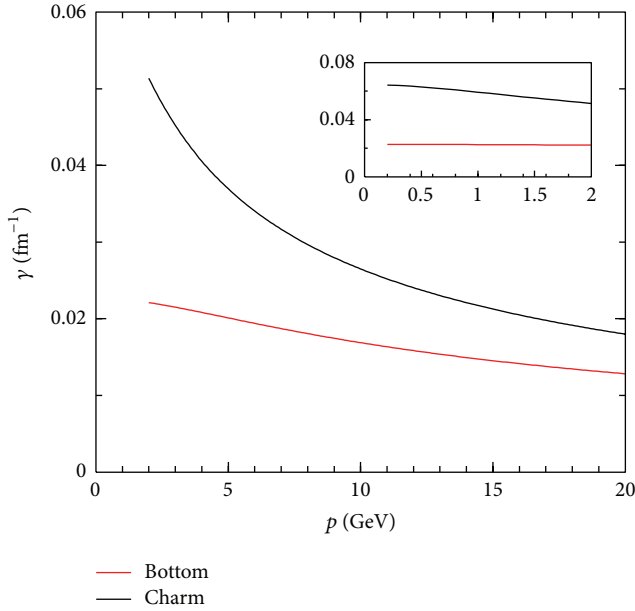


FIGURE 1: Drag coefficients of charm and bottom with their momentum at $T = 300$ MeV assuming running strong coupling, $\alpha_s(T)$, and temperature-dependent Debye screening mass, $m_D(T)$ for gluon, quark, and antiquark scattering.

where $\mathbf{p}' = \mathbf{p} - \mathbf{k}$ and $\mathbf{q}' = \mathbf{q} + \mathbf{k}$. The scattering matrix elements are given explicitly in [41] where the t channel divergence occurring due to very soft gluon exchange has been shielded by replacing t in the denominator of matrix elements by $t - m_D^2$ in an ad hoc manner, where t is the Mandelstam variable and m_D is the thermal mass of gluon. However, the same problem can be approached from hard thermal loop (HTL) perturbation theory. The gluon propagator for t channel diagram is then replaced by HTL propagator. But calculation of even the elastic matrix elements for HQs scattering with light quarks and gluons in this approach is very lengthy and radiative matrix elements are even clumsier. However, an outline of calculating collisional drag and diffusion coefficients in HTL perturbation theory approach is given for the interested readers in the Appendix. Here we proceed with the conventional process of shielding t channel divergence with the gluon thermal mass, m_D .

The integrations in (15) have been performed using the standard techniques [23–25, 37]. Results of the present calculation of drag coefficients are plotted with respect to momenta of charm and bottom (Figure 1). We can observe that the momentum dependence of γ is nonnegligible for the shown momentum range. The value of γ for charm due to collisional processes at $p = 5$ GeV is about 0.036 fm^{-1} which reduces to a value of 0.018 fm^{-1} at $p = 10$ GeV (can be compared with, e.g., [42–45]). In the inset, the drag coefficients of HQs due to elastic collision are plotted in the lower momentum region, where the drag remains more or less constant with \mathbf{p} . Therefore, it is clear that had we taken the value of drag at low momentum and extrapolated that value to higher momentum, the final result would have been overestimated. The diffusion coefficient of HQ can be evaluated from Einstein relation $D = \gamma MT$. Later, it will be seen

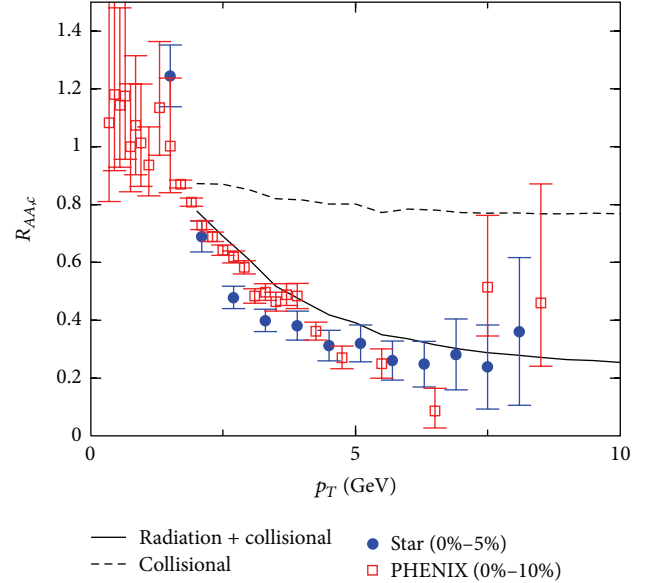


FIGURE 2: Suppression of transverse momentum of charm quarks in QGP as a function p_T .

that the momentum dependence of transport coefficients of a high energy HQ will have considerable effects on the nuclear suppression factor, R_{AA} of HQ.

However, there are also radiative processes taking place in the medium. The radiative drag can be obtained in the present formalism by computing the radiative energy loss of a HQ passing through QGP. In the next section, we will discuss the methods and intricacies of calculating the transport coefficients in radiative domain.

4.2. Radiative Processes. It is already known that the two mechanisms of energy loss of heavy quarks are collisional and radiative energy loss. Though at low transverse momentum (p_T) region the collisional and radiative losses of HQs are comparable (see Figure 5), the radiative one tends to dominate with increasing momentum. So it is worthwhile, after discussing about evaluation of collisional transport coefficients (drag, diffusion) within the ambit of $T = 0$ perturbative QCD (pQCD) [37] in the previous section, to contemplate on radiative processes and to inspect how pQCD approach can be utilized in finding out radiative transport coefficients.

It is well known from QED that for high energies radiative energy loss becomes dominant [46]. Also the hard thermal loop calculations in context of QCD show that the radiative energy loss contributes to the same order of strong coupling as that of collisional loss [47]. The above discussions tempt one to infer that the observed large suppression of heavy quarks at RHIC is predominantly due to bremsstrahlung processes [25, 28], at least at high p_T , but, as already said, the comparable values of energy losses in low momentum region leave an ample room for ambiguity in this statement particularly at “not-so-high” p_T (~ 2 GeV) region.

Theoretical estimate of nuclear suppression factor (R_{AA}) for charm quarks in [28] shows ~ 4 times more suppression due to inclusion of radiation (Figure 2) with the same initial conditions. Inclusion of radiative processes leads to a good

description of charm R_{AA} at RHIC energies. At LHC energy (2.76 TeV/A), the collisional energy loss due to hard (momentum transfer > 2 GeV) collisions could be about one-third of the total [29]. The rest may be attributed to radiative loss.

From the discussion on collisional transport coefficients we know that (collisional) drag is given by [37]

$$\gamma_{\text{coll}} = -\frac{1}{p} \left(\frac{dE}{dx} \right)_{\text{coll}}, \quad (16)$$

where p is the momentum of the probe. We employ a similar argument and relate radiative energy loss $((dE/dx)_{\text{rad}})$ to inelastic drag (γ_{rad}) in the same way. The effective drag obtained is a summation of collisional and radiative parts. As energy loss is related with the transport properties like drag offered by the medium, we must concentrate on more and more accurate determination of radiative energy loss which will enable us to understand the properties of QGP.

The radiative energy loss in general has been studied in [48–53] incorporating Landau-Pomeranchuk-Migdal (LPM) effect [54, 55], to be discussed later, due to multiple scattering. The authors of [56] treat the problem of radiative energy loss of HQs by building a model in scalar QCD approach. Attempts have been taken [25, 28, 30] to incorporate the formalism of [48], the Gyulassy-Wang potential model (GWPM), to compute the radiative energy loss of heavy quarks traveling through QGP. In stead of going to the energy loss in GWPM approach directly, we may try to acquire some familiarity with the model and the notations used for the description of it.

4.2.1. Gyulassy Wang Potential Model (GWPM) and Radiation Spectrum. To analyze the multiple scattering and the induced gluon radiation in GWPM, certain simplifications have to be made. For example, [49] assumes static interaction between propagating parton and bath particles. This interaction is modelled by a static Debye screening potential. Now, it is possible to approximate the effective average random colour field produced by the bath particles by a potential provided the distance between two successive scatterers is large compared to colour screening length (μ^{-1}) . The screened potential is given by

$$\begin{aligned} V_{AA'}^a(\vec{q}) &= A_{AA'}^a(\vec{q}) e^{-i\vec{q}\cdot\vec{x}} \\ &= g T_{AA'}^a \frac{e^{-i\vec{q}\cdot\vec{x}}}{\vec{q}^2 + \mu^2}, \end{aligned} \quad (17)$$

where μ is the colour screening mass, T^a are the generators corresponding to the representation of target partons at \vec{x} transferring (three) momentum \vec{q} , and g is the coupling. The Feynman diagrams contributing to induced gluon radiation from a single quark-quark scattering are given in Figure 3.

The calculation of Feynman diagrams is done in light-cone coordinates [57, 58] where light-cone representations of four-vectors are done in the following way:

$$\begin{aligned} p &= (p^+, p^-, p_\perp) \\ &= (p_0 + p_3, p_0 - p_3, p_\perp). \end{aligned} \quad (18)$$

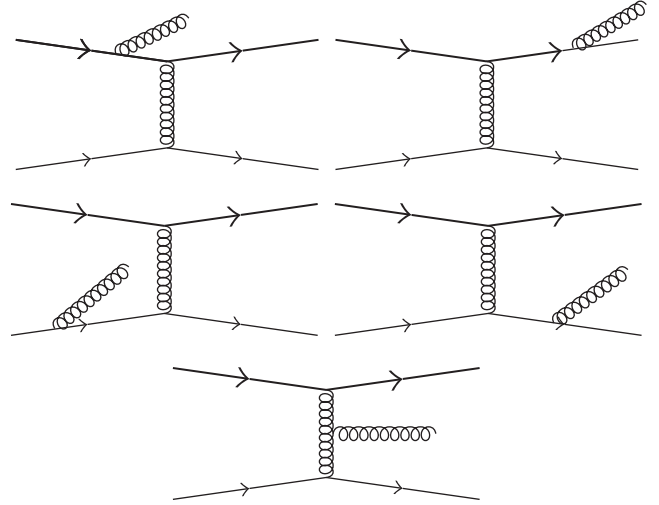


FIGURE 3: Feynman diagrams for gluon radiation from a single quark-quark (qq') scattering.

In the potential model, one can neglect radiation from the target lines (external lines appearing at the bottom of gluon propagator in Figure 3) provided one decides to work in light cone gauge, $A^+ = 0$, for emitted gluon fields (For details see [59]). For radiation in the midrapidity region, the celebrated Gunion-Bertsch distribution formula (GB formula) for soft gluon radiation [60] can be reproduced from this approach.

We now discuss the GB formula and recent attempts to generalize. (Interested readers are referred to the Appendix for other such very recent endeavors.) We will see that this formula and/or its generalizations will play a significant role in finding out the energy loss due to gluon emission of quarks. The early attempts of generalizing GB formula [61–63] consider the general $gg \rightarrow ggg$ matrix element elegantly written by [64] and factoring out the elastic $gg \rightarrow gg$ scattering amplitude to obtain the distribution of emitted gluon $(\sim |M_{gg \rightarrow ggg}|^2 / |M_{gg \rightarrow gg}|^2)$. We can write the following form of gluon distribution [63], (for details, see Appendix of [63])

$$\begin{aligned} \frac{dn_g}{d^2k_\perp d\eta} &= \left[\frac{dn_g}{d^2k_\perp d\eta} \right]_{\text{GB}} \left[\left(1 + \frac{t}{2s} + \frac{5t^2}{2s^2} - \frac{t^3}{s^3} \right) \right. \\ &\quad \left. - \left(\frac{3}{2\sqrt{s}} + \frac{4t}{s\sqrt{s}} - \frac{3t^2}{2s^2\sqrt{s}} \right) k_\perp \right. \\ &\quad \left. + \left(\frac{5}{2s} + \frac{t}{2s^2} + \frac{5t^2}{s^3} \right) k_\perp^2 \right], \end{aligned} \quad (19)$$

where η is the rapidity of the radiated gluon, and the subscript GB has been used to indicate the gluon spectrum obtained using the approximation considered in [60] (see also [65]) which is generally given by

$$\left[\frac{dn_g}{d^2k_\perp d\eta} \right]_{\text{GB}} = \frac{C_A \alpha_s}{\pi^2} \frac{q_\perp^2}{k_\perp^2 \left[(\vec{k}_\perp - \vec{q}_\perp)^2 + m_D^2 \right]}, \quad (20)$$

where $m_D = \sqrt{(2\pi/3)\alpha_s(T)(C_A + N_F/2)T}$ is the thermal mass of the gluon [66, 67], N_F is the number of flavours contributing in the gluon self-energy loop, $C_A = 3$ is the Casimir invariant for the SU(3) adjoint representation, α_s is the temperature-dependent strong coupling [68], k_\perp is the transverse momentum of the emitted gluon, and q_\perp is the transverse momentum transfer. In general, one introduces the thermal mass in the denominator of (20) to shield the divergence arising from collinearity (i.e., when $\vec{k}_\perp = \vec{q}_\perp$) of emitted gluon. But, for the present case (19) is written under the assumption that $\vec{q}_\perp \gg \vec{k}_\perp$, and hence there is no need to write the m_D^2 factor in GB spectrum.

Now, we must consider multiple scattering encountered by incoming particles, too. The many-body effect due to presence of medium results in interference of scattering amplitudes. This interference effect is called LPM effect [54, 55]. LPM effect is discussed in QED domain in [69]. LPM suppression can be understood in a qualitative manner as an interplay between two time scales, the formation time (τ_f) and the scattering time (τ_{sc}). τ_f is the time needed for the emission of the induced gluon. Actually, τ_f determines the time span after which a radiation can be separately identified from the parent parton from which the radiation is being given off. Now, a collision just before formation of the gluon results in suppression of the radiation. This destructive interference is called LPM effect and in the next section we will see that it puts a constraint on the phase space of the emitted gluon. If k_0 is the energy of the emitted (soft) gluon and k_\perp is its transverse momentum, then formation time $\tau_f \sim 2k_0/k_\perp^2$ [49]. When this τ_f is much less than collision time, that is, separation between two scattering centres, L , then the intensity of radiation is additive and *Bethe-Heitler (BH) limit* is reached. In the *factorization limit*, $L \ll \tau_f$, the interference in radiation amplitude takes place and LPM effect dominates.

After this brief discussion on possible effects of multiple scattering, emitted gluon distribution due to multiple scattering in terms of that due to single scattering can be written as [49]

$$\frac{dn_g^{(m)}}{d^2k_\perp d\eta} = C_m(k) \frac{dn_g^{(1)}}{d^2k_\perp d\eta}, \quad (21)$$

where “ m ” stands for multiple scattering and “1” stands for single scattering. C_m is called radiation formation factor characterizing the interference pattern due to multiple scattering. Naturally, in the BH limit, $C_m \approx m$, which implies that scattering amplitudes are just additive and the resultant intensity shows no interference pattern. On the other hand, the factorization limit gives [49, 50]

$$C_m(k) \approx \frac{8}{9} \left[1 - \left(-\frac{1}{8} \right)^m \right] \quad \text{for quarks} \\ \approx 2 \left(1 - \frac{1}{2^m} \right) \quad \text{for gluons.} \quad (22)$$

Equation (22) shows that the interference effect due to many multiple scatterings for quarks leaves corresponding radiation spectrum a factor of $8/9$ of that due to single scattering.

It can also be checked that the gluon intensity radiated by gluon jet is $9/4$ times higher than that radiated by quark jets in multiple scattering. Thus, the LPM effect in QCD depends on colour representation due to nonabelian nature of the problem under discussion.

4.2.2. Energy Loss of Light Particles in GWPM. The energy loss in potential model can be evaluated by integrating over the transverse momentum and rapidity of emitted gluon. The phase space is, of course, constrained by LPM effect due to multiple scattering. The multiple scattering is implemented through the differential change of the factor C_m with number of scattering m , dC_m/dm , which can be approximated as a θ -function [49]. Also, the emitted gluon must have energy less than that of the parent parton. So the energy loss formula implementing the energy constraint gives

$$\Delta E_{\text{rad}} = \frac{E_{m+1} - E_m}{m} \\ = \int d^2k_\perp d\eta \frac{dn_g}{d^2k_\perp d\eta} k_0 \frac{C_{m+1} - C_m}{m} \theta(E - k_\perp \cosh \eta) \\ = \int d^2k_\perp d\eta \frac{dn_g}{d^2k_\perp d\eta} k_0 \frac{dC_m}{dm} \theta(E - k_\perp \cosh \eta) \\ \sim \int d^2k_\perp d\eta \frac{dn_g}{d^2k_\perp d\eta} k_0 \theta(\tau_{sc} - \tau_f) \theta(E - k_\perp \cosh \eta), \quad (23)$$

where E is the energy of the parent parton and $k_0 = k_\perp \cosh \eta$, E_{m+1} denotes energy loss in $(m+1)$ th, collision and E_m is the corresponding value in the m th collision. The first θ -function involving scattering time τ_{sc} [70] gives a lower limit of k_\perp , that is, $k_\perp > \Lambda \cosh \eta$. The second θ -function yields $k_\perp < E/\cosh \eta$. Utilizing (23), [63] compares the energy loss (Figure 4) of a gluon jet passing through gluonic plasma obtained by generalized GB formulae given in [61–63]. We will see how (23) can be employed to find out HQ energy loss in the next section.

4.2.3. Energy Loss of HQs and Radiative Drag. While calculating the radiative energy loss of HQs [56] takes the GB distribution for small and moderate x and for mass $m \neq 0$. The distribution, so obtained, can be shown to yield GB distribution when $x \ll 1$ and when $m = 0$. However the authors of [25, 28] use the original GB distribution formula weighted by a radiative suppression factor, called “dead-cone” factor, originating due to mass of HQs. Since dead-cone factor plays an important role in radiative energy loss of heavy quarks, we will pause here to spend some words on dead-cone effect in QCD [71] and its generalizations.

The dead-cone suppression obtained in [71] actually has an analogy with radiated power distribution of a nonrelativistic, accelerating charge particle. The average power radiated per unit solid angle is given by [72]

$$\frac{dP}{d\Omega} \propto \left| \dot{\vec{\beta}} \right|^2 \sin^2 \theta, \quad (24)$$

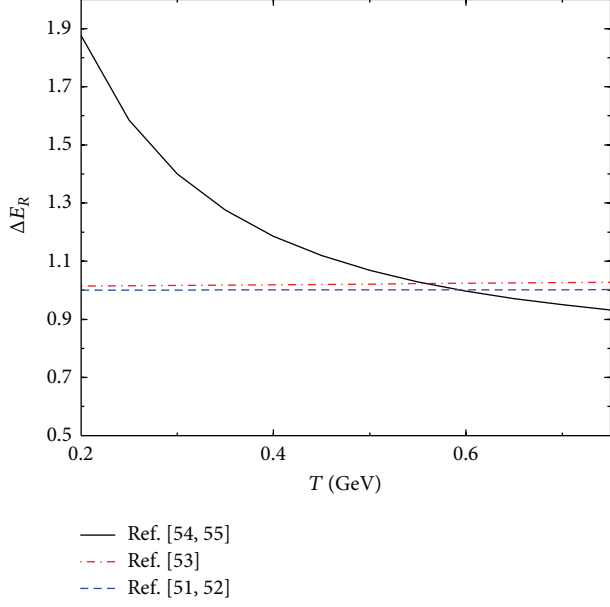


FIGURE 4: Temperature variation of ΔE_R , that is, ΔE normalized by the corresponding value obtained from GB approximation, of a 15 GeV gluon due to traversal of 4 fm in a gluonic heat bath. Solid (dashed) line indicates result for the gluon spectrum obtained (Color online) in [61, 63]. The dot-dashed line stands for the results for the gluon spectrum of [62].

where θ is the angle between acceleration $\dot{\vec{\beta}}$ of the particle and the direction of propagation of radiation, \vec{n} . This is a simple $\sin^2\theta$ behaviour showing no radiation at $\theta = 0$ (or $n\pi$, $n \in \mathbb{Z}$). It can be shown [73] that the behaviour of (24) is, indeed, similar to what one gets for conventional dead cone [71]. Qualitatively speaking, it is hard to cause a deceleration of a high energy heavy quarks along their directions of motion, and this is why the bremsstrahlung radiation is suppressed along this direction (see Figure 24). Indeed, the distribution of radiated gluons emanating from HQs is shown to be related to those from light quarks (LQs) by the following formula [71] (for small radiation angle θ):

$$dP_{\text{HQ}} = \left(1 + \frac{\theta_0^2}{\theta^2}\right)^{-2} dP_{\text{LQ}}, \quad (25)$$

where $\theta_0 = m/E$, m is the mass, and E is the energy of heavy quark. It is worth noting that when $E \rightarrow \infty$, the radiation from HQs converges with that of LQs. However, there are some very recent developments in generalizing the dead-cone effect either from $Qq \rightarrow Qqg$ matrix element or assuming effects of off-shellness of quarks which, after being produced, take some time to become on-shell. The details may be seen in the Appendix.

The radiative transport coefficients like drag and diffusion have been evaluated in [25, 28] employing potential approach. The radiative drag coefficient can be obtained by finding out the radiative energy loss of HQs passing through medium. The GB spectrum for emitted gluon, weighted by the dead-cone factor and the energy of gluon $k_0 (=k_\perp \cosh \eta)$, is integrated over the transverse momentum (k_\perp) and rapidity

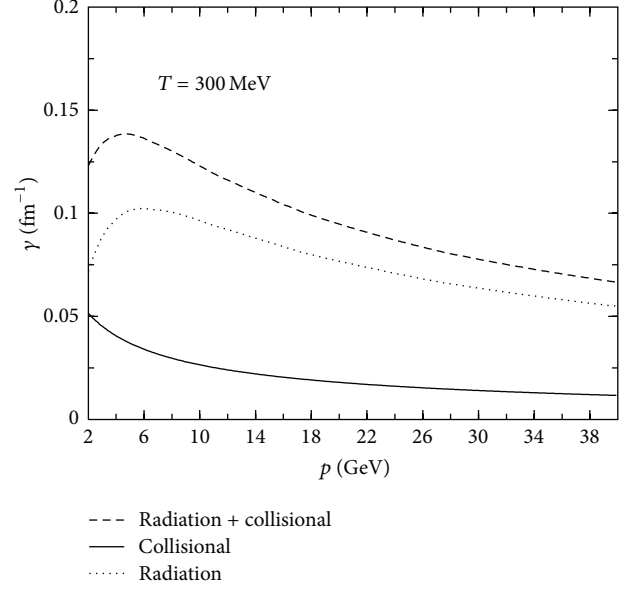


FIGURE 5: Drag coefficients of charm assuming running strong coupling, $\alpha_s(T)$ and temperature dependent Debye screening mass, $m_D(T)$ due to its interaction with thermal gluons, quarks, and antiquarks.

(η) of the emitted gluon. As already stated, the lower and upper limits of k_\perp have been obtained from the θ -functions of (23). The average energy loss per collision, ΔE_{rad} , can be written with the help of (23) as

$$\Delta E_{\text{rad}} = \langle n_g k_0 \rangle = \int d\eta d^2k_\perp \frac{dn_g}{d\eta d^2k_\perp} \times k_0 \Theta(\tau_{\text{sc}} - \tau_F) \Theta(E - k_\perp \cosh \eta) F_{\text{DC}}^2, \quad (26)$$

where the formation time of the emitted gluon [49], $\tau_F = (C_A/2C_2) 2 \cosh \eta/k_\perp$, and $C_A/2C_2 = N^2/(N^2 - 1)$ for quarks with $C_2 = C_F = 4/3$. Dead-cone factor of (25) ($dP_{\text{HQ}}/dP_{\text{LQ}}$) can be written in the following way, provided one replaces $k_\perp/k_0 \sim \sin \theta \sim \theta$ for small θ :

$$F_{\text{DC}}^2 = \left(\frac{k_\perp^2}{k_0^2 \theta_0^2 + k_\perp^2} \right)^2, \quad (27)$$

where dE/dx can be obtained if one multiplies ΔE_{rad} with Λ , which can be obtained from [70]. Drag (γ) and diffusion ($D = \gamma m T$) coefficients in [28] are functions of momentum as well as temperature. The effective drag can be obtained by adding collisional and radiative drags, $\gamma_{\text{eff}} = \gamma_{\text{coll}} + \gamma_{\text{rad}}$. The momentum dependence of the drag coefficient of the charm quark propagating through the QGP is displayed in Figure 5 for $T = 300$ MeV. For $p_T \sim 2$ GeV of charm quarks the collisional and radiative contributions tend to merge with each other. However, it is interesting to note the dominance of radiative drag in Figure 5 over its collisional counterpart for higher momentum.

5. Space-Time Evolution

Once we know the total drag (γ_{eff}) and diffusion (D_{eff}) coefficients, we need the initial conditions for both the HQ and the QGP background which is also evolving with time as follows.

$$\partial_\mu T^{\mu\nu} = 0, \quad (28)$$

where $T^{\mu\nu} = (\epsilon + P)u^\mu u^\nu - g^{\mu\nu}P$ is the energy momentum tensor for ideal fluid, ϵ is the energy density, P is the pressure, u^μ is the hydrodynamic four velocity, and $g^{\mu\nu}$ is the metric tensor. We will solve this equation for longitudinal expansion assuming boost invariance along the z direction [74]. It is expected that the central rapidity region of the system formed after nuclear collisions at RHIC and LHC energy is almost net baryon free. Therefore, the equation governing the conservation of net baryon number need not be considered here. Under this circumstance, (28) reduces to:

$$\frac{\partial \epsilon}{\partial \tau} + \frac{\epsilon + P}{\tau} = 0. \quad (29)$$

To solve (29), we use the relation $P = c_s^2 \epsilon$, where c_s is the velocity of sound and τ is time. With this we arrive at the relation

$$\epsilon \tau^{1+c_s^2} = C, \quad (30)$$

where C is a constant. For the ideal equation of state, $c_s^2 = 1/\sqrt{3}$, (30) reads $\epsilon \tau^{4/3} = C$. In terms of temperature, this relation can be written as $\tau T^3 = C$.

The total amount of energy dissipated by a heavy quark in the expanding QGP depends on the path length it traverses. Each parton traverses a different path length which depends on the geometry of the system and on the point where it is created. The probability that a parton is produced at a point (r, ϕ) in the plasma depends on the number of binary collisions at that point which can be taken as [75]

$$P(r, \phi) = \frac{2}{\pi R^2} \left(1 - \frac{r^2}{R^2}\right) \theta(R - r), \quad (31)$$

where R is the nuclear radius. It should be mentioned here that the expression in (31) is an approximation for the collisions with zero impact parameter. A very high energy parton created at (r, ϕ) in the transverse plane propagates a distance $L = \sqrt{R^2 - r^2 \sin^2 \phi} - r \cos \phi$ in the medium provided its direction remains unaltered. In the present work, we use the following equation for the geometric average of the integral involving drag coefficient

$$\Gamma = \frac{\int r dr d\phi P(r, \phi) \int^{L/\nu} d\tau \gamma(\tau)}{\int r dr d\phi P(r, \phi)}, \quad (32)$$

where ν is the velocity of the propagating partons. Similar averaging has been performed for the diffusion coefficient, too. For a static system, the temperature dependence of the drag and diffusion coefficients of the heavy quarks enters via

the thermal distributions of light quarks and gluons through which it is propagating. However, in the present scenario, the variation of temperature with time is governed by the equation of state or velocity of sound of the thermalized system undergoing hydrodynamic expansion. In such a scenario the quantities like Γ (32) and hence the HQ suppression become sensitive to c_s .

6. Initial Conditions and Nuclear Modification Factor

In order to solve (11), the initial distribution functions, $f_{\text{in}}(p_T, t)$ for charm and bottom quarks have been supplied from the well-known MNR code [39]. The ratio between the solution of Fokker-Planck equation at the transition temperature, $T_c = 175$ MeV, and the initial distribution function of HQ is the required nuclear modification factor, R_{AA} of open HQ. But in order to compare results from the present formalism with experimental data from RHIC and LHC, we need to have R_{AA} of nonphotonic single electron originating from the decays of D and B mesons.

Therefore, the hadronization of charm and bottom quarks to D and B mesons, respectively, are done by using Peterson fragmentation function [76] as

$$f(z) \propto \frac{1}{[z[z - 1/z - \epsilon_Q/(1-z)]^2]}, \quad (33)$$

where z is the fraction of momentum carried by the hadrons and ϵ_Q is 0.05 for charm and $(m_c/m_b)^2 \epsilon_Q$ for bottom where $m_c(m_b)$ is the mass of charm (bottom). One may use different kinds of available fragmentation functions, but the final result will not be sensitive to the choice of $f(z)$. In point of fact, describing hadronization has always been a formidable task because the hadron bound states are nonperturbative in nature. The fragmentation scheme is a popular method to deal with hadronization. For more relevant information, interested readers are referred to [77, 78], which discusses coalescence model, a hadronization formulation based on recombination of heavy flavours.

Both the final solution of FP Equation and the initial distribution of HQ are convoluted with the above fragmentation function (33) and their ratio will give R_{AA} of D and B mesons. The final and initial distribution functions are obtained for the single electrons originated from the decays of D and B mesons and the final nuclear modification factor is

$$R_{AA}^{D(B) \rightarrow e} = \frac{f^{D(B) \rightarrow e}(p_T, T_c)}{f^{D(B) \rightarrow e}(p_T, T_i)}. \quad (34)$$

Now, once we know how to determine R_{AA} , we will compare our results with the RHIC and LHC data. In the process of doing so, we will study the effects of the equation of state on the nuclear suppression of heavy flavours in quark gluon plasma and estimate the initial entropy density of the QGP formed at the RHIC. For this purpose, the experimental data on the charged particle multiplicity and the nuclear suppression of single electron spectra originating from the semileptonic decays of D and B mesons have been employed. We have

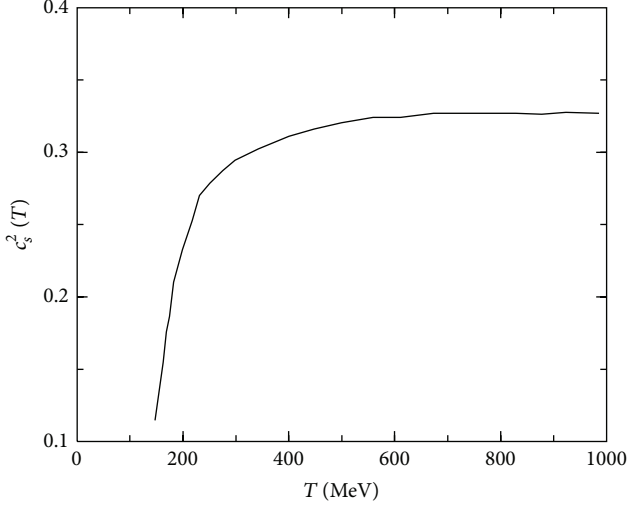


FIGURE 6: Velocity of sound squared as a function temperature [8].

used inputs from lattice QCD (LQCD) to minimize the model dependence of the results.

The initial entropy density and the thermalization time (τ_i) for the QGP can be constrained to the measured (final) multiplicity by the following relation [79] which is boost invariant:

$$s_i \tau_i = \kappa \frac{1}{A_\perp} \frac{dN}{dy}, \quad (35)$$

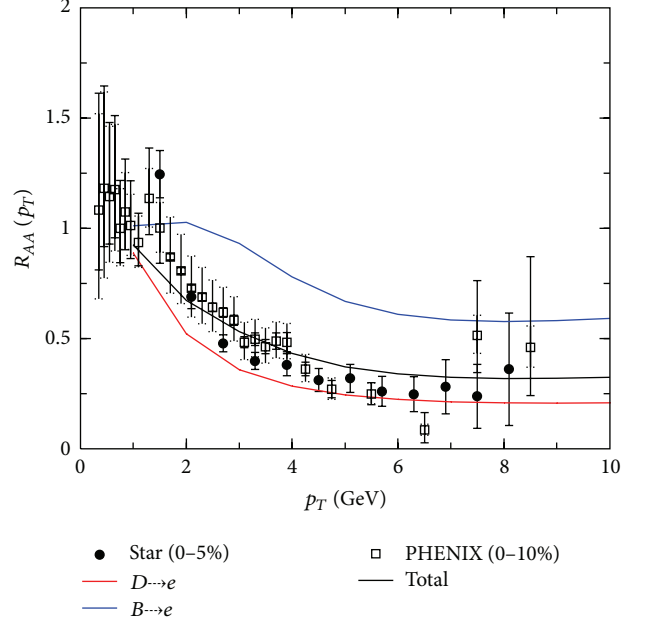
where A_\perp is the transverse area of the system which can be determined from the collision geometry and κ is a known constant (≈ 3.7 for massless Bosons).

Equation of state (EoS), which is taken as $P = c_s^2 \epsilon$ for almost baryon free QGP expected at RHIC energy, also has its own role to play in the space-time evolution of QGP. This sound velocity squared appearing in the EoS shows a significant variation with temperature in LQCD calculations (Figure 6).

In Figure 10, we show the variation of T_i with c_s^2 obtained by constraints imposed by the experimental data on R_{AA} and dN/dy . The value of T_i varies from 210 to 300 MeV depending on the value of c_s^2 . It is interesting to note that the lowest value of T_i obtained from the present analysis is well above the quark-hadron phase transition temperature, indicating the fact that the system formed in Au + Au collisions at $\sqrt{s_{NN}} = 200$ GeV might be formed in the partonic phase.

The data for R_{AA} of D^0 from ALICE are also contrasted with our results (see Figure 11) when $c_s^2 = 1/3$ [12]. The EoS sets the expansion time scale for the system as $\tau_{exp} \sim [(1/\epsilon)d\epsilon/d\tau]^{-1} \sim \tau/(1 + c_s^2)$ indicating the fact that lower value of c_s^2 makes the expansion time scale longer, that is, the rate of expansion is slower. This issue is further discussed in details in [80].

The result of R_{AA} , where the EoS contains temperature-dependent c_s^2 , is displayed in Figure 7. Here, the experimentally measured suppression [13, 14] has been reproduced reasonably well at $T_i = 250$ MeV and $\tau_i = 0.83$ fm/c. The T_i value, however, may increase if we take into account the transverse expansion because the inflation dilutes the medium.


 FIGURE 7: Variation of R_{AA} with p_T for the space time evolution with initial condition $T_i = 250$ MeV and $\tau_i = 0.84$ fm/c and the EoS which includes the variation of c_s^2 with T (colour online).

Now, we know that larger c_s^2 makes the QGP life time smaller leading to lesser suppression of HQ propagating through QGP for a shorter time. Therefore, when the value of c_s^2 is taken to be $1/3$, that is, the highest possible value, the maximum value of T_i , which is in this analysis 300 MeV, will be reached. The value of s_i at $c_s^2 = 1/3$ is $\sim 59/\text{fm}^3$. These values of T_i and s_i are considered as the highest values of them admitted by the data. The result for the highest value of c_s^2 is illustrated in Figure 8. Likewise, the result of R_{AA} in the case when $c_s^2 = 1/5$ is depicted in Figure 9. In this case, the data is well reproduced at $T_i = 210$ MeV and $s_i \sim 19.66/\text{fm}^3$.

Now, it is expected that the central rapidity region of the system formed after nuclear collisions at high energy RHIC and LHC run is almost net baryon free. Therefore, the equation governing the conservation of net baryon number need not be considered here and all our calculations are valid for zero baryonic chemical potential ($\mu_B = 0$) cases. One may be interested in calculating transport coefficients in $\mu_B \neq 0$ case which may be of importance in low energy RHIC run [81, 82] and GSI-FAIR [83]. This aspect is discussed in the next section.

7. Drag and Diffusion at Finite Baryonic Chemical Potential

The nuclear collisions at low energy RHIC run [81, 82] and GSI-FAIR [83] are expected to create a thermal medium with large baryonic chemical potential (μ_B) and moderate temperature (T). So the effect of baryonic chemical potential (μ_B) on the transport coefficients of HQ should also be taken into account. Both the temperature (T) and quark chemical potential, $\mu (= \mu_B/3)$, dependence of drag enter through the thermal distribution.

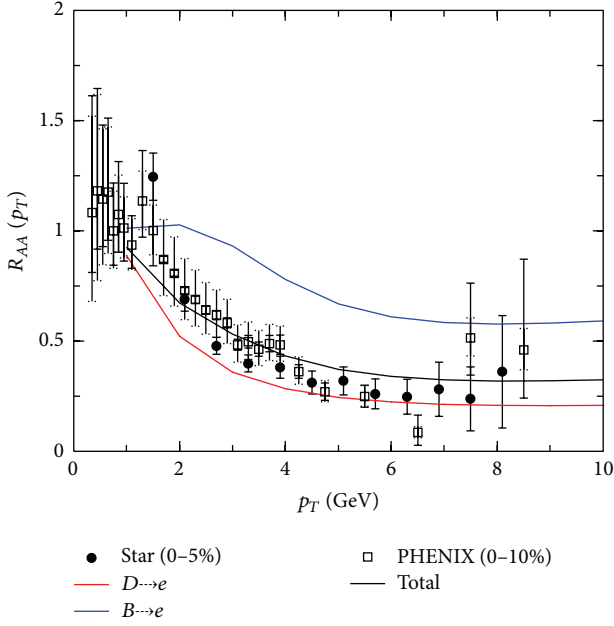


FIGURE 8: Variation of R_{AA} with p_T for $c_s^2 = 1/3$ and $T_i = 300$ MeV (colour online).

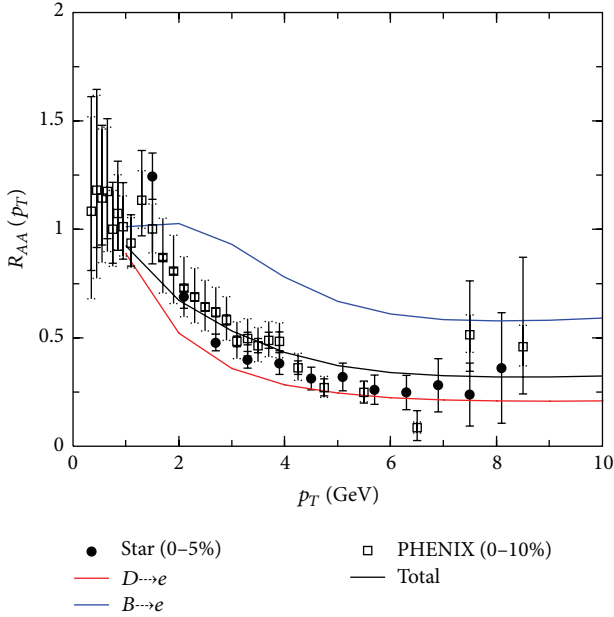


FIGURE 9: Variation of R_{AA} with p_T for $c_s^2 = 1/5$ and $T_i = 210$ MeV (colour online).

The variation of the drag coefficients of charm quarks (due to its interactions with quarks and antiquarks) with the baryonic chemical potential for different T is displayed in Figure 12. The drag coefficient for the process: $Qg \rightarrow Qg$ is $\sim 8.42 \times 10^{-3} \text{ fm}^{-1}$ ($1.86 \times 10^{-2} \text{ fm}^{-1}$) for $T = 140$ MeV (190 MeV) (not displayed in Figure 12). The T and μ dependence of the drag and diffusion coefficients may be understood as follows. As discussed earlier, the drag may be defined as the thermal average of the momentum transfer weighted by the square of the invariant transition amplitude for the reactions $qQ \rightarrow qQ$, $Q\bar{q} \rightarrow Q\bar{q}$, and $gQ \rightarrow gQ$.

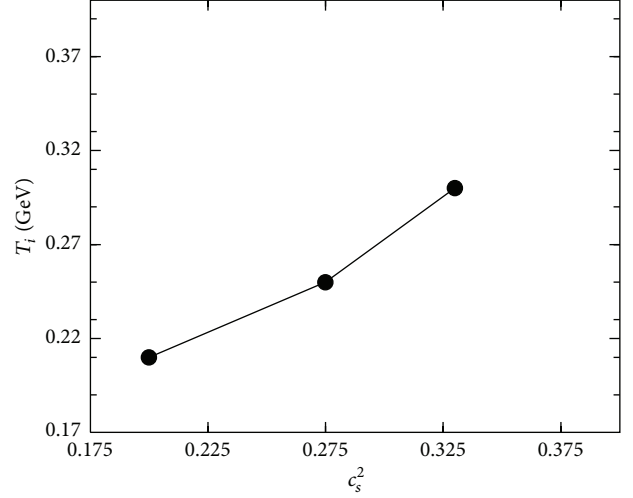


FIGURE 10: The variation of T_i with c_s^2 for fixed dN/dy .

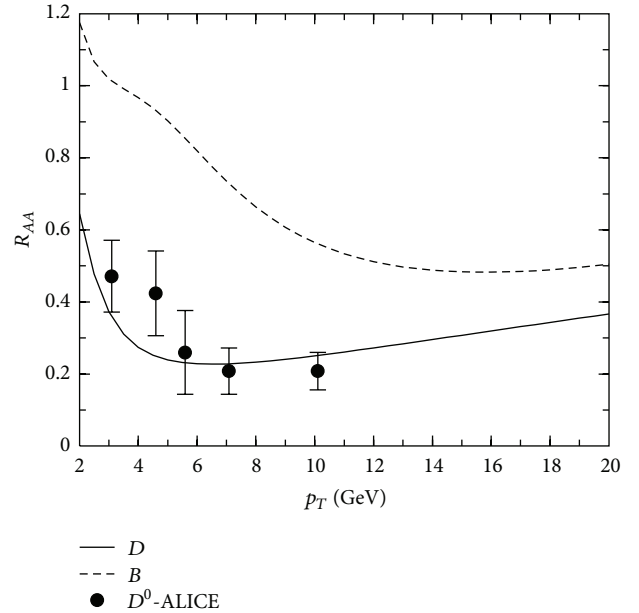


FIGURE 11: R_{AA} as a function of p_T for D and B mesons at LHC. Experimental data taken from [16].

The average momentum of the quarks of the thermal bath increases with both T and μ . The increase in average momenta enables the thermal quarks to transfer larger momentum and thus, in turn, enhances the drag coefficient. This trend is clearly observed in the results displayed in Figure 12 for charm quark. The drag due to the process $Qq \rightarrow Qq$ is larger than the $Q\bar{q} \rightarrow Q\bar{q}$ interaction because of non-zero chemical potential, the Q propagating through which the medium encounters more q than \bar{q} at a given μ . For vanishing chemical potential, the contributions from quarks and anti-quarks are same.

In the same way, it may be argued that the diffusion coefficient involves the square of the momentum transfer, which should also increase with T and μ as observed in Figure 13. The diffusion coefficient for charm quarks due to its interaction with gluons is given by $\sim 1.42 \times 10^{-3} \text{ GeV}^2/\text{fm}$

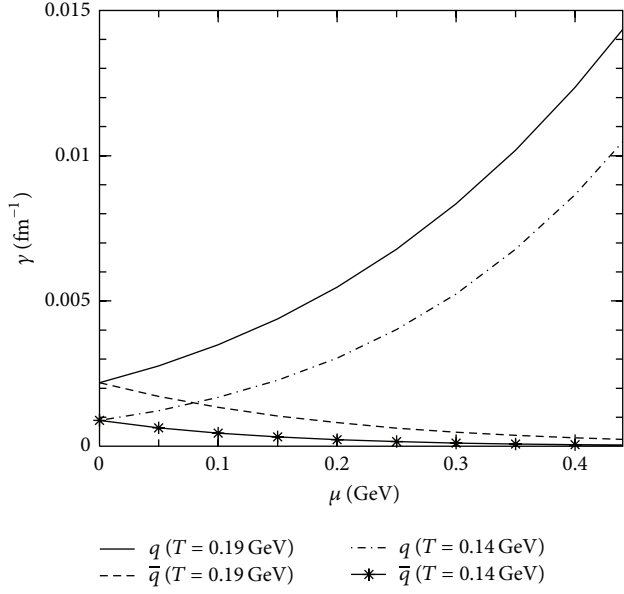


FIGURE 12: Variation of the drag coefficient of charm quark due to its interactions with light quarks and anti-quarks as a function of μ for different temperatures.

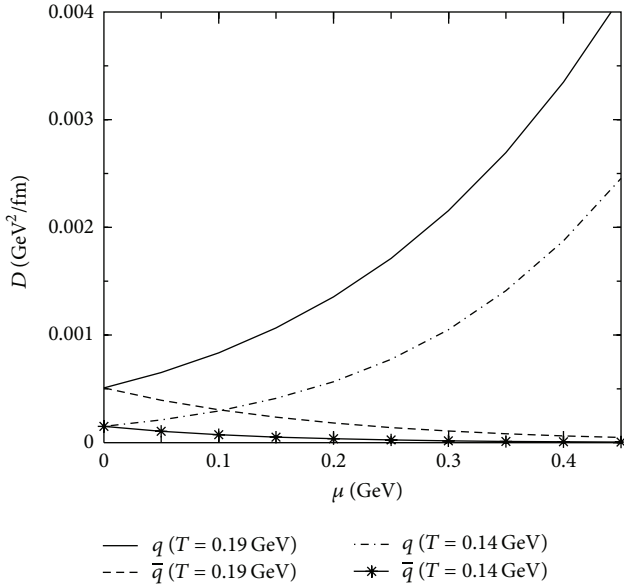


FIGURE 13: Variation of the diffusion coefficient of charm quark due to its interactions with light quarks and anti-quarks as a function of μ for different temperatures.

$(4.31 \times 10^{-3} \text{ GeV}^2/\text{fm})$ for $T = 140 \text{ MeV}$ (190 MeV). The drag and diffusion coefficients for bottom quarks are displayed in Figures 14 and 15, respectively, showing qualitatively similar behaviour as charm quarks. The drag coefficients for bottom quarks due to the process $Qg \rightarrow Qg$ are given by $\sim 3.15 \times 10^{-3} \text{ fm}^{-1}$ and $6.93 \times 10^{-3} \text{ fm}^{-1}$ at $T = 140 \text{ MeV}$ and 190 MeV respectively. The corresponding diffusion coefficients are $\sim 1.79 \times 10^{-3} \text{ GeV}^2/\text{fm}$ and $5.38 \times 10^{-3} \text{ GeV}^2/\text{fm}$ at $T = 140 \text{ MeV}$ and 190 MeV , respectively. The μ dependent drag and diffusion coefficients will be used later to evaluate the nuclear

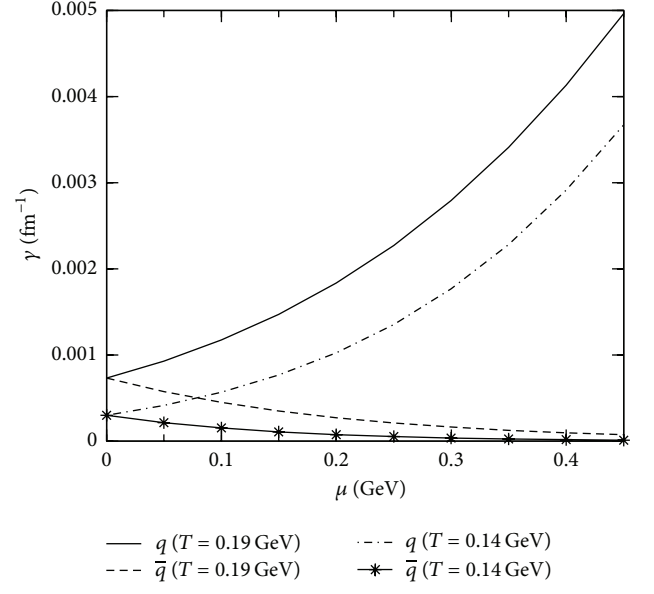


FIGURE 14: The same as Figure 12 for bottom quark.

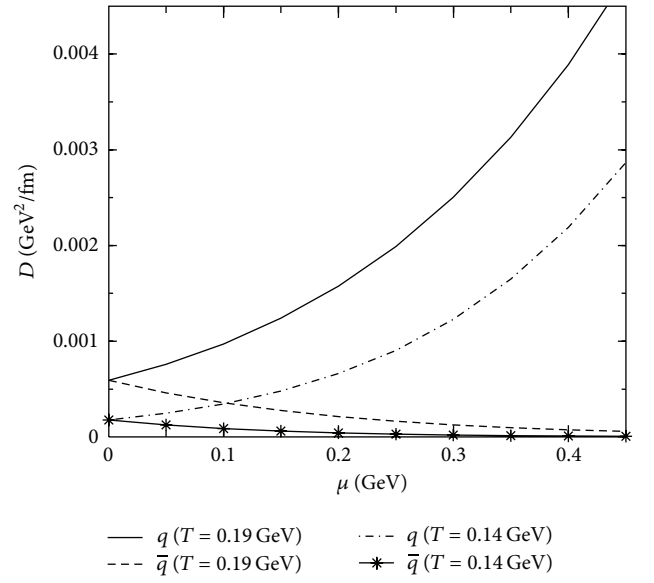


FIGURE 15: The same as Figure 13 for bottom quark.

suppression of the heavy flavours for low energy RHIC experiments.

8. Nuclear Suppression in Baryon Rich QGP

For low energy collisions, the radiative energy loss of heavy quarks will be much smaller than the loss caused by elastic processes as they are produced with very low momentum. Moreover, the thermal production of charm and bottom quarks can be ignored in the range of temperature and baryonic chemical potential under study. Therefore, we can apply the FP equation for the description of HQ evolution in the baryon rich QGP. Here we need to solve the FP equation for non-zero μ_B . The drag and diffusion coefficients are functions of both the thermodynamical variables: μ_B and T .

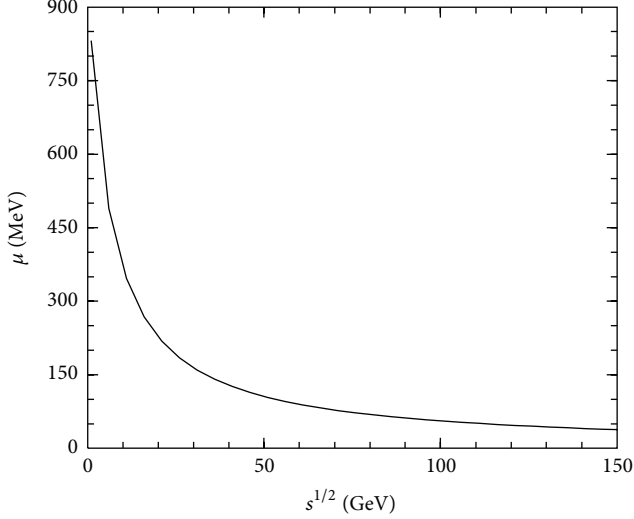


FIGURE 16: Variation of μ_B with respect to the $\sqrt{s_{NN}}$.

The energy ($\sqrt{s_{NN}}$) dependence of the chemical potential can be obtained from the parametrization of the experimental data on hadronic ratios as [84] (see also [85])

$$\mu_B(s_{NN}) = a \left(1 + \frac{\sqrt{s_{NN}}}{b} \right)^{-1}, \quad (36)$$

where $a = 0.967 \pm 0.032$ GeV and $b = 6.138 \pm 0.399$ GeV. The parametrization in (36) gives the values of μ_B . At midrapidity, the chemical potential of the system decreases with respect to the colliding energy as observed in Figure 16. So the composition of matter produced at LHC and RHIC is different from the matter produced at low energy collision. At LHC and RHIC, the matter produced at the midrapidity is almost baryon free, whereas the matter produced at the low colliding energy is dominated by baryons.

To take care of this extra baryons, we need to solve the baryon-number conservation equation along with the energy-momentum conservation equation; that is, we simultaneously solve

$$\begin{aligned} \partial_\mu T^{\mu\nu} &= 0, \\ \partial_\mu n_B^\mu &= 0 \end{aligned} \quad (37)$$

for (1 + 1) dimension with boost invariance along the longitudinal direction [74]. In the above equation, $n_B^\mu = n_B u^\mu$ is the baryonic flux and u^μ is the hydrodynamic 4-velocity. The initial baryonic chemical potential carried by the quarks ($\mu = \mu_B/3$) is shown in Table 1 for various $\sqrt{s_{NN}}$ under consideration.

The value of the multiplicities for various $\sqrt{s_{NN}}$ has been calculated from the equation below [86] as

$$\frac{dN}{dy} = \frac{dn_{pp}}{dy} \left[(1-x) \frac{\langle N_{part} \rangle}{2} + x \langle N_{coll} \rangle \right] \quad (38)$$

N_{coll} is the number of collisions and contributes x fraction to the multiplicity dn_{pp}/dy measured in pp collision. The

TABLE 1: The values center of mass energy $\sqrt{s_{NN}}$, dN/dy , initial temperature (T_i), and quark chemical potential used in the present calculations.

$\sqrt{s_{NN}}$ (GeV)	dN/dy	T_i (MeV)	μ (MeV)
39	617	240	62
27	592	199	70
17.3	574	198	100
7.7	561	197	165

number of participants, N_{part} , contributes a fraction $(1-x)$ to dn_{pp}/dy , which is given by

$$\frac{dn_{pp}}{dy} = 2.5 - 0.25 \ln(s) + 0.023 \ln^2(s). \quad (39)$$

The values of N_{part} and N_{coll} are estimated for (0%–5%) centrality by using Glauber model [87]. The value of x depends very weakly on $\sqrt{s_{NN}}$ [88], and in the present work we have taken $x = 0.1$ for all the energies.

We need the initial heavy quark momentum distributions for solving the FP equation. For low collision energy, rigorous QCD-based calculations for heavy flavour production are not available. In the present work, the initial HQ distribution is obtained from pQCD calculation [41, 89] for the processes $gg \rightarrow Q\bar{Q}$ and $q\bar{q} \rightarrow Q\bar{Q}$. To demonstrate the effect of non-zero baryonic chemical potential, we evaluate R_{AA} for $\mu = 200$ MeV and $\mu = 0$ for a given $T_i = 200$ MeV. The results are displayed in Figure 17 representing the combined effects of temperature and baryon density on the drag and diffusion coefficients. The drag of the heavy quarks due to its interaction with quarks is larger than that due to its interactions with the anti-quarks (Figure 12), resulting in larger suppression in the former case than the latter. The net suppression of the electron spectra from the Au+Au collisions compared to p + p collisions is affected by quarks, anti-quarks, and gluons. The results for net suppressions are displayed for $\mu = 200$ MeV (dashed line) and $\mu = 0$ (with asterisk). The experimental detection of the non-zero baryonic effects will shed light on the net baryon density (and hence baryon stopping) in the central rapidity region. However, whether the effects of non-zero baryonic chemical potential are detectable or not will depend on the overall experimental performance.

The results for R_{AA} are shown in Figure 18 for various $\sqrt{s_{NN}}$ with inputs from Table 1. We observe that at large p_T the suppression is similar for all energies under consideration. This is because the collisions at high $\sqrt{s_{NN}}$ are associated with large temperature but small baryon density at midrapidity, which is compensated by large baryon density and small temperature at low $\sqrt{s_{NN}}$ collisions. Low p_T particles predominantly originate from low temperature and low density part of the evolution where drag is less and so is the nuclear suppression.

In our earlier work [23], we have evaluated the R_{AA} for nonphotonic single electron spectra resulting from the semileptonic decays of hadrons containing heavy flavours and observed that the data from RHIC collisions at $\sqrt{s_{NN}} = 200$ GeV are well reproduced by enhancing the pQCD cross

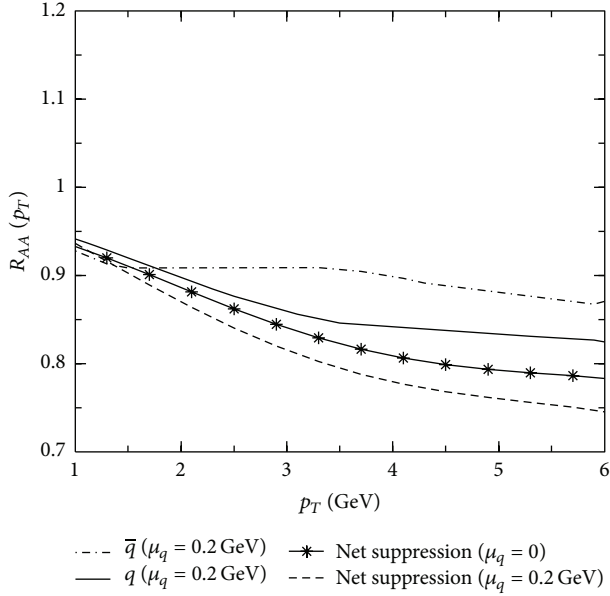


FIGURE 17: The nuclear suppression factor R_{AA} as a function of p_T due to the interaction of the charm quark (solid line) and anti-quark (dashed-dot line) for $\mu = 200$ MeV. The net suppressions including the interaction of quarks, anti-quarks, and gluons for $\mu = 200$ MeV (dashed line) and $\mu = 0$ (with asterisk) are also shown.

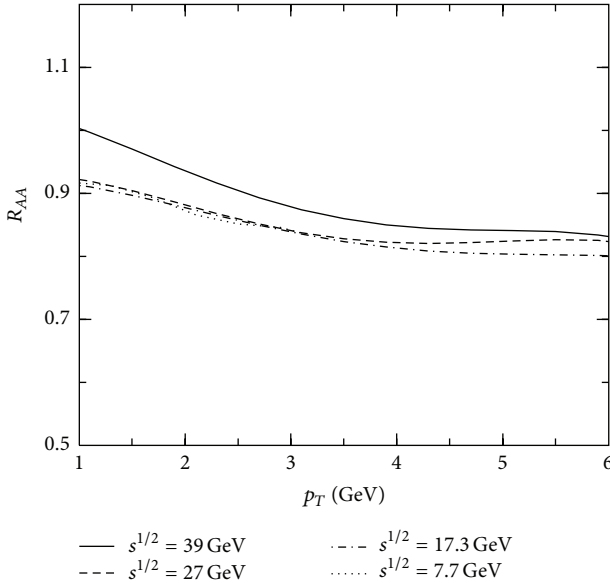


FIGURE 18: Nuclear suppression factor, R_{AA} , as function of p_T for various $\sqrt{s_{NN}}$.

sections by a factor 2 and with an equation of state $P = \epsilon/4$ for collisional loss. In the same spirit, we evaluate R_{AA} with twice enhanced pQCD cross section and keeping all other quantities unaltered (Figure 19). The results in Figure 19 show stronger suppression as compared to the results displayed in Figure 18, but it is similar in all the energies under consideration. When we have enhanced the pQCD cross section for the interaction of the heavy quarks with the thermal system by a factor of two—the resulting suppressions in R_{AA} are between 20% and 30% for $\sqrt{s_{NN}} = 39 - 7.7$ GeV.

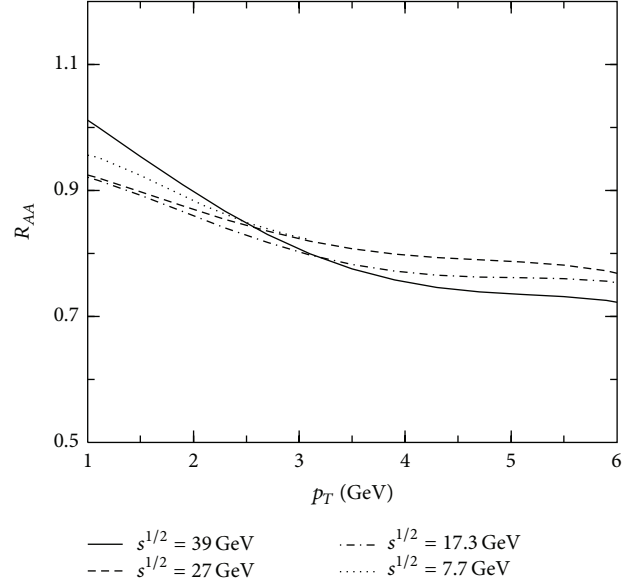


FIGURE 19: The same as Figure 18 with enhancement of cross section by a factor of 2.

9. Glimpses of Elliptic Flow

However, apart from the nuclear suppression factor R_{AA} , another experimental observable of heavy flavour, elliptic flow (v_2), can be studied within the framework of Fokker-Planck equation. The elliptic flow (v_2) of the produced particles has been considered as one of the most promising signals for the early thermalization of the matter formed in heavy ion collision. If we consider a thermalized ellipsoidal spatial domain of QGP, originated due to noncentral nucleus nucleus collisions, with major and minor axes of lengths l_y and l_x (determined by the collision geometry), respectively, then the pressure gradient is larger along the minor axis compared to that along the major axis because $l_y > l_x$. Now, pressure gradient is force and hence force along the minor axis is larger than that along the major axis. Consequently, the HQ moves faster in this direction. Therefore, the momentum distribution of electrons originating from the decays of charmed hadrons (D mesons) produced from the charm quark fragmentation will be anisotropic, and since v_2 is the second Fourier's coefficient of the momentum distribution, the spatial anisotropy is thus reflected in the momentum space anisotropy.

v_2 is sensitive to the initial conditions and the equation of state (EoS) of the evolving matter formed in heavy ion collision [90–92]. Several theoretical attempts have been made in this direction to study both the nuclear suppression factor and elliptic flow of the heavy flavour within a single framework. Although several authors have reproduced the large suppression of high momentum heavy quarks reasonably well yet it is still difficult to explain HQ elliptic flow simultaneously within the same set of initial parameters. It is also imperative to mention that no calculation with radiative energy loss is still able to reproduce heavy flavour elliptic flow. After this brief discussion, we refer the interested readers

to [18, 27, 32, 33, 56, 93–96] for more interesting aspects of elliptic flow.

10. Summary and Discussions

In summary, we have tried to give a systematic account of evaluating collisional and radiative transport coefficients of heavy quarks passing through quark-gluon plasma. The nuclear suppression factor (R_{AA}) of heavy quarks has been evaluated using Fokker-Planck equation. The present paper confines the discussions within perturbative QCD. Recently, the authors of [97] find out the drag force and R_{AA} of charm quarks propagating through thermalized QGP within the framework of both AdS/CFT and AdS/non-CFT. Interested readers are referred to [98, 99] for similar discussions.

We have studied the momentum dependence of transport coefficients and observe that the momentum dependence is crucial in reproducing the trend in the p_T dependence of the experimental data. Also, the dead-cone factor (F_{DC}) weighted by the Gunion-Bertsch spectrum for radiated gluon from heavy quarks is implemented. It is worth mentioning that though the present paper speaks at length about elastic as well as bremsstrahlung energy loss of HQs and tells about dominance of the latter in high p_T region, yet there are a plethora of articles which show the importance of elastic energy loss in context of experimental observables in entire momentum range attainable by HQs [18, 93, 100]. This issue, as a matter of fact, still awaits an unambiguous settlement.

Momentum independent transport coefficients in non-zero baryonic chemical potential region have also been studied and theoretical estimates of the suppression factor are provided. In the Appendix, we have discussed the calculation of elastic transport coefficients within the ambit of QCD hard thermal loop perturbation theory. Also, radiative suppression due to off-shellness of produced partons, which we may call the “dead cone due to virtuality,” has also been discussed. This effect of off-shellness of heavy quarks as well as HTL calculations may be extended to encompass radiative processes which, as we have already discussed, will play the most significant part in high energy regime. The calculations of R_{AA} including the aspects just mentioned may be contrasted with the experimental data.

Though [18, 23–25, 27, 34, 56, 93, 95] attempt to study R_{AA} and v_2 of the heavy quark, yet the role of hadronic matter has been ignored. However, to make the characterization of QGP reliable, the role of the hadronic phase should be taken into consideration and its contribution must be subtracted out from the observables. Although a large amount of work has been done on the diffusion of heavy quarks in QGP, the diffusion of heavy mesons in hadronic matter has received much less attention so far. Recently, the diffusion coefficient of D meson has been evaluated using heavy meson chiral perturbation theory [101] and also by using the empirical elastic scattering amplitudes [102] of D mesons with thermal hadrons. The interactions of D meson with pions, nucleons, kaons, and eta particles have been evaluated using Born amplitudes [103] and unitarized chiral effective $D\pi$ interactions [104, 105]. D and B -meson scattering lengths have also been used as dynamical input to study the drag and

diffusion coefficients [106, 107]. All these studies observed that the magnitude of both the transport coefficients is significant, indicating substantial amount of interaction of the heavy mesons with the thermal bath. The results may have significant impact on the experimental observables like the suppression of single electron spectra [108] originating from the decays of heavy mesons produced in nuclear collisions at RHIC and LHC energies.

Appendix

A. Hard Thermal Loop (HTL) Approximations and Transport Coefficients

We have used $T = 0$ pQCD matrix elements for calculating collisional transport coefficients so far. The t channel divergence due to soft intermediary gluon exchange has been shielded by an ad hoc replacement of t by $t - m_D^2$, where m_D is the (static) Debye screening mass of gluon. Here we use thermal resummed (HTL) gluon propagators [66, 67, 109] for calculating the matrix elements for the processes like $Qq \rightarrow Qq$ and $Qg \rightarrow Qg$, where $Q(q)$ stands for heavy (light) quark and g stands for gluon, for a self-consistent shielding of t channel divergence. Since the light quarks and gluons of thermal bath are hard, that is, their momenta are $\sim T$, we may neglect the vertex correction (assuming $g \ll 1$) arising due to ggg or qqg vertex. The effect of full gluon spectral function on the collisional drag coefficient will be investigated for HQs.

B. HTL Gluon Propagator

For finding out the HTL gluon propagator ($\Delta^{\mu\nu}$), we need HTL approximated self-energy of gluon which goes as an input to $\Delta^{\mu\nu}$ to be used as effective thermal propagator regularizing the t channel divergence. The gluon self-energy in HTL approximation is discussed in detail in [66, 67]. In this section, we give only an outline of the scheme. There are four diagrams which contribute to gluon self-energy (Figure 20). The loop integrations can be written down easily if we keep in mind that the loop momentum, $K = (k_0, \vec{k})$, is much larger compared to external gluon momentum, that is, $K \gg P$, which enables us to use simplified ggg vertex [66]. Our goal will be to find out T^2 contributions of self-energy which is the leading behaviour of self-energy in terms of temperature, T . This T^2 contribution of self-energy is called the “hard thermal loop” contribution. We may argue that the hard thermal loop contribution of the gluon self-energy is due to momenta $\sim T$ if we look at the generic integral of the type

$$\int_0^\infty k f(k) dk = \frac{\pi^2 T^2}{12}, \quad (\text{B.1})$$

which appears during self-energy calculation. f in (B.1) is the distribution function and the leading contribution in (B.1) is given by $k \sim T$. Henceforth, we obtain a scale of momentum $\sim T$, which will be called “hard” compared to another “soft” scale $\sim gT$, where $g(\ll 1)$ is the colour charge. HTL gluon propagators are to be used for processes exchanging very soft

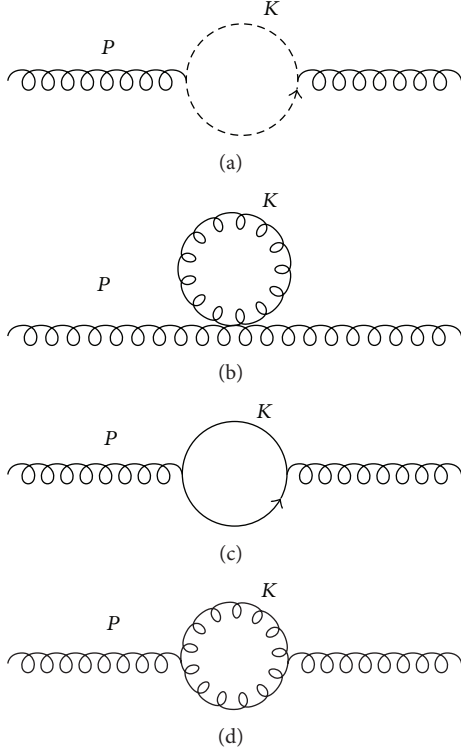


FIGURE 20: Feynman diagrams contributing to gluon self-energy up to one loop. (a) Ghost-gluon loop. (b) Four-gluon vertex. (c) Quark-antiquark pair creation. (d) Three-gluon vertex.

gluons. As the t channel divergence is equivalent to dominance of soft gluon exchange processes, the use of HTL propagator is justified and consistent.

Now, let us define the following useful quantities [66] required to write down the gluon propagator in thermal medium. Let u_μ be the fluid 4-velocity, with normalization condition $u^\mu u_\mu = 1$. The fluid 4-velocity gives rise to two directions, and so any 4-vector P^μ can be decomposed into components parallel and perpendicular to the fluid velocity

$$\begin{aligned}\omega &= P \cdot u, \\ \tilde{P}_\mu &= P_\mu - u_\mu (P \cdot u),\end{aligned}\quad (\text{B.2})$$

where

$$\begin{aligned}P^2 &= \omega^2 - p^2, \\ \tilde{P}^2 &= -p^2.\end{aligned}\quad (\text{B.3})$$

Equations (B.2) and (B.3) are valid in the local rest frame of fluid, that is, in a frame where $u = (1, \vec{0})$. Similarly, a tensor orthogonal to u_μ can be defined as

$$\tilde{g}_{\mu\nu} = g_{\mu\nu} - u_\mu u_\nu. \quad (\text{B.4})$$

The longitudinal and transverse projection tensors, $\mathcal{P}_L^{\mu\nu}$ and $\mathcal{P}_T^{\mu\nu}$, respectively, are defined as [109]

$$\begin{aligned}\mathcal{P}_L^{\mu\nu} &= -\frac{1}{P^2 p^2} (\omega P^\mu - P^2 u^\mu) (\omega P^\nu - P^2 u^\nu), \\ \mathcal{P}_T^{\mu\nu} &= \tilde{g}_{\mu\nu} + \frac{\tilde{P}_\mu \tilde{P}_\nu}{p^2}\end{aligned}\quad (\text{B.5})$$

which are orthogonal to P^μ as well as to each other, that is,

$$P_\mu \mathcal{P}_L^{\mu\nu} = P_\mu \mathcal{P}_T^{\mu\nu} = \mathcal{P}_L^{\mu\nu} \mathcal{P}_T^{\nu\rho} = 0, \quad (\text{B.6})$$

but

$$\mathcal{P}_i^{\mu\rho} \mathcal{P}_{i\nu\rho} = \mathcal{P}_i^{\mu\nu}, \quad i = L, T. \quad (\text{B.7})$$

The HTL gluon propagator, which is given by

$$\Delta^{\mu\nu} = \frac{\mathcal{P}_T^{\mu\nu}}{-P^2 + \Pi_T} + \frac{\mathcal{P}_L^{\mu\nu}}{-P^2 + \Pi_L} + (\alpha - 1) \frac{P^\mu P^\nu}{P^2}, \quad (\text{B.8})$$

will need HTL approximated longitudinal and transverse self-energies Π_L and Π_T , respectively, too. Π_L and Π_T are given by

$$\Pi_L(P) = (1 - x^2) \pi_L(x), \quad \Pi_T(P) = \pi_T(x), \quad (\text{B.9})$$

where $x = \omega/|\vec{p}|$ ($P \equiv (\omega, \vec{p})$, see Figure 20) and scaled self-energies π_T and π_L are given by [66]

$$\begin{aligned}\pi_T(x) &= m_D^2 \left[\frac{x^2}{2} + \frac{x}{4} (1 - x^2) \ln \left(\frac{1+x}{1-x} \right) - i \frac{\pi}{4} x (1 - x^2) \right], \\ \pi_L(x) &= m_D^2 \left[1 - \frac{x}{2} \ln \left(\frac{1+x}{1-x} \right) + i \frac{\pi}{2} x \right],\end{aligned}\quad (\text{B.10})$$

where m_D is the thermal mass of gluon and is given by $m_D^2 = g^2 T^2 (C_A + N_f/2)/6$, where $C_A = 3$ is the Casimir of adjoint representation of SU(3) and $N_f = 2$ is the number of flavours.

C. Finding Out Matrix Elements for Qq Scattering

From Figure 21, we can calculate the t -channel matrix element for the process $Qq \rightarrow Qq$. We will use the HTL gluon propagator [66]. Pictorially, an HTL propagator will be denoted by a solid circle. We can write the amplitude in Feynman Gauge ($\alpha = 1$) from Figure 21 as

$$\begin{aligned}-iM_t &= \bar{u}(p_3) (-ig\gamma^\mu t_{ji}^a) u(p_1) [-i\Delta_{\mu\nu}] \\ &\quad \times \bar{u}(p_4) (-ig\gamma^\nu t_{lk}^a) u(p_2),\end{aligned}\quad (\text{C.1})$$

where g is strong coupling and $g^2 = 4\pi\alpha_s$. i, j, k, l ($i \neq j, k \neq l$) are quark colours and “ a ” is the colour of intermediary gluon

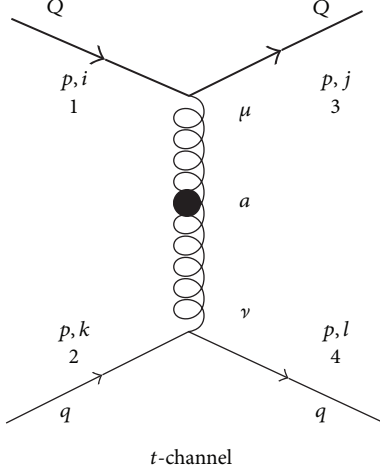


FIGURE 21: $Qq \rightarrow Qq$ Feynman diagram. Bold lines are for heavy quarks (Q).

with polarizations μ, ν . After squaring and averaging over spin and colour as well as using (B.8), we get

$$\begin{aligned}
& \frac{|M_{Qq}|^2}{4C_{Qq}g^4} \\
&= 2 \frac{p_4 \cdot \mathcal{P}_T \cdot p_3 p_2 \cdot \mathcal{P}_T \cdot p_1}{(t - \Pi_T)^2} + 2 \frac{p_4 \cdot \mathcal{P}_L \cdot p_3 p_2 \cdot \mathcal{P}_L \cdot p_1}{(t - \Pi_L)^2} \\
&+ 2 \frac{p_4 \cdot \mathcal{P}_T \cdot p_1 p_2 \cdot \mathcal{P}_T \cdot p_3}{(t - \Pi_T)^2} + 2 \frac{p_4 \cdot \mathcal{P}_L \cdot p_1 p_2 \cdot \mathcal{P}_L \cdot p_3}{(t - \Pi_L)^2} \\
&+ 2A \frac{p_4 \cdot \mathcal{P}_L \cdot p_3 p_2 \cdot \mathcal{P}_T \cdot p_1 + p_4 \cdot \mathcal{P}_T \cdot p_3 p_2 \cdot \mathcal{P}_L \cdot p_1}{(t - \Pi_T)^2 (t - \Pi_L)^2} \\
&+ 2A \frac{p_4 \cdot \mathcal{P}_L \cdot p_1 p_2 \cdot \mathcal{P}_T \cdot p_3 + p_4 \cdot \mathcal{P}_T \cdot p_1 p_2 \cdot \mathcal{P}_L \cdot p_3}{(t - \Pi_T)^2 (t - \Pi_L)^2} \\
&- 2p_4 \cdot p_2 \left[\frac{p_3 \cdot \mathcal{P}_T \cdot p_1}{(t - \Pi_T)^2} + \frac{p_3 \cdot \mathcal{P}_L \cdot p_1}{(t - \Pi_L)^2} \right] \\
&- 2p_3 \cdot p_1 \left[\frac{p_4 \cdot \mathcal{P}_T \cdot p_2}{(t - \Pi_T)^2} + \frac{p_4 \cdot \mathcal{P}_L \cdot p_2}{(t - \Pi_L)^2} \right] \\
&+ p_3 \cdot p_1 p_4 \cdot p_2 \left[\frac{2}{(t - \Pi_T)^2} + \frac{1}{(t - \Pi_L)^2} \right] \\
&+ m^2 \left[2 \frac{p_4 \cdot \mathcal{P}_T \cdot p_2}{(t - \Pi_T)^2} + 2 \frac{p_4 \cdot \mathcal{P}_L \cdot p_2}{(t - \Pi_L)^2} \right] \\
&- m^2 \left[2 \frac{p_4 \cdot p_2}{(t - \Pi_T)^2} + \frac{p_4 \cdot p_2}{(t - \Pi_L)^2} \right], \tag{C.2}
\end{aligned}$$

where $C_{Qq} = 2/9$ is the Color factor, $Q^2 \equiv t = (p_1 - p_3)^2$, and $A = t^2 - t(\text{Re } \Pi_T + \text{Re } \Pi_L) + \text{Re } \Pi_T \Pi_L^*$, and we have used the following relations:

$$p_1 \cdot \mathcal{P}_L \cdot p_2 = p_3 \cdot \mathcal{P}_L \cdot p_4 = p_4 \cdot \mathcal{P}_L \cdot p_1 = p_2 \cdot \mathcal{P}_L \cdot p_3 \tag{C.3}$$

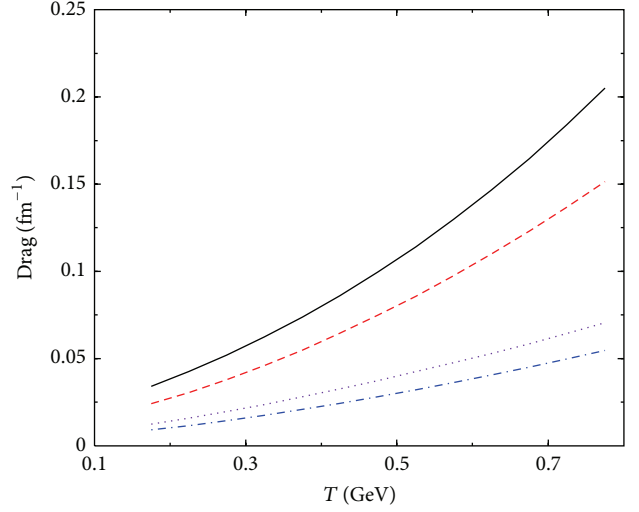


FIGURE 22: Variation of drag of heavy quarks of momentum 1 GeV with temperature (color online).

as well as

$$\begin{aligned}
\Delta^{\mu\rho} \Delta_{\rho}^{*\nu} &= \frac{\mathcal{P}_T^{\mu\nu}}{(t - \Pi_T)^2} + \frac{\mathcal{P}_L^{\mu\nu}}{(t - \Pi_L)^2}, \\
|\Delta|^2 &= \Delta^{\mu\nu} \Delta_{\nu\mu}^* = \frac{2}{(t - \Pi_T)^2} + \frac{1}{(t - \Pi_L)^2} \tag{C.4}
\end{aligned}$$

which can be proven using (B.5) and (B.8) in the rest frame of fluid element.

The $Qq \rightarrow Qq$ scattering contains s , t , and u channel diagrams and they can easily be written just like Qq case. There are $|M_t|^2$, $|M_s|^2$ and $|M_u|^2$ as well as the interference of s , t , u channels as opposed to [47] where only s and u channel interference term exists (besides $|M_t|^2$) because gluon momenta are assumed to be much larger than that of HQ.

D. Results and Discussions on Collisional Drag and Diffusion Coefficients Using HTL Propagator

We have found out the matrix elements for relativistic heavy quark scattering elastically with light quarks and gluons of QGP with arbitrary scattering angle. The variations of drags with temperature for HQs with momentum, $p = 1$ GeV, as a function of temperature are displayed in Figure 22. The results clearly indicate an enhancement and rapid variation of drag using HTL propagator (γ_{HTL}) compared to that in $T = 0$ pQCD (γ). The increase is more prominent for charm than bottom. We have explicitly checked that, in the static limit, the drag and diffusion using HTL propagator approaches that in $T = 0$ pQCD. γ_{HTL} is greater than γ for the entire momentum range considered here. Again, drag being the measure of energy loss, increase in drag results in

more suppression of heavy flavours measured at RHIC and LHC energies. From Figure 22, we observe that at 400 MeV temperature γ_{HTL} charm quark is $\sim 33\%$ more than the γ , whereas the corresponding difference is $\sim 25\%$ for bottom quarks. We also observe that this difference increases with the increase in temperature. Diffusion coefficients, plotted in Figure 23, seem to be more sensitive to the use of effective propagator in a sense that we observe 100% change between the diffusion using HTL propagator (D_{HTL}) and that in $T = 0$ pQCD (D) at $T = 400$ MeV and this difference increases with T . Though unlike drag, this difference is not much (3.5%) for a difference in charm and bottom quark masses.

The authors of [47] also calculate the energy loss of heavy quarks using HTL propagator and get a drag which is 16% less than that obtained in the present paper at HQ momentum 4 GeV and $T = 250$ MeV. The authors of [18] calculates diffusion coefficient of a nonrelativistic heavy quark in leading order as well as in next to leading order. The leading order result surpasses the present result by 25% at $T = 300$ MeV and at a very low momentum (0.2 GeV) of HQ.

However, radiative transport coefficients like drag are also needed for we have seen that radiation becomes very important in high energy regime. We can even extend the present calculation of collisional drag and diffusion using HTL propagator to radiative domains, but that will increase the complexity of problem.

E. Recent Efforts of Generalizing GB Formula

Gunion-Bertsch formula is derived in the mid-rapidity region and there is another very recent development in this field proposed in [110] where a generalized Gunion-Bertsch formula for arbitrary forward and backward rapidity region has been derived. This modification will be needed when one needs to compute cross sections and rates. Now, this calculation involves two parts (a) keeping a factor $(1 - x)^2$, where x is the fraction of light cone momentum carried by the emitted gluon and (b) combination of calculations obtained from both $A^+ = 0$ and $A^- = 0$ gauge conditions for emitted gluon polarization. The final form of $M_{qq' \rightarrow qq'g}$ can be written as follows:

$$|M_{qq' \rightarrow qq'g}|^2 = 12g^2 |M_{qq' \rightarrow qq'}|_{sa}^2 (1 - \bar{x})^2 \times \frac{q_{\perp}^2}{k_{\perp}^2 (\vec{q}_{\perp} - \vec{k}_{\perp})^2}, \quad (\text{E.1})$$

where

$$\bar{x} = \frac{k_{\perp} e^{|\eta|}}{\sqrt{s}}, \quad (\text{E.2})$$

where η is the rapidity of the emitted gluon. With this, the exact differential cross section ($d\sigma/d\eta$) for the process $qq' \rightarrow qq'g$ is shown to be reproduced by using (E.1) for all rapidity ranges.

In all these calculations, we tacitly assume that the incoming jet is hard enough so that eikonal approximation (straight path) for it is always valid. But there has been a

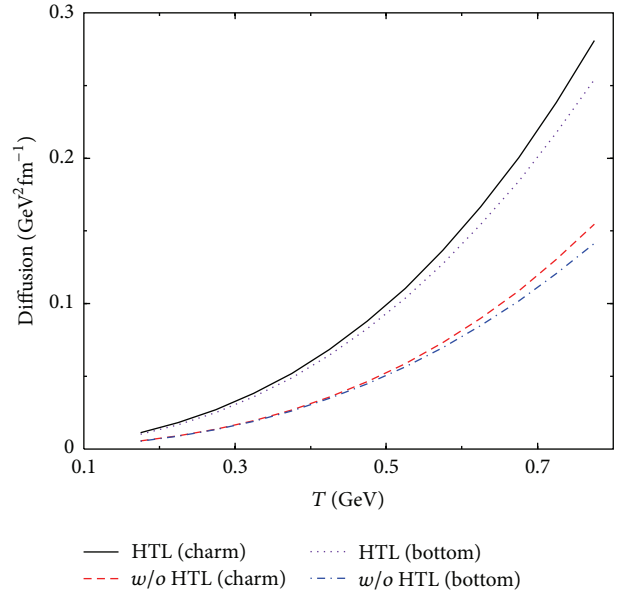


FIGURE 23: Variation of diffusion of heavy quarks of momentum 1 GeV with temperature (color online).

recent attempt of relaxing the eikonal approximation in [111] and 15%–20% suppression in the differential cross section of $2 \rightarrow 3$ processes for moderately hard jets because of the noneikonal effects that have been found.

F. Dead-Cone Effect Revisited and Other Aspects of Energy Loss

The authors of [112] compute the HQ-LQ \rightarrow HQ-LQ-g scattering amplitude for soft gluon emission and find out a general expression for radiative suppression factor for dead-cone effect. In the limit $m \ll \sqrt{s}$ and $\theta \rightarrow 0$, they reproduce (25). In the backward rapidity region, the gluon emission does not depend on the mass and in $\theta \sim \pm\pi$ region there is no suppression, in contrast with what we get from [71] (see [73] also). The authors of [113] evaluate the HQ energy loss employing the generalized dead-cone factor in [112]. They report similar energy loss for both massless and massive quark jets.

However, the high energy quarks and gluons produced from the hard collisions of the partons from the colliding nucleons are off-shell and their colour fields are stripped off; that is, they have no field to radiate. Therefore, the parton virtuality creates its own dead cone which may be large depending on the magnitude of the virtuality. The forbidden zone around the direction of motion of the partons due to its virtuality will here be called virtual dead cone. If the virtuality does not disappear before the hadronization of the QGP, then the dead cone suppression due to virtuality will play a decisive role in QGP diagnostics by jet quenching. The conventional dead-cone (due to the mass of the quark) becomes important when the virtuality of the quarks reduces to zero.

For the demonstration of suppression of soft gluon radiation due to virtuality, we can take up the $e^+e^- \rightarrow QQg$ process,

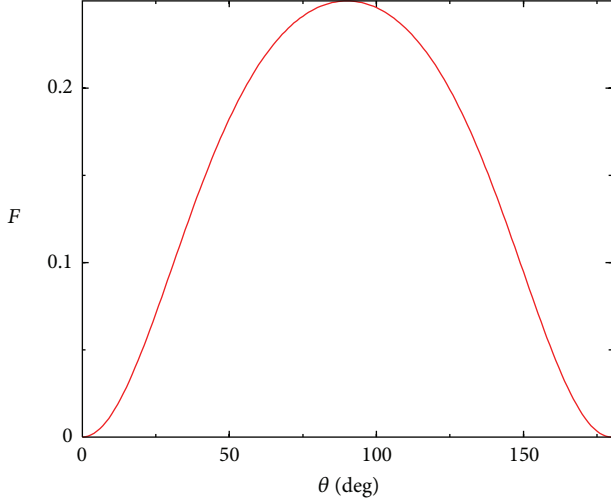


FIGURE 24: Plot of the spectrum F in $V = 0$ limit (F.2), $m = 1.5$ GeV, $\beta = 0.5$.

where Q is heavy quark. The spectrum of the soft gluons emitted by the virtual quarks can be shown to be [114]

$$F = 4\beta^2 \left(\frac{V^4/k_0^2 E^2 + 4V^2/k_0 E + 4\sin^2\theta}{(V^4/k_0^2 E^2 + 4V^2/k_0 E + 4(1 - \beta^2 \cos^2\theta))^2} \right), \quad (\text{F.1})$$

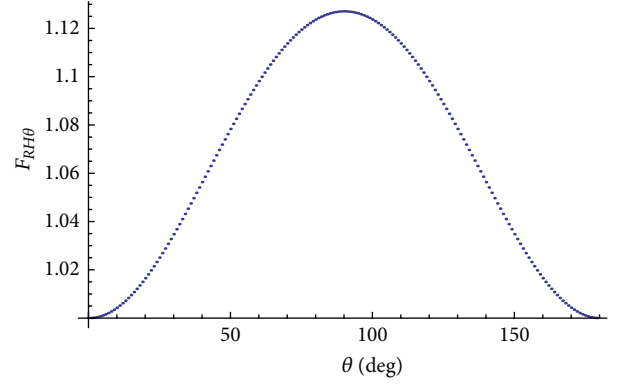
where external quarks are assumed to be on the verge of being on-shell so that Dirac's equation can be applied. V is the virtuality parameter defined by the equation, $V^2 = q^2 - m^2$ where q^2 is four-momentum square of external virtual particles and m is its mass, if any. $q^2 = m^2$ implies $V = 0$; that is, the particle becomes on-shell. One can show that the spectrum is that of gluons emitted from on-shell quarks when $V = 0$. k_0 is the energy of the soft gluon emitted at angle θ with the parent quark whose velocity is β and energy is E . The virtuality is replaced by $V = \sqrt{q^2 - m^2} = \sqrt{E^2 - p^2 - m^2}$. The emitted gluon carry a fraction of parent parton energy consistent with $|\vec{p}_i| \sin\theta \gg k_0$ (for dominance of soft gluon emission). Different limits of F given in (F.1) will be worth exploring.

- (i) For zero virtuality ($V = 0$) of the massive quark, (F.1) reduces to the conventional dead-cone factor (Figure 24) as

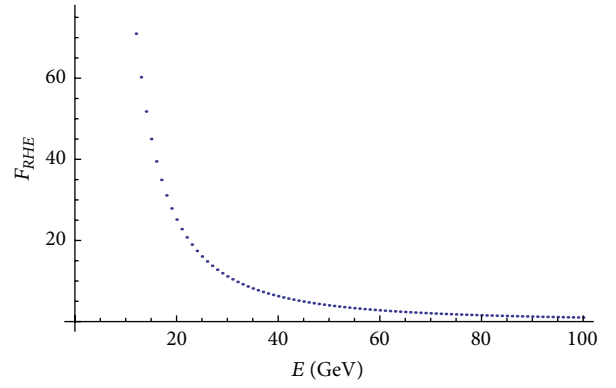
$$F \longrightarrow \frac{\beta^2 \sin^2\theta}{(1 - \beta^2 \cos^2\theta)^2}. \quad (\text{F.2})$$

This is the well-known conventional dead cone for a gluon emitted by a massive quark for large angles. The divergence of the factor is shielded by the quark mass or virtuality through $\beta (< 1)$. In fact, for on-shell quarks with small θ , one can show that (F.2) (see [71]) boils down to

$$F = \frac{1}{\theta^2} \frac{1}{(1 + \theta_0^2/\theta^2)^2}, \quad \theta_0 = \frac{m}{E}, \quad (\text{F.3})$$



(a)



(b)

FIGURE 25: The variation of (a) $F_{RH0}(E, \theta)$, defined in the text with θ for $E = 1.5$ GeV, (b) with E for $\theta = \pi/4$ for virtual heavy quarks (colour online). The results displayed in this figure are evaluated for heavy quark mass, $m = 1.27$ GeV, and emitted gluon energy, $k_0 = 20$ MeV and $\beta = 0.5$. The quark virtuality is defined as $V^2 = E^2 - \beta^2 E^2 - m^2$.

and for highly virtual quarks (large V) the F can be written as:

$$F = \frac{\omega^2}{E^2}. \quad (\text{F.4})$$

- (ii) Now, the light quark limit ($\beta = 1$) can be investigated. For $V = 0$, $\beta = 1$,

$$F \sim \frac{1}{\sin^2\theta}. \quad (\text{F.5})$$

For light quarks, (F.5) ensures the absence of dead-cone suppression at $\theta = 0$ and π for vanishing virtuality.

In Figure 25, the suppression of the energy loss, F for heavy quarks is displayed. The variation of $F_{RH0} = F(E = 1.5 \text{ GeV}, \theta)/F(E = 1.5 \text{ GeV}, \theta = 0)$ with θ is depicted in Figure 26(a). It is interesting to note that for vanishingly small virtuality the suppression is similar to that of a conventional dead cone that appears for massive on-shell quarks (Figure 24). In Figure 25(b), the variation of $F_{RHE} = F(E, \theta = \pi/4)/F(E = 100 \text{ GeV}, \theta = \pi/4)$ with E is displayed for heavy

quarks. For large virtuality (which increases with parton energy, E), the suppression is large.

Figure 26 illustrates the suppression of the energy loss for light quarks. In Figure 26(a), the variation of $F_{RL\theta} = F(E = 3 \text{ GeV}, \theta)/F(E = 3 \text{ GeV}, \theta = 0)$ with θ is shown for light partons. It is important to note that the variation of $F_{RL\theta}$ with θ for light quark with low virtuality is drastically different from the corresponding quantity, $F_{RH\theta}$, for heavy quark. This is obvious because for low virtuality the light partons are not subjected to any dead-cone suppression at $\theta = 0$ and π unlike heavy quarks. Moreover, the $\sin^{-2}\theta$ behaviour for light quarks (F.5) ensures a minimum at $\theta = \pi/2$ as opposed to a maximum at the same θ for heavy quarks. In Figure 26(b), the variation of $F_{RLE} = F(E, \theta = \pi/4)/F(E = 100 \text{ GeV}, \theta = \pi/4)$ with E is depicted. We note that the suppression is large for high E and the behaviour of F_{RLE} is similar to F_{RHE} which indicates that the suppression due to virtuality overwhelm the effects due to the conventional dead-cone.

The energy loss ($\Delta E(L)$) of quarks as a function of path length (L) traversed by the off-shell parton in vacuum can be evaluated (see [115] for details) by using the emitted gluon spectrum given by (E.1). The results are displayed in Figure 27. We note that the energy loss of light and heavy quarks differ significantly at large path length or time when the propagating quarks acquire enough field to radiate. However, at small path length, the value of ΔE for light and heavy quarks is similar.

When we want to talk about radiative energy loss of high energy partons, we mean that the absorption of radiation given off is absorbed in the medium. So, we must take into account the interaction of emitted radiation with the medium. Consequently, the dispersion relation of the emitted gluon should change. This change in gluon dispersion relation is encoded in the thermal quark self-energy, and as the inverse of imaginary part of self energy gives radiation production rate, the formation time of radiation is also modified. This effect of modified dispersion relation of emitted gluon (or photon) is called Ter-Mikaelian (TM) effect [69]. The QCD analogue of TM effect is discussed in [116, 117]. The authors of [56] implement TM effect by replacing $x^2 m^2$ by $x^2 m^2 + (1-x)m_D^2$, where m_D is thermal mass of gluon. However, the authors of [116] repeats the single, double, and multiple scattering calculations of [49] by assuming a modified dispersion relation, $k^2 = \omega_0^2(T)$, of emitted gluon. ω_0 parametrizes gluon self-energy in medium. The authors of [116] show that in the phase space region where abelian radiation does not occur, the gluon radiation is suppressed due to polarization properties of the medium. The authors of [117, 118] extend the results of [116] using 1-Loop HTL self-energy of gluons. The authors of [118] show a $\sim 30\%$ decrease in the 1st order in opacity fractional energy loss for heavy quarks of 10 GeV energy when TM effect is taken into account, whereas the authors of [56] show ~ 1.5 times increase in radiative energy spectra per unit length when gluon thermal mass is taken into consideration. Such changes indicate that one can barely neglect the effect of gluon interaction with medium while probing QGP.

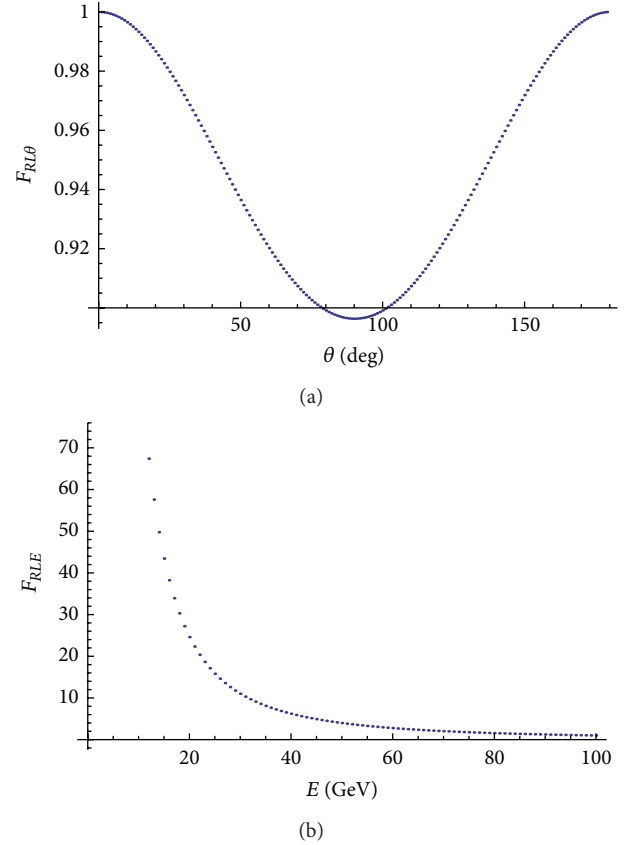


FIGURE 26: The variation of (a) $F_{RL\theta}(E, \theta)$, defined in the text with θ for $E = 3 \text{ GeV}$, (b) with E for $\theta = \pi/4$ for virtual light partons (colour online). The results displayed in this figure are evaluated for vanishing quark mass, $\beta = 0.95$, and emitted gluon energy, $k_0 = 10 \text{ MeV}$. The quark virtuality is defined as $V^2 = E^2(1 - \beta^2)$.

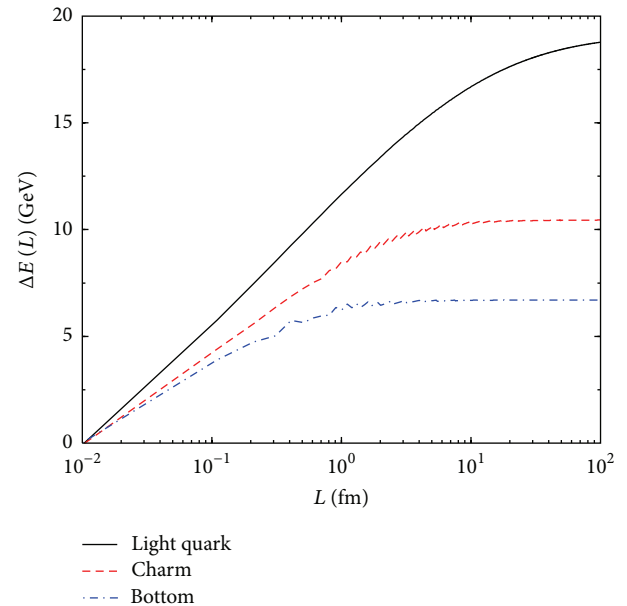


FIGURE 27: Variation of energy loss, ΔE as a function of path traversed, L in vacuum. The energy of the quark is taken as $E = 20 \text{ GeV}$.

So far, we have talked about the energy loss of HQs in an infinite medium. But, how does the energy loss depend on the size of medium? The authors show that length dependent energy loss $\Delta E(L)$ is $\propto L^2$, when we are considering the coherent region; that is, the emitted gluon energy is soft and is within the factorization and the Bethe-Heitler limits (see [119]). When gluon energy (k_0) is of the order of that of parent parton (E), the energy loss per unit length becomes independent of length of medium. This is the limit ($k_0 \sim E$) when evaluation of transport coefficients without addressing to size of medium works more efficiently.

There is also a path integral approach of radiative energy loss proposed in [120, 121]. Path integral approach is shown to be equivalent to the approach of [51, 52] in [119]. An alternate formalism (GLV) proposed in [53, 122] performs a systematic expansion in opacity (the mean number of jet scatterings). Opacity is quantitatively given by $\bar{n} = L/\lambda$, where L is the target thickness and λ is the mean free path. One analytic limit applies to plasmas where mean number of scattering is small [50]. The other limit applies to thick plasma where $\bar{n} \gg 1$ [51, 52].

Acknowledgments

Surasree Mazumder and Trambak Bhattacharyya are supported by DAE, Government of India. Santosh K. Das acknowledges the support by the ERC StG under the QGP-Dyn Grant no. 259684. The authors thank Jan-e Alam and Md. Younus for fruitful discussions and critical reading of the paper. The authors also take the opportunity to thank the anonymous reviewers for their relevant suggestions which have undoubtedly helped to increase the quality of paper.

References

- [1] D. J. Gross and F. Wilczek, "Ultraviolet behavior of non-Abelian gauge theories," *Physical Review Letters*, vol. 30, p. 1343, 1973.
- [2] D. J. Gross and F. Wilczek, "Asymptotically free gauge theories. I," *Physical Review D*, vol. 8, no. 10, pp. 3633–3652, 1973.
- [3] H. D. Politzer, "Reliable perturbative results for strong interactions?" *Physical Review Letters*, vol. 30, p. 1346, 1973.
- [4] J. C. Collins and M. J. Perry, "Superdense matter: neutrons or asymptotically free quarks?" *Physical Review Letters*, vol. 34, p. 1353, 1975.
- [5] N. Cabibbo and G. Parisi, "Exponential hadronic spectrum and quark liberation," *Physics Letters B*, vol. 59, p. 67, 1975.
- [6] F. Karsch, "Lattice QCD at high temperature and density," *Lecture Notes in Physics*, vol. 583, pp. 209–249, 2002.
- [7] F. Karsch, "Lattice results on QCD thermodynamics," *Nuclear Physics A*, vol. 698, pp. 199–208, 2002.
- [8] S. Borsányi, G. Endrődi, Z. Fodor et al., "The QCD equation of state with dynamical quarks," *Journal of High Energy Physics*, vol. 11, p. 077, 2010.
- [9] Y. Aoki, G. Endrődi, Z. Fodor, S. D. Katz, and K. K. Szabó, "The order of the quantum chromodynamics transition predicted by the standard model of particle physics," *Nature*, vol. 443, no. 7112, pp. 675–678, 2006.
- [10] S. Borsányi, G. Endrődi, Z. Fodor et al., "Transition temperature and the equation of state from lattice QCD, Wuppertal-Budapest results," *Journal of Physics G*, vol. 38, no. 12, Article ID 124101, 2011.
- [11] P. Kovtun, D. T. Son, and O. A. Starinets, "Viscosity in strongly interacting quantum field theories from black hole physics," *Physical Review Letters*, vol. 94, Article ID 111601, 2005.
- [12] A. Adams, L. D. Carr, T. Schaefer, P. Steinberg, and J. E. Thomas, "Strongly correlated quantum fluids: ultracold quantum gases, quantum chromodynamic plasmas, and holographic duality," *New Journal of Physics*, vol. 14, Article ID 115009, 2012.
- [13] S. S. Adler, S. Afanasiev, C. Aidala et al., "Nuclear modification of electron spectra and implications for heavy quark energy loss in Au + Au collisions at $\sqrt{s_{NN}} = 200$ GeV," *Physical Review Letters*, vol. 96, Article ID 032301, 2006.
- [14] B. I. Abelev, M. M. Aggarwal, Z. Ahammed et al., "Transverse momentum and centrality dependence of high- p_T nonphotonic electron suppression in Au + Au collisions at $\sqrt{s_{NN}} = 200$ GeV," *Physical Review Letters*, vol. 98, Article ID 192301, 2007.
- [15] B. Abelev, J. Adam, D. Adamova et al., "Production of muons from heavy flavour decays at forward rapidity in pp and Pb-Pb collisions at $\sqrt{s_{NN}} = 2.76$ TeV," *Physical Review Letters*, vol. 109, Article ID 112301, 2012.
- [16] A. Rossi, "D meson nuclear modification factors in Pb-Pb collisions at $\sqrt{s_{NN}} = 2.76$ TeV, measured with the ALICE detector," in *Proceedings of Quark Matter Conference*, Annecy, France, May 2011.
- [17] A. Adare, S. Afanasiev, C. Aidala et al., "Energy loss and flow of heavy quarks in Au + Au collisions at $\sqrt{s_{NN}} = 200$ GeV," *Physical Review Letters*, vol. 98, Article ID 172301, 2007.
- [18] G. D. Moore and D. Teaney, "How much do heavy quarks thermalize in a heavy ion collision?" *Physical Review C*, vol. 71, Article ID 064904, 2005.
- [19] C. M. Ko and W. Liu, "Suppression of heavy quarks in heavy-ion collisions," *Nuclear Physics A*, vol. 783, pp. 233–240, 2007.
- [20] A. Adil and I. Vitev, "Collisional dissociation of heavy mesons in dense QCD matter," *Physics Letters B*, vol. 649, p. 139, 2007.
- [21] N. Armesto, M. Cacciari, A. Dainese, C. A. Salgado, and U. A. Wiedemann, "How sensitive are high- p_T electron spectra at RHIC to heavy quark energy loss?" *Physics Letters B*, vol. 637, p. 362, 2006.
- [22] P. B. Gossiaux and J. Aichelin, "Toward an understanding of the single electron data measured at the BNL Relativistic Heavy Ion Collider (RHIC)," *Physical Review C*, vol. 78, Article ID 014904, 2008.
- [23] S. K. Das, J. Alam, and P. Mohanty, "Probing quark gluon plasma properties by heavy flavors," *Physical Review C*, vol. 80, Article ID 054916, 8 pages, 2009.
- [24] S. K. Das, J. Alam, and P. Mohanty, "Drag of heavy quarks in quark gluon plasma at energies available at the CERN Large Hadron Collider (LHC)," *Physical Review C*, vol. 82, Article ID 014908, 2010.
- [25] S. K. Das, J. Alam, P. Mohanty, and B. Sinha, "Nuclear suppression at low energy in relativistic heavy ion collisions," *Physical Review C*, vol. 81, Article ID 044912, 2010.
- [26] J. Uphoff, O. Fochler, Z. Xu, and C. Greiner, "Elliptic flow and energy loss of heavy quarks in ultrarelativistic heavy ion collisions," *Physical Review C*, vol. 84, Article ID 024908, 2011.
- [27] W. M. Alberico, A. Beraudo, A. De Pace et al., "Heavy-flavour spectra in high-energy nucleus-nucleus collisions," *The European Physical Journal C*, vol. 71, p. 1666, 2011.
- [28] S. Mazumder, T. Bhattacharyya, J. Alam, and S. K. Das, "Momentum dependence of drag coefficients and heavy flavor

- suppression in quark gluon plasma,” *Physical Review C*, vol. 84, Article ID 044901, 2011.
- [29] M. Younus and D. K. Srivastava, “Empirical determination of charm quark energy loss and its consequences for azimuthal anisotropy,” *Journal of Physics G*, vol. 39, Article ID 095003, 2012.
- [30] M. G. Mustafa, D. Pal, D. K. Srivastava, and M. H. Thoma, “Radiative energy-loss of heavy quarks in a quark-gluon plasma,” *Physics Letters B*, vol. 428, p. 234, 1998.
- [31] C. Young, B. Schenke, S. Jeon, and C. Gale, “MARTINI event generator for heavy quarks: Initialization, parton evolution, and hadronization,” *Physical Review C*, vol. 86, Article ID 034905, 7 pages, 2012.
- [32] S. Cao, G. Qin, and S. Bass, “A systematic study of heavy quark energy loss in a hot and dense QCD medium,” <http://arxiv.org/abs/1205.2396>.
- [33] T. Lang, H. Hees, J. Steinheimer, and M. Bleicher, “Charm quark transport in Pb+Pb reactions at $\sqrt{s_{NN}} = 2.76$ TeV from a (3 + 1) dimensional hybrid approach,” <http://arxiv.org/abs/1208.1643>.
- [34] S. K. Das, V. Chandra, and J. Alam, “Heavy-quark transport coefficients in a hot viscous quark-gluon plasma medium,” <http://arxiv.org/abs/1210.3905>.
- [35] S. Chakravorty and D. Syam, “Pre-thermalization quark momentum distribution in the quark-gluon plasma,” *Lettere Al Nuovo Cimento Series 2*, vol. 41, no. 11, p. 381, 1984.
- [36] J. Alam, B. Sinha, and S. Raha, “Successive equilibration in quark-gluon plasma,” *Physical Review Letters*, vol. 73, p. 1895, 1994.
- [37] B. Svetitsky, “Diffusion of charmed quarks in the quark-gluon plasma,” *Physical Review D*, vol. 37, no. 9, pp. 2484–2491, 1988.
- [38] H. M. Antia, *Numerical Methods for Scientists and Engineers*, Tata McGraw-Hill, 1991.
- [39] M. L. Mangano, P. Nason, and G. Ridolfi, “Heavy-quark correlations in hadron collisions at next-to-leading order,” *Nuclear Physics B*, vol. 373, no. 2, pp. 295–345, 1992.
- [40] H. van Hees and R. Rapp, “Thermalization of heavy quarks in the quark-gluon plasma,” *Physical Review C*, vol. 71, Article ID 034907, 2005.
- [41] B. L. Combridge, “Associated production of heavy flavour states in pp and $\bar{p}p$ interactions: some QCD estimates,” *Nuclear Physics B*, vol. 151, p. 429, 1979.
- [42] M. G. Mustafa, D. Pal, and D. K. Srivastava, “Propagation of charm quarks in equilibrating quark-gluon plasma,” *Physical Review C*, vol. 57, p. 889, 1998.
- [43] H. Van Hees, M. Mannarelli, V. Greco, and R. Rapp, “T-matrix approach to heavy quark diffusion in the QGP,” *European Physical Journal C*, vol. 61, no. 4, pp. 799–806, 2009.
- [44] P. B. Gossiaux, J. Aichelin, and T. Gousset, “Theory of heavy quark energy loss,” *Progress of Theoretical Physics Supplements*, vol. 193, p. 110, 2012.
- [45] M. He, R. J. Fries, and R. Rapp, “Heavy-quark diffusion and hadronization in quark-gluon plasma,” *Physical Review C*, vol. 86, Article ID 014903, 15 pages, 2012.
- [46] W. R. Leo, *Techniques for Nuclear and Particle Physics Experiments*, Springer, Berlin, Germany, 1987.
- [47] E. Braaten and M. H. Thoma, “Energy loss of a heavy quark in the quark-gluon plasma,” *Physical Review D*, vol. 44, p. R2625, 1991.
- [48] M. Gyulassy, M. Plumer, M. H. Thoma, and X. N. Wang, “High p_T probes of nuclear collisions,” *Nuclear Physics A*, vol. 538, p. 37c, 1992.
- [49] X. N. Wang, M. Gyulassy, and M. Plümer, “Landau-Pomeranchuk-Migdal effect in QCD and radiative energy loss in a quark-gluon plasma,” *Physical Review D*, vol. 51, p. 3436, 1995.
- [50] M. Gyulassy and X.-N. Wang, “Multiple collisions and induced gluon bremsstrahlung in QCD,” *Nuclear Physics B*, vol. 420, no. 3, pp. 583–614, 1994.
- [51] R. Baier, Yu. L. Dokshitzer, S. Peigné, and D. Schiff, “Induced gluon radiation in a QCD medium,” *Physics Letters B*, vol. 345, p. 277, 1995.
- [52] R. Baier, Yu. L. Dokshitzer, A. H. Mueller, S. Peigné, and D. Schiff, “Radiative energy loss of high energy quarks and gluons in a finite-volume quark-gluon plasma,” *Nuclear Physics B*, vol. 483, pp. 291–320, 1997.
- [53] M. Gyulassy, P. Levai, and I. Vitev, “Non-abelian energy loss at finite opacity,” *Physical Review Letters*, vol. 85, no. 26, pp. 5535–5538, 2000.
- [54] L. D. Landau and I. Ya. Pomeranchuk, “Electron-avalanche process at high energies,” *Doklady Akademii Nauk SSSR*, vol. 92, p. 535, 1953.
- [55] A. B. Migdal, “Bremsstrahlung and pair production in condensed media at high energies,” *Physical Review*, vol. 103, p. 1811, 1956.
- [56] P. B. Gossiaux, J. Aichelin, T. Gousset, and V. Guiho, “Competition of heavy quark radiative and collisional energy loss in deconfined matter,” *Journal of Physics G: Nuclear and Particle Physics*, vol. 37, no. 9, Article ID 094019, 2010.
- [57] Y. S. Kim and M. Noz, “Dirac’s light-cone coordinate system,” *American Journal of Physics*, vol. 50, no. 8, pp. 721–724, 1982.
- [58] L. McLerran, “Three lectures on the physics of small x and high gluon density,” in *Proceedings of the 8th Mexican School on Particles and Fields*, vol. 490 of *AIP Conference Proceedings*, pp. 42–79, 1998.
- [59] R. Thomas, *Energy loss of quarks by gluon radiation in deconfined matter [Ph.D. thesis]*, Institut für Theoretische Physik, 2003.
- [60] J. F. Gunion and G. Bertsch, “Hadronization by color bremsstrahlung,” *Physical Review D*, vol. 25, no. 3, pp. 746–753, 1982.
- [61] S. K. Das and J. Alam, “Soft gluon multiplicity distribution revisited,” *Physical Review D*, vol. 82, Article ID 051502(R), 2010.
- [62] R. Abir, C. Greiner, M. Martinez, and M. G. Mustafa, “Generalization of Gunion-Bertsch formula for soft gluon emission,” *Physical Review D*, vol. 83, Article ID 011501, 2011.
- [63] T. Bhattacharyya, S. Mazumder, S. K. Das, and J. Alam, “Examination of the Gunion-Bertsch formula for soft gluon radiation,” *Physical Review D*, vol. 85, Article ID 034033, 2012.
- [64] F. A. Berends, R. Kleiss, P. De Causmaecker, R. Gastmans, and T. T. Wu, “Single bremsstrahlung processes in gauge theories,” *Physics Letters B*, vol. 103, p. 124, 1981.
- [65] S. M. H. Wong, “Thermal and chemical equilibration in a gluon plasma,” *Nuclear Physics A*, vol. 607, p. 442, 1996.
- [66] M. Le Bellac, *Thermal Field Theory*, Cambridge Monographs on Mathematical Physics, Cambridge University Press, Cambridge, UK, 1996.
- [67] J. I. Kapusta and C. Gale, *Finite-Temperature Field Theory*, Cambridge Monographs on Mathematical Physics, Cambridge University Press, Cambridge, UK, 2nd edition, 2006.
- [68] O. Kaczmarek and F. Zantow, “Static quark-antiquark interactions in zero and finite temperature QCD: I. Heavy quark free energies, running coupling, and quarkonium binding,” *Physical Review D*, vol. 71, Article ID 114510, 2005.

- [69] S. Klein, "Suppression of bremsstrahlung and pair production due to environmental factors," *Reviews of Modern Physics*, vol. 71, p. 1501, 1999.
- [70] M. H. Thoma, "Parton interaction rates in the quark-gluon plasma," *Physical Review D*, vol. 49, p. 451, 1994.
- [71] Y. L. Dokshitzer and D. E. Kharzeev, "Heavy-quark colorimetry of QCD matter," *Physics Letters, Section B: Nuclear, Elementary Particle and High-Energy Physics*, vol. 519, no. 3-4, pp. 199–206, 2001.
- [72] J. D. Jackson, *Classical Electrodynamics*, John Wiley & Sons, New York, NY, USA, 1998.
- [73] K. M. Paul, *From Higgs to top to color [Ph.D. thesis]*, University of Illinois at Urbana-Champaign, 2002.
- [74] J. D. Bjorken, "Highly relativistic nucleus-nucleus collisions: the central rapidity region," *Physical Review D*, vol. 27, p. 140, 1983.
- [75] S. Turbide, C. Gale, S. Jeon, and G. D. Moore, "Energy loss of leading hadrons and direct photon production in evolving quark-gluon plasma," *Physical Review C*, vol. 72, Article ID 014906, 2005.
- [76] C. Peterson, D. Schlatter, I. Schmitt, and P. M. Zerwas, "Scaling violations in inclusive e^+e^- annihilation spectra," *Physical Review D*, vol. 27, p. 105, 1983.
- [77] R. J. Fries, V. Greco, and P. Sorensen, "Coalescence models for hadron formation from quark-gluon plasma," *Annual Review of Nuclear and Particle Science*, vol. 58, p. 177, 2008.
- [78] V. Greco, H. van Hees, and R. Rapp, "Heavy quark dynamics in the QGP," in *International Workshop on Early Physics with Heavy-Ion Collisions at the LHC*, vol. 1422 of *AIP Conference Proceedings*, pp. 117–126, 2012.
- [79] R. C. Hwa and K. Kajantie, "Diagnosing quark matter by measuring the total entropy and the photon or dilepton emission rates," *Physical Review D*, vol. 32, p. 1109, 1985.
- [80] S. Mazumder and J. Alam, "Effects of equation of state on nuclear suppression and the initial entropy density of quark gluon plasma," *Physical Review C*, vol. 85, Article ID 044918, 2012.
- [81] T. Sakaguchi, "PHENIX plans for RHIC low energy run," in *Proceedings of the 5th International Workshop on Critical Point and Onset of Deconfinement (CPOD '09)*, Long Island, NY, USA, June 2009.
- [82] B. I. Abelev, "Identified particle production, azimuthal anisotropy, and interferometry measurements in Au + Au collisions at $\sqrt{s_{NN}} = 9.2$ GeV," *Physical Review C*, vol. 81, Article ID 024911, 2010.
- [83] J. M. Heuser, "The compressed baryonic matter experiment at FAIR: physics of strangeness and charm, status of preparations," *Journal of Physics G*, vol. 35, Article ID 044049, 2008.
- [84] O. Ristea, "Study of the chemical freeze-out in nucleus-nucleus collisions," *Romanian Reports in Physics*, vol. 56, pp. 659–666, 2004.
- [85] A. Andronic, P. Braun-Munzinger, and J. Stachel, "Hadron production in central nucleus-nucleus collisions at chemical freeze-out," *Nuclear Physics A*, vol. 772, no. 3-4, pp. 167–199, 2006.
- [86] D. Kharzeev and M. Nardi, "Hadron production in nuclear collisions at RHIC and high-density QCD," *Physics Letters B*, vol. 507, p. 121, 2001.
- [87] R. J. Glauber, "High-energy collision theory," in *Lectures in Theoretical Physics, Vol. I. Lectures Delivered at the Summer Institute for Theoretical Physics, University of Colorado, Boulder, 1958*, W. E. Brittin and L. G. Dunham, Eds., pp. 315–414, Interscience Publishers, New York, NY, USA, 1959.
- [88] B. B. Back, M. D. Baker, M. Ballintijn et al., "Collision geometry scaling of Au + Au pseudorapidity density from $\sqrt{s_{NN}} = 19.6$ to 200 GeV," *Physical Review C*, vol. 70, Article ID 021902, 2004.
- [89] R. D. Field, *Application of Perturbative QCD*, Addison-Wesley, New York, NY, USA, 1989.
- [90] T. Hirano, N. van der Kolk, and A. Bilandzic, "Hydrodynamics and flow," *Lecture Notes in Physics*, vol. 785, pp. 139–178, 2010.
- [91] P. Huovinen and P. V. Ruuskanen, "Hydrodynamic models for heavy ion collisions," *Annual Review of Nuclear and Particle Science*, vol. 56, p. 163, 2006.
- [92] D. A. Teaney, "Viscous hydrodynamics and the quark gluon plasma," <http://arxiv.org/abs/0905.2433>.
- [93] H. van Hees, V. Greco, and R. Rapp, "Heavy-quark probes of the quark-gluon plasma and interpretation of recent data taken at the BNL Relativistic Heavy Ion Collider," *Physical Review C*, vol. 73, Article ID 034913, 2006.
- [94] H. van Hees, M. Mannarelli, V. Greco, and R. Rapp, "Nonperturbative heavy-quark diffusion in the quark-gluon plasma," *Physical Review Letters*, vol. 100, no. 19, Article ID 192301, 2008.
- [95] Y. Akamatsu, T. Hatsuda, and T. Hirano, "Heavy quark diffusion with relativistic Langevin dynamics in the quark-gluon fluid," *Physical Review C*, vol. 79, Article ID 054907, 2009.
- [96] S. K. Das and J. Alam, "Elliptic flow of heavy flavors," <http://arxiv.org/abs/1008.2643>.
- [97] S. K. Das and A. Davody, "A non-conformal holographic model for D-meson suppression at LHC energy," <http://arxiv.org/abs/1211.2925>.
- [98] S. S. Gubser, "Drag force in AdS/CFT," *Physical Review D*, vol. 74, no. 12, Article ID 126005, 4 pages, 2006.
- [99] G. C. Giecold, "Heavy quark in an expanding plasma in AdS/CFT," *Journal of High Energy Physics*, vol. 06, p. 002, 2009.
- [100] M. G. Mustafa, "Energy loss of charm quarks in the quark-gluon plasma: Collisional vs radiative losses," *Physical Review C*, vol. 72, Article ID 014905, 2005.
- [101] M. Laine, "Heavy flavour kinetic equilibration in the confined phase," *Journal of High Energy Physics*, vol. 04, p. 124, 2011.
- [102] M. He, R. J. Fries, and R. Rapp, "Thermal relaxation of charm in hadronic matter," *Physics Letters B*, vol. 701, p. 445, 2002.
- [103] S. Ghosh, S. K. Das, S. Sarkar, and J. Alam, "Drag coefficient of D mesons in hot hadronic matter," *Physical Review D*, vol. 84, Article ID 011503, 2011.
- [104] L. M. Abreu, D. Cabrera, F. J. Llanes-Estrada, and J. M. Torres-Rincon, "Charm diffusion in a pion gas implementing unitarity, chiral and heavy quark symmetries," *Annals of Physics*, vol. 326, no. 10, pp. 2737–2772, 2011.
- [105] L. Abreu, D. Cabrera, and J. M. Torres-Rincon, "Transport properties of bottomed mesons in a hot mesonic gas," *Physical Review D*, vol. 87, Article ID 034019, 2013.
- [106] S. K. Das, S. Ghosh, S. Sarkar, and J. Alam, "Drag and diffusion coefficients of B mesons in hot hadronic matter," *Physical Review D*, vol. 85, Article ID 074017, 2012.
- [107] D. Cabrera, L. M. Abreu, F. J. Llanes-Estrada, and J. M. Torres-Rincon, "Heavy flavor relaxation in a hadronic medium," *Nuclear Physics A*, 2013.
- [108] S. K. Das, S. Ghosh, S. Sarkar, and J. Alam, "Heavy flavor suppression: role of hadronic matter," <http://arxiv.org/abs/1303.2476>.
- [109] H. Heiselberg and X.-N. Wang, "Thermal equilibration in an expanding parton plasma," *Nuclear Physics B*, vol. 462, no. 2-3, pp. 389–411, 1996.

- [110] O. Fochler, J. Uphoff, Z. Xu, and C. Greiner, “Radiative parton processes in perturbative QCD—an improved version of the Gunion and Bertsch cross section from comparisons to the exact result,” <http://arxiv.org/abs/1302.5250>.
- [111] R. Abir, “Jet-parton inelastic interaction beyond eikonal approximation,” *Physical Review D*, vol. 87, Article ID 034036, 2013.
- [112] R. Abir, C. Greiner, M. Martinez, M. G. Mustafa, and J. Uphoff, “Soft gluon emission off a heavy quark revisited,” *Physical Review D*, vol. 85, no. 5, Article ID 054012, 2012.
- [113] R. Abir, U. Jamil, M. G. Mustafa, and D. K. Srivastava, “Heavy quark energy loss and D -mesons in RHIC and LHC energies,” *Physics Letters B*, vol. 715, p. 183, 2012.
- [114] T. Bhattacharyya and J. Alam, “Dead cone due to parton virtuality,” *International Journal of Modern Physics A*, vol. 28, Article ID 1350031, 2013.
- [115] B. Z. Kopeliovich, I. K. Potashnikova, and I. Schmidt, “Why heavy and light quarks radiate energy with similar rates,” *Physical Review C*, vol. 82, Article ID 037901, 2010.
- [116] B. Kampfer and O. Pavlenko, “The Ter-Mikaelian and Landau-Pomeranchuk effects for induced soft gluon radiation in a QCD medium,” *Physics Letters B*, vol. 477, p. 171, 2000.
- [117] M. Djordjevic and M. Gyulassy, “Where is the charm quark energy loss at RHIC?” *Physics Letters B*, vol. 560, pp. 37–43, 2003.
- [118] M. Djordjevic, “Ter-Mikaelian effect on QCD radiative energy loss,” *Physical Review C*, vol. 68, Article ID 034914, 2003.
- [119] R. Baier, D. Schiff, and B. G. Zakharov, “Energy loss in perturbative QCD,” *Annual Review of Nuclear and Particle Science*, vol. 50, p. 37, 2000.
- [120] B. G. Zakharov, “Fully quantum treatment of the Landau-Pomeranchuk-Migdal effect in QED and QCD,” *Journal of Experimental and Theoretical Physics Letters*, vol. 63, pp. 952–957, 1996.
- [121] B. G. Zakharov, “Landau-Pomeranchuk-Migdal effect for finite-size targets,” *Journal of Experimental and Theoretical Physics Letters*, vol. 64, p. 781, 1996.
- [122] M. Gyulassy, P. Levai, and I. Vitev, “Reaction operator approach to non-abelian energy loss,” *Nuclear Physics B*, vol. 594, no. 1-2, pp. 371–419, 2001.

Research Article

Calibrating the In-Medium Behavior of Quarkonia

Helmut Satz

Fakultät für Physik, Universität Bielefeld, D-33501 Bielefeld, Germany

Correspondence should be addressed to Helmut Satz; satz@physik.uni-bielefeld.de

Received 20 March 2013; Accepted 3 April 2013

Academic Editor: Jan E. Alam

Copyright © 2013 Helmut Satz. This is an open access article distributed under the Creative Commons Attribution License, which permits unrestricted use, distribution, and reproduction in any medium, provided the original work is properly cited.

Quarkonium production has been considered as a tool to study the medium formed in high-energy nuclear collisions, assuming that the formation of a hot and dense environment modifies the production pattern observed in elementary collisions. The basic features measured there are the relative fractions of hidden to open heavy flavor and the relative fractions of the different hidden heavy flavor states. Hence the essential question is if and how these quantities are modified in nuclear collisions. We show how the relevant data must be calibrated; that is, what reference has to be used, in order to determine this in a model-independent way.

The original suggestion for charmonium production as a means to test the formation of a deconfined medium in high-energy nuclear collisions was based on the idea that color screening in such a medium would prevent the binding of charm quarks to a color neutral J/ψ [1]. The J/ψ production process in elementary hadronic collisions (taking pp as an example) begins with the formation of a $c\bar{c}$ pair; this pair can then either lead to open charm production (about 90%) or subsequently bind to form a charmonium state (about 10% for all charmonia). A schematic illustration (Figure 1) shows the dominant high-energy reaction through gluon fusion.

The initial $c\bar{c}$ production can be calculated in terms of the parton distribution functions f_p of the relevant hadrons and the perturbative partonic cross-section. The full description of charmonium binding has so far resisted various theoretical attempts; on the other hand, the process is in good approximation independent of the incident hadronic collision energy [2, 3]. This is a consequence of the fact that the heavy quark propagator in the reaction $gg \rightarrow c\bar{c}$ strongly dampens the mass variation of the $c\bar{c}$ pair with incident energy. Thus the fractions of the produced $c\bar{c}$ system into hidden versus open charm as well as those for the different charmonium states are approximately constant; once determined at one energy, they remain the same also for different energies. As a result, the phenomenological color evaporation model [4–7] provides a good description of charmonium production through the form

$$\sigma_{hh \rightarrow J/\psi}(s) = g_{c\bar{c} \rightarrow J/\psi} \sigma_{hh \rightarrow c\bar{c}}(s), \quad (1)$$

and correspondingly for the other charmonium states. Here the constant $g_{c\bar{c} \rightarrow J/\psi}$ specifies what fraction of the total $c\bar{c}$ production cross-section goes into J/ψ production; in pp collisions, it is typically about 2%. The set of the different constants $g_{c\bar{c} \rightarrow i}$ for the different charmonium states i thus effectively characterizes charmonium production in the absence of a medium.

A further important aspect of quarkonium production in elementary collisions is that the observed (1S) ground states J/ψ and Υ are in both cases partially produced through feed-down from higher excited states [8–11]. Of the observed J/ψ rates, only some 60% is a directly produced $J/\psi(1S)$ state; about 30% comes from $\chi_c(1P)$ and 10% from $\psi'(2S)$ decay. Because of the narrow width of the excited states, their decay occurs well outside any interaction region.

The features we have here summarized for charm and charmonium production are readily extended to that of bottom and bottomonium. To simplify the discussion, we will continue referring to the charmonium case, keeping in mind that all arguments apply as well to bottomonia. Given the patterns observed in elementary collisions, we want to see how they are modified in the presence of a medium, as provided by nuclear collisions. From the point of view of production dynamics, one way such modifications can arise is as *initial state effects*, which take place before the $c\bar{c}$ pair is produced. The main possibilities considered so far are nuclear modifications of the parton distribution functions (shadowing or antishadowing) and a possible energy loss of

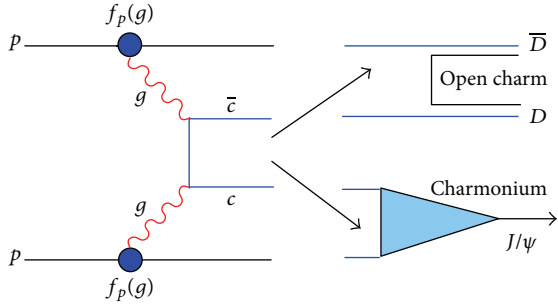


FIGURE 1: Schematic view of J/ψ production in pp collisions.

the partons passing through the nuclear medium to produce the $c\bar{c}$. Once produced, the pair can encounter *final state effects*, either in the form of a phase space shift already of the $c\bar{c}$, for example, through an energy loss of the unbound charm quarks, or through effects on the nascent or fully formed charmonium state. Such effects may arise from the passage through the cold nuclear medium or because of the presence of the medium newly produced in the nuclear collision. The latter is evidently what we have in mind when we want to use quarkonia to study quark-gluon plasma production. The difficulties encountered over the past years [12, 13] in arriving at a conclusive analysis of the relevant nuclear collision data on J/ψ production are largely due to the problem of parametrizing the different effects and then constructing a convincing model correctly incorporating all of them. We want to show here that today experimental means have become available which allow us to calibrate the measured results in a way which avoids these difficulties.

Before we turn to the problem of determining medium effects on quarkonium production, we recall the two main conceptual approaches on what may happen; the two can perhaps best be labelled *suppression* and *enhancement*. Color screening in a quark-gluon plasma will decrease the quarkonium binding, both in strength and in its spatial range, and this should for sufficiently energetic nucleus-nucleus collisions lead to quarkonium dissociation or melting. Since the larger and less tightly bound states will melt at lower temperature or energy density than the ground states, color screening will produce *sequential suppression* [14, 15]. We illustrate this for the J/ψ . After an initial threshold melting the ψ' and hence removing its feed-down component for J/ψ production, there will be a second threshold for χ_c melting and then finally a third, at which the direct $J/\psi(1S)$ is dissociated. The resulting pattern is illustrated in Figure 2. We have here introduced something denoted as J/ψ survival probability. Theoretically, this is the chance of a J/ψ to persist as a bound state in a deconfined medium. How to properly define this quantity as a useful observable in experimental studies is the subject of this paper.

The other alternative, J/ψ enhancement, assumes, in accord with color screening and the resulting suppression, that at sufficiently high energies there is an almost complete dissociation of the J/ψ 's produced in primary nucleon-nucleon interactions. On the other hand, at such collision energies, these interactions lead to abundant $c\bar{c}$ production;

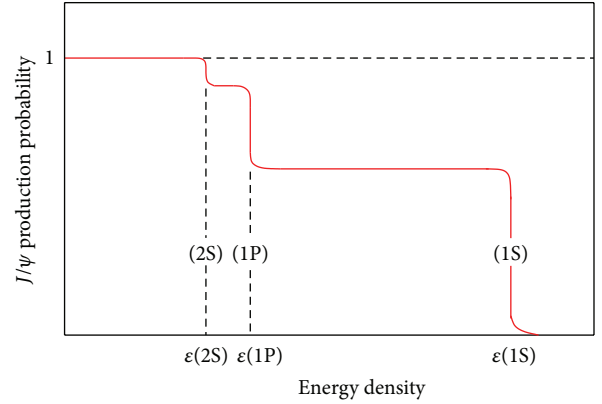


FIGURE 2: Schematic view of sequential J/ψ suppression in a deconfined medium.

the rate for this process grows faster than that for the production of light quarks, and if the $c\bar{c}$ pairs remain present in the evolution of the medium, the system will at the hadronisation point show an oversaturation of charm, compared to the predicted thermal abundance. If these charm quarks have become part of an equilibrated medium and as such undergo hadronisation in the form of statistical combination, then such secondary charmonium formation can convert more $c\bar{c}$ pairs into J/ψ 's than the dynamical primary production mechanism, thus leading to an effective J/ψ enhancement [16–19], as shown in Figure 3. We note that this scenario invokes a new and so far unknown binding dynamics to form charmonia; the outcome is assumed to be determined simply by the relative abundance of charm quarks [20].

We now come to our central question: how to calibrate the J/ψ survival? Since we are interested in using quarkonium production as a tool to study the medium produced in nuclear collisions, our primary concern is not if such collisions produce more or fewer $c\bar{c}$ pairs than proton-proton collisions, but rather if the presence of the medium modifies the fraction of produced $c\bar{c}$ pairs going into charmonium formation. In other words, the crucial quantity is the amount of charmonium production relative to that of open charm [21]. To illustrate, in pp collisions, about 2% of the total $c\bar{c}$ production goes into J/ψ 's. If in high-energy nuclear collisions the total $c\bar{c}$ production rate was reduced by a factor two, but we still have 2% of these going into J/ψ 's, then evidently AA collisions do not modify J/ψ binding. This is, of course, strictly true only for fully integrated rates, which is difficult to check; we return to the issue of phase space variations shortly. But we note here already that in the example just given the number of J/ψ 's produced in AA collisions would be half of that obtained by scaling the results from pp interactions. That is, however, not an indication of any J/ψ suppression; it is just the consequence of having fewer $c\bar{c}$ pairs to start with, the formation probability of charmonia has remained the same as in pp collisions, 2%. It is thus crucial to correctly calibrate the survival in nuclear collisions.

To achieve that, we recall in both sequential suppression and statistical enhancement state that the total number of $c\bar{c}$ pairs produced in nuclear collisions is distributed among

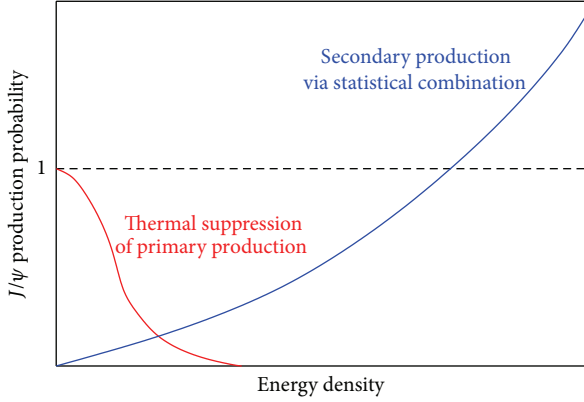


FIGURE 3: Schematic view of secondary production through statistical combination.

hidden and open charm differently than it is in proton-proton collisions. The essential observable is thus the ratio of charmonium states to open charm in nuclear collisions, compared to that in pp interactions. Sequential suppression predicts it to decrease with centrality and eventually vanish, statistical enhancement has it increasing with centrality, in many studies beyond the pp value. Hence the relevant observable is the fraction of charmonia to open charm, or more generally, that of quarkonia to the relevant open heavy flavor production [21, 22]. In this quantity, if measured over the entire phase space, the effects of possible initial state nuclear modifications—shadowing/antishadowing, parton energy loss—cancel out, so that whatever changes it shows relative to the pp pattern are due to final state effects.

It should be noted here that in actual applications, it will most likely not be necessary (nor generally possible) to measure the total open charm production rate. The relative abundances of the different open charm states produced in high energy collisions are so far found to be in good agreement with the predictions of the statistical hadronisation model [23, 24], with a universal hadronisation temperature of some 150–170 MeV. For open charm production, this model assumes an initial dynamical (perturbative) $c\bar{c}$ production; subsequently, at the hadronisation point, the charm quarks thus produced form open charm hadrons according to their statistical abundances. The relative production rates are thus totally determined in terms of the mass of the open charm state and the universal hadronisation temperature. Such a description is found to hold very well for open charm production in high-energy interactions from e^+e^- annihilation through pp and pA collisions; studies of the AA behavior are underway. However, the model does not work for charmonium production, neither in elementary (e^+e^- , pp) nor in nuclear interactions, since the binding mechanism forming charmonia is evidently of dynamical and not of statistical origin. In nuclear collisions, there are in addition medium effects on the binding.

As a consequence, we expect that the *relative abundances* of the different open charm states will not depend on the collision energy and remain essentially the same for elementary and nuclear collisions. Analogous to (1), the production

rate $N(hh \rightarrow D_i)$ for a specific open charm state D_i is then a constant fraction of the total open charm rate $N(hh \rightarrow c\bar{c})$:

$$N(hh \rightarrow D_i) \approx \bar{g}_{c\bar{c} \rightarrow D_i} N(hh \rightarrow c\bar{c}). \quad (2)$$

The crucial observable, the rate of $(J/\psi)/$ open charm, can thus in good approximation be taken as the rate of $(J/\psi)/D_i$ for a specific D -meson state. This will, of course, greatly facilitate the analysis.

The final state effect of interest to us is that caused by the newly produced medium. We, therefore, have to check to what extent the nascent or fully formed J/ψ is already dissociated by the cold nuclear matter of the target or the projectile. This can be done by studying the ratio hidden to open charm in high-energy pA collisions. It is in fact known that in such interactions there exist reductions of J/ψ production beyond the scaled pp results, but the origin of these is not unambiguously clarified. They could arise largely from initial state effects; but if there is a stronger suppression of ψ' than of J/ψ at energies for which the state is formed inside the nuclear medium, this would indicate that there the interaction depends on its physical size. The different fates of the different quarkonium states in *cold* nuclear matter are due to their different sizes, in a *hot* medium due to the different binding energies. And dissociation by color screening should start with a threshold, while the breakup in nuclear matter is presumably continuous. Measurements of charmonia relative to open charm in pA up to highest energies (RHIC, LHC) are, therefore, of great importance.

First applications of the in-medium charmonium study based on the relative survival of charmonia versus open charm were started last year, using LHC data from ALICE and CMS [25–28]. In Figure 4(a), we show mid-rapidity ALICE data for J/ψ production at intermediate transverse momenta, compared to open charm production in a similar kinematic region. In Figure 4(b), the comparison is extended to larger transverse momenta, using CMS data for J/ψ production. In both cases, J/ψ production relative to pp results, scaled by the number of collisions, decreases with increasing centrality, as seen by the corresponding R_{AA} values.

This decrease has at times been considered as suppressed J/ψ production. However, that is incorrect; the corresponding R_{AA} for open charm production, as determined through D measurements, shows within errors the same behavior. In other words, the reduction of the J/ψ is in complete agreement with that of open charm; there is neither suppression nor enhancement; the fraction of the produced $c\bar{c}$ pairs going into J/ψ production has remained the same in the AA collisions which are considered here as in the corresponding pp interactions:

$$R_{AA} \left(\frac{J}{\psi} \right) = \frac{N_{AA}(J/\psi)}{n_c N_{pp}(J/\psi)} = \frac{N_{AA}(c\bar{c})}{n_c N_{pp}(c\bar{c})} = R_{AA}(c\bar{c}) \quad (3)$$

with n_c denoting the scaling factor for the number of collisions at the corresponding centrality. We, therefore, have

$$\frac{N_{AA}(J/\psi)}{N_{AA}(c\bar{c})} = \frac{N_{pp}(J/\psi)}{N_{pp}(c\bar{c})} = g_{c\bar{c} \rightarrow J/\psi} \quad (4)$$

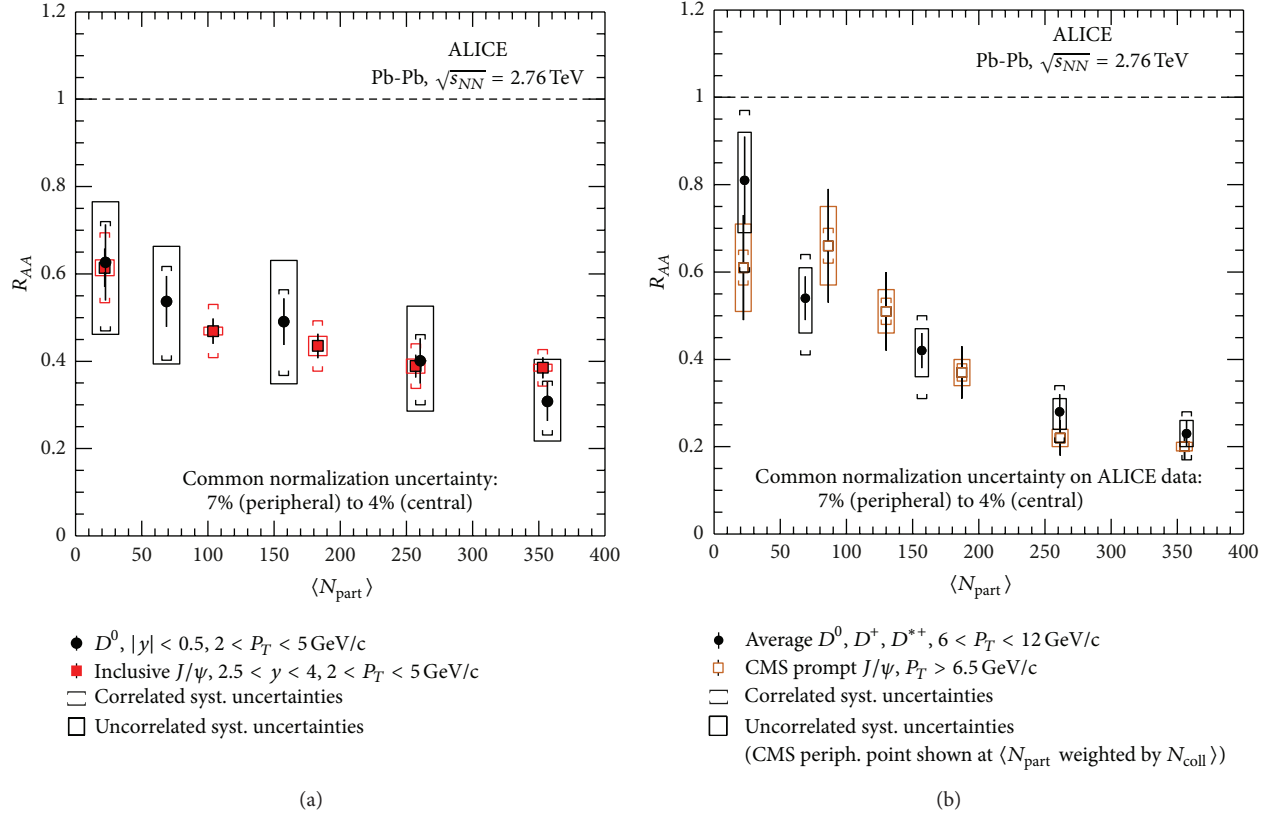


FIGURE 4: LHC data from ALICE and CMS [26–28], comparing J/ψ production to open charm production at intermediate (a) and high (b) transverse momenta.

at all centralities, in the kinematic regime indicated. If we divide the J/ψ rates by the open charm rates in the same kinematic region (large P_T), this ratio becomes centrality independent, and if we normalize it to the corresponding value from pp collisions, it becomes unity. The correct and model-independent J/ψ survival probability for experimental study is thus

$$S_{J/\psi} = \frac{(N_{AA}(J/\psi)/N_{AA}(c\bar{c}))}{(N_{pp}(J/\psi)/N_{pp}(c\bar{c}))} = \frac{1}{g_{c\bar{c} \rightarrow J/\psi}} \left(\frac{N_{AA}(J/\psi)}{N_{AA}(c\bar{c})} \right). \quad (5)$$

In the kinematic regime considered so far, it is indeed unity, there is neither suppression nor enhancement.

At the LHC, corresponding data for low P_T open charm production is not yet available. At RHIC, however, it is provided by the PHENIX and STAR collaborations [29–33], and the relevant comparisons of J/ψ versus open charm production are shown in Figure 5. At high P_T we have a similar behavior as at the LHC, no change of J/ψ production relative to open charm. At low P_T , however, the $R_{AA}(c\bar{c})$ of open charm is within errors unity over the whole centrality range; in contrast, $R_{AA}(J/\psi)$ decreases strongly and thus here gives the correct J/ψ survival probability. We see that now with increasing centrality, a smaller and smaller fraction of $c\bar{c}$ pairs go into J/ψ production, with a suppression of up

to 75% for the most central collisions. The J/ψ production finally surviving could conceivably be large due to corona interactions [34].

In this context it seems of interest to note that a decrease of the open charm production rates between central and forward rapidity is observed in both pA and AA collisions relative to pp collisions, at Fermilab (pA) and at RHIC (Cu-Cu). We note in particular in the Fermilab data based on 800 GeV pA collisions (see Figure 6) that at forward rapidity there is a suppression of open charm production, relative to scaled pp rates [35–38], while at midrapidity there is not. A similar effect is observed in Cu-Cu collisions with $\sqrt{s} = 200$ GeV at RHIC [39]. If this is passed on to charmonium production, one expects for RHIC and LHC data a smaller $R_{AA}(J/\psi)$ at forward than at mid-rapidity, simply because there are fewer $c\bar{c}$ pairs there to form charmonia, no matter how. Such an effect was indeed observed at RHIC and has often been considered a puzzle [40].

The aim of this work was to show how quarkonium production has to be calibrated in order to obtain experiment-based, model-independent information on suppression or enhancement due to the hot medium formed in nuclear collisions. The data cited are given for illustration, to make the point. In a more complete study, the transverse momentum range of J/ψ and open charm should be correlated more precisely. The crucial question now remains, of course, how

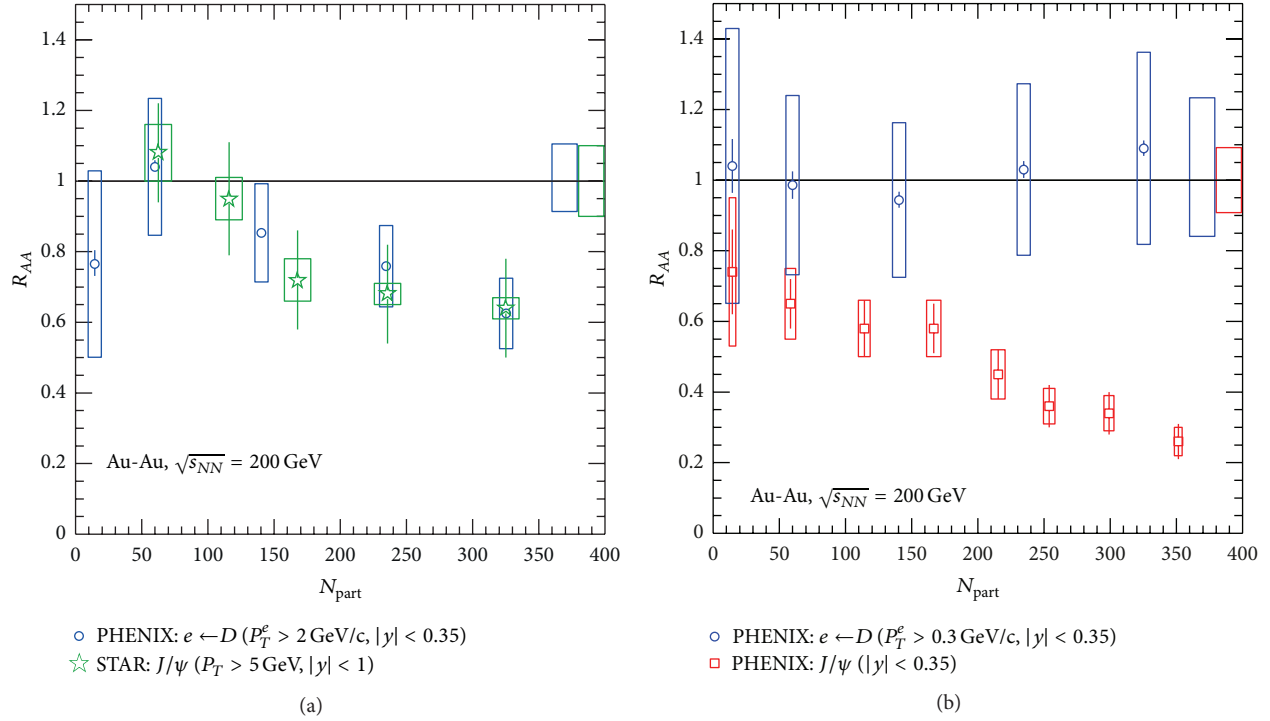


FIGURE 5: RHIC data from PHENIX and STAR [30–33], comparing J/ψ production to open charm production at high (a) and low (b) transverse momenta.

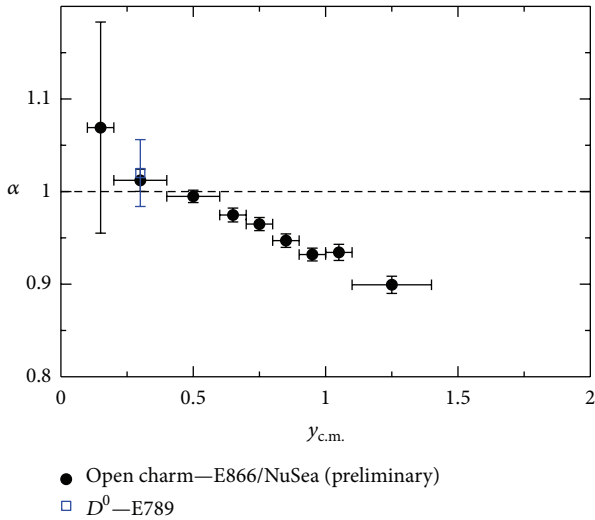


FIGURE 6: The rapidity dependence of open charm production in pA collisions at 800 GeV, parametrized in the form $\sigma_{pA} = A^\alpha \sigma_{pp}$ [35–38].

the open charm rates for low P_T production at the LHC will behave. That kinematic region is responsible for the bulk of $c\bar{c}$ production, and the issue to be decided is if nuclear collisions do or do not lead to an overall reduction. At RHIC, that is, not the case, as Figure 5(b) shows.

Acknowledgments

It is a pleasure for the author to thank Zaida Conesa del Valle, Torsten Dahms, Louis Kluberg, Mike Leitch, Carlos Lourenço, and Jürgen Schukraft for helpful discussions. Particular thanks go to Torsten Dahms also for pointing out the applicability of RHIC data for the analysis and for providing the author with the corresponding Figures.

References

- [1] T. Matsui and H. Satz, “ J/ψ suppression by quark-gluon plasma formation,” *Physics Letters B*, vol. 178, no. 4, pp. 416–422, 1986.
- [2] R. Gavai, D. Kharzeev, H. Satz et al., “Quarkonium production in hadronic collisions,” *International Journal of Modern Physics A*, vol. 10, pp. 3043–3070, 1995.
- [3] R. Vogt, “Quarkonium baseline predictions,” in *Hard Probes in Heavy-Ion Collisions at the LHC*, M. Mangano, H. Satz, and U. Wiedemann, Eds., CERN Yellow Report, 2004.
- [4] M. B. Einhorn and S. D. Ellis, “Hadronic production of the new resonances: probing gluon distributions,” *Physical Review D*, vol. 12, no. 7, pp. 2007–2014, 1975.
- [5] H. Fritzsch, “Producing heavy quark flavors in hadronic collisions: a test of quantum chromodynamics,” *Physics Letters B*, vol. 67, no. 2, pp. 217–221, 1977.
- [6] M. Glück, J. F. Owens, and E. Reya, “Gluon contribution to hadronic J/ψ production,” *Physical Review D*, vol. 17, pp. 2324–2331, 1978.

- [7] J. Babcock, D. Sivers, and S. Wolfram, “Quantum-chromodynamic estimates for heavy-particle production,” *Physical Review D*, vol. 18, no. 1, pp. 162–181, 1978.
- [8] L. Antoniazzi, M. Arenton, Z. Cao et al., “Production of J/ψ via ψ' and χ_c decay in 300 GeV/c proton- and π^\pm -nucleon interactions,” *Physical Review Letters*, vol. 70, no. 4, pp. 383–386, 1983.
- [9] P. Faccioli, C. Lourenço, J. Seixas, H. K. Wöhri et al., “Study of ψ' and χ_c decays as feed-down sources of J/ψ hadro-production,” *Journal of High Energy Physics*, vol. 2008, no. 10, pp. 1–15, 2008.
- [10] A. Adare, S. Afanasiev, C. Aidala et al., “Ground and excited state charmonium production in $p + p$ collisions at $\sqrt{s} = 200$ GeV,” *Physical Review D*, vol. 85, p. 092004, 2012.
- [11] N. Brambilla, M. Kramer, R. Mussa et al., “Heavy quarkonium physics,” CERN Yellow Report, Quarkonium Working Group, 2005.
- [12] H. Satz, “Colour deconfinement and quarkonium binding,” *Journal of Physics G*, vol. 32, no. 3, pp. R25–R69, 2006.
- [13] L. Kluberg and H. Satz, “Color deconfinement and charmonium production in nuclear Collisions,” in *Landolt-Börnstein Set 2010: Relativistic Heavy Ion Physics*, R. Stock, Ed., Springer, 2010.
- [14] F. Karsch and H. Satz, “The spectral analysis of strongly interacting matter,” *Zeitschrift für Physik C*, vol. 51, no. 2, pp. 209–224, 1991.
- [15] F. Karsch, D. Kharzeev, and H. Satz, “Sequential charmonium dissociation,” *Physics Letters B*, vol. 637, no. 1-2, pp. 75–80, 2006.
- [16] P. Braun-Munzinger and J. Stachel, “On charm production near the phase boundary,” *Nuclear Physics A*, vol. 690, no. 1–3, pp. 119–126, 2001.
- [17] R. L. Thews, M. Schroedter, and J. Rafelski, “Enhanced J/ψ production in deconfined quark matter,” *Physical Review C*, vol. 63, no. 5, p. 054905, 2001.
- [18] L. Grandchamp and R. Rapp, “Charmonium suppression and regeneration from SPS to RHIC,” *Nuclear Physics A*, vol. 709, no. 1–4, pp. 415–439, 2002.
- [19] R. L. Thews and M. L. Mangano, “Momentum spectra of charmonium produced in a quark-gluon plasma,” *Physical Review C*, vol. 73, no. 1, p. 014904, 2006.
- [20] P. Braun-Munzinger and J. Stachel, “Charmonium from statistical hadronization of heavy quarks—a probe for deconfinement in the quark-gluon plasma,” in *Landolt-Börnstein Set 2010: Relativistic Heavy Ion Physics*, R. Stock, Ed., Springer, 2010.
- [21] K. Sridhar and H. Satz, “Charmonium production versus open charm in nuclear collisions,” *Physical Review D*, vol. 50, no. 5, pp. 3557–3559, 1994.
- [22] A. Andronic, P. Braun-Munzinger, and K. Redlich, “Statistical hadronization of heavy quarks in ultra-relativistic nucleus-nucleus collisions,” *Nuclear Physics A*, vol. 789, no. 1–4, pp. 334–356, 2007.
- [23] F. Becattini, P. Castorina, J. Manninen, and H. Satz, “The thermal production of strange and non-strange hadrons in e^+e^- collisions,” *The European Physical Journal C*, vol. 56, no. 4, pp. 493–510, 2008.
- [24] A. Andronic, F. Beutler, P. Braun-Munzinger, K. Redlich, and J. Stachel, “Statistical hadronization of heavy flavor quarks in elementary collisions: successes and failures,” *Physics Letters B*, vol. 678, no. 4, pp. 350–354, 2009.
- [25] Z. Conesa del Valle, Quark Matter 2012, Washington and private communication.
- [26] B. Abelev, J. Adam, D. Adamová et al., “Suppression of high transverse momentum D mesons in central Pb-Pb collisions at $\sqrt{s_{NN}} = 2.76$,” *Journal of High Energy Physics*, vol. 2012, no. 9, pp. 1–37, 2012.
- [27] B. Abelev, J. Adam, D. Adamová et al., “ J/ψ suppression at forward rapidity in Pb-Pb collisions at $\sqrt{s_{NN}} = 2.76$ TeV,” *Physical Review Letters*, vol. 109, no. 7, p. 072301, 2012.
- [28] S. Chatrchyan, V. Khachatryan, A. M. Sirunyan et al., “Suppression of non-prompt J/ψ , prompt J/ψ , and $Y(1S)$ in PbPb collisions at $\sqrt{s_{NN}} = 2.76$ TeV,” *Journal of High Energy Physics*, vol. 2012, no. 5, pp. 1–54, 2012.
- [29] T. Dahms, private communication.
- [30] A. Adare, S. Afanasiev, C. Aidala et al., “Heavy-quark production in $p+p$ and energy loss and flow of heavy quarks in Au+Au collisions at $\sqrt{s_{NN}} = 200$ GeV,” *Physical Review C*, vol. 84, no. 4, p. 044905, 2011.
- [31] A. Adare, S. Afanasiev, C. Aidala et al., “ J/ψ production versus centrality, transverse momentum, and rapidity in Au+Au collisions at $\sqrt{s_{NN}} = 200$ GeV,” *Physical Review Letters*, vol. 98, no. 23, p. 232301, 2007.
- [32] F. Akram and M. A. K. Lodhi, “ B_c absorption cross sections by ρ mesons,” *Physical Review C*, vol. 84, no. 6, p. 064912, 2011.
- [33] L. Adamczyk, G. Agakishiev, M. M. Aggarwal et al., “ J/ψ production at high transverse momenta in $p + p$ and Au + Au collisions at $\sqrt{s_{NN}} = 200$ GeV,” *Physics Letters B*, vol. 722, no. 1-3, pp. 55–62, 2013, arXiv:1208.2736 [nucl-ex].
- [34] S. Digal, H. Satz, and R. Vogt, “Charmonium production and corona effect,” *Physical Review C*, vol. 85, no. 3, p. 034906, 2012.
- [35] M. Leitch, private communication.
- [36] M. J. Leitch, J. Boissevain, T. A. Carey et al., “Nuclear dependence of neutral D production by 800 GeV/c protons,” *Physical Review Letters*, vol. 72, p. 2542, 1994.
- [37] M. J. Leitch and J. C. Peng, E866/NuSea, private communication.
- [38] S. Klinksieck, *Ph. D. thesis*, The University of New Mexico, 2005.
- [39] N. Apadula, in *Proceedings of the 29th Winter Workshop on Nuclear Dynamics*, Squaw Valley, Calif, USA, February 2013.
- [40] R. Granier de Cassagnac, “Quarkonia production in cold and hot matters,” *Journal of Physics G*, vol. 35, no. 10, p. 104023, 2008.

Research Article

On the Higher Moments of Particle Multiplicity, Chemical Freeze-Out, and QCD Critical Endpoint

A. Tawfik^{1,2}

¹ Egyptian Center for Theoretical Physics (ECTP), MTI University, Cairo 11571, Egypt

² Research Center for Einstein Physics, Freie-University Berlin, Berlin, Germany

Correspondence should be addressed to A. Tawfik; a.tawfik@eng.mti.edu.eg

Received 6 January 2013; Revised 11 May 2013; Accepted 2 June 2013

Academic Editor: Edward Sarkisyan-Grinbaum

Copyright © 2013 A. Tawfik. This is an open access article distributed under the Creative Commons Attribution License, which permits unrestricted use, distribution, and reproduction in any medium, provided the original work is properly cited.

We calculate the first six nonnormalized moments of particle multiplicity within the framework of the hadron resonance gas model. In terms of the lower order moments and corresponding correlation functions, general expressions of higher order moments are derived. Thermal evolution of the first four normalized moments and their products (ratios) are studied at different chemical potentials, so that it is possible to evaluate them at chemical freeze-out curve. It is found that a nonmonotonic behaviour reflecting the dynamical fluctuation and strong correlation of particles starts to appear from the normalized third order moment. We introduce novel conditions for describing the chemical freeze-out curve. Although the hadron resonance gas model does not contain any information on the criticality related to the chiral dynamics and singularity in the physical observables, we are able to find out the location of the QCD critical endpoint at $\mu \sim 350$ MeV and temperature $T \sim 162$ MeV.

1. Introduction

Recently, the higher order multiplicity moments have gained prominence in high energy physics with a huge hope in pinpointing the QCD critical endpoint (CEP) [1] connecting the first order boundary separating the hadronic from the partonic matter at high density with the cross-over boundary at low density [2, 3]. It is clear that the hadron resonance gas partition function is an approximation to a nonsingular part of the free energy of QCD in the hadronic phase. There are large theoretical uncertainties of its location, and even its existence is not fully confirmed yet [4–6]. The characteristic feature of CEP is critical dynamical fluctuations [7–14]. The higher order moments are conjectured to reflect the large fluctuations associating the hadron-quark phase transition. This was the motivation of a remarkable number of experimental and theoretical studies [1, 15–20]. Recently, various calculations have shown that the higher order moments of the multiplicity distributions of some conserved quantities, such as net-baryon, net-charge, and net-strangeness, are sensitive to the correlation length ξ [21–23], which in turn is related to

the higher order moments, themselves. In realistic heavy-ion collisions, the correlation length is found to remain finite.

Apparently, it should not be an exception that the strongly interacting QCD matter undergoes phase transition(s) at extreme conditions, as almost all matter types suffer from such a critical change as the extreme conditions change. The lattice QCD calculations predict that a cross-over takes place between the hadronic phase and the Quark Gluon Plasma (QGP) phase, when the temperature exceeds critical value of $T_c \simeq 150 - 190$ MeV. As given in [3, 24, 25], depending on the different parameters (for instance, the quark flavours and their masses) and on the lattice configurations, lattice QCD assigns different values to T_c . Furthermore, the value of T_c depends on the baryon chemical potential μ . With vanishing μ , the lattice QCD calculations [26] show that the higher order susceptibilities can be related to the higher order moments of the corresponding multiplicity distributions. They also show nonmonotonic behavior near T_c . Apparently, the QCD phase diagram including CEP can be mapped out using this characteristic behaviour. In the literature, one finds that the QCD phase diagram has been determined using

various criteria, such as critical energy density [27–29] or line of constant physics [3]. Also the chemical freeze-out curve can be characterized assuming constant physics. For a recent and extensive review, we refer to [30] and the references therein.

At large chemical potential μ , various calculations based on QCD-based models indicate that the transition from the hadronic phase to the QGP phase is of first order. The endpoint connecting this line with the one of the cross-over (at small μ) is likely of second order [4–6, 31, 32]. Therefore, the phase transition should be accompanied with large fluctuations in different physical quantities. Experimentally, we study the QCD phase diagram by varying the colliding energy in heavy-ion collisions and determining the critical temperature T_c [2]. The possibility of finding QCD CEP has motivated the RHIC beam energy scan program [33]. By tuning the collision energy from a center-of-mass energy of 200 GeV down to 5 GeV, we are able to vary the baryon chemical potential from ~ 2 to ~ 500 MeV. Nevertheless, there are large theoretical uncertainties of its location and even its existence is not fully confirmed [4–6, 34]. The higher order moments of various physical quantities are conjectured to reflect the nonmonotonic behaviour near the QCD CEP. In the present work, we give a systematic study for the higher order moments of the multiplicity distribution and show their ability to represent the fluctuations along the QCD phase diagram.

Many reasons speak for utilizing the physical resonance gas model (HRG) in predicting the hadron abundances and their thermodynamics. The HRG model seems to provide a good description for the thermal evolution of the thermodynamic quantities in the hadronic matter [3, 7–9, 27–29, 35, 36] and has been successfully utilized to characterize the conditions deriving from the chemical freeze-out at finite densities [37, 38]. In light of this, HRG can be used in calculating the higher order moments of particle multiplicity using a grand canonical partition function of an ideal gas with all experimentally observed states up to a certain large mass as constituents. The HRG grand canonical ensemble includes two important features [3]; the kinetic energies and the summation over all degrees of freedom and energies of resonances. On other hand, it is known that the formation of resonances can only be achieved through strong interactions [39]; *resonances (fireballs) are composed of further resonances (fireballs), which in turn consist of resonances (fireballs) and so on*. In other words, the contributions of the hadron resonances to the partition function are the same as that of free particles with some effective mass. At temperatures comparable to the resonance half-width, the effective mass approaches the physical one [3]. Thus, at high temperatures, the strong interactions are conjectured to be taken into consideration through including heavy resonances. It is found that hadron resonances with masses up to 2 GeV are representing suitable constituents for the partition function [3, 7–9, 27–29, 35, 36]. Such a way, the singularity expected at the Hagedorn temperature [27, 28] can be avoided and the strong interactions are assumed to be considered. Nevertheless, the validity of HRG is limited to temperatures below the critical one, T_c .

In this paper, we study the first six nonnormalized higher order moments of the particle multiplicity in the hadron resonance gas (HRG) model, which is introduced in Section 2. In Section 2.1, we suggest an answer to the question: what is needed when going from “trivial” lower order to “sophisticated” higher order moments? Based on results, general expressions for arbitrary higher moments are deduced, so that it is possible to conclude that going from lower to higher order moments is achievable through a series of lower order moments and correlation functions. The thermal evolution of the first four normalized moments and their products (ratios) are studied at different chemical potentials μ in Section 2.2. Therefore, it is possible to evaluate them at the chemical freeze-out curve, which is characterized by constant s/T^3 at all values of μ , where s and T are entropy density and temperature, respectively. Sections 3 and 4 are devoted to introduce novel conditions describing the chemical freeze-out curve and define the location of the QCD critical endpoint.

2. Higher Order Moments of the Particle Multiplicity

In a grand canonical ensemble, it is straightforward to derive an expression for the pressure. In Section 2.1, we give a list of different moments of particle multiplicity. As we move from lower order to higher order multiplicities, certain distribution functions are being added/subtracted. These distribution functions represent higher order correlations. In Section 2.2, we list out various normalized higher order moments, the normalization being based on the variance σ . The products (ratios) of normalized moments are elaborated in Section 2.3.

The hadron resonances treated as a free gas [3, 27–29, 35] are conjectured to add to the thermodynamic pressure in the hadronic phase (below T_c). This statement is valid for free as well as for strongly interacting resonances. It has been shown that the thermodynamics of strongly interacting system can also be approximated to an ideal gas composed of hadron resonances with masses ≤ 2 GeV [3, 40]. Therefore, the confined phase of QCD, the hadronic phase, is modelled as a noninteracting gas of resonances. The grand canonical partition function reads

$$Z(T, \mu, V) = \text{Tr} \left[\exp^{(\mu N - H)/T} \right], \quad (1)$$

where H is the Hamiltonian of the system and T is the temperature. The Hamiltonian is given by the sum of the kinetic energies of relativistic Fermi and Bose particles. The main motivation of using this Hamiltonian is that it contains all relevant degrees of freedom of confined and strongly interacting matter. It includes implicitly the interactions that result in resonance formation. In addition, it has been shown that this model can submit a quite satisfactory description of particle production in heavy-ion collisions. With the above assumptions the dynamics of the partition function can be calculated exactly and be expressed as a sum over

single-particle partition functions Z_i^1 of all hadrons and their resonances. Consider the following:

$$\begin{aligned} \ln Z(T, \mu_i, V) &= \sum_i \ln Z_i^1(T, V) \\ &= \sum_i \pm \frac{Vg_i}{2\pi^2} \int_0^\infty k^2 dk \ln \left\{ 1 \pm \exp \left[\frac{\mu_i - \epsilon_i}{T} \right] \right\}, \end{aligned} \quad (2)$$

where $\epsilon_i(k) = (k^2 + m_i^2)^{1/2}$ is the i th particle dispersion relation, g_i is spin-isospin degeneracy factor, and \pm stands for bosons and fermions, respectively.

Before the discovery of QCD, a probable phase transition of a massless pion gas to a new phase of matter was speculated [41]. Based on statistical models like Hagedorn [42, 43] and Bootstrap [44, 45], the thermodynamics of such an ideal pion gas is studied, extensively. After the QCD, the new phase of matter is known as Quark Gluon Plasma (QGP). The physical picture was that at T_c the additional degrees of freedom carried by QGP are to be released resulting in an increase in the thermodynamic quantities like energy and pressure densities. The success of hadron resonance gas model in reproducing lattice QCD results at various quark flavours and masses (below T_c) changed this physical picture drastically. Instead of releasing additional degrees of freedom at $T > T_c$, the interacting system reduces its effective degrees of freedom at $T < T_c$. In other words, the hadron gas has much more degrees of freedom than QGP.

At finite temperature T and baryon chemical potential μ_i , the pressure of the i th hadron or resonance species reads

$$p(T, \mu_i) = \pm \frac{g_i}{2\pi^2} T \int_0^\infty k^2 dk \ln \left\{ 1 \pm \exp \left[\frac{\mu_i - \epsilon_i}{T} \right] \right\}. \quad (3)$$

As no phase transition is conjectured in HRG, summing over all hadron resonances results in the final thermodynamic pressure in the hadronic phase.

The switching between hadron and quark chemistry is given by the relations between the *hadronic* chemical potentials and the quark constituents; $\mu_i = 3n_b\mu_q + n_s\mu_s$, where $n_b(n_s)$ being baryon (strange) quantum number. The chemical potential assigned to the light quarks is $\mu_q = (\mu_u + \mu_d)/2$, and the one assigned to strange quark reads $\mu_s = \mu_q - \mu_s$. The strangeness chemical potential μ_s is calculated as a function of T and μ_i under the assumption that the overall strange quantum number has to remain conserved in heavy-ion collisions [3].

2.1. Nonnormalized Higher Order Moments. As given in the introduction, the higher order moments can be studied in different physical quantities. For example, the higher order moments of charged-particle multiplicity distribution have been predicted four decades ago [46]. Recently, the higher order moments of various multiplicity distributions have been reported by STAR measurements [15–19] and lattice QCD calculations [47–49]. The empirical relevance of the higher order moments to the experimental measurements has been suggested in [1]. Accordingly, the measurement of

the correlation length seems to be very much crucial. In a future work, we shall discuss the experimental signatures of the higher order moments. Another ingredient would be the experimental sensitivity for the suggested signatures, which are based on singular behavior of thermodynamic functions. For the time being, we just want to mention that the experimental measurements apparently take place at the final state of the collision, which would mean that the signals have to survive the extreme conditions in such high energy collisions. It has been pointed out that the contribution of the critical fluctuations to the higher order moments is proportional to a positive power of ξ . The latter is conjectured to diverge at QCD CEP, and such an assumption is valid in the thermodynamic limit.

In the present work, we first study the contribution of the hadron resonance mass spectrum in clarifying the interrelations between the various nonnormalized and normalized moments. The motivation of using resonance gas is clear [27–29]. As introduced about five decades ago, the resonance gas is only valid below T_c [3, 27–29, 35, 42, 43]. Therefore, the present work is valid in the hadronic phase, only.

For the i th particle, the “first” order moment is given by the derivative of $p = -T\partial \ln Z(T, V, \mu_i)/\partial V$ with respect to the dimensionless quantity μ_i/T . When taking into account the antiparticles, we add a negative sign to the chemical potential. The first derivative describes the multiplicity distribution or an expectation operator, which is utilized to estimate the number or multiplicity density

$$m_1(T, \mu_i) = \pm \frac{g_i}{2\pi^2} T \int_0^\infty \frac{e^{(\mu_i - \epsilon_i)/T} k^2 dk}{1 \pm e^{(\mu_i - \epsilon_i)/T}}. \quad (4)$$

The “second” order moment is known as the variance. It gives the susceptibility of the measurements. Consider the following:

$$\begin{aligned} m_2(T, \mu_i) &= \pm \frac{g_i}{2\pi^2} T \int_0^\infty \frac{e^{(\mu_i - \epsilon_i)/T} k^2 dk}{1 \pm e^{(\mu_i - \epsilon_i)/T}} \\ &\quad - \frac{g_i}{2\pi^2} T \int_0^\infty \frac{e^{2(\mu_i - \epsilon_i)/T} k^2 dk}{(1 \pm e^{(\mu_i - \epsilon_i)/T})^2}. \end{aligned} \quad (5)$$

The “third” order moment measures the lopsidedness of the distribution. As given in Section 2.2, the normalization of third order moment is known as skewness or the asymmetry in the distribution. Skewness tells us about the direction of variation of the data set. Consider the following:

$$\begin{aligned} m_3(T, \mu_i) &= \pm \frac{g_i}{2\pi^2} T \int_0^\infty \frac{e^{(\mu_i - \epsilon_i)/T} k^2 dk}{1 \pm e^{(\mu_i - \epsilon_i)/T}} \\ &\quad - \frac{g_i}{2\pi^2} 3T \int_0^\infty \frac{e^{2(\mu_i - \epsilon_i)/T} k^2 dk}{(1 \pm e^{(\mu_i - \epsilon_i)/T})^2} \\ &\quad \pm \frac{g_i}{2\pi^2} 2T \int_0^\infty \frac{e^{3(\mu_i - \epsilon_i)/T} k^2 dk}{(1 \pm e^{(\mu_i - \epsilon_i)/T})^3}. \end{aligned} \quad (6)$$

In general, the normalization of r th order moment is obtained by dividing it by σ^r , where σ is the standard deviation.

The normalization is assumed to remove the brightness dependence.

The “fourth” order moment compares the tallness and skinniness or shortness and squatness, that is, shape, of a certain measurement to its normal distribution. It is defined as the uncertainty is an uncertainty or “*the location- and scale-free movement of probability mass from the shoulders of a distribution into its center and tails and to recognize that it can be formalized in many ways*” [50]. Consider the following:

$$\begin{aligned}
m_4(T, \mu_i) = & \pm \frac{g_i}{2\pi^2} T \int_0^\infty \frac{e^{(\mu_i - \varepsilon_i)/T} k^2 dk}{1 \pm e^{(\mu_i - \varepsilon_i)/T}} \\
& - \frac{g_i}{2\pi^2} 7T \int_0^\infty \frac{e^{2(\mu_i - \varepsilon_i)/T} k^2 dk}{(1 \pm e^{(\mu_i - \varepsilon_i)/T})^2} \\
& \pm \frac{g_i}{2\pi^2} 12T \int_0^\infty \frac{e^{3(\mu_i - \varepsilon_i)/T} k^2 dk}{(1 \pm e^{(\mu_i - \varepsilon_i)/T})^3} \\
& - \frac{g_i}{2\pi^2} 6T \int_0^\infty \frac{e^{4(\mu_i - \varepsilon_i)/T} k^2 dk}{(1 \pm e^{(\mu_i - \varepsilon_i)/T})^4}.
\end{aligned} \tag{7}$$

The “fifth” order moment measures the asymmetry sensitivity of the “fourth” order moment. Consider the following:

$$\begin{aligned}
m_5(T, \mu_i) = & \pm \frac{g_i}{2\pi^2} T \int_0^\infty \frac{e^{(\mu_i - \varepsilon_i)/T} k^2 dk}{1 \pm e^{(\mu_i - \varepsilon_i)/T}} \\
& - \frac{g_i}{2\pi^2} 15T \int_0^\infty \frac{e^{2(\mu_i - \varepsilon_i)/T} k^2 dk}{(1 \pm e^{(\mu_i - \varepsilon_i)/T})^2} \\
& \pm \frac{g_i}{2\pi^2} 50T \int_0^\infty \frac{e^{3(\mu_i - \varepsilon_i)/T} k^2 dk}{(1 \pm e^{(\mu_i - \varepsilon_i)/T})^3} \\
& - \frac{g_i}{2\pi^2} 60T \int_0^\infty \frac{e^{4(\mu_i - \varepsilon_i)/T} k^2 dk}{(1 \pm e^{(\mu_i - \varepsilon_i)/T})^4} \\
& \pm \frac{g_i}{2\pi^2} 24T \int_0^\infty \frac{e^{5(\mu_i - \varepsilon_i)/T} k^2 dk}{(1 \pm e^{(\mu_i - \varepsilon_i)/T})^5}.
\end{aligned} \tag{8}$$

The “sixth” order moment is generally associated with compound options. Consider the following:

$$\begin{aligned}
m_6(T, \mu_i) = & \pm \frac{g_i}{2\pi^2} T \int_0^\infty \frac{e^{(\mu_i - \varepsilon_i)/T} k^2 dk}{1 \pm e^{(\mu_i - \varepsilon_i)/T}} \\
& - \frac{g_i}{2\pi^2} 31T \int_0^\infty \frac{e^{2(\mu_i - \varepsilon_i)/T} k^2 dk}{(1 \pm e^{(\mu_i - \varepsilon_i)/T})^2} \\
& \pm \frac{g_i}{2\pi^2} 180T \int_0^\infty \frac{e^{3(\mu_i - \varepsilon_i)/T} k^2 dk}{(1 \pm e^{(\mu_i - \varepsilon_i)/T})^3} \\
& - \frac{g_i}{2\pi^2} 390T \int_0^\infty \frac{e^{4(\mu_i - \varepsilon_i)/T} k^2 dk}{(1 \pm e^{(\mu_i - \varepsilon_i)/T})^4}
\end{aligned}$$

$$\begin{aligned}
& \pm \frac{g_i}{2\pi^2} 360T \int_0^\infty \frac{e^{5(\mu_i - \varepsilon_i)/T} k^2 dk}{(1 \pm e^{(\mu_i - \varepsilon_i)/T})^5} \\
& - \frac{g_i}{2\pi^2} 120T \int_0^\infty \frac{e^{6(\mu_i - \varepsilon_i)/T} k^2 dk}{(1 \pm e^{(\mu_i - \varepsilon_i)/T})^6}.
\end{aligned} \tag{9}$$

Thus, from (4)–(9), a general expression for the r th order moment can be deduced

$$m_r(T, \mu_i) = \frac{g_i}{2\pi^2} T \sum_{l=1}^r a_{r,l} \int_0^\infty \frac{e^{l(\mu_i - \varepsilon_i)/T}}{(1 \pm e^{(\mu_i - \varepsilon_i)/T})^l} k^2 dk, \tag{10}$$

where the coefficients read

$$a_{r,l} = (\pm 1)^l (-1)^{l+1} [l a_{r-1,l} + (l-1) a_{r-1,l-1}], \tag{11}$$

where $l \leq r$ and $a_{r,l}$ vanishes for all $r < 1$. It is obvious that the coefficients of a certain moment are to be determined from a long chain of all previous ones. Such a conclusion dates back to about four decades [46], where it has been shown that the coefficients are related to high order correlation functions. Should this assumption is proven to be valid, then expression (11) gets a novel interpretation. It seems to sum up the correlation functions up to the r th order. According to [46] and when neglecting the two-particle correlations C_2 , then the higher order moments read

$$m_2 = \langle (\delta N)^2 \rangle \approx 2 \langle N \rangle, \tag{12}$$

$$m_3 = \langle (\delta N)^3 \rangle \approx 4 \langle N \rangle + C_3,$$

$$m_4 \approx \langle (\delta N)^4 \rangle = 6m_3 + 3m_2^2 - 8m_2 + 8C_4, \tag{13}$$

where $\delta N = N - \langle N \rangle$,

$$\begin{aligned}
C_3(p_1, p_2, p_3) = & \sum_{p_1} \langle p_1 p_1 p_1 \rangle + 3 \sum_{p_1 < p_2} \langle p_1 p_2 p_2 \rangle \\
& + 6 \sum_{p_1 < p_2 < p_3} \langle p_1 p_2 p_3 \rangle,
\end{aligned} \tag{14}$$

$$\begin{aligned}
C_4(p_1, p_2, p_3, p_4) = & \sum_{p_1 < p_2} \langle p_1 p_2 p_2 p_2 \rangle + \sum_{p_1 < p_2 < p_3} \langle p_1 p_2 p_3 p_3 \rangle \\
& + 8 \sum_{p_1 < p_2 < p_3 < p_4} \langle p_1 p_2 p_3 p_4 \rangle,
\end{aligned} \tag{15}$$

and p_i is the i th particle. To the second order moment m_2 , we have to add the effects of the two particle correlation function, $2 \sum C_2$. The third order moment m_3 gets approximately three times this amount. The three and four particle correlations, (14) and (15) appear first in third and fourth moments (13) and (14), respectively.

When ignoring these high order correlations, we are left with the widely used two particle correlations. In the present work, we restrict the discussion to this type, only. It is of great interest, as it is accessible experimentally and achievable numerically. The two particle correlations are suggested as

a probe for the bulk QCD medium, energy loss, medium response, jet properties, and intensity interferometry [51–57]. In addition to this list of literature, the comprehensive review [58, 59] can be recommended.

Taking into account the particle multiplicities, then expressions (12) and (13) can be rewritten as follows:

$$\begin{aligned} m_2 &= \langle (\delta N)^2 \rangle \simeq \langle N^2 \rangle - \langle N \rangle^2, \\ m_3 &= \langle (\delta N)^3 \rangle \simeq \langle N^3 \rangle - \langle N^2 \rangle \langle N \rangle + 2 \langle N^3 \rangle^3, \\ m_4 &= \langle (\delta N)^4 \rangle - 3 \langle (\delta N)^2 \rangle^2 \simeq \langle N^4 \rangle - 2 \langle N^2 \rangle^2 \\ &\quad - 5 \langle N^2 \rangle^2 + 6 \langle N \rangle^2 \langle N^2 \rangle. \end{aligned} \quad (16)$$

As mentioned in Section 2.1, the experimental signals for the higher order moments shall be discussed in a future work.

As given in (10), the dependence of first six nonnormalized moments on lower ones can explicitly be deduced as follows:

$$\begin{aligned} m_1 &= \frac{g_i}{2\pi^2} T \int_0^\infty \frac{e^{(\mu_i - \varepsilon_i)/T} k^2 dk}{1 \pm e^{(\mu_i - \varepsilon_i)/T}}, \\ m_2 &= m_1 - \frac{g_i}{2\pi^2} T \int_0^\infty \frac{e^{2(\mu_i - \varepsilon_i)/T} k^2 dk}{(1 \pm e^{(\mu_i - \varepsilon_i)/T})^2}, \\ m_3 &= -2m_1 + 3m_2 + 2 \frac{g_i}{2\pi^2} T \int_0^\infty \frac{e^{3(\mu_i - \varepsilon_i)/T} k^2 dk}{(1 \pm e^{(\mu_i - \varepsilon_i)/T})^3}, \\ m_4 &= 6m_1 - 11m_2 + 6m_3 - 6 \frac{g_i}{2\pi^2} T \int_0^\infty \frac{e^{4(-\varepsilon_i + \mu_i)/T} k^2 dk}{(1 \pm e^{(-\varepsilon_i + \mu_i)/T})^4}, \\ m_5 &= -24m_1 + 50m_2 - 35m_3 + 10m_4 \\ &\quad + 24 \frac{g_i}{2\pi^2} T \int_0^\infty \frac{e^{5(-\varepsilon_i + \mu_i)/T} k^2 dk}{(1 \pm e^{(-\varepsilon_i + \mu_i)/T})^5}, \\ m_6 &= 120m_1 - 274m_2 + 225m_3 - 85m_4 + 15m_5 \\ &\quad - 120 \frac{g_i}{2\pi^2} T \int_0^\infty \frac{e^{6(-\varepsilon_i + \mu_i)/T} k^2 dk}{(1 \pm e^{(-\varepsilon_i + \mu_i)/T})^6}. \end{aligned} \quad (17)$$

Naively spoken, we conclude that raising lower order moments to higher ones is achievable through a series of all lower order moments and an additional term reflecting the correlations, themselves [46]. From (17), the additional terms are proportional to $\langle N \rangle^r$. Apparently, they are essential in order to judge whether going from lower to higher order moments would make the signatures of dynamical fluctuations clearer than when excluding them.

The first and second terms can be generalized. Then, a general expression would read

$$\begin{aligned} m_r &= (-)^{r-1} (r-1) c_{m_1}^{r-1} m_1 \\ &\quad - [(r-1) c_{m_2}^{r-1} + (r-2)!] m_2 + \mathcal{O}(m_{>2}), \end{aligned} \quad (18)$$

where c_{m_r} is the coefficient of the r th moment. The last term in (18) can be elaborated when higher order moments are calculated. The latter are essential in order to find out a clear pattern.

Figure 1 presents the results of the higher order moments as calculated in the HRG model. As introduced previously, raising the orders of multiplicity moments results in new coefficients and new integrals. The earlier are partly characterized in (18). The dimensionless nonnormalized moments are given depending on the temperature T in the left panel of Figure 1. The new coefficients that resulted in when going from lower to higher order moments are depicted in the right panel. The integrals can be compared with the correlation functions [46]. We find that these integrals are related to $\langle N \rangle^r$, where r is the order of the moment. It is obvious that successive moments have a difference of about one order of magnitude. Therefore, higher order $\langle N \rangle^r$ can be disregarded with reference to their vanishing contributions.

In order to draw a picture about the contributions of the integrals appearing in (17), the phase space integral can be replaced by a series representation. For the i th particle species, the pressure can be expressed as

$$\begin{aligned} P(T, \mu_i) &= \frac{g_i}{2\pi^2} T^4 \sum_{n=1}^{\infty} (\pm)^{n+1} e^{n(\mu_i/T)} \left(n \frac{m_i}{T} \right)^2 \\ &\quad \times n^{-4} K_2 \left(n \frac{m_i}{T} \right), \end{aligned} \quad (19)$$

where K_2 is modified Bessel function of the second kind and the factor $(\pm)^{n+1}$ represents fermions and bosons, respectively. In deriving previous expression, we expand the functions appearing in (4), for instance. The resulting expression is applicable as long as $\mu_i < m_i$ is valid. Then, the derivatives with respect to μ/T leads to

$$\begin{aligned} m_r(T, \mu_i) &= \frac{g_i}{2\pi^2} T^4 \sum_{n=1}^{\infty} (\pm)^{n+1} e^{n(\mu_i/T)} \left(n \frac{m_i}{T} \right)^2 \\ &\quad \times n^{r-4} K_2 \left(n \frac{m_i}{T} \right), \end{aligned} \quad (20)$$

which is valid for all order moments of order $r \geq 1$.

For completeness, we mention here that taking into consideration one particle and its antiparticle is not rare in the literature. In this case, the expression (19) can be rewritten as

$$\begin{aligned} P(T, \mu_i) &= \frac{g_i}{\pi^2} T^4 \sum_{n=1}^{\infty} (\pm)^{n+1} \left(n \frac{m_i}{T} \right)^2 n^{-4} \\ &\quad \times K_2 \left(n \frac{m_i}{T} \right) \cosh \left(n \frac{\mu_i}{T} \right), \end{aligned} \quad (21)$$

and accordingly,

$$\begin{aligned} m_r(T, \mu_i) &= \frac{g_i}{2\pi^2} T^4 \sum_{n=1}^{\infty} (\pm)^{n+1} \left(n \frac{m_i}{T} \right)^2 n^{-4} \\ &\quad \times K_2 \left(n \frac{m_i}{T} \right) \frac{\partial^r}{\partial \mu^r} \cosh \left(n \frac{\mu_i}{T} \right). \end{aligned} \quad (22)$$

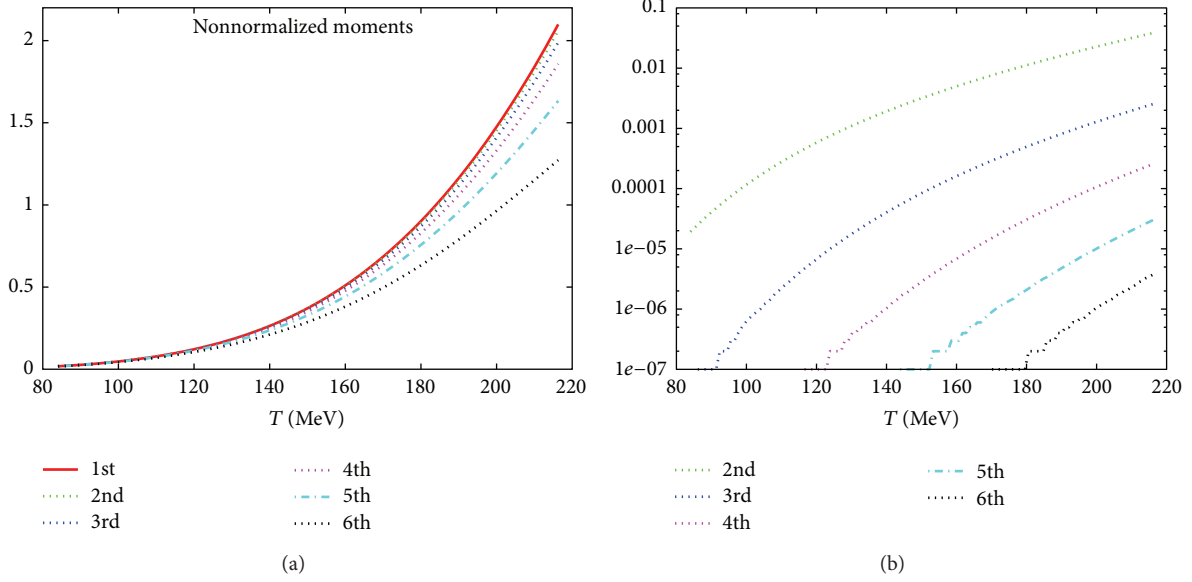


FIGURE 1: (a) Depicts dimensionless nonnormalized moments depending on the temperature. (b) Shows the evolution of the so-called correlation parts (the integrals appearing in (17)) with the temperature. (b) Shows the new coefficients that resulted in when going from lower to higher order moments of multiplicities in a log scale.

Comparing (20) with (19), we conclude that calculating higher order moments is associated with a gradual change in n . Expression (10) reflects almost the same behaviour, where higher order moments are associated with change in the coefficients.

2.2. Normalized Higher Order Moments. The normalization of higher order moments which can be deduced through derivatives with respect to the chemical potential μ of given charges, apparently gives additional insights about the properties of higher order moments. From statistical point of view, the normalization is done with respect to the standard deviation σ , which is related to ξ . Therefore, it provides a tool to relate moments with various orders to the experimental measurement. The susceptibility of the distribution gives a measure for σ . Should we are interested on the multiplicity, then the susceptibility is simply given by the derivative of first order moments with respect to μ . It has been shown that the susceptibility is related to $\sim \xi^2$ [1]. The results of σ in hadronic, bosonic, and fermionic resonances are calculated at different μ and given in Figure 2. As discussed earlier, the strange quantum number has to remain conserved in high energy collisions. As per the standard model, this is one of the global symmetries in strong interactions. The procedure of keeping strange degrees of freedom conserved in HRG is introduced in [3]. This is the origin of the μ dependence, especially in the bosonic gas. Although baryon chemical potential μ vanishes per definition, the chemical potential associated with strange quark μ_s remains finite. The dependence of μ_s on μ is depicted in Figure 16. Another feature in these calculations is the assumption that the freeze-out boundary is determined by constant s/T^3 , where s is

the entropy density [37]. At chemical freeze-out boundary, the dependence of σ on μ is given in Figure 5.

The ‘‘third’’ order moment normalized to σ^3 is known as ‘‘skewness.’’ For standard Gaussian distribution, the skewness is obviously vanishing. Therefore, the skewness is an ideal quantity probing the non-Gaussian fluctuation feature as expected near T_c . The QCD CEP is conjectured to be sensitive to skewness. Experimentally, it has been shown that the skewness S is related to $\sim \xi^{4.5}$ [21]. The skewness for bosonic and fermionic resonance gas, respectively, reads

$$\begin{aligned}
 S_b &= -\frac{1}{2} \frac{\pi}{\sqrt{g_i}} T^{3/2} \\
 &\times \frac{\int_0^\infty \text{csch}[(\varepsilon_i - \mu_i)/2T]^4 \sinh[(\varepsilon_i - \mu_i)/T] k^2 dk}{\left[\int_0^\infty (\cosh[(\varepsilon_i - \mu_i)/T] - 1)^{-1} k^2 dk \right]^{3/2}}, \\
 S_f &= 8 \frac{\pi}{\sqrt{g_i}} T^{3/2} \\
 &\times \frac{\int_0^\infty \text{csch}[(\varepsilon_i - \mu_i)/T]^3 \sinh[(\varepsilon_i - \mu_i)/(2T)]^4 k^2 dk}{\left[\int_0^\infty (\cosh[(\varepsilon_i - \mu_i)/T] + 1)^{-1} k^2 dk \right]^{3/2}}.
 \end{aligned} \tag{23}$$

At different chemical potentials, the skewness S is calculated depending on T and given in Figure 3. It is worthwhile to notice that the values of S in the fermionic resonance gas are much larger than the S values in the bosonic resonance gas, especially at small chemical potentials. But at large chemical potential, this observation is exactly the opposite. The value of μ , at which the large (or small) skewness is flipped, seems to reflect the nature of phase transition, where

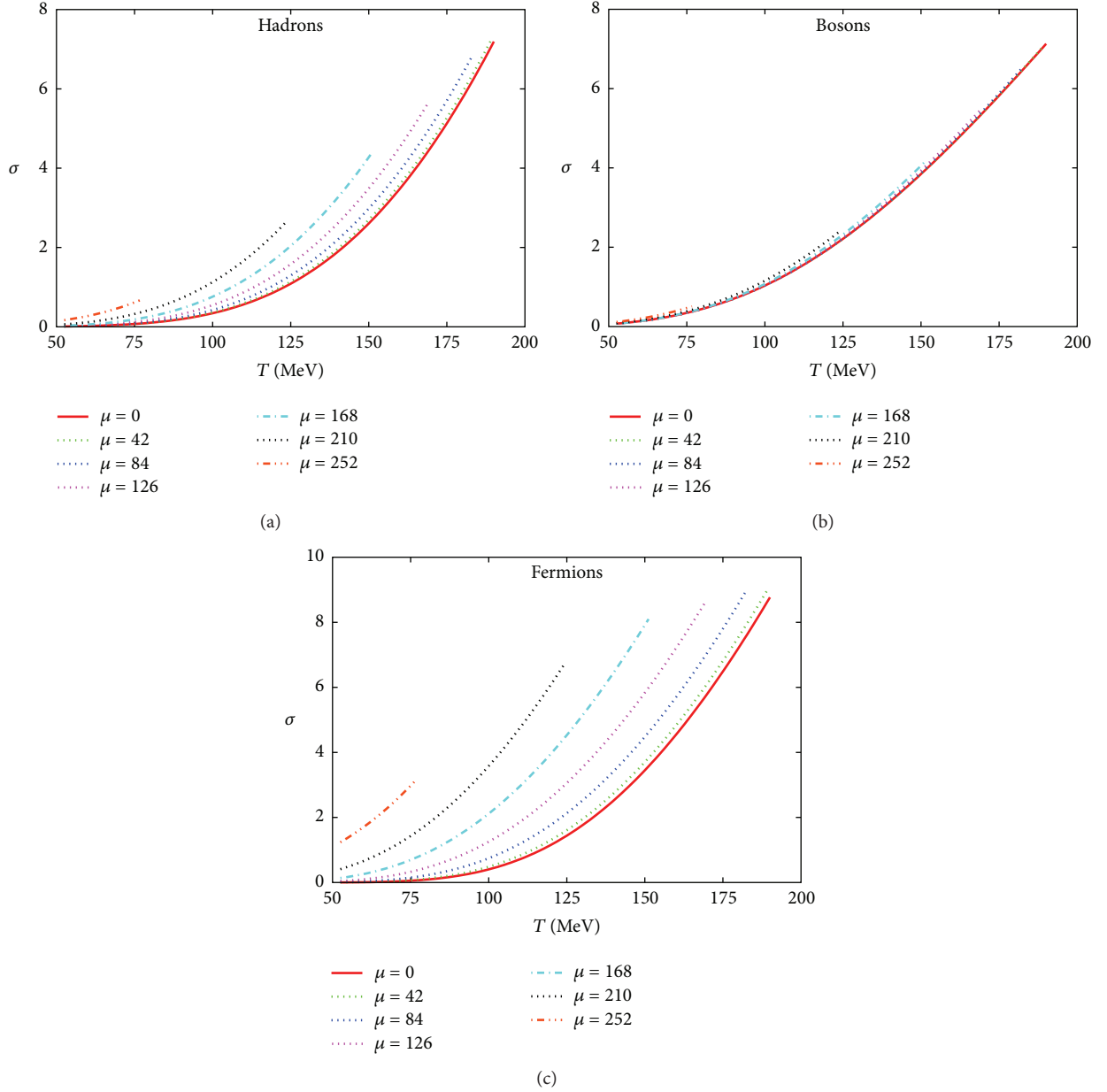


FIGURE 2: Results for σ in hadronic (a), bosonic (b), and fermionic (c) resonances are given in dependence on T for various baryon chemical potentials (given in MeV).

the fermionic and/or bosonic degrees of freedom turn out to be undistinguishable. Such an observation shall be utilized in positioning the QCD CEP, Section 3.

The normalization of fourth order moment is known as, heteroskedacity or kurtosis. It means varying volatility or more accurately, varying variance. Actually, the kurtosis is given by normalized fourth order moment minus 3. The subtraction of 3, which arises from the Gaussian distribution, is usually omitted [50, 60, 61]. Therefore, the kurtosis is an ideal quantity for probing the non-Gaussian fluctuation feature as expected near T_c and CEP. A sign change of skewness or kurtosis is conjectured to indicate that the system crosses the phase boundary [26, 62, 63]. As HRG is valid

below T_c , the sign change is not accessible. It has been shown that kurtosis κ is related to $\sim \xi^7$ [21]. Consider the following:

$$\begin{aligned} \kappa_b &= -\frac{\pi^2}{g_i} T^3 \\ &\times \left(\int_0^\infty \left\{ \cosh \left[\frac{\varepsilon_i - \mu_i}{T} \right] + 2 \right\} \operatorname{csch} \left[\frac{\varepsilon_i - \mu_i}{2T} \right]^4 k^2 dk \right. \\ &\quad \left. \times \left(\left[\int_0^\infty \left(1 - \cosh \left[\frac{\varepsilon_i - \mu_i}{T} \right] \right)^{-1} k^2 dk \right]^2 \right)^{-1} \right)^{-3}, \end{aligned}$$

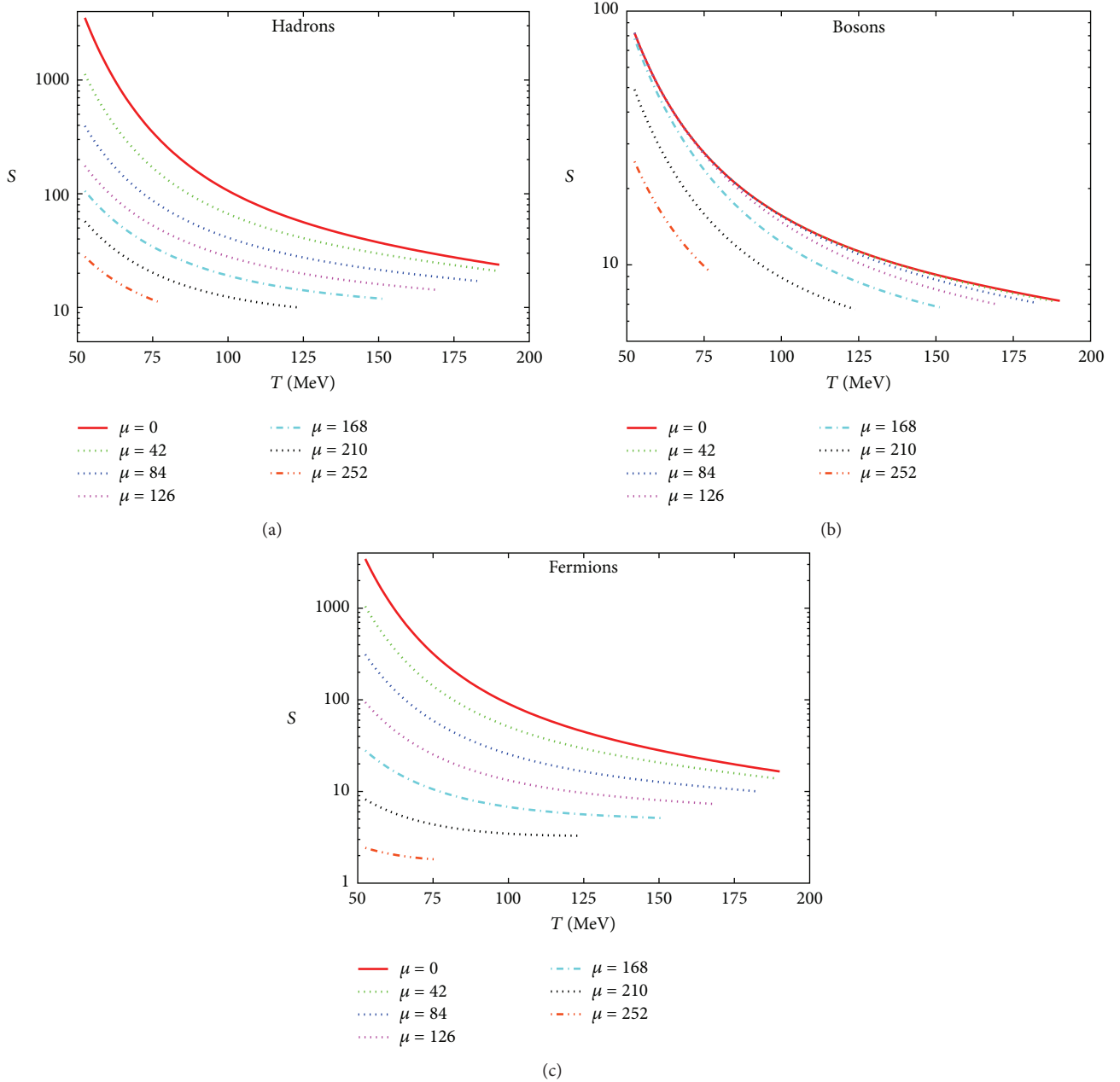


FIGURE 3: At various baryon chemical potentials (given in MeV), the skewness S for hadronic (a), bosonic (b), and fermionic (c) resonance gas is given as function of T .

$$\begin{aligned}
 \kappa_f &= \frac{\pi^2}{g_i} T^3 \\
 &\times \left(\int_0^\infty \left\{ \cosh \left[\frac{\varepsilon_i - \mu_i}{T} \right] - 2 \right\} \operatorname{sech} \left[\frac{\varepsilon_i - \mu_i}{2T} \right]^4 k^2 dk \right. \\
 &\times \left. \left(\left[\int_0^\infty \left(\cosh \left[\frac{\varepsilon_i - \mu_i}{T} \right] + 1 \right)^{-1} k^2 dk \right]^2 \right)^{-1} \right) - 3.
 \end{aligned} \tag{24}$$

2.3. Products of Higher Order Moments. There are several techniques to scale the correlation functions. The survey system's optional statistics module represents the most common technique, that is, Pearson or product moment correlation. This module includes the so-called partial correlation which seems to be useful when the relationship between two variables is to be highlighted, while effect of one or two other variables can be removed. In the present work, we study the products of higher order moments of the distributions of conserved quantities. The justification of this step is that certain products can be directly connected to the corresponding susceptibilities in lattice QCD simulation and

related to long range correlations [26, 64, 65]. Seeking for simplicity, we start with the Boltzmann approximation.

2.3.1. Modified Bessel Function: Boltzmann Statistics. When relativistic momentum integrals are replaced by summation over modified Bessel functions, the products of higher order moments in Boltzmann approximation read

$$\begin{aligned} \frac{\sigma^2}{\langle N \rangle} &= \frac{\sum_{n=1}^{\infty} (\pm)^{n+1} e^{n(\mu_i/T)} (n(m_i/T))^2 n^{-2} K_2(n(m_i/T))}{\sum_{n=1}^{\infty} (\pm)^{n+1} e^{n(\mu_i/T)} (n(m_i/T))^2 n^{-3} K_2(n(m_i/T))}, \\ S\sigma &= \frac{\sum_{n=1}^{\infty} (\pm)^{n+1} e^{n(\mu_i/T)} (n(m_i/T))^2 n^{-1} K_2(n(m_i/T))}{\sum_{n=1}^{\infty} (\pm)^{n+1} e^{n(\mu_i/T)} (n(m_i/T))^2 n^{-2} K_2(n(m_i/T))}, \\ \kappa\sigma^2 &= \frac{\sum_{n=1}^{\infty} (\pm)^{n+1} e^{n(\mu_i/T)} (n(m_i/T))^2 K_2(n(m_i/T))}{\sum_{n=1}^{\infty} (\pm)^{n+1} e^{n(\mu_i/T)} (n(m_i/T))^2 n^{-2} K_2(n(m_i/T))} \\ &\quad - 3 \frac{g_i}{2\pi^2} T^4 \sum_{n=1}^{\infty} (\pm)^{n+1} e^{n(\mu_i/T)} \\ &\quad \times \left(n \frac{m_i}{T} \right)^2 n^{-2} K_2 \left(n \frac{m_i}{T} \right), \\ \frac{\kappa\sigma}{S} &= \left(2\pi^2 \sum_{n=1}^{\infty} (\pm)^{n+1} e^{n(\mu_i/T)} \left(n \frac{m_i}{T} \right)^2 K_2 \left(n \frac{m_i}{T} \right) - 3g_i T^4 \right. \\ &\quad \times \left. \left(\sum_{n=1}^{\infty} (\pm)^{n+1} e^{n(\mu_i/T)} \left(n \frac{m_i}{T} \right)^2 n^{-2} K_2 \left(n \frac{m_i}{T} \right) \right)^2 \right) \\ &\quad \times \left(2\pi^2 \sum_{n=1}^{\infty} (\pm)^{n+1} e^{n(\mu_i/T)} \left(n \frac{m_i}{T} \right)^2 n^{-1} K_2 \left(n \frac{m_i}{T} \right) \right)^{-1}. \end{aligned} \quad (25)$$

The origin of the second term in all expressions containing κ is obvious. Expressions (25) justify the conclusions in [66] that are in Boltzmann approximation

$$\frac{\sigma^2}{\langle N \rangle} = S\sigma \simeq 1, \quad (26)$$

while

$$\kappa\sigma^2 = \frac{\kappa\sigma}{S} \simeq 1 - 3 \frac{g_i}{2\pi^2} T^4 \exp \left[\frac{\mu_i}{T} \right] \left(\frac{m_i}{T} \right)^2 K_2 \left(\frac{m_i}{T} \right). \quad (27)$$

These expressions are valid in the final state, which can be characterized by chemical and thermal freeze-out. In other words, these expressions are functions of the chemical potential. Using relativistic momentum integrals (see Section 2.3.2) shows that the products of moments result in a constant dependence on T [66].

2.3.2. Relativistic Momentum Integrals: Quantum Statistics. The fluctuations of conserved quantities are assumed to be sensitive to the structure of the hadronic system in its final state. As mentioned above, crossing the phase boundary or passing through critical endpoint is associated with large

fluctuations. The most proposed fluctuation of observables is variations of second order moments of the distribution, such as particle ratio [11–14] and charged dynamical measurement [67]. Then, the fluctuations are approximately related to ξ^2 [23].

The ratio of standard deviation σ^2 and the mean multiplicity $\langle N \rangle$ for fermions and bosons read

$$\frac{\sigma^2}{\langle N \rangle} = \frac{1}{2} \frac{\int_0^{\infty} (1 \pm \operatorname{csch}[(\varepsilon_i - \mu_i)/T])^{-1} k^2 dk}{\int_0^{\infty} (1 \pm e^{(\varepsilon_i - \mu_i)/T})^{-1} k^2 dk}, \quad (28)$$

where \pm stands for fermions and bosons, respectively. The results are given in Figure 4. We notice that the bosonic resonance gas results in smaller values than the fermionic one, especially in final state. Furthermore, we notice that $\sigma^2/\langle N \rangle$ decreases with increasing μ of the bosons at middle temperature. This is exactly the opposite in the fermionic resonance gas. This would give an explanation for the observation that the results in hadron resonances are not spread as in the other two sectors. Figure 5 shows the dependence of $\sigma^2/\langle N \rangle$ on μ at the chemical freeze-out boundary, which is characterized by $s/T^3 = 7$. The ratio $\sigma^2/\langle N \rangle$ is equivalent to m_2/m_1 , (32). The dependence of bosonic and fermionic σ on μ is given in Figure 5, as well. We notice that σ is smaller than $\sigma^2/\langle N \rangle$, especially at small μ . At large μ both quantities are almost equal.

The multiplication of skewness S by the standard deviation σ is directly related to the thermodynamics of the number susceptibility of the lattice QCD. In HRG, the bosonic and fermionic products read

$$\begin{aligned} (S\sigma)_b &= -\frac{1}{4} \frac{\int_0^{\infty} \operatorname{csch}[(\varepsilon_i - \mu_i)/T]^4 \sinh[(\varepsilon_i - \mu_i)/T] k^2 dk}{\int_0^{\infty} (1 - \cosh[(\varepsilon_i - \mu_i)/T])^{-1} k^2 dk}, \\ (S\sigma)_f &= 4 \frac{\int_0^{\infty} \operatorname{csch}[(\varepsilon_i - \mu_i)/T]^3 \sinh[(\varepsilon_i - \mu_i)/(2T)]^4 k^2 dk}{\int_0^{\infty} (\cosh[(\varepsilon_i - \mu_i)/T] + 1)^{-1} k^2 dk}. \end{aligned} \quad (29)$$

The product $S\sigma$ is equivalent to m_3/m_2 (33). The results are given in Figure 6. It is obvious that $S\sigma \simeq 1$ for either bosons or fermions. Then, for hadrons, $S\sigma \simeq 2$. Nevertheless, the fine structure seems to reveal interesting features.

The dependence of σ and $\sigma^2/\langle N \rangle$ on T is illustrated in Figures 2 and 4, respectively. It is obvious that both quantities have a monotonic behavior. Their dependences on μ are given in Figure 5. Also, this type of dependences seems to be monotonic. As given in Figure 6, the product $S\sigma$ has a characteristic dependence on T . Regardless of the tiny change, we notice that increasing μ increases the bosonic $S\sigma$ product but decreases the fermionic $S\sigma$ product. In both cases, it forms a folding fan. The hadronic product makes an amazing bundle in the middle (at a characteristic T). This will be discussed in details in Section 3. When S is studied

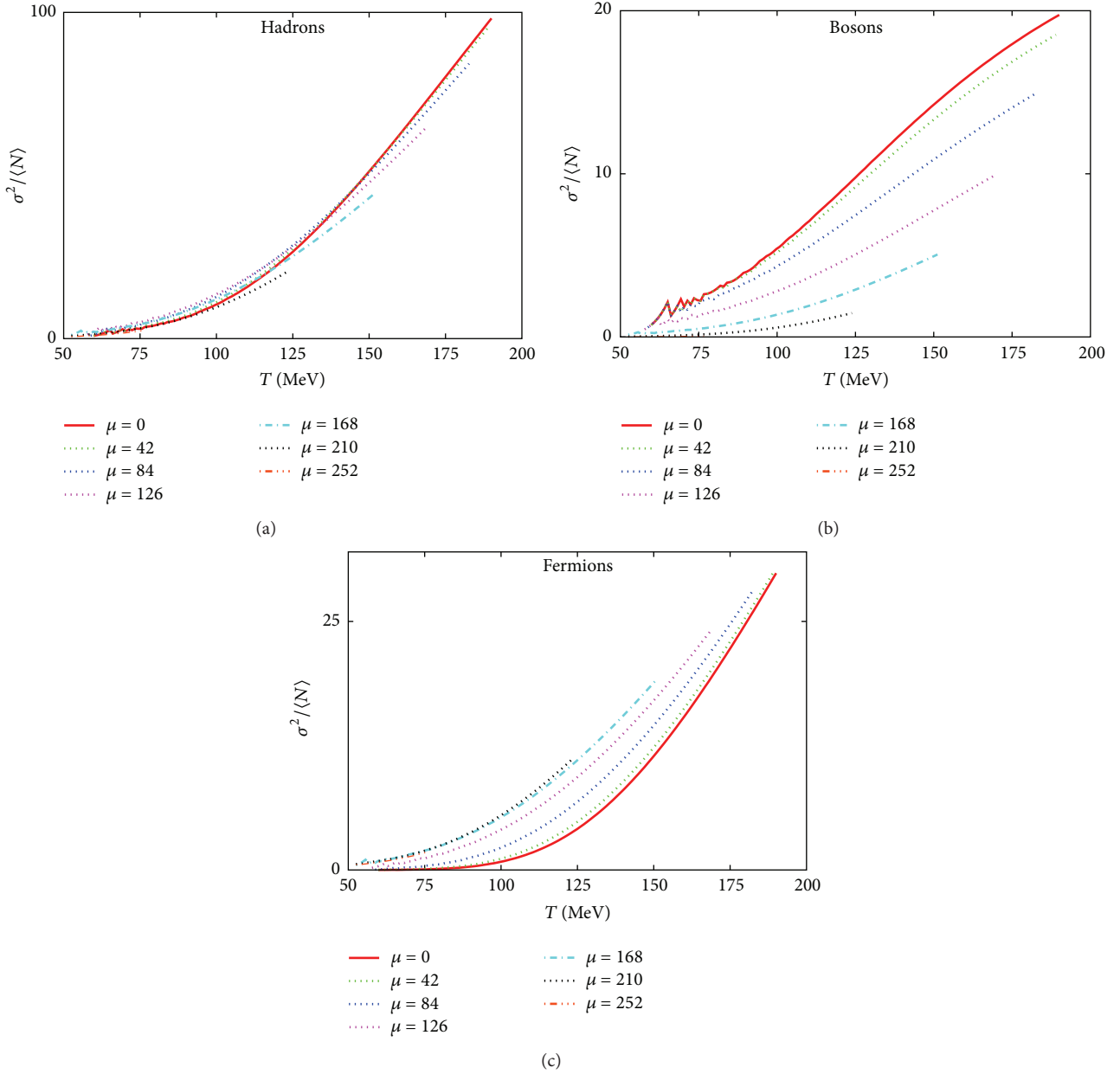


FIGURE 4: The ratio $\sigma^2/\langle N \rangle$ is given depending on T at different chemical potentials μ for hadronic (a), bosonic (b), and fermionic (c) resonance gas.

as a function of μ and given in Figure 15, we find that $S(\mu)_b$ remains almost constant, while $S(\mu)_f$ raises with increasing μ . We also notice that both curves cross at a certain point. This is not the case of the μ dependence of σ and $\sigma^2/\langle N \rangle$, Figure 5. So far, we conclude that starting from the third normalized moment, a nonmonotonic behavior appears. Thus, the kurtosis and its products should be expected to highlight such a nonmonotonic behavior [26, 64, 68].

The multiplication of kurtosis by σ^2 called κ^{eff} [69] is apparently equivalent to the ratio of third order moment to second order moment (34). In lattice QCD and QCD-like

models, κ^{eff} is found to diverge near the critical endpoint [26, 64]. In HRG, the bosonic and fermionic products read

$$\begin{aligned}
 (\kappa\sigma^2)_b &= -\frac{1}{4} \left(\int_0^\infty \left\{ \cosh \left[\frac{\varepsilon_i - \mu_i}{T} \right] + 2 \right\} \right. \\
 &\quad \left. \times \text{csch} \left[\frac{\varepsilon_i - \mu_i}{2T} \right]^4 k^2 dk \right)
 \end{aligned}$$

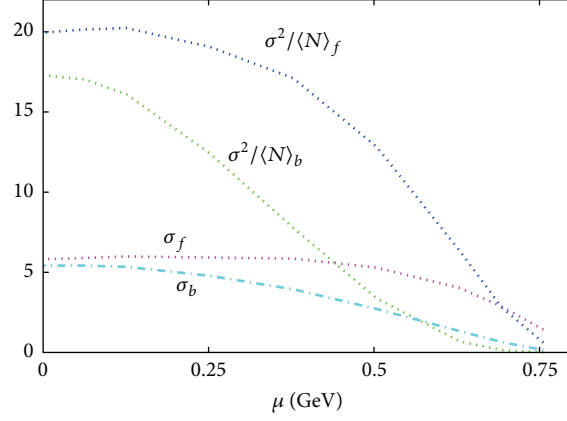


FIGURE 5: The ratio $\sigma^2/\langle N \rangle$ and σ are given depending on μ for boson and fermion resonances.

$$\begin{aligned}
& \times \left(\int_0^\infty \left(1 - \cosh \left[\frac{\varepsilon_i - \mu_i}{T} \right] \right)^{-1} k^2 dk \right)^{-1} \\
& + \frac{3g_i}{4\pi^2} \frac{1}{T^3} \int_0^\infty \left(1 - \cosh \left[\frac{\varepsilon_i - \mu_i}{T} \right] \right)^{-1} k^2 dk, \\
(\kappa\sigma^2)_f & \\
& = \frac{1}{4} \left(\int_0^\infty \left\{ \cosh \left[\frac{\varepsilon_i - \mu_i}{T} \right] - 2 \right\} \right. \\
& \quad \times \operatorname{sech} \left[\frac{\varepsilon_i - \mu_i}{2T} \right]^4 k^2 dk \\
& \quad \times \left(\int_0^\infty \left(\cosh \left[\frac{\varepsilon_i - \mu_i}{T} \right] + 1 \right)^{-1} k^2 dk \right)^{-1} \\
& \quad - \frac{3g_i}{4\pi^2} \frac{1}{T^3} \int_0^\infty \left(\cosh \left[\frac{\varepsilon_i - \mu_i}{T} \right] + 1 \right)^{-1} k^2 dk. \tag{30}
\end{aligned}$$

When ignoring the constant term in (24), then the second terms in the previous expressions entirely disappear. The results are given in Figure 7. In the hadronic sector, the dependence of $\kappa\sigma^2$ on the temperature T at different μ values is given in Figure 7(a). We notice that increasing T is accompanied with a drastic declination in $\kappa\sigma^2$. Also, we find that $\kappa\sigma^2$ flips its sign at large T . When comparing the thermal evolution of $\kappa\sigma^2$ with the one of $S\sigma$, Figure 6, we simply find that the latter is much drastically changing than the former. Also, when comparing their dependence on the chemical potentials at the freeze-out boundary, Figures 9 and 14, it is apparent that the μ dependence increases when the normalized fourth order moment is included. The product $\kappa\sigma^2$ calculated at the freeze-out boundary leads to some interesting findings. First, $\kappa\sigma^2$ almost vanishes or even flips its sign. Second, the T and μ corresponding to vanishing $\kappa\sigma^2$ are coincident with the phenomenologically measured freeze-out parameters. Third, the freeze-out boundaries of bosons and

fermions are crossing at a point located very near to the one assumed by the lattice QCD calculations to be the QCD CEP, Section 4.

The skewness and kurtosis can be combined through the standard deviation as follows:

$$\begin{aligned}
\left(\frac{\kappa\sigma}{S} \right)_b & = \left(-\frac{1}{4}\pi^2 T^3 \int_0^\infty \left\{ 2 + \cosh \left[\frac{\varepsilon_i - \mu_i}{T} \right] \right\} \right. \\
& \quad \times \operatorname{csch} \left[\frac{\varepsilon_i - \mu_i}{2T} \right]^4 k^2 dk \\
& \quad \left. + \frac{3}{4} g_i \left(\int_0^\infty \left(1 - \cosh \left[\frac{\varepsilon_i - \mu_i}{T} \right] \right)^{-1} k^2 dk \right)^2 \right) \\
& \quad \times \left(\frac{1}{4}\pi^2 T^3 \int_0^\infty \operatorname{csch} \left[\frac{\varepsilon_i - \mu_i}{2T} \right]^4 \right. \\
& \quad \left. \times \sinh \left[\frac{\varepsilon_i - \mu_i}{T} \right] k^2 dk \right)^{-1},
\end{aligned}$$

$$\begin{aligned}
\left(\frac{\kappa\sigma}{S} \right)_f & = \left(\frac{1}{4}\pi^2 T^3 \int_0^\infty \left\{ \cosh \left[\frac{\varepsilon_i - \mu_i}{T} \right] - 2 \right\} \right. \\
& \quad \times \operatorname{sech} \left[\frac{\varepsilon_i - \mu_i}{2T} \right]^4 k^2 dk \\
& \quad \left. - \frac{3}{4} g_i \left(\int_0^\infty \left(1 + \cosh \left[\frac{\varepsilon_i - \mu_i}{T} \right] \right)^{-1} k^2 dk \right)^2 \right) \\
& \quad \times \left(4\pi^2 T^3 \int_0^\infty \operatorname{csch} \left[\frac{\varepsilon_i - \mu_i}{T} \right]^3 \right. \\
& \quad \left. \times \sinh \left[\frac{\varepsilon_i - \mu_i}{2T} \right]^4 k^2 dk \right)^{-1}. \tag{31}
\end{aligned}$$

Also when ignoring the constant term in (24), the second terms in previous expressions disappear. The results of $\kappa\sigma/S$ are given in Figure 8. In the fermionic sector, $\kappa\sigma/S$ decreases with increasing T . Increasing μ makes the decrease much

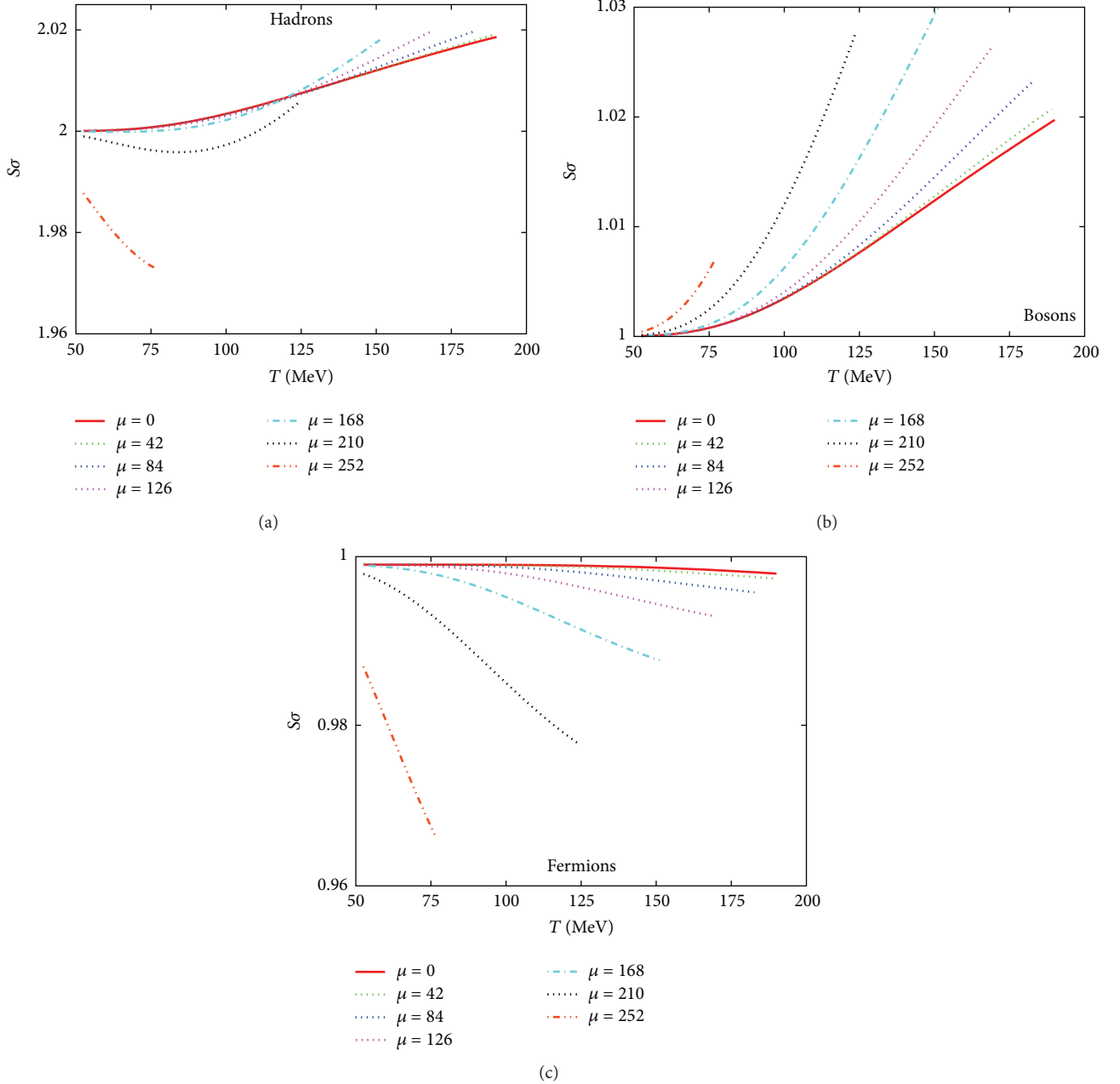


FIGURE 6: The product $S\sigma$ is given depending on T at different μ_b values (given in MeV).

faster. Despite the drastic change in $\kappa\sigma/S$, this behavior can be compared with $S\sigma$, Figure 6, qualitatively. In the bosonic sector, there is a very slow decrease with increasing μ . The same sector in $S\sigma$, Figure 6, shows a very slow but an increasing dependence on T . Therefore, in the hadronic sector, $\kappa\sigma/S$ is overall diminishing with increasing T . The declination becomes faster for larger μ . Figure 9 illustrates the μ dependence, that is, $\kappa\sigma/S$ is estimated at the freeze-out curve. We notice that the bosons result in an almost unvarying $\kappa\sigma/S$ with growing μ . Therefore, the overall decrease in the hadronic sector is originated in the fermionic degrees of freedom.

From (28)–(31), we summarize that

$$\frac{\sigma^2}{\langle N \rangle} \equiv \frac{m_2}{m_1}, \quad (32)$$

$$S\sigma \equiv \frac{m_3}{m_2}, \quad (33)$$

$$\kappa\sigma^2 \equiv \frac{m_4}{m_2}, \quad (34)$$

$$\frac{\kappa\sigma}{S} \equiv \frac{m_4}{m_3}. \quad (35)$$

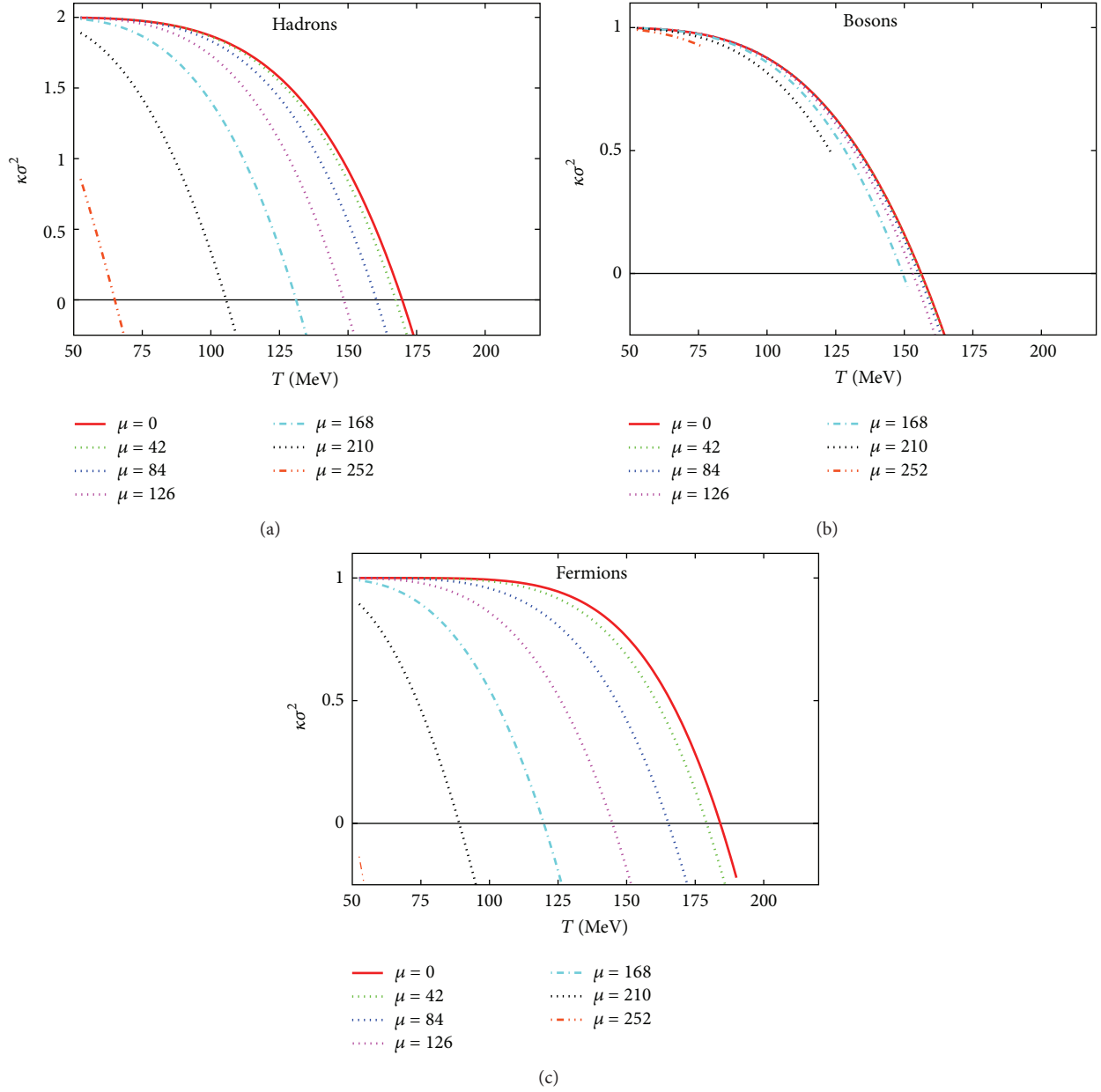


FIGURE 7: The product $\kappa\sigma^2$ is given as a function of T at various μ -values for hadronic (a), bosonic (b), and fermionic (c) resonance gas.

Obviously, other products would complete missing ratios, for example,

$$\begin{aligned} S\chi &\equiv \frac{m_3}{m_1}, \\ \frac{\kappa\chi^2}{\langle N \rangle} &\equiv \frac{m_4}{m_1}, \end{aligned} \quad (36)$$

relating third and fourth order moments to the first one, respectively. As discussed above, the susceptibility χ is equivalent to σ^2 . These products seem to be sensitive to the volume independent multiplicities.

The results of $S\chi \equiv S\sigma^2$ are given in Figure 10. At the freeze-out boundary, the μ dependence of $S\sigma^2$ seems to be much stronger than the μ dependence on $S\sigma$, Figure 11.

The thermal evolution of $\kappa\sigma^4/\langle N \rangle$ is illustrated in Figure 12. Increasing T is accompanied by an almost overall increase of $\kappa\sigma^4/\langle N \rangle$ values. At low T , fluctuations appear. In bosonic sector, increasing μ leads to an obvious decrease in $\kappa\sigma^4/\langle N \rangle$ so that the curves are distributed over a wide range. This is not the case for the fermionic sector. Figure 12(a) shows the results in the hadronic sector. At the freeze-out boundary, the values of $\kappa\sigma^4/\langle N \rangle$ at various μ -values are given in Figure 13. At large μ , both bosonic and fermionic ratios vanish. With decreasing μ , there is a bounce. It reaches its

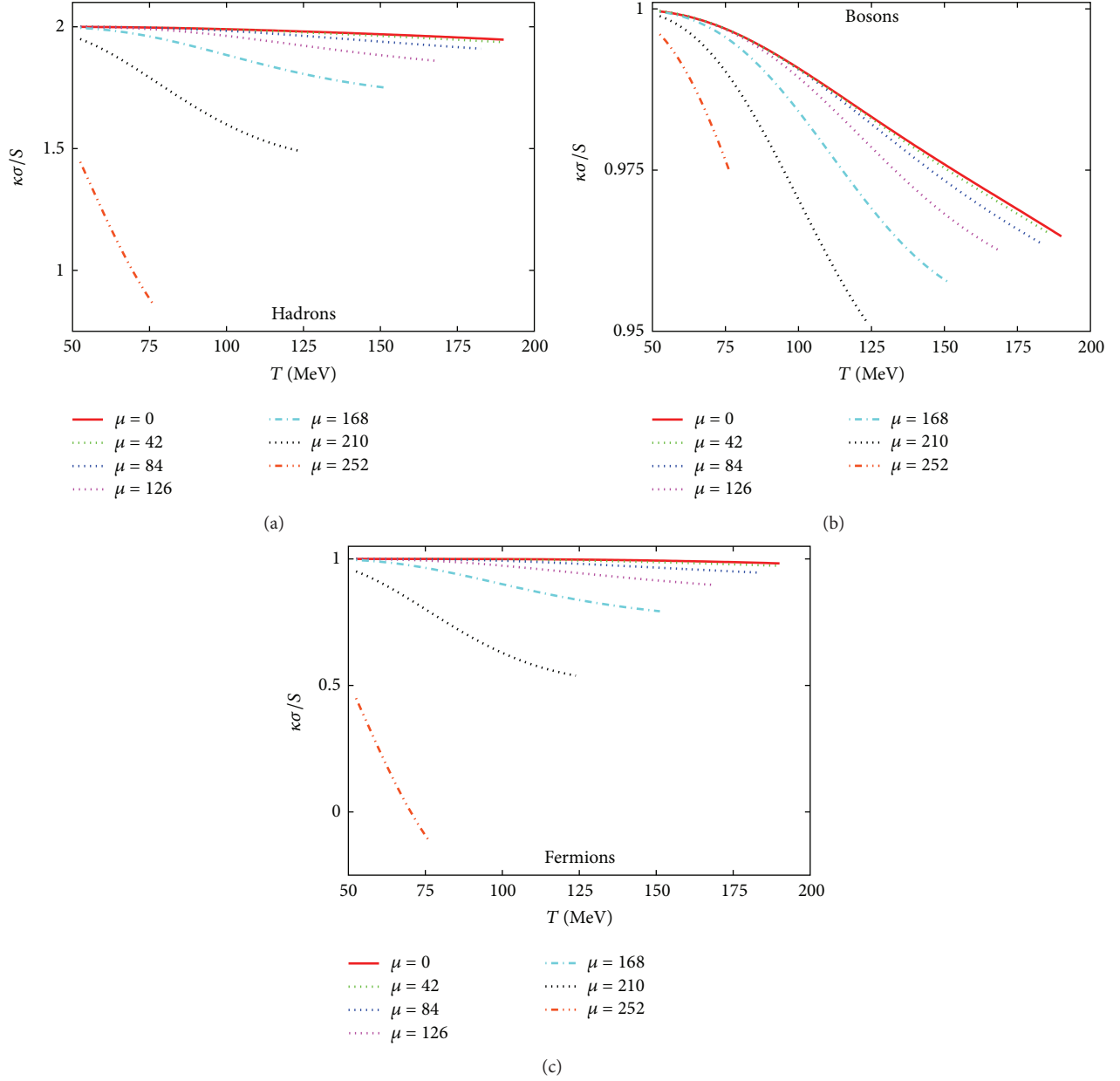


FIGURE 8: $\kappa\sigma^4/S$ as a function T at different chemical potentials for hadrons (a), bosons (b), and fermions (c).

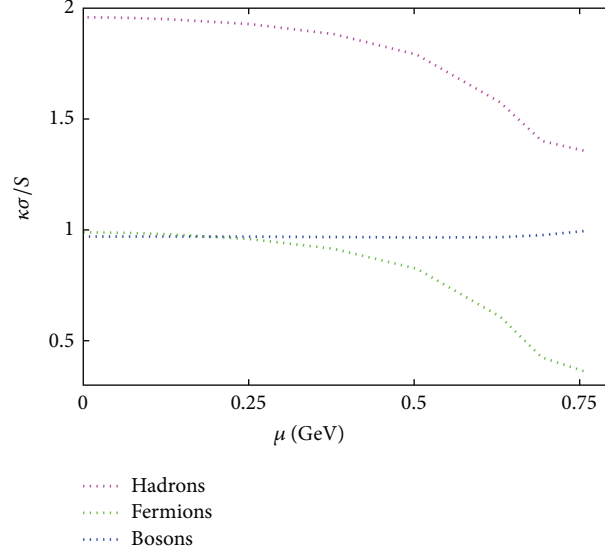
maximum over ~ 0.25 GeV. Then both curves come closer to each other. They cross again over ~ 0.2 GeV. Continue decreasing μ results in another bounce off. At smaller μ , the fermionic sector switches again to positive values, while the bosonic sector results in large negative values of $\kappa\sigma^4/\langle N \rangle$. For hadrons, $\kappa\sigma^4/\langle N \rangle$ remains almost negative. At very low μ , it turns out to small positive values.

3. Chemical Freeze-Out

In the rest frame of produced particle, the hadronic matter can be determined by constant degrees of freedom, for instance, $s/T^3(4/\pi^2) = \text{const}$ [70]. The chemical freeze-out

is related to the particle creation. Therefore, the abundance of different particle species is controlled by chemical potential, which obviously depends on T . With the beam energy, T is increasing, while the baryon densities at midrapidity are decreasing. The estimation of the macroscopic parameters of the chemical freeze-out can be extracted from particle ratio. These parameters collected over the last two decades seem to follow regular patterns as the beam energy increases [30, 37]. The higher order moments have been suggested to control the chemical freeze-out, so that several conditions have been proposed [71–73].

As introduced in Section 2.3.2, the thermal evolution of $\kappa\sigma^2$ declines. This result seems to update previous ones [48, 74], where $\kappa\sigma^2$ is assumed to remain finite and positive with

FIGURE 9: The dependence of $\kappa\sigma^2/S$ on the chemical potential μ .

increasing μ . In the present work, we find that the sign of $\kappa\sigma^2$ is flipped at high T [71–73]. It has been found that the T and μ parameters, at which the sign is flipped, amazingly coincide with the ones of the chemical freeze-out, Figure 14. Also, we find that the freeze-out boundaries of bosons and fermions are crossing at one point located at the hadronic curve. This point is close to the one that lattice QCD calculations suggest for QCD CEP, Section 4. The results are given in Figure 14. Vanishing $\kappa\sigma^2$ leads to

$$\begin{aligned}
 & \int_0^\infty \left\{ \cosh \left[\frac{(\varepsilon_i - \mu_i)}{T} \right] + 2 \right\} \operatorname{csch} \left[\frac{(\varepsilon_i - \mu_i)}{2T} \right]^4 k^2 dk \\
 &= \frac{3g_i}{\pi^2} \frac{1}{T^3} \left[\int_0^\infty \left(1 - \cosh \left[\frac{(\varepsilon_i - \mu_i)}{T} \right] \right)^{-1} k^2 dk \right]^2, \\
 & \int_0^\infty \left\{ \cosh \left[\frac{(\varepsilon_i - \mu_i)}{T} \right] - 2 \right\} \operatorname{sech} \left[\frac{(\varepsilon_i - \mu_i)}{2T} \right]^4 k^2 dk \\
 &= \frac{3g_i}{\pi^2} \frac{1}{T^3} \left[\int_0^\infty \left(\cosh \left[\frac{(\varepsilon_i - \mu_i)}{T} \right] + 1 \right)^{-1} k^2 dk \right]^2.
 \end{aligned} \tag{37}$$

The rhs and lhs in both expressions can be rewritten as

$$16 \frac{\pi^2}{g_i} T^3 \kappa = 48 \frac{\pi^2}{g_i} T^3 \chi^2, \tag{38}$$

which is valid for bosons and fermions. Then, the chemical freeze-out is defined, if the condition

$$\kappa(T, \mu) = 3\chi^2(T, \mu) \tag{39}$$

is fulfilled. At chemical freeze-out curve, a naive estimation leads to $\xi \sim 3^{1/3}$ fm. In doing this, it is assumed that the proportionality coefficients of $\kappa \sim \xi^7$ and $\chi \sim \xi^2$, are equal.

In the heavy-ion collisions, ξ has been measured [75]. Near a critical point, the experimental value ~ 2 -3 fm (only factor 3 larger) agrees well with our estimation.

At the chemical freeze-out curve, the intensive parameters T and μ which are related to the extensive properties entropy and particle number, respectively, have to be determined over a wide range of beam energies. Left panel of Figure 14 collects a large experimental data set. For a recent review, we refer to [30] and the references therein. The double-dotted curve represents a set of T and μ , at which $\kappa\sigma^2$ vanishes. It is obvious that this curve reproduces very well the experimental data. As given above, at this curve the normalized fourth order moment κ is equal to three times the squared susceptibility χ . This new condition seems to guarantee the condition introduced in [37]; $s/T^3 = \text{const.}$, right panel of Figure 14, at least over the range $0 < \mu < 0.6$ GeV. When excluding all degrees of freedom but the fermionic ones, s/T^3 decreases with increasing μ (dashed curve). An opposite dependence is accompanied with the bosonic degrees of freedom (dotted curve).

4. QCD Critical Endpoint

In the right panel of Figure 14, it is interesting to notice that both fermionic and bosonic curves intersect at the hadronic curve at one point. Also, in the freeze-out diagram, all curves crossing at one point, left panel of Figure 14. Furthermore, based on nonperturbative convergence radius, the critical endpoint as calculated in lattice QCD [5, 6] given by solid square in Figure 14 is located very near to the crossing point. It is clear that the HRG model does not contain any information on criticality related with the chiral dynamics and singularity in physical observables required to locate the CP. The HRG partition function is an approximation to a nonsingular part of the free energy of QCD in the hadronic phase. It can be used only as the reference for LGT calculations or HIC to

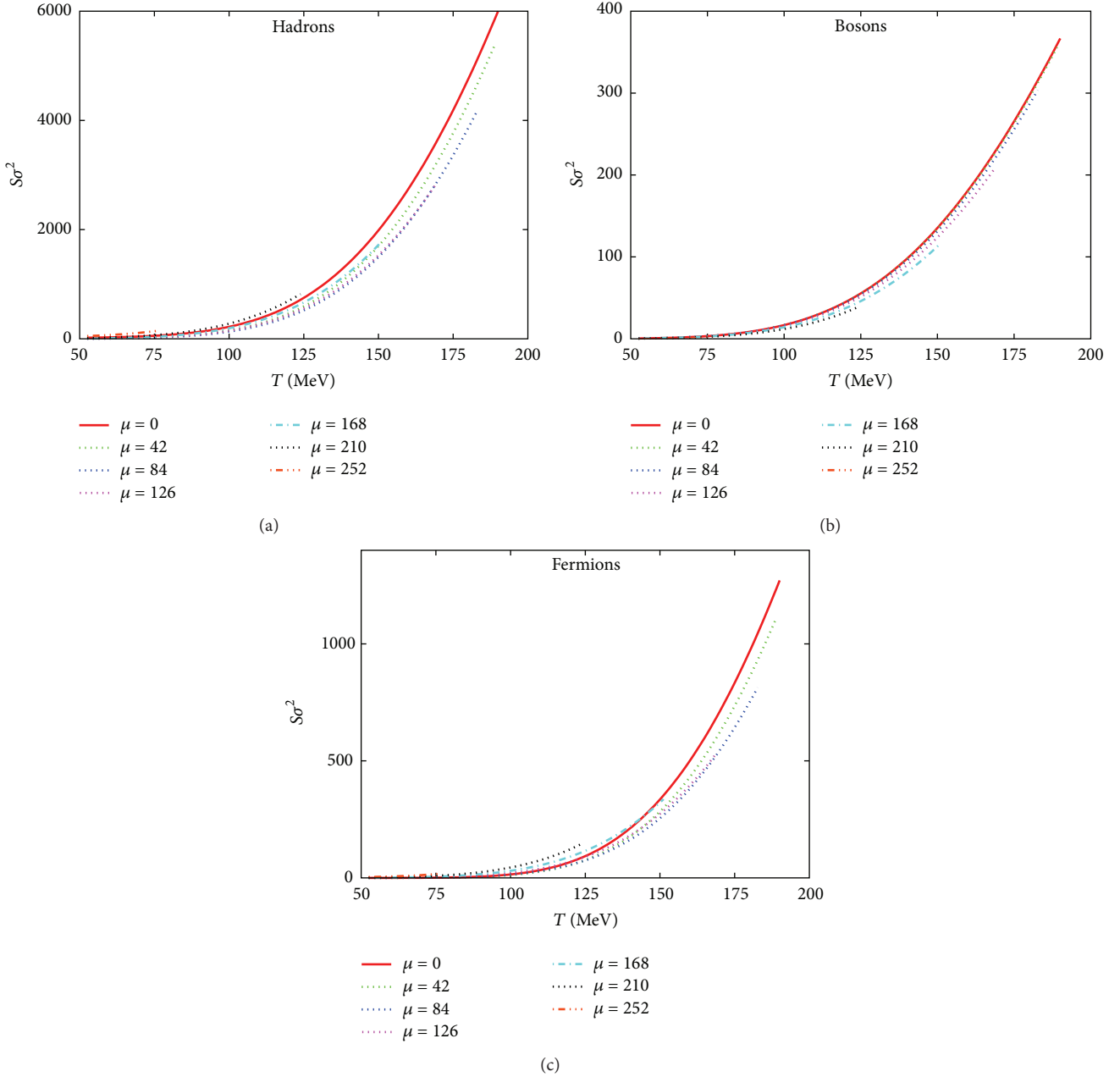


FIGURE 10: The thermal evolution of $S\sigma^2$ for hadrons (a), bosons (b), and fermions (c) at different μ -values (given in MeV).

verify the critical behavior, but it can not be used as an origin to search for the chiral critical structure in QCD medium. This is the motivation of Figure 15.

In Figure 15, the skewness and kurtosis of bosons and fermions calculated at the freeze-out curve are given depending on μ (left panel) and center-of-mass energy \sqrt{s} (right panel). It seems that the evolution of fermionic and bosonic skewness and kurtosis coincide at one point, marked with the vertical band. This fact would reflect the nature of the phase transition. It would be the critical endpoint connecting cross-over with the first order deconfinement phase transitions. At QCD CEP, the phase transition is conjectured to be of second order. It is worthwhile to mention that the crossing point is

amazingly coincident with the QCD CEP measured in lattice QCD [5, 6], Figure 14, regardless of its uncertainties.

From (23) and (24), the following expressions have to be solved in μ , individually and/or dependently, in order to determine μ of the crossing point:

$$\begin{aligned}
 & - \frac{\int_0^\infty \text{csch}[(\varepsilon_i - \mu_i)/2T]^4 \sinh[(\varepsilon_i - \mu_i)/T] k^2 dk}{\left[\int_0^\infty (\cosh[(\varepsilon_i - \mu_i)/T] - 1)^{-1} k^2 dk \right]^{3/2}} \\
 & = 16 \left(\int_0^\infty \text{csch}\left[\frac{\varepsilon_i - \mu_i}{T}\right]^3 \sinh\left[\frac{\varepsilon_i - \mu_i}{2T}\right]^4 k^2 dk \right)
 \end{aligned}$$

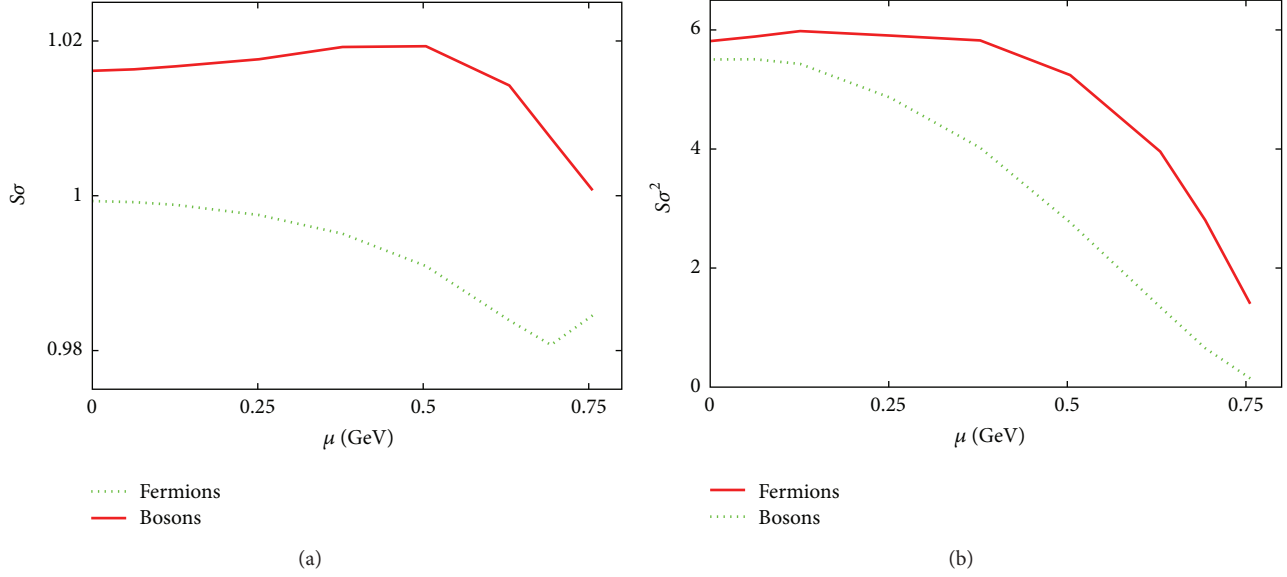


FIGURE 11: The dependence of $S\sigma$ (a) and $S\sigma^2$ (b) of bosons and fermions on the chemical potential μ (given in MeV).

$$\begin{aligned}
 & \times \left(\left[\int_0^\infty \left(\cosh \left[\frac{\varepsilon_i - \mu_i}{T} \right] + 1 \right)^{-1} k^2 dk \right]^{3/2} \right)^{-1}, \\
 & - \frac{\int_0^\infty \{ \cosh [(\varepsilon_i - \mu_i)/T] + 2 \} \operatorname{csch} [(\varepsilon_i - \mu_i)/(2T)]^4 k^2 dk}{\left[\int_0^\infty (1 - \cosh [(\varepsilon_i - \mu_i)/T])^{-1} k^2 dk \right]^2} \\
 & = \int_0^\infty \left\{ \cosh \left[\frac{\varepsilon_i - \mu_i}{T} \right] - 2 \right\} \operatorname{sech} \left[\frac{\varepsilon_i - \mu_i}{2T} \right]^4 k^2 dk \\
 & \times \left(\left[\int_0^\infty \left(\cosh \left[\frac{\varepsilon_i - \mu_i}{T} \right] + 1 \right)^{-1} k^2 dk \right]^2 \right)^{-1}.
 \end{aligned} \tag{40}$$

Due to the mathematical difficulties in dealing with these expressions, the integral over phase space has to be simplified. A suitable simplification is given in Section 2.3.1.

$$\begin{aligned}
 \frac{P(T, \mu_q, \mu_s)}{T^4} &= \pm \frac{1}{2\pi^2 T^3} \sum_{i=1}^{\infty} g_i m_i^2 \sum_{n=1}^{\infty} \frac{(\pm)^{n+1}}{n^2} \\
 & \times K_2 \left(n \frac{m_i}{T} \right) \exp \left[n \frac{(3n_b + n_s) \mu_q - n_s \mu_s}{T} \right],
 \end{aligned} \tag{41}$$

where n_b and n_s being baryon (strange) quantum number and μ_q (μ_s) is the baryon (strange) chemical potential of light and strange quarks, respectively. The quarks chemistry is introduced in Section 2. Accordingly, the difference between baryons and fermions is originated in the exponential function. For simplicity, we consider one fermion and one boson particle. Then, the baryon chemical potential μ at the chemical freeze-out curve at which the fermionic and bosonic

skewness (or kurtosis) curves of these two particles cross with each other can be given as

$$\mu_b = 3n_b \mu_q = T \ln \left[\frac{g_b m_b^2 K_2(m_b/T)}{g_f m_f^2 K_2(m_f/T)} \right]. \tag{42}$$

In the relativistic limit, $K_2(m/T) \approx 2T^2/m^2 - 1/2$ while in the nonrelativistic limit $K_2(m/T) \approx \sqrt{\pi T/2m} \exp(-m/T)(1 + 15T/8m)$. It is obvious that the bosonic and fermionic degrees of freedom play an essential role in determining (42). Furthermore, it seems that the chemical potential of strange quark has no effect at the crossing point.

The dependence of μ_s on μ_b as calculated in HRG is given in Figure 16. As mentioned above, μ_s is calculated to guarantee strange number conservation in heavy-ion collisions. At small μ_b , μ_s has a linear dependence, $\mu_s = 0.25\mu_b$ (Hooke's limit). At large μ_b , the dependence is no longer linear.

As discussed earlier, the critical behavior and the existence of QCD CEP can be identified by means of signatures sensitive to singular parts of the free energy, especially the ones reflecting dynamical fluctuations of conserved charges, such as baryon number and charge density [76]. The reason that the fermionic and bosonic higher order moments are crossing on a point very near the QCD CEP shall be elaborated in a forthcoming work [77].

5. Conclusion

In the present work, the first six nonnormalized order moments of the particle multiplicity are calculated in the hadron resonance gas model. General expressions for arbitrary higher order moments are deduced in terms of lower

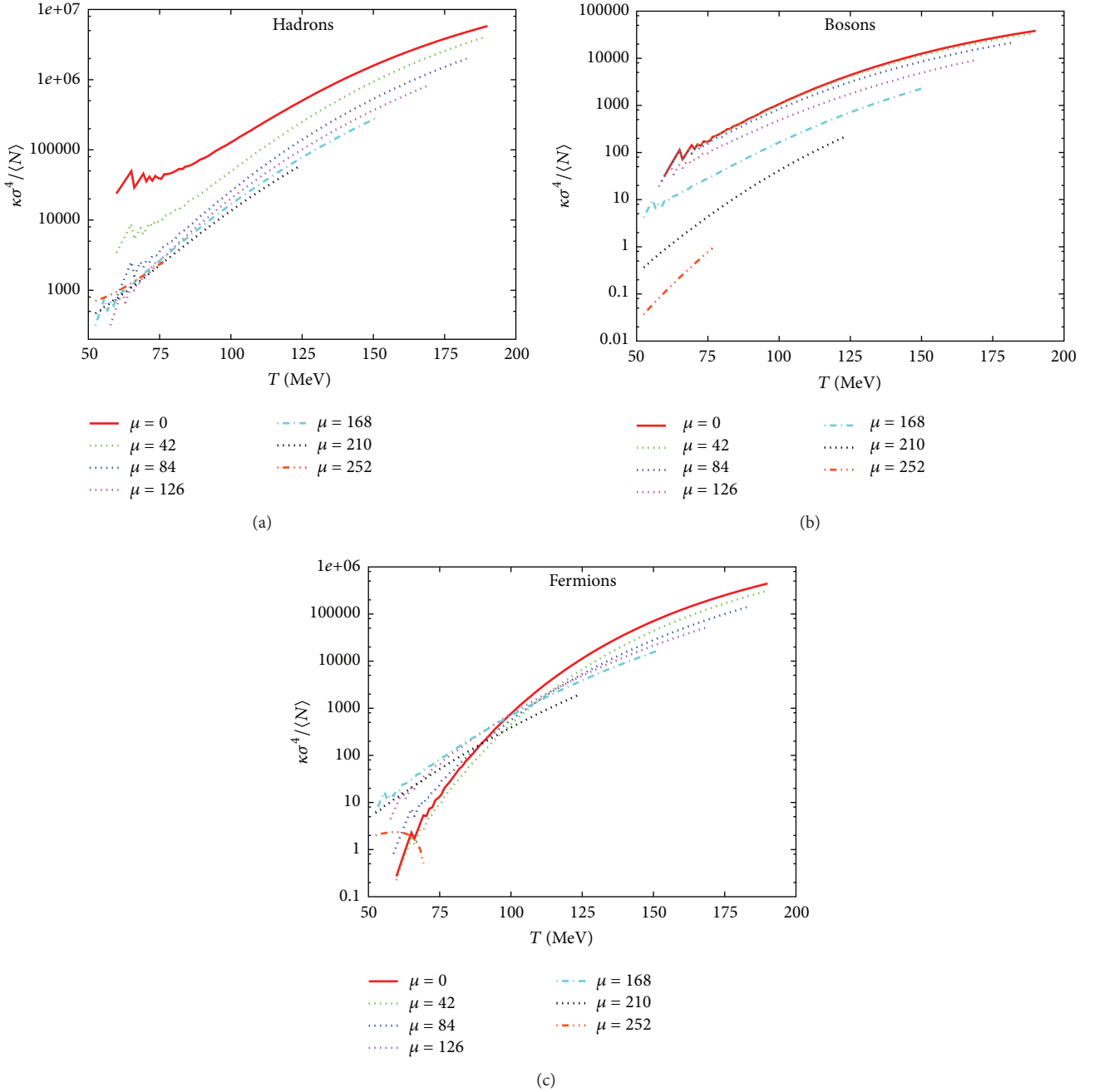


FIGURE 12: Thermal evolution of $\kappa\sigma^4/\langle N \rangle$ for hadrons (a), bosons (b) and fermions (c) at different chemical potentials (given in MeV).

ones. We concluded that going from lower to higher order moments is possible through adding up a series that consists of all lower order moments plus correlation functions. We studied the thermal evolution of the first four normalized order moments and their products (ratios) at different chemical potentials μ . By doing that, it was possible to evaluate first four normalized moments at the chemical freeze-out curve. The freeze-out curve is characterized by constant s/T^3 at all values of μ , where s and T are entropy density and

temperature, respectively. It has been found that nonmonotonic behavior reflecting dynamical fluctuation and strong correlations appears starting from the normalized third order moment (skewness S). Furthermore, nonmonotonicity is observed in the normalized fourth order moment, the kurtosis κ , and its products. These are novel observations. Although HRG is exclusively applicable below T_c , that is, it does not include deconfinement phase transition, it is apparent that the higher order moments are able to give

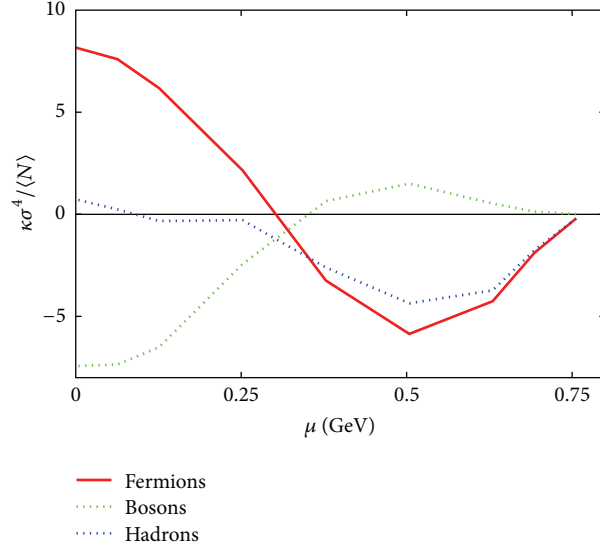


FIGURE 13: The ratio $\kappa\sigma^4/\langle N \rangle$ is given in depending on μ for boson and fermion resonances.

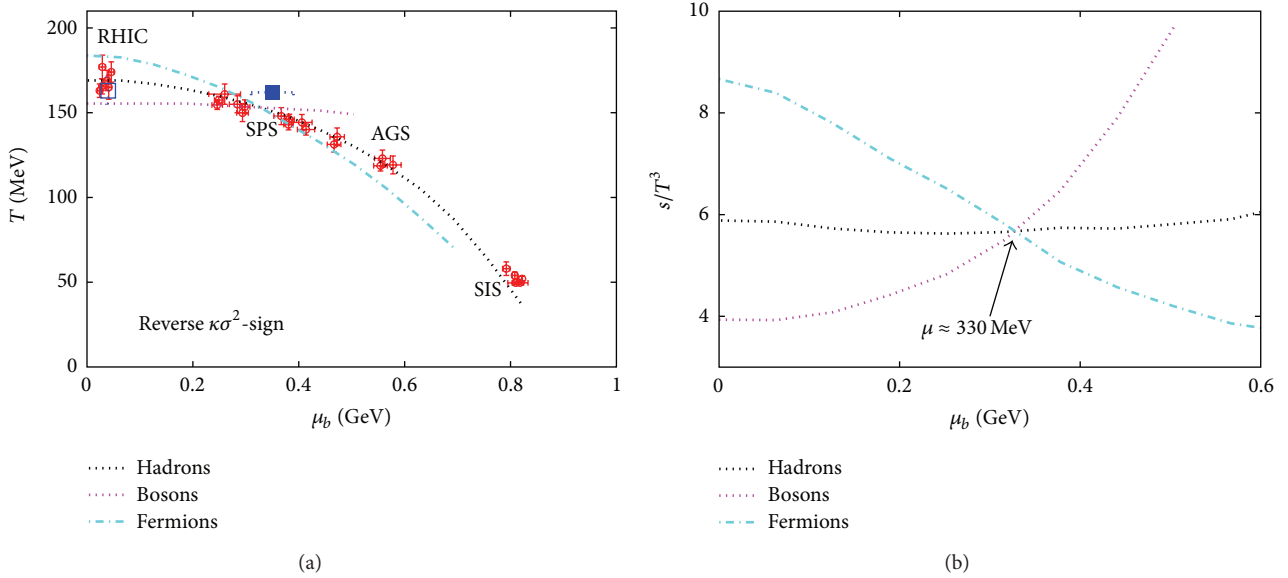


FIGURE 14: (a) illustrates the chemical freeze-out boundary. The experimental data are given by the solid circles. The curves represent the results of hadron, boson, and fermion gas determined when the sign of $\kappa\sigma^2$ is flipped. (b) gives the corresponding s/T^3 values. The lattice QCD endpoint is marked by solid square.

signatures for the critical phase transition. The accuracy of our calculations made it possible to have clear evidence on the phase transition. Based on these findings, we introduced novel conditions characterizing the chemical freeze-out curve and the location of the QCD critical endpoint as follows. The chemical freeze-out curve is described by $\kappa = 3\chi^2$, where χ is the susceptibility in particle number, that is, the second order moment. The location of QCD critical endpoint (at T and μ axes) is positioned when the condition

$S_b = S_f$ or $\kappa_b = \kappa_f$ is fulfilled. The subscripts b and f refer to bosons and fermions, respectively. Accordingly, the QCD endpoint is positioned at $\mu \sim 350$ MeV and $T \sim 162$ MeV. We are able to estimate these two quantities, although the hadron resonance gas model basically does not contain information on criticality related with the chiral dynamics and singularity in physical observables required to locate the critical endpoint. After submitting this work, a new paper was posted in arXiv, in which the authors used the second order

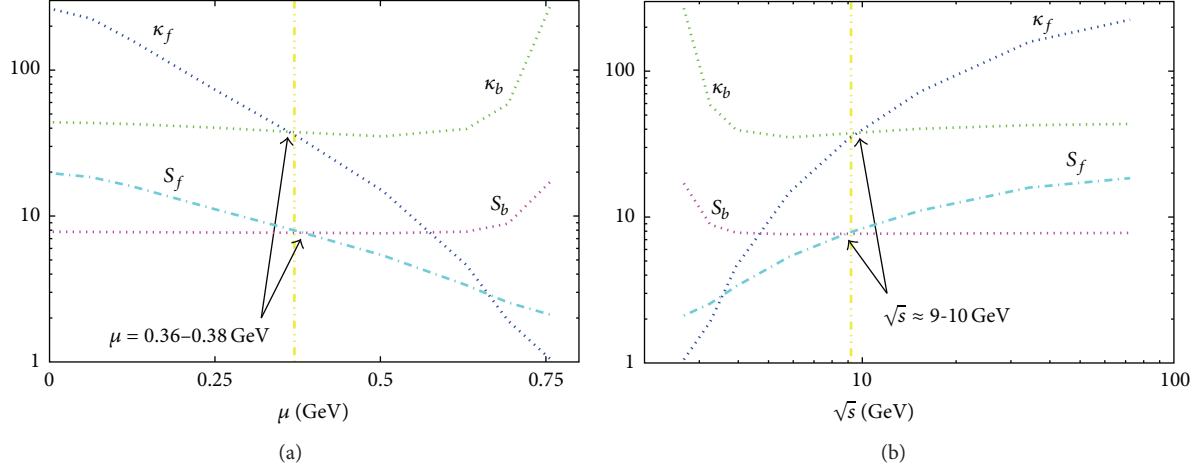


FIGURE 15: Left panel: Skewness and kurtosis at the freeze-out boundary for fermions and bosons. The curves of both quantities are crossing at almost the same μ -value. The corresponding T -values are almost equal.

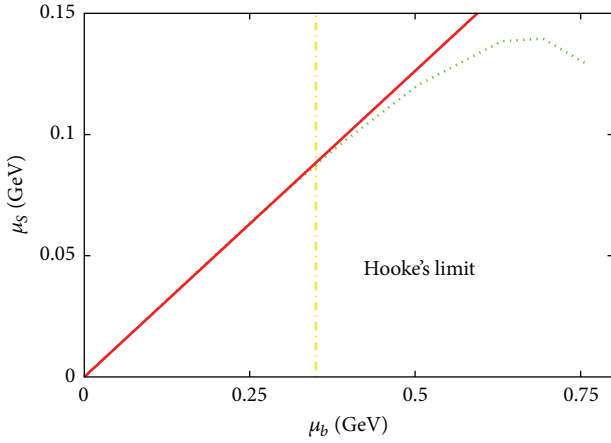


FIGURE 16: μ_s as a function of μ_b in hadron resonance gas model (dotted curve). The linear fitting is given by solid curve.

moment (susceptibility) and the fourth order one (kurtosis) that are apparently sensitive to the phase transition [78].

Acknowledgment

This work is partly supported by the German-Egyptian Scientific Projects (GESp ID: 1378).

References

- [1] C. Athanasiou, K. Rajagopal, and M. Stephanov, "Using higher moments of fluctuations and their ratios in the search for the QCD critical point," *Physical Review D*, vol. 82, no. 7, Article ID 074008, 2010.
- [2] J. Adams, M. M. Aggarwal, Z. Ahammed et al., "Experimental and theoretical challenges in the search for the quark gluon plasma: the STAR Collaboration's critical assessment of the evidence from RHIC collisions," *Nuclear Physics A*, vol. 757, p. 102, 2005.
- [3] A. Tawfik, "QCD phase diagram: a comparison of lattice and hadron resonance gas model calculations," *Physical Review D*, vol. 71, Article ID 054502, 2005.
- [4] M. A. Stephanov, "QCD phase diagram and the critical point," *International Journal of Modern Physics A*, vol. 20, p. 4387, 2005.
- [5] Z. Fodor and S. D. Katz, "Critical point of QCD at finite T and μ , lattice results for physical quark masses," *Journal of High Energy Physics*, vol. 0404, p. 50, 2004.
- [6] R. V. Gavai and S. Gupta, "QCD at finite chemical potential with six time slices," *Physical Review D*, vol. 78, no. 11, Article ID 114503, 2008.
- [7] A. Tawfik, "Phase space and dynamical fluctuations of kaon-to-pion ratios," *Progress of Theoretical Physics*, vol. 126, no. 2, pp. 279–292, 2011.
- [8] A. Tawfik, "Matter—antimatter asymmetry in heavy-ion collisions," *International Journal of Theoretical Physics*, vol. 51, pp. 1396–1407, 2012.
- [9] A. Tawfik, "Antiproton-to-proton ratios for ALICE heavy-ion collisions," *Nuclear Physics A*, vol. 859, no. 1, pp. 63–72, 2011.
- [10] A. Tawfik, "Event-by-event fluctuations of particle ratios in heavy-ion collisions," *FIZIKA B*, vol. 18, pp. 141–150, 2009.
- [11] A. Tawfik, "Dynamical fluctuations in baryon-meson ratios," *Journal of Physics G*, vol. 40, Article ID 055109, 2013.
- [12] A. Tawfik, "Fluctuations of particle yield ratios in heavy-ion collisions," *Indian Journal of Physics*, vol. 86, pp. 1139–1146, 2012.
- [13] A. Tawfik, "Black box QGP," <http://arxiv.org/abs/hep-ph/0604037>.
- [14] M. I. Adamovich, M. M. Aggarwal, N. P. Andreeva et al., "Factorial moments of Si-28 induced interactions with Ag(Br) nuclei," *Acta Physica Hungarica A*, vol. 13, no. 4, pp. 213–221, 2001.
- [15] X. Luo, "Search for the QCD critical point by higher moments of net-proton multiplicity distributions at RHIC," *Acta Physica Polonica B*, vol. 5, no. 2, p. 497, 2012.
- [16] X. Luo, "Probing the QCD critical point with higher moments of net-proton multiplicity distributions," *Journal of Physics: Conference Series*, vol. 316, Article ID 012003, 2011.
- [17] M. M. Aggarwal, Z. Ahammed, A. V. Alakhverdyants et al., "Higher moments of net proton multiplicity distributions at RHIC," *Physical Review Letters*, vol. 105, Article ID 022302, 2010.

- [18] T. J. Tarnowsky, "Searching for the QCD critical point using particle ratio fluctuations and higher moments of multiplicity distributions," *Journal of Physics G*, vol. 38, Article ID 124054, 2011.
- [19] T. K. Nayak, "Study of the fluctuations of net-charge and net-protons using higher order moments," *Nuclear Physics A*, vol. 830, pp. 555C–558C, 2009.
- [20] M. A. York and G. D. Moore, "Exploring the phase diagram with Taylor series: epic voyage or just another bad trip," <http://arxiv.org/abs/1106.2535>.
- [21] M. A. Stephanov, "Non-Gaussian fluctuations near the QCD critical point," *Physical Review Letters*, vol. 102, no. 3, Article ID 032301, 2009.
- [22] Y. Zhou, S. S. Shi, K. Xiao, K. J. Wu, and F. Liu, "Higher moments of net-baryon distribution as probes of QCD critical point," *Physical Review C*, vol. 82, Article ID 014905, 2010.
- [23] M. Stephanov, K. Rajagopal, and E. Shuryak, "Event-by-event fluctuations in heavy ion collisions and the QCD critical point," *Physical Review D*, vol. 60, no. 11, Article ID 114028, 32 pages, 1999.
- [24] Y. Aoki, G. Endrodi, Z. Fodor, S. D. Katz, and K. K. Szabó, "The order of the quantum chromodynamics transition predicted by the standard model of particle physics," *Nature*, vol. 443, no. 7112, pp. 675–678, 2006.
- [25] M. Cheng, N. H. Christ, S. Datta et al., "The transition temperature in QCD," *Physical Review D*, vol. 74, Article ID 054507, 2006.
- [26] M. Cheng, P. Hegde, C. Jung et al., "Baryon number, strangeness and electric charge fluctuations in QCD at high temperature," *Physical Review D*, vol. 79, Article ID 074505, 2009.
- [27] F. Karsch, K. Redlich, and A. Tawfik, "Hadron resonance mass spectrum and lattice QCD thermodynamics," *European Physical Journal C*, vol. 29, no. 4, pp. 549–556, 2003.
- [28] F. Karsch, K. Redlich, and A. Tawfik, "Thermodynamics at non-zero baryon number density: a comparison of lattice and hadron resonance gas model calculations," *Physics Letters B*, vol. 571, no. 1-2, pp. 67–74, 2003.
- [29] K. Redlich, F. Karsch, and A. Tawfik, "Heavy-ion collisions and lattice QCD at finite baryon density," *Journal of Physics G*, vol. 30, no. 8, pp. S1271–S1274, 2004.
- [30] J. Cleymans, H. Oeschler, K. Redlich, and S. Wheaton, "Comparison of chemical freeze-out criteria in heavy-ion collisions," *Physical Review C*, vol. 73, no. 3, Article ID 034905, 2006.
- [31] S. Ejiri, "Canonical partition function and finite density phase transition in lattice QCD," *Physical Review D*, vol. 78, Article ID 074507, 2008.
- [32] E. S. Bowman and J. I. Kapusta, "Critical points in the linear σ model with quarks," *Physical Review D*, vol. 79, Article ID 015202, 2009.
- [33] B. I. Abelev, M. M. Aggarwal, Z. Ahammed et al., "Identified particle production, azimuthal anisotropy, and interferometry measurements in Au + Au collisions at $\sqrt{s_{NN}} = 9.2$ -GeV," *Physical Review C*, vol. 81, Article ID 024911, 2010.
- [34] S.-X. Qin, L. Chang, H. Chen, Y.-X. Liu, and C. D. Roberts, "Phase diagram and critical end point for strongly interacting quarks," *Physical Review Letters*, vol. 106, Article ID 172301, 2011.
- [35] A. Tawfik, "Influence of strange quarks on the QCD phase diagram and chemical freeze-out," *Journal of Physics G*, vol. 31, no. 6, pp. S1105–S1110, 2005.
- [36] A. Tawfik, "In-medium modifications of hadron properties," *Indian Journal of Physics*, vol. 85, no. 5, pp. 755–766, 2011.
- [37] A. Tawfik, "A universal description for the freezeout parameters in heavy-ion collisions," *Nuclear Physics A*, vol. 764, no. 1–4, pp. 387–392, 2006.
- [38] A. Tawfik, "Condition driving chemical freeze-out," *Europhysics Letters*, vol. 75, no. 3, pp. 420–426, 2006.
- [39] R. Hagedorn, "Statistical thermodynamics of strong interactions at high-energies," *Nuovo Cimento, Supplemento*, vol. 3, pp. 147–186, 1965.
- [40] R. Venugopalan and M. Prakash, "Thermal properties of interacting hadrons," *Nuclear Physics A*, vol. 546, no. 4, pp. 718–760, 1992.
- [41] M. Gell-Mann and M. Lévy, "The axial vector current in beta decay," *Il Nuovo Cimento*, vol. 16, no. 4, pp. 705–726, 1960.
- [42] R. Hagedorn, "Statistical thermodynamics of strong interactions at high energies. 3. Heavy-pair (quark) production rates," *Nuovo Cimento, Supplemento*, vol. 6, pp. 311–354, 1968.
- [43] R. Hagedorn, "Hadronic matter near the boiling point," *Il Nuovo Cimento A*, vol. 56, no. 4, pp. 1027–1057, 1968.
- [44] R. J. Eden, P. V. Landshoff, D. I. Olive, and J. C. Polkinghorne, *The Analytic S-Matrix*, Cambridge University Press, London, UK, 1966.
- [45] J. Letessier and J. Rafelski, *Hadrons and Quark-Gluon Plasma*, Cambridge University Press, 2002.
- [46] V. Gupta, "Predictions for the higher moments of the charged-particle multiplicity distribution," *Lettere al Nuovo Cimento*, vol. 5, no. 1, pp. 108–111, 1972.
- [47] B.-J. Schaefer and M. Wagner, "QCD critical region and higher moments for three flavor models," *Physical Review D*, Article ID 034027, 2012.
- [48] C. Miao, "Higher moments of charge fluctuations in QCD at high temperature," *Nuclear Physics A*, vol. 830, pp. 705C–708C, 2009.
- [49] P. Hegde, "Fluctuations and higher moments of conserved charges from the lattice," in *Proceedings of the 19th Particles and Nuclei International Conference (PANIC '11)*, vol. 1441 of *AIP Conference Proceedings*, pp. 898–900, July 2011.
- [50] K. P. Ballanda and H. L. MacGillivray, "Kurtosis: a critical review," *American Statistician*, vol. 42, pp. 111–119, 1988.
- [51] R. Singer, Y. Cho, T. Fields et al., "Two-particle rapidity correlations in 205 GeV/c pp interactions," *Physics Letters B*, vol. 49, p. 481, 1974.
- [52] U. Heinz and B. V. Jacak, "Two-particle correlations in relativistic heavy-ion collisions," *Annual Review of Nuclear and Particle Science*, vol. 49, pp. 529–579, 1999.
- [53] S. Chapman, J. R. Nix, and U. Heinz, "Extracting source parameters from Gaussian fits to two-particle correlations," *Physical Review C*, vol. 52, no. 5, pp. 2694–2703, 1995.
- [54] E. Braidot, "Two-particle correlations at forward rapidity in STAR," *Nuclear Physics A*, vol. 854, pp. 168–174, 2011.
- [55] C. Adler, Z. Ahammed, C. Allgower et al., "Elliptic flow from two and four particle correlations in Au + Au collisions at $\sqrt{s_{NN}} = 130$ -GeV," *Physical Review C*, vol. 66, Article ID 034904, 2002.
- [56] G. A. Kozlov, "New features of two-particle correlations," *Physics of Particles and Nuclei*, vol. 36, no. 2, pp. S190–S197, 2005.
- [57] R. Perez-Ramos, "Single inclusive distribution and two-particle correlations inside one jet at 'modified leading logarithmic approximation' of quantum chromodynamics II. Steepest descent evaluation at small x ," *Journal of High Energy Physics*, vol. 2006, no. 9, article 014, 2006.

- [58] E. A. De Wolf, I. M. Dremin, and W. Kittel, "Scaling laws for density correlations and fluctuations in multiparticle dynamics," *Physics Report*, vol. 270, no. 3, pp. 1–141, 1996.
- [59] W. Kittel and E. A. De Wolf, *Soft Multihadron Dynamics*, World Scientific, Singapore, 2005.
- [60] N. L. Johnson, S. Kotz, and N. Balakrishnan, *Continuous Univariate Distribution*, Houghton Mifflin, Boston, MA, 1970.
- [61] C. T. Hsu and D. N. Lawley, "The derivation of the fifth and sixth moments of the distribution of b_2 in samples from a normal population," *Biometrika*, vol. 31, pp. 238–248, 1940.
- [62] M. Asakawa, S. Ejiri, and M. Kitazawa, "Third moments of conserved charges as probes of QCD phase structure," *Physical Review Letters*, vol. 103, no. 26, Article ID 262301, 2009.
- [63] M. Kitazawa, M. Asakawa, and S. Ejiri, "Third moments of conserved charges in QCD phase diagram," *PoS LAT2009*, vol. 174, 2009.
- [64] B. Stokic, B. Friman, and K. Redlich, "Kurtosis and compressibility near the chiral phase transition," *Physics Letters B*, vol. 673, pp. 192–196, 2009.
- [65] R. V. Gavai and S. Gupta, "Lattice QCD predictions for shapes of event distributions along the freezeout curve in heavy-ion collisions," *Physics Letters B*, vol. 696, no. 5, pp. 459–463, 2011.
- [66] F. Katsch and K. Redlich, "Probing freeze-out conditions in heavy ion collisions with moments of charge fluctuations," *Physics Letters B*, vol. 695, pp. 136–142, 2010.
- [67] B. I. Abelev, M. M. Aggarwal, Z. Ahammed et al., "Beam-energy and system-size dependence of dynamical net charge fluctuations," *Physical Review C*, vol. 79, Article ID 024906, 2009.
- [68] X. Luo, B. Mohanty, H. G. Ritter, and N. Xu, "Higher moments of net-proton multiplicity distributions," *Physics of Atomic Nuclei*, vol. 75, no. 6, pp. 676–678, 2012.
- [69] T. Schuster, "Net-baryon-, net-proton-, and net-charge kurtosis in heavy-ion collisions within a relativistic transport approach," *The European Physical Journal C*, vol. 72, p. 2143, 2012.
- [70] J. Cleymans, M. Stankiewicz, P. Steinberg, and S. Wheaton, "The origin of the difference between multiplicities in e^+e^- annihilation and heavy ion collisions," submitted to *Physics Letters B*.
- [71] B. Friman, F. Karsch, K. Redlich, and V. Skokov, "Fluctuations as probe of the QCD phase transition and freeze-out in heavy ion collisions at LHC and RHIC," *The European Physical Journal C*, vol. 71, p. 1694, 2011.
- [72] R. V. Gavai and S. Gupta, "Lattice QCD predictions for shapes of event distributions along the freezeout curve in heavy-ion collisions," *Physics Letters B*, vol. 696, pp. 459–463, 2011.
- [73] F. Karsch, "Moments of charge fluctuations, pseudo-critical temperatures and freeze-out in heavy-ion collisions," *Journal of Physics G*, vol. 38, no. 12, Article ID 124098, 2011.
- [74] F. Karsch, B.-J. Schaefer, M. Wagner, and J. Wambach, "Towards finite density QCD with Taylor expansions," *Physics Letters B*, vol. 698, no. 3, pp. 256–264, 2011.
- [75] B. Berdnikov and K. Rajagopal, "Slowing out of equilibrium near the QCD critical point," *Physical Review D*, vol. 61, Article ID 105017, 9 pages, 2000.
- [76] E. Nakano, B.-J. Schaefer, B. Stokic, B. Friman, and K. Redlich, "Fluctuations and isentropes near the chiral critical endpoint," *Physics Letters B*, vol. 682, no. 4-5, pp. 401–407, 2010.
- [77] A. Tawfik, "Chemical freeze-out and higher order multiplicity moments," <http://arxiv.org/abs/1306.1025>.
- [78] A. Nakamura and K. Nagata, "Probing QCD phase structure by baryon multiplicity distribution," <http://arxiv.org/abs/1305.0760>.

Review Article

Role of Magnetic Interaction in Dense Plasma

S. Sarkar,¹ K. Pal,² and A. K. Dutt-Mazumder¹

¹ High Energy Nuclear and Particle Physics Division, Saha Institute of Nuclear Physics, 1/AF Bidhannagar, Kolkata 700 064, India

² Serampore College, Serampore 712201, India

Correspondence should be addressed to S. Sarkar; sreemoyee.sarkar@saha.ac.in

Received 21 March 2013; Revised 12 June 2013; Accepted 16 June 2013

Academic Editor: Jan E. Alam

Copyright © 2013 S. Sarkar et al. This is an open access article distributed under the Creative Commons Attribution License, which permits unrestricted use, distribution, and reproduction in any medium, provided the original work is properly cited.

Quasiparticle excitations and associated phenomena of energy and momentum transfer rates have been calculated in terms of the drag and the diffusion coefficients exposing clearly the dominance of the magnetic interaction over its electric counterpart. The results have been compared with the finite temperature results highlighting the similarities and dissimilarities in the two extreme regimes of temperature and density. Non-Fermi-liquid behavior of various physical quantities like neutrino mean free path and thermal relaxation time due to the inclusion of magnetic interaction has clearly been revealed. All the results presented in the current review are pertinent to the degenerate and ultradegenerate plasma.

1. Introduction

Understanding the properties of the hot and dense ultrarelativistic plasma has been at the forefront of contemporary research for the past few decades. Interests in this regime cover a broad area starting from the laboratory based heavy ion collisions (HIC) to the wider domain of naturally occurring astrophysical sites like neutron stars, supernovae, and white dwarfs and so forth.

In the present review we mainly focus on the properties of plasma with high chemical potential (μ) and zero or low temperature (T). It is to be noted that the theoretical calculations so far involving both the quantum electrodynamics and quantum chromodynamics (QED/QCD) have been confined largely to the domain of high temperature particularly to address the issues related to heavy ion collisions. The main motivation for this has been the possibility of quark-hadron phase transition which might occur in HIC mimicking the conditions of microsecond old universe. Studies with dense plasma on the other hand find their applications mainly in astrophysics.

Several calculations have recently been performed exposing subtle departure of the characteristic behavior of the

quasiparticle excitations in dense plasma than their high temperature counterparts. For example, the role of magnetic interaction in dense plasma, as we shall see, modifies the fermion self-energy in a nontrivial way involving fractional powers of the excitation energy [1] leading to phenomena not seen in the high temperature plasma. In fact the transverse or magnetic interaction seems to dominate over the corresponding electric or longitudinal interactions [1] in degenerate electron or quark matter. It is to be noted that such departures can only be significant in the relativistic plasma as in the nonrelativistic case magnetic interactions are $\beta = v/c$ suppressed [2–5]. The introduction of magnetic interaction changes some of the characteristic behaviours of dense plasma which show departure from the normal Fermi liquid case. In this review this particular aspect will be illuminated upon further.

Our discussion starts with the quasiparticle damping rate (γ). In the relativistic case $\gamma \sim (E - \mu)$ [6] unlike the known non-relativistic scenario where $\gamma \sim (E - \mu)^2$. Here, E is the energy of the quasiparticle and μ is the chemical potential [6–8]. More importantly the infrared behavior of this quantity differs dramatically from the high temperature case [6–8]. In a plasma the other quantities of interest have been the

drag (η) and the diffusion coefficients (\mathcal{B}) which eventually determine the equilibration time scale of the plasma. These two quantities are actually related to the energy loss and the momentum transfer due to the scattering of the constituent particles of the plasma. In high temperature case they are known to be connected *via* the Einstein relation. We address this issue to see the scaling behavior of these quantities in the domain of zero and high temperature plasma [2].

Recently the implications of the medium modified quasi-particle self-energies have been discussed by several authors showing their significance in the cooling behavior of neutron stars. The appearance of logarithmic terms in the specific heat, emissivity, and thermal relaxation time of the degenerate matter has been found to be of crucial importance. How the medium modified dispersion relation changes the cooling behavior of neutron star has been first exposed in [9] and later in [3, 5, 10].

The plan of the review is as follows. In Section 2 we have shown the behavior of quasiparticle damping rate in ultradegenerate plasma. In this section we compare the results of quasiparticle lifetime in the extreme limits of high temperature and high density. For the former it is known that the damping rate for the exchange of static gauge boson remains unscreened even when one uses hard thermal loop corrected propagator for the gauge bosons [11, 12]. It has been shown in the literatures that a further resummation is required to resolve this issue by invoking Bloch-Nordseick techniques as discussed in great detail in [13, 14]. For the degenerate case, as we shall see this problem does not appear. In this context however we shall expose the relative importance of the magnetic interaction over the electric part unlike the hot relativistic plasma.

In this review we also calculate the drag and the diffusion coefficients for both degenerate and ultradegenerate cases. Different properties of η and \mathcal{B} in the zero temperature and low temperature limit have been reported in Section 3. In Section 4 explicit analysis has been presented to exhibit how the nature of neutrino mean free path changes with the inclusion of the transverse mode. One distinguishing feature of the present work is to show the structure of the fermion self-energy near the Fermi surface. Of particular importance is the vanishing group velocity at the Fermi surface which in turn is responsible for the non-Fermi liquid (NFL) corrections. Section 5 describes the implication of the neutrino mean free path *vis-a-vis* cooling of the neutron star specially focusing on NFL corrections to the various physical quantities. We calculate the thermal relaxation time exposing the role of magnetic interaction further in Section 6 where we also discuss NFL corrections.

In the last two sections of this review we estimate the neutrino mean free path and thermal relaxation time of degenerate matter. At very high density nowadays it is well known that quark matter is expected to form a color superconducting color-flavour locked (CFL) phase [15]. In this phase all quark excitations are gapped, and the mean free path or the thermal relaxation time is modified by exponential factor involving gap parameter [16–18]. However, in order to highlight particular aspects of NFL behaviour of the relativistic plasma we deal with only ungapped quark

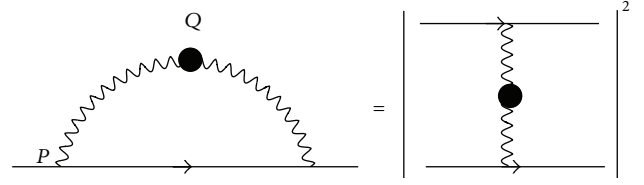


FIGURE 1: Fermion self-energy with resummed photon propagator.

matter. The extension of the present calculation for the gapped quark matter is straightforward.

2. Damping Rate

The propagation of a particle immersed in plasma gets modified through interaction with the medium. In case of ultradegenerate ($T = 0$, $\mu \neq 0$) plasma these medium modified particles (quasiparticles) scatter with the other particles close to the Fermi surface. Information about the quasiparticle lifetime is obtained from the retarded propagator. The damping rate is expected to follow exponential decay in time $S_R(t, p) \sim e^{-Et} e^{-\gamma t}$, so that $|S_R(t, p)|^2 \sim e^{-\Gamma t}$, where $\Gamma = \gamma/2$. The life time of the single-particle excitation is then $\tau(p) = 1/\Gamma(p)$. The concept of quasiparticles becomes meaningful only if their life time is long or in other words the damping width is much smaller than its energy. In a plasma the damping rate of the quasiparticle can be written in terms of the imaginary part of the fermion self-energy or the scattering rate (see Figure 1). Mathematically one writes [19]

$$\gamma(E) = -\frac{1}{4E} \text{Tr} [\text{Im} \Sigma(p_0 + i\sigma\mathbf{p}) \not{P}] \Big|_{p_0=E}, \quad (1)$$

where Σ is the fermion self-energy, $\sigma \rightarrow 0^+$, and we have used $P_\mu = (p_0, \mathbf{p})$. The aforementioned expression is true for both the high temperature and the zero temperature plasmas. The one-loop electron self-energy is given by

$$\Sigma(P) = e^2 \int \frac{d^4 q}{(2\pi)^4} \gamma_\mu S_f(P-Q) \gamma_\nu \Delta_{\mu\nu}(Q). \quad (2)$$

In the previous equation $S_f(P-Q)$ is the free fermion propagator and $\Delta_{\mu\nu}(Q)$ is the photon propagator.

Focusing on (2) we can see that it involves the boson propagator ($\Delta_{\mu\nu}$) which is well known to diverge in the infrared regime. This is a generic feature of both the high temperature and the zero temperature plasmas. In case of hot QED or QCD plasmas one handles this problem by employing the hard thermal loop (HTL) prescription which was originally developed in [11, 12]. In this method the exchanged momentum (\mathbf{q}) integration is performed in two domains by introducing an intermediate cut-off parameter (q^*), below which the one-loop corrected dressed boson propagator has to be used and the bare propagator can be used to perform the integration above q^* (Braaten and Yuan's prescription) [20].

For electric interaction this is sufficient to remove the infrared singularity associated with the exchange of massless

bosons (photons or gluons). The interaction mediated by the transverse bosons on the other hand still poses a problem at high temperature [13, 14]. We shall discuss this further at the end of this section where we compare the zero temperature case with the corresponding high temperature calculations. It might be mentioned that to construct the one-loop corrected photon propagator one needs to evaluate the photon self-energy in dense plasma [21]. In the ultradegenerate case, the dominant contribution to the photon self-energy comes from the loop momentum $\sim \mu$, and the external momentum for the soft modes is assumed to be $\mathbf{q} \sim e\mu$ (Figure 2). This, in principle, runs similar to the HTL approximation where the loop momentum is $\sim T$ and the external momentum is $\sim eT$. Likewise for the degenerate case one can construct hard dense loop (HDL) propagator where loop momentum is assumed to be $\sim \mu$ [21].

The structure of the dressed photon propagator in the Coulomb gauge can be written as [19]

$$\Delta_{\mu\nu}(Q) = \delta_{\mu 0} \delta_{\nu 0} \Delta_l(Q) + P_{\mu\nu}^t \Delta_t(Q), \quad (3)$$

with $P_{ij}^t = (\delta_{ij} - \hat{q}_i \hat{q}_j)$, $\hat{q}^i = \mathbf{q}^i / |\mathbf{q}|$, $P_{i0}^t = P_{0i}^t = P_{00}^t = 0$, and Δ_l , Δ_t are given by [19]

$$\Delta_l(q_0, q) = \frac{-1}{q^2 + \Pi_l}, \quad (4)$$

$$\Delta_t(q_0, q) = \frac{-1}{q_0^2 - q^2 - \Pi_t}. \quad (5)$$

$\Delta_{l,t}$ are the longitudinal and the transverse components of the boson propagator, and $\Pi_{l,t}$ are the longitudinal and transverse parts of the self-energy [19]:

$$\begin{aligned} \Pi_l(q_0, q) &= m_D^2 \left[1 - \frac{q_0}{2q} \ln \left(\frac{q_0 + q}{q_0 - q} \right) \right], \\ \Pi_t(q_0, q) &= m_D^2 \left[\frac{q_0^2}{2q^2} + \frac{q_0(1 - (q_0^2/q^2))}{4q} \ln \left(\frac{q_0 + q}{q_0 - q} \right) \right], \end{aligned} \quad (6)$$

where the Debye mass is $m_D = e\mu/\pi$.

The bosonic spectral functions are the imaginary part of the propagators:

$$\rho_{l,t}(q_0, \mathbf{q}) = 2 \text{Im} \Delta_{l,t}(q_0 + i\sigma, \mathbf{q}), \quad (7)$$

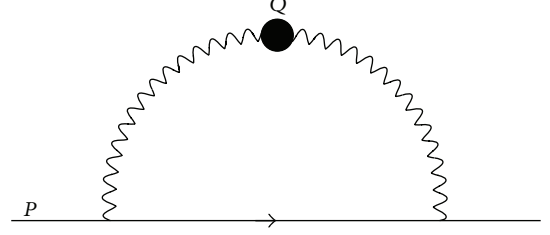


FIGURE 2: Feynman diagram for $e^- e^- \rightarrow e^- e^-$ scattering process with effective photon propagator.

where $\rho_{l,t}$ in the HDL approximations are given by [6]

$$\begin{aligned} \rho_l(q_0, q) &= \frac{2\pi m_D^2 x \Theta(1-x^2)}{2[q^2 + m_D^2(1-(x/2)\ln|(x+1)/(x-1)|)]^2 + (m_D^4 \pi^2 x^2/4)}, \\ \rho_t(q_0, q) &= 2\pi m_D^2 x(1-x^2) \Theta(1-x^2) \\ &\quad \times \left(\left[2q^2(x^2-1) - m_D^2 x^2 \left(1 + \frac{(1-x^2)}{2x} \ln \left| \frac{x+1}{x-1} \right| \right) \right]^2 \right. \\ &\quad \left. + \frac{m_D^4 \pi^2 x^2 (1-x^2)^2}{4} \right)^{-1}, \end{aligned} \quad (8)$$

with $x = q_0/q$.

To calculate γ in the ultradegenerate plasma the energy of the quasiparticle is therefore considered to be hard, that is, $E \sim \mu$. Hence, for the quasiparticle with momentum close to the Fermi momentum the electron-photon vertex can be replaced by the bare one and the one-loop self-energy is dominated by the photon with soft momentum ($\mathbf{q} \sim e\mu$). So, the calculation of imaginary part of Σ can be performed with the help of the free fermion spectral function $\rho_f(P-Q) = 2\pi \varepsilon(k_0) \delta(k_0^2 - E_k^2) (\varepsilon(k_0) = k_0/|k_0|)$ and the medium modified $\rho_{l,t}$ [6]. Explicitly,

$$\begin{aligned} \gamma(E) &= \frac{\pi e^2}{E} \int \frac{d^3 q}{(2\pi)^3} \int_{-\infty}^{\infty} \frac{dk_0}{2\pi} \rho_f(k_0) \int_{-\infty}^{\infty} \frac{dq_0}{2\pi} \\ &\quad \times (1 + n(q_0) - \bar{n}(k_0)) \delta(E - k_0 - q_0) \\ &\quad \times \{ [p_0 k_0 + \mathbf{p} \cdot \mathbf{k}] \\ &\quad \times \rho_l(q_0, q) + 2 [p_0 k_0 - (\mathbf{p} \cdot \hat{\mathbf{q}})(\mathbf{k} \cdot \hat{\mathbf{q}})] \rho_t(q_0, q) \}. \end{aligned} \quad (9)$$

In the previous equation $n(q_0)$ and $\bar{n}(k_0)$ are the boson and fermion distribution functions. In case of the cold plasma these distribution functions can be replaced by $(1 + n(q_0)) = \Theta(q_0)$ and $\bar{n}(k_0) = \Theta(\mu - E + q_0)$, where Θ represents the step function. These theta functions, as we shall see, restrict the

phase space of the q_0 integration severely. This eventually with the help of the HDL propagator makes γ finite [13, 14, 21]. To proceed further an approximation in the region $(E - \mu)/m_D = \nu \ll 1$ has been made. This is due to the fact that scatterings close to the Fermi surface are only relevant as mentioned earlier. To perform the q integration the integration domain is divided into two sectors. In the soft sector ($q < q^*$) with the HDL corrected spectral function mentioned in (8) one obtains [6]

$$\gamma_{\text{soft}}(E) \approx \frac{e^2 m_D \nu}{24\pi} + \frac{e^2 m_D^4 \nu^2}{32\pi} \left(\frac{\pi}{2m_D^3} - \frac{1}{q^{*3}} \right). \quad (10)$$

Only the leading order terms in $(E - \mu)/m_D$ have been retained in writing the previous equation. For the hard momentum region $q > q^*$ bare propagator is sufficient to calculate the damping rate:

$$\gamma_{\text{hard}}(E) \approx \frac{e^2 m_D^4 \nu^2}{32\pi} \left(\frac{1}{q^{*3}} - \frac{1}{q_{\text{max}}^3} \right), \quad (11)$$

where $q_{\text{max}} \approx \mu$ is the maximum momentum transfer that is allowed by kinematics.

Two points are to be noted here. One that q^* dependent term appear only at the higher orders that is, the leading order result is independent of q^* . Second upon summation the q^* terms cancel out exactly. The total damping rate is then given by [6]

$$\gamma(E) \approx \mathcal{G}_1 \nu + \mathcal{G}_2 \nu^2 + \dots, \quad (12)$$

where $\mathcal{G}_1 = (e^2 m_D)/(24\pi)$ and $\mathcal{G}_2 = (e^2 m_D)/32$. In the last equation the first term corresponds to the magnetic interaction, and the second term comes from the electric interaction revealing the fact that the magnetic interaction here dominates over the electric one. In this connection we can recall the results of the damping rate in case of the high temperature plasma with vanishing chemical potential. These are given by [13, 14]

$$\gamma_t = \frac{e^2 T}{2\pi} \int_0^{\omega_p} \frac{dq}{q}, \quad \gamma_l \sim e^2 T, \quad (13)$$

where ω_p is the plasma frequency related to the Debye mass ($\omega_p = m_D/\sqrt{3}$).

The last equations have been obtained by using the one-loop corrected dressed propagator which makes γ_l finite. The transverse part, on the other hand, remains divergent that can be cured by another resummation as discussed in [13, 14]. In the case of dense QED or QCD matter interestingly the second resummation is not required. This happens, as indicated above, due to the restrictions imposed by the Pauli blocking which severely cuts off the phase space. A comparative study between high and zero temperature damping rates has been listed in Table 1 [22].

In the nonrelativistic case the excitation energy dependence of γ can be derived from the simple phase-space factor without performing any rigorous calculation. A particle with energy $E > \mu$ interacts with the particle of energy $E_k < \mu$.

The scattered particles are now in the energy state $E_{p'} > \mu$ and $E_{k'} > \mu$. The total probability of the scattering process is proportional to $\int \delta(E + E_k - E_{p'} - E_{k'}) d^3 k d^3 p'$. For $E - \mu \ll \mu$, the permissible regions of variation for the scattered particles are $\mu < E_{p'} < E + E_k - \mu$ and $2\mu - E < E_k < \mu$. The integral over $d^3 k$ and $d^3 p'$ can be computed with the approximation $E_k \approx E_{p'} \approx \mu$, that is, scattering occurs near the Fermi surface. The scattering probability is then $(E - \mu)^2$ [23]. Similar arguments can be made for the transverse sector which will render the damping rate of the particle $\sim (E - \mu)$ at the leading order for relativistic case.

3. Drag and Diffusion Coefficients

3.1. Zero Temperature Plasma. Next we review the drag and diffusion coefficients in zero temperature relativistic plasma and see how the magnetic interaction changes the behavior of these coefficients. These two are the important quantities to study the equilibration properties of the plasma as mentioned earlier and are related to the energy and the momentum transfer per scattering, respectively. η can thus be defined as follows [24]:

$$\eta = \frac{1}{E} \left(-\frac{dE}{dx} \right). \quad (14)$$

The energy loss $-(dE/dx)$ can be calculated by averaging over the interaction rate (Γ) times the energy transfer per scattering ω [25]:

$$\frac{dE}{dx} = \int d\Gamma \omega, \quad (15)$$

where $\Gamma = \gamma/2$. Inserting the energy exchange ω in the expression of γ to calculate dE/dx from the previous equation we obtain (Figure 2)

$$\begin{aligned} -\frac{dE}{dx} &= \frac{\pi e^2}{E} \int \frac{d^3 q}{(2\pi)^3} \int_{-\infty}^{\infty} \frac{dk_0}{2\pi} \rho_f(k_0) \int_{-\infty}^{\infty} \frac{dq_0}{2\pi} q_0 \\ &\times (1 + n(q_0) - \bar{n}(k_0)) \delta(E - k_0 - q_0) \\ &\times [p_0 k_0 + \mathbf{p} \cdot \mathbf{k}] \rho_t(q_0, q) \\ &+ 2 [p_0 k_0 - (\mathbf{p} \cdot \hat{\mathbf{q}})(\mathbf{k} \cdot \hat{\mathbf{q}})] \rho_t(q_0, q). \end{aligned} \quad (16)$$

The basic assumption behind the calculation of η lies in the fact that $(E - \mu)/m_D = \nu \ll 1$. Taking into consideration the previous assumption in case of the hard photon exchange we get [2],

$$\left(-\frac{dE}{dx} \right) \approx \frac{e^2 \nu^3 m_D^5}{16\pi} \int \frac{dq}{q^4}. \quad (17)$$

The above expression is infrared divergent with algebraic dependence. Here, it would be worthwhile to comment that in case of the high temperature plasma the divergence is logarithmic ($e^4 T^2/24\pi E$) $\int (dq/q)$. The divergence is even worse in case of the ultradegenerate plasma. But we show below that with the HDL propagator and Pauli blocking one

TABLE 1: Comparison of high and zero temperature damping rates.

	γ in high temperature plasma	γ in zero temperature plasma
Fermion	$f(E) = \frac{1}{e^{\beta(E-\mu)} + 1}$	$f(E) = \Theta(\mu - E + q_0)$
Boson	$n(E) = \frac{1}{e^{\beta E} - 1}$	$1 + n(E) = \Theta(q_0)$
Longitudinal contribution	$\gamma_l \sim e^2 T$	$\gamma_l \approx \frac{e^2 \nu^2 m_D}{64}$
Transverse contribution	$\gamma_t \sim \frac{e^2 T}{2\pi} \int_0^{q^*} \frac{dq}{q}$	$\gamma_t \approx \frac{e^2 \nu m_D}{24\pi}$
Infrared behaviour	IR divergent after the HTL resummation	Finite with HDL resummation
Dominance	γ_l and γ_t contribute at the same order ($O(e^2)$)	Dominant contribution from γ_t

can render η finite. In the soft sector η is given by the following expression:

$$\begin{aligned} \eta|_{\text{soft}}(E) &\simeq \frac{e^2}{8\pi^2 E} \\ &\times \int_D dq q \int dq_0 q_0 \left\{ \rho_l(q_0, q) + \left(1 - \frac{q_0^2}{q^2}\right) \rho_t(q_0, q) \right\}. \end{aligned} \quad (18)$$

The integration domain (D) above is restricted by the Θ functions:

$$\begin{aligned} D : 0 \leq q_0 \leq E - \mu; \\ q_0 \leq q \leq q^*. \end{aligned} \quad (19)$$

After explicit calculation, the electric and the magnetic contributions to the expressions of η take the following form [2]:

$$\begin{aligned} \eta|_{\text{soft}}^l &\simeq \frac{e^2 m_D^2 \nu^3}{96E} - \frac{e^2 m_D^5 \nu^3}{72\pi q^{*3} E}, \\ \eta|_{\text{soft}}^t &\simeq \frac{e^2 m_D^2 \nu^2}{48\pi E} - \frac{e^2 m_D^5 \nu^3}{144\pi q^{*3} E}. \end{aligned} \quad (20)$$

In the last two equations the leading order terms are independent of the cut-off parameter as they appear only at $O(e^2)$. In the region of hard photon momentum exchange we obtain [2]

$$\eta|_{\text{hard}} \simeq \frac{e^2 m_D^5 \nu^3}{48\pi E} \left[\frac{1}{q^{*3}} - \frac{1}{\mu^3} \right]. \quad (21)$$

On addition of the soft and the hard sectors it can be seen that the expression of the drag coefficient becomes [2],

$$\eta \simeq \mathcal{H}_1 \nu^3 + \mathcal{H}_2 \nu^3 + \dots, \quad (22)$$

where $\mathcal{H}_1 = (e^2 m_D^2)/(48\pi E)$ and $\mathcal{H}_2 = (e^2 m_D^2)/(96E)$. In the previous equation the first term corresponds to the magnetic interaction, and the second term has come from

the longitudinal interaction. From (21) it is important to note that the hard sector involves even higher power. The entire contribution at the leading order then comes from the soft sector alone, and Braaten and Yuan's prescription is not required in case of the ultradegenerate plasma [2]. The final expression of η reveals that with the magnetic interaction η changes significantly from the Fermi liquid result. In the Fermi liquid theory, since the magnetic interaction is suppressed in comparison with the electric sector η goes with $(E-\mu)^3$. Here, we can recall the result of the drag coefficient in case of high temperature plasma and compare the same with the previous result. The coefficient at high temperature looks like [25–29]

$$\eta \simeq \frac{e^4 T^2}{36\pi E} \left(-\frac{1}{2} + \frac{3}{2} \log \left| \frac{q_{\text{max}}}{m_D} \right| + \frac{1}{2} \log \left| \frac{2}{\sqrt{\pi}} \right| \right). \quad (23)$$

From the previous result it is clear that there is no splitting between electric and magnetic modes, and in hot plasma both contribute at the same order. A comparative study between high temperature and zero temperature η can be found in [22]:

Another important quantity to study the equilibration property of the plasma is the momentum diffusion coefficient B_{ij} . The coefficient is related to the interaction rate *via* the following relation [24]:

$$B_{ij} = \int d\Gamma q_i q_j. \quad (24)$$

Decomposing B_{ij} into longitudinal (B_l) and transverse components (B_t) we get the following expression,

$$B_{ij} = B_t \left(\delta_{ij} - \frac{p_i p_j}{p^2} \right) + B_l \frac{p_i p_j}{p^2}. \quad (25)$$

$B_{l,t}$ are the longitudinal, transverse squared momenta acquired by the particle through collision with the plasma. The longitudinal momentum diffusion coefficient is related to the drag coefficient *via* the Einstein relation in case of equilibrating plasma. Like η longitudinal momentum

diffusion coefficient ($B_l = \mathcal{B}$, suppressing the index l) can be expressed as

$$\begin{aligned} \mathcal{B} &= \frac{\pi e^2}{E} \int \frac{d^3 q}{(2\pi)^3} \int_{-\infty}^{\infty} \frac{dk_0}{2\pi} \rho_f(k_0) \int_{-\infty}^{\infty} \frac{dq_0}{2\pi} q_{\parallel}^2 \\ &\times (1 + n(q_0) - \bar{n}(k_0)) \delta(E - k_0 - q_0) \\ &\times [p_0 k_0 + \mathbf{p} \cdot \mathbf{k}] \rho_t(q_0, q) \\ &+ 2 [p_0 k_0 - (\mathbf{p} \cdot \hat{\mathbf{q}})(\mathbf{k} \cdot \hat{\mathbf{q}})] \rho_t(q_0, q). \end{aligned} \quad (26)$$

Here, q_{\parallel} is the longitudinal exchanged momentum transfer in a scattering and $q_{\parallel} = q \cos \theta$. Explicitly \mathcal{B} is then given by [2]

$$\mathcal{B} \simeq \mathcal{B}_1 v^3 + \mathcal{B}_2 v^4 + \dots, \quad (27)$$

where $\mathcal{B}_1 = (e^2 m_D^3)/(72\pi)$ and $\mathcal{B}_2 = (e^2 m_D^3)/128$. In this case also the electric and magnetic modes split as the magnetic mode is $\sim (E-\mu)^3$ whereas electric mode is $\sim (E-\mu)^4$. One can relate the leading order terms of η and \mathcal{B} from (22) and (27) *via* a common relation, namely, Einstein's relation as in case of high temperature plasma. In ultradegenerate plasma the relation can be written as $\mathcal{B} = 3E(E-\mu)\eta/4$.

In the high temperature and zero chemical potential regime \mathcal{B} has the following expression [25–29]:

$$\mathcal{B} \simeq \frac{e^4 T^3}{18\pi} \left(-\frac{1}{2} + \frac{3}{2} \log \left| \frac{q_{\max}}{m_D} \right| + \frac{1}{2} \log \left| \frac{2}{\sqrt{\pi}} \right| \right). \quad (28)$$

In case of high temperature plasma from (23) and (28), Einstein's relation becomes $\mathcal{B} = 2TE\eta$.

From (22), (23), (27), and (28) it can be seen that zero temperature η and \mathcal{B} show entirely different characteristics from the high temperature case. The logarithmic dependence in high temperature takes an algebraic form in the ultradegenerate limit [22].

3.2. Low Temperature Plasma. In this section we extend our calculations to include finite temperature effects in the domain where $|E - \mu| \sim T \ll e\mu \ll \mu$. Moreover, we also go beyond the leading order calculations as previously reported above. Finally we shall see how the leading order zero temperature results appear as a limiting case from our present analysis including higher order correction terms.

For the soft sector contribution we take T/m_D as an expansion parameter and $\alpha = (E - \mu)/T \sim 1$. We start with the following expression for the soft sector [4]:

$$\begin{aligned} \eta_{\parallel}^{\text{soft}}(E) &\simeq \frac{e^2}{8\pi^2 E} \int_0^{q^*} dq q^3 \int_{-1}^1 dx x (1 + n(qx) - \bar{n}(E - \mu - qx)) \\ &\times \{ \rho_t(qx, q) + (1 - x^2) \rho_t(qx, q) \}. \end{aligned} \quad (29)$$

The previous equation can easily be derived from (16). After subtracting the energy independent part from the above equation we get,

$$\begin{aligned} \eta_{\parallel}^{\text{soft}}(E) - \eta_{\parallel E=\mu}^{\text{soft}} &= -\frac{e^2}{8\pi^2 E} \int_0^{q^*} dq q^3 \int_{-1}^1 dx x (\bar{n}(E - \mu - qx) - \bar{n}(-qx)) \\ &\times \left[(1 - x^2) \rho_t(qx, q) + \rho_t(qx, q) \right]. \end{aligned} \quad (30)$$

We substitute q and q_0 by introducing dimensionless variables z and v in the above equation:

$$q = \frac{2q_s z}{(\pi v)^{1/3}}, \quad q_0 = T v, \quad (31)$$

where q_s is the screening length in the magnetic sector and given by $(\pi m_D^2 q_0/2)^{1/3}$. This fractional power in the transverse sector will eventually show up in different coefficients as we show below. The previous substitutions actually yields,

$$q = m_D a^{1/3} z, \quad x = \frac{a^{2/3} v}{z}. \quad (32)$$

After performing the q_0 and q integrations we obtain [4]:

$$\begin{aligned} \eta_{\parallel}^{\text{soft}}(E) - \eta_{\parallel E=\mu}^{\text{soft}} &= \frac{e^2 m_D^2}{E} \\ &\times \left\{ \frac{1}{48\pi} \left(\frac{T}{m_D} h_1 \left(\frac{(E - \mu)}{T} \right) \right)^2 \right. \\ &- \frac{3 \times 2^{1/3}}{72\pi^{7/3}} \left(\frac{T}{m_D} h_2 \left(\frac{(E - \mu)}{T} \right) \right)^{8/3} \\ &\left. - \frac{6 \times 2^{2/3}}{9\pi^{11/3}} \left(\frac{T}{m_D} h_3 \left(\frac{(E - \mu)}{T} \right) \right)^{10/3} \right\}, \end{aligned} \quad (33)$$

where

$$\begin{aligned} h_1 \left(\frac{(E - \mu)}{T} \right) &= [\Gamma(3) (\text{Li}_2(-e^{-\alpha}) - \text{Li}_2(-e^{\alpha}))]^{1/2}, \\ h_2 \left(\frac{(E - \mu)}{T} \right) &= \left[\Gamma \left(\frac{11}{3} \right) (\text{Li}_{8/3}(-e^{-\alpha}) - \text{Li}_{8/3}(-e^{\alpha})) \right]^{3/8}, \\ h_3 \left(\frac{(E - \mu)}{T} \right) &= \left[\Gamma \left(\frac{13}{3} \right) (\text{Li}_{10/3}(-e^{-\alpha}) - \text{Li}_{10/3}(-e^{\alpha})) \right]^{3/10}. \end{aligned} \quad (34)$$

In case of the longitudinal sector we substitute $q = q_s y$ and $q_0 = Tu/y$ or $q = m_D y$ and $x = au/y$. Since screening length is different in electric and magnetic sectors the substitutions therefore involve different coefficients of m_D

and T for the transverse and the longitudinal cases [1] as can be seen from the structure of $\rho_{l,t}$ (8). For the leading term in the longitudinal sector one writes,

$$\eta_l^{\text{soft}}(E) - \eta_{l,E=\mu}^{\text{soft}} = \frac{e^2 m_D^2}{96E} \left(\frac{T}{m_D} g_1 \left(\frac{(E-\mu)}{T} \right) \right)^3, \quad (35)$$

where

$$g_1 \left(\frac{(E-\mu)}{T} \right) = [\Gamma(4) (\text{Li}_3(-e^{-\alpha}) - \text{Li}_3(-e^{\alpha}))]^{1/3}. \quad (36)$$

The final expression for drag coefficient then becomes [4]

$$\begin{aligned} \eta = \frac{e^2 m_D^2}{E} & \left\{ \frac{1}{48\pi} \left(\frac{T}{m_D} h_1 \left(\frac{(E-\mu)}{T} \right) \right)^2 \right. \\ & - \frac{3 \times 2^{1/3}}{72\pi^{7/3}} \left(\frac{T}{m_D} h_2 \left(\frac{(E-\mu)}{T} \right) \right)^{8/3} \\ & \left. - \frac{6 \times 2^{2/3}}{9\pi^{11/3}} \left(\frac{T}{m_D} h_3 \left(\frac{(E-\mu)}{T} \right) \right)^{10/3} \right\} \\ & + \frac{e^2 m_D^2}{96E} \left(\frac{T}{m_D} g_1 \left(\frac{(E-\mu)}{T} \right) \right)^3. \end{aligned} \quad (37)$$

From the previous expression it is evident that η is polylogarithmic in nature and contains fractional powers in $(E-\mu)$. The fractional powers indicate the nonanalytic behavior of η . Significant it is to note that here the subleading transverse term is greater than the leading order longitudinal one. Thus we see that here too the transverse contribution dominates over the longitudinal one. In the zero temperature limit the functions behave as $h_i(\alpha) \rightarrow |\alpha|$ and $g_i(\alpha) \rightarrow |\alpha|$. Hence, η in the limit becomes [4]

$$\eta = \mathcal{H}_1 v^2 - \mathcal{H}_3 v^{8/3} + \mathcal{H}_2 v^3 + \dots. \quad (38)$$

In the last equation $\mathcal{H}_3 = (3 \times 2^{1/3} e^2 m_D^2)/(72\pi^{7/3} E)$, and $\mathcal{H}_1, \mathcal{H}_2$ are the same as before. We can infer from the previous observations that the inclusion of transverse interaction for a relativistic particle changes the nature of η . In the nonrelativistic case considering only the electric interaction η goes as $(E-\mu)^3$, but with the inclusion of the transverse sector we see that anomalous fractional powers appear. Like η one can also compute the longitudinal momentum diffusion coefficient in the low temperature limit. The expression for

the longitudinal momentum diffusion coefficient as defined in (26) can be written as [4]

$$\begin{aligned} \mathcal{B} = e^2 m_D^3 & \left\{ \frac{1}{72\pi} \left(\frac{T}{m_D} h_4 \left(\frac{(E-\mu)}{T} \right) \right)^3 \right. \\ & - \frac{3 \times 2^{1/3}}{99\pi^{7/3}} \left(\frac{T}{m_D} h_5 \left(\frac{(E-\mu)}{T} \right) \right)^{11/3} \\ & \left. - \frac{20 \times 2^{2/3}}{39\pi^{11/3}} \left(\frac{T}{m_D} h_6 \left(\frac{(E-\mu)}{T} \right) \right)^{13/3} \right\} \\ & + \frac{e^2 m_D^3}{128} \left(\frac{T}{m_D} g_2 \left(\frac{(E-\mu)}{T} \right) \right)^4, \end{aligned} \quad (39)$$

where

$$\begin{aligned} h_4 \left(\frac{(E-\mu)}{T} \right) & = [\Gamma(4) (\text{Li}_3(-e^{-\alpha}) - \text{Li}_3(-e^{\alpha}))]^{1/3}, \\ h_5 \left(\frac{(E-\mu)}{T} \right) & = \left[\Gamma \left(\frac{14}{3} \right) (\text{Li}_{11/3}(-e^{-\alpha}) - \text{Li}_{11/3}(-e^{\alpha})) \right]^{3/11}, \\ h_6 \left(\frac{(E-\mu)}{T} \right) & = \left[\Gamma \left(\frac{16}{3} \right) (\text{Li}_{13/3}(-e^{-\alpha}) - \text{Li}_{13/3}(-e^{\alpha})) \right]^{3/13}, \\ g_2 \left(\frac{(E-\mu)}{T} \right) & = [\Gamma(5) (\text{Li}_4(-e^{-\alpha}) - \text{Li}_4(-e^{\alpha}))]^{1/4}. \end{aligned} \quad (40)$$

The final expression for \mathcal{B} in the extreme zero temperature limit becomes [4]

$$\mathcal{B} = \mathcal{B}_1 v^3 - \mathcal{B}_3 v^{11/3} + \mathcal{B}_2 v^4 + \dots, \quad (41)$$

$\mathcal{B}_3 = (2^{1/3} e^2 m_D^3)/(33\pi^{7/3})$, \mathcal{B}_1 , and \mathcal{B}_2 are the same as earlier. It is to be noted that, for the low temperature case, so far, no reference has been made to the case of hard momentum regime. This is justified as we have seen before that up to the order of our interest the hard sector does not contribute, and the entire contribution comes from the soft sector alone.

Furthermore, it is worthwhile to mention that the NFL behaviour of these coefficients is related to the dynamical screening involving “ ω ” in the static limit when one evaluates Π_t . To see this one can recall the expressions for the polarization functions in (6). In the static limit ($q_0/q \sim 0$) the functions become

$$\Pi_l = m_D^2, \quad \Pi_t = \frac{im_D^2 \pi \omega}{4q}. \quad (42)$$

The “ ω ” that appears in the denominator of (5) from the Π_t above along with the Pauli blocking is responsible for this NFL behavior.

In Figures 3 and 4 η and \mathcal{B} versus energy of the incoming fermion in the small temperature ($T/T_f \ll 1$) region ($T_f = \mu/k_B$ is the Fermi temperature) have been plotted. From the figures, it is evident that with increasing T/T_f , both η and \mathcal{B} decrease. This nature is consistent with what one finds for the fermionic damping rate at small temperature [1].

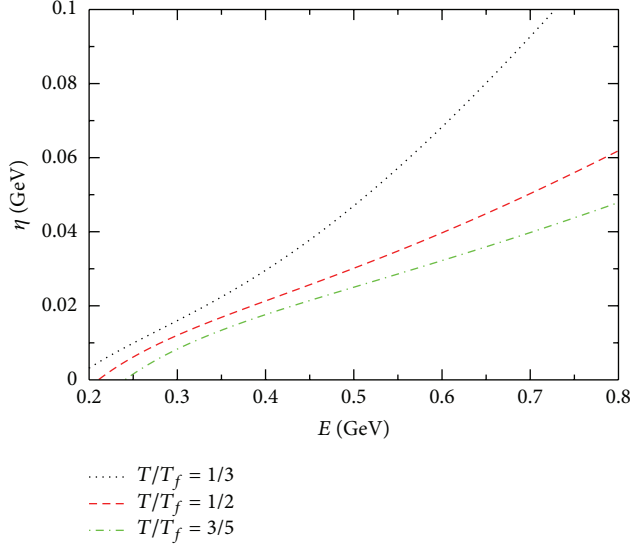


FIGURE 3: Energy dependence of the drag coefficient at $T/T_f = 1/3$ (dotted curve), $T/T_f = 1/2$ (dashed curve), and $T/T_f = 3/5$ (dash dotted curve) [10].

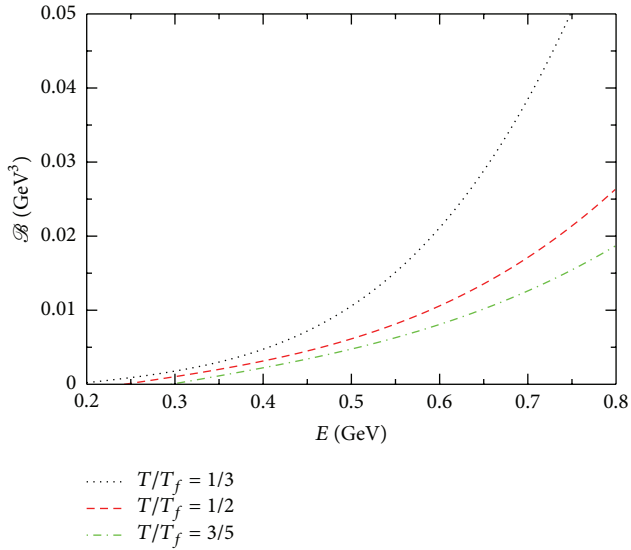


FIGURE 4: Energy dependence of the diffusion coefficient at $T/T_f = 1/3$ (dotted curve), $T/T_f = 1/2$ (dashed curve), and $T/T_f = 3/5$ (dash dotted curve) [10].

4. Neutrino Mean Free Path

In this section we calculate the neutrino mean free path (MFP) for cold and warm QCD matters. When a new star is born following a supernova explosion, it starts emitting neutrinos *via* the direct or the modified Urca processes. Emission of these neutrinos is responsible for the initial cooling of the star so produced. For quark matter, the dominant contribution to the emission of neutrinos is given by the β decay and the electron capture [9]. These reactions are named as “quark direct Urca” processes which have been studied in detail by Iwamoto [30, 31]. For quark matter, the

MFP was previously derived in [30] where the calculations were restricted to the leading order by assuming free Fermi gas interactions. In this context we recall two important works on the neutrino MFP in QED plasma. One is due to Tubbs and Schramm [32], and the other is done by Lamb and Pethick [33]. In [32], MFP was calculated in the neutranized core and just outside the core. On the other hand, it has been shown in [33] that neutrino degeneracy reduces the neutrino MFP which suggests that neutrino may flow out of the core rather slowly. Here, we revisit the calculation and go beyond the leading order results to incorporate the NFL corrections both for degenerate and nondegenerate neutrinos.

In the interior of a neutron star, there are two distinct phenomena for which the neutrino mean free path is calculated: one is absorption, and the other involves scattering of neutrinos [31]. The corresponding mean free paths are denoted as $l_{\text{mean}}^{\text{abs}}$ and $l_{\text{mean}}^{\text{scatt}}$, and combine them to obtain the total mean free path [34]:

$$\frac{1}{l_{\text{mean}}^{\text{total}}} = \frac{1}{l_{\text{mean}}^{\text{abs}}} + \frac{1}{l_{\text{mean}}^{\text{scatt}}}. \quad (43)$$

In our model the Lagrangian density is described by [30]

$$\mathcal{L}_{Wx}(x) = \frac{G}{\sqrt{2}} l_{\mu}(x) \mathcal{J}_W^{\mu}(x) + \text{H.C.}, \quad (44)$$

where the weak coupling constant is $G \approx 1.166 \times 10^{-11}$ in MeV units, and l_{μ} and \mathcal{J}_W^{μ} are the lepton and hadron charged weak currents, respectively. The weak currents are

$$\begin{aligned} l_{\mu}(x) &= \bar{e}\gamma_{\mu}(1 - \gamma_5)\nu_e + \bar{\mu}\gamma_{\mu}(1 - \gamma_5)\nu_{\mu} + \dots, \\ \mathcal{J}_W^{\mu}(x) &= \cos\theta_c \bar{u}\gamma^{\mu}(1 - \gamma_5)d + \sin\theta_c \bar{u}\gamma^{\mu}(1 - \gamma_5)s + \dots, \end{aligned} \quad (45)$$

where θ_c is the Cabibbo angle ($\cos^2\theta_c \approx 0.948$) [35].

The mean free path is determined by the quark neutrino interaction in dense quark matter *via* weak processes. We consider the simplest β decay reactions: the absorption process

$$d + \nu_e \longrightarrow u + e^{-} \quad (46)$$

and the other is its inverse relation

$$u + e^{-} \longrightarrow d + \nu_e \quad (47)$$

The neutrino mean free path is related to the total interaction rate due to neutrino emission averaged over the initial quark spins and summed over the final state phase space and spins. It is given by [31]

$$\begin{aligned} \frac{1}{l_{\text{mean}}^{\text{abs}}(E_{\nu}, T)} &= \frac{g}{2E_{\nu}} \int \frac{d^3 p_d}{(2\mathbf{p})^3} \frac{1}{2E_d} \int \frac{d^3 p_u}{(2\mathbf{p})^3} \frac{1}{2E_u} \\ &\times \int \frac{d^3 p_e}{(2\mathbf{p})^3} \frac{1}{2E_e} (2\pi)^4 \delta^4(P_d + P_{\nu} - P_u - P_e), \\ &|M|^2 \{n(p_d)[1 - n(p_u)][1 - n(p_e)] \\ &\quad - n(p_u)n(p_e)[1 - n(p_d)]\}, \end{aligned} \quad (48)$$

where g is the spin and color degeneracy, which in the present case is considered to be 6. Here, E , p , and n_p are the energy, momentum, and distribution function for the corresponding particle. $|M|^2$ is the squared invariant amplitude averaged over initial d quark spin and summed over final spins of u quark and electron as given by [31]

$$|M|^2 = \frac{1}{2} \sum_{\sigma_u, \sigma_d, \sigma_e} |M_{fi}|^2 = 64G^2 \cos^2 \theta_c (P_d \cdot P_\nu) (P_u \cdot P_e). \quad (49)$$

Here, we work with the two flavor system as the interaction involving strange quark is Cabibbo suppressed [9, 36].

4.1. Degenerate Neutrinos. In this section we consider the case of degenerate neutrinos. When the neutrino chemical potential (μ_ν) is considered to be much larger than the temperature (T), the neutrinos become degenerate. This is also termed as trapped neutrino matter. In this case both the direct (46) and inverse (47) processes can occur, and both terms in (48) under curly brackets are retained [31]. Consequently, the β equilibrium condition becomes $\mu_d + \mu_\nu = \mu_u + \mu_e$. Neglecting the quark-quark interactions and by using (48) and (49), the mean free path becomes

$$\begin{aligned} \frac{1}{l_{\text{mean}}^{\text{abs},D}} &= \frac{3}{4\pi^5} G^2 \cos^2 \theta_c \int d^3 p_d \int d^3 p_u \\ &\times \int d^3 p_e (1 - \cos \theta_{d\nu}) (1 - \cos \theta_{ue}) \\ &\times \delta^4 (P_d + P_\nu - P_u - P_e) [1 + e^{-\beta(E_\nu - \mu_\nu)}] \\ &\times n(p_d) [1 - n(p_u)] [1 - n(p_e)]. \end{aligned} \quad (50)$$

In the square bracket, the second term $e^{-\beta(E_\nu - \mu_\nu)}$ is due to the inverse process (47). One can neglect the mass effect on the neutrino MFP as the masses of u , d quark and electron are very small. To perform the momentum integration we define $p \equiv |p_d + p_\nu| = |p_u + p_e|$ as a variable. Following the same procedure as described by Iwamoto [31] one has

$$\sin \theta_{d\nu} d\theta_{d\nu} = \frac{p dp}{p_f(d) p_f(\nu)}, \quad (51)$$

$$(1 - \cos \theta_{d\nu}) (1 - \cos \theta_{ue}) \simeq \frac{p^4 - 2p^2 p_f^2 + p_f^4}{4p_f(d) p_f(\nu) p_f(u) p_f(e)}, \quad (52)$$

$$\begin{aligned} d^3 p_d &= 2\pi \sin \theta_{d\nu} d\theta_{d\nu} p_d^2 dp_d \\ &= 2\pi \frac{p_f(d)}{p_f(\nu)} p dp \frac{dp_d}{dE_d} dE_d \\ &= 2\pi \frac{p_f(d)}{p_f(\nu)} p dp \frac{dp_d}{d\omega}, \end{aligned} \quad (53)$$

$$d^3 p_u = 2\pi \frac{p_f(u) p_f(e)}{p} dE_e \frac{dp_u}{d\omega}, \quad (54)$$

where we denote the single particle energy $E_{d(u)}$ as ω . For the free case $dp/d\omega$ is the inverse quark velocity. It is well known that this slope of the dispersion relation changes in matter due to the scattering from the Fermi surface and excitation of the Dirac vacuum. The modified dispersion relation can be obtained by computing the on-shell one-loop self-energy. For quasiparticles with momenta close to the Fermi momentum, the one-loop self-energy is dominated by the soft gluon exchanges [8]. The quasiparticle energy ω satisfies the relation [8, 21]

$$\omega = E_p(\omega) - \text{Re} \Sigma(\omega, p(\omega)), \quad (55)$$

where we have retained only the real part of self-energy since the imaginary part of Σ turns out to be negligible compared to its real part [1, 37]. For the detailed analysis we refer the reader to [11, 12, 21].

The analytical expressions for one-loop quark self-energy can be written as [1, 8, 37–40]

$$\Sigma = \frac{g^2 C_F}{12\pi^2} (\omega - \mu) \ln \left(\frac{m_D}{\omega - \mu} \right) + i \frac{g^2 C_F}{24\pi} |\omega - \mu|. \quad (56)$$

It exhibits a logarithmic singularity close to the Fermi surface, that is, when $\omega \rightarrow \mu$.

$dp(\omega)/d\omega$ can be obtained by differentiating the dispersion relation (55) with respect to p . At leading order in T/μ this yields

$$\begin{aligned} \frac{dp(\omega)}{d\omega} &\simeq \left(1 - \frac{\partial}{\partial \omega} \text{Re} \Sigma(\omega) \right) \frac{E_p(\omega)}{p(\omega)} \\ &= \left[1 + \frac{C_F \alpha_s}{3\pi} \ln \left(\frac{m_D}{T} \right) \right] \frac{E_p(\omega)}{p(\omega)}, \end{aligned} \quad (57)$$

where α_s is the strong coupling constant, $C_F = (N_c^2 - 1)/(2N_c)$, and N_c is the color factor. Using (57), (50), and (52)–(54), the neutrino mean free path can be determined for two conditions. For $|p_f(u) - p_f(e)| \geq |p_f(d) - p_f(\nu)|$

$$\begin{aligned} \frac{1}{l_{\text{mean}}^{\text{abs},D}} &= \frac{4}{\pi^3} G^2 \cos^2 \theta_c \frac{\mu_u^2 \mu_e^3}{\mu_\nu^2} \left[1 + \frac{1}{2} \left(\frac{\mu_e}{\mu_u} \right) + \frac{1}{10} \left(\frac{\mu_e}{\mu_u} \right)^2 \right] \\ &\times [(E_\nu - \mu_\nu)^2 + \pi^2 T^2] \left[1 + \frac{C_F \alpha_s}{3\pi} \ln \left(\frac{m_D}{T} \right) \right]^2. \end{aligned} \quad (58)$$

To derive (58), we use the chemical equilibrium condition $p_f(u) + p_f(e) = p_f(d) + p_f(\nu)$ neglecting the masses for quarks and electrons. For the phase-space integral we have [31, 41]

$$\begin{aligned} &\int_0^\infty dE_d \int_0^\infty dE_u \\ &\times \int_0^\infty dE_e [1 + e^{-\beta(E_\nu - \mu_\nu)}] n(p_d) \\ &\times [1 - n(p_u)] [1 - n(p_e)] \delta(E_d + E_\nu - E_u - E_e) \\ &\simeq \frac{1}{2} [(E_\nu - \mu_\nu)^2 + \pi^2 T^2]. \end{aligned} \quad (59)$$

Similarly, for $|p_f(d) - p_f(\nu)| \geq |p_f(u) - p_f(e)|$, the corresponding expression for mean free path can be obtained by replacing $\mu_u \leftrightarrow \mu_d$ and $\mu_e \leftrightarrow \mu_\nu$ in (58).

The other contribution to the mean free path comes from the quark-neutrino scattering. The neutrino scattering process from degenerate quarks is given by

$$q_i + \nu_e(\bar{\nu}_e) \longrightarrow q_i + \nu_e(\bar{\nu}_e) \quad (60)$$

for each quark component of flavor i ($= u$ or d). The scattering mean free path of the neutrinos in degenerate case can be calculated similarly as evaluated by Lamb and Pethick in [33] for electron-neutrino scattering. Assuming $m_{q_i}/p_{f_i} \ll 1$ and including the suitable modifications of the phase space, the mean free path is given by

$$\frac{1}{l_{\text{mean}}^{\text{scatt},D}} = \frac{3}{16} n_{q_i} \sigma_0 \left[\frac{(E_\nu - \mu_\nu)^2 + \pi^2 T^2}{m_{q_i}^2} \right] \times \left[1 + \frac{C_F \alpha_s}{3\pi} \ln \left(\frac{m_D}{T} \right) \right]^2 \Lambda(x_i). \quad (61)$$

Here, m_{q_i} is the quark mass. C_{V_i} and C_{A_i} are the vector and axial vector coupling constant given in Table II of [31]. The expression of (61) has been found to be in agreement with the results reported in [33] for dense and cold QED plasmas by making suitable changes for the color factors and by dropping the second square bracketed term. In (61) the constants $\sigma_0 \equiv 4G^2 m_{q_i}^2 / \pi$ [32], and n_{q_i} is the quark number density:

$$n_{q_i} = 2 \int \frac{d^3 p}{(2\mathbf{p})^3} \frac{1}{e^{\beta(E_{q_i} - \mu_{q_i})}}, \quad (62)$$

where 2 is the quark spin degeneracy factor. Explicit form of $\Lambda(x_i)$ can be written as [31, 33]

$$\Lambda(x_i) = \frac{4}{3} \frac{\text{Min}(\mu_\nu, \mu_{q_i})}{\mu_{q_i}} \times \left[(C_{V_i}^2 + C_{A_i}^2) \left(2 + \frac{1}{5} x_i^2 \right) + 2C_{V_i} C_{A_i} x_i \right], \quad (63)$$

and $x_i = \mu_\nu / \mu_{q_i}$ if $\mu_\nu < \mu_{q_i}$, and $x_i = \mu_{q_i} / \mu_\nu$ if $\mu_\nu > \mu_{q_i}$.

4.2. Nondegenerate Neutrinos. The mean free path has been also derived for nondegenerate neutrinos, that is, when $\mu_\nu \ll T$. This is the case for untrapped neutrino matter. For this case the inverse process (47) does not contribute to the MFP. Hence we neglect the second term in the curly braces of (48). Here, only those fermions take part in the reaction whose momenta lie close to their respective Fermi surfaces. It is to be mentioned here, if quarks are treated as free, as discussed in [31, 42, 43], the matrix element vanishes since u, d quarks and electrons are collinear in momenta. The inclusion of strong interactions between quarks relaxes these kinematic restrictions resulting in a nonvanishing squared matrix amplitude. Since the neutrinos are produced thermally, we neglect the neutrino momentum in energy-momentum conservation relation [31]. This is not the case

for degenerate neutrinos where $p_\nu \gg T$, and therefore such approximation is not valid there. By doing angular average over the direction of the outgoing neutrino, from (49) the squared matrix element is given by [9]:

$$|M|^2 = 64G^2 \cos^2 \theta_c p_f^2 (V_d \cdot P_\nu) (V_u \cdot P_e) = 64G^2 \cos^2 \theta_c p_f^2 E_\nu \mu_e \frac{C_F \alpha_s}{\pi}, \quad (64)$$

where $V = (1, v_f)$ is the four velocity. To calculate (64) we have used the chemical equilibrium condition $\mu_d = \mu_u + \mu_e$ and also the relations derived from Fermi liquid theory [9]

$$v_F = 1 - \frac{C_F \alpha_s}{2\pi}; \quad \delta\mu = \frac{C_F \alpha_s}{\pi} \mu. \quad (65)$$

Putting $|M|^2$ in (48) we have

$$\frac{1}{l_{\text{mean}}^{\text{abs},ND}} = \frac{3C_F \alpha_s}{4\mathbf{p}^6} G^2 \cos^2 \theta_c \int d^3 p_d \int d^3 p_u \int d^3 p_e \delta^4(p_d + P_\nu - p_u - p_e) n(p_d) [1 - n(p_u)] [1 - n(p_e)]. \quad (66)$$

Neglecting the neutrino momentum in the neutrino momentum conserving δ function, the integrals can be decoupled into two parts. Following the procedure described by Iwamoto [31], the angular integral is given by

$$\mathcal{A} = \int d\Omega_d \int d\Omega_u \int d\Omega_e \delta(p_d - p_u - p_e) = \frac{8\pi^2}{\mu_d \mu_u \mu_e} \quad (67)$$

and the other part

$$\mathcal{D} = \int_0^\infty p_d^2 \frac{dp_d}{dE_d} dE_d \int_0^\infty p_u^2 \frac{dp_u}{dE_u} dE_u \int_0^\infty p_e^2 dE_e \quad (68)$$

$$\delta(E_d + E_\nu - E_u - E_e) n(p_d) [1 - n(p_u)] [1 - n(p_e)].$$

Changing the variables to $x_d = (E_d - \mu_d)\beta$, $x_u = -(E_u - \mu_u)\beta$, and $x_e = -(E_e - \mu_e)\beta$ and denoting the single particle energy $E_{u(d)}$ as ω we have from (68)

$$\mathcal{D} = \int_{-\infty}^\infty dx_d dx_u dx_e \frac{dp_d(\omega)}{d\omega} \frac{dp_u(\omega)}{d\omega} p_d^2 p_u^2 p_e^2 \delta \times (x_d + x_u + x_e + \beta E_\nu) n(x_d) n(-x_u) n(-x_e). \quad (69)$$

As the contribution dominates near the Fermi surfaces, extension of lower limit is reasonable [41, 44].

The integration of (69) can be performed using (57) and following the procedure defined in [37, 41, 44] to give

$$\mathcal{D} = \mu_d^2 \mu_u^2 \mu_e^2 \frac{(E_\nu^2 + \pi^2 T^2)}{2(1 + e^{-\beta E_\nu})} \left[1 + \frac{C_F \alpha_s}{3\pi} \ln \left(\frac{m_D}{T} \right) \right]^2. \quad (70)$$

Using (66), (67), and (70), the mean free path at leading order in T/μ is given by

$$\frac{1}{l_{\text{mean}}^{\text{abs},ND}} = \frac{3C_F \alpha_s}{\pi^4} G^2 \cos^2 \theta_c \mu_d \mu_u \mu_e \times \frac{(E_\nu^2 + \pi^2 T^2)}{(1 + e^{-\beta E_\nu})} \left[1 + \frac{C_F \alpha_s}{3\pi} \ln \left(\frac{m_D}{T} \right) \right]^2. \quad (71)$$

The first term is known from [31], and the additional terms are higher order corrections to the previous results derived in the present work.

For the scattering of nondegenerate neutrinos in quark matter, the expression of mean free path was given by Iwamoto [31]. We incorporate the anomalous effect which enters through phase space modification giving rise to

$$\frac{1}{l_{\text{mean}}^{\text{scatt,ND}}} = \frac{C_{V_i}^2 + C_{A_i}^2}{20} n_{q_i} \sigma_0 \times \left(\frac{E_\nu}{m_{q_i}} \right)^2 \left(\frac{E_\nu}{\mu_i} \right) \left[1 + \frac{C_F \alpha_s}{3\pi} \ln \left(\frac{m_D}{T} \right) \right]^2. \quad (72)$$

Here, we have assumed $m_{q_i}/p_{f_i} \ll 1$. The constants σ_0 and number density n_{q_i} have been defined earlier.

We now estimate the numerical values of the neutrino mean free paths. Here, E_ν is set to be equal to $3T$ and $m_q = 10$ MeV [31, 34]. For the quark chemical potential, following [9], we take $\mu_q \approx 500$ MeV corresponding to densities $\rho_b \approx 6\rho_0$, where ρ_0 is the nuclear matter saturation density. The electron chemical potential is determined by using the charge neutrality and beta equilibrium conditions which yields $\mu_e = 11$ Mev. The other parameters used are the same as [9].

From Figure 5, we find for degenerate neutrinos at the anomalous logarithmic terms reduce the value of the mean free path appreciably both in the low and high temperature regimes. Figure 6 shows that for nondegenerate neutrinos NFL correction is quite large at low temperature while at higher temperature it tends to merge. It is interesting to see from these two plots that NFL correction to the MFP in degenerate neutrinos is less than that of nondegenerate neutrinos [3]. This reduced mean free path is expected to influence the cooling of the compact stars.

5. Cooling of Neutron Star

To analyze the cooling of the compact star [45–47], the specific heat capacity of the quark matter core needs to be taken into consideration along with the emissivity via the cooling equation [9, 36]

$$\frac{\partial u}{\partial t} = \frac{\partial u}{\partial T} \frac{\partial T}{\partial t} = C_v(T) \frac{dT}{dt} = -\epsilon(T), \quad (73)$$

where u is the internal energy, C_v is the specific heat at constant volume and baryon number, ϵ is the emissivity, t is time, and T is the temperature, and we have assumed that there is no surface emission.

Emissivity under different scenarios both for quark and nuclear matters has been studied extensively. For the specific heat however earlier literatures were concerned only with the kinetic energy contribution without paying much attention to the QCD interaction. Recently several authors have shown that the interaction can lead to a significant correction to C_v . It has been shown that this interaction mediated by the gluons can give rise to a leading $T \ln T^{-1}$ term in the specific heat [48, 49]. This logarithmic enhancement comes from long-range chromomagnetic fields which eventually leads to non-Fermi-liquid behavior. The calculation of C_v including NFL

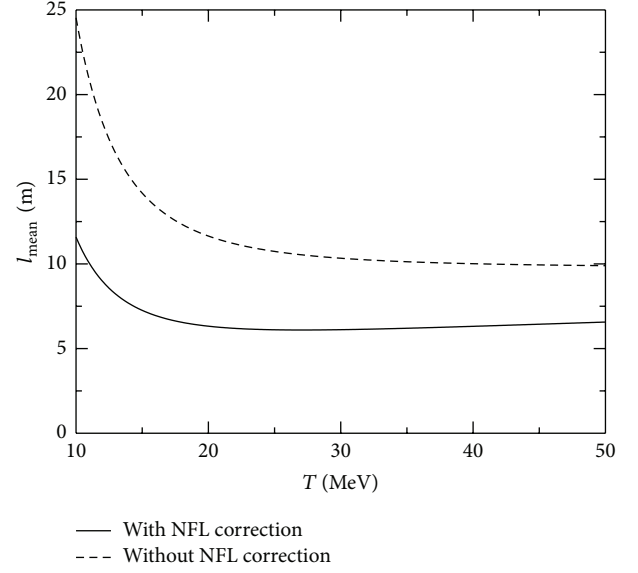


FIGURE 5: Neutrino mean free path in quark matter for degenerate neutrinos [3].

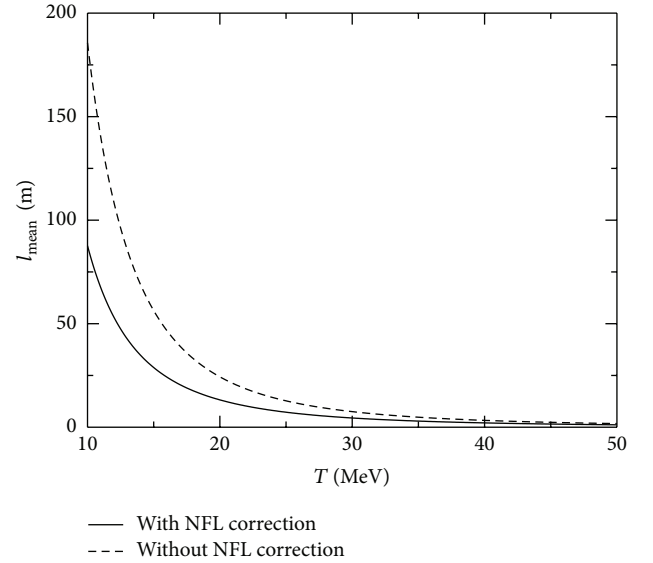


FIGURE 6: Neutrino mean free path in quark matter for nondegenerate neutrinos [3].

correction has been done in [48, 49] which we quote here for further use:

$$C_v = \frac{N_c N_f}{3} \mu^2 T + \frac{N_c N_f}{9\pi} \mu^2 C_F \alpha_s T \ln \left(\frac{0.28 m_D}{T} \right). \quad (74)$$

On the other hand, the neutrino emissivity of degenerate quark matter was first derived by Iwamoto [31]. Latter Schäfer and Schwenzer [9] calculated the neutrino emissivity including the corrections for NFL effects. The calculation has been made by considering the energy loss due to neutrino emission from the core of the neutron star. Alternatively, one

can also determine the neutrino emissivity from the mean free path by evaluating the integral [31]

$$\begin{aligned} \epsilon &= \int \frac{d^3 p_\nu}{(2\mathbf{p})^3} \frac{E_\nu}{I_{\text{mean}}^{\text{abs,ND}}(-E_\nu, T)} \\ &\approx \frac{457}{630} G^2 \cos^2 \theta_c \alpha_s \mu_u \mu_d \mu_e T^6 \left(1 + \frac{C_F \alpha_s}{3\pi} \log \left(\frac{m_D}{T} \right) \right)^2. \end{aligned} \quad (75)$$

This is the same as given in [9]. In this context, it is to be mentioned that without such non-Fermi liquid effects we have $\epsilon \sim T^6$ and $C_\nu \sim T$. In this case the temperature scales turn out to be $T \propto 1/t^{1/4}$ [9]. With logarithmic corrections included, no simple analytic solution is possible, and we solve (73) numerically.

We observe from Figure 7 that the cooling of neutron star is significantly faster with NFL corrections as compared to the Fermi liquid result [9].

6. Thermal Relaxation Time

In this section we address the issue of thermal conduction that follows the initial cooling by the neutrino emission. This phenomenon is intimately connected to the thermal relaxation mechanism. A new born star emits a large amount of neutrinos to cool the core, but the crust remains hot. Hence, a temperature gradient is set up between the crust and the core. Immediately after the neutrino emission discussed earlier in the paper thermal energy gradually flows from outer crust to the inner core by heat conduction which, alternatively, might be viewed as the propagation of the cooling waves from the center towards the surface leading to thermalization. We in this section estimate the thermalization time scale (τ_κ) and reveal the NFL behavior of the quantity in the context of the neutron star crust. In the latter the electrons constitute an almost ideal Fermi gas and scatter between themselves. The kinetic theory definition of τ_κ is

$$\tau_\kappa = \frac{3\kappa}{C_\nu}. \quad (76)$$

In case of the strongly degenerate electron gas the electron thermal conductivity (κ_e) can be expressed in terms of the thermal current J_T as follows:

$$\kappa_e = \frac{J_T}{T\nu_e}, \quad \nu_e = \nu_{ei} + \nu_{ee}, \quad (77)$$

where ν_e is the total effective collision frequency. In the neutron star crust the main components that contribute to different transport coefficients are electrons and ions. Hence, the total collision frequency is the sum of the partial collision frequencies of electron-ion (ν_{ei}) and electron-electron (ν_{ee}). Evidently κ_e is related to κ_{ee} and κ_{ei} via the following expression [50, 51]:

$$\begin{aligned} \frac{1}{\kappa_e} &= \frac{1}{\kappa_{ei}} + \frac{1}{\kappa_{ee}}, \\ \kappa_{ei} &= \frac{J_T}{T\nu_{ei}}, \quad \kappa_{ee} = \frac{J_T}{T\nu_{ee}}. \end{aligned} \quad (78)$$

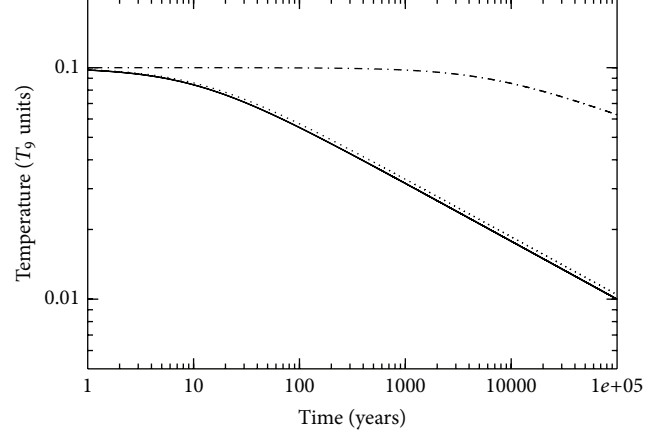


FIGURE 7: The cooling behavior of neutron star with core as neutron matter and degenerate quark matter. The dotted line represents the Fermi liquid result; the solid line gives the result including non-Fermi liquid correction. The dash-dotted line gives the cooling behavior of the neutron star core made up of purely neutron matter.

Thus the derivation of κ_{ee} involves the calculation of ν_{ee} . To derive ν_{ee} we start with the Boltzmann equation which describes the kinetics of the particles:

$$\left(\frac{\partial}{\partial t} + \mathbf{v}_p \cdot \nabla_r + \mathbf{F} \cdot \nabla_p \right) n_p = -\mathcal{E} [n_p], \quad (79)$$

where \mathbf{p} is the momentum of the quasiparticle, \mathbf{F} is the external force, \mathbf{v}_p is the velocity of the heat carrier, and n_p is the distribution function of electrons. The right hand side of the Boltzmann equation is the collision integral describing the rate of scattering of fermions. In the presence of a weak stationary temperature gradient Boltzmann equation takes the following form:

$$\mathbf{v}_p \cdot \nabla_r n_p = -\mathcal{E} [n_p]. \quad (80)$$

The Fermi-Dirac distribution functions deviate from equilibrium distribution functions n_i due to the presence of a weak temperature gradient, which we write as

$$\tilde{n}_i = n_i + \frac{\partial n_i}{\partial \epsilon_i} \Phi_i \frac{\nabla T}{T}, \quad (81)$$

where

$$n_i = \left\{ \exp \left(\frac{\epsilon_i - \mu}{T} \right) + 1 \right\}^{-1}, \quad (82)$$

ϵ is the particle energy, μ is the chemical potential, and T is the temperature. The term with Φ measures the deviation from equilibrium. The collision integral can be written as follows:

$$\begin{aligned} \mathcal{E} [n_p] &= \nu \nu' \int_{p', k, k'} \tilde{n}_p \tilde{n}_k (1 \pm \tilde{n}_p) (1 \pm \tilde{n}_k) \\ &\quad - \tilde{n}_p \tilde{n}_k' (1 \pm \tilde{n}_p) (1 \pm \tilde{n}_k) (2\pi)^4 \delta^4 \\ &\quad \times (p + k - p' - k') |M|^2. \end{aligned} \quad (83)$$

In the previous equation ν, ν' are the degeneracy factors and $|M|^2$ is the squared matrix element for the $2 \rightarrow 2$ scattering process. The \pm sign is meant for stimulated emission or Pauli blocking. Since we consider only the electron-electron scattering, the negative sign will remain in the phase space factor. We write the previous equation in the form $|X\rangle = I|\Phi\rangle$, where $|X\rangle = (\epsilon_p - \mu)v_p$ and I is the integral operator. The thermal conductivity κ_{ee} is then given by the maximum of the following equation [52, 53]:

$$\kappa_{ee} = \frac{\langle X | \Phi \rangle^2}{T \langle \Phi | I | \Phi \rangle}; \quad (84)$$

$\langle \cdot | \cdot \rangle$ denotes an inner product; for $\Psi = \Phi$ the quantity $\langle X | \Psi \rangle^2 / T \langle \Psi | I | \Psi \rangle$ is minimal with the minimal value κ_{ee} . With the help of this definition one can write

$$\begin{aligned} \frac{1}{\kappa_{ee}} &\geq \left(\nu \int_p \frac{(\epsilon_p - \mu)}{T} v_z n_p (1 - n_p) \Psi_p \right)^{-2} \\ &\times \nu \nu' \int_{p,p',k,k'} n_p n_k (1 - n'_p) (1 - n'_k) \\ &\times (2\pi)^4 \delta^4(p + k - p' - k') |M|^2 \\ &\times \frac{(\Psi_p + \Psi_k - \Psi_{p'} - \Psi_{k'})^2}{4}; \end{aligned} \quad (85)$$

the first bracketed term in the denominator is the thermal current J_T . In principle Φ should be determined by minimizing (84) using the variational principle. But in the present scenario we consider the simplest trial function as [50, 52]

$$\Psi_p \propto (\epsilon_p - \mu) v_z. \quad (86)$$

The term in the bracket can be averaged over the z axis keeping x and ϕ fixed using the previous trial function, where, ϕ is the azimuthal angle between v_p and v_k . After averaging we obtain [52]

$$(\Psi_p + \Psi_k - \Psi_{p'} - \Psi_{k'})^2 = \frac{2}{3} \omega^2 (1 - x^2) (1 - \cos \phi). \quad (87)$$

For small energy transfer the electron-electron scattering squared matrix element is given by [52]

$$|M|^2 = 32e^4 \left[\frac{1}{(q^2 + \Pi_l)} + \frac{(1 - x^2) \cos \phi}{(q^2 - \omega^2 + \Pi_t)} \right]^2. \quad (88)$$

The medium modified photon propagator in the previous equation contains the polarization functions $\Pi_l(q_0, q)$ and $\Pi_t(q_0, q)$, which describe plasma screening of interparticle interaction by longitudinal and transverse plasma perturbations, respectively. Now, we first analyze the denominator

of (85). The denominator is the thermal current as defined earlier and is given by

$$\begin{aligned} J_T &= \nu \int_p \frac{(\epsilon_p - \mu)}{T} v_z n_p (1 - n_p) \Psi_p \\ &= \frac{\nu \mu^2 T^2}{6}. \end{aligned} \quad (89)$$

Here, the degeneracy factor for electrons is $\nu = 2$.

The fermionic dispersion relation gets modified due to the inclusion of the fermion self-energy in the presence of the medium. Hence, energy momentum relation changes from the vacuum. For the momentum integration in the phase-space integral in (85) we will use the medium modified dispersion relation given in (55). For this one needs to know the fermion self-energy. The fermion self-energy for the QCD matter has already been quoted in (56). In case of electrons at low temperature with NLO correction it is given by the following [1]:

$$\begin{aligned} \Sigma(\epsilon, k) &= e^2 m \\ &\times \left\{ \frac{\epsilon}{12\pi^2 m} \left[\log \left(\frac{4\sqrt{2}m}{\pi\epsilon} \right) + 1 \right] \right. \\ &+ \frac{i\epsilon}{24\pi m} + \frac{2^{1/3} \sqrt{3}}{45\pi^{7/3}} \left(\frac{\epsilon}{m} \right)^{5/3} (\text{sgn}(\epsilon) - \sqrt{3}i) \\ &+ \frac{i}{64\sqrt{2}} \left(\frac{\epsilon}{m} \right)^2 - 20 \frac{2^{2/3} \sqrt{3}}{189\pi^{11/3}} \left(\frac{\epsilon}{m} \right)^{7/3} (\text{sgn}(\epsilon) + \sqrt{3}i) \\ &- \frac{6144 - 256\pi^2 + 36\pi^4 - 9\pi^6}{864\pi^6} \left(\frac{\epsilon}{m} \right)^3 \\ &\left. \times \left[\log \left(\frac{0.928m}{\epsilon} \right) - \frac{i\pi \text{sgn}(\epsilon)}{2} \right] + \mathcal{O} \left(\left(\frac{\epsilon}{m} \right)^{11/3} \right) \right\}, \end{aligned} \quad (90)$$

where $m^2 = m_D^2/2$ and ϵ is chosen to be $(\epsilon_k - \mu)$. The phase-space correction due to the medium modified dispersion relation can now be written as [10]

$$\begin{aligned} \frac{dk}{d\epsilon_k} &\simeq 1 + \frac{e^2}{12\pi^2} \log \left(\frac{4}{\pi\lambda} \right) \\ &+ \frac{2^{2/3} e^2 \lambda^{2/3}}{9\sqrt{3}\pi^{7/3}} - \frac{40 \times 2^{1/3} e^2 \lambda^{4/3}}{27\sqrt{3}\pi^{11/3}} \dots \\ &= (1 + \beta), \end{aligned} \quad (91)$$

where $\lambda = T/m_D$. The expression for κ_{ee}^{-1} now becomes

$$\frac{1}{\kappa_{ee}} = \frac{\mathcal{P}}{T^2} \frac{dk}{d\epsilon_k} \frac{dp}{d\epsilon_p} I_{\kappa_{ee}} \left(\frac{T}{m_D} \right), \quad (92)$$

where $\mathcal{P} = 3e^4/4\pi^5$ and

$$I_{\kappa_{ee}} \left(\frac{T}{m_D} \right) \equiv \int_0^\infty \frac{d\omega}{\omega} \frac{\omega^2/4T^2}{(\sinh(\omega/2T))^2} \times \int_0^1 dx \int_0^{2\pi} \frac{d\phi}{2\pi} x^2 (1-x^2) (1-\cos\phi) \times \left| \frac{1}{1+(xm_D/\omega)^2 \chi_l(x)} - \frac{\cos\phi}{1+(xm_D/\omega)^2 \chi_t(x)/(1-x^2)} \right|^2. \quad (93)$$

In the previous equation we have used the following expression [10, 52]:

$$\int d\epsilon_p d\epsilon_k n_{\epsilon_p} n_{\epsilon_k} (1-n_{(\epsilon_p+\omega)}) (1-n_{(\epsilon_k-\omega)}) = (1+\beta) T^2 \frac{\omega^2/4T^2}{(\sinh(\omega/2T))^2}; \quad (94)$$

while writing the previous equation we have considered the medium modified phase-space factor only for the particle with momentum k . One can in principle take the correction for both the particles with momentum p and k , but that will contribute at higher order in coupling constant.

The final expression for the electron thermal conductivity now takes the following form [10]:

$$\kappa_{ee} = \left[\frac{\mathcal{P}}{T^2} (1+\beta) \times \left\{ 2\lambda^2 \zeta(3) + \frac{(2\pi)^{2/3}}{3} \lambda^{8/3} \zeta\left(\frac{11}{3}\right) \Gamma\left(\frac{14}{3}\right) + \frac{\pi^5}{15} \lambda^3 \right\} \right]^{-1}. \quad (95)$$

Unlike the Fermi-liquid result where $\kappa_{ee} \propto 1/T$, here the temperature dependence is nonanalytical and anomalous in nature. This is reminiscent of other quantities involving ultradegenerate plasma presented in the previous sections [1, 3–5]. κ_{ee} involves fractional powers in (T/m_D) coming from the medium modified phase space factor too.

For the estimation of relaxation time the other quantity which we require is the specific heat. For the degenerate electron gas it can be written as [48, 49]

$$C_v = \frac{\mu^2 T}{3} + \frac{m_D^2 T}{36} \left(\ln\left(\frac{4}{\pi\lambda}\right) + \gamma_E - \frac{6}{\pi^2} \zeta'(2) - 3 \right) - 40 \frac{2^{2/3} \Gamma(8/3) \zeta(8/3) m_D^3}{27 \sqrt{3} \pi^{7/3}} \lambda^{5/3} + 560 \frac{2^{1/3} \Gamma(10/3) \zeta(10/3) m_D^3}{81 \sqrt{3} \pi^{11/3}} \lambda^{7/3}. \quad (96)$$

With (95) and (96) the relaxation time for thermal conduction can be written as [10]

$$\tau_{\kappa_{ee}} = 3 \left[\frac{\mathcal{P}}{T^2} (1+\beta) \times \left\{ 2\lambda^2 \zeta(3) + \frac{(2\pi)^{2/3}}{3} \lambda^{8/3} \zeta\left(\frac{11}{3}\right) \times \Gamma\left(\frac{14}{3}\right) + \frac{\pi^5}{15} \lambda^3 \right\} \right]^{-1} \times \left(\left[\frac{\mu^2 T}{3} + \frac{m_D^2 T}{36} \left(\ln\left(\frac{4}{\pi\lambda}\right) + \gamma_E - \frac{6}{\pi^2} \zeta'(2) - 3 \right) - 40 \frac{2^{2/3} \Gamma(8/3) \zeta(8/3) m_D^3}{27 \sqrt{3} \pi^{7/3}} \lambda^{5/3} + 560 \frac{2^{1/3} \Gamma(10/3) \zeta(10/3) m_D^3}{81 \sqrt{3} \pi^{11/3}} \lambda^{7/3} \right] \right)^{-1}. \quad (97)$$

The thermal relaxation time up to NLO terms contains some anomalous fractional powers originated from the transverse interaction. This in turn changes the temperature dependence of $\tau_{\kappa_{ee}}$ nontrivially. The departure from the Fermi liquid result ($\tau_{\kappa_{ee}} \propto 1/T^2$) is evident from the final expression of $\tau_{\kappa_{ee}}$.

In Figures 8, 9, 10, and 11 we have plotted κ_{ee} and $\tau_{\kappa_{ee}}$ with T using (95) and (97). From the plots it can be seen that the inclusion of both the medium modified propagator and β decreases the value of κ_{ee} and $\tau_{\kappa_{ee}}$. It shows strong deviation from the Fermi liquid in both cases. In Figures 9 and 11 it has been shown that β reduces both the thermal conductivity and the thermal relaxation time. This has a serious implication on the total electron conductivity κ_e . In [50] it has been shown that magnetic interaction decreases κ_{ee} which in turn increases the electron-electron collision frequency. Thus to the total electron thermal conductivity electron-electron scattering dominates over electron-ion scattering. The phase space correction due to the medium modified electron dispersion relation further enhances the electron-electron collision frequency [10].

7. Conclusion

Investigation of the quasiparticle excitation in ultradegenerate plasma has been the cardinal focus of the present review. The main interesting feature which has been exposed here is the role of magnetic interaction mediated by the transverse gauge bosons leading to the phenomena very different from its high temperature counterpart. In particular the NFL behaviour of various quantities like C_v , κ_{ee} , and $l_{\text{mean}}^{\text{total}}$ involving excitations near the Fermi surface is a very special characteristic behaviour of degenerate or ultradegenerate plasma. We also show clearly how the dynamical screening leads to finite damping rate emanating from the restricted phase space driven by the Pauli blocking. Besides the damping rate we also present results for the drag and the

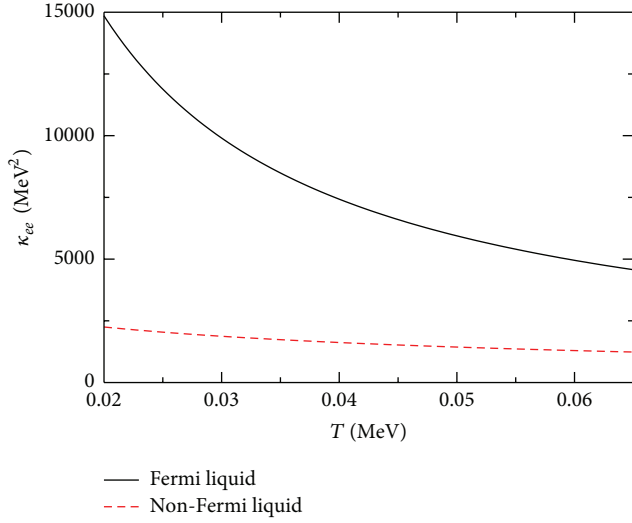


FIGURE 8: Temperature dependence of the electron thermal conductivity and comparison between the Fermi liquid and the non-Fermi-liquid NLO results where $\beta \neq 0$.

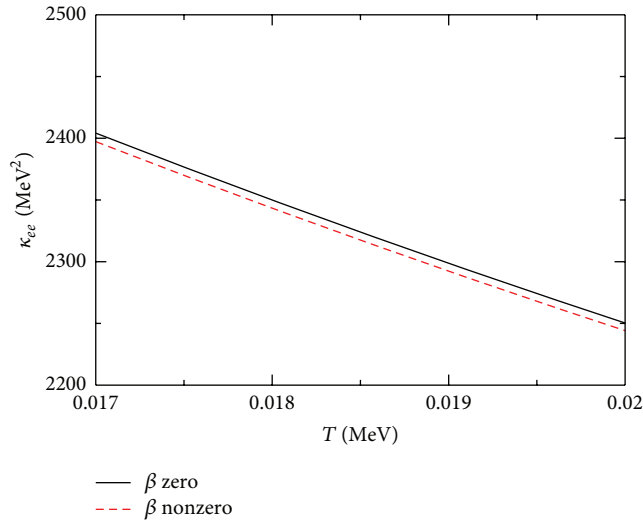


FIGURE 9: The reduction of κ_{ee} with the inclusion of β .

diffusion coefficients, that is, the energy and the momentum relaxation of the quasiparticle excitation in such a plasma revealing further the domination of the magnetic interaction over the electric interactions in ultradegenerate plasma. This separation between the longitudinal and the transverse sectors is a very special feature of the cold and dense plasma which is not seen in the finite temperature case.

Another aspect of the present work has been the modification of the quasiparticle dispersion relation which changes the phase-space in a nontrivial way leading to modification of $\tau_{\kappa_{ee}}$ and l_{mean} . Further investigations along this line are pertinent to understand various phenomena of astrophysical interests. Some of these extensions have recently been undertaken by various authors showing the importance of

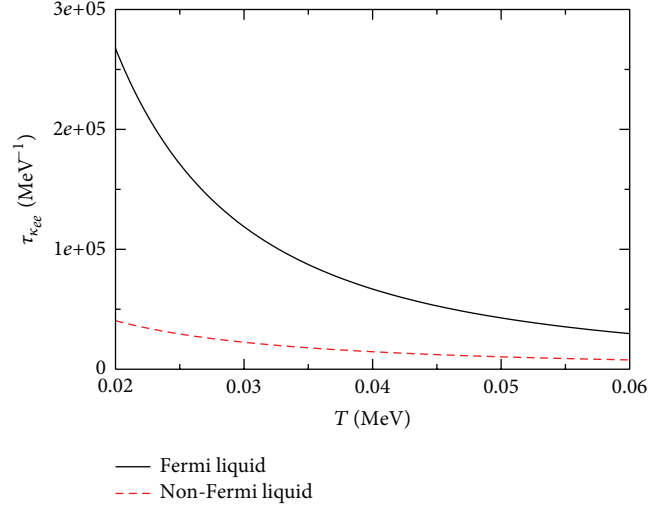


FIGURE 10: Temperature dependence of the thermal relaxation time and comparison between the Fermi liquid and the non-Fermi-liquid NLO results where $\beta \neq 0$.

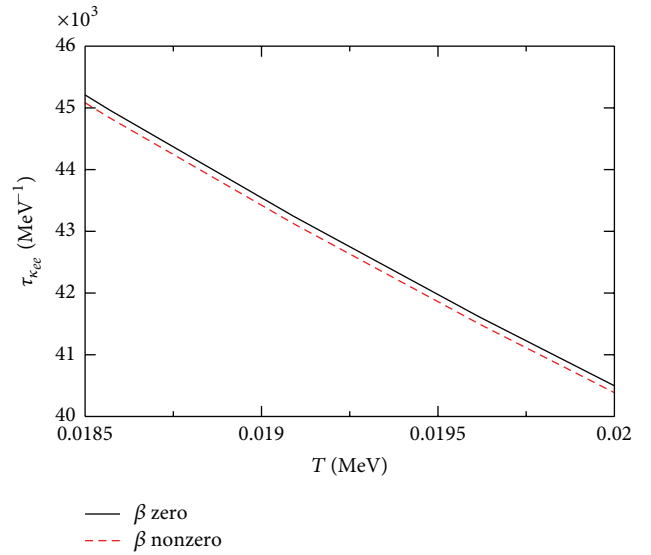


FIGURE 11: The reduction of $\tau_{\kappa_{ee}}$ with the inclusion of β .

this emerging area particularly due to the possibility of experiments in the domain of high chemical potential and low temperature in addition to its relevance in the astrophysical context.

References

- [1] A. Gerhold and A. Rebhan, “Fermionic dispersion relations in ultradegenerate relativistic plasmas beyond leading logarithmic order,” *Physical Review D*, vol. 71, no. 8, Article ID 085010, 6 pages, 2005.
- [2] S. Sarkar and A. K. Dutt-Mazumder, “Energy and momentum relaxation of heavy fermion in dense and warm plasma,” *Physical Review D*, vol. 82, no. 5, Article ID 056003, 7 pages, 2010.

- [3] K. Pal and A. K. Dutt-Mazumder, “Non-Fermi liquid corrections to the neutrino mean free path in dense quark matter,” *Physical Review D*, vol. 84, no. 3, Article ID 034004, 6 pages, 2011.
- [4] S. Sarkar and A. K. Dutt-Mazumder, “Non-Fermi liquid behavior of the drag and diffusion coefficients in QED plasma,” *Physical Review D*, vol. 84, no. 9, Article ID 096009, 7 pages, 2011.
- [5] S. P. Adhya, P. K. Roy, and A. K. Dutt-Mazumder, “Next-to-leading order non-Fermi-liquid corrections to the neutrino emissivity and cooling of the neutron star,” *Physical Review D*, vol. 86, no. 3, Article ID 034012, 8 pages, 2012.
- [6] M. Le Bellac and C. Manuel, “Damping rate of quasiparticles in degenerate ultrarelativistic plasmas,” *Physical Review D*, vol. 55, no. 5, pp. 3215–3218, 1997.
- [7] B. Vanderheyden and J. Ollitrault, “Damping rates of hard momentum particles in a cold ultrarelativistic plasma,” *Physical Review D*, vol. 56, no. 8, pp. 5108–5122, 1997.
- [8] C. Manuel, “Dispersion relations in ultradegenerate relativistic plasmas,” *Physical Review D*, vol. 62, no. 7, Article ID 076009, 7 pages, 2000.
- [9] T. Schäfer and K. Schwenzer, “Neutrino emission from ungapped quark matter,” *Physical Review D*, vol. 70, no. 11, Article ID 114037, 7 pages, 2004.
- [10] S. Sarkar and A. K. Dutt-Mazumder, “Non-Fermi liquid behavior of thermal relaxation time in degenerate electron plasma,” *Physical Review D*, vol. 87, no. 7, Article ID 076003, 8 pages, 2013.
- [11] R. D. Pisarski, “Scattering amplitudes in hot gauge theories,” *Physical Review Letters*, vol. 63, no. 11, pp. 1129–1132, 1989.
- [12] E. Braaten and R. D. Pisarski, “Soft amplitudes in hot gauge theories: a general analysis,” *Nuclear Physics B*, vol. 337, no. 3, pp. 569–634, 1990.
- [13] J. P. Blaizot and E. Iancu, “Lifetime of quasiparticles in hot QED plasmas,” *Physical Review Letters*, vol. 76, no. 17, pp. 3080–3083, 1996.
- [14] J. P. Blaizot and E. Iancu, “Lifetimes of quasiparticles and collective excitations in hot QED plasmas,” *Physical Review D*, vol. 55, no. 2, pp. 973–996, 1997.
- [15] M. Alford, K. Rajagopal, and F. Wilczek, “Color-flavor locking and chiral symmetry breaking in high density QCD,” *Nuclear Physics B*, vol. 537, no. 1–3, pp. 443–458, 1999.
- [16] P. Jaikumar, M. Prakash, and T. Schafer, “Neutrino emission from Goldstone modes in dense quark matter,” *Physical Review D*, vol. 66, no. 6, Article ID 063003, 12 pages, 2002.
- [17] S. Reddy, M. Sadzikowski, and M. Tachibana, “Neutrino rates in color flavor locked quark matter,” *Nuclear Physics A*, vol. 714, no. 1–2, pp. 337–351, 2003.
- [18] J. Kundu and S. Reddy, “Neutrino scattering off pair-breaking and collective excitations in superfluid neutron matter and in color-flavor-locked quark matter,” *Physical Review C*, vol. 70, no. 5, Article ID 055803, 15 pages, 2004.
- [19] M. Le Bellac, *Thermal Field Theory*, Cambridge Monographs on Mathematical Physics, Cambridge University Press, Cambridge, UK, 1996.
- [20] E. Braaten and T. C. Yuan, “Calculation of screening in a hot plasma,” *Physical Review Letters*, vol. 66, no. 17, pp. 2183–2186, 1991.
- [21] C. Manuel, “Hard dense loops in a cold non-Abelian plasma,” *Physical Review D*, vol. 53, no. 10, pp. 5866–5873, 1996.
- [22] S. Sarkar and A. K. Dutt-Mazumder, “Drag and diffusion coefficients in extreme scenarios of temperature and chemical potential,” <http://arxiv.org/abs/1303.3353>.
- [23] A. A. Abrikosov, L. P. Gorkov, and I. E. Dzyaloshinski, *Methods of Quantum Field Theory in Statistical Physics*, Dover, New York, NY, USA, 1963.
- [24] B. Svetitsky, “Diffusion of charmed quarks in the quark-gluon plasma,” *Physical Review D*, vol. 37, no. 9, pp. 2484–2491, 1988.
- [25] E. Braaten and M. H. Thoma, “Energy loss of a heavy fermion in a hot QED plasma,” *Physical Review D*, vol. 44, no. 4, pp. 1298–1310, 1991.
- [26] G. D. Moore and D. Teaney, “How much do heavy quarks thermalize in a heavy ion collision?” *Physical Review C*, vol. 71, no. 6, Article ID 064904, 19 pages, 2005.
- [27] A. K. Dutt-Mazumder, J. Alam, P. Roy, and B. Sinha, “Stopping power of hot QCD plasma,” *Physical Review D*, vol. 71, no. 9, Article ID 094016, 9 pages, 2005.
- [28] P. Roy, A. K. Dutt-Mazumder, and J. Alam, “Energy loss and dynamical evolution of quark pT spectra,” *Physical Review C*, vol. 73, no. 4, Article ID 044911, 4 pages, 2006.
- [29] A. Beraudo, A. de Pace, W. M. Alberico, and A. Molinari, “Transport properties and Langevin dynamics of heavy quarks and quarkonia in the quark gluon plasma,” *Nuclear Physics A*, vol. 831, no. 1–2, pp. 59–90, 2009.
- [30] N. Iwamoto, “Quark beta decay and the cooling of neutron stars,” *Physical Review Letters*, vol. 44, no. 24, pp. 1637–1640, 1980.
- [31] N. Iwamoto, “Neutrino emissivities and mean free paths of degenerate quark matter,” *Annals of Physics*, vol. 141, no. 1, pp. 1–49, 1982.
- [32] D. L. Tubbs and D. N. Schramm, “Neutrino opacities at high temperatures and densities,” *The Astrophysical Journal*, vol. 201, pp. 467–488, 1975.
- [33] D. Q. Lamb and C. J. Pethick, “Effects of neutrino degeneracy in supernova models,” *The Astrophysical Journal Letters*, vol. 209, part 2, pp. L77–L81, 1976.
- [34] I. Sagert and J. Schaffner-Bielich, “Asymmetric neutrino emission in quark matter and pulsar kicks,” <http://arxiv.org/abs/astro-ph/0612776>.
- [35] N. Barash-Schmidt, R. L. Kelly, C. P. Horne et al., “Review of particle properties,” *Reviews of Modern Physics*, vol. 52, no. 2, part 2, pp. S1–S286, 1980.
- [36] D. Boyanovsky and H. J. de Vega, “Specific heat of normal, degenerate quark matter: non-Fermi liquid corrections,” *Physical Review D*, vol. 63, no. 11, Article ID 114028, 9 pages, 2001.
- [37] K. Sato and T. Tatsumi, “Spontaneous magnetization in QCD and non-Fermi-liquid effects,” *Nuclear Physics A*, vol. 826, no. 1–2, pp. 74–100, 2009.
- [38] T. Schäfer and K. Schwenzer, “Non-Fermi liquid effects in QCD at high density,” *Physical Review D*, vol. 70, no. 5, Article ID 054007, 8 pages, 2004.
- [39] W. E. Brown, J. T. Liu, and H. C. Ren, “Perturbative nature of color superconductivity,” *Physical Review D*, vol. 61, no. 11, Article ID 114012, 7 pages, 2000.
- [40] W. E. Brown, J. T. Liu, and H. C. Ren, “Non-Fermi liquid behavior, the Becchi-Rouet-Stora-Tyutin identity in the dense quark-gluon plasma, and color superconductivity,” *Physical Review D*, vol. 62, no. 5, Article ID 054013, 13 pages, 2000.
- [41] S. L. Shapiro and S. A. Teukolsky, *Black Holes, White Dwarfs and Neutron Stars*, Wiley-Interscience, New York, NY, USA, 1983.
- [42] R. C. Duncan, S. L. Shapiro, and I. Wasserman, “Equilibrium composition and neutrino emissivity of interacting quark matter in neutron stars,” *The Astrophysical Journal*, vol. 267, pp. 358–370, 1983.

- [43] X. Huang, Q. Wang, and P. Zhuang, "Neutrino emission from direct Urca processes in pion condensed quark matter," *Physical Review D*, vol. 76, no. 9, Article ID 094008, 11 pages, 2007.
- [44] D. G. Yakovlev, A. D. Kaminker, O. Y. Gnedin, and P. Haensel, "Neutrino emission from neutron stars," *Physics Report*, vol. 354, no. 1-2, pp. 1-155, 2001.
- [45] D. G. Yakovlev and C. J. Pethick, "Neutron star cooling," *Annual Review of Astronomy and Astrophysics*, vol. 42, pp. 169-210, 2004.
- [46] J. P. Finley, H. Ogelman, and U. Kiziloglu, "ROSAT observations of PSR 0656 + 14: a pulsating and cooling neutron star," *The Astrophysical Journal Letters*, vol. 394, no. 1, pp. L21-L24, 1992.
- [47] R. E. Rutledge, L. Bildsten, E. F. Brown, G. G. Pavlov, and V. E. Zavlin, "The quiescent x-ray spectrum of the neutron star in centaurus x-4 observed with Chandra/ACIS-S," *The Astrophysical Journal Letters*, vol. 551, no. 2, pp. 921-928, 2001.
- [48] A. Gerhold, A. Ipp, and A. Rebhan, "Anomalous specific heat in high-density QED and QCD," *Physical Review D*, vol. 69, no. 1, Article ID 011901(R), 4 pages, 2004.
- [49] A. Gerhold, A. Ipp, and A. Rebhan, "Non-Fermi-liquid specific heat of normal degenerate quark matter," *Physical Review D*, vol. 70, no. 10, Article ID 105015, 17 pages, 2004.
- [50] P. S. Shternin and D. G. Yakovlev, "Electron thermal conductivity owing to collisions between degenerate electrons," *Physical Review D*, vol. 74, no. 4, Article ID 043004, 8 pages, 2006.
- [51] P. S. Shternin and D. G. Yakovlev, "Electron-muon heat conduction in neutron star cores via the exchange of transverse plasmons," *Physical Review D*, vol. 75, no. 10, Article ID 103004, 15 pages, 2007.
- [52] H. Heiselberg and C. J. Pethick, "Transport and relaxation in degenerate quark plasmas," *Physical Review D*, vol. 48, no. 6, pp. 2916-2928, 1993.
- [53] G. Baym and C. J. Pethick, *Landau Fermi-Liquid Theory Concepts and Applications*, Wiley-Interscience, New York, NY, USA, 1991.

Review Article

Particle Production in Strong Electromagnetic Fields in Relativistic Heavy-Ion Collisions

Kirill Tuchin

Department of Physics and Astronomy, Iowa State University, Ames, IA 50011, USA

Correspondence should be addressed to Kirill Tuchin; tuchink@gmail.com

Received 31 December 2012; Accepted 11 April 2013

Academic Editor: Jan E. Alam

Copyright © 2013 Kirill Tuchin. This is an open access article distributed under the Creative Commons Attribution License, which permits unrestricted use, distribution, and reproduction in any medium, provided the original work is properly cited.

I review the origin and properties of electromagnetic fields produced in heavy-ion collisions. The field strength immediately after a collision is proportional to the collision energy and reaches $\sim m_\pi^2$ at RHIC and $\sim 10m_\pi^2$ at LHC. I demonstrate by explicit analytical calculation that after dropping by about one-two orders of magnitude during the first fm/c of plasma expansion, it freezes out and lasts for as long as quark-gluon plasma lives as a consequence of finite electrical conductivity of the plasma. Magnetic field breaks spherical symmetry in the direction perpendicular to the reaction plane, and therefore all kinetic coefficients are anisotropic. I examine viscosity of QGP and show that magnetic field induces azimuthal anisotropy on plasma flow even in spherically symmetric geometry. Very strong electromagnetic field has an important impact on particle production. I discuss the problem of energy loss and polarization of fast fermions due to synchrotron radiation, consider photon decay induced by magnetic field, elucidate J/ψ dissociation via Lorentz ionization mechanism, and examine electromagnetic radiation by plasma. I conclude that *all* processes in QGP are affected by strong electromagnetic field and call for experimental investigation.

1. Origin and Properties of Electromagnetic Field

1.1. Origin of Magnetic Field. We can understand the origin of magnetic field in heavy-ion collisions by considering collision of two ions of radius R with electric charge Ze (e is the magnitude of electron charge) at impact parameter \mathbf{b} . According to the Biot and Savart law they create magnetic field that in the center-of-mass frame has magnitude

$$B \sim \gamma Ze \frac{b}{R^3} \quad (1)$$

and points in the direction perpendicular to the reaction plane (span by the momenta of ions). Here $\gamma = \sqrt{s_{NN}}/2m_N$ is the Lorentz factor. At RHIC heavy ions are collided at 200 GeV per nucleon, hence $\gamma = 100$. Using $Z = 79$ for gold and $b \sim R_A \approx 7$ fm we estimate $eB \approx m_\pi^2 \sim 10^{18}$ G. To appreciate how strong is this field, compare it with the following numbers: the strongest magnetic field created on earth in a form of electromagnetic shock wave is $\sim 10^7$ G [1],

and magnetic field of a neutron star is estimated to be $10^{10} - 10^{13}$ G, that of a magnetar up to 10^{15} G [2]. It is perhaps the strongest magnetic field that has ever existed in nature.

It has been known for a long time that classical electrodynamics breaks down at the critical (Schwinger) field strength $F = m_e^2/e$ [3]. In cgs units the corresponding magnetic field is 10^{13} G. Because $m_\pi/m_e = 280$, electromagnetic fields created at RHIC and LHC are well above the critical value. This offers a unique opportunity to study the super-strong electromagnetic fields in laboratory. The main challenge is to identify experimental observables that are sensitive to such fields. The problem is that nearly all observables studied in heavy-ion collisions are strongly affected both by the strong color forces acting in quark-gluon plasma (QGP) and by electromagnetic fields often producing qualitatively similar effects. An outstanding experimental problem thus is to separate the two effects. In Sections 2–7 I examine several processes strongly affected by intense magnetic fields and discuss their phenomenological significance. But first, in this section, let me derive a quantitative estimate of electromagnetic field.

Throughout this paper, the heavy-ion collision axis is denoted by z . Average magnetic field then points in the y -direction; see Figures 1 and 7. Plane xz is the reaction plane, and b is the impact parameter.

1.2. Magnetic Field in Vacuum

1.2.1. Time Dependence. To obtain a quantitative estimate of magnetic field we need to take into account a realistic distribution of protons in a nucleus. This has been first done in [5] (in the case of high-energy pp collisions, magnetic field was first estimated in [9] who also pointed out a possibility of formation of W -condensate [9, 10]). Magnetic field at point \mathbf{r} created by two heavy ions moving in the positive or negative z -direction can be calculated using the Liénard-Wiechert potentials as follows:

$$e\mathbf{E}(t, \mathbf{r}) = \alpha_{\text{em}} \sum_a \frac{(1 - v_a^2) \mathbf{R}_a}{R_a^3 [1 - (\mathbf{R}_a \times \mathbf{v}_a)^2 / R_a^2]^{3/2}}, \quad (2)$$

$$e\mathbf{B}(t, \mathbf{r}) = \alpha_{\text{em}} \sum_a \frac{(1 - v_a^2) (\mathbf{v}_a \times \mathbf{R}_a)}{R_a^3 [1 - (\mathbf{R}_a \times \mathbf{v}_a)^2 / R_a^2]^{3/2}}, \quad (3)$$

with $\mathbf{R}_a = \mathbf{r} - \mathbf{r}_a(t)$, where sums run over all Z protons in each nucleus, their positions and velocities being \mathbf{r}_a and \mathbf{v}_a . The magnitude of velocity v_a is determined by the collision energy $\sqrt{s_{NN}}$ and the proton mass m_p , $v_a^2 = 1 - (2m_p / \sqrt{s_{NN}})^2$. These formulas are derived in the eikonal approximation, assuming that protons travel on straight lines before and after the scattering. This is a good approximation, since baryon stopping is a small effect at high energies. Positions of protons in heavy ions can be determined by one of the standard models of the nuclear charge density $\rho(\mathbf{r}_a)$. Reference [5] employed the ‘‘hard sphere’’ model, while [4] used a bit more realistic Woods-Saxon distribution.

Numerical integration in (3) including small contribution from baryon stopping yields for magnetic field the result shown in Figure 2 as a function of the proper time $\tau = (t^2 - z^2)^{1/2}$. Evidently, magnetic field rapidly decreases as a power of time, so that after first 3 fm it drops by more than three orders of magnitude.

1.2.2. Event-by-Event Fluctuations in Proton Positions. Nuclear charge density ρ provides only event-averaged distribution of protons. The actual distribution in a given event is different form ρ implying that in a single event there is not only magnetic field along the y -direction, but also other components of electric and magnetic fields. This leads to event-by-event fluctuations of electromagnetic field [4]. Shown in Figure 3 are electric and magnetic field components at $t = 0$ at the origin (denoted by a black dot in Figure 1) in AuAu collisions at $\sqrt{s_{NN}} = 200$ GeV.

Figure 3 clearly shows that although on average the only nonvanishing component of the field is B_y , which is also clear

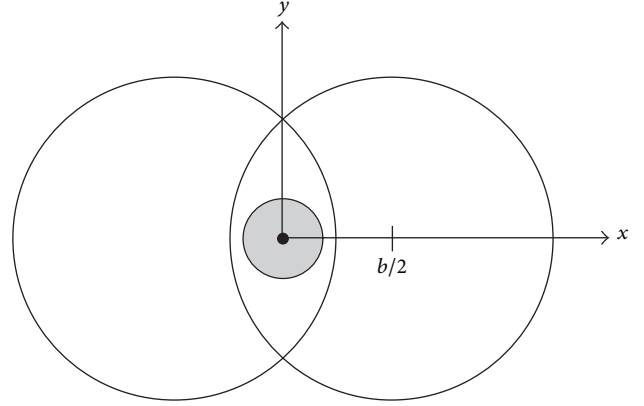


FIGURE 1: Heavy-ion collision geometry as seen along the collision axis z . Adapted from [4].

from the symmetry considerations, other components are finite in each event and are of the same order of magnitude

$$\langle |B_x| \rangle \approx \langle |E_x| \rangle \approx \langle |E_y| \rangle. \quad (4)$$

To appreciate the magnitude of electric field produced in heavy-ion collisions note that $E \sim m_\pi^2 = 10^{21}$ V/cm. The corresponding intensity is 10^{39} W/cm² which is instructive to compare with the power generated by the most powerful state-of-the-art lasers: 10^{23} W/cm².

Electromagnetic fields created in heavy-ion collisions were also examined in more elaborated approaches in [11–13]. They yielded qualitatively similar results on electromagnetic field strength and its relaxation time.

1.3. Magnetic Field in Quark-Gluon Plasma

1.3.1. Liénard-Wiechert Potentials in Static Medium. In the previous section, I discussed electromagnetic field in vacuum. A more realistic estimate must include medium effects. Indeed, the state-of-the-art phenomenology of quark-gluon plasma (QGP) indicates that strongly interacting medium is formed at as early as 0.5 fm/c. Even before this time, strongly interacting medium exists in a form of *Glasma* [14, 15]. Therefore, a calculation of magnetic field must involve response of medium determined by its electrical conductivity. It has been found in the lattice calculations that the gluon contribution to electrical conductivity of static quark-gluon plasma is [16]

$$\sigma = (5.8 \pm 2.9) \frac{T}{T_c} \text{ MeV}, \quad (5)$$

where T is plasma temperature and T_c it critical temperature. This agrees with [17] but is at odds with an earlier calculation [18]. It is not clear whether (5) adequately describes the electromagnetic response of realistic quark-gluon plasma because it neglects quark contribution and

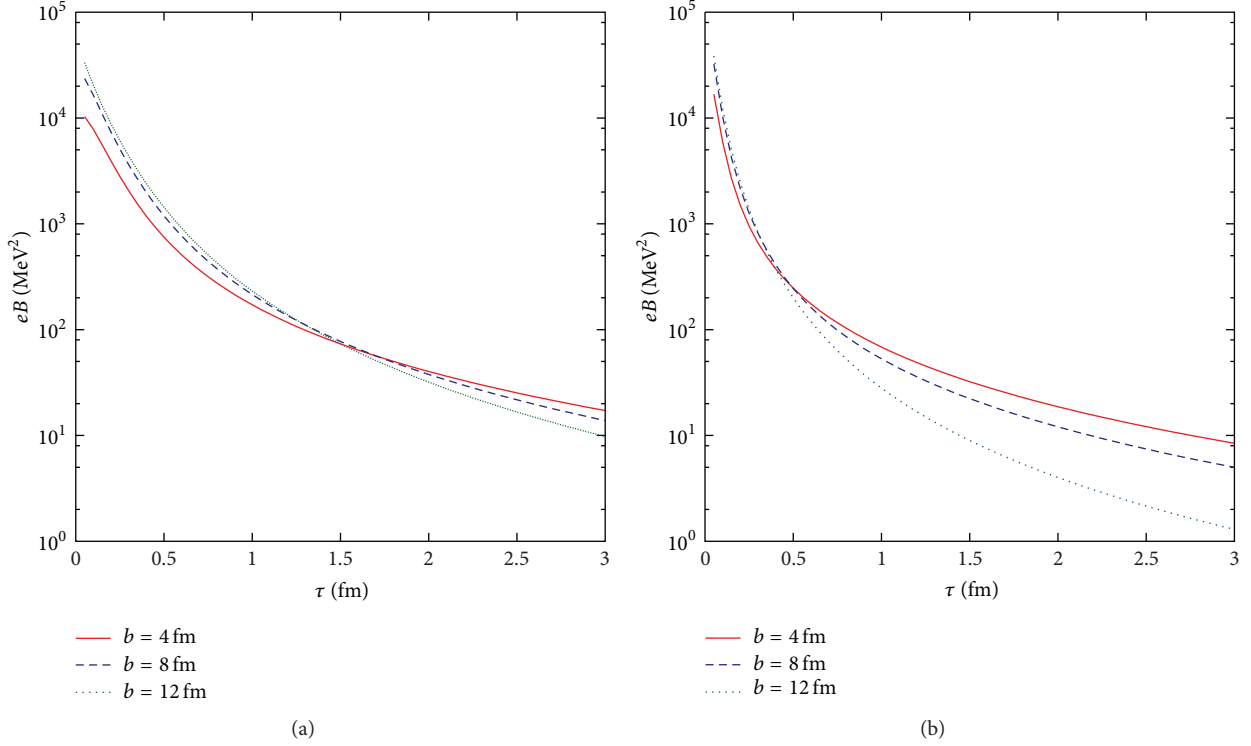


FIGURE 2: Magnetic field $\mathbf{B} = B\hat{y}$ (multiplied by e) at the origin $\mathbf{r} = 0$ produced in collision of two gold ions at beam energies (a) $\sqrt{s_{NN}} = 62$ GeV and (b) $\sqrt{s_{NN}} = 200$ GeV. Adapted from [5]. Note that eB is the same in Gauss and Lorentz-Heaviside units in contrast to B .

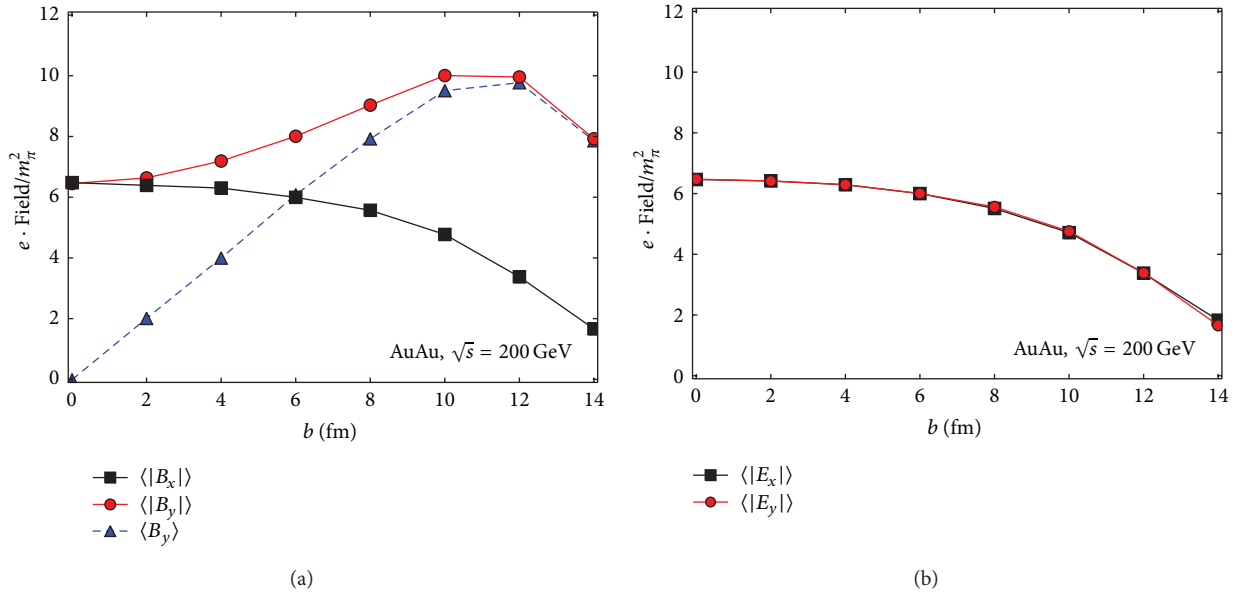


FIGURE 3: The mean absolute value of (a) magnetic field and (b) electric field at $t = 0$ and $\mathbf{r} = 0$ as a function of impact parameter b for AuAu collision at $\sqrt{s_{NN}} = 200$ GeV.

assumes that medium is static. Theoretical calculations are of little help at the temperatures of interest, since the perturbation theory is not applicable. In absence of a sensible alternative I will use (5) as a best estimate of electrical conductivity. If medium is static then T is constant as a

function of time t . The static case is considered in this section, while in the next section I consider expanding medium.

In medium, magnetic field created by a charge e moving in z -direction with velocity v is a solution of the following

equations:

$$\nabla \cdot \mathbf{B} = 0, \quad \nabla \times \mathbf{E} = -\frac{\partial \mathbf{B}}{\partial t}, \quad (6)$$

$$\nabla \cdot \mathbf{E} = e\delta(z-vt)\delta(\mathbf{b}), \quad (7)$$

$$\nabla \times \mathbf{B} = \frac{\partial \mathbf{E}}{\partial t} + \sigma \mathbf{E} + ev\hat{\mathbf{z}}\delta(z-vt)\delta(\mathbf{b}),$$

where we used the Ohm's law $\mathbf{j} = \sigma \mathbf{E}$ to describe currents induced in the medium. Position of the observation point is specified by the longitudinal and transverse coordinates z and \mathbf{b} , $\mathbf{r} = z\hat{\mathbf{z}} + \mathbf{b}$. Taking curl of the second equation in (7) and substituting (6) we get

$$\nabla^2 \mathbf{B} = \frac{\partial^2 \mathbf{B}}{\partial t^2} + \sigma \frac{\partial \mathbf{B}}{\partial t} - ev\nabla \times [\hat{\mathbf{z}}\delta(z-vt)\delta(\mathbf{b})]. \quad (8)$$

The particular solution reads

$$\mathbf{B}(z, \mathbf{b}, t) = \int_0^t dt' \int_{-\infty}^{\infty} dz \int d^2\mathbf{b}' G(z-z', \mathbf{b}-\mathbf{b}', t-t') ev \times \nabla' [\hat{\mathbf{z}}\delta(z'-vt')\delta(\mathbf{b}')], \quad (9)$$

where Green's function $G(z-z', \mathbf{b}-\mathbf{b}', t-t')$ satisfies the following equation:

$$\nabla^2 G - \frac{\partial^2 G}{\partial t^2} - \sigma \frac{\partial G}{\partial t} = -\delta(z-z')\delta(\mathbf{b}-\mathbf{b}')\delta(t-t'), \quad (10)$$

which is solved by

$$\begin{aligned} G(z-z', \mathbf{b}-\mathbf{b}', t-t') &= \int \frac{d^2 k_{\perp}}{(2\pi)^2} e^{i(\mathbf{b}-\mathbf{b}') \cdot \mathbf{k}_{\perp}} \int_{-\infty}^{\infty} \frac{dk_z}{2\pi} e^{ik_z(z-z')} \\ &\times \int_{-\infty}^{\infty} \frac{d\omega}{2\pi} e^{-i\omega(t-t')} \frac{1}{k_z^2 + k_{\perp}^2 - \omega^2 - i\omega\sigma}, \end{aligned} \quad (11)$$

where $\mathbf{k} = k_z \hat{\mathbf{z}} + \mathbf{k}_{\perp}$. Plugging this into (9) and substituting for the expression in the square brackets in (9) its Fourier image, we obtain

$$\begin{aligned} \mathbf{B}(z, \mathbf{b}, t) &= 2\pi ev \int \frac{d^2 k_{\perp}}{(2\pi)^2} e^{i\mathbf{b} \cdot \mathbf{k}_{\perp}} \int_{-\infty}^{\infty} \frac{dk_z}{2\pi} e^{ik_z z} \\ &\times \int_{-\infty}^{\infty} \frac{d\omega}{2\pi} e^{-i\omega t} \frac{i\mathbf{k} \times \hat{\mathbf{z}}}{k_z^2 + k_{\perp}^2 - \omega^2 - i\omega\sigma} \\ &\times \delta(\omega - k_z v) \end{aligned} \quad (12)$$

$$\begin{aligned} &= e \int \frac{d^2 k_{\perp}}{(2\pi)^2} e^{i\mathbf{b} \cdot \mathbf{k}_{\perp}} \\ &\times \int_{-\infty}^{\infty} \frac{d\omega}{2\pi} e^{-i\omega t} e^{i\omega z/v} \\ &\times \frac{i\mathbf{k}_{\perp} \times \hat{\mathbf{z}}}{\omega^2/v^2 + k_{\perp}^2 - \omega^2 - i\omega\sigma}. \end{aligned} \quad (13)$$

We are interested in the y -component of the field. Noting that $(\mathbf{k}_{\perp} \times \hat{\mathbf{z}}) \cdot \hat{\mathbf{y}} = -k_{\perp} \cos \phi$, where ϕ is the azimuthal angle in the transverse plane, and integrating over $d^2 k_{\perp}$ we derive

$$eB_y = \frac{\alpha_{em}}{\pi} \int_{-\infty}^{\infty} s(\omega) K_1(s(\omega)b) e^{i\omega(z/v-t)} d\omega, \quad (14)$$

where $\alpha_{em} = e^2/4\pi$, and we introduced notation

$$s(\omega) = \omega \sqrt{\frac{1}{v^2} - \epsilon(\omega)}, \quad (15)$$

where $\epsilon(\omega)$ is the dielectric constant of the plasma with the following frequency dependence:

$$\epsilon(\omega) = 1 + \frac{i\sigma}{\omega}. \quad (16)$$

Equation (14) is actually valid for any functional form of $\epsilon(\omega)$ [19], which can be easily verified by using electric displacement \mathbf{D} instead of \mathbf{E} in (7). In this case (16) can be viewed as a low frequency expansion of $\epsilon(\omega)$. Magnetic field in this approximation is quasistatic. Therefore, we could have neglected the second time derivative in (8), and then keeping only the leading powers of ω we would have derived (14) with $s^2 = i\omega\sigma$. After integration over ω this gives (21). Let us take notice of the fact that neglecting the second time derivative in (8) yields *diffusion equation* for magnetic field in plasma.

It is instructive to compare time dependence of magnetic field created by moving charges in vacuum and in plasma. In vacuum, setting $\sigma = 0$ in (13) and integrating first over ω and then over \mathbf{k}_{\perp} give

$$e\mathbf{B} = \hat{\mathbf{y}} \alpha_{em} \frac{b\gamma}{(b^2 + \gamma^2(t-z)^2)^{3/2}}, \quad (17)$$

where we used $v \approx 1$. This coincides with (3) for a single proton when we take $\mathbf{R}_a = \mathbf{b} + (z-vt)\hat{\mathbf{z}}$. Consider field strength (17) at the origin $z = 0$. At times $t < b/\gamma$ the field is constant, while at $t \gg b/\gamma$ it decreases as $B_{\infty} \propto 1/t^3$. At the time $t \approx b$ the ratio between these two is

$$\frac{B_0}{B_{\infty}} = \frac{1}{\gamma^3} \ll 1, \quad (18)$$

which is a very small number ($\sim 10^{-6}$ at RHIC).

In matter $\sigma > 0$. Let me write the modified Bessel function appearing in (14) as follows:

$$sK_1(sb) = \int_0^{\infty} \frac{J_1(xb)x^2 dx}{x^2 + s^2}. \quad (19)$$

Substituting (19) into (14) and using (16), we have ($v = 1$)

$$e\mathbf{B} = \frac{\alpha_{em}}{\pi} \hat{\mathbf{y}} \int_0^{\infty} dx \int_{-\infty}^{\infty} d\omega \frac{J_1(xb)x^2}{x^2 - i\omega\sigma} e^{i\omega(z-t)}. \quad (20)$$

Closing the contour in the lower half-plane of complex ω picks a pole at $\omega = -ix^2/\sigma$. We have

$$\begin{aligned} e\mathbf{B} &= \frac{2\alpha_{em}}{\sigma} \hat{\mathbf{y}} \int_0^{\infty} dx x^2 J_1(xb) e^{-(x^2/\sigma)(t-z)} \\ &= \hat{\mathbf{y}} \frac{\alpha_{em} b\sigma}{2(t-z)^2} e^{-b^2\sigma/4(t-z)}. \end{aligned} \quad (21)$$

At $z = 0$ this function vanishes at $t = 0$ and $t \rightarrow \infty$ and has maximum at the time instant $t = b^2\sigma/8$ which is much larger than b/γ . The value of the magnetic field at this time is

$$eB_{\max} = \frac{32e^{-2}\alpha_{\text{em}}}{b^3\sigma}. \quad (22)$$

(Here e is the base of natural logarithm.) This is smaller than the maximum field in vacuum

$$\frac{B_{\max}}{B_0} = \frac{32e^{-2}}{\sigma b\gamma} \quad (23)$$

but is still a huge field. We compare the two solutions (17) and (21) in Figure 4. We see that in a conducting medium magnetic field stays for a long time.

One essential component is still missing in our arguments—time dependence of plasma properties due to its expansion. Let us now turn to this problem.

1.3.2. Magnetic Field in Expanding Medium. So far I treated quark-gluon plasma as a static medium. Expanding medium temperature and hence conductivity are functions of time. In Bjorken scenario [20], expansion is isentropic, that is, $nV = \text{const}$, where n is the particle number density and V is plasma volume. Since $n \sim T^3$ and at early times expansion is one-dimensional $V \sim t$ it follows that $T \propto t^{-1/3}$. (Eventually, we will consider the midrapidity region $z = 0$, therefore distinction between the proper time and t is not essential.) Equation (5) implies that $\sigma \sim t^{-1/3}$. I will parameterize conductivity as follows:

$$\sigma(t) = \sigma_0 \left(\frac{t_0}{t_0 + t} \right)^{1/3}, \quad (24)$$

where I took $t_0 \approx 0.5$ fm to be the initial time (or longitudinal size) of plasma evolution. Suppose that plasma lives for 10 fm/c and then undergoes phase transition to hadronic gas at T_c . Then employing (5) we estimate $\sigma_0 \approx 16$ MeV. Let me define another parameter that I will need in the forthcoming calculation:

$$\beta = \frac{4\sigma_0}{3t_0} \approx 43 \frac{\text{MeV}}{\text{fm}}. \quad (25)$$

Magnetic field in expanding medium is still governed by (8). As was explained in the preceding subsection, time evolution of magnetic field is quasi-static, which allows me to neglect the second time derivative. Let me introduce a new “time” variable ρ as follows:

$$\rho = \left(\frac{1+t}{t_0} \right)^{4/3} - 1. \quad (26)$$

Field $\mathbf{B}(z, \mathbf{b}, \rho)$ satisfies equation

$$\nabla^2 \mathbf{B} = \beta \frac{\partial \mathbf{B}}{\partial \rho} - e\nu \nabla \times \{ \hat{\mathbf{z}} \delta [z - \nu t(\rho)] \delta(\mathbf{b}) \}, \quad (27)$$

where

$$t(\rho) = t_0 \left[(\rho + 1)^{3/4} - 1 \right]. \quad (28)$$

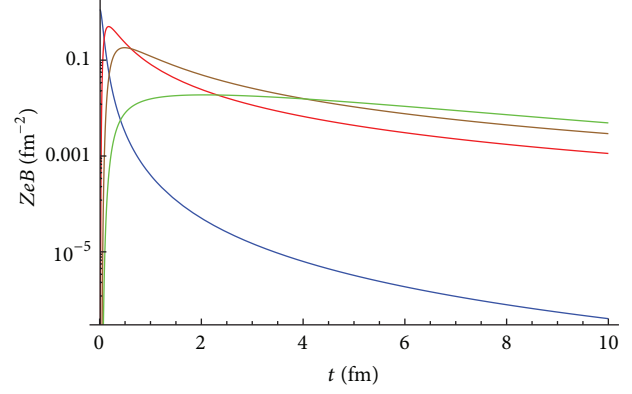


FIGURE 4: Relaxation of magnetic field at $z = 0$ in vacuum (blue), in static conducting medium at $\sigma = 5.8$ MeV (red) and at $\sigma = 16$ MeV (brown), and in the expanding medium (green). Units of B is $\text{fm}^{-2} \approx 2m_\pi^2$, $b = 7$ fm, $Z = 79$ (gold nucleus), $\gamma = 100$ (RHIC).

Its solution can be written as

$$\begin{aligned} \mathbf{B}(z, \mathbf{b}, \rho) &= \int_0^\rho d\rho' \int_{-\infty}^\infty dz \\ &\times \int d^2 \mathbf{b}' \mathfrak{G}(z - z', \mathbf{b} - \mathbf{b}', \rho - \rho') e\nu \\ &\times \nabla \{ \hat{\mathbf{z}} \delta [z - \nu t(\rho)] \delta(\mathbf{b}) \}, \end{aligned} \quad (29)$$

in terms of Green's function $\mathfrak{G}(z - z', \mathbf{b} - \mathbf{b}', \rho - \rho')$ satisfying

$$\nabla^2 \mathfrak{G} - \beta \frac{\partial \mathfrak{G}}{\partial \rho} = -\delta(z - z') \delta(\mathbf{b} - \mathbf{b}') \delta(\rho - \rho'). \quad (30)$$

To solve this equation we represent \mathfrak{G} as three-dimensional Fourier integral with respect to the space coordinates and Laplace transform with respect to the “time” coordinate:

$$\mathfrak{G}(z, \mathbf{b}, \rho) = \int \frac{d^3 k}{(2\pi)^3} e^{i(\mathbf{k}_\perp \cdot \mathbf{b} + k_z z)} \int_C \frac{d\lambda}{2\pi i} e^{\lambda \rho} \frac{1}{k_\perp^2 + k_z^2 + \beta \lambda}, \quad (31)$$

with the contour C running parallel to the imaginary axis to the right of all integrand singularities. Now I would like to write the expression in the curly brackets in (29) also as Fourier-Laplace expansion. To this end we calculate

$$\begin{aligned} f_{\mathbf{k}, \lambda} &= \int d^2 \mathbf{b} \int_{-\infty}^\infty dz \\ &\times \int_0^\infty d\rho e^{-i(\mathbf{k}_\perp \cdot \mathbf{b} + k_z z)} e^{-\lambda \rho} \delta(z - \nu t(\rho)) \delta(\mathbf{b}) \end{aligned} \quad (32)$$

$$= \int_0^\infty d\rho e^{-ik_z \nu t_0 [(\rho+1)^{3/4} - 1]} e^{-\lambda \rho}. \quad (33)$$

Therefore,

$$\begin{aligned} & ev\nabla \times \{\widehat{\mathbf{z}}\delta [z - vt(\rho)] \delta(\mathbf{b})\} \\ &= ev \int \frac{d^3k}{(2\pi)^3} e^{i(\mathbf{k}_\perp \cdot \mathbf{b} + k_z z)} \\ & \quad \times \int_C \frac{d\lambda}{2\pi i} e^{\lambda\rho} i\mathbf{k}_\perp \times \widehat{\mathbf{z}} f_{\mathbf{k},\lambda}. \end{aligned} \quad (34)$$

Substituting (31) and (34) into (29) we obtain upon integration over the volume and time as follows:

$$\begin{aligned} \mathbf{B}(z, \mathbf{b}, \rho) &= \int \frac{d^3k}{(2\pi)^3} e^{i(\mathbf{k}_\perp \cdot \mathbf{b} + k_z z)} \\ & \quad \times \int_C \frac{d\lambda}{2\pi i} e^{\lambda\rho} \frac{ev i\mathbf{k}_\perp \times \widehat{\mathbf{z}}}{k_\perp^2 + k_z^2 + \beta\lambda} f_{\mathbf{k},\lambda} \theta(\rho), \end{aligned} \quad (35)$$

where θ is the step function. Taking consequent integrals over λ and k_z gives

$$\begin{aligned} \mathbf{B}(0, \mathbf{b}, \rho) &= \frac{ev}{\beta} \int \frac{d^2k_\perp}{(2\pi)^2} e^{i\mathbf{k}_\perp \cdot \mathbf{b}} \int_{-\infty}^{\infty} \frac{dk_z}{2\pi} i\mathbf{k}_\perp \\ & \quad \times \widehat{\mathbf{z}} \int_0^\rho d\rho' e^{-ik_z v t_0 [(\rho'+1)^{3/4} - 1]} \\ & \quad \times e^{-((k_\perp^2 + k_z^2)/\beta)(\rho - \rho')} \\ &= \frac{ev}{\beta} \int \frac{d^2k_\perp}{(2\pi)^2} e^{i\mathbf{k}_\perp \cdot \mathbf{b}} \frac{1}{2\pi} i\mathbf{k}_\perp \\ & \quad \times \widehat{\mathbf{z}} \int_0^\rho d\rho' e^{-(k_\perp^2/\beta)(\rho - \rho')} \\ & \quad \times \frac{\sqrt{\pi\beta}}{\sqrt{\rho - \rho'}} e^{-v^2 t_0^2 \beta [(\rho'+1)^{3/4} - 1]^2 / 4(\rho - \rho')}. \end{aligned} \quad (36)$$

Consider now B_y . Integrating over azimuthal angle ϕ and then over k_\perp as in (13), (14) yields

$$\begin{aligned} & eB_y(0, \mathbf{b}, \rho) \\ &= \frac{\alpha_{\text{em}} v \beta^{3/2}}{2\sqrt{\pi}} \int_0^\rho d\zeta \zeta^{-5/2} \\ & \quad \times e^{-\mathbf{b}^2 \beta / 4\zeta} e^{-v^2 t_0^2 \beta [(\rho - \zeta + 1)^{3/4} - 1]^2 / 4\zeta}, \end{aligned} \quad (37)$$

where $\zeta = \rho - \rho'$.

The results of a numerical calculation of (37) are shown in Figure 4. We see that expansion of plasma tends to increase the relaxation time, although this effect is rather modest. We conclude that due to finite electrical conductivity of QGP, magnetic field essentially freezes in the plasma for as long as plasma exists. Similar phenomenon, known as skin effect, exists in good conductors placed in time-varying magnetic field: conductors expel time dependent magnetic fields from conductor volume confining them into a thin layer of width $\delta \sim \omega^{-1/2}$ on the surface.

1.3.3. Diffusion of Magnetic Field in QGP. The dynamics of magnetic field relaxation in conducting plasma can be understood in a simple model [21]. Suppose at some initial time $t = 0$ magnetic field $\mathbf{B}(0, \mathbf{r})$ permeates the plasma. The problem is to find the time dependence of the field at $t > 0$. In this model, the field sources turn off at $t = 0$ and do not at all contribute to the field at $t > 0$. Electromagnetic field is governed by the following equations:

$$\nabla \times \mathbf{B} = \mathbf{j}, \quad \mathbf{j} = \sigma \mathbf{E}, \quad (38)$$

$$\nabla \times \mathbf{E} = -\frac{\partial \mathbf{B}}{\partial t}, \quad \nabla \cdot \mathbf{B} = 0,$$

that lead to the diffusion equation for \mathbf{B} , after we neglect the second-time derivative as discussed previously as follows:

$$\nabla^2 \mathbf{B} = \sigma \frac{\partial \mathbf{B}}{\partial t}. \quad (39)$$

For simplicity we treat electrical conductivity σ as constant. Initial condition at $t = 0$ reads

$$\mathbf{B}(0, \mathbf{r}) = \mathbf{B}_0 e^{-\mathbf{b}^2/R^2}, \quad (40)$$

where the Gaussian profile is chosen for illustration purposes, and R is the nuclear radius. Solution to the problem (39), (40) is

$$\mathbf{B}(t, \mathbf{r}) = \int dV' \mathbf{B}(0, \mathbf{r}') G(t, \mathbf{r} - \mathbf{r}'), \quad (41)$$

where Green's function is

$$G(t, \mathbf{r}) = \frac{1}{(4\pi t/\sigma)^{3/2}} \exp\left[-\frac{\mathbf{r}^2}{4t/\sigma}\right]. \quad (42)$$

Integrating over the entire volume we derive

$$\mathbf{B}(t, \mathbf{r}) = \mathbf{B}_0 \frac{R^2}{R^2 + 4t/\sigma} \exp\left[-\frac{\mathbf{b}^2}{R^2 + 4t/\sigma}\right]. \quad (43)$$

It follows from (43) that as long as $t \ll t_{\text{relax}}$, where t_{relax} is a characteristic time $t_{\text{relax}} = R^2\sigma/4$ and magnetic field \mathbf{B} is approximately time independent. This estimate is the same as the one we arrived at after (21).

In summary, magnetic field in quark-gluon plasma appears to be extremely strong and slowly varying function of time for most of the plasma lifetime. At RHIC it decreases from $eB \approx (2.5m_\pi)^2$ right after the collision to $eB \approx (m_\pi/4)^2$ at $t \approx 5$ fm see Figure 4. This has a profound impact on all the processes occurring in QGP.

1.3.4. Schwinger Mechanism. Schwinger mechanism of pair production [3] is operative if electric field exceeds the critical value of m^2/e , where m is mass of lightest electrically charged particle. Indeed, in order to excite a fermion out of the Dirac sea, electric force $e\mathbf{E}$ must do work along the path $d\ell$ satisfying

$$\int_0^\ell e\mathbf{E} \cdot d\ell' > 2m. \quad (44)$$

If $\mathbf{E} = \text{const}$, then $E \geq m/\ell e$. The maximal value of ℓ is the fermion Compton's wavelength $\ell \sim \lambda = 1/m$ implying that the minimum (or critical) value of electric field is

$$E_c = \frac{m^2}{e}. \quad (45)$$

Notice that in stronger fields $\ell \sim m/eE < \lambda$. Figure 3 indicates that electron-positron pairs are certainly produced at RHIC. An important question then is the role of these pairs in the electromagnetic field relaxation in plasma. There are two associated effects: (i) before e^-e^+ pairs thermalize, they contribute to the Foucault currents; (ii) after they thermalize, their density contributes to the polarization of plasma in electric field and hence to its conductivity.

Since space dimensions of QGP are much less than $\lambda_e = 380 \text{ fm}$, it may seem inevitable that space dependence of electric field (in addition to its time dependence) has a significant impact on the Schwinger process in heavy-ion collisions. However, this conclusion is premature. Indeed, suppose that electric field is a slow function of coordinates. Then $\mathbf{E}(\mathbf{r}) \approx \mathbf{E}(0) + \mathbf{r} \cdot \nabla \mathbf{E}(0)$. Work done by electric field is

$$\int_0^\ell e\mathbf{E}(0) \cdot d\boldsymbol{\ell}' + \int_0^\ell (\mathbf{r} \cdot \nabla) e\mathbf{E}(0) \cdot d\boldsymbol{\ell}' \sim eE\ell + \frac{e\ell^2 E(0)}{\lambda}, \quad (46)$$

where λ is length scale describing space variation of electric field. In order that contribution of space variation to work be negligible, the second term in the r.h.s. of (46) must satisfy $e\ell^2 E(0)/\lambda \ll m$. Employing the estimate $\ell \sim m/eE(0)$ that we obtained after (45) implies $m/eE(0)\lambda \ll 1$. Following [22] I define the inhomogeneity parameter

$$\tilde{\gamma} = \frac{m}{\lambda eE} \quad (47)$$

that describes the effect of spatial variation of electric field on the pair production rate. For electrons $m = 0.5 \text{ MeV}$ in QGP $\lambda \sim 0.5 \text{ fm}$ at $eE \sim m_\pi^2$ we have $\tilde{\gamma} \sim 0.01$. Therefore, somewhat counter intuitively, electric field can be considered as spatially homogeneous. The same conclusion can be derived from results of [23]. Schwinger mechanism in spatially dependent electric fields was also discussed in [24, 25].

In view of smallness of $\tilde{\gamma}$ one can employ the extensive literature on Schwinger effect in time-dependent spatially-homogeneous electric fields. As far as heavy-ion physics is concerned, the most comprehensive study has been done in [6, 26, 27] who developed an approach to include the effect of backreaction. They argued that time evolution of electric field can be studied in adiabatic approximation and used the kinetic approach to study the time evolution. Their results are exhibited in Figure 5. Similar results were obtained in [28]. We observe that response time of the current density of Schwinger pairs $\sim 10^4 \text{ fm}/c$ is much larger than the plasma lifetime $\sim 10 \text{ fm}/c$, and therefore no sizable electric current is generated.

In summary, strong electric field is generated in heavy-ion collisions in every event but averages to zero in a large event ensemble. This field exceeds the critical value for electrons and light u, d quarks. However, during the plasma lifetime no significant current of Schwinger pairs is generated.

2. Flow of Quark-Gluon Plasma in Strong Magnetic Field

2.1. Azimuthal Asymmetry. Magnetic field is known to have a profound influence on kinetic properties of plasmas. Once the spherical symmetry is broken, distribution of particles in plasma is only axially symmetric with respect to the magnetic field direction. This symmetry, however, is not manifest in the plane span by magnetic field and the impact parameter vectors, namely, xy -plane in Figure 1. Charged particles moving along the magnetic field direction y are not influenced by the magnetic Lorentz force, while those moving the xz -plane (i.e., the reaction plane) are affected the most. The result is azimuthally anisotropic flow of expanding plasma in the xy -plane even when initial plasma geometry is completely spherically symmetric. The effect of weak magnetic field on quark-gluon plasma flow was first considered in [29] who argued that magnetic field is able to enhance the azimuthal anisotropy of produced particles up to 30%. This conclusion was reached by utilizing a solution of the magnetohydrodynamic equations in weak magnetic field.

A characteristic feature of the viscous pressure tensor in magnetic field is its azimuthal anisotropy. This anisotropy is the result of suppression of the momentum transfer in QGP in the direction perpendicular to the magnetic field. Its macroscopic manifestation is decrease of the viscous pressure tensor components in the plane perpendicular to the magnetic field, which coincides with the reaction plane in the heavy-ion phenomenology. Since Lorentz force vanishes in the direction parallel to the field, viscosity along that direction is not affected at all. In fact, the viscous pressure tensor component in the reaction plane is twice as small as the one in the field direction. As the result, transverse flow of QGP develops azimuthal anisotropy in presence of the magnetic field. Clearly, this anisotropy is completely different from the one generated by the anisotropic pressure gradients and exists even if the later is absent. In fact, because spherical symmetry in magnetic field is broken, viscous effects in plasma cannot be described by only two parameters: shear η and bulk viscosity ζ . Rather the viscous pressure tensor of magnetoactive plasma is characterized by seven viscosity coefficients, among which five are shear viscosities and two are bulk ones.

2.2. Viscous Pressure in Strong Magnetic Field

2.2.1. Viscosities from Kinetic Equation. Generally, calculation of the viscosities requires knowledge of the strong interaction dynamics of the QGP components. However, in strong magnetic field these interactions can be considered as a perturbation, and viscosities can be analytically calculated using the kinetic equation [30–33]. To apply this approach to QGP in strong magnetic field we start with kinetic equation for the distribution function f of a quark flavor of charge ze as follows:

$$p^\mu \partial_\mu f = zeB^{\mu\nu} \frac{\partial f}{\partial u^\mu} u_\nu + \mathcal{E}[f, \dots], \quad (48)$$

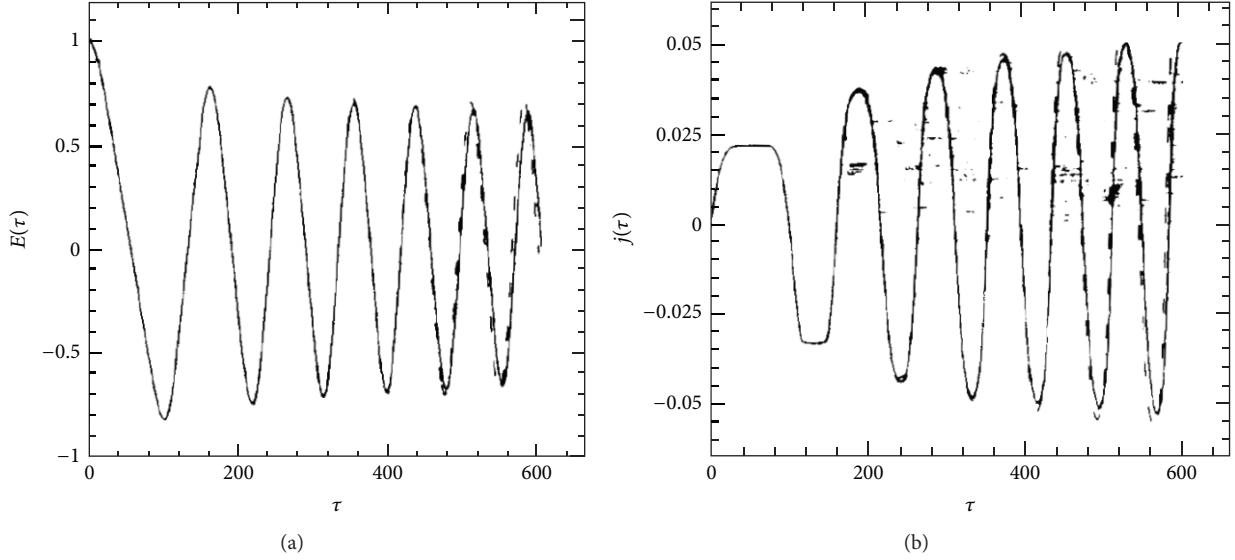


FIGURE 5: Time dependence of electric field due to the Schwinger mechanism back reaction and the corresponding electric current density of Schwinger pairs. Dimensionless time variable is defined as $\tau = t/\lambda$. For electrons $\lambda = 380$ fm. Plasma undergoes phase transition at about $\tau = 1/38$. Adapted from [6].

where \mathcal{C} is the collision integral and $B^{\mu\nu}$ is the electromagnetic tensor, which contains only magnetic field components in the laboratory frame. Ellipsis in the argument of \mathcal{C} indicates the distribution functions of other quark flavors and gluons (I will omit them in the following). The equilibrium distribution reads

$$f_0 = \frac{\rho}{4\pi m^3 T K_2(\beta m)} e^{-\beta p \cdot U(x)}, \quad (49)$$

where $U(x)$ is the macroscopic velocity of the fluid, $p^\mu = mu^\mu$ is particle momentum, $\beta = 1/T$, and ρ is the mass density. Since $(\partial f_0/\partial u^\mu) \propto u_\mu$, the first term on the r.h.s. of (48) as well as the collision integral vanishes in equilibrium. Therefore, we can write the kinetic equation as an equation for δf :

$$p^\mu \partial_\mu f_0 = ze B^{\mu\nu} \frac{\partial(\delta f)}{\partial u^\mu} u_\nu + \mathcal{C}[\delta f], \quad (50)$$

where δf is a deviation from equilibrium. Differentiating (49) we find

$$\partial_\mu f_0 = -f_0 \frac{1}{T} p^\lambda \partial_\mu U_\lambda(x). \quad (51)$$

Since $U^\lambda = (\gamma_V, \gamma_V \mathbf{V})$ and $p^\lambda = (\varepsilon, \mathbf{p}) = (\gamma_V m, \gamma_V m \mathbf{v})$ it follows that

$$p \cdot U = \frac{m}{\sqrt{1-v^2} \sqrt{1-V^2}} (1 - \mathbf{v} \cdot \mathbf{V}). \quad (52)$$

Thus, in the comoving frame

$$\partial_\mu f_0|_{\mathbf{v}=0} = f_0 \frac{1}{T} p_\nu \partial_\mu V^\nu. \quad (53)$$

Substituting (53) in (50) yields

$$-\frac{f_0}{T} p^\mu p^\nu V_{\mu\nu} = ze B^{\mu\nu} \frac{\partial(\delta f)}{\partial u^\mu} u_\nu + \mathcal{C}[\delta f], \quad (54)$$

where I defined

$$V_{\mu\nu} = \frac{1}{2} (\partial_\mu V_\nu + \partial_\nu V_\mu). \quad (55)$$

and used $u^\mu u^\nu \partial_\mu V_\nu = u^\mu u^\nu V_{\mu\nu}$.

Since the time derivative of f_0 is irrelevant for the calculation of the viscosity I will drop it from the kinetic equation. All indices thus become the usual three-vector ones. To avoid confusion we will label them by the Greek letters from the beginning of the alphabet. Introducing $b_{\alpha\beta} = B^{-1} \varepsilon_{\alpha\beta\gamma} B_\gamma$, we cast (54) in the form

$$\frac{1}{T} p^\alpha u^\beta V_{\alpha\beta} f_0 = -ze B b_{\alpha\beta} v^\beta \frac{\partial(\delta f)}{\partial v_\alpha} \frac{1}{\varepsilon} - \mathcal{C}[\delta f]. \quad (56)$$

The viscous pressure generated by a deviation from equilibrium is given by the tensor

$$-\Pi_{\alpha\beta} = \int p_\alpha p_\beta \delta f \frac{d^3 p}{\varepsilon}. \quad (57)$$

Effectively it can be parameterized in terms of the viscosity coefficients as follows (we neglect the bulk viscosities):

$$\Pi_{\alpha\beta} = \sum_{n=0}^4 \eta_n V_{\alpha\beta}^{(n)}, \quad (58)$$

where the linearly independent tensors $V_{\alpha\beta}^{(n)}$ are given by

$$V_{\alpha\beta}^{(0)} = \left(3b_\alpha b_\beta - \delta_{\alpha\beta}\right) \left(b_\gamma b_\delta V_{\gamma\delta} - \frac{1}{3}\nabla \cdot \mathbf{V}\right), \quad (59a)$$

$$V_{\alpha\beta}^{(1)} = 2V_{\alpha\beta} + \delta_{\alpha\beta} V_{\gamma\delta} b_\gamma b_\delta - 2V_{\alpha\gamma} b_\gamma b_\beta - 2V_{\beta\gamma} b_\gamma b_\alpha + (b_\alpha b_\beta - \delta_{\alpha\beta}) \nabla \cdot \mathbf{V} + b_\alpha b_\beta V_{\gamma\delta} b_\gamma b_\delta, \quad (59b)$$

$$V_{\alpha\beta}^{(2)} = 2(V_{\alpha\gamma} b_{\beta\gamma} + V_{\beta\gamma} b_{\alpha\gamma} - V_{\gamma\delta} b_{\alpha\gamma} b_{\beta\delta}), \quad (59c)$$

$$V_{\alpha\beta}^{(3)} = V_{\alpha\gamma} b_{\beta\gamma} + V_{\beta\gamma} b_{\alpha\gamma} - V_{\gamma\delta} b_{\alpha\delta} b_{\alpha\gamma} b_{\beta\delta} - V_{\gamma\delta} b_{\beta\delta} b_{\alpha\gamma} b_\delta, \quad (59d)$$

$$V_{\alpha\beta}^{(4)} = 2(V_{\gamma\delta} b_{\alpha\delta} b_{\alpha\gamma} b_{\beta\delta} + V_{\gamma\delta} b_{\beta\delta} b_{\alpha\gamma} b_\delta). \quad (59e)$$

Here b_α is a unit vector in the direction of magnetic field. For the calculation of the shear viscosities η_n , $n = 0, \dots, 4$ we can set $\nabla \cdot \mathbf{V} = 0$ and $V_{\alpha\beta} b_\alpha b_\beta = 0$.

Let us expand δf to the second order in velocities in terms of the tensors $V_{\alpha\beta}^{(n)}$ as follows:

$$\delta f = \sum_{n=0}^4 g_n V_{\alpha\beta}^{(n)} v^\alpha v^\beta. \quad (60)$$

Then, substituting (60) into (58) and requiring consistency of (57) and (58) yield

$$\eta_n = -\frac{2}{15} \int \varepsilon v^4 g_n d^3 p. \quad (61)$$

This gives the viscosities in the magnetic field in terms of the deviation of the distribution function from equilibrium. Transition to the nonrelativistic limit in (61) is achieved by the replacement $\varepsilon \rightarrow m$ [30].

2.2.2. Collisionless Plasma. In strong magnetic field we can determine g_n by the method of consecutive approximations. Writing $\delta f = \delta f^{(1)} + \delta f^{(2)}$ and substituting into (56), we find

$$\frac{1}{T} p^\alpha v^\beta V_{\alpha\beta} f_0 = -ze B b_{\alpha\beta} v^\beta \frac{\partial (\delta f^{(1)} + \delta f^{(2)})}{\partial v_\alpha} \frac{1}{\varepsilon} + \mathcal{E} [\delta f^{(1)}]. \quad (62)$$

Here I assumed that the deviation from equilibrium due to the strong magnetic field is much larger than due to the particle collisions. The explicit form of \mathcal{E} is determined by the strong interaction dynamics but drops off the equation in the leading order. The first correction to the equilibrium distribution obeys the equation

$$\frac{1}{T} p^\alpha v^\beta V_{\alpha\beta} f_0 = -ze B b_{\alpha\beta} v^\beta \frac{\partial \delta f^{(1)}}{\partial v_\alpha} \frac{1}{\varepsilon}. \quad (63)$$

Using (60), we get

$$b_{\alpha\beta} v^\beta \frac{\partial \delta f^{(1)}}{\partial v_\alpha} = 2b_{\alpha\beta} v^\beta \sum_{n=0}^4 g_n V_{\alpha\gamma}^{(n)} v_\gamma. \quad (64)$$

Substituting (64) into (63) and using (59a), (59b), (59c), (59d), and (59e) yield

$$\begin{aligned} \frac{\varepsilon}{TzeB} p_\alpha v^\beta V_{\alpha\beta} f_0 = & -2b_{\beta\gamma} v_\alpha v_\gamma \\ & \times \left[g_1 (2V_{\alpha\beta} - 2V_{\beta\gamma} b_\gamma b_\alpha) + 2g_2 V_{\beta\gamma} b_\gamma b_\alpha \right. \\ & + g_3 (V_{\alpha\gamma} b_{\beta\gamma} + V_{\beta\gamma} b_{\alpha\gamma} - V_{\gamma\delta} b_\alpha b_\delta) \\ & \left. + 2g_4 V_{\gamma\delta} b_{\beta\gamma} b_\alpha b_\delta \right], \end{aligned} \quad (65)$$

where I used the following identities $b_{\alpha\beta} b_\alpha = b_{\alpha\beta} b_\beta = b_{\alpha\beta} v_\alpha v_\beta = 0$. Clearly, (65) is satisfied only if $g_1 = g_2 = 0$. Concerning the other two coefficients, we use the identities

$$b_{\alpha\beta} b_{\beta\gamma} = b_\gamma b_\alpha - \delta_{\alpha\gamma} b^2, \quad (66a)$$

$$\begin{aligned} \varepsilon_{\alpha\beta\gamma} \varepsilon_{\delta\epsilon\zeta} = & \delta_{\alpha\delta} (\delta_{\beta\epsilon} \delta_{\gamma\zeta} - \delta_{\beta\zeta} \delta_{\gamma\epsilon}) - \delta_{\alpha\epsilon} (\delta_{\beta\delta} \delta_{\gamma\zeta} - \delta_{\beta\zeta} \delta_{\gamma\delta}) \\ & + \delta_{\alpha\zeta} (\delta_{\beta\delta} \delta_{\gamma\epsilon} - \delta_{\beta\zeta} \delta_{\gamma\delta}) \end{aligned} \quad (66b)$$

that we substitute into (65) to derive

$$\begin{aligned} -\frac{\varepsilon}{2TzeB} p^\alpha v^\beta V_{\alpha\beta} f_0 = & g_3 [2V_{\alpha\beta} b_\alpha b_\beta - 4V_{\alpha\beta} v_\alpha b_\beta (\mathbf{b} \cdot \mathbf{v})] \\ & + 2g_4 V_{\alpha\beta} v_\alpha b_\beta (\mathbf{b} \cdot \mathbf{v}). \end{aligned} \quad (67)$$

Since $p_\alpha = \varepsilon v_\alpha$, we obtain

$$g_3 = \frac{g_4}{2} = -\frac{\varepsilon^2 f_0}{4TzeB}. \quad (68)$$

Using (49), (68) in (61) in the comoving frame (of course η_n s do not depend on the frame choice) and integrating using 3.547.9 of [34], we derive [35]

$$\eta_3 = \frac{K_3(\beta m)}{K_2(\beta m)} \frac{\rho T}{2zeB}. \quad (69)$$

The nonrelativistic limit corresponds to $m \gg T$ in which case we get

$$\eta_3^{\text{NR}} = \frac{\rho T}{2zeB}. \quad (70)$$

In the opposite ultrarelativistic case $m \ll T$ (high-temperature plasma)

$$\eta_3^{\text{UR}} = \frac{2nT^2}{zeB}, \quad (71)$$

where $n = \rho/m$ is the number density.

2.2.3. Contribution of Collisions. In the relaxation-time approximation we can write the collision integral as

$$\mathcal{E} [\delta f] = -\nu \delta f, \quad (72)$$

where ν is an effective collision rate. Strong field limit means that

$$\omega_B \gg \nu, \quad (73)$$

where $\omega_B = zeB/\varepsilon$ is the synchrotron frequency. Whether ν itself is function of the field depends on the relation between the Larmor radius $r_B = v_T/\omega_B$, where v_T is the particle velocity in the plane orthogonal to \mathbf{B} and the Debye radius r_D . If

$$r_B \gg r_D, \quad (74)$$

then the effect of the field on the collision rate ν can be neglected [30]. Assuming that (74) is satisfied, the collision rate reads

$$\nu = n\nu\sigma_t, \quad (75)$$

where σ_t is the transport cross-section, which is a function of the saturation momentum Q_s [36, 37]. We estimate $\sigma_t \sim \alpha_s^2/Q_s^2$, with $Q_s \sim 1 \text{ GeV}$ and $n = P/T$ with pressure $\alpha_s^2 P \sim 1 \text{ GeV/fm}^3$; we get $\nu \sim 40 \text{ MeV}$. Inequality (73) is well satisfied since $eB \simeq m_\pi^2$ [5, 11], and m is in the range between the current and the constituent quark masses. On the other hand, applicability of the condition (74) is marginal and is very sensitive to the interaction details. In this section we assume that (74) holds in order to obtain the analytic solution. Additionally, the general condition for the applicability of the hydrodynamic approach $\ell = 1/\nu \ll L$, where ℓ is the mean free path and L is the plasma size is assumed to hold. Altogether we have $r_D \ll r_B \ll \ell \ll L$.

Equation for the second correction to the equilibrium distribution $\delta f^{(2)}$ follows from (62) after substitution (72)

$$\frac{zeB}{\varepsilon} b_{\alpha\beta} v_\beta \frac{\partial \delta f^{(2)}}{\partial v_\alpha} = -\nu \delta f^{(1)}. \quad (76)$$

Now, plugging

$$\delta f^{(1)} = [g_3 V_{\alpha\beta}^{(3)} + g_4 V_{\alpha\beta}^{(4)}] v_\alpha v_\beta, \quad (77a)$$

$$\delta f^{(2)} = [g_1 V_{\alpha\beta}^{(1)} + g_2 V_{\alpha\beta}^{(2)}] v_\alpha v_\beta, \quad (77b)$$

into (76) yields

$$\begin{aligned} & \frac{2zeB}{\varepsilon} \left\{ g_1 [2V_{\beta\alpha} b_{\alpha\gamma} v_\beta v_\gamma - 2V_{\beta\alpha} b_{\alpha\gamma} v_\beta v_\gamma (\mathbf{v} \cdot \mathbf{b})] \right. \\ & \quad \left. + 2g_2 V_{\beta\alpha} b_{\alpha\gamma} v_\beta v_\gamma (\mathbf{v} \cdot \mathbf{b}) \right\} \\ & = -\nu g_3 \left\{ -2V_{\beta\alpha} b_{\alpha\gamma} v_\beta v_\gamma - 6V_{\beta\alpha} b_{\alpha\gamma} v_\beta v_\gamma (\mathbf{v} \cdot \mathbf{b}) \right\}, \end{aligned} \quad (78)$$

where I used $g_4 = 2g_3$. It follows that

$$g_1 = \frac{g_2}{4} = \frac{\nu g_3}{2\omega_B}. \quad (79)$$

With the help of (80), (49), and (65) we obtain [35]

$$\eta_1 = \frac{\eta_2}{4} = \frac{8}{5\sqrt{2\pi}} \frac{\rho^2 \sigma_t T^{3/2}}{(zeB)^2 m^{1/2}} \frac{K_{7/2}(\beta m)}{K_2(\beta m)}. \quad (80)$$

2.3. Azimuthal Asymmetry of Transverse Flow: A Simple Model. To illustrate the effect of the magnetic field on the viscous flow of the electrically charged component of the quark-gluon plasma I will assume that the flow is non-relativistic and use the Navier-Stokes equations that read

$$\rho \left(\frac{\partial V_\alpha}{\partial t} + V_\beta \frac{\partial V_\alpha}{\partial x_\beta} \right) = -\frac{\partial P}{\partial x_\alpha} + \frac{\partial \Pi_{\alpha\beta}}{\partial x_\beta}, \quad (81)$$

where $\Pi_{\alpha\beta}$ is the viscous pressure tensor, $\rho = mn$ is mass density, and P is pressure. I will additionally assume that the flow is nonturbulent and that the plasma is non-compressible. The former assumption amounts to dropping the terms non-linear in velocity, while the later implies vanishing divergence of velocity

$$\nabla \cdot \mathbf{V} = 0. \quad (82)$$

Because of the approximate boost invariance of the heavy-ion collisions, we can restrict our attention to the two dimensional flow in the xy -plane corresponding to the central rapidity region.

The viscous pressure tensor in vanishing magnetic field is isotropic in the xy -plane and is given by

$$\Pi_{\alpha\beta}^0 = \eta \left(\frac{\partial V_\alpha}{\partial x_\beta} + \frac{\partial V_\beta}{\partial x_\alpha} \right) = 2\eta \begin{pmatrix} V_{xx} & V_{xy} \\ V_{yx} & V_{yy} \end{pmatrix}, \quad (83)$$

where the superscript 0 indicates absence of the magnetic field. In the opposite case of very strong magnetic field the viscous pressure tensor has a different form (58). Neglecting all η_n with $n \geq 1$, we can write

$$\Pi_{\alpha\beta}^\infty = \eta_0 \begin{pmatrix} -V_{yy} & 0 \\ 0 & 2V_{yy} \end{pmatrix} = 2\eta_0 \begin{pmatrix} \frac{1}{2}V_{xx} & 0 \\ 0 & V_{yy} \end{pmatrix}, \quad (84)$$

where we also used (82). Notice that $\Pi_{xx}^\infty = (1/2)\Pi_{yy}^\infty = (1/2)\Pi_{xx}^0$ indicating that the plasma flows in the direction perpendicular to the magnetic field with twice as small viscosity as in the direction of the field. The later is not affected by the field at all, because the Lorentz force vanishes in the field direction. Substituting (84) into (81) we derive the following two equations characterizing the plasma velocity in the strong magnetic field [35]:

$$\rho \frac{\partial V_x}{\partial t} = -\frac{\partial P}{\partial x} + \eta_0 \frac{\partial^2 V_x}{\partial x^2}, \quad \rho \frac{\partial V_y}{\partial t} = -\frac{\partial P}{\partial y} + 2\eta_0 \frac{\partial^2 V_y}{\partial y^2}. \quad (85)$$

Additionally, we need to set the initial conditions

$$V_x|_{t=0} = \varphi_1(x, y), \quad V_y|_{t=0} = \varphi_2(x, y). \quad (86)$$

The solution to the the problem (85), (86) is

$$\begin{aligned}
V_x(x, y, t) &= \int_{-\infty}^{\infty} dx' \varphi_1(x', y) G_{1/2}(x - x', t) \\
&\quad - \frac{1}{\rho} \int_0^t dt' \int_{-\infty}^{\infty} dx' G_{1/2}(x - x', t - t') \frac{\partial P(x', y, t')}{\partial x'},
\end{aligned} \tag{87a}$$

$$\begin{aligned}
V_y(x, y, t) &= \int_{-\infty}^{\infty} dy' \varphi_2(x, y') G_1(y - y', t) \\
&\quad - \frac{1}{\rho} \int_0^t dt' \int_{-\infty}^{\infty} dy' G_1(y - y', t - t') \frac{\partial P(x, y', t')}{\partial y'}.
\end{aligned} \tag{87b}$$

Here Green's function is given by

$$G_k(y, t) = \frac{1}{\sqrt{4\pi a^2 kt}} e^{-y^2/4a^2 kt} \tag{88}$$

and the diffusion coefficient by

$$a^2 = \frac{2\eta_0}{\rho}. \tag{89}$$

Suppose that the pressure is isotropic; that is, it depends on the coordinates x, y only via the radial coordinate $r = \sqrt{x^2 + y^2}$; accordingly we pass from the integration variables x' and y' to r' in (87a) and (87b) correspondingly. At later times we can expand Green's function (88) in inverse powers of t . The first terms in the r.h.s. of (87a) and (87b) are subleading, and we obtain

$$\begin{aligned}
V_x(x, y, t) &\approx -\frac{1}{\rho} \int_0^t ds \int_{-\infty}^{\infty} dr \frac{1}{\sqrt{2\pi a^2 s}} \frac{\partial P(r, t - s)}{\partial r} \\
&= -\frac{1}{\rho} \int_0^t ds \frac{1}{\sqrt{2\pi a^2 s}} [P(R(s), t - s) - P(0, t - s)],
\end{aligned} \tag{90a}$$

and by the same token

$$\begin{aligned}
V_y(x, y, t) &\approx -\frac{1}{\rho} \int_0^t ds \frac{1}{\sqrt{4\pi a^2 s}} [P(R(s), t - s) - P(0, t - s)],
\end{aligned} \tag{90b}$$

where $R(t)$ denotes the boundary beyond which the density of the plasma is below the critical value. We observe that $V_x/V_y = \sqrt{2}$. Consequently, the azimuthal anisotropy of the hydrodynamic flow is [35]

$$\frac{V_x^2 - V_y^2}{V_x^2 + V_y^2} = \frac{1 - (1/2)}{1 + (1/2)} = \frac{1}{3}. \tag{91}$$

Since I assumed that the initial conditions and the pressure are isotropic, the azimuthal asymmetry (91) is generated exclusively by the magnetic field.

We see that at later times after the heavy-ion collision, flow velocity is proportional to $\eta_0^{-1/2}$, where η_0 is the finite shear viscosity coefficient; see (87a) and (87b). If the system is such that in absence of the magnetic field it were azimuthally symmetric, then the magnetic field induces azimuthal asymmetry of 1/3; see (91). The effect of the magnetic field on flow is strong and must be taken into account in phenomenological applications. Neglect of the contribution by the magnetic field leads to underestimation of the phenomenological value of viscosity extracted from the data [38–40]. In other words, the more viscous QGP in magnetic field produces the same azimuthal anisotropy as a less viscous QGP in vacuum.

A model that I considered in this section to illustrate the effect of the magnetic field on the azimuthal anisotropy of a viscous fluid flow does not take into account many important features of a realistic heavy-ion collision. To be sure, a comprehensive approach must involve numerical solution of the relativistic magnetohydrodynamic equations with a realistic geometry. A potentially important effect that I have not considered here is plasma instabilities [41, 42], which warrant further investigation.

The structure of the viscous stress tensor in very strong magnetic field (84) is general, model independent. However, as explained, the precise amount of the azimuthal anisotropy that it generates cannot be determined without taking into account many important effects. Even so, I draw the reader's attention to the fact that analysis of [29] using quite different arguments arrived at similar conclusion. Although a more quantitative numerical calculation is certainly required before a final conclusion can be made, it looks very plausible that the QGP viscosity is significantly higher than the presently accepted value extracted without taking into account the magnetic field effect [38–40] and is perhaps closer to the value calculated using the perturbative theory [43, 44].

3. Energy Loss and Polarization due to Synchrotron Radiation

3.1. Radiation of Fast Quark in Magnetic Field. General problem of charged fermion radiation in external magnetic field was solved in [45–47]. It has important applications in collider physics; see, for example, [48, 49]. In heavy-ion phenomenology, synchrotron radiation provides one of the mechanisms of energy loss in quark-gluon plasma, which is an important probe of QGP [50, 51] (synchrotron radiation in chromo-magnetic fields was discussed in [52–54]).

A typical diagram contributing to the synchrotron radiation, that is, radiation in external magnetic field, by a quark is shown in Figure 6 [21]. This diagram is proportional to $(eB)^n$, where n is the number of external field lines. In strong field, powers of eB must be summed up, which may be accomplished by exactly solving the Dirac equation for the relativistic fermion and then calculating the matrix element for the transition $q \rightarrow q + g$. Such calculation has been done in QED for some special cases including the homogeneous

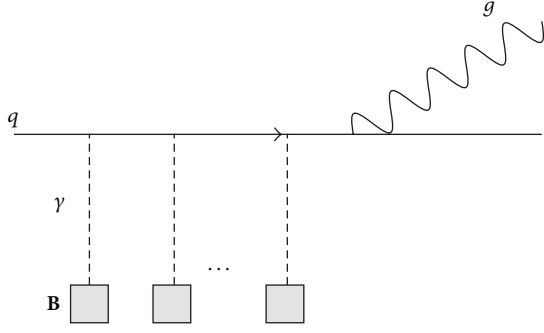


FIGURE 6: A typical diagram contributing to the synchrotron radiation by a quark.

constant field and can be readily generalized for gluon radiation. Intensity of the radiation can be expressed via the invariant parameter χ defined as

$$\chi^2 = -\frac{\alpha_{\text{em}} Z_q^2 \hbar^3}{m^6} (F_{\mu\nu} p^\nu)^2 = \frac{\alpha_{\text{em}} Z_q^2 \hbar^3}{m^6} (\mathbf{p} \times \mathbf{B})^2, \quad (92)$$

where the initial quark 4-momentum is $p^\mu = (\varepsilon, \mathbf{p})$ and Z_q is the quark charge in units of the absolute value of the electron charge e . At high energies,

$$\chi \approx \frac{Z_q B \varepsilon}{B_c m}. \quad (93)$$

The regime of weak fields corresponds to $\chi \ll 1$, while in strong fields $\chi \gg 1$. In our case, $eB/eB_c \approx (m_\pi/m_u)^2 \gg 1$ (at RHIC), and therefore $\chi \gg 1$. In terms of χ , spectrum of radiated gluons of frequency ω can be written as [45]

$$\frac{dI}{d\omega} = -\alpha_s C_F \frac{m^2 \omega}{\varepsilon^2} \times \left\{ \int_x^\infty \text{Ai}(\xi) d\xi + \left(\frac{2}{x} + \frac{\omega}{\varepsilon} \chi x^{1/2} \right) \text{Ai}'(x) \right\}, \quad (94)$$

where I is the intensity

$$x = \left(\frac{\hbar \omega}{\varepsilon' \chi} \right)^{2/3}, \quad (95)$$

and ε' is quark's energy in the final state. Ai is the Ayri function. Equation (94) is valid under the assumption that the initial quark remains ultrarelativistic, which implies that the energy loss due to the synchrotron radiation $\Delta\varepsilon$ should be small compared to the quark energy itself $\Delta\varepsilon \ll \varepsilon$.

Energy loss by a relativistic quark per unit length is given by [48]

$$\frac{d\varepsilon}{dl} = - \int_0^\infty d\omega \frac{dI}{d\omega} = \alpha_s C_F \frac{m^2 \chi^2}{2} \int_0^\infty \frac{4 + 5\chi x^{3/2} + 4\chi^2 x^3}{(1 + \chi x^{3/2})^4} \text{Ai}'(x) x dx. \quad (96)$$

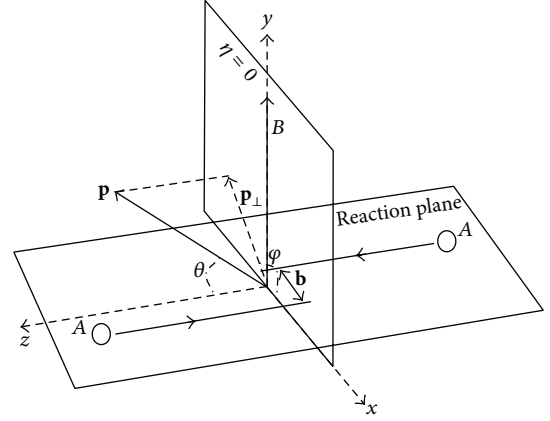


FIGURE 7: Geometry of a heavy-ion collision. \mathbf{p} denotes momentum of a fast quark. Two orthogonal planes are the reaction plane span by the initial heavy-ion momenta and the mid rapidity plane $\theta = \pi/2$, which is labeled as $\eta = 0$.

In two interesting limits, energy loss behaves quite differently. At $\eta = \varphi = 0$ we have [48]

$$\frac{d\varepsilon}{dl} = -\frac{2\alpha_s \hbar C_F (Z_q eB)^2 \varepsilon^2}{3m^4}, \quad \chi \ll 1, \quad (97a)$$

$$\frac{d\varepsilon}{dl} = -0.37\alpha_s \hbar^{-1/3} C_F (Z_q eB \varepsilon)^{2/3}, \quad \chi \gg 1. \quad (97b)$$

In the strong field limit energy loss is independent of the quark mass, whereas in the weak field case it decreases as m^{-4} . Since $\chi \propto \hbar$, limit of $\chi \ll 1$ corresponds to the classical energy loss.

To apply this result to heavy-ion collisions we need to write down the invariant χ in a suitable kinematic variables. The geometry of a heavy-ion collision is depicted in Figure 7. Magnetic field \mathbf{B} is orthogonal to the reaction plane span by the impact parameter vector \mathbf{b} and the collision axis (z -axis). For a quark of momentum \mathbf{p} we define the polar angle θ with respect to the z -axis and azimuthal angle φ with respect to the reaction plane. In this notation, $\mathbf{B} = B\hat{\mathbf{y}}$ and $\mathbf{p} = p_z \hat{\mathbf{z}} + p_\perp (\hat{\mathbf{x}} \cos \varphi + \hat{\mathbf{y}} \sin \varphi)$, where $p_\perp = |\mathbf{p}| \sin \theta \approx \varepsilon \sin \theta$. Thus, $(\mathbf{B} \times \mathbf{p})^2 = B^2 (p_z^2 + p_\perp^2 \cos^2 \varphi)$. Conventionally, one expresses the longitudinal momentum and energy using the rapidity η as $\varepsilon = m_\perp \cosh \eta$ and $p_z = m_\perp \sinh \eta$, where $m_\perp^2 = m^2 + p_\perp^2$. We have

$$\chi^2 = \frac{\hbar^2 (eB)^2}{m^6} p_\perp^2 (\sinh^2 \eta + \cos^2 \varphi). \quad (98)$$

In Figure 8 a numerical calculation of the energy loss *per unit length* in a constant magnetic field using (96) and (98) is shown [21]. We see that energy loss of a u quark with $p_\perp = 10$ GeV is about 0.2 GeV/fm at RHIC and 1.3 GeV/fm at LHC. This corresponds to the loss of 10% and 65% of its initial energy after traveling 5 fm at RHIC and LHC, respectively. Therefore, energy loss due to the synchrotron radiation at LHC gives a phenomenologically important contribution to the total energy loss.

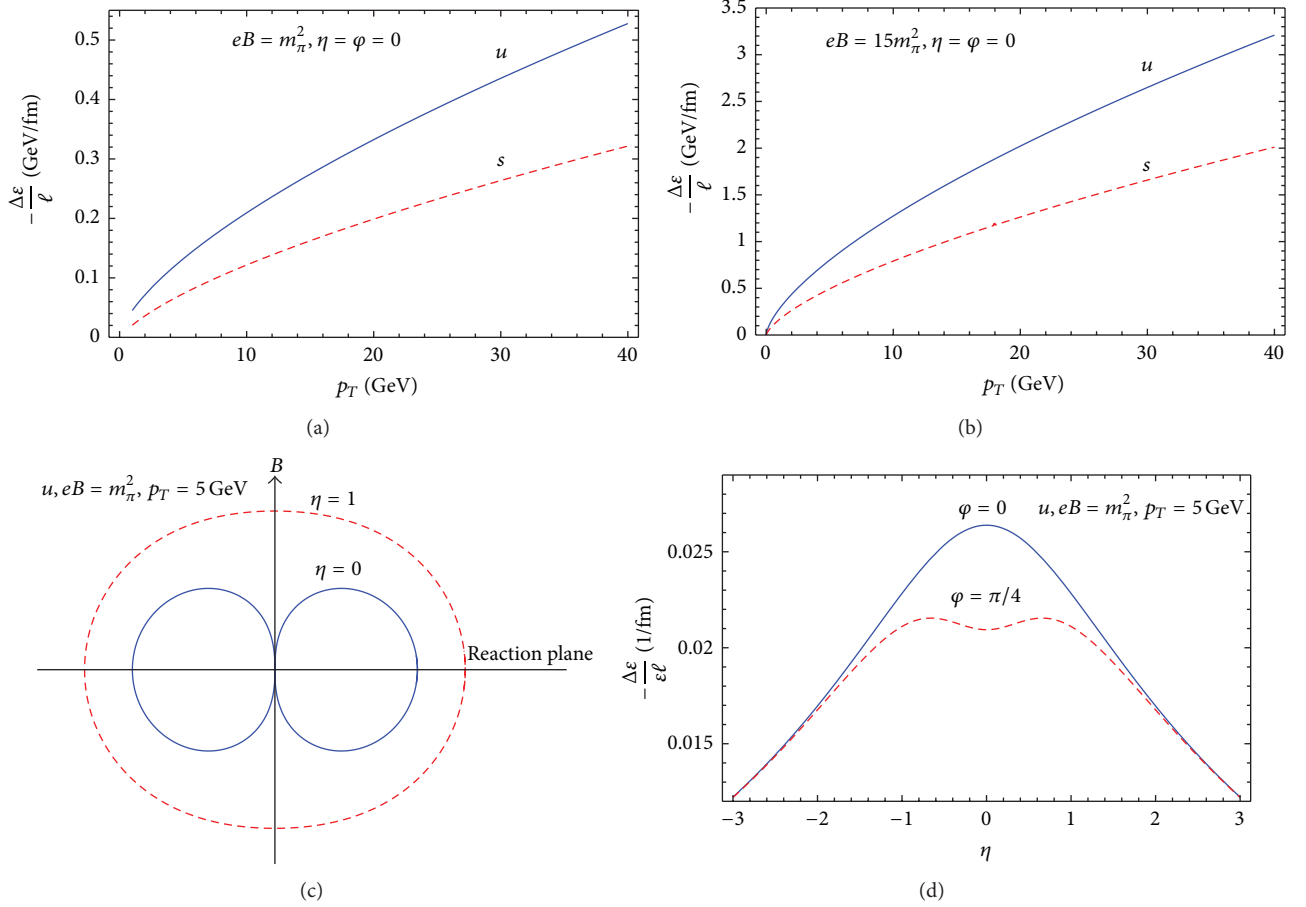


FIGURE 8: Energy loss per unit length by quarks moving in constant external magnetic field as a function of (a) p_T at RHIC at $\eta = \varphi = 0$, (b) p_T at LHC at $\eta = \varphi = 0$, (c) azimuthal angle φ with respect to the reaction plane for $p_T = 5$ GeV and $\eta = 0, 1$, and (d) fractional energy loss versus rapidity η at $p_T = 5$ GeV and $\varphi = 0, \pi/4$.

Energy loss due to the synchrotron radiation has a very nontrivial azimuthal angle and rapidity dependence that comes from the corresponding dependence of the χ -parameter (98). As can be seen in Figure 8(c), energy loss has a minimum at $\varphi = \pi/2$ that corresponds to quark's transverse momentum \mathbf{p}_\perp being parallel (or antiparallel) to the field direction. It has a maximum at $\varphi = 0, \pi$ when \mathbf{p}_\perp is perpendicular to the field direction and thus lying in the reaction plane. It is obvious from (98) that at midrapidity $\eta = 0$ the azimuthal angle dependence is much stronger pronounced than in the forward/backward direction. Let me emphasize that the energy loss (96) divided by m^2 , that is, $d\varepsilon/(dl m^2)$ scales with χ . In turn, χ is a function of magnetic field, quark mass, rapidity, and azimuthal angle. Therefore, all the features seen in Figure 8 follow from this scaling behavior.

3.2. Azimuthal Asymmetry of Gluon Spectrum. In magnetic field gluon spectrum is azimuthally asymmetric. It is customary to describe this asymmetry by Fourier coefficients of intensity defined as

$$I(\varphi) = \bar{I} \left(1 + 2 \sum_{n=1}^{\infty} v_n \cos(n\varphi) \right), \quad (99)$$

$$v_n = \frac{1}{2\pi\bar{I}} \int_{-\pi}^{\pi} I(\varphi) \cos(n\varphi) d\varphi.$$

Azimuthal averaged intensity is $\bar{I} = \int_{-\pi}^{\pi} I(\varphi) d\varphi / 2\pi$. In strong fields $\chi \gg 1$, and we can write

$$\begin{aligned} I(\varphi) &= 0.37\alpha_s C_F m^2 \chi^{2/3} \\ &= 0.37\alpha_s C_F (eB p_\perp)^{2/3} (\sinh^2 \eta + \cos^2 \varphi)^{1/3}. \end{aligned} \quad (100)$$

We have

$$\begin{aligned} v_n &= \frac{\int_{-\pi}^{\pi} I(\varphi) \cos(n\varphi) d\varphi}{\int_{-\pi}^{\pi} I(\varphi) d\varphi} \\ &= \frac{\int_{-\pi}^{\pi} (\sinh^2 \eta + \cos^2 \varphi)^{1/3} \cos(n\varphi) d\varphi}{\int_{-\pi}^{\pi} (\sinh^2 \eta + \cos^2 \varphi)^{1/3} d\varphi}. \end{aligned} \quad (101)$$

At $\eta = 0$ the Fourier coefficients w_n can be calculated analytically using formula 3.631.9 of [34] as follows:

$$v_n = \frac{B(4/3, 4/3)}{B((4/3) + (n/2), (4/3) - (n/2))}, \quad \text{if } n \in \text{even}; \quad (102)$$

$$v_n = 0, \quad \text{if } n \in \text{odd},$$

where B is Euler's beta function. The corresponding numerical values of the lowest harmonics are $v_2 = 0.25$, $v_4 = -0.071$, $v_6 = 0.036$, $v_8 = -0.022$, and $v_{10} = 0.015$.

3.3. Polarization of Light Quarks. Synchrotron radiation leads to polarization of electrically charged fermions, this is known as the Sokolov-Ternov effect [46]. It was applied to heavy-ion collisions in [21]. Unlike energy loss that I discussed so far, this is a purely quantum effect. It arises because the probability of the spin-flip transition depends on the orientation of the quark spin with respect to the direction of the magnetic field and on the sign of fermion's electric charge. The spin-flip probability per unit time reads [46]

$$w = \frac{5\sqrt{3}\alpha_s C_F}{16} \frac{\hbar^2}{m^2} \left(\frac{\varepsilon}{m}\right)^5 \left(\frac{Z_q e |\mathbf{v} \times \mathbf{B}|}{\varepsilon}\right)^3 \times \left(1 - \frac{2}{9}(\boldsymbol{\zeta} \cdot \mathbf{v})^2 - \frac{8\sqrt{3}}{15} \text{sign}(e_q)(\boldsymbol{\zeta} \cdot \hat{\mathbf{z}})\right), \quad (103)$$

where $\boldsymbol{\zeta}$ is a unit axial vector that coincides with the direction of quark spin in its rest frame and $\mathbf{v} = \mathbf{p}/\varepsilon$ is the initial fermion velocity.

The nature of this spin-flip transition is transparent in the nonrelativistic case, where it is induced by the interaction Hamiltonian [49] as follows:

$$\mathcal{H} = -\boldsymbol{\mu} \cdot \mathbf{B} = -\left(\frac{geZ_q \hbar}{2m}\right) \mathbf{s} \cdot \mathbf{B}. \quad (104)$$

It is seen that negatively charged quarks and antiquarks (e.g., \bar{u} and \bar{d}) tend to align against the field, while the positively charged ones (e.g., u and d) align parallel to the field.

Let $n_{\uparrow(\downarrow)}$ be the number of fermions or antifermions with given momentum and spin direction parallel (antiparallel) to the field produced in a given event. At initial time $t = t_0$ the spinasymmetry defined as

$$A = \frac{n_{\uparrow} - n_{\downarrow}}{n_{\uparrow} + n_{\downarrow}} \quad (105)$$

vanishes. Equation (103) implies that at later times, a beam of nonpolarized fermions develops a finite asymmetry given by [46]

$$A = \frac{8\sqrt{3}}{15} \left(1 - e^{-(t-t_0)/\tau}\right), \quad (106)$$

where

$$\tau = \frac{8}{5\sqrt{3}m\alpha_s C_F} \left(\frac{m}{\varepsilon}\right)^2 \left(\frac{m^2}{Z_q e |\mathbf{v} \times \mathbf{B}|}\right)^3 \quad (107)$$

is the characteristic time over which the maximal possible asymmetry is achieved. This time is extremely small on the scale of t_0 . For example, it takes only $\tau = 6 \cdot 10^{-8}$ fm for a d quark of momentum $p_{\perp} = 1$ GeV at $\eta = \varphi = 0$ at RHIC to achieve the maximal asymmetry of $A_m = 8/5\sqrt{3} = 92\%$. Therefore, quarks and antiquarks are polarized almost instantaneously after being released from their wave functions. However, subsequent interaction with QGP and fragmentation washes out the polarization of quarks.

A more sensitive probe are leptons weakly interacting with QGP and not undergoing a fragmentation process. Thus, their polarization can present a direct experimental evidence for the existence and strength of magnetic field. In case of muons we can estimate τ by replacing $\alpha_s C_F \rightarrow \alpha_{em}$. For muons we get $\tau = 0.3$ fm/c, which is still much smaller than magnetic field life-time. Observation of such a lepton polarization asymmetry is perhaps the most definitive proof of existence of the strong magnetic field at early times after a heavy-ion collision regardless of its later time-dependence.

In summary, energy loss per unit length for a light quark with $p_T = 15$ GeV is about 0.27 GeV/fm at RHIC and 1.7 GeV/fm at LHC, which is comparable to the losses due to interaction with the plasma. Thus, the synchrotron radiation alone is able to account for quenching of jets at LHC with p_{\perp} as large as 20 GeV. Synchrotron radiation is definitely one of missing pieces in the puzzle of the jet energy loss in heavy-ion collisions. Quarks and leptons are expected to be strongly polarized in plasma in the direction parallel or anti-parallel to the magnetic field depending on the sign of their electric charge.

4. Photon Decay

In this section I consider pair production by photon in external magnetic field [55], which is a cross-channel of synchrotron radiation discussed in the previous section. Specifically, we are interested to determine photon decay rate w in the process $\gamma B \rightarrow f \bar{f} B$, where f stands for a charged fermion, as a function of photon's transverse momentum k_T , rapidity η , and azimuthal angle φ . Origin of these photons in heavy-ion collisions will not be of interest to us in this section.

Characteristic frequency of a fermion of species a of mass m_a and charge $z_a e$ (e is the absolute value of electron charge) moving in external magnetic field B (in a plane perpendicular to the field direction) is

$$\hbar\omega_B = \frac{z_a e B}{\varepsilon}, \quad (108)$$

where ε is the fermion energy. Here—in the spirit of the adiabatic approximation— B is a slow function of time. Calculation of the photon decay probability significantly simplifies if motion of electron is quasiclassical; that is, quantization of fermion motion in the magnetic field can be neglected. This condition is fulfilled if $\hbar\omega_B \ll \varepsilon$. This implies that

$$\varepsilon \gg \sqrt{zeB}. \quad (109)$$

For RHIC it is equivalent to $\varepsilon \gg m_{\pi}$, for LHC $\varepsilon \gg 4m_{\pi}$.

Photon decay rate was calculated in [45] and, using the quasi-classical method, in [56]. It reads

$$w = -\sum_a \frac{\alpha_{\text{em}} z_a^3 eB}{m_a \kappa_a} \int_{(4/\kappa_a)^{2/3}}^{\infty} \frac{2(x^{3/2} + 1/\kappa_a) \text{Ai}'(x)}{x^{11/4} (x^{3/2} - 4/\kappa_a)^{3/2}}, \quad (110)$$

where summation is over fermion species and the invariant parameter κ is defined as

$$\kappa_a^2 = -\frac{\alpha_{\text{em}} z_a^2 \hbar^3}{m_a^6} (F_{\mu\nu} k^\nu)^2 = \frac{\alpha_{\text{em}} z_a^2 \hbar^3}{m_a^6} (\mathbf{k} \times \mathbf{B})^2, \quad (111)$$

with the initial photon 4-momentum $k^\mu = (\hbar\omega, \mathbf{k})$. With notations of Figure 7, $\mathbf{k} = k_z \hat{\mathbf{z}} + k_\perp (\hat{\mathbf{x}} \cos \varphi + \hat{\mathbf{y}} \sin \varphi)$, where $k_\perp = |\mathbf{k}| \sin \theta = \hbar\omega \sin \theta$. Thus, $(\mathbf{B} \times \mathbf{k})^2 = B^2 (k_z^2 + k_\perp^2 \cos^2 \varphi)$. Employing $\hbar\omega = k_\perp \cosh \eta$ and $k_z = k_\perp \sinh \eta$, we write

$$\kappa_a = \frac{\hbar(z_a eB)}{m_a^3} k_\perp \sqrt{\sinh^2 \eta + \cos^2 \varphi}. \quad (112)$$

Plotted in Figure 9 is the photon decay rate (110) for RHIC and LHC. The survival probability of photons in magnetic field is $P = 1 - w\Delta t$, where Δt is the time spent by a photon in plasma. Estimating $\Delta t = 10$ fm we determine that photon survives with probability $P_{\text{RHIC}} \approx 97\%$ at RHIC, while only $P_{\text{LHC}} \approx 80\%$ at LHC. Such strong depletion can certainly be observed in heavy-ion collisions at LHC.

Azimuthal distribution of the decay rate of photons at LHC is azimuthally asymmetric as can be seen in Figure 10 [55]. The strongest suppression is in the B field direction, that is, in the direction orthogonal to the reaction plane. At $\eta \geq 1$ the φ dependence of κ_a is very weak which is reflected in nearly symmetric azimuthal shape of the dashed line in Figure 10.

To quantify the azimuthal asymmetry it is customary to expand the decay rate in Fourier series with respect to the azimuthal angle. Noting that w is an even function of φ , we have

$$w(\varphi) = \frac{1}{2} w_0 + \sum_{n=1}^{\infty} w_n \cos(n\varphi), \quad (113)$$

$$w_n = \frac{1}{\pi} \int_{-\pi}^{\pi} w(\varphi) \cos(n\varphi) d\varphi.$$

In strong fields $\kappa_a \gg 1$. For example, for $\gamma \rightarrow \mu^+ \mu^-$ at RHIC at $\varphi = \eta = 0$ and $k_T = 1$ GeV we get $\kappa_\mu = 19$. Therefore, we can expand the rate (110) at large κ_a as [45]

$$\begin{aligned} w &\approx \frac{3^{1/6} 5 \Gamma^2(2/3)}{2^{4/3} 7 \pi^{1/2} \Gamma(7/6)} \sum_a \frac{\alpha_{\text{em}} eB z_a^3}{m_a \kappa_a^{1/3}} \\ &\equiv \frac{A}{(\sinh^2 \eta + \cos^2 \varphi)^{1/6}}, \quad \kappa_a \gg 1. \end{aligned} \quad (114)$$

At $\eta = 0$ the Fourier coefficients w_n can be calculated analytically using formula 3.631.9 of [34]

$$\begin{aligned} w_{2k} &= \frac{3 \cdot 2^{1/3} A}{B((5/6) + k, (5/6) - k)}, \\ w_{2k+1} &= 0, \quad k = 0, 1, 2, \dots, \end{aligned} \quad (115)$$

where B is the Euler's beta function and A is defined in (114). Substituting these expressions into (113) we find

$$w = \frac{1}{2} w_0 \left[1 - \sum_{k=1}^{\infty} \frac{\sqrt{\pi} \Gamma(-1/6)}{2^{2/3} B((5/6) + k, (5/6) - k)} \cos(2k\varphi) \right]. \quad (116)$$

The first few terms in this expansion read

$$w = \frac{1}{2} w_0 \left(1 - \frac{2}{5} \cos(2\varphi) + \frac{14}{55} \cos(4\varphi) - \dots \right), \quad (117)$$

What is measured experimentally is not the decay rate, but rather the photon spectrum. This spectrum is modified by the survival probability P which is obviously azimuthally asymmetric. To quantify this asymmetry, we write using (113)

$$P = \bar{P} \left(1 + \sum_{k=1}^{\infty} v_{2k} \cos(2\varphi k) \right), \quad (118)$$

$$v_{2k} = -\frac{1 - \bar{P}}{\bar{P}} \frac{2w_{2k}}{w_0},$$

where $\bar{P} = \langle 1 - w\Delta t \rangle_\varphi = 1 - w_0 \Delta t$ is the survival probability averaged over the azimuthal angle. Since $w_0 \Delta t \ll 1$, as can be seen in Figure 9, we can estimate using (114) and (115)

$$\begin{aligned} v_{2k} &\approx -\frac{2w_{2k}}{w_0} w_0 \Delta t \\ &= -\frac{2w_{2k}}{w_0} \Delta t \frac{5 \cdot 6^{2/3} \Gamma(2/3)}{7\pi} \sum_a \frac{\alpha_{\text{em}} (eB)^{2/3} z_a^{8/3}}{(k_T)^{1/3}}. \end{aligned} \quad (119)$$

In particular, the ‘‘elliptic flow’’ coefficient is [55]

$$v_2 = \Delta t \frac{2 \cdot 6^{2/3} \Gamma(2/3)}{7\pi} \sum_a \frac{\alpha_{\text{em}} (eB)^{2/3} z_a^{8/3}}{(k_T)^{1/3}}. \quad (120)$$

For example, at $k_T = 1$ GeV and $\Delta t \sim 10$ fm/c one expects $v_2 \approx 2\%$ at RHIC and $v_2 \approx 14\%$ at LHC only due to the presence of magnetic field. We see that decay of photons in external magnetic field significantly contributes to the photon asymmetry in heavy-ion collisions along with other possible effects.

In summary, I calculated photon pair-production rate in external magnetic field created in off-central heavy-ion collisions. Photon decay leads to depletion of the photon yield by a few percent at RHIC and by as much as 20% at the LHC. The decay rate depends on the rapidity and azimuthal angle. At midrapidity the azimuthal asymmetry of the decay rate translates into asymmetric photon yield and contributes to the ‘‘elliptic flow.’’ Let me also quote a known result that photons polarized parallel to the field are 3/2 times more likely to decay than those polarized transversely [45]. Therefore, polarization of the final photon spectrum perpendicular to the field is a signature of existence of strong magnetic field. Finally, photon decay necessarily leads to enhancement of dilepton yield.

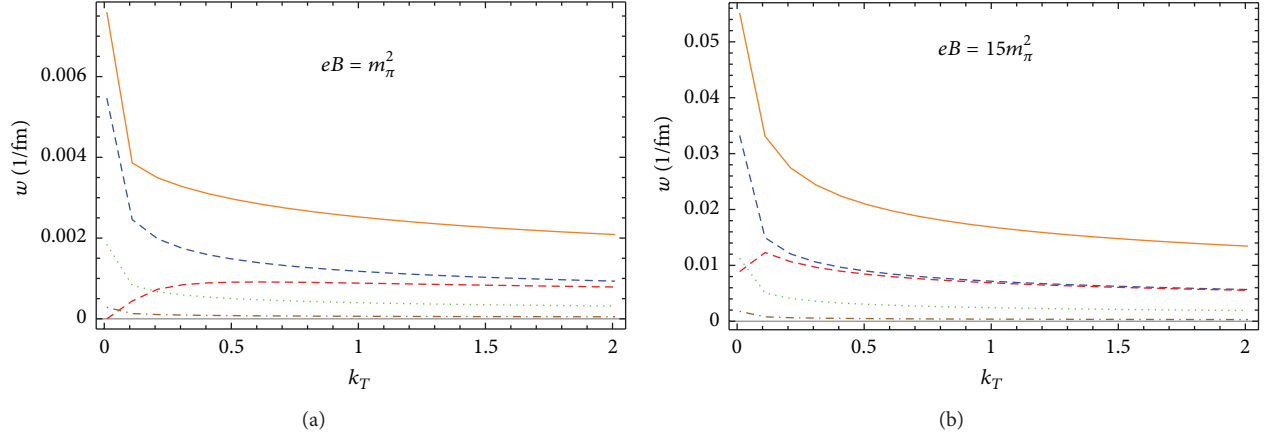


FIGURE 9: Decay rate of photons moving in reaction plane in magnetic field as a function of transverse momentum k_T : (a) at RHIC, (b) at LHC. Broken lines from bottom to top give contributions of $\gamma \rightarrow d\bar{d}$, $\gamma \rightarrow u\bar{u}$, $\gamma \rightarrow \mu^+\mu^-$, and $\gamma \rightarrow e^+e^-$ channels. Upper solid line is the total rate.

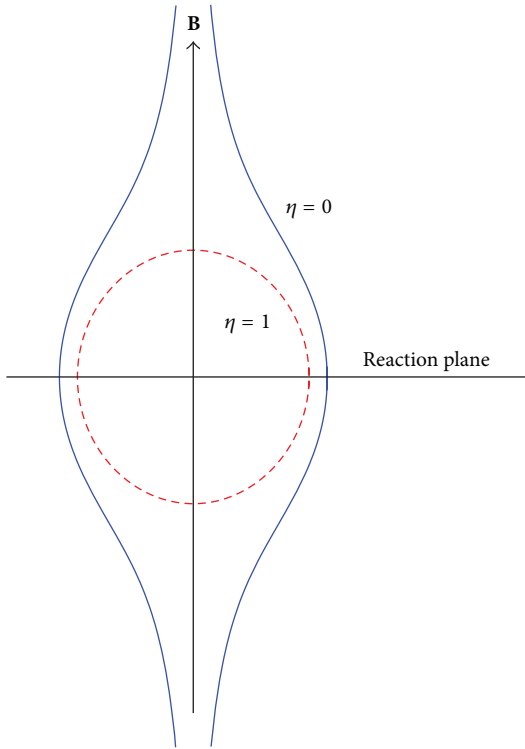


FIGURE 10: Azimuthal distribution of the decay rate of photons at different rapidities at LHC. Only contribution of the $\gamma \rightarrow e^+e^-$ channel is shown. Note that the rate w vanishes at $\eta = 0$ and $\varphi = \pi/2$, that is, in the direction of \mathbf{B} . However, it happens at so small values of $|\varphi - \pi/2|$ that it is beyond the experimental resolution and is not shown in the figure.

5. Quarkonium Dissociation in Magnetic Field

5.1. Effects of Magnetic Field on Quarkonium. Strong magnetic field created in heavy-ion collisions generates a number of remarkable effects on quarkonium production, some of which I will describe in this section. Magnetic field can be treated as static if the distance λ over which it significantly

varies is much larger than the quarkonium radius. If Δt is magnetic field life-time, then $\lambda \sim c\Delta t$. For a quarkonium with binding energy ε_b and radius α_s/ε_b , the quasi-static approximation applies when $\varepsilon_b\lambda/\alpha_s \gg 1$. Estimating conservatively $\lambda \sim 2$ fm we get for J/ψ : $\varepsilon_b\lambda/\alpha_s \approx 23$, which is comfortably large to justify the quasi-static approximation, where I assumed that ε_b is given by its vacuum value. As temperature T increases ε_b drops. Temperature dependence of ε_b is model dependent; however, it is certain that eventually it vanishes at some finite temperature T_0 . Therefore, only in the close vicinity of T_0 , that is, at very small binding energies, the quasi-static approximation is not applicable. I thus rely on the quasi-static approximation to calculate J/ψ dissociation [57, 58].

Magnetic field has a three-fold effect on quarkonium.

- (1) *Lorentz ionization.* Consider quarkonium traveling with constant velocity in magnetic field in the laboratory frame. Boosting to the quarkonium comoving frame, we find mutually orthogonal electric and magnetic fields given by (121a), (121b), and (122). In the presence of an electric field quark and anti-quark have a finite probability to tunnel through the potential barrier thereby causing quarkonium dissociation. In atomic physics such a process is referred to as Lorentz ionization. In the nonrelativistic approximation, the tunneling probability is of order unity when the electric field E in the comoving frame satisfies $eE \gtrsim m^{1/2}\varepsilon_b^{3/2}$ (for weakly bound states), where m is quark mass; see (144). This effect causes a significant increase in quarkonium dissociation rate; numerical calculation for J/ψ is shown in Figure 13.
- (2) *Zeeman effect.* Energy of a quarkonium state depends on spin S , orbital angular momentum L , and total angular momentum J . In a magnetic field these states split; the splitting energy in a weak field is $\Delta M = (eB_0/2m)gJ_z$, where $J_z = -J, -J+1, \dots, J$ is projection of the total angular momentum on the direction of magnetic field, m is quark mass, and g is Landé factor depending on J, L , and S in a well-known way; see, for

example, [59]. For example, J/ψ with $S = 1$, $L = 0$, and $J = 1$ ($g \approx 2$) splits into three states with $J_z = \pm 1, 0$ and with mass difference $\Delta M = 0.15$ GeV, where we used $eB_0 = 15m_\pi^2$. Thus, the Zeeman effect leads to the emergence of new quarkonium states in plasma.

- (3) *Distortion of the quarkonium potential in magnetic field.* This effect arises in higher-order perturbation theory and becomes important at field strengths of order $B \sim 3\pi m^2/e^3$ [60]. This is $3\pi/\alpha$ times stronger than the critical Schwinger's field. Therefore, this effect can be neglected at the present collider energies.

Some of the notational definitions used in this section: \mathbf{V} and \mathbf{P} , are velocity and momentum of quarkonium in the lab frame; M is its mass; \mathbf{p} is the momentum of quark or antiquark in the comoving frame; m is its mass; \mathbf{B}_0 is the magnetic field in the lab frame, \mathbf{E} and \mathbf{B} are electric and magnetic fields in the comoving frame; γ_L is the quarkonium Lorentz factor; and γ is a parameter defined in (139). I use Gauss units throughout the section; note that expressions eB , eE , and eB_0 are the same in Gauss and Lorentz-Heaviside units.

5.2. Lorentz Ionization: Physical Picture. In this section I focus on Lorentz ionization, which is an important mechanism of J/ψ suppression in heavy-ion collisions [57, 58]. Before we proceed to analytical calculations it is worthwhile to discuss the physics picture in more detail in two reference frames: the quarkonium proper frame and the lab frame. In the quarkonium proper frame the potential energy of, say, antiquark (with $e < 0$) is a sum of its potential energy in the binding potential and its energy in the electric field $-eEx$, where x is the electric field direction; see Figure 11. Since $|e|Ex$ becomes large and negative at large and negative x (far away from the bound state) and because the quarkonium potential has finite radius, this region opens up for the motion of the antiquark. Thus there is a quantum mechanical probability to tunnel through the potential barrier formed on one side by the vanishing quarkonium potential and on the other by increasing absolute value of the antiquark energy in electric field. Of course the total energy of the antiquark (not counting its mass) is negative after tunneling. However, its kinetic energy grows proportionally to eEx as it goes away. By picking up a light quark out of vacuum it can hadronize into a D -meson.

If we now go to the reference frame where $E = 0$ and there is only magnetic field B (we can always do so since $E < B$), then the entire process looks quite different. An energetic quarkonium travels in external magnetic field and decays into quark-antiquark pair that can later hadronize into D -mesons. This happens in spite of the fact that J/ψ mass is smaller than masses of two D -mesons due to additional momentum $e\mathbf{A}$ supplied by the magnetic field. Similarly a photon can decay into electron-positron pair in external magnetic field.

5.3. Quarkonium Ionization Rate

5.3.1. Comoving Frame. Consider a quarkonium traveling with velocity \mathbf{V} in constant magnetic field \mathbf{B}_0 . Let \mathbf{B} and \mathbf{E}

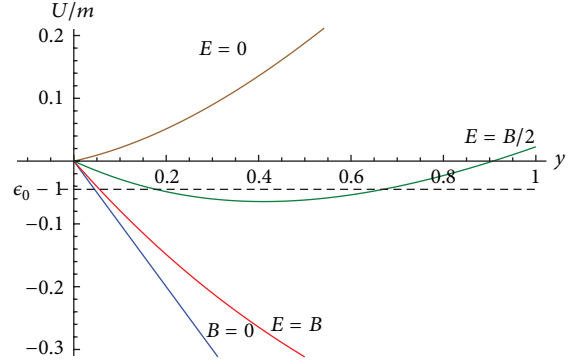


FIGURE 11: Effective potential $U(x) = \sqrt{m^2 + (p_z + eBx)^2 + p_x^2} - eEx - \sqrt{m^2 + p_x^2 + p_z^2}$ for $p_x = 0$, $p_z = m/6$, and $B = m$ (except the blue line where $B = 0$). The width of the potential barrier decreases with E and increases with B . $1 - \epsilon_0$ corresponds to the binding energy in units of m .

be magnetic and electric fields in the comoving frame, and let subscripts \parallel and \perp denote field components parallel and perpendicular to \mathbf{V} correspondingly. Then,

$$E_{\parallel} = 0, \quad \mathbf{E}_{\perp} = \gamma_L \mathbf{V} \times \mathbf{B}_0, \quad (121a)$$

$$B_{\parallel} = \frac{\mathbf{B}_0 \cdot \mathbf{V}}{V}, \quad \mathbf{B}_{\perp} = \gamma_L \frac{(\mathbf{V} \times \mathbf{B}_0) \times \mathbf{V}}{V^2}, \quad (121b)$$

where $\gamma_L = (1 - V^2)^{-1/2}$. Clearly, in the comoving frame $\mathbf{B} \cdot \mathbf{E} = 0$. If quarkonium travels at angle ϕ with respect to the magnetic field in the laboratory frame, then

$$B = B_0 \sqrt{\cos^2 \phi (1 - \gamma_L^2) + \gamma_L^2}, \quad E = B_0 \gamma_L V \sin \phi. \quad (122)$$

We choose y and x axes of the comoving frame such that $\mathbf{B} = B\hat{y}$ and $\mathbf{E} = E\hat{x}$. A convenient gauge choice is $\mathbf{A} = -Bx\hat{z}$ and $\varphi = -Ex$. For a future reference we also define a useful dimensionless parameter ρ [61]:

$$\rho = \frac{E}{B} = \frac{\gamma_L V \sin \phi}{\sqrt{\cos^2 \phi (1 - \gamma_L^2) + \gamma_L^2}}. \quad (123)$$

Note that (i) $0 \leq \rho \leq 1$ because $B^2 - E^2 = B_0^2 \geq 0$ and (ii) when quarkonium moves perpendicularly to the magnetic field \mathbf{B}_0 , $\rho = V$.

5.3.2. WKB Method. I assume that the force binding q and \bar{q} into quarkonium as a short-range one, that is, $(M\epsilon_b)^{1/2}R \ll 1$, where ϵ_b and M are binding energy and mass of quarkonium, respectively, and R is the radius of the nuclear force given by $R \approx (\alpha_s/\sigma)^{1/2}$, where $\sigma = 1$ GeV/fm is the string tension. For example, the binding energy of c and \bar{c} in J/ψ in vacuum is $\epsilon_b = 0.64$ GeV $\ll M/R^2 = M\sigma/\alpha_s \approx 3$ GeV. This approximation is even better at finite temperature on account of ϵ_b decrease. Regarding J/ψ as being bound by a short-range force enables us to calculate the dissociation probability

w with exponential accuracy $w \approx e^{-f}$, independently of the precise form of the quarkonium wave function. This is especially important, since solutions of the relativistic two-body problem for quarkonium are not readily available.

It is natural to study quarkonium ionization in the comoving frame [57]. As explained in the Introduction, ionization is quantum tunneling through the potential barrier caused by the electric field \mathbf{E} . In this subsection I employ the quasiclassical WKB approximation to calculate the quarkonium decay probability w . For the gauge choice specified in Section 5.3.1, quark energy ϵ_0 ($\epsilon_0 < m$) in electromagnetic field can be written as

$$\begin{aligned}\epsilon_0 &= \sqrt{m^2 + (\mathbf{p} - e\mathbf{A})^2} + e\varphi \\ &= \sqrt{m^2 + (p_z + eBx)^2 + p_x^2 + p_y^2} - eEx.\end{aligned}\quad (124)$$

In terms of ϵ_0 , quarkonium binding energy is $\epsilon_b = m - \epsilon_0$. To simplify notations, we will set $p_x = 0$, because the quark moves constant momentum along the direction of magnetic field.

The effective potential $U(x) = \epsilon_0(x) - \sqrt{m^2 + \mathbf{p}^2}$ corresponding to (124) is plotted in Figure 11. We can see that the tunneling probability is finite only if $E > 0$. It is largest when $B = 0$. It has been already noted before in [61–63] that the effect of the magnetic field is to stabilize the bound state. In spite of the linearly rising potential (at $B > E$) tunneling probability is finite as the result of rearrangement of the QED vacuum in electric field.

Ionization probability of quarkonium equals its tunneling probability through the potential barrier. The later is given by the transmission coefficient

$$w = e^{-2 \int_0^{y_1} \sqrt{-p_y^2} dy} \equiv e^{-f}. \quad (125)$$

In the nonrelativistic approximation one can also calculate the preexponential factor, which appears due to the deviation of the quark wave function from the quasi-classical approximation. This is discussed later in Section 5.5.2. We now proceed with the calculation of function f . Since $B > E$ (125) can be written as [57]

$$p_x^2 = -e^2 (B^2 - E^2) (x - x_1) (x - x_2), \quad (126)$$

where

$$x_{1,2} = \frac{\epsilon_0 E - p_z B \mp \sqrt{(\epsilon_0 E - p_z B)^2 - (B^2 - E^2) (-\epsilon_0^2 + m^2 + p_z^2)}}{e(B^2 - E^2)}. \quad (127)$$

Define dimensionless variables $\epsilon_0 = \epsilon_0/m$ and $q = p_z/m$. Integration in (74) gives

$$\begin{aligned}\frac{f}{m^2} &= \frac{\sqrt{-\epsilon_0^2 + 1 + q^2} (\epsilon_0 E - qB)}{e(B^2 - E^2)} \\ &\quad - \frac{(\epsilon_0 E - qB)^2 - (B^2 - E^2) (-\epsilon_0^2 + 1 + q^2)}{e(B^2 - E^2)^{3/2}} \\ &\quad \times \ln \left\{ \frac{\epsilon_0 E - qB + \sqrt{(B^2 - E^2) (-\epsilon_0^2 + 1 + q^2)}}{\sqrt{(\epsilon_0 E - qB)^2 - (B^2 - E^2) (-\epsilon_0^2 + 1 + q^2)}} \right\}.\end{aligned}\quad (128)$$

$w = e^f$ gives the corresponding ionization probabilities, at a given q . The largest probability corresponds to smallest f , which occurs at momentum q_m determined by [62]

$$\frac{\partial f(q_m)}{\partial q_m} = 0. \quad (129)$$

Using (128) and parameter ρ defined in (123), we find [57]

$$\begin{aligned}\frac{\rho (\epsilon_0 - \rho q_m)}{1 - \rho^2} \ln \left\{ \frac{\epsilon_0 \rho - q_m + \sqrt{1 - \rho^2} \sqrt{-\epsilon_0^2 + 1 + q_m^2}}{\sqrt{(\epsilon_0 - \rho q_m)^2 - 1 + \rho^2}} \right\} \\ = \frac{\sqrt{-\epsilon_0^2 + 1 + q_m^2}}{\sqrt{1 - \rho^2}}.\end{aligned}\quad (130)$$

This is an implicit equation for the extremal momentum $q_m = q_m(\epsilon_0, \rho)$. Substituting q_m into (128) one obtains $f = f(\epsilon_0, \rho)$, which by means of (125) yields the ionization probability. The quasi-classical approximation that we employed in this section is valid in as much as $f(q_m) \gg 1$.

In order to compare with the results obtained in [62] using the imaginary time method, we can rewrite (130) in terms of an auxiliary parameter τ_0 as

$$\tau_0 = \frac{\sqrt{1 - \rho^2} \sqrt{-\epsilon_0^2 + 1 + q_m^2}}{\rho (\epsilon_0 - \rho q_m)}, \quad (131a)$$

$$\frac{\tanh \tau_0}{\tau_0} = \rho \frac{\epsilon_0 - \rho q_m}{\epsilon_0 \rho - q_m}. \quad (131b)$$

Taking advantage of these equations, (128) can be cast into a more compact form as follows

$$f_m = \frac{m^2 \tau_0 \rho}{eE \sqrt{1 - \rho^2}} [1 - \epsilon_0 (\epsilon_0 - q_m \rho)], \quad (132)$$

where we denoted $f_m = f(q_m)$. This agrees with results of [62].

5.3.3. *Special Case: Crossed Fields.* An important limiting case is crossed fields $E = B$. Since also $\mathbf{E} \perp \mathbf{B}$ (see Section 5.3.1), both field invariants vanish. Nevertheless, quarkonium ionization probability is finite [62]. This limit is obtained by taking $\rho \rightarrow 1$ in the equations from the previous section. Employing (131a) and (131b) we get the following condition for extremum:

$$\epsilon_0^2 - 1 + 2q_m^2 - 3\epsilon_0 q_m = 0, \quad (133)$$

with the solution

$$q_m = \frac{1}{4} \left(3\epsilon_0 - \sqrt{\epsilon_0^2 + 8} \right). \quad (134)$$

Substituting into (132) produces

$$f_m = \frac{2}{3} \frac{m^2}{eE} \frac{(-\epsilon_0^2 + 1 + q_m^2)^{3/2}}{\epsilon_0 - q_m}. \quad (135)$$

5.4. *Nonrelativistic Approximation.* A very useful approximation of the relativistic formulas derived in the previous section is the nonrelativistic limit because (i) it provides a very good numerical estimate (see Figure 12), and (ii) it allows us to eliminate the parametric dependence in (128), (130) and write $f(q_m)$ explicitly in terms of ρ and ϵ_0 , and (iii) spin effects can be accounted for [57, 58].

5.4.1. *Arbitrary Binding.* Motion of a particle can be treated non-relativistically if its momentum is much less than its mass. In such a case $\epsilon_0 \approx m$ or $\epsilon_b = m - \epsilon_0 \ll m$. Additionally, motion of a charged particle in electromagnetic field is non-relativistic if $E \ll B$. Indeed, the average velocity of a nonrelativistic particle is of order $v \sim E/B = \rho$. Thus, the non-relativistic limit is obtained by taking the limits $\epsilon_b = \epsilon_0/m \ll 1$ and $\rho \ll 1$. In these limits the extremum conditions (131a), (131b) reduce to

$$\tau_0 = \frac{\sqrt{2\epsilon_b + q_m^2}}{\rho}, \quad (136a)$$

$$\frac{\tanh \tau_0}{\tau_0} = \frac{\rho}{\rho - q_m}. \quad (136b)$$

Out of two solution to (136a) we pick the following one:

$$q_m = -\sqrt{\tau_0^2 \rho^2 - 2\epsilon_b}. \quad (137)$$

The sign of q_m is fixed using (136b) by noticing that $\tanh \tau_0 / \tau_0 < 1$. Eliminating q_m gives

$$\tau_0^2 - (\tau_0 \coth \tau_0 - 1)^2 = \gamma^2, \quad (138)$$

where

$$\gamma = \frac{\sqrt{2\epsilon_b}}{\rho}, \quad (139)$$

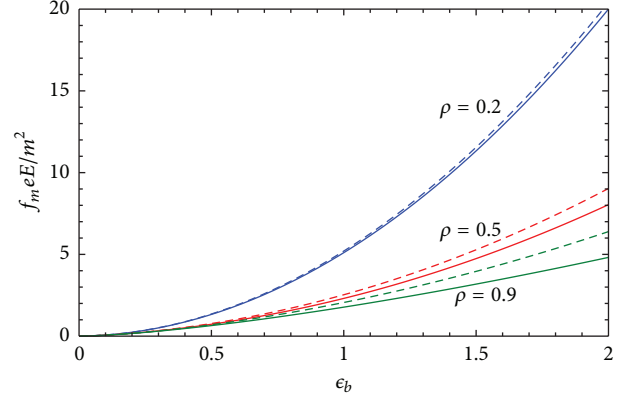


FIGURE 12: Dimensionless function $f_m eE/m^2$ versus ϵ_b for different values of ρ . The solid line is the full relativistic calculation, the dashed line is the nonrelativistic approximation. J/ψ binding energy in vacuum corresponds to $\epsilon_b = 0.68$.

where γ is analogous to the adiabaticity parameter of Keldysh [64]. Taking the non-relativistic limit of (132) and using (137) yields

$$f_m = \frac{2m^2 (2\epsilon_b)^{3/2}}{3eE} g(\gamma), \quad (140)$$

where $g(\gamma)$ is the Keldysh function [64]

$$g(\gamma) = \frac{3\tau_0}{2\gamma} \left[1 - \frac{1}{\gamma} \left(\frac{\tau_0^2}{\gamma^2} - 1 \right)^{1/2} \right]. \quad (141)$$

In Figure 12 we show the dimensionless ratio $f_m eE/m^2$ as a function of the binding energy ϵ_b (in units of m) for several values of ρ . The vacuum binding energy of J/ψ corresponds to $\epsilon_b = 0.68$. We observe an excellent agreement between the full relativistic calculation and the non-relativistic approximation. At $\rho = 0.9$ and $\epsilon_b = 0.68$ the difference between the two lines is 10% and can be further improved by considering higher order corrections to f_m [63].

5.4.2. *Weak Binding.* Of special interest is the limit of weak binding $\gamma \ll 1$; that is, $\sqrt{2\epsilon_b} \ll \rho$. Expanding (138) at small γ and τ_0 yields

$$\tau_0 = \gamma \left(1 + \frac{1}{18} \gamma^2 \right), \quad (142)$$

and substituting into (141) and subsequently into (140) yields

$$f_m = \frac{2}{3} \frac{m^2}{eE} (2\epsilon_b)^{3/2}. \quad (143)$$

Hence, the quarkonium dissociation probability reads [65]

$$w = \exp \left\{ -\frac{2}{3} \frac{(2\epsilon_b m)^{3/2}}{meE} \right\}. \quad (144)$$

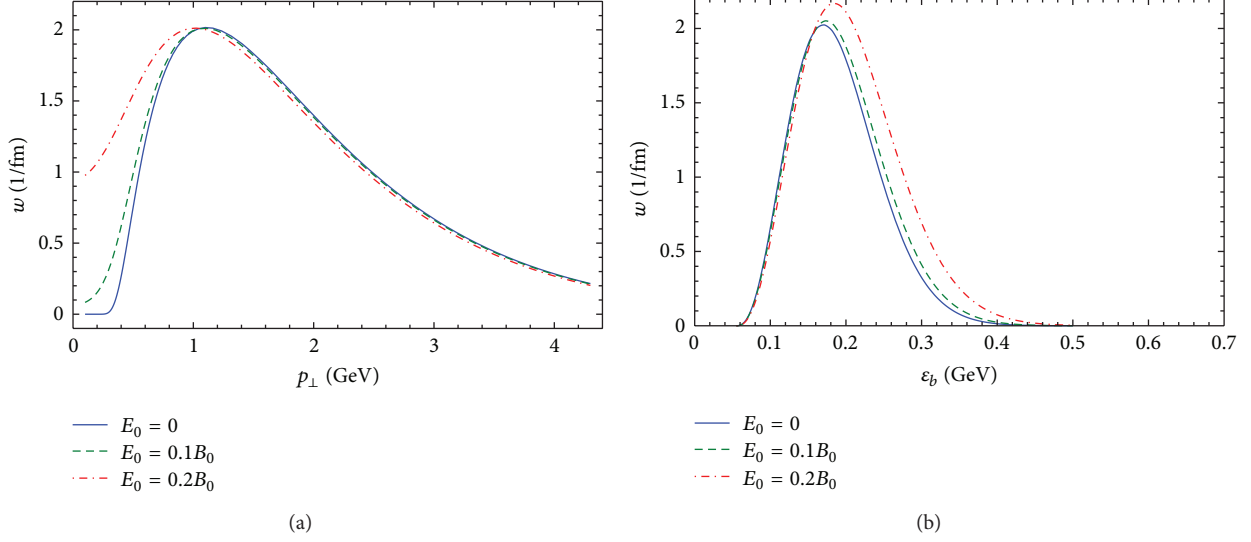


FIGURE 13: Dissociation rate of J/ψ at $eB_0 = 15m_{\pi}^2$, $\phi = \pi/2$ (in the reaction plane), and $\eta = 0$ (midrapidity) as a function of (a) P_{\perp} at $\varepsilon_b = 0.16$ GeV and (b) ε_b at $P_{\perp} = 1$ GeV.

Since the quasi-classical approximation employed in this paper is valid if $f(q_m) \gg 1$, it follows that the binding energy must satisfy

$$\frac{(eE)^{2/3}}{m^{1/3}} \ll \varepsilon_b \ll \rho^2 m. \quad (145)$$

Note also that we work in the approximation of the short-range binding potential meaning that $\sqrt{2\varepsilon_b} \ll 1/(mR)$; see Section 5.1.

5.4.3. Strong Binding. In the limit $\gamma \gg 1$, (138) and (141) imply that

$$\tau_0 = \frac{\gamma^2}{2}, \quad g(\gamma) = \frac{3\gamma}{8}. \quad (146)$$

Substituting (146) into (140), we derive

$$f_m = \frac{\varepsilon_b^2 B}{eE E}. \quad (147)$$

Thus, quarkonium dissociation probability in the case of strong binding is

$$w = \exp \left\{ -\frac{\varepsilon_b^2 B}{eE E} \right\}. \quad (148)$$

This formula is valid when

$$\rho^2 m, \quad \sqrt{eE\rho} \ll \varepsilon_b \ll \frac{1}{R}. \quad (149)$$

5.4.4. Contribution of Quark Spin. So far I have neglected the contribution of quark spin. In order to take into account the effect of spin interaction with the external field, we can use squared Dirac equation for a bispinor ψ as follows:

$$\left[(\varepsilon - e\rho)^2 - (\mathbf{p} - e\mathbf{A})^2 - m^2 + e\Sigma \cdot \mathbf{B} - ie\boldsymbol{\alpha} \cdot \mathbf{E} \right] \psi = 0, \quad (150)$$

where

$$\Sigma = \begin{pmatrix} \boldsymbol{\sigma} & 0 \\ 0 & \boldsymbol{\sigma} \end{pmatrix}, \quad \boldsymbol{\alpha} = \begin{pmatrix} \boldsymbol{\sigma} & 0 \\ 0 & -\boldsymbol{\sigma} \end{pmatrix}. \quad (151)$$

Operators Σ_y and α_x do not commute. Therefore, in order to apply the WKB method for calculation of the ionization probability one actually needs to square (150), which leads to a differential equation of the fourth order in derivatives. The problem becomes more tractable in the non-relativistic case and for crossed fields. Spin effects in crossed fields were discussed in [66].

With quark spin taken into account, the non-relativistic version of (124) becomes

$$\frac{1}{2m} \left[(p_z + eBx)^2 + p_x^2 \right] - eEx - \frac{\mu}{s} \mathbf{s} \cdot \mathbf{B} = -\varepsilon_b, \quad (152)$$

and hence

$$p_x^2 = 2m \left(-\varepsilon_b + \frac{\mu}{s} \mathbf{s} \cdot \mathbf{B} + eEx \right) - (p_z + eBx)^2, \quad (153)$$

where μ is the quark magnetic moment and s is the projection of spin in the direction of the magnetic field. For a point quark, $\mu = \mu_B = e\hbar/2mc$. The effect of quark spin on quarkonium dissociation probability can be taken into account by replacing $\varepsilon_b \rightarrow \varepsilon_b' = \varepsilon_b - (\mu/s) \mathbf{s} \cdot \mathbf{B}$ in formulas for f_m . With this replacement, all results of this section apply to a particle with spin. Note that effective binding energy ε_b' decreases if spin is parallel to the magnetic field and increases if it is antiparallel. In particular, in the case of weak binding

$$w = \sum_{s=\pm 1/2} \exp \left\{ -\frac{2(2\varepsilon_b' m + 2seB)^{3/2}}{3meE} \right\}. \quad (154)$$

Since the non-relativistic limit provides a good approximation of the full relativistic formulas, we will implement the quark spin dependence using the non-relativistic prescription [57, 58].

5.5. Effect of Electric Field Produced in the Lab Frame

5.5.1. Origin of Electric Field in the Lab Frame. So far I have entirely neglected possible existence of electric field in the lab frame. This field, which we will be denoted by \mathbf{E}_0 , can have two origins: (i) asymmetry of nucleon distributions in the colliding heavy ions (see Figure 3(b)) and (ii) chiral magnetic effect (CME) [5, 67–72], which has recently attracted a lot of attention. In a nutshell, if a metastable P - and CP -odd bubble is induced by axial anomaly in the hot nuclear matter, then in the presence of external magnetic field \mathbf{B}_0 the bubble generates an electric field which is *parallel* to the magnetic one. According to [68] the value of the electric field \mathbf{E}_0 in the bubble is

$$\mathbf{E}_0 = -N_c \sum_f \frac{e_f^2}{4\pi^2} \frac{\Theta}{N_f} \mathbf{B}_0 = -\frac{2}{3} \frac{\alpha\Theta}{\pi} \mathbf{B}_0, \quad (155)$$

where the sum runs over quark flavors f and it is assumed that only three lightest flavors contribute. The value of the Θ -angle fluctuates from event to event. CME refers to the macroscopic manifestation of this effect—separation of electric charges with respect to the reaction plane. This effect is a possible explanation of experimentally observed charge asymmetry fluctuations [73–75].

No matter what is the origin of electric field in the lab frame, it averages to zero over an ensemble of events. We are interested to know the effect of this field on quarkonium dissociation—this is the problem we are turning to now [58].

5.5.2. Quarkonium Dissociation Rate. Ionization probability of quarkonium equals its tunneling probability through the potential barrier. In the WKB approximation the later is given by the transmission coefficient and was calculated in Section 5.3. In this method contribution of the quark spin can be easily taken into account. Another method of calculating the ionization probability, the imaginary time method [76–78], was employed in [61–63]. It also yielded in the non-relativistic approximation the preexponential factor that appears due to the deviation of the quark wave function from the quasi-classical approximation. Such a calculation requires matching quark wave function inside and outside the potential barrier [65]. Extension of this approach to the relativistic case is challenging due to analytical difficulties of the relativistic two-body problem. Fortunately, it was argued in Section 5.3, that the non-relativistic approximation provides a very good accuracy in the $\epsilon_b \ll m$ region, which is relevant in the quarkonium dissociation problem [57, 62].

Given the electromagnetic field in the laboratory frame $\mathbf{B}_0, \mathbf{E}_0$, the electromagnetic field \mathbf{B}, \mathbf{E} in the comoving frame moving with velocity \mathbf{V} is given by

$$\mathbf{E} = E_0 \left\{ \gamma_L (\mathbf{b}_0 + \rho_0^{-1} \mathbf{V} \times \mathbf{b}_0) - (\gamma_L - 1) \mathbf{V} \frac{\mathbf{V} \cdot \mathbf{b}_0}{V^2} \right\}, \quad (156a)$$

$$\mathbf{B} = B_0 \left\{ \gamma_L (\mathbf{b}_0 - \rho_0 \mathbf{V} \times \mathbf{b}_0) - (\gamma_L - 1) \mathbf{V} \frac{\mathbf{V} \cdot \mathbf{b}_0}{V^2} \right\}, \quad (156b)$$

where $\mathbf{b}_0 = \mathbf{B}_0/B_0$ is a unit vector in the magnetic field direction, $\rho_0 = E_0/B_0 = 2\alpha|\Theta|/3\pi$ (see (155)) and $\gamma_L = 1/\sqrt{1-V^2}$. It follows from (156a) and (156b) that

$$E = E_0 \sqrt{1 + \gamma_L^2 (\mathbf{b}_0 \times \mathbf{V})^2 (1 + \rho_0^{-2})}, \quad (157a)$$

$$B = B_0 \sqrt{1 + \gamma_L^2 (\mathbf{b}_0 \times \mathbf{V})^2 (1 + \rho_0^2)}. \quad (157b)$$

Using (157a) and (157b), we find that the angle θ between the electric and magnetic field in the comoving frame is

$$\begin{aligned} \cos \theta &= \frac{\mathbf{E} \cdot \mathbf{B}}{EB} \\ &= \frac{1}{\sqrt{[1 + \gamma_L^2 (\mathbf{b}_0 \times \mathbf{V})^2 (1 + \rho_0^{-2})] [1 + \gamma_L^2 (\mathbf{b}_0 \times \mathbf{V})^2 (1 + \rho_0^2)]}}, \end{aligned} \quad (158)$$

where we used the relativistic invariance of $\mathbf{E} \cdot \mathbf{B}$.

It is useful to introduce dimensionless parameters γ, ϵ and ρ as [62]

$$\gamma = \frac{1}{\rho} \sqrt{\frac{2\epsilon_b}{m}}, \quad \rho = \frac{E}{B}, \quad \epsilon = \frac{eE}{m^2} \left(\frac{m}{2\epsilon_b} \right)^{3/2}, \quad (159)$$

where m is quark mass and ϵ_b is quarkonium binding energy. I will treat the quarkonium binding potential in the non-relativistic approximation, which provides a very good accuracy to the dissociation rate [57, 62]. The quarkonium dissociation rate in the comoving frame in the non-relativistic approximation is given by [61]

$$w = \frac{8\epsilon_b}{\epsilon} P(\gamma, \theta) C^2(\gamma, \theta) e^{-(2/3\epsilon)g(\gamma, \theta)}, \quad (160)$$

where function g reads

$$g = \frac{3\tau_0}{2\gamma} \left[1 - \frac{1}{\gamma} \left(\frac{\tau_0^2}{\gamma^2} - 1 \right) \sin \theta - \frac{\tau_0^2}{3\gamma^2} \cos^2 \theta \right]. \quad (161)$$

and functions P and C are given in the following formulas:

$$\begin{aligned} P &= \frac{\gamma^2}{\tau_0} \left[\left(\tau_0 \coth \tau_0 + \frac{\sinh \tau_0 \cosh \tau_0}{\tau_0} - 2 \right) \sin^2 \theta \right. \\ &\quad \left. + \sinh^2 \tau_0 \cos^2 \theta \right]^{-1/2}, \\ C &= \exp \left[\ln \frac{\tau_0}{2\gamma} + \int_0^{\tau_0} d\tau \left(\frac{\gamma}{\xi(\tau)} - \frac{1}{\tau_0 - \tau} \right) \right], \end{aligned} \quad (162)$$

$$\begin{aligned} \xi(\tau) &= \left\{ \frac{1}{4} (\tau_0^2 - \tau^2)^2 \cos^2 \theta \right. \\ &\quad \left. + \tau_0^2 \left[\left(\frac{\cosh \tau_0 - \cos \tau}{\sinh \tau_0} \right)^2 \right. \right. \\ &\quad \left. \left. - \left(\frac{\sinh \tau}{\sinh \tau_0} - \frac{\tau}{\tau_0} \right)^2 \right] \sin^2 \theta \right\}^{1/2}. \end{aligned}$$

The contribution of quark spin is taken into account by replacing $\varepsilon_b \rightarrow \varepsilon'_b = \varepsilon_b - (e/m)\mathbf{s} \cdot \mathbf{B}$ [57]. Function g represents the leading quasi-classical exponent, P is the prefactor for the S -wave state of quarkonium, and C accounts for the Coulomb interaction between the valence quarks. Parameter τ_0 satisfies the following equation:

$$\tau_0^2 - \sin^2\theta(\tau_0 \coth \tau_0 - 1)^2 = \gamma^2 \quad (163)$$

which establishes its dependence on θ and γ . Note that in the limit $E \rightarrow 0$ the dissociation rate (160) exponentially vanishes. This is because pure magnetic field cannot force a charge to tunnel through a potential barrier.

In the case that mechanism (i) is responsible for generation of electric field, \mathbf{E}_0 is the field permitting the entire plasma in a single event. Event average is then obtained by averaging (160) over an ensemble of events. In the case that mechanism (ii) is operative, averaging is more complicated. Equation (160) gives the quarkonium dissociation rate in a bubble with a given value of Θ . Its derivation assumes that the dissociation process happens entirely inside a bubble and that Θ is constant inside the bubble. Since in a relativistic heavy-ion collision many bubbles can be produced with a certain distribution of Θ s (with average $\langle \Theta \rangle = 0$) more than one bubble can affect the dissociation process. This will result in a distractive interference leading to reduction of the CP -odd effect on quarkonium dissociation. However, if a typical bubble size R_0 is much larger than the size of quarkonium R_f , then the dissociation is affected by one bubble at a time independently of others, and hence the interference effect can be neglected. In this case (74) provides, upon a proper average, a reasonable estimate of quarkonium dissociation in a heavyion collision. We can estimate the bubble size as the size of the sphaleron, which is of the order of the chromomagnetic screening length $\sim 1/g^2T$, whereas the quarkonium size is of the order α_s/ε_b . Consequently, at small coupling and below the zero-field dissociation temperature (i.e., when ε_b is not too small) R_0 is parametrically much larger than R_f . A more quantitative estimate of the sphaleron size is $R_0 \simeq 1.2/\alpha_s N_c T \simeq 0.4 \text{ fm}$ [79]; whereas $R_f \simeq \alpha_s/\varepsilon_b \simeq 0.1\text{--}0.2 \text{ fm}$. Thus, based on this estimate bubble interference can be neglected in the first approximation. However, since the ratio R_f/R_0 is actually not so small this effect nevertheless warrants further investigation.

To obtain the experimentally observed J/ψ dissociation rate we need to average (74) over the bubbles produced in a given event and then over all events. To this end it is important to note that because the dissociation rate depends only on ρ_0^2 it is insensitive to the sign of the \mathbf{E}_0 field, or, in other words, it depends only on absolute value of Θ but not on its sign. Therefore, it stands to reason that although the precise distribution of Θ s is not known, (74) gives an approximate event average with parameter Θ representing a characteristic absolute value of the theta angle.

5.5.3. Limiting Cases. Before I proceed with the numerical calculations, let us consider for illustration several limiting cases. If quarkonium moves with non-relativistic velocity, then in the comoving frame electric and magnetic fields are

approximately parallel $\theta \approx 0$, whereas in the ultrarelativistic case they are orthogonal $\theta \approx \pi/2$; see (158). In the later case the electromagnetic field in the comoving frame does not depend on E_0 as seen in (157a) and (157b) and therefore the dissociation rate becomes insensitive to the CME. In our estimates I will assume that $\rho_0 < 1$ which is the relevant phenomenological situation. Indeed, it was proposed in [68] that $\rho_0 \sim \alpha \ll 1$ produces charge fluctuations with respect to the reaction plane of the magnitude consistent with experimental data.

(1) $\theta \geq 0$; that is, electric and magnetic fields are approximately parallel. This situation is realized in the following two cases. (i) Non-relativistic quarkonium velocities: $V \ll \rho_0$ or (ii) motion of quarkonium at small angle ϕ to the direction of the magnetic field \mathbf{b}_0 : $\phi \ll \rho_0/\gamma_L V$. In both cases $E \approx E_0$ and $B \approx B_0$. This is precisely the case where the dissociation rate exhibits its strongest sensitivity to the strength of the electric field \mathbf{E}_0 generated by the local parity violating QCD effects. Depending on the value of the γ parameter defined in (159) we can distinguish the case of strong electric field $\gamma \gg 1$ and weak electric field $\gamma \ll 1$ [63]. In the former case, $g = (3/8)\gamma$, $P = (8/e)^{1/2}\gamma e^{-\gamma^2/2}$, and $C = e^{\pi\gamma/2}/\gamma$. Substituting into (74) the dissociation rate reads

$$\begin{aligned} w &= \frac{8\varepsilon_b}{\varepsilon\gamma} \sqrt{\frac{8}{e}} e^{-\gamma^2/2} e^{-\gamma/4\varepsilon} \\ &= \frac{16\varepsilon_b^2 m}{eB_0} \sqrt{\frac{8}{e}} e^{-\varepsilon_b/\rho_0^2 m} e^{-\varepsilon_b^2/\rho_0 e E_0}, \quad \gamma \gg 1. \end{aligned} \quad (164)$$

In the later case, $g = P = C = 1$ and

$$\begin{aligned} w &= \frac{8\varepsilon_b}{\varepsilon} e^{-2/3\varepsilon} \\ &= \frac{8\varepsilon_b m^2}{eE_0} \left(\frac{2\varepsilon_b}{m}\right)^{3/2} e^{-(2m^2/3eE_0)(2\varepsilon_b/m)^{3/2}}, \quad \gamma \ll 1, \end{aligned} \quad (165)$$

where the electromagnetic field in the comoving frame equals one in the laboratory frame as was mentioned previously.

(2) $\theta \sim \pi/2$; that is, electric and magnetic fields are approximately orthogonal (note that the limit $\gamma \gg 1$ is different in $\theta = \pi/2$ and $\theta < (\pi/2)$ cases [61]). This occurs for an ultra-relativistic motion of quarkonium $V \rightarrow 1$. In this case

$$B = E = B_0 \gamma_L |\mathbf{b}_0 \times \mathbf{V}| \sqrt{1 + \rho_0^2}. \quad (166)$$

This case was discussed in detail in our previous paper [57]. In particular for $\gamma \ll 1$, we get

$$w = \frac{8\varepsilon_b m^2}{eE} \left(\frac{2\varepsilon_b}{m}\right)^{3/2} e^{-(2m^2/3eE)(2\varepsilon_b/m)^{3/2}}. \quad (167)$$

Due to (164) and (167) dependence of w on E_0 is weak unless $\rho_0 \gg 1$.

5.6. Dissociation Rate of J/ψ . One of the most interesting applications of this formalism is calculation of the dissociation rate of J/ψ which is considered a litmus test of the

quark-gluon plasma [80]. Let z be the heavy ions collision axis; heavy-ion collision geometry implies that $\mathbf{b}_0 \cdot \hat{\mathbf{z}} = 0$. The plane containing z -axis and perpendicular to the magnetic field direction is the reaction plane. We have

$$(\mathbf{b}_0 \times \mathbf{V})^2 = V_z^2 + V_\perp^2 \sin^2 \phi, \quad (168)$$

where ϕ is the angle between the directions of \mathbf{B}_0 and \mathbf{V}_\perp , and I denoted vector components in the xy -plane by the subscript \perp . We can express the components of the quarkonium velocity \mathbf{V} in terms of the rapidity η as $V_z = \tanh \eta$, $V_\perp = P_\perp / (M_\perp \cosh \eta)$, where \mathbf{P} and M are the quarkonium momentum and mass and $M_\perp^2 = M^2 + P_\perp^2$.

Results of numerical calculations are exhibited in Figures 13–15 [58]. In Figure 13 I show the dissociation rate of J/ψ for several values of the electric field \mathbf{E}_0 induced by the Chiral Magnetic Effect. Note that the typical size of the medium traversed by a quarkonium in magnetic field can be estimated very conservatively as a few fm. Therefore, $\omega \sim 0.3\text{--}0.5 \text{ fm}^{-1}$ corresponds to complete destruction of J/ψ s. This means that in the magnetic field of strength $eB_0 \sim 15m_\pi^2$ all J/ψ s with $P_\perp \geq 0.5 \text{ GeV}$ are destroyed independently of the strength of E_0 . Since magnetic field strength decreases towards the QGP periphery, most of J/ψ surviving at later times originate from that region. Effect of electric field \mathbf{E}_0 is strongest at low P_\perp , which is consistent with our discussion in the previous section. The dissociation rate at low P_\perp exponentially decreases with decrease of E_0 . Probability of quarkonium ionization by the fields below $E_0 \leq 0.1B_0$ (i.e., $\rho_0 \leq 0.1$) is exponentially small. This is an order of magnitude higher than the estimate $\rho_0 \sim \alpha$ of electric field due to CME effect as proposed in [68].

As the plasma temperature varies, so is the binding energy of quarkonium, although the precise form of the function $\varepsilon_b(T)$ is model dependent. The dissociation rate picks at some $\varepsilon_b^0 < \varepsilon_b^{\text{vac}}$ (see Figure 13(b)), where $\varepsilon_b^{\text{vac}}$ is the binding energy in vacuum, indicating that J/ψ breaks down even before ε_b drops to zero, which is the case at $\mathbf{B}_0 = 0$. This ε_b^0 is a strong function of E_0 as can be seen in Figure 14. It satisfies the equation $\partial\omega/\partial\varepsilon_b = 0$. In the case $\gamma \ll 1$ (165) and (167) imply that

$$\varepsilon_b^0 = \frac{m}{2} \left(\frac{5eE}{2m^2} \right)^{2/3}, \quad \gamma \ll 1. \quad (169)$$

At $\gamma \gg 1$ and $\theta = \pi/2$ we employ (164) to derive the condition $(\varepsilon_b^0)^2 + eB\varepsilon_b^0/2m - eE^2/B = 0$. In view of (166) $E \approx B$, and we obtain

$$\varepsilon_b^0 = \frac{eB}{4m} \left(\sqrt{\frac{16m^2}{eB} + 1} - 1 \right) \approx \sqrt{eB}, \quad \gamma \gg 1, \quad (170)$$

where in the last step I used that $eB \ll m^2$. For a given function $\varepsilon_b(T)$ one can convert ε_b^0 into the dissociation temperature, which is an important phenomenological parameter.

In the absence of electric field \mathbf{E}_0 , the dissociation probability peaks in the direction perpendicular to the direction of magnetic field \mathbf{b}_0 , that is, in the reaction plane. Dissociation

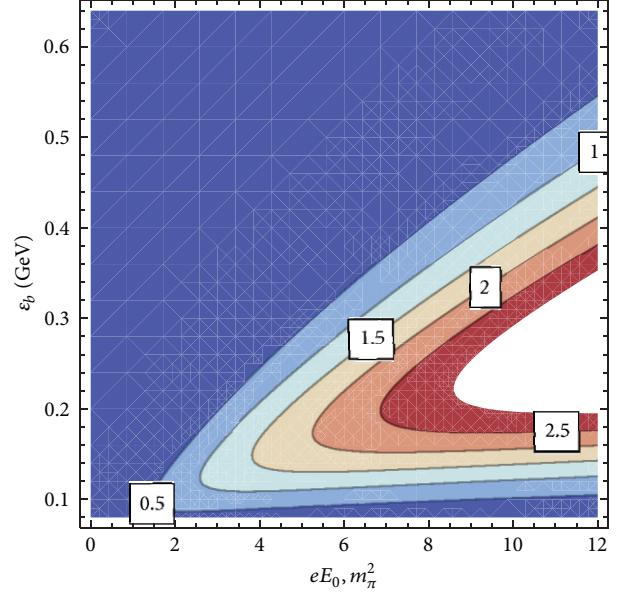


FIGURE 14: Contour plot of the dissociation rate of J/ψ as a function of ε_b and eE_0 at $eB_0 = 15m_\pi^2$, $\phi = \pi/2$ (in the reaction plane), $\eta = 0$ (midrapidity), and $P_\perp = 0.1 \text{ GeV}$. Numbers inside boxes indicate the values of ω in $1/\text{fm}$.

rate vanishes in the \mathbf{b}_0 direction. Indeed, for $\mathbf{V} \cdot \mathbf{b}_0 = 0$ (157a) and (157b) imply that $E = 0$. This feature is seen in Figure 15(a). At finite \mathbf{E}_0 the dissociation probability is finite in the \mathbf{b}_0 direction making the azimuthal distribution more symmetric. The shape of the azimuthal distribution strongly depends on quarkonium velocity, while at low V the strongest dissociation is in the direction of the reaction plane, at higher V the maximum shifts towards small angles around the \mathbf{b}_0 direction. Extrema of the azimuthal distribution are roots of the equation $\partial\omega/\partial\phi = 0$. At $\gamma \ll 1$ it yields minimum at $\phi_0 = 0$, maximum at $\phi_0 = \pi/2$ and another maximum that satisfies the condition (neglecting the spin-dependence of ε_b)

$$eE_0 \sqrt{1 + \gamma_L^2 (V_z^2 + V_\perp^2 \sin^2 \phi_0) (1 + \rho_0^{-2})} = \frac{2m^2}{3} \left(\frac{2\varepsilon_b}{m} \right)^{3/2}. \quad (171)$$

In order to satisfy (171) ϕ_0 must decrease when V increases and vice versa. This features are seen in Figure 15(a).

Spectrum of quarkonia surviving in the electromagnetic field is proportional to the survival probability $P = 1 - \omega t$, where t is the time spent by the quarkonium in the field. Consider P as a function of the angle χ between the quarkonium velocity and the reaction plane $\chi = \pi/2 - \phi$. Fourier expansion of P in χ reads

$$P(\chi) = \frac{1}{2} P_0 + \sum_{n=1}^{\infty} P_n \cos(n\chi), \quad (172)$$

$$P_n = \frac{1}{\pi} \int_{-\pi}^{\pi} P(\chi) \cos(n\chi) d\chi.$$

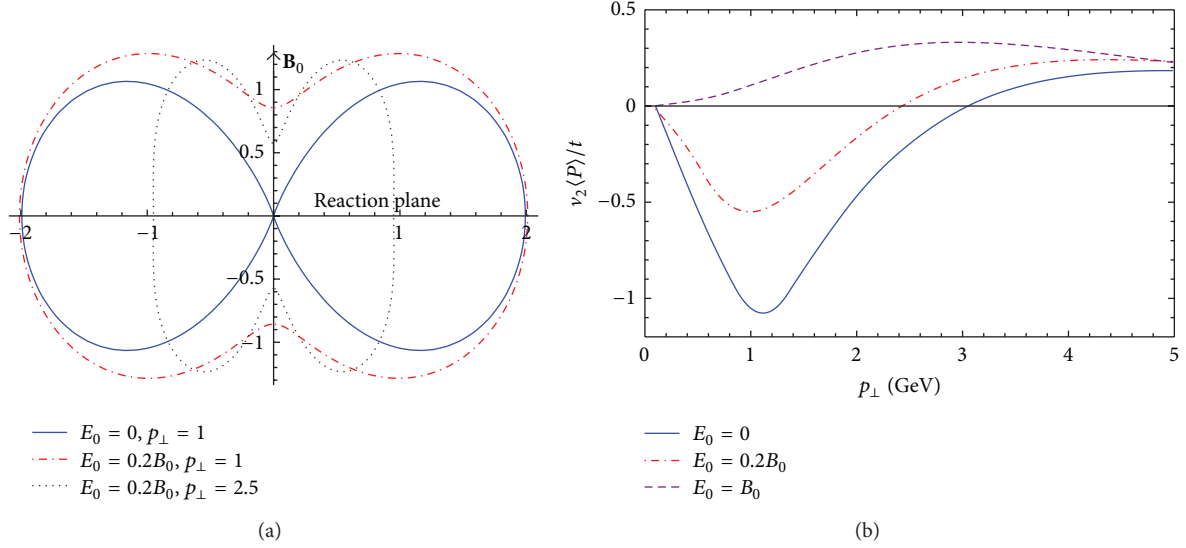


FIGURE 15: (a) Angular distribution of J/ψ dissociation rate at $eB_0 = 15m_\pi^2$, $\eta = 0$ at different E_0 and P_\perp (in GeV's). Magnetic field \mathbf{B}_0 points in the positive vertical direction. Reaction plane coincides with the horizontal plane. (b) Rescaled second Fourier-harmonic v_2 of the azimuthal distribution as a function of P_\perp . $\langle P \rangle$ is the azimuthal average of the survival probability, and t is the time spent by J/ψ in the P -odd bubble.

Ellipticity of the distribution is characterized by the “elliptic flow” coefficient v_2 defined as

$$v_2 = \frac{P_2}{(1/2)P_0} = \frac{\int_{-\pi}^{\pi} (1 - wt) \cos 2\chi d\chi}{\pi \langle P \rangle} \quad (173)$$

$$= -\frac{t}{\pi \langle P \rangle} \int_{-\pi}^{\pi} w \cos 2\chi d\chi,$$

where $\langle P \rangle$ denotes average of P over the azimuthal angle. These formulas are applicable only as long as $wt < 1$ because otherwise there are no surviving quarkonia. In Figure 15(b) [58] I show $v_2 \langle P \rangle / t$, which is independent of t , as a function of P_\perp . As expected, in the absence of the CME, v_2 is negative at low P_\perp and positive at high P_\perp . v_2 changes sign at P_\perp that depends on the strength of the electric field. It decreases as E_0 increases until at $E_0 \approx B_0$ it becomes positive at all P_\perp . Figure 15(b) provides the low bound for v_2 because $\langle P \rangle < 1$ and $t \gtrsim 1$ fm. We thus expect that magnetic field strongly modifies the azimuthal distribution of the produced J/ψ s. Role of the magnetic field in generation of azimuthal anisotropies in heavy-ion collisions has been pointed out before in [29, 55].

In summary, we observed that J/ψ dissociation energy increases with magnetic field strength and quarkonium momentum. As a consequence, *quarkonia dissociate at lower temperature* than one would have expected based on calculations neglecting magnetic field [57, 58]. Figure 13 indicates that in heavy-ion collisions at the LHC, all J/ψ 's moving with $P_\perp > 0.5$ GeV in the reaction plane would dissociate with probability of order unity even if the QGP effect was completely negligible. If electric field fluctuations shown in Figure 3 are taken into account, then even low P_\perp J/ψ 's are destroyed. However, chiral magnetic effect has negligible effect on J/ψ dissociation.

Although magnetic fields in pp and pA collisions are much weaker than in AA collisions, they are still strong enough to cause J/ψ dissociation at sufficiently high momenta P_\perp . A truly spectacular feature of such process would be J/ψ decay into two heavier D -mesons.

The effect of J/ψ dissociation in a magnetic field vanishes in the direction parallel to the magnetic field, that is, perpendicular to the reaction plane. Therefore, J/ψ dissociation gives negative contribution to the total azimuthal asymmetry coefficient v_2 . It remarkable that presence of electric field reverses this effect making v_2 positive.

6. Electromagnetic Radiation by Quark-Gluon Plasma in Magnetic Field

6.1. Necessity to Quantize Fermion Motion. In Section 3 we discussed synchrotron radiation of *gluons* by *fast* quarks. Our main interest was the energy loss problem. In this section we turn to the problem of electromagnetic radiation by QGP, namely, radiation of *photons* by thermal fermions [7]. In this case quasi-classical approximation that we employed in Sections 3 and 4 is no longer applicable, and one has to take into account quantization of fermion motion in magnetic field.

Electromagnetic radiation by quarks and antiquarks of QGP moving in external magnetic field originates from two sources: (i) synchrotron radiation and (ii) quark and antiquark annihilation. QGP is transparent to the emitted electromagnetic radiation because its absorption coefficient is suppressed by α^2 . Thus, QGP is shining in magnetic field. The main goal of this paper is to calculate the spectrum and angular distribution of this radiation. In strong magnetic field it is essential to account for quantization of fermion spectra. Indeed, spacing between the Landau levels is of the order

eB/ε (ε being quark energy), while their thermal width is of the order T . Spectrum quantization is negligible only if $eB/\varepsilon \ll T$ which is barely the case at RHIC and certainly not the case at LHC (at least during the first few fms of the evolution). Fermion spectrum quantization is important not only for hard and electromagnetic probes but also for the bulk properties of QGP.

6.2. Synchrotron Radiation. Motion of charged fermions in external magnetic field, which I will approximately treat as spatially homogeneous, is quasi-classical in the field direction and quantized in the *reaction plane*, which is perpendicular to the magnetic field and span by the impact parameter and the heavy-ion collision axis. In high energy physics one usually distinguishes the *transverse plane*, which is perpendicular to the collision axis and span by the magnetic field and the impact parameter. In this section I use notation in which three vectors are discriminated by the bold face and their component along the field direction by the plain face. Momentum projections onto the transverse plane are denoted by subscript \perp .

In the configuration space, charged fermions move along spiral trajectories with the symmetry axis aligned with the field direction. Synchrotron radiation is a process of photon γ radiation by a fermion f with electric charge $e_f = z_f e$ in external magnetic field B as follows:

$$f(e_f, j, p) \longrightarrow f(e_f, k, q) + \gamma(\mathbf{k}), \quad (174)$$

where \mathbf{k} is the photon momentum, p, q are the momentum components along the magnetic field direction, and indices $j, k = 0, 1, 2, \dots$ label the discrete Landau levels in the reaction plane. The Landau levels are given by

$$\begin{aligned} \varepsilon_j &= \sqrt{m^2 + p^2 + 2je_f B}, \\ \varepsilon_k &= \sqrt{m^2 + q^2 + 2ke_f B}. \end{aligned} \quad (175)$$

In the constant magnetic field only momentum component along the field direction is conserved. Thus, the conservation laws for synchrotron radiation read

$$\varepsilon_j = \omega + \varepsilon_k, \quad p = q + \omega \cos \theta, \quad (176)$$

where ω is the photon energy and θ is the photon emission angle with respect to the magnetic field. Intensity of the synchrotron radiation was derived in [81]. In [82–85] it was thoroughly investigated as a possible mechanism for γ -ray bursts. In particular, synchrotron radiation in electromagnetic plasmas was calculated. Spectral intensity of angular distribution of synchrotron radiation by a fermion in the j th Landau state is given by

$$\frac{dI^j}{d\omega d\Omega} = \sum_f \frac{z_f^2 \alpha}{\pi} \omega^2 \sum_{k=0}^j \Gamma_{jk} \{ |\mathcal{M}_\perp|^2 + |\mathcal{M}_\parallel|^2 \} \delta(\omega - \varepsilon_j + \varepsilon_k), \quad (177)$$

where $\Gamma_{jk} = (1 + \delta_{j0})(1 + \delta_{k0})$ accounts for the double degeneration of all Landau levels except the ground one.

The squares of matrix elements \mathcal{M} , which appear in (177), corresponding to photon polarization perpendicular and parallel to the magnetic field are given by, respectively,

$$\begin{aligned} 4\varepsilon_j \varepsilon_k |\mathcal{M}_\perp|^2 &= (\varepsilon_j \varepsilon_k - pq - m^2) [I_{j,k-1}^2 + I_{j-1,k}^2] \\ &\quad + 2\sqrt{2je_f B} \sqrt{2ke_f B} [I_{j,k-1} I_{j-1,k}], \\ 4\varepsilon_j \varepsilon_k |\mathcal{M}_\parallel|^2 &= \cos^2 \theta \left\{ (\varepsilon_j \varepsilon_k - pq - m^2) [I_{j,k-1}^2 + I_{j-1,k}^2] \right. \\ &\quad \left. - 2\sqrt{2je_f B} \sqrt{2ke_f B} [I_{j,k-1} I_{j-1,k}] \right\} \\ &\quad - 2 \cos \theta \sin \theta \left\{ p \sqrt{2ke_f B} [I_{j-1,k} I_{j-1,k-1} + I_{j,k-1} I_{j,k}] \right. \\ &\quad \left. + q \sqrt{2je_f B} [I_{j,k} I_{j-1,k} + I_{j-1,k-1} I_{j,k-1}] \right\} \\ &\quad + \sin^2 \theta \left\{ (\varepsilon_j \varepsilon_k + pq - m^2) [I_{j-1,k-1}^2 + I_{j,k}^2] \right. \\ &\quad \left. + 2\sqrt{2je_f B} \sqrt{2ke_f B} (I_{j-1,k-1} I_{j,k}) \right\}, \end{aligned} \quad (178)$$

where for $j \geq k$,

$$I_{j,k} \equiv I_{j,k}(x) = (-1)^{j-k} \sqrt{\frac{k!}{j!}} e^{-x/2} x^{(j-k)/2} L_k^{j-k}(x), \quad (179)$$

and $I_{j,k}(x) = I_{k,j}(x)$ when $k > j$. ($I_{j,-1}$ are identically zero.) The functions $L_k^{j-k}(x)$ are the generalized Laguerre polynomials. Their argument is

$$x = \frac{\omega^2}{2e_f B} \sin^2 \theta. \quad (180)$$

Angular distribution of radiation is obtained by integrating over the photon energies and remembering that ε_k also depends on ω by virtue of (175) and (176) as follows:

$$\begin{aligned} \frac{dI^j}{d\Omega} &= \sum_f \frac{z_f^2 \alpha}{\pi} \sum_{k=0}^j \frac{\omega^* (\varepsilon_j - \omega^*)}{\varepsilon_j - p \cos \theta - \omega^* \sin^2 \theta} \\ &\quad \times \Gamma_{jk} \{ |\mathcal{M}_\perp|^2 + |\mathcal{M}_\parallel|^2 \}, \end{aligned} \quad (181)$$

where photon energy ω is fixed to be

$$\begin{aligned} \omega^* &= \frac{1}{\sin^2 \theta} \left\{ (\varepsilon_j - p \cos \theta) \right. \\ &\quad \left. - \left[(\varepsilon_j - p \cos \theta)^2 - 2e_f B (j - k) \sin^2 \theta \right]^{1/2} \right\}. \end{aligned} \quad (182)$$

In the context of heavy-ion collisions the relevant observable is the differential photon spectrum. For ideal plasma in

equilibrium each quark flavor gives the following contribution to the photon spectrum:

$$\begin{aligned} \frac{dN^{\text{synch}}}{dt d\Omega d\omega} &= \sum_f \int_{-\infty}^{\infty} dp \frac{e_f B (2N_c) V}{2\pi^2} \\ &\times \sum_{j=0}^{\infty} \sum_{k=0}^j \frac{dI^j}{\omega d\omega d\Omega} (2 - \delta_{j,0}) f(\varepsilon_j) [1 - f(\varepsilon_k)], \end{aligned} \quad (183)$$

where $2N_c$ accounts for quarks and antiquarks each of N_c possible colors, and $(2 - \delta_{j,0})$ sums over the initial quark spin.

Index f indicates different quark flavors. V stands for the plasma volume. The statistical factor $f(\varepsilon)$ is

$$f(\varepsilon) = \frac{1}{e^{\varepsilon/T} + 1}. \quad (184)$$

The δ -function appearing in (177) can be re-written using (175) and (176) as

$$\delta(\omega - \varepsilon_j + \varepsilon_k) = \sum_{\pm} \frac{\delta(p - p_{\pm}^*)}{|(p/\varepsilon_j) - (q/\varepsilon_k)|}, \quad (185)$$

where

$$p_{\pm}^* = \frac{\left\{ \cos\theta (m_j^2 - m_k^2 + \omega^2 \sin^2\theta) \pm \sqrt{[(m_j + m_k)^2 - \omega^2 \sin^2\theta][(m_j - m_k)^2 - \omega^2 \sin^2\theta]} \right\}}{2\omega \sin^2\theta}. \quad (186)$$

The following convenient notation was introduced:

$$m_j^2 = m^2 + 2j e_f B, \quad m_k^2 = m^2 + 2k e_f B. \quad (187)$$

The physical meaning of (186) is that synchrotron radiation of a photon with energy ω at angle θ by a fermion undergoing transition from j th to k th Landau level is possible only if the initial quark momentum along the field direction equals p_{\pm}^* .

Another consequence of the conservation laws (176) is that for a given j and k the photon energy cannot exceed a certain maximal value that will be denoted by $\omega_{s,jk}$. Indeed, inspection of (186) reveals that this equation has a real solution only in two cases:

$$(i) m_j - m_k \geq \omega \sin\theta, \quad \text{or} \quad (ii) m_j + m_k \leq \omega \sin\theta. \quad (188)$$

The first case is relevant to the synchrotron radiation, while the second one is relevant to the one-photon pair annihilation as discussed in the next section. Accordingly, allowed photon energies in the $j \rightarrow k$ transition satisfy

$$\omega \leq \omega_{s,jk} \equiv \frac{m_j - m_k}{\sin\theta} = \frac{\sqrt{m^2 + 2j e_f B} - \sqrt{m^2 + 2k e_f B}}{\sin\theta}. \quad (189)$$

No synchrotron radiation is possible for $\omega > \omega_{s,jk}$. In particular, when $j = k$, $\omega_{s,jk} = 0$, that is, no photon is emitted, which is also evident in (182). The reason is clearly seen in the frame where $p = 0$: since $\varepsilon_j \geq \varepsilon_k$, constraints (175) and (176) hold only if $\omega = 0$.

Substituting of (177) into (183) yields the spectral distribution of the synchrotron radiation rate per unit volume

$$\begin{aligned} \frac{dN^{\text{synch}}}{V dt d\Omega d\omega} &= \sum_f \frac{2N_c z_f^2 \alpha}{\pi^3} e_f B \\ &\times \sum_{j=0}^{\infty} \sum_{k=0}^j \omega (1 + \delta_{k0}) \vartheta(\omega_{s,ij} - \omega) \\ &\times \int dp \sum_{\pm} \frac{\delta(p - p_{\pm}^*)}{|(p/\varepsilon_j) - (q/\varepsilon_k)|} \\ &\times \{ |\mathcal{M}_{\perp}|^2 + |\mathcal{M}_{\parallel}|^2 \} f(\varepsilon_j) [1 - f(\varepsilon_k)], \end{aligned} \quad (190)$$

where ϑ is the step function.

The natural variables to study the synchrotron radiation are the photon energy ω and its emission angle θ with respect to the magnetic field. However, in high energy physics particle spectra are traditionally presented in terms of rapidity y (which for photons is equivalent to pseudo-rapidity) and transverse momentum k_{\perp} . k_{\perp} is a projection of three-momentum \mathbf{k} onto the transverse plane. These variables are not convenient to study electromagnetic processes in external magnetic field. In particular, they conceal the azimuthal symmetry with respect to the magnetic field direction. To change variables, let z be the collision axis, and let $\hat{\mathbf{y}}$ be the direction of the magnetic field. In spherical coordinates photon momentum is given by $\mathbf{k} = \omega(\sin\alpha \cos\phi \hat{\mathbf{x}} + \sin\alpha \sin\phi \hat{\mathbf{y}} + \cos\alpha \hat{\mathbf{z}})$, where α and ϕ are the polar and azimuthal angles with respect to z -axis. The plane xz is the

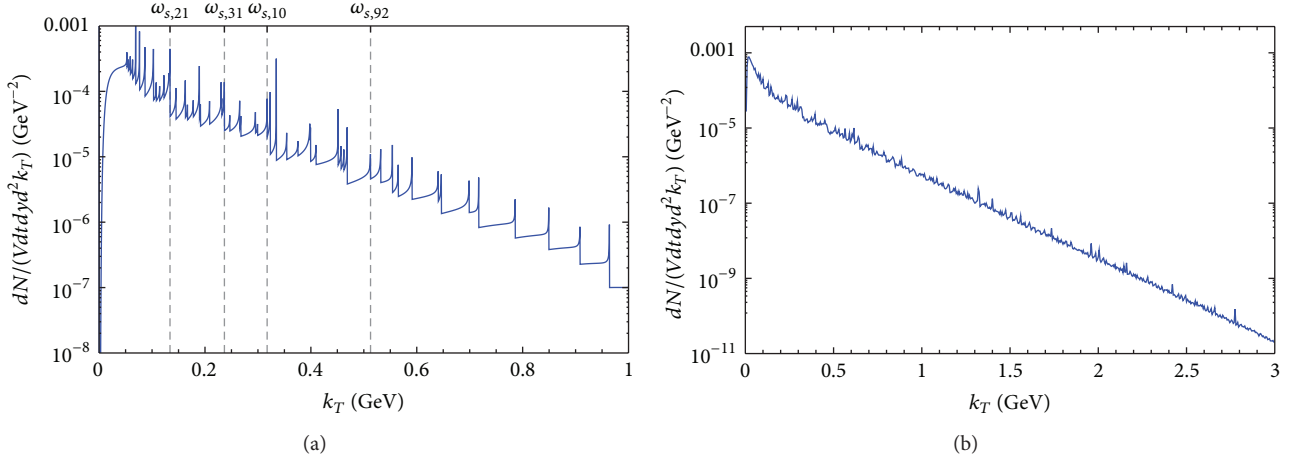


FIGURE 16: Spectrum of synchrotron radiation by u quarks at $eB = m_\pi^2$, $y = 0$, and $\phi = \pi/3$: (a) contribution of 10 lowest Landau levels $j \leq 10$; several cutoff frequencies are indicated; (b) summed over all Landau levels. $m_u = 3$ MeV, $T = 200$ MeV. Adopted from [7].

reaction plane. By definition, $\hat{\mathbf{k}} \cdot \hat{\mathbf{y}} = \cos \theta$ implying that $\cos \theta = \sin \alpha \sin \phi$. Thus,

$$k_\perp = \sqrt{k_x^2 + k_y^2} = \frac{\omega \cos \theta}{\sin \phi}, \quad y = -\text{Lntan} \frac{\alpha}{2}. \quad (191)$$

The second of these equations is the definition of (pseudo-)rapidity. Inverting (191) yields

$$\omega = k_\perp \cosh y, \quad \cos \theta = \frac{\sin \phi}{\cosh y}. \quad (192)$$

Because $dy = dk_z/\omega$ the photon multiplicity in a unit volume per unit time reads

$$\frac{dN^{\text{synch}}}{dV dt d^2 k_\perp dy} = \omega \frac{dN^{\text{synch}}}{dV dt d^3 k} = \frac{dN^{\text{synch}}}{dV dt \omega d\omega d\Omega}. \quad (193)$$

Figure 16 displays the spectrum of synchrotron radiation by u quarks as a function of k_\perp at fixed ϕ [7]. At midrapidity $y = 0$ (192) implies that $k_\perp = \omega$. Contribution of d and s quarks is qualitatively similar. At $eB \gg m^2$, quark masses do not affect the spectrum much. The main difference stems from the difference in electric charge. In panel (a) only the contributions of the first ten Landau levels are displayed. The cutoff frequencies $\omega_{s,jk}$ can be clearly seen, and some of them are indicated on the plot for convenience. The azimuthal distribution is shown in Figure 17. Note that at midrapidity $\phi = \pi/2 - \theta$. Therefore, the figure indicates that photon production in the direction of magnetic field (at $\phi = \pi/2$) is suppressed. More photons are produced in the direction of the reaction plane $\phi = 0$. This results in the ellipticity of the photon spectrum that translates into the positive ‘‘elliptic flow’’ coefficient v_2 . It should be noted that the classical synchrotron radiation has a similar angular distribution.

In order to compare the photon spectrum produced by synchrotron radiation to the photon spectrum measured in heavy-ion collisions, the u , d , and s quarks contributions were summed up. Furthermore, the experimental data from [8]

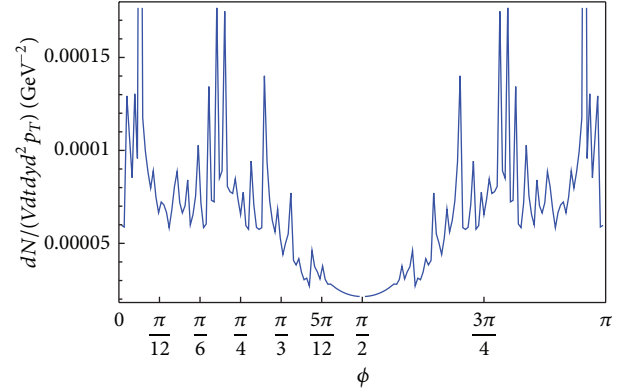


FIGURE 17: Azimuthal distribution of synchrotron radiation by u quarks at $k_\perp = 0.2$ GeV, $eB = m_\pi^2$, and $y = 0$. $m_u = 3$ MeV. Adopted from [7].

was divided by Vt , where t is the magnetic field relaxation time. The volume of the plasma can be estimated as $V = \pi R^2 t$ with $R \approx 5$ fm being the nuclear radius. Therefore,

$$\begin{aligned} \frac{dN_{\text{exp}}^y}{dV dt d^2 k_\perp dy} &= \frac{dN_{\text{exp}}^y}{d^2 k_\perp dy} \frac{1}{\pi R^2 t^2} \\ &= \frac{dN_{\text{exp}}^y}{d^2 k_\perp dy} \left(\frac{\text{GeV}}{14.9} \right)^4 \left(\frac{1 \text{ fm}}{t} \right)^2. \end{aligned} \quad (194)$$

The results are plotted in Figure 18. In panel (a) it is seen that synchrotron radiation gives a significant contribution to the photon production in heavy-ion collisions at RHIC energy. This contribution is larger at small transverse momenta. This may explain enhancement of photon production observed in [8]. Panel (b) indicates the increase of the photon spectrum produced by the synchrotron radiation mechanism at the LHC energy. This increase is due to enhancement of the magnetic field strength, but mostly because of increase of plasma temperature. This qualitative features can be better

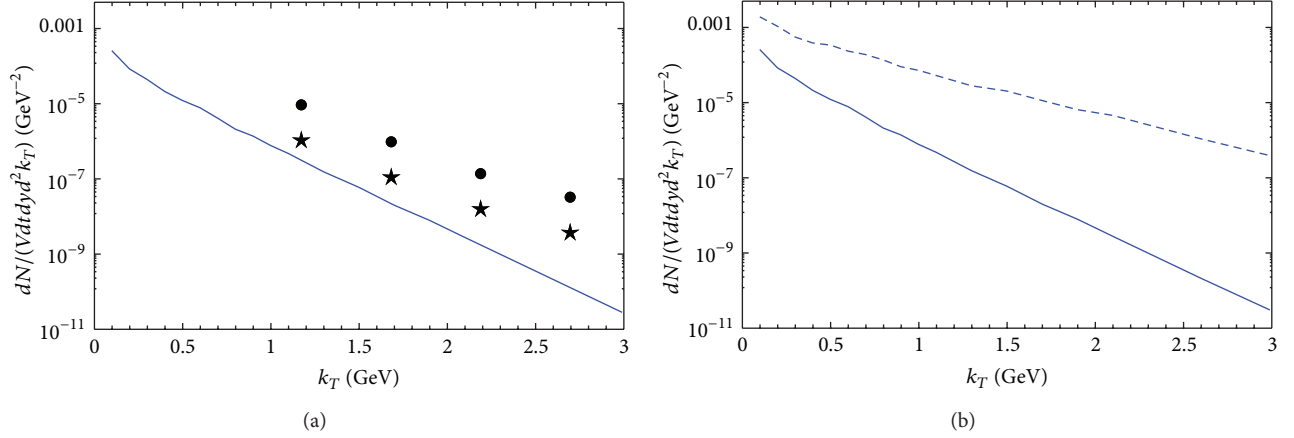


FIGURE 18: Azimuthal average of the synchrotron radiation spectrum of u, d, s quarks and their corresponding antiquarks. (a) $eB = m_\pi^2$, $y = 0$ compared to the experimental data from [8] divided by $Vt = 25\pi \text{ fm}^4$ (dots) and $Vt = 9 \times 25\pi \text{ fm}^4$ (stars); (b) $eB = m_\pi^2$, $T = 200 \text{ MeV}$, and $y = 0$ (solid line) compared to $eB = 15m_\pi^2$, $T = 400 \text{ MeV}$, and $y = 0$ (dashed line). $m_u = 3 \text{ MeV}$, $m_d = 5 \text{ MeV}$, and $m_s = 92 \text{ MeV}$. Adopted from [7].

understood by considering the limiting cases of low and high photon energies.

One possible way to ascertain the contribution of electromagnetic radiation in external magnetic field is to isolate the azimuthally symmetric component with respect to the direction of the magnetic field. It seems that synchrotron radiation dominates the photon spectrum at low k_\perp . Thus, azimuthal symmetry can be easily checked by simply plotting the multiplicity versus ω , θ , and φ , where ω is photon energy, θ is emission angle with respect to the magnetic field, and φ is azimuthal angle around the magnetic field direction (which is perpendicular both to the collision axis and to the impact parameter). In Figure 16(a) it is also seen that in these variables it may be possible to discern the cutoff frequencies $\omega_{s,jk}$ that appear as resonances (in Figure 16 $y = 0$ so $k_\perp = \omega$). Note that averaging over the azimuthal angle α around the collision axis direction destroys these features; see Figure 18.

6.2.1. Low Photon Energy. The low energy part of the photon spectrum satisfies the condition $\omega \ll \sqrt{e_f B}$. The corresponding initial quark momentum components along the field p and energy ε_j follow from (186) and (175) and are given by

$$p_\pm^* \approx \frac{(j-k)e_f B (\cos\theta \pm 1)}{\omega \sin^2\theta} + \mathcal{O}(\omega), \quad (195)$$

$$\varepsilon_j \approx |p_\pm^*| + \mathcal{O}(\omega).$$

Evidently, $\varepsilon_j \gg eB$. In practice, magnetic field strength satisfies $\sqrt{eB} \geq T$, so that $\varepsilon_j \gg T$. Therefore, synchrotron radiation is dominated by fermion transitions from low Landau levels due to the statistical factors appearing in (183).

For a qualitative discussion it is sufficient to consider the $1 \rightarrow 0$ transition. In this case the matrix elements (178) read

$$|\mathcal{M}^{1,0}|^2 = \frac{1}{2\varepsilon_1 \varepsilon_0} \left\{ I_{1,0}^2 (\varepsilon_1 \varepsilon_0 - pq \cos^2\theta - m^2) + \cos\theta \sin\theta q \sqrt{2e_f B} I_{1,0} I_{0,0} \right\}. \quad (196)$$

Assuming that the field strength is supercritical; that is, $e_f B \gg m^2$, but keeping all powers of ω (for future reference) (186) reduces to

$$p_\pm^* \approx \frac{1}{2\omega \sin^2\theta} \left\{ 2e_f B (\cos\theta \pm 1) + \omega^2 \sin^2\theta (\cos\theta \mp 1) \right\}. \quad (197)$$

Furthermore, using the conservation laws (176) we obtain in this approximation

$$\varepsilon_{1\pm} = \frac{1}{2\omega \sin^2\theta} \left| 2e_f B (\cos\theta \pm 1) - \omega^2 \sin^2\theta (\cos\theta \mp 1) \right|,$$

$$q_\pm = \frac{1}{2\omega \sin^2\theta} (2e_f B - \omega^2 \sin^2\theta) (\cos\theta \pm 1),$$

$$\varepsilon_{0\pm} = |q|. \quad (198)$$

The values of the nonvanishing matrix elements $I_{j,k}$ defined by (179) are

$$I_{1,0}(x) = -x^{1/2} e^{-x/2}, \quad I_{0,0}(x) = e^{-x/2}. \quad (199)$$

TABLE 1: The upper summation limit in (190) that yields the 5% accuracy. j_{\max} is the highest Landau level of the initial quark that is taken into account at this accuracy. Throughout the table $y = 0$.

f	u	u	u	u	u	u	s	u	u	s
eB/m_π^2	1	1	1	1	1	1	1	15	15	15
T , GeV	0.2	0.2	0.2	0.2	0.2	0.2	0.2	0.4	0.4	0.4
ϕ	$\frac{\pi}{3}$	$\frac{\pi}{3}$	$\frac{\pi}{3}$	$\frac{\pi}{3}$	$\frac{\pi}{6}$	$\frac{\pi}{12}$	$\frac{\pi}{3}$	$\frac{\pi}{3}$	$\frac{\pi}{3}$	$\frac{\pi}{3}$
k_\perp , GeV	0.1	1	2	3	1	1	1	1	2	1
x	0.096	9.6	38	86	29	35	19	0.64	2.6	1.3
j_{\max}	30	40	90	150	120	200	90	8	12	16

For $j = 1, k = 0$ we write using (189) $\omega_{s,10} = \sqrt{2e_f B} \sin \theta$. Then (180) implies $x = \omega^2/\omega_{s,10}^2$. Substituting (197)–(199) into (196) gives

$$\left| \mathcal{M}_\pm^{1,0} \right|^2 = \frac{1}{2} x e^{-x} \left[1 - \frac{\cos \theta (1+x) \pm (1-x)}{\cos \theta (1-x) \pm (1+x)} \cos^2 \theta - \frac{2(1-x) \cos \theta \sin^2 \theta}{\cos \theta (1-x) \pm (1+x)} \right]. \quad (200)$$

According to (190) the contribution of the $1 \rightarrow 0$ transition to the synchrotron radiation reads [7]

$$\begin{aligned} & \frac{dN^{\text{synch},10}}{V dt d\Omega d\omega} \\ &= \sum_f \frac{2N_c z_f^2 \alpha}{\pi} \omega \Gamma \frac{e_f B}{2\pi^2} \sum_\pm f(\varepsilon_1) [1 - f(\varepsilon_0)] \left| \mathcal{M}_\pm^{1,0} \right|^2 \\ & \quad \times \frac{(1-x) \cos \theta \pm (1+x)}{-2x(\cos \theta \mp 1)} \vartheta(\omega_{s,10} - \omega). \end{aligned} \quad (201)$$

Consider radiation spectrum at $\theta = \pi/2$, that is, perpendicular to the magnetic field. The spectrum increases with x and reaches maximum at $x = 1$. Since $x = \omega^2/(2e_f B)$, spectrum decreases with increase of B at fixed ω . This feature holds at low x part of the spectrum for other emission angles and even for transitions from higher excited states. However, at high energies, it is no longer possible to approximate the spectrum by the contribution of a few low Landau levels. In that case the typical values of quantum numbers are $j, k \gg 1$. For example, to achieve the numerical accuracy of 5%, sum over j must run up to a certain j_{\max} . Some values of j_{\max} are listed in Table 1 [7].

6.2.2. High Photon Energy. The high energy tail of the photon spectrum is quasi-classical and approximately continuous. In this case the Laguerre polynomials can be approximated by the Airy functions or the corresponding modified Bessel functions. The angular distribution of the spectrum can be found in [82]

$$\frac{dN^{\text{synch}}}{V dt d\Omega d\omega} = \sum_f \frac{z_f^2 \alpha}{\pi} \frac{n_f \omega m^2}{4T^3} \sqrt{\frac{e_f B T \sin \theta}{m^3}} e^{-\omega/T}, \quad (202)$$

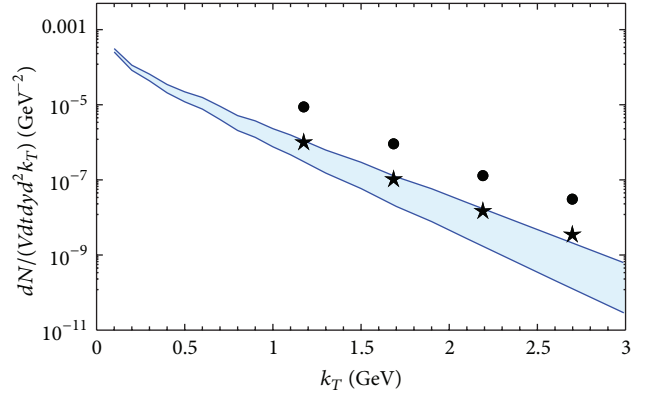


FIGURE 19: Variation of the synchrotron spectrum with plasma temperature. Lower line: $T = 200$ MeV, upper line: $T = 250$ MeV; Other parameters are the same as in Figure 18(a). Adopted from [7].

provided that $\omega \gg m \sqrt{mT/e_f B \sin \theta}$. Here n_f is number density of flavor f , which is independent of B as follows:

$$n_f = \frac{2 \cdot 2N_c e_f B}{4\pi^2} \sum_{j=0}^{\infty} \int_{-\infty}^{\infty} dp e^{-\varepsilon_j/T} \approx \frac{4N_c}{\pi^2} T^3. \quad (203)$$

Here summation over j was replaced by integration. It follows that this part of the spectrum increases with magnetic field strength as \sqrt{B} and with temperature as $\sqrt{T} e^{-\omega/T}$. Therefore, variation of the spectrum with T is much stronger than with B . The T dependence is shown in Figure 19.

Unlike time-dependence of magnetic field, time-dependence of temperature is non-negligible even during the first few fm/c. Final synchrotron spectrum, which is an average over all temperatures, is dominated by high temperatures/early times. However, the precise form of time-dependence of temperature is model-dependent. Therefore, the spectrum is presented at fixed temperatures, so that a reader can appreciate its qualitative features in a model-independent way.

6.3. Pair Annihilation. The theory of one-photon pair annihilation was developed in [86, 87]. It was shown in [88] that in the super-critical regime $eB \gg m^2$ one-photon annihilation is much larger than the two-photon annihilation. In this section the one-photon annihilation of q and \bar{q} pairs in the QGP is calculated.

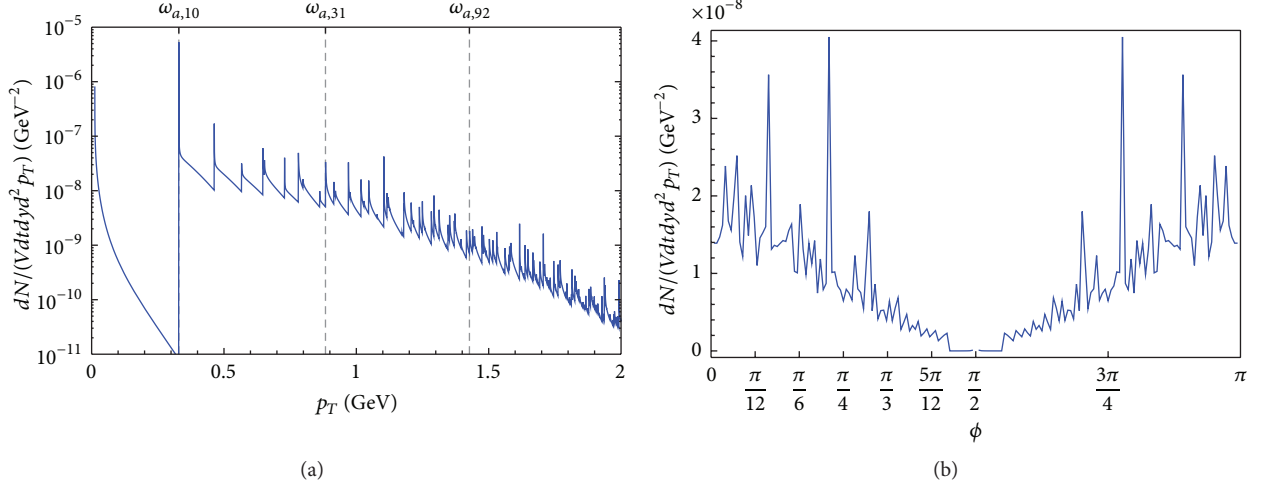


FIGURE 20: Photon spectrum in one-photon annihilation of u and \bar{u} quarks. $eB = m_\pi^2$, $y = 0$. (a) k_\perp -spectrum at $\phi = \pi/3$, (b) azimuthal angle distribution at $k_\perp = 1$ GeV. Adopted from [7].

For $q\bar{q}$ pair annihilation the conservation of energy and momentum is given by

$$\varepsilon_j + \varepsilon_k = \omega, \quad p + q = \omega \cos \theta. \quad (204)$$

The spectral density of the annihilation rate per unit volume reads

$$\begin{aligned} & \frac{dN^{\text{annih}}}{V dt d\omega d\Omega} \\ &= \sum_f \frac{\alpha z_f^2 \omega N_c}{4\pi e_f B} \sum_{j=0}^{\infty} \sum_{k=0}^{\infty} \int dp \frac{2e_f B}{2\pi^2} f(\varepsilon_j) \int dq \frac{2e_f B}{2\pi^2} f(\varepsilon_k) \\ & \quad \times \delta(p + q - \omega \cos \theta) \delta(\varepsilon_j + \varepsilon_k - \omega) \\ & \quad \times \{ |\mathcal{T}_\perp|^2 + |\mathcal{T}_\parallel|^2 \}, \end{aligned} \quad (205)$$

where the matrix elements \mathcal{T} can be obtained from (178) by making substitutions $\varepsilon_k \rightarrow -\varepsilon_k$, $q \rightarrow -q$ and are given by

$$\begin{aligned} & 4\varepsilon_j \varepsilon_k |\mathcal{T}_\perp|^2 \\ &= (\varepsilon_j \varepsilon_k - pq + m^2) [I_{j,k-1}^2 + I_{j-1,k}^2] \\ & \quad - 2\sqrt{2j e_f B} \sqrt{2k e_f B} [I_{j,k-1} I_{j-1,k}], \\ & 4\varepsilon_j \varepsilon_k |\mathcal{T}_\parallel|^2 \\ &= \cos^2 \theta \left\{ (\varepsilon_j \varepsilon_k - pq + m^2) [I_{j,k-1}^2 + I_{j-1,k}^2] \right. \\ & \quad \left. + 2\sqrt{2j e_f B} \sqrt{2k e_f B} [I_{j,k-1} I_{j-1,k}] \right\} \end{aligned}$$

$$\begin{aligned} & - 2 \cos \theta \sin \theta \left\{ -p \sqrt{2k e_f B} [I_{j-1,k} I_{j-1,k-1} + I_{j,k-1} I_{j,k}] \right. \\ & \quad \left. + q \sqrt{2j e_f B} [I_{j,k} I_{j-1,k} + I_{j-1,k-1} I_{j,k-1}] \right\} \\ & + \sin^2 \theta \left\{ (\varepsilon_j \varepsilon_k + pq + m^2) [I_{j-1,k-1}^2 + I_{j,k}^2] \right. \\ & \quad \left. - 2\sqrt{2j e_f B} \sqrt{2k e_f B} (I_{j-1,k-1} I_{j,k}) \right\}, \end{aligned} \quad (206)$$

with the same functions $I_{i,j}$ as in (179). Integration over q removes the delta function responsible for the conservation of momentum along the field direction. The remaining delta function is responsible for energy conservation and can be written in exactly the same form as in (185) with particle energies and momenta now obeying the conservation laws (204). It is straightforward to see that momentum p_\pm^* is still given by (190), (187). The photon spectrum produced by annihilation of quark in state j with antiquark in state k has a threshold $\omega_{a,ij}$ that is given by the case (ii) in (188) as follows:

$$\omega \geq \omega_{a,ij} = \frac{m_j + m_k}{\sin \theta} = \frac{\sqrt{m^2 + 2j e_f B} + \sqrt{m^2 + 2k e_f B}}{\sin \theta}. \quad (207)$$

Thus, the spectral density of the annihilation rate per unit volume is

$$\begin{aligned} & \frac{dN^{\text{annih}}}{V dt d\omega d\Omega} \\ &= \sum_f \frac{\alpha z_f^2 \omega N_c}{4\pi^5} e_f B \sum_{j=0}^{\infty} \sum_{k=0}^{\infty} \vartheta(\omega - \omega_{a,ij}) \\ & \quad \times \int dp \sum_{\pm} \frac{\delta(p - p_\pm^*)}{|(p/\varepsilon_j) - (q/\varepsilon_k)|} \\ & \quad \times \{ |\mathcal{T}_\perp|^2 + |\mathcal{T}_\parallel|^2 \} f(\varepsilon_j) f(\varepsilon_k). \end{aligned} \quad (208)$$

Passing to γ and p_{\perp} variables in place of ω and θ is similar to (193).

The results of the numerical calculations are represented in Figure 20. Panel (a) shows the spectrum of photons radiated in annihilation of u and \bar{u} . We conclude that contribution of the annihilation channel is negligible as compared to the synchrotron radiation.

In summary, results of the calculations presented in this section indicate that photon production by QGP due to its interaction with external magnetic field gives a considerable contribution to the total photon multiplicity in heavy-ion collisions. This is seen in Figure 18 where the model calculation is compared with the experimental data [8]. The largest contribution to the photon multiplicity arises from photon momenta of the order of \sqrt{eB} . This may provide an explanation of the photon excess observed by the PHENIX experiment [8]. Similar mechanism may also be responsible for enhancement of low mass di-lepton production that proceeds via emission of virtual photon which subsequently decays into dilepton pair.

7. Summary

Analytical and numerical calculations indicate existence of extremely powerful electromagnetic fields in relativistic heavy-ion collisions. They are the strongest electromagnetic fields that exist in nature. They evolve slowly on characteristic QGP time scale and therefore have a profound effect on dynamics of QGP. In this review I described the recent progress in understanding of particle production in presence of these fields. Treating the fields as quasi-static and spatially homogeneous allowed us to use analytical results derived over the past half century. This is, however, the main source of uncertainty that can be clarified only in comprehensive numerical approach based on relativistic magnetohydrodynamics.

I discussed many spectacular effects caused by magnetic field. All of them have direct phenomenological relevance. Breaking of spherical symmetry by magnetic field in the direction perpendicular to the collision axis results in azimuthal asymmetry of particle production in the reaction plane. Fast quarks moving in magnetic field radiate a significant fraction of their energy. All electromagnetic probes are also naturally affected by magnetic field. Therefore, all experimental processes that are being used to study the properties of QGP have strong magnetic field dependence. In addition, the QCD phase diagram is modified by magnetic field as has been extensively studied using model calculations [89–110] and lattice simulations [111–123]. Entanglement of effects produced by magnetic field with conventional QGP ones makes it difficult to quantify the role of magnetic field in QGP dynamics. A unique observable is polarization of leptons escaping from QGP, which can be induced only by magnetic field see Section 3.3.

Profound influence of magnetic field on properties of QGP is truly remarkable. Hopefully, progress in theory will soon be matched by experimental investigations that will eventually discover properties of QCD at high temperatures and strong electromagnetic fields.

Acknowledgment

This work was supported in part by the U.S. Department of Energy under Grant no. DE-FG02-87ER40371.

References

- [1] B. A. Boyko, A. I. Bykov, M. I. Dolotenko et al., “With record magnetic fields to the 21st century,” in *Proceedings of the 12th IEEE International Pulsed Power Conference*, pp. 746–749, June 1999.
- [2] C. Kouveliotou, R. C. Duncan, and C. Thompson, “Feature,” *Scientific American*, vol. 288, no. 2, pp. 34–41, 2003.
- [3] J. S. Schwinger, “On gauge invariance and vacuum polarization,” *Physical Review*, vol. 82, pp. 664–679, 1951.
- [4] A. Bzdak and V. Skokov, “Event-by-event fluctuations of magnetic and electric fields in heavy ion collisions,” *Physics Letters B*, vol. 710, pp. 171–174, 2012.
- [5] D. E. Kharzeev, L. D. McLerran, and H. J. Warringa, “The effects of topological charge change in heavy ion collisions: ‘event by event P and CP violation,’” *Nuclear Physics A*, vol. 803, no. 3–4, pp. 227–253, 2008.
- [6] Y. Kluger, J. M. Eisenberg, B. Svetitsky, F. Cooper, and E. Mottola, “Fermion pair production in a strong electric field,” *Physical Review D*, vol. 45, no. 12, pp. 4659–4671, 1992.
- [7] K. Tuchin, “Electromagnetic radiation by quark-gluon plasma in a magnetic field,” *Physical Review C*, vol. 87, Article ID 024912, 8 pages, 2013.
- [8] A. Adare, S. Afanasiev, C. Aidala et al., “Enhanced production of direct photons in Au+Au collisions at $\sqrt{s_{NN}} = 200$ GeV and implications for the initial temperature,” *Physical Review Letters*, vol. 104, no. 13, Article ID 132301, 6 pages, 2010.
- [9] J. Ambjorn and P. Olesen, “W-condensate formation in high energy collisions,” *Physics Letters B*, vol. 257, pp. 201–206, 1991.
- [10] P. Olesen, “W condensation at the LHC?” In press, <http://arxiv.org/abs/1207.7045>.
- [11] V. V. Skokov, A. Y. Illarionov, and V. D. Toneev, “Estimate of the magnetic field strength in heavy-ion collisions,” *International Journal of Modern Physics A*, vol. 24, no. 31, pp. 5925–5932, 2009.
- [12] V. Voronyuk, V. D. Toneev, W. Cassing, E. L. Bratkovskaya, V. P. Konchakovski, and S. A. Voloshin, “Electromagnetic field evolution in relativistic heavy-ion collisions,” *Physical Review C*, vol. 83, no. 5, Article ID 054911, 2011.
- [13] W.-T. Deng and X.-G. Huang, “Event-by-event generation of electromagnetic fields in heavy-ion collisions,” *Physical Review C*, vol. 85, Article ID 044907, 8 pages, 2012.
- [14] T. Lappi and L. McLerran, “Some features of the glasma,” *Nuclear Physics A*, vol. 772, no. 3–4, pp. 200–212, 2006.
- [15] J.-P. Blaizot, F. Gelis, J. Liao, L. McLerran, and R. Venugopalan, “Thermalization and bose-einstein condensation in overpopulated glasma,” In press, <http://arxiv.org/abs/1210.6838>.
- [16] H. T. Ding, A. Francis, O. Kaczmarek, F. Karsch, E. Laermann, and W. Soeldner, “Thermal dilepton rate and electrical conductivity: an analysis of vector current correlation functions in quenched lattice QCD,” In press, <http://arxiv.org/abs/1012.4963>.
- [17] G. Aarts, C. Allton, J. Foley, S. Hands, and S. Kim, “Spectral functions at small energies and the electrical conductivity in hot quenched lattice QCD,” *Physical Review Letters*, vol. 99, no. 2, Article ID 022002, 4 pages, 2007.
- [18] S. Gupta, “Analyticity and the phase diagram of QCD,” *Physics Letters B*, vol. 588, no. 1–2, pp. 136–144, 2004.

- [19] J. D. Jackson, *Classical Electrodynamics*, 3rd edition, 1998.
- [20] J. D. Bjorken, “Highly relativistic nucleus-nucleus collisions: the central rapidity region,” *Physical Review D*, vol. 27, no. 1, pp. 140–151, 1983.
- [21] K. Tuchin, “Synchrotron radiation by fast fermions in heavy-ion collisions,” *Physical Review C*, vol. 83, no. 3, Article ID 039903, 1 pages, 2011, Erratum: *Physical Review C*, vol. 82, article ID 034904, 2010.
- [22] G. V. Dunne and C. Schubert, “Worldline instantons and pair production in inhomogeneous fields,” *Physical Review D*, vol. 72, no. 10, Article ID 105004, 12 pages, 2005.
- [23] R.-C. Wang and C. Y. Wong, “Finite-size effect in the Schwinger particle-production mechanism,” *Physical Review D*, vol. 38, pp. 348–359, 1988.
- [24] C. Martin and D. Vautherin, “Finite-size and dynamical effects in pair production by an external field,” *Physical Review D*, vol. 40, pp. 1667–1673, 1989.
- [25] S. P. Kim and D. N. Page, “Improved approximations for fermion pair production in inhomogeneous electric fields,” *Physical Review D*, vol. 75, Article ID 045013, 9 pages, 2007.
- [26] F. Cooper, J. M. Eisenberg, Y. Kluger, E. Mottola, and B. Svetitsky, “Particle production in the central rapidity region,” *Physical Review D*, vol. 48, no. 1, pp. 190–208, 1993.
- [27] Y. Kluger, J. M. Eisenberg, B. Svetitsky, F. Cooper, and E. Mottola, “Pair production in a strong electric field,” *Physical Review Letters*, vol. 67, no. 18, pp. 2427–2430, 1991.
- [28] N. Tanji, “Dynamical view of pair creation in uniform electric and magnetic fields,” *Annals of Physics*, vol. 324, no. 8, pp. 1691–1736, 2009.
- [29] R. K. Mohapatra, P. S. Saumia, and A. M. Srivastava, “Enhancement of flow anisotropies due to magnetic field in relativistic heavy-ion collisions,” *Modern Physics Letters A*, vol. 26, p. 2477, 2011.
- [30] E. M. Lifshitz and L. P. Pitaevskiy, *Physical Kinetics*, Pergamon Press, 1981.
- [31] H. Van Erkelens and W. A. Van Leeuwen, “Relativistic Boltzmann theory for a plasma: I. The entropy production,” *Physica A*, vol. 89, pp. 113–126, 1977.
- [32] H. Van Erkelens and W. A. Van Leeuwen, “Relativistic Boltzmann theory for a plasma: II. Reciprocal relations,” *Physica A*, vol. 89, pp. 225–244, 1977.
- [33] H. Van Erkelens and W. A. Van Leeuwen, “Relativistic Boltzmann theory for a plasma: III. Viscous phenomena,” *Physica A*, vol. 90, pp. 97–108, 1978.
- [34] I. S. Gradshteyn and I. M. Ryzhik, *Table of Integrals, Series, and Products*, Edited by: A. Jeffrey, D. Zwillinger, Academic Press, 7th edition, 2007.
- [35] K. Tuchin, “On viscous flow and azimuthal anisotropy of the quark-gluon plasma in a strong magnetic field,” *Journal of Physics G*, vol. 39, no. 2, Article ID 025010, 2012.
- [36] L. V. Gribov, E. M. Levin, and M. G. Ryskin, “Semihard processes in QCD,” *Physics Reports*, vol. 100, no. 1-2, pp. 1–150, 1983.
- [37] J. P. Blaizot and A. H. Mueller, “The early stage of ultra-relativistic heavy ion collisions,” *Nuclear Physics B*, vol. 289, pp. 847–860, 1987.
- [38] H. Song and U. W. Heinz, “Suppression of elliptic flow in a minimally viscous quark-gluon plasma,” *Nuclear Physics B*, vol. 658, pp. 279–283, 2008.
- [39] P. Romatschke and U. Romatschke, “Viscosity information from relativistic nuclear collisions: how perfect is the fluid observed at RHIC?” *Physical Review Letters*, vol. 99, no. 17, Article ID 172301, 4 pages, 2007.
- [40] K. Dusling and D. Teaney, “Simulating elliptic flow with viscous hydrodynamics,” *Physical Review C*, vol. 77, Article ID 034905, 19 pages, 2008.
- [41] E. S. Weibel, “Spontaneously growing transverse waves in a plasma due to an anisotropic velocity distribution,” *Physical Review Letters*, vol. 2, pp. 83–84, 1959.
- [42] S. Mrowczynski, “Color collective effects at the early stage of ultrarelativistic heavy-ion collisions,” *Physical Review C*, vol. 49, pp. 2191–2197, 1994.
- [43] P. B. Arnold, G. D. Moore, and L. G. Yaffe, “Transport coefficients in high temperature gauge theories. 2. Beyond leading log,” *Journal of High Energy Physics*, vol. 305, p. 51, 2003.
- [44] G. Baym, H. Monien, C. J. Pethick, and D. G. Ravenhall, “Transverse interactions and transport in relativistic quark-gluon and electromagnetic plasmas,” *Physical Review Letters*, vol. 64, no. 16, pp. 1867–1870, 1990.
- [45] A. I. Nikishov and V. I. Ritus, “Quantum processes in the field of a plane electromagnetic wave and in a constant field. I,” *Soviet Physics*, vol. 19, pp. 529–541, 1964.
- [46] A. A. Sokolov and I. M. Ternov, “On polarization and spin effects in synchrotron radiation theory,” *Soviet Physics—Doklady*, vol. 8, p. 1203, 1964, *Doklady Akademii Nauk SSSR*, vol. 153, pp. 1052, 1964, *PHDOE*, vol. 8, pp. 1203–1205, 1964.
- [47] V. I. Ritus, “Quantum effects of the interaction of elementary particles with an intense electromagnetic field,” *Journal of Soviet Laser Research*, vol. 6, no. 5, pp. 497–617, 1985.
- [48] V. B. Berestetsky, E. M. Lifshitz, and L. P. Pitaevsky, *Quantum Electrodynamics*, vol. 4 of *Course Of Theoretical Physics*, Pergamon, Oxford, UK, 1982.
- [49] J. D. Jackson, “On understanding spin-flip synchrotron radiation and the transverse polarization of electrons in storage rings,” *Reviews of Modern Physics*, vol. 48, pp. 417–433, 1976.
- [50] M. Gyulassy and X. N. Wang, “Multiple collisions and induced gluon bremsstrahlung in QCD,” *Nuclear Physics B*, vol. 420, no. 3, pp. 583–614, 1994.
- [51] R. Baier, Y. L. Dokshitzer, S. Peigne, and D. Schi, “Induced gluon radiation in a QCD medium,” *Physics Letters B*, vol. 345, pp. 277–286, 1995.
- [52] E. V. Shuryak and I. Zahed, “Jet Quenching in high energy heavy ion collisions by QCD synchrotron-like radiation,” *Physical Review D*, vol. 67, Article ID 054025, 2003.
- [53] D. E. Kharzeev, “Universal upper bound on the energy of a parton escaping from the strongly coupled quark-gluon matter,” In press, <http://arxiv.org/abs/0806.0358>.
- [54] B. G. Zakharov, “Parton energy loss due to synchrotron-like gluon emission,” *JETP Letters*, vol. 88, no. 8, pp. 475–480, 2008.
- [55] K. Tuchin, “Photon decay in a strong magnetic field in heavy-ion collisions,” *Physical Review C*, vol. 83, no. 1, Article ID 017901, 3 pages, 2011.
- [56] V. N. Baier and V. M. Katkov, “Quantum effects in magnetic bremsstrahlung,” *Physics Letters A*, vol. 25, no. 7, pp. 492–493, 1967.
- [57] K. Marasinghe and K. Tuchin, “Quarkonium dissociation in quark-gluon plasma via ionization in a magnetic field,” *Physical Review C*, vol. 84, no. 4, Article ID 044908, 8 pages, 2011.
- [58] K. Tuchin, “ J/ψ dissociation in parity-odd bubbles,” *Physics Letters B*, vol. 705, pp. 482–486, 2011.

- [59] L. D. Landau and L. E. Lifshitz, *Quantum Mechanics Non-Relativistic Theory*, Butterworth-Heinemann, 3rd edition.
- [60] B. Machet and M. I. Vysotsky, "Modification of Coulomb law and energy levels of the hydrogen atom in a superstrong magnetic field," *Physical Review D*, vol. 83, no. 2, Article ID 025022, 12 pages, 2011.
- [61] V. S. Popov, B. M. Karnakov, and V. D. Mur, "Quasiclassical theory of atomic ionization in electric and magnetic fields," *Physics Letters A*, vol. 229, no. 5, pp. 306–312, 1997.
- [62] V. S. Popov, B. M. Karnakov, and V. D. Mur, "Relativistic version of the imaginary time method," *Physics Letters A*, vol. 250, pp. 20–24, 1998.
- [63] V. S. Popov, B. M. Karnakov, and V. D. Mur, "Ionization of atoms in electric and magnetic fields and the imaginary time method," *Journal of Experimental and Theoretical Physics*, vol. 86, no. 5, pp. 860–874, 1998.
- [64] L. V. Keldysh, "Diagram technique for nonequilibrium processes," *Soviet Physics*, vol. 20, pp. 1018–1026, 1965.
- [65] L. D. Landau and L. E. Lifshitz, *Quantum Mechanics Non-Relativistic Theory*, Butterworth-Heinemann, 3rd edition.
- [66] V. S. Popov, "Tunnel and multiphoton ionization of atoms and ions in a strong laser field (Keldysh theory)," *Physics-Usp ekhi*, vol. 47, no. 9, pp. 855–885, 2004.
- [67] D. Kharzeev, "Parity violation in hot QCD: why it can happen, and how to look for it," *Physics Letters B*, vol. 633, pp. 260–264, 2006.
- [68] D. Kharzeev and A. Zhitnitsky, "Charge separation induced by P-odd bubbles in QCD matter," *Nuclear Physics A*, vol. 797, no. 1-2, pp. 67–79, 2007.
- [69] K. Fukushima, D. E. Kharzeev, and H. J. Warringa, "Chiral magnetic effect," *Physical Review D*, vol. 78, no. 7, Article ID 074033, 14 pages, 2008.
- [70] D. E. Kharzeev, "Topologically induced local P and CP violation in QCD \times QED," *Annals of Physics*, vol. 325, pp. 205–218, 2010.
- [71] G. Basar, G. V. Dunne, and D. E. Kharzeev, "Chiral magnetic spirals," *Physical Review Letters*, vol. 104, no. 23, Article ID 232301, 4 pages, 2010.
- [72] M. Asakawa, A. Majumder, and B. Muller, "Electric charge separation in strong transient magnetic fields," In press, <http://arxiv.org/abs/1003.2436>.
- [73] B. I. Abelev, M. M. Aggarwal, Z. Ahammed et al., "Azimuthal charged-particle correlations and possible local strong parity violation," *Physical Review Letters*, vol. 103, no. 25, Article ID 251601, 7 pages, 2009.
- [74] B. I. Abelev, M. M. Aggarwal, Z. Ahammed et al., "Observation of charge-dependent azimuthal correlations and possible local strong parity violation in heavy ion collisions," *Physical Review C*, vol. 81, Article ID 054908, 2010.
- [75] N. N. Ajitanand, R. A. Lacey, A. Taranenko, and J. M. Alexander, "New method for the experimental study of topological effects in the quark-gluon plasma," *Physical Review C*, vol. 83, no. 1, 5 pages, 2011.
- [76] A. M. Perelomov, V. S. Popov, and M. V. Terentev, *Zhurnal Eksperimental'noi i Teoreticheskoi Fiziki*, vol. 50, p. 1393, 1966.
- [77] A. M. Perelomov, V. S. Popov, and M. V. Terentev, *Zhurnal Eksperimental'noi i Teoreticheskoi Fiziki*, vol. 51, p. 309, 1966.
- [78] V. S. Popov, V. P. Kuznetsov, and A. M. Perelomov, *Zhurnal Eksperimental'noi i Teoreticheskoi Fiziki*, vol. 53, p. 331, 1967.
- [79] G. D. Moore and M. Tassler, "The sphaleron rate in SU(N) gauge theory," *Journal of High Energy Physics*, vol. 1102, article 105, 2011.
- [80] T. Matsui and H. Satz, " J/ψ suppression by quark-gluon plasma formation," *Physics Letters B*, vol. 178, no. 4, pp. 416–422, 1986.
- [81] A. A. Sokolov and I. M. Ternov, *Synchrotron Radiation*, Pergamon Press, Oxford, UK, 1968.
- [82] M. G. Baring, "Synchrotron emission, pair production and annihilation in strongly magnetized relativistic plasmas," *Monthly Notices of the Royal Astronomical Society*, vol. 235, pp. 51–78, 1988.
- [83] H. Herold, H. Ruder, and G. Wunner, "Cyclotron emission in strongly magnetized plasmas," *Astronomy & Astrophysics*, vol. 115, no. 1, pp. 90–96, 1982.
- [84] A. K. Harding and R. Preece, "Quantized synchrotron radiation in strong magnetic fields," *Astrophysical Journal*, vol. 319, pp. 939–950, 1987.
- [85] H. G. Latal, "Cyclotron radiation in strong magnetic fields," *Astrophysical Journal*, vol. 309, pp. 372–382, 1986.
- [86] A. K. Harding, "One-photon pair annihilation in magnetized relativistic plasmas," *Astrophysical Journal*, vol. 300, pp. 167–177, 1986.
- [87] G. Wunner, J. Paez, H. Herold, and H. Ruder, "One-quantum annihilation of polarized electron-positron pairs in strong magnetic fields," *Astronomy & Astrophysics*, vol. 170, no. 1, pp. 179–186, 1986.
- [88] G. Wunner, "Comparison of 1γ and 2γ pair annihilation in strong magnetic fields," *Physical Review Letters*, vol. 42, pp. 79–82, 1979.
- [89] A. J. Mizher, M. N. Chernodub, and E. S. Fraga, "Phase diagram of hot QCD in an external magnetic field: Possible splitting of deconfinement and chiral transitions," *Physical Review D*, vol. 82, no. 10, Article ID 105016, 16 pages, 2010.
- [90] E. S. Fraga and A. J. Mizher, "Can a strong magnetic background modify the nature of the chiral transition in QCD?" *Nuclear Physics A*, vol. 820, pp. 103c–106c, 2009.
- [91] E. S. Fraga and L. F. Palhares, "Deconfinement in the presence of a strong magnetic background: an exercise within the MIT bag model," *Physical Review D*, vol. 86, Article ID 016008, 7 pages, 2012.
- [92] R. Gatto and M. Ruggieri, "Deconfinement and chiral symmetry restoration in a strong magnetic background," *Physical Review D*, vol. 83, no. 3, Article ID 034016, 12 pages, 2011.
- [93] R. Gatto and M. Ruggieri, "Dressed Polyakov loop and phase diagram of hot quark matter in a magnetic field," *Physical Review D*, vol. 82, no. 5, Article ID 054027, 10 pages, 2010.
- [94] A. A. Osipov, B. Hiller, A. H. Blin, and J. da Providencia, "Dynamical chiral symmetry breaking by a magnetic field and multi-quark interactions," *Physics Letters B*, vol. 650, pp. 262–267, 2007.
- [95] K. Kashiwa, "Entanglement between chiral and deconfinement transitions under strong uniform magnetic background field," *Physical Review D*, vol. 83, no. 11, Article ID 117901, 4 pages, 2011.
- [96] C. V. Johnson and A. Kundu, "External fields and chiral symmetry breaking in the Sakai-Sugimoto model," *Journal of High Energy Physics*, vol. 2008, no. 12, p. 53, 2008.
- [97] S. Kanemura, H. T. Sato, and H. Tochimura, "Thermodynamic Gross-Neveu model in a constant electromagnetic field," *Nuclear Physics B*, vol. 517, no. 1–3, pp. 567–598, 1998.
- [98] J. Alexandre, K. Farakos, and G. Koutsoumbas, "Magnetic catalysis in three-dimensional QED at finite temperature: beyond the constant mass approximation," *Physical Review D*, vol. 63, no. 6, Article ID 065015, 13 pages, 2001.

- [99] N. O. Agasian and S. M. Fedorov, "Quark-hadron phase transition in a magnetic field," *Physics Letters B*, vol. 663, pp. 445-449, 2008.
- [100] F. Preis, A. Rebhan, and A. Schmitt, "Inverse magnetic catalysis in dense holographic matter," *Journal of High Energy Physics*, vol. 2011, article 33, 2011.
- [101] V. P. Gusynin, V. A. Miransky, and I. A. Shovkovy, "Dimensional reduction and catalysis of dynamical symmetry breaking by a magnetic field," *Nuclear Physics B*, vol. 462, no. 2-3, pp. 249-290, 1996.
- [102] V. A. Miransky and I. A. Shovkovy, "Magnetic catalysis and anisotropic confinement in QCD," *Physical Review D*, vol. 66, no. 4, Article ID 045006, 9 pages, 2002.
- [103] M. N. Chernodub, "Superconductivity of QCD vacuum in strong magnetic field," *Physical Review D*, vol. 82, no. 8, Article ID 085011, 17 pages, 2010.
- [104] Y. Hidaka and A. Yamamoto, "Charged vector mesons in a strong magnetic field," In press, <http://arxiv.org/abs/1209.0007>.
- [105] M. N. Chernodub, "Vafa-Witten theorem, vector meson condensates, and magnetic-field-induced electromagnetic superconductivity of vacuum," *Physical Review D*, vol. 86, no. 10, Article ID 107703, 2 pages, 2012.
- [106] J. K. Boomsma and D. Boer, "Influence of strong magnetic fields and instantons on the phase structure of the two-flavor Nambu-Jona-Lasinio model," *Physical Review D*, vol. 81, Article ID 074005, 9 pages, 2010.
- [107] I. A. Shushpanov and A. V. Smilga, "Quark condensate in a magnetic field," *Physics Letters B*, vol. 402, no. 3-4, pp. 351-358, 1997.
- [108] T. D. Cohen, D. A. McGady, and E. S. Werbos, "Chiral condensate in a constant electromagnetic field," *Physical Review C*, vol. 76, no. 5, Article ID 055201, 9 pages, 2007.
- [109] N. O. Agasian, "Chiral thermodynamics in a magnetic field," *Physics of Atomic Nuclei*, vol. 64, pp. 554-560, 2001, *Yadernaya Fizika*, vol. 64, pp. 608, 2001.
- [110] B. V. Galilo and S. N. Nedelko, "Impact of the strong electromagnetic field on the QCD effective potential for homogeneous Abelian gluon field configurations," *Physical Review D*, vol. 84, no. 9, Article ID 094017, 8 pages, 2011.
- [111] M. D'Elia, S. Mukherjee, and F. Sanfilippo, "QCD phase transition in a strong magnetic background," *Physical Review D*, vol. 82, no. 5, Article ID 051501, 5 pages, 2010.
- [112] P. Cea and L. Cosmai, "Color dynamics in external fields," *Journal of High Energy Physics*, vol. 508, p. 79, 2005.
- [113] P. Cea and L. Cosmai, "Abelian chromomagnetic fields and confinement," *Journal of High Energy Physics*, vol. 302, p. 31, 2003.
- [114] P. Cea, L. Cosmai, and M. D'Elia, "QCD dynamics in a constant chromomagnetic field," *Journal of High Energy Physics*, vol. 712, p. 97, 2007.
- [115] G. S. Bali, F. Bruckmann, G. Endrődi et al., "The QCD phase diagram for external magnetic fields," *Journal of High Energy Physics*, vol. 2012, article 44, 2012.
- [116] G. S. Bali, F. Bruckmann, G. Endrodi et al., "The finite temperature QCD transition in external magnetic fields," In press, <http://arxiv.org/abs/1111.5155>.
- [117] G. S. Bali, F. Bruckmann, G. Endrodi, Z. Fodor, S. D. Katz, and A. Schafer, "QCD quark condensate in external magnetic fields," *Physical Review D*, vol. 86, no. 7, Article ID 071502, 6 pages, 2012.
- [118] E.-M. Ilgenfritz, M. Kalinowski, M. Muller-Preussker, B. Petersson, and A. Schreiber, "Two-color QCD with staggered fermions at finite temperature under the influence of a magnetic field," *Physical Review D*, vol. 85, no. 11, Article ID 114504, 12 pages, 2012.
- [119] Y. Aoki, G. Endrodi, Z. Fodor, S. D. Katz, and K. K. Szabó, "The order of the quantum chromodynamics transition predicted by the standard model of particle physics," *Nature*, vol. 443, no. 7112, pp. 675-678, 2006.
- [120] S.-I. Nam and C.-W. Kao, "Chiral restoration at finite T under the magnetic field with the meson-loop corrections," *Physical Review D*, vol. 83, no. 9, Article ID 096009, 14 pages, 2011.
- [121] M. D'Elia and F. Negro, "Chiral properties of strong interactions in a magnetic background," *Physical Review D*, vol. 83, Article ID 114028, 2011.
- [122] P. V. Buividovich, M. N. Chernodub, D. E. Kharzeev, T. Kalaydzhyan, E. V. Luschevskaya, and M. I. Polikarpov, "Magnetic-field-induced insulator-conductor transition in SU(2) quenched lattice gauge theory," *Physical Review Letters*, vol. 105, no. 13, Article ID 132001, 2010.
- [123] F. Bruckmann and G. Endrodi, "Dressed Wilson loops as dual condensates in response to magnetic and electric fields," *Physical Review D*, vol. 84, Article ID 074506, 2011.

Review Article

On Collective Properties of Dense QCD Matter

Igor Dremin,¹ Martin Kirakosyan,¹ and Andrei Leonidov^{1,2}

¹*P.N. Lebedev Physical Institute, Leninsky pr. 53, Moscow 119991, Russia*

²*Institute of Experimental and Theoretical Physics and Moscow Institute of Physics and Technology, Moscow, Russia*

Correspondence should be addressed to Martin Kirakosyan; martin.kirakosyan@cern.ch

Received 15 March 2013; Accepted 5 June 2013

Academic Editor: Jan E. Alam

Copyright © 2013 Igor Dremin et al. This is an open access article distributed under the Creative Commons Attribution License, which permits unrestricted use, distribution, and reproduction in any medium, provided the original work is properly cited.

A short review of the two recently analyzed collective effects in dense non-Abelian matter, the photon and dilepton production in nonequilibrium glasma and polarization properties of turbulent Abelian and non-Abelian plasmas, is given.

1. Introduction

Working out a quantitative description of the properties of dense strongly interacting matter produced in ultrarelativistic heavy ion collisions presents one of the most fascinating problems in high energy physics. The main goal of the present review is to expand an analysis of various properties of dense non-Abelian matter presented in [1] by discussing, in particular, several new topics [2–4], enriching our understanding of the early stages of ultrarelativistic heavy ion collisions.

The conceptually simplest way of organizing experimental information obtained at RHIC [5–8] and LHC [9–11] into a more or less coherent framework is to describe the late stages of these collisions in terms of standard relativistic hydrodynamical expansion of primordial quark-gluon matter that, after a short transient period, reaches sufficient level of local isotropization and equilibration allowing the usage of hydrodynamics in its standard form. In particular, the presence of strong elliptic flow suggests the picture of strongly coupled and, therefore, low viscosity matter. A detailed discussion of the corresponding issues can be found in, for example, reviews [12, 13] devoted to RHIC and LHC results, respectively. The collective effects can also become pronounced in high-multiplicity proton-proton collisions [14].

The actual physical picture is, most likely, much more complicated. In the absence of realistic mechanisms leading to extremely fast isotropization needed for describing the experimental data within the framework of standard hydro [15], the recent discussion [16–19] focused on building

a generalization of hydrodynamical approach on systems with anisotropic pressure that naturally arise in the glasma-based description of the physics of the early stages of heavy ion collisions [1, 20, 21]. Of particular interest are results of [18, 19] showing, within the AdS-CFT duality paradigm, that hydrodynamic description can be valid for unexpectedly large pressure gradients. The new paradigm of anisotropic hydrodynamics is, in our opinion, one of the most promising new approaches to the physics of high energy nuclear collisions.

At the most fundamental level a description of early stages of high energy nuclear collisions in the weak coupling regime is based on the idea that large gluon density and, correspondingly, large occupation numbers of low energy gluon modes make it natural to use tree-level Yang-Mills equations with sources in the strong field regime as a major building block for the theoretical description of ultrarelativistic nuclear collisions. At the early stage a strongly nonisotropic tree-level gluon field configuration arising immediately after collision, the glasma [20, 21] is formed. A very recent development [22] suggests that temporal evolution of glasma involves formation of a transient coherent object, the gluon condensate. This can have interesting experimental consequences, in particular for photon and dilepton production [2] discussed in Section 2.

The glasma is, however, unstable with respect to boost-noninvariant quantum fluctuations [23–25]. At later stages of its evolution these instabilities were shown to drive a system towards a state characterized by the turbulent Kolmogorov momentum spectrum of its modes [26]. The same

Kolmogorov spectrum was earlier discovered in a simplified scalar model of multiparticle production in heavy ion collisions [27, 28]. A possible relation between these instabilities and low effective viscosity in expanding geometry was recently discussed in [29].

The origin of the initial glasma instabilities and the physical picture underlying the turbulent-like glasma at later stages of its evolution, however, do still remain unclear. One possible scenario is that of the Weibel-type instabilities of soft field modes present both in QED and QCD plasma having their origin in the momentum anisotropy of hard sources [30–36] that eventually lead to the formation of the turbulent Kolmogorov cascade [37–40].

Of major importance to the physics of turbulent quantum field theory that provide another important benchmark for the physics of heavy ion collisions are also the fixed-box studies in the framework of classical statistical lattice gauge theory [41–43] and a study of the turbulent cascade in the isotropic QCD matter in [44]. Let us also note that there is no doubt that the genuinely stochastic nature of the classical Yang-Mills equation [45] should by itself play an important role in the physics of turbulent non-Abelian matter. The precise relation is however still to be studied.

The importance of turbulent effects, discussed in Section 3, makes it natural to study their effects on physically important quantities like shear viscosity. The corresponding calculation, discussed in Section 3.1 below was made in [46–48] in a setting generalizing the one used in the earlier studies of turbulent QED plasma [49, 50], in which turbulent plasma is described as a system of hard thermal modes and the stochastic turbulent fields characterized by some spatial and temporal correlation lengths. It was shown that plasma turbulence can serve as a natural source of the above-mentioned anomalous smallness of viscosity of strongly interacting matter created in high energy heavy ion collisions. The relation between the anomalously small viscosity of turbulent plasmas and anomalously large jet quenching in them [51] is described in Section 3.2.

The physics of turbulence, both in liquids [52–58] and plasma [59], is essentially that of space-time structures that appear at the event-by-event level and, after averaging, give rise to Kolmogorov (or, more generally, multifractal) scaling of the structure functions. The event-by-event stochastic inhomogeneity of turbulent plasma can therefore play an important role in forming its physical properties. In Section 3.3 we consider, following [3, 4], the turbulent contributions to the most fundamental physical characteristics of plasma, the properties of its collective modes, and plasmons for ultrarelativistic Abelian plasmas. The generalization of these results to the non-Abelian case is considered in Section 3.4. These results are new. The effects in question can broadly be described as nonlinear Landau damping [50]. One of the most interesting effects we see is a nonlinear Landau instability for transverse plasmons at large turbulent fields, that is, a phenomenon similar to nonlinear Landau damping. The origin of the phenomena considered in the paper is in the stochastic inhomogeneity of the turbulent electromagnetic fields in QED plasma; in this respect they are similar to the phenomenon of the stochastic transition radiation [60–62].

In particular, similarly to the stochastic transition radiation, the turbulent contributions to plasmon properties discussed in this paper vanish in the limit of vanishing correlation length of the stochastic turbulent fields. Finally, in Section 3.1, we consider the anomalous turbulent contributions to plasma viscosity [46–48].

2. Photons and Dileptons from Glasma

In this paragraph we will present, following [2], the main results on photon and dilepton production in glasma.

2.1. Thermalizing Glasma: Basic Facts. Let us first discuss the kinetic framework for glasma evolution as developed in [22]. Evolution of primordial non-Abelian matter produced in ultrarelativistic heavy ion collisions proceeds through several stages. A natural separation of scales is provided by the saturation momentum Q_{sat} . At earliest times $0 \leq t \sim 1/Q_{\text{sat}}$ the system can be described in terms of coherent chromoelectric and chromomagnetic flux tubes. The physics of this stage is that of gluons, so in terms of electromagnetic signals this stage is of no special interest. The density of quarks becomes substantial at times closer to the thermalization time t_{therm} , so in studying the nonequilibrium contributions to photon and dilepton production we will focus at the time interval $1/Q_{\text{sat}} \ll t \ll t_{\text{therm}}$.

Let us assume that the gluon momentum density f_g can be written in the following form:

$$f_g = \frac{\Lambda_s}{\alpha_s p} F_g \left(\frac{p}{\Lambda} \right), \quad (1)$$

where the infrared and ultraviolet momentum cutoffs Λ_s and Λ are defined as follows. Initially, at $t_0 \sim 1/Q_{\text{sat}}$, we have $\Lambda(t_0) = \Lambda_s(t_0) \sim Q_{\text{sat}}$, whereas at thermalization time $\Lambda_s(t_{\text{therm}}) \sim \alpha_s T_i$ and $\Lambda(t_{\text{therm}}) \sim T_i$. In estimating the physical cross-sections one can use the following simple parametrization of f_g as a function of the gluon energy E_g :

$$\begin{aligned} f_g(E_g) &= \text{const.}, & E_g < \Lambda_s, \\ f_g(E_g) &= \text{const.} \frac{\Lambda_s}{E_g}, & \Lambda_s < E_g < \Lambda, \\ f_g(E_g) &= 0, & E_g > \Lambda. \end{aligned} \quad (2)$$

A key physical point of primary importance for the physics of the early stage of heavy ion collisions is that the phase space for the gluons is initially overoccupied so that the number density of gluons n_g and their energy density ϵ_g are related by

$$\frac{n_g}{\epsilon_g^{3/4}} \sim \frac{1}{\alpha_s^{1/4}}, \quad (3)$$

while for a thermally equilibrated Bose system it is necessary that this ratio should be less than a number of the order 1. This fact is a basis for the hypothesis [22] that the “extra” gluonic degrees of freedom are hidden in the highly coherent

color singlet and spin singlet configuration that can be (approximately) described as a transient Bose condensate with a density

$$f_{\text{cond}} = n_{\text{cond}} \delta^3(p). \quad (4)$$

It is natural to think that the condensate is formed by gluons with masses of order of the natural infrared cutoff of the problem, the Debye mass:

$$M_{\text{Debye}}^2 \sim \Lambda \Lambda_s. \quad (5)$$

One of the key features arising in many problems related to physical properties of primordial strongly interacting matter in heavy ion collisions is the natural asymmetry between longitudinal and transverse degrees of freedom which in the problem under consideration is parametrized by the fixed asymmetry between the typical transverse and longitudinal pressures δ that can conveniently be parametrized by the relation between the longitudinal pressure P_L and energy density ϵ :

$$P_L = \delta \epsilon, \quad (6)$$

where $0 \leq \delta \leq 1/3$, with $\delta = 0$ and $\delta = 1/3$ corresponding to the free-streaming (thus maximal anisotropy between the longitudinal and transverse pressure) and the isotropic expansion, respectively. The pressure anisotropy does of course reflect the difference of characteristic scales of transverse and longitudinal momenta.

The time evolution of the scales Λ_s and Λ was found to be [22]

$$\begin{aligned} \Lambda_s &\sim Q_s \left(\frac{t_0}{t} \right)^{(4+\delta)/7}, \\ \Lambda &\sim Q_s \left(\frac{t_0}{t} \right)^{(1+2\delta)/7} \end{aligned} \quad (7)$$

which, in turn, leads to the following temporal evolution of the gluon density and Debye mass:

$$\begin{aligned} n_g &\sim \frac{Q_s^3}{\alpha_s} \left(\frac{t_0}{t} \right)^{(6+5\delta)/7}, \\ M_{\text{Debye}}^2 &\sim \Lambda \Lambda_s \sim Q_{\text{sat}}^2 \left(\frac{t_0}{t} \right)^{(5+3\delta)/7} \end{aligned} \quad (8)$$

and, finally, the thermalization time:

$$t_{\text{therm}} \sim t_0 \left(\frac{1}{\alpha_s} \right)^{7/(3-\delta)}. \quad (9)$$

The description of the model is completed by introducing the quark distribution function:

$$f_q = F_q \left(\frac{p}{\Lambda} \right) \quad (10)$$

and assuming, for simplicity, the proportionality between the condensate density and that of gluons [22]:

$$n_{\text{cond}} = \kappa n_{\text{gluon}}, \quad (11)$$

where κ is a constant of order 1.

2.2. Electromagnetic Particle Production from the Glasma. Let us start with deriving a rate of photon production from glasma. The standard expression for the fixed-box photon production rate from the Compton channel $gq \rightarrow \gamma q$ reads

$$\begin{aligned} E \frac{dN}{d^4x d^3p} &\propto F_q \left(\frac{E}{\Lambda} \right) \frac{1}{E} \int_{\mu^2}^{\infty} ds (s - \mu^2) \sigma_{gq \rightarrow \gamma q}(s) \\ &\times \int_{s/4E}^{\infty} dE_g f_g(E_g) \left[1 - F_q \left(\frac{E_g}{\Lambda} \right) \right], \end{aligned} \quad (12)$$

where E is the photon energy and \mathbf{p} its three-momentum. The lower limit for integration over gluon energy E_g follows from kinematics; μ^2 is an infrared cutoff needed to regularize the $t(u)$ channel singularity for diagrams with massless particle exchange which in our case is the Debye mass $\mu^2 = \Lambda \Lambda_s$, and $\sigma_{gq \rightarrow \gamma q}(s)$ is the cross-section for gluon Compton effect $gq \rightarrow \gamma q$.

In the high energy limit and for small quark densities F_q , (12) simplifies to

$$\begin{aligned} E \frac{dN}{d^4x d^3p} &\propto F_q \left(\frac{E}{\Lambda} \right) \frac{\Lambda_s \Lambda}{E} \int_1^{\infty} dy \ln y \int_{(y\Lambda_s, \Lambda)/4E}^{\infty} dE_g f_g(E_g). \end{aligned} \quad (13)$$

Using the explicit parametrization of gluon density equation (2), it is straightforward to obtain

$$E \frac{dN}{d^4x d^3p} \propto F_q \left(\frac{E}{\Lambda} \right) \Lambda \Lambda_s \phi \left(\frac{E}{\Lambda} \right), \quad (14)$$

where $\phi(E/\Lambda)$ is some analytically calculable function. Let us thus assume that the photon production rate from glasma is given by

$$\frac{dN}{d^4x dy d^2k_T} = \frac{\alpha}{\pi} \Lambda_s \Lambda g \left(\frac{E}{\Lambda} \right), \quad (15)$$

where y is the photon rapidity.

To obtain the overall rate, we need to integrate over longitudinal coordinates. We assume that the early time expansion is purely longitudinal and that, in the integration, the space-time rapidity is strongly correlated with that of the momentum space-rapidity. We then have that

$$\frac{dN}{d^2r_T dy d^2k_T} \sim \alpha \int t dt \Lambda_s \Lambda g \left(\frac{k_T}{\Lambda} \right). \quad (16)$$

Using the result of the previous section for the time dependence of the scales Λ and Λ_s , we get

$$t dt = \kappa' \frac{d\Lambda}{\Lambda} \frac{1}{Q_{\text{sat}}^2} \left(\frac{Q_{\text{sat}}}{\Lambda} \right)^{14/(1+2\delta)}. \quad (17)$$

The constant κ' is of order 1.

Doing the integration over Λ in (16), we find that

$$\frac{dN}{d^2r_T dy d^2k_T} \sim \alpha \left(\frac{Q_{\text{sat}}}{k_T} \right)^{(9-3\delta)/(1+2\delta)}. \quad (18)$$

Now integrating over d^2r_T and identifying the overlap cross-section as proportional to the number of participants, we finally obtain

$$\frac{dN_\gamma}{dyd^2k_T} = \alpha R_0^2 N_{\text{part}}^{2/3} \left(\frac{Q_{\text{sat}}}{k_T} \right)^\eta, \quad (19)$$

where $\eta = (9 - 3\delta)/(1 + 2\delta)$. The factor of $N_{\text{part}}^{2/3}$ arises because the number of participants in a collision is proportional to the nuclear volume $R^3 \sim N_{\text{part}}$, and R_0 is a constant with dimensions of a length. A detailed analysis [2] shows that the formula (19) should be valid for the transverse momenta in the interval $1 \text{ GeV} \leq k_T \leq 10 \text{ GeV}$. The analytical results are compared to RHIC data in Figure 1 (for details of the comparison see [2]).

From Figure 1 we see that our simple model provides a good description of the experimental data.

The analysis of dilepton production is more complicated because there are two sources of dileptons. The first is due to annihilation of quarks in the glasma. The expression for the static rate of production of dilepton pairs with invariant mass M for massless quarks and leptons reads

$$\begin{aligned} \frac{dN^{l+l}}{d^4x dM^2} &\sim M^2 \sigma_{q\bar{q} \rightarrow l+l} (M^2) \int_0^\infty dE_q F_q \left(\frac{E_q}{\Lambda} \right) \\ &\times \int_{M^2/4E_q}^\infty dE_{\bar{q}} F_{\bar{q}} \left(\frac{E_{\bar{q}}}{\Lambda} \right) \\ &= M^2 \sigma_{q\bar{q} \rightarrow l+l} (M^2) \Lambda^2 \\ &\times \int_0^\infty dy F_q(y) \int_{M^2/4\Lambda^2 y}^\infty dx F_q(x). \end{aligned} \quad (20)$$

Taking into account that $M^2 \sigma_{q\bar{q} \rightarrow l+l} (M^2) \sim \text{const.}$, we can already see the scaling behavior of the static dilepton production rate (24), that is,

$$\frac{dN^{l+l}}{d^4x dM^2} \sim \Lambda^2 \Phi \left(\frac{M}{\Lambda} \right) \quad (21)$$

with $\Phi(M/\Lambda) \equiv \int_0^\infty dy F_q(y) \int_{(M/\Lambda)^2/4y}^\infty dx F_q(x)$. To further explicitly demonstrate the scaling behavior of the static dilepton production rate (24), let us consider two examples with explicit forms of quark distribution function.

First let us consider a simple hard-cutoff quark distribution function $F_q = \theta(\Lambda - E)$. In this case we can easily obtain

$$\frac{dN^{l+l}}{d^4x dM^2} \sim \Lambda^2 \left[1 - \frac{(M/\Lambda)^2}{4} + \frac{(M/\Lambda)^2}{4} \ln \frac{(M/\Lambda)^2}{4} \right]. \quad (22)$$

Second let us consider an exponential quark distribution function $F_q = \exp(-E/\Lambda)$. In this case we get the following result:

$$\begin{aligned} \frac{dN^{l+l}}{d^4x dM^2} &\sim \Lambda^2 \sqrt{\frac{M^2}{\Lambda^2}} K_1 \left(\frac{M}{\Lambda} \right) \\ &= M \Lambda K_1 \left(\frac{M}{\Lambda} \right) \equiv \Lambda^2 \left[\frac{M}{\Lambda} K_1 \left(\frac{M}{\Lambda} \right) \right], \end{aligned} \quad (23)$$

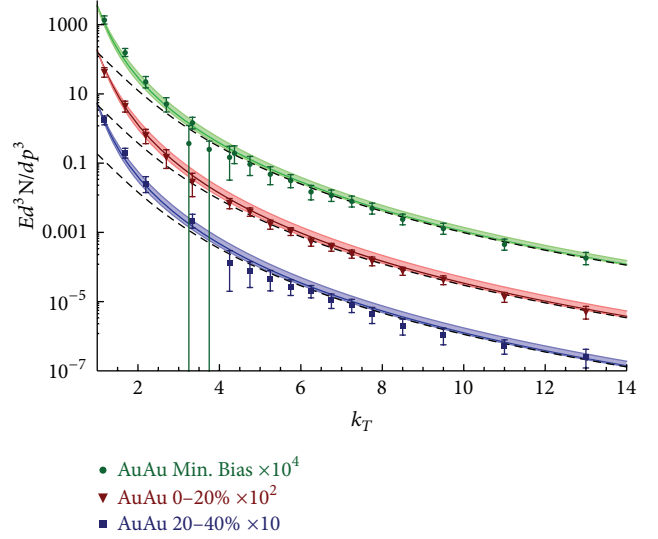


FIGURE 1: Comparison between the PHENIX photon data and the present model for three centrality bins [2]. The best fit corresponds to $\delta = 0.144 \pm 0.0045$. The parameter λ controls the x dependence of the saturation momentum with the best fit value $\lambda = 0.29 \pm 0.05$. For each of three color bands, the η (or δ) varies as $\eta = 6.65 \mp 0.60$ ($\delta \approx 0.144 \pm 0.045$) at $\lambda = 0.29$.

where $K_1(M/\Lambda)$ is a Bessel function. This leads to the simple conjecture for the dilepton rate due to the annihilation mechanism:

$$\frac{dN_{DY}}{d^4x dM^2} = \alpha^2 \Lambda^2 g' \left(\frac{M}{\Lambda} \right) \quad (24)$$

which, in the direct analogy with the above-described calculation for photons, leads to

$$\frac{dN_{DY}}{dy dM^2} \sim \alpha^2 R_0^2 N_{\text{part}}^{2/3} \left(\frac{Q_{\text{sat}}}{M} \right)^\eta \quad (25)$$

with $\eta = 4(3 - \delta)/(1 + 2\delta)$.

The second possible source of dileptons is the annihilation of gluons into a quark loop from which the quarks then subsequently decay into a virtual photon and eventually the dilepton: see the illustration in Figure 2. Such a virtual process is naively suppressed by factors of α_s . Here, however, the gluons arise from a highly coherent condensate, and the corresponding factors of α_s are compensated by inverse factors $1/\alpha_s$ from the coherence of the condensate. In other words, the usual power counting for diagrams in terms of α_s has to be changed when the coherent condensate with high occupation is present.

Here we estimate the rate for the three-gluon decay of the condensate into a dilepton. On dimensional grounds, we expect that

$$\frac{dN_{C \rightarrow DY}}{d^4x dy dM^2} = \alpha^2 \frac{(\alpha_s n_{\text{gluon}})^3}{M_{\text{Debye}}^7} g'' \left(\frac{M}{M_{\text{Debye}}} \right), \quad (26)$$

where we have assumed that the condensate density is of the order of the gluon number density as in (17) and that

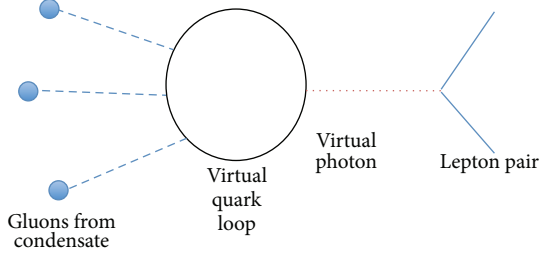


FIGURE 2: Three gluons from the condensate annihilate into a virtual quark loop, that subsequently decays into a virtual photon and then into a dilepton.

the typical scale for the energy of gluons in the condensate is of order of the Debye mass. Integration over time leads to

$$\frac{dN_{C \rightarrow DY}}{dydM^2} \sim \alpha^2 R_0'^2 N_{\text{part}}^{2/3} \left(\frac{Q_{\text{sat}}}{M} \right)^{\eta'}, \quad (27)$$

where

$$\eta'_{\text{perturbative}} = \frac{9(3-\delta)}{5+3\delta}. \quad (28)$$

The analytical results are compared to RHIC data in Figure 3 (for details of the comparison see [2]).

From Figure 3 we see that our simple model provides a good description of the experimental data.

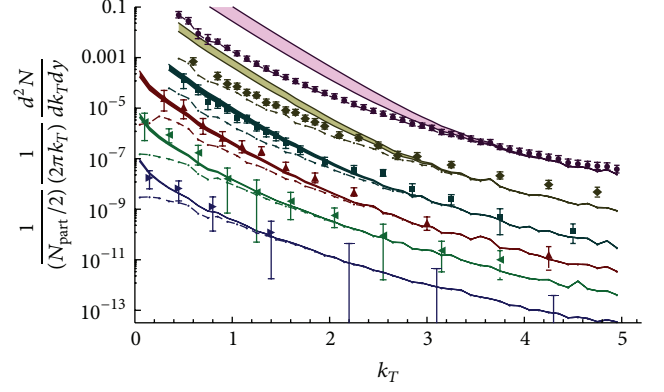
3. Turbulent Plasma

It is well known that experimentally observed physical properties of usual electromagnetic plasmas are dramatically different from predictions based on textbook equilibrium Vlasov plasma [49, 50]. A picture accommodating these observations is that of turbulent plasma, in which in addition to hard particles and soft self-consistent mean field there exist random electromagnetic fields leading, for example, to anomalously small viscosity and conductivity of turbulent plasma as compared to the equilibrium one. In this section we consider the key physical characteristics of turbulent ultrarelativistic plasma, its anomalously small viscosity [46–48], and anomalously large jet quenching [51] as well its polarization properties in the Abelian [3, 4] and non-Abelian cases.

3.1. Turbulent Anomalous Viscosity. One of the most important requirements for any scenario describing the relevant physics of the early stage of nuclear collisions is its ability of explaining an (effectively) small viscosity characterizing collective expansion of dense matter created in these collisions. Let us recall the standard kinetic theory expression for shear viscosity:

$$\eta = \frac{1}{3} n \langle p \rangle_T \lambda_f, \quad (29)$$

where n is the density of the medium, $\langle p \rangle_T$ is the thermal momentum of particles, and λ_f is the mean free path.



- $m_{ee} < 100 \text{ MeV}/c^2 \times 10^1$
- $200 \text{ MeV}/c^2 \leq m_{ee} < 300 \text{ MeV}/c^2 \times 10^0$
- ▲ $500 \text{ MeV}/c^2 \leq m_{ee} < 750 \text{ MeV}/c^2 \times 10^{-2}$
- ◆ $100 \text{ MeV}/c^2 \leq m_{ee} < 200 \text{ MeV}/c^2 \times 10^1$
- ▲ $300 \text{ MeV}/c^2 \leq m_{ee} < 500 \text{ MeV}/c^2 \times 10^{-1}$
- ▶ $810 \text{ MeV}/c^2 \leq m_{ee} < 990 \text{ MeV}/c^2 \times 10^{-3}$

FIGURE 3: (Color online) The comparison between the PHENIX dilepton data and the model [2]. Min. Bias Au + Au $\sqrt{s_{NN}} = 200 \text{ GeV}$. For each color band, the η' (or δ) varies as $\eta' \approx 4.73 \pm 0.20$ ($\delta = 0.144 \mp 0.045$) at $\lambda = 0.29$.

In the standard perturbative case the source of λ_f is perturbative scattering which is parametrically weak and, therefore, leads to very large values of λ_f and, consequently, shear viscosity η . The situation is dramatically different in turbulent plasmas [46–48], where particle scatters on strong turbulent fields. The physical picture is here that of plasma particles scattering on domains of coherent turbulent fields, the size of the domains being controlled by the corresponding correlation length l , so that

$$\lambda_f = \frac{\langle p \rangle_T^2}{g^2 Q^2 \langle B^2 \rangle l}, \quad (30)$$

leading to the anomalously small turbulent shear viscosity [46–48]

$$\eta_A \approx \frac{(9/4) s T^3}{g^2 Q^2 \langle B^2 \rangle l} \quad (31)$$

valid for the nearly equilibrated plasma.

3.2. Turbulent Jet Quenching. Another very attractive feature of the turbulent plasma scenario is its natural ability to describe the observed strong jet quenching, that is, large energy loss experienced by fast particles propagating through early QCD matter [51]. Indeed, it is easy to calculate transverse broadening $\langle (\Delta p_\perp)^2 \rangle$ induced by the same process of particle scattering on turbulent field domains and the corresponding (anomalous) jet quenching parameter \hat{q}_A :

$$\hat{q}_A = g^2 Q^2 \langle B^2 \rangle l. \quad (32)$$

Leading, in particular, to an interesting relation between the two above-discussed anomalous quantities [51]:

$$\frac{\eta_A}{s} \propto \frac{T^3}{\bar{q}_A}, \quad (33)$$

that is, the smaller is the anomalous turbulent viscosity, the large is the anomalous turbulent jet quenching.

3.3. Turbulent Polarization: QED Plasma. Let us first consider polarization properties of the turbulent ultrarelativistic QED plasma [3, 4]. A weakly turbulent plasma is described as perturbation of an equilibrated system of (quasi-)particles by weak turbulent fields $F_{\mu\nu}^T$. In the collisionless Vlasov approximation we employ, the plasma properties are defined by the following system of equations ($F_{\mu\nu}^R$ is a regular nonturbulent field):

$$\begin{aligned} p^\mu \left[\partial_\mu - eq (F_{\mu\nu}^R + F_{\mu\nu}^T) \frac{\partial}{\partial p_\nu} \right] f(p, x, q) &= 0, \\ \partial^\mu (F_{\mu\nu}^R + F_{\mu\nu}^T) &= j_\nu(x) = e \sum_{q,s} \int dp p_\nu q f(p, x, q). \end{aligned} \quad (34)$$

The stochastic ensemble of turbulent fields is assumed to be Gaussian and characterized by the following correlators:

$$\langle F_{\mu\nu}^T \rangle = 0, \quad \langle F^{T\mu\nu}(x) F^{T\mu'\nu'}(y) \rangle = K^{\mu\nu\mu'\nu'}(x, y). \quad (35)$$

Following [46–48] we use the parametrization of $K^{\mu\nu\mu'\nu'}(x, y)$ of the form

$$K^{\mu\nu\mu'\nu'}(x) = K_0^{\mu\nu\mu'\nu'} \exp \left[-\frac{t^2}{2\tau^2} - \frac{r^2}{2a^2} \right]. \quad (36)$$

By definition, turbulent polarization is defined as a response to a regular perturbation that depends on turbulent fields. In the linear response approximation it is fully described by the polarization tensor $\Pi^{\mu\nu}(k)$ which can be computed by taking a variational derivative of the averaged induced current $\langle j^\mu(k | F^R, F^T) \rangle_{F^T}$ over the regular gauge potential A_ν^R :

$$\Pi^{\mu\nu}(k) = \frac{\delta \langle j^\mu(k | F^R, F^T) \rangle_{F^T}}{\delta A_\nu^R}, \quad (37)$$

$$\langle j^\mu(k | F^R, F^T) \rangle_{F^T} = e \sum_{q,s} \int dP p_\nu q \langle \delta f(p, k, q | F^R, F^T) \rangle_{F^T}. \quad (38)$$

To organize the calculation in the efficient way it is useful to rewrite (34) as follows:

$$f = f^{eq} + G p^\mu F_{\mu\nu} \partial_p^\mu f, \quad G \equiv \frac{eq}{i((pk) + i\epsilon)}, \quad (39)$$

where f^{eq} is a distribution function characterizing the original nonturbulent plasma and introduces the following systematic expansion in the turbulent and regular fields:

$$\begin{aligned} \delta f &= \sum_{m=0} \sum_{n=0} \rho^m \tau^n \delta f_{mn}, \\ F^{\mu\nu} &= \sum_{m=0} \sum_{n=0} \rho^m \tau^n F_{mn}^{\mu\nu}, \end{aligned} \quad (40)$$

where powers of ρ count those of F^R and powers of τ count those of F^T . Turbulent polarization is described by contributions of the first order in the regular and the second in the turbulent fields. The lowest nontrivial contribution to the induced current (38) is thus given by δf_{12} :

$$\delta f \simeq \delta f_{\text{HTL}} + \langle \delta f_{12} \rangle_I + \langle \delta f_{12} \rangle_{\text{II}}, \quad (41)$$

where

$$\begin{aligned} \delta f_{\text{HTL}} &= G p_\mu F_{10}^{\mu\nu} \partial_{\mu,p} f^{eq}, \\ \langle \delta f_{12} \rangle_I &= G p_\mu \langle F_{01}^{\mu\nu} \partial_{\nu,p} G p_{\mu'} F_{10}^{\mu'\nu'} \partial_{\nu',p} G p_\rho F_{01}^{\rho\sigma} \rangle \partial_{\sigma,p} f^{eq}, \\ \langle \delta f_{12} \rangle_{\text{II}} &= G p_\mu \langle F_{01}^{\mu\nu} \partial_{\nu,p} G p_{\mu'} F_{01}^{\mu'\nu'} \partial_{\nu',p} G p_\rho F_{10}^{\rho\sigma} \rangle \partial_{\sigma,p} f^{eq}. \end{aligned} \quad (42)$$

Generically one has the following decomposition of the polarization tensor:

$$\begin{aligned} \Pi_{ij}(\omega, \mathbf{k}; l) &= \left(\delta_{ij} - \frac{k_i k_j}{k^2} \right) \Pi_T(\omega, |\mathbf{k}|; l) + \frac{k_i k_j}{k^2} \Pi_L(\omega, |\mathbf{k}|; l), \end{aligned} \quad (43)$$

where $l \equiv \sqrt{2}(\tau a) / \sqrt{\tau^2 + a^2}$. In the leading order in turbulent fields its components can be rewritten as sums of the leading hard thermal loops (HTL) contributions and the gradient expansion in the scale of turbulent fluctuations l :

$$\Pi_{L(T)}(\omega, \mathbf{k}; l) = \Pi_{L(T)}^{\text{HTL}}(\omega, \mathbf{k}) + \Pi_{L(T)}^{\text{turb}}(\omega, \mathbf{k} | l),$$

$$\begin{aligned} \Pi_{L(T)}^{\text{turb}}(\omega, |\mathbf{k}|; l) &= \sum_{n=1}^{\infty} \frac{(|\mathbf{k}| l)^n}{k^2} \left[\phi_{L(T)}^{(n)}(x) \langle E_{\text{turb}}^2 \rangle + \chi_{L(T)}^{(n)}(x) \langle B_{\text{turb}}^2 \rangle \right], \end{aligned} \quad (44)$$

where $x = \omega/|\mathbf{k}|$, and the HTL contributions to the polarization tensor read

$$\Pi_L^{\text{HTL}}(\omega, |\mathbf{k}|) = -m_D^2 x^2 \left[1 - \frac{x}{2} L(x) \right],$$

$$\Pi_T^{\text{HTL}}(\omega, |\mathbf{k}|) = m_D^2 \frac{x^2}{2} \left[1 + \frac{1}{2x} (1 - x^2) L(x) \right], \quad (45)$$

$$L(x) \equiv \ln \left| \frac{1+x}{1-x} \right| - i\pi\theta(1-x); \quad m_D^2 = \frac{e^2 T^2}{3}.$$

The computation of turbulent polarization was carried out to second order in the gradient expansion [3, 4]. To the leading order in the gradient expansion one gets

$$\begin{aligned}
\phi_{IT}^{(1)}(x) &= \frac{ie^4}{6\pi\sqrt{\pi}} 2x \left[\frac{4 + 10x^2 - 6x^4}{3(1-x^2)} + x(1-x^2)L(x) \right], \\
\phi_{IL}^{(1)}(x) &= -\frac{ie^4}{6\pi\sqrt{\pi}} \frac{8x^3}{3(1-x^2)^2}, \\
\chi_{IT}^{(1)}(x) &= \frac{ie^4}{6\pi\sqrt{\pi}} 4x \left[\frac{-2 + 6x^2}{3(1-x^2)} + xL(x) \right], \\
\chi_{IL}^{(1)}(x) &= -\frac{ie^4}{6\pi\sqrt{\pi}} \frac{8x^3}{3(1-x^2)^2}.
\end{aligned} \tag{46}$$

Let us first discuss the turbulent contributions to the imaginary part of the polarization tensor [3, 4]. These can be summarized as follows. The sign of the imaginary part of the turbulent contribution to the polarization operator in the time-like domain $x > 1$ is negative and corresponds to turbulent damping of time-like collective excitations. This refers to both transverse and longitudinal modes. As the HTL contribution in this domain is absent, this turbulent damping is a universal phenomenon present for all ω, k such that $\omega > k$ and all values of the parameters involved ($l, \langle B^2 \rangle, \langle E^2 \rangle$). The turbulent damping leads to an attenuation of the propagation of collective excitations at some characteristic distance. The situation in the space-like domain $x < 1$ is more diverse. In contrast with the time-like domain the gradient expansion for the imaginary part of the polarization tensor starts from the negative HTL contribution corresponding to Landau damping. The imaginary parts of turbulent contributions to the longitudinal polarization tensor are negative and are thus amplifying the Landau damping. The most interesting contributions come from the turbulent contributions to the transverse polarization tensor. The electric contribution $\text{Im}[\phi_T^{(1)}(x)]$ in the space-like domain is positive at all x while the magnetic contribution $\text{Im}[\chi_T^{(1)}(x)]$ is negative for $x < x^* \approx 0.43$ and positive for $x > x^*$. This means that the turbulent plasma becomes unstable for sufficiently strong turbulent fields.

It is also of interest to analyze the effects of turbulence on the properties of collective excitations of QED plasma, the plasmons [4]. The plasmons are characterized by dispersion relations $\omega_{T(L)}(|\mathbf{k}|)$ that are read from the solutions of dispersion equation for the corresponding components of dielectric permittivity, which are just a real part of zeroes of inverse transverse and longitudinal wave propagators:

$$\text{Re} \left[\mathbf{k}^2 \left(1 - \frac{\Pi_L(k^0, |\mathbf{k}|)}{\omega^2} \right) \Big|_{k^0=\omega_L(|\mathbf{k}|)} \right] = 0, \tag{47}$$

$$\text{Re} \left[\mathbf{k}^2 - (k^0)^2 + \Pi_T(k^0, |\mathbf{k}|) \Big|_{k^0=\omega_T(|\mathbf{k}|)} \right] = 0.$$

Thus, real part of polarization tensor corresponds to propagation of plasmons in a medium, while its imaginary part defines plasmon smearing.

Let us focus first on a shift of plasmons dispersion relations in turbulent medium. In general dispersion equations can be solved only numerically. Analytical expressions can be obtained in certain limits. Let us focus on the deeply time-like regime of $x \gg 1$. In nonturbulent HTL Vlasov plasma the time-like plasmon modes do not decay, since imaginary part of polarization tensor in that limit is zero. For frequencies $(k/\omega_{pl}) \ll 1$ the corresponding solutions of dispersion equations may be expanded as powers of $|\mathbf{k}|/\omega_{pl}$:

$$\begin{aligned}
\omega_L^2(|\mathbf{k}|)_{\text{HTL}} &= \omega_{pl}^2 \left(1 + \frac{3}{5} \left(\frac{|\mathbf{k}|}{\omega_{pl}} \right)^2 + O \left(\left(\frac{|\mathbf{k}|}{\omega_{pl}} \right)^4 \right) \right), \\
\omega_T^2(|\mathbf{k}|)_{\text{HTL}} &= \omega_{pl}^2 \left(1 + \frac{6}{5} \left(\frac{|\mathbf{k}|}{\omega_{pl}} \right)^2 + O \left(\left(\frac{|\mathbf{k}|}{\omega_{pl}} \right)^4 \right) \right),
\end{aligned} \tag{48}$$

where we have used a standard definition for the plasma frequency $\omega_{pl}^2 = m_D^2/3$.

In a turbulent plasma plasmons decay even in a Vlasov limit since polarization tensor has imaginary part. As to the turbulent modifications of the HTL dispersion relation (48), it can be conveniently written as

$$\begin{aligned}
\omega_L^2(|\mathbf{k}|)_{\text{turb}} &= (\omega_{plL}^{\text{turb}})^2 \left(1 + \frac{3}{5} y_L^2 \right) - \frac{e^4 l^2}{6\pi^2} \left(\frac{24}{5} \langle E^2 \rangle + \frac{64}{15} \langle B^2 \rangle \right) y_L^2 \\
&\quad + O(y_L^4), \\
\omega_T^2(|\mathbf{k}|)_{\text{turb}} &= (\omega_{plT}^{\text{turb}})^2 \left(1 + \frac{3}{5} y_T^2 \right) - \frac{e^4 l^2}{6\pi^2} \left(\frac{24}{7} \langle E^2 \rangle + \frac{32}{15} \langle B^2 \rangle \right) y_T^2 \\
&\quad + O(y_T^4),
\end{aligned} \tag{49}$$

where

$$\begin{aligned}
y_L &= \frac{|\mathbf{k}|}{\omega_{plL}^{\text{turb}}}, \quad y_T = \frac{|\mathbf{k}|}{\omega_{plT}^{\text{turb}}}, \\
(\omega_{plL}^{\text{turb}})^2 &= \omega_{plL}^2 - \frac{e^4 l^2}{6\pi^2} \left(\frac{16}{3} \langle E^2 \rangle + \frac{8}{3} \langle B^2 \rangle \right), \\
(\omega_{plT}^{\text{turb}})^2 &= \omega_{plT}^2 - \frac{e^4 l^2}{6\pi^2} \left(\frac{128}{15} \langle E^2 \rangle + \frac{8}{3} \langle B^2 \rangle \right).
\end{aligned} \tag{50}$$

Now let us consider the plasmon smearing. It can be easily seen that a rate of decay for plasmons is connected to the imaginary part of polarization tensor by a formula:

$$\Gamma_{T(L)} = \sqrt{-\text{Im}(\Pi_{T(L)})}. \tag{51}$$

In the time-like region considered previously the imaginary parts of both transverse and longitudinal components of

polarization tensor are negative so that there is no instability for time-like modes. It should also be noted that turbulent smearing is a leading order effect in (kl) as compared to the turbulent modification of plasmon dispersion relations.

3.4. Turbulent Polarization: QCD Plasma. Let us now discuss a generalization of the results of [3, 4] on the polarization properties on the non-Abelian QCD plasma.

The generalization of (34) to the non-Abelian case reads

$$p^\mu \left[\partial_\mu - g f_{abc} A_\mu^b Q^c \frac{\partial}{\partial Q^a} - g Q_a F_{\mu\nu}^a \frac{\partial}{\partial p_\nu} \right] = 0, \quad (52)$$

where the fields $F_{\mu\nu}$ satisfy the Yang-Mills equations:

$$D^\mu F_{\mu\nu}^a = j_\nu^a. \quad (53)$$

The main distinction from the Abelian case is the dependence of the distribution function on the color spin Q , where for $SU(3)Q = (Q^1, Q^2, \dots, Q^8)$, so that $f(x, p, Q)$. The components of color spin $Q = (Q^1, Q^2, \dots, Q^8)$ are dynamic variables satisfying the Wong equation:

$$\frac{dQ^a}{d\tau} = -g f^{abc} p^\mu A_\mu^b Q^c \quad (54)$$

which, with (52), (53), completes the dynamical description of QCD plasma.

The description of the properties of turbulent QCD plasma is based on separating the regular and turbulent contributions of the distribution functions and gauge potentials A_μ^a :

$$f = f^R + f^T, \quad A_\mu^a = A_\mu^{Ra} + A_\mu^{Ta}, \quad (55)$$

where we assume that $\langle A_\mu^a \rangle = A_\mu^{Ra}$ and $\langle A_\mu^{Ta} \rangle = 0$.

It is possible to define gauge transformations of regular and turbulent gauge potentials in such a way that

$$\begin{aligned} \delta A_\mu^{Ra} &= \partial_\mu \alpha^a + g f^{abc} A_\mu^{Rb} \alpha^c, \\ \delta A_\mu^{Ta} &= g f^{abc} A_\mu^{Tb} \alpha^c \end{aligned} \quad (56)$$

which is technically equivalent to choosing the background field gauge. A very useful property following from this choice is that the basic property of turbulent fields $\langle A_\mu^{Ta} \rangle = 0$ is gauge invariant. The corresponding decomposition of gauge field strength reads

$$F_{\mu\nu}^a = F_{\mu\nu}^{Ra} + \mathbf{F}_{\mu\nu}^{Ta} + \mathcal{F}_{\mu\nu}^{Ta}, \quad (57)$$

where

$$\begin{aligned} F_{\mu\nu}^{Ra} &= \partial_\mu A_\nu^{Ra} - \partial_\nu A_\mu^{Ra} + g f^{abc} A_\mu^{Rb} A_\nu^{Rc}, \\ \mathcal{F}_{\mu\nu}^{Ta} &= \partial_\mu A_\nu^{Ta} - \partial_\nu A_\mu^{Ta} + g f^{abc} A_\mu^{Tb} A_\nu^{Tc}, \\ \mathbf{F}_{\mu\nu}^{Ta} &= g f^{abc} (A_\mu^{Tb} A_\nu^{Rc} + A_\mu^{Rb} A_\nu^{Tc}). \end{aligned} \quad (58)$$

The computation of polarization properties proceeds through expanding f^R, f^T in a series in the regular potential ($f^{(0)} \sim (A^R)^0, f^{(1)} \sim (A^R)^1, \dots$). Assuming $f^{R(0)}(x, p, Q) = f^{eq}(p)$, we have

$$(p^\mu \partial_\mu) f^{T(0)} = g p^\mu Q_a \mathcal{F}_{\mu\nu}^{Ta} \frac{\partial}{\partial p_\nu} f^{R(0)}. \quad (59)$$

The corresponding equations for the first-order turbulent contributions to the distribution function read

$$\begin{aligned} (p^\mu \partial_\mu) f^{T(1)} &= g p^\mu f^{abc} A_\mu^{Tb} Q^c \frac{\partial}{\partial Q^a} f^{R(1)} \\ &+ g^2 p^\mu f^{abc} A_\mu^{Rb} Q^c \frac{1}{(p\partial)} p^{\mu'} \mathcal{F}_{\mu'\nu}^{Ta} \frac{\partial}{\partial p_\nu} f^{R(0)} \\ &+ g p^\mu Q_a \mathbf{F}_{\mu\nu}^{Ta} \frac{\partial}{\partial p_\nu} f^{R(0)} + g p^\mu Q_a \mathcal{F}_{\mu\nu}^{Ta} \frac{\partial}{\partial p_\nu} f^{R(1)} \\ &+ g^2 p^\mu p^\nu p'^\mu Q^a F_{\mu\nu}^{Ra} \frac{\partial}{\partial p_\nu} \frac{1}{(p^\mu \partial_\mu)} Q_c \mathcal{F}_{\mu'\nu'}^{Tc} \frac{\partial}{\partial p_{\nu'}} f^{R(0)} \\ &+ g^2 p^\mu f^{abc} A_\mu^{Rb} Q^c \frac{\partial}{\partial Q^a} \frac{1}{(p^\mu \partial_\mu)} p_d^{\mu'} \mathcal{F}_{\mu'\nu}^{Td} \frac{\partial}{\partial p_{\mu\nu}} f^{R(0)}, \end{aligned} \quad (60)$$

$$\begin{aligned} (p^\mu \partial_\mu) f^{R(1)} &= g p^\mu f^{abc} \left\langle A_\mu^{Tb} Q^c \frac{\partial}{\partial Q^a} f^{T(1)} \right\rangle \\ &+ g p^\mu Q_a \left\langle \mathcal{F}_{\mu\nu}^{Ta} \frac{\partial}{\partial p_\nu} f^{T(1)} \right\rangle + g p^\mu Q_a \left\langle \mathbf{F}_{\mu\nu}^{R} \frac{\partial}{\partial p_\nu} f^{T(0)} \right\rangle \\ &+ g p^\mu Q_a F_{\mu\nu}^{Ra} \frac{\partial}{\partial p_\nu} f^{R(0)}. \end{aligned} \quad (61)$$

Substituting (59) and (60) to (61) one arrives at the final expression for the first-order regular correction to the distribution function. A detailed analysis shows that in the relevant long wavelength limit we are left with only two contributions:

$$f^{R(1)} = \text{HTL} + I_1 + I_2, \quad (62)$$

where

$$\begin{aligned} I_1 &= g^3 p^\mu f^{abc} \\ &\times \left\langle A_\mu^{Tb} Q^c \frac{\partial}{\partial Q^a} p^{\mu'} \frac{1}{p^\mu \partial_\mu} f^{def} A_{\mu'}^{Re} Q^f \right. \\ &\quad \times \left. \frac{\partial}{\partial Q^d} \frac{1}{p^\mu \partial_\mu} p^{\mu'} Q_g \mathcal{F}_{\mu'\nu} \right\rangle \\ &\times \frac{\partial}{\partial p_\nu} f^{R(0)}, \end{aligned}$$

$$I_2 = g^2 p^\mu f^{abc} \times \left\langle A_\mu^{Tb} Q^c \frac{\partial}{\partial Q^a} \frac{1}{(p^\mu \partial_\mu)} p^{\mu'} Q_a F_{\mu'\nu}^{Td} \right\rangle \frac{\partial}{\partial p_\nu} f^{R(0)}. \quad (63)$$

Averaging over the stochastic color fields involves two two-point correlators:

$$\begin{aligned} \langle A_\mu^{Ta}(x) A_\nu^{Tb}(y) \rangle &= G_{\mu\nu}^{ab}(x, y), \\ \langle \mathcal{F}_{\mu\nu}^{Ta}(x) U^{ab}(x, y) \mathcal{F}_{\mu'\nu'}^{Tb}(y) \rangle &= K_{\mu\nu\mu'\nu'}^{ab}(x, y). \end{aligned} \quad (64)$$

We will restrict our consideration to the plasma which is on average homogeneous, $K_{\mu\nu\mu'\nu'}^{Ta}(x, y) = K_{\mu\nu\mu'\nu'}^{Ta}(x - y)$ (same for $G_{\mu\nu}^{ab}$), and assume that the stochastic correlators are symmetric under permutations of both color and Lorentz indices.

Let us choose the following explicit parametrization for the non-Abelian correlation function $G_{\mu\nu}^{ab}$:

$$G_{\mu\nu}^{ab} = \delta_{ab} \left[g_{\mu\nu} g_{\nu 0} \langle A_0^2 \rangle + \frac{1}{3} \hat{\delta}_{\mu\nu} \langle \mathbf{A}^2 \rangle \right] \exp \left[-\frac{r^2}{2a^2} - \frac{t^2}{2\tau^2} \right]. \quad (65)$$

Defining $f^{Ra(1)}(x, p) = \int Q^a dQ f^{R(1)}(x, p, Q)$, we get

$$\left[(p^\mu \partial_\mu) + p\gamma \right] f^{R(1)} = \int Q^l dQ (\text{HTL} + I_1 + I_2), \quad (66)$$

where

$$\gamma = g^2 \frac{N^2 - 1}{4N} \sqrt{\pi} l \left[\langle A_0^2 \rangle + \left\langle \frac{1}{3} \mathbf{A}^2 \right\rangle \right] \quad (67)$$

and $l = 1/\sqrt{(1/2a^2) + (1/2\tau^2)}$. Let us stress that only the sum of contributions from HTL, I_1 , and I_2 , is gauge invariant.

Detailed calculations show that to the leading order there is no contribution from the non-Abelian correlator $G_{\mu\nu}^{ab}$, so that the only modification distinguishing QCD plasma from the QED one is an overall normalization so that

$$\begin{aligned} \phi_{T,L}(x) &\longrightarrow C_{q(g)} \phi_{T,L}(x), \\ \chi_{T,L}(x) &\longrightarrow C_{q(g)} \chi_{T,L}(x), \end{aligned} \quad (68)$$

where for quarks

$$C_q = g^4 N_q \frac{N^2 - 1}{4N} \quad (69)$$

and for gluons

$$C_g = \frac{2g^3 N^2}{N + (N_q/2)}, \quad (70)$$

where we have taken into account a necessity of introducing an infrared cutoff at m_D when computing the integral $\int dp(df/dp)$ for massless bosons.

From the above analysis we can conclude that, apart from trivial color factors, in the considered approximation, the properties of the turbulent non-Abelian plasma are equivalent to those of the Abelian one.

4. Conclusions

In the present paper we have reviewed several results related to the important role played by collective effects in the physics of heavy ion collisions and, more broadly, dense non-Abelian matter. The results on anomalous viscosity [46–48] and anomalous jet quenching [51] are not new and are included for making the discussion of the properties of turbulent ultrarelativistic plasma self-contained. The main emphasis is made on new results on photon and dilepton production in glasma [2], polarization properties of ultrarelativistic Abelian [3, 4] and non-Abelian turbulent plasmas.

Discussing electromagnetic signals originating from glasma and, possibly, gluon condensate we have demonstrated that the unusual properties of photon and dilepton spectra observed at RHIC can naturally be described by taking into account collective gluon degrees of freedom.

The analysis of polarization properties of Abelian [3, 4] and non-Abelian ultrarelativistic turbulent plasmas revealed interesting structure of turbulent contributions to both imaginary and real parts of the polarization tensor and, correspondingly, to the plasmon properties. In particular, we have described an interesting instability of turbulent plasma for strong enough turbulent fields and have shown that the polarization properties of turbulent non-Abelian plasmas are, up to the trivial color factors, in the considered approximation equivalent to those of the Abelian one.

With a wealth of new experimental data and theoretical ideas the physics of high energy heavy ion collisions remains a truly exciting domain of research. We are sure that in the near future we will see rapid progress both in the quality of experimental data and that of theoretical research.

References

- [1] I. M. Dremin and A. V. Leonidov, “The quark-gluon medium,” *Physics-Uspekhi*, vol. 53, no. 11, pp. 1123–1149, 2010.
- [2] M. Chiu, T. K. Hemmick, V. Khachatryan, A. Leonidov, J. Liao, and L. McLerran, “Production of photons and dileptons in the Glasma,” *Nuclear Physics A*, vol. 900, p. 16, 2013.
- [3] M. Kirakosyan, A. Leonidov, and B. Müller, “Turbulence-induced instabilities in EP and QGP,” *Acta Physica Polonica B*, vol. 6, p. 403, 2013.
- [4] M. Kirakosyan, A. Leonidov, and B. Müller, “On collective properties of turbulent QED plasma,” <http://arxiv.org/abs/1305.4414>.
- [5] I. Arsene, I. G. Bearden, D. Beavis et al., “Quark-gluon plasma and color glass condensate at RHIC? The perspective from the BRAHMS experiment,” *Nuclear Physics A*, vol. 757, p. 1, 2005.
- [6] B. B. Back, M. D. Baker, M. Ballintijn et al., “The PHOBOS perspective on discoveries at RHIC,” *Nuclear Physics A*, vol. 757, p. 28, 2005.
- [7] J. Adams, M. M. Aggarwal, Z. Ahammed et al., “Experimental and theoretical challenges in the search for the quark-gluon plasma: the STAR Collaboration’s critical assessment of the evidence from RHIC collisions,” *Nuclear Physics A*, vol. 757, p. 102, 2005.
- [8] K. Adcox, S. S. Adler, S. Afanasie et al., “Formation of dense partonic matter in relativistic nucleus-nucleus collisions at RHIC: experimental evaluation by the PHENIX Collaboration,” *Nuclear Physics A*, vol. 757, p. 184, 2005.

- [9] K. Aamodt, B. Abelev, A. A. Quintana et al., “Elliptic flow of charged particles in Pb-Pb collisions at $\sqrt{s_{NN}} = 2.76$ TeV,” *Physical Review Letters*, vol. 105, Article ID 252302, 11 pages, 2010.
- [10] G. Aad, “Measurement of the pseudorapidity and transverse momentum dependence of the elliptic flow of charged particles in lead-lead collisions at $\sqrt{s_{NN}} = 2.76$ TeV with the ATLAS detector,” *Physics Letters B*, vol. 707, no. 3-4, pp. 330–348, 2012.
- [11] C. M. S. Collaboration, “Azimuthal correlations of charged hadrons in Pb+Pb collisions at $\sqrt{s_{NN}} = 2.76$ TeV,” Tech. Rep. CMS PAS HIN-10-002, 2013.
- [12] U. W. Heinz, “Thermalization at RHIC,” *AIP Conference Proceedings*, vol. 739, 18 pages, 2005.
- [13] B. Müller, J. Schukraft, and B. Wyslouch, “First results from Pb+Pb collisions at the LHC,” *Annual Review of Nuclear and Particle Science*, vol. 62, pp. 361–386, 2012.
- [14] CMS Collaboration, “Jet properties in low and high multiplicity events in pp collisions at $\sqrt{s_{NN}} = 2.76$ TeV,” Tech. Rep. CMS-PAS-FSQ-12-022, 2013.
- [15] C. Gale, S. Jeon, B. Schenke, P. Tribedy, and R. Venugopalan, “Event-by-event anisotropic flow in heavy-ion collisions from combined Yang-Mills and viscous fluid dynamics,” *Physical Review Letters*, vol. 110, no. 1, Article ID 012302, 5 pages, 2013.
- [16] R. Ryblewski, “Collective phenomena in the early stages of relativistic heavy ion collisions,” <http://arxiv.org/pdf/1305.3812.pdf>.
- [17] W. Florkowski, M. Martinez, R. Ryblewski, and M. Strickland, “Anisotropic hydrodynamics—basic concepts,” in *Proceedings of the Xth Quark Confinement and the Hadron Spectrum, PoS(Confinement X) 221*, Munich, Germany, Octobre 2012.
- [18] M. Heller, R. A. Janik, and P. Witaszyk, “Characteristics of thermalization of boost-invariant plasma from holography,” *Physical Review Letters*, vol. 108, no. 20, Article ID 201602, 2012.
- [19] M. Heller, R. A. Janik, and P. Witaszyk, “Numerical relativity approach to the initial value problem in asymptotically anti-de Sitter spacetime for plasma thermalization: an ADM formulation,” *Physical Review D*, vol. 85, no. 12, Article ID 126002, 2012.
- [20] A. Kovner, L. McLerran, and H. Weigert, “Gluon production from non-Abelian Weizsäcker-Williams fields in nucleus-nucleus collisions,” *Physical Review D*, vol. 52, no. 11, pp. 6231–6237, 1995.
- [21] T. Lappi and L. McLerran, “Some features of the glasma,” *Nuclear Physics A*, vol. 772, no. 3-4, pp. 200–212, 2006.
- [22] J.-P. Blaizot, F. Gelis, J. Liao, L. McLerran, and R. Venugopalan, “Bose-Einstein condensation and thermalization of the quark-gluon plasma,” *Nuclear Physics A*, vol. 873, pp. 68–80, 2012.
- [23] P. Romatschke and R. Venugopalan, “Collective non-abelian instabilities in a melting color glass condensate,” *Physical Review Letters*, vol. 96, no. 6, Article ID 062302, 2006.
- [24] P. Romatschke and R. Venugopalan, “Signals of a Weibel instability in the melting color glass condensate,” *The European Physical Journal A*, vol. 29, no. 1, pp. 71–75, 2006.
- [25] P. Romatschke and R. Venugopalan, “The unstable glasma,” *Physical Review D*, vol. 74, no. 4, Article ID 045011, 13 pages, 2006.
- [26] K. Fukushima and F. Gelis, “The evolving Glasma,” *Nuclear Physics A*, vol. 874, pp. 108–129, 2012.
- [27] K. Dusling, T. Epelbaum, F. Gelis, and R. Venugopalan, “Role of quantum fluctuations in a system with strong fields: Onset of hydrodynamical flow,” *Nuclear Physics A*, vol. 850, no. 1, pp. 69–109, 2011.
- [28] T. Epelbaum and F. Gelis, “Role of quantum fluctuations in a system with strong fields: Spectral properties and thermalization,” *Nuclear Physics A*, vol. 872, no. 1, pp. 210–244, 2011.
- [29] K. Dusling, T. Epelbaum, F. Gelis, and R. Venugopalan, “Instability induced pressure isotropization in a longitudinally expanding system,” *Physical Review D*, vol. 86, no. 8, Article ID 085040, 19 pages, 2012.
- [30] E. S. Weibel, “Spontaneously growing transverse waves in a plasma due to an anisotropic velocity distribution,” *Physical Review Letters*, vol. 2, no. 3, pp. 83–84, 1959.
- [31] S. Mrowczynski, “Stream instabilities of the quark-gluon plasma,” *Physics Letters B*, vol. 214, no. 4, pp. 587–590, 1988.
- [32] Y. E. Pokrovsky and A. V. Selikhov, “Filamentation in a quark-gluon plasma,” *JETP Letters*, vol. 47, pp. 12–14, 1988.
- [33] S. Mrowczynski, “Plasma instability at the initial stage of ultrarelativistic heavy-ion collisions,” *Physics Letters B*, vol. 314, no. 1, pp. 118–121, 1993.
- [34] S. Mrowczynski, “Color filamentation in ultrarelativistic heavy-ion collisions,” *Physics Letters B*, vol. 393, no. 1-2, pp. 26–30, 1997.
- [35] P. Arnold, J. Lenaghan, and G. D. Moore, “QCD plasma instabilities and bottom-up thermalization,” *Journal of High Energy Physics*, vol. 08, article 002, 2003.
- [36] P. Arnold, J. Lenaghan, G. D. Moore, and L. G. Yaffe, “Apparent thermalization due to plasma instabilities in the quark-gluon plasma,” *Physical Review Letters*, vol. 94, no. 7, Article ID 072302, 2005.
- [37] A. Kurkela and G. D. Moore, “Thermalization in weakly coupled nonabelian plasmas,” *Journal of High Energy Physics*, vol. 1112, article 44, 2011.
- [38] A. Kurkela and G. D. Moore, “Bjorken flow, plasma instabilities, and thermalization,” *Journal of High Energy Physics*, vol. 1204, article 120, 2012.
- [39] A. Ipp, A. Rebhan, and M. Strickland, “Non-Abelian plasma instabilities: SU(3) versus SU(2),” *Physical Review D*, vol. 84, no. 5, Article ID 056003, 7 pages, 2011.
- [40] M. E. Carrington and A. Rebhan, “Perturbative and non-perturbative Kolmogorov turbulence in a gluon plasma,” *The European Physical Journal C*, vol. 71, article 1787, 2011.
- [41] J. Berges, S. Scheffler, and D. Sexty, “Bottom-up isotropization in classical-statistical lattice gauge theory,” *Physical Review D*, vol. 77, no. 3, Article ID 034504, 11 pages, 2008.
- [42] J. Berges, D. Gelfand, S. Scheffler, and D. Sexty, “Simulating plasma instabilities in SU(3) gauge theory,” *Physics Letters B*, vol. 677, no. 3-4, pp. 210–213, 2009.
- [43] J. Berges, S. Scheffler, and D. Sexty, “Turbulence in nonabelian gauge theory,” *Physics Letters B*, vol. 681, no. 4, pp. 362–366, 2009.
- [44] A. H. Mueller, A. I. Soshi, and S. M. H. Wong, “On Kolmogorov wave turbulence in QCD,” *Nuclear Physics B*, vol. 760, no. 1-2, pp. 145–165, 2007.
- [45] T. Kunihiro, B. Müller, A. Ohnishi, A. Schafer, T. Takahashi, and A. Yamamoto, “Chaotic behavior in classical Yang-Mills dynamics,” *Physical Review D*, vol. 82, no. 11, Article ID 114015, 9 pages, 2010.
- [46] M. Asakawa, S. A. Bass, and B. Müller, “Anomalous viscosity of an expanding quark-gluon plasma,” *Physical Review Letters*, vol. 96, no. 25, Article ID 252301, 2006.
- [47] M. Asakawa, S. A. Bass, and B. Müller, “Anomalous transport processes in anisotropically expanding Quark-Gluon plasmas,” *Progress of Theoretical Physics*, vol. 116, no. 4, pp. 725–755, 2007.

- [48] M. Asakawa, S. A. Bass, and B. Müller, “Anomalous transport processes in turbulent non-Abelian plasmas,” *Nuclear Physics A*, vol. 854, no. 1, pp. 76–80, 2011.
- [49] V. N. Tsytovich, *Theory of Turbulent Plasma*, Springer, New York, NY, USA, 1977.
- [50] S. Ichimaru, *Statistical Plasma Physics*, Westview Press, Boulder, Colo, USA, 1991.
- [51] A. Majumder, B. Müller, and X. N. Wang, “Small shear viscosity of a Quark-Gluon plasma implies strong jet quenching,” *Physical Review Letters*, vol. 99, Article ID 192301, 4 pages, 2007.
- [52] N. Okamoto, K. Yoshimatsu, K. Schneider et al., “Coherent vortices in high resolution direct numerical simulation of homogeneous isotropic turbulence: a wavelet viewpoint,” *Physics of Fluids*, vol. 19, Article ID 11509, 13 pages, 2007.
- [53] K. P. Zybin, V. A. Sirota, A. S. Il’in, and A. V. Gurevich, “Generation of small-scale structures in well-developed turbulence,” *Journal of Experimental and Theoretical Physics*, vol. 105, no. 2, pp. 455–466, 2007.
- [54] K. P. Zybin, V. A. Sirota, A. S. Ilyin, and A. V. Gurevich, “Lagrangian statistical theory of fully developed hydrodynamical turbulence,” *Physical Review Letters*, vol. 100, no. 17, Article ID 174504, 2008.
- [55] K. P. Zybin and V. A. Sirota, “Lagrangian and eulerian velocity structure functions in hydrodynamic turbulence,” *Physical Review Letters*, vol. 104, no. 15, Article ID 154501, 2010.
- [56] K. P. Zybin, V. A. Sirota, and A. S. Ilyin, “Structure functions of fully developed hydrodynamic turbulence: an analytical approach,” *Physical Review E*, vol. 82, Article ID 056324, 14 pages, 2010.
- [57] K. P. Zybin and V. A. Sirota, “Longitudinal and transverse velocity scaling exponents from merging of the vortex filament and multifractal models,” <http://arxiv.org/abs/1204.1465>.
- [58] K. P. Zybin and V. A. Sirota, “On the multifractal structure of fully developed turbulence,” <http://arxiv.org/abs/1305.0027>.
- [59] J. A. Krommes, “Fundamental statistical descriptions of plasma turbulence in magnetic fields,” *Physics Report*, vol. 360, no. 5-6, pp. 1–352, 2002.
- [60] V. V. Tamoykin, “Cherenkov and transient radiation of uniformly moving charge in random inhomogeneous medium,” *Astrophysics and Space Science*, vol. 16, no. 1, pp. 120–129, 1972.
- [61] M. R. Kirakosyan and A. V. Leonidov, “Stochastic jet quenching in high energy nuclear collisions,” <http://arxiv.org/abs/arXiv:0810.5442>.
- [62] M. R. Kirakosyan and A. V. Leonidov, “Energy loss in stochastic Abelian medium,” <http://arxiv.org/abs/0809.2179>.

Research Article

Viscous Coefficients of a Hot Pion Gas

Sourav Sarkar

Theoretical Physics Division, Variable Energy Cyclotron Centre, 1/AF, Bidhannagar, Kolkata 700064, India

Correspondence should be addressed to Sourav Sarkar; sourav@vecc.gov.in

Received 26 March 2013; Accepted 20 May 2013

Academic Editor: Edward Sarkisyan-Grinbaum

Copyright © 2013 Sourav Sarkar. This is an open access article distributed under the Creative Commons Attribution License, which permits unrestricted use, distribution, and reproduction in any medium, provided the original work is properly cited.

The steps essentially involved in the evaluation of transport coefficients in linear response theory using Kubo formulas are to relate the defining *retarded* correlation function to the corresponding *time-ordered* one and to evaluate the latter in the conventional perturbation expansion. Here we evaluate the viscosities of a pion gas carrying out both the steps in the *real-time* formulation. We also obtain the viscous coefficients by solving the relativistic transport equation in the Chapman-Enskog approximation to leading order. An in-medium $\pi\pi$ cross-section is used in which spectral modifications are introduced in the propagator of the exchanged ρ .

1. Introduction

One of the most interesting results from experiments at the Relativistic Heavy Ion Collider (RHIC) is the surprisingly large magnitude of the elliptic flow of the emitted hadrons. Viscous hydrodynamic simulations of heavy ion collisions require a rather small value of η/s , η being the coefficient of shear viscosity and s the entropy density, for the theoretical interpretation of this large collective flow. The value being close to $1/4\pi$, the quantum lower bound for this quantity [1], matter produced in these collisions is believed to be almost a perfect fluid [2].

This finding has led to widespread interest in the study of nonequilibrium dynamics, especially in the microscopic evaluation of the transport coefficients of both partonic as well as hadronic forms of strongly interacting matter. In the literature one comes across basically two approaches that have been used to determine these quantities. One is the kinetic theory method in which the nonequilibrium distribution function which appears in the transport equation is expanded in terms of the gradients of the flow velocity field. The coefficients of this expansion which are related to the transport coefficients are then perturbatively determined using various approximation methods. The other approach is based on response theory in which the nonequilibrium transport coefficients are related by Kubo formulas to equilibrium correlation functions. They are then perturbatively evaluated using the techniques of thermal field theory. Alternatively, the

Kubo formulas can be directly evaluated on the lattice [3] or in transport cascade simulations [4] to obtain the transport coefficients.

Thermal quantum field theory has been formulated in the imaginary as well as real-time [5–9]. For time independent quantities such as the partition function, the imaginary time formulation is well suited and stands as the only simple method of calculation. However, for time dependent quantities like two-point correlation functions, the use of this formulation requires a continuation to imaginary time and possibly back to real-time at the end. On the other hand, the real-time formulation provides a convenient framework to calculate such quantities, without requiring any such continuation at all.

A difficulty with the real-time formulation is, however, that all two-point functions take the form of 2×2 matrices. But this difficulty is only apparent. Such matrices are always diagonalisable, and it is the 11 component of the diagonalised matrix that play the role of the single function in the imaginary time formulation. It is only in the calculation of this 11 component to higher order in perturbation that the matrix structure appears in a nontrivial way.

In the literature transport coefficients are evaluated using the imaginary time formulation [10–12]. Such a coefficient is defined by the *retarded* correlation function of the components of the energy-momentum tensor. As the conventional perturbation theory applies only to *time-ordered* correlation

functions, it is first necessary to relate the two types of correlation functions using the Källén-Lehmann spectral representation [13–16]. We find this relation directly in real-time formulation. The time-ordered correlation function is then calculated also in the covariant real-time perturbative framework to finally obtain the viscosity coefficients of a pion gas.

We also calculate the viscous coefficients in a kinetic theory framework by solving the transport equation in the Chapman-Enskog approximation to the leading order. This approach being computationally more efficient [12] has been mostly used in the literature to obtain the viscous coefficients. The $\pi\pi$ cross-section is a crucial dynamical input in these calculations. Scattering amplitudes evaluated using chiral perturbation theory [17, 18] to lowest order have been used in [19, 20], and unitarization improved estimates of the amplitudes were used in [21] to evaluate the shear viscosity. Phenomenological scattering cross-section using experimental phase shifts has been used in [20, 22–24] in view of the fact that the $\pi\pi$ cross-section estimated from lowest order chiral perturbation theory is known to deviate from the experimental data beyond centre of mass energy of 500 MeV primarily due to the ρ pole which dominates the cross-section in the energy region between 500–1000 MeV. All these approaches have used a vacuum cross section. To construct an in-medium cross-section we employ an effective Lagrangian approach which incorporates ρ and σ meson exchange in $\pi\pi$ scattering. Medium effects are then introduced in the ρ propagator through one-loop self-energy diagrams [25].

In Section 2 we derive the spectral representations for the retarded and time-ordered correlation functions in the real-time version of thermal field theory. We also review the formulation of the nonequilibrium density operator and obtain the expressions for the viscosities in terms of equilibrium (retarded) two-point functions. The time-ordered function is then calculated to lowest order with complete propagators in the equilibrium theory. In Section 3 we briefly recapitulate the expressions for the viscosities obtained by solving the Uehling-Uhlenbeck transport equation in the kinetic theory framework. We then evaluate the $\pi\pi$ cross-section in the medium briefly discussing the one-loop ρ self-energy due to πh ($h = \pi, \omega, h_1, a_1$) loops evaluated in the real-time formulation discussed previously. We end with a summary in Section 4.

2. Viscous Coefficients in the Linear Response Theory

2.1. Real-Time Formulation. In this section we review the real-time formulation of equilibrium thermal field theory leading to the spectral representations of bosonic two-point functions [16]. This formulation begins with a comparison between the time evolution operator $e^{-iH(t_2-t_1)}$ of quantum theory and the Boltzmann weight $e^{-\beta H} = e^{-iH(\tau-i\beta-\tau)}$ of statistical physics, where we introduce τ as a complex variable. Thus while for the time evolution operator, the times t_1 and t_2 ($t_2 > t_1$) are any two points on the real line, the Boltzmann weight involves a path from τ to $\tau - i\beta$ in the complex time plane. Setting this $\tau = -T$, where T is

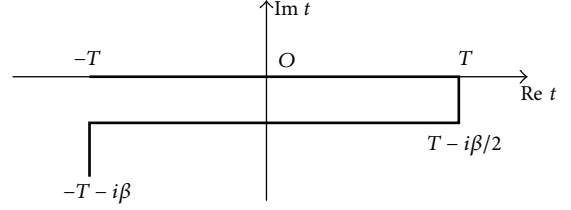


FIGURE 1: The contour C in the complex time plane used here for the real-time formulation.

real, positive, and large, we can get the contour C shown in Figure 1, lying within the region of analyticity in this plane and accommodating real-time correlation functions [6, 8].

Let a general bosonic interacting field in the Heisenberg representation be denoted by $\Phi_l(x)$, whose subscript l collects the index (or indices) denoting the field component and derivatives acting on it. Although we will call its two-point function as propagator, $\Phi_l(x)$ can be an elementary field or a composite local operator. (If $\Phi_l(x)$ denotes the pion field, it will, of course, not have any index.)

The thermal expectation value of the product $\Phi_l(x)\Phi_{l'}^\dagger(x')$ may be expressed as

$$\begin{aligned} \langle \Phi_l(x) \Phi_{l'}^\dagger(x') \rangle &= \frac{1}{Z} \sum_{m,n} e^{-\beta E_m} \\ &\times \langle m | \Phi_l(x) | n \rangle \langle n | \Phi_{l'}^\dagger(x') | m \rangle, \end{aligned} \quad (1)$$

where $\langle O \rangle$ for any operator O denotes *equilibrium* ensemble average:

$$\langle O \rangle = \frac{\text{Tr}(e^{-\beta H} O)}{Z}, \quad Z = \text{Tr} e^{-\beta H}. \quad (2)$$

Note that we have two sums in (1), one to evaluate the trace and the other to separate the field operators. They run over a complete set of states, which we choose as eigenstates $|m\rangle$ of four-momentum P_μ . Using translational invariance of the field operator:

$$\Phi_l(x) = e^{iP \cdot x} \Phi_l(0) e^{-iP \cdot x}, \quad (3)$$

we get

$$\begin{aligned} \langle \Phi_l(x) \Phi_{l'}^\dagger(x') \rangle &= \frac{1}{Z} \sum_{m,n} e^{-\beta E_m} e^{i(k_m - k_n) \cdot (x - x')} \\ &\times \langle m | \Phi_l(0) | n \rangle \langle n | \Phi_{l'}^\dagger(0) | m \rangle. \end{aligned} \quad (4)$$

Its spatial Fourier transform is

$$\begin{aligned} &\int d^3 x e^{-ik \cdot (x - x')} \langle \Phi_l(x) \Phi_{l'}^\dagger(x') \rangle \\ &= \frac{(2\pi)^3}{Z} \sum_{m,n} e^{-\beta E_m} e^{i(E_m - E_n)(\tau - \tau')} \delta^3(\mathbf{k}_m - \mathbf{k}_n + \mathbf{k}) \\ &\times \langle m | \Phi_l(0) | n \rangle \langle n | \Phi_{l'}^\dagger(0) | m \rangle, \end{aligned} \quad (5)$$

where the times τ, τ' are on the contour C . We now insert unity on the left of (5) in the form

$$1 = \int_{-\infty}^{\infty} dk'_0 \delta(E_m - E_n + k'_0). \quad (6)$$

(We reserve k_0 for the variable conjugate to the real-time.) Then it may be written as

$$\begin{aligned} & \int d^3x e^{-ik \cdot (x-x')} \langle \Phi_I(x) \Phi_I^\dagger(x') \rangle \\ &= \int \frac{dk'_0}{2\pi} e^{-ik'_0(\tau-\tau')} M_{II'}^+(k'_0, \mathbf{k}), \end{aligned} \quad (7)$$

where the spectral function M^+ is given by [$k'_\mu = (k'_0, \mathbf{k})$] as follows:

$$\begin{aligned} M_{II'}^+(k') &= \frac{(2\pi)^4}{Z} \sum_{m,n} e^{-\beta E_m} \delta^4(k_m - k_n + k') \\ &\times \langle m | \Phi_I(0) | n \rangle \langle n | \Phi_I^\dagger(0) | m \rangle. \end{aligned} \quad (8)$$

In just the same way, we can work out the Fourier transform of $\langle \Phi_I^\dagger(x') \Phi_I(x) \rangle$ as follows:

$$\begin{aligned} & \int d^3x e^{-ik \cdot (x-x')} \langle \Phi_I^\dagger(x') \Phi_I(x) \rangle \\ &= \int \frac{dk'_0}{2\pi} e^{-ik'_0(\tau-\tau')} M_{II'}^-(k'_0, \mathbf{k}), \end{aligned} \quad (9)$$

with a second spectral function M^- given by

$$\begin{aligned} M_{II'}^-(k') &= \frac{(2\pi)^4}{Z} \sum_{m,n} e^{-\beta E_m} \delta^4(k_n - k_m + k') \\ &\times \langle m | \Phi_I^\dagger(0) | n \rangle \langle n | \Phi_I(0) | m \rangle. \end{aligned} \quad (10)$$

The two spectral functions are related by the KMS relation [26, 27]

$$M_{II'}^+(k) = e^{\beta k_0} M_{II'}^-(k), \quad (11)$$

in momentum space, which may be obtained simply by interchanging the dummy indices m, n in one of $M_{II'}^\pm(k)$ and using the energy conserving δ -function.

We next introduce the *difference* of the two spectral functions:

$$\rho_{II'}(k) \equiv M_{II'}^+(k) - M_{II'}^-(k) \quad (12)$$

and solve this identity and the KMS relation (11) for $M_{II'}^\pm(k)$ as follows:

$$\begin{aligned} M_{II'}^+(k) &= \{1 + f(k_0)\} \rho_{II'}(k), \\ M_{II'}^-(k) &= f(k_0) \rho_{II'}(k), \end{aligned} \quad (13)$$

where $f(k_0)$ is the distribution-like function

$$f(k_0) = \frac{1}{e^{\beta k_0} - 1}, \quad -\infty < k_0 < \infty. \quad (14)$$

In terms of the true distribution function

$$n(|k_0|) = \frac{1}{e^{\beta|k_0|} - 1}, \quad (15)$$

it may be expressed as

$$\begin{aligned} f(k_0) &= f(k_0) \{\theta(k_0) + \theta(-k_0)\} \\ &= n\epsilon(k_0) - \theta(-k_0). \end{aligned} \quad (16)$$

With the previous ingredients, we can build the spectral representations for the two types of thermal propagators. First consider the *time-ordered* one:

$$\begin{aligned} -iD_{II'}(x, x') &= \langle T_c \Phi_I(x) \Phi_I^\dagger(x') \rangle \\ &= \theta_c(\tau - \tau') \langle \Phi_I(x) \Phi_I^\dagger(x') \rangle \\ &\quad + \theta_c(\tau' - \tau) \langle \Phi_I^\dagger(x') \Phi_I(x) \rangle. \end{aligned} \quad (17)$$

Using (7), (9), and (13), we see that its spatial Fourier transform is given by [6]

$$\begin{aligned} D_{II'}(\tau - \tau', \mathbf{k}) &= i \int_{-\infty}^{\infty} \frac{dk'_0}{2\pi} \rho_{II'}(k'_0, \mathbf{k}) \\ &\times e^{-ik'_0(\tau-\tau')} \{\theta_c(\tau - \tau') + f(k'_0)\}. \end{aligned} \quad (18)$$

As $T \rightarrow \infty$, the contour of Figure 1 simplifies, reducing essentially to two parallel lines, one the real axis and the other shifted by $-i\beta/2$, points which will be denoted, respectively, by subscripts 1 and 2, so that $\tau_1 = t$, $\tau_2 = t - i\beta/2$ [8]. The propagator then consists of four pieces, which may be put in the form of a 2×2 matrix. The contour ordered θ 's may now be converted to the usual time ordered ones. If τ, τ' are both on line 1 (the real axis), the τ and t orderings coincide, $\theta_c(\tau_1 - \tau'_1) = \theta(t - t')$. If they are on two different lines, the τ ordering is definite, $\theta_c(\tau_1 - \tau'_2) = 0$, $\theta_c(\tau_2 - \tau'_1) = 1$. Finally if they are both on line 2, the two orderings are opposite, $\theta_c(\tau_2 - \tau'_2) = \theta(t' - t)$.

Back to real-time, we can work out the usual temporal Fourier transform of the components of the matrix to get

$$\mathbf{D}_{II'}(k_0, \mathbf{k}) = \int_{-\infty}^{\infty} \frac{dk'_0}{2\pi} \rho_{II'}(k'_0, \mathbf{k}) \mathbf{\Lambda}(k'_0, k_0), \quad (19)$$

where the elements of the matrix $\mathbf{\Lambda}$ are given by [16]

$$\begin{aligned} \Lambda_{11} &= -\Lambda_{22}^* = \frac{1}{k'_0 - k_0 - i\eta} + 2\pi i f(k'_0) \delta(k'_0 - k_0), \\ \Lambda_{12} &= \Lambda_{21} = 2\pi i e^{\beta k'_0/2} f(k'_0) \delta(k'_0 - k_0). \end{aligned} \quad (20)$$

Using relation (16), we may rewrite (20) in terms of n as follows:

$$\begin{aligned} \Lambda_{11} &= -\Lambda_{22}^* = \frac{1}{k'_0 - k_0 - i\eta\epsilon(k_0)} + 2\pi i n\epsilon(k_0) \delta(k'_0 - k_0), \\ \Lambda_{12} &= \Lambda_{21} = 2\pi i \sqrt{n(1+n)} \epsilon(k_0) \delta(k'_0 - k_0). \end{aligned} \quad (21)$$

The matrix Λ and hence the propagator $\mathbf{D}_{ll'}$ can be diagonalised to give

$$\mathbf{D}_{ll'}(k_0, \mathbf{k}) = \mathbf{U} \begin{pmatrix} \bar{D}_{ll'} & 0 \\ 0 & -\bar{D}_{ll'}^* \end{pmatrix} \mathbf{U}, \quad (22)$$

where $\bar{D}_{ll'}$ and \mathbf{U} are given by

$$\bar{D}_{ll'}(k_0, \mathbf{k}) = \int_{-\infty}^{\infty} \frac{dk'_0}{2\pi} \frac{\rho_{ll'}(k'_0, \mathbf{k})}{k'_0 - k_0 - i\eta\epsilon(k_0)}, \quad (23)$$

$$\mathbf{U} = \begin{pmatrix} \sqrt{1+n} & \sqrt{n} \\ \sqrt{n} & \sqrt{1+n} \end{pmatrix}.$$

Equation (22) shows that \bar{D} can be obtained from any of the elements of the matrix \mathbf{D} , say D_{11} . Omitting the indices ll' , we get

$$\text{Re } \bar{D} = \text{Re } D_{11}, \quad \text{Im } \bar{D} = \tanh\left(\frac{\beta|k_0|}{2}\right) \text{Im } D_{11}. \quad (24)$$

Looking back at the spectral functions $M_{ll'}^\pm$ defined by (8) and (10), we can express them as usual four-dimensional Fourier transforms of ensemble average of the operator products, so that $\rho_{ll'}$ is the Fourier transform of that of the commutator:

$$\rho_{ll'}(k_0, \mathbf{k}) = \int d^4y e^{ik \cdot (y-y')} \langle [\Phi_l(y), \Phi_{l'}(y')] \rangle, \quad (25)$$

where the time components of y and y' are on the real axis in the τ -plane. Taking the spectral function for the free scalar field

$$\rho_0 = 2\pi\epsilon(k_0) \delta(k^2 - m^2), \quad (26)$$

we see that \bar{D} becomes the free propagator, $\bar{D}(k_0, \mathbf{k}) = -1/(k^2 - m^2)$.

We next consider the *retarded* thermal propagator:

$$D_{ll'}^R(x, x') = i\theta_c(\tau - \tau') \langle [\Phi_l(\mathbf{x}, \tau), \Phi_{l'}(\mathbf{x}', \tau')] \rangle, \quad (27)$$

where again τ, τ' are on the contour C (Figure 1). Noting equations (7), (9), and (12) the three-dimensional Fourier transform may immediately be written as

$$D_{ll'}^R(\tau - \tau', \mathbf{k}) = i\theta_c(\tau - \tau') \int_{-\infty}^{\infty} \frac{dk'_0}{2\pi} e^{-ik'_0(\tau - \tau')} \rho_{ll'}(k'_0, \mathbf{k}). \quad (28)$$

As before we isolate the different components with real-times and take the Fourier transform with respect to real-time. Thus for the 11 component we simply have

$$D_{ll'}^R(t - t', \mathbf{k})_{11} = i\theta(t - t') \int_{-\infty}^{\infty} \frac{dk'_0}{2\pi} e^{-ik'_0(t - t')} \rho_{ll'}(k'_0, \mathbf{k}), \quad (29)$$

whose temporal Fourier transform gives

$$D_{ll'}^R(k_0, \mathbf{k})_{11} = \int_{-\infty}^{\infty} \frac{dk'_0}{2\pi} \frac{\rho_{ll'}(k'_0, \mathbf{k})}{k'_0 - k_0 - i\eta}. \quad (30)$$

This 11 component suffices for us, but we also display the complete matrix as follows:

$$\mathbf{D}_{ll'}^R(k_0, \mathbf{k}) = \begin{pmatrix} D_{ll'}^R(k_0, \mathbf{k})_{11} & 0 \\ \rho_{ll'}(k_0) \left\{ \sqrt{\frac{n}{n+1}} \theta(k_0) + \sqrt{\frac{n+1}{n}} \theta(-k_0) \right\} & -D_{ll'}^{R*}(k_0, \mathbf{k})_{11} \end{pmatrix}. \quad (31)$$

Though we deal with matrices in real-time formulation, it is the 11 component that is physical. Equations (23) and (30) then show that we can continue the *time-ordered* two-point function into the *retarded* one by simply changing the *ie* prescription as follows:

$$D_{ll'}^R(k_0 + i\eta, \mathbf{k})_{11} = \bar{D}_{ll'}(k_0 + i\eta\epsilon(q_0)) \longrightarrow k_0 + i\eta, \mathbf{k}. \quad (32)$$

The point to note here is that for the time-ordered propagator, it is the *diagonalised* matrix and not the matrix itself, whose 11 component can be continued in a simple way.

2.2. Transport Coefficients. We now use the linear response approach to arrive at expressions of the transport coefficients as integrals of retarded Green's functions over space. We follow the method proposed by Zubarev [28], which is excellently reviewed in [10]. Here the system is supposed to be in the hydrodynamical stage where the mean free time of the constituent particles is much shorter than the relaxation time of the whole system under consideration. Thus local equilibrium will be attained quickly, while global equilibrium will be approaching gradually. Since the system is assumed to be not far from equilibrium, we may retain only linear terms in space-time gradients of thermodynamical parameters, like temperature and velocity fields. We assume the energy-momentum of the system to be conserved as follows:

$$\partial_\mu T^{\mu\nu}(\mathbf{x}, t) = 0. \quad (33)$$

The nonequilibrium density matrix operator is constructed in the Heisenberg picture, where it is independent of time as follows:

$$\frac{d\rho}{dt} = 0. \quad (34)$$

Following Zubarev, we construct the operator $B(\mathbf{x}, t)$ as follows:

$$B(\mathbf{x}, t) = \epsilon \int_{-\infty}^t dt_1 e^{\epsilon(t_1 - t)} F^\nu(\mathbf{x}, t_1) T_{0\nu}(\mathbf{x}, t_1), \quad (35)$$

$(\epsilon \longrightarrow 0^+),$

where $F^\nu(\mathbf{x}, t) = \beta(\mathbf{x}, t)u^\nu(\mathbf{x}, t)$. Here $\beta(\mathbf{x}, t)$ is a Lorentz invariant quantity defining the local temperature, and $u^\nu(\mathbf{x}, t)$ is the four-velocity field of the fluid

$$u^\nu(\mathbf{x}, t)u_\nu(\mathbf{x}, t) = 1. \quad (36)$$

The construction (35), which smooths out the oscillating terms, resembles the one used in the formal theory of scattering [28, 29] and selects out the retarded solution.

The expression (35) is actually independent of t ; the time derivative is

$$\begin{aligned} \frac{d}{dt}B(\mathbf{x}, t) &= \epsilon F^\nu(\mathbf{x}, t)T_{0\nu}(\mathbf{x}, t) \\ &- \epsilon^2 \int_{-\infty}^t dt_1 e^{\epsilon(t_1-t)} F^\nu(\mathbf{x}, t_1)T_{0\nu}(\mathbf{x}, t_1). \end{aligned} \quad (37)$$

As $T_{0\nu}$ and F^ν are finite, the right hand side of (37) goes to zero as $\epsilon \rightarrow 0$. Also integrating (35) by parts, we get

$$\begin{aligned} B(\mathbf{x}, t) &= F^\nu(\mathbf{x}, t)T_{0\nu}(\mathbf{x}, t) \\ &- \int_{-\infty}^t dt_1 e^{\epsilon(t_1-t)} \left(F^\nu \frac{dT_{0\nu}}{dt} + \frac{dF^\nu}{dt} T_{0\nu} \right). \end{aligned} \quad (38)$$

We now consider the space integral of (38). Using the energy-momentum conservation rule (33), we integrate the second term in (38) by parts and neglect the surface integrals to get

$$\begin{aligned} \int d^3x B(\mathbf{x}, t) &= \int d^3x F^\nu(\mathbf{x}, t)T_{0\nu}(\mathbf{x}, t) \\ &- \int d^3x \int_{-\infty}^t dt_1 e^{\epsilon(t_1-t)} T_{\mu\nu}(\mathbf{x}, t_1) \partial^\mu F^\nu(\mathbf{x}, t_1) \\ &\equiv A - B, \end{aligned} \quad (39)$$

where we have abbreviated the first and second terms by A and $-B$, respectively. Then the nonequilibrium statistical density matrix is given by

$$\rho = e^{-A+B} / \text{Tr} e^{-A+B}. \quad (40)$$

The first term A in (39) characterises local equilibrium:

$$\rho_0 = e^{-A} / \text{Tr} e^{-A} \quad (41)$$

where the second term B including the thermodynamical force $\partial^\mu F^\nu$ describes deviation from equilibrium.

In order to expand ρ in a series in B we define the function

$$Q(\tau) = e^{-(1-\tau)A} e^{\tau(-A+B)} \quad (42)$$

such that the boundary conditions at $\tau = 0$ and $\tau = 1$ correspond to the equilibrium and nonequilibrium density matrices as follows:

$$Q(\tau = 0) = e^{-A} = \rho_0, \quad Q(\tau = 1) = e^{-A+B} = \rho. \quad (43)$$

We then differentiate $Q(\tau)$ with respect to τ to get

$$\frac{dQ(\tau)}{d\tau} = e^{-(1-\tau)A} B e^{(1-\tau)A} Q(\tau) \quad (44)$$

which can be integrated to give

$$Q(\tau) = Q(0) + \int_0^\tau d\tau' e^{-(1-\tau')A} B e^{(1-\tau')A} Q(\tau'). \quad (45)$$

It can be solved iteratively. Keeping up to the first order term (linear response) and setting $\tau = 1$, we get the required result

$$\rho = \rho_0 \left[1 + \int_0^1 e^{-\tau A} B e^{\tau A} \right]. \quad (46)$$

Applying this formula to the energy-momentum tensor, we get its response to the thermodynamical forces as [10]

$$\begin{aligned} \langle T_{\mu\nu}(\mathbf{x}, t) \rangle &= \langle T_{\mu\nu}(\mathbf{x}, t) \rangle_0 \\ &+ \int d^3x' \int_{-\infty}^t dt' e^{\epsilon(t_1-t)} \\ &\times (T_{\mu\nu}(\mathbf{x}, t), T_{\rho\sigma}(\mathbf{x}', t')) \partial^\rho F^\sigma(\mathbf{x}', t'), \end{aligned} \quad (47)$$

where

$$\begin{aligned} (T_{\mu\nu}(\mathbf{x}, t), T_{\rho\sigma}(\mathbf{x}', t')) &= \int_0^1 d\tau \left\{ \langle T_{\mu\nu}(\mathbf{x}, t) e^{-\tau A} T_{\rho\sigma}(\mathbf{x}', t') e^{\tau A} \rangle_0 \right. \\ &\left. - \langle T_{\mu\nu}(\mathbf{x}, t) \rangle_0 \langle T_{\rho\sigma}(\mathbf{x}', t') \rangle_0 \right\} \end{aligned} \quad (48)$$

is the correlation function to be evaluated. As the correlation is assumed to vanish as $t' \rightarrow -\infty$, it can be put in terms of the conventional retarded Green's function. Omitting indices, it is

$$(T(\mathbf{x}, t), T(\mathbf{x}', t')) = \frac{1}{\beta} \int_{-\infty}^t dt' \langle T(\mathbf{x}, t), T(\mathbf{x}', t') \rangle_{\text{ret}} \quad (49)$$

with

$$\langle T(\mathbf{x}, t), T(\mathbf{x}', t') \rangle_{\text{ret}} \equiv i\theta(t-t') \langle [T(\mathbf{x}, t), T(\mathbf{x}', t')] \rangle_0. \quad (50)$$

We now use (47) to obtain the expectation value of the viscous-shear stress part of the nonequilibrium energy momentum tensor which is given by

$$T^{\mu\nu} = T^{\mu\nu(0)} + \pi^{\mu\nu} + (P^\mu u^\nu + P^\nu u^\mu), \quad (51)$$

where $T^{\mu\nu(0)} = (\epsilon + p)u^\mu u^\nu - g^{\mu\nu}p$ is the equilibrium part, $\pi^{\mu\nu}$ is the viscous-shear stress tensor, and P^μ is the heat current. Also, with a view to separate scalar, vector and tensor processes, the quantity $T_{\rho\sigma} \partial^\rho F^\sigma$ in (39) is expanded as

$$T_{\rho\sigma} \partial^\rho F^\sigma = \beta \pi_{\rho\sigma} \partial^\rho u^\sigma + \beta P_\rho (\beta \partial^\rho \beta + u \cdot \partial u^\rho) - \beta \bar{p} \partial \cdot u \quad (52)$$

with $\bar{p} = p - c_s^2 \epsilon$, c_s being the sound velocity. Using now the fact that the correlation function between operators of

different ranks vanishes in an isotropic medium, one can write from (47)

$$\begin{aligned} & \langle \pi_{\mu\nu}(\mathbf{x}, t) \rangle \\ &= \langle \pi_{\mu\nu}(\mathbf{x}, t) \rangle_0 + \int d^3x' \int_{-\infty}^t dt' e^{\epsilon(t_1-t)} \\ & \quad \times (\pi_{\mu\nu}(\mathbf{x}, t), \pi_{\rho\sigma}(\mathbf{x}', t')) \beta(\mathbf{x}', t') \partial^\rho u^\sigma(\mathbf{x}', t') \end{aligned} \quad (53)$$

with $\langle \pi_{\mu\nu}(\mathbf{x}, t) \rangle_0 = 0$. Following Hosoya et al. [10], we write the correlation function as

$$\begin{aligned} (\pi_{\mu\nu}, \pi_{\rho\sigma}) &= \frac{1}{10} \left[\Delta_{\mu\rho} \Delta_{\nu\sigma} + \Delta_{\mu\sigma} \Delta_{\nu\rho} - \frac{2}{3} \Delta_{\mu\nu} \Delta_{\rho\sigma} \right] \\ & \quad \times (\pi^{\alpha\beta}, \pi_{\alpha\beta}), \end{aligned} \quad (54)$$

where $\Delta_{\mu\nu} = g_{\mu\nu} - u_\mu u_\nu$. Assuming now that changes in the thermodynamic forces are small over the correlation length of the two-point function, the factor $\beta \partial^\rho u^\sigma$ can be taken out of the integral giving finally:

$$\langle \pi^{\mu\nu}(\mathbf{x}, t) \rangle = \eta \left[\Delta_\rho^\mu \Delta_\sigma^\nu (\partial^\rho u^\sigma + \partial^\sigma u^\rho) - \frac{2}{3} \Delta^{\mu\nu} \Delta_{\rho\sigma} \partial^\rho u^\sigma \right], \quad (55)$$

where

$$\begin{aligned} \eta &= \frac{1}{10} \int_{-\infty}^0 dt_1 e^{\epsilon(t_1-t)} \int_{-\infty}^{t_1} dt' \\ & \quad \times \int d^3x' \langle \pi^{\alpha\beta}(\mathbf{x}, t), \pi_{\alpha\beta}(\mathbf{x}', t') \rangle_{\text{ret}} \\ &= \frac{1}{10} \int_{-\infty}^0 dt_1 e^{\epsilon t_1} \int_{-\infty}^{t_1} dt' i \int d^3x' \theta(-t') \\ & \quad \times \langle [\pi^{\alpha\beta}(0, 0), \pi_{\alpha\beta}(\mathbf{x}', t')] \rangle_0; \quad (\mathbf{x} \rightarrow 0, t \rightarrow 0). \end{aligned} \quad (56)$$

Again, starting with the pressure $p(\mathbf{x}, t)$ on the l.h.s of (47) and following the steps as described previously, we obtain

$$\langle p(\mathbf{x}, t) \rangle = \langle p(\mathbf{x}, t) \rangle_0 - \zeta \partial_\rho u^\rho(\mathbf{x}, t), \quad (57)$$

where the bulk viscosity ζ is given in terms of a retarded correlation function by

$$\zeta = \int_{-\infty}^0 dt_1 e^{\epsilon(t_1-t)} \int_{-\infty}^{t_1} dt' \int d^3x' \langle \tilde{p}(\mathbf{x}, t), \tilde{p}(\mathbf{x}', t') \rangle_{\text{ret}}. \quad (58)$$

Here $\tilde{p}(\mathbf{x}, t) = p(\mathbf{x}, t) - c_s^2 \epsilon(\mathbf{x}, t)$ with $\epsilon(\mathbf{x}, t)$ the energy density and $c_s^2 = \langle \partial p / \partial \epsilon \rangle_0$.

Recall that $\langle \dots \rangle_0$ denotes *equilibrium* ensemble average. From now on we will drop the subscript "0" on the correlation functions.

2.3. Perturbative Evaluation. Clearly the spectral forms and their interrelations derived in Section 2.1 hold also for the

two-point function appearing in (56) for the shear viscosity. We begin with four-dimensional Fourier transforms. To calculate the 11 element of the retarded two-point function

$$\begin{aligned} \Pi_{11}^R(q) &= i \int d^4x e^{iq(x-x')} \theta(t-t') \\ & \quad \times \langle [\pi_{\alpha\beta}(\mathbf{x}, t), \pi^{\alpha\beta}(\mathbf{x}', t')] \rangle, \end{aligned} \quad (59)$$

we consider the corresponding time-ordered one

$$\Pi_{11}(q) = i \int d^4x e^{iq(x-x')} \langle T \pi_{\alpha\beta}(\mathbf{x}, t) \pi^{\alpha\beta}(\mathbf{x}', t') \rangle, \quad (60)$$

which can be calculated perturbatively. The viscous stress tensor can be extracted from the energy momentum tensor using the formula

$$\pi_{\alpha\beta}(x) = \left(\Delta_\alpha^\rho \Delta_\beta^\sigma - \frac{1}{3} \Delta_{\alpha\beta} \Delta^{\rho\sigma} \right) T_{\rho\sigma}(x), \quad (61)$$

where $T_{\mu\nu} = -g_{\mu\nu} \mathcal{L} + (\partial \mathcal{L} / \partial (\partial^\mu \vec{\phi})) \cdot \partial_\nu \vec{\phi}$ in which $\vec{\phi}(x)$ denotes the pion triplet. We take the lowest-order chiral Lagrangian given by [18]

$$\begin{aligned} \mathcal{L} &= \frac{1}{2} \partial_\mu \vec{\phi} \cdot \partial^\mu \vec{\phi} - \frac{1}{2} m_\pi^2 \vec{\phi} \cdot \vec{\phi} + \mathcal{L}_{\text{int}}, \\ \mathcal{L}_{\text{int}} &= -\frac{1}{6f_\pi^2} [\partial_\mu \vec{\phi} \cdot \partial^\mu \vec{\phi} \vec{\phi} \cdot \vec{\phi} - \vec{\phi} \cdot \partial_\mu \vec{\phi} \vec{\phi} \cdot \partial^\mu \vec{\phi}] \\ & \quad + \frac{m_\pi^2}{4!f_\pi^2} (\vec{\phi} \cdot \vec{\phi})^2. \end{aligned} \quad (62)$$

The time-ordered correlator, to leading order, is then given by Wick contractions of pion fields in $\pi_{\alpha\beta}$ which is obtained as

$$\pi_{\alpha\beta}(x) = \left(\Delta_\alpha^\rho \Delta_\beta^\sigma - \frac{1}{3} \Delta_{\alpha\beta} \Delta^{\rho\sigma} \right) \partial_\rho \vec{\phi}(x) \cdot \partial_\sigma \vec{\phi}(x). \quad (63)$$

In the so-called skeleton expansion, these contractions are expressed in terms of complete propagators (see Figure 2) to get

$$\Pi_{11}(q) = i \int \frac{d^4l}{(2\pi)^4} N(l, q) D_{11}(l) D_{11}(l-q), \quad (64)$$

where D_{11} is given by (19) and $N(l, q)$ is determined by the derivatives acting on the pion fields as follows:

$$N(l, q) = -g_\pi \left[\mathbf{l}^2 (\mathbf{l} - \mathbf{q})^2 + \frac{1}{3} [\mathbf{l} \cdot (\mathbf{l} - \mathbf{q})]^2 \right], \quad (65)$$

where the pion isospin degeneracy factor $g_\pi = 3$.

To work out the l_0 integral in (64), it is more convenient to use Λ_{11} given by (20) than by (21). Closing the contour in the upper or lower half l_0 -plane, we get

$$\begin{aligned} \Pi_{11}(q) &= \int \frac{d^3l}{(2\pi)^3} N(\mathbf{l}, \mathbf{q}) \int \frac{dk_0'}{2\pi} \rho(k_0', \mathbf{l}) \\ & \quad \times \frac{dk_0''}{2\pi} \rho(k_0'', \mathbf{l} - \mathbf{q}) K(q_0, k_0', k_0''), \end{aligned} \quad (66)$$

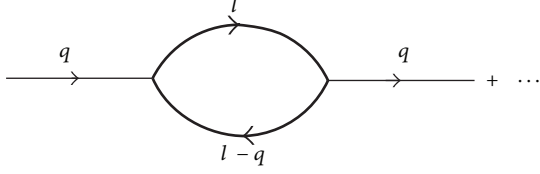


FIGURE 2: The first term in the so-called skeleton expansion of the two-point function. Heavy lines denote full propagators.

where

$$K = \frac{\{1 + f(k'_0)\} f(k''_0)}{q_0 - (k'_0 - k''_0) + i\eta} - \frac{f(k'_0) \{1 + f(k''_0)\}}{q_0 - (k'_0 - k''_0) - i\eta}. \quad (67)$$

The imaginary part of Π_{11} arises from the factor K as follows:

$$\begin{aligned} \text{Im } K &= -\pi \left[\{1 + f(k'_0)\} f(k''_0) + f(k'_0) \{1 + f(k''_0)\} \right] \\ &\quad \times \delta(q_0 - (k'_0 - k''_0)) \\ &= -\pi \coth\left(\frac{\beta q_0}{2}\right) \{f(k''_0) - f(k'_0)\} \\ &\quad \times \delta(q_0 - (k'_0 - k''_0)), \end{aligned} \quad (68)$$

where its real part is given by the principal value integrals.

Having obtained the real and imaginary parts of $\Pi_{11}(q)$, we use relations similar to (24) to build the 11 element of the diagonalised Π matrix:

$$\begin{aligned} \bar{\Pi} &= \int \frac{d^3 l}{(2\pi)^3} N(\mathbf{l}, \mathbf{q}) \int \frac{dk'_0}{2\pi} \rho(k'_0, \mathbf{l}) \int \frac{dk''_0}{2\pi} \rho(k''_0, \mathbf{l} - \mathbf{q}) \\ &\quad \times \frac{\{1 + f(k'_0)\} f(k''_0) - f(k'_0) \{1 + f(k''_0)\}}{q_0 - (k'_0 - k''_0) + i\eta \epsilon(q_0)}. \end{aligned} \quad (69)$$

Finally $\bar{\Pi}$ can be continued to Π_{11}^R by a relation similar to (31) as follows:

$$\begin{aligned} \Pi_{11}^R &= \int \frac{d^3 l}{(2\pi)^3} N(\mathbf{l}, \mathbf{q}) \\ &\quad \times \int \frac{dk'_0}{2\pi} \rho(k'_0, \mathbf{l}) \frac{dk''_0}{2\pi} \rho(k''_0, \mathbf{l} - \mathbf{q}) \\ &\quad \times \frac{\{1 + f(k'_0)\} f(k''_0) - f(k'_0) \{1 + f(k''_0)\}}{q_0 - (k'_0 - k''_0) + i\eta}. \end{aligned} \quad (70)$$

Note that in (69), (70), we retain the $f(k'_0)f(k''_0)$ terms in the numerator to put it in a more convenient form. Change the signs of k'_0 and k''_0 in the first and second term, respectively.

Noting relations like $1 + f(-k_0) = -f(k_0)$ and $\rho(-k_0) = -\rho(k_0)$, we get

$$\begin{aligned} \Pi_{11}^R(q) &= \int \frac{d^3 l}{(2\pi)^3} N(\mathbf{l}, \mathbf{q}) \\ &\quad \times \int \frac{dk'_0}{2\pi} \frac{dk''_0}{2\pi} \rho(k'_0, \mathbf{l}) \rho(k''_0, \mathbf{l} - \mathbf{q}) \\ &\quad \times f(k'_0) f(k''_0) W(q_0, k'_0 + k''_0), \end{aligned} \quad (71)$$

where

$$W = \frac{1}{q_0 + k'_0 + k''_0 + i\eta} - \frac{1}{q_0 - (k'_0 + k''_0) + i\eta}. \quad (72)$$

Returning to the expression (56) for η , we now get the three-dimensional spatial integral of the retarded correlation function by setting $\mathbf{q} = 0$ in (59) and Fourier inverting with respect to q_0 as follows:

$$\begin{aligned} &i \int d^3 x' \theta(-t') \langle [\pi^{\alpha\beta}(\vec{0}, 0), \pi_{\alpha\beta}(\mathbf{x}', t')] \rangle \\ &= - \int dq_0 e^{iq_0 t'} \Pi_{11}^R(q_0, \mathbf{q} = 0). \end{aligned} \quad (73)$$

This completes our use of the real-time formulation to get the required result. The integrals appearing in the expression for η have been evaluated in [10, 11], which we describe in the following for completeness.

As shown in [10], the integral over t_1 , t' , and q_0 in (56) and (73) may be carried out trivially to give

$$\eta = \frac{i}{10} \frac{d}{dq_0} \Pi_{11}^R(q_0) \Big|_{q_0=0}. \quad (74)$$

The q_0 dependence of Π_{11}^R is contained entirely in W as follows:

$$\begin{aligned} &\frac{d}{dq_0} W(q_0) \Big|_{q_0=0} \\ &= -\frac{1}{(k'_0 + k''_0 - i\eta)^2} + \frac{1}{(k'_0 + k''_0 + i\eta)^2} \\ &= 2\pi i \delta'(k'_0 + k''_0). \end{aligned} \quad (75)$$

Changing the integration variables in (71) from k'_0, k''_0 to $\bar{k}_0 = k'_0 + k''_0$ and $k_0 = (1/2)(k'_0 - k''_0)$, we get

$$\eta = \int \frac{d^3 l}{(2\pi)^3} N(\mathbf{l}) \int \frac{dk_0}{(2\pi)^2} F(k_0, \mathbf{l}), \quad (76)$$

where

$$\begin{aligned} F(k_0, \mathbf{l}) &= \frac{d}{d\bar{k}_0} \left\{ \rho\left(\frac{\bar{k}_0}{2} + k_0, \mathbf{l}\right) \rho\left(\frac{\bar{k}_0}{2} - k_0, \mathbf{l}\right) \right. \\ &\quad \left. \times f\left(\frac{\bar{k}_0}{2} + k_0\right) f\left(\frac{\bar{k}_0}{2} - k_0\right) \right\} \Big|_{\bar{k}_0=0}. \end{aligned} \quad (77)$$

It turns out that the integral over k_0 becomes undefined, if we try to evaluate $F(k_0)$ with the free spectral function $\rho_0(k)$ given by (26). As pointed out in [10], we have to take the spectral function for the complete propagator that includes the self-energy of the pion, leading to its finite width Γ in the medium

$$\rho(k_0, \mathbf{l}) = \frac{1}{i} \left[\frac{1}{(k_0 - i\Gamma)^2 - \omega^2} - \frac{1}{(k_0 + i\Gamma)^2 - \omega^2} \right], \quad (78)$$

$$\omega = \sqrt{\mathbf{l}^2 + m_\pi^2}.$$

Note that this form of the spectral function trivially follows on replacing $i\eta$ (where $\eta \rightarrow 0^+$) with $i\Gamma$ in the free spectral function (26) which can be written as

$$\rho_0(k_0, \mathbf{l}) = \frac{1}{i} \left[\frac{1}{(k_0 - i\eta)^2 - \omega^2} - \frac{1}{(k_0 + i\eta)^2 - \omega^2} \right]. \quad (79)$$

Then $F(k_0, \mathbf{l})$ becomes

$$F = -8 \frac{k_0^2 e^{\beta k_0}}{(e^{\beta k_0} - 1)^2} \frac{\beta \Gamma^2}{\{(k_0 - i\Gamma)^2 - \omega^2\}^2 \{(k_0 + i\Gamma)^2 - \omega^2\}^2}, \quad (80)$$

having double poles at $k_0 = 2\pi i n / \beta$ for $n = \pm 1, \pm 2, \dots$ and also at $k_0 = \pm \omega \pm i\Gamma$. The integral over k_0 may now be evaluated by closing the contour in the upper/lower half plane to get

$$\int_{-\infty}^{+\infty} \frac{dk_0}{(2\pi)^2} F(k_0, \mathbf{l}) = -\frac{1}{8\pi} \frac{\beta}{\omega^2 \Gamma} n(\omega) \{1 + n(\omega)\}, \quad (81)$$

where we retain only the leading (singular) term for small Γ . In this approximation (76) gives

$$\eta = \frac{g_\pi \beta}{30\pi^2} \int_0^\infty dl \frac{l^6}{\omega^2 \Gamma} n(\omega) \{1 + n(\omega)\}. \quad (82)$$

Proceeding analogously as mentioned above, the lowest order contribution to the bulk viscosity can be obtained as [10]

$$\zeta = \frac{g_\pi \beta}{4\pi^2} \int_0^\infty dl \frac{l^2 (l^2/3 - c_s^2 \omega^2)^2}{\omega^2 \Gamma} n(\omega) \{1 + n(\omega)\}. \quad (83)$$

The width $\Gamma(l)$ at different temperatures is known [30] from chiral perturbation theory. The quantity Γ can also be interpreted as the collision frequency, and the inverse of which is the relaxation time τ . For collisions of the form $\pi(l) + \pi(k) \rightarrow \pi(l') + \pi(k')$ this is given by (see, e.g., [25])

$$\Gamma(l) = \tau^{-1}(l)$$

$$= \int \frac{k^2 dk}{2\pi^2 \omega_k} \frac{\sqrt{s(s - 4m_\pi^2)}}{2\omega_l} n(\omega_k)$$

$$\times (1 + n(\omega_{l'})) (1 + n(\omega_{k'})) \frac{1}{2} \int d\Omega \frac{d\sigma}{d\Omega}, \quad (84)$$

where $d\sigma/d\Omega$ is the $\pi\pi$ cross-section. Note that the lowest order formulae for the shear and bulk viscosities obtained previously in the linear response approach coincide with the expressions which result from solving the transport equation in the relaxation-time approximation.

3. Viscous Coefficients in the Kinetic Theory Approach

The kinetic theory approach is suitable for studying transport properties of dilute systems. Here one assumes that the system is characterized by a distribution function which gives the phase space probability density of the particles making up the fluid. Except during collisions, these (on-shell) particles are assumed to propagate classically with well-defined position, momenta, and energy. It is possible to obtain the nonequilibrium distribution function by solving the transport equation in the hydrodynamic regime by expanding the distribution function in a local equilibrium part along with nonequilibrium corrections. This expansion in terms of gradients of the velocity field is used to linearize the transport equation. The coefficients of expansion which are related to the transport coefficients satisfy linear integral equations. The standard method of solution involves the use of polynomial functions to reduce these integral equations to algebraic ones.

3.1. Transport Coefficients at First Chapman-Enskog Order. The evolution of the phase space distribution of the pions is governed by the (transport) equation:

$$p^\mu \partial_\mu f(x, p) = C[f], \quad (85)$$

where $C[f]$ is the collision integral. For binary elastic collisions $p + k \rightarrow p' + k'$ which we consider, this is given by [22]

$$C[f] = \int d\Gamma_k d\Gamma_{p'} d\Gamma_{k'}$$

$$\times [f(x, p') f(x, k') \{1 + f(x, p)\}$$

$$\times \{1 + f(x, k)\} - f(x, p) f(x, k)$$

$$\times \{1 + f(x, p')\} \{1 + f(x, k')\}] W, \quad (86)$$

where the interaction rate is as follows:

$$W = \frac{s}{2} \frac{d\sigma}{d\Omega} (2\pi)^6 \delta^4(p + k - p' - k'), \quad (87)$$

and $d\Gamma_q = d^3q / (2\pi)^3 q_0$. The $1/2$ factor comes from the indistinguishability of the initial state pions.

For small deviation from local equilibrium, we write, in the first Chapman-Enskog approximation,

$$f(x, p) = f^{(0)}(x, p) + \delta f(x, p), \quad (88)$$

$$\delta f(x, p) = f^{(0)}(x, p) [1 + f^{(0)}(x, p)] \phi(x, p),$$

where the equilibrium distribution function (in the new notation) is given by

$$f^{(0)}(x, p) = \left[e^{(p^\mu u_\mu(x) - \mu_\pi(x))/T(x)} - 1 \right]^{-1}, \quad (89)$$

with $T(x)$, $u_\mu(x)$, and $\mu_\pi(x)$ representing the local temperature, flow velocity, and pion chemical potential, respectively. Putting (88) in (85), the deviation function $\phi(x, p)$ is seen to satisfy

$$p^\mu \partial_\mu f^{(0)}(x, p) = -\mathcal{L}[\phi], \quad (90)$$

where the linearized collision term

$$\begin{aligned} \mathcal{L}[\phi] = & f^{(0)}(x, p) \int d\Gamma_k d\Gamma_{p'} d\Gamma_{k'} f^{(0)}(x, k) \\ & \times \{1 + f^{(0)}(x, p')\} \{1 + f^{(0)}(x, k')\} \\ & \times [\phi(x, p) + \phi(x, k) - \phi(x, p') - \phi(x, k')] W. \end{aligned} \quad (91)$$

Using the form of $f^{(0)}(x, p)$ as given in (89) on the left side of (90) and eliminating time derivatives with the help of equilibrium thermodynamic laws, we arrive at [31]

$$\begin{aligned} [Q\partial_\nu u^\nu + p_\mu \Delta^{\mu\nu} (p \cdot u - h) (T^{-1} \partial_\nu T - D u_\nu) \\ - \langle p_\mu p_\nu \rangle \langle \partial^\mu u^\nu \rangle] f^{(0)} (1 + f^{(0)}) = -T \mathcal{L}[\phi], \end{aligned} \quad (92)$$

where $D = u^\mu \partial_\mu$, $\nabla_\mu = \Delta_{\mu\nu} \partial^\nu$, $\Delta_{\mu\nu} = g_{\mu\nu} - u_\mu u_\nu$, and $\langle \cdot \rangle$ indicates a space-like symmetric and traceless combination. In this equation,

$$Q = -\frac{1}{3} m_\pi^2 + (p \cdot u)^2 \left\{ \frac{4}{3} - \gamma' \right\} + p \cdot u \{ (\gamma'' - 1) h - \gamma''' T \}, \quad (93)$$

where

$$\begin{aligned} \gamma' &= \frac{(S_2^0/S_2^1)^2 - (S_3^0/S_2^1)^2 + 4z^{-1} S_2^0 S_3^1 / (S_2^1)^2 + z^{-1} S_3^0 / S_2^1}{(S_2^0/S_2^1)^2 - (S_3^0/S_2^1)^2 + 3z^{-1} S_2^0 S_3^1 / (S_2^1)^2 + 2z^{-1} S_3^0 / S_2^1 - z^{-2}}, \\ \gamma'' &= 1 + \frac{z^{-2}}{(S_2^0/S_2^1)^2 - (S_3^0/S_2^1)^2 + 3z^{-1} S_2^0 S_3^1 / (S_2^1)^2 + 2z^{-1} S_3^0 / S_2^1 - z^{-2}}, \\ \gamma''' &= \frac{S_2^0/S_2^1 + 5z^{-1} S_3^1/S_2^1 - S_3^0 S_3^1 / (S_2^1)^2}{(S_2^0/S_2^1)^2 - (S_3^0/S_2^1)^2 + 3z^{-1} S_2^0 S_3^1 / (S_2^1)^2 + 2z^{-1} S_3^0 / S_2^1 - z^{-2}}, \end{aligned} \quad (94)$$

with $z = m_\pi/T$ and $h = m_\pi S_3^1/S_2^1$. The functions $S_n^\alpha(z)$ are integrals over Bose functions [31] and are defined as $S_n^\alpha(z) = \sum_{k=1}^{\infty} e^{k\mu_\pi/T} k^{-\alpha} K_n(kz)$, $K_n(x)$ denoting the modified Bessel function of order n . The left hand side of (90) is thus expressed in terms of thermodynamic forces with different tensorial ranks. In order to be a solution of this equation ϕ must also be a linear combination of the corresponding thermodynamic forces. It is typical to take ϕ as

$$\phi = A \partial \cdot u + B_\mu \nabla^{\mu\nu} (T^{-1} \partial_\nu T - D u_\nu) - C_{\mu\nu} \langle \partial^\mu u^\nu \rangle \quad (95)$$

which on substitution into (92) and comparing coefficients of the (independent) thermodynamic forces on both sides yields the set of equations:

$$\begin{aligned} \mathcal{L}[A] &= -Q f^{(0)}(p) \frac{\{1 + f^{(0)}(p)\}}{T}, \\ \mathcal{L}[C_{\mu\nu}] &= -\langle p_\mu p_\nu \rangle f^{(0)}(p) \frac{\{1 + f^{(0)}(p)\}}{T} \end{aligned} \quad (96)$$

ignoring the equation for B_μ which is related to thermal conductivity. These integral equations are to be solved to get the coefficients A and $C_{\mu\nu}$. It now remains to link these to the viscous coefficients ζ and η . This is achieved by means of the dissipative part of the energy-momentum tensor resulting from the use of the nonequilibrium distribution function (88) in

$$T^{\mu\nu} = \int d\Gamma_p p^\mu p^\nu f(p) = T^{\mu\nu(0)} + \Delta T^{\mu\nu}, \quad (97)$$

where

$$\begin{aligned} \Delta T^{\mu\nu} &= \int d\Gamma_p f^{(0)}(1 + f^{(0)}) C_{\alpha\beta} \langle p^\alpha p^\beta \rangle \langle \partial^\mu u^\nu \rangle \\ &+ \int d\Gamma_p f^{(0)}(1 + f^{(0)}) Q A \Delta^{\mu\nu} \partial_\sigma u^\sigma. \end{aligned} \quad (98)$$

Again, for a small deviation $\phi(x, p)$, close to equilibrium, so that only first-order derivatives contribute, and the dissipative tensor can be generally expressed in the form [32, 33]

$$\Delta T^{\mu\nu} = -2\eta \langle \partial^\mu u^\nu \rangle - \zeta \Delta^{\mu\nu} \partial_\sigma u^\sigma. \quad (99)$$

Comparing, we obtain the expressions of shear and bulk viscosity as follows:

$$\begin{aligned} \eta &= -\frac{1}{10} \int d\Gamma_p C_{\mu\nu} \langle p^\mu p^\nu \rangle f^{(0)}(p) \{1 + f^{(0)}(p)\}, \\ \zeta &= - \int d\Gamma_p Q A f^{(0)}(p) \{1 + f^{(0)}(p)\}. \end{aligned} \quad (100)$$

The coefficients A and $C_{\mu\nu}$ are perturbatively obtained from (96) by expanding in terms of orthogonal polynomials which reduces the integral equations to algebraic ones. After a tedious calculation using the Laguerre polynomial of 1/2 integral order, the first approximation to the shear and bulk viscosity comes out as

$$\begin{aligned} \eta &= \frac{T}{10} \frac{\gamma_0^2}{c_{00}}, \\ \zeta &= T \frac{\alpha_2^2}{a_{22}}, \end{aligned} \quad (101)$$

where

$$\begin{aligned}
\gamma_0 &= -10 \frac{S_3^2(z)}{S_2^1(z)}, \\
c_{00} &= 16 \left\{ I_1(z) + I_2(z) + \frac{1}{3} I_3(z) \right\}, \\
\alpha_2 &= \frac{z^3}{2} \left[\frac{1}{3} \left(\frac{S_3^0}{S_2^1} - z^{-1} \right) \right. \\
&\quad + \left(\frac{S_2^0}{S_2^1} + \frac{3 S_3^1}{z S_2^1} \right) \left\{ (1 - \gamma'') \frac{S_3^1}{S_2^1} + \gamma''' z^{-1} \right\} \\
&\quad \left. - \left(\frac{4}{3} - \gamma' \right) \left\{ \frac{S_3^0}{S_2^1} + 15z^{-2} \frac{S_3^2}{S_2^1} + 2z^{-1} \right\} \right], \\
a_{22} &= 2z^2 I_3(z).
\end{aligned} \tag{102}$$

The integrals $I_\alpha(z)$ are given by

$$\begin{aligned}
I_\alpha(z) &= \frac{z^4}{[S_2^1(z)]^2} e^{(-2\mu_\pi/T)} \\
&\quad \times \int_0^\infty d\psi \cosh^3 \psi \sinh^7 \psi \\
&\quad \times \int_0^\pi d\Theta \sin \Theta \frac{1}{2} \frac{d\sigma}{d\Omega}(\psi, \Theta) \int_0^{2\pi} d\phi \\
&\quad \times \int_0^\infty d\chi \sinh^{2\alpha} \chi \int_0^\pi d\theta \sin \theta \\
&\quad \times \frac{e^{2z \cosh \psi \cosh \chi}}{(e^E - 1)(e^F - 1)(e^G - 1)(e^H - 1)} M_\alpha(\theta, \Theta),
\end{aligned} \tag{103}$$

where μ_π is the chemical potential of pions. The exponents in the Bose functions are given by

$$\begin{aligned}
E &= z (\cosh \psi \cosh \chi - \sinh \psi \sinh \chi \cos \theta) - \frac{\mu_\pi}{T}, \\
F &= z (\cosh \psi \cosh \chi - \sinh \psi \sinh \chi \cos \theta') - \frac{\mu_\pi}{T},
\end{aligned} \tag{104}$$

$$G = E + 2z \sinh \psi \sinh \chi \cos \theta,$$

$$H = F + 2z \sinh \psi \sinh \chi \cos \theta',$$

and the functions $M_\alpha(\theta, \Theta)$ represent

$$\begin{aligned}
M_1(\theta, \Theta) &= 1 - \cos^2 \Theta, \\
M_2(\theta, \Theta) &= \cos^2 \theta + \cos^2 \theta' - 2 \cos \theta \cos \theta' \cos \Theta, \\
M_3(\theta, \Theta) &= [\cos^2 \theta - \cos^2 \theta']^2.
\end{aligned} \tag{105}$$

The relative angle θ' is defined by $\cos \theta' = \cos \theta \cos \Theta - \sin \theta \sin \Theta \cos \phi$.

Note that the differential cross-section which appears in the denominator is the dynamical input in the expressions for η and ζ . It is this quantity that we turn to in the next section.

3.2. The $\pi\pi$ Cross-Section with Medium Effects. The strong interaction dynamics of the pions enters the collision integrals through the cross-section. In Figure 3, we show the $\pi\pi$ cross-section as a function of the centre of mass energy of scattering. The different curves are explained in the following. The filled squares referred to as experiment is a widely used resonance saturation parametrization [23, 34] of isoscalar and isovector phase shifts obtained from various empirical data involving the $\pi\pi$ system. The isospin averaged differential cross-section is given by

$$\frac{d\sigma(s)}{d\Omega} = \frac{4}{q_{cm}^2} \left[\frac{1}{9} \sin^2 \delta_0^0 + \frac{5}{9} \sin^2 \delta_0^2 + \frac{1}{3} \cdot 9 \sin^2 \delta_1^1 \cos^2 \theta \right], \tag{106}$$

where

$$\begin{aligned}
\delta_0^0 &= \frac{\pi}{2} + \arctan \left(\frac{E - m_\sigma}{\Gamma_\sigma/2} \right), \\
\delta_1^1 &= \frac{\pi}{2} + \arctan \left(\frac{E - m_\rho}{\Gamma_\rho/2} \right), \\
\delta_0^2 &= -\frac{0.12p}{m_\pi}.
\end{aligned} \tag{107}$$

The widths are given by $\Gamma_\sigma = 2.06p$ and $\Gamma_\rho = 0.095p((p/m_\pi)/(1 + (p/m_\rho)^2))^2$ with $m_\sigma = 5.8m_\pi$ and $m_\rho = 5.53m_\pi$.

To get a handle on the dynamics, we now evaluate the $\pi\pi$ cross-section involving ρ and σ meson exchange processes using the interaction Lagrangian as follows:

$$\mathcal{L} = g_\rho \vec{p}^\mu \cdot \vec{\pi} \times \partial_\mu \vec{\pi} + \frac{1}{2} g_\sigma m_\sigma \vec{\pi} \cdot \vec{\pi} \sigma, \tag{108}$$

where $g_\rho = 6.05$ and $g_\sigma = 2.5$. In the matrix elements corresponding to s -channel ρ and σ exchange diagrams which appear for total isospin $I = 1$ and 0, respectively, we

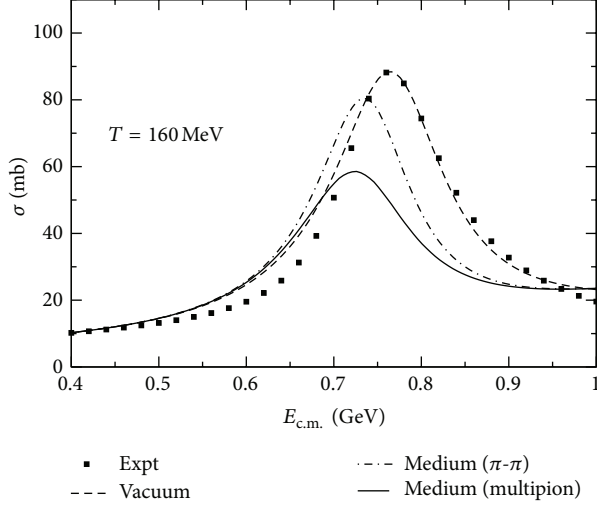


FIGURE 3: The $\pi\pi$ cross-section as a function of centre of mass energy. The dotted line indicates the cross-section obtained using (109) which agrees well with the experimental values (106) shown by filled squares. The dashed and solid lines depict the in-medium cross-section for $\pi\pi$ and πh ($h = \pi, \omega, h_1, a_1$) loops, respectively, in the ρ self-energy evaluated at $T = 160$ MeV.

introduce a decay width in the corresponding propagator. We get [25]

$$\begin{aligned}
\mathcal{M}_{I=0} &= g_\sigma^2 m_\sigma^2 \left[\frac{3}{s - m_\sigma^2 + im_\sigma \Gamma_\sigma} + \frac{1}{t - m_\sigma^2} + \frac{1}{u - m_\sigma^2} \right] \\
&\quad + 2g_\rho^2 \left[\frac{s - u}{t - m_\rho^2} + \frac{s - t}{u - m_\rho^2} \right], \\
\mathcal{M}_{I=1} &= g_\sigma^2 m_\sigma^2 \left[\frac{1}{t - m_\sigma^2} - \frac{1}{u - m_\sigma^2} \right] \\
&\quad + g_\rho^2 \left[\frac{2(t - u)}{s - m_\rho^2 + im_\rho \Gamma_\rho} + \frac{t - s}{u - m_\rho^2} - \frac{u - s}{t - m_\rho^2} \right], \\
\mathcal{M}_{I=2} &= g_\sigma^2 m_\sigma^2 \left[\frac{1}{t - m_\sigma^2} + \frac{1}{u - m_\sigma^2} \right] \\
&\quad + g_\rho^2 \left[\frac{u - s}{t - m_\rho^2} + \frac{t - s}{u - m_\rho^2} \right].
\end{aligned} \tag{109}$$

The differential cross-section is then obtained from $d\sigma/d\Omega = |\mathcal{M}|^2/64\pi^2 s$, where the isospin averaged amplitude is given by $|\mathcal{M}|^2 = (1/9) \sum (2I + 1) |\mathcal{M}_I|^2$.

The integrated cross-section, after ignoring the $I = 2$ contribution is shown by the dotted line (indicated by ‘‘vacuum’’) in Figure 3 and is seen to agree reasonably well with the experimental cross-section up to a centre of mass energy of about 1 GeV beyond which the theoretical estimate gives higher values. We hence use the experimental cross-section beyond this energy.

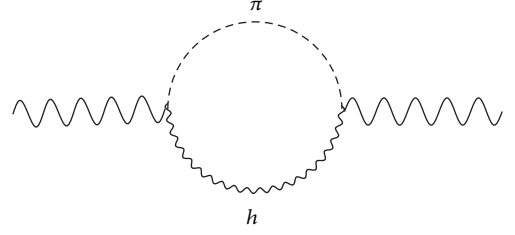


FIGURE 4: πh self-energy diagrams where h stands for $\pi, \omega, h_1,$ and a_1 mesons.

After this normalisation to data, we now turn to the in-medium cross-section by introducing the effective propagator for the ρ in the previous expressions for the matrix elements. This is obtained in terms of the self-energy by solving the Dyson equation and is given by

$$D_{\mu\nu} = D_{\mu\nu}^{(0)} + D_{\mu\sigma}^{(0)} \Pi^{\sigma\lambda} D_{\lambda\nu}, \tag{110}$$

where $D_{\mu\nu}^{(0)}$ is the vacuum propagator for the ρ meson and $\Pi^{\sigma\lambda}$ is the self-energy function obtained from one-loop diagrams shown in Figure 4. The standard procedure [35] to solve this equation in the medium is to decompose the self-energy into transverse and longitudinal components. For the case at hand the difference between these components is found to be small and is hence ignored. We work with the polarization averaged self-energy function defined as

$$\Pi = \frac{1}{3} (2\Pi^T + q^2 \Pi^L), \tag{111}$$

where

$$\Pi^T = -\frac{1}{2} \left(\Pi_\mu^\mu + \frac{q^2}{q^2} \Pi_{00} \right), \tag{112}$$

$$\Pi^L = \frac{1}{q^2} \Pi_{00}, \quad \Pi_{00} \equiv u^\mu u^\nu \Pi_{\mu\nu}.$$

The in-medium propagator is then written as

$$D_{\mu\nu}(q_0, \vec{q}) = \frac{-g_{\mu\nu} + q_\mu q_\nu / q^2}{q^2 - m_\rho^2 - \text{Re} \Pi(q_0, \vec{q}) + i \text{Im} \Pi(q_0, \vec{q})}. \tag{113}$$

The scattering, decay, and regeneration processes which cause a gain or loss of ρ mesons in the medium are responsible for the imaginary part of its self-energy. The real part on the other hand modifies the position of the pole of the spectral function.

As discussed in Section 2.1, in the real-time formulation of thermal field theory the self-energy assumes a 2×2 matrix structure of which the 11 component is given by

$$\Pi_{\mu\nu}^{11}(q) = i \int \frac{d^4 k}{(2\pi)^4} N_{\mu\nu}(q, k) D_\pi^{11}(k) D_h^{11}(q - k), \tag{114}$$

where D^{11} is the 11 component of the scalar propagator given by $D^{11}(k) = \Delta(k) + 2\pi i f^{(0)}(k) \delta(k^2 - m^2)$. It turns out that

the self-energy function mentioned above can be obtained in terms of the 11 component through the relations [35, 36]

$$\begin{aligned} \text{Re } \Pi_{\mu\nu} &= \text{Re } \Pi_{\mu\nu}^{11}, \\ \text{Im } \Pi_{\mu\nu} &= \epsilon(q_0) \tanh\left(\frac{\beta q_0}{2}\right) \text{Im } \Pi_{\mu\nu}^{11}. \end{aligned} \quad (115)$$

Tensor structures associated with the two vertices and the vector propagator are included in $N_{\mu\nu}$ and are available in [37] where the interactions were taken from chiral perturbation theory. It is easy to perform the integral over k_0 using suitable contours to obtain

$$\begin{aligned} \Pi^{\mu\nu}(q_0, \mathbf{q}) &= \int \frac{d^3k}{(2\pi)^3} \frac{1}{4\omega_\pi\omega_h} \\ &\times \left[\frac{\left(1 + f^{(0)}(\omega_\pi)\right) N_1^{\mu\nu} + f^{(0)}(\omega_h) N_3^{\mu\nu}}{q_0 - \omega_\pi - \omega_h + i\eta\epsilon(q_0)} \right. \\ &+ \frac{-f^{(0)}(\omega_\pi) N_1^{\mu\nu} + f^{(0)}(\omega_h) N_4^{\mu\nu}}{q_0 - \omega_\pi + \omega_h + i\eta\epsilon(q_0)} \\ &+ \frac{f^{(0)}(\omega_\pi) N_2^{\mu\nu} - f^{(0)}(\omega_h) N_3^{\mu\nu}}{q_0 + \omega_\pi - \omega_h + i\eta\epsilon(q_0)} \\ &\left. + \frac{-f^{(0)}(\omega_\pi) N_2^{\mu\nu} - \left(1 + f^{(0)}(\omega_h)\right) N_4^{\mu\nu}}{q_0 + \omega_\pi + \omega_h + i\eta\epsilon(q_0)} \right], \end{aligned} \quad (116)$$

where $f^{(0)}(\omega) = 1/(e^{(\omega-\mu_\pi)/T} - 1)$ is the Bose distribution function with arguments $\omega_\pi = \sqrt{\mathbf{k}^2 + m_\pi^2}$ and $\omega_h = \sqrt{(\mathbf{q}-\mathbf{k})^2 + m_h^2}$. Note that this expression is a generalized form for the in-medium self-energy obtained by Weldon [38]. The subscript $i (= 1, \dots, 4)$ on $N^{\mu\nu}$ in (116) corresponds to its values for $k_0 = \omega_\pi, -\omega_\pi, q_0 - \omega_h,$ and $q_0 + \omega_h,$ respectively. It is easy to read off the real and imaginary parts from (116). The angular integration can be carried out using the δ -functions in each of the four terms in the imaginary part which define the kinematically allowed regions in q_0 and \mathbf{q} where scattering, decay, and regeneration processes occur in the medium leading to the loss or gain of ρ mesons [37]. The vector mesons $\omega, h_1,$ and a_1 which appear in the loop have negative G -parity and have substantial 3π and $\rho\pi$ decay widths [39]. The (polarization averaged) self-energies containing these unstable particles in the loop graphs have thus been folded with their spectral functions as follows:

$$\begin{aligned} \Pi(q, m_h) &= \frac{1}{N_h} \int_{(m_h-2\Gamma_h)^2}^{(m_h+2\Gamma_h)^2} dM^2 \\ &\times \frac{1}{\pi} \text{Im} \left[\frac{1}{M^2 - m_h^2 + iM\Gamma_h(M)} \right] \Pi(q, M) \end{aligned} \quad (117)$$

with $N_h = \int_{(m_h-2\Gamma_h)^2}^{(m_h+2\Gamma_h)^2} dM^2 (1/\pi) \text{Im}[1/(M^2 - m_h^2 + iM\Gamma_h(M))]$. The contributions from the loops with heavy mesons may

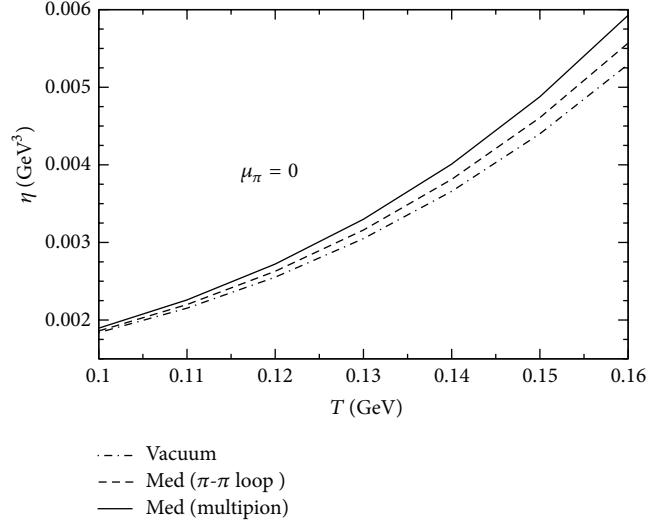


FIGURE 5: The shear viscosity as a function of temperature in the Chapman-Enskog approximation. The dash-dotted line indicates use of the vacuum cross-section, and the dashed and solid lines correspond to in-medium cross-section for the $\pi\pi$ and multipion cases respectively.

then be considered as a multipion contribution to the ρ self-energy.

The in-medium cross-section is now obtained by using the full ρ -propagator (113) in place of the usual vacuum propagator $D_{\mu\nu}^{(0)}$ in the scattering amplitudes. The long dashed line in Figure 3 shows a suppression of the peak when only the $\pi\pi$ loop is considered. This effect is magnified when the πh loops (solid line indicated by multipion) are taken into account and is also accompanied by a small shift in the peak position. Extension to the case of finite baryon density can be done using the spectral function computed in [40] where an extensive list of baryon (and antibaryon) loops are considered along with the mesons. A similar modification of the $\pi\pi$ cross-section for a hot and dense system was seen also in [41].

We plot η versus T in Figure 5 obtained in the Chapman-Enskog approximation showing the effect of the in-medium ρ propagation in the pion gas [25]. We observe $\sim 10\%$ change at $T = 150$ MeV due to medium effects compared to the vacuum when all the loops in the ρ self-energy are considered. The effect reduces with temperature to less than 5% at 100 MeV.

We noted in Section 2 that the lowest order result for η in the response theory framework coincides with that obtained in the relaxation time approximation which is in fact the simplest way to linearize the transport equation. Here one assumes that $f(x, p)$ goes over to the equilibrium distribution $f^{(0)}(x, p)$ as a result of collisions, and this takes place over a relaxation time $\tau(p)$ which is the inverse of the collision frequency defined in (84). The right hand side of (85) is then given by $-E_p[f(x, p) - f^{(0)}(x, p)]/\tau(p)$ which subsequently leads to the expressions (82) and (83) for the shear and bulk viscosities [42]. In Figure 6 we show the temperature dependence of η in the relaxation time approximation. The values in this case are lower than that obtained in the

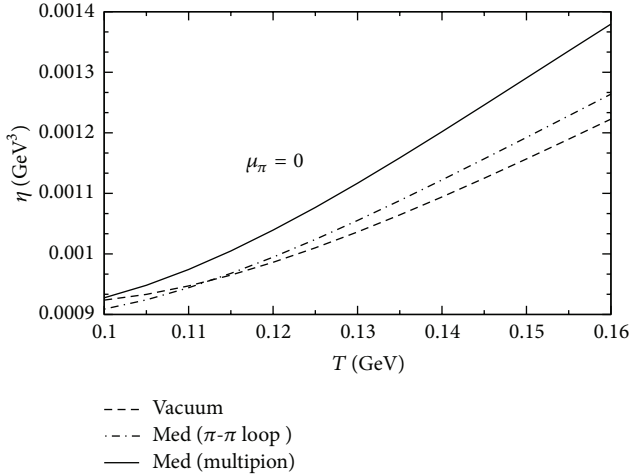


FIGURE 6: The shear viscosity as a function of temperature in the relaxation time approximation. The dash-dotted and solid lines correspond to the use of in-medium cross-sections in (84) for $\pi\pi$ and multipion loops, respectively. The dashed line represents the vacuum case.

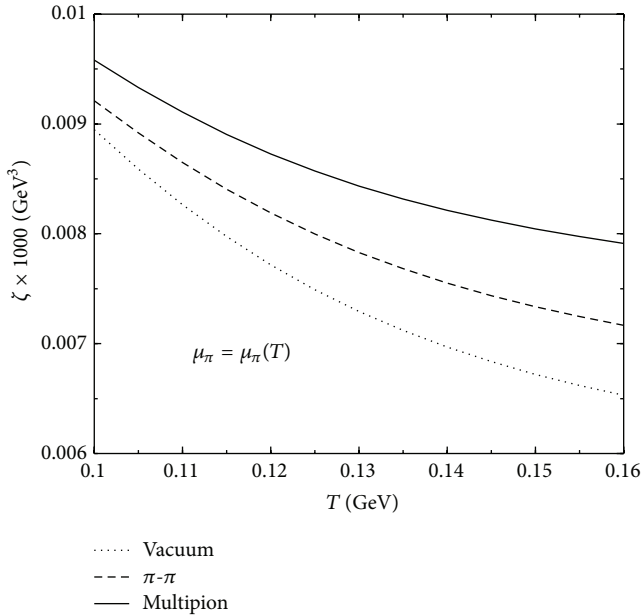


FIGURE 7: The bulk viscosity as a function of temperature for a chemically frozen pion gas. The dashed and solid lines correspond to the use of in-medium cross-sections in (84) for $\pi\pi$ and multipion loops, respectively. The dotted line represents the vacuum case.

Chapman-Enskog method, though the effect of the medium is larger. In addition to the fact that the expressions for the viscosities are quite different in two approaches, the difference in the numerical values obtained in the two cases also depends significantly on the energy dependence of the $\pi\pi$ cross-section [43].

In Figure 7 we show the numerical results for the bulk viscosity of a pion gas as function of T . It is seen from an analysis of the left hand side of the transport equation that, while the shear viscosity depends on elastic processes, bulk viscosity is sensitive to number changing processes. However, in heavy ion collision experiments matter is known to undergo early chemical freezeout. Number changing (inelastic) processes having much larger relaxation times go out of equilibrium at this point and a temperature dependent chemical potential results for each species so as to conserve the number corresponding to the measured particle ratios. We hence use a temperature dependent pion chemical potential taken from [44] in this case. It is interesting to observe that ζ decreases with T in contrast to η which increases. The trend followed by ζ is similar to the findings of [45]. Additional discussions concerning the temperature dependence of viscosities for a chemically frozen pion gas are available in [31].

4. Summary and Conclusion

To summarize, we have calculated the shear viscosity coefficient of a pion gas in the real-time version of thermal field theory. It is simpler to the imaginary version in that we do not have to continue to imaginary time at any stage of the calculation. As an element in the theory of linear response, a transport coefficient is defined in terms of a retarded thermal two-point function of the components of the energy-momentum tensor. We derive Källén-Lehmann representation for any (bosonic) two-point function of both time-ordered and retarded types to get the relation between them. Once this relation is obtained, we can calculate the retarded function in the Feynman-Dyson framework of the perturbation theory.

Clearly the method is not restricted to transport coefficients. Any linear response leads to a retarded two-point function, which can be calculated in this way. Also quadratic response formulae have been derived in the real-time formulation [46].

We have also evaluated the viscous coefficients in the kinetic theory approach to leading order in the Chapman-Enskog expansion. Here we have incorporated an in-medium $\pi\pi$ cross-section and found a significant effect in the temperature dependence of the shear viscosity.

The viscous coefficients and their temperature dependence could affect the quantitative estimates of signals of heavy ion collisions particularly where hydrodynamic simulations are involved. For example, it has been argued in [47] that corrections to the freeze-out distribution due to bulk viscosity can be significant. As a result the hydrodynamic description of the p_T spectra and elliptic flow of hadrons could be improved by including a realistic temperature dependence of the viscous coefficients. Such an evaluation essentially requires the consideration of a multicomponent gas preferably containing nucleonic degrees of freedom, so that extensions to finite baryon chemical potential can be made. Work in this direction is in progress.

Acknowledgments

The author gratefully acknowledges the contribution from his collaborators S. Mallik, S. Ghosh, and S. Mitra to various topics presented here.

References

- [1] P. Kovtun, D. T. Son, and A. O. Starinets, “Viscosity in strongly interacting quantum field theories from black hole physics,” *Physical Review Letters*, vol. 94, no. 11, Article ID 111601, 4 pages, 2005.
- [2] L. P. Csernai, J. I. Kapusta, and L. D. McLerran, “Strongly interacting low-viscosity matter created in relativistic nuclear collisions,” *Physical Review Letters*, vol. 97, no. 15, Article ID 152303, 4 pages, 2006.
- [3] H. B. Meyer, “Transport properties of the quark-gluon plasma,” *The European Physical Journal A*, vol. 47, p. 86, 2011.
- [4] N. Demir and S. A. Bass, “Shear-viscosity to entropy-density ratio of a relativistic hadron gas,” *Physical Review Letters*, vol. 102, no. 17, Article ID 172302, 4 pages, 2009.
- [5] T. Matsubara, “A new approach to quantum-statistical mechanics,” *Progress of Theoretical Physics*, vol. 14, pp. 351–378, 1955.
- [6] R. Mills, *Propagators for Many Particle Systems*, Gordon and Breach, New York, NY, USA, 1969.
- [7] H. Matsumoto, Y. Nakano, and H. Umezawa, “An equivalence class of quantum field theories at finite temperature,” *Journal of Mathematical Physics*, vol. 25, no. 10, pp. 3076–3085, 1984.
- [8] A. J. Niemi and G. W. Semenoff, “Finite-temperature quantum field theory in Minkowski space,” *Annals of Physics*, vol. 152, no. 1, pp. 105–129, 1984.
- [9] R. L. Kobes and G. W. Semenoff, “Discontinuities of green functions in field theory at finite temperature and density,” *Nuclear Physics B*, vol. 260, no. 3-4, pp. 714–746, 1985.
- [10] A. Hosoya, M. Sakagami, and M. Takao, “Nonequilibrium thermo field dynamics in field theory: transport coefficients,” *Annals of Physics*, vol. 154, p. 229, 1982.
- [11] R. Lang, N. Kaiser, and W. Weise, “Shear viscosity of a hot pion gas,” *The European Physical Journal A*, vol. 48, article 109, 2012.
- [12] S. Jeon, “Computing spectral densities in finite temperature field theory,” *Physical Review D*, vol. 47, no. 10, pp. 4586–4607, 1993.
- [13] G. K. Källen, “On the definition of the renormalization constants in quantum electrodynamics,” *Helvetica Physica Acta*, vol. 25, p. 417, 1952.
- [14] H. Lehmann, “Über Eigenschaften von Ausbreitungsfunktionen und Renormierungskonstanten quantisierter Felder,” *Il Nuovo Cimento*, vol. 11, no. 4, pp. 342–357, 1954.
- [15] A. L. Fetter and J. D. Walecka, *Quantum Theory of Many-Particle Systems*, Dover Publications, New York, NY, USA, 2003.
- [16] S. Mallik and S. Sarkar, “Real-time propagators at finite temperature and chemical potential,” *The European Physical Journal C*, vol. 61, no. 3, pp. 489–494, 2009.
- [17] S. Weinberg, “Phenomenological lagrangians,” *Physica A*, vol. 96, no. 1-2, pp. 327–340, 1979.
- [18] J. Gasser and H. Leutwyler, “Chiral perturbation theory to one loop,” *Annals of Physics*, vol. 158, no. 1, pp. 142–210, 1984.
- [19] A. Dobado and S. N. Santalla, “Pion gas viscosity at low temperature and density,” *Physical Review D*, vol. 65, no. 9, Article ID 096011, 13 pages, 2002.
- [20] J. W. Chen, Y. H. Li, Y. F. Liu, and E. Nakano, “QCD viscosity to entropy density ratio in the hadronic phase,” *Physical Review D*, vol. 76, no. 11, Article ID 114011, 8 pages, 2007.
- [21] A. Dobado and F. J. Llanes-Estrada, “Viscosity of meson matter,” *Physical Review D*, vol. 69, no. 11, Article ID 116004, 2004.
- [22] D. Davesne, “Transport coefficients of a hot pion gas,” *Physical Review C*, vol. 53, no. 6, pp. 3069–3084, 1996.
- [23] M. Prakash, M. Prakash, R. Venugopalan, and G. Welke, “Non-equilibrium properties of hadronic mixtures,” *Physics Report*, vol. 227, no. 6, pp. 321–366, 1993.
- [24] K. Itakura, O. Morimatsu, and H. Otomo, “Shear viscosity of a hadronic gas mixture,” *Physical Review D*, vol. 77, no. 1, Article ID 014014, 19 pages, 2008.
- [25] S. Mitra, S. Ghosh, and S. Sarkar, “Effect of a spectral modification of the ρ meson on the shear viscosity of a pion gas,” *Physical Review C*, vol. 85, no. 6, Article ID 064917, 8 pages, 2012.
- [26] R. Kubo, “Statistical-mechanical theory of irreversible processes. I. General theory and simple applications to magnetic and conduction problems,” *Journal of the Physical Society of Japan*, vol. 12, pp. 570–586, 1957.
- [27] P. C. Martin and J. Schwinger, “Theory of many-particle systems. I,” *Physical Review*, vol. 115, no. 6, pp. 1342–1373, 1959.
- [28] D. N. Zubarev, *Nonequilibrium Statistical Thermodynamics*, Plenum, New York, NY, USA, 1974.
- [29] M. Gell-Mann and M. L. Golberger, “The formal theory of scattering,” *Physical Review*, vol. 91, no. 2, pp. 398–408, 1953.
- [30] J. L. Goity and H. Leutwyler, “On the mean free path of pions in hot matter,” *Physics Letters B*, vol. 228, no. 4, pp. 517–522, 1989.
- [31] S. Mitra and S. Sarkar, “Medium effects on the viscosities of a pion gas,” *Physical Review D*, vol. 87, no. 9, Article ID 094026, 12 pages, 2013.
- [32] P. Chakraborty and J. I. Kapusta, “Quasiparticle theory of shear and bulk viscosities of hadronic matter,” *Physical Review C*, vol. 83, no. 1, Article ID 014906, 17 pages, 2011.
- [33] P. H. Polak, W. A. van Leeuwen, and S. R. de Groot, “On relativistic kinetic gas theory. X. Transport coefficients in the intermediate relativistic regime. Values for special models,” *Physica*, vol. 66, no. 3, pp. 455–473, 1973.
- [34] G. Bertsch, M. Gong, L. McLerran, P. V. Ruuskanen, and E. Sarkkinen, “Cascade simulation of ultrarelativistic collisions,” *Physical Review D*, vol. 37, no. 5, pp. 1202–1209, 1988.
- [35] M. Le Bellac, *Thermal Field Theory*, Cambridge Monographs on Mathematical Physics, Cambridge University Press, Cambridge, Mass, USA, 1996.
- [36] S. Sarkar, B. K. Patra, V. J. Menon, and S. Mallik, “Spectral representation at finite temperature,” *Indian Journal of Physics*, vol. 76A, pp. 385–391, 2002.
- [37] S. Ghosh, S. Sarkar, and S. Mallik, “Analytic structure of ρ meson propagator at finite temperature,” *The European Physical Journal C*, vol. 70, no. 1-2, pp. 251–262, 2010.
- [38] H. A. Weldon, “Simple rules for discontinuities in finite-temperature field theory,” *Physical Review D*, vol. 28, no. 8, pp. 2007–2015, 1983.
- [39] K. Nakamura, K. Hagiwara, K. Hikasa et al., “Review of particle physics,” *Journal of Physics G*, vol. 37, Article ID 075021, 2010.
- [40] S. Ghosh and S. Sarkar, “ ρ self-energy at finite temperature and density in the real-time formalism,” *Nuclear Physics A*, vol. 870-871, pp. 94–111, 2011.
- [41] H. W. Barz, G. Bertsch, P. Danielewicz, and H. Schulz, “Pion-pion cross section in a dense and hot pionic gas,” *Physics Letters B*, vol. 275, no. 1-2, pp. 19–23, 1992.

- [42] S. Gavin, "Transport coefficients in ultra-relativistic heavy-ion collisions," *Nuclear Physics A*, vol. 435, no. 3-4, pp. 826–843, 1985.
- [43] A. Wiranata and M. Prakash, "Shear viscosities from the Chapman-Enskog and the relaxation time approaches," *Physical Review C*, vol. 85, no. 5, Article ID 054908, 14 pages, 2012.
- [44] T. Hirano and K. Tsuda, "Collective flow and two-pion correlations from a relativistic hydrodynamic model with early chemical freeze-out," *Physical Review C*, vol. 66, no. 5, Article ID 054905, 14 pages, 2002.
- [45] E. Lu and G. D. Moore, "Bulk viscosity of a pion gas," *Physical Review C*, vol. 83, no. 4, Article ID 044901, 7 pages, 2011.
- [46] M. E. Carrington, H. Defu, and R. Kobes, "Nonlinear response from transport theory and quantum field theory at finite temperature," *Physical Review D*, vol. 64, no. 2, Article ID 025001, 15 pages, 2001.
- [47] K. Dusling and T. Schafer, "Bulk viscosity, particle spectra, and flow in heavy-ion collisions," *Physical Review C*, vol. 85, no. 4, Article ID 044909, 19 pages, 2012.

Review Article

Charge Radii and Quadrupole Moments of the Low-Lying Baryons in the Chiral Constituent Quark Model

Neetika Sharma and Harleen Dahiya

Department of Physics, Dr. B.R. Ambedkar National Institute of Technology, Jalandhar 144011, India

Correspondence should be addressed to Harleen Dahiya; dahiyah@nitj.ac.in

Received 16 December 2012; Revised 15 April 2013; Accepted 13 May 2013

Academic Editor: Jan E. Alam

Copyright © 2013 N. Sharma and H. Dahiya. This is an open access article distributed under the Creative Commons Attribution License, which permits unrestricted use, distribution, and reproduction in any medium, provided the original work is properly cited.

The chiral constituent quark model (χ CQM) with general parameterization method (GPM) has been formulated to calculate the charge radii of the spin $(1/2)^+$ octet and $(3/2)^+$ decuplet baryons and quadrupole moments of the spin $(3/2)^+$ decuplet baryons and spin $(3/2)^+ \rightarrow (1/2)^+$ transitions. The implications of such a model have been investigated in detail for the effects of symmetry breaking and GPM parameters pertaining to the one-, two-, and three-quark contributions. Our results are not only comparable with the latest experimental studies but also agree with other phenomenological models. It is found that the χ CQM is successful in giving a quantitative and qualitative description of the charge radii and quadrupole moments.

1. Introduction

The internal structure of baryons is determined in terms of electromagnetic Dirac and Pauli form factors $F_1(Q^2)$ and $F_2(Q^2)$ or equivalently in terms of the electric and magnetic Sachs form factors $G_E(Q^2)$ and $G_M(Q^2)$ [1]. The electromagnetic form factors are the fundamental quantities of theoretical and experimental interest which are further related to the static low energy observables of charge radii and magnetic moments. One of the main challenges in the theoretical and experimental hadronic physics is to understand the structure of hadrons within the quantum chromodynamics (QCD) in terms of these moments. Although QCD is accepted as the fundamental theory of strong interactions, the direct prediction of these kinds of observables from the first principle of QCD still remains a theoretical challenge as they lie in the nonperturbative regime of QCD.

Following the discoveries that the quarks and antiquarks carry only 30% of the total proton spin [2, 3], the orbital angular momentum of quarks and gluons is expected to make a significant contribution. In addition to this, there is a significant contribution coming from the strange quarks in the nucleon which are otherwise not present in the valence structure. It therefore becomes interesting to discuss

the interplay between the spin of nonvalence quark and the orbital angular momentum in understanding the spin structure of baryons. Further, the experimental developments [4–6], providing information on the radial variation of the charge, and magnetization densities of the proton give the evidence for the deviation of the charge distribution from spherical symmetry. On the other hand, it is well known that the quadrupole moment of the nucleon should vanish on account of its spin-1/2 nature. This observation has naturally turned to be the subject of intense theoretical and experimental activity.

The mean square charge radius (r_B^2), giving the possible “size” of baryon, has been investigated experimentally with the advent of new facilities at JLAB, SELEX Collaborations [7–13]. Several measurements have been made for the charge radii of p , n , and Σ^- in electron-baryon scattering experiments [13, 14] giving $r_p = 0.877 \pm 0.007$ fm ($r_p^2 = 0.779 \pm 0.025$ fm² [15]) and $r_n^2 = -0.1161 \pm 0.0022$ fm² [12]. The recent measurement of $r_{\Sigma^-}^2$ [13, 14] is particularly interesting as it gives the first estimate for the charge form factor of a strange baryon at low momentum transfer.

The $\Delta(1232)$ resonance is the lowest-lying excited state of the nucleon in which the search for quadrupole strength

has been carried out [16–19]. The spin and parity selection rules in the $\gamma + p \rightarrow \Delta^+$ transition allow three contributing photon absorption amplitudes, the magnetic dipole G_{M1} , the electric quadrupole moment G_{E2} , and the charge quadrupole moment G_{C2} . The G_{M1} amplitude gives us information on magnetic moment, whereas the information on the intrinsic quadrupole moment can be obtained from the measurements of G_{E2} and G_{C2} amplitudes [12]. If the charge distribution of the initial and final three-quark states was spherically symmetric, the G_{E2} and G_{C2} amplitudes of the multipole expansion would be zero [20]. However, the recent experiments at Mainz, Bates, Bonn, and JLab Collaborations [7–11, 21, 22] reveal that these quadrupole amplitudes are clearly nonzero [12]. The ratio of electric quadrupole amplitude to the magnetic dipole amplitude is at least $E2/M1 \equiv -0.025 \pm 0.005$, and a comparable value of same sign and magnitude has been measured for the $C2/M1$ ratio [12]. Further, the quadrupole transition moment (Q^{Δ^+N}) measured by LEGS and Mainz collaborations ($-0.108 \pm 0.009 \pm 0.034 \text{ fm}^2$ [16–18] and $-0.0846 \pm 0.0033 \text{ fm}^2$ [19], resp.) also leads to the conclusion that the nucleon and the Δ^+ are *intrinsically* deformed.

The naive quark model (NQM) [23–27] is one of the simplest model to describe the hadron properties and interactions in the low energy regime. This model is able to provide a simple intuitive picture of the hadron structure in terms of three valence quarks (qqq) for baryons and quark antiquark ($q\bar{q}$) for mesons. It allows the direct calculations of the low energy hadronic matrix elements including their spectra and successfully accounts for many of the low energy properties of the hadrons in terms of the valence quarks [28–32]. Interestingly, with the inclusion of the spin-spin interactions generated configuration mixing [28] between the valence quarks, the NQM has not only given an accurate description of the hadron spectroscopy data but also has been able to describe some subtle features of the data including the $N - \Delta$ mass difference, photohelicity amplitudes, and baryon magnetic moments [29–36]. However, some major findings on the experimental front discussed below have brought into prominence the inadequacies of the NQM.

The measurements in the deep inelastic scattering (DIS) experiments [2, 3] indicate that the valence quarks of the proton carry only about 30% of its spin and also establish the asymmetry of the quark distribution functions [37–41]. This is referred to as the “proton spin problem” in NQM. Several effective and phenomenological models have been developed to explain the “proton spin problem” by including spontaneous breaking of chiral symmetry and have been further applied to study the electromagnetic properties of baryons.

For the calculations pertaining to the baryon charge radii, NQM leads to vanishing charge radii for the neutral baryons like n , Σ^0 , Ξ^0 , and Λ . This is in contradiction to the experimental data. The inclusion of quark spin-spin interactions in NQM modify the baryon wavefunction to some extent leading to the breaking of the SU(3) symmetry and a nonvanishing neutron charge mean square radius [29–32]. A likely cause of these dynamical shortcomings

is that the NQM does not respect chiral symmetry whose spontaneous breaking leads to the emission of Goldstone bosons (GBs). In this context, it becomes important to incorporate the effect of chiral symmetry breaking (χ SB) in the phenomenological models to obtain a reasonable agreement with the data. On the other hand, a wide variety of accurately measured data have been accumulated for the static low energy properties of baryons, for example, masses, electromagnetic moments, charge radii, and low energy dynamical properties such as scattering lengths and decay rates, which has renewed considerable interest in the low energy baryon spectroscopy. The direct calculations of these quantities from the first principle of QCD are extremely difficult as they require the nonperturbative methods. Several effective and phenomenological models such as Lattice QCD, effective field theories, QCD sum rules, and variants of quark models have been developed to explain the failures of the NQM and further applied to study the properties of baryons.

Some of the important models measuring the charge radii of octet baryon are the Skyrme model with bound state approach [42–44], slow-rotor approach [45], semibosonized SU(3) NJL model [46], cloudy bag model [47], variants of constituent quark models [48–54], $1/N_c$ expansion approach [55–58], perturbative chiral quark model ($P\chi$ QM) [59], heavy-baryon chiral perturbation theory (HB χ PT) [60], chiral perturbation theory (χ PT) [61, 62], Lattice QCD [63], and so forth. The charge radii of decuplet baryons have been studied within the framework of Lattice QCD [64–66], quark model [67], $1/N_c$ expansion [55, 56], chiral perturbation theory [68], and so forth. The results for different theoretical models are however not consistent with each other.

There have been a lot of theoretical investigations in understanding the implications of the $C2/M1$ and $E2/M1$ ratios in finding out the exact sign of deformation in the spin $(1/2)^+$ octet baryons. However, there is a little consensus between the results even with respect to the sign of the nucleon deformation. Some of the models predict the deformation in nucleon as oblate [69, 70], some predict a prolate nucleon deformation [71–80] whereas others speak about “deformation” without specifying the sign. The quadrupole moment of the $(3/2)^+$ decuplet baryons has also been studied using the variants of the constituent quark model (CQM) [81–84], chiral quark soliton model (χ QSM) [85], spectator quark model [86–88], slow-rotator approach (SRA) [89, 90], skyrme model [91, 92], general parametrization method [93, 94], light cone QCD sum rules (QCDSR) [95, 96], large N_c [97, 98], chiral perturbation theory (χ PT) [99–103], Lattice QCD (LQCD) [104–108], and so forth. In this case also, the results for different theoretical models are not consistent in terms of sign and magnitude with each other.

As the hadron structure is sensitive to the pion cloud in the low energy regime, a coherent understanding is necessary as it will provide a test for the QCD-inspired effective field theories. One of the important nonperturbative approaches which finds its application in the low energy regime is the chiral constituent quark model (χ CQM) [109,

110]. It is one of the most convenient languages for the treatment of light hadrons at low energies using the effective interaction Lagrangian approach of the strong interactions. The χ CQM coupled with the “quark sea” generation through the chiral fluctuation of a constituent quark GBs [111–119] successfully explains the “proton spin problem” [117–119], hyperon β decay parameters [120, 121], strangeness content in the nucleon [122–124], magnetic moments of octet and decuplet baryons including their transitions [125–127], magnetic moments of $(1/2)^-$ octet baryon resonances [128], magnetic moments of $(1/2)^-$ and $(3/2)^-$ Λ resonances [129], charge radii [130], quadrupole moment [131], and so forth. The model is successfully extended to predict the important role played by the small intrinsic charm (IC) content in the nucleon spin in the SU(4) χ CQM [132] and to calculate the magnetic moment of spin $(1/2)^+$ and spin $(3/2)^+$ charm baryons including their radiative decays [133]. In view of the above developments in the χ CQM, it become desirable to extend the model to calculate the charge radii and quadrupole moment of the spin $(1/2)^+$ octet and spin $(3/2)^+$ decuplet baryons.

The purpose of the present communication is to calculate the charge radii of the spin $(1/2)^+$ octet and spin $(3/2)^+$ decuplet baryons and quadrupole moment of the spin $(3/2)^+$ decuplet baryons including the spin $(3/2)^+ \rightarrow (1/2)^+$ transitions within the framework of χ CQM using a general parametrization method (GPM) [134–138]. In order to understand the role of pseudoscalar mesons in the baryon charge radii and quadrupole moment, we will compare our results with NQM as well as other phenomenological models. The detailed analysis of SU(3) symmetry breaking would also be carried out in the χ CQM. Further, we aim to discuss the implications of GPM parameters by calculating the extent to which the three-quark term contributes.

2. Charge Radii and Quadrupole Moments

The mean square charge radii (r_B^2) and quadrupole moments (Q_B) are the lowest order moments of the charge density ρ in a low-momentum expansion. The charge radii contain fundamental information about the possible “size” of the baryons whereas the “shape” of a spatially extended particle is determined by its quadrupole moment [139–142].

The mean square charge radius r_B^2 of a given baryon is a scalar under spatial rotation and is defined as

$$\langle r^2 \rangle = \int d^3r \rho(\mathbf{r}) r^2, \quad (1)$$

where $\rho(\mathbf{r})$ is the charge density. The *intrinsic* quadrupole moment with respect to the body frame of axis is defined as

$$Q_0 = \int d^3r \rho(\mathbf{r}) (3z^2 - r^2). \quad (2)$$

For the charge density concentrated along the z -direction, the term proportional to $3z^2$ dominates, Q_0 is positive, and the particle is prolate shaped. If the charge density is concentrated in the equatorial plane perpendicular to z axis, the term

proportional to r^2 dominates, Q_0 is negative, and the particle is oblate shaped.

The most general form of the multipole expansion of the nucleon charge density ρ in the spin-flavor space can be expressed as

$$\begin{aligned} \rho = & A' \sum_{i=1}^3 e_i \mathbf{1} - B' \sum_{i \neq j}^3 e_i \left[2\sigma_i \cdot \sigma_j - (3\sigma_{iz}\sigma_{jz} - \sigma_i \cdot \sigma_j) \right] \\ & - C' \sum_{i \neq j \neq k}^3 e_i \left[2\sigma_j \cdot \sigma_k - (3\sigma_{jz}\sigma_{kz} - \sigma_j \cdot \sigma_k) \right]. \end{aligned} \quad (3)$$

The charge radii operator composed of the sum of one-, two-, and three-quark terms is expressed as

$$\widehat{r}^2 = A \sum_{i=1}^3 e_i \mathbf{1} + B \sum_{i \neq j}^3 e_i \sigma_i \cdot \sigma_j + C \sum_{i \neq j \neq k}^3 e_i \sigma_j \cdot \sigma_k, \quad (4)$$

whereas the quadrupole moment operator composed of a two- and three-quark term can be expressed as

$$\begin{aligned} \widehat{Q} = & B' \sum_{i \neq j}^3 e_i (3\sigma_{iz}\sigma_{jz} - \sigma_i \cdot \sigma_j) \\ & + C' \sum_{i \neq j \neq k}^3 e_i (3\sigma_{jz}\sigma_{kz} - \sigma_j \cdot \sigma_k). \end{aligned} \quad (5)$$

The coefficients called GPM parameters of the charge radii and quadrupole moments are related to each other as $A = A'$, $B = -2B'$, and $C = -2C'$. These GPM parameters are to be determined from the experimental observations on charge radii and quadrupole moment.

Before calculating the matrix elements corresponding to the charge radii and quadrupole moment, it is essential to simplify various operator terms involved in (4). It can be easily shown that

$$\begin{aligned} \sum_{i \neq j} e_i (\sigma_i \cdot \sigma_j) &= 2J \cdot \sum_i e_i \sigma_i - 3 \sum_i e_i, \\ \sum_{i \neq j \neq k} e_i (\sigma_j \cdot \sigma_k) &= \pm 3 \sum_i e_i - \sum_{i \neq j} e_i (\sigma_i \cdot \sigma_j), \end{aligned} \quad (6)$$

where +ve sign holds for $J = 3/2$ and –ve sign for $J = 1/2$ states leading to different operators for spin $(1/2)^+$ and spin $(3/2)^+$ baryons:

Operator	$\sum_{i \neq j} e_i (\sigma_i \cdot \sigma_j)$	$\sum_{i \neq j \neq k} e_i (\sigma_j \cdot \sigma_k)$
$J = \frac{1}{2}$	$3 \sum_i e_i \sigma_{iz} - 3 \sum_i e_i$	$-3 \sum_i e_i \sigma_{iz}$
$J = \frac{3}{2}$	$5 \sum_i e_i \sigma_{iz} - 3 \sum_i e_i$	$6 \sum_i e_i - 5 \sum_i e_i \sigma_{iz}$

(7)

The charge radii operators for the spin $(1/2)^+$ octet and spin $(3/2)^+$ decuplet baryons can now be expressed as

$$\widehat{r}_B^2 = (A - 3B) \sum_i e_i + 3(B - C) \sum_i e_i \sigma_{iz}, \quad (8)$$

$$\widehat{r}_{B^*}^2 = (A - 3B + 6C) \sum_i e_i + 5(B - C) \sum_i e_i \sigma_{iz}. \quad (9)$$

It is clear from the above equations that the determination of charge radii basically reduces to the evaluation of the flavor ($\sum_i e_i$) and spin ($\sum_i e_i \sigma_{iz}$) structure of a given baryon. The charge radii squared $r_{B(B^*)}^2$ for the octet (decuplet) baryons can now be calculated by evaluating matrix elements corresponding to the operators in (8) and (9) and are given as

$$r_B^2 = \langle B | \widehat{r}_B^2 | B \rangle, \quad r_{B^*}^2 = \langle B^* | \widehat{r}_{B^*}^2 | B^* \rangle. \quad (10)$$

Here $|B\rangle$ and $|B^*\rangle$, respectively, denote the spin-flavor wavefunctions for the spin $(1/2)^+$ octet and the spin $(3/2)^+$ decuplet baryons.

The quadrupole moment operators for the spin $(1/2)^+$, spin $(3/2)^+$ baryons, and spin $(3/2)^+ \rightarrow (1/2)^+$ transitions can be calculated from the operator in (5) and are expressed as

$$\begin{aligned} \widehat{Q}_B &= B' \left(3 \sum_{i \neq j} e_i \sigma_{iz} \sigma_{jz} - 3 \sum_i e_i \sigma_{iz} + 3 \sum_i e_i \right) \\ &\quad + C' \left(3 \sum_{i \neq j \neq k} e_i \sigma_{jz} \sigma_{kz} + 3 \sum_i e_i \sigma_{iz} \right), \\ \widehat{Q}_{B^*} &= B' \left(3 \sum_{i \neq j} e_i \sigma_{iz} \sigma_{jz} - 5 \sum_i e_i \sigma_{iz} + 3 \sum_i e_i \right) \\ &\quad + C' \left(3 \sum_{i \neq j \neq k} e_i \sigma_{jz} \sigma_{kz} + 5 \sum_i e_i \sigma_{iz} - 6 \sum_i e_i \right), \\ \widehat{Q}_{B^*B} &= 3B' \sum_{i \neq j} e_i \sigma_{iz} \sigma_{jz} + 3C' \sum_{i \neq j \neq k} e_i \sigma_{jz} \sigma_{kz}. \end{aligned} \quad (11)$$

It is clear from the above equations that the determination of quadrupole moment basically reduces to the evaluation of the flavor ($\sum_i e_i$), spin ($\sum_i e_i \sigma_{iz}$), and tensor terms ($\sum_i e_i \sigma_{iz} \sigma_{jz}$) and ($\sum_i e_i \sigma_{jz} \sigma_{kz}$) for a given baryon.

Using the three-quark spin-flavor wavefunctions for the spin $(1/2)^+$ octet and spin $(3/2)^+$ decuplet baryons, the quadrupole moment can now be calculated by evaluating the matrix elements of operators in (11). We now have

$$\begin{aligned} Q_B &= \langle B | \widehat{Q}_B | B \rangle, & Q_{B^*} &= \langle B^* | \widehat{Q}_{B^*} | B^* \rangle, \\ Q_{B \rightarrow B^*} &= \langle B^* | \widehat{Q}_{B^*B} | B \rangle. \end{aligned} \quad (12)$$

3. Naive Quark Model (NQM)

The appropriate operators for the spin and flavor structure of baryons in NQM are defined as

$$\begin{aligned} \sum_i e_i &= \sum_{q=u,d,s} n_q^B + \sum_{\bar{q}=\bar{u},\bar{d},\bar{s}} n_{\bar{q}}^B \\ &= n_u^B u + n_d^B d + n_s^B s + n_{\bar{u}}^B \bar{u} + n_{\bar{d}}^B \bar{d} + n_{\bar{s}}^B \bar{s}, \\ \sum_i e_i \sigma_{iz} &= \sum_{q=u,d,s} (n_{q_+}^B q_+ + n_{q_-}^B q_-) \\ &= n_{u_+}^B u_+ + n_{u_-}^B u_- + n_{d_+}^B d_+ + n_{d_-}^B d_- + n_{s_+}^B s_+ + n_{s_-}^B s_-, \end{aligned} \quad (13)$$

where n_q^B ($n_{\bar{q}}^B$) is the number of quarks with charge q (\bar{q}) and $n_{q_+}^B$ ($n_{q_-}^B$) is the number of polarized quarks q_+ (q_-). For a given baryon $u = -\bar{u}$ and $u_+ = -u_-$, with similar relations for the d and s quarks. The general expression for the charge radii of any of the spin $(1/2)^+$ octet baryon in (4) can be expressed as

$$\begin{aligned} \widehat{r}_B^2 &= (A - 3B) \left(\sum_{u,d,s} n_q - \sum_{\bar{u},\bar{d},\bar{s}} n_{\bar{q}} \right) q \\ &\quad + 3(B - C) \left(\sum_{u,d,s} n_{q_+} - \sum_{u,d,s} n_{q_-} \right) q_+. \end{aligned} \quad (14)$$

Before we discuss the details of the charge radii calculations, it is essential to define the octet and decuplet wavefunctions. The ‘‘mixed’’ state octet baryon wavefunction generated by the spin-spin forces [33, 34] which improves the predictions of the various spin-related properties [117–119] is expressed as

$$|B\rangle \equiv \left| 8, \frac{1}{2}^+ \right\rangle = \cos \theta |56, 0^+\rangle_{N=0} + \sin \theta |70, 0^+\rangle_{N=2}, \quad (15)$$

with

$$\begin{aligned} |56, 0^+\rangle_{N=0} &= \frac{1}{\sqrt{2}} (\varphi' \chi' + \varphi'' \chi'') \psi^s(0^+), \\ |70, 0^+\rangle_{N=2} &= \frac{1}{2} [(\varphi' \chi'' + \varphi'' \chi') \psi'(0^+) \\ &\quad + (\varphi' \chi' - \varphi'' \chi'') \psi''(0^+)]. \end{aligned} \quad (16)$$

Here θ is the mixing angle and χ , φ , and ψ are the spin, isospin, and spatial wavefunctions. For the details of the wavefunction, we refer the readers to [33, 34]. Using the

TABLE 1: Charge radii of octet baryons in $\text{NQM}_{\text{config}}$ in terms of the GPM parameters. The results in NQM without configuration can easily be calculated by substituting $\theta = 0$.

Charge radii	$\text{NQM}_{\text{config}}$
r_p^2	$(A - 3B)[2u + d] + (B - C) [\cos^2\theta(4u_+ - d_+) + \sin^2\theta(2u_+ + d_+)]$
r_n^2	$(A - 3B)[u + 2d] + (B - C) [\cos^2\theta(-u_+ + 4d_+) + \sin^2\theta(u_+ + 2d_+)]$
$r_{\Sigma^+}^2$	$(A - 3B)[2u + s] + (B - C) [\cos^2\theta(4u_+ - s_+) + \sin^2\theta(2u_+ + s_+)]$
$r_{\Sigma^-}^2$	$-(A - 3B)[2d + s] - (B - C) [\cos^2\theta(4d_+ - s_+) + \sin^2\theta(2d_+ + s_+)]$
$r_{\Sigma^0}^2$	$(A - 3B)[u + d + s] + (B - C) [\cos^2\theta(2u_+ + 2d_+ - s_+) + \sin^2\theta(u_+ + d_+ + s_+)]$
$r_{\Xi^0}^2$	$(A - 3B)[u + 2s] + (B - C) [\cos^2\theta(-u_+ + 4s_+) + \sin^2\theta(u_+ + 2s_+)]$
$r_{\Xi^-}^2$	$-(A - 3B)[d + 2s] + (B - C) [\cos^2\theta(-d_+ + 4s_+) + \sin^2\theta(d_+ + 2s_+)]$
r_{Λ}^2	$(A - 3B)[u + d + s] + (B - C) [\cos^2\theta(3s_+) + \sin^2\theta(u_+ + d_+ + s_+)]$
$r_{\Sigma\Lambda}^2$	$(A - 3B)[u + d + s] + \sqrt{3}(B - C) [u_+ - d_+]$

TABLE 2: Charge radii of decuplet baryons in NQM in terms of GPM parameters.

Charge radii	NQM
$r_{\Delta^{++}}^2$	$\frac{1}{2} [(A - 3B + 6C)(3u) + 5(B - C)(3u_+)]$
$r_{\Delta^+}^2$	$(A - 3B + 6C)(2u + d) + 5(B - C)(2u_+ + d_+)$
$r_{\Delta^0}^2$	$(A - 3B + 6C)(u + 2d) + 5(B - C)(u_+ + 2d_+)$
$r_{\Delta^-}^2$	$-(A - 3B + 6C)(3d) - 5(B - C)(3d_+)$
$r_{\Sigma^{*+}}^2$	$(A - 3B + 6C)(2u + s) + 5(B - C)(2u_+ + s_+)$
$r_{\Sigma^{*-}}^2$	$-(A - 3B + 6C)(2d + s) - 5(B - C)(2d_+ + s_+)$
$r_{\Sigma^{*0}}^2$	$(A - 3B + 6C)(u + d + s) + 5(B - C)(u_+ + d_+ + s_+)$
$r_{\Xi^{*0}}^2$	$(A - 3B + 6C)(u + 2s) + 5(B - C)(u_+ + 2s_+)$
$r_{\Xi^{*-}}^2$	$-(A - 3B + 6C)(d + 2s) - 5(B - C)(d_+ + 2s_+)$
$r_{\Omega^-}^2$	$-(A - 3B + 6C)(3s) - 5(B - C)(3s_+)$

“mixed” wavefunction (15), the charge radii for the p and Σ^+ from (14) can now be expressed as

$$\begin{aligned}
r_p^2 &= (A - 3B)(2u + d) + 3(B - C) \\
&\quad \times \left[\cos^2\theta \left(\frac{4}{3}u_+ - \frac{1}{3}d_+ \right) + \sin^2\theta \left(\frac{2}{3}u_+ + \frac{1}{3}d_+ \right) \right], \\
r_{\Sigma^+}^2 &= (A - 3B)(2u + s) + 3(B - C) \\
&\quad \times \left[\cos^2\theta \left(\frac{4}{3}u_+ - \frac{1}{3}s_+ \right) + \sin^2\theta \left(\frac{2}{3}u_+ + \frac{1}{3}s_+ \right) \right].
\end{aligned} \tag{17}$$

The expressions for the charge radii of other octet baryons in NQM with configuration mixing ($\text{NQM}_{\text{config}}$) are presented in Table 1. The results without configuration mixing can easily be obtained by taking the mixing angle $\theta = 0$.

Configuration mixing generated by the spin-spin forces does not affect the spin $(3/2)^+$ decuplet baryons. The wavefunction in this case is given as

$$|B^*\rangle \equiv \left| 10, \frac{3}{2}^+ \right\rangle = |56, 0^+\rangle_{N=0} = \chi^s \varphi^s \psi^s (0^+), \tag{18}$$

Using the baryon wavefunction from the above equation and the charge radii operator from (9), the general expression for the charge radii of spin $(3/2)^+$ baryons can be expressed as

$$\begin{aligned}
\widehat{r}_{B^*}^2 &= (A - 3B + 6C) \left(\sum_{u,d,s} n_q - \sum_{\bar{u},\bar{d},\bar{s}} n_{\bar{q}} \right) q \\
&\quad + 5(B - C) \left(\sum_{u,d,s} n_{q_+} - \sum_{u,d,s} n_{q_-} \right) q_+.
\end{aligned} \tag{19}$$

As an example, the charge radii for Δ^+ baryon can be expressed as

$$r_{\Delta^+}^2 = (A - 3B + 6C)(2u + d) + 5(B - C)(2u_+ + d_+). \tag{20}$$

The expressions for the charge radii of other decuplet baryons in NQM are presented in Table 2.

For the spin $(1/2)^+$ octet baryons, the quadrupole moment of p and Σ^+ in NQM can be expressed as

$$\begin{aligned}
Q_p &= 3B'(2u + d - 2u_+ - d_+) \\
&\quad + C'(-4u + d + 4u_+ - d_+), \\
Q_{\Sigma^+} &= 3B'(2u + s - 2u_+ - s_+) \\
&\quad + C'(-4u + s + 4u_+ - s_+).
\end{aligned} \tag{21}$$

For the spin $(3/2)^+$ decuplet baryons, the quadrupole moment of Δ^+ and Ξ^{*-} can be expressed as

$$\begin{aligned} Q_{\Delta^+} &= B' (6u + 3d + 2u_+ + d_+) \\ &\quad + C' (-6u - 3d + 10u_+ + 5d_+), \\ Q_{\Xi^{*-}} &= B' (3d + 6s + d_+ + 2s_+) \\ &\quad + C' (-3d - 6s + 5d_+ + 10s_+). \end{aligned} \quad (22)$$

Similarly, for the spin $(3/2)^+ \rightarrow (1/2)^+$ transitions, the quadrupole moment of the $\Delta^+ p$ and $\Sigma^{*-} \Sigma^-$ transitions can be expressed as

$$\begin{aligned} Q_{\Delta^+ p} &= 2\sqrt{2}B' (u_+ - d_+) + 2\sqrt{2}C' (-u + d), \\ Q_{\Sigma^{*-} \Sigma^-} &= 2\sqrt{2}B' (d_+ - s_+) + 2\sqrt{2}C' (-d + s). \end{aligned} \quad (23)$$

The expressions for quadrupole moment of the other $(1/2)^+$ octet and $(3/2)^+$ decuplet baryons and for spin $(3/2)^+ \rightarrow (1/2)^+$ transitions in NQM can similarly be calculated. The results are presented in Tables 7, 8, and 9.

4. Chiral Constituent Quark Model (χ CQM)

In light of the recent developments and successes of the χ CQM in explaining the low energy phenomenology [117–127], we formulate the quadrupole moments for the $(3/2)^+$ decuplet baryons and spin $(3/2)^+ \rightarrow (1/2)^+$ transitions. The basic process in the χ CQM is the Goldstone boson (GB)

emission by a constituent quark which further splits into a $q\bar{q}$ pair as

$$q_{\pm} \longrightarrow \text{GB}^0 + q'_{\mp} \longrightarrow (q\bar{q}') + q'_{\mp}, \quad (24)$$

where $q\bar{q}' + q'$ constitute the “quark sea” [111–116]. The effective Lagrangian describing the interaction between quarks and a nonet of GBs is

$$\mathcal{L} = g_8 \bar{q} \Phi' q, \quad (25)$$

with

$$q = \begin{pmatrix} u \\ d \\ s \end{pmatrix},$$

$$\Phi' = \begin{pmatrix} \frac{\pi^0}{\sqrt{2}} + \beta \frac{\eta}{\sqrt{6}} + \zeta \frac{\eta'}{\sqrt{3}} & \pi^+ & \alpha K^+ \\ \pi^- & -\frac{\pi^0}{\sqrt{2}} + \beta \frac{\eta}{\sqrt{6}} + \zeta \frac{\eta'}{\sqrt{3}} & \alpha K^0 \\ \alpha K^- & \alpha \bar{K}^0 & -\beta \frac{2\eta}{\sqrt{6}} + \zeta \frac{\eta'}{\sqrt{3}} \end{pmatrix}, \quad (26)$$

where $\zeta = g_1/g_8$, g_1 and g_8 are the coupling constants for the singlet and octet GBs, respectively. If the parameter $a (= |g_8|^2)$ denotes the transition probability of chiral fluctuation of the splitting $u(d) \rightarrow d(u) + \pi^{+(-)}$, then $\alpha^2 a$, $\beta^2 a$ and $\zeta^2 a$, respectively, denote the probabilities of transitions of $u(d) \rightarrow s + K^{-(0)}$, $u(d, s) \rightarrow u(d, s) + \eta$, and $u(d, s) \rightarrow u(d, s) + \eta'$. SU(3) symmetry breaking is introduced by considering $M_s > M_{u,d}$ as well as by considering the masses of GBs to be nondegenerate ($M_{K,\eta} > M_{\pi}$ and $M_{\eta'} > M_{K,\eta}$) [111–119].

In terms of the quark contents, the GB field can be expressed as

$$\Phi' = \begin{pmatrix} \phi_{uu}u\bar{u} + \phi_{ud}d\bar{d} + \phi_{us}s\bar{s} & \phi_{ud}u\bar{d} & \phi_{us}u\bar{s} \\ \phi_{du}d\bar{u} & \phi_{dd}d\bar{d} + \phi_{ds}s\bar{s} & \phi_{ds}d\bar{s} \\ \phi_{su}s\bar{u} & \phi_{sd}s\bar{d} & \phi_{ss}s\bar{s} + \phi_{sd}d\bar{d} + \phi_{ss}s\bar{s} \end{pmatrix}, \quad (27)$$

where

$$\begin{aligned} \phi_{uu} = \phi_{dd} &= \frac{1}{2} + \frac{\beta}{6} + \frac{\zeta}{3}, & \phi_{ss} &= \frac{2\beta}{3} + \frac{\zeta}{3}, \\ \phi_{us} = \phi_{ds} = \phi_{su} = \phi_{sd} &= -\frac{\beta}{3} + \frac{\zeta}{3}, \\ \phi_{du} = \phi_{ud} &= -\frac{1}{2} + \frac{\beta}{6} + \frac{\zeta}{3}, & \varphi_{ud} = \varphi_{du} &= 1, \\ \varphi_{us} = \varphi_{ds} = \varphi_{su} = \varphi_{sd} &= \alpha. \end{aligned} \quad (28)$$

A redistribution of flavor and spin structure takes place in the interior of baryon due to the chiral symmetry breaking,

and the modified flavor and spin content of the baryon can be calculated by substituting for every constituent quark:

$$\begin{aligned} q &\longrightarrow P_q q + |\psi(q)|^2, \\ q_{\pm} &\longrightarrow P_q q_{\pm} + |\psi(q_{\pm})|^2. \end{aligned} \quad (29)$$

Here $P_q = 1 - \sum P_q$ is the transition probability of no emission of GB from any of the q quark with

$$\begin{aligned} \sum P_u &= a (\phi_{uu}^2 + \phi_{ud}^2 + \phi_{us}^2 + \varphi_{ud}^2 + \varphi_{us}^2), \\ \sum P_d &= a (\phi_{du}^2 + \phi_{dd}^2 + \phi_{ds}^2 + \varphi_{du}^2 + \varphi_{ds}^2), \end{aligned}$$

$$\sum P_s = a (\phi_{su}^2 + \phi_{sd}^2 + \phi_{ss}^2 + \varphi_{su}^2 + \varphi_{sd}^2), \quad (30)$$

and $|\psi(q)|^2$ ($|\psi(q_{\pm})|^2$) are the transition probabilities of the emission of q (q_{\pm}) quark:

$$\begin{aligned} |\psi(u)|^2 &= a \left[(2\phi_{uu}^2 + \phi_{ud}^2 + \phi_{us}^2 + \varphi_{ud}^2 + \varphi_{us}^2)u + \phi_{uu}^2\bar{u} \right. \\ &\quad \left. + (\phi_{ud}^2 + \varphi_{ud}^2)(d + \bar{d}) + (\phi_{us}^2 + \varphi_{us}^2)(s + \bar{s}) \right], \\ |\psi(d)|^2 &= a \left[(\phi_{du}^2 + 2\phi_{dd}^2 + \phi_{ds}^2 + \varphi_{du}^2 + \varphi_{ds}^2)d + \phi_{dd}^2\bar{d} \right. \\ &\quad \left. + (\phi_{du}^2 + \varphi_{du}^2)(u + \bar{u}) + (\phi_{ds}^2 + \varphi_{ds}^2)(s + \bar{s}) \right], \\ |\psi(s)|^2 &= a \left[(\phi_{su}^2 + \phi_{sd}^2 + 2\phi_{ss}^2 + \varphi_{su}^2 + \varphi_{sd}^2)s + \phi_{ss}^2\bar{s} \right. \\ &\quad \left. + (\phi_{su}^2 + \varphi_{su}^2)(u + \bar{u}) + (\phi_{sd}^2 + \varphi_{sd}^2)(d + \bar{d}) \right], \\ |\psi(u_{\pm})|^2 &= a \left[(\phi_{uu}^2 + \phi_{ud}^2 + \phi_{us}^2)u_{\mp} + \varphi_{ud}^2d_{\mp} + \varphi_{us}^2s_{\mp} \right], \\ |\psi(d_{\pm})|^2 &= a \left[\varphi_{du}^2u_{\mp} + (\phi_{du}^2 + \phi_{dd}^2 + \phi_{ds}^2)d_{\mp} + \varphi_{ds}^2s_{\mp} \right], \\ |\psi(s_{\pm})|^2 &= a \left[\varphi_{su}^2u_{\mp} + \varphi_{sd}^2d_{\mp} + (\phi_{su}^2 + \phi_{sd}^2 + \phi_{ss}^2)s_{\mp} \right]. \end{aligned} \quad (31)$$

After the inclusion of ‘‘quark sea,’’ the charge radii for the spin $(1/2)^+$ octet baryons, in χ CQM with configuration mixing (χ CQM_{config}), can be obtained by substituting (29) for each quark in (17). The charge radii for the case of p and Σ^+ are now expressed as

$$\begin{aligned} r_p^2 &= (A - 3B) (2P_u u + 2|\psi(u)|^2 + P_d d + |\psi(d)|^2) \\ &\quad + 3(B - C) \left[\cos^2\theta \left(\frac{4}{3}P_u u_+ + \frac{4}{3}|\psi(u_+)|^2 \right. \right. \\ &\quad \left. \left. - \frac{1}{3}P_d d_+ - \frac{1}{3}|\psi(d_+)|^2 \right) \right. \\ &\quad \left. + \sin^2\theta \left(\frac{2}{3}P_u u_+ + \frac{2}{3}|\psi(u_+)|^2 \right. \right. \\ &\quad \left. \left. + \frac{1}{3}P_d d_+ + \frac{1}{3}|\psi(d_+)|^2 \right) \right], \\ r_{\Sigma^+}^2 &= (A - 3B) (2P_u u + 2|\psi(u)|^2 + P_s s + |\psi(s)|^2) \\ &\quad + 3(B - C) \left[\cos^2\theta \left(\frac{4}{3}P_u u_+ + \frac{4}{3}|\psi(u)|^2 \right. \right. \\ &\quad \left. \left. - \frac{1}{3}P_s s_+ - \frac{1}{3}|\psi(s)|^2 \right) \right. \\ &\quad \left. + \sin^2\theta \left(\frac{2}{3}P_u u_+ + \frac{2}{3}|\psi(u_+)|^2 \right. \right. \\ &\quad \left. \left. + \frac{1}{3}P_s s_+ + \frac{1}{3}|\psi(s_+)|^2 \right) \right]. \end{aligned} \quad (32)$$

The charge radii in the χ CQM_{config} for other spin $(1/2)^+$ octet baryons are presented in Table 3. The results without

configuration mixing can easily be obtained by taking the mixing angle $\theta = 0$.

Similarly, for the spin $(3/2)^+$ decuplet baryons, the charge radii are modified on substituting for each quark from (29). For example, the charge radii for Δ^+ in χ CQM can be expressed as

$$\begin{aligned} r_{\Delta^+}^2 &= (A - 3B + 6C) (2P_u u + 2|\psi(u)|^2 + P_d d + |\psi(d)|^2) \\ &\quad + 5(B - C) (2P_u u_+ + 2|\psi(u_+)|^2 + P_d d_+ + |\psi(d_+)|^2). \end{aligned} \quad (33)$$

The charge radii of the other decuplet baryons can be calculated similarly and are detailed in Table 4.

After the inclusion of ‘‘quark sea,’’ the quadrupole moment for the spin $(1/2)^+$ octet baryons vanishes on account of the effective cancelation of contribution coming from the ‘‘quark sea’’ and the orbital angular momentum as observed spectroscopically. For the spin $(3/2)^+$ decuplet baryons, the quadrupole moment in χ CQM can be obtained by substituting (29) for each quark in (21). The quadrupole moment of Δ^+ and Ξ^{*-} in χ CQM can be expressed as

$$\begin{aligned} Q^{\Delta^+} &= 4B' + 2C' - (B' + 5C')a \left(2 + \frac{\beta^2}{3} + \frac{2\zeta^2}{3} \right), \\ Q^{\Xi^{*-}} &= -4B' - 2C' + (B' + 5C')a \left(\frac{4\alpha^2}{3} + \beta^2 + \frac{2\zeta^2}{3} \right). \end{aligned} \quad (34)$$

Similarly, the quadrupole moment of $\Delta^+ p$ and $\Sigma^{*-}\Sigma^-$ transitions in χ CQM can be expressed as

$$\begin{aligned} Q^{\Delta^+ p} &= 2\sqrt{2} \left[B' \left(1 - a \left(1 + \alpha^2 + \frac{\beta^2}{3} + \frac{2\zeta^2}{3} \right) \right) - C' \right], \\ Q^{\Sigma^{*-}\Sigma^-} &= 2\sqrt{2}B'a \left(\frac{\alpha^2}{3} - \frac{\beta^2}{3} \right). \end{aligned} \quad (35)$$

The expressions for the quadrupole moment of other $(3/2)^+$ decuplet baryons and spin $(3/2)^+ \rightarrow (1/2)^+$ transitions in χ CQM can similarly be calculated. The results are presented in Tables 8 and 9.

5. Results and Discussion

The calculations of charge radii and quadrupole moment of octet and decuplet baryons involve two set of parameters the SU(3) symmetry breaking parameters of χ CQM and the GPM parameters. The χ CQM parameters a , $a\alpha^2$, $a\beta^2$, and $a\zeta^2$ represent, respectively, the probabilities of fluctuations to pions K , η , and η' . A best fit of χ CQM parameters can be obtained by carrying out a fine grained analysis of the spin and flavor distribution functions [117–119] leading to

$$a = 0.12, \quad \alpha = 0.7, \quad \beta = 0.4, \quad \zeta = -0.15. \quad (36)$$

TABLE 3: Charge radii of octet baryons in $\chi\text{CQM}_{\text{config}}$ in terms of SU(3) symmetry breaking parameters and GPM parameters. These results are obtained by substituting $q \rightarrow P_q q + |\psi(q)|^2$ and $q_{\pm} \rightarrow P_q q_{\pm} + |\psi(q_{\pm})|^2$ for every constituent quark in NQM. Results in χCQM without configuration mixing can easily be obtained by substituting the mixing angle $\theta = 0$.

Charge radii	$\chi\text{CQM}_{\text{config}}$
r_p^2	$A - 3B + (B - C) \left[\cos^2\theta (3 - a(4 + 2\alpha^2 + \beta^2 + 2\zeta^2)) + \sin^2\theta \left(1 - \frac{a}{3}(6 + \beta^2 + 2\zeta^2)\right) \right]$
r_n^2	$(B - C) \left[\cos^2\theta \left(-2 + \frac{a}{3}(3 + 9\alpha^2 + 2\beta^2 + 4\zeta^2)\right) + \sin^2\theta (a(-1 + \alpha^2)) \right]$
$r_{\Sigma^+}^2$	$A - 3B + (B - C) \left[\cos^2\theta \left(3 - \frac{a}{3}(12 + 5\alpha^2 + 4\beta^2 + 6\zeta^2)\right) + \sin^2\theta \left(1 - \frac{a}{3}(6 + \alpha^2 + 2\zeta^2)\right) \right]$
$r_{\Sigma^-}^2$	$A - 3B + (B - C) \left[\cos^2\theta \left(-1 + \frac{a}{3}(7\alpha^2 + 2\zeta^2)\right) + \sin^2\theta \left(-1 + \frac{a}{3}(5\alpha^2 + 2\beta^2 + 2\zeta^2)\right) \right]$
$r_{\Sigma^0}^2$	$(B - C) \left[\cos^2\theta \left(1 - \frac{a}{3}(6 - \alpha^2 + 2\beta^2 + 2\zeta^2)\right) + \sin^2\theta \left(\frac{a}{3}(-3 + 2\alpha^2 + \beta^2)\right) \right]$
$r_{\Xi^0}^2$	$(B - C) \left[\cos^2\theta \left(-2 + \frac{a}{3}(3 + 5\alpha^2 + 6\beta^2 + 4\zeta^2)\right) + \sin^2\theta \left(\frac{a}{3}(-3 + \alpha^2 + 2\beta^2)\right) \right]$
$r_{\Xi^-}^2$	$A - 3B + (B - C) \left[\cos^2\theta \left(-1 + \frac{a}{3}(2\alpha^2 + 5\beta^2 + 2\zeta^2)\right) + \sin^2\theta \left(-1 + \frac{a}{3}(4\alpha^2 + 3\beta^2 + 2\zeta^2)\right) \right]$
r_{Λ}^2	$(B - C) \left[\cos^2\theta \left(-1 + \frac{a}{3}(3\alpha^2 + 4\beta^2 + 2\zeta^2)\right) + \sin^2\theta \left(\frac{a}{9}(-9 + 6\alpha^2 + 7\beta^2 + 2\zeta^2)\right) \right]$
$r_{\Sigma\Lambda}^2$	$(B - C) \left[\sqrt{3} - \frac{a}{\sqrt{3}}(3 + 3\alpha^2 + \beta^2 + 2\zeta^2) \right]$

TABLE 4: Charge radii of decuplet baryons in χCQM in terms of SU(3) symmetry breaking parameters and GPM parameters. These results are obtained by substituting $q \rightarrow P_q q + |\psi(q)|^2$ and $q_{\pm} \rightarrow P_q q_{\pm} + |\psi(q_{\pm})|^2$ for every constituent quark in NQM.

Charge radii	χCQM
$r_{\Delta^{++}}^2$	$A + 2B + C - \frac{5a}{6}(B - C)(9 + 3\alpha^2 + 2\beta^2 + 4\zeta^2)$
$r_{\Delta^+}^2$	$A + 2B + C - \frac{5a}{3}(B - C)(6 + \beta^2 + 2\zeta^2)$
$r_{\Delta^0}^2$	$5a(B - C)(-1 + \alpha^2)$
$r_{\Delta^-}^2$	$A + 2B + C - \frac{5a}{3}(B - C)(6\alpha^2 + \beta^2 + 2\zeta^2)$
$r_{\Sigma^{*+}}^2$	$A + 2B + C - \frac{5a}{3}(B - C)(6 + \alpha^2 + 2\zeta^2)$
$r_{\Sigma^{*-}}^2$	$A + 2B + C - \frac{5a}{3}(B - C)(5\alpha^2 + 2\beta^2 + 2\zeta^2)$
$r_{\Sigma^{*0}}^2$	$\frac{5a}{3}(B - C)(-3 + 2\alpha^2 + \beta^2)$
$r_{\Xi^{*0}}^2$	$\frac{5a}{3}(B - C)(-3 + \alpha^2 + 2\beta^2)$
$r_{\Xi^{*-}}^2$	$A + 2B + C - \frac{5a}{3}(B - C)(4\alpha^2 + 3\beta^2 + 2\zeta^2)$
$r_{\Omega^-}^2$	$A + 2B + C - \frac{5a}{3}(B - C)(3\alpha^2 + 4\beta^2 + 2\zeta^2)$

The mixing angle θ is fixed from the consideration of neutron charge radius [28]. This set of parameters has already been tested for a wide variety of low energy matrix elements and has been able to give a simultaneous fit to the quantities describing proton spin and flavor structure [117–119], weak vector-axial vector form factors [120, 121], strangeness

content in the nucleon [122–124], octet and decuplet baryons magnetic moments [125–127], and so forth.

The order of GPM parameters corresponding to the one-, two-, and three-quark terms decreases with the increasing complexity of terms and obeys the hierarchy $A > B > C$ [143, 144]. These are fitted by using the available experimental values for the charge radii and quadrupole moment of nucleon as input. In the present case, we have used $r_p = 0.877 \pm 0.007$ fm [12], $r_n^2 = -0.1161 \pm 0.0022$ fm² [12], and $Q_{\Delta^{*N}} = -0.0846 \pm 0.0033$ fm² [19]. The set of GPM parameters obtained after χ^2 minimization are as follows:

$$A = 0.879, \quad B = 0.094, \quad C = 0.016. \quad (37)$$

For the quadrupole moment calculations, best fit set of parameters obtained after χ^2 minimization are as follows:

$$B' = -0.047, \quad C' = -0.008, \quad (38)$$

obeying the hierarchy $B' > C'$ [143, 144] corresponding to the two- and three-quark contribution. Since we also intend to investigate the extent to which the three-quark term contributes, we calculate the charge radii corresponding to the one- and two-quark terms only by taking $C = 0$. Similarly, if we intend to calculate the charge radii corresponding to just the one-quark term, we can take $B = C = 0$.

Using the set of parameters discussed above, we have calculated the numerical values for the charge radii of octet and decuplet baryons in $\chi\text{CQM}_{\text{config}}$ and presented the results in Tables 5 and 6, respectively. To understand the implications of chiral symmetry breaking and ‘‘quark sea,’’ we have also presented the results of NQM as well as comparing our results with the predictions of other available phenomenological models. Since the calculations in χCQM have been carried

TABLE 5: Charge radii of octet baryons calculated in χ CQM in comparison with other phenomenological models (in units of fm^2).

Charge radii	NQM	RCQM [51]	HB χ PT [60]	χ PT [61, 62]	CCQM [52]	P χ QM [59]	$1/N_c$ [57, 58]	Lattice [63]	χ CQM _{config}		
									With SU(3) symmetry	With SU(3) symmetry breaking	
										A = 0.879 B = 0.094 C = 0.0	A = 0.879 B = 0.094 C = 0.016
r_p^2 $r_p = 0.877 \pm 0.007$	0.813	—	0.735	0.717	0.82	0.72 ± 0.09	0.779	0.685	0.732	0.801	0.766
r_n^2 -0.1161 ± 0.0022	-0.138	—	-0.113	-0.113	-0.13	-0.111 ± 0.014	-0.116	-0.158	-0.087	-0.140	-0.116
$r_{\Sigma^+}^2$	0.813	0.79	1.366	0.60 ± 0.02	1.13	0.81 ± 0.10	0.928	0.749	0.732	0.802	0.767
$r_{\Sigma^-}^2$ 0.61 ± 0.21 [13]	0.675	0.49	0.798	0.67 ± 0.03	0.72	0.71 ± 0.07	0.672	0.657	0.646	0.678	0.664
$r_{\Sigma^0}^2$	0.069	0.15	—	-0.03 ± 0.01	0.20	0.05 ± 0.01	0.128	—	0.043	0.062	0.052
$r_{\Xi^0}^2$	-0.138	0.14	-0.122	0.13 ± 0.03	-0.19	0.14 ± 0.02	0.132	-0.082	-0.087	-0.145	-0.120
$r_{\Xi^-}^2$	0.675	0.47	0.997	0.49 ± 0.05	0.54	0.62 ± 0.07	0.520	0.502	0.646	0.683	0.669
r_{Λ}^2	-0.069	0.038	-0.284	0.11 ± 0.02	0.03	0.05 ± 0.01	0.050	0.010	-0.042	-0.076	-0.063
$r_{\Sigma\Lambda}^2$	0.135	-0.12	0.074	0.03 ± 0.01	—	0.0	-0.066	—	0.085	0.132	0.109

TABLE 6: Charge radii of decuplet baryons calculated in χ CQM in comparison with other phenomenological models (in units of fm^2).

Charge radii	NQM	FTQM [67]	CCQM [52]	$1/N_c$ [57, 58]	Lattice [64–66]	χ CQM		
						With SU(3) symmetry	With SU(3) symmetry breaking	
							A = 0.879 B = 0.094 C = 0.0	A = 0.879 B = 0.094 C = 0.016
$r_{\Delta^{++}}^2$	1.084	1.18	0.43	1.011	—	0.938	0.961	0.996
$r_{\Delta^+}^2$	1.084	0.82	0.43	1.011	0.410 (57)	0.938	0.946	0.983
$r_{\Delta^0}^2$	0.0	0.16	0.00	0.0	—	0.0	-0.030	-0.025
$r_{\Delta^-}^2$	1.084	0.84	0.43	1.011	-0.410 (57)	0.938	1.006	1.033
$r_{\Sigma^{*+}}^2$	1.084	0.97	0.42	1.086	0.399 (45)	0.938	0.940	0.978
$r_{\Sigma^{*-}}^2$	1.084	0.84	0.37	0.845	-0.360 (32)	0.938	1.013	1.038
$r_{\Sigma^{*0}}^2$	0.0	0.34	0.03	0.127	0.020 (7)	0.0	-0.036	-0.030
$r_{\Xi^{*0}}^2$	0.0	0.49	0.06	0.244	0.043 (10)	0.0	-0.043	-0.035
$r_{\Xi^{*-}}^2$	1.084	0.82	0.33	0.692	-0.330 (20)	0.938	1.019	1.043
$r_{\Omega^-}^2$	0.390	0.78	0.29	0.553	—	0.245	0.429	0.355

out using the GPM, the NQM results have also been presented by including the one-, two-, and three-quark contributions of the GPM parameters. It is clear from Tables 1 and 2 that if we consider the contribution coming from one-quark term only, the charge radii of the charged baryons are equal whereas all neutral baryons have zero charge radii. These predictions are modified on the inclusion of two- and three-quark terms of GPM and are further modified on the inclusion of “quark sea” and SU(3) symmetry breaking effects. Thus, it seems that the GPM parameters alone are able to explain the experimentally observed nonzero charge radii of the neutral baryons. However, NQM is unable to account for the “proton spin problem” and other related quantities; the results have been presented for χ CQM. The importance of

strange quark mass has been investigated by comparing the χ CQM results with and without SU(3) symmetry breaking. The SU(3) symmetry results can be easily derived from Tables 3 and 4 by considering $\alpha = \beta = 1$ and $\zeta = -1$. The SU(3) breaking results are in general higher in magnitude than the SU(3) symmetric results, and the values obtained are also in agreement with the other models.

For the case of octet baryons, it can be easily shown from Table 5 that in the SU(3) symmetric limit, octet baryon charge radii can be expressed in terms of the nucleon charge radii leading to the following relations:

$$r_{\Sigma^+}^2 = r_p^2, \quad r_{\Xi^-}^2 = r_{\Sigma^-}^2 = r_p^2 + r_n^2, \quad (39)$$

TABLE 7: Quadrupole moments of the octet baryons in NQM using the GPM.

Baryons	NQM
p	$3B'(2u+d-2u_+-d_+)+C'(-4u+d+4u_+-d_+)$
n	$3B'(u+2d-u_+-2d_+)+C'(u-4d-u_++4d_+)$
Σ^+	$3B'(2u+s-2u_+-s_+)+C'(-4u+s+4u_+-s_+)$
Σ^-	$3B'(2d+s-2d_+-s_+)+C'(-4d+s+4d_+-s_+)$
Σ^0	$3B'(u+d+s-u_+-d_+-s_+)$ $+C'(-2u-2d+s+2u_++2d_+-s_+)$
Ξ^0	$3B'(u+2s-u_+-2s_+)+C'(u-4s-u_++4s_+)$
Ξ^-	$3B'(d+2s-d_+-2s_+)+C'(d-4s-d_++4s_+)$
Λ^0	$3B'(u+d+s-u_+-d_+-s_+)+3C'(-s+s_+)$

The inclusion of SU(3) symmetry breaking changes this pattern considerably, and we get

$$r_{\Sigma^+}^2 > r_p^2, \quad r_{\Xi^-}^2 > r_{\Sigma^-}^2 > r_p^2 + r_n^2. \quad (40)$$

Also we have

$$2r_{\Lambda}^2 = -2r_{\Sigma^0}^2 = r_{\Xi^0}^2 = r_n^2, \quad (41)$$

which has its importance in the isospin limit where the three-quark core in neutral baryons does not contribute to the charge radii. In the limit of SU(3) symmetry breaking, a nonvanishing value for the neutral baryons charge radii is generated by the ‘‘quark sea’’ through the chiral fluctuations of constituent quarks leading to

$$r_{\Lambda}^2 > -r_{\Sigma^0}^2, \quad r_{\Xi^0}^2 > r_n^2. \quad (42)$$

The exact order of SU(3) symmetry breaking effects can be easily found from Table 3. Since experimental information is not available for some of these octet charge radii, the accuracy of these relations can be tested by the future experiments. It is interesting to note that the relation for the Σ baryon charge radii,

$$r_{\Sigma^+}^2 - 2r_{\Sigma^0}^2 - r_{\Sigma^-}^2 = 0, \quad (43)$$

holds good even after incorporating SU(3) symmetry breaking. Since this relation is independent of SU(3) symmetry breaking parameters, any refinement in the Σ baryon charge radii data would have important implications for SU(3) symmetry breaking. Further, our predicted value $r_{\Sigma^-}^2 = 0.664$ is clearly of the order of proton charge radius and is also in agreement with the recent SELEX collaboration experimental results [12]. It would be important to mention here that the χ CQM parameters play an important role in the SU(3) symmetry breaking effects whereas the assumed parametrization plays a dominant role in the valence quark distributions.

In Table 3, we have presented the results for the case with configuration mixing generated by the spin-spin forces. We have not presented the results without configuration mixing which can easily be obtained by taking the mixing angle $\theta = 0$. It has been observed that configuration mixing decreases the overall magnitudes of the charge radii in χ CQM, but

the change is very small as compared to the other low energy properties like spin distribution function, magnetic moments, and so forth [117–127].

On comparing our results with the other phenomenological models, we find that for the case of charged octet baryons, our results are in fair agreement in sign and magnitude with the other model predictions. However, for the neutral octet baryons n , Σ^0 , Ξ^0 , and Λ , different models show opposite sign. For example, if we consider the charge radii for the Λ baryon, our model prediction (-0.063) is opposite in sign to the predictions of the relativistic constituent quark model (RCQM) [51], covariant constituent quark model (CCQM) [52], $1/N_c$ expansion [55, 56], and P χ QM [59]. On the other hand, it is in agreement with the sign of HB χ PT [60]. A similar trend has been observed for the charge radii of $\Sigma\Lambda$ transition. The difference in the sign may be due to the chiral fluctuation of a constituent quark leading to the reversal of sign in case of neutral octet baryons. This can perhaps be substantiated by a measurement of charge radii of other baryons.

The spin $(3/2)^+$ decuplet baryon charge radii, presented in Table 6, are in general higher than the octet baryon charge radii which are in line with the trend followed by the octet and decuplet baryons for the other low energy hadronic matrix elements such as magnetic moments. In this case also, the inclusion of SU(3) symmetry breaking increases the predictions of charge radii. It can be easily shown that SU(3) symmetry results in the following relations for the decuplet baryons:

$$r_{\Delta^{++}}^2 = r_{\Delta^+}^2 = r_{\Delta^-}^2 = r_{\Sigma^{*+}}^2 = r_{\Sigma^{*-}}^2 = r_{\Xi^{*-}}^2. \quad (44)$$

These results are affected by the inclusion of SU(3) symmetry breaking and give

$$r_{\Xi^{*-}}^2 > r_{\Sigma^{*-}}^2 > r_{\Delta^-}^2 > r_{\Delta^{++}}^2 > r_{\Delta^+}^2 > r_{\Sigma^{*+}}^2. \quad (45)$$

Some relations, derived in $1/N_c$ expansion of QCD [55–58], are found to be independent of SU(3) symmetry breaking parameters in χ CQM. Even though the individual charge radii are affected by SU(3) symmetry breaking, the effects are canceled exactly for the following relations:

$$\begin{aligned} 2r_{\Delta^{++}}^2 - r_{\Delta^+}^2 - r_{\Delta^0}^2 - r_{\Delta^-}^2 &= 0, \\ 2r_{\Delta^{++}}^2 - 3r_{\Delta^+}^2 + 3r_{\Delta^0}^2 + r_{\Delta^-}^2 &= 0, \\ r_{\Sigma^{*+}}^2 - 2r_{\Sigma^{*0}}^2 - r_{\Sigma^{*-}}^2 &= 0. \end{aligned} \quad (46)$$

In this case also, SU(3) symmetry breaking is expected to reduce the charge radii with increasing strangeness content. As a consequence, Δ^- , Σ^- , and Ξ^- should have successively decreasing charge radii. However, this suppression disappears in χ CQM due to the effect of ‘‘quark sea,’’ and the charge radii of Δ^+ , Σ^{*-} , and Ξ^{*0} are of almost the same order as that of Σ^{*+} , Ξ^{*-} , and Σ^{*0} , respectively. Again, the sign and magnitude of the decuplet baryon charge radii in χ CQM are in fair agreement with the other phenomenological models with the exception for neutral baryons. One of the important predictions in χ CQM is a nonzero Λ^0 charge radii which

TABLE 8: Quadrupole moments of the decuplet baryons in NQM and χ CQM using the GPM.

Baryon	NQM	χ CQM
Δ^{++}	$B' (9u + 3u_+) + C' (-9u + 15u_+)$	$8B' + 4C' - (B' + 5C') \frac{a}{3} (9 + 3\alpha^2 + 2\beta^2 + 4\zeta^2)$
Δ^+	$B' (3(2u + d) + 2u_+ + d_+) + C' (-3(2u + d) + 5(2u_+ + d_+))$	$4B' + 2C' - (B' + 5C') \frac{a}{3} (6 + \beta^2 + 2\zeta^2)$
Δ^0	$B' (3(u + 2d) + u_+ + 2d_+) + C' (-3(u + 2d) + 5(u_+ + 2d_+))$	$(B' + 5C')a(-1 + \alpha^2)$
Δ^-	$B' (9d + 3d_+) + C' (-9d + 15d_+)$	$-4B' - 2C' + (B' + 5C') \frac{a}{3} (6\alpha^2 + \beta^2 + 2\zeta^2)$
Σ^{*+}	$B' (3(2u + s) + 2u_+ + s_+) + C' (-3(2u + s) + 5(2u_+ + s_+))$	$4B' + 2C' - (B' + 5C') \frac{a}{3} (6 + \alpha^2 + 2\zeta^2)$
Σ^{*-}	$B' (3(2d + s) + 2d_+ + s_+) + C' (-3(2d + s) + 5(2d_+ + s_+))$	$-4B' - 2C' + (B' + 5C') \frac{a}{3} (5\alpha^2 + 2\beta^2 + 2\zeta^2)$
Σ^{*0}	$B' (3(u + d + s) + u_+ + d_+ + s_+)$ $+ C' (-3(u + d + s) + 5(u_+ + d_+ + s_+))$	$(B' + 5C') \frac{a}{3} (-3 + 2\alpha^2 + \beta^2)$
Ξ^{*0}	$B' (3(u + 2s) + u_+ + 2s_+) + C' (-3(u + 2s) + 5(u_+ + 2s_+))$	$(B' + 5C') \frac{a}{3} (-3 + \alpha^2 + 2\beta^2)$
Ξ^{*-}	$B' (3(d + 2s) + d_+ + 2s_+) + C' (-3(d + 2s) + 5(d_+ + 2s_+))$	$-4B' - 2C' + (B' + 5C') \frac{a}{3} (4\alpha^2 + 3\beta^2 + 2\zeta^2)$
Ω^-	$B' (9s + 3s_+) + C' (-9s + 15s_+)$	$-4B' - 2C' + (B' + 5C') \frac{a}{3} (3\alpha^2 + 4\beta^2 + 2\zeta^2)$

TABLE 9: Quadrupole moments of the spin $(3/2)^+ \rightarrow (1/2)^+$ transitions in NQM and χ CQM using the GPM.

Baryon	NQM	χ CQM
$\Delta^+ p$	$2\sqrt{2}B' (u_+ - d_+) + 2\sqrt{2}C' (-u + d)$	$2\sqrt{2}B' \left(1 - \frac{a}{3}(3 + 3\alpha^2 + \beta^2 + 2\zeta^2)\right) - 2\sqrt{2}C'$
$\Sigma^{*+} \Sigma^+$	$2\sqrt{2}B' (u_+ - s_+) + 2\sqrt{2}C' (-u + s)$	$2\sqrt{2}B' \left(1 - \frac{a}{3}(3 + 2\alpha^2 + 2\beta^2 + 2\zeta^2)\right) - 2\sqrt{2}C'$
$\Sigma^{*-} \Sigma^-$	$2\sqrt{2}B' (d_+ - s_+) + 2\sqrt{2}C' (-d + s)$	$\frac{2\sqrt{2}}{3} B' a (\alpha^2 - \beta^2)$
$\Sigma^{*0} \Sigma^0$	$\sqrt{2}B' (u_+ + d_+ - 2s_+) + \sqrt{2}C' (-u - d + 2s)$	$\sqrt{2}B' \left(1 - a\left(1 + \frac{\alpha^2}{3} + \beta^2 + \frac{2}{3}\zeta^2\right)\right) - \sqrt{2}C'$
$\Xi^{*0} \Xi^0$	$2\sqrt{2}B' (u_+ - s_+) + 2\sqrt{2}C' (-u + s)$	$2\sqrt{2}B' \left(1 - \frac{a}{3}(3 + 2\alpha^2 + 2\beta^2 + 2\zeta^2)\right) - 2\sqrt{2}C'$
$\Xi^{*-} \Xi^-$	$2\sqrt{2}B' (d_+ - s_+) + 2\sqrt{2}C' (-d + s)$	$\frac{2\sqrt{2}}{3} B' a (\alpha^2 - \beta^2)$
$\Sigma^{*0} \Lambda$	$\sqrt{6}B' (u_+ - d_+) + \sqrt{6}C' (-u + d)$	$\sqrt{6}B' \left(1 - \frac{a}{3}(3 + 3\alpha^2 + \beta^2 + 2\zeta^2)\right) - \sqrt{6}C'$

vanishes in NQM as well as in some other models. This is further endorsed by the predictions of the field theoretical quark model (FTQM) calculations [67]. The contribution of the three-quark term in the case of decuplet baryons is exactly opposite to that for the octet baryons. Unlike the octet baryon case, the inclusion of the three-quark term increases the value of the baryon charge radii.

For the sake of completeness, certain relations between the octet and decuplet baryon charge radii can also be tested for the spacing between the levels. In NQM, we have

$$r_{\Sigma^+}^2 - r_{\Sigma^{*+}}^2 = r_{\Xi^0}^2 - r_{\Xi^{*0}}^2 = r_{\Sigma^+}^2 - r_{\Sigma^{*+}}^2 = r_{\Xi^0}^2 - r_{\Xi^{*0}}^2 = r_n^2. \quad (47)$$

In χ CQM, the inclusion of SU(3) symmetry breaking effects creates a spacing between the octet and decuplet baryon charge radii as

$$r_p^2 - r_{\Delta^+}^2 = r_{\Sigma^+}^2 - r_{\Sigma^{*+}}^2 = -0.31,$$

$$r_{\Sigma^-}^2 - r_{\Sigma^{*-}}^2 = r_{\Xi^-}^2 - r_{\Xi^{*-}}^2 = -0.48,$$

$$r_n^2 - r_{\Delta^0}^2 = r_{\Xi^0}^2 - r_{\Xi^{*0}}^2 = -0.09. \quad (48)$$

We have calculated the numerical values for the quadrupole moment for the $(3/2)^+$ decuplet baryons in χ CQM and presented the results in Table 10. The results of the spin $(3/2)^+ \rightarrow (1/2)^+$ transitions have been presented in Table 11. To understand the implications of chiral symmetry breaking and “quark sea,” we have also presented the results of NQM. Since the calculations in χ CQM have been carried out using the GPM, the NQM results have also been presented by including the two- and three- quark term contributions of the GPM parameters so that the contribution of the “quark sea” effects can be calculated explicitly. For the case of spin $(1/2)^+$ octet baryons, we find that the quadrupole moments are zero for all the cases in NQM. Even if we consider the contribution coming from two-quark terms with the

TABLE 10: Quadrupole moments of the spin $(3/2)^+$ decuplet baryons in χ CQM using GPM and SU(3) symmetry breaking.

Baryon	NQM fm^2	CQM [84] 10^{-2}fm^2	χ PT [99–103] 10^{-1}fm^2	SRA [89, 90] 10^{-1}fm^2	Skyrme [91, 92] 10^{-2}fm^2	χ CQM with SU(3)		
						GPM [93, 94] fm^2	Symmetry fm^2	Symmetry breaking fm^2
Δ^{++}	-0.409	-9.3	-0.8 ± 0.5	-0.87	-8.8	-0.12	-0.3437	-0.3695
Δ^+	-0.204	-4.6	-0.3 ± 0.2	-0.31	-2.9	-0.06	-0.1719	-0.1820
Δ^0	0.0	0.0	0.12 ± 0.05	0.24	2.9	0.0	0.0	0.0055
Δ^-	0.204	4.6	0.6 ± 0.3	0.80	8.8	0.06	0.1719	0.1930
Σ^{*+}	-0.204	-5.4	-0.7 ± 0.3	-0.42	-7.1	-0.069	-0.1719	-0.1808
Σ^{*-}	0.204	4.0	4.0 ± 0.2	0.52	7.1	0.039	0.1719	0.1942
Σ^{*0}	0.0	-0.7	-0.13 ± 0.07	0.05	0.0	0.014	0.0	0.0067
Ξ^{*0}	0.0	-1.3	-0.35 ± 0.2	-0.07	-4.6	-0.1719	0.0	0.0079
Ξ^{*-}	0.204	3.4	0.2 ± 0.1	0.35	4.6	0.024	0.1719	0.1954
Ω^-	0.204	2.8	0.09 ± 0.05	0.24	0.0	0.014	0.1719	0.1966

inclusion of “quark sea” and SU(3) symmetry breaking effects, the quadrupole moments still remain zero. In the case of $(3/2)^+$ decuplet baryons, the quadrupole moments of the charged baryons are equal whereas all neutral baryons have zero quadrupole moment.

For the $(3/2)^+$ decuplet and radiative decays of baryons, it can be easily shown that in the SU(3) symmetric limit, the magnitude of quadrupole moments can be expressed by the following relations:

$$\begin{aligned} \frac{Q^{\Delta^{++}}}{2} &= Q^{\Delta^+} = Q^{\Delta^-} = Q^{\Sigma^{*+}} = Q^{\Sigma^{*-}} = Q^{\Xi^{*-}} = Q^{\Omega^-}, \\ Q^{\Delta^+ p} &= Q^{\Sigma^{*+} \Sigma^+} = 2Q^{\Sigma^{*0} \Sigma^0} = Q^{\Xi^{*0} \Xi^0} = \frac{2}{\sqrt{3}} Q^{\Sigma^{*0} \Lambda}. \end{aligned} \quad (49)$$

The inclusion of SU(3) symmetry breaking changes this pattern considerably, and we obtain

$$\begin{aligned} Q^{\Omega^-} > Q^{\Xi^{*-}} > Q^{\Sigma^{*-}} > Q^{\Delta^-} > \frac{Q^{\Delta^{++}}}{2} > Q^{\Delta^+} > Q^{\Sigma^{*+}}, \\ 2Q^{\Sigma^{*0} \Sigma^0} > Q^{\Xi^{*0} \Xi^0} = Q^{\Sigma^{*+} \Sigma^+} > Q^{\Delta^+ p} = \frac{2}{\sqrt{3}} Q^{\Sigma^{*0} \Lambda}. \end{aligned} \quad (50)$$

Also we have

$$Q^{\Xi^{*0}} = Q^{\Sigma^{*0}} = Q^{\Delta^0}, \quad (51)$$

which has its importance in the isospin limit where the three-quark core in neutral baryons does not contribute to the quadrupole moment. In the limit of SU(3) symmetry breaking, a nonvanishing value for the neutral baryons quadrupole moment is generated by the “quark sea” through the chiral fluctuations of constituent quarks leading to

$$Q^{\Xi^{*0}} > Q^{\Sigma^{*0}} > Q^{\Delta^0}. \quad (52)$$

In the SU(3) limit, the transition moments involving the negatively charged baryons are zero:

$$Q^{\Xi^{*-} \Xi^-} = Q^{\Sigma^{*-} \Sigma^-} = 0. \quad (53)$$

This is because if flavor symmetry is exact, U-spin conservation forbids such transitions. The exact order of SU(3) symmetry breaking effects can be easily found from Tables 10 and 11. Since there is no experimental or phenomenological information available for any of these quadrupole moments, the accuracy of these relations can be tested by the future experiments.

For the spin $(3/2)^+$ decuplet baryons presented in Table 10, quadrupole moments results in NQM using the GPM predict an oblate shape for all positively charged baryons (Δ^{++} , Δ^+ , and Σ^{*+}), prolate shape for negatively charged baryons (Δ^- , Σ^{*-} , Ξ^{*-} , and Ω^-). It is important to mention here that the NQM is unable to explain the deformation in neutral baryons (Δ^0 , Σ^{*0} , and Ξ^{*0}). On incorporating the effects of chiral symmetry breaking and “quark sea” in the χ CQM, a small amount of prolate deformation in neutral baryons (Δ^0 , Σ^{*0} , and Ξ^{*0}) is observed. The trend of deformations is however the same for the positively and negatively charged baryons in χ CQM and NQM. The other phenomenological models also observe a similar trend, for example, light cone QCD sum rules [95, 96], spectator quark model [86–88], Lattice QCD [104–108], χ PT [99–103], chiral quark soliton model (χ QSM) [85], and so forth.

For the case of spin $(3/2)^+ \rightarrow (1/2)^+$ transitions in Table 11, it is observed that quadrupole moments of all the transitions are oblate in shape. This result is further endorsed by the predictions of Skyrme model [91, 92]. The effects of chiral symmetry breaking can further be substantiated by a measurement of the other transition quadrupole moments.

6. Summary and Conclusion

To summarize, χ CQM is able to provide a fairly good description of the charge radii of spin $(1/2)^+$ octet and spin $(3/2)^+$ decuplet baryons and quadrupole moments of spin $(3/2)^+$ decuplet baryons and spin $(3/2)^+ \rightarrow (1/2)^+$ transitions using general parameterization method (GPM). The most significant prediction of the model for the charge

TABLE 11: Quadrupole moments of the spin $(3/2)^+ \rightarrow (1/2)^+$ decuplet to octet transitions in χ CQM using GPM and SU(3) symmetry breaking.

Baryon	NQM fm ²	Skyrme [91, 92] 10 ⁻² fm ²	GPM [93, 94] fm ²	χ CQM with SU(3)	
				Symmetry fm ²	Symmerty breaking fm ²
$\Delta^+ p$	-0.110	-5.2	-0.082	-0.0608	-0.0846
-0.0846 ± 0.0033					
$\Sigma^{*+} \Sigma^+$	-0.110	-0.93	-0.076	-0.0608	-0.0864
$\Sigma^{*-} \Sigma^-$	0.0	0.93	0.014	-0.0608	-0.0018
$\Sigma^{*0} \Sigma^0$	-0.055	0.0	-0.031	0.0	-0.0441
$\Xi^{*0} \Xi^0$	-0.110	2.91	-0.031	-0.0608	-0.0864
$\Xi^{*-} \Xi^-$	0.0	-2.91	0.007	0.0	-0.0018
$\Sigma^{*0} \Lambda$	-0.096	-4.83	-0.041	-0.0526	-0.0733

radii is the nonzero value pertaining to the neutral octet baryons (n , Σ^0 , Ξ^0 , and Λ) and decuplet baryons (Δ^0 , Σ^{*0} , Ξ^{*0}). For the quadrupole moment, prolate shape is observed for the spin $(3/2)^+$ neutral decuplet baryons (Δ^0 , Σ^{*0} , and Ξ^{*0}). The effects of SU(3) symmetry breaking have also been investigated, and the results show considerable improvement over the SU(3) symmetric case. We have also studied the implications of GPM parameters, particularly, the contribution of the three-quark term in the octet and decuplet baryon. We find that the sign of the three-quark term contribution is opposite in the case of octet and decuplet baryons charge radii. New experiments aimed at measuring the charge radii and quadrupole moment of the other baryons are needed for a profound understanding of the hadron structure in the nonperturbative regime of QCD.

In conclusion, we would like to state that at-the-leading-order constituent quarks and the weakly interacting Goldstone bosons constitute the appropriate degrees of freedom in the nonperturbative regime of QCD. The SU(3) symmetry breaking parameters pertaining to the strangeness contribution and the GPM parameters pertaining to the one-, two-, and three-quark contributions are the key in understanding the octet and decuplet baryon charge radii and quadrupole moment.

Acknowledgments

The authors would like to thank the Department of Atomic Energy, Government of India for the financial support through Grant no. 2010/37P/48/BRNS/1445.

References

- [1] R. G. Sachs, "High-energy behavior of nucleon electromagnetic form factors," *Physical Review*, vol. 126, no. 6, pp. 2256–2260, 1962.
- [2] J. Ashman, B. Badelek, G. Baum et al., "A measurement of the spin asymmetry and determination of the structure function g_1 in deep inelastic muon-proton scattering," *Physics Letters B*, vol. 206, no. 2, pp. 364–370, 1988.
- [3] J. Ashman, B. Badelek, G. Baum et al., "An investigation of the spin structure of the proton in deep inelastic scattering of

polarised muons on polarised protons," *Nuclear Physics B*, vol. 328, no. 1, pp. 1–35, 1989.

- [4] J. J. Kelly, "Nucleon charge and magnetization densities from Sachs form factors," *Physical Review C*, vol. 66, no. 6, Article ID 065203, 2002.
- [5] J. Friedrich and T. Walcher, "A coherent interpretation of the form factors of the nucleon in terms of a pion cloud and constituent quarks," *The European Physical Journal A*, vol. 17, pp. 607–623, 2003.
- [6] S. L. Glashow, "The unmellisonant quark," *Physica A*, vol. 96, no. 1-2, pp. 27–30, 1979.
- [7] S. Taylor, G. S. Mutchler, G. Adams et al., "Radiative decays of the $\Sigma^0(1385)$ and $\Lambda(1520)$ hyperons," *Physical Review C*, vol. 71, no. 5, Article ID 054609, 2005.
- [8] O. Gayou, K. Wijesooriya, A. Afanasev et al., "Measurements of the elastic electromagnetic form factor ratio $\mu_p G_{Ep}/G_{Mp}$ via polarization transfer," *Physical Review C*, vol. 64, no. 3, Article ID 038202, 2001.
- [9] O. Gayou, K. A. Aniol, T. Averett et al., "Measurement of G_{Ep}/G_{Mp} in $e^- p \rightarrow ep^-$ to $Q^2 = 5.6 \text{ GeV}^2$," *Physical Review Letters*, vol. 88, no. 9, Article ID 092301, 2002.
- [10] V. Punjabi, C. F. Perdrisat, K. A. Aniol et al., "Proton elastic form factor ratios to $Q^2=3.5 \text{ GeV}^2$ by polarization transfer," *Physical Review C*, vol. 71, Article ID 055202, 2005.
- [11] C. B. Crawford, A. Sindile, T. Akdogan et al., "Measurement of the proton's electric to magnetic form factor ratio from $^1H^- (e^-, e' p)$," *Physical Review Letters*, vol. 98, no. 5, Article ID 052301, 2007.
- [12] K. Nakamura, "Review of particle physics," *Journal of Physics G*, vol. 37, no. 7, Article ID 075021, 2010.
- [13] I. Eschrich, H. Krügeri, J. Simon et al., "Measurement of the S^- charge radius by S^- -electron elastic scattering," *Physics Letters B*, vol. 522, no. 3-4, pp. 233–239, 2001.
- [14] M. I. Adamovich, Y. A. Alexandrov, S. P. Baranov et al., "First observation of $S^- - e^-$ elastic scattering in the hyperon beam experiment WA89 at CERN," *The European Physical Journal C*, vol. 8, no. 1, pp. 59–66, 1999.
- [15] R. Rosenfelder, "Coulomb corrections to elastic electron-proton scattering and the proton charge radius," *Physics Letters B*, vol. 479, no. 4, pp. 381–386, 2000.
- [16] G. Blanpied, M. Blecher, A. Caracappa et al., " $N \rightarrow \Delta$ Transition from simultaneous measurements of $p(\gamma^-, \pi)$ and $p(\gamma^-, \gamma)$," *Physical Review Letters*, vol. 79, pp. 4337–4340, 1997.

- [17] R. Beck, H. P. Krahn, J. Ahrens et al., "Measurement of the $E2/M1$ Ratio in the $N \rightarrow \Delta$ Transition using the reaction $p(\gamma^-, p)\pi^0$," *Physical Review Letters*, vol. 78, no. 4, pp. 606–609, 1997.
- [18] G. Blanpied, M. Blecher, A. Caracappa et al., " $N \rightarrow \Delta$ transition and proton polarizabilities from measurements of $p(\gamma^-, \gamma)$, $p(\gamma^-, \pi^0)$ and $p(\gamma^-, \pi^+)$," *Physical Review C*, vol. 64, no. 2, Article ID 025203, 2001.
- [19] L. Tiator, D. Drechsel, S. S. Kamalov, and S. N. Yang, "Electromagnetic form factors of the $\Delta(1232)$ excitation," *The European Physical Journal A*, vol. 17, no. 3, pp. 357–363, 2003.
- [20] C. Becchi and G. Morpurgo, "Vanishing of the $E2$ part of the $N^*33 \rightarrow N + \gamma$ amplitude in the non-relativistic quark model of "elementary" particles," *Physics Letters*, vol. 17, no. 3, pp. 352–354, 1965.
- [21] A. M. Bernstein, "Deviation of the nucleon shape from spherical symmetry: experimental status," *The European Physical Journal A*, vol. 17, no. 3, pp. 349–355, 2003.
- [22] C. N. Papanicolas, "Nucleon deformation: a status report," *The European Physical Journal A*, vol. 18, no. 2-3, pp. 141–145, 2003.
- [23] M. Gell-Mann, "A schematic model of baryons and mesons," *Physics Letters*, vol. 8, no. 3, pp. 214–215, 1964.
- [24] R. P. Feynman, M. Gell-Mann, and G. Zweig, "Group $U(6) \hat{=} U(6)$ generated by current components," *Physical Review Letters*, vol. 13, no. 22, pp. 678–680, 1964.
- [25] G. Zweig, "An model for strong interaction symmetry and its breaking I," CERN Reports 8182/TH401, 1964.
- [26] G. Zweig, "An model for strong interaction symmetry and its breaking II," CERN Reports 8419/TH412, 1964.
- [27] G. Morpurgo, "Is a nonrelativistic approximation possible for the internal dynamics of 'elementary' particles?" *Physics*, vol. 2, pp. 95–104, 1965.
- [28] A. De Rújula, H. Georgi, and S. L. Glashow, "Hadron masses in a gauge theory," *Physical Review D*, vol. 12, no. 1, pp. 147–162, 1975.
- [29] N. Isgur and G. Karl, "Ground-state baryon magnetic moments," *Physical Review D*, vol. 21, no. 11, pp. 3175–3179, 1980.
- [30] N. Isgur, G. Karl, and D. W. L. Sprung, "Neutron charge form factor in a quark model with hyperfine interactions," *Physical Review D*, vol. 23, pp. 163–164, 1981.
- [31] N. Isgur, G. Karl, and R. Koniuk, "D waves in the nucleon: a test of color magnetism," *Physical Review D*, vol. 25, no. 9, pp. 2394–2398, 1982.
- [32] P. Geiger and N. Isgur, "Strange hadronic loops of the proton: a quark model calculation," *Physical Review D*, vol. 55, no. 1, pp. 299–310, 1997.
- [33] A. L. Yaouanc, L. Oliver, O. Pène, and J. C. Raynal, "Combined effects of internal quark motion and $SU(6)$ breaking on the properties of the baryon ground state," *Physical Review D*, vol. 15, no. 3, pp. 844–853, 1977.
- [34] M. Gupta and A. N. Mitra, "Even-wave harmonic-oscillator theory of baryonic states. IV. Structure functions versus slope of neutron charge form factor," *Physical Review D*, vol. 18, no. 5, pp. 1585–1590, 1978.
- [35] M. Gupta, S. K. Sood, and A. N. Mitra, "Resonance photocouplings with a "mixed" nucleon and the even-wave harmonic-oscillator theory of baryonic states," *Physical Review D*, vol. 16, no. 1, pp. 216–219, 1977.
- [36] M. Gupta, S. K. Sood, and A. N. Mitra, "Even-wave harmonic-oscillator theory of baryonic states. V. Polarized photoproduction of single pions," *Physical Review D*, vol. 19, pp. 104–111, 1979.
- [37] P. Amaudruz, M. Arneodo, A. Arvidson et al., "Gottfried sum from the ratio F_2^n/F_2^p ," *Physical Review Letters*, vol. 66, no. 21, pp. 2712–2715, 1991.
- [38] M. Arneodo, A. Arvidson, B. Badelek et al., "Reevaluation of the Gottfried sum," *Physical Review D*, vol. 50, no. 1, pp. R1–R3, 1994.
- [39] E. A. Hawker, T. C. Awes, M. E. Beddo et al., "Measurement of the light antiquark flavor asymmetry in the nucleon sea," *Physical Review Letters*, vol. 80, no. 17, pp. 3715–3718, 1998.
- [40] J. C. Peng, G. T. Garvey, T. C. Awes et al., " \bar{d}/\bar{u} asymmetry and the origin of the nucleon sea," *Physical Review D*, vol. 58, no. 9, Article ID 092004, 1998.
- [41] R. S. Towell, P. L. McGaughey, T. C. Awes et al., "Improved measurement of the \bar{d}/\bar{u} asymmetry in the nucleon sea," *Physical Review D*, vol. 64, no. 5, Article ID 052002, 2001.
- [42] J. Kunz and P. J. Mulders, "Electromagnetic properties of hyperons in the bound-state approach to the Skyrme model," *Physical Review D*, vol. 41, no. 5, pp. 1578–1585, 1990.
- [43] J. Kunz, P. J. Mulders, and G. A. Miller, "Charge distributions of hyperons," *Physics Letters B*, vol. 255, no. 1, pp. 11–17, 1991.
- [44] C. Gobbi, S. Boffi, and D. O. Riska, "Mean square radii of hyperons in the bound-state soliton model," *Nuclear Physics A*, vol. 547, no. 4, pp. 633–644, 1992.
- [45] B. Schwesinger and H. Weigel, " $SU(3)$ symmetry breaking for masses, magnetic moments and sizes of baryons," *Nuclear Physics A*, vol. 540, no. 3-4, pp. 461–477, 1992.
- [46] H. Kim, A. Blotz, M. V. Polyakov, and K. Goeke, "Electromagnetic form factors of the $SU(3)$ octet baryons in the semibosonized $SU(3)$ Nambu-Jona-Lasinio model," *Physical Review D*, vol. 53, no. 7, pp. 4013–4029, 1996.
- [47] D. H. Lu, A. W. Thomas, and A. G. Williams, "Electromagnetic form factors of the nucleon in an improved quark model," *Physical Review C*, vol. 57, no. 5, pp. 2628–2637, 1998.
- [48] G. Wagner, A. J. Buchmann, and A. Faessler, "Exchange currents in octet hyperon charge radii," *Physical Review C*, vol. 58, no. 6, pp. 3666–3669, 1998.
- [49] N. Barik, S. N. Jena, and D. P. Rath, "Nucleon form factors and static properties of baryons in a quark model," *Physical Review D*, vol. 41, no. 5, pp. 1568–1577, 1990.
- [50] M. Warns, W. Pfeil, and H. Rollnik, "Electromagnetic properties of hyperons in a relativised quark model," *Physics Letters B*, vol. 258, no. 3-4, pp. 431–440, 1991.
- [51] T. V. Cauteren, D. Merten, T. Corthals et al., "Electric and magnetic form factors of strange baryons," *The European Physical Journal A*, vol. 20, no. 2, pp. 283–291, 2004.
- [52] K. Berger, R. F. Wagenbrunn, and W. Plessas, "Covariant baryon charge radii and magnetic moments in a chiral constituent-quark model," *Physical Review D*, vol. 70, no. 9, Article ID 094027, 2004.
- [53] B. J. Diaz, D. O. Riska, and F. Coester, "Baryon form factors of relativistic constituent-quark models," *Physical Review C*, vol. 69, Article ID 035212, 2004.
- [54] B. J. Diaz, D. O. Riska, and F. Coester, "Erratum: baryon form factors of relativistic constituent-quark models," *Physical Review C*, vol. 75, Article ID 069902, 2007.
- [55] A. J. Buchmann and R. F. Lebed, "Large N_c , constituent quarks, and N, Δ charge radii," *Physical Review D*, vol. 62, no. 9, Article ID 096005, 2000.
- [56] A. J. Buchmann, "Charge form factors and nucleon shape," *AIP Conference Proceedings*, vol. 904, pp. 110–125.

- [57] A. J. Buchmann and R. F. Lebed, “Baryon charge radii and quadrupole moments in the $1/N_c$ expansion: the 3-flavor case,” *Physical Review D*, vol. 67, Article ID 016002, 17 pages, 2003.
- [58] A. J. Buchmann, “Structure of strange baryons,” in *Proceedings of the International Conference on Hypernuclear and Strange Particle Physics (HYP '06)*, Mainz, Germany, October 2006.
- [59] S. Cheedket, V. E. Lyubovitskij, T. Gutsche, A. Faessler, K. Pumsa-Ard, and Y. Yan, “Electromagnetic form factors of the baryon octet in the perturbative chiral quark model,” *The European Physical Journal A*, vol. 20, no. 2, pp. 317–327, 2004.
- [60] S. J. Puglia, M. J. R. Musolf, and S. L. Zhu, “Octet baryon charge radii, chiral symmetry, and decuplet intermediate states,” *Physical Review D*, vol. 36, Article ID 034014, 2001.
- [61] B. Kubis and U. G. Meissner, “Baryon form factors in chiral perturbation theory,” *The European Physical Journal C*, vol. 18, no. 4, pp. 747–756, 2001.
- [62] D. Arndt and B. C. Tiburzi, “Charge radii of the meson and baryon octets in quenched and partially quenched chiral perturbation theory,” *Physical Review D*, vol. 68, no. 9, Article ID 094501, 2003.
- [63] P. Wang, D. B. Leinweber, A. W. Thomas, and R. D. Young, “Chiral extrapolation of octet-baryon charge radii,” *Physical Review D*, vol. 79, no. 9, Article ID 094001, 2009.
- [64] D. B. Leinweber, T. Draper, and R. M. Woloshyn, “Decuplet baryon structure from lattice QCD,” *Physical Review D*, vol. 46, no. 7, pp. 3067–3085, 1992.
- [65] D. Arndt and B. C. Tiburzi, “Electromagnetic properties of the baryon decuplet in quenched and partially quenched chiral perturbation theory,” *Physical Review D*, vol. 68, Article ID 114503, 2003.
- [66] S. Boinepalli, D. B. Leinweber, P. J. Moran, A. G. Williams, J. M. Zanotti, and J. B. Zhang, “Electromagnetic structure of decuplet baryons towards the chiral regime,” *Physical Review D*, vol. 80, no. 5, Article ID 054505, 2009.
- [67] R. K. Sahoo, A. R. Panda, and A. Nath, “Magnetic moments and charge radii of decuplet baryons in a field-theoretic quark model,” *Physical Review D*, vol. 52, no. 7, pp. 4099–4105, 1995.
- [68] L. S. Geng, J. M. Camalich, and M. J. V. Vacas, “Electromagnetic structure of the lowest-lying decuplet resonances in covariant chiral perturbation theory,” *Physical Review D*, vol. 80, no. 3, Article ID 034027, 2009.
- [69] C. Alexandrou, P. de Forcrand, T. Lippert et al., “ N to Δ electromagnetic transition form factors from lattice QCD,” *Physical Review D*, vol. 69, no. 11, Article ID 114506, 2004.
- [70] C. Alexandrou, P. de Forcrand, H. Neff et al., “ N to Δ electromagnetic-transition form factors from lattice QCD,” *Physical Review Letters*, vol. 94, no. 2, Article ID 021601, 2005.
- [71] G. Clement and M. Maamache, “Are the N and Δ deformed MIT bags?” *Annals of Physics*, vol. 165, no. 1, pp. 1–16, 1985.
- [72] A. B. Migdal, “Traektorii Redzhe i forma adronov,” *Pis'Ma V ZhETF*, vol. 46, no. 7, pp. 256–258, 1987.
- [73] A. B. Migdal, “Regge trajectories and the shape of hadrons,” *JETP Letters*, vol. 46, no. 7, pp. 322–325, 1987.
- [74] A. J. Buchmann, “ N -to- Δ quadrupole transition in the constituent quark model,” in *Proceedings of the 8th International Conference on the Structure of Baryons (Baryons' 98)*, D. W. Menze and B. Metsch, Eds., p. 731, World Scientific, Singapore, 1999.
- [75] A. J. Buchmann, E. Hernandez, and A. Faessler, “Electromagnetic properties of the Δ (1232),” *Physical Review C*, vol. 55, no. 1, pp. 448–463, 1997.
- [76] A. J. Buchmann and E. M. Henley, “Intrinsic quadrupole moment of the nucleon,” *Physical Review D*, vol. 63, Article ID 015202, 2001.
- [77] A. J. Buchmann and E. M. Henley, “Quadrupole moments of baryons,” *Physical Review D*, vol. 65, no. 7, Article ID 073017, 2002.
- [78] A. J. Buchmann, J. A. Hester, and R. F. Lebed, “Quadrupole moments of N and Δ in the $1/N_c$ expansion,” *Physical Review D*, vol. 66, no. 5, Article ID 056002, 2002.
- [79] A. J. Buchmann, “Size and shape of baryons in a large N_c quark model,” in *Proceedings of the Institute for Nuclear Theory, Phenomenology of Large N_c QCD*, R. F. Lebed, Ed., vol. 12, p. 224, World Scientific, 2002.
- [80] A. J. Buchmann and R. F. Lebed, “Baryon charge radii and quadrupole moments in the $1/N_c$ expansion: the 3-flavor case,” *Physical Review D*, vol. 67, Article ID 016002, 2003.
- [81] N. Isgur, G. Karl, and R. Koniuk, “ D waves in the nucleon: a test of color magnetism,” *Physical Review D*, vol. 25, pp. 2394–2398, 1982.
- [82] W. J. Leonard and W. J. Gerace, “Quark-meson coupling model for baryon wave functions and properties,” *Physical Review D*, vol. 41, pp. 924–936, 1990.
- [83] G. Wagner, A. J. Buchmann, and A. Faessler, “Electromagnetic properties of decuplet hyperons in a chiral quark model with exchange currents,” *Journal of Physics G*, vol. 26, no. 3, article 267, 2000.
- [84] M. I. Krivoruchenko and M. M. Giannini, “Quadrupole moments of the decuplet baryons,” *Physical Review D*, vol. 43, no. 11, pp. 3763–3765, 1991.
- [85] T. Ledwig, A. Silva, and M. Vanderhaeghen, “Electromagnetic properties of the Δ (1232) and decuplet baryons in the self-consistent $SU(3)$ chiral quark-soliton model,” *Physical Review D*, vol. 79, no. 9, Article ID 094025, 2009.
- [86] G. Ramalho and M. T. Pena, “Electromagnetic form factors of the Δ in an S-wave approach,” *Journal of Physics G*, vol. 36, no. 8, Article ID 085004, 2009.
- [87] G. Ramalho, M. T. Pena, and F. Gross, “Electric quadrupole and magnetic octupole moments of the Δ ,” *Physics Letters B*, vol. 678, no. 4, pp. 355–358, 2009.
- [88] G. Ramalho, M. T. Pena, and F. Gross, “Electromagnetic form factors of the Δ with D-waves,” *Physical Review D*, vol. 81, no. 11, Article ID 113011, 2010.
- [89] B. Schwesinger and H. Weigel, “ $SU(3)$ symmetry breaking for masses, magnetic moments and sizes of baryons,” *Nuclear Physics A*, vol. 540, no. 3–4, pp. 461–477, 1992.
- [90] J. Kroll and B. Schwesinger, “Electric quadrupole moments of the decuplet and the strangeness content of the proton,” *Physics Letters B*, vol. 334, pp. 287–289, 1994.
- [91] Y. Oh, “Electric quadrupole moments of the decuplet baryons in the Skyrme model,” *Modern Physics Letters A*, vol. 10, pp. 1027–1034, 1995.
- [92] A. Abada, H. Weigel, and H. Reinhardt, “Radiative decays of hyperons in the Skyrme model: view the MathML source transitions ratios $E2/M1$,” *Physics Letters B*, vol. 366, pp. 26–31, 1996.
- [93] A. J. Buchmann and E. M. Henley, “Quadrupole moments of baryons,” *Physical Review D*, vol. 65, no. 7, Article ID 073017, 2002.
- [94] A. J. Buchmann and E. M. Henley, “Baryon octupole moments,” *The European Physical Journal A*, vol. 35, no. 3, pp. 267–269, 2008.

- [95] K. Azizi, “Magnetic dipole, electric quadrupole and magnetic octupole moments of the Δ baryons in light cone QCD sum rules,” *The European Physical Journal C*, vol. 61, no. 2, pp. 311–319, 2009.
- [96] T. M. Aliev, K. Azizi, and M. Savci, “Electric quadrupole and magnetic octupole moments of the light decuplet baryons within light cone QCD sum rules,” *Physics Letters*, vol. 681, no. 3, pp. 240–246, 2009.
- [97] A. J. Buchmann, J. A. Hester, and R. F. Lebed, “Quadrupole moments of N and Δ in the $1/N_c$ expansion,” *Physical Review D*, vol. 66, no. 5, Article ID 056002, 2002.
- [98] A. J. Buchmann and R. F. Lebed, “Baryon charge radii and quadrupole moments in the $1/N_c$ expansion: the 3-flavor case,” *Physical Review D*, vol. 67, Article ID 016002, 2003.
- [99] M. N. Butler, M. J. Savage, and R. P. Springer, “Electromagnetic moments of the baryon decuplet,” *Physical Review D*, vol. 49, pp. 3459–3465, 1994.
- [100] M. K. Banerjee and J. Milana, “Decuplet reexamined in chiral perturbation theory,” *Physical Review D*, vol. 54, no. 9, pp. 5804–5811, 1996.
- [101] D. Arndt and B. C. Tiburzi, “Electromagnetic properties of the baryon decuplet in quenched and partially quenched chiral perturbation theory,” *Physical Review D*, vol. 68, no. 11, Article ID 114503, 2003.
- [102] D. Arndt and B. C. Tiburzi, “Erratum: electromagnetic properties of the baryon decuplet in quenched and partially quenched chiral perturbation theory,” *Physical Review D*, vol. 65, no. 5, Article ID 059904, 2004.
- [103] L. S. Geng, J. M. Camalich, and M. J. V. Vacas, “Electromagnetic structure of the lowest-lying decuplet resonances in covariant chiral perturbation theory,” *Physical Review D*, vol. 80, Article ID 034027, 2009.
- [104] D. B. Leinweber, T. Draper, and R. M. Woloshyn, “Decuplet baryon structure from lattice QCD,” *Physical Review D*, vol. 46, pp. 3067–3085, 1992.
- [105] C. Alexandrou, T. Korzec, T. Leontiou, J. W. Negele, and A. Tsapalis, “Electromagnetic form factors of the Delta baryon,” *PoSLATTICE*, 2007, p. 149, 2006.
- [106] C. Alexandrou, T. Korzec, G. Koutsou et al., “Quark transverse charge densities in the delta-(1232) from lattice QCD,” *Nuclear Physics A*, vol. 825, no. 1-2, pp. 115–144, 2009.
- [107] C. Alexandrou, T. Korzec, G. Koutsou et al., “Delta-baryon electromagnetic form factors in lattice QCD,” *Physical Review D*, vol. 79, Article ID 014507, 2009.
- [108] S. Boinepalli, D. B. Leinweber, P. J. Moran, A. G. Williams, J. M. Zanotti, and J. B. Zhang, “Electromagnetic structure of decuplet baryons towards the chiral regime,” *Physical Review D*, vol. 80, Article ID 054505, 2009.
- [109] S. Weinberg, “Phenomenological lagrangians,” *Physica A*, vol. 96, no. 1-2, pp. 327–340, 1979.
- [110] A. Manohar and H. Georgi, “Chiral quarks and the non-relativistic quark model,” *Nuclear Physics B*, vol. 234, no. 1, pp. 189–212, 1984.
- [111] T. P. Cheng and L. F. Li, “Flavor and spin contents of the nucleon in the quark model with chiral symmetry,” *Physical Review Letters*, vol. 74, pp. 2872–2875, 1995.
- [112] T. P. Cheng and L. F. Li, “Chiral quark model of nucleon spin-flavor structure with SU(3) and axial-U(1) breakings,” *Physical Review D*, vol. 57, pp. 344–349, 1998.
- [113] X. Song, J. S. McCarthy, and H. J. Weber, “Nucleon spin-flavor structure in the SU(3)-breaking chiral quark model,” *Physical Review D*, vol. 55, no. 5, pp. 2624–2629, 1997.
- [114] X. Song, “New relations and constraints on quark spin-flavor content in the symmetry-breaking chiral quark model,” *Physical Review D*, vol. 57, pp. 4114–4123, 1998.
- [115] J. Linde, T. Ohlsson, and H. Snellman, “Octet baryon magnetic moments in the chiral quark model with configuration mixing,” *Physical Review D*, vol. 57, pp. 452–464, 1998.
- [116] J. Linde, T. Ohlsson, and H. Snellman, “Decuplet baryon magnetic moments in the chiral quark model,” *Physical Review D*, vol. 57, no. 9, pp. 5916–5919, 1998.
- [117] H. Dahiya and M. Gupta, “Chiral quark model with configuration mixing,” *Physical Review D*, vol. 64, Article ID 014013, 2001.
- [118] H. Dahiya and M. Gupta, “Chiral quark model (χ QM) and the nucleon spin,” *International Journal of Modern Physics A*, vol. 19, no. 29, Article ID 5027, 2004.
- [119] H. Dahiya and M. Gupta, “Chiral constituent quark model and the coupling strength of η ,” *International Journal of Modern Physics A*, vol. 21, no. 21, Article ID 4255, 2006.
- [120] N. Sharma, H. Dahiya, P. K. Chatley, and M. Gupta, “Weak vector and axial-vector form factors in the chiral constituent quark model with configuration mixing,” *Physical Review D*, vol. 79, Article ID 077503, 2009.
- [121] N. Sharma, H. Dahiya, and P. K. Chatley, “Extraction of the CKM matrix element V_{us} from the hyperon semileptonic decays,” *The European Physical Journal A*, vol. 44, no. 1, pp. 125–128, 2010.
- [122] H. Dahiya and M. Gupta, “ x -dependence of the quark distribution functions in the χ CQM,” *The European Physical Journal C*, vol. 52, no. 3, pp. 571–579, 2007.
- [123] H. Dahiya and M. Gupta, “Spin and flavor strange quark content of the nucleon,” *Physical Review D*, vol. 78, Article ID 014001, 2008.
- [124] N. Sharma and H. Dahiya, “Quark sea asymmetries of the octet baryons,” *Physical Review D*, vol. 81, Article ID 114003, 2010.
- [125] H. Dahiya and M. Gupta, “Octet magnetic moments and the Coleman-Glashow sum rule violation in the chiral quark model,” *Physical Review D*, vol. 66, Article ID 051501, 2002.
- [126] H. Dahiya and M. Gupta, “Octet and decuplet baryon magnetic moments in the chiral quark model,” *Physical Review D*, vol. 67, p. 114015, 2003.
- [127] H. Dahiya and M. Gupta, “SU(4) chiral quark model with configuration mixing,” *Physical Review D*, vol. 67, Article ID 074001, 2003.
- [128] N. Sharma, A. M. Torres, K. P. Khemchandani, and H. Dahiya, “Magnetic moments of the low-lying $(1/2)^-$ octet baryon resonances,” *The European Physical Journal A*, vol. 49, article 11, 2013.
- [129] A. M. Torres, K. P. Khemchandani, N. Sharma, and H. Dahiya, “Magnetic moments of the low-lying $J^P = (1/2)^-, (3/2)^- \Lambda$ resonances within the framework of the chiral quark model,” *The European Physical Journal A*, vol. 48, article 185, 2012.
- [130] N. Sharma and H. Dahiya, “Charge radii of octet and decuplet baryons,” in *AIP Conference Proceedings*, vol. 1388, pp. 458–460, 2011.
- [131] N. Sharma and H. Dahiya, “Quadrupole moments of low-lying baryons with spin- $(1/2)^+$, spin- $(3/2)^+$, and spin- $(3/2)^+$ to $(1/2)^+$ transitions,” *Pramana*, vol. 80, no. 2, pp. 237–249, 2013.
- [132] H. Dahiya and M. Gupta, “SU(4) chiral quark model with configuration mixing,” *Physical Review D*, vol. 67, no. 7, Article ID 074001, 2003.
- [133] N. Sharma, H. Dahiya, P. K. Chatley, and M. Gupta, “Spin $(1/2)^+$, spin $(3/2)^+$, and transition magnetic moments of low lying and

- charmed baryons,” *Physical Review D*, vol. 81, no. 7, Article ID 073001, 2010.
- [134] G. Morpurgo, “Field theory and the nonrelativistic quark model: a parametrization of the baryon magnetic moments and masses,” *Physical Review D*, vol. 40, pp. 2997–3011, 1989.
- [135] G. Morpurgo, “Field theory and the nonrelativistic quark model: a parametrization of the meson masses,” *Physical Review D*, vol. 41, no. 9, pp. 2865–2870, 1990.
- [136] G. Dillon and G. Morpurgo, “Relation of constituent quark models to QCD: why several simple models work ‘so well,’” *Physical Review D*, vol. 53, pp. 3754–3769, 1996.
- [137] G. Dillon and G. Morpurgo, “Chiral QCD, general QCD parametrization, and constituent quark models,” *Physical Review D*, vol. 68, Article ID 014001, 2003.
- [138] G. Dillon and G. Morpurgo, “Baryon octet magnetic moments to all orders in flavor breaking: an application to the problem of the strangeness in the nucleon,” *Physical Review D*, vol. 75, no. 7, Article ID 073007, 2007.
- [139] A. J. Buchmann and E. M. Henley, “Intrinsic quadrupole moment of the nucleon,” *Physical Review C*, vol. 63, no. 1, Article ID 015202, 8 pages, 2000.
- [140] A. J. Buchmann, “Electromagnetic $N \rightarrow \Delta$ transition and neutron form factors,” *Physical Review Letters*, vol. 93, Article ID 212301, 4 pages, 2004.
- [141] A. J. Buchmann, “Structure of strange baryons,” in *Proceedings of the Shape of Hadrons Workshop*, C. N. Papanicolas and A. M. Bernstein, Eds., Athens, Greece, 2006.
- [142] A. J. Buchmann, “Charge form factors and nucleon shape,” *AIP Conference Proceedings*, vol. 904, pp. 110–125, 2007.
- [143] G. Morpurgo, “Smallness of gluon coupling to constituent quarks in baryons and validity of nonrelativistic quark model,” *Physical Review D*, vol. 46, no. 9, pp. 4068–4075, 1992.
- [144] G. Dillon and G. Morpurgo, “General QCD parametrization of the charge radii of p , n and Δ^+ ,” *Physics Letters B*, vol. 448, no. 1-2, pp. 107–110, 1999.

Research Article

Ridge and Transverse Correlation without Long-Range Longitudinal Correlation

Charles B. Chiu¹ and Rudolph C. Hwa²

¹ Center for Particles and Fields and Department of Physics, University of Texas at Austin, Austin, TX 78712, USA

² Institute of Theoretical Science and Department of Physics, University of Oregon, Eugene, OR 97403-5203, USA

Correspondence should be addressed to Rudolph C. Hwa; hwa@uoregon.edu

Received 19 March 2013; Accepted 16 May 2013

Academic Editor: Jan E. Alam

Copyright © 2013 C. B. Chiu and R. C. Hwa. This is an open access article distributed under the Creative Commons Attribution License, which permits unrestricted use, distribution, and reproduction in any medium, provided the original work is properly cited.

A simple phenomenological relationship between the ridge distribution in $\Delta\eta$ and the single-particle distribution in η can be established from the PHOBOS data on both distributions. The implication points to the possibility that it is not necessary to have long-range longitudinal correlation to explain the data. An interpretation of the relationship is then developed, based on the recognition that longitudinal uncertainty of the initial configuration allows for non-Hubble-like expansion at early time. It is shown that the main features of the ridge structure can be explained in a model where transverse correlation stimulated by semihard partons is the principal mechanism. This work is related to the azimuthal anisotropy generated by minijets in Au-Au collisions at 0.2 TeV on the one hand and to the ridge structure seen in pp collisions at 7 TeV on the other hand.

1. Introduction

The ridge structure in two-particle correlation has been studied in nuclear collisions at the Relativistic Heavy-Ion Collider (RHIC) for several years [1–5] and has recently also been seen in pp collisions at the Large Hadron Collider (LHC) [6]. The nature of that structure is that it is narrow in $\Delta\phi$ (azimuthal angle ϕ relative to that of the trigger) but broad in $\Delta\eta$ (pseudorapidity η relative to the trigger). In [3], the range in $\Delta\eta$ is found to be as large as 4. So far there is no consensus on the origin of the ridge formation [7]. It has been pointed out that the wide $\Delta\eta$ distribution implies long-range correlation [8–10]. That is, a view based partially on the conventional estimate that the correlation length is about 2 [11]. We make here a comparison between the η ranges of single-particle distribution and two-particle correlation, using only the experimental data from PHOBOS [3, 12]. It is found that the large- $\Delta\eta$ ridge distribution is related simply to a shift of the inclusive distribution and an integral over the trigger η . That is a phenomenological observation without any theoretical input. Any successful model of ridge formation should be able to explain that relationship.

There are subtleties about the single-particle distribution for all charges, $dN^{\text{ch}}/d\eta$, that to our knowledge has not been satisfactorily explained in all its details. Since it sums over all charges, hadrons of different types are included, making $dN^{\text{ch}}/d\eta$ to be quite different from dN^{π}/dy , which can be fitted by a Gaussian distribution in y with width $\sigma_{\pi} = 2.27$ [13, 14]. That difference cannot be readily accounted for in any simple hadronization scheme. Fortunately, detailed examination of $dN^{\text{ch}}/d\eta$ is not required before we find its relationship to the ridge distribution $dN_R^{\text{ch}}/d\Delta\eta$, since both are for unidentified charged hadrons, and the empirical verification is based on the data from the same experimental group (PHOBOS).

As a consequence of the phenomenological relationship, we consider the possibility that there is no intrinsic long-range longitudinal correlation apart from what gives rise to the single-particle distribution. We have found that to generate $dN_R^{\text{ch}}/d\Delta\eta$ it is only necessary to have transverse correlation at different points in η , provided that at early time the small- x partons do not expand in Hubble-like manner. If spatial uncertainty of wee partons is allowed at early time, the identification of spatial and momentum rapidities may

not be valid near the tip of the forward light cone. Therein lies the origin of transverse correlation due to the possibility of near crossing of soft- and hard-parton trajectories. The energy lost by a hard parton enhances the thermal energies of the medium partons in the vicinity of the hard parton's trajectory. The transverse broadening of any small- x parton that passes through the cone of that enhancement leads to measurable effect of the ridge. The parton model that we use does not rely on flux tubes or hydrodynamics.

Recently, the existence of ridge has been called into question by investigations on the effect of fluctuations of the initial configurations in heavy-ion collisions [15, 16]. Using hydrodynamical model and transport theory to relate the eccentricities of the spatial initial state in the transverse plane to the azimuthal momentum anisotropy in the final state, it has been shown that the harmonic coefficients v_n observed in the data can be understood in terms of such transverse fluctuations [17–25]. That is, however, only one of the possible interpretations of v_n . The effect of minijets on the initial configuration can yield similar consequences. Data on two-dimensional (2D) angular correlation with p_T integrated have been analyzed by model fits; it is found that the same-side 2D peak can account for all higher Fourier components with $n > 2$ [26]. In [27], it is shown that the data on v_n can also be well reproduced by taking the minijets into account in the recombination model without the details of hydrodynamics. Here, we raise the issue about the effect of longitudinal fluctuations that seem to be as important as transverse fluctuations but have hardly been investigated.

After the phenomenological relationship between $dN_R^{\text{ch}}/d\Delta\eta$ and $dN^{\text{ch}}/d\eta$ is established in Section 2, we give our interpretation of the phenomenon in Section 3. We show the possibility that the ridge can have the observed properties in the absence of long-range longitudinal correlation. Section 3 includes many subsections in which both longitudinal and transverse aspects of the correlation are examined in the parton model. Connections between what we do here with azimuthal anisotropy generated by minijets in Au-Au collisions at RHIC and with the ridge structure found in pp collisions at LHC are given in Section 4. Our conclusion is given in Section 5.

2. Comparison between Ridge and Inclusive Distributions

Our focus is on the PHOBOS data on two-particle correlation measured with a trigger particle having transverse momentum $p_T^{\text{trig}} > 2.5$ GeV/c in Au + Au collisions at $\sqrt{s_{NN}} = 200$ GeV [3]. The pseudorapidity acceptance of the trigger is $0 < \eta^{\text{trig}} < 1.5$. The per-trigger ridge yield integrated over $|\Delta\phi| < 1$, denoted by $(1/N^{\text{trig}})dN_R^{\text{ch}}/d\Delta\eta$, includes all charged hadrons with $p_T^a \geq 7$ MeV/c at $\eta^a = 3$ and $p_T^a \geq 35$ MeV/c at $\eta^a = 0$, where the superscript a stands for associated particle in the ridge. For simplicity, we use the notation $\eta^{\text{trig}} = \eta_1$, $\eta^a = \eta_2$, $\Delta\eta = \eta_2 - \eta_1$, $\phi^{\text{trig}} = \phi_1$, $\phi^a = \phi_2$, $\Delta\phi = \phi_2 - \phi_1$. Since all ridge particles are included in the range $|\Delta\phi| < 1$, the $\Delta\phi$ dependence of the ridge structure does not show up in the properties of $dN_R^{\text{ch}}/d\Delta\eta$. We have previously

studied the $\Delta\phi$ dependence of the ridge [28], which will be summarized in Section 3.2. Here we focus on our aim to relate the ridge distribution in $\Delta\eta$ to the single-particle distribution in η . We first make a phenomenological observation using only PHOBOS data for both distributions. After showing their relationship, we then make an interpretation that does not involve extensive modeling.

To do meaningful comparison, it is important to use single-particle η distribution, $dN^{\text{ch}}/d\eta$, that has the same kinematical constraints as the ridge distribution. That is, it involves an integration over p_T and a sum over all charged hadrons

$$\frac{dN^{\text{ch}}}{d\eta} = \sum_h \int dp_T p_T \rho_1^h(\eta, p_T), \quad (1)$$

where $\rho_1^h(\eta, p_T) = dN^h/p_T dp_T d\eta$, and the lower limit of the p_T integration is $35(1 - \eta/3.75)$ MeV/c in keeping with the acceptance window of p_T^a [3]. The data on $(1/N^{\text{trig}})dN_R^{\text{ch}}/d\Delta\eta$ are for 0–30% centrality. PHOBOS has the appropriate $dN^{\text{ch}}/d\eta$ for 0–6%, 6–15%, 15–25%, and 25–35% centralities [12], as shown in Figure 1(a). Thus we average them over those four bins. The result is shown in Figure 1(b) by the small circles for 0–30% centrality. Those points are fitted by the three Gaussian distributions, located at $\eta = 0$ and $\pm\hat{\eta}$,

$$\frac{dN^{\text{ch}}}{d\eta} = A \left\{ \exp\left[\frac{-\eta^2}{2\sigma_0^2}\right] + a_1 \exp\left[\frac{-(\eta - \hat{\eta})^2}{2\sigma_1^2}\right] + a_1 \exp\left[\frac{-(\eta + \hat{\eta})^2}{2\sigma_1^2}\right] \right\} \quad (2)$$

shown by the solid (red) line in that figure with $A = 468$, $\sigma_0 = 2.69$, $a_1 = 0.31$, $\hat{\eta} = 2.43$, $\sigma_1 = 1.15$. The dashed line shows the central Gaussian, while the dash-dotted line shows the two side Gaussians. The purpose of the fit is mainly to give an analytic representation of $dN^{\text{ch}}/d\eta$ to be used for comparison with the ridge distribution. Nevertheless, it is useful to point out that the width σ_0 of the central Gaussian in η is larger than the width of the pion γ -distribution, $\sigma_\pi = 2.27$, mentioned in Section 1. The two side Gaussians are undoubtedly related to the production of protons, since BRAHMS data show significant p/π ratio above $\eta = 2$ and $p_T > 1$ GeV/c [29]. The value of $\hat{\eta}$ in (2) being > 2 is a result of the enhancement by proton production. Any treatment of correlation among charged particles without giving proper attention to the protons is not likely to reproduce the inclusive distribution given by (2), whose η width is significantly stretched by the side Gaussians.

We now propose the formula

$$\frac{1}{N^{\text{trig}}} \frac{dN_R^{\text{ch}}}{d\Delta\eta} = r \int_0^{1.5} d\eta_1 \left. \frac{dN^{\text{ch}}}{d\eta_2} \right|_{\eta_2=\eta_1+\Delta\eta}, \quad (3)$$

where r is a parameter that summarizes all the experimental conditions that lead to the magnitude of the ridge distribution measured relative to the single-particle distribution. In particular, r does not depend on η_1 or η_2 ; otherwise, the equation is meaningless in comparing the η dependencies.

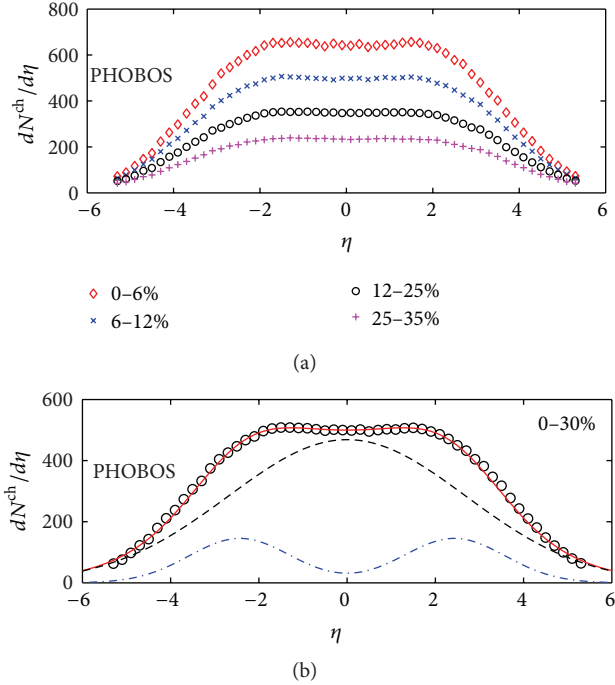


FIGURE 1: Pseudorapidity distribution in Au-Au collisions at $\sqrt{s_{NN}} = 200$ GeV for (a) various centrality bins and (b) 0–30% centrality. Data are from [12]. The (red) line in (b) is a fit using (2), whose first term is represented by the dashed line and the other two terms by the dash-dotted line (color online).

There is no theoretical input in (3), except for the question behind the proposal: how much of the $\Delta\eta$ distribution can be accounted for by just a mapping of $dN^{\text{ch}}/d\eta_2$ with a shift due to the definition $\Delta\eta = \eta_2 - \eta_1$, and an integration over η_1 due to the trigger acceptance, $0 < \eta_1 < 1.5$? Another way of asking the question is how would the range of correlation be affected if the experimental statistics were high enough so that the trigger's η range can be very narrow around $\eta_1 = 0$?

The proposed formula in (3) is tested by substituting the fit of $dN^{\text{ch}}/d\eta$ according to (2) into the integrand on the right-hand side. The result is shown in Figure 2 with r being adjusted to fit the height of the ridge distribution; its value is 4.4×10^{-4} . The peak in the data around $\Delta\eta = 0$ is, of course, due to the jet component associated with the trigger jet and is not relevant to our comparison here. That component has been studied in the recombination model as a consequence of thermal-shower recombination that can give a good description of the peak both in $\Delta\eta$ and $\Delta\phi$ [30]. For the ridge considered here, it is evident that the large $\Delta\eta$ distribution in Figure 2 is well reproduced by (3). Since our concern is to elucidate the implications of the range of $\Delta\eta$, we leave the fluctuation from the flat distribution in the interval $-2 < \Delta\eta < -1$ as an experimental problem. In qualitative terms, the width of the ridge distribution is due partly to the width of $dN^{\text{ch}}/d\eta$ and partly to the smearing of η_1 , which adds another 1.5 to the width. No intrinsic dynamics of long-range longitudinal correlation has been put in. Note that the center of the plateau in $\Delta\eta$ is at -0.75 , which is the

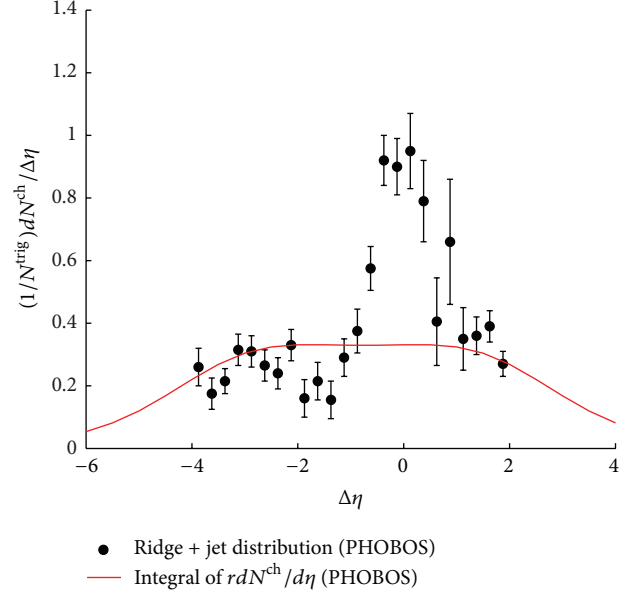


FIGURE 2: Two-particle correlation of charged particles. Data are from [3] that include both ridge and jet components. The line is a plot according to (3) using η distribution from Figure 1 [12] (color online).

average of the shift due to η_1 being integrated from 0 to 1.5. It suggests that if η_1 were fixed at $\eta_1 \approx 0$ when abundant data become available, then the width of $dN^{\text{ch}}/d\Delta\eta$ would be only as wide as that of the single-particle $dN^{\text{ch}}/d\eta$. No theoretical prejudice has influenced these observations.

3. Interpretation of Phenomenological Observation

We now consider an interpretation of what (3) implies, given the empirical support for its validity from Figure 2. First, we ask what the implication of the phenomenological observation is in terms of the range of longitudinal correlation. Then we describe a model for ridge formation first for azimuthal dependence at mid-rapidity then for larger pseudorapidity pertinent to the data. The considerations from various perspectives lead to the notion of transverse correlation that will become the core element of our model to explain the ridge phenomenon.

3.1. Range of Longitudinal Correlation. Since the observed ridge distribution integrates over trigger η , we write it as

$$\frac{1}{N^{\text{trig}}} \frac{dN^{\text{ch}}}{d\Delta\eta} = \int_0^{1.5} d\eta_1 \sum_{h_2} \int dp_2 p_2 R^{h_2}(\eta_1, \eta_2, p_2) \Big|_{\eta_2 = \eta_1 + \Delta\eta}, \quad (4)$$

where we exhibit also explicitly the sum over the hadron type of the ridge particle h_2 and the integral over its transverse momentum, denoted by p_2 . According to the definition of

correlation $C_2(1, 2) = \rho_2(1, 2) - \rho_1(1)\rho_1(2)$, we can express the per-trigger ridge correlation as

$$R^{h_2}(\eta_1, \eta_2, p_2) = \sum_{h_1} \int dp_1 p_1 \frac{\rho_2^{h_1 h_2(B+R)}(\eta_1, p_1, \eta_2, p_2)}{\rho_1^{h_1}(\eta_1, p_1)} - \rho_1^{h_2(B)}(\eta_2, p_2), \quad (5)$$

where p_1 is the transverse momentum of the trigger particle; B and R in the superscript denote background and ridge, respectively. The jet component in the associated-particle distribution is excluded in (5).

On the other hand, with (1) substituted into (3) we have, using η_2 and p_2 instead of η and p_T ,

$$\frac{1}{N^{\text{trig}}} \frac{dN_R^{\text{ch}}}{d\Delta\eta} = \int_0^{1.5} d\eta_1 \sum_{h_2} \int dp_2 p_2 r \rho_1^{h_2}(\eta_2, p_2) \Big|_{\eta_2=\eta_1+\Delta\eta}. \quad (6)$$

Comparing (6) to (4) we see that the ridge distribution $R^{h_2}(\eta_1, \eta_2, p_2)$ is to be related to the phenomenological quantity $r\rho_1^{h_2}(\eta_2, p_2)$. Thus the crux of the relationship between the ridge and inclusive distributions involves the interpretation of $r\rho_1^{h_2}$. To that end let us first write $\rho_1^{h_2}$ in the form

$$\rho_1^{h_2}(\eta_2, p_2) = \frac{dN^{h_2}}{d\eta_2 p_2 d p_2} = H^{h_2}(\eta_2, p_2) V(p_2), \quad (7)$$

$$V(p_2) = e^{-p_2/T},$$

where $V(p_2)$ is the transverse component that contains the explicit exponential behavior of p_2 . Although $H^{h_2}(\eta_2, p_2)$ has some mild p_2 dependence due mainly to mass effects of h_2 , the average transverse momentum $\langle p_2 \rangle$ is determined primarily by the inverse slope T and is not dependent on η_2 . This is an approximate statement that is based on the BRAHMS data [13, 14], which show that $\langle p_T \rangle$ is essentially independent of rapidity. Since r serves as the phenomenological bridge between R^{h_2} and $\rho_1^{h_2}$, the key question to address is which of the two components, the longitudinal $H^{h_2}(\eta_2, p_2)$ or the transverse $V(p_2)$, does the two-particle correlation generated by a trigger at η_1 exert its most important influence in relating R^{h_2} to $\rho_1^{h_2}$?

If there is longitudinal correlation from early times as in [8–10, 31], then its effect must be to convert $H^{h_2}(\eta_2, p_2)$ to $R^{h_2}(\eta_1, \eta_2, p_2)$. In that case $V(p_2)$ is relegated to the secondary role due to radial flow (which is, nevertheless, essential in explaining the $\Delta\phi$ restriction as in [9, 10, 32, 33]). On the other hand, if there is no intrinsic long-range longitudinal correlation, then $H^{h_2}(\eta_2, p_2)$ is unaffected, and the ridge can only arise from the change in the transverse component, $V(p_2)$, due to a hard scattering that leads to the trigger. Without phenomenology one would think that the first option is more reasonable, when $|\Delta\eta| \sim 4$ is regarded as large, and especially when there is an inclination based on theoretical ideas that prefer the existence of long-range correlation. With the ridge phenomenology described by (3) pointing to direct relevance of $H^{h_2}(\eta_2, p_2)$, the question

becomes that of asking: $|\Delta\eta|$ is large compared to what? If it is now recognized that $|\Delta\eta|$ is not large compared to the η_2 range of $\rho_1^{h_2}(\eta_2, p_2)$ after the widening due to η_1 smearing (remarked at the end of the previous section) is taken into account, then the need for a long-range dynamical correlation to account for the structure of $R^{h_2}(\eta_1, \eta_2, p_2)$ is lost. We describe below a possible explanation based on the second option of no long-range correlation. The key is to accept the suggestion of the data that the unmodified longitudinal component $H^{h_2}(\eta_2, p_2)$ is sufficient.

A series of articles have treated the subject of ridge formation in the recombination model [34], beginning with (a) the early observation of pedestal in jet correlation [30, 35], to (b) its effects on azimuthal anisotropy of single-particle distribution at mid-rapidity [36, 37], and then to (c) the dependence on the azimuthal angle ϕ_s of the trigger relative to the reaction plane [28, 38–40]. Forward productions in d-Au and Au-Au collisions have also been studied in [41, 42]. Our consideration here of ridge formation at $|\Delta\eta| > 2$ is an extension of earlier studies with the common theme that ridges are formed as a consequence of energy loss by semihard or hard partons as they traverse the medium. The details involve careful treatment of the hadronization process with attention given to both the longitudinal and transverse components. The ϕ dependence has been studied thoroughly in [28, 40], and the η dependence should take into account of the experimental fact that the p/π ratio can be large (>2.5) at large η [29] so that $H^{h_2}(\eta_2, p_2)$ in (7) can be properly reproduced.

3.2. Azimuthal Dependence of the Ridge. We give in this subsection a brief summary of the $\Delta\phi$ distribution that we have obtained previously in our treatment of the ridge formation [28]. In so doing we also explain more thoroughly an aspect of the basic elements of our model.

The tenets of our interpretation of the ridge structure are that its formation is due to (a) the passage of a semihard parton through the medium and (b) the conversion of the energy loss by the parton to the thermal energy of the soft partons in the vicinity of its trajectory. Hadronization of the enhanced thermal partons forms the ridge standing above the background. In [28], we have considered the geometry of the trajectory of a semihard parton traversing the medium in the transverse plane at mid-rapidity, $|\eta| < 1$, taking into account the azimuthal angle ϕ_s of the trajectory that is to be identified with the trigger direction relative to the reaction plane. Along that trajectory, labeled by points (x, y) in the transverse plane, the medium expands in the direction $\psi(x, y)$. If $\psi(x, y)$ is approximately equal to ϕ_s for most of the points (x, y) along the trajectory of the semihard parton, then the thermal partons enhanced by successive soft emissions are carried by the flow along in the same direction; the effects reinforce one another and lead to the formation of a ridge in a narrow cone. On the other hand, if the two directions are orthogonal, then the soft partons emitted from the various points along the trajectory are dispersed over a range of surface area, so their hadronization leads to no pronounced effect. These extreme

possibilities suggest a correlation function between ϕ_s and ψ , which we assume to have the Gaussian form

$$C(x, y, \phi_s) = \exp \left[-\frac{(\phi_s - \psi(x, y))^2}{2\lambda} \right], \quad (8)$$

where the width-squared λ is a parameter to be determined. This correlation is the central element of our Correlated Emission Model (CEM) [28].

Considerable care is given to the calculation of the observed ridge yield $Y(\phi_s)$ as a function of ϕ_s . It involves integrations over the path length of the trajectory of the semihard parton and its point of creation in the medium whose density depends on nuclear overlap, and so forth. To compare with the data on $Y(\phi_s)$, we also have to integrate over all ϕ of the ridge particle. It is found that by adjusting the value of λ it is possible to fit the data on $Y(\phi_s)$ in the entire range $0 < \phi_s < \pi/2$ for both 0–5% and 20–60% centralities. The value determined is $\lambda = 0.11$, corresponding to a width $\sigma_c = \sqrt{\lambda} = 0.34$ rad, which is much smaller than the width of the ridge itself, $\Delta\phi \sim 1$. We have been able to show that using $\lambda = 0.11$ the calculated distribution of the ridge $dN_R/\Delta\phi$ agrees well with the data. We further made a prediction on the existence of an asymmetry property of the ridge $R(\phi, \phi_s)$ in its ϕ dependence relative to ϕ_s . That prediction was subsequently verified by the STAR data [43, 44].

The mechanism for ϕ correlation described above will form the basis of transverse correlation when we move away from mid-rapidity to $|\eta| > 1$. It is necessary, however, to start the consideration with a discussion of the forward-moving soft partons relative to the semihard partons at early time.

3.3. Longitudinal Initial Configuration. We now extend the mechanism for ridge formation at mid-rapidity described above to $|\eta| > 1$. Of course, without examining $dN_R/d\Delta\eta d\Delta\phi$ at $|\Delta\eta| > 1$ one cannot strictly refer to the structure at $|\Delta\eta| < 1$ as ridge, which by definition has a flat distribution in $\Delta\eta$, but is restricted in $|\Delta\phi|$. We have actually considered the $\Delta\eta$ behavior before we investigated the $\Delta\phi$ structure at a time when the ridge was referred to as pedestal [30]. Calculation was done in the framework where the trigger is formed by thermal-shower recombination and the associated particles in the ridge by the recombination of enhanced thermal partons. In view of our present phenomenological finding in Figure 2 and expressed in (3) and (6), we reformulate our model here with attention given to the initial configuration relevant to the problem at hand.

In Section 3.3 we have discussed the correlation between the semihard parton at ϕ_s and the local flow direction at $\psi(x, y)$, expressed in (8) for $|\eta| < 1$. To extend the same mechanism to $|\eta| > 1$, it is important to recognize first that the longitudinal momenta of the hadrons produced outside the mid-rapidity region are not generated by the semihard parton, as it would be ruled out simply by energy conservation. In accordance with the original parton model [45], the right- and left-moving partons in the initial configuration provide the main thrust for forward and backward momenta. To be more quantitatively pertinent to the ridge structure observed in [3], let us recall that the pseudorapidity ranges

of the trigger and ridge particles are $0 < \eta^{\text{trig}} < 1.5$ and $-4 < \Delta\eta < 2$. For the sake of discussing positive momentum fractions, let us reverse the signs of η without loss of generality and regard $\eta_1 > -1.5$ and $\eta_2 < 2.5$ so that $-2 < \eta_2 - \eta_1 < 4$. Let us be generous and set $\eta_2 < 3$; it corresponds to $\theta_2 > 0.1$. That is, a ridge particle has $p_T/p_L = \tan\theta_2 > 0.1$. Assuming an average $\langle p_T \rangle \sim 0.4$ GeV/c implies $p_L < 4$ GeV/c. The coalescing quarks that form a pion at such a p_L would have on average a longitudinal momentum of $k_L < 2$ GeV/c (even less for a proton). For $\sqrt{s_{NN}} = 200$ GeV, the corresponding momentum fraction x of the quarks is $2k_L/\sqrt{s} < 0.02$. Those soft partons do not have very large x , being very nearly in the wee region [45]. Thus the kinematics of the particles in the ridge does not indicate that the coalescing quarks are very much in the forward (or backward) fragmentation region.

For $\sqrt{s}/2 = 100$ GeV, the Lorentz contraction factor is sometimes taken to be $\gamma \sim 100$, but that corresponds to $x = 1$, where no quarks exist. If we take the average valence-quark momentum fraction to be $\langle x_{\text{val}} \rangle \sim 1/4$, then the corresponding γ is ~ 25 and $\Delta z_{\text{val}} \sim 2R_A/\gamma \sim 0.5$ fm, which has a width that is not very thin. When two such slabs overlap in the initial configuration, the wee partons of the Au-Au colliding system can occupy a wider longitudinal space ($\Delta z \sim 2$ fm) of uncertainty due to quantum fluctuations—1 fm on each side of the overlapping slabs consisting of soft parton with x much smaller than $\langle x_{\text{val}} \rangle$. Our point is then that in that space of $\Delta z \sim 2$ fm in the initial configuration quantum fluctuations free us from requiring the soft partons to follow a Hubble-like expansion, that is, the faster partons are on the outer edges of that longitudinal space, right-moving ones on the right side, and left-moving ones on the left. Note that we have this freedom because we have not restricted ourselves to a dynamical picture of flux tube being stretched by receding thin disks, as in [9, 10, 31].

For a trigger particle to have $p_T^{\text{trig}} > 2.5$ GeV/c, the initiating semihard or hard parton must have $k_T > 3$ GeV/c and is created at early time. In Figure 3 we show a sketch of the initial configuration in x - z plane that depicts the relationship among various possible momentum vectors at that time. The horizontal thickness of the shaded region is $\Delta z \sim 2$ fm and the vertical height is $2R_A \sim 12$ fm for central collisions, thus not to scale. The central slab marked by a darker region of $\Delta z_{\text{val}} \sim 0.5$ fm represents the longitudinal extent in which the valence quarks are contracted. The (red) arrow labeled k_1 is the semihard parton that initiates the trigger; it starts from inside the narrow slab because the longitudinal momenta of the colliding partons before scattering are high. The two other (blue) arrows labeled by k_2 and k_2' represent two possible soft partons with $k_L \leq 2$ GeV/c, originating from outside the inner slab, since their Δz is larger than Δz_{val} . We place those vectors in such positions to emphasize the possibility that they can originate from the opposite sides of the slab. That is what we mean by expansion at early time that is not of Hubble-type. The conical region (shaded green) around vector k_1 represents the vicinity of the trajectory of the semihard parton where the thermal partons are enhanced due to the energy loss by the semihard parton. Note that since the soft partons k_2 and k_2' have larger Δz than that of the valence quarks, they can cross the conical region, so the transverse

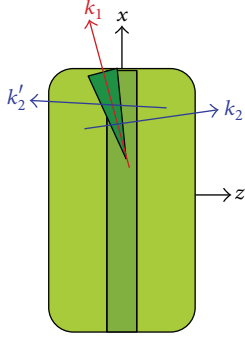


FIGURE 3: A sketch of initial configuration in x - z plane at early time. Horizontal thickness of the medium is $\Delta z \sim 2$ fm; the inner vertical slab indicates the relative thickness (~ 0.5 fm) of the overlapping contracted disks in which the valence quarks are restricted. Red arrow represents semihard parton surrounded in medium by a cone of enhanced thermal partons. Blue arrows represent soft partons with $k_i \lesssim 2$ GeV/c that originate from outside the slab and can therefore interact with the cone (color online).

components of the soft partons can be broadened by their interaction with the enhanced thermal partons.

3.4. Transverse Correlation. The discussion above on the space-momentum relationship between the semihard and soft partons at early time in the uncertainty region Δz gives the conceptual basis for our view of how hadrons in the ridge are formed at late time. Our main point about the initial longitudinal uncertainty is that the forward-moving soft partons that eventually hadronize can be influenced by the semihard parton because the soft-parton trajectory starting from the left side of the central slab shown in Figure 3 can traverse the cone of enhanced thermal partons. To be more quantitative we return to the general factorizable form of the single-particle distribution given in (7) where p_2 refers to the transverse component p_T of particle 2. The effect of the semihard parton on particle 2 is the transverse broadening of the soft parton k_2 in Figure 3, in much the same way that the Cronin effect is conventionally explained in terms of initial-state broadening [46]. That is, the p_2 dependence is affected if (a) there is a semihard parton k_1 , and (b) k_2 (and other soft partons not shown in Figure 3) passes through the cone in the vicinity of k_1 . We denote the case without the semihard parton by $V_B(p_2)$ representing the background, where

$$V_B(p_2) = \exp\left(-\frac{p_2}{T_0}\right), \quad (9)$$

and the case with semihard parton and with ϕ in the vicinity of the cone by

$$V_{B+R}(p_2) = \exp\left(-\frac{p_2}{T}\right), \quad (10)$$

where $T > T_0$ is a result of the interaction with the enhanced thermal partons. Then the ridge has a transverse component that rises above the background and has the p_T dependence

$$V_R(p_2) = V_{B+R}(p_2) - V_B(p_2). \quad (11)$$

This is the essence of transverse broadening due to the presence of semihard parton. Since the soft partons k_2 must pass through the enhanced cone (narrow in ϕ) in order to develop transverse broadening, they contribute to the ridge only within the $\Delta\phi$ interval around ϕ_1 , discussed in [28].

The transverse correlation that we refer to is not what one usually associates with the correlation between hadrons in the fragments of a high- p_T jet. All of those fragments are in a small range of $\Delta\eta$ and have transverse-momentum fractions that are correlated. They populate the peak in Figure 2. In our problem about the ridge we have been concerned with the transverse momentum of a particle associated with a trigger outside that peak. The former reveals the effect of the medium on the jet, while the latter reveals the effect of the jet on the medium. That is the basic difference between the jet and ridge components of the associated particles. Since semihard or hard scattering takes place early, transverse broadening can take place for soft partons (the medium) moving through the interaction zone, leading to the ridge structure.

It is important to note that although the exponential p_T behaviors of the thermal partons have been parametrized by T_0 and T , there is no implication that those parameters are conventional temperatures and that hydrodynamics is valid from the beginning of the evolution process to the end. We have referred to T as the inverse slope, as is appropriate for an exponential peak at low p_T in any hadron scattering. The word thermal is used in reference to the soft component with the assumption that just before hadronization the bulk partons in the local system has an underlying thermal distribution as opposed to a power-law behaved hard component above the background. We do not assume that the global system is equilibrated at an early universal time and that the whole system can be adequately treated by hydrodynamics without considering the effects of the minijets. Our emphasis on semihard partons as the generators of the ridge and our reliance on non-Hubble-like expansion in the initial longitudinal configuration are features that explicitly depend on the departure from the usual assumptions of global thermalization in hydro calculations.

3.5. The Ridge. We may now write the per-trigger ridge correlation distribution $R^{h_2}(\eta_1, \eta_2, p_2)$ that is introduced in (4) and (5) in the form

$$R^{h_2}(\eta_1, \eta_2, p_2) = cH^{h_2}(\eta_2, p_2)V_R(\Delta\eta, p_2), \quad (12)$$

where, for $\Delta\eta$ in the range of the ridge, $V_R(\Delta\eta, p_2)$ may be approximated by $V_R(p_2)$ given in (11), that is,

$$\begin{aligned} V_R(p_2) &= e^{-p_2/T} - e^{-p_2/T_0} \\ &= e^{-p_2/T} \left(1 - e^{-p_2/T'}\right), \quad T' = \frac{T_0 T}{T - T_0}. \end{aligned} \quad (13)$$

As we have seen in Figure 2 and (3) that range of $\Delta\eta$ where $T > T_0$ is no more than the η_2 range of $dN^{\text{ch}}/d\eta_2$, which in turn is determined by the η_2 range of $H^{h_2}(\eta_2, p_2)$ in (12). Thus in practice we may suppress the $\Delta\eta$ dependence in $V_R(\Delta\eta, p_2)$. The constant c in (12) characterizes the magnitude of the

ridge, which can depend on many factors that include the fluctuations in the initial configuration, the details of correlation dynamics, the experimental cuts, the $\Delta\phi$ interval where the ridge is formed, and the related scheme of background subtraction. Its value (that was not calculated) does not affect the relationship between the η dependencies of the two sides of (12).

The expression for $V_R(p_2)$ in (13) was first obtained in [36, 37] as a description of the ridge distribution without trigger. It was noted there that $V_R(p_T) \rightarrow 0$ as $p_T \rightarrow 0$ and that p_T/T' sets the scale for $v_2(p_T, b)$ for $p_T < 0.5$ GeV/c in agreement with the data on it. More recently, a detailed study of $v_2(p_T, b)$ and the inclusive distribution has been carried out in [27], where it is found that $T_0 = 0.245$ GeV and $T = 0.283$ GeV, so that $T' = 1.825$ GeV. Although our conclusion to be drawn below does not depend on the precision of those values, more comments on that subject will be given in Section 4.

To proceed, we now substitute (12) in (4) and use (7) to eliminate $H^{h_2}(\eta_2, p_2)$, thus obtaining

$$\frac{1}{N^{\text{trig}}} \frac{dN_R^{\text{ch}}}{d\Delta\eta} = \int_0^{1.5} d\eta_1 \sum_{h_2} \int dp_2 p_2 \frac{cV_R(p_2)}{V(p_2)} \rho_1^{h_2}(\eta_2, p_2) \Big|_{\eta_2=\eta_1+\Delta\eta}, \quad (14)$$

where $V(p_2)$ in (7) and here are identical to $V_{B+R}(p_2)$ in (10). Comparing this equation with (6), we come to the conclusion that r is a phenomenological approximation of $cV_R(p_2)/V(p_2)$ in the region where it contributes most to the integral over p_2 . From (13) we get $V_R(p_2)/V(p_2) = 1 - e^{-p_2/T'}$. The integrand in (14) is severely damped by the exponential decrease of $\rho_1^{h_2}(\eta_2, p_2)$ for $p_2 > 1$ GeV/c, since $T' \gg T$. Thus $cV_R(p_2)/V(p_2)$ may be approximated by a constant r in the region where the integrand is maximum at around $p_2 \sim 0.5$ GeV/c. In so doing, we obtain (6) and therefore the phenomenological relation given by (3).

Let us give an overview of what we have done. The LHS of (14) is the measured ridge distribution in $\Delta\eta$, which is related to the two-particle distribution $\rho_2^{h_1, h_2}(\eta_1, p_1, \eta_2, p_2)$ through the definitions given in (4) and (5). Instead of concentrating on $\rho_2^{h_1, h_2}$ and examining the dynamics of long-range longitudinal correlation, we have found through the phenomenological observation made in (3), and thus (6), that the correlation data can largely be understood by focussing on the relation given in (12), where the ridge correlation is expressed in terms of the component in the transverse-momentum part of the single-particle distribution that exhibit the same $V_R(p_2)$ behavior at various $\Delta\eta$ values in the range where (6) is valid without any $\Delta\eta$ dependence in the longitudinal component, that is, transverse correlation. Thus the ridge is generated by the same dynamical mechanism at any η in the range where single-particle distribution can reach. That mechanism depends on semihard or hard partons (with or without trigger) whose energy loss to the medium leads to transverse broadening of small- x partons that encounter the enhanced region of thermal partons.

The transverse-momentum distribution of the ridge particles is the same for any η , and the η range of the ridge is no more than that of the single-particle inclusive distribution because the partonic origin of the longitudinal momentum of any particle is the same.

4. Relationship to Azimuthal Quadrupole at RHIC and the Ridge in pp Collisions at LHC

Having described how the ridge phenomenon observed by PHOBOS can be understood in terms of transverse correlation without longitudinal correlation, we now solidify that description by connecting the dynamical mechanism to other features observed at RHIC and LHC that exhibit more quantitative behaviors. They are (a) azimuthal quadrupole (usually referred to as elliptic flow in fluid description) generated by minijets in noncentral Au-Au collisions at RHIC and (b) the ridge phenomenon found in pp collisions at LHC.

In establishing the relationship between (6) and (14), we made the argument that $cV_R(p_2)/V(p_2)$ in (14) can be approximated by a constant r in the p_2 region where the integrand has a maximum. The PHOBOS experiment provides no details about the p_T of the associated particles, since it is integrated over the entire detected region [3]. Thus the approximation made cannot be done without some quantitative knowledge of the p_2 dependence. In (13) we show the functional form of $V_R(p_2)$, while in (7) $V(p_2)$ is given. Their p_2 behaviors have been examined in great detail in the study of the p_T spectra and azimuthal anisotropies of pions and protons produced in Au-Au collisions at various centralities [27], without being concerned about correlations. It is therefore important to note here that the subject matter of transverse correlation, discussed in Section 3.4, is intimately related to the p_T , and ϕ dependences of single-particle distribution without triggers. The connection between the two is the ridge.

The basic physical origin of the ridge is the pervasive presence of semihard partons. Whether or not the semihard parton is detected by a trigger, its effect on the single-particle distribution ρ^h is always present. Thus in [27] ρ^h for hadron h has been written in the form at mid-rapidity, low p_T and impact parameter b

$$\rho^h(p_T, \phi, b) = B^h(p_T, b) + R^h(p_T, \phi, b) + M^h(p_T, \phi, b), \quad (15)$$

where the three terms correspond to base, ridge, and minijets, respectively. The base, $B^h(p_T, b)$, has no ϕ dependence; its p_T dependence is

$$B^h(p_T, b) = \mathcal{N}_h(p_T, b) V_B(p_T), \quad (16)$$

where $\mathcal{N}_h(p_T, b)$ is a normalization factor for hadron h that depends on the hadronic wave function. $V_B(p_T)$ is given in (9). The ridge term has a specific ϕ dependence due to semihard partons in the initial configuration and can be shown to account for the observed $v_2(p_T, b)$ without using hydrodynamics [27]. For our purpose here we mention only

that after averaging over all ϕ the resultant $\overline{R}^h(p_T, b)$ has the form

$$\overline{R}^h(p_T, b) = \mathcal{N}_h(p_T, b) V_R(p_T), \quad (17)$$

where $V_R(p_T)$ is as given in (13). The main point we want to stress is that the per-trigger correlation distribution $R^{h_2}(\eta_1, \eta_2, p_2)$ discussed in Section 3.5 involves the same $V_R(\Delta\eta, p_2)$ as the $V_R(p_T)$ in (17) embedded in the single-particle distribution $\rho^h(p_T, \phi, b)$. Although $V_R(\Delta\eta, p_2)$ has not been measured directly, the form of $V_R(p_T)$ has been tested by the p_T dependence of $v_2(p_T, b)$, as described in [27]. The values of T_0 and T determined there lead to our conclusion in Section 3.5 that $cV_R(p_2)/V(p_2)$ inside the integral in (14) can be approximated by a constant r , since the high- p_2 region is suppressed by $\rho_1^{h_2}(\eta_2, p_2)$. Thus our proposal in (3) is confirmed.

The above discussion refers to different aspects of the Au-Au collisions at RHIC. Now, we turn to a different connection between the ridge found at RHIC and the ridge observed in pp collisions at LHC, which is a study of autocorrelation between two particles produced at 7 TeV without using triggers [6]. That connection, as stunning as it was at the time of discovery, provides another quantitative verification of the concept of transverse correlation discussed here.

In pp collisions one does not expect even at 7 TeV the formation of a dense system that can be treated by hydrodynamics. Since our approach has been to emphasize that the origin of the ridge is not to be found in hydro flow but in minijet production, it is then very natural to apply our model to pp collisions at LHC. In [6], reported by CMS, it is found that the two-particle correlation function develops a ridge structure at $|\Delta\eta| > 2$ and that the ridge yield increases significantly with event multiplicity N in the region $1 < p_T < 3$ GeV/c but not outside that region. That is a direct statement on the p_T dependence of the ridge that is highly relevant to what we have regarded as transverse correlation. Indeed, the problem has been studied in [47], where the two particles at η_1 and η_2 separated by at least 2 units are treated as longitudinally independent, but transversely correlated in the factorizable form

$$Y_R(p_T, N) \propto NV_R(p_{T_1})V_R(p_{T_2}), \quad (18)$$

where $V_R(p_{T_i})$ is as given in (13). The factorized form in (18) is an explicit expression of the assumption that there is no longitudinal correlation, yet there exist correlations between particles produced at widely separated η_1 and η_2 because their p_T distributions are both enhanced by a common semihard jet [47]. The values of T_0 and T in $V_R(p_{T_i})$ are adjusted to fit the data. Excellent results are obtained by virtue of the p_{T_i} dependence in (13) that has a peak in just the region where the CMS data show the ridge structure. Thus our approach to the present problem receives strong support from the dual properties that we are able (a) to relate the ridges in these two very different systems and (b) to show that the transverse correlation with the same p_T dependence (except for the numerical values of T and T_0) is responsible for both systems.

It is of interest to also remark here about the ridge found in pPb collisions at $\sqrt{s_{NN}} = 5.02$ TeV at LHC

[48–51]. Comparison between the pp and pPb collision systems can best be made by examining [6, 48], which report data obtained by the same experimental group (CMS) and analyzed in the same way. Indeed, similar properties of the same-side ridge are found in that the associated yields at $2 < |\Delta\eta| < 4$ are most pronounced in the region $1 < p_T < 2$ GeV/c and at high event multiplicities. Since the results are on autocorrelation without trigger, it is not possible to apply the method used in Section 2 to relate single-particle distribution to the $\Delta\eta$ dependence of the ridge structure. It should be recognized that in autocorrelation the two particles at η_1 and η_2 can be separated by $|\Delta\eta| = 4$ but on opposite sides of an undetected semihard jets with $\eta_{1,2} - \eta_{\text{jet}} = \pm 2$ thus not correlated to the jet with a range as long as 4. Note, however, that the p_T dependences of the ridges in the pp and pPb systems are similar and are consistent with transverse correlation discussed here, as noted in [47]. An important difference is the dependence on event multiplicity. The high-multiplicity events in pPb collisions are consequences of particle production in multiple soft proton-nucleon scatterings, whereas in pp collisions those events arise from rare multiple hard-scattering processes. Thus to understand fully the ridge structure in pPb collisions in the framework of the present approach requires detailed study that has not yet been undertaken.

5. Conclusion

An issue that this study has brought up is the usage of the word “large” in referring to the range of $\Delta\eta$ in the ridge structure. Our phenomenological observation in (3), substantiated by Figures 1 and 2, does not reveal any quantitative definition of what large $\Delta\eta$ means. To be able to relate large $\Delta\eta$ to dynamical long-range correlation is a worthy theoretical endeavor but more can be added to its phenomenological relevance if it can also elucidate the empirical connection between the two sides of (3).

The approach that we have taken involves no long-range longitudinal correlation for the ridge. The observed ridge distribution is interpreted in our approach as being due to transverse correlation with a range in $\Delta\eta$, that is, no more than that of the single-particle distribution. That is, the p_T distributions of the detected hadrons in the ridge have a larger inverse slope than that of the particles outside, which have larger $\Delta\phi$ than the ridge width. We have described a partonic basis for how the transverse correlation can arise; it emphasizes the point that without semihard partons there can be no ridge (with or without trigger detection).

If a hard (or semihard) scattering is likened to an earthquake, then the ridge is the counterpart of tsunami, and the thermal medium carrying the enhancement is the ocean water. Transverse correlation is the rise in water level at various points along a coast hit by the tsunami. Although the tsunami damage is insensitive to the horizontal separation among the coastal cities, it should not be interpreted as evidence for long-range horizontal (longitudinal) correlation. The buildings in different cities are not horizontally correlated, but their uprooting by vertical displacements is a sign of

transverse correlation caused by the tsunamis. Similarly, there is transverse correlation at various points in the ridge but no long-range longitudinal correlation. Where the analogy fails, as all analogies do at some point, is that our expanding system illustrated in Figure 3 is not Hubble-like in the initial configuration and that the soft partons must intersect the enhanced cone of the hard parton in order to carry the effect of enhancement at $|\Delta\eta| > 1$. That is where the restriction in $\Delta\phi$ enters in the ridge problem. There is no such complication in the earthquake/tsunami example, which is strictly a classical case of wave propagation. Another point where the analogy may be misleading is that in the case of the tsunami the energy of wave propagation is provided entirely by the earthquake. In our problem, the momenta of the forward-moving soft partons are in the initial state whether or not there is a hard (or semihard) scattering. They are the medium; their transverse momenta can be enhanced to form a ridge in the same way that the ocean water can be perturbed by the earthquake to develop a tsunami, whose underlying medium, however, does not expand. Note that in both cases the detection of trigger or earthquake is not essential in assessing the effect of ridge or tsunami. The main point of the analogy is to illustrate the meaning of transverse correlation at separated rapidities without longitudinal correlation (and without suggesting similarity in dynamics).

A crucial point in our interpretation of the ridge phenomenon is that the quantum fluctuation of the longitudinal coordinates of the initial configuration is important, as illustrated in Figure 3. Because of the possibility that low- x partons with positive momenta do not necessarily have to be located on the positive side of the thinner slab to which the high- x partons are contracted, the usual approximation that equates spatial rapidity with momentum rapidity should not be extended to the neighborhood of the tip of the forward light cone. Fluctuations of the initial longitudinal configuration are not usually considered. Here we find that longitudinal fluctuation of the initial parton configuration can be the source of the longitudinal structure in the ridge phenomenon. Fluctuations of the initial transverse configuration have been investigated vigorously in recent years, leading to results according to hydrodynamical expansion that have significant phenomenological consequences on the transverse structure quantified by the azimuthal harmonics, one of which being the diminution of the ridge itself. That approach relies heavily on the validity of hydrodynamics, which has not been used here. The relevance of higher-harmonic fluctuations has also been challenged by a study of the p_T -integrated 2D angular correlation [26]. The transverse momentum distributions of the base and ridge that we rely on have been studied in detail in connection with $v_2(p_T)$ generated by minijets in Au-Au collisions at RHIC and with ridge formation in pp collisions at LHC; they all have the same structure.

Finally, we return to Figure 2 and note that this investigation was motivated by the observation made on the empirical relationship between the ridge distribution in $\Delta\eta$ and the single-particle distribution in η shown in that figure. A number of previous studies on the origin of the ridge structure are based on other approaches, the first being by Wong in the momentum-kick model [52, 53], followed by

others, such as in flux-tube initiated hydrodynamics [54], and especially a large group working in the framework of Color Glass Condensate, as in [10, 31, 55], which led more recently to [56–58] on the ridge formation in pp and pPb collisions. In all those investigations, the authors focus on different mechanisms that offer various sufficient but not necessary explanations of the ridges. In most of those approaches, the emphases are on long-range correlation, and none of them recognize the relationship exhibited in Figure 2, which should therefore provide a useful constraint on all the models proposed.

To sum up our work here, we have two important findings to emphasize. One is the phenomenological relationship between $dN_R^{\text{ch}}/d\Delta\eta$ and $dN^{\text{ch}}/d\eta$ that shows the absence of necessity for intrinsic long-range correlation in η . The other is an interpretation of that relationship in terms of transverse correlation without long-range longitudinal correlation.

Acknowledgment

This work was supported, in part, by the U.S. Department of Energy under Grant no. DE-FG02-92ER40972.

References

- [1] J. Adams, M. M. Aggarwal, Z. Ahammed et al., “Minijet deformation and charge-independent angular correlations on momentum subspace (η, ϕ) in Au-Au collisions at $\sqrt{s_{NN}} = 130$ GeV,” *Physical Review C*, vol. 73, Article ID 064907, 10 pages, 2006.
- [2] B. I. Abelev, M. M. Aggarwal, Z. Ahammed et al., “Long range rapidity correlations and jet production in high energy nuclear collisions,” *Physical Review C*, vol. 80, Article ID 064912, 9 pages, 2009.
- [3] B. Alver, B. B. Back, M. D. Baker et al., “High transverse momentum triggered correlations over a large pseudorapidity acceptance in Au + Au collisions at $\sqrt{s_{NN}} = 200$ GeV,” *Physical Review Letters*, vol. 104, Article ID 062301, 4 pages, 2010.
- [4] B. I. Abelev, M. M. Aggarwal, Z. Ahammed et al., “Three-particle coincidence of the long range pseudorapidity correlation in high energy nucleus-nucleus collisions,” *Physical Review Letters*, vol. 105, Article ID 022301, 7 pages, 2010.
- [5] M. Daugherty, “Anomalous centrality variation of minijet angular correlations in Au-Au collisions at 62 and 200 GeV from STAR,” *Journal of Physics G*, vol. 35, no. 10, Article ID 104090, 2008.
- [6] V. Khachatryan, A. M. Sirunyan, A. Tumasyan et al., “Observation of long-range, near-side angular correlations in proton-proton collisions at the LHC,” *Journal of High Energy Physics*, vol. 2010, p. 91, 2010.
- [7] INT Workshop on The Ridge Correlation in High Energy Collisions at RHIC and LHC, May 2012, <http://www.int.washington.edu/PROGRAMS/12-51w/>.
- [8] A. Dumitru, F. Gelis, L. McLerran, and R. Venugopalan, “Glasma flux tubes and the near side ridge phenomenon at RHIC,” *Nuclear Physics A*, vol. 810, no. 1–4, pp. 91–108, 2008.
- [9] S. Gavin, L. McLerran, and G. Moschelli, “Long range correlations and the soft ridge in relativistic nuclear collisions,” *Physical Review C*, vol. 79, no. 5, Article ID 051902, 2009.

- [10] G. Moschelli and S. Gavin, “Soft contribution to the hard ridge in relativistic nuclear collisions,” *Nuclear Physics A*, vol. 836, pp. 43–58, 2010.
- [11] W. Kittel and E. A. de Wolf, *Soft Multihadron Dynamics*, World Scientific, Singapore, 2005.
- [12] B. B. Back, M. D. Baker, D. S. Barton et al., “Significance of the fragmentation region in ultrarelativistic heavy-ion collisions,” *Physical Review Letters*, vol. 91, Article ID 052303, 4 pages, 2003.
- [13] I. G. Bearden, D. Beavis, C. Besliu et al., “Nuclear Stopping in Au + Au collisions at $\sqrt{s_{NN}} = 200$ GeV,” *Physical Review Letters*, vol. 93, Article ID 102301, 5 pages, 2004.
- [14] I. G. Bearden, D. Beavis, C. Besliu et al., “Charged meson rapidity distributions in central Au + Au collisions at $\sqrt{s_{NN}} = 200$ GeV,” *Physical Review Letters*, vol. 94, Article ID 162301, 4 pages, 2005.
- [15] B. Alver and G. Roland, “Collision-geometry fluctuations and triangular flow in heavy-ion collisions,” *Physical Review C*, vol. 81, Article ID 054905, 2010.
- [16] B. H. Alver, C. Gombeaud, M. Luzum, and J. Y. Ollitrault, “Triangular flow in hydrodynamics and transport theory,” *Physical Review C*, vol. 82, no. 3, Article ID 034913, 9 pages, 2010.
- [17] D. Teaney and L. Yan, “Triangularity and dipole asymmetry in relativistic heavy ion collisions,” *Physical Review C*, vol. 83, Article ID 064904, 16 pages, 2011.
- [18] J. Xu and C. M. Ko, “Triangular flow in heavy ion collisions in a multiphase transport model,” *Physical Review C*, vol. 84, Article ID 014903, 7 pages, 2011.
- [19] R. S. Bhalerao, M. Luzum, and J. Y. Ollitrault, “Understanding anisotropy generated by fluctuations in heavy-ion collisions,” *Physical Review C*, vol. 84, Article ID 054901, 8 pages, 2011.
- [20] P. Sorensen, “Higher flow harmonics in heavy ion collisions from STAR,” *Journal of Physics G*, vol. 38, Article ID 124029, 12 pages, 2011.
- [21] R. A. Lacey, A. Taranenko, R. Wei et al., “Azimuthal anisotropy: transition from hydrodynamic flow to jet suppression,” *Physical Review C*, vol. 82, Article ID 034910, 4 pages, 2010.
- [22] G.-Y. Qin, H. Petersen, S. A. Bass, and B. Müller, “Translation of collision geometry fluctuations into momentum anisotropies in relativistic heavy-ion collisions,” *Physical Review C*, vol. 82, Article ID 064903, 14 pages, 2010.
- [23] L. X. Han, G. L. Ma, Y. G. Ma et al., “Initial fluctuation effect on harmonic flows in high-energy heavy-ion collisions,” *Physical Review C*, vol. 84, Article ID 064907, 9 pages, 2011.
- [24] B. Shenke, S. Jeon, and C. Gale, “Higher flow harmonics from (3 + 1)D event-by-event viscous hydrodynamics,” *Physical Review C*, vol. 85, Article ID 024901, 10 pages, 2012.
- [25] F. G. Gardim, F. Grassi, M. Luzum, and J. Y. Ollitrault, “Anisotropic flow in event-by-event ideal hydrodynamic simulations of $\sqrt{s_{NN}} = 200$ GeV Au + Au collisions,” *Physical Review Letters*, vol. 109, Article ID 202302, 5 pages, 2012.
- [26] T. A. Trainor, D. J. Prindle, and R. L. Ray, “Challenging claims of nonjet “higher harmonic” components in 2D angular correlations from high-energy heavy-ion collisions,” *Physical Review C*, vol. 86, Article ID 064905, 13 pages, 2012.
- [27] R. C. Hwa and L. Zhu, “Effects of minijets on hadronic spectra and azimuthal harmonics in Au-Au collisions at 200 GeV,” *Physical Review C*, vol. 86, Article ID 024901, 12 pages, 2012.
- [28] C. B. Chiu and R. C. Hwa, “Dependence of ridge formation on trigger azimuth: correlated emission model,” *Physical Review C*, vol. 79, Article ID 034901, 10 pages, 2009.
- [29] I.G. Arsenej, I.G. Bearden, D. Beavis et al., “Rapidity dependence of the proton-to-pion ratio in Au+Au and p+p collisions at $\sqrt{s_{NN}} = 62.4$ and 200 GeV,” *Physics Letters B*, vol. 684, p. 22, 2010.
- [30] C. B. Chiu and R. C. Hwa, “Pedestal and peak structure in jet correlation,” *Physical Review C*, vol. 72, Article ID 034903, 8 pages, 2005.
- [31] K. Dusling, F. Gelis, T. Lappi, and R. Venugopalan, “Long range two-particle rapidity correlations in A + A collisions from high energy QCD evolution,” *Nuclear Physics A*, vol. 836, no. 1-2, pp. 159–182, 2010.
- [32] S. A. Voloshin, “Transverse radial expansion in nuclear collisions and two particle correlations,” *Physics Letters B*, vol. 632, no. 4, pp. 490–494, 2006.
- [33] E. Shuryak, “Origin of the “ridge” phenomenon induced by jets in heavy ion collisions,” *Physical Review C*, vol. 76, Article ID 047901, 4 pages, 2007.
- [34] R. C. Hwa and C. B. Yang, “Recombination of shower partons at high p_T in heavy-ion collisions,” *Physical Review C*, vol. 70, Article ID 024905, 11 pages, 2004.
- [35] J. Adams, C. Adler, M. M. Aggarwal et al., “Distributions of charged hadrons associated with high transverse momentum particles in pp and Au + Au collisions at $\sqrt{s_{NN}} = 200$ GeV,” *Physical Review Letters*, vol. 95, Article ID 152301, 6 pages, 2005.
- [36] R. C. Hwa, “Elliptic flow arising from ridges due to semi-hard scattering,” *Physics Letters B*, vol. 666, pp. 228–231, 2008.
- [37] C. B. Chiu, R. C. Hwa, and C. B. Yang, “Azimuthal anisotropy: ridges, recombination, and breaking of quark number scaling,” *Physical Review C*, vol. 78, Article ID 044903, 16 pages, 2008.
- [38] A. Feng, “Reaction plane dependent away-side modification and near-side ridge in Au + Au collisions,” *Journal of Physics G*, vol. 35, no. 10, Article ID 104082, 2008, Quark Matter, Jaipur, India, 2008.
- [39] H. Agakishiev, M. M. Aggarwal, Z. Ahammed et al., “Measurements of dihadron correlations relative to the event plane in Au + Au collisions at $\sqrt{s_{NN}} = 200$ GeV,” <http://arxiv.org/abs/1010.0690>.
- [40] R. C. Hwa and L. Zhu, “Relationship between the azimuthal dependencies of nuclear modification factor and ridge yield,” *Physical Review C*, vol. 81, Article ID 034904, 10 pages, 2010.
- [41] R. C. Hwa, C. B. Yang, and R. J. Fries, “Forward production in $d + Au$ collisions by parton recombination,” *Physical Review C*, vol. 71, Article ID 024902, 9 pages, 2005.
- [42] R. C. Hwa and L. Zhu, “Forward production of protons and pions in heavy-ion collisions,” *Physical Review C*, vol. 78, Article ID 024907, 7 pages, 2008.
- [43] J. R. Konzer, “Is the ridge formed by aligned jet propagation and medium flow?” *Nuclear Physics A*, vol. 830, pp. 621c–622c, 2009.
- [44] P. K. Netrakanti, “Addressing the physics of the ridge by 2- and 3-particle correlations at STAR,” *Nuclear Physics A*, vol. 830, pp. 681c–684c, 2009.
- [45] R. P. Feynman, *Photon-Hadron Interaction*, Benjamin Press, Reading, Mass, USA, 1972.
- [46] J. W. Cronin, H. J. Frisch, M. J. Shochet, J. P. Boymond, P. A. Piroué, and R. L. Sumner, “Production of hadrons at large transverse momentum at 200, 300, and 400 GeV,” *Physical Review D*, vol. 11, pp. 3105–3123, 1975.
- [47] R. C. Hwa and C. B. Yang, “Ridge formation induced by jets in pp collisions at 7 TeV,” *Physical Review C*, vol. 83, Article ID 024911, 5 pages, 2011.

- [48] S. Chatrchyan, V. Khachatryan, A.M. Sirunyan et al., “Observation of long-range, near-side angular correlations in pPb collisions at the LHC,” *Physics Letters B*, vol. 718, pp. 795–814, 2013.
- [49] B. Abelev, J. Adam, D. Adamová et al., “Pseudorapidity density of charged particles in p + Pb collisions at $\sqrt{s_{NN}} = 200$ TeV,” *Physical Review Letters*, vol. 110, Article ID 032301, 10 pages, 2013.
- [50] B. Abelev, J. Adam, D. Adamová et al., “Long-range angular correlations on the near and away side in p-Pb collisions at $\sqrt{s_{NN}} = 5.02$ TeV,” *Physics Letters B*, vol. 719, pp. 29–41, 2013.
- [51] G. Aad, T. Abajyan, B. Abbott et al., “Observation of associated near-side and away-side long-range correlations in $\sqrt{s_{NN}} = 5.02$ TeV proton-lead collisions with the ATLAS detector,” <http://arxiv.org/abs/1212.5198>.
- [52] C. Y. Wong, “Momentum kick model description of the near-side ridge and jet quenching,” *Physical Review C*, vol. 78, Article ID 064905, 21 pages, 2008.
- [53] C. Y. Wong, “Momentum kick model analysis of PHENIX near-side ridge data and photon jet,” *Physical Review C*, vol. 80, Article ID 034908, 15 pages, 2009.
- [54] K. Werner, M. Luzum, and J. Ollitrault, “Event-by-event simulation of the three-dimensional hydrodynamic evolution from flux tube initial conditions in ultrarelativistic heavy ion collisions,” *Physical Review C*, vol. 82, Article ID 044904, 26 pages, 2010.
- [55] F. Gelis, E. Iancu, J. Jalilian-Marian, and R. Venugopalan, “The color glass condensate,” *Annual Review of Nuclear and Particle Science*, vol. 60, pp. 463–489, 2010.
- [56] K. Dusling and R. Venugopalan, “Evidence for BFKL and saturation dynamics from dihadron spectra at the LHC,” *Physical Review D*, vol. 87, Article ID 051502, 7 pages, 2013.
- [57] K. Dusling and R. Venugopalan, “Explanation of systematics of CMS p + Pb high multiplicity dihadron data at $\sqrt{s_{NN}} = 5.02$ TeV,” *Physical Review D*, vol. 87, Article ID 054014, 12 pages, 2013.
- [58] K. Dusling and R. Venugopalan, “Comparison of the color glass condensate to di-hadron correlations in proton-proton and proton-nucleus collisions,” <http://arxiv.org/abs/1302.7018>.